UNIVERSITY OF CALIFORNIA, SAN DIEGO

State-Resolved Photochemistry and Spectroscopic Characterization of Atmospherically Relevant Hydroperoxides

A dissertation submitted in partial satisfaction of the
requirements for the degree Doctor of Philosophy

in

Chemistry

by

Jamie Matthews

Committee in charge:

Professor Amitabha Sinha, Chair
Professor Robert E. Continetti
Professor Gourisankar Ghosh
Professor Douglas Magde
Professor Clifford M. Surko

2008

The Dissertation of Jamie Matthews is approved, and it is acceptable in quality and form for publication on microfilm and electronically:

_____

_____

_____

_____

_____

Chair

University of California, San Diego

2008

To

Eli, Sari, Sagiv, Tal

and Brian

TABLE OF CONTENTS

Signature Page……..... iii

Dedication.……..……..... iv

Table of Contents…… v

List of Figures….…… xvii

List of Tables…..…… xxviii

Acknowledgements.…… xxxvi

Vita…….…… xxxix

Abstract…..……. xlii

Chapter 1 Introduction…..…….…….. 1

1.1 Photochemical Processes: Reactions Initiated by Absorption of Light…..…….……..……..….. 1

1.2 Properties of Hydroperoxides and their Role in the Atmosphere…… 3

1.3 State Selected Experiments on the Ground and Electronically Excited States……...… 7

1.4 References…….…… 22

Chapter 2 Photodissociation of Vibrationally Excited Pernitric Acid: HO_2NO_2 ($2\nu_1$) + 390 nm……. 25

2.1 Introduction…….…….. 25

2.2 Experiment…….……... 27

2.2.1 Experimental Apparatus…..……..... 27

2.2.2 PNA Synthesis.…….. 29

2.3 Results and Discussion…..……..... 30

2.3.1 Sample Analysis, HOONO Formation and Action Spectra of HO_2NO_2..... 30

2.3.2 Lifetime of Vibrationally Excited HO_2NO_2 ($2\nu_1$) Molecule..... 34

2.3.3 OH + NO_3 Channel Product State Distribution and Translational Energy Release..... 35

2.3.4 Direct Detection of the HO_2 + NO_2* Channel: $2\nu_1$ Quantum Yields Estimates..... 36

2.4 Summary..... 39

2.5 Future Studies on PNA..... 40

2.6 Acknowledgment..... 41

2.7 References..... 50

Chapter 3 *Ab Initio* Study of Structure, Thermochemistry and Vibrational Spectra of Peroxynitric Acid..... 52

3.1 Introduction..... 52

3.2 Computational Methods..... 55

3.3 Results and Discussion..... 56

3.3.1 Rotational Confomers of HO_2NO_2..... 56

3.3.2 Global Minimum Energy Structure of HO_2NO_2..... 58

3.3.3 Thermochemistry of Peroxynitric Acid..... 61

3.3.3.1 D_0 Evaluation Using the Direct method..... 62

3.3.3.2 D_0 Evaluation Using the Isodesmic Reaction Method..... 65

3.3.3.3 *Ab Initio* and Experiment D_0 Comparison…….. 67

3.3.4 Vibrational Frequencies, Anharmonicities and OH Stretching Overtones…….. 68

3.4 Conclusions…….. 75

3.5 Acknowledgement…… 76

3.6 References…… 105

Chapter 4 Characterization of the Unimolecular Photodissociation of Peroxynitrous Acid in the $2\nu_{OH}$ Region……..….. 108

4.1 Introduction…….. 108

4.1.1 Properties of Peroxynitrous Acid…….. 108

4.1.2 Photodissociation dynamics of the $2\nu_{OH}$ Band……. 110

4.1.3 The Spectroscopy of the $2\nu_{OH}$ Band……. 112

4.1.4 ^{15}N Isotope Studies……... 113

4.2 Experiment……... 113

4.2.1 Experiment Apparatus…….. 113

4.2.2 HOONO Synthesis…… 114

4.3 Results and Analysis…… 117

4.3.1 Room Temperature Vibrational Overtone Action Spectrum…… 117

4.3.2 OH Fragment Product State Distributions and Translational Energy Release…… 118

4.3.3 One Dimensional *Ab Initio* Study of *cis-cis*, *cis-perp* and *trans-perp*……..... 123

4.3.4 Phase Space Theory Simulations…….. 127

4.3.5 Searching for the *cis-perp* Conformer…….…….. 136

4.3.6 *Ab Initio* Two-Dimension Study of the

Influence of Torsion on Overtone Intensity…….. 137

4.4 Discussion…….…… 143

4.5 Conclusions…….…….. 150

4.6 Acknowledgement.…… 151

4.7 References…….…… 187

Chapter 5 State-Resolved Photodissociation Dynamics of *cis-cis* Peroxynitrous

Acid in the $3\nu_{OH}$ Region: Action Spectra and Energetics……... 191

5.1 Introduction…….…….. 191

5.2 Experiment…….……... 193

5.3 Results…….…….. 194

5.3.1 The Second ($3\nu_{OH}$) Overtone Vibrational Action Spectra…..… 194

5.3.2 *Ab Initio* Study of *cis-perp* HOONO

and Second Overtone Intensity……. 197

5.3.3 $HOO^{14}NO$ and $HOO^{15}NO$ Isotope Study…….……. 199

5.3.4 OH Fragment Internal and Translational Energy Release.…… 200

5.3.5 Phase-Space Theory and OH Fragment Product

State Simulations…….. 204

5.4 Discussion…….…… 206

5.5 Conclusions…….…….. 211

5.6 Acknowledgment…..……. 212

5.7 References…… 225

Chapter 6 Unimolecular Dissociation and Thermochemistry of

Methyl Hydroperoxide…… 227

6.1 Introduction…….. 227

6.2 Experiment……... 230

6.2.1 Synthesis of Methyl Hydroperoxide……. 230

6.2.2 Experimental Apparatus…… 232

6.2.3 Computation Methods……... 233

6.3 Results and Analysis…… 234

6.3.1 Vibrational Action Spectrum of $4\nu_{OH}$ and $5\nu_{OH}$……..... 234

6.3.2 Fragment Energy Release from $4\nu_{OH}$ and $5\nu_{OH}$ Excitation….. 237

6.3.3 *Ab initio* Determination of CH_3OOH Thermochemistry…….. 241

6.4 Summary…….. 245

6.5 Acknowledgements…….. 246

6.6 References…… 263

Chapter 7 Probing the Room Temperature Vibrational Overtones of

Methyl Hydroperoxide…….……..…… 265

7.1 Introduction…….. 265

7.2 Experiment……..……. 268

7.2.1 Room Temperature Apparatus…….. 268

7.2.2 Computational Methods……. 270

7.3 Results…….. 271

7.3.1 Room Temperature Overtones Action Spectra……. 271

7.3.2 *Ab Initio* Spectral Simulation using Vibration-Torsion Model……... 274

7.4 Discussion……..…… 284

7.5 Conclusions…….. 290

7.6 Acknowledgements…….…….. 292

7.7 References…….…… 321

Chapter 8 State-Resolved First and Second OH-Stretching Overtones Action Spectra of Jet Cooled Methyl Hydroperoxide……. 324

8.1 Introduction…….…….. 324

8.2 Experiment…..……... 328

8.2.1 Room Temperature Apparatus…….…….. 328

8.2.2 Molecular Beam Apparatus…..…….. 329

8.3 Results and Analysis…….…… 331

8.3.1 Comparison between Room Temperature and Molecular Beam Action Spectra……... 331

8.3.2 The $2\nu_{OH}$ Band…….…….. 335

8.3.3 The $2\nu_{OH} + \nu_{COOH}$ Band…….…… 340

8.3.4 The $3\nu_{OH}$ Band…….…….. 342

8.4 Discussion…….…… 345

8.5 Conclusions…….…….. 358

8.6 References…….…… 387

Chapter 9 Intramolecular Vibrational Energy Redistribution Controlled Photodissociation Dynamics of Hydrogen Peroxide and

Methyl Hydroperoxide…….... 390

9.1 Introduction……..…….. 390

9.2 Experiment…….……... 393

9.3 Results and Discussion…..…… 395

9.4 Conclusions……..…….. 407

9.5 References.…… 419

Chapter 10 The near-UV and Overtone Absorption Cross Sections of Methyl Hydroperoxide: A Mechanism of Tropospheric OH Production…….... 422

10.1 Introduction…….…… 422

10.2 Experiment……..……. 425

10.3 Results…….…… 427

10.4 Discussion…….…….. 430

10.5 Conclusions…….…… 434

10.6 Acknowledgements…….…… 435

10.7 References…….…….. 445

Chapter 11 Vibrational Overtone Initiated Unimolecular Dissociation of Hydroxymethyl Hydroperoxide: Thermochemistry and Dissociation Rates…… 447

11.1 Introduction…...…. 447

11.2 Experiment…….……. 451

11.2.1 Synthesis of Hydroxymethyl Hydroperoxide.....……. 451

11.2.2 Experimental Apparatus…….……. 452

11.3 Results and Discussion…….…….. 453

11.3.1 Vibrational Overtone Spectra…..……. 453

11.3.2 OH Fragment Product State Distribution…….…… 456

11.3.3 Phase-Space Simulations and D_0 Estimate…….……. 458

11.3.4 Unimolecular Dissociation Rate Measurements…….……. 460

11.3.5 RRKM Calculations…….…… 463

11.4 Summary and Conclusions…..…… 466

11.5 Future Studies…….…… 471

11.6 Acknowledgements…….…… 472

11.7 References…….…….. 493

Appendix A Supplementary Equipment Operation and Maintenance…….…... 496

A.1 Introduction…….……. 496

A.2 GCR-270 Laser System…….…….. 496

A.2.1 Basic Turning-On Procedure…….…… 496

A.2.2 Basic Turning-Off Procedure…….……... 499

A.2.3 Maximizing the Power Output…….……. 499

A.2.4 Internal Cooling System Maintenance…….……. 500

A.2.5 Flashlamps Maintenance and Replacement…….……. 502

A.3 MOPO-730 Laser…….…… 505

A.3.1 Basic Operation Procedure…….……... 505

A.3.2 Writing Calibration Table…….…… 507

A.3.3 MOPO Alignment…….…… 509

A.3.4 Optics Replacement…….……. 511

A.4 NY82-10 / NY82-20 Laser System……. 511

A.4.1 YAG Turning-On Procedure……..... 511

A.4.2 YAG Turning-Off Procedure……..…….…… 512

A.4.3 Dye Laser Turning-On Procedure……..…….…….. 512

A.4.4 Basic Dye Laser Turning-Off Procedure…….…… 513

A.4.5 Basic Dye Laser Operation…….…….. 513

A.4.6 Internal Dieonized Water System…….…… 515

A.4.7 Dye Circulator…….…….. 516

A.4.8 NY82-20 and NY81-20 Flashlamps Replacement…….……... 517

A.5 Frequency Mixing using Inrad Autotracker III…….……... 519

A.6 Photomultiplier Tube…….……... 523

A.7 Delay Generator…….…….. 524

A.8 Data Acquisition Program…….……... 527

A.9 Molecular Beam Apparatus…….…… 529

A.10 Liquid Nitrogen Level Controller…….……. 531

Appendix B GAUSSIAN03 and ACESII Operation…...…….. 554

B.1 GAUSSIAN03 Operation…….…… 554

B.1.1 Basic Linux and GAUSSIAN03 Commands…..……... 554

B.1.2 GAUSSIAN03 Input File…….……. 556

B.1.3 GAUSSIAN03 Output File…….…….. 562

B.1.4 Useful GAUSSIAN03 Keywords…….……. 565

B.2 ACESII Operation…….……... 573

B.2.1 Basic ACESII Commands…….……..…….. 573

B.2.2 ACESII Input ZMAT File…… 574

B.2.3 ACESII Output File…….. 576

B.2.4 Useful ACESII Keywords…… 577

B.3 Acknowledgment……. 585

B.4 References……... 585

Appendix C OH Fragment Translational and

Rotational Energy Release Analysis…….. 587

C.1 Introduction……. 587

C.2 OH Fragment Translational Energy Release……... 588

C.3 OH Fragment Ro-Vibrational Population and Energy……. 591

C.4 OH Fragment Λ-Doublet splitting……... 594

C.5 Linewidth and Area Analysis with PeakFit……. 595

C.5.1 Differences in Integrated Intensities and Linewidths…..... 595

C.5.2 Evaluating the Integrated Signal Intensities……. 596

C.5.3 Evaluating the Transition Linewidth……. 597

C.6 References……... 616

Appendix D Mathematica Codes Used with Data Analysis……... 617

D.1 Introduction…. 617

D.2 Evaluating the Average Rotational-Vibrational

internal energy of PNA……... 618

D.3 Evaluating the Densities of States in PNA using

Whitten-Rabinovitch Approximation…….. 619

D.4 3-Parameter Extrapolation of $E(n \rightarrow \infty)$: Basis

Set Limit Evaluations…….. 621

D.5 HO_2NO_2 O-H Stretching Polynomial Fit and

Morse Parameters (ω_e, $\omega_e\chi_e$)……... 623

D.6 PNA Vibrational Transition Strengths…… 625

D.7 Internal Energy of *cis-cis* HOONO……. 636

D.8 Two-Dimension OH-Stretch / HOON-Torsion

Oscillator Strength Evaluation for *cis-cis* HOONO

Using CCSD(T)/cc-pVTZ Dipole Moment Surface…… 639

D.9 Quantum Yield Calculation of

cis-cis HOONO in the $2\nu_{OH}$ Region…… 676

D.10 Vibrational Term Value Calculation *cis-cis* HOONO…..…….. 680

D.11 Internal Energy of CH_3OOH……. 684

D.12 Two-Dimension OH-Stretch / HOON-Torsion

Oscillator Strength Evaluation for CH_3OOH Using

CCSD(T)/cc-pVTZ Dipole Moment Surface……. 686

D.13 "Franck-Condon" OH-Stretch / HOON-Torsion

Oscillator Model for CH_3OOH Using CCSD(T)/cc-pVTZ

Dipole Moment Surface……. 716

D.14 Calculating the Percent Enhancement in

OH Yield from CH_3OOH……. 732

D.15 RRKM Rate Calculation……... 735

Appendix E FORTRAN Code Used in Phase Space Simulations……. 740

E.1 Introduction…….. 740

E.2 Phase-Space Simulation for

cis-cis HOONO ($h\nu = 6381.23\ cm^{-1}$)…….…….. 742

E.3 Phase-Space Simulation for

trans-perp HOONO ($h\nu = 6971.35\ cm^{-1}$)…… 747

E.4 Phase-Space Simulation for HMHP ($h\nu = 13\ 330\ cm^{-1}$)…..……. 753

E.5 References…….…… 759

Appendix F Schrödinger Equation Solver FGH1D, HITRAN and

Rotational Structure Analysis with PGOPHER…….. 760

F.1 Schrödinger Equation Solver FGH1D…….……. 760

F.2 The HITRAN Database Application…….…… 763

F.3 Rotational Band Contour Simulation Program PGOPHER…..……. 765

F.4 References…….…… 819

LIST OF FIGURES

Figure 1.1: Solar flux as a function of wavelength at various altitudes……. 14

Figure 1.2: Solar flux as a function of wavelength at various angles....……. 15

Figure 1.3: The absorption cross-sections of CH_3OOH, HOOH, and HO_2NO_2……. 16

Figure 1.4: Ground state potential energy diagram…… 17

Figure 1.5: Ground and electronically excited states potential energy diagrams…… 18

Figure 1.6: Potential energy diagrams depicting the ViMP process……... 19

Figure 1.7: Potential energy diagrams comparing ViMP and direct photolysis……. 20

Figure 1.8: The absorption bands of NO_2 in the visible spectral region……. 21

Figure 2.1: PNA schematic energy level diagram…….. 43

Figure 2.2: Experimental diagram for the HO_2NO_2 $2\nu_1$ + 390 nm experiments…… 44

Figure 2.3: HOONO ($2\nu_1$) action spectra from various sources……. 45

Figure 2.4: Unimolecular dissociation overtone action spectra of HO_2NO_2…….. 46

Figure 2.5: Birge-Sponer plot associated with the OH-stretching overtones of PNA……. 47

Figure 2.6: Vibrational overtone action spectra of HO_2NO_2 ($2\nu_1$)……. 48

Figure 2.7: Nascent rotational state distribution of the OH ($v=0, {}^2\Pi_{3/2}$) manifold…. 49

Figure 3.1: Two perspective views of the HO_2NO_2 global minimum structure……. 100

Figure 3.2: Several rotational conformers of HO_2NO_2…….. 101

Figure 3.3: The absorption spectrum in the fundamental region of HO_2NO_2…… 102

Figure 3.4: O-H stretching potential generated using single point energy calculations…… 103

Figure 3.5: Dipole moments functions and Morse wavefunction……... 104

Figure 4.1: HOONO schematic potential energy diagram…….. 167

Figure 4.2: Schematic of HOONO experimental apparatus…… 168

Figure 4.3: Action spectrum of room temperature HOONO…….. 169

Figure 4.4: Dependence of HOONO ($2\nu_{OH}$) action spectra on

the probed nascent OH rotational state……. 170

Figure 4.5: Nascent rotational state distributions of the OH fragment……... 171

Figure 4.6: CCSD(T)/cc-pVTZ one-dimensional slices of the OH potentials…… 172

Figure 4.7: *Cis-cis* HOONO one-dimensional

dipole moments μ_x, μ_y, μ_z functions……. 173

Figure 4.8: Simulated HOONO ($2\nu_{OH}$) action spectrum…….……... 174

Figure 4.9: Phase-space simulations for peaks *A*, *B* and *C*

using D_0 = 19.9 kcal/mol ……...…….. 175

Figure 4.10: Phase-space simulations for peaks *A*, *B* and *C*

using D_0 = 19.4 kcal/mol ……...…….. 176

Figure 4.11: Phase-space simulations for peak *D*……... 177

Figure 4.12: Density of rotational-vibrational states of HOONO at 298 K…….. 178

Figure 4.13: *Ab initio* potential for HOON torsional state…….. 179

Figure 4.14: Adiabatic torsional potentials for the OH stretching states…… 180

Figure 4.15: Adiabatic torsional potentials for OH V = 0, 1, 2, 3…….. 181

Figure 4.16: The torsional and OH-stretching eigenfunctions…… 182

Figure 4.17: Variation in the X, Y, and Z dipole moment components……. 183

Figure 4.18: Simulated $2\nu_{OH}$ action spectrum…… 184

Figure 4.19: Action spectra of $HOO^{15}NO$ and $HOO^{14}NO$……. 185

Figure 4.20: Phase-space simulations for peak *C*

at 6720 cm^{-1} and the peak at 6625 cm^{-1}…….. 186

Figure 5.1: Action spectrum of room temperature HOONO ($3\nu_{OH}$)…….. 215

Figure 5.2: "High" pressure HOONO overview action spectrum…….. 216

Figure 5.3: Rotational band contour simulation of *trans-perp* HOONO $3\nu_1$ band… 217

Figure 5.4: Adiabatic torsional potentials for the

$V_{OH} = 0$ and $V_{OH} = 3$ stretching states…….. 218

Figure 5.5: Simulated overtone action spectrum of HOONO ($3\nu_{OH}$)……. 219

Figure 5.6: $HOO^{15}NO$ isotopic shifts in the $2\nu_1 + \nu_3$ and the $3\nu_1$ regions…….. 220

Figure 5.7: Nascent OH rotational state distributions of peaks *A* and *C*…… 221

Figure 5.8: Nascent OH rotational state distributions of peak D…… 222

Figure 5.9: Phase-space simulations of peaks *A* and *C*…… 223

Figure 5.10: Phase-space simulations of peak *D*……..... 224

Figure 6.1: Schematic energy level diagram of CH_3OOH……. 256

Figure 6.2: Schematic of the experimental apparatus……. 257

Figure 6.3: Vibrational overtone action spectrum of the CH_3OOH $5\nu_{OH}$ band…….. 258

Figure 6.4: Vibrational overtone action spectrum

of CH_3OOH and HOOH $5\nu_{OH}$ bands…… 259

Figure 6.5: Vibrational overtone action spectrum

of CH_3OOH and HOOH $4\nu_{OH}$ bands…… 260

Figure 6.6: CH_3OOH ($5\nu_{OH}$) nascent rotational product state distributions……... 261

Figure 6.7: CH_3OOH ($4\nu_{OH}$) nascent rotational product state distributions…….. 262

Figure 7.1: Schematic of the ViMP experiments conducted on CH_3OOH……. 302

Figure 7.2: Schematic of the experimental apparatus used in recording
the $2\nu_{OH}$ and $3\nu_{OH}$ overtone regions……. 303

Figure 7.3: Schematic of the experimental apparatus used in recording
the $4\nu_{OH}$ overtone region…….. 304

Figure 7.4: CH_3OOH molecule and its a-, b- and c- principle inertial axes……..... 305

Figure 7.5: The low pressure vibrational overtone spectra of CH_3OOH…… 306

Figure 7.6: The $2\nu_{OH}$ ViMP and one-color two-photon action spectra…….. 307

Figure 7.7: The $4\nu_{OH}$ unimolecular and ViMP action spectra…… 308

Figure 7.8: Simulated MHP absorption in the fundamental region…… 309

Figure 7.9: *Ab initio* potential for HOOC torsional
motion and dipole moments functions…….. 310

Figure 7.10: *Ab initio* potential slice for O-H stretching motion…… 311

Figure 7.11: CCSD(T)/cc-pVTZ adiabatic torsional potentials of CH_3OOH……. 312

Figure 7.12: Adiabatic torsional potentials for the OH V =0, 2 stretching states….. 313

Figure 7.13: $\mu_\alpha(\tau)$ transition dipole moment functions…….. 314

Figure 7.14: $\mu_\alpha(r|\tau_{eq.})$ transition dipole moment functions……. 315

Figure 7.15: Simulated $2\nu_{OH}$ action spectrum considering $\mu(r,\tau)$ and $\mu(r)$……. 316

Figure 7.16: Simulated $3\nu_{OH}$ action spectrum considering $\mu(r,\tau)$ and $\mu(r)$……. 317

Figure 7.17: Simulated $4\nu_{OH}$ action spectrum considering $\mu(r,\tau)$ and $\mu(r)$……. 318

Figure 7.18: Simulated $5\nu_{OH}$ action spectrum considering $\mu(r,\tau)$ and $\mu(r)$……. 319

Figure 7.19: 3-D representations of the natural bond orbital…….. 320

Figure 8.1: Adiabatic torsional potentials for the first few OH stretching states…… 370

Figure 8.2: Two-dimensional dipole moment function…….. 371

Figure 8.3: Schematic of the DFM IR apparatus…… 372

Figure 8.4: The room temperature high pressure overview
action spectra of CH_3OOH and CD_3OOH ……..…. 373

Figure 8.5: The $2\nu_{CH}$ region action spectrum of CH_3OOH…… 374

Figure 8.6: The "low resolution" $2\nu_{OH}$ jet spectra of MHP……..……. 375

Figure 8.7: The $2\nu_{OH}$ "high resolution" jet spectra of MHP……... 376

Figure 8.8: $2\nu_{OH}$ rotational band contour simulations at 5 K……. 377

Figure 8.9: The $3\nu_{OH}$ jet spectrum of MHP…… 378

Figure 8.10: $2\nu_{OH}$ rotational band contour simulations at T = 18.7 K…… 379

Figure 8.11: $\mu_\alpha(\tau)$ (= $\mu_a(\tau)$, $\mu_b(\tau)$, $\mu_c(\tau)$) transition dipole moment functions…… 380

Figure 8.12: Product of torsion wavefunctions……... 381

Figure 8.13: Transition dipole moment μ_a and μ_b for various states…….. 382

Figure 8.14: $2\nu_{OH}$ action spectra of CD_3OOH…… 383

Figure 8.15: Action spectra and rotational band contours
of CH_3OOH at T = 17 and 298 K……... 384

Figure 8.16: Action spectra and rotational band contour
of jet cooled CD_3OOH at 10 K……... 385

Figure 8.17: Action spectra of CH_3OOH ($3\nu_{OH} + \nu_{COOH}$) and
rotational band contour simulation at 298 K……. 386

Figure 9.1: Schematic diagram illustrating IVR……. 412

Figure 9.2: Overview action spectra of CH_3OOH and HOOH……... 413

Figure 9.3: Normal modes representation of hydrogen peroxide…… 414

Figure 9.4: ViMP action spectrum of HOOH monitoring OH(V= 0, 1, 2)……. 415

Figure 9.5: Expended view of the vibrational states of HOOH…….. 416

Figure 9.6: ViMP action spectrum of CH_3OOH monitoring OH(V= 0, 1, 2)……. 417

Figure 9.7: Relaxed OH product from the CH_3OOH ViMP ($2\nu_{OH}$ + 532 nm)…..... 418

Figure 10.1: Schematic of the experimental absorption cross-section apparatus….. 437

Figure 10.2: The room temperature electronic

UV absorption cross-sections of methyl hydroperoxide……. 438

Figure 10.3: Room temperature action spectrum of the CH_3OOH $5\nu_{OH}$ band……... 439

Figure 10.4: The UV electronic absorption data and solar flux…….. 440

Figure 10.5: The fractional photolysis rate, J_λ as a function of wavelength……... 441

Figure 10.6: The percent enhancement in the yield of OH radicals from MHP..…... 442

Figure 10.7: Electronic, and overtones, absorption cross-sections of HO_2NO_2……. 443

Figure 10.8: The percent enhancement in the yield of HO_2 radicals from PNA…… 444

Figure 11.1: Energy level diagram of HMHP's conformers……... 477

Figure 11.2: Schematic energy level diagram for vibrational

overtone initiated unimolecular dissociation of HMHP……. 478

Figure 11.3: $4\nu_{OH}$ action spectra of HMHP and HMHP-d_2…… 479

Figure 11.4: The variations in the HMHP ($4\nu_{OH}$) band shape

and intensity as a function of H_2O_2 concentration…….. 480

Figure 11.5: $5\nu_{OH}$ action spectra of HMHP and HMHP-d_2…… 481

Figure 11.6: The one-color three-photon dissociation of H_2O_2 in the $5\nu_{OH}$ band….. 482

Figure 11.7: Nascent rotational state distributions of the OH fragment……. 483

Figure 11.8: Raw sum of the nascent rotational state distributions
of the OH from HMHP and HOOH……... 484

Figure 11.9: $4\nu_2$ phase-space simulations……..…..….. 485

Figure 11.10: $4\nu_2$ and $5\nu_1$ phase-space simulations……...…...….. 486

Figure 11.11: Unimolecular dissociation rate measurements……. 487

Figure 11.12: Unimolecular dissociation rate measurement
at various frequencies..... 488

Figure 11.13: Direct comparison of the measured OH
rotational product state distributions…… 489

Figure 11.14: CCSD/cc-pVDZ O-O stretching potential energy diagram……. 490

Figure 11.15: Schematic illustrating the IVR in HMHP molecule……. 491

Figure 11.16: Action spectra of HMHP in the region of
the first ($2\nu_{OH}$) OH-stretching overtones region…….. 492

Figure A.1: The GCR-270 YAG controller…… 534

Figure A.2: The GCR-270 YAG with cover open…….. 535

Figure A.3: The GCR-270 YAG controller in LONG PULSE MODE…….. 536

Figure A.4: The GCR-270 YAG controller in EXTERNAL Q-SWITCH MODE…. 537

Figure A.5: The GCR-270 YAG SHG/THG harmonic generator housing…… 538

Figure A.6: The GCR-270 power supply unit showing the DI and particle filters…. 539

Figure A.7: The GCR-270 power supply unit showing oscillator board…… 540

Figure A.8: Top view of the GCR-270 laser……... 541

Figure A.9: GCR-270 flashlamp housing……... 542

Figure A.10: MOPO-730 showing the power oscillator (PO)

and master oscillator (MO) stages……. 543

Figure A.11: MOPO-730 schematics…….. 544

Figure A.12: NY82-20/NY81-20 YAG controller…….. 545

Figure A.13: NY81-20/NY82-20 Deionizing filter…… 546

Figure A.14: NY82-20 YAG laser…….. 547

Figure A.15: NY82-20 YAG laser showing oscillator cladding……. 548

Figure A.16: NY82-20 YAG laser showing oscillator cladding bolt……. 549

Figure A.17: Inrad Autotracker controller…….. 550

Figure A.18: Electronics rack…… 551

Figure A.19: Pulsed-valve assembly……... 552

Figure A.20: Liquid nitrogen controller board…… 553

Figure C.1: OH ($v=0, {}^2\Pi_{3/2}$) in its N=2 (a) and N=4 (b) rotational states……... 601

Figure C.2: Screen caption of the PeakFit program main menu……. 602

Figure C.3: The import menu used in loading files in PeakFit program…… 603

Figure C.4: Selecting X and Y columns to load in PeakFit program……. 604

Figure C.5: Selecting from the "AutoFit" menu the Fitting Routine…….. 605

Figure C.6: Initial AutoFit screen caption of the auto-fitting Method I……. 606

Figure C.7: Selecting the "Full Peak Fit with Graphical Update" option……... 607

Figure C.8: The resulting fit using the Auto Fit routine……. 608

Figure C.9: Additional values are shown post fitting……. 609

Figure C.10: Manual adjustments to the position, intensities and widths…….. 610

Figure C.11: Screen capture of PeakFit main screen showing graphical display of un-calibrated spectral line…… 611

Figure C.12: Screen capture of PeakFit showing data points graphically…….. 612

Figure C.13: Screen capture of PeakFit showing the points separation……. 613

Figure C.14: Screen capture of PeakFit showing the frequency separation…… 614

Figure C.15: Screen capture of PeakFit showing a fully calibrated spectra…… 615

Figure F.1: The HOON-torsion potential of *cis-cis* HOONO…… 771

Figure F.2: FGH1D program default settings……. 772

Figure F.3: FGH1D program after selecting the "Read File"……. 773

Figure F.4: FGH1D program after selecting the "Read ClipBoard"…….. 774

Figure F.5: FGH1D program adjustable "Points" parameter…….. 775

Figure F.6: FGH1D program adjustable "Mass" parameter……... 776

Figure F.7: FGH1D program after all the required parameters are inserted..…..…… 777

Figure F.8: FGH1D program showing the solutions to the Schrödinger equation…. 778

Figure F.9: FGH1D program displaying additional values…… 779

Figure F.10: FGH1D program also showing fitting parameters……. 780

Figure F.11: FGH1D program displaying the fitted eigenvalues parameters……. 781

Figure F.12: FGH1D program showing the "Copy to Clipboard" option…….. 782

Figure F.13: The first four eigenvectors ($V_\tau = 0 – 4$) associated with the HOON torsion potential…….. 783

Figure F.14: Computer screen caption of the HITRAN program……... 784

Figure F.15: HITRAN program displaying the various options……. 785

Figure F.16: HITRAN program prompting the user to select the input file…… 786

Figure F.17: HITRAN program; Selecting "NO"……... 787

Figure F.18: HITRAN program displaying the input file HITRAN04.PAR…….. 788

Figure F.19: HITRAN program simulation output file……... 789

Figure F.20: HITRAN program simulation output file optio...…….. 790

Figure F.21: HITRAN program selecting the Spectral Range option……..... 791

Figure F.22: HITRAN program selecting the temperature parameter…… 792

Figure F.23: HITRAN program selecting the "Molecule" option…….. 793

Figure F.24: HITRAN program showing the "Run Select" option…… 794

Figure F.25: HITRAN program showing the lines selected……... 795

Figure F.26: Plot option in the HITRAN program……. 796

Figure F.27: Plot intensity option in the HITRAN program……... 797

Figure F.28: HITRAN program displaying the transitions……. 798

Figure F.29: Computer screen caption of the Specsim code……... 799

Figure F.30: Specsim prompts the user to enter the transition linewidth and number of data points per said FWHM…… 800

Figure F.31: The simulated absorption spectrum of water in the $2\nu_{OH}$ region…… 801

Figure F.32: Computer screen caption of the program PGOPHER…… 802

Figure F.33: PGOPHER showing the "Paste Overlay" option……... 803

Figure F.34: PGOPHER showing the expended view of the overlay of CD_3OOH… 804

Figure F.35: PGOPHER showing the "Overlays" screen……... 805

Figure F.36: PGOPHER showing the "Constants" screen…….. 806

Figure F.37: PGOPHER showing "Add New…" and "Species" options……... 807

Figure F.38: PGOPHER showing “Asymmetric Molecule” options…….. 808

Figure F.39: PGOPHER showing “Asymmetric Manifold” options…….. 809

Figure F.40: PGOPHER showing “New Asymmetric Top” options…….. 810

Figure F.41: PGOPHER showing parameters of the initial state…… 811

Figure F.42: PGOPHER showing the “Constants” of upper state…….. 812

Figure F.43: PGOPHER showing upper state constants……. 813

Figure F.44: PGOPHER showing the “Add Transition Moments” option……. 814

Figure F.45: PGOPHER showing a-, b-, and c-

Cartesian Transition Moments Parameters……. 815

Figure F.46: PGOPHER showing current simulation temperature……. 816

Figure F.47: PGOPHER showing the simulation of CD_3OOH $|2\ 1^+>$ state…… 817

Figure F.48: PGOPHER showing simulation and experimental spectrum……. 818

LIST OF TABLES

Table 2.1: $HO_2NO_2(2\nu_1 + 390\ nm) \rightarrow OH + NO_3$ Channel Energy Partitioning….. 42

Table 3.1: Z-matrices Used with CCSD(T)/cc-pVDZ Energies, frequencies and Structure Calculations for *cis-cis* and *cis-perp'* HO_2NO_2 Conformers….. 78

Table 3.2: CCSD(T)/cc-pVDZ Equilibrium Structure and Energies for Conformers of HO_2NO_2…… 79

Table 3.3: CCSD(T)/cc-pVDZ Harmonic Frequencies of the Rotomers…… 80

Table 3.4: Equilibrium Geometry Parameters for HO_2NO_2……..... 81

Table 3.5: Equilibrium Rotational Constants of HO_2NO_2…….. 82

Table 3.6: HO_2NO_2 Z-matrices Used with CCSD(T)/cc-pVDZ Energies Calculations……. 83

Table 3.7: HO_2 Z-matrices Used with CCSD(T)/cc-pVξZ (ξ = D, T, Q) Energies Calculations……. 84

Table 3.8: NO_2 Z-matrices Used with CCSD(T)/cc-pVξZ (ξ = D, T, Q) Energies Calculations……. 85

Table 3.9: OH Z-matrices Used with CCSD(T)/cc-pVξZ (ξ = D, T, Q) Energies Calculations……. 86

Table 3.10: NO_3 Z-matrices Used with CCSD(T)/cc-pVξZ (ξ = D, T, Q) Energies Calculations……... 87

Table 3.11: Sum of Electronic and ZPE[a] for Reactant and Products in: $HO_2NO_2 \rightarrow HO_2 + NO_2$ and $HO_2NO_2 \rightarrow OH + NO_3$……. 88

Table 3.12: Thermochemistry of HO_2NO_2 Using the Direct Method:

$HO_2NO_2 \rightarrow HO_2 + NO_2$ and $HO_2NO_2 \rightarrow OH + NO_3$……. 88

Table 3.13: H_2O Z-matrices Used with CCSD(T)/cc-pVξZ (ξ = D, T, Q)

Energies Calculations……... 89

Table 3.14: H_2O_2 Z-matrices Used with CCSD(T)/cc-pVξZ (ξ = D, T, Q)

Energies Calculations……... 90

Table 3.15: $HONO_2$ Z-matrices Used with CCSD(T)/cc-pVξZ (ξ = D, T, Q) Energies

Calculations…….…. 91

Table 3.16: Sum of Electronic and ZPE[a] for Species in the Isodesmic

Reaction: $HO_2NO_2 + H_2O \rightarrow H_2O_2 + HONO_2$……. 92

Table 3.17: Thermochemistry of HO_2NO_2 Using the Isodesmic Reaction:

$HO_2NO_2 + H_2O \rightarrow H_2O_2 + HONO_2 \quad \Delta H^o_r$……. 93

Table 3.18: Harmonic Vibrational Frequencies for HO_2NO_2…… 94

Table 3.19: HO_2NO_2 Z-matrix Used with MP2/cc-pVTZ

Harmonic Frequencies and Anharmonicities……... 95

Table 3.20: Harmonic Frequencies and Anharmonicities of HO_2NO_2

Computed at MP2/cc-pVTZ…… 96

Table 3.21: Morse Parameters for OH Stretching mode of $HONO_2$,

HONO, HO_2NO_2, CH_3OH, HOCl and HO_2NO_2……. 97

Table 3.22: Predicted OH Overtone Transition Frequencies, Oscillator Strengths

and Absorption Cross-Sections for HO_2NO_2…… 98

Table 3.23: QCISD/cc-pVTZ Dipole Moment Points as a Function of

O-H bond length and Dipole Derivatives…… 99

Table 4.1: Fragment Energy Disposal

cis-cis HOONO($2\nu_{OH}$ region) → OH + NO_2……. 152

Table 4.2: *cis-cis* HOONO Z-matrix Used with CCSD(T)/cc-pVTZ Energies Calculations……. 153

Table 4.3: *cis-perp* HOONO Z-matrix Used with CCSD(T)/cc-pVTZ Energies Calculations……. 154

Table 4.4: *trans-perp* HOONO Z-matrix Used with CCSD(T)/cc-pVTZ Energies Calculations……. 155

Table 4.5: Equilibrium Geometry Parameters for *cis-cis, cis-perp* and *trans-perp* calculated at CCSD(T)/cc-pVTZ…….. 156

Table 4.6: Harmonic Frequencies for *cis-cis, cis-perp* and *trans-perp* calculated at CCSD(T)/cc-pVTZ……... 157

Table 4.7: CCSD(T)/cc-pVTZ Morse Parameters for OH Stretching mode of $HONO_2$, HONO, HO_2NO_2, CH_3OH, HOCl and HO_2NO_2…… 158

Table 4.8: Predicted OH Overtone Transition Frequencies and Absorption Cross-Sections for *cis-cis, cis-perp and trans-perp*……. 169

Table 4.9: Rotational Constants, Harmonic Frequencies, Dipoles, Ionization Potentials and Polarizabilities for Reactants and Products Used with Phase-Space Simulation…… 160

Table 4.10: Equilibrium Geometry Parameters of *cis-perp* HOONO…… 161

Table 4.11: Harmonic Frequencies of *cis-perp* HOONO……... 162

Table 4.12: CCSD(T)/cc-pVTZ O-H stretch / HOON torsion vibrational levels, transition frequencies and oscillator strengths…… 163

Table 4.13: ACESII Z-matrix Used with CCSD(T)/cc-pVTZ

Single Point Dipole Moment Evaluations…… 164

Table 4.14: Vibrational Frequencies, Anharmonicities and Isotope Shift of *cis-cis* HOONO…… 165

Table 4.15: Isotopic shift constrained band assignments for *cis-cis* HOONO spectral features……. 166

Table 5.1: Vibrational Frequencies, Anharmonicities and Isotope Shift of *cis-cis* HOONO……. 213

Table 5.2: Fragment Energy Disposal HOONO($3\nu_{OH}$ region) → OH + NO_2…… 214

Table 6.1: Fragment Energy Disposal CH_3OOH ($5\nu_{OH}$ region) → OH + CH_3O….. 248

Table 6.2: CH_3OOH Z-matrices Used with CCSD(T)/cc-pVξZ (ξ = D, T, Q) Calculations…… 249

Table 6.3: Equilibrium Geometry Parameters for CH_3OOH…….. 250

Table 6.4: Equilibrium Rotational Constants of CH_3OOH…… 251

Table 6.5: Sum of Electronic and ZPE for Species in the Isodesmic Reaction: $CH_3OOH + H_2O \rightarrow H_2O_2 + CH_3OH$…….. 252

Table 6.6: Thermochemistry of CH_3OOH using the isodesmic reaction: $CH_3OOH + H_2O \rightarrow H_2O_2 + CH_3OH$ ΔH_r^o…….. 252

Table 6.7: OH Z-matrices Used with UCCSD(T)/cc-pVξZ (ξ = D, T, Q) Calculations…… 253

Table 6.8: CH_3O Z-matrices Used with UCCSD(T)/cc-pVξZ (ξ = D, T, Q) Calculations…… 254

Table 6.9: Sum of Electronic and ZPE[a] for Species in the Reaction:

$CH_3OOH \rightarrow OH + CH_3O$…….. 255

Table 7.1: Harmonic Frequencies, Anharmonicities and Isotope Shifts of CH_3OOH Computed at MP2/aug-cc-pVTZ……... 293

Table 7.2: CH_3OOH ACESII Z-matrices Used with CCSD(T)/cc-pVTZ…….. 294

Table 7.3: CH_3OOH ACESII Z-matrices Used with CCSD(T)/cc-pVTZ SP Energy and Dipole Moments Calculations……... 295

Table 7.4: Potential and Kinetic Energy Parameters for the OH Vibrational Levels of CH_3OOH…….. 296

Table 7.5: Bond Interaction Energies of CH_3OOH at Vibrational Excitation Corresponding to $0\nu_{OH}$ and $5\nu_{OH}$…….. 296

Table 7.6: Calculated Oscillator Strength for the Various Transitions in CH_3OOH……... 297

Table 7.7: CCSD(T)/cc-pVTZ OH-Stretch / COOH-Torsion Vibrational Levels and Oscillator Strengths in the First ($2\nu_{OH}$) OH-Stretching Overtone Region…… 298

Table 7.8: CCSD(T)/cc-pVTZ OH-Stretch / COOH-Torsion Vibrational Levels and Oscillator Strengths in the Second ($3\nu_{OH}$) OH-Stretching Overtone Region…… 299

Table 7.9: CCSD(T)/cc-pVTZ OH-Stretch / COOH-Torsion Vibrational Levels and Oscillator Strengths in the Third ($4\nu_{OH}$) OH-Stretching Overtone Region…… 300

Table 7.10: CCSD(T)/cc-pVTZ OH-Stretch / COOH-Torsion Vibrational Levels and Oscillator Strengths in the Fourth ($3\nu_{OH}$)

OH-Stretching Overtone Region…… 301

Table 8.1: Rotational and Vibrational Parameters for the Torsion Substates Associated with the OH Vibrational Ground State, $|0\ m^{+/-}>$, of CH_3OOH……. 360

Table 8.2: Harmonic Frequencies, Anharmonicities and Isotope Shifts of CH_3OOH Computed at MP2/aug-cc-pVTZ…….. 361

Table 8.3: CCSD(T)/cc-pVTZ Transition Dipole Moments for the Various Matrix Elements $<0\ 0^{+/-}|\mu_\alpha|2\ 0^{+/-}>$……...…… 362

Table 8.4: Experimental Parameters used for the $2\nu_{OH}$ Rotational Band Contour at 5 K…… 362

Table 8.5: Experimental Parameters used for the $2\nu_{OH} + \nu_{COOH}$ Rotational Band Contour at 9 K…… 363

Table 8.6: Experimental Parameters used for the $3\nu_{OH} + \nu_{COOH}$ Rotational Band Contour at 19 K…….. 364

Table 8.7: Scaled Rotational Parameters for the Torsion Substates Associated with the OH Vibrational Ground State, $|0\ 0^{+/-}>$, of CD_3OOH…….. 364

Table 8.8: Experimental Parameters used for the $2\nu_{OH} + \nu_{COOH}$ Rotational Band Contours of CD_3OOH……..... 365

Table 8.9: Experimental Parameters used for the $2\nu_{OH}$ Rotational Band Contour of CD_3OOH at 4.2 K…… 365

Table 8.10: Experimental Parameters used for the $2\nu_{OH}$ Rotational Band Contour of CD_3OOH at 9.5 K…….. 366

Table 8.11: Experimental Parameters used for the $2\nu_{OH}$ Rotational Band Contour of CH_3OOH at 17 K……... 367

Table 8.12: Experimental Parameters used for the $2\nu_{OH}$ Rotational Band Contour of CH_3OOH at 298 K……. 368

Table 8.13: Experimental Parameters used for the $3\nu_{OH} + \nu_{COOH}$ Rotational Band Contour of CH_3OOH at 298 K..…… 369

Table 9.1: Harmonic Frequencies, and Anharmonicities of HOOH Computed at MP2/cc-pVQZ…….. 409

Table 9.2: The OH Fragment Vibrational Product State Branching Ratio of Hydrogen Peroxide in the Stretching Overtones and Bend-Stretch Regions at Photolysis Wavelength λ_2 = 532 nm…… 409

Table 9.3: The OH Fragment Vibrational Product State Branching Ratio of Methyl Hydroperoxide in the Stretching Overtones and Bend-Stretch Regions at Photolysis Wavelength λ_2 = 532 nm…… 410

Table 9.4: The OH Fragment Vibrational Product State Branching Ratio of Hydrogen Peroxide in the Stretching Overtones and Bend-Stretch Regions at Photolysis Wavelength λ_2 = 355 nm…… 410

Table 9.5: The OH Fragment Vibrational Product State Branching Ratio of Methyl Hydroperoxide in the Stretching Overtones and Bend-Stretch Regions at Photolysis Wavelength λ_2 = 355 nm…….. 411

Table 10.1: Absorption Cross-Sections for CH_3OOH…… 436

Table 11.1: Rotational Constants and Scaled[a] Harmonic Frequencies

for Reactant and Products Used with Phase-Space Simulation……... 473

Table 11.2: Dipoles, Ionization Potentials and Polarizabilities for Reactants and Products Used with Phase-Space Simulation……... 474

Table 11.3: HMHP Dissociation Rates Resulting from Excitation at Various Wavelengths in the Vicinity of Peroxide and Alcohol $4\nu_{OH}$ Bands…… 474

Table 11.4: CCSD(T)/cc-pVDZ Rotational Constants and Scaled Harmonic Frequencies Used with RRKM Rates Calculations for HMHP and HMHP-d_2…….. 475

Table 11.5: RRKM Rates Calculated for Excitation of the Peroxide and Alcohol $4\nu_{OH}$ Stretching Overtones of HMHP and HMHP-d_2…… 476

Table A.1: MOPO System Optical Components replacement parts……..…… 533

Table C.1: OH Fragment Rotational Energy Distribution…….. 600

Table F.1: CCSD(T)/cc-pVTZ HOONO Torsion Potential Used with FGH1D Program to Obtain Eigenvalues and Eigenfunctions……. 769

Table F.2: Molecules Available in the HITRAN Database…… 770

ACKNOWLEDGEMENTS

I would like to express my deepest gratitude to Professor Amitabha Sinha whose devotion, talent, enthusiasm and support has inspired me to what has now become this dissertation. This work would not have been possible without the guidance he has provided me with.

I would also like to thank my fellow lab partners Dr. M. Shane Bowen, Melanie McWilliams, and our postdoctoral fellows Dr. Ramesh Sharma, Dr. Shuping Li and Dr. Montu Hazra for their help, support and encouragement. I would also like to acknowledge the assistance I received from the undergraduate students Matthew Gonzales, Sujitra Pookpanratana, Jonas Opperman and Jordan Fine.

In addition to the guidance received from my lab partners of old and new, I would also like to thank our collaborators Professor Joseph S. Francisco and Dr. Mónica Martínez-Avilés of Purdue University, Professor Paul O. Wennberg, Dr. Juliane L. Fry, Dr. Coleen M. Roehl of Caltech University, and also Professor Henrik G. Kjaergaard and Dr. Daniel P. Schofield of University of Otago- New Zealand. Many thanks for the invaluable interactions.

To my dear UCSD friends who were always there to lend a hand, Professor Katja Lindenberg, Dr. Michael Hale, Katheryn Sanchez, and John D. Savee- Thank you all very much.

Chapter 2, in part, is a reprint of the material as it appears in Journal of Physical Chemistry *A* 108, 8134 (2004). J. Matthews, R. Sharma, and A. Sinha, American Chemical Society, 2004. The dissertation author was the primary investigator and author of this paper.

Chapter 3, in part, is a reprint of the material as it appears in Journal of Chemical Physics 121, 5720 (2004). J. Matthews, J. S. Francisco, and A. Sinha, American Institute of Physics, 2004. The dissertation author was the primary investigator and author of this paper.

Chapter 4, in part, is a reprint of the material as it appears in Journal of Chemical Physics 120, 10543 (2004). J. Matthews, J. S. Francisco, and A. Sinha, American Institute of Physics, 2004. And in Journal of Chemical Physics 122, 104313 (2005). J. Matthews, and A. Sinha, American Institute of Physics, 2005.The dissertation author was the primary investigator and author of these papers.

Chapter 5, in part, is a reprint of the material as it appears in Journal of Chemical Physics 120, 10543 (2004). J. Matthews, J. S. Francisco, and A. Sinha, American Institute of Physics, 2004. And in American Chemical Society 125, 134318 (2005). D. P. Schofield, and H. G. Kjaergaard; J. Matthews, and A. Sinha, American Chemical Society, 2005. The dissertation author was the primary investigator and author of these papers.

Chapter 6, in part, is a reprint of the material as it appears in Journal of Chemical Physics 122, 221101 (2005). J. Matthews, J. S. Francisco, and A. Sinha, American Institute of Physics, 2005. The dissertation author was the primary investigator and author of this paper.

Chapter 7, in part, is a reprint of the material as it appears in Journal of Chemical Physics 129, 074316 (2008). J. Matthews, M. Martínez-Avilés, J. S. Francisco, and A. Sinha, American Institute of Physics, 2008. The dissertation author was the primary investigator and author of this paper.

Chapter 10, in part, is a reprint of the material as it appears in Proceedings of the National Academy of Sciences 102, 7449 (2005). J. Matthews, J. S. Francisco, and A. Sinha, National Academy of Sciences of the USA, 2005. The dissertation author was the primary investigator and author of this paper.

Chapter 11, in part, is a reprint of the material as it appears in Journal of Chemical Physics 128, 184306 (2008). J. Matthews, J. L. Fry, C. M. Roehl, P. O. Wennberg, A. Sinha, American Institute of Physics, 2008. The dissertation author was the primary investigator and author of this paper.

VITA

2002	Bachelor of Science in Chemical Physics University of California, San Diego
2004	Master of Science in Chemistry University of California, San Diego
2008	Doctor of Philosophy in Physical Chemistry University of California, San Diego

PUBLICATIONS

"Photodissociation of vibrationally excited pernitric acid: HO_2NO_2 ($2\nu_1$) + 390 nm", Jamie Matthews, Ramesh Sharma and Amitabha Sinha, J. Phys. Chem A. **108**, 8134 (2004)

"Relative vibrational overtone intensity of *cis– cis* and *trans– perp* peroxynitrous acid", Jamie Matthews, Amitabha Sinha and Joseph S. Francisco, J. Chem. Phys. **120**, 10543 (2004)

"High level *ab initio* study of the structure and vibrational spectra of HO_2NO_2", Jamie Matthews, Amitabha Sinha and Joseph S. Francisco, J. Chem. Phys. **121**, 5720 (2004)

"State-resolved unimolecular dissociation of *cis- cis* HOONO: Product state distributions and action spectrum in the $2\nu_{OH}$ band region", Jamie Matthews, and Amitabha Sinha, J. Chem. Phys. **122**, 104313 (2005)

"The importance of weak absorption features in promoting tropospheric radical production", Jamie Matthews, Amitabha Sinha and Joseph S. Francisco, PNAS, **102**, 7449 (2005)

"Unimolecular dissociation and thermochemistry of CH_3OOH", Jamie Matthews, Amitabha Sinha and Joseph S. Francisco, J. Chem. Phys. **122**, 221101 (2005)

"The OH-stretching and OOH-bending overtone spectrum of HOONO", Daniel P. Schofield, Jamie Matthews, Amitabha Sinha, and Henrik G. Kjaergaard, J. Chem. Phys. **123**, 134318 (2005)

"OH-Stretch vibrational spectroscopy of hydroxymethyl hydroperoxide", Juliane L. Fry, Jamie Matthews, Joseph R. Lane, Coleen M. Roehl, Amitabha Sinha, Henrik G. Kjaergaard, and Paul O. Wennberg, J. Phys. Chem. A **110**, 7072 (2006)

"Atmospheric hydroxyl radical production from electronically excited NO_2 and H_2O", Shuping Li, Jamie Matthews, and Amitabha Sinha, Science **319**, 1657 (2008)

"Vibrational overtone initiated unimolecular dissociation of $HOCH_2OOH$ and $HOCD_2OOH$: Evidence for mode selective behavior", Jamie Matthews, Juliane L. Fry, Coleen M. Roehl, Paul O. Wennberg, and Amitabha Sinha, J. Chem. Phys. **128**, 184306 (2008)

"Probing OH stretching overtones of CH_3OOH through action spectroscopy: Influence of dipole moment dependence on HOOC Torsion", Jamie Matthews, Mónica Martínez-Avilés, Joseph S. Francisco, and Amitabha Sinha, J. Chem. Phys. **129**, 074316 (2008)

ABSTRACT OF THE DISSERTATION

State-Resolved Photochemistry and Spectroscopic Characterization of Atmospherically Relevant Hydroperoxides

by

Jamie Matthews

Doctor of Philosophy in Chemistry

University of California, San Diego

Professor Amitabha Sinha, Chair

This dissertation focuses on the photodissociation dynamics, thermochemistry, spectroscopy and structure of important hydroperoxide molecules which influence the oxidation capacity of the atmosphere. Since hydroperoxides such as CH_3OOH, $HOCH_2OOH$, HO_2NO_2 and HOOH species serve as reservoir for the HO_x (=HO_2 + OH) radicals, a thorough examination of excited state and ground state photochemistry of these species is needed.

In this dissertation, the photodissociation dynamics of vibrationally excited HO_2NO_2 molecule is examined, and its first OH-stretching state dissociation quantum yield is assessed in order to quantify its contribution to the HO_x budget. An *ab initio* study is used to obtain bond dissociation energies, vibrational spectra and absorption cross-sections.

The HOONO molecule is an important structural isomer of nitric acid. Studies of HOONO molecule have primarily focused on the vibrational structure, spectra and energetics of vibrational states in the vicinity of the first and second OH-stretching overtones. From these measurements, the heat of formation and vibrational band assignment of *cis*-*cis* HOONO are determined.

Organic hydroperoxides such as CH_3OOH and $HOCH_2OOH$ are fundamental systems to explore the flow of energy among different vibrational modes. In $HOCH_2OOH$, the dissociation rates that are extracted from the third OH-stretching overtone suggest that excitation of the alcohol OH-stretch result in dissociation rates that are substantially slower than rates resulting from excitation of the peroxide OH-stretch where IVR is evidently more restricted. Non-statistical behavior is also observed in CH_3OOH, where the excitation of HOO-bending mode and CH-stretching modes result in more complete IVR due to strong state-mixing compared with excitation of the OH-stretching modes; as inferred from the quantities of vibrationally excited OH product formed. Enhanced IVR mixing is also observed in HOOH molecule, suggesting mode-selective behavior is a common occurrence in hydroperoxide molecules.

Lastly, rotational band analysis of jet-cooled CH_3OOH facilitates band assignment and structure of the first and second OH-stretching overtones and their corresponding torsional states. The analysis also shows that interactions between the bright OH-state and dark background states lead to inhomogeneous line broadening and band perturbations. These interactions predominantly arise from interaction between the symmetric HOOC-torsion/OH-stretching states and the CH-states of the methyl rotor.

Chapter 1

Introduction

1.1 Photochemical Processes: Reactions Initiated by Absorption of Light

A chemical change that results in the breaking and/or formation of bonds that is initiated by absorption of light is a common occurrence in many chemical environments. For example, in the atmosphere, these processes occur naturally in the presence of sunlight. Since the atmosphere represents an important dynamic environment where the actinic photon flux from the sun varies with altitude and with angle the sun forms with respect to the earth's surface normal, it has captured the attention of many researchers.[1-3] The actinic solar flux as a function of altitude is shown in Fig. 1.1 for several altitudes ranging from 0 to 50 km.[4] The figure shows that while penetration of longer wavelengths ($\lambda > 320$ nm), in particular visible (VIS) and near infrared (IR) radiation is fairly independent of altitude, penetration of short wavelengths ($\lambda < 320$ nm) are strongly affected by the air column above it. Conversely, the variation in solar flux with time of day is shown for a particular altitude (5 km) as function of solar zenith angle (SZA) in Fig. 1.2.[4] The subtle differences in the solar flux when the sun is at $0 - 40^{o}$ which corresponds to time of day 12:00 through 14:00 compared with 18:00 when the sun is at ~90^{o} SZA, has been thought to affect dramatically atmospheric reactions.[5-7]

As the sun goes down, the extended path-length the light travels through the atmosphere leads to preferential depletion of ultraviolet (UV) radiation through scattering and absorption relative to the longer wavelengths.[1,2,5-7] In recent years, a great deal of

effort has been dedicated in order to address several unexplained observations. One of these phenomena involve the production of HO_x (= OH + HO_2) radicals under low ultraviolet light conditions occurring at high solar zenith angle (see Fig. 1.2).[5-8] Normally, at low SZA, where UV radiation is abundant, HO_x production is initiated when ozone molecules (O_3) absorb photons to produce $O(^1D)$ atoms as follows:[9,10]

$$O_3 + h\nu(\leq 320\ nm) \rightarrow O(^1D) + O_2 \qquad (1.1)$$

These highly reactive oxygen atoms can subsequentially react with water (H_2O) or methane (CH_4) molecules to form hydroxyl radical (OH):[9,10]

$$O(^1D) + H_2O\ (or\ CH_4) \rightarrow OH + OH\ (or\ CH_3) \qquad (1.2)$$

However, under low UV condition, which occur at sunrise and sunset, researchers have measured HO_x concentrations that are unexplained by conventional models and simulations which predominantly consider HO_x production via ultraviolet photolysis of ozone and other OH containing species.

To appreciate the importance of HO_x radicals and the great interest they have generated, it is important to point out that despite their relatively low concentrations measuring ~10^7 molecule/cm^3,[3] they are responsible for converting pollutants that lead to the destruction of ozone in the stratosphere and formation of smog (ozone) in the troposphere to more inert species and ultimately to their removal from their atmosphere. For example, the dissociation of nitrogen dioxide (NO_2) leads to major ground-level urban air pollution:[1-3,10-13]

$$NO_2 + h\nu\ (\leq 420\ nm) \rightarrow O(^3P) + NO \qquad (1.3)$$

$$O(^3P) + O_2 \rightarrow O_3\ (smog) \qquad (1.4)$$

However, in the presence of hydroxyl radicals, NO_2 can be converted to the relatively more inert nitric acid which eventually gets removed from the atmosphere via rainout:[2]

$$OH + NO_2 \rightarrow HONO_2 \qquad (1.5)$$

Thus, in order to evaluate the oxidation power of the atmosphere, quantifying the sources and mechanisms leading to the production of HO_x radical is essential.

Donaldson and coworkers were first to show that a fraction of the missing HO_x source can be accounted by considering low-lying overtones photolysis of HO_x containing molecules.[14-16] These photolysis transitions occur at wavelengths $500 < \lambda < 1500$ nm that are not significantly attenuated by atmospheric absorption (see Figs 1.1 and 1.2). These so called HO_x containing molecules to a large extent have been identified as hydroperoxides. The dissertation chapters focus on such hydroperoxide species and present new results regarding their energetics, dissociation dynamics and spectroscopy.

1.2 Properties of Hydroperoxides and their Role in the Atmosphere

The various systems that are explored in the dissertation chapters are inorganic and organic hydroperoxides. Namely, these are peroxynitric acid (HO_2NO_2, PNA), peroxynitrous acid (HOONO) hydrogen peroxide (HOOH), methyl hydroperoxide (CH_3OOH, MHP), and hydroxymethyl hydroperoxide ($HOCH_2OOH$, HMHP). With the exclusion of HOONO, numerous studies, including field campaigns and atmospheric models have pointed out their atmospheric significance as HO_x reservoir species because of their relatively large concentrations.[17-19] Presently, experiments are underway to asses the contribution of the HOONO species.

To fully appreciate the importance of hydroperoxides, one must gain general knowledge of their properties. Hydroperoxides are mainly formed via the radical-radical association reaction involving the OH or HO_2 radical with NO_2, HO_2 or RO_2:[1,20]

$$HO_2 + NO_2 \rightarrow HO_2NO_2 \quad (1.6)$$

$$HO + NO_2 \rightarrow HOONO \quad (1.7)$$

$$HO_2 + HO_2 \rightarrow HOOH + O_2 \quad (1.8)$$

$$HO_2 + CH_3O_2 \rightarrow CH_3OOH + O_2 \quad (1.9)$$

Principally, hydroperoxides are removed by oxidation, photolysis and rainout processes:[20]

$$XOOH + OH \rightarrow \text{products} \quad (1.10)$$

$$XOOH + h\nu \rightarrow XO + OH \quad (X = CH_3, NO_2, H, \text{etc.}) \quad (1.11)$$
$$\rightarrow \quad X + HO_2$$

Removal via photolytic processes occurs predominately in the UV region where the molecules absorb strongly. The absorption cross-section curves of HOOH, CH_3OOH, and HO_2NO_2 are shown in Fig. 1.3.[20,21] The figure shows that hydroperoxides have strong continuous electronic absorption bands in the region of 200 – 300 nm. Thus, photons are expected absorb strongly over this absorption region. Looking at the solar flux curves shown in Figs. 1.1, and 1.2 it is clear that under some SZA, a photon absorbed by an hydroperoxide XOOH molecule (where X = H, NO_2, CH_3, $HOCH_2$), may indeed produce HO_x radical.

In the dissertation chapters, the bond dissociation energies ranging from 20 – 43 kcal/mol are determined for all hydroperoxides with the exception of HOOH molecule. The generally weak peroxide O–O bond dissociation energy associated with

hydroperoxides suggests that it is also possible to photolyze them via overtone excitation. As discussed below, the relatively anharmonic O-H stretching potential makes excitation of overtones an efficient process which carries relatively large transition strength. These facts support the findings of Donaldson and coworkers who have, for example, demonstrated that overtone initiated photodissociation of HO_2NO_2 leads to significant enhancement of photolysis rate of PNA and HO_x production at high solar zenith angle.[14]

Aside from their atmospheric significance as reservoir species, hydroperoxides can also provide insight to the flow of vibrational energy in the molecule which can ultimately provide an additional probe of the unimolecular dissociation dynamics. Much of the framework to understanding the flow of vibrational energy is based on the assumption that energy absorbed by molecules is fully randomized and distributed statistically among the various vibrational degrees of freedom.[22] There are however several known examples where the energy is restricted to a smaller set of vibrational modes. Mode selective behavior has been observed in molecules such as water, hypochlorous acid, and stilbene.[23-25]

In recent year it has also been demonstrated that it may be possible to use vibrational excitation to control the reactivity of a particular reaction site and therefore affect the outcome of reaction. For example, Crim and coworkers have observed bond-selective reaction by exciting various vibrational coordinates of HOD and methane-d_1 prior to their reactions with hydrogen and chlorine atoms respectively.[26-27] In addition, they have compared the resulting product of two-step state selected dissociation from a vibrationally excited molecule to that resulting from dissociation of HOOH that is not vibrationally excited but pumped with a single UV photon of *equivalent* photon energy.[28]

Understanding of these state-selected dissociation, aside from their importance in validating quantum calculations, also reveal non-statistical behavior which can not be described with RRKM theory.[29]

Chapters in this dissertation present the experimental and theoretical properties obtained for the hydroperoxides ranging from thermochemistry to dissociation dynamics and spectroscopy. Chapter 2 looks at the dissociation dynamics and dissociation quantum yields of vibrationally excited HO_2NO_2 molecule in the first OH-stretching overtone region. Chapter 3 complements the experiments with high-level *ab initio* study which investigates the structure, thermochemistry and vibrational spectra of PNA. Chapters 4 and 5 present results on the dissociation dynamics, phase-space calculations, and vibrational spectra resulting from the unimolecular decay of peroxynitrous acid in the first and second OH-stretching overtones regions respectively. These studies are also accompanied by an *ab initio* study of structure and vibrational spectra of HOONO. Chapter 6 is a first in a series investigating CH_3OOH. The chapter focuses on the unimolecular dissociation of the vibrationally excited molecule in the third ($4\nu_{OH}$) and fourth ($5\nu_{OH}$) OH-stretching overtones. Chapter 7 presents results of high-level *ab initio* calculations simulating the vibrational spectra in the vicinity of the $2\nu_{OH} - 5\nu_{OH}$ stretching states and examines the influence of the HOOC-torsion on the OH-stretching mode in CH_3OOH. The first ($2\nu_{OH}$) and second ($3\nu_{OH}$) OH-stretching overtones and second ($3\nu_{CH}$) CH-stretching overtones regions of jet-cooled methyl hydroperoxide molecule are then further investigated and spectroscopic information pertaining to theses vibrational levels are reported in Chapter 8. Chapter 9 explores the vibrational mode selective behavior of methyl hydroperoxide and hydrogen peroxide which are excited in

their first and second OH-stretch and second CH-stretch/HOO-bend regions. The data suggests that enhanced vibrational state mixing associated with HOO bending mode compared to excitation of zeroth-order pure OH stretching states leads to significantly less vibrationally excited OH product in CH_3OOH and HOOH. Chapter 10 reviews findings of photolysis rate under atmospheric conditions of MHP and PNA from photon absorption in the 360 – 640 nm regions which corresponds to electronic excitation of weak absorption tail as well as overtone excitation. The dissertation chapter also quantifies the atmospheric contribution to the HO_x reservoir of absorption in the near-UV/VIS spectral region of methyl hydroperoxide by comparing their relative photolysis rates to known UV photolysis rate. The chapter also invokes similar approach with peroxynitric acid by comparing its near UV/VIS and IR photolysis rate to UV photolysis. Lastly, Chapter 11 covers the thermochemistry vibrational spectra of $HOCH_2OOH$ molecule. In addition, the mode-selective dissociation of $HOCH_2OOH$ and $HOCD_2OOH$ are also examined by measuring their dissociation rates resulting from excitation of peroxide vs. alcohol OH-stretches in the third OH-stretching overtone region. The experimental dissociation rates are then compared with predictions of RRKM theory. The experiments described above utilize several state-select techniques which in conjunction with complementary *ab initio* methods has facilitated the current findings. These experimental techniques are discussed below.

1.3 State Selected Experiments on the Ground and Electronically Excited States

As described above, experiments conducted in the laboratory probe the spectroscopic, thermochemical and dissociation dynamics associated with hydroperoxide molecules. The experimental data presented throughout the dissertation chapters are

obtained by employing several laser techniques to obtain the pertaining information. Data obtained by the experiments are then interpreted with the aid of *ab initio* methods and/or data analysis methods which are presented throughout the dissertation chapters and appendices.

The majority of the experiments are conducted in a photolysis chamber maintained at room temperature through which the sample is flowed slowly while maintaining constant sample pressure ranging from 20 to 150 mTorr ($6.0 \times 10^{14} - 4.5 \times 10^{15}$ molec/cm^3). Under these conditions, the spectral congestion that is typically present due to the thermal energy obstructs the fine rotational structure associated with the vibrational bands. For experiments where the rotational information is needed, experiments are conducted under jet-free expansion environment where ~4 Torr sample seeded in 500 to 2280 Torr of helium is allowed to pass through a pulse valve into a vacuum chamber. The expansion leads to cooling which allowing to achieve temperatures ranging from 4 to 20 K.

Perhaps one of the simplest methods for accessing the dissociative part of the ground state potential is by exciting the molecule to a high vibrational overtone level which lies near the dissociation threshold:

$$X–Y + h\nu \rightarrow [X–Y]^{\ddagger} \rightarrow X + Y \qquad (1.12)$$

In the above reaction, if the combined photon energy, hν, and the parent's internal energy, E_{int}, is grater than the bond dissociation energy, D_0, the energized parent molecule, $[X–Y]^{\ddagger}$, will dissociate and result in fragments that are traveling in opposing direction, each carrying energy partitioned into internal (rotation, vibration, electronic) and translational degrees of freedom. Fig. 1.4(a) shows a potential energy diagram where

the molecule is excited to a vibrational level which lies above the dissociation threshold, resulting in prompt dissociation of the parent molecule. The lower panel in the figure depicts a situation where the molecule is vibrationally excited to a ro-vibrational state with photon energy which is less than the dissociation threshold ($h\nu < D_0$). In the presence of thermal energy, where high rotational and/or vibrational hot-band states in the parent molecule are also populated, the excitation will result in a dissociation quantum yield of less than unity. This process is referred to as thermally assisted unimolecular dissociation.

In both examples above, the resulting fragments X and Y carry translational energy that in the parent molecular reference frame is labeled E_t, as well as internal energy labeled $E^X_{int}(\Omega,v,J)$ for fragment X and $E^Y_{int}(\Omega,v,J)$. Applying conservation of energy:

$$E^{XY}_{int} + h\nu - D_0 = E^X_{int}(\Omega,v,J) + E^Y_{int}(\Omega,v,J) + E_t \qquad (1.13)$$

One can see that by mapping out the internal energy of the fragments and their translational energy, it is possible to obtain the bond dissociation energy; a parameter which is of practical significance.

The effectiveness of the experiment is very much depended on the choice of the vibrational excitation coordinate. The equations governing the harmonic oscillator forbid transitions differing from $\Delta v = \pm 1$.[30] Thus, to access high vibrational levels of a harmonic-like oscillator, one may need to produce several sequential $\Delta v = +1$ transitions. Alternatively, one will choose to excite vibrational overtones of modes that are more anharmonic such as C–H, N–H and O–H stretching modes of which one or more are present in hydroperoxides. What makes these modes relatively simple to excite is the fact

that their small reduced-mass leads to vibrational levels that have higher frequencies, thus requiring less quantum units of excitation to access the same region of the potential compared with low frequency vibrational modes. The basis for overtone excitation can be understood in term of the mechanical and electrical anharmonicities terms in the general expression:[31,32]

$$f = 4.072 \times 10^{-7}\ [\text{cm D}^{-2}]\ \nu_{0\rightarrow v}\ |\boldsymbol{\mu}_{0\rightarrow v}|^2 \qquad (1.14)$$

Where the transition strength, f, is proportional to the transition frequency, $\nu_{0\rightarrow v}$, and the transition dipole moment, $\boldsymbol{\mu}_{0\rightarrow v}$. For a particular transition, the transition dipole moment, $\boldsymbol{\mu}_{0\rightarrow v}$, is given by:

$$\boldsymbol{\mu}_{0\rightarrow v} = \langle \Psi_v | \boldsymbol{\mu}(q) | \Psi_0 \rangle \qquad (1.15)$$

Equation 1.15 contains both the harmonic and anharmonic (mechanical and electrical) terms where the wavefunctions, Ψ, of the anharmonic oscillator can be expressed in terms of a linear combinations of harmonic oscillator basis functions, φ:[30]

$$|\Psi_v\rangle = \sum c_i |\varphi_i\rangle = c_0|\varphi_0\rangle + c_1|\varphi_1\rangle + c_2|\varphi_2\rangle + \ldots \qquad (1.16)$$

Also, the electrical anharmonicity which arising from the expansion of the electrical dipole moment can be written as follows:

$$\boldsymbol{\mu}(q) = \sum (\partial^n \boldsymbol{\mu}(q)/\partial q^n)|_{q=q_o}\ q^n/n! = \qquad (1.17)$$

$$\boldsymbol{\mu}(q_0) + (\partial \boldsymbol{\mu}(q)/\partial q)|_{q=q_o}\ q + (\partial^2 \boldsymbol{\mu}(q)/\partial q^2)|_{q=q_o}\ q^2/2! + \ldots$$

Note that in the harmonic oscillator approximation the terms associated with the mechanical anharmonicity vanish. And, even though the electrical anharmonicity has non-zero terms even for the harmonic oscillator, those are typically neglected.

Another commonly occurring excitation scheme involves exciting molecules from their electronic ground state to another bound or repulsive electronically excited state. In Fig. 1.5(a), the molecule is excited from its ground vibrational level to a bound electronic state. This excitation scheme is extensively used throughout the dissertation chapters to probe the resulting OH(v,J) fragment states using the laser-induced fluorescence technique (LIF). By contrast, Fig. 1.5(b) depicts a situation where the upper state is repulsive which means that upon accessing the potential, prompt dissociation will occur. Unlike the situation depicted in Figs. 1.4(a) and 1.4(b) which correspond to near-threshold dissociation, electronic excitation typically generates species that carry more energy (internal + translational) dictated by the characteristics of the electronic state from which they are dissociated from. Thus, one may obtain information pertaining to the electronic excited state of the parent molecule, such as product branching ratio, fragment recoil velocities, fragment alignment and energy distribution by studying such excitation processes.

A third method that is used to investigate hydroperoxides in several of the dissertation chapters combines the two methods discussed above. Developed by Crim and coworkers,[28,33,34] the vibrationally mediated photodissociation (ViMP) technique involves a two-step sequential excitation where the first step involves vibrational exciting of the molecule to a bound state followed by a subsequent excitation of the vibrationally excited molecule to an electronically excited state by a second photon at some short time after the vibrational excitation has occurred. Typically, a UV or VIS photon is chosen to for the second electronic excitation step. The choice of wavelength for the second step is dictated by factors that enhance the signal levels by increasing the transition strength and by

minimizing the interferences from ground state absorption. The stages of the ViMP process are depicted in Fig. 1.6. In the figure, the molecule is vibrationally excited to a bound vibrational state and subsequently dissociated on the electronically excited state. Absorption from the ground state or other low lying states is not possible since each photon by it self falls short of directly accessing the excited electronic state.

In terms of its applicability, the ViMP method permits for dissociation dynamics studies of vibrationally excited species with good signal-to-noise and, because of its selectivity, interferences from impurities can be minimized with proper choice of excitation wavelengths. In addition, unlike some absorption technique, it can be extended to molecular beam experiments where the thermal distribution of states is quenched to a small manifold of rotational states. The ViMP method can also be used in order to study the differences in dissociation dynamics of vibrationally excited molecule with electronically prepared molecule having *equivalent* energy which carries no vibrational excitation. For example, in Fig. 1.7 the photodissociation dynamic from the electronically excited state accessed via a single photon is compared with the dissociation dynamics from the ViMP process. Even though the dissociation process leads to formation of same fragments X and Y, these products are formed with different distribution of quantum states due to the fact that in the ViMP process intramolecular vibrational energy redistribution (IVR) can play an important role in determining the final product states. Thus, the ViMP technique can be used to probe the extent of IVR associated with excitation of different vibrational modes.

In the excitation and dissociation schemes described above the molecule not only absorbs a photon(s), but the photon(s) also fragments the parent molecule. In essence, the

signal from these experiments is proportional to the absorption cross-section, quantum yields and detection efficiencies of the X and Y fragments. Photoacoustic spectroscopy is an absorption technique which although less sensitive than LIF has the advantage that absorption features of molecules can be characterized regardless of whether the states they are excited to lead to dissociation or not. In photoacoustic spectroscopy, the absorbed photon is converted to heat and pressure changes which is captured with a microphone. For example, Fig. 1.8(a) shows the visible absorption spectrum of NO_2 generated by exciting the bound states B^2B_1 and A^2B_2 from the ground X^2A_1 state. The panel below is the reference absorption spectrum obtained from the HITRAN database (see Fig. 1.8(b)).[35] The specific wavelengths used and their power settings, focusing conditions etc. in the studies of hydroperoxides are described in the experimental section of each chapter.

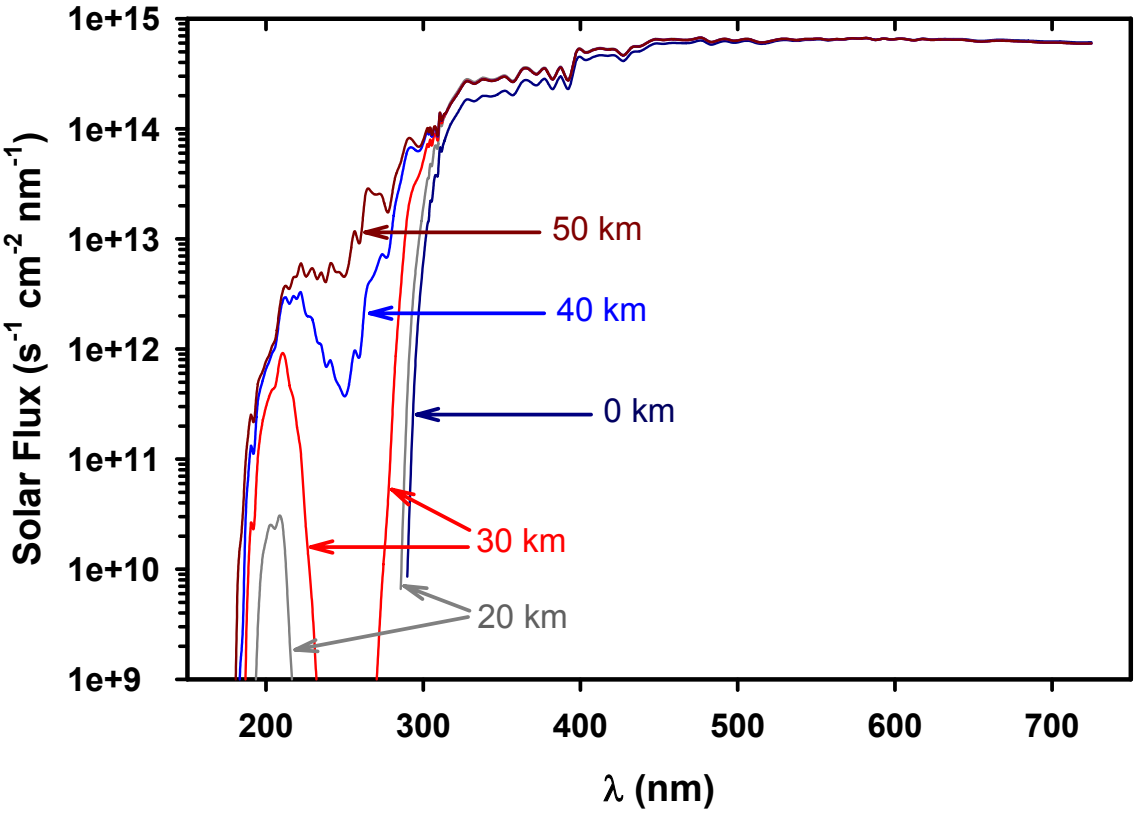

Figure 1.1: Solar flux as a function of wavelength measured during summertime at noon for 0, 20, 30, 40 and 50 km above sea level obtained from data in Ref. 4.
[File: F1.1_solar_ alt]

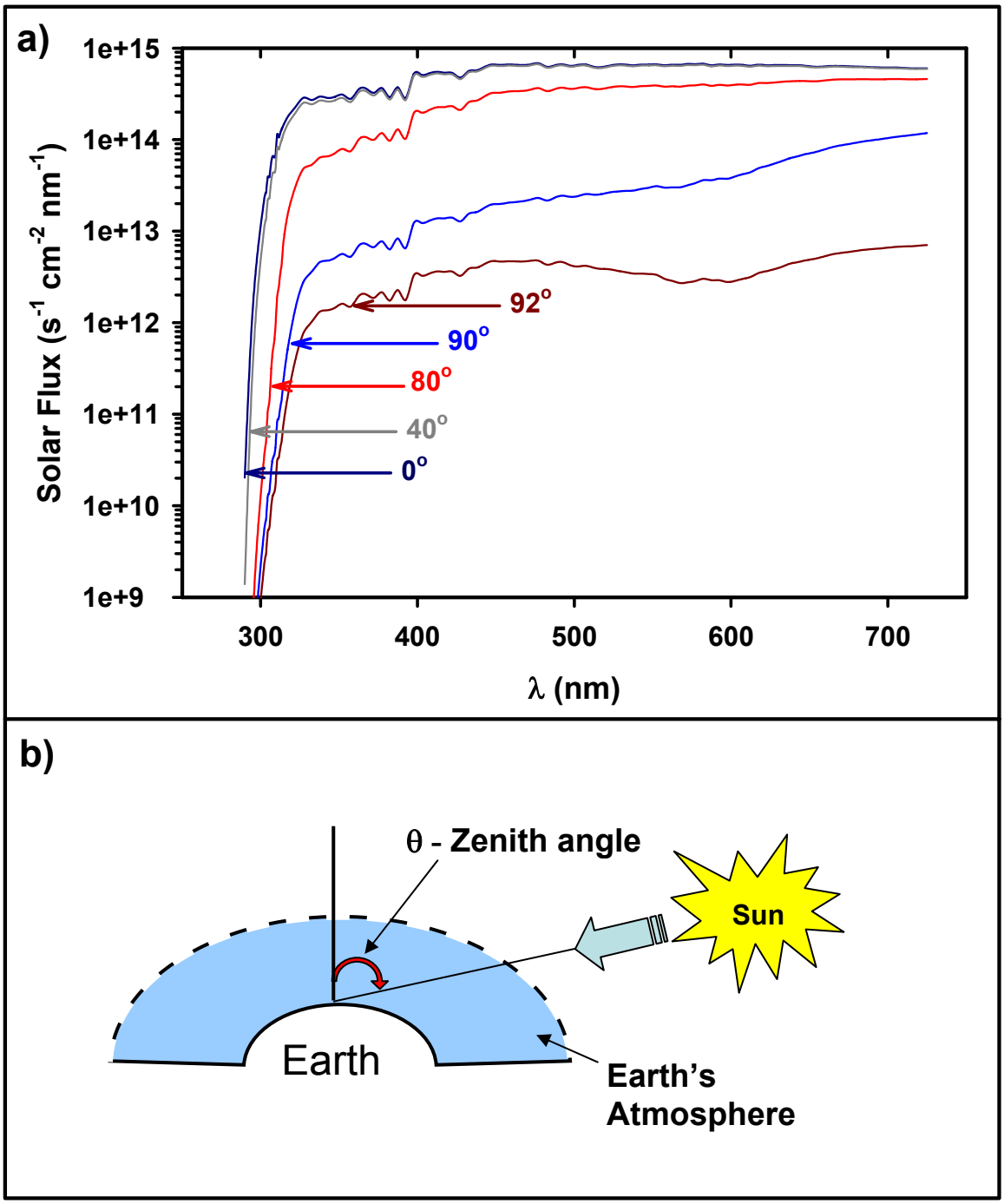

Figure 1.2: a) Solar flux as a function of wavelength measured during summertime at 0, 40, 80, 90 and 92° solar zenith angles obtained from data in Ref. 4. b) The solar zenith angle is defined as angle the sun makes with respect to the earth normal.
[File: F1.2_solar_ sza]

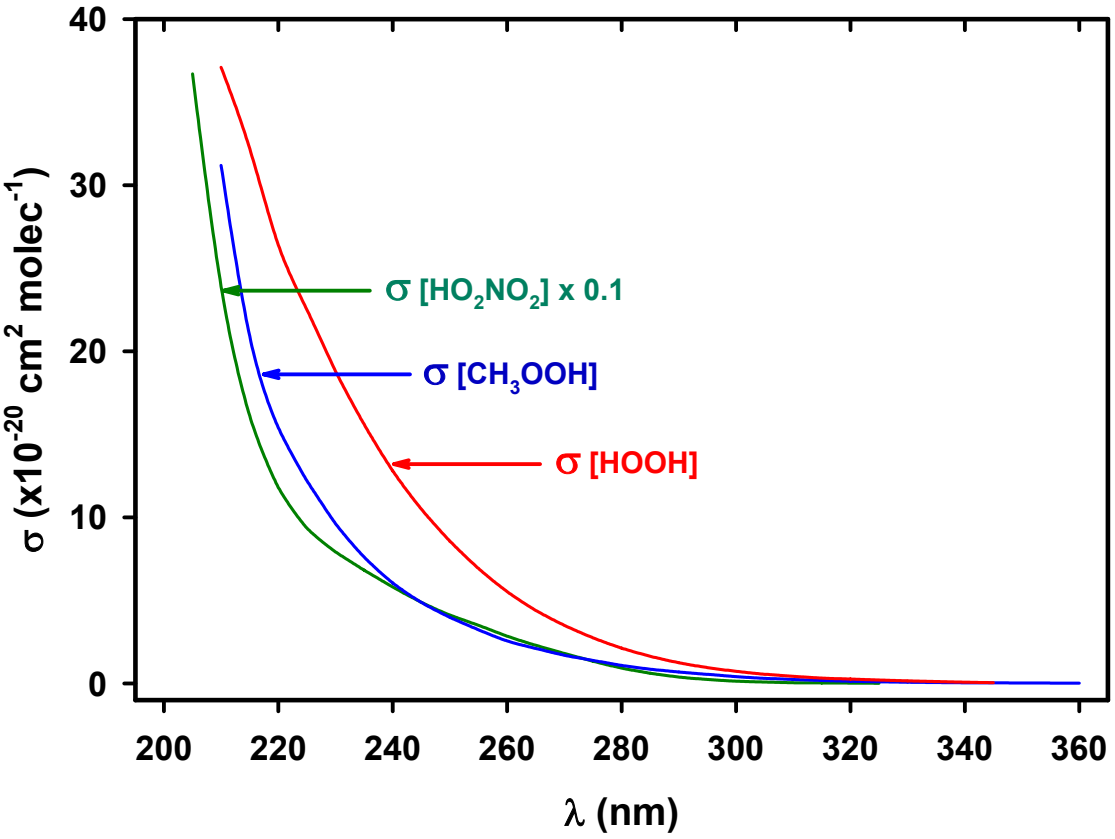

Figure 1.3: The absorption cross-sections of CH_3OOH, HOOH, and HO_2NO_2 in the UV spectral region obtained from data in Refs. 20-21. [File: F1.3_xsections]

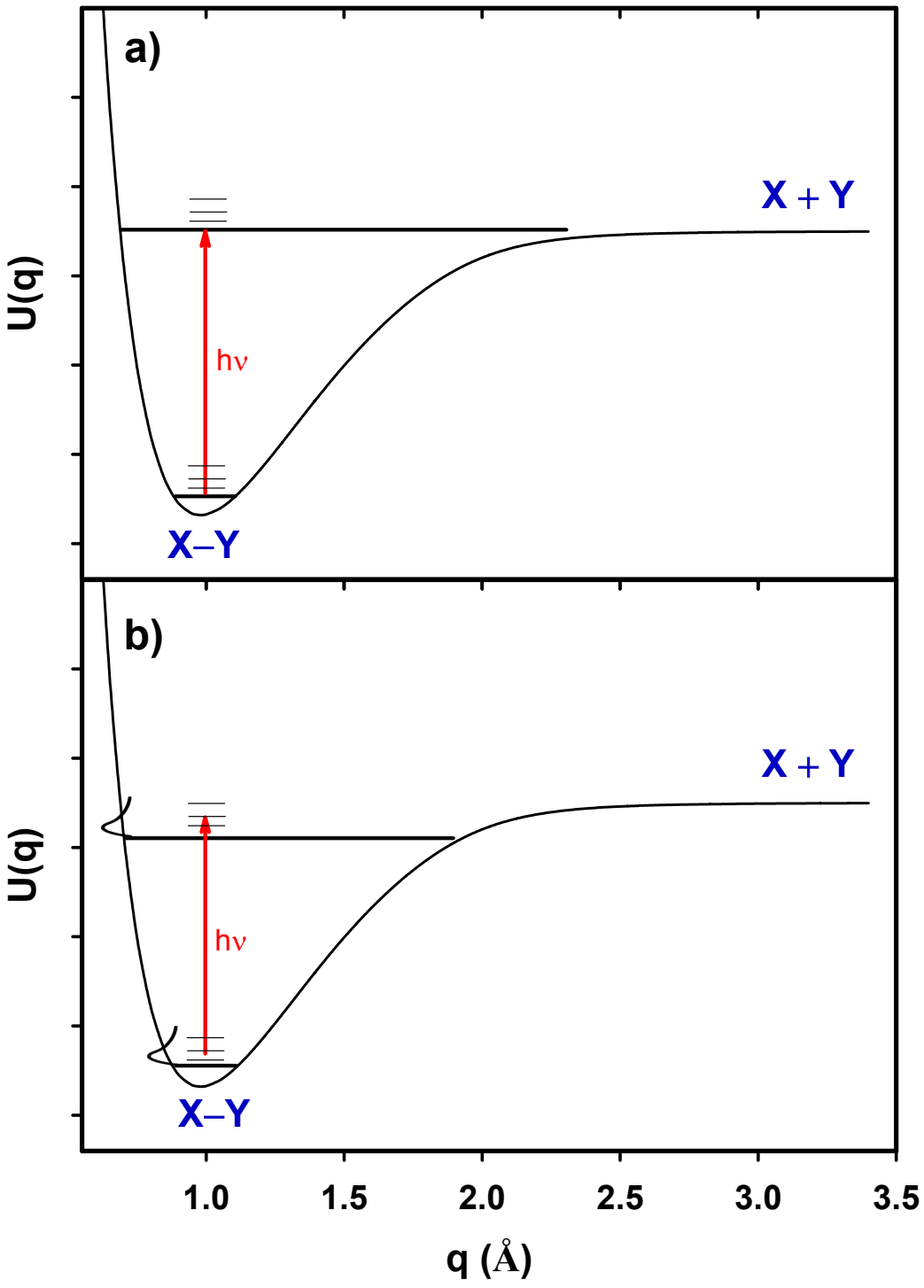

Figure 1.4: Ground state potential energy diagram depicting a) transition in which the photon energy exceeds the dissociation threshold and b) transition in which the photon energy lies below the dissociation threshold. [File: F1.4_gspotential]

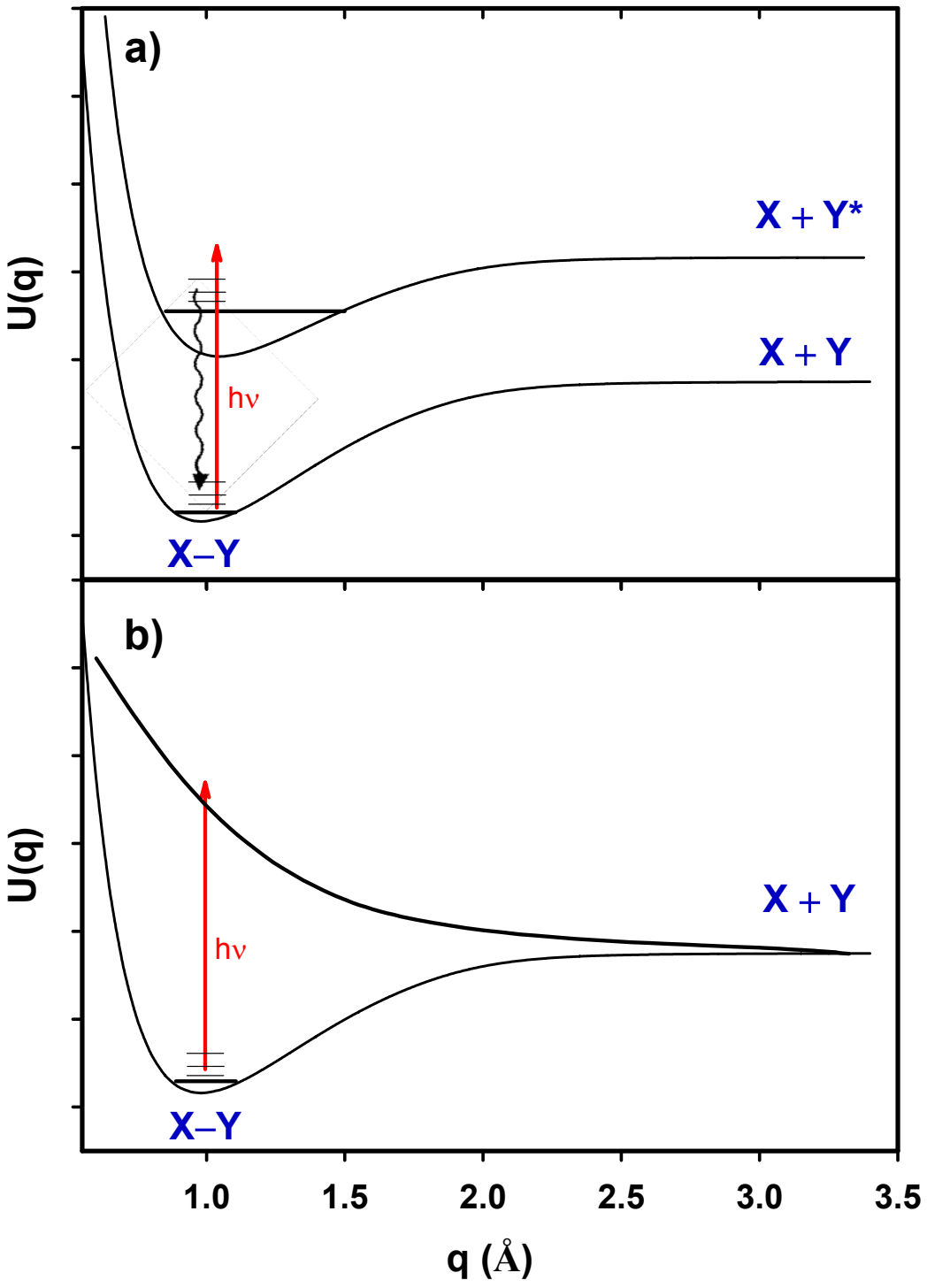

Figure 1.5: Ground and electronically excited states potential energy diagrams depicting a) transition between two bound states. The squiggly line indicates the emission of photon occurring when the electron relaxes back to its ground state. b) Transition between a bound and a repulsive state which results in prompt dissociation.
[File: F1.5_elec_potential]

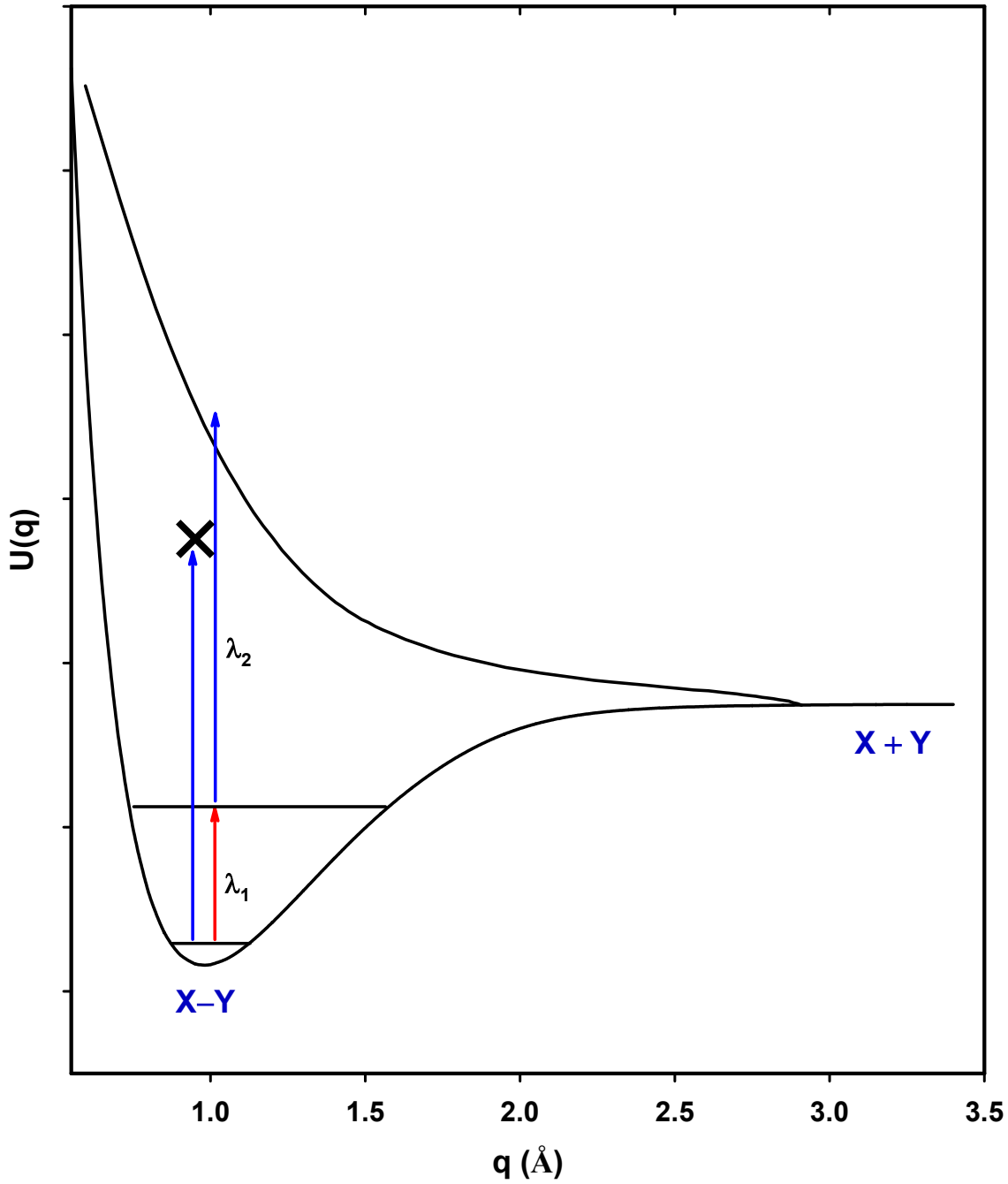

Figure 1.6: Potential energy diagrams depicting the ViMP process where initially, the molecule is vibrationally excited on its ground state (λ_1). Subsequently, the vibrationally excited molecule is excited to a repulsive excited state which results in prompt dissociation (λ_2). The dissociating photon is chosen such that direct electronic excitation from the vibrational ground state is not possible. [File: F1.6_vimp]

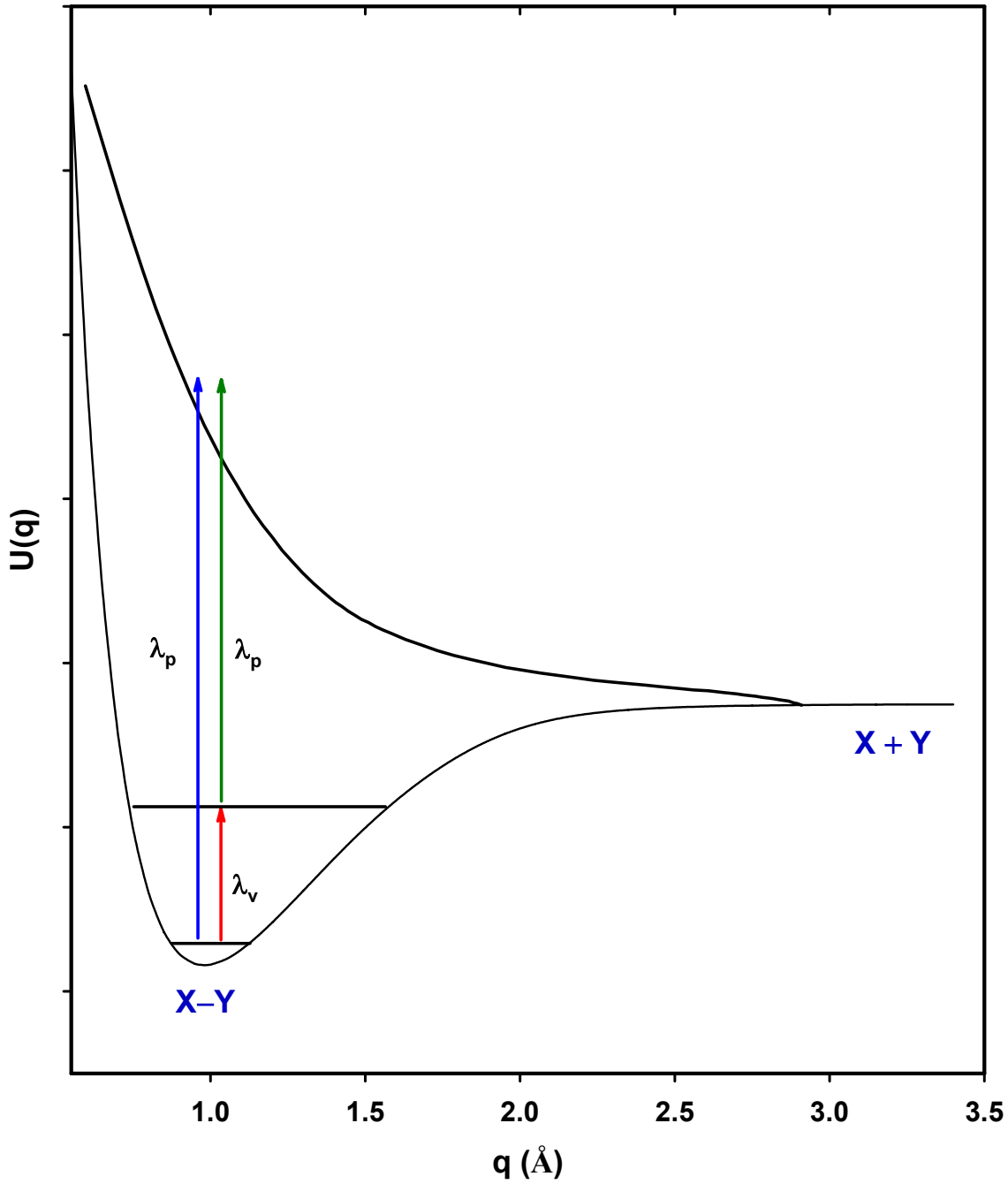

Figure 1.7: Potential energy diagrams comparing the ViMP process ($\lambda_v + \lambda_p$) with direct photolysis having *equivalent* photon energy. [File: F1.7_vimpvssingle]

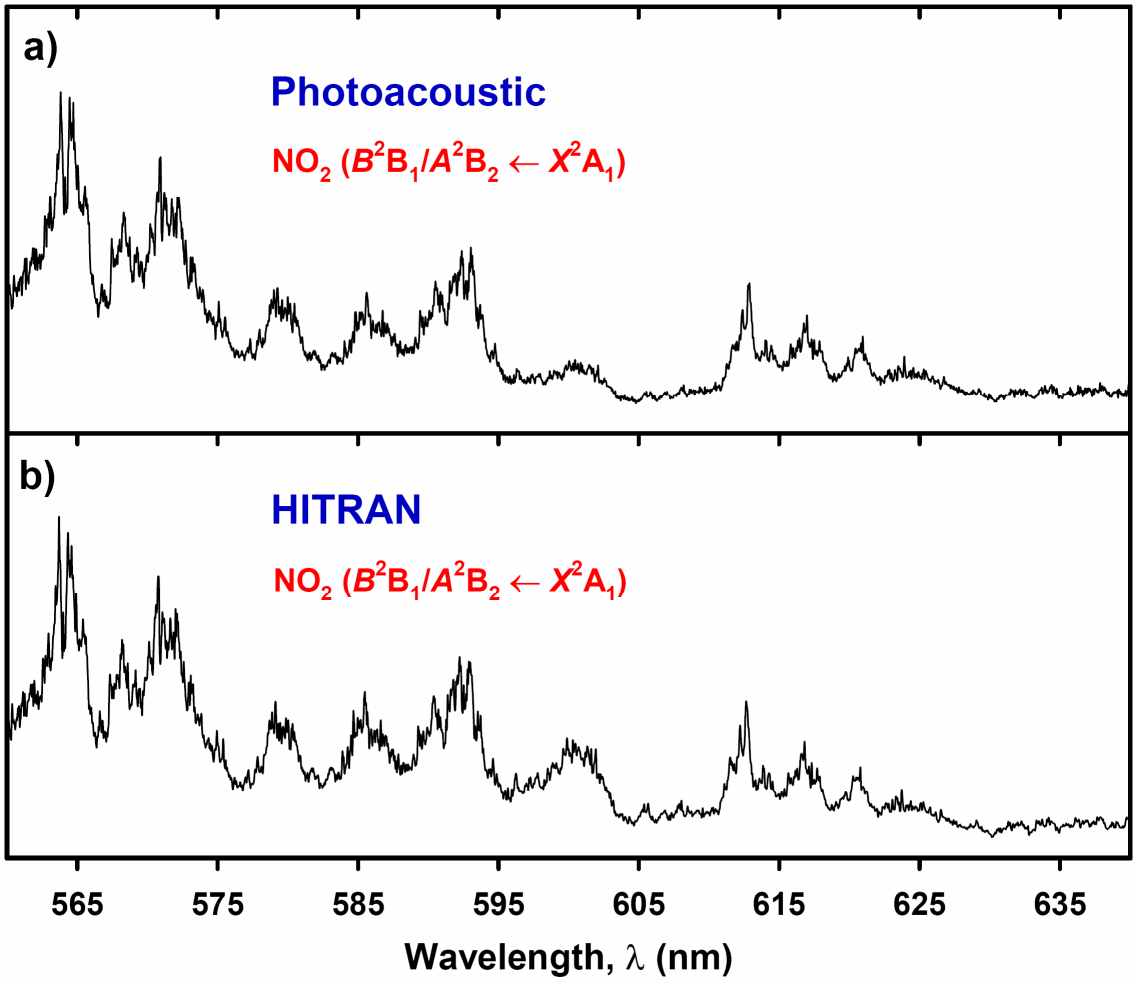

Figure 1.8: a) The absorption bands of NO_2 in the visible spectral region generated using photoacoustic spectroscopy. b) Absorption bands of NO_2 obtained from the HITRAN database.[35] [File: F1.8_NO2]

1.4 References

1. G. P. Brasseur, J. J. Orlando, and G. S. Tyndall, *Atmospheric Chemistry andGlobal Change* (Oxford University Press, New York 1999).

2. B. J. Finlayson-Pitts, J. N., Jr. Pitts, *Atmospheric Chemistry* (Wiley, New York, 1986).

3. S. P. Sander, R. R. Friedl, D. M. Golden, M. J. Kurylo, R. E. Huie, V. L. Orkin, G. K. Moortgat, A. R. Ravishankara, C. E. Kolb, M. J. Molina, B. J. Finlayson-Pitts, Chemical kinetics and photochemical data for use in stratospheric modeling, Evaluation #14, *JPL Publ.*, **02-25** (2003).

4. S. Madronich, S. Flocke, J. Zeng, I. Petropavlovskikh, and J. Lee-Taylor, Tropospheric Ultraviolet-Visible Model, version 4.1(2002). http://cprm.acd.ucar.edu/Models/TUV/Interactive_TUV/

5. R. J. Salawitch, S. C. Wofsy, P. O. Wennberg, R. C. Cohen, J. G. Anderson, D. W. Fahey, R. S. Gao, E. R. Keim, E. L. Woodbridge, R. M. Stimpfle, J. P. Koplow, D. W. Kohn, C. R. Webster, R. D. May, L. Pfister, E. W. Gottlieb, H. A. Michelsen, G. K. Yue. M. J. Prather, J. C. Wilson, C. A. Brock, H. H. Jonsson, J. E. Dye, D. Baumgardner, M. H. Proffitt, M. Loewenstein, J. R. Podolske, J. W. Elkins, G. S. Dutton, E. J. Hintsa, A. E. Dessler, E. M. Weinstock, K. K. Kelly, K. A. Boering, B. C. Daube, K. R. Chan, S. W. Bowen, Geophys. Res. Lett. **21**, 2551 (1994).

6. P. O. Wennberg, R. J. Salawitch, D. J. Donaldson, T. F. Hanisco, E. J. Lanzendorf, K. K. Perkins, S. A. Lloyd, V. Vaida, R. S. Gao, E. J. Hintsa, R. C. Cohen, W. H. Swartz, T. L. Kusterer, D. E. Anderson, Geophys. Res. Lett. **26**, 1373 (1999).

7. C. M. Roehl, S. A. Nizkorodov, G. H. Zhang, A. Blake, P. O. Wennberg, J. Phys. Chem. A. **106**, 3766 (2002).

8. L. Jaegle′, D. J. Jacob W. H. Brune, I. Faloona, D. Tan, B. G. Heikes, Y. Kondo, G. W. Sachse, B. Anderson, G. L. Gregory, *et al.*, J. Geophys. Res. **105**, 3877 (2000).

9. D. Kley, Science **276**, 1043 (1997).

10. R. B. Chatfield, and P. J. Crutzen, J. Geophys. Res. **89**, 7111 (1984).

11. P. J. Crutzen, *Pure Appl. Geophys.* **106**, 1385 (1973).

12. J. A. Logan, M. J. Prather, S. C. Wofsy, M. B. McElroy, *J. Geophys. Res.* **86**, 7210 (1981).

13. P. S. Monks, *Chem. Soc. Rev*. **34**, 376 (2005).

14. D. J. Donaldson, G. J. Frost, K. H. Rosenlof, A. F. Tuck, V. Vaida, Geophys. Res. Lett. **24**, 2651 (1997).

15. D. J. Donaldson, J. J. Orlando, S. Amann, G. S. Tyndall, R. J. Proos, B. R. Henry, V. Vaida, J. Phys. Chem. A **102**, 5171 (1998).

16. D. J. Donaldson, A. F. Tuck, V. Vaida, Phys. Chem. Earth C **25**, 223 (2000).

17. M. J. Prather, and D. J. Jacob, Geophys. Res. Lett. **24**, 3189 (1997).

18. L. Jaegle′, D. J. Jacob, P. O. Wennberg, C. M. Spivakovsky, T. F. Hanisco, E. J. Lanzendorf, E. J. Hinsta, D. W. Fahey, E. R. Keim, M. H. Proffitt, *et al.*, Geophys. Res. Lett. **24**, 3181 (1997).

19. F. Ravetta, D. J. Jacob, W. H. Brune, B. G. Heikes, B. E. Anderson, D. R. Blake, G. L. Gregory, G. W. Sachse, S. T. Sandholm, R. E. Shetter, *et al.*, *J*. Geophys. Res.-Atmos. **106(D23)**, 32709 (2001).

20. G. L. Vaghjiani, and A. R. Ravishankara, J. Geophys. Res. **94(D3)**, 3487 (1989).

21. G. Knight, A. R. Ravishankara, J. B. Burkholder, Phys. Chem. Chem. Phys. **4**, 1432 (2002).

22. D. J. Nesbitt and R. W. Field, J. Phys. Chem. **100**, 12735 (1996).

23. R. L. Vander Wal, J. L. Scott, and F. F. Crim, J. Chem. Phys. **94**, 3548 (1991).

24. R. J. Barnes, G. Dutton, and A. Sinha, J. Phys. Chem. A. **101**, 8374 (1997).

25. M. J. Cox, and F. F. Crim, J. Phys. Chem. A **109**, 11673 (2005).

26. A. Sinha, M. C. Hsiao, and F. F. Crim, J. Chem. Phys. **94**, 4928 (1991).

27. R. J. Holiday, C. H. Kwon, C. J. Annesley, and F. F. Crim, J. Chem. Phys. **125**, 133101 (2006).

28. T. M. Ticich, M. D. Likar, H. –R. Dübal, L. J. Butler, F. F. Crim, J. Chem. Phys. **87**, 5820 (1987).

29. P. J. Robinson and K. A. Holbrook, *Unimolecular Reactions* (Wiley, New York, 1972).

30. I. N. Levine, *Quantum Chemistry, 5th ed.* (Prentice Hall, New Jersey 2000).

31. P. W. Atkins, *Molecular Quantum Mechanics, 2nd ed*. (Oxford University Press, Oxford 1983).

32. H. G. Kjaergaard, B. R. Henry, J. Chem. Phys. **96**, 4841 (1992).

33. F. F. Crim, Annu. Rev. Phys. Chem. **44**, 397 (1993).

34. F. F. Crim, J. Phys. Chem **100**, 12725 (1996).

35. L. S. Rothman *et al*., J. Quant. Spectrosc. Radiat. Transfer **82,** 5 (2003).

Chapter 2

Photodissociation of Vibrationally Excited Pernitric Acid: HO_2NO_2 ($2\nu_1$) + 390 nm

2.1 Introduction

Peroxynitric acid (PNA, HO_2NO_2) is formed in the atmosphere via a three-body recombination reaction involving the HO_2 and NO_2 radicals and, hence, provides a temporary reservoir for these species.[1] As discussed in Chapter 1, its removal from the atmosphere occurs predominantly by oxidation with OH radical, and direct photodissociation by photon absorption. The relatively weak HO_2─NO_2 bond strength implies that PNA molecules can be dissociated not only via the absorption of UV photons on a repulsive excited electronic state, but also through unimolecular dissociation initiated by overtone excitation on its ground electronic surface.[2,3]

From thermochemical data,[4] it is estimated that threshold energies for opening the lowest energy $HO_2 + NO_2$ product channel from bond fission to be ~8110 cm^{-1} and the threshold for opening the $HO + NO_3$ channel is much higher at ~13 780 cm^{-1}. In the next dissertation chapter, high-level *ab initio* study using CCSD(T) basis set limit extrapolation is used to estimate the bond dissociation energies of the $HO_2 + NO_2$ and $HO + NO_3$ channels. The difference between the threshold energy for opening the $HO_2 + NO_2$ channel ($D_0[HO_2 + NO_2]$ = 8110 cm^{-1}), and the band center for exciting the first ($2\nu_1$) OH stretching overtone of PNA (6910 cm^{-1}),[5] suggests that unimolecular dissociation can occur upon excitation to the $2\nu_1$ level only with the assistance of

substantial thermal energy. At room temperature, the average internal thermal energy (vib. + rot.) of PNA is estimated to be 700 cm^{-1}, where $E_{vib} \approx 390$ cm^{-1} and $E_{rot} \approx 310$ cm^{-1}. Thus, only states associated with the high-energy tail of the Boltzmann distribution have sufficient energy to make up the ~1200 cm^{-1} energy deficit required to open the $HO_2 + NO_2$ pathway. Appendix *D* contains the Mathematica code used in evaluating the average thermal energy associated with PNA sample at room temperature with parameters given in Ref. 6. Roehl *et al.* have investigated the quantum yield for unimolecular dissociation of PNA upon excitation to several vibrational levels in the vicinity of the $2\nu_1$ band as a function of temperature and pressure.[7] They find that at 295 K, the quantum yield for unimolecular dissociation for the $2\nu_1$ band is ~27 % and is independent of pressure over the 2 – 40 Torr range used in the study.[7]

The UV absorption spectrum of PNA has been investigated by several groups and consists of a broad absorption feature between 190 and 360 nm (see Fig. 1.3).[4,8,9] *Ab initio* calculations[10] suggest the presence of two excited singlet electronic states in the near UV region both of which are dissociative along the HO_2─NO_2 and the HO─ONO_2 coordinates. The first excited singlet state, 2^1A, is located 5.05 eV above the ground state while the second is at 5.52 eV. Quantum yield measurements from the photodissociation of PNA have been investigated at 248 nm and indicate that the primary channels are those associated with the formation of OH and HO_2 photofragments:[10]

$$HO_2NO_2 \rightarrow OH + NO_3 \ (34\%) \qquad (2.1a)$$

$$HO_2 + NO_2 \ (56\%) \qquad (2.1b)$$

The quantum yields for the above two channels were determined respectively by measuring the *total yield* of OH and NO_2 fragments resulting from 248 nm photolysis and

thus, do not preclude the possibility that some of the fragments shown in the above equations are formed in excited electronic states. In fact emission from electronically excited NO_2 has been reported in the 248 nm photodissociation study of Macleod *et al.* [11]

This dissertation chapter presents results of vibrationally mediated photodissociation (ViMP) experiments used to selectively excite and investigate the dissociation dynamics and photochemistry of PNA. Figure 2.1 illustrates the approach used in these ViMP experiments. As discussed below, comparing vibrational band intensities of PNA appearing in the ViMP action spectra with their known total integrated infrared absorption cross-sections provides a means for estimating the unimolecular dissociation quantum yields of the bands in the absence of collisions.

2.2 Experiment

2.2.1 Experimental Apparatus

As shown in Figure 2.1, the experimental excitation-detection pump-pump-probe scheme requires three laser systems. Infrared light (λ_1) is used to vibrationally state-select PNA molecules by excitation in the vicinity of the $2\nu_1$ band. The vibrationally excited molecules are subsequently dissociated by promotion to an electronic excited state using a second photon at ~390 nm (λ_2). Finally, the OH fragments resulting from the photodissociation are probed by laser-induced fluorescence with a third laser (λ_3). Thus the effective total energy the PNA molecule is pumped with corresponds to equivalent single photon excitation energy of ~307 nm.

The experimental apparatus used in the investigation of HO_2NO_2 is shown in Figure 2.2. Infrared radiation (λ_1) for exciting the first OH stretching overtone of PNA

($2\nu_1$ and $3\nu_1$) is generated by the OPO laser system. The idler beam from the OPO laser provides the required tunable radiation between 6600 – 11 000 cm^{-1} with a bandwidth of ~0.4 cm^{-1} and pulse energies ranging from 4 – 6 mJ and 9 – 12 mJ in the $2\nu_1$ and $3\nu_1$ regions respectively. The $4\nu_1$ band is examined by generating tunable infrared radiation from a dye laser operating with LDS-765 dye and pumped by the NY82-20 laser. Typical pulse energies range from 18 – 22 mJ. Radiation at ~390 nm for exciting the electronic transition in the second step of the double resonance (λ_2) is generated by frequency mixing the visible output of the same dye laser system operating with R-640 dye and the fundamental of the Nd:Yag laser. Typical output pulse energies from the mixing process range between 8 and 10 mJ.

The resulting OH photofragments in the ViMP excitation are probed via the *A–X* transition at ~308 nm using laser-induced fluorescence (LIF). The 308 nm radiation, which has a bandwidth of 0.17 cm^{-1}, is generated by frequency doubling the output of the NY81-20 dye laser system operating with DCM dye. The probe and photolysis laser beams are combined on a dichroic mirror and directed into the photolysis cell after passing through a collimating lens system. The vibrational excitation lasers propagates counter to the other two beams and is focused into the center of the cell using a 400 mm lens.

For some of the Doppler profile measurements, the probe laser is introduced orthogonal to the other two beams. The time delay between λ_1 and λ_2 is typically fixed at 20 ns, although for experiments probing the unimolecular dissociative lifetime of the vibrational states, this delay is varied between 7 and 50 ns. The probe laser pulse (λ_3)

typically occur ~ 80 ns after the OPO (λ_1) and its intensity is greatly attenuated in order to avoid saturation of the OH transitions as well as prevent photolysis of the PNA. The OH fluorescence excited by the probe laser is collected using an f/1 lens system and imaged onto an end-on photomultiplier (EMI 9635QB). The combination of a color glass filter (Schott UG-11), a 308 nm interference filter, and a 355 nm edge filter located in front of the photomultiplier provides discrimination against scattered laser light. For detection of NO_2 fluorescence the Schott UG-11 color glass filter is replaced with a GG-420 filter and the 308 nm interference and edge filters are removed. Signal from the PMT is sent to a gated charge integrator (LeCroy, 2249SG ADC) and subsequently digitized and passed to a laboratory computer for storage and analysis.

2.2.2 PNA Synthesis

We generate HO_2NO_2 (PNA) in a manner similar to that described in the literature using the following reaction scheme: [8,12]

$$H_2O_2 + BF_4NO_2 \rightarrow HO_2NO_2 + HF + BF_3 \qquad (2.2)$$

Due to the danger associated with generation of hydroperoxides and their by-products, extreme caution must be exercised when mixing the reagents. 5 mL of H_2O_2 (~90%) is kept in a jacketed glass tube maintained at -13^0C using a chiller circulating 1:1 ethylene glycol-water mixture. Since the BF_4NO_2 (Acros, AC17438-0050) solid is highly hydroscopic, ~2 g of BF_4NO_2 solid is initially transferred to a pre-weighed small, capped glass container in a glove bag purged with dry nitrogen. The H_2O_2 is *slowely* added dropwise to the solid. The resulting bursts of brown and white fumes, by-products of the reaction are allowed to escape from the synthesis flask before dropping more of the solid. After adding all the H_2O_2 into the synthesis tube over a period of ~20 minutes, the

synthesis tube is capped, removed from the glove bag and cooled down further to –17° C. The sample tube is then pumped-on to remove volatile species such as N_2, NO_2 and $HONO_2$. During the experimental runs the chiller maintains temperatures ranging from –13 to –10° C which regulates the partial pressure of HO_2NO_2 in the sample cell. The HO_2NO_2 sample is slowly flowed into the photolysis cell and under normal operating conditions, although the sample reservoir is kept cold, the photolysis cell is at room temperature and typically, operating pressures range between 80 and 100 mTorr.

All components coming in contact with the reagent prior to entering the photolysis cell are made of either glass or Teflon in order to minimize loss of PNA. Under these operating conditions, the PNA samples last about 7 to 10 days before requiring replacement. Concentrated H_2O_2 used in the synthesis is prepared by bubbling N_2 through a 50% H_2O_2 (Fisher, H341-500) solution over a period of several days in order to remove the more volatile water component; the final H_2O_2 concentration is estimated by noting its volume change.

2.3 Results and Discussion

2.3.1 Sample Analysis, HOONO Formation and Action Spectra of HO_2NO_2

As a first step, prior to using the ViMP technique to investigate the photochemistry of PNA, the influence of infrared excitation (λ_1) alone is examined on the sample. The right side of Figure 2.1 illustrates the bond fission pathways associated with the dissociation of HO_2NO_2 (PNA) and their corresponding threshold energies. As noted above, in these room temperature measurements the initial thermal energy associated with the high energy tail of the Boltzman distribution combined with the $2\nu_1$ photon energy, is sufficient for opening the $HO_2 + NO_2$ pathway. By contrast the $OH + NO_3$

channel is not accessible at these vibrational excitation energies. Thus based on energetics it is not expected that OH fragments will be generated solely from the infrared excitation of PNA in the $2\nu_1$ spectral region.

In actual fact, a freshly prepared PNA samples do give rise to OH signal when exposed to infrared radiation tuned to the vicinity of the $2\nu_1$ vibration. Monitoring the yield of the OH fragments using the $Q_1(2)$ transition, for example, while scanning the wavelength of the infrared excitation laser (λ_1) at 0.008 nm/s and averaging 20 shots/bin, generates an action spectrum like the one shown in Figure 2.3(a). This signal is due to OH fragment generated through the unimolecular dissociation of HOONO impurity present in the PNA sample. Not only is the thermochemistry for opening the HOONO → OH + NO_2 ($D_0 \approx 19.8$ kcal/mol) [13, 14] consistent with the energy associated with the $2\nu_1$ excitation, but also the band centers of the four primary spectral features observed in Fig. 2.3(a) match up with those reported in Ref. 15 for HOONO generated using the three-body recombination reaction OH + NO_2 + M → HOONO + M shown in Fig. 2.3(b).

The HOONO signal from the PNA source remains strong only for the first one to two days of use of a freshly prepared PNA sample, suggesting that it is rather volatile and disappears following extended pumping. Prior studies have not reported detecting HOONO impurity in their PNA samples,[4,5,7-9] although it is clear that its presence can potentially interfere with the study of PNA photochemistry. All experiments on PNA reported below are conducted after the OH signal from HOONO ($2\nu_1$) reached negligible levels.

After eliminating the HOONO interference the influence of infrared excitation on PNA sample is probed. As expected on the basis of known thermochemistry and also by

prior measurements, the $0 \rightarrow 2\nu_1$ excitation of PNA leads to opening the $HO_2 + NO_2$ pathway. The production of HO_2 is verified by conducting the infrared excitation experiments in the presence of added NO. The addition of NO initiates the following reaction with the HO_2 photofragments:

$$HO_2 + NO \rightarrow OH + NO_2 \quad (k = 8.6 \times 10^{-12}\ cm^3\ molecule^{-1}\ s^{-1}) \qquad (2.3)$$

To detect the OH fragment, the delay between the overtone excitation laser and probe laser is increased from 20 to 11 000 ns to allow sufficient reagent reaction time. The OH fragments are then detected by LIF. Thus, the above reaction provides a convenient, although indirect, means for monitoring the formation of HO_2 photofragments. Figure 2.4(a) displays a vibrational overtone action spectrum of HO_2NO_2 over the region of the $0 \rightarrow 2\nu_1$ transitions obtained by this method where the resulting OH molecules are monitored using the $Q_1(2)$ transition. Comparing Fig. 2.3(a) and Fig. 2.4(a), it is clear that although the HOONO and HO_2NO_2 spectra are distinct, there are substantial regions of overlap in the vicinity of their respective $2\nu_1$ bands. Consequently care must be taken in order to avoid excitation of the unwanted species.

Using the NO titration reaction, it is also possible to obtain overtone spectra for the $3\nu_1$ and $4\nu_1$ bands shown in Figs. 2.4(b) and 2.4(c) respectively. These spectra are generated by tuning the infrared light over the region shown and allowing sufficient time for the HO_2 to convert in the presence of NO to OH while monitoring the $Q_1(2)$ transition. The bands in the spectra appear to be broad and featureless with small shoulders lying to the blue of the main band. This shoulder is likely due to the combination band involving the OH-stretch/HOON-torsion in PNA ($\alpha\nu_1 + \nu_{12}$ with $\alpha =$

2, 3 and 4). The bands structure and position are consistent with those reported in Refs. 5 and 7. From the bands position reported here a Birge-Sponer plot associated with excitation of the OH-stretching modes of PNA is constructed and as shown in figure 2.5. From the plot, the mechanical frequency, ω_0, is found to be 3628 cm^{-1} and the mechanical anharmonicity, $\omega_e\chi_e$, is found to be -88 cm^{-1}. The fact that the overtones are aligned on the diagonal line in Fig. 2.5 suggests that the bands are not strongly perturbed by interactions with other vibrational modes in PNA although these interactions, if present, would appear more noticeably under molecular beam conditions.

After examining the overtone spectra from the $2\nu_1 - 4\nu_1$ vibrational levels we focused on the ViMP experiments. In these measurements, vibrationally excited PNA molecules to the $2\nu_1$ level by the OPO (λ_1) are subsequently promoted to an electronic excited state using ~390 nm light (λ_2) (see Fig. 2.1). The choice of wavelength for λ_2 is dictated by a desire to maximize the ViMP signal from PNA while minimizing background signal initiated by λ_2 alone. In particular, the absorption cross-section of both $HONO_2$ and HOOH is weak at 390 nm and NO_2 is not expected to fluoresce when excited at this wavelength as it leads to dissociation.

One advantage of this experimental approach is that the excited electronic state of PNA naturally gives rise to OH fragments,[11] and hence it is not necessary to add nitric oxide in order to record a vibrational action spectrum. Figure 2.6(b) shows a vibrational overtone action spectrum of HO_2NO_2 ($2\nu_1$) obtained using the ViMP technique. The spectrum is generated by scanning λ_1 while monitoring the yield of OH photofragments using the $Q_1(4)$ transition. Action spectra generated by monitoring yields of other OH

rotational states give similar results. While the feature at 7075 cm^{-1} is due to hydrogen peroxide (see Chapter 9), the combination of λ_1 and λ_2 effectively prevents HNO_3 species from contributing at these wavelengths. Thus, by tuning λ_1 to ~6910 cm^{-1}, the peak of PNA $2\nu_1$ band, and subsequent photolysis of the vibrationally excited molecules using 390 nm light, the near UV photochemistry of PNA can be investigated without interferences. Recall that the combination of $2\nu_1$ + 390 nm corresponds to an effective single photon excitation of ~307 nm (see Fig. 1.3).

2.3.2 Lifetime of Vibrationally Excited HO_2NO_2 ($2\nu_1$) Molecule

Another aspect of the PNA vibrationally mediated action spectra that can be examined is whether they change as the time delay between λ_1 and λ_2 is varied. By varying this time delay the lifetime distribution of those states of the $2\nu_{OH}$ vibrational band that have sufficient energy to undergo unimolecular dissociation on the ground electronic surface can be probed. For a given time delay (Δt) between λ_1 and λ_2, only ro-vibrational states that *do not* undergo unimolecular dissociation during Δt can subsequently interact with λ_2 and produce OH photofragements through promotion to the repulsive electronic excited state. Thus, action spectra of these predissociative vibrational states taken under different time delay settings may exhibit different intensity distributions. The ViMP action spectrum presented in Figure 2.6(b) corresponds to Δt = 25 ns, and we find that the spectrum does not change noticeably as Δt is reduced to ~7 ns, the temporal resolution limit of our laser system. Thus, these room temperature measurements suggest that the majority of PNA states that undergo unimolecular dissociation upon excitation through the $0 \rightarrow 2\nu_1$ band, apparently do so on a time scale

much faster than ~7 ns. This observation is consistent with the lack of pressure dependence reported in the quantum yield measurements of Roehl *et al.* over the 2 − 40 Torr range.[7]

Also, note that the width of the $2\nu_1$ band generated by monitoring HO_2 formation by the addition of NO (Fig. 2.6(a)) is broader than that obtained using the ViMP excitation (Fig. 2.6(b)). This is likely due to the fact that action spectra generated by monitoring unimolecular reaction is biased (due to energy constraint) in favor of states in the $2\nu_1$ band with high internal energy while the action spectra generated by state selected electronic photodissociation are expected to be equally sensitive to all the states of $2\nu_1$ that *do not* undergo unimolecular dissociation.

2.3.3 OH + NO_3 Channel Product State Distribution and Translational Energy Release

Using sub-Doppler resolution, the energy disposal for the OH + NO_3 channel resulting from the ViMP photodissociation of PNA are determined. Taking into account the photon energies associated with λ_1 and λ_2, the average thermal energy in PNA (700 cm^{-1}) and the bond energy for opening the OH + NO_3 channel (13 780 cm^{-1}), the available energy associated with this dissociation pathway is estimated to be ~19 500 cm^{-1}. By scanning the probe laser in BURST mode using 5 μstep and 30 shots / bin (see Appendix *A*) over the rotational transitions of the OH fragment's *A*–*X*(0,0) band and examining both their intensity and Doppler linewidths, we find that 470 cm^{-1} of the available energy goes into rotational and 8420 cm^{-1} into translational excitation of the OH fragment. The nascent OH energy disposal results are shown in Figure 2.7. Within our detection limit, we do not observe any vibrationally excited OH fragment. Applying

momentum and energy conservation, we infer that the partner NO_3 fragment receives ~2310 cm^{-1} of translational and ~8250 cm^{-1} of internal excitation. The amount of internal energy available for NO_3 is insufficient to form in its electronic excited state. Product state distributions and linewidth analysis preformed in this chapter are explained in further details in Appendix *C*. Table 2.1 gives summary of the energy partitioning associated with the OH + NO_3 channel.

2.3.4 Direct Detection of the HO_2 + NO_2* Channel: $2\nu_1$ Quantum Yields Estimates

Obtaining detailed information regarding energy disposal for the HO_2 + NO_2 pathway in is difficult. However, substantial amount of the NO_2 fragments are generated in electronic excited states from the ViMP process. This is confirmed by recording an action spectrum that monitors the total visible fluorescence (400 – 640 nm) as a function of λ_1 with λ_2 fixed at 390 nm (see Fig. 1.8 for NO_2 bands in the visible spectral region). Figure 2.6(c) shows an action spectrum obtained by this method. The signal to noise ratio in this spectra is considerably better than that obtained by monitoring OH fragments in a single quantum state. In fact, taking into account the photomultiplier response, filter transmissions and relative fluorescence signals from NO_2 versus OH, it is estimated that the HO_2 + NO_2 channel is at least ~10 times more favored over the OH + NO_3 channel at these excitation energies. This is to be compared with the results at 248 nm, where the yield of the HO_2 + NO_2 channel is ~2 times that of the OH + NO_3 channel.[10]

The improved signal to noise associated with monitoring the NO_2 fluorescence in these experiments permits detection of relatively weak vibrational bands such as the ν_1 + $2\nu_3$ combination band (involving O-H stretch and OOH bend) located at 6250 cm^{-1}. By detecting this lower energy combination band it is relatively simple to compare the

integrated intensities of the $\nu_1 + 2\nu_3$ and $2\nu_1$ bands with their known integrated infrared absorption cross sections and to estimate the quantum yield for unimolecular dissociation associated with the $2\nu_1$ state.

As noted above, Roehl *et al.* have determined the quantum yield for unimolecular dissociation of several near threshold vibrational levels of PNA as a function of temperature and pressure by comparing the relative yield of HO_2 fragments from these levels with those from the much higher energy $3\nu_1$ band, whose dissociation quantum yield they assumed to be unity.[7] Their experiments relied on using the HO_2 + NO titration reaction to convert HO_2 photofragments to OH for the purposes of monitoring HO_2 fragment yields and, thus, were conducted under conditions of high pressure (>2 Torr).

The present experiments provide a complementary method for estimating the unimolecular dissociation quantum yields at low pressure (70 - 80 mTorr) in the absence of collisions and without requiring nitric oxide. This is accomplished by noting that the integrated signal intensity, S^i, for the i-th vibrational band appearing in the ViMP spectrum is directly proportional to the product of the following factors:

$$S^i \propto n_0 \times \sigma^i_{IR} \times f^i_S \times \sigma^i_{UV} \times \sigma^i_{EM} \qquad (2.4)$$

In the above expression n_0 is the number density of PNA molecules in the excitation volume, σ_{IR} is the bands integrated infrared absorption cross section, f_S is the *fraction of vibrationally excited molecules that survive* and *do not* undergo unimolecular dissociation, σ_{UV} is the cross-section for absorption of UV light by these vibrationally excited molecules and σ_{EM} is their cross section for producing electronically excited NO_2.

Since excitation to the first excited singlet electronic state of HO_2NO_2 involves an $n \rightarrow \pi^*$ transition that is primarily localized on the NO_2 chromophore, [10] the Franck-Condon factors associated with electronic excitation are likely to be most sensitive to initial vibrational motion in the parent molecule involving the NO_2 moiety. Since the $2\nu_1$ and $\nu_1 + 2\nu_3$ vibrations involve primarily motion on the OH-stretch/HOO-bend portion of PNA, these states are likely to have comparable Franck-Condon factors. In addition, as the OH stretching state is the "bright" state in overtone spectroscopy, it is likely that the intensity of the $\nu_1 + 2\nu_3$ combination band arises from mixing of this state with the "bright" $2\nu_1$ state.[16] This is also consistent with the fact that stretch-bend coupling is very common in many other molecules.[17] Thus, assuming that state mixing is strong in vibrationally excited PNA, excitation of these vibrational spectral features having comparable energies are expected, on average, to differ little with regards to either their ability to absorb λ_2 or in their propensity for producing excited NO_2 fragments upon vibrationally mediated photodissociation; hence, they will have similar values for σ_{UV} and σ_{EM}.

Strong state mixing and concomitant statistical behavior also seem reasonable given that the vibrational state density of PNA at energies corresponding to $2\nu_1$ is ~ 10^3 states/cm^{-1} based on Whitten–Rabinovitch density of vibrational states calculations (see Appendix *D*).[18] Hence, under these conditions taking the ratio of integrated intensities of two spectral features in the action spectra, S^i and S^j, gives:

$$(S^i/S^j) \approx (\sigma^i_{IR}/\sigma^j_{IR}) \times (f^i_S/f^j_S) \qquad (2.5)$$

Thus, if the total integrated infrared absorption cross sections are known, then one can determine the unimolecular dissociation quantum yield of one vibrational level relative to another. In PNA the $\nu_1 + 2\nu_3$ band is lower in energy compared to the $2\nu_1$ band by about 650 cm^{-1}, and its unimolecular dissociation quantum yield is observed to be negligible due to energy constraints. In fact, the data of Roehl *et al.* show that the unimolecular dissociation quantum yield for the $\nu_1 + 2\nu_3$ band is ~6 % at room temperature (implying that f^j_S=0.94).[7] Consequently we use the $\nu_1 + 2\nu_3$ band as our reference state and take f^j_S ≈1 for this combination band. Using the experimentally determined integrated intensity ratio for the $\nu_1 + 2\nu_3$ and $2\nu_1$ bands (found to be: 0.041 from the action spectra), and their corresponding integrated infrared absorption cross-sections ($2\nu_1$: 9.5×10^{-19} and $\nu_1+2\nu_3$: 2.7×10^{-20} cm molecule),[6] we estimate f^j_S for the $2\nu_1$ band to be ~70%. Hence, at room temperature dissociation quantum yield for the $2\nu_1$ state is ~30 ± 5 %.

The extent to which the relative UV absorption of the two vibrational levels change with λ_2 is also examined by carrying out separate experiments using λ_2 = 367 nm. Consistent with the assumption that the two vibrational levels exhibit similar behavior in the second step of the double resonance excitation, the vibrational band intensity ratio did not change when λ_2 was changed from 390 to 367 nm. In addition, power dependence studies involving the λ_1 laser, that the vibrational band intensity ratio is not affected by saturation of the infrared transitions of the stronger $2\nu_1$ band. Our finding for the $2\nu_1$ dissociation quantum yield is consistent with the earlier results of Roehl *et al.* who report a unimolecular dissociation quantum yield of ~27% at room temperature.[7]

2.4 Summary

In summary, the ViMP technique is used to investigate the photochemistry of HO_2NO_2 free from interference of various impurities that are typically present in PNA samples. The combination of $2\nu_1$ + 390 nm is used in providing information on the energy disposal for the minor OH + NO_3 channel resulting from electronic photodissociation of PNA. The primary channel, associated with NO_2 + HO_2 pathway, is detected through monitoring NO_2* fluorescence. The NO_2 fluorescence is sufficiently intense to allow us to record action spectra of both the $2\nu_1$ and $\nu_1 + 2\nu_3$ bands. Comparing integrated intensities of these bands appearing in the state selected action spectra with their known infrared absorption cross-section allows determining the quantum yield for unimolecular dissociation for the predissociative $2\nu_1$ level.

This parameter is important in assessing the infrared initiated photochemistry of HO_2NO_2 in the atmosphere. The present measurements indicate that the states associated with the $2\nu_1$ level that have sufficient energy to undergo unimolecular dissociate at room temperature, do so on a time scale faster than ~7 ns. In addition, the quantum yield for unimolecular dissociation of the HO_2NO_2 $2\nu_1$ state is determined to be 30 ± 5 % in the absence of collisions at 298 K. The present results are in good agreement with the earlier results of Roehl *et al.* obtained at high pressure using the HO_2 + NO → OH + NO_2 reaction to monitor formation of HO_2 from excitation of HO_2NO_2 in the region of the $2\nu_1$ level.[7] In Chapter 9 the photolysis rate of PNA is assessed under atmospheric conditions using the dissociation quantum yield parameter.

2.5 Future Studies on PNA

The substantial signal levels arising from NO_2 fluorescence in the ViMP technique ($2\nu_1$ + 390nm) suggests that it should be possible to investigate the PNA under molecular beam conditions. To date, only the ground state spectroscopic parameters are characterized for this important atmospheric molecule.[19] By obtaining the overtone spectra of a jet cooled sample, one may obtain important and relevant information on the band structure and the extant of the interactions between the $2\nu_1$ and the $\nu_1 + 2\nu_3$ states.

2.6 Acknowledgment

Chapter 2, in part, is a reprint of the material as it appears in Journal of Physical Chemistry *A* **108**, 8134 (2004). J. Matthews, R. Sharma, and A. Sinha, American Chemical Society, 2004. The dissertation author was the primary investigator and author of this paper.

Table 2.1: $HO_2NO_2(2\nu_1 + 390\ nm) \rightarrow OH + NO_3$ Channel Energy Partitioning.[a]

Fraction, f	$E_{translational}$	$E_{internal}$
f [OH]	43 %	2 %
f [NO_3]	12 %	43 %
f [Total]	55 %	45 %

[a] Off the total available excess energy of ~19 600 cm^{-1}.

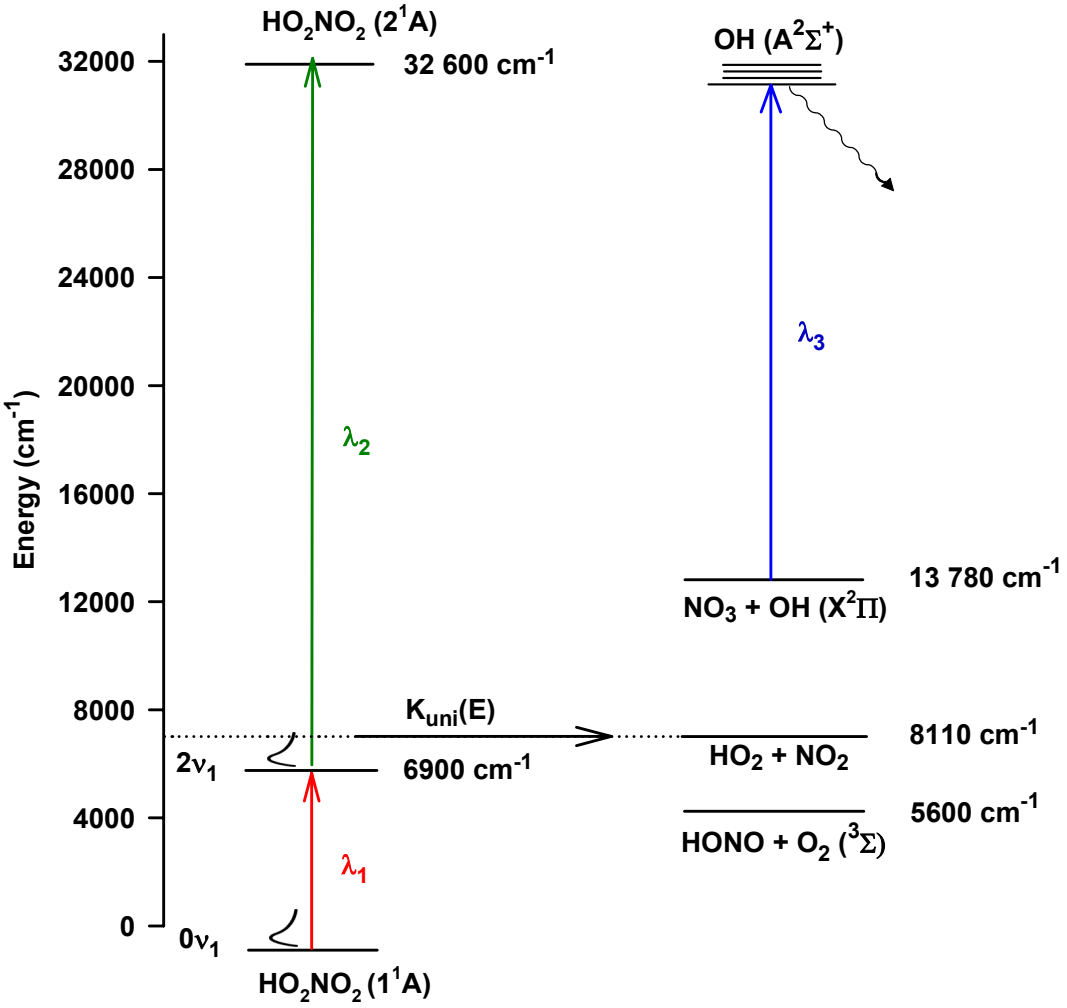

Figure 2.1: Schematic energy level diagram illustrating photodissociation of vibrationally excited HO_2NO_2. Laser λ_1 vibrationally excites room temperature PNA molecules to the $2\nu_1$ level where λ_2 subsequently further promotes these state-selected molecules to a dissociative electronic excited state. The resulting OH photofragments are probed via LIF using λ_3. PNA molecules excited to states of the $2\nu_1$ vibrational level having sufficient initial thermal energy can also undergo unimolecular dissociation on the ground electronic surface. The threshold energies for opening the various product channels shown are estimated using the enthalpy data of Refs. 4 and 7.
[File: F2.1_EPD]

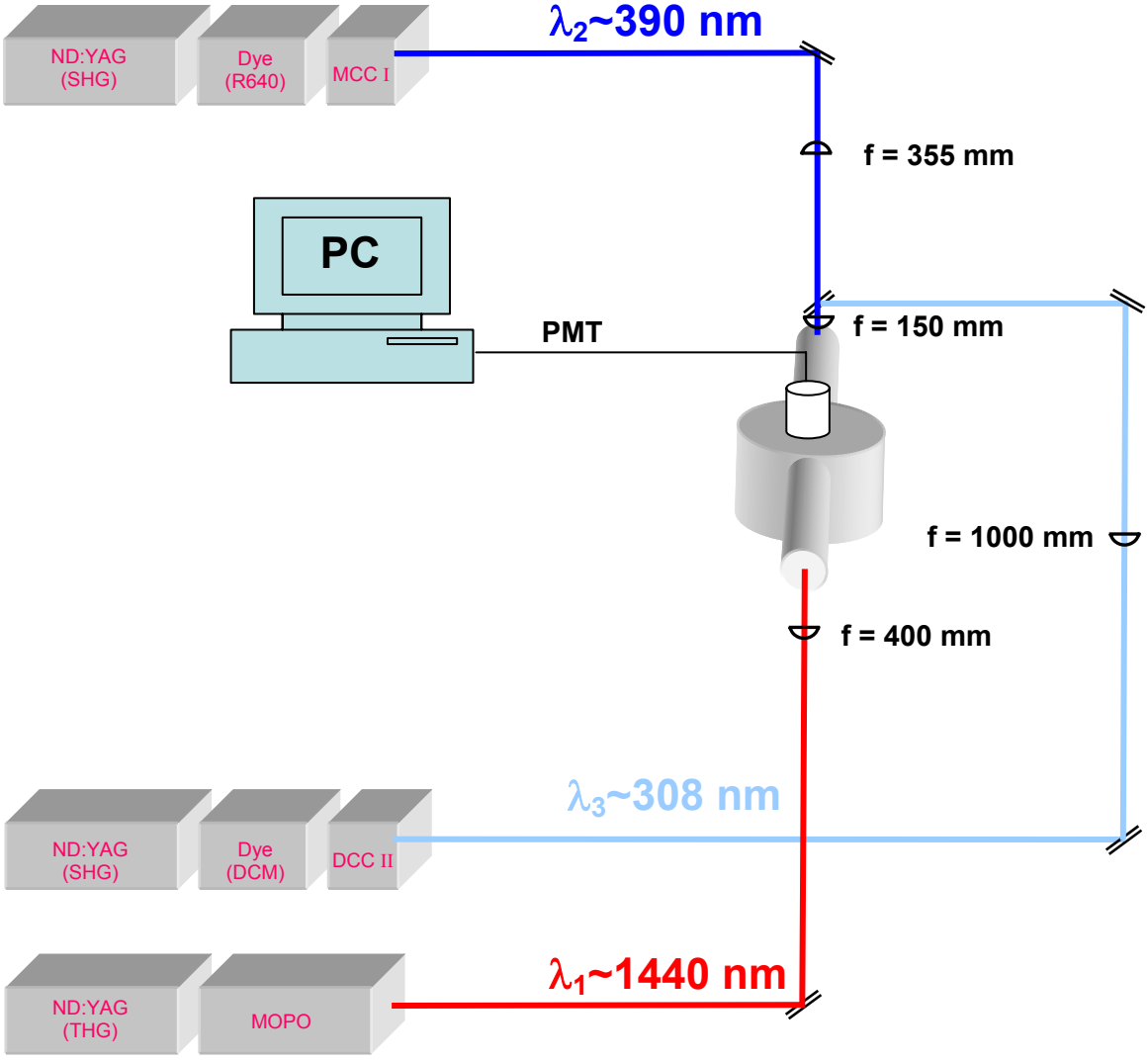

Figure 2.2: Experimental diagram for the HO_2NO_2 $2\nu_1$ + 390 nm experiments. Typical pulse energies from the MOPO (λ_1) in the $2\nu_1$ region range between 4 – 6 mJ. The photolysis laser (λ_2) with energies in the range of at 8 – 10 mJ typically fires 20 ns after the vibrational excitation laser. The firing of the probe beam (λ_3) is delayed by 40 ns from the photolysis laser and is greatly attenuated (< 1 μJ) to prevent photolysis of PNA and saturation of the OH lines. The 400 mm, 1000 mm, 150 mm and 355 mm lenses are located 20", 77", 13" and 35" from the center of the cell respectively.
[File: F2.2_apparatus]

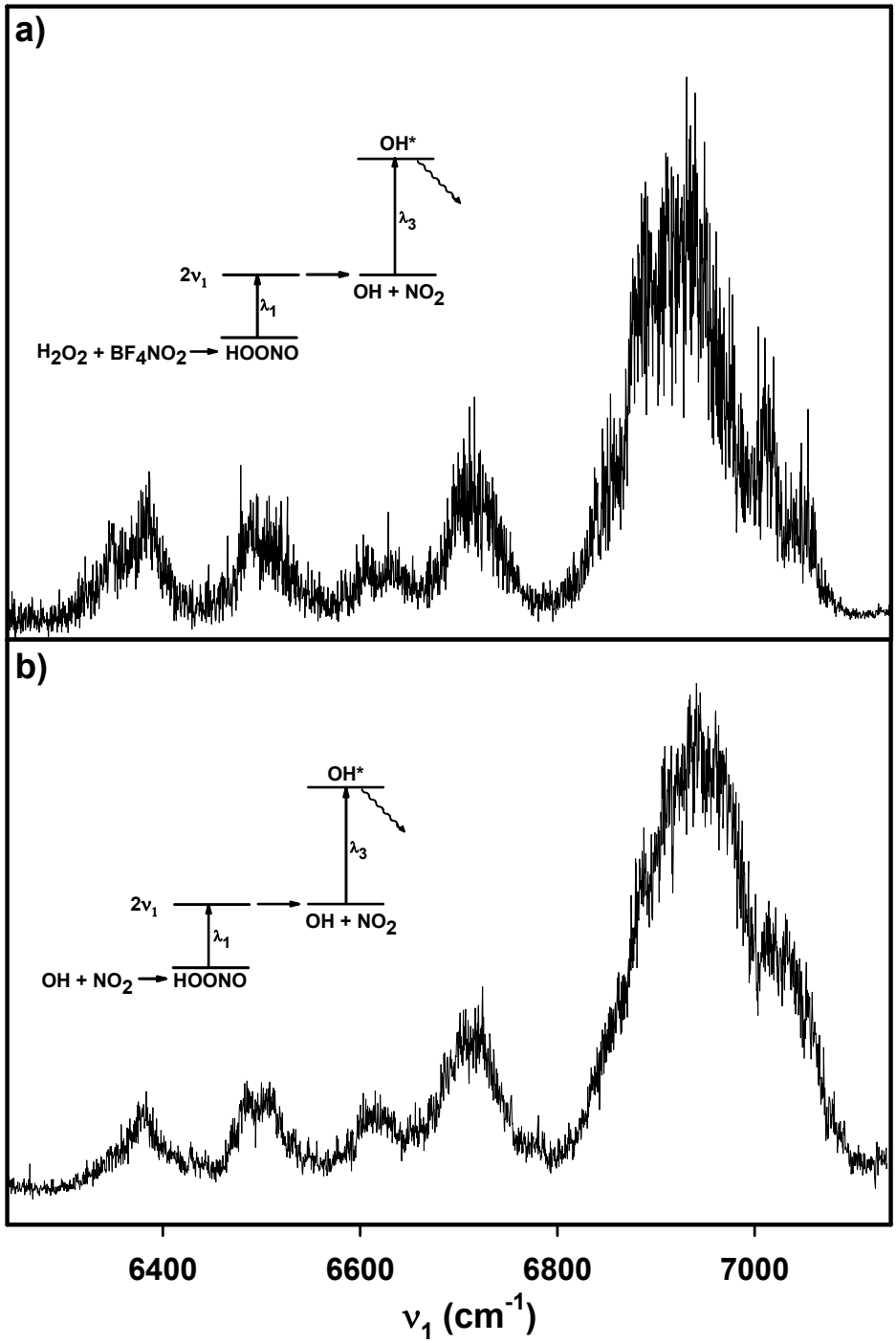

Figure 2.3: a) HOONO ($2\nu_1$) action spectra arising from the H_2O_2 + BF_4NO_2 source. The spectra is generated by scanning the IR laser (λ_1) while monitoring OH fragment yield through the $Q_1(2)$ transition(λ_3). b) HOONO($2\nu_1$) action spectra generated from the OH + NO_2 + M three-body recombination reaction. The OH radicals required for the three-body reaction are generated using the H + NO_2 reaction with hydrogen atoms being produced by passing H_2 through a microwave discharge in a side arm reactor.

[File: F2.3_HOONO_spectra]

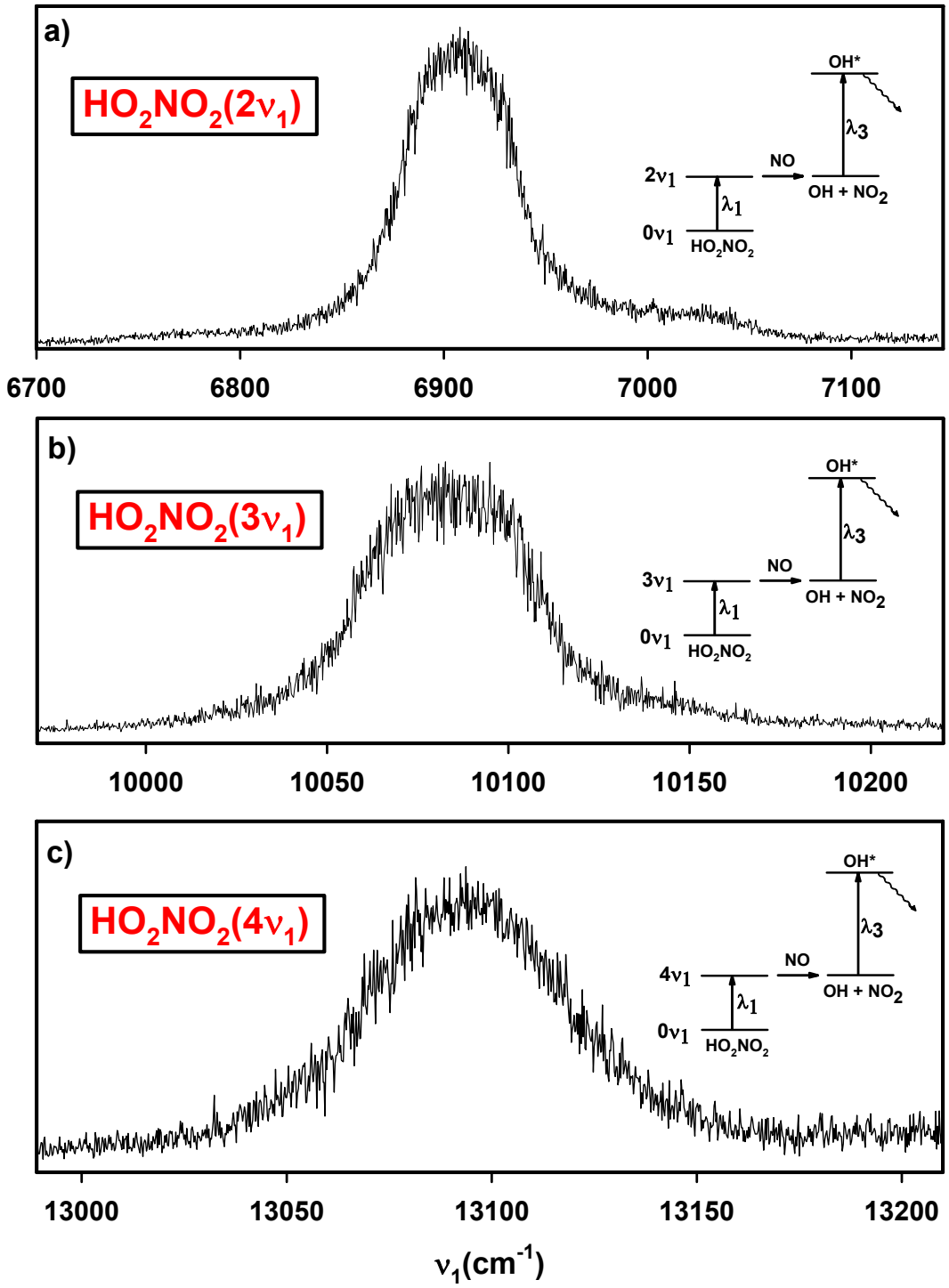

Figure 2.4: Vibrational overtone action spectra of HO_2NO_2 generated by exciting PNA to the (a) first OH-stretching overtone ($2\nu_1$), (b) second OH-stretching overtone ($3\nu_1$) and

(c) third OH-stretching overtone ($4\nu_1$) and then converting the HO_2 photoproduct to OH through its reaction with NO. [File: F2.4_PNA_tit_spectra]

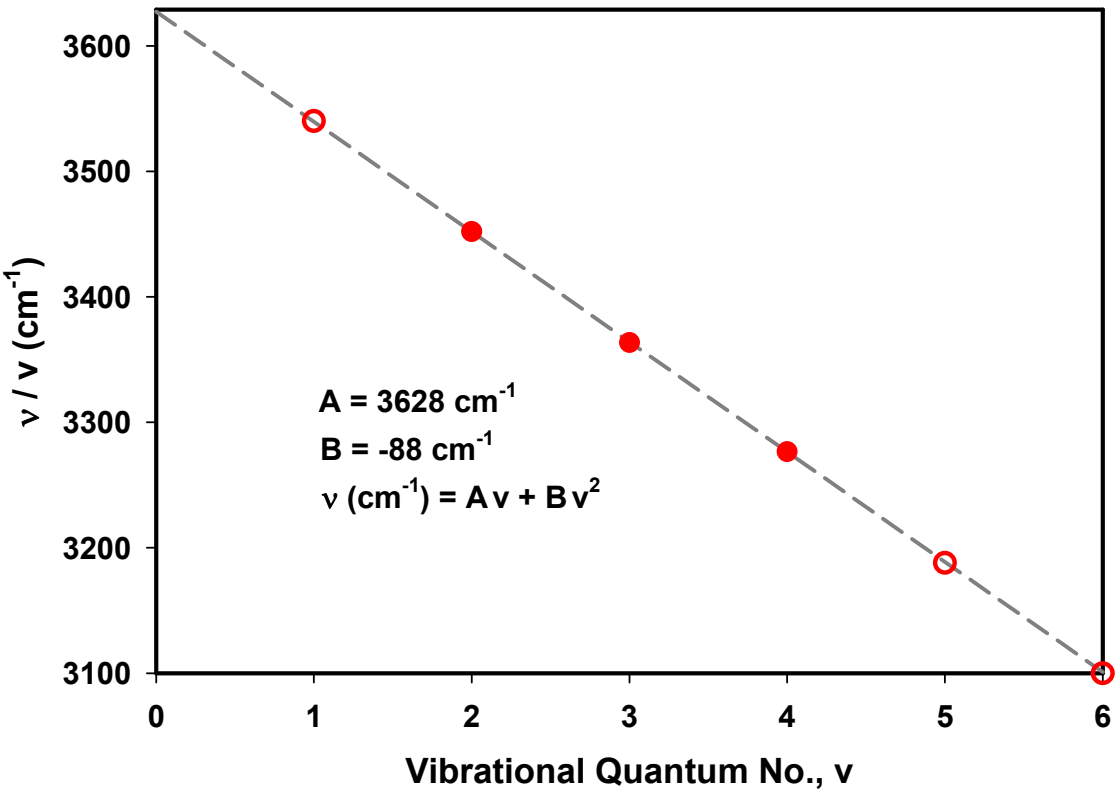

Figure 2.5: Birge-Sponer plot associated with the OH-stretching overtones of PNA. The closed circles indicate experimental frequencies obtained from Fig. 2.4 and the open circles indicate the extrapolated band positions. [File: F2.5_BS]

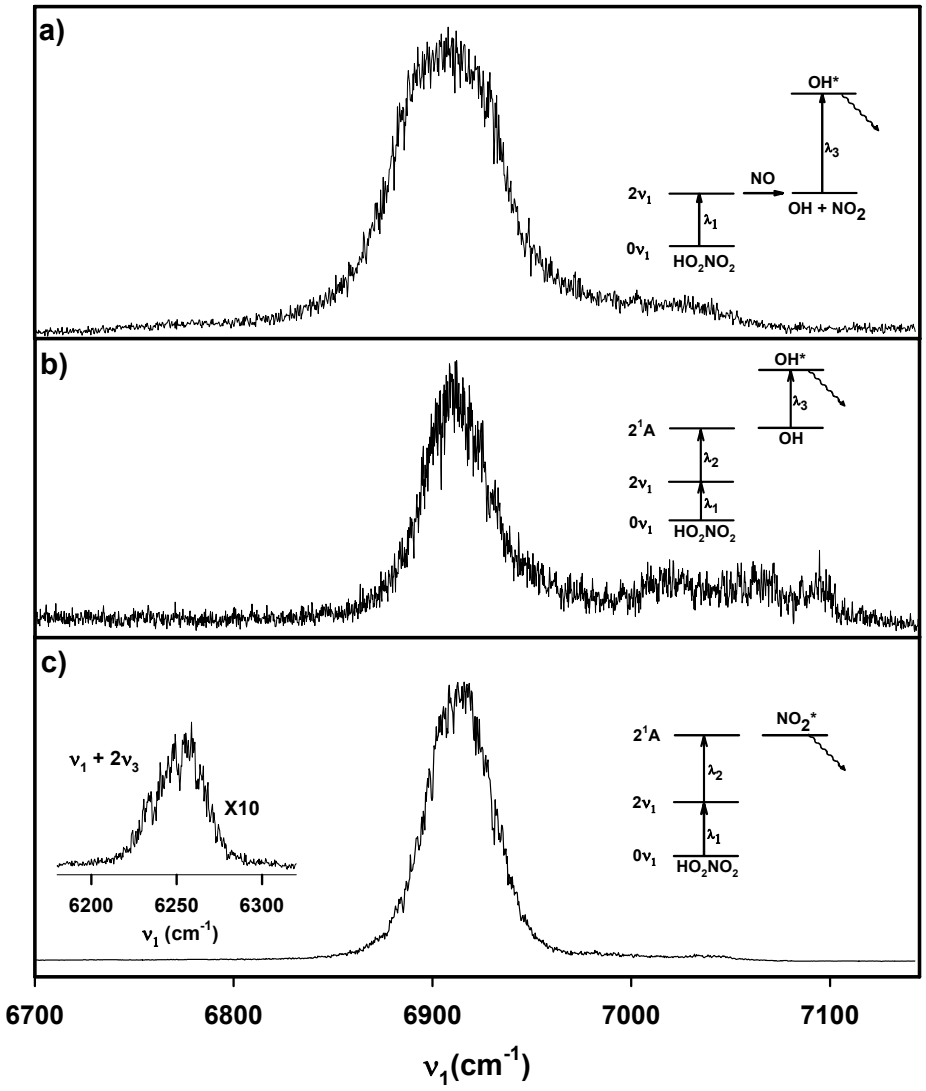

Figure 2.6: a) Vibrational overtone action spectra of HO_2NO_2 ($2\nu_1$). This spectrum is generated by exciting PNA to the $2\nu_1$ level and then converting the unimolecular dissociation products, HO_2, to OH through its reaction with NO, which is also added to the reaction cell. In the spectrum the yield of OH radicals is monitored using the $Q_1(2)$ transition as the $0 \rightarrow 2\nu_1$ excitation frequency is scanned. b) Vibrational overtone action spectra of HO_2NO_2 ($2\nu_1$) from the $2\nu_1$ + 390 nm photodissociation. This spectrum is generated by scanning λ_1 while monitoring OH photofragments through the $Q_1(4)$ transition. No nitric oxide is present and the time delay between λ_1 and λ_2 is set at 25 ns. c) Vibrational overtone action spectra of HO_2NO_2 ($2\nu_1$) generated via the $2\nu_1$ + 390 nm photodissociation, but monitoring total NO_2 fluorescence while scanning λ_1. The weak $\nu_1 + 2\nu_3$ combination band is shown in the inset. The assignment is from Ref. 7.
[File: F2.6_PNA_vimp_spectra]

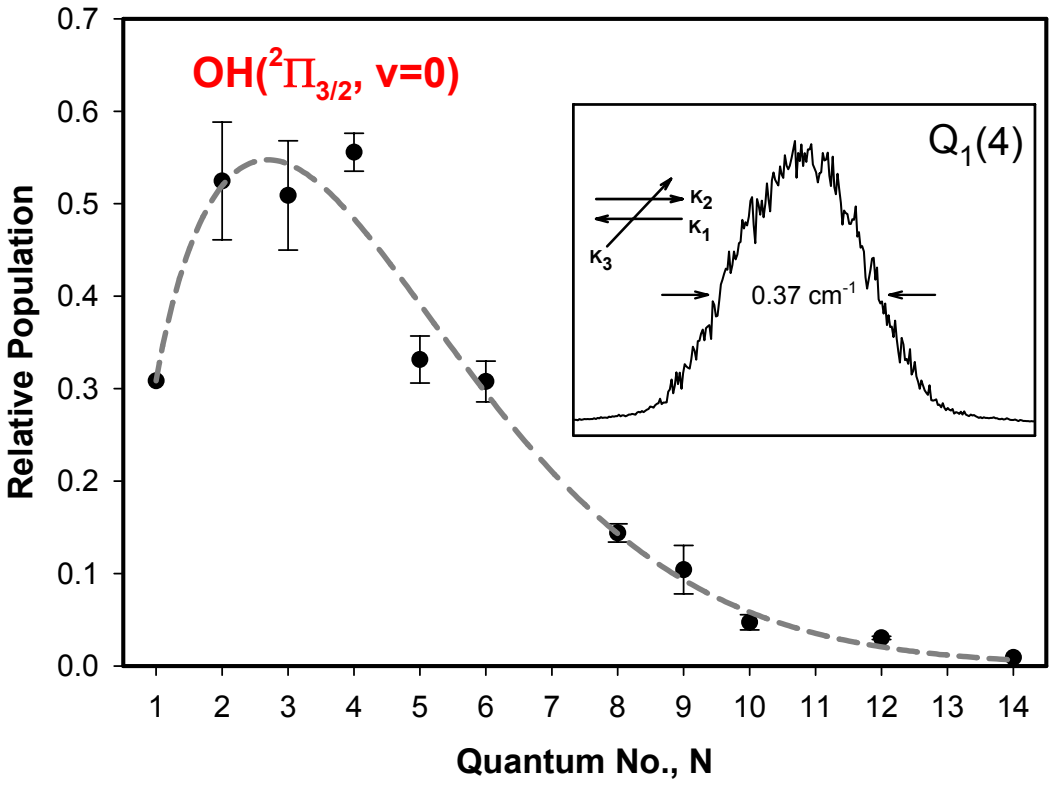

Figure 2.7: Nascent rotational state distribution of the OH (v=0, $^2\Pi_{3/2}$) manifold resulting from the $2\nu_1$ + 390 nm excitation of PNA. The inset shows the Doppler width associated with the $Q_1(4)$ transition with the 0.17 cm^{-1} probe laser linewidth convoluted out.
[File: F2.5_psd]

2.7 References

1. G. P. Brasseur, J. J Orlando, G. S. Tyndall, *Atmospheric Chemistry and Global Change* (Oxford University Press, New York, 1999).

2. D. J. Donaldson, G. J. Frost, K. H. Rosenlof, A. F. Tuck, V. Vaida, Geophys. Res. Lett. **24**, 2651 (1997).

3. D. J. Donaldson, A. F. Tuck, V. Vaida, Phys. Chem. Earth C. **25**, 223 (2000).

4. W. B. DeMore, *et al.,* JPL Publication 94-26, NASA/ JPL (Pasadena, CA. **1994**).

5. H. Zhang, C. M. Roehl, S. P. Sander, P. O. Wennberg, J. Geophys. Res. **105**, 14593 (2000).

6. Z. Chen, T. P. Hamilton, J. Phys. Chem. **100**, 15731 (1996).

7. C. M. Roehl, S. A. Nizkorodov, G. H. Zhang, A. Blake, P. O. Wennberg, J. Phys. Chem. A. **106**, 3766 (2002).

8. L. T. Molina, M. J. Molina, J. Photochem. **15**, 97 (1981).

9. G. Knight, A. R. Ravishankara, J. B. Burkholder, Phys. Chem. Chem. Phys. **4**, 1432 (2002).

10. C. M. Roehl, T. L. Mazely, R. R. Friedl, Y. Li, J. S. Francisco, S. P. Sander, J. Phys. Chem. A. **105**, 1592 (2001).

11. H. Macleod, G, P. Smith, D. M. Golden, J. Geophys. Res. **93**, 3813 (1998).

12. R. A. Kenley, P. L. Trevor, B. Y. Lan, J. Am. Chem. Soc. **103**, 2203 (1981).

13. Y. Li, J. S. Francisco, J. Chem. Phys. **113**, 7976 (2000).

14. D. A. Dixon, D. C. Feller, G. Zhan, J. S. Francisco, J. Phys. Chem. A. **106**, 3191 (2002).

15. S. A. Nizkorodov, and P. O. Wennberg, J. Phys. Chem. **106**, 855 (2002).

16. D. J. Nesbitt, R. W. Field, J. Phys. Chem. **100**, 12735 (1996).

17. M. Quack, Annu. Rev. Phys. Chem. **41**, 839 (1990).

18. P. J. Robinson and K. A. Holbrook, *Unimolecular Reactions* (Wiley, New York, 1972).

19. R. D. Suenram, F. J. Lovas, and H. M Pickett, J. Mol. Specrosc. **116**, 406 (1986).

Chapter 3

Ab Initio Study of Structure, Thermochemistry and Vibrational Spectra of Peroxynitric Acid

3.1 Introduction

While the photodissociation experiments on peroxynitric acid (HO_2NO_2, PNA) presented in Chapter 2 provide with wealth of information on the dissociation dynamics, vibrational and electronic spectroscopy, *ab initio* method can provide with supplementary information regarding its molecular structure, thermochemistry and spectroscopic parameters which are often difficult to extract from laboratory studies. In essence, *ab initio* studies provide experimentalists with additional tools which can be used in making predictions while probing the various properties of the molecule. For example, the detection of the signature of PNA in the atmosphere often involves searching for its vibrational and/or rotational signature in a collected atmospheric sample. Niki *et al.* used Fourier transform infrared spectroscopy to first detect gas-phase pernitric acid under laboratory conditions.[1] However, not all the vibrational frequencies have been detected experimentally. *Ab initio* studies can, in principle, aid in the assignment of vibrational bands and aid in locating the missing bands. To that end, using high level *ab initio* computational study we investigate the ground state and equilibrium geometry of PNA in order to obtain vibrational frequencies and rotational constants. We then evaluate and compare our *ab initio* structure to that reported by, Suenram *et al.* who used microwave spectroscopy to investigate the lowest torsional mode and derive rotational constants for HO_2NO_2.[2] In essence, this dissertation chapter takes advantage of these experimental

values in order to provide a comparison between our computed *ab initio* values and experimental thus providing a benchmark to our high-level *ab initio* parameters.

This study also presents initial results of the molecule's conformational preferences which are otherwise difficult to obtain experimentally. Using the CCSD(T)/cc-pVDZ level of theory, we perform conformational study associated with the O'NO"O and NO"OH torsion dihedral angles shown in Fig. 3.1. From the vibrational analysis, of the nine available configurations, only the *cis-perp* and *trans-perp* where the H-atom is in out-of-plane configurations correspond to minimum energy structure. Determining the number of allowed PNA conformers is important since in general, different molecular configuration correspond to different energies thus giving rise to different bond dissociation energies and stabilities. As already stated, HO_2NO_2 is formed in the atmosphere via a three-body recombination reaction involving the HO_2 and NO_2 radicals and, hence, provides a temporary reservoir for these species.[3]

$$HO_2 + NO_2 + M \leftrightarrow HO_2NO_2 + M \qquad (3.1)$$

As discussed in Chapter 1 and 2, reaction 3.1 is important for evaluating the oxidation power of HO_x in the atmosphere. More importantly, the removal of pollutants such as nitrogen dioxide (NO_2) via this reaction from the atmosphere will depend to a large extant on the reverse reaction and on the molecule's binding energies. If for example the binding energy for HO_2NO_2 is small, it would result in a rapid decomposition to its constituents and therefore exclude this reaction of becoming an efficient removal mechanism of atmospheric NO_2.

In the previous chapter, we recorded predissociation spectra of PNA out of $2\nu_1$. Quantum yields measurements of this band centered at 6905 cm^{-1} suggest that only 30 %

of the states undergo photodissociation. Roehl *et al.* who have also investigated the vibrational bands in the $2\nu_1$ region, suggested that the OH-stretch / HOO-bend combination mode ($2\nu_1 + \nu_3$) with band origin at 8250 cm^{-1} has a unity dissociation quantum yields ($\Phi = 1$).[4] Therefore, one may infer that the bond dissociation energy of the $HO_2 + NO_2$ channel lies in the range of $6900 < D_0 < 8250$ cm^{-1}. In fact, recent measurements by Ravishankara and coworkers who derived heats of formation from decomposition rates of PNA pin ΔH_f^{298} $[HO_2NO_2] = -12.6 \pm 1$ kcal / mol.[5] Using the heats of formation[6] of HO_2 and NO_2 we find that the bond dissociation energy of $D_0[HO_2\text{-}NO_2] = 23.3$ kcal /mol = 8149.2 cm^{-1} is indeed consistent with the previous range estimated for D_0. In this chapter we examine the bond dissociation energy associated with $HO_2 + NO_2$ and $OH + NO_3$ channels of PNA using *ab initio* methods. In order to evaluate the bond energy, we utilize coupled-cluster calculation with single, double and perturbative triple excitation (CCSD(T)) in conjunction with the Dunning basis sets cc-pVξZ (ξ = D, T, Q) and basis set limit extrapolation to obtain the most accurate energies to date using the isodesmic reaction scheme. We then compare the *ab initio* bond dissociation energies to that reported by Ravishankara and coworkers and based on this value, estimate the quantum yields of HO_2NO_2 from $2\nu_1$ excitation.[5]

Equally important to obtaining thermochemical information on the molecule, this study aims to also provide with overtones absorption cross-section. Donaldson and coworkers have shown that the overtone-initiated photolysis of PNA is a significant source of atmospheric HOx at high solar zenith angle (SZA).[7] Based on known absorption cross-sections of PNA, they evaluated the photolysis rates of the overtones

and compared it to that of UV.[8,9] The relatively large absorption cross-section associated with OH-stretching mode of PNA and the difficulties in determining these absorption cross-sections accurately using experimental techniques, have lead us to re-examination of said $1\nu_1$ through $6\nu_1$ overtones transition frequencies and cross-sections.

3.2 Computational Methods

We use the GAUSSIAN98 and GAUSSIAN03 programs to determine the optimized geometries, energies, vibrational frequencies, anharmonicities and dipole moment of HO_2NO_2.[10, 11] For detailed description of running these programs as well as ACESII program on our workstations refer to Appendix *B*. All stationary points were characterized by vibrational frequency calculations. Several *ab initio* methods are used in this study. These include the quadratic configuration interaction theory with single and double excitations (QCISD) as well as the QCISD(T) method where perturbative correction for triple excitations are also included. In addition, coupled cluster theory with single and double excitation (CCSD(T) method) is also used. The Pople double and triple zeta split valance basis sets are used and augmented with high angular momentum polarization functions. Specifically these are the 6-311++G(2d,2p) and 6-311++G(2df,2p) basis sets.[12] In addition, the Dunning basis sets are also used and these include the cc-pVDZ, aug-cc-pVDZ, cc-pVTZ and aug-cc-pVTZ basis sets.[13] The vibrational anharmoncities are calculated at the MP2/cc-pVTZ level and the vibrational overtone intensity and transition frequency calculations are carried out respectively at the QCISD and CCSD(T) level of theory using the cc-pVTZ and aug-cc-pVTZ basis sets. In order to evaluate the bonds dissociation energies of HO_2NO_2, we obtain the equilibrium and zero points energies of PNA, H_2O, H_2O_2, $HONO_2$, HO_2, NO_2, OH, NO_3. These energy

evaluations where used in conjunction to CCSD(T)/complete basis set (CBS) limit (CCSD(T)/cc-pVξZ (ξ = D, T, Q)) and the isodesmic reaction scheme as follows:[13,14]

$$HO_2NO_2 + H_2O \rightarrow H_2O_2 + HONO_2 \qquad \Delta_r H^o_{0\,k} \qquad (3.2)$$

In the above reaction, the number and types of bonds breaking and forming are preserved leading to cancellation of errors associated with solving for the energies due to the difficulties arising with incorporating electron correlations (electron-electron repulsion forces) in the Schrödinger equation.

3.3 Results and Discussion

3.3.1 Rotational Confomers of HO_2NO_2

To start investigating the structure of the transient PNA molecule we proceed by probing its equilibrium geometry. In HO_2NO_2, there are two major dihedral angles that define the molecule's conformation; they correspond to the angles formed by the O'NO"O and NO"OH group of atoms (see Fig. 3.1). For convenience we refer to the different rotational conformers by specifying the respective dihedral angles τ(O'NO"O) and τ(NO"OH). Configurations with dihedral angles fixed at 0^o, 90^o and 180^o are designated as *cis*, *perp* and *trans* respectively. The different conformers of HO_2NO_2 are shown in Fig. 3.2. Globally optimized structure of HO_2NO_2 has been reported previously.[15] However, these earlier calculations did not investigate the conformational dependence of the molecule's energy. In the present study preliminary optimizations of all the rotational conformers of HO_2NO_2 were carried at the B3LYP and MP2 levels of theory using the cc-pVDZ basis. These calculations were then used as starting points for higher electron correlation calculations using the CCSD(T) method. As an example, the keywords and input Z-matrices used with the *cis-cis* and *cis-perp'* calculations are shown

in Table 3.1. For explanation on the keywords used in current and subsequent tables as well as general GAUSSIAN03 operation see Appendix *B*. Note that in the *cis-cis* optimization, both D2 and D3 dihedral are kept fixed at 0^o where in the *cis-perp'* optimization, only D2 is fixed to 0^o while D3 is set to 90^o but then unconstrained and allowed to relax. The optimized structures and relative energies for the different rotomers obtained using the CCSD(T)/cc-pVDZ method are given in Table 3.2. In the table, the prime labeling indicates full optimization of that particular dihedral angle starting from the given position. Thus, the label *cis-perp*' indicates that while the τ(O'NO"O) dihedral angle is kept fixed at 0^o, the τ(NO"OH) dihedral angle, initially set to 90^o, is fully optimized. Looking at Table 3.2, we find that in HO_2NO_2, the highest-energy conformers correspond to the *cis-trans* and *trans-trans* structures. Apparently in both of these cases the energetically unfavorable structure results from the NO"OH dihedral angle being in the *trans* position. Interestingly, by contrast in the structurally related molecule, peroxynitrous acid (HOONO) discussed in Chapter 4, the optimal position for the NO"OH dihedral angle is in the *cis* conformation.[16] Apparently this difference between the two molecules arises due to the possibility of intramolecular hydrogen bonding in HOONO, which stabilizes its *cis* structure. The vibrational frequencies of the various conformers, given in Table 3.3, suggest that none of the structures with the NO"OH dihedral angle in the *trans* position is a minimum energy structure as they have one imaginary frequency (ν_{12}) indicated with an *i* suffix. In particular both the *cis-trans* and *trans-trans* structures have imaginary frequencies for the ν_{12} mode indicating that they are first order saddle points.

A preliminary examination of the energies in Table 3.2, shows that the barrier for rotation of the NO"OH angle is only slightly asymmetric with energy difference on the order of a fraction of a mHartree (~11 cm^{-1}). Structures in the *cis* conformation, i.e. *cis-cis* and *cis-perp* conformations, are first order saddle points despite the fact that they are lower in energy than the *cis-trans* and the *trans-trans* structures. The lower energy structures are found to be those in which NO"OH dihedral angles are out-of-plane i.e. the *perp* position. The *cis-perp*, *trans-perp'*, and *perp-perp* structures all are lower energy structures with no imaginary frequencies indicating that they are indeed minimum energy structures. No minimum energy structure with τ(O'NO"O) in the *perp* position or *gauche* (~60^o) position could be found. However, as Table 3.2 shows, the global minimum energy structure at CCSD(T)/cc-pVDZ has the NO"OH dihedral angles of about ~84^o out of the plane. The O'NO"O dihedral angle is close to the *cis* conformation, but is approximately ~12^o out of the plane as shown in Fig. 3.1(b). A higher level optimization calculation at the CCSD(T)/cc-pVQZ confirms that indeed the NO"OH dihedral angle is ~84^o and the O'NO"O dihedral angle is slightly closer to the *cis* configuration at ~11^o.

3.3.2 Global Minimum Energy Structure of HO_2NO_2

From the conformational study, we find that the global minimum structure has no symmetry elements and the plane of the HO_2 group is roughly perpendicular to the plane of the NO_2 group, i.e., 84.0^o at the CCSD(T)/cc-pVDZ and cc-pVQZ levels of theory. As noted by Saxon and Liu, [17] this dihedral configuration is similar to the situation in H_2O_2. In fact, several hydroperoxides such as the *trans-perp* peroxynitrous acid (HOONO)[18], methyl hydroperoxide (CH_3OOH)[19] and hydroxymethyl hydroperoxide ($HOCH_2OOH$)[20] have the respective dihedral angles of 97^o, 114^o and 75^o. The origin for the out of plane

configuration adopted by the HO_2 group in HO_2NO_2 can be rationalized by noticing that the HO_2 radical in its ground electronic state has its unpaired electron in the singly occupied out-of-plane ^2A" orbital; thus, the bonding interaction of the NO_2 moiety must assume an out-of-plane orientation as the two radicals approach one another to form HO_2NO_2. Previous *ab initio* studies have obtained similar results for the HO_2NO_2 structure at lower levels of theory. Saxon and Liu preformed Hartree-Fock optimization with the Pople 6-31G and 6-31G** basis sets, [17] while Chen and Hamilton improved the basis set quality using 6-31++G** basis with the Hartree-Fock and B3LYP hybrid density functional method.[15] The two results showed significant structural variation. For example, there is an increase of 0.158Å in the NO" bond length in going from HF (Hartree-Fock) to the B3LYP (Becke 3-Parameter, Lee, Yang and Parr) wave functions. The study of Chen and Hamilton also showed that higher order angular momentum functions, such as the addition of *f*-polarization functions were critical and significantly affected the NO and NO' bonds.[15] The general observations from these earlier studies were that while the Hartree-Fock method tends to predict bond lengths that were too short, consistent with the fact that HF method lacks the proper treatment of the electron correlation neglecting the instantaneous coulomb repulsion arising between two electrons with opposing spins. In contrast, the MP2 method predictions overestimated the bond length. A comparison of the MP2/6-311++G** results of Jitariu and Hirst with the MP2/6-311++G(2df,2pd) results of Chen and Hamilton show that there is also a basis set dependence.[15,21]

The highest level of theory reported in the literature prior to the present work is the QCISD/6-31G* optimization by Chen and Hamilton and a CCSD(T)/cc-pVDZ

optimization by Roehl *et al.*[15,22] Neither of these prior calculations, however, has used basis sets with high angular momentum functions in conjunction with the coupled cluster methods. As shown in Table 3.4 the present optimizations for HO_2NO_2 have been preformed with the QCISD, QCISD(T), and CCSD(T) coupled-cluster methods with both Pople and Dunning basis sets.[12,13] It is interesting to note that there is very little difference between the optimized QCISD/6-31G** structure of Hamilton and Chen and the QCISD/cc-pVDZ results shown in Table 3.4. However, when the triple excitations are included in the QCISD wave function, all the bond lengths are significantly lengthened. For example, the NO bonds are increased by a ~0.006 Å and the NO" bond increased by ~ 0.037 Å. This is also seen when one compares the QCISD and CCSD(T) results with the aug-cc-pVTZ and cc-pVQZ basis sets. This observation indicates that inclusion of triple excitation in the coupled-cluster wave functions is also important in converging the structure. From the QCISD(T) calculations with the Pople triple zeta basis set, a clear basis set dependence is seen. There is a 0.021Å decrease in the OO" bond length in going from the 6-31G* to 6-311++G(2df,2p) basis set suggesting that calculations with the smaller basis set may not provide an accurate representation of the experimental geometry for HO_2NO_2. A comparison between the QCISD(T) results using 6-311++G(2d,2p) and 6-311++G(2df,2p) basis sets highlight the importance of *f*-polarization in converging the geometry as exemplified by the fact that there is still a 0.011Å difference between the results for the OO" bond distance. We find that the QCISD(T)/6-311++G(2df,2p) and CCSD(T)/aug-cc-pVTZ results are very similar. However, looking at the CCSD(T)/cc-pVQZ column suggests that the inclusion of an *f*-wave function on the H-atom and *g*-functions on the O- and N- atoms results in an

additional decrease in the bond lengths and angles. This is likely due to the fact that the large basis-set increases in the spatial volume the electron is allowed to occupy thus reducing the electron-electron repulsive interactions and allowing the bond lengths to decrease. Although there are no reported experimental structural parameters with which we can directly compare the results of our calculations, experimental rotational constants from microwave measurements provide some basis for evaluating the quality and reliabilities of the present calculations. In Table 3.5, the computed equilibrium rotational constants are listed along with the experimental microwave results of Suenram *et al.* for the ground vibrational state.[2] One can see a clear convergence between the *ab initio* results using the CCSD(T)/aug-cc-pVTZ, CCSD(T)/cc-pVQZ wavefunctions and the microwave experiments. The respective deviation in the *A*, *B*, and *C* rotational constants are 0.30 %, 0.04 %, and 0.04 % for the aug-cc-pVTZ and 0.60 %, 1.0 % and 1.0 % for the cc-pVQZ levels. Moreover, the QCISD(T) results with the 6-311++G(2df, 2p) basis set are also of comparable agreement with experiments. Even in the computed rotational constants results, one can see the basis set effects previously discussed. The rotational constants with the largest deviation are those using smaller basis sets, i.e. 6-31G(d) and cc-pVDZ basis sets. One can also see the importance in the addition of *f*-polarization functions in converging the results toward experiments. Given the nice agreement between the experimental rotational constants and the CCSD(T) level, it is reasonable to assume that the geometrical parameters given in Table 3.4 using this basis are close to the experimental values.

3.3.3 Thermochemistry of Peroxynitric Acid

Exploring the ground equilibrium geometries of PNA with various *ab initio* methods as indicated in the previous sections have allowed us to quantitatively evaluate the agreement between these methods with experimental PNA structure. It is clear that the CCSD(T) wave functions in conjunction with the Dunning basis functions give best agreement with available experimental data for PNA. Therefore, we prefer using this method to evaluate the thermochemical properties of PNA. The bond dissociation energies of the OH + NO_3 and HO_2 + NO_2 channels are important for many atmospheric models. From an experimental point of view it is difficult to obtain *exact* value for D_0 from unimolecular photodissociation on the ground state since the detection of nascent HO_2 + NO_2 channel is difficult using direct methods and apparently, the OH + NO_3 channel is not accessible from unimolecular on the ground electronic state (See Chapter *2*). Thus, *ab initio* methods can provide aid in the absence of experimental techniques to determine these bond dissociation energies. Two standard methods are used in evaluating D_0. In the first, the bond dissociation energy is evaluated by computing the differences in the equilibrium and ZPE energies of the species in the reactions below using CCSD(T)/CBS:

$$HO_2NO_2 \rightarrow HO_2 + NO_2 \qquad (3.3a)$$

$$HO_2NO_2 \rightarrow OH + NO_3 \qquad (3.3b)$$

The more accurate method for computing the bond dissociation energies involves the isodesmic reaction scheme (reaction 3.2) which is discussed in the following section.

3.3.3.1 D_0 Evaluation Using the Direct Method

The direct method requires calculating the bottom of the well (equilibrium) energies for the five species in reactions 3.3(a) and 3.3(b) at the CCSD(T)/cc-pVDZ,

CCSD(T)/cc-pVTZ and CCSD(T)/cc-pVQZ levels of theory. For efficiency reasons, we start the series by initially converging the cc-pVDZ structure for each molecule as well as obtaining the ZPE correction using a frequency calculation. The optimized geometries from the cc-pVDZ are subsequently used in computing the cc-pVTZ energies. It is not necessary to obtain the ZPE at the cc-pVTZ or at higher levels since typically, the zero point energy corrections are relatively small and are not affected as drastically as the equilibrium energy by the size of the basis sets.[14] The input Z-matrices used for computing the series of equilibrium and ZPE energies are shown in Tables 3.6 – 3.10 for HO_2NO_2, HO_2, NO_2, OH, NO_3. For details on the keywords used and specifics on running these calculations on the workstations see Appendix *B*. As shown in the tables, the keywords used except those controlling the calculation level (basis-sets) for each of molecules in the series are identical; thus ensuring consistent level of calculation and convergence criteria. The CCSD(T) energies associated with each of the calculations are then extracted from the output file. Also extracted are the zero-point energy calculations from the CCSD(T)/cc-pVDZ calculations. We then apply the ZPE correction associated with each molecule to each of the cc-pVξZ (ξ = D, T, Q) energy calculation. The CCSD(T) energies and their zero-point energy corrections are shown in Table 3.11. Note that as outlined in the previous section, the ZPE corrections are relatively small compared with the total electronic energies. In addition, it can be shown that increasing the level of theory will have no drastic effect on the ZPE correction. Therefore, using a single ZPE evaluation for each molecule is sufficiently accurate as well as very efficient method to employ with molecules consist of more than three atoms.

Also shown in Table 3.11 are the extrapolated energies values from the CCSD(T)/CBS. Dunning and coworkers have shown that consistent increase in the basis set within a family of correlation consistent sets lead to a convergence toward complete basis set limit of parameters such as equilibrium geometry, harmonic frequencies, and energies.[13] The widely used equation which applies to these sets of calculations with the purpose of achieving convergence to the limit has the functional form:[13-14,19]

$$E(n) = A(\infty) + B \exp[-(n-1)] + C \exp[-(n-1)^2] \qquad (3.4)$$

Where n is the cardinal number in the cc-pVξZ basis sets with DZ (=2) , TZ (=3) and QZ (=4). $A(\infty)$ is the estimated CBS limit as $n \rightarrow \infty$ and is the parameter of interest. Since the equation has three unknowns (A, B and C), at least three energies evaluations ($E(n)$) as a function of n are required in order to extract the basis set limit parameter, $A(\infty)$. The Mathematica code used for the basis set limit evaluations is provided in Appendix *D*.

With the values obtained in Table 3.11 using equation 3.4 and equations 3.3(a)-3.3(b), one may readily obtain the dissociation energies associated with each channel. D_0 is simply obtained by summing the CBS energies of the fragments and subtracting from it the CBS energy of PNA. The energies differences between products and reactant obtained from the direct method are shown in Table 3.12 in units of kcal/mol. There is a significant difference in D_0 associated with the cc-pVDZ and cc-pVTZ levels as there is an increase of ~4.5 kcal/mol in of D_0[HOO-NO_2] corresponding to basis functions increase. Going from cc-pVTZ to cc-pVQZ the difference in values is reduced to ~1.1 kcal/mol and at its convergence limit, the difference between CBS−∞ and cc-pVQZ is reduced to ~0.6 kcal/mol which is within the typical uncertainties associated with these

ab initio methods. Similarly, the differences in D_0 associated with the OH + NO_3 channel are reduced from ~3.4 kcal/mol to ~0.16 kcal/mol going from the DZ to CBS−∞ limit suggesting converges in the series.

3.3.3.2 D_0 Evaluation Using the Isodesmic Reaction Method

In the isodesmic reaction scheme, generally speaking, the underlying approach in constructing a valid reaction involving reactants → products is in the conservation of the types and numbers of bonds breaking and bonds forming. Moreover, in contrast to the direct method which involves taking energy differences between products and reactants where typically the products have multiplicity of 2 and the reactant of 1, the isodesmic reaction scheme invokes computation of D_0 using only closed-shell species (2S + 1 = 1; S=0). Thus, eliminating the potential errors associated with spin-contamination of open-shell species.[13] In this particular case, the chosen isodesmic reaction involves PNA and water to form hydrogen peroxide and nitric acid; species of which their heats of formations are well characterized.[6] Examining the reactant side of Eq. 3.2 we find that there are three O−H bonds, a single O−O bond, a single N−O bond and two N=O bonds. This is also occurring on the products side of Eq. 3.2. Thus, the net effect of "decomposing" PNA and water and "reassembling" hydrogen peroxide and nitric acid results in a zero change to numbers and types of bond. In addition, all the species participating in this reaction are closed shell molecules with multiplicity of 1 on their ground electronic state.

As with the direct method, we start off by computing the cc-pVξZ (ξ = D, T, Q) energies and frequencies at the cc-pVDZ for the species in Eq. 3.2. The Z-matrices used for HO_2NO_2, H_2O, H_2O_2 and $HONO_2$ are given in Tables 3.6 and 3.13-3.15 respectively.

As before, the CCSD(T) and ZPE are then summed for each specie as shown in Table 3.16. We then use Eq. 3.4 as before to fit the cc-pVξZ (ξ = D, T, Q) energies using non-linear fit (see Appendix *D*) to obtained the CCSD(T)/CBS energies for each of the species. These energies are also given for comparison in Table 3.16. Note that as before, the zero point energies are relatively small compared with the energies associated with the electrons and are sufficient to be computed at the CCSD(T)/cc-pVDZ level.

Having calculated the relevant energies associated with reaction 3.2, we can proceed by calculating the heat of reaction $\Delta_r H^0$ by noting that:

$$\Delta H_r^0 = \Sigma \text{ E[products]} - \Sigma \text{ E[reactants]} \qquad (3.5)$$

Where the Σ E[products] term is the sum of the energies of H_2O_2 and $HONO_2$ and the Σ E[reactants] term is the sum of the HO_2NO_2 and H_2O energies. The heats of reaction (ΔH_r^0) associated with each calculation level are shown in Table 3.17. As the experimental heats of formation of all the species but PNA are known in the isodesmic reaction, the heats of reaction can be readily used to obtain the heat of formation (ΔH_f^0) of PNA at a given level of theory using:

$$\Delta H_f^0 [HO_2NO_2] = \Delta H_f^0 [H_2O_2] + \Delta H_f^0 [HONO_2] - \Delta H_f^0 [H_2O] - \Delta H_r^0 \qquad (3.6)$$

Taking the heats of formation of -31.02, -29.69, and -57.1 kcal/mol for H_2O_2, $HONO_2$ and H_2O respectively, a value of -9.88 kcal/mol is backed out from equation 3.6 kcal/mol for PNA at the CCSD(T)/CBS level.[6] At this level of theory, using experimental heats of formation ($\Delta H_f^0 [HO_2]$ = 3.01 kcal/mol, $\Delta H_f^0 [NO_2]$ = 8.84 kcal/mol, $\Delta H_f^0 [OH]$ = 8.84 kcal/mol, $\Delta H_f^0 [NO_3]$ = 18.53 kcal/mol)[6], the respective bond dissociation energies are 21.74 and 37.26 kcal/mol for the $HO_2 + NO_2$ and $OH + NO_3$ channels. The heats of

formation and bond dissociation energies are also summarized in Table 3.17. Note that the convergence in the bond energies are occurring faster where, for example the energy differences between the cc-pVDZ and cc-pVTZ are ~0.35 kcal/mol while the differences between the cc-pVQZ and CBS are ~0.22 kcal/mol. Recall that with the direct method the same differences correspond to ~4.5 and ~0.6 kcal/mol respectively. The relatively small differences in energies between the levels of theory provide us with the confidence in the series convergence. The difference between the direct and isodesmic method for the HO_2 + NO_2 and OH + NO_3 channel are 1.34 kcal/mol (6% difference) and 3.94 kcal/mol (11% difference) respectively at the CCSD(T)/CBS level.

3.3.3.3 *Ab Initio* and Experiment D_0 Comparison

The value for $\Delta H_f^{298\,K}$ [HO_2NO_2] = -12.6 ± 1 kcal/mol from the Ravishankara group can be compared directly with our CCSD(T)/CSB heat of formation values by extrapolating ΔH_f obtained using the isodesmic reaction to 298 K.[5] Using the values of Ref. 6, at 298 K, we find that $\Delta H_f^{298\,K}$ [HO_2NO_2] = -11.25 kcal/mol. This value is slightly lower than that reported by the Ravishankara. The HO_2 – NO_2 bond dissociation energy inferred from their work corresponds to 23.1 kcal/mol which is 1.36 kcal/mol higher than our best value. Since both values are above the $2\nu_1$ band, it is difficult to gauge which value is more consistent with PNA's actual D_0 value. However, using a simple quantum yield model which combines the initial thermal energy with the photon energy at $2\nu_1$, one can directly compare the experimental quantum yields with our best value:

$$\Phi = \exp[(h\nu + 3kT/2 - D_0)/kT] \qquad (3.7)$$

In the above equation, k is Boltzmann factor, hν =6950 cm^{-1} correspond to photon energy used in exciting the $2\nu_1$ band and is combined with the initial average internal rotational energy associated with thermal distribution of states, $3kT/2 \approx 310\ cm^{-1}$. At room temperature (T = 298.15 K) using the D_0 value inferred from Ref. 5 gives a quantum yield Φ, of ~2 % while the *ab initio* D_0 value gives Φ ~ 19 %. Experimental dissociation quantum yields measured at the $2\nu_1$ and discussed in Chapter 2 and by Rohel *et al.* have shown that 30 ± 5 % and 27 % respectively of those states undergo photodissociation.[4] In essence, this quantum yield value is more consistent with the *ab initio* D_0 than that of Ravishankara and coworkers. In fact, using the experimental quantum yield to back out D_0 from equation 3.7, we find a value $D_0[HO_2NO_2]$ = 21.5 kcal/mol Which is in excellent agreement with the *ab initio* D_0 of 21.74 kcal/mol.

3.3.4 Vibrational Frequencies, Anharmonicities and OH Stretching Overtones

The first detection of HO_2NO_2 in the stratosphere was achieved by measurements of Rinsland *et al.*[23] who detected the vibrational mode at 802.7 cm^{-1} in the infrared region of the solar spectra. Laboratory measurements by May and Friedl refined the spectroscopic analysis of this band.[24] Current field measurements on PNA involve detection using near infrared to excite OH stretching overtone transitions.[25] Of the twelve HO_2NO_2 vibrational modes, all are infrared active and have been experimentally observed except for the ν_{11} band, which corresponds to asymmetric O'NO" / ONO" bends (see Fig 3.2(a)). Unlike the Hartree-Fock level of theory, where all the harmonic vibrational frequencies are significantly too high, the couple-cluster results shown in Table 3.18 appear to be more consistent with experiments. Note that in Table 3.18 we make the comparison between the experimental transition frequencies and the theoretical

harmonic frequencies associated with v_i=0 (i = 1 – 12) of each vibrational mode. It is interesting to note that for the vibrational frequency calculations on HO_2NO_2, electron correlation seem more important than basis set size in obtaining good agreement with experiment. For example, the RMS error between calculated harmonic frequencies and experimental fundamental transition frequencies for QCISD(T)/6-31G(d) and CCSD(T)/aug-cc-pVTZ methods shown in Table 5 is 4.4% and 4.9%, respectively. Our vibrational mode assignment is consistent with the reassignment of Chen and Hamilton,[15] however we note that many of the vibrational modes are considerably mixed. The state mixing to a large extant will depend on the coupling between the various vibrational modes and their "efficiencies" in distributing the energy deposited in a particular band among the rest of the vibrational modes.

We predict the coupling, vibrational frequencies and anharmonicities on the ground state of PNA at the MP2/cc-pVTZ level by running GAUSSIAN03.[11] The Z-matrix for the calculation is given in Table 3.19. The anharmonicites, along with the harmonic frequencies and coupling matrix calculated at the same level of theory, are presented in Table 3.20. Using the parameters in Table 3.20 we estimate the position of the $\nu_1 + 2\nu_3$ stretch-bend combination band to occur at 6277 cm^{-1}. The strong coupling between the OH stretch (ν_1) and the HOO bend (ν_3), suggests that this band should exhibit some intensity arising from state mixing. This result is consistent with earlier assignment of the peak occurring at 6250 cm^{-1} in the experimental action spectrum shown in Chapter 2 and Ref. 4 to the $\nu_1 + 2\nu_3$ band. Figure 3.3 shows the predicted spectra of PNA in the IR region involving fundamental transitions frequencies as a function of intensities in units of cm^2/molecule obtained from the MP2/cc-pVTZ level. Note that the

high frequency OH–stretching mode (ν_1) is not the most intense feature in the spectrum. In fact, its intensity is ~5 times weaker than the NO'–stretching mode (ν_2) in the fundamental region. Even the OOH bending mode (ν_3) carries more intensity than the OH stretch. This situation is quickly reversed in the overtones region where the OH vibrational transitions dominate the absorption spectrum.

As previously stated, the OH-stretching overtones not only play an important role in the photodissociation of PNA in the atmosphere but also in various detection schemes involving excitation of the OH overtones. Therefore, determining the bands positions as well as their absorption cross-sections is key for understanding the vibrational spectrum of PNA. Our approach to obtaining information about the OH stretching overtone involves first determining the vibrational frequency (ω_e) and anharmonicity ($\omega_e\chi_e$) by modeling the OH stretch of HO_2NO_2 as an anharmonic-oscillator and using a Morse potential to describe motion along this coordinate. We determine the equilibrium geometry by running GAUSSIAN98 at the CCSD(T)/aug-cc-pVTZ level of theory. We then determine the force constant and anharmonicity as a function of the OH displacement coordinate, $q=r-r_e$, by carrying out a series of single-point *ab initio* calculations which stretch the O-H coordinate over a range of $r_e \pm 0.4$ Å in increments of 0.1 Å while keeping all other coordinates fixed at their equilibrium value. Essentially, this calculation is carried out on the optimized structure of PNA at the CCSD(T)/aug-cc-pVTZ level using similar keywords as in Table 3.6 and dropping the OPT=EF keyword thus, resulting in constrained single point (SP) energy calculation. This procedure then provides us with a one dimensional grid of discrete points that represents changes in the potential energy V(q) for motion along the OH stretching coordinate. The choice of step

size in the above procedure is critical for subsequent accurate evaluation of numerical derivatives of the potential energy and dipole moment functions, and the value of 0.1 Å for the step size was chosen on the basis of those recommended in Refs. 27 and 28. Since the OH stretching coordinate is approximated as a Morse oscillator, the Birge-Spooner expression allows the overtone transition frequencies (ν) to be estimated through the equation:

$$\nu(cm^{-1}) = v\omega_e - (v^2+v)\omega_e\chi_e \qquad (3.8)$$

In the above expression v is the vibrational level while ω_e and $\omega_e\chi_e$ are the local-mode vibrational frequency and anharmonicity respectively. These parameters are extracted from the *ab initio* potential energy curve V(q) by noting that for a Morse potential, the frequency and anharmonicity depend on the reduced mass of the oscillator and on the second and third order force constants, F_{ii} and F_{iii} through the following expressions[29]

$$\omega_e\ (cm^{-1}) = \omega_e/2\pi c = (F_{ii}G_{ii})^{1/2}/2\pi c \qquad (3.9)$$

$$\omega_e\chi_e\ (cm^{-1}) = \omega_e\chi_e/2\pi c = (hG_{ii}/72\pi^2 c)\ (F_{iii}/F_{ii})^2 \qquad (3.10)$$

In the above equations G_{ii} is reciprocal of the O-H oscillator's reduced mass, h is Plank's constant and c the velocity of light. We determine the force constants F_{ii} and F_{iii} by fitting the discrete set of *ab initio* potential energy points represented by V(q) with a 7-th order polynomial in the displacement coordinate and then numerically evaluating the second and third order derivatives about the equilibrium position. From this procedure we obtain values for ω_e and $\omega_e\chi_e$. The *ab initio* OH stretching potential V(r) as a function of r generated at the CCSD(T)/aug-cc-pVTZ is shown in Fig. 3.4 along with the first few vibrational levels associated with the Morse potential. The Mathematica code used in obtaining the Morse parameters is provided in Appendix *D*.

As it is difficult to carry out *ab initio* calculation of the frequency and anharmonicity at the level required to match experimental accuracy, we scale the *ab initio* values using scaling parameters.[18,29] The scaling parameters for a particular level of theory are determined by running calculations at that same level on several reference molecules for which experimental data for ω_e and $\omega_e\chi_e$ are available. We have done this using nitric acid, methanol, *trans* HONO, and HOCl. The result from this scaling is that ω_e=3714 cm^{-1} and $\omega_e\chi_e$=85 cm^{-1} for HO_2NO_2. By comparison, the experimental value for these parameters are ω_e=3716 cm^{-1} and $\omega_e\chi_e$=88 cm^{-1}. Table 3.21 summarizes the harmonic frequencies and anharmonicities of PNA as well as the values for the reference molecules used for the evaluations of the average scaling parameters ($<f_{\omega e}>$=0.99568 and $<f_{\omega e\chi e}>$=0.86595). The predicted OH overtone frequencies using these scaled values of ω_e and $\omega_e\chi_e$ and Eq. 3.8 are presented in Table 3.22. The agreement between experimental and calculated OH overtone frequencies is excellent. The error between the measured and calculated transition frequencies increase slightly with vibrational level and for the highest level measured ($4\nu_{OH}$); the error is ~ 0.39 %. The corresponding vibrational overtone oscillator strength, *f*, for transition from the ground state to an excited vibrational level v is given by the expression: [27,29]

$$f = 4.702 \times 10^{-7}\ [\text{cm D}^{-2}]\ \nu_{0\rightarrow v}\ |\boldsymbol{\mu}_{0\rightarrow v}|^2 \qquad (3.11)$$

In the above equation $\nu_{0\rightarrow v}$ is the transition frequency in cm^{-1} and $\boldsymbol{\mu}_{0\rightarrow v} = <0|\boldsymbol{\mu}(r\text{-}r_e)|v>$ is the transition dipole moment matrix element between the ground and excited vibrational level. The *ab initio* dipole moment function ($\boldsymbol{\mu}(q= r\text{-}r_e)$) in the above equation is obtained in a manner similar to V(q) i.e., by stretching the O-H bond by $r_e \pm 0.4$ Å in increments of 0.1 Å. However, as neither GAUSSIAN98 nor GAUSSIAN03 calculate dipole moments

at the CCSD(T) level of theory, we perform the dipole calculations at the QCISD/cc-pVTZ level using the keyword DENSITY=CURRENT. This allows dipole moments to be calculated using the generalized density for the specified level of theory and provides dipole moments that are correct analytical derivatives of the energy.[29] In essence, this procedure requires to re-optimize the PNA molecule at that level of theory and then stretch and compress the O-H bond by $r_e \pm 0.4$ Å in order to obtain the X, Y and Z dipole moment components. In general, GAUSSIAN98/GAUSSIAN03 produces gradients or post SCF (self-consistent field) densities only for methods which analytic gradients are available (MP2, MP3, MP4SDQ, CI, CCD, and QCI). The dipole moment values over the grid of points are shown in Table 3.23. The general trend that emerges from the table suggests that the three dipole moment components increase with the stretching of the O-H.

To continue solving for equation 3.11 we use a nonlinear 7th order polynomial to fit the dipole moment points and make use of a seventh order Taylor expansion about the equilibrium position (r_e) to obtain the dipole moment function in terms of q:

$$\boldsymbol{\mu}(q) = \sum (\partial^n \boldsymbol{\mu}/\partial q^n)|_{q=qo}\, q^n /n! \qquad (3.12)$$

The appropriate Morse wavefunction[34-37] along with each component of the *ab initio* dipole moment function is substituted into the Eq. 3.11 and the resulting matrix element integral evaluated numerically. The expansion coefficients (derivatives) for each component of the dipole moment are given in Table 3.23 as well. The analytical Morse oscillator wave functions which are also required in order to evaluate the $|\boldsymbol{\mu}_{0\rightarrow v}|^2$ term in Eq. 3.11 can be expressed in terms of the generalized Laguerre polynomials, $L^b_n(z)$, where the eigenfunctions, v, have the generalized form:

$$|v> = N_v\, e^{-z/2}\, z^{b/2}\, L^b_n(z) \tag{3.13}$$

N_v is the normalization constant defined as follows:

$$N_v = (v!\bullet a\bullet b/\Gamma(k-v))^{1/2} \tag{3.14}$$

The term k in the Gamma function is simply the ratio between the harmonic and anharmonic frequencies:

$$k = (\omega_e/\omega_e\chi_e) \tag{3.15}$$

and,

$$z = k\, \exp[-a(r-r_e)] \tag{3.16}$$

with a and b equal:

$$a = 0.243559\, (\mu\bullet\, \omega_e\chi_e)^{1/2} \tag{3.17}$$

$$b = k-2v-1 \tag{3.18}$$

The full program used in the evaluations of the dipole moment expansion functions and the Morse wave functions in Eq. 3.11 is provided in Appendix *D*. Plots for the dipole moment functions and the first few normalized Morse eigenfunction are shown in Fig. 3.5. Note that the term $|\boldsymbol{\mu}_{0\rightarrow v}|^2$ is a geometrical sum of the three components of the transition dipole moments. I.e., proper evaluation of $|\boldsymbol{\mu}_{0\rightarrow v}|^2$ involves adding the squared components of $\boldsymbol{\mu}_x$, $\boldsymbol{\mu}_y$, $\boldsymbol{\mu}_z$ in the following manner:

$$|\boldsymbol{\mu}_{0\rightarrow v}|^2 = |<0|\boldsymbol{\mu}_x|v>|^2 + |<0|\boldsymbol{\mu}_y|v>|^2 + |<0|\boldsymbol{\mu}_z|v>|^2 \tag{3.19}$$

The sum in equation 3.19 is then combined with the appropriate transition frequency in accords with Eq. 3.11 to provide with the total oscillator strength as given in Table 3.22. The unitless oscillator strength, *f*, can readily be transformed to integrated absorption cross-sections ($\int\sigma(\nu)d\nu$) which are also given in Table 3.23 using:[34]

$$f = 4e^{-2}m_e c^2\epsilon_0 \int \sigma(\nu)d\nu = 1.1296 \times 10^{12} \int \sigma(\nu)d\nu \qquad (3.20)$$

With e being the charge of the electron, is m_e the electron mass, c is the speed of light and ϵ_0 is the permittivity of vacuum. The results of the calculations match the experimental values reasonably well with the predicted values for $2\nu_{OH}$ and $3\nu_{OH}$ being within ~15% of the experimental value. Based on the work presented in Chapter 2 in is clear that HO_2NO_2 samples generated in the lab typically contain other OH molecules which lead to complication in measuring absolute absorption cross sections. In addition, it is difficult to estimate accurately the concentration of PNA in a typical sample as the concentrations of these impurities (such as HOONO) changes with usage and their decomposition products generate additional complications. Thus, *ab initio* predictions of absorption cross-sections can help with validating some of the experimental data which are obtained in the lab for PNA.

3.4 Conclusions

The study presented in Chapter 3 investigates the structure, thermochemistry and vibrational spectroscopy of PNA. The best estimates for the structure is PNA presented here is obtained through a high level *ab initio* optimization using coupled-cluster and configuration-interaction methods with high angular momentum basis sets. We have found that a reasonable structure is obtained with the coupled-cluster methods using triple excitations and high angular momentum or quadruple excitation basis sets. In a separate study, an investigation of the torsional potential have confirmed that the global minimum energy structure of PNA has the NO"OH dihedral angle of $\tau \approx 84^o$ out of the plane and the O'NO"O dihedral angle is slightly in the *cis* conformation with $\tau \approx 12^o$ out of the plane. A comparison with microwave data currently available for HO_2NO_2, suggests that

ab initio equilibrium rotational constants calculated at the CCSD(T)/aug-cc-pVTZ and CCSD(T)/cc-pVQZ levels of theory are quite accurate and could be used in conjunction with measured rotational constants of multiple isotopomers to extract an experimentally determined structure of HO_2NO_2.

An additional advantage that the *ab initio* study has over experimental studies is in determining the bond dissociation energies for the $HO_2 + NO_2$ and $OH + NO_3$ channels which are difficult to obtain experimentally due to impurities and detection techniques. The value of -9.88 kcal/mol is extracted for the heat of formation of HO_2NO_2 (ΔH_f^0) using basis-set limit extrapolation in conjunction to the isodesmic reaction scheme. At room temperature, this value corresponds to $\Delta H_f^{298\ K}$ [HO_2NO_2] = -11.25 kcal/mol which differ by 1.35 kcal/mol from that reported in Ref. 5. This ΔH_f^0 value suggests that the bond dissociation energy $D_0[HO_2 + NO_2]$ = 21.74 kcal/mol is consistent with quantum yield measurements from the first OH stretching overtone.

Vibrational frequencies of the twelve fundamental bands as well as several OH stretching overtones have also been calculated at the coupled-cluster level of theory and provide a reliable spectroscopic database to assist atmospheric detection and monitoring of various vibrational bands of HO_2NO_2. The present calculations of the OH stretching overtone oscillator strength corroborate results of previous calculations carried out at lower level and should be useful for evaluating the importance of HO_2NO_2 overtone initiated chemistry in the atmosphere.

3.5 Acknowledgement

Chapter 3, in part, is a reprint of the material as it appears in Journal of Chemical Physics 121, 5720 (2004). J. Matthews, J. S. Francisco, and A. Sinha, American Institute of Physics, 2004. The dissertation author was the primary investigator and author of this paper.

Table 3.1: Z-matrices Used with CCSD(T)/cc-pVDZ Energies, frequencies and Structure Calculations for *cis-cis* and *cis-perp'* HO_2NO_2 Conformers

cis-cis Conformer

```
#p ccsd(t,maxcyc=300)/cc-pVDZ  trans=iabc  scf=(direct,tight)
opt=ef  freq=noraman

cis-cis hoono2 optimization

0 1
O
N 1 B1
O 2 B2 1 A1
O 2 B3 1 A2 3 D1 0
O 4 B4 2 A3 3 D2 0
H 5 B5 4 A4 2 D3 0
     Variables:
B1=1.20638
B2=1.20407
B3=1.51505
B4=1.42728
B5=0.97565
A1=133.30168
A2=109.7543
A3=108.00166
A4=101.81448
D1=178.35107
     Constants:
D2=0.0
D3=0.0
```

cis-perp' Conformer

```
#p ccsd(t,maxcyc=300)/cc-pVDZ  trans=iabc  scf=(direct,tight)
opt=ef  freq=noraman

cis-perp' hoono2 optimization

0 1
O
N 1 B1
O 2 B2 1 A1
O 2 B3 1 A2 3 D1 0
O 4 B4 2 A3 3 D2 0
H 5 B5 4 A4 2 D3 0
     Variables:
B1=1.20638
B2=1.20407
B3=1.51505
B4=1.42728
B5=0.97565
A1=133.30168
A2=109.7543
A3=108.00166
A4=101.81448
D1=178.35107
D3=90.0
     Constants:
D2=0.0
```

Table 3.2: CCSD(T)/cc-pVDZ Equilibrium Structure and Energies for Conformers of HO_2NO_2 [a]

Conformer	r(O-N)	r(O'-N)	r(O"-N)	r(O"-O)	r(O-H)	∠(ONO')	∠(ONO")	∠(NO"O')	∠(O"OH)	τ(ONO"O)	τ(O'NO"O)	τ(NO"OH)	E (opt.) (hartree)	E (rel.) (kcal mol^{-1})
global min.	1.200	1.200	1.518	1.418	0.976	133.6	109.9	108.1	101.6	177.9	-12.3	84.0	-355.19609	0.0
cis-cis	1.198	1.217	1.452	1.450	0.986	131.9	111.6	109.9	100.1	180.0	0.0	0.0	-355.19335	1.7
cis-perp	1.201	1.198	1.522	1.419	0.975	133.7	109.4	108.2	101.3	180.7	0.0	90.0	-355.19562	0.3
cis-trans	1.205	1.199	1.467	1.468	0.975	133.1	109.3	105.9	95.7	180.0	0.0	180.0	-355.18931	4.3
trans-cis	1.217	1.198	1.452	1.450	0.986	132.0	116.4	109.9	100.1	180.0	180.0	0.0	-355.19335	1.7
trans-perp	1.199	1.201	1.522	1.419	0.975	133.7	116.8	108.2	101.2	182.0	180.0	90.0	-355.19565	0.3
trans-trans	1.199	1.205	1.466	1.468	0.975	133.1	117.6	105.9	95.7	180.1	180.0	180.0	-355.18931	4.3
trans-perp'	1.199	1.201	1.522	1.418	0.975	133.7	116.8	108.3	101.4	182.1	180.0	86.7	-355.19567	0.3
cis-perp'	1.201	1.199	1.522	1.418	0.975	133.7	109.4	108.3	101.4	180.5	0.0	87.9	-355.19563	0.3
perp'-perp'	1.200	1.201	1.517	1.419	0.976	133.6	116.5	108.1	101.6	182.2	169.4	83.8	-355.19609	0.0

[a] **Bond distances are in Angstroms and bond angles are in degrees.**

Table 3.3: CCSD(T)/cc-pVDZ Harmonic Frequencies of the Rotomers (cm^{-1})

Conformer	ν_1	ν_2	ν_3	ν_4	ν_5	ν_6	ν_7	ν_8	ν_9	ν_{10}	ν_{11}	ν_{12}
global min.	3728	1821	1426	1355	929	807	727	640	450	370	299	132
cis-cis	3564	1789	1475	1326	906	841	727	687	515	384	305	118*i*
cis-perp	3731	1823	1421	1356	930	806	725	639	449	368	314	128
cis-trans	3760	1809	1392	1346	908	833	728	634	510	331	145	275*i*
trans-cis	3563	1789	1476	1326	906	841	727	687	515	383	308	115*i*
trans-trans	3759	1810	1392	1347	908	833	728	635	510	331	146	273*i*
trans-perp'	3729	1823	1424	1356	930	806	725	638	448	367	311	127
cis-perp'	3730	1823	1422	1356	930	806	725	638	448	368	312	126
perp'-perp'	3728	1820	1427	1355	929	808	728	641	452	368	300	133

Table 3.4: Equilibrium Geometry Parameters for HO_2NO_2 (Distances in Å, Angles in deg)

	QCISD				QCISD(T)			CCSD(T)				
	6-31G** [a]	cc-pVDZ	aug-cc-pVDZ	cc-pVTZ	6-31G(d)	6-311++G(2d,2p)	6-311++G(2df,2p)	cc-pVDZ	aug-cc-pVDZ	cc-pVTZ	aug-cc-pVTZ	cc-pVQZ
r(O-N)	1.205	1.196	1.201	1.190	1.211	1.201	1.196	1.200	1.206	1.196	1.196	1.193
r(O'-N)	1.205	1.196	1.199	1.189	1.210	1.200	1.195	1.200	1.204	1.194	1.195	1.192
r(O"-N)	1.477	1.484	1.480	1.459	1.512	1.513	1.496	1.518	1.515	1.491	1.496	1.483
r(O"-O)	1.419	1.409	1.415	1.400	1.430	1.420	1.409	1.418	1.427	1.411	1.414	1.406
r(O-H)	0.971	0.974	0.973	0.966	0.982	0.967	0.968	0.976	0.976	0.968	0.971	0.967
∠(ONO')	132.7	133.1	132.7	132.6	133.3	133.3	133.4	133.6	133.3	133.2	133.3	133.1
∠(ONO")	110.1	110.0	110.0	110.2	109.9	109.8	109.9	109.9	109.8	109.9	109.8	110.0
∠(NO"O)	108.6	108.7	108.6	109.3	108.0	108.5	108.8	108.1	108.0	108.8	108.7	108.9
∠(O"OH)	102.1	102.0	102.3	102.6	101.8	102.1	102.5	101.6	101.8	102.1	102.3	102.4
τ(ONO"O)	169.0	177.8	178.2	178.0	178.0	178.4	178.2	177.9	178.4	178.2	178.5	178.1
τ(O'NO"O)	-	-13.0	-11.3	-11.9	-11.9	-10.9	-11.2	-12.2	-10.5	-11.2	-10.2	-11.3
τ(NO"OH)	83.8	84.2	85.0	83.4	85.4	85.6	84.8	84.2	85.7	84.1	85.9	84.0
E (hartree)	-	-355.16332	-355.25112	-355.50002	-355.13800	-355.43080	-355.53817	-355.19609	-355.29191	-355.55309	-355.58566	-355.66443

[a] **Reference 15.**

Table 3.5: Equilibrium Rotational Constants of HO_2NO_2 (cm^{-1})

Method	Basis Set	Rotational constants (cm^{-1}) [a]		
		A	B	C
QCISD	cc-pVDZ	0.399799	0.156950	0.114220
	aug-cc-pVDZ	0.398393	0.154609	0.113817
	cc-pVTZ	0.406910	0.159358	0.115971
QCISD(T)	6-31G(d)	0.388690	0.152969	0.111193
	6-311++G(2d,2p)	0.393994	0.153566	0.111856
	6-311++G(2df,2p)	0.398844	0.155902	0.113486
CCSD(T)	cc-pVDZ	0.393199	0.153888	0.112035
	aug-cc-pVDZ	0.391020	0.153205	0.111436
	cc-pVTZ	0.399585	0.156271	0.113736
	aug-cc-pVTZ	0.398793	0.155546	0.113270
	cc-pVQZ	0.402404	0.157224	0.114462
Expt.[b]		0.400093	0.155616	0.113318

[a] Calculated constants correspond to equilibrium structure while experimental values are for vibrational ground state. [b] Reference 2.

Table 3.6: HO_2NO_2 Z-matrices Used with CCSD(T)/cc-pVDZ Energies Calculations

CCSD(T) /cc-pVDZ

```
#p ccsd(t,maxcyc=300)/cc-pVDZ  trans=iabc  scf=(direct,tight)
opt=ef  freq=noraman

hoono2 optimization and ZPE at ccsd(t)/cc-pvdz

0 1
O
N 1 B1
O 2 B2 1 A1
O 2 B3 1 A2 3 D1 0
O 4 B4 2 A3 3 D2 0
H 5 B5 4 A4 2 D3 0
     Variables:
B1=1.20638
B2=1.20407
B3=1.51505
B4=1.42728
B5=0.97565
A1=133.30168
A2=109.7543
A3=108.00166
A4=101.81448
D1=178.35107
D2=-10.53076
D3=85.71068
```

CCSD(T) /cc-pVTZ

```
#p ccsd(t,maxcyc=300)/cc-pVTZ  trans=iabc  scf=(direct,tight)
opt=(ef,readfc)  geom=check guess=read

hoono2 optimization at ccsd(t)/cc-pvtz

0 1
```

CCSD(T) /cc-pVQZ

```
#p ccsd(t,maxcyc=300)/cc-pVQZ  trans=iabc  scf=(direct,tight)
opt=(ef,readfc)  geom=check guess=read

hoono2 optimization at ccsd(t)/cc-pvqz

0 1
```

Table 3.7: HO_2 Z-matrices Used with CCSD(T)/cc-pVξZ (ξ = D, T, Q) Energies Calculations

CCSD(T) /cc-pVDZ
#p uccsd(t,maxcyc=300)/cc-pvdz scf=(direct,tight) trans=iabc opt= ef freq=noraman HO2 optimization and ZPE at ccsd(t)/cc-pvdz 0 2 H O 1 rh O 2 ro 1 a Variables: rh=0.9831 ro=1.3264 a=104.4704
CCSD(T) /cc-pVTZ
#p uccsd(t,maxcyc=300)/cc-pvtz scf=(direct,tight) trans=iabc opt=(ef,readfc) geom=check guess=read HO2 optimization at ccsd(t)/cc-pvtz 0 2
CCSD(T) /cc-pVQZ
#p uccsd(t,Maxcyc=300)/cc-pvtz scf=(direct,tight) trans=iabc opt=(ef,readfc) freq=noraman geom=check guess=read HO2 optimization at ccsd(t)/cc-pvqz 0 2

Table 3.8: NO_2 Z-matrices Used with CCSD(T)/cc-pVξZ (ξ = D, T, Q) Energies Calculations

CCSD(T) /cc-pVDZ
#p uccsd(t,maxcyc=300)/cc-pvdz scf=(direct,tight) trans=iabc opt= ef freq=noraman NO2 optimization and ZPE at ccsd(t)/cc-pvdz 0 2 N O 1 rn O 1 rn 2 a Variables: rn=1.22 a=133.7
CCSD(T) /cc-pVTZ
#p uccsd(t,maxcyc=300)/cc-pvtz scf=(direct,tight) trans=iabc opt=(ef,readfc) geom=check guess=read NO2 optimization at ccsd(t)/cc-pvtz 0 2
CCSD(T) /cc-pVQZ
#p uccsd(t,Maxcyc=300)/cc-pvtz scf=(direct,tight) trans=iabc opt=(ef,readfc) freq=noraman geom=check guess=read NO2 optimization at ccsd(t)/cc-pvqz 0 2

Table 3.9: OH Z-matrices Used with CCSD(T)/cc-pVξZ (ξ = D, T, Q) Energies Calculations

CCSD(T) /cc-pVDZ
#p uccsd(t,maxcyc=300)/cc-pvdz scf=(direct,tight) trans=iabc opt= ef freq=noraman OH optimization and ZPE at ccsd(t)/cc-pvdz 0 2 O H 1 rh Variables: rh=0.9831
CCSD(T) /cc-pVTZ
#p uccsd(t,maxcyc=300)/cc-pvtz scf=(direct,tight) trans=iabc opt=(ef,readfc) geom=check guess=read OH optimization at ccsd(t)/cc-pvtz 0 2
CCSD(T) /cc-pVQZ
#p uccsd(t,Maxcyc=300)/cc-pvtz scf=(direct,tight) trans=iabc opt=(ef,readfc) freq=noraman geom=check guess=read OH optimization at ccsd(t)/cc-pvqz 0 2

Table 3.10: NO_3 Z-matrices Used with CCSD(T)/cc-pVξZ (ξ = D, T, Q) Energies Calculations

CCSD(T) /cc-pVDZ

#p uccsd(t,maxcyc=300)/cc-pvdz scf=(direct,tight) trans=iabc opt= ef freq=noraman

NO3 optimization and ZPE at ccsd(t)/cc-pvdz

0 2
N
X 1 1.0
O 1 r 2 90.0
O 1 r2 2 90.0 3 d2
O 1 r2 2 90.0 3 -d2
Variables:
r=1.4779
r2=1.2138
d2=113.7069

CCSD(T) /cc-pVTZ

#p uccsd(t,maxcyc=300)/cc-pvtz scf=(direct,tight) trans=iabc opt=(ef,readfc) geom=check guess=read

NO3 optimization at ccsd(t)/cc-pvtz

0 2

CCSD(T) /cc-pVQZ

#p uccsd(t,Maxcyc=300)/cc-pvtz scf=(direct,tight) trans=iabc opt=(ef,readfc) freq=noraman geom=check guess=read

NO3 optimization at ccsd(t)/cc-pvqz

0 2

Table 3.11: Sum of Electronic and ZPE[a] for Reactant and Products in:

$HO_2NO_2 \rightarrow HO_2 + NO_2$ and $HO_2NO_2 \rightarrow OH + NO_3$

CCSD(T) Level	Sum of electronic and ZPE[b]				
	HO_2NO_2[c]	HO_2[d]	NO_2[e]	OH[f]	NO_3[g]
cc-pVDZ	-355.1671966	-150.5446278	-204.5957014	-75.55091560	-279.5569691
cc-pVTZ	-355.5241934	-150.6986509	-204.7914520	-75.62928450	-279.8301482
cc-pVQZ	-355.6355336	-150.7458990	-204.8537864	-75.65319470	-279.9169424
CBS	-355.6984362	-150.7725041	-204.8891463	-75.66664356	-279.9661559

[a] From CCSD(T)/cc-pVDZ level of theory.
[b] In units of hartree (E_h).
[c] ZPE[HO_2NO_2] = 0.028897 E_h
[d] ZPE[HO_2] = 0.014071 E_h
[e] ZPE[NO_2] = 0.008807 E_h
[f] ZPE[OH] = 0.008439 E_h
[g] ZPE[NO_3] = 0.011716 E_h

Table 3.12: Thermochemistry of HO_2NO_2 Using the Direct Method:[a]

$HO_2NO_2 \rightarrow HO_2 + NO_2$ and $HO_2NO_2 \rightarrow OH + NO_3$

	D_0[HOO–NO_2]	D_0[HO–NO_3]
CCSD(T)/cc-pVDZ	16.86	37.22
CCSD(T)/cc-pVTZ	21.39	40.64
CCSD(T)/cc-pVQZ	22.50	41.04
CCSD(T)/CBS	23.08	41.20

[a] In units of kcal/mol.

Table 3.13: H_2O Z-matrices Used with CCSD(T)/cc-pVξZ (ξ = D, T, Q) Energies Calculations

CCSD(T) /cc-pVDZ
#p ccsd(t,maxcyc=300)/cc-pvdz scf=(direct,tight) trans=iabc opt= ef freq=noraman H2O optimization and ZPE at ccsd(t)/cc-pvdz 0 1 O H 1 r H 1 r 2 a Variables: r=0.96641743 a=104.02181062
CCSD(T) /cc-pVTZ
#p ccsd(t,maxcyc=300)/cc-pvtz scf=(direct,tight) trans=iabc opt=(ef,readfc) geom=check guess=read H2O optimization at ccsd(t)/cc-pvtz 0 1
CCSD(T) /cc-pVQZ
#p ccsd(t,Maxcyc=300)/cc-pvtz scf=(direct,tight) trans=iabc opt=(ef,readfc) freq=noraman geom=check guess=read H2O optimization at ccsd(t)/cc-pvqz 0 1

Table 3.14: H_2O_2 Z-matrices Used with CCSD(T)/cc-pVξZ (ξ = D, T, Q) Energies Calculations

CCSD(T) /cc-pVDZ

#p ccsd(t,maxcyc=300)/cc-pvdz scf=(direct,tight) trans=iabc opt= ef freq=noraman

H2O2 optimization and ZPE at ccsd(t)/cc-pvdz

0 1
O
O 1 r1
H 1 r2 2 a1
H 2 r2 1 a1 3 d1 0
Variables:
r1=1.46985513
r2=0.97131271
a1=98.85505493
d1=117.9243648

CCSD(T) /cc-pVTZ

#p ccsd(t,maxcyc=300)/cc-pvtz scf=(direct,tight) trans=iabc opt=(ef,readfc) geom=check guess=read

H2O2 optimization at ccsd(t)/cc-pvtz

0 1

CCSD(T) /cc-pVQZ

#p ccsd(t,Maxcyc=300)/cc-pvtz scf=(direct,tight) trans=iabc opt=(ef,readfc) freq=noraman geom=check guess=read

H2O2 optimization at ccsd(t)/cc-pvqz

0 1

Table 3.15: $HONO_2$ Z-matrices Used with CCSD(T)/cc-pVξZ (ξ = D, T, Q) Energies Calculations

CCSD(T) /cc-pVDZ

#p ccsd(t,maxcyc=300)/cc-pvdz scf=(direct,tight) trans=iabc opt= ef freq=noraman

HONO2 optimization and ZPE at ccsd(t)/cc-pvdz

0 1
N
O 1 rno1
O 1 rno2 2 aono2
O 1 rno3 2 aono3 3 180.0 0
H 2 roh 1 ahon 3 0.0 0
Variables:
rno1=1.4070789
rno2=1.21378235
rno3=1.19812684
roh=0.97209972
aono2=115.59243717
aono3=114.00660745
ahon=101.94482153

CCSD(T) /cc-pVTZ

#p ccsd(t,maxcyc=300)/cc-pvtz scf=(direct,tight) trans=iabc opt=(ef,readfc) geom=check guess=read

HONO2 optimization at ccsd(t)/cc-pvtz

0 1

CCSD(T) /cc-pVQZ

#p ccsd(t,Maxcyc=300)/cc-pvtz scf=(direct,tight) trans=iabc opt=(ef,readfc) freq=noraman geom=check guess=read

HONO2 optimization at ccsd(t)/cc-pvqz

0 1

Table 3.16: Sum of Electronic and ZPE[a] for Species in the Isodesmic Reaction: $HO_2NO_2 + H_2O \rightarrow H_2O_2 + HONO_2$

CCSD(T) Level	Sum of electronic and ZPE[b]			
	HO_2NO_2[c]	H_2O[d]	H_2O_2[e]	$HONO_2$[f]
cc-pVDZ	**-355.1671966**	**-76.2198000**	**-151.1678563**	**-280.2105835**
cc-pVTZ	**-355.5241934**	**-76.3107115**	**-151.3324467**	**-280.493342**
cc-pVQZ	**-355.6355336**	**-76.3382927**	**-151.3820554**	**-280.5821122**
CSB	**-355.6984362**	**-76.3537886**	**-151.4098896**	**-280.6323289**

[a] From CCSD(T)/cc-pVDZ level of theory.

[b] In units of hartree (E_h).

[c] ZPE[HO_2NO_2] = 0.028897 E_h

[d] ZPE[H_2O] = 0.021505 E_h

[e] ZPE[H_2O_2] = 0.026164 E_h

[f] ZPE[$HONO_2$] = 0.026476 E_h

TABLE 3.17: Thermochemistry of HO_2NO_2 Using the Isodesmic Reaction:[a]

$$HO_2NO_2 + H_2O \rightarrow H_2O_2 + HONO_2 \qquad \Delta H^o_r$$

CCSD(T) Level	ΔH^o_r	ΔH^o_f [HO_2NO_2]	D_0[HOO–NO_2]	D_0[HO–NO_3]
cc-pVDZ	**5.37**	**-8.97**	**20.83**	**36.35**
cc-pVTZ	**5.72**	**-9.33**	**21.18**	**36.70**
cc-pVQZ	**6.06**	**-9.67**	**21.52**	**37.04**
CBS	**6.28**	**-9.88**	**21.74**	**37.26**

[a] In units of kcal/mol using Ref. 6 for the heats of formation of the species involed.

Table 3.18: Harmonic Vibrational Frequencies for HO_2NO_2 (cm^{-1})

Mode number	Mode description	QCISD			QCISD(T)	CCSD(T)		Expt. [a]
		cc-pVDZ	aug-cc-pVDZ	cc-pVTZ	6-31G(d)	cc-pVDZ	aug-cc-pVTZ	
1	OH str.	3757	3734	3792	3632	3728	3634	3540[b]
2	asym. NO' str.	1828	1771	1800	1782	1821	1794	1728[b]
3	O"OH bend	1453	1447	1470	1435	1426	1438	1397[b]
4	sym. NO' str.	1393	1366	1382	1337	1355	1343	1304[b]
5	O"O str.	981	973	1029	935	929	937	945[c]
6	NO" scissor	840	831	862	793	807	798	803[b]
7	umbrella	762	761	784	711	727	715	722[c]
8	sym. NOO, O"NO bend	682	683	709	639	640	643	654[c]
9	N-O" str.	508	513	537	458	450	466	483[c]
10	HOO"N tors.	381	374	380	367	368	368	340[c]
11	asym. NOO, O"NO bend	307	311	300	299	299	300	-
12	O"-NO_2 tors.	138	135	139	133	132	131	145[d]

[a] Observed transition frequencies [b] Reference 1. [c] Reference 26. [d] Reference 2.

Table 3.19: HO_2NO_2 Z-matrix Used with MP2/cc-pVTZ Harmonic Frequencies and Anharmonicities

MP2/cc-pVTZ
#p mp2/cc-pvtz scf=direct trans=iabc density=current opt=ef freq=(noraman,vibrot,anharmonic)
hoono2 geometry optimization and anharmonic freq. calculation
0 1 O N 1 B1 O 2 B2 1 A1 O 2 B3 1 A2 3 D1 0 O 4 B4 2 A3 3 D2 0 H 5 B5 4 A4 2 D3 0 Variables: B1=1.1993 B2=1.1965 B3=1.5503 B4=1.4059 B5=0.9739 A1=135.03 A2=109.26 A3=107.63 A4=101.75 D1=178.66 D2=-9.42 D3=88.0

Table 3.20: Harmonic Frequencies and Anharmonicities of HO_2NO_2 Computed at MP2/cc-pVTZ (cm^{-1})

$(\omega_e)_i$	148	313	372	444	661	739	790	987	1317	1426	1929	3768
$(\omega_e\chi_e)_{ij}$	12	11	10	9	8	7	6	5	4	3	2	1
1	0.722	-0.973	-1.09	-0.532	-0.256	-0.195	-0.469	-2.96	-0.402	-23.4	-6.32	-86
2	-0.886	-1.08	-2.08	4.04	-0.642	-5.51	-3.82	-0.523	-4.0	1.08	-8.50	
3	-0.755	1.16	1.95	-2.19	-1.26	0.283	-0.812	-14.0	0.001	-11.3		
4	-0.484	-0.715	-1.03	5.79	2.28	-9.31	-3.23	-0.905	-4.0			
5	-1.49	-1.51	-2.11	-0.021	-6.62	-2.29	-0.381	-5.80				
6	0.431	1.06	0.457	-6.88	-1.45	-1.41	-0.066					
7	-0.374	-1.49	-3.02	-7.63	-5.96	0.30						
8	0.717	-4.97	-4.12	-0.770	-2.91							
9	0.003	-0.678	3.30	-4.73								
10	-3.43	-10.3	-10.6									
11	1.68	-1.02										
12	-1.53											

Table 3.21: Morse Parameters for OH Stretching mode of $HONO_2$, HONO, HO_2NO_2, CH_3OH, HOCl and HO_2NO_2 (cm^{-1})

		Ab initio	**Experimental**	**Scale factors**	**Ab-initio Scaled[a]**
$HONO_2$	ω_e	**3737**	**3707[b]**	**0.99197**	**3721**
	$\omega_e\chi_e$	**93**	**79[b]**	**0.84946**	**80**
trans-HONO	ω_e	**3773**	**3751[c]**	**0.99417**	**3757**
	$\omega_e\chi_e$	**95**	**81[c]**	**0.85263**	**82**
CH_3OH	ω_e	**3856**	**3853[d]**	**0.99922**	**3839**
	$\omega_e\chi_e$	**97**	**85[d]**	**0.87629**	**84**
HOCl	ω_e	**3789**	**3779[e]**	**0.99736**	**3773**
	$\omega_e\chi_e$	**96**	**85[e]**	**0.88542**	**83**
HO_2NO_2	ω_e	**3730**	**3716[f]**	**0.99625**	**3714**
	$\omega_e\chi_e$	**98**	**88[f]**	**0.89796**	**85**

[a] Using average scale factors from reference molecules at CCSD(T)/aug-cc-pVTZ ($<f_{\omega e}>=0.99568$ and $<f_{\omega e\chi e}>=0.86595$). [b] Ref. 30. [c] Ref. 31. [d] Ref. 32. [e] Ref. 33. [f] Ref. 9.

Table 3.22: Predicted OH Overtone Transition Frequencies, Oscillator Strengths and Absorption Cross-Sections for HO_2NO_2

Overtone Transition	HO_2NO_2				
	ν_{OH} (cm^{-1})		f	σ (cm molec.$^{-1}$)	
	calc. [a]	expt.		calc. [b]	expt.
V=1	3544	3540[c]	8.3×10^{-6}	0.74×10^{-17}	0.72×10^{-17} [c]
V=2	6918	6900[c]	1.0×10^{-6}	9.03×10^{-19}	9.5×10^{-19} [c]
V=3	10 122	10 090[c]	4.1×10^{-8}	3.61×10^{-20}	3.3×10^{-20} [c]
V=4	13 156	13 105[d]	2.0×10^{-9}	1.79×10^{-21}	3.0×10^{-21} [d]
V=5	16 020	-	1.8×10^{-10}	1.56×10^{-22}	-
V=6	18 714	-	2.5×10^{-11}	2.19×10^{-23}	-

[a] Using scaled CCSD(T)/aug-cc-pVTZ. [b] Using a dipole function calculated at QCISD/cc-pVTZ. [c] Reference 4. [d] Reference 9.

Table 3.23: QCISD/cc-pVTZ Dipole Moment Points as a Function of O-H Bond Length and Dipole Derivatives [a]

r (Å)	X	Y	Z	$(\frac{\partial^n \mu}{\partial q^n})_{eq}$		X	Y	Z
0.6657	1.2055	0.3525	1.1705	n=0	(D)	1.495	0.496	1.423
0.7657	1.3170	0.4046	1.2565	n=1	(D Å^{-1})	0.711	0.395	0.479
0.8657	1.4146	0.4529	1.3423	n=2	(D Å^{-2})	-2.078	-0.815	-1.331
0.9657	1.4954	0.4959	1.4225	n=3	(D Å^{-3})	-4.331	-3.376	-8.575
1.0657	1.5554	0.5307	1.4893	n=4	(D Å^{-4})	-2.233	-3.829	7.344
1.1657	1.5904	0.5541	1.5343	n=5	(D Å^{-5})	93.333	143.333	196.667
1.2657	1.5969	0.5635	1.5502	n=6	(D Å^{-6})	53.333	66.667	246.667
1.3657	1.5730	0.5568	1.5324	n=7	(D Å^{-7})	-1.0×10^3	-13×10^3	-6.5×10^3

[a] **Bond lengths in units of Å and Dipole moments in units of Debye.**

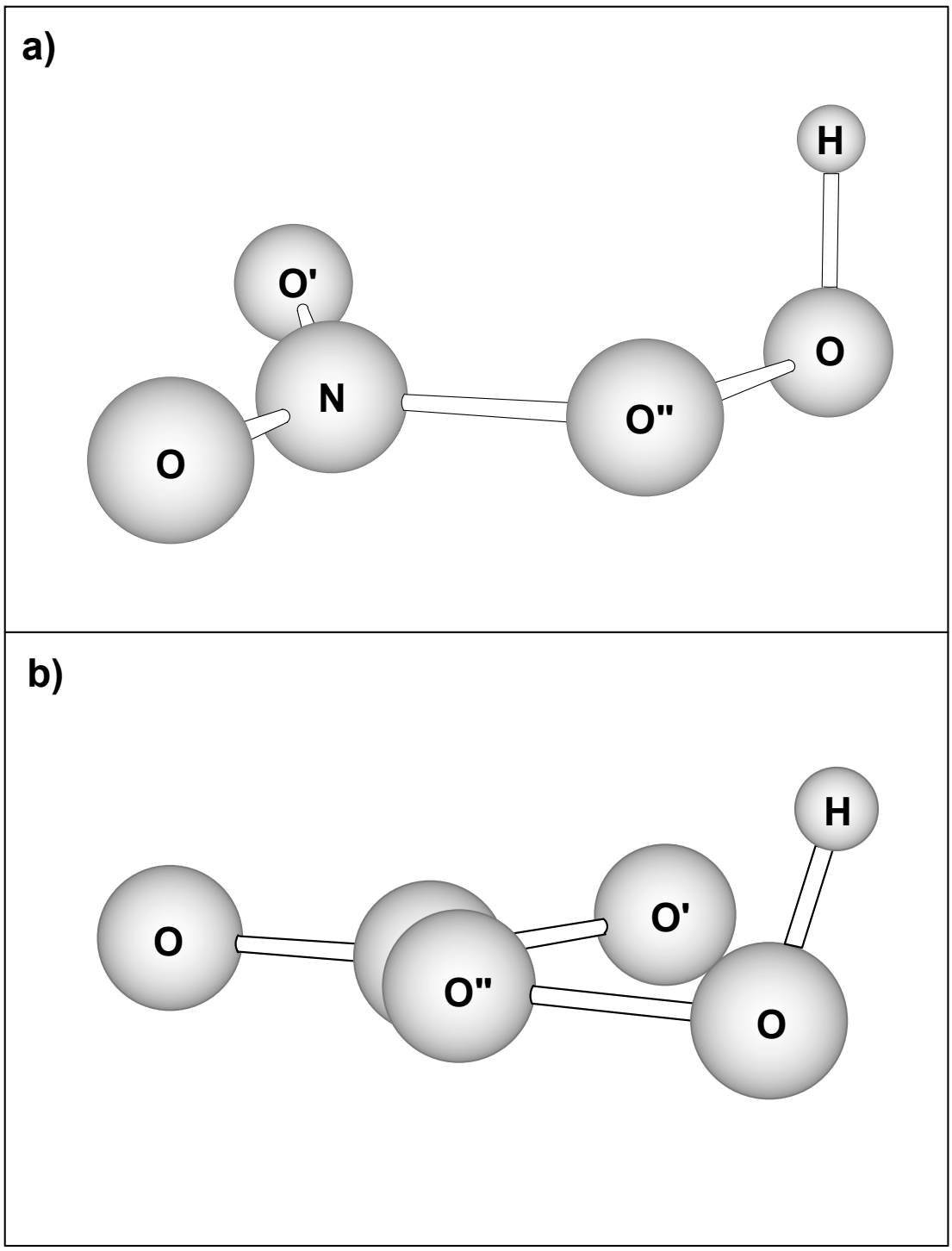

Figure 3.1: Two perspective views of the HO_2NO_2 global minimum structure optimized at the CCSD(T)/aug-cc-pVQZ level. Detailed geometrical parameters are given in Table 3.4. [File: F3.1_molec]

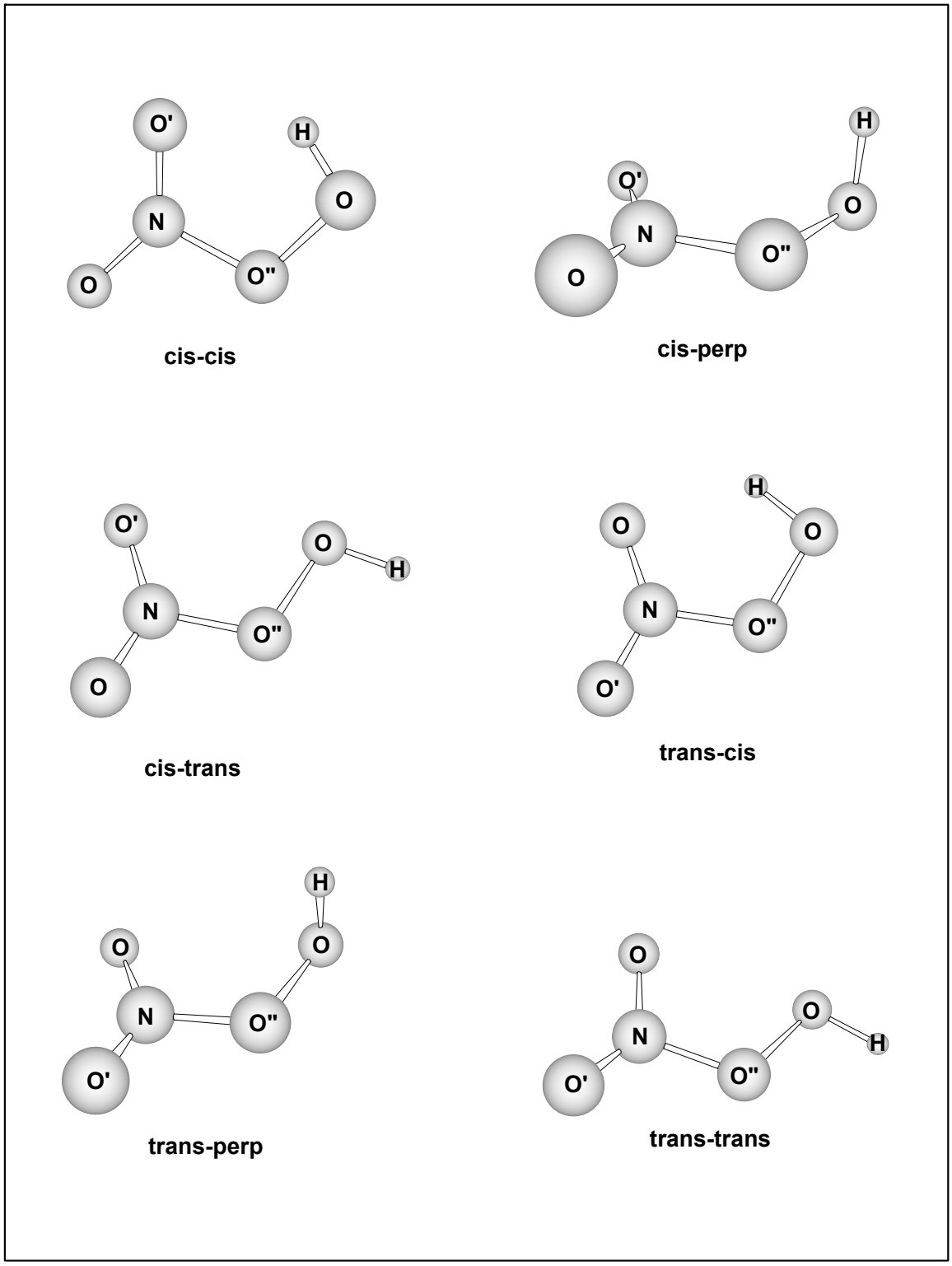

Figure 3.2: Several rotational conformers of HO_2NO_2 for which energies have been calculated in Table 3.1. Note that the NO' and NO bond lengths are not identical. [File: F3.2_confor]

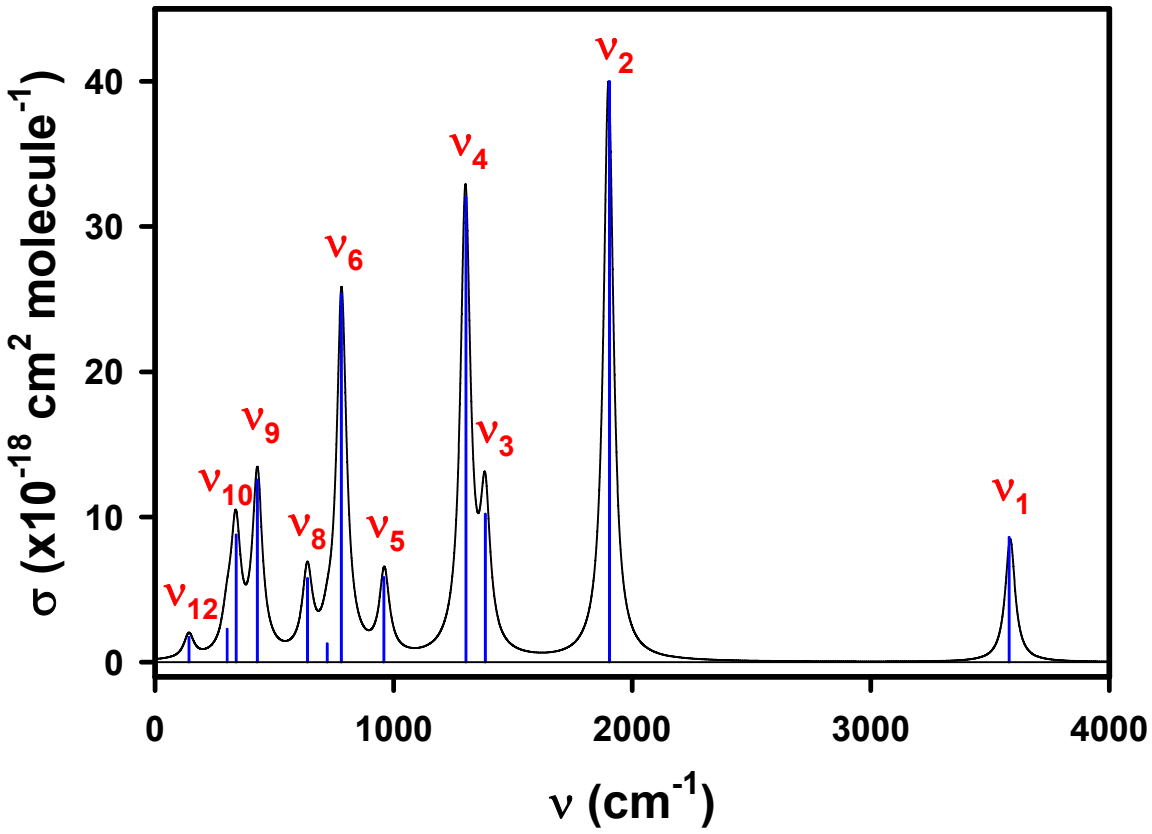

Figure 3.3: The absorption spectrum in the fundamental region of HO_2NO_2 predicted by the MP2/cc-pVTZ level. Note that the most intense transition does not involve O-H stretching mode but corresponds to N-O' stretching mode. [File: F3.3_spectra]

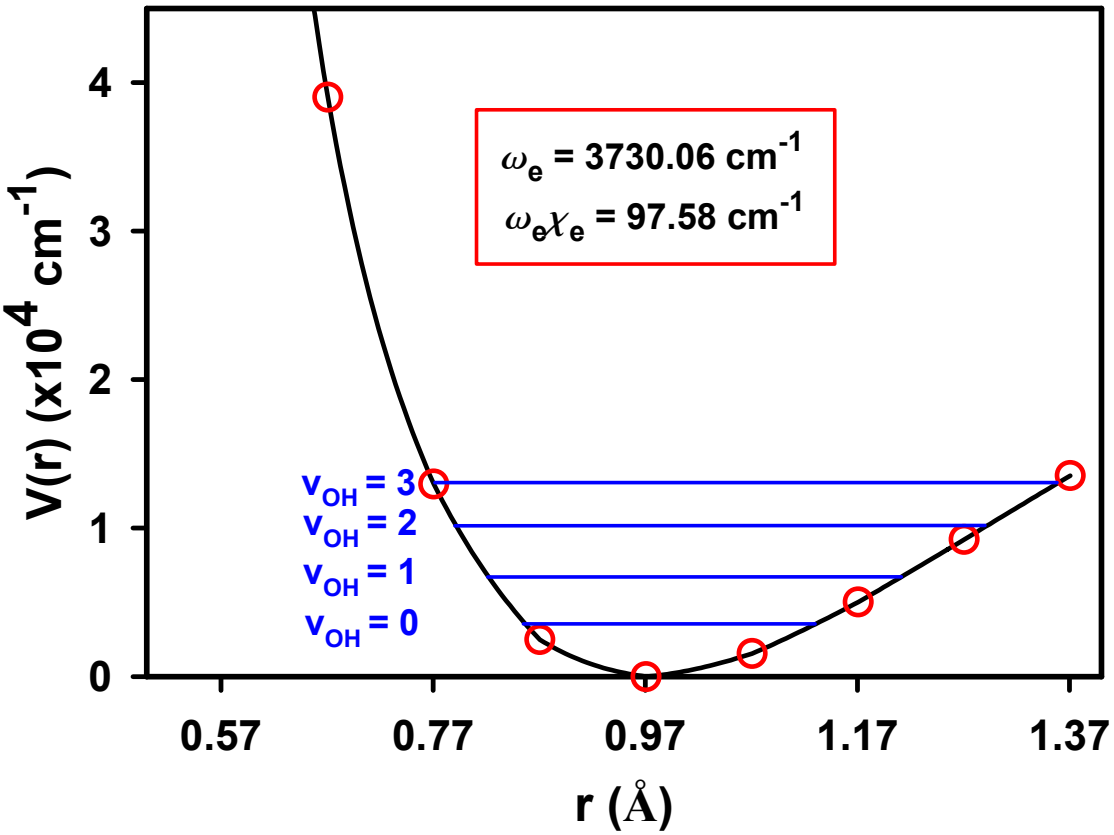

Figure 3.4: O-H stretching potential generated using single point calculations at the CCSD(T)/aug-cc-pVTZ level of theory. The potential is obtained by stretching and compressing the O-H bond by ± 0.4 Å from the optimized equilibrium (r_e ~ 0.97 Å) in steps of 0.1 Å (see text). The second and third derivatives of the potential with respect to r provide with the harmonic and anharmonic frequencies. The first few OH levels are also shown relative to ZPE. [File: F3.4_potential]

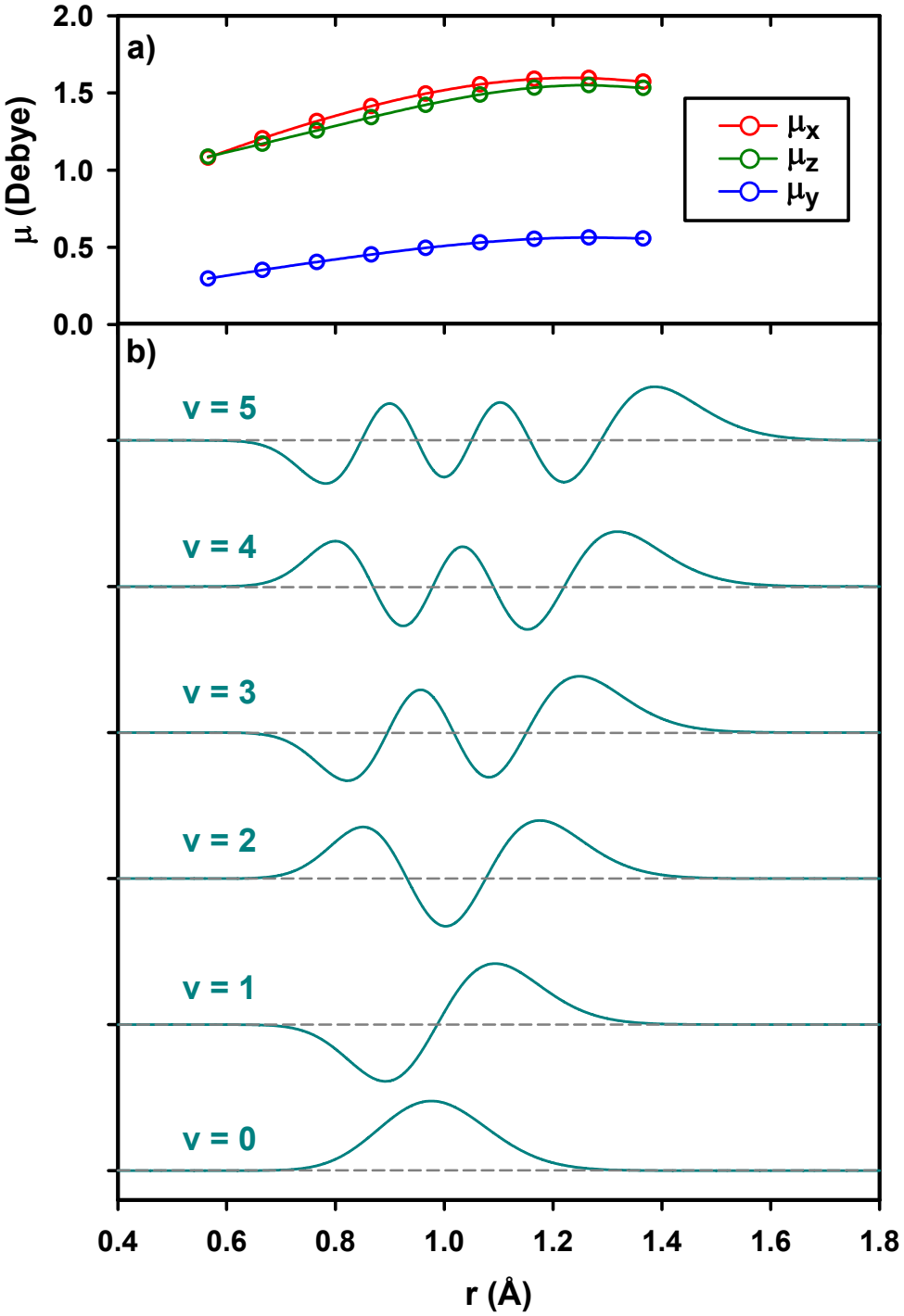

Figure 3.5: a) The three components of the dipole moments functions associated with the O-H stretching mode obtained from single point calculations at the QCISD/cc-pVTZ level of theory. b) Morse oscillator wave functions associated with v = 0 – 5 of the OH stretching modes. [File: F3.5_wavefunctions]

3.6 References

1. H. Niki, P. D. Maker, C. M. Savage and L. P. Breitenbach, Chem.Phys. Lett. **45**, 564 (1977).

2. R. D. Suenram, F. J. Lovas, and H. M. Pickett, J. Mol. Spectrosc. **116**, 406 (1986).

3. G. Brasseur, J. J. Orlando, and G. S. Tyndall, *Atmospheric Chemistry and Global Change* (Oxford University Press 1999).

4. C. M. Roehl, S. A. Nizkorodov, H. G. Zhang, A. Blake, and P. O. Wennberg, J. Phys. Chem. A. **106**, 3766 (2002).

5. T. Gierczak, E. Jimenez, V. Riffault, J. B. Burkholder, A. R. Ravishankara, J. Phys. Chem A. **109**, 586 (2005).

6. D. R. Lide, ed., *CRC Handbook of Chemistry and Physics, Internet Version 2007, 87th Edition*, <http://www.hbcpnetbase.com> (Taylor and Francis, Boca Raton, Florida 2007).

7. D. J. Donaldson, G. J. Frost, K. H. Rosenlof, A. F. Tuck, and V. Vaida, Geophys. Res. Lett. **24**, 2651 (1997).

8. W. B. DeMore, *et al.* JPL Publication 94-26, NASA/ JPL, Pasadena, CA. (1994).

9. H. Zhang, C. M. Roehl, S. P. Sander, and P. O. Wennberg, J. Geophys. Res. **105**, 14593 (2000).

10. M. J. Frisch, G. W. Trucks, H. B. Schlegel, G. E. Scuseria, M. A. Robb, J. R. Cheeseman, V. G. Zakrzewski, J. A. Montgomery, Jr., R. E. Stratmann, J. C. Burant, S. Dapprich, J. M. Millam, A. D. Daniels, K. N. Kudin, M. C. Strain, O. Farkas, J. Tomasi, V. Barone, M. Cossi, R. Cammi, B. Mennucci, C. Pomelli, C. Adamo, S. Clifford, J. Ochterski, G. A. Petersson, P. Y. Ayala, Q. Cui, K. Morokuma, N. Rega, P. Salvador, J. J. Dannenberg, D. K. Malick, A. D. Rabuck, K. Raghavachari, J. B. Foresman, J. Cioslowski, J. V. Ortiz, A. G. Baboul, B. B. Stefanov, G. Liu, A. Liashenko, P. Piskorz, I. Komaromi, R. Gomperts, R. L. Martin, D. J. Fox, T. Keith, M. A. Al-Laham, C. Y. Peng, A. Nanayakkara, M. Challacombe, P. M. W. Gill, B. Johnson, W. Chen, M. W. Wong, J. L. Andres, C. Gonzalez, M. Head-Gordon, E. S. Replogle, and J. A. Pople, Gaussian 98, Revision A.11.3, (Gaussian, Inc., Pittsburgh PA, 2002).

11. M. J. Frisch G. W. Trucks, H. B. Schlegel, G. E. Scuseria, M. A. Robb, J. R. Cheeseman, J. A. Montgomery, Jr., T. Vreven, K. N. Kudin, J. C. Burant, J. M. Millam, S. S. Iyengar, J. Tomasi, V. Barone, B. Mennucci, M. Cossi, G. Scalmani, N. Rega, G. A. Petersson, H. Nakatsuji, M. Hada, M. Ehara, K. Toyota, R. Fukuda, J. Hasegawa, M. Ishida, T. Nakajima, Y. Honda, O. Kitao, H. Nakai, M. Klene, X. Li, J. E. Knox, H. P. Hratchian, J. B. Cross, C. Adamo, J. Jaramillo, R. Gomperts, R. E. Stratmann, O.

Yazyev, A. J. Austin, R. Cammi, C. Pomelli, J. W. Ochterski, P. Y. Ayala, K. Morokuma, G. A. Voth, P. Salvador, J. J. Dannenberg, V. G. Zakrzewski, S. Dapprich, A. D. Daniels, M. C. Strain, O. Farkas, D. K. Malick, A. D. Rabuck, K. Raghavachari, J. B. Foresman, J. V. Ortiz, Q. Cui, A. G. Baboul, S. Clifford, J. Cioslowski, B. B. Stefanov, G. Liu, A. Liashenko, P. Piskorz, I. Komaromi, R. L. Martin, D. J. Fox, T. Keith, M. A. Al-Laham, C. Y. Peng, A. Nanayakkara, M. Challacombe, P. M. W. Gill, B. Johnson, W. Chen, M. W. Wong, C. Gonzalez, and J. A. Pople, Gaussian 03, Revision B.04, (Gaussian, Inc., Pittsburgh PA, 2003).

12. K. Raghavachari, G. W. Trucks, J. A. Pople, M. Head-Gordon, Chem. Phys. Lett. 157, 179 (1989); R. Krishnan, J. S. Binkley, R. Seeger, J. A. Pople, J. Chem. Phys. **72**, 650 (1980).

13. T. H. Dunning Jr., J. Chem. Phys. **90**, 1007 (1989); K. A. Peterson, D. E. Woon, T. H. Dunning Jr., J. Chem. Phys. **100**, 7410 (1994).

14. J. S. Francisco, J. Chem. Phys. **115**, 6373 (2001).

15. Z. Chen, and T. P. Hamilton, J. Phys. Chem. **100**, 15731 (1996).

16. Y. Li and J. S. Francisco, J. Chem. Phys.**113**, 7976 (2000).

17. R. P. Saxon and B. Liu, J. Phys. Chem. **89**, 1227 (1985).

18. J. Matthews, A. Sinha, and J. Francisco, J. Chem. Phys. **120**, 10543 (2004).

19. J. Matthews, A. Sinha, and J. Francisco, J. Chem. Phys. **122**, 221101 (2005).

20. J. L. Fry, J. Matthews, J. R. Lane, C. M. Roehl, A. Sinha, H. G. Kjaergaard, and P. O. Wennberg, J. Phys. Chem A. **110**, 7072 (2006).

21. L. C. Jitariu and D. M. Hirst, J. Phys. Chem. **103**, 6673 (1999).

22. C. M. Roehl, T. L. Mazely, R. R. Friedl, Y. Li, J. S. Francisco, and S. P. Sander, J. Phys. Chem. A. **105**, 1592 (2001).

23. C. P. Rinsland, R. Zander, C. B. Farmer, R. H. Norton, L. R. Brown, J. M. Russell, and J. H. Park, Geophys. Res. Lett. **13**, 761 (1986).

24. R. D. May and R. R. Friedl, J. Quant. Spect. Rad. Trans. **50**, 257(1993).

25. R. J. Salawitch, P. O. Wennberg, G. C. Toon, B. Sen, and J. F. Blavier, Geophys. Res. Lett. **29**, 1762 (2002).

26. E. H. Appelman and D. Gosztola, J. Inorg. Chem. **34**, 787 (1995).

27. H. G. Kjaergaard, and B. R. Henry, J. Chem. Phys. **96**, 4841 (1992).

28. H. G. Kjaergaard, and B. R. Henry, J. Phys. Chem. **99**, 899 (1995).

29. R. G. Low, and H. G. Kjaergaard, J. Chem. Phys. **110**, 9104 (1999).

30. A. Sinha, R. L. Van Der Wal, and F. F. Crim, J. Chem. Phys. **91**, 2929 (1989); **92**, 401 (1989).

31. D. Luckhaus, J. Chem. Phys. **118**, 8797 (2003).

32. K. R. Lange, N. P. Weels, K. S. Plegge, and J. A. Phillips, J. Phys. Chem. A. **105**, 3481 (2001).

33. R. J. Barnes, *The State-Resolved Photochemistry of Small Molecules on Their Ground and Electronic Excited States* (University of California-San Diego, 1999).

34. P. W. Atkins, *Molecular Quantum Mechanics, 2nd ed*. (Oxford University Press, Oxford, 1983).

35. P. M. Morse, Phys. Rev. **34**, 57 (1929).

36. M. L. Sage, Chem. Phys. **35**, 375 (1978).

37. J. A. C. Gallas, Phys. Rev. A **21**, 1829 (1980); J. A. C. Gallas, J. Chem. Phys. **69**, 612 (1978).

Chapter 4

Characterization of the Unimolecular Photodissociation of Peroxynitrous Acid in the $2\nu_{OH}$ Region

4.1 Introduction

4.1.1 Properties of Peroxynitrous Acid

Peroxynitrous acid (HOONO) is a structural isomer of nitric acid ($HONO_2$). And similarly to nitric acid, it is formed via a three-body radical-radical recombination reaction of hydroxyl (OH) with nitrogen dioxide (NO_2):

$$OH + NO_2 + M \rightarrow HONO_2 + M \quad (k_1^{298K} = 1.9\times10^{-30}\ cm^6\ molecule^2\ s^{-1}) \quad (4.1)$$

$$OH + NO_2 + M \rightarrow HOONO + M \quad (k_2^{298K} = 1.1\times10^{-32}\ cm^6\ molecule^2\ s^{-1}) \quad (4.2)$$

Recent pressure and temperature dependence studies of the above competing reactions have shown that the branching ratio, f[HOONO] / f[$HONO_2$] may be as high as 20 %.[1] Apparently, the resulting branching ratio of these two closely related molecules is attributed their significant energetics differences. Several *ab initio* studies have investigated the energetics of HOONO which is shown in figure 4.1. According to some of the studies, HOONO molecule has up to three conformers; namely, these are the *cis-cis*, *cis-perp* and *trans-perp*.[2-8] The labeling of the conformational configuration is chosen based on the two dihedral angles τ_{ONOO} and τ_{HOON} which correspond to the torsional motion and provide with the pathways for converting between the conformers of HOONO. For example, the notation *cis-cis* simply corresponds to $\tau_{ONOO} = 0^o$ and $\tau_{HOON} = 0^o$ while the *trans-perp* notation corresponds to $\tau_{ONOO} = 180^o$ and $\tau_{HOON} = 90^o$. As will be

discussed at a later point, in HOONO none of the angles correspond exactly to 0^o, 180^o or 90^o, but rather labeled in that fashion to indicate the rough angles representing the dihedral geometry. Of the three conformers, *cis-cis* HOONO is the most stable because of apparently, the intermolecular hydrogen bonding that is formed between the terminal oxygen and the hydrogen atoms. Comparing the energetics of the *cis-cis* conformer to nitric acid suggests that about ~27 kcal/mol separate these two isomers apart; making the nitric acid isomer chemically "inert" molecule relative to HOONO.[9] In fact, considering the energetics of HOONO suggest that HOONO can fall apart to produce its OH and NO_2 constituents simply from the presence of thermal ambient energy.

Despite its gentle nature, there has been a great deal of effort in characterizing the structure, energetics and spectroscopy of HOONO since its initial detection in the gas-phase.[10] Looking at figure 4.1 raises some issues regarding the conformers of HOONO. Several *ab initio* studies investigating HOONO produced conflicting results as to the number of actual stable conformers the molecule has. For example, from calculations at the G2 level of theory McGrath and Rowland have suggested the possibility of three conformers where the *cis-perp* configuration that is predicted to be ~1.2 kcal/mol above the *cis-cis* energy minimum, and thus lies 2.5 kcal below the *trans-perp* configuration.[2] However, at higher level, using the CCSD(T)/cc-pVTZ method, Fry *et al.* apparently were unable to detect a stationary point on the HOONO potential corresponding to the *cis-perp* configuration.[11] Therefore, these studies have suggested that HOONO only exists in either the *cis-cis* and the *trans-perp* configuration.[11] The differences in the structure of *cis-cis* and *trans-perp* HOONO give rise to two different O-H stretching modes associated with these two modes. At the CCSD(T)/cc-pVTZ level, the harmonic

frequencies associated with the *cis-cis* and *trans-perp* conformers are 3521 cm^{-1} and 3780 cm^{-1} respectively. The relatively low frequency compared with typical OH-stretching associated with the *cis-cis* conformer is due to the "closed" ring-like geometry.

Spectroscopic identification of the *trans-perp* HOONO under jet cooled conditions has confirmed that the binding energy of the *trans-perp* is 16.2 kcal/mol.[12,13] However, the inability by the Lester group to detect the *cis-perp* and more importantly, *cis-cis* HOONO under their experiments conditions have resulted in ambiguities to the makeup of the HOONO action spectrum in both the first and second OH stretching overtones regions.[12-14] When first recorded under room temperature conditions, it was initially suggested by Nizkorodov and Wennberg that HOONO $2\nu_{OH}$ spectrum is composed of the three conformers reported at the G2 level.[2,10] In addition, Fry *et al.* have experimentally shown that at room temperature, under thermal equilibrium conditions, the *trans-perp* rapidly converts to the *cis-cis* conformer, thus, concluding that only a single conformer exists at 298 K.[11] To date however, this conformer has not been detected under molecular beam conditions.

4.1.2 Photodissociation dynamics of the $2\nu_{OH}$ Band

The interesting part about the number of conformer at room temperature reported by Ref 11 is embedded in the HOONO $2\nu_{OH}$ action spectrum. In contrast to high-resolution studies conducted by Lester and coworkers[12-13] on the $2\nu_1$ jet-cooled *trans-perp* molecule and the analysis of the pure rotational spectrum recorded by Drouin *et al.*[15] on the *cis-cis*, the medium resolution room temperature spectrum of HOONO in the region of its first and second OH stretching overtones remains only partially understood. The complexity of these spectra results primarily from the presence of thermal energy,

which leads to hot band transitions and overlapping of spectral features. Furthermore, both the $2\nu_{OH}$ and $3\nu_{OH}$ spectra consists of a weak *cis*-*cis* OH stretching overtone peak followed by a much stronger, broad spectral feature located respectively at ~570 and 730 cm^{-1} to the blue.[10,11,16,17] The $3\nu_{OH}$ data will be discussed in details in Chapter 5. Regardless, the $2\nu_{OH}$ observation is puzzling in itself since the OH stretching states are expected to be the "bright" state in overtone spectroscopy[18,19] and the preponderance of the *cis*-*cis* conformer, as found by the temperature dependent studies,[11] would then suggest that its OH stretching overtone transitions should correspond to the strongest features in the experimental spectrum.

The fact that the $2\nu_{OH}$ action spectrum region supposedly consists of a single conformer suggest that there is significant activity from additional vibrational modes other than the OH stretching modes. If these modes originate from transitions above the ground state (hot bands), or alternatively, these transitions originate from the different conformers of HOONO, a careful analysis of the nascent fragment energy release resulting from excitation of features within the vibrational overtone spectrum, can constrain their assignment to a particular state. This approach is expected to be sensitive for vibrational bands near the dissociation threshold where the influence of energy constraint is greatly magnified. In addition, it has the advantage of circumventing the need for rotationally resolved spectra for ascertaining conformer identity. This study examines the first OH stretching overtone using Doppler resolution laser-induced fluorescence to detect the nascent distribution of the OH fragments. Our measurements provide direct information regarding the internal and translational energy of the OH fragment and by inference, the energy in the partner NO_2 moiety. Subsequent fitting of

this energy disposal data using phase-space theory provides an estimate of the HO-ONO bond energy for the *cis-cis* isomer as well as the conformational identity of all major spectral features in the $2\nu_{OH}$ room temperature action spectrum. In particular, our energy disposal measurements show that the strongest features in the action spectrum, those occurring ~570 cm^{-1} to the blue of the *cis-cis* $2\nu_{OH}$ band, are not due to the *trans-perp* isomer, but instead correspond to hot bands of *cis-cis* HOONO associated with vibrational levels that lie on average ~ 600 cm^{-1} above the ground state.

4.1.3 The Spectroscopy of the $2\nu_{OH}$ Band

In an attempt to identify the states contributing to the $2\nu_{OH}$ action spectra we have also carried out theoretical studies by initially using a simple one dimensional *ab initio* dipole function, and treating the OH stretching potential as a Morse oscillator. Subsequently, we then re-examine our work using a two-dimensional dipole surface that takes into account the influence of the HOON torsion on the OH stretching overtones intensity. The two-dimensional *ab initio* calculations which conducted at the CCSD(T)/cc-pVTZ level of theory consist of two parts. In the first part, we confirm that the *cis-perp* configuration, which lies ~650 cm^{-1} above the *cis-cis* state, does not correspond to a bound localized minimum on the HOONO potential and hence is not responsible for the strong transitions observed in the experiments. Part two of the calculations involve spectral simulations using a two-dimensional dipole surface, which is calculated at the CCSD(T)/cc-pVTZ level of theory and takes into account the influence of HOON torsional motion on the OH stretching overtone. These simulations show that HOON-torsion/OH-stretch combination bands originating from ground and torsionally excited *cis-cis* states can qualitatively account for the observed intensity

distribution appearing in the $2\nu_{OH}$ action spectrum. In particular, the model reproduces the strong-broad spectral features in the action spectrum occurring ~570 cm^{-1} to the blue of the *cis-cis* $2\nu_{OH}$ overtone peak.

4.1.4 ^{15}N Isotope Studies

In order to test the predictions made by our *ab initio* two-dimensional model we have also carried our measurements on $HOO^{15}NO$ in the region of its first OH stretching overtone ($2\nu_{OH}$) where the bands position are recorded and compared with those of $HOO^{14}NO$. Even though prediction of this two-dimensional model qualitatively agree with the observed action spectrum, an ^{15}N isotope shifts reveals some of its limitations and suggests that a more elaborate multi-dimensional treatment taking into account additional modes are likely needed in order to fully explain the room temperature HOONO action spectrum.

4.2 Experiment

4.2.1 Experiment Apparatus

The experimental apparatus is similar to that used with the predissociation HO_2NO_2 experiments presented in Chapter 2. Infrared radiation for exciting the first OH stretching overtone of HOONO, $2\nu_{OH}$, is generated by an optical parametric oscillator (Spectra Physics: MOPO-730), which is pumped by the third-harmonic of an injection seeded Nd: YAG laser (Spectra Physics: GCR-270). The beam from the OPO laser provides the tunable infrared radiation between 6200 – 7200 cm^{-1} with a bandwidth of ~0.4 cm^{-1} and pulse energies ranging from 6 – 10 mJ over this spectral region. The OH photofragments resulting from unimolecular dissociation are probed via the *A-X*(0, 0) transition at ~308 nm using laser induced fluorescence (LIF). The 308 nm laser radiation,

which has a bandwidth of 0.13 cm^{-1}, is generated by frequency doubling the output of a second Nd:YAG laser (Continuum: NY81-20) pumped dye laser (Continuum: ND60).

The bandwidth of the probe laser is determined in a separate measurement by recording LIF line profiles of thermal OH generated in a microwave discharge, and deconvoluting from these profiles the estimated contribution due to room temperature Doppler broadening (~0.097 cm^{-1}) as described in Appendix *C*. The vibrational excitation laser propagates counter to the probe beam and is focused into the center of the cell using a 400 mm lens. Figure 4.2 shows a schematic of the experimental apparatus used. The probe laser pulse typically fires ~ 10 – 15 ns after the OPO and its intensity is greatly attenuated in order to avoid photodissociation of the HOONO sample as well as saturating the OH transitions. We typically use probe energies ranging from 0.1 – 0.2 μJ and it is collimated prior to entering the photolysis cell using a +300 / -150 lens system. The probe beam diameter is about 0.2 – 0.25 cm corresponding to fluency 4.07×10^{-6} J cm^{-2}. The OH fluorescence excited by the probe laser is collected using an f/1 lens system and imaged onto an end-on photomultiplier (EMI 9813QB). A color glass filter (Schott UG-11) located in front of the photomultiplier provides discrimination against scattered laser light. Signal from the PMT is sent to a gated charge integrator (LeCroy, 2249SG ADC) and subsequently digitized and passed to a laboratory computer for storage and analysis.

4.2.2 HOONO Synthesis

HOONO molecule is generated using three different sources to verify that the features and their relative intensities appearing in the spectrum are independent of source chemistry. In the first and primary synthesis route, we use the three-body recombination

reaction of OH + NO_2 + M in a side arm reactor attached to the photolysis cell to generate HOONO. Hydrogen atoms are generated by passing ~10% H_2 diluted in helium through a glass tube to which is attached an Evenson cavity microwave discharge operating at 2450 MHz and ~30 W of power. This is typically achieved by flowing 5 mTorr of H_2 gas in ~50 mTorr of He while the gate valve is kept opened one full revolution from the off position. Products from the discharge are combined further down stream with NO_2 to make OH radicals and the mixture is passed through a six feet section of $^1/_8$" OD Teflon tubing to enhance the three-body recombination. The OH and NO_2 radicals travel through the tubing and enter the main photolysis cell. By passing the OH + NO_2 mixture through the constrained environment fashioned by the Teflon tubing, the amount of NO_2 required to produce HOONO is significantly reduced. In addition, the narrow tubing provides a convenient way to maintain the required pressure differential between the high-pressure source region and the low-pressure photolysis cell. For example, 100 mTorr of pressure in the photolysis chamber correspond to ~9 Torr in the $^1/_8$" OD Teflon tubing.

We optimize the formation of HOONO by monitoring OH concentration reaching the photolysis cell using laser induced fluorescence, while varying the flow of NO_2 in the side arm reactor. Initially the NO_2 flow is increased till the weak OH signal in the cell just disappears due to formation of HOONO in the side arm reactor. This typically require a flow of 30 – 35 mTorr of NO_2 bringing the total pressure inside the cell to ~85 mTorr. The signal is then further adjusted by monitoring the resulting OH signal generated from the unimolecular dissociation of HOONO excited at 6935 cm^{-1}. At this frequency we find that flowing the reagents faster by opening the gate valve and reducing

the total pressure to 45 – 65 mTorr provide with signal levels that are sufficiently large for scanning over HOONO transitions and obtaining product state distributions measurements. Typically, the photolysis cell operates in the pressure range between 30 – 90 mTorr for the "low" pressure measurements and this value is increased by the addition of extra helium to ~2 Torr for the "high" pressure studies.

We make isotopically labeled $HOO^{15}NO$ using the same procedure outlined above, except with the $^{14}NO_2$ replaced by $^{15}NO_2$ (Icon Isotopes: 99% isotopic purity). Isotope shift measurements are conducted by sending a portion of the infrared OPO output into a photoacoustic cell containing H_2O or CO_2 and simultaneously recording photoacoustic signal from these reference molecules while scanning the OPO output over the HOONO spectrum. The shifts in the HOONO peaks upon isotope substitution are determined by noting the changes in their peak position relative to the fixed transitions of the reference molecules.[20] For a guideline using the HITRAN database see Appendix *F*.

As an alternative source of HOONO, we use the $BF_4NO + H_2O_2$ reaction.[15] The ~90% H_2O_2 used in this reaction is generated by bubbling N_2 through 50 % H_2O_2 solution over a period of several days in order to remove as much of the water present in the mixture. The hydrogen peroxide is then flowed slowly through a $^1/_8$" OD insert in a glass tube with dimensions of 1 cm in diameter and 15 cm in length filled with ~4 cm of solid BF_4NO. Under identical pressure conditions, this source chemistry produces ~3 times *weaker* signal than the $OH + NO_2$ reaction. Also, when the solid in the tube becomes moist due to the residual water present in the H_2O_2, signal levels drop sharply and require that the BF_4NO be replaced. This typically occurs within a few hours of usage.

We also use the reaction of H_2O_2 and BF_4NO_2 as reported in Chapter 2 to record a spectrum. However, signal levels from this source are rather weak and short lasting. HOONO production from this source is likely involved conversion of BF_4-NO_2 to BF_4-NO in the presence of water, but the mechanism is uncharacterized.

4.3 Results and Analysis

4.3.1 Room Temperature Vibrational Overtone Action Spectrum

The room temperature action spectra of gas phase HOONO in the region of its first OH stretching overtone ($2\nu_{OH}$) are shown in Fig 4.3. These spectra are generated by monitoring yields of nascent OH($v=0$, $^2\Pi_{3/2}$) fragments in the N=2 rotational state as the wavelength of the vibrational excitation laser is scanned. Each of the three panels corresponds to spectra generated using the different HOONO source chemistry described in the experimental section. In the first panel, Fig. 4.3(a), HOONO sample is generated from the OH + NO_2 reaction taken at 45 mTorr of total pressure. The second panel, Fig 4.3(b), corresponds to HOONO sample generated from the H_2O_2 + BF_4NO reaction taken at ~85 mTorr total pressure. And finally, in panel 4.3(c) HOONO is generated as a byproduct in the H_2O_2 + BF_4NO_2 HO_2NO_2 liquid phase reaction outlined in Chapter 2. For convenience, we label the main peaks *A* – *E*. The fact that all features, show up consistently in all three spectra indicates that they originate from a species common to all three sources (HOONO).

Several theoretical studies investigating the dissociation energy for the *cis-cis* isomer report values ranging from, D_0 = 18.3 – 19.8 kcal/mol.[2-8] Since at least one or more vibrational states lie below the dissociation threshold, energy constraint may influence the appearance of these bands in the predissociation action spectrum. Fig. 4.4

demonstrates the effects of energy constrains on the relative intensities of the band in the predissociation spectrum. In essence, this figure shows the variation in the $2\nu_{OH}$ action spectrum as a result of monitoring different nascent OH rotational N-levels. Each panel corresponds to scanning the IR laser (λ_1) over the region shown and probing the indicated nascent OH rotational state (λ_2). In these scans the total pressure in the cell is 60 mTorr, the pump – probe delays are set to 20 ns, and the OPO scan rate is chosen to be 0.008 nm/s while averaging 20 shots/bin. The spectra are area normalized. The dashed vertical lines in Fig. 4.4 indicate the range of values reported for D_0.

It is clear from the figure that while peaks *A – C* are sensitive to which rotational states the OH is probed, features *D* and *E* exhibit substantial intensity even when the OH(N=6) state is monitored. This finding brings out two possibilities. In the first, assuming that all bands belong to a single *cis-cis* conformer, the observed spectrum is likely due to the fact that the while the total energy (photon + internal) associated with excitation of peaks *A – C* is below the dissociation threshold, peaks *D – E* carry sufficient energy to overcome D_0 to produce these highly excited OH rotational states (N= 5, 6). This also suggests that the bond dissociation energy lies over peak *C* and therefore D_0 is greater than 19.4 kcal/mol. The second scenario, involves the assumption that two or more conformers of HOONO present in our room temperature spectrum were each conformer has different D_0 and intensity distribution which give rise to the observed spectrum.

4.3.2 OH Fragment Product State Distributions and Translational Energy Release

In order to investigate the energetics associated with the vibrational bands in Figs. 4.3 and 4.4 using a more systematic approach, we map out the resulting nascent OH

rotational product state distribution arising from unimolecular dissociation of HOONO. We probe the OH fragment using laser-induced fluorescence (LIF) via the diagonal $A^2\Sigma \leftarrow X^2\Pi$ transitions. The positions of the OH spectral features are identified using the work of Dieke and Crosswhite[21] and are scanned over using the "BURST" mode "Probe Scan" routine at a rate of 5 μsteps and 30 shots/bin averaging as described in Appendix *A*. The measured integrated LIF line intensities are converted to relative population using the procedure described in Appendix *C*. The extent of fragment alignment is assumed to be negligible in these near threshold dissociation measurements.[22] The various panels in Fig. 4.5 display the normalized nascent rotational distributions for the OH ($X^2\Pi_{3/2}$; v"=0) and OH ($X^2\Pi_{1/2}$; v"=0) spin-orbit manifolds resulting from excitation within various spectral features, marked *A – E*, in the HOONO ($2\nu_{OH}$) spectrum (see Fig. 4.3).

The data show that for the photolysis wavelengths corresponding to excitation at 6381, 6497, and 6718 cm^{-1}, the maximum in the nascent rotational population for the lower OH ($^2\Pi_{3/2}$) spin-orbit sate occurs at N=1 and then monotonically decrease as the OH rotational quantum number N increases. By contrast the population in the corresponding upper $^2\Pi_{1/2}$ spin-orbit state, which is the less populated spin-orbit state, goes through a maximum at intermediate values of the rotational quantum number, typically N=2, before decreasing towards zero at higher values of N. The average rotational energy associated with these rotational state distributions, shown in Figs. 4.5(a)-4.5(c), are fairly modest with the average rotational energy, weighted over both spin-orbit state, being about 60, 80, and 100 cm^{-1} for OH fragments generated respectively from features *A*, *B*, and *C*. In contrast to these distributions, the OH

rotational distributions resulting from excitation of spectral features *D* and *E* are qualitatively different. Figures 4.5(d) and 4.5(e) show the distributions obtained by exciting respectively at 6935 $cm^{-1}$and 7027 cm^{-1}. The OH $^2\Pi_{3/2}$ rotational state distributions arising from excitation within peak *D* and *E* both exhibit a maximum peaking around N=2 or 3, instead of monotonically decreasing from a maximum at N=1 as found for the peaks at lower excitation energy. The average rotational energy arising from excitation of feature *D* and *E* correspond respectively to 243 and 265 cm^{-1} and is significantly hotter than found from excitation of features *A – C*.

Figure 4.5(d) also compares the OH $^2\Pi_{3/2}$ distribution arising from excitation near the center of feature *D* at 6935 cm^{-1}, as a function of HOONO source chemistry. We do this in order to examine the influence, if any, of the source conditions on the energy disposal. Both the OH + NO_2 + M and BF_4NO + H_2O_2 sources give similar results within the estimated uncertainties as indicated by comparing the distribution represented respectively by the circles and square symbols in Fig. 4.5(d). In addition, we have investigated the variation in the OH product state distribution for excitation at different points within the ~125 cm^{-1} width associated with band *D*. Comparing results from excitation at the left end of the band at 6835 cm^{-1}, denoted as feature $D^{'}$ in Fig. 4.3(a), with results from the center of the band at 6935 cm^{-1}, we find that both give similar results as shown in Fig. 4.5(f).

The OH rotational energy release data are summarized in Table 4.1. The table shows that in going from feature *A* to feature *B* the excitation energy in the OH fragment, on average, increases by ~20 cm^{-1} or, by ~25%. Similarly, going from peak *B* to peak *C* results in a ~20% increase in the OH fragment rotational energy. Note that peaks *A* and *B*

are separated by 120 cm^{-1} same as peaks *B* and *C*. By contrast, in going from peak *C* to peak *D*, which corresponds to an identical change in the photon excitation energy, the OH fragment rotational energy changes by over ~240% (see Table 4.1). Thus, the rotational energy disposal data suggests that there is apparently a qualitative change in the dynamics associated with excitation of feature *D* compared to the features *A* – *C*. Scanning the probe laser over the Q branch region of the OH $A^2\Sigma \leftarrow X^2\Pi(1,1)$ band shows no discernible signal attributable to vibrationally excited OH from feature *D* or *E*, consistent with the available energy expected on the basis of the estimated HO-ONO bond dissociation energy for the either the *trans-perp*, *cis-perp* or *cis-cis* isomers.

A further probe of the dissociation dynamics results from measuring the population distributions among the fine-structure levels of the OH fragment. In its ground electronic state each rotational level of OH is split into two lambda-doublet components due to the interaction between electronic and rotational angular momentum. The two lambda doublet components are labeled as (A') or (A") depending on whether the electronic wave function is symmetric or anti-symmetric with respect to reflection in the plane of rotation.[23] For the OH radical in the high N limit, the (A') states have the orbital containing the unpaired electron lying in the plane of rotation, while the (A") states have this orbital perpendicular to the plane. Strict selection rules constrain the Q branch transitions to probing only the anti-symmetric lambda doublet states, while the P and R branch transitions probe the symmetric component. For excitation within the spectral feature marked *D*, where relatively high OH rotational states are populated, we find that both lambda doublet components are equally populated for the N = 5, 6 and 8 rotational states investigated, consistent with what might be expected for the dissociation dynamics

being statistical. The population analysis preformed for the two Λ–doublet components is discussed in further details in Appendix *C*.

Apart from fragment internal energy, the unimolecular decomposition of HOONO can also channel available energy into relative translation. The substantial mass difference between the OH and NO_2 moieties ensures that the lighter OH fragment receives much of this excitation. We quantify the amount of energy appearing in relative translation by examining Doppler-broadened LIF line profiles of the OH fragments. The relatively small amount of available energy associated with these near threshold dissociation, combined with the probe laser resolution, results in our being able to measure Doppler broadening associated with only the two lowest OH rotational levels, N = 1 and 2, arising from the photolysis of spectral features *A* – *E*. These rotational lines are scanned using the BURST mode routine taking 3 μsteps per burst with 30 shots/bin averaging as described in Appendix *A*. After deconvoluting out the 0.13 cm^{-1} U.V. probe laser linewidth as well as the contribution from initial thermal motion of the parent molecule (0.051cm^{-1}) as described in Appendix *C*, we find that the OH fragments in the N = 1 and 2 rotational states exhibit measurable broadening over this spectral region corresponding to an average translational energy over this region of ~560 cm^{-1} and ~235 cm^{-1} associated respectively with the two rotational states. The individual translational energies arising from excitation of features *A* – *E* are listed in Table 4.1.

Interestingly, all translations energy release values obtained over this entire spectral range fall within a fairly narrow value; all within 10 – 20% of the average value. Comparing the OH rotational versus translational energy release, it appears that most of its energy appears in translation. The amount of translational energy imparted to the

partner NO_2 fragment can be estimated on the basis of momentum conservation (see Appendix *C*) as shown in Table 4.1.

As Fig. 4.3 indicates, the room temperature spectrum is dominated by much stronger feature(s) appearing ~ 570 cm^{-1} to the blue of the *cis-cis* $2\nu_{OH}$ band around 6935cm^{-1}. The fact that the *cis-cis* $2\nu_1$ band is not the dominant feature in this spectral region, even though it is consider the "bright" state in overtone spectroscopy, is due to a combination of reasons having to do with the energy dependence of the dissociation quantum yields, the inherently low oscillator strength of the *cis-cis* $2\nu_{OH}$ band, as well as the overlapping of multiple vibrational bands in the vicinity of 6935 cm^{-1} which gives this region additional intensity. These issues will be discussed in further details below. In addition, the relatively weak signal from the *cis-cis* conformer at 6365 cm^{-1} could also be attributed to the possibility that one or more of the other conformers (*cis-perp*, trans-*perp*) are also present and relative to their population and/or intensity, the *cis-cis* conformer is not the dominate specie. The presence of other conformers could, in principle, give rise to the complex action spectrum. We engage this possibility using *ab initio* techniques where we initially investigate the likelihood that the *cis-perp* and *trans-perp* conformers contributing to our action spectra based on their band position and absorption cross-section.

4.3.3 One Dimensional *Ab Initio* Study of *cis-cis*, *cis-perp* and *trans-perp*

The $2\nu_{OH}$ overtone action spectra and OH rotational product state distributions suggest that the bands in the $2\nu_{OH}$ region carry different energies. In particular, the spectra show that the *cis-cis* zeroth-order OH stretching band at 6365 cm^{-1} is not the dominating feature suggesting that other OH stretching modes associated with the *cis-*

perp and *trans-perp* may be a contributing source in the action spectrum.[2-3,5] The two respective conformers have been reported to lie ~1.2 kcal and ~3.4 kcal/mol above the ground state of *cis-cis* HOONO[2-3,5] and calculations at the QCISD(T)/6-311G(d,p) and G2 level of theory have indicated that the *cis-perp* conformer may exist.[2]

Our intensities and band origin calculations on the three conformers are conducted at the CCSD(T)/cc-pVTZ level using GAUSSIAN03[24] in a similar manner presented in Chapter 3 with PNA. Initially, the geometry corresponding to stationary points of the three conformers is found via the optimization procedure discussed in Appendix *B*. The Z-matrices used for this optimization procedure are shown in Tables 4.2 – 4.4 for the *cis-cis*, *cis-perp* and *trans-perp* respectively. The procedure used in obtaining the correct Z-matrix for the elusive *cis-perp* is discussed in details in the following section. We check that indeed these optimizations result in minimum on the global potential by computing the harmonic frequencies. The resulting equilibrium geometries and harmonic frequencies are given in Tables 4.5 and 4.6 respectively. From these tables we find similarities between the *cis-perp* and *trans-perp* in term of their OH stretching frequencies (ν_1). In fact, the range of frequencies $\nu_2 - \nu_8$ all vary only slightly between the three conformers. Interestingly, ν_9 which is associated with the HOON torsion diverge for the three conformers.

To continue in evaluating the contribution of the three conformer in the $2\nu_{OH}$ action spectra, we generate one-dimension O-H stretching potentials by generating a grid of energy points starting from the equilibrium geometry r_e and stretch and compress the O-H by $r_e \pm 0.4$ Å in increments of 0.1 Å as outlined in Chapter 3. The OH-stretching potentials associated with the *cis-cis*, *cis-perp* and *trans-perp* are shown in Fig 4.6. The

figure shows that the *cis-perp* and *trans-perp* potentials are similar; they both have stiffer potential with bond equilibrium, r_e, that are ~0.015 Å shorter than that of the *cis-cis*. These differences arise from the fact that the H-atom is "pulled" toward the terminal O-atom in the *cis-cis* geometry leading to a more "loose" potential. The harmonic and anharmonic scaled frequencies associated with these potentials are obtained in a similar manner described Chapter 3 for PNA using the program in Appendix *D*. Briefly, we generate similar OH-stretching potentials for the reference molecules (HO_2NO_2,[25] $HONO_2$,[26] CH_3OH,[27] *trans* HONO,[28] HOCl [29]) at the CCSD(T)/cc-pVTZ level. For these molecules both the harmonic and anharmonic frequencies are experimentally known. From the OH stretching potentials we obtain the Morse parameters by noting that the harmonic and anharmonic frequencies associated with the potential via the expressions:[30]

$$\omega_e\ (cm^{-1}) = \omega_e/2\pi c = (F_{ii}G_{ii})^{1/2}/2\pi c \qquad (4.3)$$

$$\omega_e\chi_e\ (cm^{-1}) = \omega_e\chi_e/2\pi c = (hG_{ii}/72\pi^2 c)\ (F_{iii}/F_{ii})^2 \qquad (4.4)$$

In the expressions above, F_{ii} and F_{iii} are the respective second and third order force constants, h is Planck's constant, G_{ii} is the inverse of the reduced mass, and c is the speed of light. The force constants are then obtained by fitting the calculated potential with a 7th order polynomial and obtaining its second and third order derivatives ($\partial^2 V(r)/\partial r^2$, $\partial^3 V(r)/\partial r^3$). These parameters are summarized in Table 4.7. Again, the scaled parameters obtained for the *cis-cis* (ω_e = 3492 cm^{-1} and $\omega_e\chi_e$ = 92 cm^{-1}) differ significantly than those of *cis-perp* (ω_e = 3719 cm^{-1} and $\omega_e\chi_e$ = 86 cm^{-1}) and *trans-perp* (ω_e = 3744 cm^{-1} and $\omega_e\chi_e$ = 86 cm^{-1}). Indeed, the relatively high anharmonic frequency and low harmonic frequency are characteristics of the *cis-cis* conformer.

With the scaled Morse parameters extracted from the OH-stretching potentials we proceed in generating the Morse wave functions that are required in order to obtain the transition strength according to:[31-32]

$$f = 4.702\text{x}10^{-7}\ [\text{cm D}^{-2}]\ \nu_{0\rightarrow v}\ |\boldsymbol{\mu}_{0\rightarrow v}|^2 \qquad (4.5)$$

In the above equation $\nu_{0\rightarrow v}$ is the transition frequency in cm^{-1} and $\boldsymbol{\mu}_{0\rightarrow v} = \langle 0|\boldsymbol{\mu}(r\text{-}r_e)|v\rangle$ is the transition dipole moment matrix element between the ground and excited vibrational level. The *ab initio* dipole moment function ($\boldsymbol{\mu}(q= r\text{-}r_e)$) in the above equation is obtained in a manner similar to obtaining V(q) i.e., by stretching the O-H bond by $r_e \pm 0.4$ Å in increments of 0.1 Å. However, a notable difference is that these dipole moment points are calculated using GAUSSIAN03 at the QCISD/cc-pVTZ level due to the incapacity of the code to generate correct analytical derivatives of the energy at the CCSD(T)/cc-pVTZ level.[24] The X-, Y-, and Z- dipole moments associated with conformers of HOONO are shown in Fig. 4.7. As predicted, the *cis-cis* conformer has no dipole moment component along the z-axis since the O-H stretching and compressing motion takes place in the XY-plane. Evaluation of expression 4.5 with the appropriate Morse wave functions[33-35] and dipole moments as described in Chapter 3 and in Appendix *D* results in the absorptions cross-sections for the overtone transitions summarized in Table 4.8 by converting the oscillator strength, *f*, to absorption coefficient, $\int\sigma(\nu)d\nu$, in units of cm/molecule using:[31]

$$f = 4e^{-2}m_e c^2\epsilon_0 \int\sigma(\nu)d\nu = 1.1296 \times 10^{12} \int\sigma(\nu)d\nu \qquad (4.6)$$

With *e* being the charge of the electron, is m_e the electron mass, *c* is the speed of light and ϵ_0 is the permittivity of vacuum. As the table shows, we find that, for example, in the

$2\nu_{OH}$ region the *cis-cis* conformer is relatively weak with about $\sim{}^{1}/_{5}{}^{th}$ the intensity of the *cis-perp* and *trans-perp* conformers.

To compare our *ab initio* findings with our one-dimensional model we generate a stick diagram including these transitions with our action spectrum. Due to quantum yields issues associated with the fact that the *cis-cis* $2\nu_1$ band lies ~595 cm^{-1} below the D_0[*cis-cis*] value, we scale its absorption cross-section according to:

$$\Phi = \exp[(h\nu + 3kT/2 - D_0)/kT] \qquad (4.7)$$

In the above equation, k is Boltzmann factor, $h\nu = 6365$ cm^{-1} correspond to photon energy used in exciting the $2\nu_1$ band and is combined with the initial average internal rotational energy associated with thermal distribution of states, $3kT/2 \approx 310$ cm^{-1}. At room temperature, (T = 298.15 K) using the D_0 value from Fig. 4.1, gives a quantum yield $\Phi \sim 0.25$. Therefore, we obtain absorption ratio for *cis-cis* : *cis-perp* : *trans-perp* of 1:17:21. Figure 4.8 compares the results of this one-dimensional $2\nu_{OH}$ spectrum simulation with the action spectrum. It is clear that while the frequencies predicted by our *ab initio* model are in reasonable agreement with the observed bands in the action spectrum, our model fails to predict the correct number of bands, suggesting that other modes are active in the $2\nu_{OH}$ region. Furthermore, Fry and coworkers have shown that the rapid isomerization rate of the *trans-perp* to *cis-cis* eliminates the *trans-perp* contribution from the spectrum.[11] Implications of the *cis-perp* conformer are discussed in further details in section 4.4.5.

4.3.4 Phase Space Theory Simulations

Additional information regarding the energetics of the near-threshold unimolecular dissociation process can be extracted by assuming that it behaves statistically. In essence, this hypothesis allows us to account for the internal energy in the undetected NO_2 fragment by modeling the HOONO dissociation dynamics in the least-biased manner. This approach was implemented successfully with the isomer of HOONO molecule, nitric acid. Crim and coworkers have shown that the $HONO_2$ molecule dissociates statistically near threshold.[26] We use phase space theory (PST), which assumes that the transition state for near threshold unimolecular reaction occurs at sufficiently large internuclear separation as to give a "loose" transition state.[36] A "loose" transition state is where the two separating fragments are free to rotate relative to one another. The only constraints invoked in PST are energy and angular momentum conservation. We perform the phase space calculations on HOONO in essentially two steps, analogous to that described for nitric acid.[26] The Fortran code used in the calculations was written by Professor A. Sinha originally for nitric acid fourth and fifth OH stretching overtones studies and is provided in Appendix *E* as reference by the dissertation author.

The first step in PST involves calculating the probability that HOONO molecules in a particular quantum state, specified by its vibrational and rotational quantum numbers, dissociates to produce OH fragments in a specified ro-vibrational state while conserving energy and angular momentum. We then average this probability over the distribution of initial HOONO states prepared by vibrational overtone excitation. We approximate *cis-cis* HOONO as a prolate symmetric top using Ray's symmetry parameter:

$$\kappa = 2B - A - C / (A - C) \qquad (4.8)$$

Where A, B and C are the rotational constants of *cis-cis* HOONO (A = 0.71404 cm^{-1}, B = 0.26512 cm^{-1}, C = 0.19317 cm^{-1}). We find that $\kappa = -0.724$ using the data of Drouin *et al.*[15] HOONO is then designated by its initial ro-vibrational states by |v, J, K>. The quantum number, v, is used as a short hand label to represent the full set of nine vibrational modes $v_1,..,v_9$ of the molecule while the quantum numbers J and K are associated respectively with the molecules rotational angular momentum and its projection on the top-axis. We denote the energy of the HOONO molecule in state |v, J, K> by E(v,J,K) and its dissociation energy by D_0. In an analogous manner, we label the OH fragment states as $|u_1, J_1, \Omega>$ using respectively the vibrational, rotational and spin-orbit quantum numbers. For these near threshold experiments, the OH fragments are all formed in their vibrational ground state. There are however two spin-orbit states of OH corresponding to $\Omega = {}^3/_2$ and ${}^1/_2$ that are separated by ~125 cm^{-1} and both are accessible in these measurements. The vibrational excitation photon of energy, hν, prepares the reacting molecule with an excess energy E, given by:

$$E = E(v, J, K) + h\nu - D_0 \qquad (4.9)$$

The probability of this energized molecule dissociating to produce $OH(u_1, J_1, \Omega)$ is then given by:

$$P(v,J,K \rightarrow u1,J1,\Omega) = \frac{N(E;v,J,K \rightarrow u1,J1,\Omega)}{\sum_{u1,J1,\Omega} N(E;v,J,K \rightarrow u1,J1,\Omega)} \qquad (4.10)$$

In the above equation $N(E; v, J, K \rightarrow u_1, J_1, \Omega)$ is the number of open channels leading to the specific OH product sate represented by $|u_1, J_1, \Omega>$, while the expression in the

denominator is the total number of open channels for all possible OH products states that are consistent with energy and angular momentum conservation. Furthermore, the numerator in Eq. 4.10, the number of open channels leading to a particular OH fragment, N(E; v, J, K → u_1, J_1,Ω) is given by:

$$N(E;\mathrm{v},J,K \rightarrow u_1,J_1,\Omega) = \sum_{u_2,N_2,K_2,J_2,J_R,L} g(K_2)h(E_t) \qquad (4.11)$$

In Eq. 4.11, u_2 and N_2 are respectively the vibrational and rotational quantum numbers of the NO_2 fragment, which we treat as a near prolate symmetric top. The quantum number K_2 is the projection of the NO_2 rotational angular momentum on the top axis. Nuclear-spin statistics remove half the rotational states of NO_2, and we approximately account for this by setting the K degeneracy, $g(K_2)$, in Eq. 4.11 to half its normal value. The usual value for symmetric tops is $g(K_2) = 2$, but we use $g(K_2) = 1$ for NO_2. The total angular momentum of the NO_2 fragment $\mathbf{J_2}$ is the vector sum of its rotational and electronic spin angular momenta. Thus for every NO_2 rotational state specified by $|N_2, K_2>$ the total angular momentum quantum number for this fragment, $\mathbf{J_2}$, can be either $\mathbf{J_2} = N_2 + {}^1/_2$ or $\mathbf{J_2} = N_2 - {}^1/_2$. We neglect the small change in energy levels due to this spin splitting and assume that both levels arising from the coupling between rotational and electronic spin angular momentum have the same energy, even though they correspond to states of different total angular momenta. A channel is open and, therefore, contributes to the summation in Eq. 4.11 if the relative translational energy available exceeds that needed to overcome the centrifugal barrier. The function $h(E_t)$ in Eq. 4.11, which accounts for this relative kinetic energy restriction, is unity for an open channel and zero otherwise.

Energy conservation restricts the range of the quantum numbers, u_2, N_2, and K_2 for the NO_2 fragment and hence also the range of the summation appearing in Eq. 4.11. For an initial HOONO state $|v, J, K\rangle$ and an OH product state $|u_1, J_1, \Omega\rangle$, the energy available to the NO_2 fragment is:

$$E_{NO2}\,(\text{available}) = E(v, J, K) + h\nu - D_0 - E_{OH}(u_1, J_1, \Omega) \qquad (4.12)$$

The range of the summation indices L and J_R in Eq. 4.11 is controlled by angular momentum conservation. The triangle inequalities for the parent angular momentum **J** and the fragment angular momenta $\mathbf{J_1}$ and $\mathbf{J_2}$ determine the possible values of the resultant angular momentum $\mathbf{J_R}$ and the orbital angular momentum, **L**, through:

$$|\mathbf{J_1} - \mathbf{J_2}| \le \mathbf{J_R} \le |\mathbf{J_1} + \mathbf{J_2}| \qquad (4.13)$$

$$|\mathbf{J} - \mathbf{J_R}| \le \mathbf{L} \le |\mathbf{J} + \mathbf{J_R}| \qquad (4.14)$$

The role played by relative translational energy constraint can be seen by noting that the effective potential for motion of the fragments along the reaction coordinate is:

$$V(r) = V_{elec}(r) + B(r)\,L(L+1) + E_\infty \qquad (4.15)$$

In Eq. 4.15, r is the center-of-mass separation of the fragments, V_{elec} is the electronic potential, and $B(r) = \hbar^2/2\mu r^2$ is the rotational constant of the dissociating complex, L is the orbital angular momentum and E_∞ is the internal energy of the separated fragments.

Since phase space theory assumes a loose transition state, we can replace V_{elec} by its asymptotic value at long range, $V_{elec} \sim C_6/r^6$, where C_6 is the total attractive constant for the long-range interaction between the fragments given by the sum of the *dipole–dipole* ($C_{d\text{-}d}$), *dipole–induced-dipole* ($C_{d\text{-}id}$), and the *dispersion energy* (C_{disp}) constants:[37]

$$C_{d\text{-}d} = -2/3kT \times (p_1\,p_2)^2 / (4\pi\varepsilon_0)^2 \qquad (4.16)$$

$$C_{d\text{-}id} = -(p_1^2\,\alpha_2 + p_2^2\,\alpha_1) / (4\pi\varepsilon_0)^2 \qquad (4.17)$$

$$C_{disp} \approx -\tfrac{3}{2} \times I_1\, I_2 / (I_1 + I_2) \times \alpha_1\alpha_2 / (4\pi\varepsilon_0)^2 \qquad (4.18)$$

Where p_1 and p_2 are the dipole moments, α_1 and α_2 are the polorizabilities, I_1 and I_2 are the ionization energies of the OH and NO_2 fragments respectively. Also appearing in the equations, k is the Boltzmann factor, T is the temperature and ε_0 is permittivity of vacuum. The parameters used in the phase-space calculation are given in Table 4.9. See Appendix *B* for "how to" calculate these quantities with GAUSSIAN03.

The "loose" transition state assumption reduces the translational energy requirement for overcoming the centrifugal barrier to:

$$L(L+1)\hbar^2 \le 6\mu C_6^{1/3}(E_t/2)^{2/3} \qquad (4.19)$$

In Eq. 4.19 E_t is the relative translational energy, which in turn is determined by energy conservation constraint to be:

$$E_t = E(v,J,K) + h\nu - D_0 - E_{NO2}(v_2,J_2,K_2) - E_{OH}(v_1,J_1,\Omega_1) \qquad (4.20)$$

In our calculations we obtain the rotational constants for HOONO from the available experimental data while for its vibrational frequencies we use results of *ab initio* calculations.[15,4] We fix the value of the C_6 at $2.0\text{x}10^{-58}$ erg/cm^6, the value found to best describe the unimolecular dissociation of nitric acid.[35] Calculating the population of a particular OH product state formed in our room temperature experiment also requires that we average the state-to-state probability given in Eq. 4.10 over the distribution of HOONO states P(v, J, K) prepared by the vibrational overtone excitation. We assume that the vibrational overtone spectrum is so dense that transitions from many initial rotational and low-frequency vibrational states occur within the laser bandwidth.[26] Thus, we

approximate the state distribution prepared by the excitation as the thermal distribution initially present in the lower vibrational levels but shifted to higher energy by the photon energy of the vibrational overtone excitation laser. For PST calculations of the *cis-cis* conformer, we typically do the thermal averaging over the six lowest vibrational modes which are 0, 290, 371, 482, 508, 629 cm^{-1}. For each of the vibration, we include the rotational manifold of states using angular momentum values ranging from $0 \leq J \leq 80$ and $K < J$. We further assume as an approximation that all transitions lying under the laser bandwidth have the same oscillator strength. Carrying out the required averaging gives the probability of producing OH fragments in a particular quantum state $|u_1, J_1, \Omega>$ starting from a thermal distribution of HOONO molecules to be:

$$P(u_1, J_1, \Omega) = \frac{\sum_{v,J,K} P(v, J, K) P(v, J, K \rightarrow u_1, J_1, \Omega)}{\sum_{u1,J1,\Omega} \sum_{v,J,K} P(v, J, K \rightarrow u_1, J_1, \Omega)} \qquad (4.21)$$

Figure 4.9 shows the "best-fit" results of applying PST to fit the measured OH fragment rotational state distributions arising from excitation within peaks *A* – *C*. These simulated PST distributions are generated using the C_6 coefficient used to fit the nitric acid data, spectroscopic parameters for the *cis-cis* HOONO isomer and a value for its D_0 of 19.9 kcal/mol. This best fit D_0 value, which is the only unknown in the simulation, is determined by varying its value by ± 1.5 kcal/mol about the theoretical predicted value[5] while looking for a simultaneous best fit, in the least-square sense, to all three product state distribution arising from excitation of peaks *A*, *B*, and *C*. For comparison, Fig. 4.10 shows the results of PST using the D_0 value of 19.4 kcal/mol. It is clear from the

simulations for peaks *A* – *C* do not do as good of a job fitting the experimental product state distributions compared to the simulations in Fig. 4.9 using D_0 of 19.9 kcal/mol. It is important to note that simulations using *trans-perp* parameters are not able to fit these measured OH product state distributions as they predict much warmer distributions for peaks *A* – *C*.

The good agreement between the experiment and PST simulations shown in Fig. 4.9 confirm that peaks *A* – *C* correspond to the *cis-cis* isomer and further more that their dissociation dynamics is consistent with a statistical distribution of the available energy. From the variation in the PST simulations with D_0, we are able to estimate the HO-ONO bond dissociation energy of the *cis-cis* isomer to be $D_0 = 19.9 \pm 0.5$ kcal/mol. This value of D_0 compares favorably with the theoretically predicted value of 19.8 kcal/mol,[5] as well as values inferred from other recent measurements.[12-13, 38]

Simulating the product state distributions arising from excitation within the broad feature labeled peak *D* is more interesting. As Fig. 4.11(a) and 4.11(b) show, the measured OH rotational distributions obtained from excitation at 6935 cm^{-1} are too cold to arise from the dissociation of the *trans-perp* isomer and too hot to be explained by a standard PST calculation using Boltzmann weighted average over the *cis-cis* vibrational levels. We interpret this finding as signifying that the transitions giving rise to features *D* originate from "high energy" *cis-cis* HOONO vibrational states. This follows since our "standard" PST calculations using the *cis-cis* parameters, start from the ground vibrational state and continue on up the energy ladder to include contributions from higher vibrational levels of the *cis-cis* well, weighing contribution from each vibrational level to the OH product state distribution by their appropriate Boltzmann factor. Thus, the

fact that the measured distributions from feature *D* are much hotter than predicted by the "standard" PST calculation using *cis-cis* parameters means that this feature has contributions arising primarily from high-energy vibrational states and not the lower ones. The lower vibrational states, which are weighted more strongly by the Boltzmann factor, would tend to favor a colder OH rotational state distribution. In order to determine the average energy of the vibrational states giving rise to peak *D*, we have also run the PST simulations considering dissociation from only one vibrational level at a time along with their associated Boltzmann distribution of rotational states. Thus, in contrast to the "standard" PST calculations, these single vibrational level PST calculations do not average over the entire distribution of thermally populated vibrational states. These single vibrational level PST calculations start from the ground state and sequentially go up the ladder of excited levels considering first the hot band ν_9, then ν_7 and so on, each time checking if the product rotational distribution arising from the particular vibrational level under consideration matches observation. Through this procedure, we find that *the OH rotational product state distribution originating from spectral feature D, can be reproduced using cis-cis parameters only by starting from initial states having ~600 ± 100 cm^{-1} of vibrational energy* as shown in Fig. 4.11(c). The same is also found for OH product states arising from excitation of feature *E* in Fig. 4.3(a). Hence we conclude that features *D* and *E* arise from excitation of *cis-cis* HOONO hot bands. We note that the average internal energy of the sample *cis-cis* HOONO molecules at room temperature is calculated to be ~ 500 cm^{-1}. The code used in calculating the ro-vibrational average energy is provided in Appendix *D*. The normalized ro-vibrational density of states associated with *cis-cis* HOONO is shown in Fig. 4.12.

4.3.5 Searching for the *cis-perp* Conformer

To this point, the *cis-perp* conformer has been excluded from the PST simulations despite the fact that states lying ~600 cm^{-1} above the *cis-cis* ground level are found to contribute to peak *D* (see Fig. 4.11(c)); even though these levels are indeed consistent with the energetics of the *cis-perp* conformer. In order to examine the possibility of a stable bound *cis-perp* configuration, we have carried out *ab initio* calculations at several levels of theory including MP2/cc-pVDZ, QCISD/cc-pVTZ, CCSD(T)/cc-pVξZ (ξ = D, T, Q) looking for stationary points on the HOONO potential associated with the *cis-perp* configuration. At all these levels of theory, we obtain stationary points associated with the *cis-perp* geometry which are shown in Table 4.10. These stationary points are confirmed with frequencies calculations shown in Table 4.11. The range of energies of which the *cis-perp* carries relative to the *cis-cis* conformer is intriguing and as shown in Table 4.10, ranges from 100 – 500 cm^{-1} depending on the level of theory.

To further investigate the *cis-cis* / *cis-perp* potential we select the CCSD(T)/cc-pVTZ level of theory since it produces similar geometries and relative energies as the CCSD(T)/cc-pVQZ level with the fraction of the computation cost. The potential in Fig 4.13(a) shows the HOON torsional potential of HOONO calculated by running GAUSSIAN03 at the CCSD(T)/cc-pVTZ level of theory.[24] This potential is obtained by gradually increasing the HOON torsional angle τ from zero to 180^{o}, in increments of 10 degrees while optimizing all other internal coordinates including the OONO torsion. In essence this potential provides the minimum energy pathway for moving the hydrogen atom out of the plane through HOON torsional motion and thus converting *cis-cis* HOONO to the *cis-perp* form.

As shown in Fig. 4.13(a), at the CCSD(T)/cc-pVTZ level of theory this torsional potential exhibits a stationary point corresponding to a shallow minimum with a well depth of only about 5 cm^{-1} near the *cis-perp* configuration at $\tau \approx 79^{o}$. At this geometry, the harmonic frequency associated with the torsion motion, ν_9 is ~82 cm^{-1} as shown in Table 4.11. Unfortunately, based on zero-point energy considerations, we conclude that *the potential is not expected to support localized bound states corresponding to the cis-perp conformer*. These findings equally eliminate the possibility that the *cis-perp* HOONO contribute in the $2\nu_{OH}$ action spectrum.

4.3.6 *Ab Initio* Two-Dimension Study of the Influence of Torsion on Overtone Intensity

As the *ab initio* search for stable *cis-perp* conformer fails to yield a localized bound state, we take a different approach to interpreting our PST results. In essence, yes, the *cis-perp* conformer is not supported by the current *ab initio* findings; this however does not mean that transitions originating from this "ledge" region of the torsional potential are not important. On the contrary, our one-dimension intensity calculations revealed that OH stretching overtone transitions from this region of the potential, where the hydrogen atom lies out-of the plane, can exhibit appreciable oscillator strength (see Table 4.8). This arises from the fact that as the hydrogen atom moves out of the plane and the hydrogen bond is broken, the vibrational frequency of the O-H stretch increases and the dipole moment develops a non-zero out-of-plane component. Fig. 4.13(b) illustrates this change in OH frequency by showing slices of the O-H stretching potential for several fixed values of the HOON torsional angle, τ. The figures show that, as the magnitude of the torsional angle increases, the O-H stretching potentials become more closed,

indicating a stiffening of the O-H bond and a corresponding increase in its vibrational frequency. This variation in the O-H potential with torsional angle is summarized in Fig. 4.13(c), which shows how the stretching frequency and anharmonicity of the OH stretching vibration changes with τ.

The development of an out-of-plane component to the dipole moment and changes in OH frequency with torsional motion, combined with the fact that the torsional mode, ν_9, is the lowest frequency mode and hence can be appreciably populated at room temperature, motivated us to look at the influence of HOON torsional motion on the HOONO overtone intensity more systematically. In order to do this, we note that the frequency of the O-H stretch is over an order of magnitude higher than that of the HOON torsion (ω_{OH} = 3493 cm^{-1}, ω_{HOON} = 263 cm^{-1}); hence an adiabatic separation in the same spirit as the Born-Openheimer approximation seems reasonable.[42,43] The idea of adiabatic separation of the low frequency torsional mode and high frequency OH stretching vibration has been successfully used to describe the spectroscopy of other molecules such as H_2O_2.[39] We generate the adiabatic potential for torsional motion associated with each O-H stretching vibrational level labeled by the quantum number, V_{OH}, by stretching and compressing the O-H bond in increments of 0.1 Å to cover a range of $\pm$ 0.4 Å about the equilibrium position associated with a given fixed value of the torsional angle τ. This procedure then generates a one-dimensional slice of the O-H stretching potential for the particular value of the torsional angle as shown in Fig. 4.13(b). This O-H stretching potential is then used as input in a one-dimensional Schrödinger equation, which is then numerically integrated (using: μ = 0.965) to determine the wavefunctions and energies, E

($V_{OH}|\tau$), of the vibrational levels that the potential supports.[40] Tutorial of using the Schrödinger equation solver is given in Appendix *F*. This procedure for generating an O-H potential and determining its associated vibrational levels and energies is repeated for each torsional angle τ in order to cover the range between $\tau = \pm 180^{\circ}$ in increments of 10°. Connecting the series of energy points corresponding to the same value of the O-H stretching quantum number, V_{OH}, over the grid of τ values, generates the adiabatic curves for torsional motion as shown in Fig. 4.14 for the first few O-H stretching states. These adiabatic torsion potentials associated with $V_{OH} = 0$, 1 and 2 in essence correspond to torsional motion associated with an O-H vibrational stretching quantum state. It is interesting to note that the adiabatic torsion curves increase in dept as a function of increasing V_{OH} quantum number as shown in Fig. 4.15. This finding suggests that in principle, while the torsion potential supports additional torsional vibrational states at high OH stretching overtones, the steepness of the potential around the ledge area (*cis-perp*) reduces further the likelihood of *cis-perp* configuration.

Finally, the eigenfunctions and energies of the levels supported by these adiabatic torsional potentials are obtained by solving the corresponding one-dimensional Schrödinger equation (using: $\mu = 1.1266$) using these adiabatic potentials as input in the FGH code.[40] The resulting eigenfunctions and energies for the V_{τ}-th adiabatic torsional level associated with the particular O-H stretching state V_{OH}, are respectively denoted by $\varphi_{V\tau}(\tau|V_{OH})$ and $E(V_{\tau}|V_{OH})$. Transition frequencies for the various overtone transitions of interest corresponding to $|V''_{OH}, V''_{\tau}> \rightarrow |V'_{OH}, V'_{\tau}>$ are then obtained by taking energy differences between the appropriate initial and final states associated with these adiabatic

stacks of levels. The calculated energies of the various adiabatic initial and final states along with their transition frequencies are summarized in Table 4.12 for excitation in the region of the $2\nu_{OH}$ level.

The oscillator strength, *f*, for transition from some initial state represented by the wavefunction $|\psi_i\rangle$ to an excited state represented by $|\psi_f\rangle$ is given by equation 4.5[31,32] In our two-dimension model, $\boldsymbol{\mu}_{i\rightarrow f} = \langle\psi_i|\boldsymbol{\mu}(r_{OH},\tau)|\psi_f\rangle$ is the transition dipole moment matrix element between the initial and final vibrational level. We approximate the wavefunctions for the initial and final states as product functions involving the HOON torsional and O-H stretching coordinates. Thus a state in our two-degree of freedom model is represented by $|\psi\rangle \approx \varphi_{V\tau}(\tau|V_{OH})\chi_{VOH}(r_{OH},\tau)$. In this equation $\varphi_{V\tau}(\tau|V_{OH})$ is the adiabatic torsional wavefunctions which we obtain as outlined above and $\chi_{VOH}(r_{OH},\tau)$ is the corresponding O-H stretch wavefunction. For a given torsional state, we approximate the O-H stretching wavefunction $\chi_{VOH}(r_{OH},\tau)$ by assuming that the torsional state, $\varphi_{V\tau}(\tau|V_{OH})$, can be characterized by a single effective torsional angle given by the root-mean square (RMS) displacement $\langle\tau^2_{HOON}\rangle^{1/2}$ associated with the state $\varphi_{V\tau}(\tau|V_{OH})$. Having found τ_{RMS}, we run GAUSSIAN03,[24] to determine the optimized parameters for HOONO associated with the HOON torsional angle fixed at the desired τ_{RMS} value. We then stretch and compress the O-H bond about these equilibrium parameters, as described earlier, to generate a one-dimensional O-H potential energy curve from which we extract the desired effective stretching wavefunctions $\chi_{VOH}(r_{OH}|\tau_{RMS})$ associated with φ

$v_\tau(\tau|V_{OH})$. Thus in essence we use the approximation $|\psi> = \varphi_{v\tau}(\tau|V_{OH})\ \chi_{VOH}(r_{OH},\tau) \approx \varphi_{v\tau}(\tau|V_{OH})\ \chi_{VOH}(r_{OH}|\tau_{RMS})$ to express the dependence of a state, labeled by the quantum numbers V_{OH} and V_τ, on the coordinates τ and r_{OH}. The first few of the $\varphi_{v\tau}(\tau|V_{OH})$ and $\chi_{VOH}(r_{OH}|\tau_{RMS})$ eigenfunctions supported by the torsion and OH stretching potentials associated with $V_{OH} = 0$ are shown in Fig. 4.16.

In order to obtain the two-dimensional dipole moment surface also required by Eq. 4.5, we form an 37×9 grid of points by varying τ between $\pm 180^o$ in steps of 10^o and r_{OH} between $r_e \pm 0.4$ Å in steps of 0.1 Å for each τ, with the three components of the dipole moments calculated at each grid point using ACESII at the CCSD(T)/cc-pVTZ level.[41] The advantages of using ACESII for these dipole moments calculations are two fold. Not only one can obtain dipole moments which are the correct analytical gradients of the CCSD(T)/cc-pVTZ energy not available with GAUSSIAN03,[24] but also these dipole moments are provided in the a-, b- and c- molecular axes frame.[41] The keywords used in generating the grid of single point dipole evaluations are shown in Table 4.13 as an example for the $\tau = 0.0^\circ$ and $r_{OH} = 1.1822$ Å corresponding to $r_e + 0.2$ Å. The keywords are unchanged for the entire grid evaluation; only the O-H separation and HOON torsion angles are changed. For full description of using ACESII on our workstations refer to Appendix *B*.

Slices through the resulting dipole surface are shown in Fig. 4.17. The variation in the three components of the dipole moment with torsional angle is shown for three fixed values of r_{OH}. For each component of the dipole moment, the two-dimensional dipole

surface is fitted over the grid points using a 10^{th} order two-dimensional Taylor expansion in the variables $(r_{OH} - r_e)$ and $(\tau - \tau_e)$ where r_e and τ_e are respectively the equilibrium values of the OH and HOON torsional coordinates. Each fitted component of the dipole moment surface, along with the wavefunctions for initial and final states are then inserted into the matrix element in Eq. 4.5 and the integral evaluated numerically. The matrix element for each of the three components of the dipole moment are subsequently squared and then summed ($\langle\psi_i|\boldsymbol{\mu_a}(r_{OH},\tau)|\psi_f\rangle^2 + \langle\psi_i|\boldsymbol{\mu_b}(r_{OH},\tau)|\psi_f\rangle^2 + \langle\psi_i|\boldsymbol{\mu_c}(r_{OH},\tau)|\psi_f\rangle^2$) to give the total oscillator strength associated with the transition. Table 4.12 summarizes the results of the transition frequency and oscillator strength calculations using the above model. The code that was used to obtain these oscillator strength values is given in Appendix *D*.

For each transition between an initial and final state, multiplying the oscillator strength associated with the transition by the Boltzmann factor appropriate for the initial state and the dissociation quantum yield for the final state, gives the effective weight the transition contributes to the action spectrum. The vibrational Boltzmann factors are calculated using the initial state energies given in Table 4.12 after subtracting out the zero-point energy (~1880 cm^{-1}). We approximate the dissociation quantum yield for each vibrational band by first shifting the entire thermal distribution of rotational states associated with its initial vibrational level by the energy of the vibrational overtone excitation photon and then determining the fraction of these states that have energies greater than D_0 = 19.9 kcal/mol. The vertical lines of varying heights appearing in the stick spectrum shown in Fig. 4.18 correspond to the transitions given in Table 4.12 with their effective weights. Broadening each stick feature in Fig. 4.18 by ~50 cm^{-1} (FWHM)

using a Gaussian line-shape, gives the simulated action spectrum envelop shown in the figure. We find that the peaks marked as *A**, *B**, and *C** in Fig. 4.18 primarily correspond to single transitions with no changes in the torsional quantum number, i.e. $\Delta V_\tau = 0$. By contrast the feature labeled *D** and *E** correspond to overlap of many transitions with their torsional quantum number changing by $\Delta V_\tau = +1$ and +2.

4.4 Discussion

The measurement of fragment energy release provides a method for confirming the conformational identity of features appearing in the room temperature HOONO action spectrum. In particular, PST calculations using $D_0 = 19.9$ kcal/mol, $C_6 = 2.0 \times 10^{-58}$ erg/cm^6 and spectroscopic parameters for *cis-cis* HOONO, OH and NO_2, are able to provide good fits to the OH fragment rotational state distributions resulting from excitation of spectral features *A*, *B*, and *C* in the region of the $2\nu_{OH}$ band. Hence, the simulations confirm that these peaks belong to the *cis-cis* conformer. The good agreement between the statistical model calculations and measurements is also consistent with *ab intio* results,[42] which indicate that there is no barrier along the OH + NO_2 dissociation pathway for *cis-cis* HOONO; hence suggesting the absent of strong energy gradients that can influence fragment energy disposal. In addition, PST simulations provide us with constrained range of acceptable values of D_0 and estimate the bond energy for breaking the HO-ONO bond in *cis-cis* HOONO to be $D_0 = 19.9 \pm 0.5$ kcal/mol. This value is in good agreement with the *ab initio* result of 19.8 kcal/mol found by Dixon *et al.* at the CCSD(T)/CBS level of theory.[5] Our D_0 value is also in good agreement with the 19.8 kcal/mol value derived by Hippler *et al*.[38] from a third-law analysis of their data and the 19.6 kcal/mol value inferred by Konen *et al*. from their

measurements of D_0 for the *trans-perp* isomer after adjusting for the energy difference between the two isomers using *ab initio* data.[12,13] Combining our measured D_0 value with the known heat-of-formation data for the OH and NO_2 fragments,[43,44] gives ΔH^0_f(*cis-cis*) = -2.49 kcal/mol.

In contrast to the situation for these lower energy peaks *A* – *C*, the analysis of the stronger features at 6935 cm^{-1} and 7050 cm^{-1}, peaks *D* and *E*, is a bit more challenging. Although the one-dimension *ab initio* intensities calculations predict that the *trans-perp* and *cis-perp* conformers carry substantial intensity in that region, phase-space calculations using the *trans-perp* parameters confirm that these strong features are not due to that isomer. This follows, as the measured rotational distributions arising from excitation at various positions within feature *D* and E are all considerably colder than PST predictions using the *trans-perp* parameters (see Fig. 4.11(a)). Thus, none of the features *A* – *E*, in the $2\nu_{OH}$ spectrum of Fig. 4.3(a), correspond to the *trans-perp* isomer. This conclusion is consistent with the results of Fry *et al*. who report that the *trans-perp* HOONO is rapidly converted to the *cis-cis* form at room temperature.[11]

The *cis-perp* conformer is also excluded since the HOON torsion potential is unable to support this configuration (see Fig. 4.13). However, the OH distributions from these spectral features can however fit to PST simulation if one considers dissociation from *cis-cis* levels with ~600 ± 100 cm^{-1} of vibrational energy as shown by the results of Fig. 4.11(c) and discussed in the previous section. Eliminating the *trans-perp* and *cis-perp* possibilities, suggests that features *D* / *E* in the $2\nu_{OH}$ spectrum must arise from hot bands associated solely with the *cis-cis* conformer.

As the HOON torsional mode of HOONO corresponds to the lowest frequency vibrational mode of the molecule, hot bands involving this mode are expected to be the most prevalent in the near threshold $2\nu_{OH}$ spectral region. In addition, these hot bands can potentially have appreciable oscillator strength since out-of-the plane motion of the hydrogen atom via torsional excitation can lead to an enhancement of the OH overtones through the development of an out-of-plane component in the dipole moment, which is otherwise absent in the planer *cis-cis* ground state (See Fig. 4.7).

These reasons have led us to extend our one dimensional calculation and take a closer look at the influence of torsional excitation on the oscillator strengths of the OH stretching overtones. Fig. 4.18(a) shows the results of this two-dimensional HOON-torsion / OH-stretch model. The main peaks appearing in the simulation shown in Fig 4.18(a) are labeled sequentially from *A** to *E**. For comparison, Fig. 4.18(b) shows a "high" pressure action spectrum of the $2\nu_{OH}$ region. We have tried to minimize the dependence on the probed OH product state by collapsing the nascent OH distribution into a thermal distribution. Under these relaxed product state detection conditions, the relative intensity appearing in the action spectra are expected to be more directly proportional to the total yield of OH fragments arising from the excitation. By working at relatively high pressure of 1 – 2 Torr (in excess helium) and increasing the time delays between photolysis and probe lasers to 1 μsec, we are able to ensure sufficient number of collisions to collapse the nascent OH fragment rotational states into a thermal distribution without appreciably affecting the much faster unimolecular dissociation of the parent molecule.

Comparing Fig. 4.18(a) with the experimental spectrum in Fig. 4.18(b) we see that the two-dimensional model provides a reasonably description of the intensity distribution seen in the $2\nu_{OH}$ action spectrum. Similar results have recently been reported by Schofield and Kjaergaard using a torsional potential calculated at a lower level of theory[45] as well as McCoy *et al.*[46] at the CCSD(T)/cc-pVTZ. Comparing peak intensity as well as peak position in Figs. 4.18(a) and 4.18(b), suggests the following possible correspondence between the simulated and the experimental peaks: $A^* \leftrightarrow A$, $B^* \leftrightarrow B$, $C^* \leftrightarrow C$, $D^* \leftrightarrow D$ and $E^* \leftrightarrow E$. First, the model predicts the presence of an intense peak roughly ~500 cm^{-1} to the blue of the *cis-cis* OH stretching overtone peak, secondly it predicts that this peak will be broader than the other features in the spectrum as it arises from the overlap of many transitions involving OH-stretch / HOON-torsional combination bands associated with changes in the quantum numbers of $\Delta V_{OH} = 2$ and $\Delta V_{\tau} = +1, +2$. In addition, the simulation show that many of the transitions that fall under spectral feature *D / E*, originate from excited torsional levels with two or more quanta of initial excitation, thus accounting for the rotationally hot OH product state distributions seen from excitation of these spectral features. The reason for why so many transitions pile up in roughly in this spectral region can be understood by looking at the torsional potentials in Fig. 4.14. There, one may observe that as the relatively flat "ledge" region of the torsional potential around 600 cm^{-1} is approached, the spacing between the torsional energy levels become rather close thus leading to many transitions having similar frequencies. Finally as shown in Fig. 4.15, the two-dimensional model predicts that as one goes up in OH stretching overtone (e.g. from $2\nu_{OH}$ to $3\nu_{OH}$), the separation between the pure *cis-cis* OH stretching overtone peak and the broad peak to its blue should

increase. This follows from the fact that as one increases excitation of the OH stretch and thus considers higher values of V_{OH}, the associated adiabatic torsional potentials become more closed leading to higher torsion frequency and a slight increase in the energy separation between the excited levels in ledge area and the ground state. This later prediction is indeed seen in the experiments which finds that the separation between *cis-cis* overtone band and the strong features occurring to its blue, increases from ~570 cm^{-1} at $2\nu_{OH}$ to ~730 cm^{-1} at $3\nu_{OH}$ as will be shown in Chapter 5.

Sadly, a closer look at the two-dimensional model also reveals some important deficiencies. In particular, the torsion – stretch model is unable to account for the measured ^{15}N isotope shifts associated with some of the peaks in the $2\nu_{OH}$ spectrum. The isotope shifts expected on the basis of the model are indicated above the respective peaks in Fig. 4.18(a) and as seen in Fig. 4.19 which directly compares between the $2\nu_{OH}$ spectra generated via the OH + $^{14}NO_2$ and OH + $^{15}NO_2$ reactions. As all the features generated by the two-dimensional model involve combinations of the OH stretch and / or HOON torsional motion, neither of which are directly affected by ^{15}N substitution, the predicted shifts are all small (<2cm^{-1}). Comparing these shifts with what is actually measured in the experiments, shown in Fig. 4.3(a) and / or Fig. 4.18(b), illustrates the models limitations. We see that the ^{15}N shifts expected for peaks *A**, *D**, and *E** agree with what is found for their corresponding experimental peaks. By contrast, the shifts for *B** and *C** do not agree with what is found for feature *B* and *C*. As the isotope shifts expected for each quanta of excitation in a given vibrational mode is known, [11] the measured shifts suggests modes other than just the HOON torsion / OH stretch combinations, both of which have minimal shifts, are likely involved in the action spectra.

Apart from the isotope shifts, we can also check the predictions of the model using product state distributions. The right side of Fig. 4.20 shows the measured versus predicted OH ($^2\Pi_{3/2}$) distribution associated with peak *C*. We note, for example, that if we take the correspondence between the simulation and experiments to be *C** ↔ *C*, then the two-dimensional model predicts that peak *C* at ~6720 cm^{-1} originates from the first overtone of the HOON torsion, the $2\nu_9$ state. The product state distribution arising from excitation of this band, must then be consistent with dissociation from a initial state having ~510 cm^{-1} of vibrational energy. However, experimentally we find that the OH fragment product state distributions arising from excitation of feature *C* are much colder than that predicted by a PST calculation from a state having 510 cm^{-1} of vibrational energy, as shown on the right side of Fig. 4.20. It is possible, however, that the simulated peak *C** actually corresponds to the weak feature appearing slightly to the left of peak *C*, labeled *C'* in Fig. 4.20. As shown on the left side of Fig. 4.20, the measured product state distribution from excitation of this weak feature is consistent with dissociation from a state having ~510 cm^{-1} of initial vibrational energy. Unfortunately, due to the weak signal levels, we can not conclusively ascertain the isotope shift associated with this feature. Irrespective of this limitation however, if *C** corresponds to the weak feature (*C'*), then peak *C* remains unaccounted for. Thus, isotope shift and OH fragment energy release data suggest that spectral features in the $2\nu_{OH}$ spectrum such as *B* and *C*, which can not be easily explained by the two-dimensional model, most likely have contributions arising from modes other than just the HOON torsional and OH stretch.

In order to obtain information about spectral features such as *B* and *C* and their contributing modes, we have used *ab initio* vibrational frequencies and anharmonicities

obtained by running GAUSSIAN03 at MP2/aug-cc-pVTZ level of theory (see Table 4.14) to generate a list of vibrational band positions from the difference in the vibrational term value for various pairs of possible upper and lower vibrational states: $\nu = G(v'_1,v'_2,..,v'_9) - G(v''_1,v''_2,..,v''_9)$. We restrict the list of potential transitions by considering only transitions originating from the ground vibrational state and just the few lowest "hot" bands. In addition, we consider only transitions corresponding to small overall changes in the total vibrational quantum numbers (total change less than seven) and further restrict these to be consistent with our measured ^{15}N isotope shifts, which we know to within an uncertainty of around ~2 cm^{-1}. Only predicted transition frequencies that fall within a range of ± 50 cm^{-1} about the center of the measured peak are considered for the assignment. The program used with the vibrational term value calculation from the harmonic and anharmonic frequencies is given in Appendix *D*.

The resulting list of constrained possible assignments is shown in Table 4.15. For example, peak *B* could be due to transition from the ground state to the $\nu_1 + 2\nu_3 + \nu_7$ or from the first excited HOON torsional sate (ν_9) to final state $\nu_1 + 2\nu_3 + \nu_7 + \nu_9$ or from ν_7 going to $2\nu_1 + \nu_8$ etc. All of these transitions are consistent with our isotope shift measurements. A similar situation also exists for peak *C*. However, for peak *C* if we also consider fragment energy release data, we can eliminate the transitions originating from the $2\nu_9$ state as this would lead OH rotational state distribution that is hotter than what is actually measured as discussed previously (see Fig. 4.20). In Table 4.15 all transitions that are inconsistent with the measured OH product state distribution are indicated in gray and thus can be eliminated. For the large feature at 6935 cm^{-1} our search for possible

vibrational assignment indicates that neither transitions starting from the ground state nor low lying excited hot band sates (e.g. one quantum of ν_9 or ν_7) are able to generate transitions consistent with the observed band position, isotope shifts and fragment energy release. Hence this finding is consistent with feature *D* arising from highly excited HOON torsional states as predicted by the two-dimensional model. From this composite investigation using isotope shift, fragment energy release and two-dimensional spectral simulation, we are able to at least limit and, in some cases even confirm the assignment of all peaks appearing in the $2\nu_{OH}$ spectrum. It appears that a complete modeling of the action spectrum to account for features such as *B* and *C* will likely require the inclusion of additional modes such as the ν_3, ν_7 and ν_8 in a multi-dimensional treatment.

4.5 Conclusions

The unimolecular dissociation of *cis-cis* HOONO, an isomer of nitric acid, is initiated by exciting the molecule in the region of the first overtone of its OH stretching motion ($2\nu_{OH}$). The resulting OH fragments are probed using laser-induced fluorescence. The dissociation dynamics is consistent with a statistical distribution of the available energy as the OH fragment rotational energy is well described by phase space theory (PST). The PST simulations give a value of $D_0 = 19.9 \pm 0.5$ kcal/mol for the *cis-cis* HO-ONO bond energy. The fragment energy release measurements confirm that all major features in the $2\nu_{OH}$ room temperature spectrum are associated with the *cis-cis* isomer. We do not see any signature of the *trans-perp* nor that of the *cis-perp* isomer in these room temperature experiments. *Ab initio* calculations of the HOON torsional potential at the CCSD(T)/cc-pVTZ level suggests that although the *cis-perp* configuration corresponds to a stationary state, it does not correspond to a stable bound conformer on

the HOONO potential. Two-dimensional spectral simulations using this torsional potential in conjunction with a two-dimensional dipole surface, that takes into account the influence of HOON torsional motion on the OH stretching overtone, suggests that the strong spectral features occurring ~570 cm^{-1} to the blue of the *cis-cis* $2\nu_{OH}$ peak, apparently arises from the overlapping of many HOON-torsion/OH stretch combination bands originating from thermally populated hot torsional sates and excited to final states associated with changes in the torsional quantum number of $\Delta V_\tau = +1$ and +2.

The combination of spectral simulation, ^{15}N isotope shift measurements and OH fragment energy release allow us assign and in some cases bracket the possible assignments of all spectral features appearing in the action spectrum. The measurement of ^{15}N isotope shifts reveal some of the limitations of the two-dimensional torsional model and suggest that inclusion of several additional modes will likely be required in order to fully explain the room temperature $2\nu_{OH}$ action spectrum.

4.6 Acknowledgement

Chapter 4, in part, is a reprint of the material as it appears in Journal of Chemical Physics 120, 10543 (2004). J. Matthews, J. S. Francisco, and A. Sinha, American Institute of Physics, 2004. And in Journal of Chemical Physics 122, 104313 (2005). J. Matthews, and A. Sinha, American Institute of Physics, 2005.The dissertation author was the primary investigator and author of this paper.

Table 4.1: Fragment Energy Disposal *cis-cis* HOONO($2\nu_{OH}$ region) → OH + NO_2 [a]

Band / Excitation	OH N-level	Doppler Width	Translation OH	Translation NO_2	Translational Total [b]	Rotational Energy [b]
A (6381 cm^{-1})	1	0.096	560	207	767 ± 90	62 ± 3
	2	0.058	206	76	282 ± 71	
B (6500 cm^{-1})	1	0.090	495	183	678 ± 141	83 ± 4
	2	0.057	203	75	278 ± 85	
C (6720 cm^{-1})	1	0.093	522	193	715 ± 101	102 ± 5
	2	0.061	230	85	315 ± 74	
D' (6855 cm^{-1})	1	0.095	542	200	742 ± 61	—
	2	0.060	220	81	301 ± 83	
D (6935 cm^{-1})	1	0.1015	625	231	856 ± 86	243 ± 8
	2	0.063	242	89	331 ± 78	
E (7027 cm^{-1})	1	0.100	607	224	831 ± 75	265 ± 7
	2	0.0697	296	109	405 ± 87	

[a] All energies and widths in cm^{-1} . [b] Uncertainties are one standard deviation.

Table 4.2: *cis-cis* HOONO Z-matrix Used with CCSD(T)/cc-pVTZ Energies Calculations

CCSD(T) /cc-pVTZ

#p ccsd(t,maxcyc=300)/cc-pVTZ trans=iabc scf=(direct,tight)
opt=ef freq=noraman
 	
hoono optimization and ZPE at ccsd(t)/cc-pvtz
 	
0 1
N
O 1 no1
O 1 no2 2 ono2
O 3 oo 1 oon 2 d1 0
H 4 ho 3 hoo 1 d2 0
Variables:
no1=1.1915513
no2=1.38482706
oo=1.43318804
ho=0.9822377
ono2=114.39570514
oon=112.95094938
hoo=99.80958663
d1=0.0
d2=0.0

Table 4.3: *cis-perp* HOONO Z-matrix Used with CCSD(T)/cc-pVTZ Energies Calculations

CCSD(T) /cc-pVTZ

#p ccsd(t,maxcyc=300)/cc-pVTZ trans=iabc scf=(direct,tight)
opt=ef freq=noraman
 	
hoono optimization and ZPE at ccsd(t)/cc-pvtz
 	
0 1
N
O 1 no1
O 1 no2 2 ono2
O 3 oo 1 oon 2 d1 0
H 4 ho 3 hoo 1 d2 0
Variables:
no1=1.17429906
no2=1.48158918
oo=1.43852968
ho=0.9750828
ono2=114.01445591
oon=110.53799758
hoo=101.17084577
d1=-6.36845919
d2=83.92733204

Table 4.4: *trans-perp* HOONO Z-matrix Used with CCSD(T)/cc-pVTZ Energies Calculations

CCSD(T) /cc-pVTZ

#p ccsd(t,maxcyc=300)/cc-pVTZ trans=iabc scf=(direct,tight)
opt=ef freq=noraman

hoono optimization and ZPE at ccsd(t)/cc-pvtz
0 1 N O 1 no1 O 1 no2 2 ono2 O 3 oo 1 oon 2 d1 0 H 4 ho 3 hoo 1 d2 0 Variables: no1=1.16922 no2=1.46814 oo=1.43139 ho=0.96629 ono2=108.75409 oon=105.50865 hoo=100.75761 d1=176.83592 d2=97.59464

Table 4.5: Equilibrium Geometry Parameters for *cis-cis, cis-perp* and *trans-perp* calculated at CCSD(T)/cc-pVTZ[a]

	cis-cis	***cis-perp***	***trans-perp***
r(O-H)	**0.982**	**0.968**	**0.966**
r(O-O)	**1.433**	**1.430**	**1.431**
r(N-O)	**1.385**	**1.458**	**1.468**
r(N-O)	**1.192**	**1.169**	**1.169**
∠(H-O-O)	**99.8**	**101.9**	**100.8**
∠(O-O-N)	**113.0**	**111.4**	**105.5**
∠(O-N-O)	**114.4**	**114.5**	**108.8**
τ(O-N-O-O)	**0.0**	**-6.6**	**176.8**
τ(N-O-O-H)	**0.0**	**79.2**	**97.6**

[a] Bond distances are in angstroms and bond angles are in degrees.

Table 4.6: Harmonic Frequencies for *cis-cis, cis-perp* and *trans-perp* calculated at CCSD(T)/cc-pVTZ[a]

Frequency	*cis-cis*	*cis-perp*	*trans-perp*
ν_1	**3524**	**3755**	**3780**
ν_2	**1626**	**1724**	**1736**
ν_3	**1458**	**1400**	**1412**
ν_4	**964**	**953**	**992**
ν_5	**831**	**818**	**816**
ν_6	**716**	**543**	**497**
ν_7	**520**	**379**	**366**
ν_8	**402**	**344**	**302**
ν_9	**378**	**82**	**211**

[a] In units of cm^{-1}.

Table 4.7: CCSD(T)/cc-pVTZ Morse Parameters for OH Stretching mode of $HONO_2$, HONO, HO_2NO_2, CH_3OH, HOCl and HO_2NO_2 (cm^{-1})

		Ab initio	**Experimental**	**Scale factors**	**Ab-initio Scaled[a]**
cis-cis	ω_e	**3534**	**—**		**3492**
	$\omega_e\chi_e$	**107**	**—**		**92**
cis-perp	ω_e	**3764**	**—**		**3719**
	$\omega_e\chi_e$	**99**	**—**		**86**
trans-perp	ω_e	**3789**	**—**		**3744**
	$\omega_e\chi_e$	**99**	**—**		**86**
$HONO_2$	ω_e	**3767**	**3707[b]**	**0.98407**	**3721**
	$\omega_e\chi_e$	**94**	**79[b]**	**0.84043**	**80**
trans-HONO	ω_e	**3807**	**3751[c]**	**0.98529**	**3757**
	$\omega_e\chi_e$	**96**	**81[c]**	**0.84375**	**82**
CH_3OH	ω_e	**3880**	**3853[d]**	**0.99304**	**3839**
	$\omega_e\chi_e$	**98**	**85[d]**	**0.86735**	**84**
HOCl	ω_e	**3819**	**3779[e]**	**0.98953**	**3773**
	$\omega_e\chi_e$	**97**	**85[e]**	**0.87629**	**83**
HO_2NO_2	ω_e	**3760**	**3716[f]**	**0.98829**	**3714**
	$\omega_e\chi_e$	**99**	**88[f]**	**0.88889**	**85**

[a] Using average scale factors from reference molecules at CCSD(T)/cc-pVTZ ($<f_{\omega e}>=0.98804$ and $<f_{\omega e\chi e}>=0.86394$). [b] Ref. 26. [c] Ref. 28. [d] Ref. 27. [e] Ref. 29. [f] Ref. 25.

Table 4.8: Predicted OH Overtone Transition Frequencies and Absorption Cross-Sections for *cis-cis, cis-perp and trans-perp*

Overtone Transition	ν_{OH} (cm^{-1})[a]			σ (cm $molec.^{-1}$)[b]		
	cis-cis	***cis-perp***	***trans-perp***	***cis-cis***	***cis-perp***	***trans-perp***
V = 1	**3308**	**3547**	**3572**	**5.2×10^{-18}**	**6.1×10^{-18}**	**6.8×10^{-18}**
V = 2	**6432**	**6922**	**6972**	**1.9×10^{-19}**	**8.2×10^{-19}**	**10.0×10^{-19}**
V = 3	**9372**	**10 125**	**10 200**	**2.1×10^{-20}**	**3.5×10^{-20}**	**4.3×10^{-20}**
V = 4	**12 128**	**13 156**	**13 256**	**2.1×10^{-21}**	**1.9×10^{-21}**	**2.1×10^{-21}**
V = 5	**14 700**	**16 015**	**16 140**	**2.4×10^{-22}**	**1.7×10^{-22}**	**1.8×10^{-22}**
V = 6	**17 088**	**18 702**	**18 852**	**3.6×10^{-23}**	**2.4×10^{-23}**	**2.6×10^{-23}**

[a] Using scaled CCSD(T)/cc-pVTZ.
[b] Using a dipole function calculated at QCISD/cc-pVTZ.

Table 4.9: Rotational Constants, Harmonic Frequencies, Dipoles, Ionization Potentials and Polarizabilities for Reactants and Products Used with Phase-Space Simulation

	Molecule			
	cis-cis[a]	***trans-perp***[b]	NO_2	OH[c]
A (cm^{-1})	**0.71404**	**1.8054**	**8.001**	**-**
B (cm^{-1})	**0.26512**	**0.1660**	**0.434**	**16.978**[c]
C (cm^{-1})	**0.19317**	**0.1543**	**0.410**	**-**
D_J (cm^{-1})	**0.268×10^{-6}**	**8.3×10^{-8}**	**-**	**-**
D_{JK} (cm^{-1})	**-0.535×10^{-6}**	**-2.222×10^{-6}**	**-**	**-**
D_K (cm^{-1})	**2.0×10^{-6}**	**4.4×10^{-5}**	**-**	**-**
Dipole (D)[a]	**-**	**-**	**0.316**	**1.660**
***I* (eV)**[d]	**-**	**-**	**9.586**	**13.017**
α (m^3)[d]	**-**	**-**	**2.190×10^{-30}**	**0.955×10^{-30}**
C_6 (erg cm^6)	**2.0×10^{-58}**	**2.0×10^{-58}**		
ν_1	**3524**	**3780**	**1618**	**3768**
ν_2	**1626**	**1736**	**1320**	**-**
ν_3	**1458**	**1412**	**750**	**-**
ν_4	**964**	**992**	**-**	**-**
ν_5	**831**	**816**	**-**	**-**
ν_6	**715**	**497**	**-**	**-**
ν_7	**520**	**366**	**-**	**-**
ν_8	**402**	**302**	**-**	**-**
ν_9	**290**	**211**	**-**	**-**

[a] From *ab initio* CCSD(T)/cc-pVTZ calculations.
[b] The OH rotational lines are entered numerically in the phase-space simulations based on levels given in Ref. 21.
[c] Ref. 47.
[d] Ref. 44.

Table 4.10: Equilibrium Geometry Parameters of *cis-perp* HOONO[a]

	MP2	QCISD	CCSD(T)		
	cc-pVDZ	cc-pVTZ	cc-pVDZ	cc-pVTZ	cc-pVQZ
r (O–H)	0.974	0.965	0.975	0.968	0.967
r (O–O)	1.427	1.415	1.439	1.430	1.424
r (N–O)	1.513	1.440	1.482	1.458	1.452
r (N–O)	1.171	1.163	1.174	1.169	1.165
∠ (H–O–O)	100.9	102.5	101.2	101.9	102.2
∠ (H–O–O)	109.3	111.7	110.5	111.4	111.4
∠ (O–N–O)	113.6	114.6	114.0	114.5	114.5
τ (O–N–O–O)	-5.0	-6.8	-6.4	-6.6	-6.4
τ (N–O–O–H)	92.6	80.4	83.9	79.2	80.9
	-280.155265	-280.429952	-280.191098	-280.470704	-280.557536
	0.35	—	1.08	1.25	1.25

[a] Distances in Å, Angles in degrees.

[b] In hartree.

[c] In kcal/mol.

Table 4.11: Harmonic Frequencies of *cis-perp* HOONO (cm^{-1})

	MP2	QCISD	CCSD(T)		
	cc-pVDZ	**cc-pVTZ**	**cc-pVDZ**	**cc-pVTZ**	**cc-pVQZ**
ν_1	**3760**	**3797**	**3734**	**3755**	**3755**
ν_2	**1732**	**1773**	**1753**	**1724**	**1732**
ν_3	**1377**	**1431**	**1385**	**1400**	**1401**
ν_4	**940**	**1005**	**923**	**953**	**955**
ν_5	**817**	**849**	**796**	**818**	**820**
ν_6	**401**	**608**	**484**	**543**	**541**
ν_7	**369**	**385**	**372**	**379**	**382**
ν_8	**325**	**361**	**346**	**344**	**344**
ν_9	**216**	**137**	**154**	**82**	**110**

Table 4.12: CCSD(T)/cc-pVTZ O-H Stretch / HOON Torsion Vibrational Levels, Transition Frequencies [a] and Oscillator Strengths [b]

Initial State[c] (v''_{OH},v''_{τ})	Final State (v'_{OH}, v'_{τ})[c]										
	(2, 0) 8365	(2, 1) 8763	(2, 2) 9083	(2, 3) 9317	(2, 4) 9453	(2, 5) 9533	(2, 6) 9619	(2, 7) 9718	(2, 8) 9817	(2, 9) 9915	(2, 10) 10009
(0, 0) 1880	6485 2.76*E*-7	6883 1.15*E*-8	7204 3.01*E*-9	7438 4.07*E*-11	7573 2.02*E*-11	7653 1.22*E*-14	7739 1.04*E*-11	7838 1.88*E*-14	7937 3.99*E*-12	8036 1.2*E*-13	8129 1.69*E*-12
(0, 1) 2170	6195 9.50*E*-9	6593 2.89*E*-7	6914 3.49*E*-8	7147 1.20*E*-8	7283 5.61*E*-10	7363 2.06*E*-10	7449 8.73*E*-11	7548 4.85*E*-11	7647 1.50*E*-11	7745 1.23*E*-11	7839 1.56*E*-12
(0, 2) 2387	5978 2.36*E*-9	6375 1.36*E*-8	6696 2.70*E*-7	6930 9.40*E*-8	7065 4.60*E*-8	7145 5.54*E*-9	7232 2.64*E*-9	7330 5.35*E*-10	7429 2.60*E*-10	7528 8.73*E*-11	7621 3.88*E*-11
(0, 3) 2508	5857 1.66*E*-11	6254 3.43*E*-9	6575 9.04*E*-9	6809 2.22*E*-7	6944 2.30*E*-7	7024 1.46*E*-7	7111 2.74*E*-8	7209 6.53*E*-9	7308 1.78*E*-10	7407 2.16*E*-10	7500 3.57*E*-12
(0, 4) 2565	5800 7.83*E*-11	6197 4.34*E*-11	6518 8.53*E*-9	6752 1.33*E*-8	6888 2.65*E*-7	6968 3.23*E*-7	7054 1.56*E*-7	7153 2.46*E*-8	7251 1.01*E*-8	7350 2.52*E*-10	7444 8.87*E*-11
(0, 5) 2635	5730 2.01*E*-12	6128 1.13*E*-9	6449 1.82*E*-9	6682 4.59*E*-8	6818 1.80*E*-8	6898 2.31*E*-7	6984 3.08*E*-7	7083 1.52*E*-7	7182 2.29*E*-8	7281 1.25*E*-8	7374 1.03*E*-9
(0, 6) 2722	5643 5.53*E*-11	6041 2.77*E*-11	6362 4.28*E*-9	6595 7.52*E*-9	6731 5.41*E*-8	6811 1.30*E*-8	6897 2.26*E*-7	6996 3.03*E*-7	7095 1.69*E*-7	7193 2.06*E*-8	7287 1.39*E*-8
(0, 7) 2807	5558 4.24*E*-12	5956 3.51*E*-10	6276 2.85*E*-10	6510 7.81*E*-9	6646 9.31*E*-9	6726 4.86*E*-8	6812 1.34*E*-8	6911 2.40*E*-7	7010 3.06*E*-7	7108 1.89*E*-7	7202 1.32*E*-8
(0, 8) 2893	5472 1.42*E*-11	5870 1.97*E*-12	6191 1.13*E*-9	6425 1.38*E*-9	6560 6.48*E*-9	6640 1.17*E*-8	6726 5.58*E*-8	6825 9.15*E*-9	6924 2.43*E*-7	7023 2.89*E*-7	7116 2.20*E*-7
(0, 9) 2977	5388 4.17*E*-12	5786 1.18*E*-10	6107 5.33*E*-11	6340 2.14*E*-9	6476 1.72*E*-9	6556 6.44*E*-9	6642 1.66*E*-8	6741 6.19*E*-8	6840 4.75*E*-9	6938 2.56*E*-7	7032 2.64*E*-7
(0, 10) 3039	5326 4.58*E*-12	5723 1.91*E*-12	6044 3.85*E*-10	6278 4.15*E*-10	6414 1.46*E*-9	6493 1.99*E*-9	6580 9.68*E*-9	6679 1.80*E*-8	6777 5.89*E*-8	6876 2.45*E*-10	6969 2.54*E*-7

[a] In cm^{-1}.
[b] Entries inside table give transition frequencies followed by oscillator strengths.
[c] State energies are indicated below each state label.

Table 4.13: ACESII Z-matrix Used with CCSD(T)/cc-pVTZ Single Point Dipole Moment Evaluations

CCSD(T) /cc-pVTZ
HOONO (0,2) grid point N O 1 no1 O 1 no2 2 ono2 O 3 oo 1 oon 2 d1 H 4 ho 3 hoo 1 d2 no1=1.1915513 no2=1.38482706 oo=1.43318804 ho=1.1822377 ono2=114.39570514 oon=112.95094938 hoo=99.80958663 d1=0.0 d2=0.0 *ACES2(PRINT=0,REFERENCE=RHF,CALC=CCSD(T), BASIS=CC-PVTZ,CHARGE=0,SPHERICAL=ON,MULTI=1, PROPS=1,SCF_CONV=8,MEMORY_SIZE=800MB,DROPMO=1-4)

Table 4.14: Vibrational Frequencies, Anharmonicities and Isotope Shift of *cis-cis* HOONO (cm^{-1}) [a]

$(\omega_e)_i$	355	524	397	716	837	971	1434	1568	3487
^{15}N Isotope Shift	1.3	6.0	0.3	10.0	6.1	6.6	4.3	24.5	0.0
$(\omega_e\chi_e)_{ij}$	9	8	7	6	5	4	3	2	1
1	65.1	23.6	2.21	12.2	5.11	3.74	-39.7	-2.74	-111
2	4.4	0.72	0.38	28.8	-1.06	-3.41	-9.11	-9.72	
3	12.2	3.53	-0.79	-1.8	-8.56	-4.97	-5.95		
4	-6.02	-2.52	-4.77	-9.39	-9.12	-2.86			
5	-3.98	-4.87	-3.13	-4.72	-3.4				
6	-39.6	-16	-9.58	-28.4					
7	-15.4	-6.54	-3.53						
8	-48.2	-8.47							
9	-38.2								

[a] **Using MP2/aug-cc-pVTZ.**

Table 4.15: Isotopic shift constrained band assignments for *cis-cis* HOONO spectral features [a]

Initial State[b]	Peak *A* (6365 cm^{-1})	Peak *B* (6500 cm^{-1})	Peak C (6720 cm^{-1})	Peaks D (6935 cm^{-1}) E (7027 cm^{-1})
0 Ground state (0 cm^{-1})	$2\nu_1$ (~0)	$\nu_1+2\nu_3+\nu_7$ (~9)	$\nu_1+2\nu_3+2\nu_7$ (~9)	$2\nu_1+2\nu_9$ (~3) $2\nu_1+\nu_7+\nu_9$ (~2)
ν_9 τ(HOON) (a", 263 cm^{-1})		$\nu_1+2\nu_3+\nu_7$ $+\nu_9$ (~9)	$2\nu_1+\nu_8$ (~7)	$2\nu_1+3\nu_7$ (~2) $2\nu_1+\nu_7+\nu_9$ (~0) $2\nu_1+\nu_7+2\nu_9$ (~2) $2\nu_1+3\nu_7$ (~2) $2\nu_1+3\nu_9$ (~3)
ν_7 ∠(NOO) (a', 371 cm^{-1})		$2\nu_1+\nu_8$ (~6)	$2\nu_1+\nu_6$ (~10) $\nu_1+2\nu_3+3\nu_7$ (~9)	$2\nu_1+\nu_7+2\nu_9$ (~3)
$2\nu_9$ τ(HOON) (a', 447 cm^{-1})		$2\nu_1+\nu_8$ (~8)	$2\nu_1+\nu_5$ (~9) $2\nu_1+2\nu_7$ (~3)	$2\nu_1+2\nu_7+\nu_9$ (~2) $2\nu_1+\nu_7+2\nu_9$ (~0) $2\nu_1+3\nu_9$ (~1) $2\nu_1+\nu_7+3\nu_9$ (~2) $2\nu_1+4\nu_9$ (~3)

[a] **Transitions that are consistent with isotope shift data but not with fragment energy release are indicated in grey. The expected isotope shift is indicated in parentheses below the state label.**

[b] **Vibrational levels and state symmetry at MP2/aug-cc-pVTZ are given in parentheses.**

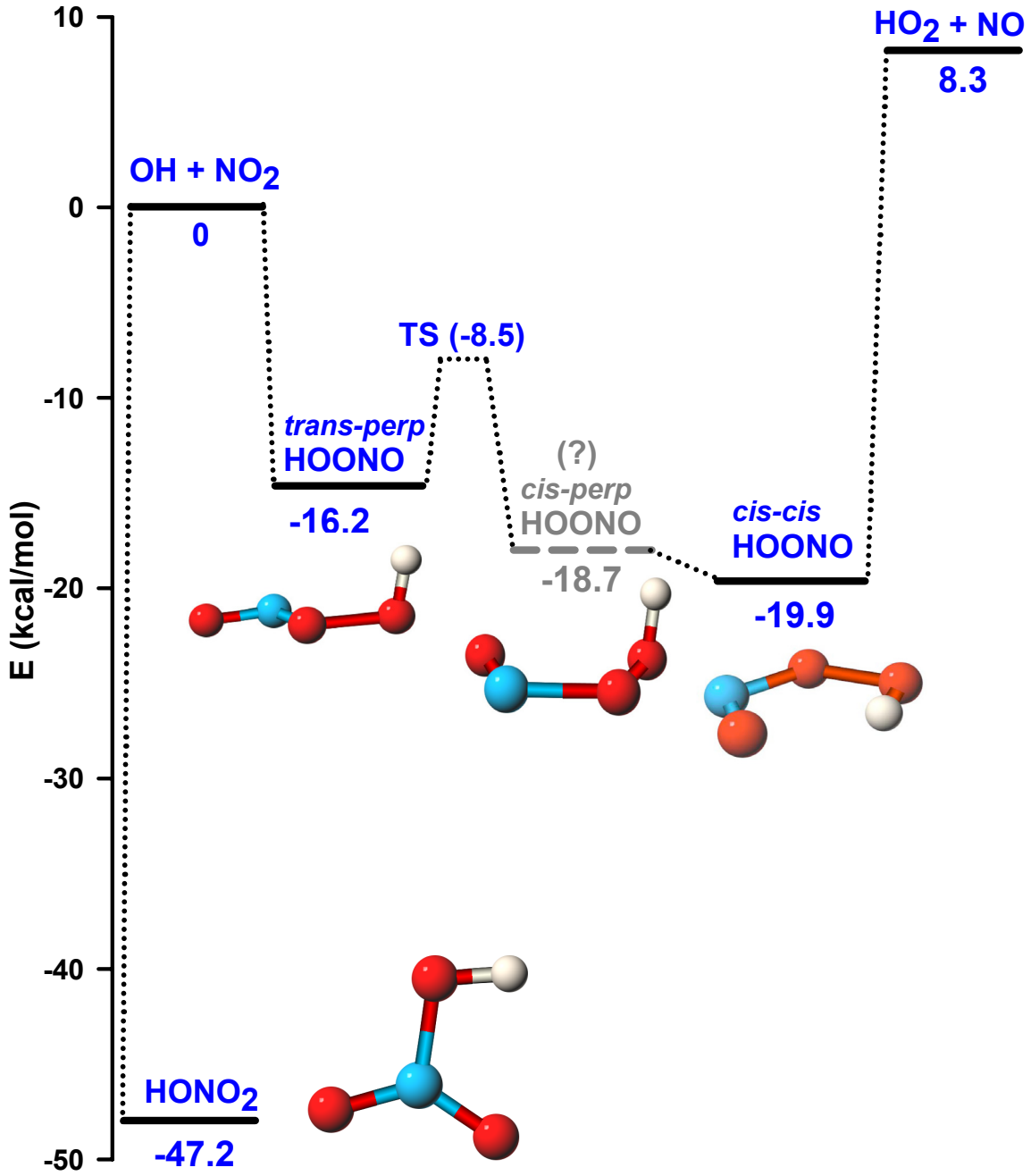

Figure 4.1: Schematic potential energy diagram showing the energies of the various HOONO conformers based on experimental data of Refs.11, 12, 13 and this work. The energies are relative to the OH + NO_2 dissociation limit. Whether the *cis-perp* configuration corresponds to a bound stable local minimum in the potential depends on the level of theory considered. [File: F4.1_epd]

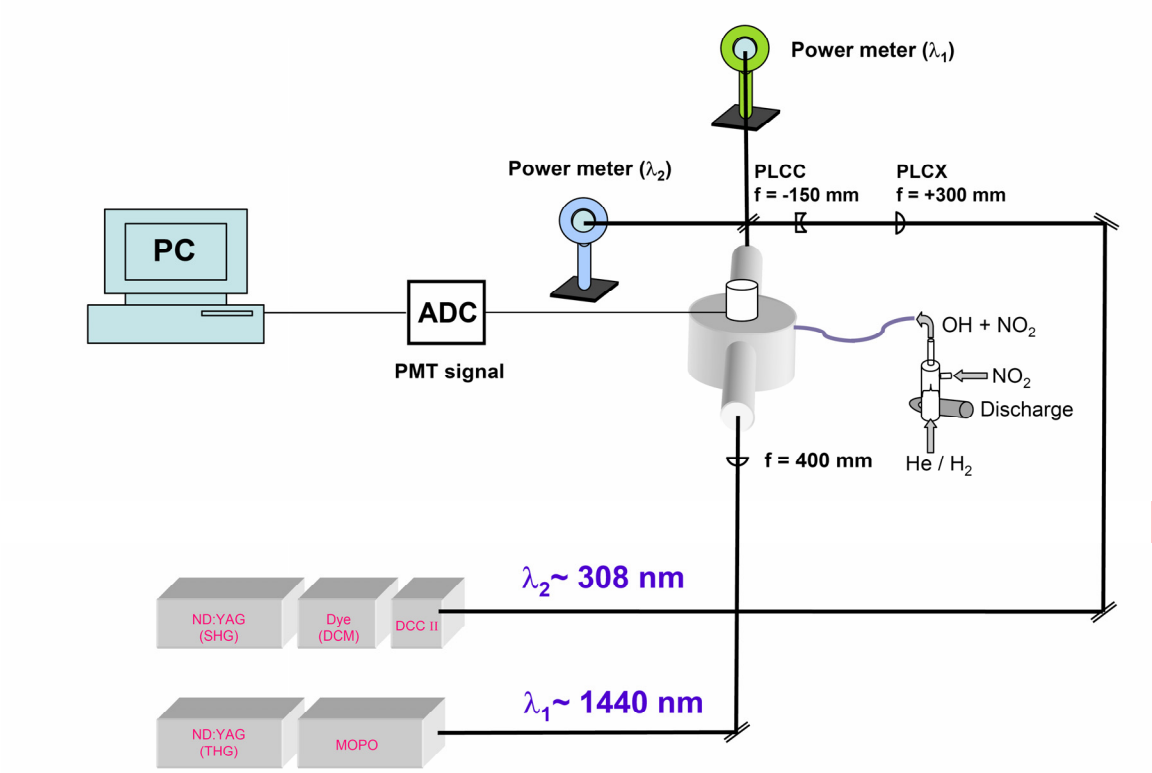

Figure 4.2: Schematic of the experimental apparatus. HOONO is generated in a side reactor is flowed through $^1/_8$" OD 6' Teflon tubing to the photolysis cell. The tunable infrared radiation used for the vibrational excitation is generated by the MOPO system and the U.V. radiation used to probe the OH transition via the $A - X(0,0)$ diagonal transition is generated by the doubling the output of the dye laser. The temporal delay between the pump and probe lasers is set to 15 ns and the probe laser is counter propagating to the IR laser. A set of plano-convex (+300 mm) and plano-concave (-150 mm) lenses collimate the probe beam to reduce scatter light. [File: F4.2_apparatus]

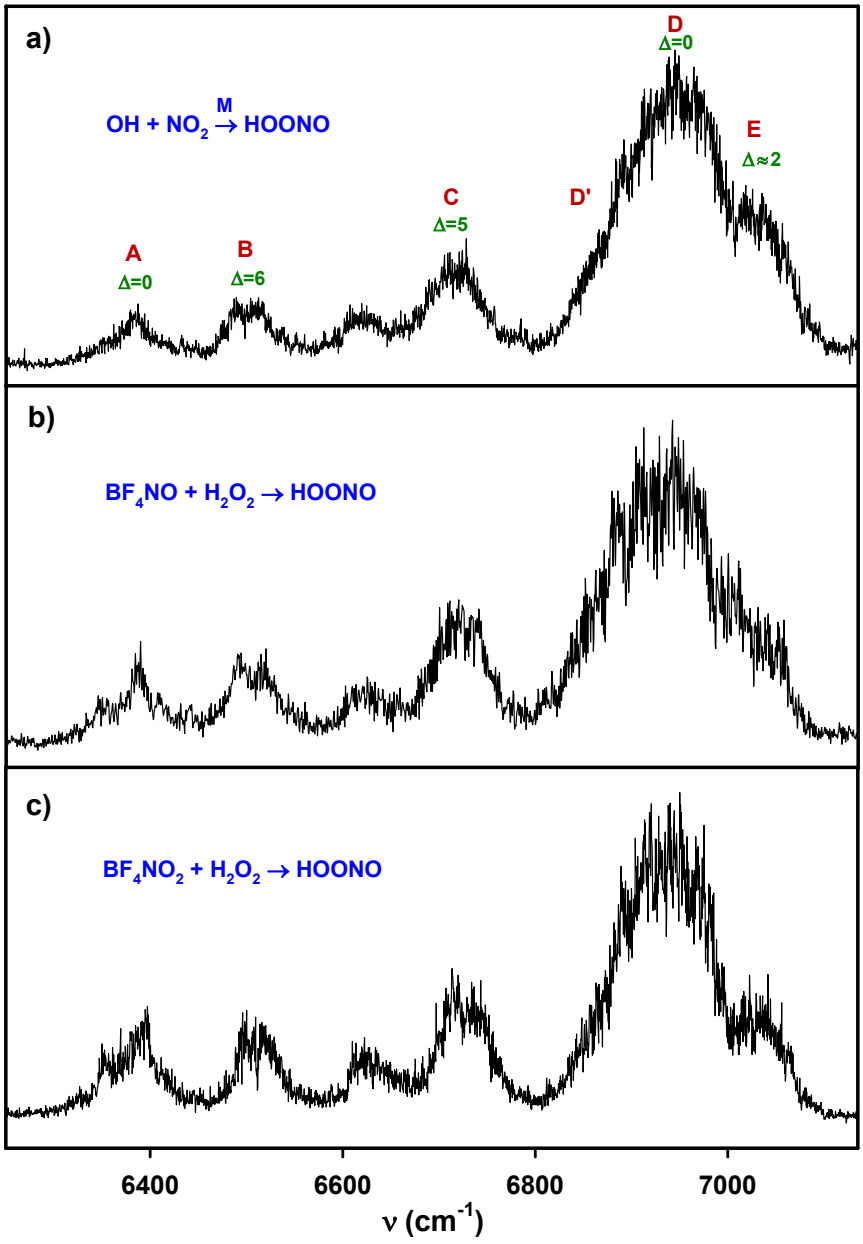

Figure 4.3: Action spectrum of room temperature HOONO obtained from three different sources in the region of its first OH stretching overtone ($2\nu_{OH}$). The spectra are generated by monitoring the total yield of nascent OH (N=2) rotational state as the infrared excitation laser is scanned. a) HOONO from the three-body recombination reaction OH + NO_2 + M. The letters A-E label the major spectral features investigated in this study. The Δ values indicated next to the spectral feature are the measured isotope shift in cm^{-1} when going from ^{14}N to ^{15}N labeled HOONO b) Action spectrum of HOONO generated from the $BF_4NO + H_2O_2$ reaction. c) Action spectrum of HOONO from the HO_2NO_2 source. [File: F4.3_HOONO_sources]

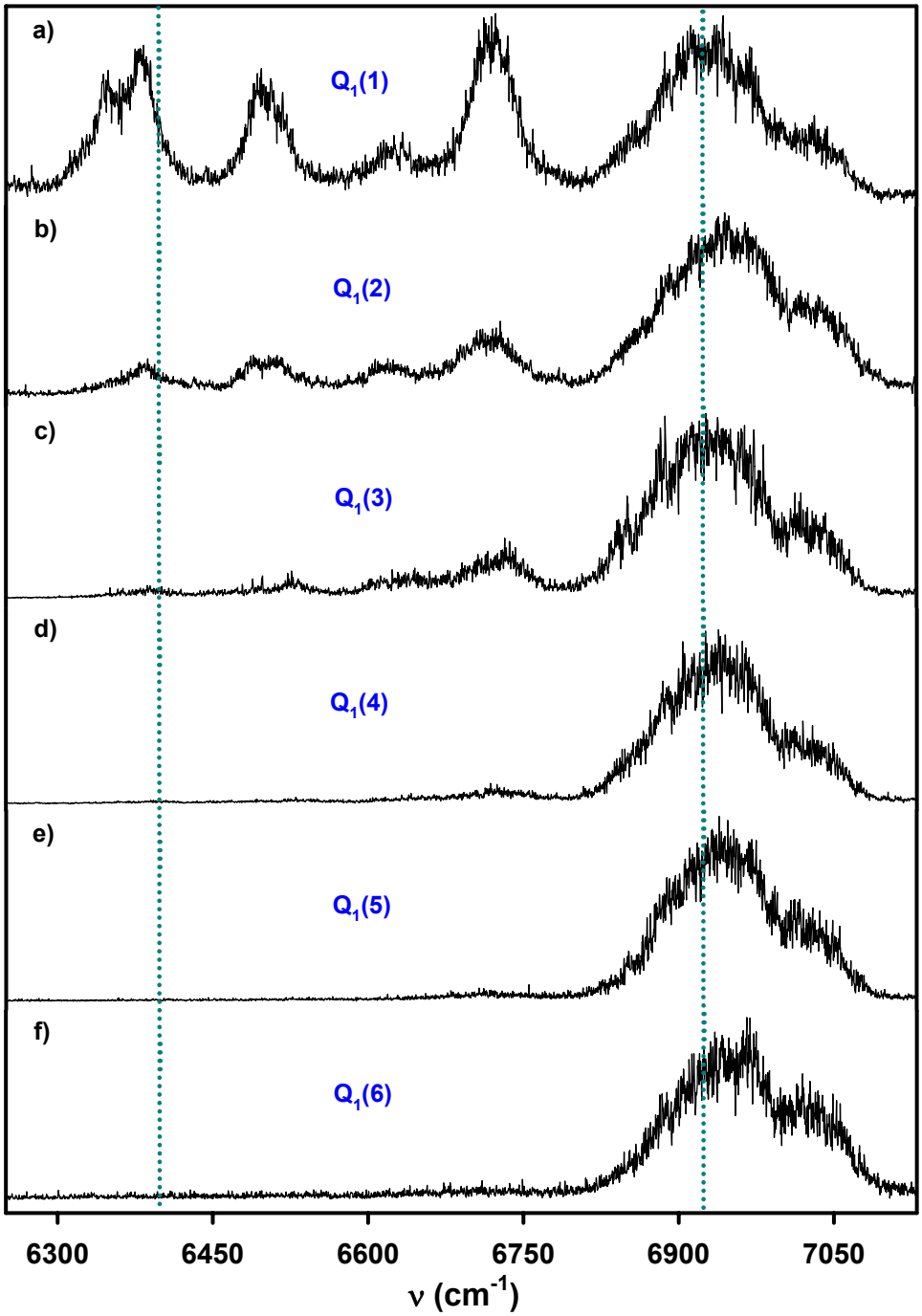

Figure 4.4: Dependence of HOONO ($2\nu_{OH}$) action spectra on the probed nascent OH rotational state. The dashed vertical line in the figure represents the range of calculated dissociation energy for the HO-ONO of D_0 = 18.3 – 19.8 kcal/mol at the CCSD(T)/CBS limit from Ref. 2-5. a) monitoring N = 1. b) monitoring N = 2. c) monitoring N = 3. d) monitoring N = 4. e) monitoring N = 5. f) monitoring N = 6. [File: F4.4_N_levels]

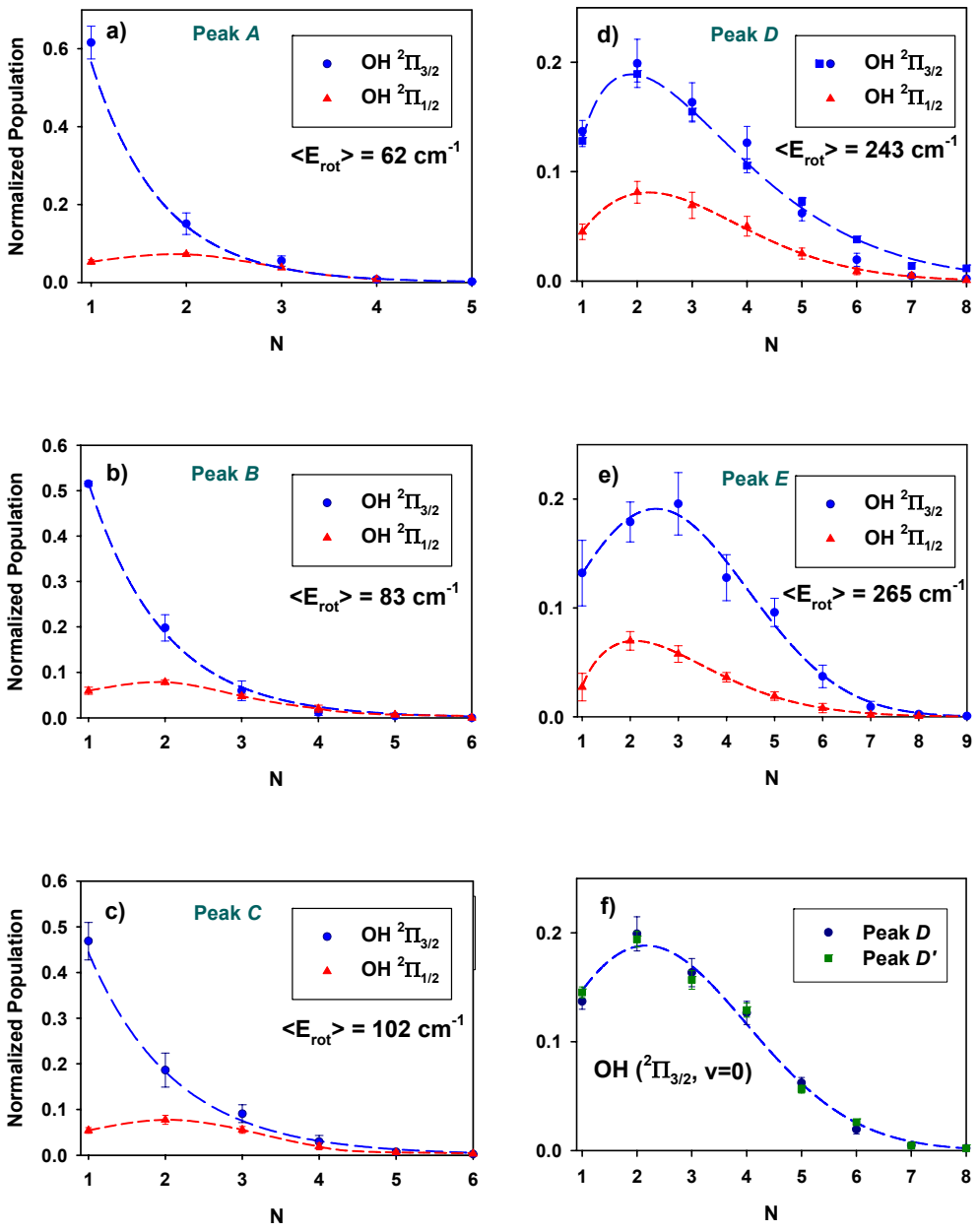

Figure 4.5: Nascent rotational state distributions of the OH (v=0, $^2\Pi_{3/2}$) and OH (v=0,$^2\Pi_{1/2}$) states resulting from excitation at various points within peaks *A* – *E* in the vicinity of the $2\nu_{OH}$ band. Except where noted, the source chemistry for these measurements is the OH + NO_2 reaction. a) Distribution resulting from excitation within peak *A*. b) Distribution resulting from excitation within peak *B*. c) Distribution resulting from excitation within peak *C*. d) Distribution resulting from excitation within peak *D*. For the $^2\Pi_{3/2}$ state, we also compare results from the BF_4NO + H_2O_2 source, represented by the squares. e) Distribution resulting from excitation within peak *E*. f) Comparison of distributions arising excitation at different points within the broad feature. Comparing results from excitation at 6855cm^{-1}, peak *D*' versus peak *D* at 6935 cm^{-1}. [File: F4.5_psd]

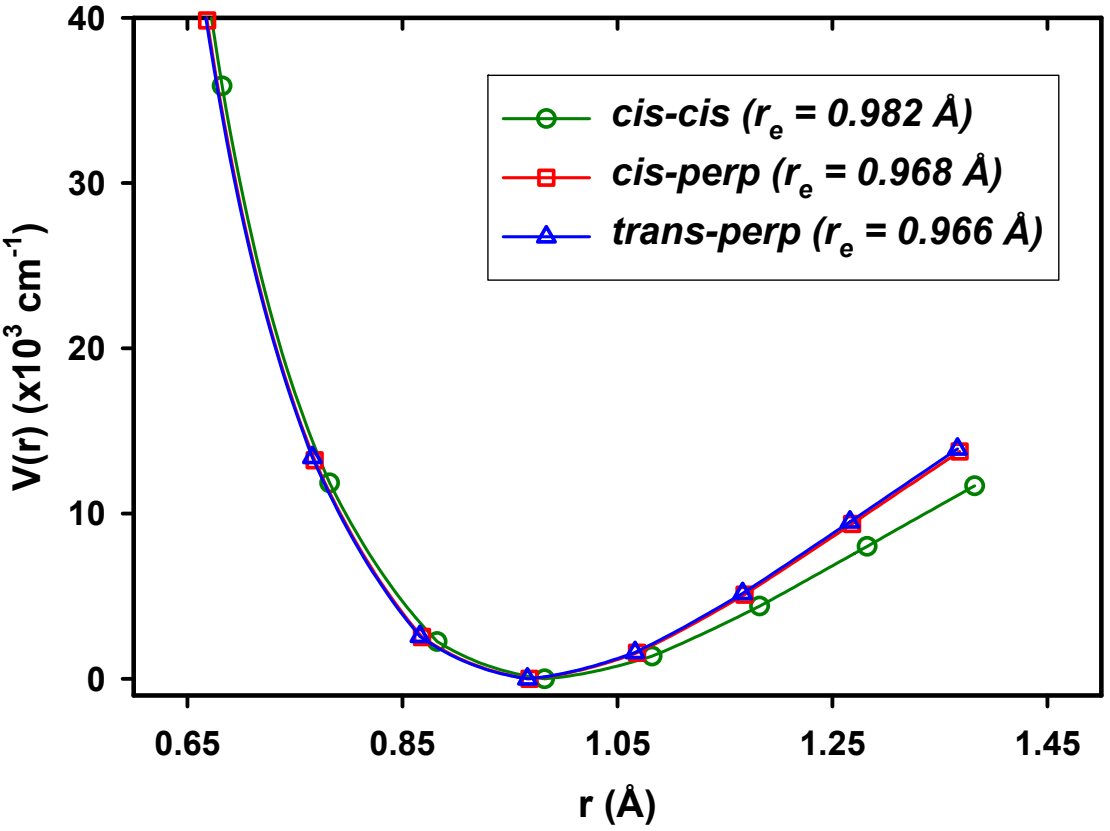

Figure 4.6: CCSD(T)/cc-pVTZ one-dimensional slices of the potential along the OH stretching coordinate for the *cis-cis* (circle), *cis-perp* (square) and *trans-perp* (triangle) conformers. The plot illustrates that the *cis-perp* and *trans-perp* conformers have a stiffer potential corresponding to a higher frequencies and lower anharmonicities compared with the "loose" *cis-cis* potential. [File: F4.6_OH_pot]

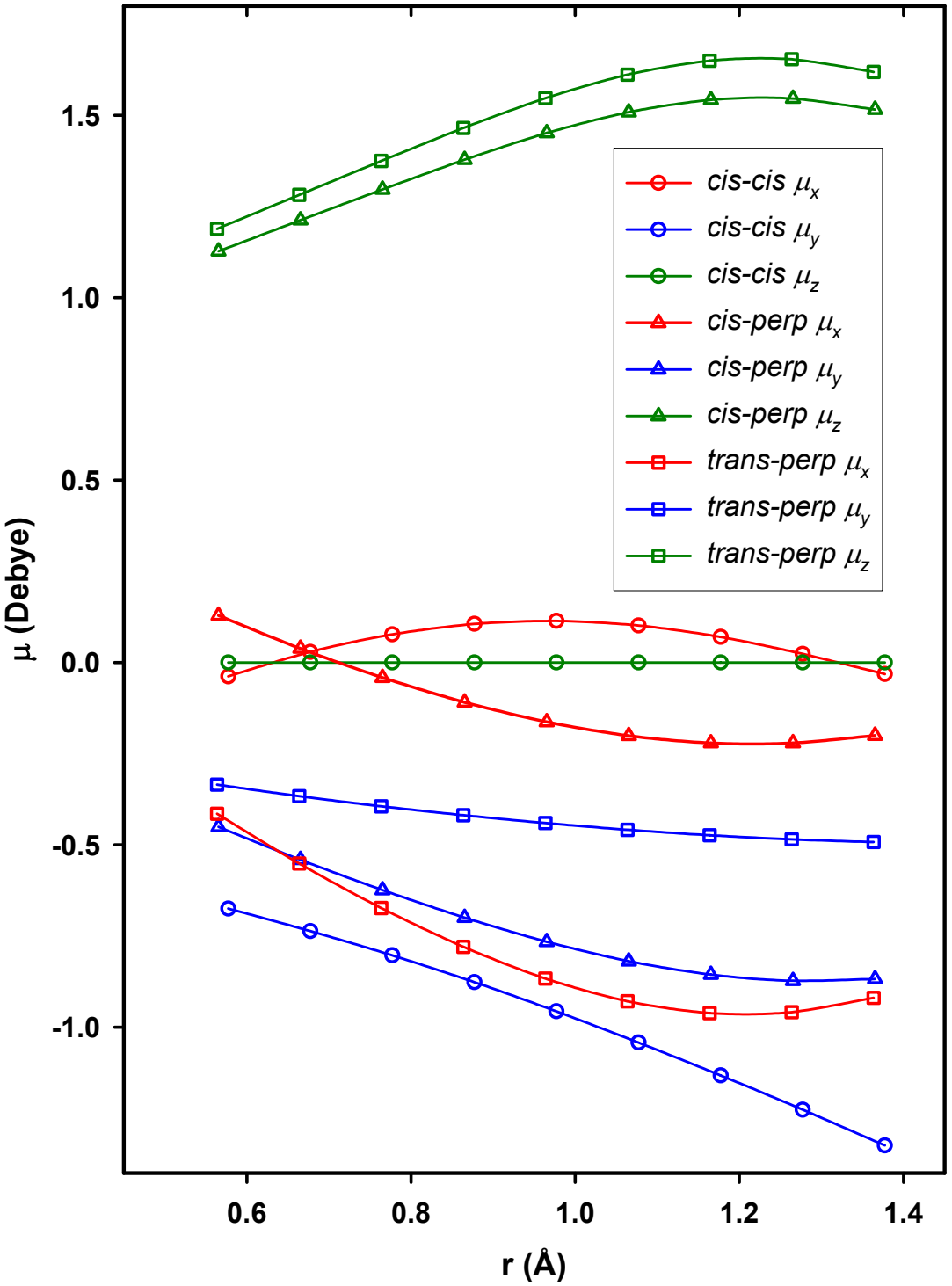

Figure 4.7: QCISD/cc-pVTZ one-dimensional dipole moments μ_x, μ_y, μ_z for the *cis-cis* (circle), *cis-perp* (triangle) and *trans-perp* (square) conformers. Note the lack of z- dipole moment component for the *cis-cis* conformer. [File: F4.7_dipoles]

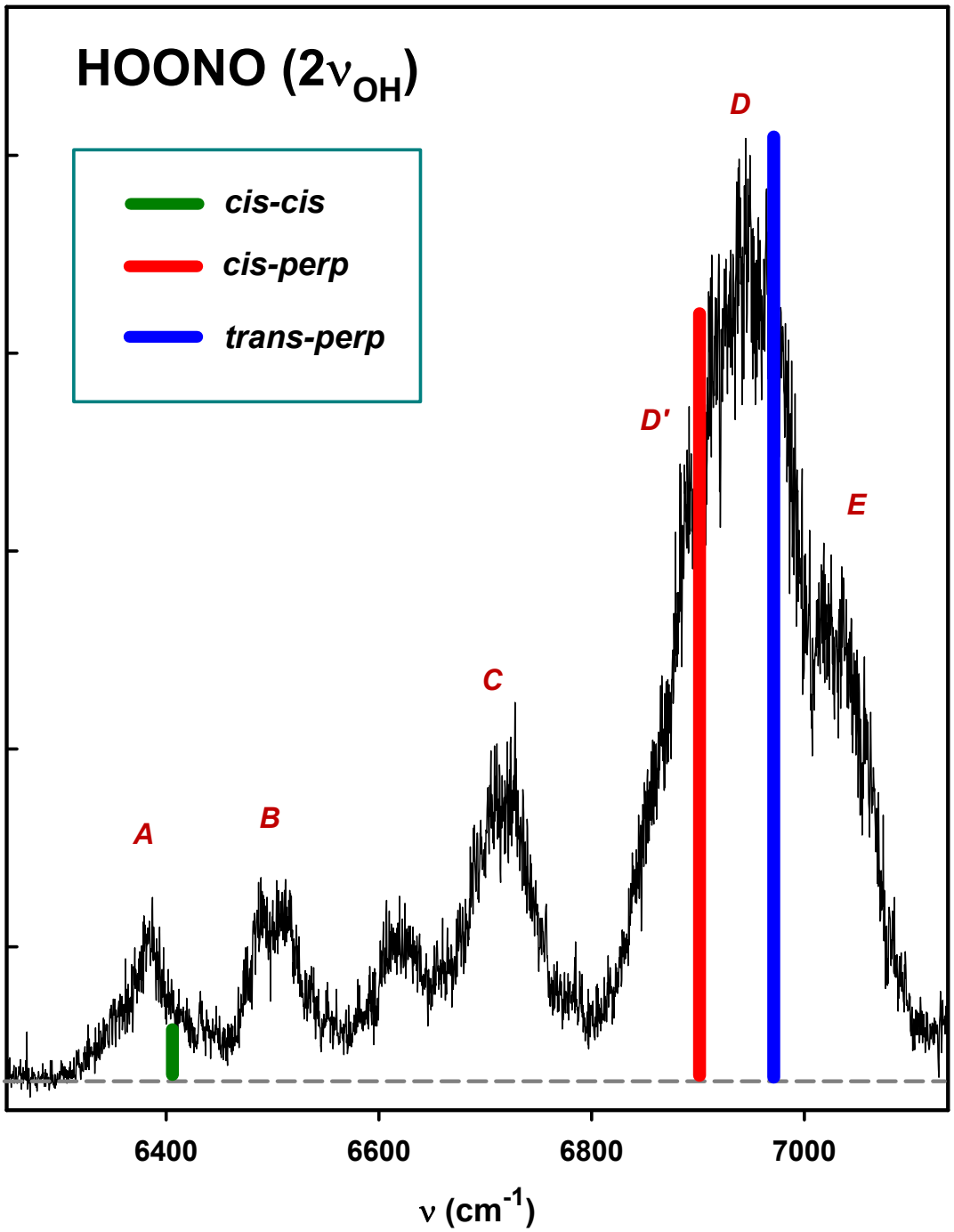

Figure 4.8: Simulated $2\nu_{OH}$ action spectrum from the one-dimensional intensity calculation using a dipole surface described in the text. The vertical sticks on the spectrum are the effective strengths of the vibrational transitions of *cis-cis* (green), *cis-perp* (red) and *trans-perp* (blue) weighted by their respective oscillator strength, and estimated quantum yield. [File: F4.8_sticks]

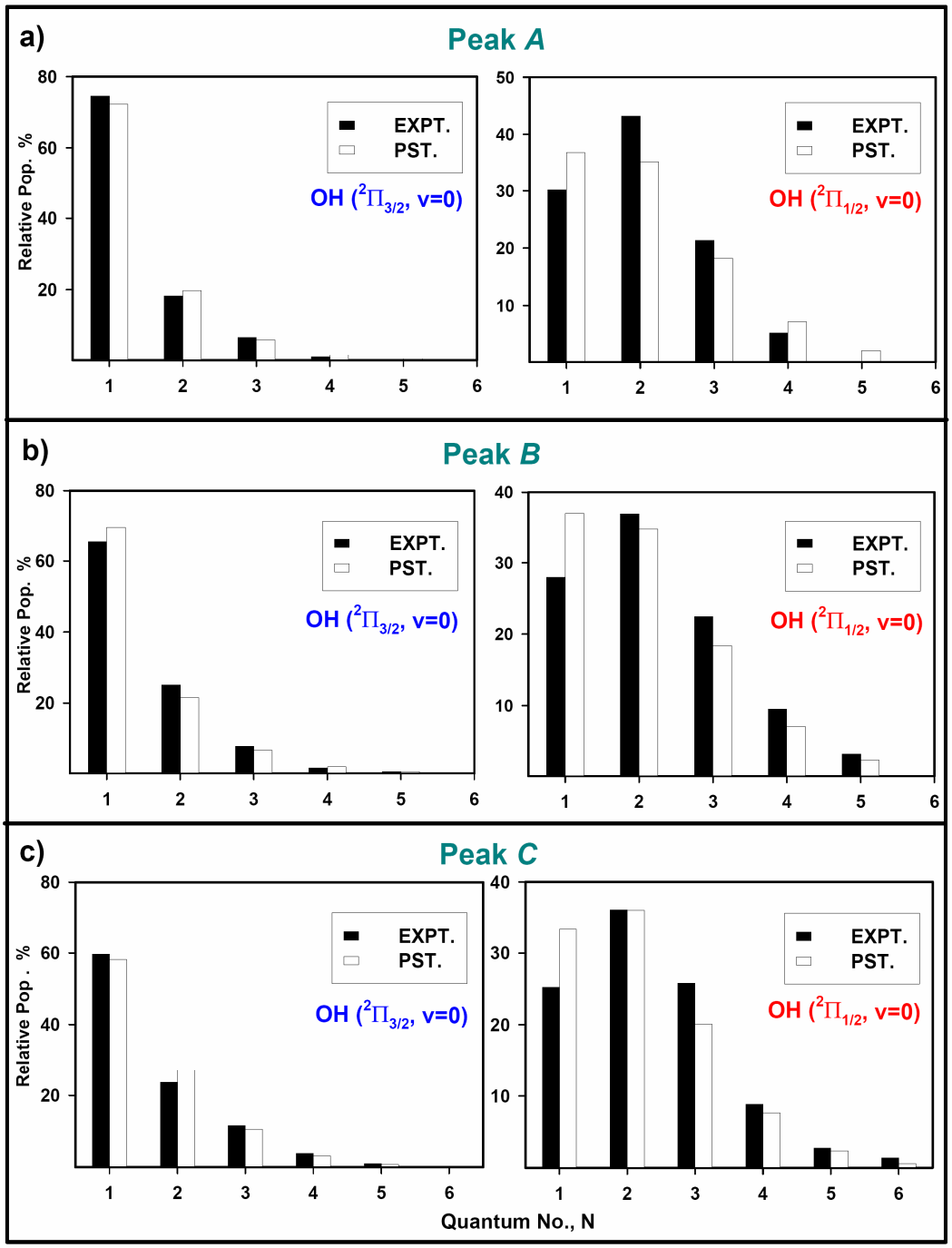

Figure 4.9: Comparison of experimental and phase-space simulation of the OH (v=0, $^2\Pi_{3/2}$) and OH (v=0,$^2\Pi_{1/2}$) product state distributions. The phase space simulation uses D_0 = 19.9 kcal/mol, $C_6 = 2.0 \times 10^{-58}$erg/cm^6, *cis-cis* HOONO spectroscopic parameters and averages over the thermal distribution of initial *cis-cis* HOONO states. a) Results for excitation within peak *A*. b) Results for excitation within peak *B*. c) Results for excitation within peak *C*. [File: F4.9_PST_199]

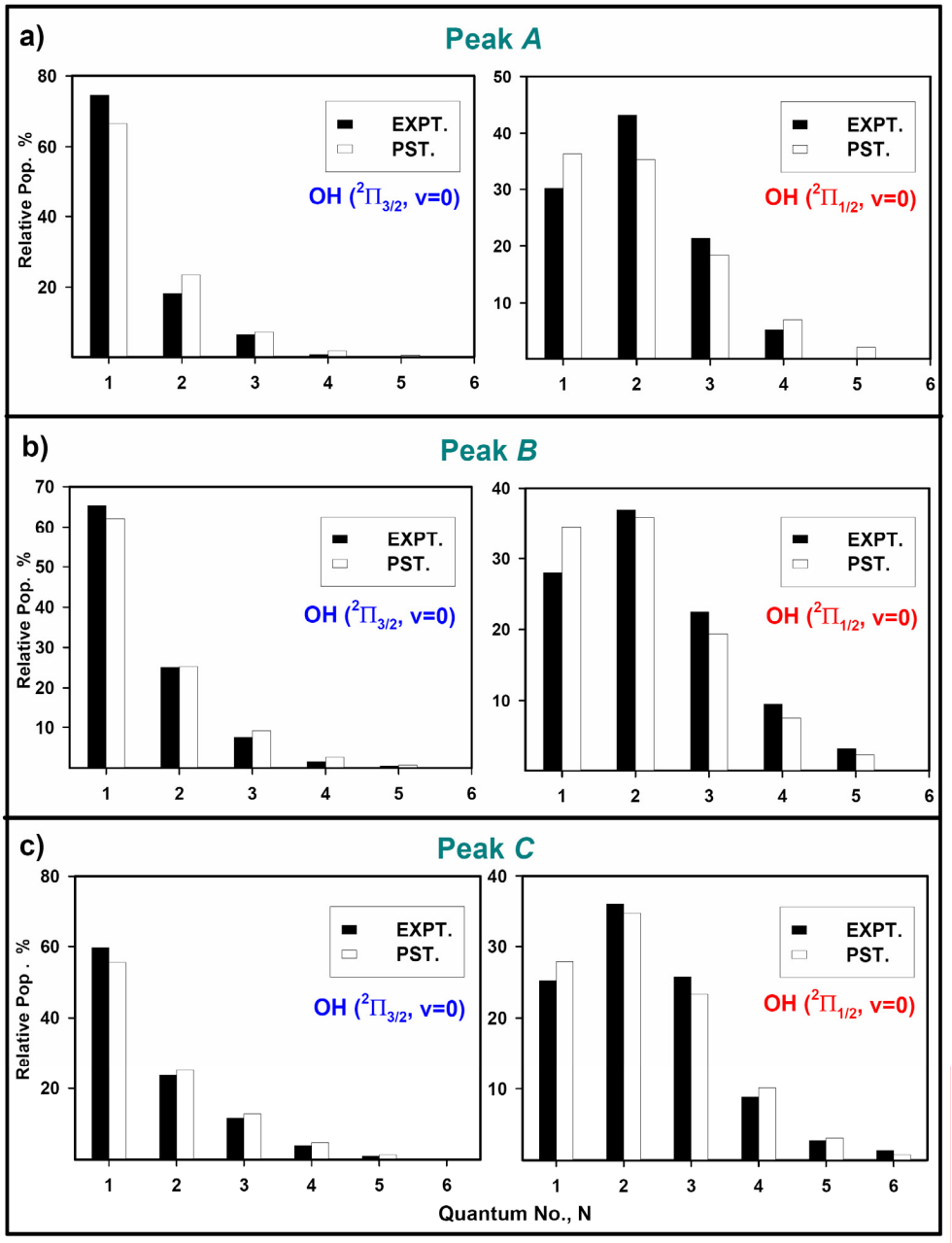

Figure 4.10: Comparison of experimental and phase-space simulation of the OH (v=0, $^2\Pi_{3/2}$) and OH (v=0,$^2\Pi_{1/2}$) product state distributions. The phase space simulation uses D_0 = 19.4 kcal/mol, $C_6 = 2.0 \times 10^{-58}$erg/cm^6 and *cis-cis* HOONO spectroscopic parameters. a) Results for excitation within peak *A*. b) Results for excitation within peak *B*. c) Results for excitation within peak *C*. [File: F4.10_PST_194]

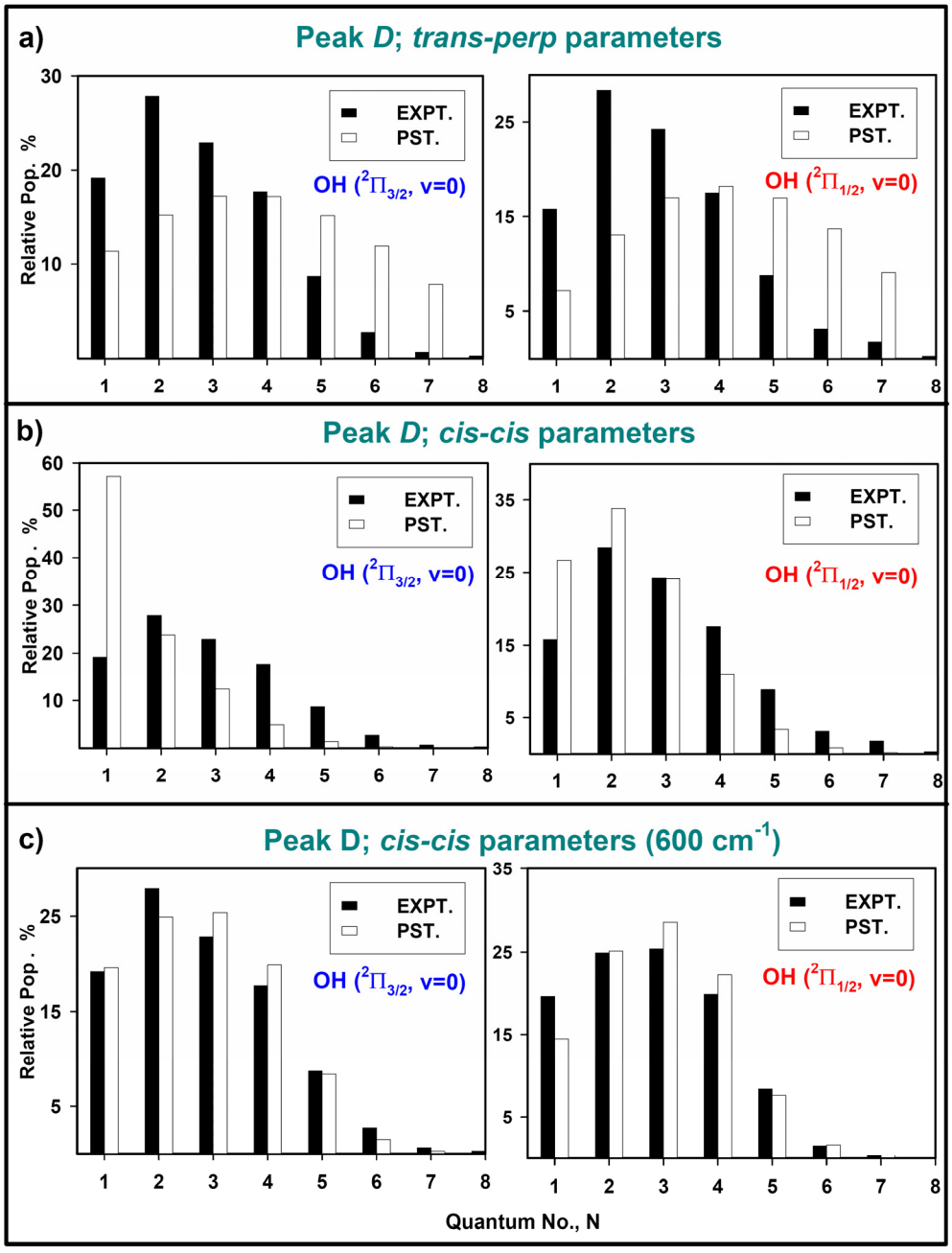

Figure 4.11: Comparison of experimental and phase-space simulation of the OH (v=0, $^2\Pi_{3/2}$) and OH (v=0,$^2\Pi_{1/2}$) product state distributions resulting from excitation within peak *D*. a) Standard PST using *trans-perp* spectroscopic parameters, D_0 = 16.2 kcal/mol, C_6= 2.0 × 10^{-58} erg/cm^6 and thermal distribution of initial states. b) Standard PST using *cis-cis* spectroscopic parameters, D_0 = 19.9 kcal/mol, C_6 = 2.0 x 10^{-58} erg/cm^6 and thermal distribution of initial states. c) PST simulation using *cis-cis* spectroscopic parameters, D_0 = 19.9 kcal/mol, C_6 = 2.0x10^{-58} erg/cm^6 and considering a single 600cm^{-1} vibrational state with corresponding thermal distribution of rotational states.
[File: F4.11_PST_transperp]

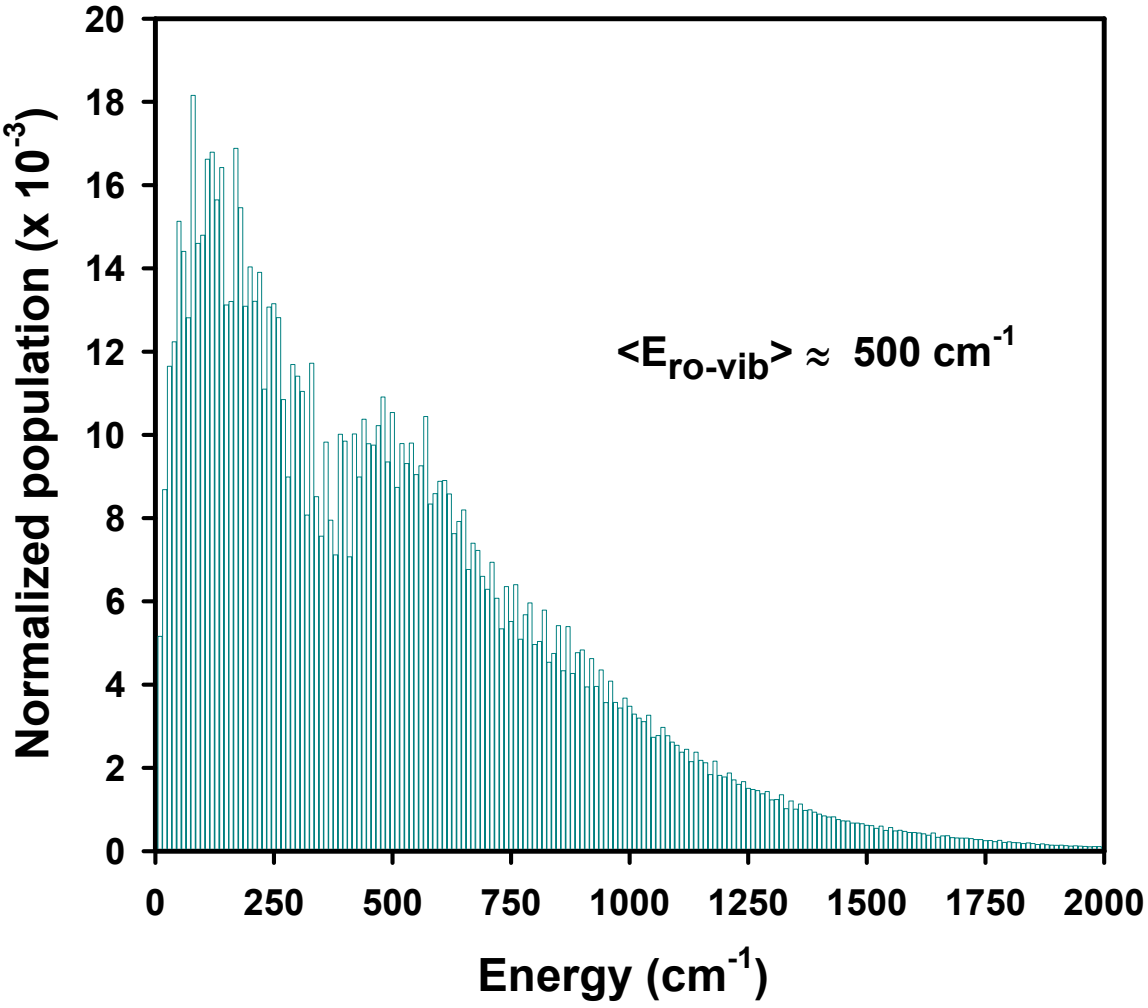

Figure 4.12: The density of rotational-vibrational states of HOONO at 298 K. The distribution is generated by counting the number of ro-vibrational states occurring in a particular energy bin. The average internal energy of HOONO is then calculated using $\langle E_{ro\text{-}vib} \rangle = \Sigma P_i \varepsilon_i / \Sigma P_i$. [File: F4.12_dos]

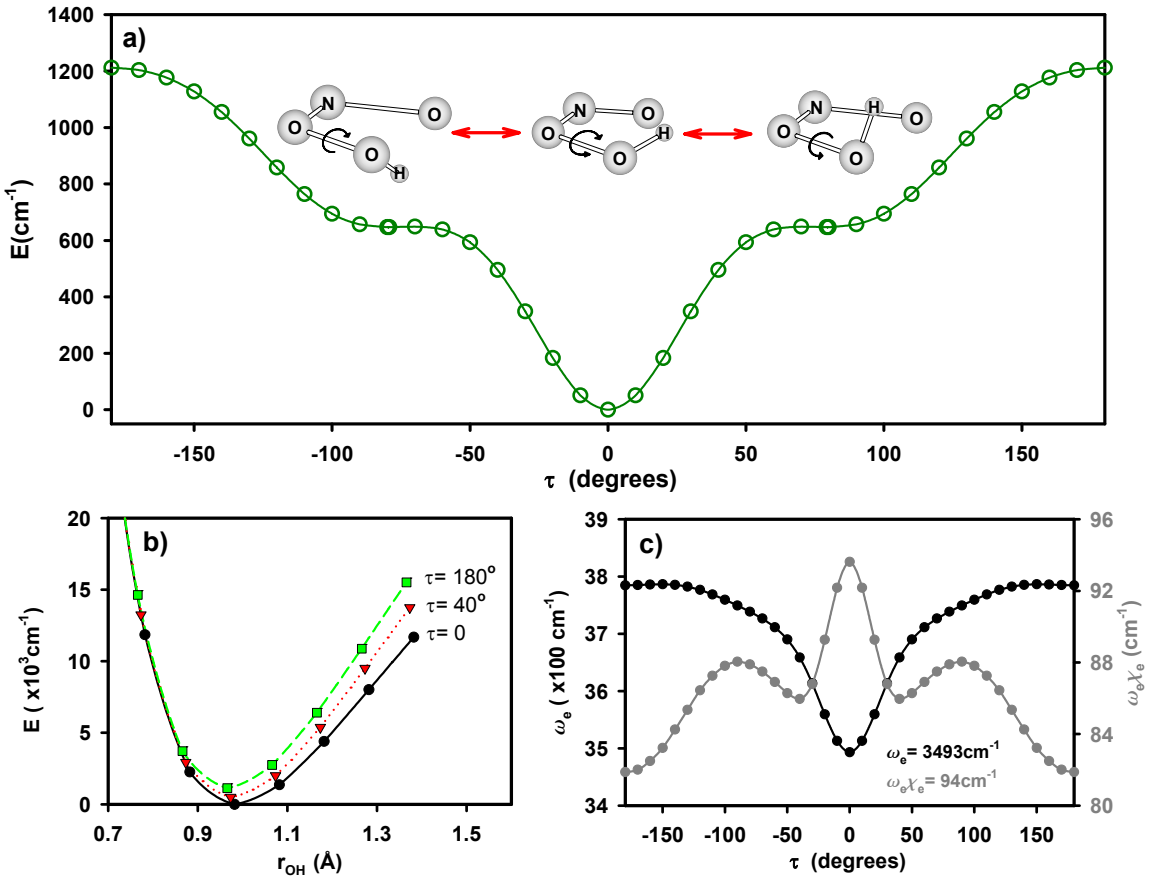

Figure 4.13: a) *Ab initio* potential for HOON torsional motion calculated at the CCSD(T)/cc-pVTZ level of theory. We consider torsional angles between $\tau = \pm 180^{o}$ in steps of 10 degrees and for each fixed value of the torsional angle, we optimize all the other coordinates. b) One-dimensional slices of the potential along the OH stretching coordinate for various fixed values of HOON torsion angle τ. c) Variation in OH stretching frequency (ω_e) and anharmonicity ($\omega_e\chi_e$) with torsion angle. Their values at $\tau = 0^{o}$ are respectively ω_e=3493 cm^{-1} and $\omega_e\chi_e$=94 cm^{-1}. [File: F4.13_torsion]

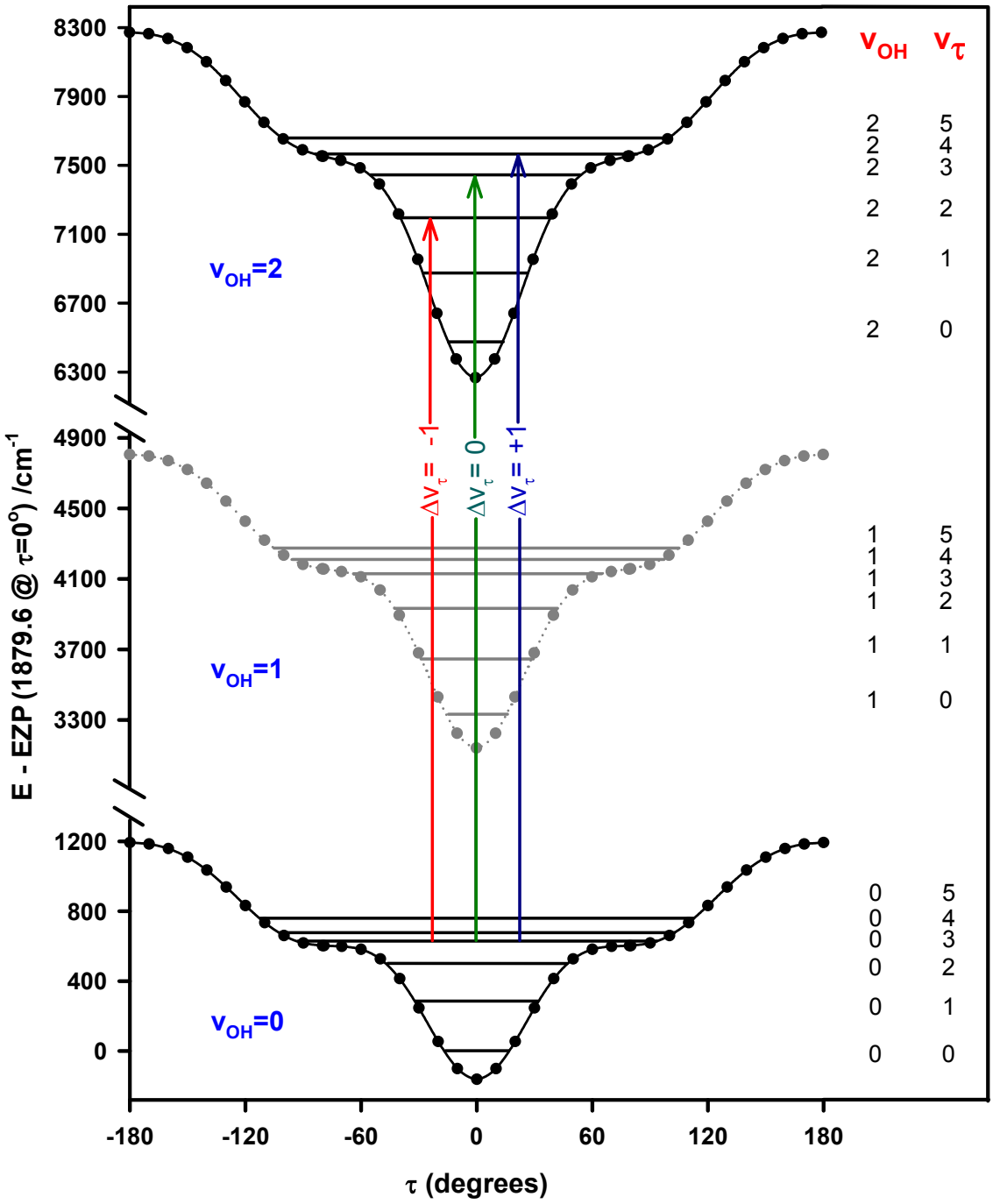

Figure 4.14: Adiabatic torsional potentials for the first few OH stretching states. The zero-point energy (~1880 cm^{-1}) has been subtracted out in the vertical energy scale. The OH stretching states are labeled by the quantum number V_{OH} while their corresponding torsional states are labeled by the quantum number V_τ. For the $2\nu_{OH}$ spectrum we consider transitions from initial states (V''_{OH}=0, V''_τ) to the final states (V'_{OH}=0, V'_τ) corresponding to $\Delta V_{OH} = 2$ and $\Delta V_\tau = 0, \pm1, \pm2$. The vertical lines in the figure indicate some of these vibrational transitions. [File: F4.14_adiabatic_transitions]

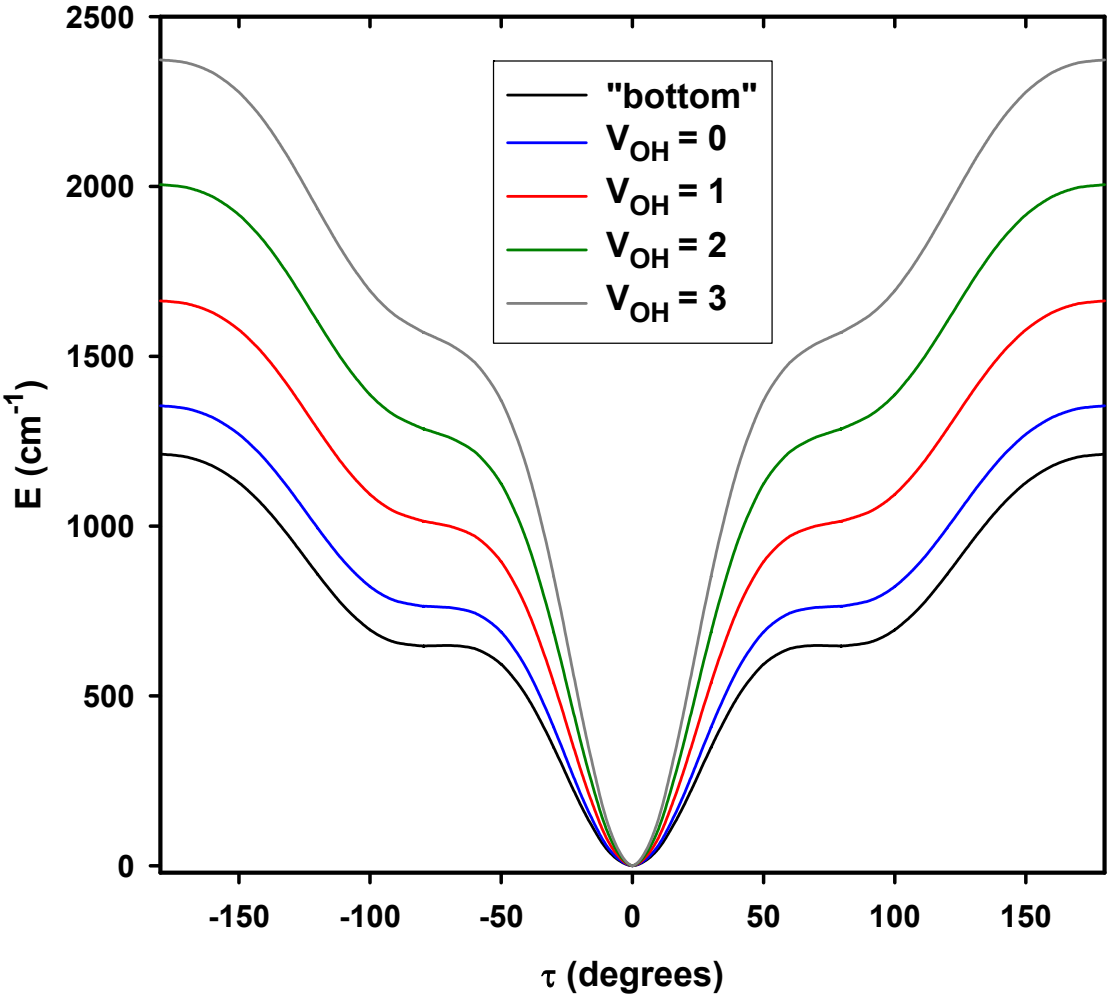

Figure 4.15: Adiabatic torsional potentials for the V_{OH} = 0, 1, 2, 3 and the torsional potential associated with the "bottom" of the stretching well. The figure shows that increasing the excitation in the OH-stretching mode leads to steeper torsion potential reducing the likelihood *cis-perp* is supported. [File: F4.15_adiabatic_curves]

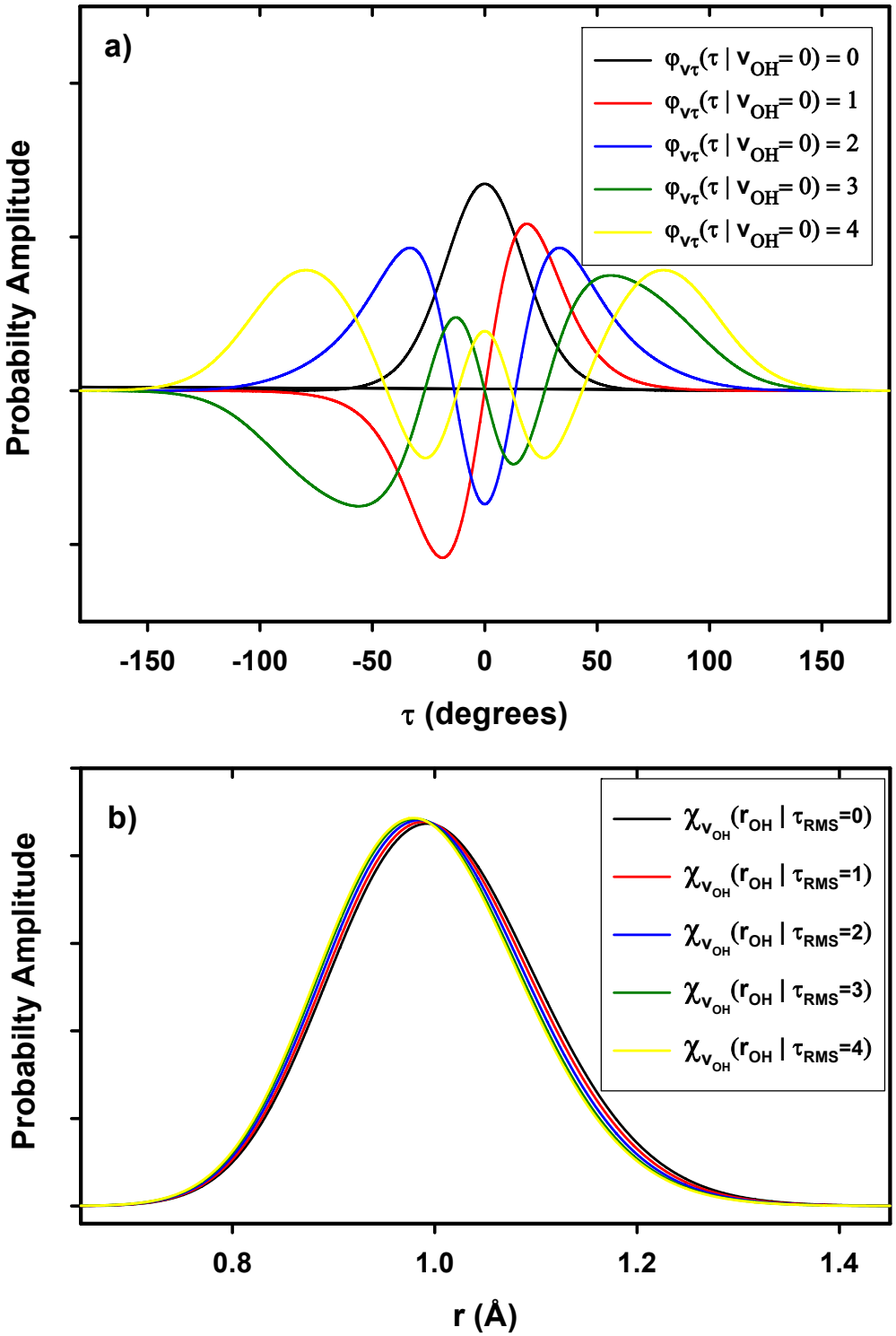

Figure 4.16: The torsional (a) and OH-stretching (b) eigenfunctions associated with the torsional potential at $V_{OH} = 0$. χ_{VOH} only change slightly with $\varphi_{V\tau}$.
[File: F4.16_eigenfunctions]

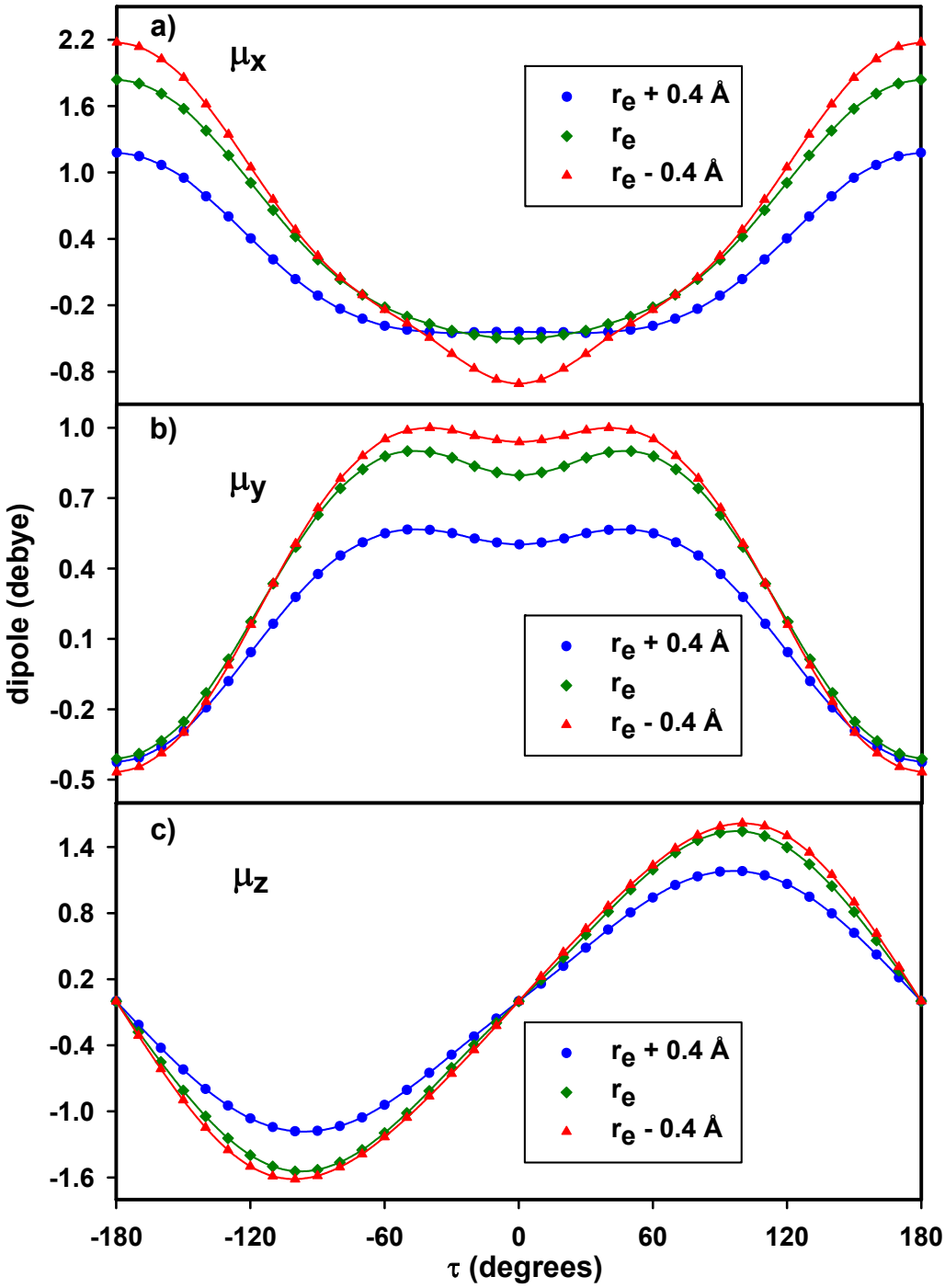

Figure 4.17: Variation in the X, Y, and Z components of the *cis-cis* HOONO dipole moment with HOON torsional angle for various values of r_{OH}. The dipole moment is computed at the CCSD(T)/cc-pVTZ level. a) variation in μ_X for r_{OHc}= re + 0.4Å, r_{OH} = re, and r_{OH} = re - 0.4 Å. b) Same as (a) but for μ_Y. c) variation in μ_Z.
[File: F4.17_dipole_surface]

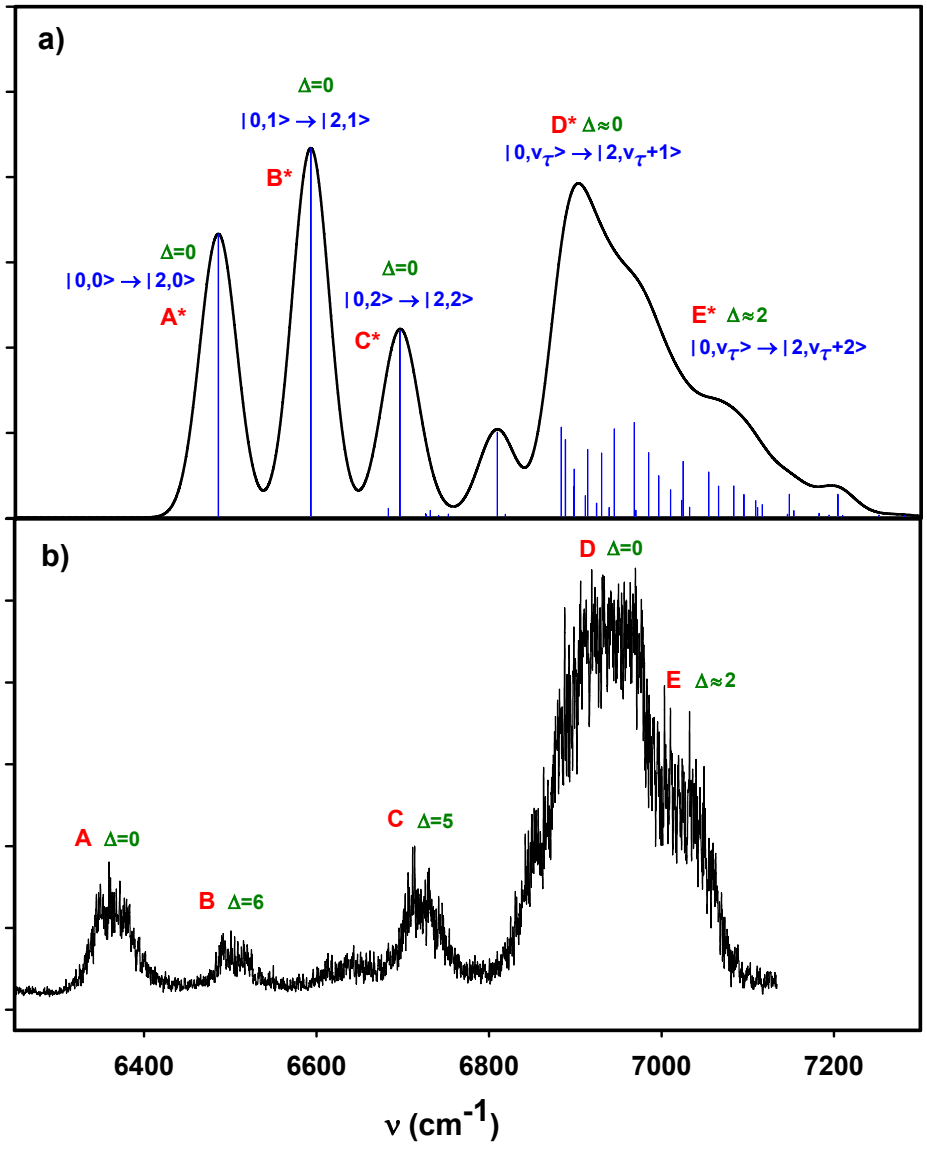

Figure 4.18: a) Simulated $2\nu_{OH}$ action spectrum resulting from the two-dimensional intensity calculation using a dipole surface computed at the CCSD(T)/cc-pVTZ level of theory and the adiabatic torsional potential. The vertical lines in the stick spectrum are the effective strengths of the vibrational transitions weighted by their respective oscillator strength, Boltzmann factor and estimated quantum yield. The influence of rotational structure associated with each vibrational transition is approximately taken into account by broadening each vertical line in the stick transition using a 50 cm^{-1} wide Gaussian envelope. The peaks are labeled *A** – *E**. The predicted assignment associated with each peak is indicated above the peak along with the corresponding ^{15}N isotope shifts, Δ, in cm^{-1}. b) Experimental action spectrum of the $2\nu_{OH}$ region taken under "high" pressure conditions monitoring the OH (N=2) rotational state. [File: F4.18_simulation]

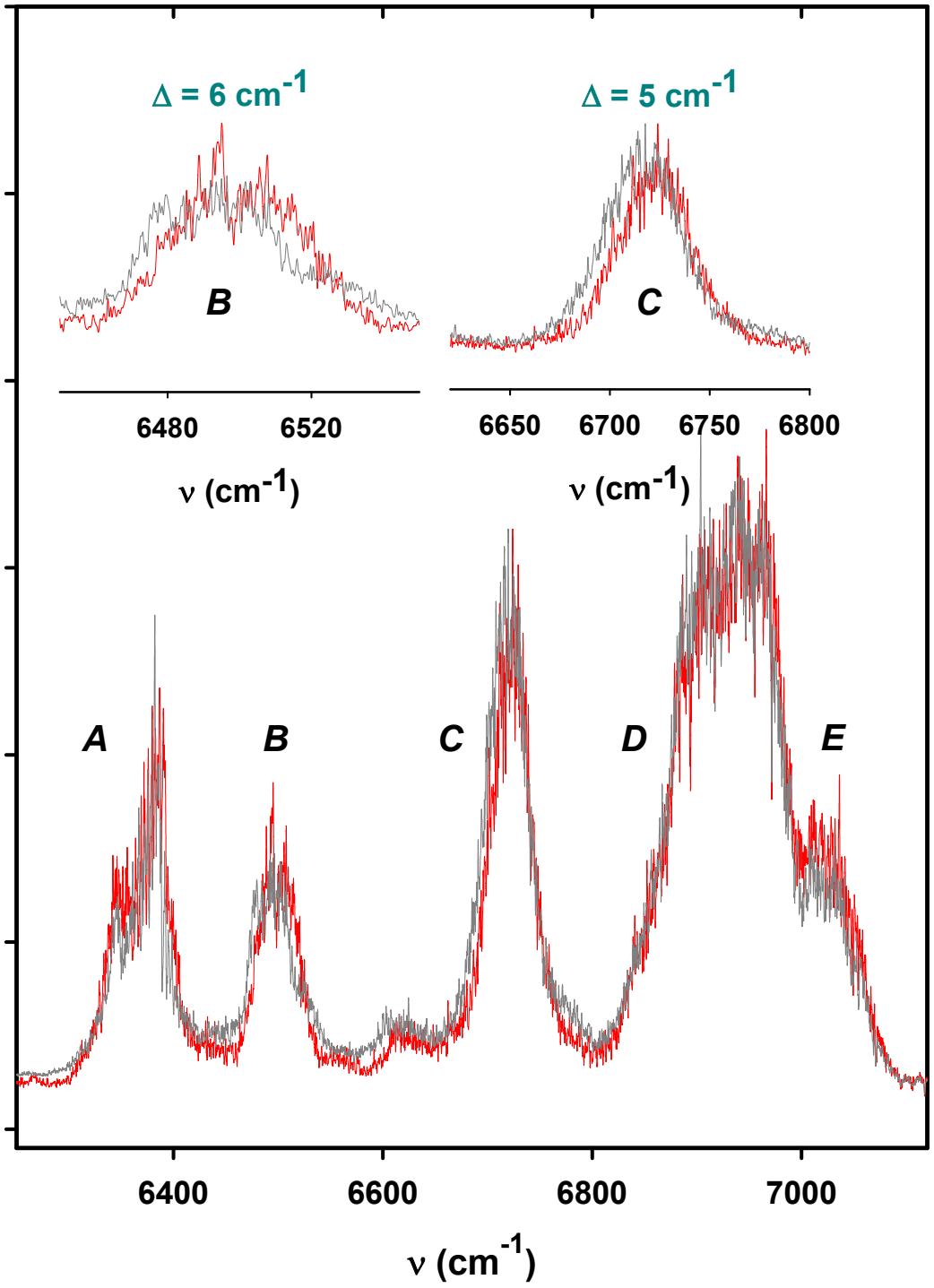

Figure 4.19: Back to back measurements of the HOONO($2\nu_{OH}$) obtained with $HOO^{15}NO$ and $HOO^{14}NO$. The measurement show that while peaks *A* and *D* do not exhibit notable shifts upon ^{15}N substitution, peaks B and C show 5 – 6 cm^{-1} shifts suggesting these modes are mixed and do not correspond to "pure" OH-stretch / HOON- torsion.
[File: F4.19_isoshift]

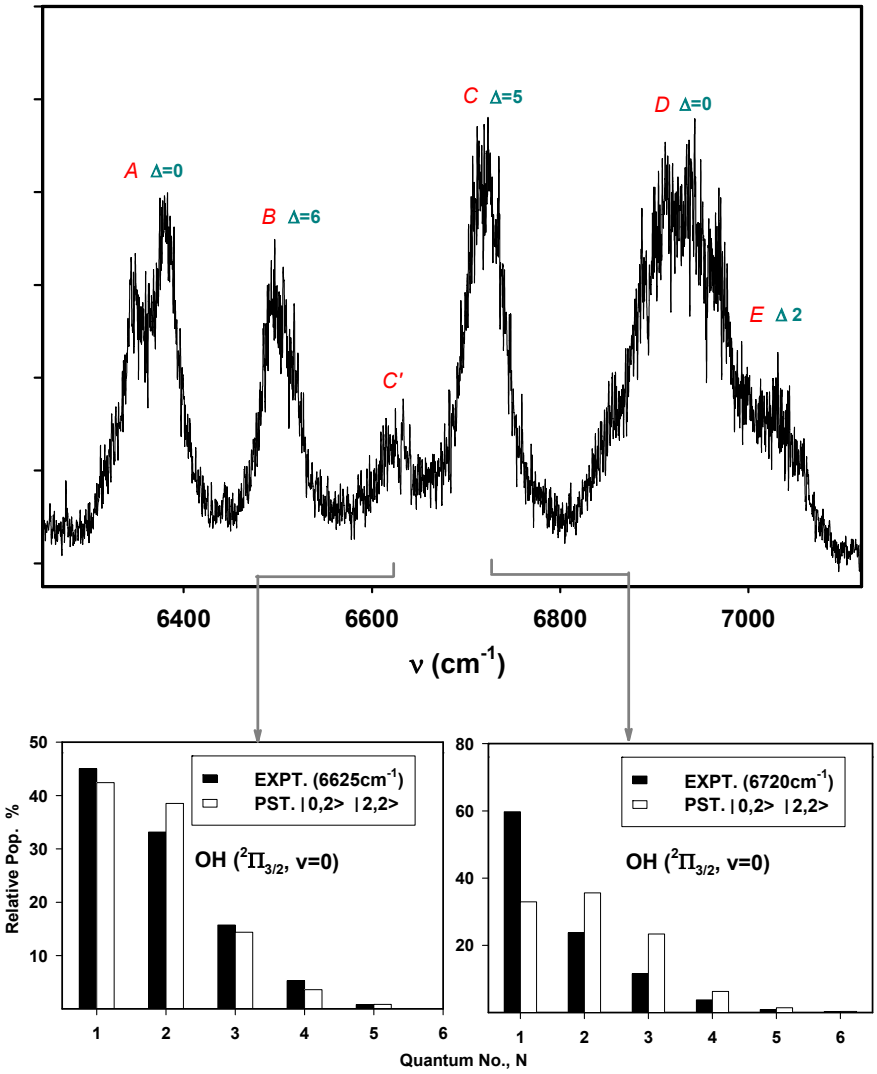

Figure 4.20: Comparison of experimentally measured product state distribution resulting from excitation within peak *C* at 6720 cm^{-1} and to the left of this peak at 6625 cm^{-1} (*C'*) with phase space simulation using states assigned to these peaks by the two-dimensional model. The PST calculations use D_0 = 19.9 kcal/mol, $C_6 = 2.0 \times 10^{-58}$ erg/cm^6 and *cis-cis* spectroscopic parameters. The two-dimensional model assigns one of these peaks to *C**, which is a state with two quanta of initial HOON torsion excitation. [File: F4.20_psd_c]

4.7 References

1. D. M. Golden, J. R. Barker, and L. L. Lohr, J. Phys. Chem. A **107**, 11057 (2003).

2. M. P. McGrath, F. S. Rowland, J. Phys. Chem. **98**, 1061 (1994).

3. Y. Zhao, K. N. Houk, and L. P. Olson, J. Phys. Chem. A **108**, 5864 (2004).

4. Y. Li, J. S. Francisco, J. Chem. Phys. **113**, 7976 (2000).

5. D. A. Dixon, D. Feller, C. G. Zhan, J. S. Francisco, J. Phys. Chem. A **106**, 3191 (2002).

6. H. W. Jin, Z.Z. Wang, Q.S. Li, and X. R. Huang, Theo.Chem. **624**, 115 (2003).

7. R. Sumathi, S. D. Peyerihoff, J. Chem. Phys. **107**, 1872 (1997).

8. D. Chakraborty, J. Park, M. C. Lin, Chem. Phys. **231**, 39 (1998).

9. G. Brasseur, J. J. Orlando, G. S. Tyndall, *Atmospheric Chemistry and Global Change* (Oxford University Press 1999); B. J. Finlayson-Pitts and J. N. Pitts, *Chemistry of the Upper and Lower Atmosphere: Theory, Experiments, and Applications*.(Academic Press, San Diego, 1999).

10. S. A. Nizkorodov, P. O. Wennberg, J. Phys. Chem. A **106**, 855 (2002).

11. J. L. Fry, S. A. Nizkorodov, M. Okumura, C. M. Roehl, J. S. Francisco, and P. O. Wennberg, J. Chem. Phys. **121**, 1432 (2004).

12. I. B. Pollack, I. M. Konen, E. X. Li, and M. I. Lester, J. Chem. Phys. **119**, 9981 (2003).

13. I. M. Konen, I. B. Pollack, E. X. J. Li, and M. I. Lester, J. Chem. Phys. **122**, 094320 (2005).

14. I. M. Konen, E. X. J. Li, T. A. Stephenson, M. I. Lester, J. Chem. Phys. **123**, 204318 (2005).

15. B. J. Drouin, J. L. Fry, and C. E. Miller, J. Chem. Phys. **120**, 5505 (2004).

16. J. Matthews, A. Sinha, J. Phys Chem. A **108**, 8134 (2004).

17. J. Matthews, A. Sinha, and J. S. Francisco, J. Chem. Phys. **120**, 10543 (2004).

18. D. J. Nesbitt, R. W. Field, J. Phys. Chem. **100**, 12735 (1996).

19. M. Quack, Annu. Rev. Phys. Chem. **41**, 839 (1990).

20. L. S. Rothman, A. Barbe, D. C. Benner, L. R. Brown, C. Camy-Peyret, M. R. Carleer, K. Chance, C. Clerbaux, V. Dana, V. M. Devi, A. Fayt, J. Fischer, J. M. Flaud, R. R. Gamache, A. Goldman, D. Jacquemart, K. W. Jucks, W. J. LaFerty, J. Y. Mandin, S. T. Massie, V. Nemtchinov, D. A. Newnham, A. Perrin, C. P. Rinsland, J. Schroeder, K. M. Smith, M. A. H. Smith, K. Tang, R. A. Toth, J. Vander Auwera, P. Varanasi, K. Yoshino, The HITRAN Molecular Spectroscopic Database: Edition of 2003, J. Quant. Spectrosc. Radiat. Transfer **82,** 5 (2003).

21. G. H. Dieke and H.M. Crosswhite, J. Quant. Spectrosc. Radiat. Transfer **2**, 97 (1962).

22. C. H. Greene and R. N. Zare, J. Chem. Phys. **78**, 6741 (1983); Annu. Rev. Phys. Chem. **33**, 119 (1982).

23. M.H. Alexander *et al.*, J. Chem. Phys. **89**, 1749 (1988).

24. Gaussian 03, Revision B.04, M. J. Frisch, G. W. Trucks, H. B. Schlegel, G. E. Scuseria, M. A. Robb, J. R. Cheeseman, J. A. Montgomery, Jr., T. Vreven, K. N. Kudin, J. C. Burant, J. M. Millam, S. S. Iyengar, J. Tomasi, V. Barone, B. Mennucci, M. Cossi, G. Scalmani, N. Rega, G. A. Petersson, H. Nakatsuji, M. Hada, M. Ehara, K. Toyota, R. Fukuda, J. Hasegawa, M. Ishida, T. Nakajima, Y. Honda, O. Kitao, H. Nakai, M. Klene, X. Li, J. E. Knox, H. P. Hratchian, J. B. Cross, V. Bakken, C. Adamo, J. Jaramillo, R. Gomperts, R. E. Stratmann, O. Yazyev, A. J. Austin, R. Cammi, C. Pomelli, J. W. Ochterski, P. Y. Ayala, K. Morokuma, G. A. Voth, P. Salvador, J. J. Dannenberg, V. G. Zakrzewski, S. Dapprich, A. D. Daniels, M. C. Strain, O. Farkas, D. K. Malick, A. D. Rabuck, K. Raghavachari, J. B. Foresman, J. V. Ortiz, Q. Cui, A. G. Baboul, S. Clifford, J. Cioslowski, B. B. Stefanov, G. Liu, A. Liashenko, P. Piskorz, I. Komaromi, R. L. Martin, D. J. Fox, T. Keith, M. A. Al-Laham, C. Y. Peng, A. Nanayakkara, M. Challacombe, P. M. W. Gill, B. Johnson, W. Chen, M. W. Wong, C. Gonzalez, and J. A. Pople, Gaussian, Inc., Wallingford CT, 2004.

25. H. Zhang, C. M. Roehl, S. P. Sander, and P. O. Wennberg, J. Geophys. Res. **105**, 14593 (2000).

26. A. Sinha, R. L. Van Der Wal, and F. F. Crim, J. Chem. Phys. **91**, 2929 (1989); **92**, 401 (1989).

27. K. R. Lange, N. P. Weels, K. S. Plegge, and J. A. Phillips, J. Phys. Chem. A. **105**, 3481 (2001).

28. D. Luckhaus, J. Chem. Phys. **118**, 8797 (2003).

29. R. J. Barnes, *The State-Resolved Photochemistry of Small Molecules on Their Ground and Electronic Excited States* (University of California-San Diego, 1999).

30. R. G. Low, and H. G. Kjaergaard, J. Chem. Phys. **110**, 9104 (1999).

31. P. W. Atkins, *Molecular Quantum Mechanics, 2nd ed*. (Oxford University Press: Oxford, 1983).

32. H. G. Kjaergaard, B. R. Henry, J. Chem. Phys. **96**, 4841 (1992).

33. P. M. Morse, Phys. Rev. **34**, 57 (1929).

34. M. L. Sage, Chem. Phys. **35**, 375 (1978).

35. J. A. C. Gallas, Phys. Rev. A **21**, 1829 (1980); J. A. C. Gallas, J. Chem. Phys. **69**, 612 (1978).

36. P. Pechukas, J. C. Light, and C. Rankin, J. Chem. Phys. **44**, 794 (1966); P. Pechukas and J. C. Light, ibid. **42**, 3281 (1965); J. C. Light, Faraday Discuss. Chem. Soc. **44**, 14 (1967).

37. I. N. Levine, *Physical Chemistry, 4th ed*. (McGraw-Hill, New York, 1995).

38. H. Hippler, S. Nasterlack, F. Striebel, Phys. Chem. Chem. Phys. **4**, 2959 (2002).

39. H. R. Dubal and F. F. Crim, J. Chem. Phys. **83**, 3863 (1985).

40. R. D. Johnson III, FGH1D program version 1.01
http://www.nist.gov/compchem/johnson/fgh/fgh1d.html

41. ACESII is a program product of the Quantum Theory Project, University of Florida. Authors: J. F. Stanton, J. Gauss, J. D. Watts, M. Nooijen, N. Oliphant, S. A. Perera, P. G. Szalay, W. J. Lauderdale, S. A. Kucharski, S. R. Gwaltney, S. Beck, A. Balková D. E. Bernholdt, K. K. Baeck, P. Rozyczko, H. Sekino, C. Hober, and R. J. Bartlett. Integral packages included are VMOL (J. Almlöf and P. R. Taylor); VPROPS (P. Taylor) ABACUS; (T. Helgaker, H. J. Aa. Jensen, P. Jørgensen, J. Olsen, and P. R. Taylor).

42. K. Doclo and U. Rothlisberger, Chem. Phys. Lett. **297**, 205 (1998).

43. B. Ruscic *et al.*, J. Phys. Chem. A **105**, 1 (2001).

44. M. W. Chase, NIST-JANAF Tables 4th ed.; J. Phys. Chem. Ref. Data Mono. **9**, Suppl. 1, (1998).

45. D. P. Schofield and H. G. Kjaergaard, J. Phys. Chem. A **109**, 1810 (2005).

46. A. B. McCoy, J. L. Fry, J. S. Francisco, A. K. Mollner, and M. Okumura, J. Chem. Phys. **122**, 104311 (2005)

47. G. Hertzberg, *Molecular Spectra and Molecular Structure Vol. I.* (Von Nostrand Reinhold Co., New York, 1950).

Chapter 5

State-Resolved Photodissociation Dynamics of *cis-cis* Peroxynitrous Acid in the $3\nu_{OH}$ Region: Action Spectra and Energetics

5.1 Introduction

In the previous dissertation chapter, spectroscopic analysis and dissociation dynamics studies of peroxynitrous acid (HOONO) have focused on the first ($2\nu_{OH}$) OH-stretching overtone region. From these studies, several important properties of HOONO have been extracted and used systematically to explain several unknowns that are associated with this molecule. The first unknown is the bond dissociation energy and the heat of formation of the *cis-cis* conformer. These values are obtained with good confidence level and are consistent with several high level *ab initio* and experimental studies.[1-8] Secondly, from phase-space theory (PST) simulations,[9] we obtain qualitatively that at room temperature, of the two known stable conformers (*cis-cis* and *trans-perp*), the *cis-cis* conformer alone can generate the vibrational signature in the $2\nu_{OH}$ band. Recall that phase-space simulations using *trans-perp* parameters could not account for *any* of the measured product state distributions on the vibrational bands in the spectrum.

In order to label the various states of *cis-cis* HOONO that gives rise to the large number of vibrational states appearing in the action spectrum we have constructed a two-dimension *ab initio* model taking to account the OH-stretching mode and its HOON-torsion. Indeed, the model has confirmed that qualitatively, transitions originating from the HOON-torsional vibrational band give rise to the various transitions appearing in the

action spectrum. Their unusual intensity however is due to the fact the pure OH stretching mode ($2\nu_1$) at 6365 cm^{-1} lies below the dissociation threshold (D_0[*cis-cis*] = 6960 cm^{-1}) and because of its dissociation quantum yield its intensity is more suppressed relative to the torsion bands (see Figs. 4.3 and 4.18).

Thus, the initial conclusion stemming from the torsion potential analysis were that apparently, transitions which originate from the *cis-cis* HOONO molecule in a *cis-perp* configuration give reasonable agreement between the simulated and observed room temperature action spectra. However, additional isotope studies of $HOO^{15}NO$ have stirred us away from this conclusions by indicating that other vibrational modes aside from those initially studied are active as well and that there is a need to develop a higher dimension *ab initio* model to account for all the interactions between these vibrational modes.

In this Chapter, we focus on the vibrational band structure of HOONO in the vicinity of the stretch-bend overtones ($2\nu_1 + \nu_3$) as well as in the vicinity of the second OH stretching overtones ($3\nu_{OH}$) regions. We take similar approach as before. We initially record their spectra and subsequently analyze them using the 2-D model developed in the previous chapter to obtain vibrational assignment of the bands appearing in the action spectra. We then examine the vibrational bands appearing in the spectrum using $HOO^{14}NO$ and $HOO^{15}NO$ isotopic study in order to confirm that our bands assignment is consistent with isotope data. In order to further gain insight, we analyze the resulting ro-vibrational and translational energy release of the OH fragment associated with these vibrational bands. The underlying idea behind this approach is that by examining the energtics of each band, it should be possible to put constraints on the total energy a particular HOONO vibrational band carries. We find that unlike the bands in the $2\nu_{OH}$

region, product state distribution and translational energy release associated with the $3\nu_{OH}$ bands carry more internal and translational energy. Lastly, the OH product state distributions are then fitted using phase-space theory.[9] In essence, these studies provide additional information which adds additional constrains on the makeup of these bands.

5.2 Experiment

The apparatus used to in these experiments is the same used in the previous dissertation chapter (see Fig. 4.2). HOONO is generated in a side reactor by discharging hydrogen gas (5 – 7 mTorr) diluted in 50 – 70 mTorr of helium in an Evenson cavity microwave operating at 2450 MHz with 30 W of power. NO_2 (~40 mTorr) is introduced down stream the reactor and allowed to react with H-atoms to generate OH radicals and subsequently $HONO_2$ and HOONO. Typical "low" pressure measurements are taken under 90 – 120mTorr of sample and for the "high" pressure measurements, the sample is diluted with ~1500 mTorr of helium buffer gas and the pump-probe delay is increased to 500 ns to ensure rotational relaxation of the OH fragment.

Tunable infrared radiation (λ_1) for the overtone initiated photolysis in the vicinity of the stretch-bend through the second OH-stretching overtone is generated by the MOPO system with typical idler pulse energies ranging between 9 to 12 mJ. The beam is focused with a 400 mm lens in the chamber's center of interaction. For measurements involving OH product state distributions and translational energy release from the weak *cis*-*cis* HOONO($3\nu_1$), the fundamental of the NY82-20 laser with linewidth of ~1.3 cm^{-1} (FWHM) is used instead. The YAG laser has pulse energies ranging from 22 to 25 mJ which are needed in order to collect reliable data with adequate signal-to-noise slightly to the red of the band center. The nascent OH product is probed (λ_2) either via the *A*-*X* (1,0)

or the *A*-*X* (0,0) transitions using the doubled output of the NY81-20 dye laser system operating with R590 or DCM respectively. The UV output with ~0.13 cm^{-1} bandwidth (FWHM) is greatly attenuated to prevent saturation of the OH lines and direct photolysis of HOONO and NO_2.

The OH fluorescence is collected using f/1 lens system and imaged onto an end-on photomultiplier tube (PMT) operating around ~2.35 kV. A Schott UG-11 glass filter and a set of 266nm diachroics provide an excellent rejection of the 282 nm (λ_2) light while enabling fluorescence collection via the *A*-*X*(1,1) transition. The set of diachoric mirrors are removed from the PMT viewing region when we photoexcite the OH fragment via the *A*-*X*(0,0) transition.

5.3 Result

5.3.1 The Second ($3\nu_{OH}$) Overtone Vibrational Action Spectra

The analysis preformed in this chapter is influenced by the action spectrum of HOONO shown in Fig. 5.1(a). The spectrum is generated by tuning the IR-pump laser over the region shown at 0.020 nm/sec averaging 30 shots/bin while monitoring the OH($^2\Pi_{3/2}$, v=0) photoproduct in its *N*=2 rotational state. The spectrum is taken under "high" pressure conditions and is normalized to laser powers over the scan region. The prominent feature at ~7680 cm^{-1} labeled as peak *A* is assigned to the stretch-bend combination mode ($2\nu_1 + \nu_3$). This assignment is based on an anharmonic frequency calculation preformed with GAUSSIAN03 at the MP2/aug-cc-pVTZ level of theory and is given in Table 5.1.[10] For information on running GAUSSIAN03 on our workstations see Appendix *B*. This vibrational band assignment is also consistent with a 3-D model of Schofield *et al*.[11,12] In the vicinity of peak *A* there are several overlapping peaks. These

bands will be discussed at a later time. The broad (~170 cm^{-1} FWHM) peak labeled as peak *C* in the action spectrum at 9450 cm^{-1} is assigned to the *cis-cis* $3\nu_1$ band. This state assignment is based on spectral simulation using an *ab initio* one-dimensional potential and dipole moment function (DMF) obtained from QCISD/cc-pVTZ level of theory discussed in Chapter 4. The band with similar intensity to the red of the $3\nu_1$ band at 9047 cm^{-1}, labeled as peak *B*, is unassigned.

More intriguingly than the assignment of peaks *A* – *C* however, just as in the first ($2\nu_{OH}$) OH-stretching overtone region, the second ($3\nu_{OH}$) OH-stretching overtone region is also dominated by a bright feature further to the blue of the $3\nu_1$ around 10 160 cm^{-1} (peak *D* in Fig. 5.1). This is surprising since in action spectroscopy one expects the bright state which is typically considered the OH-stretching overtone to carry more intensity than combination bands; especially in cases where the peaks lie above the bond dissociation limit. Recall, a similar situation was also noted in the $2\nu_{OH}$ region with the peak around 6935 cm^{-1} shown in the overview action spectrum of Fig. 5.2. The figure indeed shows that the band around 6935 cm^{-1} carries more intensity than the $2\nu_1$ band at 6365 cm^{-1}. Based on the 2-D *ab initio* simulations of the first ($2\nu_{OH}$) OH-stretching region (see Chapter 4), one expects that the intensity associated with the band at 10 160 cm^{-1} to also be due to torsionally excited *cis-cis* HOONO states.

Also shown in Fig. 5.1(b) the action spectrum of HOONO taken under similar conditions as in Fig. 5.1(a) while monitoring the OH fragment in its v=1, *N*=2 ro-vibrational state. This spectrum underlines that energetically there is a significant difference between peaks *A* – *C* and peak *D*. The vertical dashed line going trough the

spectra indicates the threshold for opening the OH(v=1) + NO_2 channel which is D_0 = 30.1 kcal/mol (10 530 cm^{-1}). Despite the fact that all the bands appearing in the action spectra including peak *D* lie below the channel threshold, it appears that peak *D* carries sufficient energy to overcome the OH(v=1) channel threshold. If one assumes that this band originates from the ground state of *cis-cis* HOONO, then energetically speaking, it is ~370 cm^{-1} deficient with respect to the OH(v=1) + NO_2 channel. Conversely, if this band were to originate from the *trans-perp* HOONO conformer which has a lower bond dissociation energy (D_0 = 16.2 kcal/mol),[13-15] then peak *D* should carry an excess of ~926 cm^{-1} over the threshold limit.

Spectroscopic measurements by Konen *et al.* of jet cooled *trans-perp* HOONO have indicated that peak *D* is inconsistent with *trans-perp* HOONO.[15] For example, they find that the trans-perp conformers has a band origin around 10 195.3 cm^{-1} where peak *D* band's origin is around 10 160 cm^{-1}. We also find differences in rotational band shape. The rotational band contour simulation of *trans-perp* HOONO $3\nu_1$ band at room temperature using spectroscopic parameters given in the paper by Konen *et al.* is shown in Fig. 5.3.[15] From the figure we find that at room temperature, the second ($3\nu_1$) OH-stretching overtone rotational band simulation of *trans-perp* HOONO does not agree with the experimental band shape. Also, recall that results by Fry *et al.* suggest that at room temperature, the isomerization rate of *trans-perp* to *cis-cis* is rapid therefore the *trans-perp* is more than likely undetected under our experimental conditions.[16] In essence, by eliminating the possibility that this state originates from the *trans-perp* conformer based on band origin and rotational band analysis as well as transitions from the ground state of *cis-cis* leaves but few choices for this band assignment. And, as before, it is likely that

this state results from hot-bands activities of *cis-cis* HOONO. Since the *cis-perp* configuration which corresponds to hot-bands of *cis-cis* plays a significant role in the first ($2\nu_{OH}$) OH-stretching overtone region, it is important to also quantify its role in the second ($3\nu_{OH}$) OH-stretching overtone region.

Several compelling reasons can be provided to this tentative assignment. In the first place, the the *cis-perp* conformer, as with the *trans-perp* conformer, has a lower D_0 (~18.3) than the more stable planner *cis-cis* conformer. This means that at photon energy corresponding to 10 160 cm^{-1}, the *cis-perp* conformer could carry sufficient energy to overcome the dissociation threshold which produces vibrationally excited OH. In addition, based on an *ab initio* one-dimensional potential and spectral simulation using dipole surface discussed in Chapter 4, at QCISD/cc-pVTZ, the *cis-perp* configuration of HOONO carries ~5 times the oscillator strength compared with that of the *cis-cis* conformer due to the out of the OON plane motion of the light H-atom. This, in turns, gives rise to a c-component transition dipole moment and enhanced transitions strength. Thirdly, recent analysis of the $2\nu_{OH}$ region of HOONO by the Li *et al*. provides initial spectroscopic evidence of *cis-perp* conformer in their jet-cooled spectrum.[17]

5.3.2 *Ab Initio* Study of *cis-perp* HOONO and Second Overtone Intensity

In order to test whether the *cis-perp* configuration is a viable option at room temperature, we use a two-dimensional *ab initio* model which takes into account the influence of the HOON-torsion on the OH-stretching mode. The 2-D model used in the simulation of the $3\nu_{OH}$ region is identical to the $2\nu_{OH}$ region discussed in the previous chapter. In our two-dimension model, $\boldsymbol{\mu}_{i\rightarrow f} = \langle\psi_i|\boldsymbol{\mu}(r_{OH},\tau)|\psi_f\rangle$ is the transition dipole

moment matrix element between the initial and final vibrational level which is used to evaluate the oscillator strength, *f*, according to: [18,19]

$$f = 4.702 \times 10^{-7}\ [\text{cm D}^{-2}]\ \nu_{0\rightarrow v}\ |\boldsymbol{\mu}_{0\rightarrow v}|^2 \qquad (5.1)$$

As before, we approximate the wavefunctions for the initial and final states as product functions involving the HOON torsional and O-H stretching coordinates. Thus, a state in our two-degree of freedom model is represented by $|\psi> \approx \varphi_{V\tau}(\tau|V_{OH})\chi_{VOH}(r_{OH},\tau)$. In this equation $\varphi_{V\tau}(\tau|V_{OH})$ is the adiabatic torsional wavefunctions which was obtain as outlined in Chapter 4 and $\chi_{VOH}(r_{OH},\tau)$ is the corresponding O-H stretch wavefunction.

The adiabatic torsional potential associated with the $V_{OH} = 0$ and $V_{OH} = 3$ are shown in Fig. 5.4. Unlike the situation in the $V_{OH} = 2$ (see Fig. 4.14) the $V_{OH} = 3$ torsion potential is more deep. Hence, not only the $V_{OH} = 3$ potential supports more torsion vibrational levels, but also, it is more steep in the region where the *cis-perp* configuration is assumed to originate from. The deep potential well can however explain why in the $2\nu_{OH}$ region the torsionally excited band at 6935 cm^{-1} is ~530 cm^{-1} to the blue of the $2\nu_1$ state and in the $3\nu_{OH}$ region the state at 10 160 cm^{-1} is 720 cm^{-1} to the blue of the $3\nu_1$ band.

The *ab initio* spectral simulation in the $3\nu_{OH}$ region is shown in Fig. 5.5. As with the two-dimensional simulations in the $2\nu_{OH}$ region (see Fig. 4.18), it predicts vibrational progressions involving $|0\ 0> \rightarrow |3\ 0>$, $|0\ 1> \rightarrow |3\ 1>$, $|0\ 2> \rightarrow |3\ 2>$, …, where $\Delta V_\tau = 0$ transitions carry substantial intensity. In addition, around peak *D* at 10 160 cm^{-1}, the simulation shows that there is additional intensity distribution due to transitions involving $\Delta V_\tau = +1$, and +2. Most of the intensity however, is attributed by the 2-D model to the

cis-cis $3\nu_1$ band. This is very similar to the situation in the $2\nu_{OH}$ region except that in the low frequency region, dissociation quantum yield associated with the $2\nu_1$ state ($|0\ 0\rangle \rightarrow |2\ 0\rangle$) has suppressed 90 % of the intensity arising from this state. The fact that dissociation quantum yield plays no role in the $3\nu_{OH}$ region, has resulted in the simulated intensity distribution which is consistent with what one may expect; the $3\nu_1$ bright state (peak *C*) has significantly more oscillator strength than combination bands and hot bands. It is also interesting to note that both peak *A* and peak *B* also remain unassigned in our simulation.

Previous three-dimensional *ab initio* studies have also failed to predict and provide explanations for this unusual band position and its intensity.[11,12] In these studies additional vibrational band was added to the interactions between the HOON-torsion mode and the OH-stretching mode. The inclusion of the HOO-bending mode (ν_3) in the *ab initio* models by Schofield *et al*.,[11,12] have improved the overall fitment of the spectra mainly in the stretch-bend region ($2\nu_1 + \nu_3$) and resulted in reduction of the relative intensity of the simulated $3\nu_1$ band but provided no additional insight to what process or which vibrational mode(s) giving rise to the bright feature at 10 160 cm^{-1}.

5.3.3 $HOO^{14}NO$ and $HOO^{15}NO$ Isotope Study

Since the 2-D and the 3-D *ab initio* simulations have failed to account for the intensity distribution of the $3\nu_{OH}$ region, we continue to probe experimentally the vibrational states in hope to obtain key measurements that could provide answers to the $3\nu_{OH}$ spectral signature. To continue with the experiments, we regenerate the action spectrum in the $3\nu_{OH}$ regions using the isotopically labeled $HOO^{15}NO$. Previously,

measuring the relative isotopic shifts between $HOO^{15}NO$ and $HOO^{14}NO$ samples, have assisted with the vibrational assignment in the $2\nu_{OH}$ region. Currently, for the $3\nu_{OH}$ spectral region, we focus mainly on peaks *A*, *B* and *D* because peak *C* is significantly broader (200 cm^{-1} FWHM) and detecting small shifts within a broad feature is difficult.

Figure 5.6 show the measured shifts associated with peaks *A*, *B* and *D*. Unlike in the $2\nu_{OH}$ region where we typically find relative shifts on the order of 5 or 6 cm^{-1}, in this region we find bands that are red-shifted by up to 50 cm^{-1}. For example, the peak labeled as A_1 in Fig. 5.6 is the $2\nu_1 + \nu_3$ and it has shifted by 5 cm^{-1} in the $HOO^{15}NO$ sample. This shift is consistent the MP2/aug-cc-pVTZ frequencies calculation in Table 5.1. In addition, mixed with this band, we find other states that do shift significantly. For example, we measure shifts associated with peaks A_3 and A_4 that are on the order of 26 and 48 cm^{-1} respectively. Looking at Table 5.1, we see that only the ^{15}N-O stretching modes can result in such large band shifts with small quanta change. Therefore, we conclude that mixing between the $2\nu_1 + \nu_3$ and the ν_2 states is likely the reason for the observed shifts. We also observe a small shift (~7 cm^{-1}) associated with peak *B*. More importantly, in peak *D*, we find no isotopic shifts ($\Delta < 2$ cm^{-1}). Looking in Table 5.1, we find that small isotopic shifts are typically consistent with transitions which involve ν_1, ν_7 and ν_9. Alternatively however, any hot-band transitions involving initial and final states that are the same, e.g. $\Delta V\tau = 0$, will also result in zero shift.

5.3.4 OH Fragment Internal and Translational Energy Release

An additional probe of the vibrational bands is their energetics. We probe the resulting OH fragment ro-vib product state distribution and translational energy release

arising from excitation of the HOONO $3\nu_{OH}$ bands. These OH fragment product state distributions have been used successfully over the $2\nu_{OH}$ region where in conjunction with implementation of statistical theory have provided compelling evidence of hot-bands activity.

In order to quantify the energy partitioning in the OH fragment resulting from excitation of the various bands we park our excitation laser (λ_1) in the vicinity of peaks *A*, *C*, and *D* (see Fig. 5.1(a)) corresponding to excitation of ~7657 cm^{-1}, ~9397 cm^{-1} and 10 160 cm^{-1} respectively and map out their resulting ro-vib OH fragment product state distributions and translational energy release. The OH rotational lines are identified based on the assignment of Dickie and Crosswhite.[20] We scan over the OH rotational lines under identical conditions using the BURST mode at 5 μsteps using 30 shots/bin and convert their relative integrated signals using the appropriate Einstein's B-coefficients,[21] and Franck-Condon,[20] factors described in Appendix *C*. The resulting normalized OH product states distributions for peaks *A* and *C* are shown in Figs. 5.7(a) and 5.7(b) respectively. The two OH rotational product state distributions associated excitation of the stretch-bend combination mode (Fig. 5.7(a)) show similar trends where the rotation population peaks at *N*=2 or *N*=3 and then monotonically decreasing to *N*=8 and *N*=7 for the two spin-orbit states ($OH(^2\Pi_{3/2})$ and $OH(^2\Pi_{1/2})$). The average rotational energy arising from excitation of this vibrational band is 247 cm^{-1}. Interestingly, in Chapter 4 of the dissertation, in the first OH-stretching overtone of *cis-cis* HOONO we find that the internal energy associated with the torsionally excited band at 7027 cm^{-1} labeled as the $|0\ v_\tau\rangle \rightarrow |2\ v_\tau +2\rangle$ transition (peak *E*) in Fig. 5.2 is $\langle E_{rot}\rangle = 265\ cm^{-1}$. The fact that this

band lies at a lower frequency but results in OH fragment which carries more rotational energy compared with the stretch-bend mode ($2\nu_1 + \nu_3$) is consistent with the fact that this band has more internal energy (~720 cm^{-1}) as it involves transitions between $|0\ v_\tau>$ and $|2\ v_\tau+2>$. This is indirectly indicates that peak *A* ($2\nu_1 + \nu_3$ state) likely originating from the ground state.

Similarly, the OH fragment product state distribution arising from excitation of the $3\nu_1$ band (peak *C*) is shown in Fig. 5.7(b). The OH($^2\Pi_{3/2}$, v=0) product has a maxima at *N*=3 and it has a long distribution of rotational states with a distribution tail down to *N*=12. The OH($^2\Pi_{1/2}$, v=0) peaks at *N*=4 and monotonically decreasing to *N*=11. The average OH rotational energy associated with this band is found to be 470 cm^{-1} which is almost two-fold increase compared with the excitation of $2\nu_1 + \nu_3$ combination mode.

Figures 5.8(a) and 5.8(b) show the nascent OH product state distributions associated with excitation of peak *D* at 10 160 cm^{-1}. As expected from looking at the OH(v=1) spectrum in Fig. 5.1(b), the product state distribution associated with this band is hotter. It peaks at *N*=4 and slowly decreasing to *N*=14 for the OH($^2\Pi_{3/2}$, v=0) state and for the OH($^2\Pi_{1/2}$, v=0), the distribution peaks at *N*=5 and decreasing to the *N*=13 rotational state. We also map out the OH(v=1) nascent product state distribution. For the two spin-orbit states, the distribution peaks at *N*=2 and monotonically decays to *N*=5 or 6 (see Fig. 5.8(b)). The calculated average ro-vib energy associated with excitation in the vicinity of peak *D* is almost a factor of two greater ($<E_{ro\text{-}vib}>$ = 897 cm^{-1}) than the OH fragment internal energy resulting from excitation in the *cis-cis* ($3\nu_1$) band. Interestingly, we note that the $2\nu_1 + \nu_3$ band (peak *A*) and the $3\nu_1$ band (peak *C*) are separated by ~1740

cm^{-1} and that the frequency separation has resulted in peak *C* having about a factor of two more OH internal energy than peak *A*. For peak *D* which is separated from the $3\nu_1$ band (peak *C*) by only 760 cm^{-1} however, we find additional two-fold increase in OH internal energy. More specifically, dissociation of peak *D* leads to population of two additional rotational state in the OH($^2\Pi_{3/2}$, v=0) fragment relative to peak *C*. These two rotational states account for about additional 1000 cm^{-1} in rotational energy. Furthermore, as seen in Fig. 5.1(b), the resulting OH fragment is formed vibrationally excited (v=1). Vibrational branching ratio of the population of v=0 and v=1 suggest that ~6% of the OH product is formed in its v=1 state. Similar results have been reported by Lester and coworkers for the *trans-perp* HOONO($3\nu_1$).[15] However, as mentioned above, differences in the band origin and rotational band simulations exclude the *trans-perp* conformer from our analysis.

The last observed rotational state associated with the OH($^2\Pi_{3/2}$ v=1) manifold is *N*=6, where the fragment contains internal energy of ~4310 cm^{-1}. Comparing this value with the ~2850 cm^{-1} of maximum internal energy associated with the *cis-cis* $3\nu_1$ band, we propose that peak *D* contains addition internal energy which is suggestive of hot-band contribution from *cis-cis* HOONO.

We also investigate the resulting translational energy of the OH + NO_2 channel by looking at the OH fragment linewidths which contain information on the Doppler line-broadening. We scan over the OH rotational using the BURST mode at 3 μsteps and 30 shots/bin and convert their convoluted Doppler profile into translational energy (see Appendix *C*). The total translational energy releases for several measure OH rotational

states and the average ro-vib energies for peaks *A*, *C*, and *D* are summarized in Table 5.2. Looking at the table, we find that the translational energy increases with increasing excitation energy going from peak *A* to *C* to *D* and in general, decreases as a function of an increasing rotational energy. For example, the total resulting translational energy from peak *D* associated with OH(v=0, N=2) is 3951 cm^{-1}. As we probe higher *N*- levels, we find that the translational energy is decreasing slowly. For the OH(v=1, *N*=1) ro-vibrational state we find that the translational energy in the OH and the NO_2 is under ~600 cm^{-1}.

5.3.5 Phase-Space Theory and OH Fragment Product State Simulations

In order to obtain additional estimates of the energy associated with the vibrational bands, we use phase-space theory to also examine the internal ro-vib energy of the OH fragment. In the previous dissertation chapter, we utilized phase-space theory (PST) to pin the bond dissociation energy of *cis-cis* HOONO using product state distributions from the $2\nu_{OH}$ region. Presently, we use phase-space theory to test how well the simulations can asses the contribution of hot-bands to the spectra using same parameters we obtained from the $2\nu_{OH}$ simulations.

Phase-space theory utilizes the assumption that near-threshold dissociation takes place when the internuclear bond distance between the OH and the ONO fragments is sufficiently large; this assumption results in a loose transition state where the two fragments can be treated as free rotors in space due to the large separation and the weak interaction forces between the separating fragments.[9] The two constraints invoked in PST are energy and angular momentum conservation. We perform phase-space calculations as described for nitric acid,[22] and HOONO in the previous dissertation chapter. The

vibrational and rotational constants for both the parent and fragment molecules used in the phase-space calculations are listed in Table 4.9. We fix the total attractive interaction parameter C_6 to 2.0 x 10^{-58} erg cm^6, a value which was obtained from the photodissociation of nitric acid,[22] and the dissociation energy D_0 to19.9 kcal/mol as obtained previously (see Chapter 4).

The results of the phase-space calculations are shown in white bars of Figs. 5.9(a) and 5.9(b) for the stretch-bend combination mode (peak *A*) and the second overtone (peak *C*) respectively. The filled bars represent the experimental product state distributions. We find good agreement between the simulation and the product state distributions resulting from excitation of the $2\nu_1 + \nu_3$ mode (peak *A*) in Fig. 5.9(a) for the OH($^2\Pi_{3/2}$) and OH($^2\Pi_{1/2}$) spin-orbit states. This is consistent with the fact that the bending mode is likely originating from the ground state of *cis-cis* HOONO and its appreciable intensity in the action spectrum is due to the resonance coupling of OH-stretch and HOO-bend in peroxides. These interactions have been characterized by the three-dimensional surface and dipole moment function (DMF) of Schofield *et al*.[11,12] The trend predicted by the PST simulation for the combination band is also consistent with the fact that the band lies above the dissociation limit where the OH rotational product state distribution has a maximum at *N*=3.

The fits between measured and simulated product state distribution for the second ($3\nu_1$) OH-stretching overtone are shown in panel 5.9(b). We find a reasonable fit for this band despite the fact that in general, PST is predicting a relatively hotter OH product state distribution than actually measured. This is likely due to the breakdown of the applicability of phase-space theory since the critical configuration no longer corresponds

to a "loose" transition state which is common with above-threshold dissociation processes where vibrationally excited product can form.[23] Nonetheless, the reasonableness of the fit provides some indication that indeed this band is associated with *cis-cis* HOONO. Off course, transitions originating from the *trans-perp* configuration will result in even hotter product state distribution because of its lower binding energy (D_0[*trans-perp*] = 16.2 kcal/mol).[15]

Similarly, Fig. 5.10 shows PST simulations for the product state distributions of the OH(v=0) and OH(v=1) manifolds arising from excitation of the band at 10 160 cm^{-1} (peak *D*). Again, we find that PST predicts a generally warmer products state distributions compared with those obtained experimentally for the OH(v=0) manifolds and a colder distribution for the OH(v=1) manifolds. These results indicate that for non-threshold dissociation processes, PST is not sensitive enough to aid in the determining the origin of these room temperature bands. More on the PST fits will be discussed in the next section.

5.4 Discussion

The action spectrum of HOONO in the $3\nu_{OH}$ region shown in Fig. 5.1 consists of several vibrational states. Based on *ab initio* anharmonic frequency calculation as well as a 3-D simulation which involve investigation of the influence of the HOON-torsion, HOO-bend and OH-stretch on the spectrum,[11,12] we conclude that peak *A* is likely the $2\nu_1 + \nu_3$ band. In addition, isotopic labeling of the nitrogen atom suggests that the stretch-bend combination mode is mixed with other vibrational states such as the N-O stretching mode. For example, looking at Table 5.1, we find that ^{15}NO-stretching (ν_2) is predicted to result in a ~25 cm^{-1} shift. Therefore, it is likely that the band A_3 (see Fig. 5.6) involve

excitation of the $2\nu_1 + \nu_2$ band. Fermi resonance between O-H and N-O stretching modes has also been observed in the $2\nu_{OH}$ region of nitric acid.[24]

Also, from the action spectra in Fig. 5.1 it appears that energy constrains play a role in producing vibrationally excited OH product from excitation of peak *D* but not from peaks *A* – *C*. Taking the bond dissociation energy of *cis*-*cis* HOONO to be D_0 = 6960 cm^{-1} (19.9 kcal/mol), then in order to observe vibrationally excited OH product from the *cis*-*cis* conformer, the OH fragment must carry at least ~3570 cm^{-1} in excess energy. This means that the total of internal energy (E_{int}) of the parent molecule and the photon energy ($h\nu$) have to exceed ~10 530 cm^{-1}. As seen in Fig. 5.1(b), none of the bands that appear in the spectrum lie above this energy level. The stretch-bend combination mode ($2\nu_1 + \nu_3$) at 7680 cm^{-1} lies about ~2850 cm^{-1} below the threshold for opening the OH(v=1) channel and the $3\nu_1$ band at 9450 cm^{-1} is energetically deficient by nearly ~ 1100 cm^{-1}. When including the internal average energy of the parent molecule that is associated with thermal distributions of state at room temperature (E_{therm} ~570 cm^{-1}), we find that *cis*-*cis* $3\nu_1$ band still lies below the OH(v=1) + NO_2 channel threshold limit. Peak *D* however, having photon energy of 10 160 cm^{-1}, and an average internal energy of ~570 cm^{-1}, has sufficient energy to produce OH(v=1) product. In essence, based on energetics, in order of this band to produce vibrationally excited OH product, it must originate from level(s) in *cis*-*cis* HOONO that carrying at least ~370 cm^{-1} in internal energy.

The resulting nascent OH product state distributions of peak *D* put additional constraints on the HOONO molecule's internal energy. Looking at Fig. 5.8(b), the

highest observed rotational state in the OH(v=1) manifold is *N*=6. This rotational level carries 4309 cm^{-1} of ro-vib energy above the zero point energy of the OH molecule. Invoking conservation of energy using:

$$E_{therm}(HOONO) + h\nu - D_0 = E_{int}(OH) + E_{trans}(OH + NO_2) + E_{int}(NO_2) \quad (5.2)$$

If we taking the internal energy of the NO_2 fragment, $E_{int}(NO_2)$, and the total translational energy, $E_{trans}(OH + NO_2)$, associated with the internal energy of the OH fragment to be zero for the OH($^2\Pi_{3/2}$, v=1, N=6) state, the above equation can be rearranged to:

$$E_{therm}(HOONO) \approx E_{int}(OH(v=1, N=6)) + D_0 - h\nu \quad (5.3)$$

For excitation energy hν = 10 160 cm^{-1} associated with peak *D* which originates from the *cis-cis* conformer and having D_0 = 6960 cm^{-1}, we find that these transitions must originate from state(s) which carry up to ~1100 cm^{-1} above the ground state. In other words, for peak *D* showing up in the OH(v=1) action spectra means it must involve transitions originating from ro-vibrational states which carry 370 – 1100 cm^{-1} above the *cis-cis* ground state. Because the ground state of *cis-cis* HOONO has insufficient energy to produce vibrationally excited OH, it is excluded from the range of applicable levels.

It is also important to consider the possibility that peaks *A* – *C* do not appear in the OH(v=1) spectrum (Fig. 5.1(b)) because their excitation may preferentially produce HOO + NO instead. Based on simple bond fission,[25] one finds that about 27.6 kcal/mol (9642.6 cm^{-1}) is needed to open the HOO + NO channel. This means that it takes about 2.5 kcal/mol (~890 cm^{-1}) *less* to open this channel compared to the OH(v=1) + NO_2 channel. Scanning over the same spectral region monitoring NO($^2\Pi_{1/2}$, v=0) in its *N*=4 rotational state has yielded no signal. It is important to note however that there are

complications in detecting NO from the overtone initiated dissociation of HOONO due to large LIF background signal from the excess NO that is present from the H + NO_2 reaction.

Spectra of peak *D* that are generated with the $HOO^{15}NO$ and of which their relative band position are compared with those of $HOO^{14}NO$, have resulted in band shifts that are <2 cm^{-1}. As mentioned above, only transitions involving the ν_1, ν_7 and ν_9 result in shifts that are less than 2 cm^{-1}. In addition, transitions that involve $\Delta V\tau = 0$ will also result in no shift. For example, the transition from $0\nu_1 + 3\nu_9$ to $3\nu_1 + 3\nu_9$ is valid based on energetics and isotope shifts, the transition from $0\nu_1 + 3\nu_8$ to $3\nu_1 + 4\nu_8$ will result in a ~6 cm^{-1} shift associated with $\Delta V\nu_8 = +1$ and therefore is not a likely transition. Thus, peak *D* is likely to consist of combination of transitions of ν_1, ν_7 or ν_9 where ΔV is unconstrained and/or any other mode(s) of which $\Delta V = 0$. Unfortunately, based on current predictions made by the 2-D and 3-D *ab initio* models,[11,12] it is quite certain that peak D *does not* purely involve ν_1 and ν_9 which correspond to the *cis-perp* configuration.

Phase-space simulations of the observed OH product state distributions in general, results in fits that are warmer than are experimentally observed. Unlike in the $2\nu_{OH}$ region where phase-space simulations are in good agreement with measured product state distributions (see Chapter 4), present simulations agree well only with product states of the $2\nu_1 + \nu_3$ band (peak *A*) which lies slightly above the dissociation limit (E_{excess} ~ 2 kcal/mol). Around ~7 kcal/mol above the dissociation limit, which corresponds to the $3\nu_1$ band (peak *C*), PST already shows breakdown in its applicability as it fails to follow closely the shape of the OH product state distribution. The breakdown of this statistical

theory has also been observed with simulations of $HONO_2$ ($6\nu_{OH}$),[22] and as shown in Chapter 11, with $HOCH_2OOH$ ($5\nu_{OH}$) where the dissociation can also result in vibrationally excited fragments. Thus, it is not surprising to find the phase-space that unable to fit peaks *D*. As shown in Fig. 5.10, the simulations for peak *D* are warmer than observed even when considering transitions which mainly originate from the ground state of *cis-cis* HOONO. This approach of using phase-space, in essence, does not permit us to identify using which hot-bands do contribute in peak *D*.

However, based on analysis of the product state distribution in the context of energy conservation, hot-bands of the *cis-cis* are the only likely explanation for the OH(v=1) product and the action spectrum in Fig. 5.1. Recall, as shown in Fig. 5.1(b) that the threshold for the OH(v=1) + NO_2 channel lies merely ~1 kcal/mol above the band center of peak *D*. In addition, linewidth measurements of the OH(v=1) rotational lines indicate the fragments are moving slowly where E_{trans}[OH(v=1, *N*=1) + NO_2] = 580 cm^{-1}. By contrast, resulting ground state fragments are fast moving, where E_{trans}[OH(v=0, *N*=2) + NO_2] = 3951 cm^{-1} (see Table 5.2). Therefore, in conjunction to the rotational OH(v=0) and OH(v=1) product state distributions, we conclude that hot-bands or, as seen in the case of *cis-perp* configuration, additional HOONO configuration may be giving rise to the peak *D* and its strong intensity.

At present time, the 2-D and 3-D *ab initio* models have precluded us from labeling this band as the *cis-perp* state even though this state has recently been reported by the Li *et al.* who recorded an isolated feature in the first ($2\nu_{OH}$) OH-stretching overtone region of their jet-cooled HOONO molecule.[17] Since under various conditions the yields of the various conformers of HOONO and $HONO_2$ are different, it is important

to note that Lester and coworkers generate HOONO via the three-body recombination reaction of OH + NO_2 from $HONO_2$ photolysis at 193 nm.[13-15,17] Based on rotational band contour analysis, they conclude that the band at 6996.2 cm^{-1} corresponds to the *cis-perp* configurations of peroxynitrous acid.[17] Their *cis-perp* configuration however corresponds to non-equilibrium trapping at these levels due to ineffective vibrational relaxation of the HOONO molecule to the ground state. If however in our case the *cis-perp* state is giving rise to the intensity to peak *D*, than it would occur under the situation where the thermal energy acts as a continuous pump which populates these vibrational levels. In other words, thermal energy, in equilibrium, transfers population between levels of *cis-cis* structure which our laser then excites. In addition, we also believe that the $3\nu_1$ band is weak due to the strong mixing as a result of intramolecular vibrational energy redistribution (IVR). These interactions lead to fractionation of the second overtone band and giving rise to its broadened band structure. These interactions which have not been accounted for in any *ab initio* model add another layer of complexity.

Finally, as been stated in the current and previous dissertation chapters, the disagreement between the observed and calculated intensities in HOONO is likely due to the fact that more sophisticated models are needed to fully account for the interactions between states of this transient molecule as evident from the isotope analysis.

5.5 Conclusions

This dissertation chapter presents the action spectra and dissociation dynamics of HOONO in the second ($3\nu_{OH}$) OH-stretching overtone region. Through measurements of the resulting nascent OH product state distributions and translational energy release of the various vibrational bands we find that while the energetics of peaks *A* and *B* are

consistent with transitions originating from the ground state of *cis-cis* HOONO, the energy associated with the peak *D* can only be accounted from transitions originating from hot-bands. Currently however, *ab initio* models overrule major contribution from the *cis-perp* configuration and can not explain the action spectra. Energetically speaking, the transitions which give rise to peak *D* originate from vibrational modes which have internal energy in the range of 370 – 1100 cm^{-1}. However, the significant vibrational activity in the $3\nu_{OH}$ region underlying the difficulties associated with identifying which mode(s) contribute to the enhanced intensity of peak *D*. We believe that a full multidimensional potential surface is needed in order to fully quantify the vibrational band assignment of HOONO.

5.6 Acknowledgment

Chapter 5, in part, is a reprint of the material as it appears in Journal of Chemical Physics 120, 10543 (2004). J. Matthews, J. S. Francisco, and A. Sinha, American Institute of Physics, 2004. And in American Chemical Society 125, 134318 (2005). D. P. Schofield, and H. G. Kjaergaard; J. Matthews, and A. Sinha, American Chemical Society, 2005. The dissertation author was the primary investigator and author of these papers.

Table 5.1: Vibrational Frequencies, Anharmonicities and Isotope Shift of *cis-cis* HOONO (cm^{-1}) [a]

$(\omega_e)_i$	355	524	397	716	837	971	1434	1568	3487
^{15}N Isotope Shift	1.3	6.0	0.3	10.0	6.1	6.6	4.3	24.5	0.0
$(\omega_e\chi_e)_{ij}$	9	8	7	6	5	4	3	2	1
1	65.1	23.6	2.21	12.2	5.11	3.74	-39.7	-2.74	-111.0
2	4.4	0.72	0.38	28.8	-1.06	-3.41	-9.11	-9.72	
3	12.2	3.53	-0.79	-1.8	-8.56	-4.97	-5.95		
4	-6.02	-2.52	-4.77	-9.39	-9.12	-2.86			
5	-3.98	-4.87	-3.13	-4.72	-3.4				
6	-39.6	-16	-9.58	-28.4					
7	-15.4	-6.54	-3.53						
8	-48.2	-8.47							
9	-38.2								

[a] Using MP2/aug-cc-pVTZ.

Table 5.2: Fragment Energy Disposal HOONO($3\nu_{OH}$ region) → OH + NO_2 [a]

OH Rotational level	E[N]	Excitation Band		
		peak *A* $2\nu_1 + \nu_3$ (7657 cm^{-1})	peak *C* $3\nu_1$ (9397 cm^{-1})	peak *D* — (10 160 cm^{-1})
v=0; $Q_1(2)$	83.90	1438 ± 244	2916 ± 169	3951 ± 316
v=0; $Q_1(3)$	202.37	1208 ± 157	2518 ± 197	3164 ± 288
v=0; $Q_1(4)$	355.87	1316 ± 150	2052 ± 156	2841 ± 231
v=0; $Q_1(5)$	544.82	1122 ± 116	1716 ± 166	2951 ± 262
v=0; $Q_1(6)$	769.17		1597 ± 107	2640 ± 245
v=0; $Q_1(8)$	1324.24		1401 ± 220	2440 ± 190
v=0; $Q_1(10)$	2019.53			2334 ± 135
v=1; $Q_1(1)$	3569.49			581 ± 161
$\langle E_{ro\text{-}vib} \rangle$		247 ± 4	470 ± 7	897 ± 23

[a] All energies and widths in cm^{-1} .

[b] Uncertainties are one standard deviation.

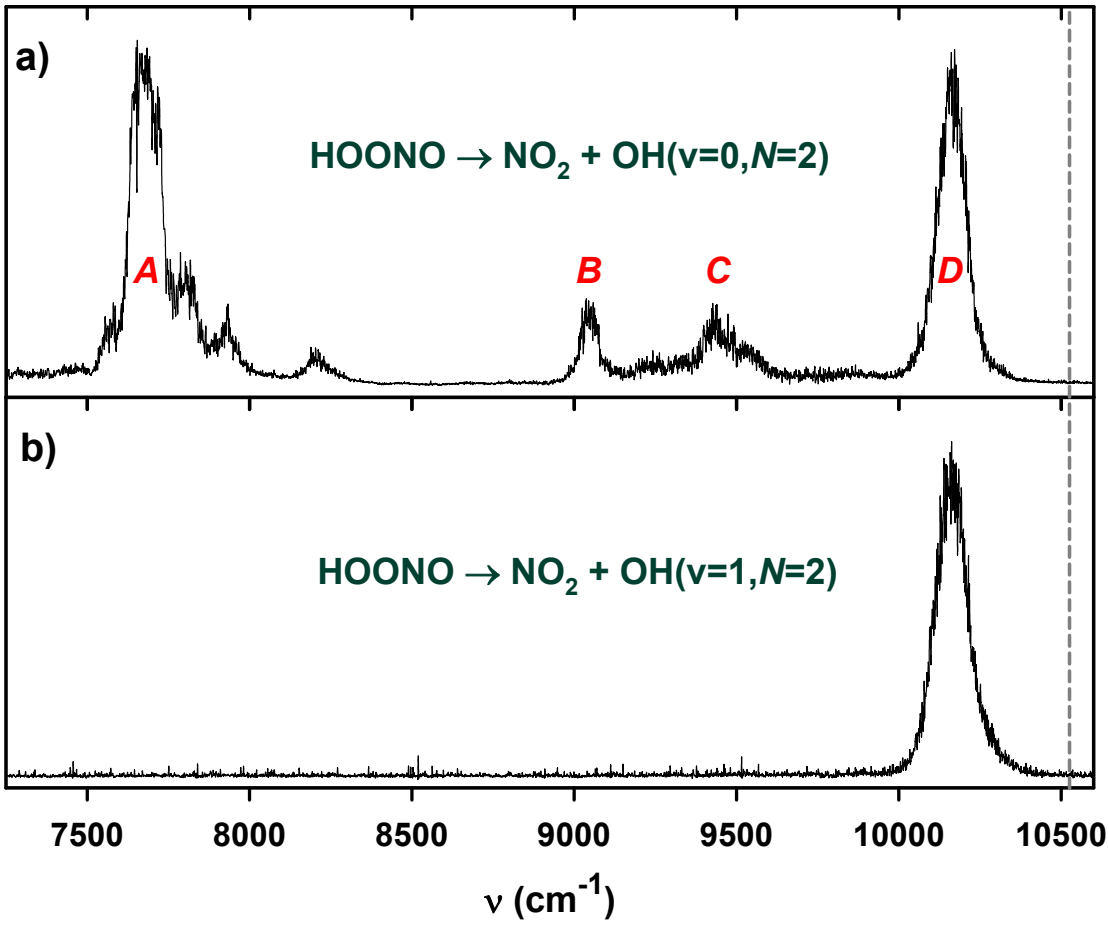

Figure 5.1: Action spectrum of room temperature HOONO obtained in its second OH stretching overtone region ($3\nu_{OH}$). a) The spectrum is generated by monitoring the yield of OH(v=0, *N*=2) rotational state as the infrared excitation laser is scanned. b) The spectrum is generated by monitoring the yield of OH(v=1, *N*=2) rotational state. [File: F5.1_3nuOH]

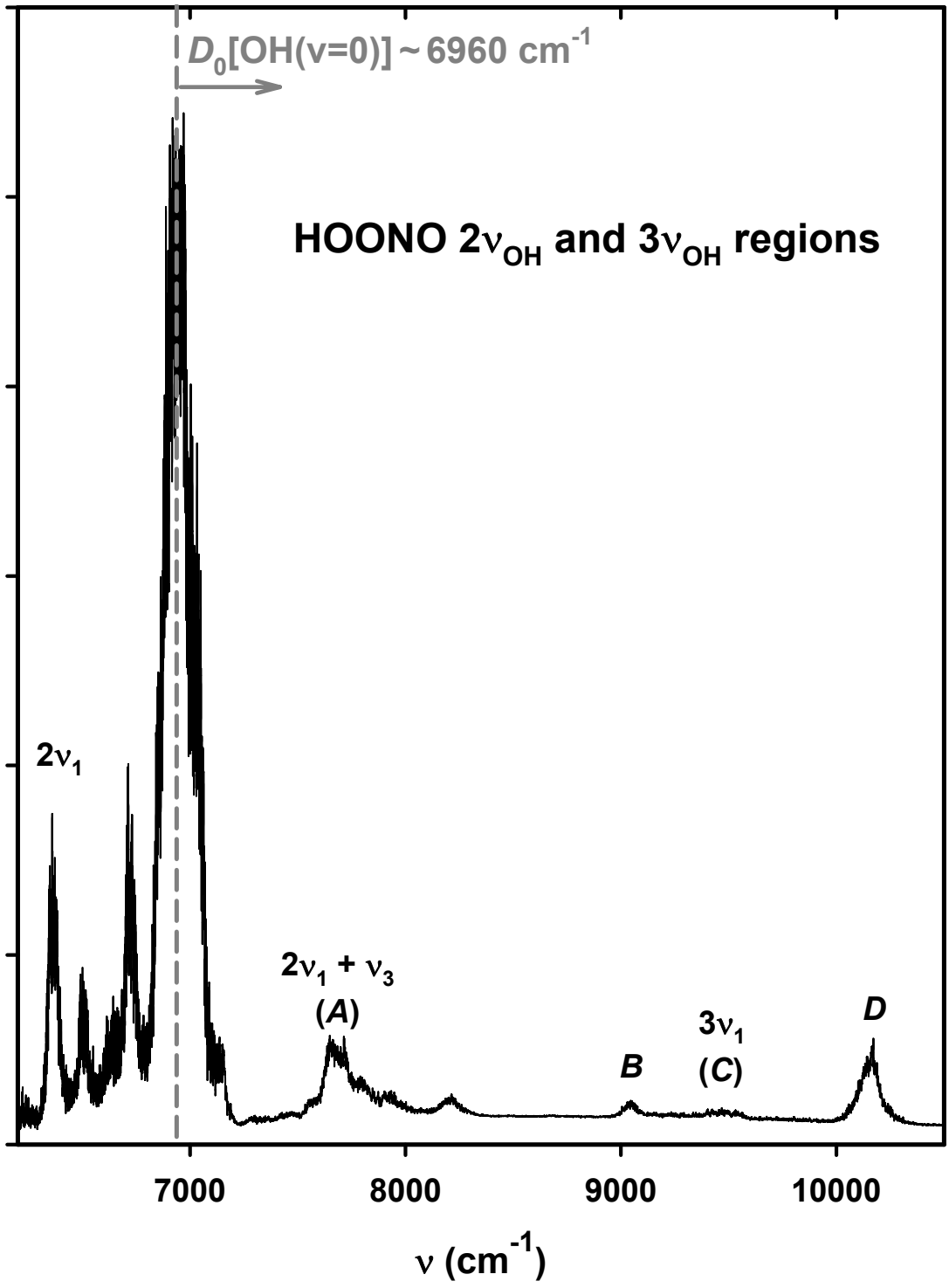

Figure 5.2: "High" pressure room temperature overview action spectrum in the first ($2\nu_{OH}$) and second ($3\nu_{OH}$) OH-stretching overtone region. The spectrum is generated by scanning the overtone excitation laser and monitoring the yield of OH(v=0, N=2). [File: F5.2_2nu_3nu]

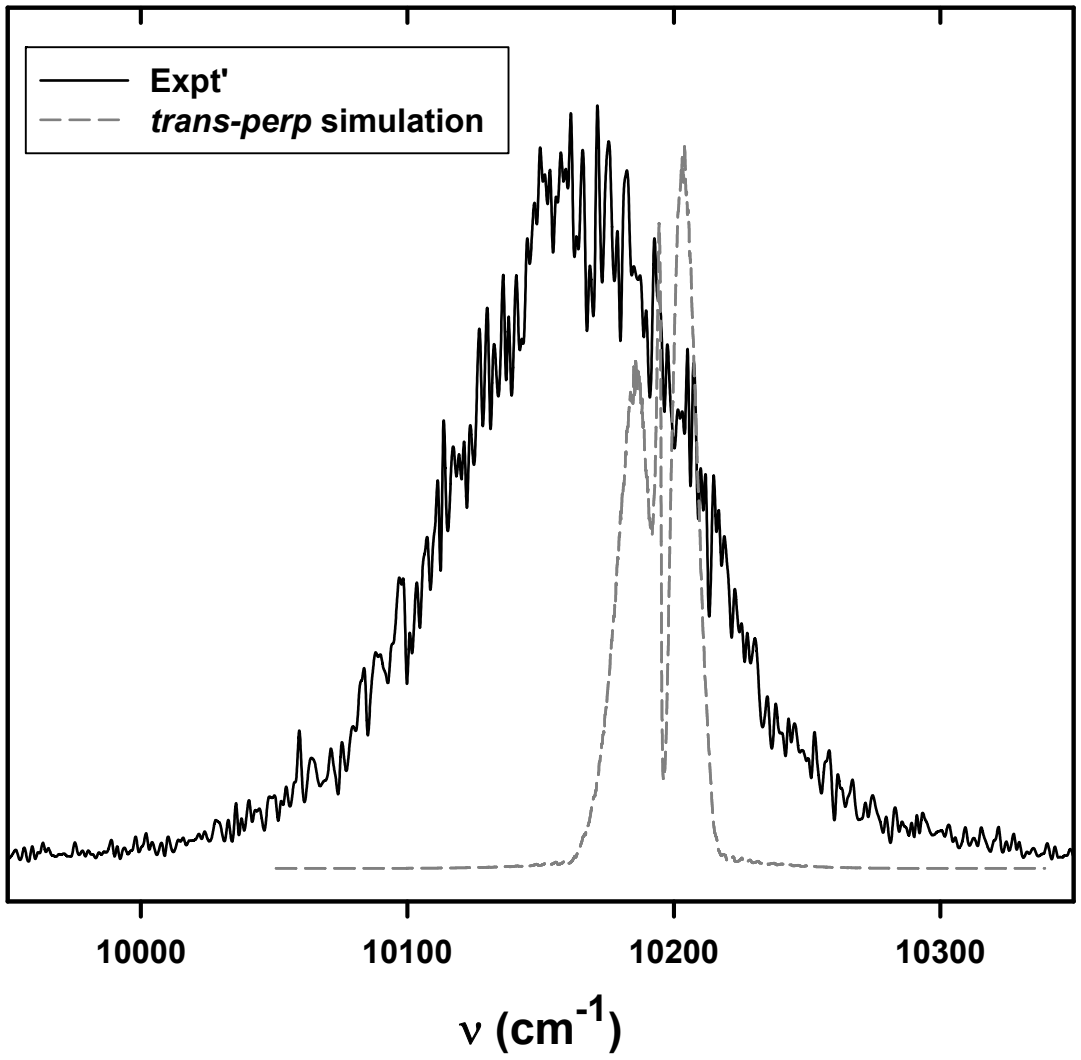

Figure 5.3: Rotational band contour simulation of *trans-perp* HOONO $3\nu_1$ band (dashed line). The parameters are obtained from Ref 17. The experimental spectrum shown in smooth line is that of the peak *D*. [File: F5.3_tp_sim]

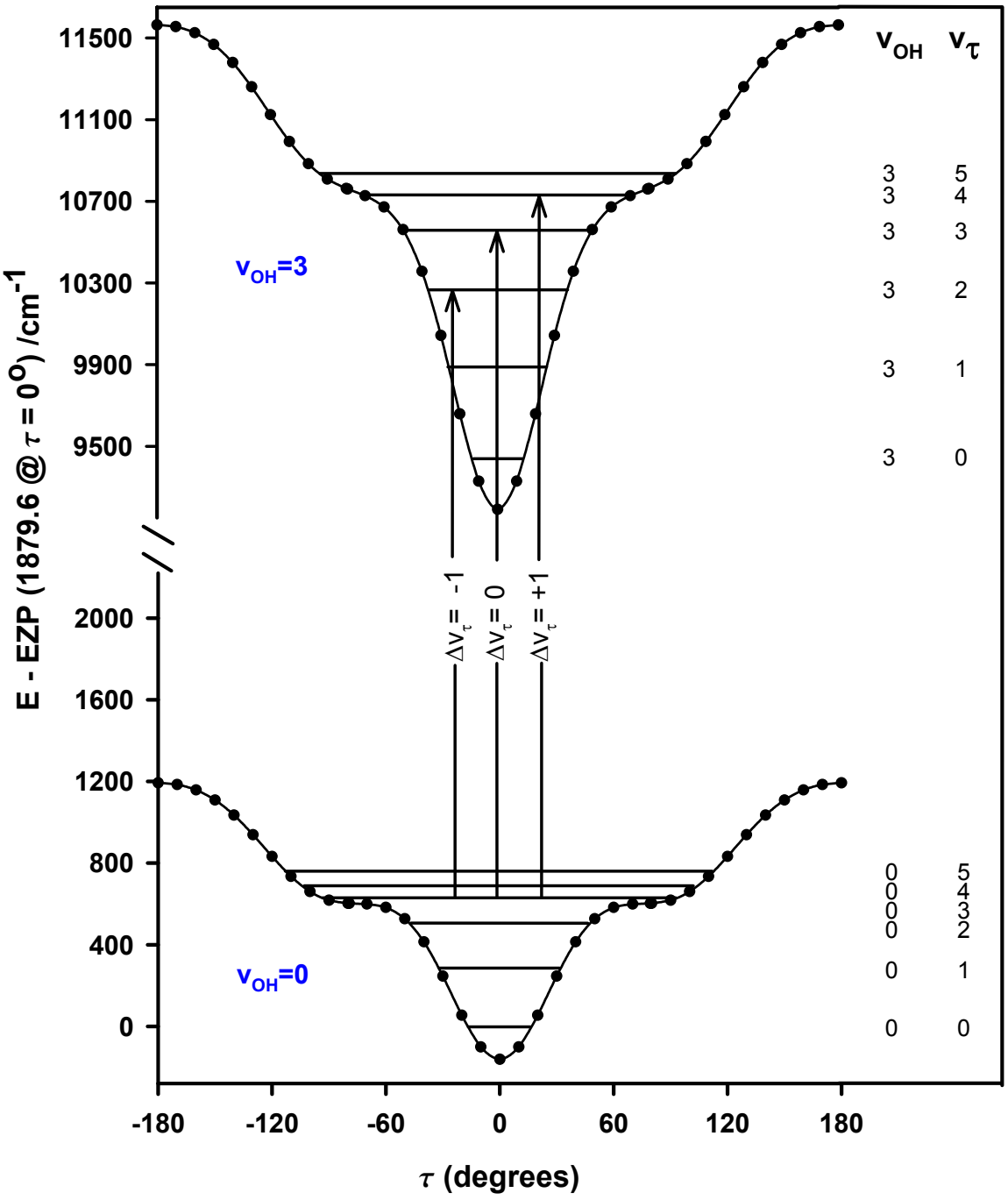

Figure 5.4: Adiabatic torsional potentials for the $V_{OH} = 0$ and $V_{OH} = 3$ stretching states. The OH stretching states are labeled by the quantum number V_{OH} while their corresponding torsional states are labeled by the quantum number V_τ. The vertical lines in the figure indicate some of these vibrational transitions.
[File: F5.4_torsion_potentials]

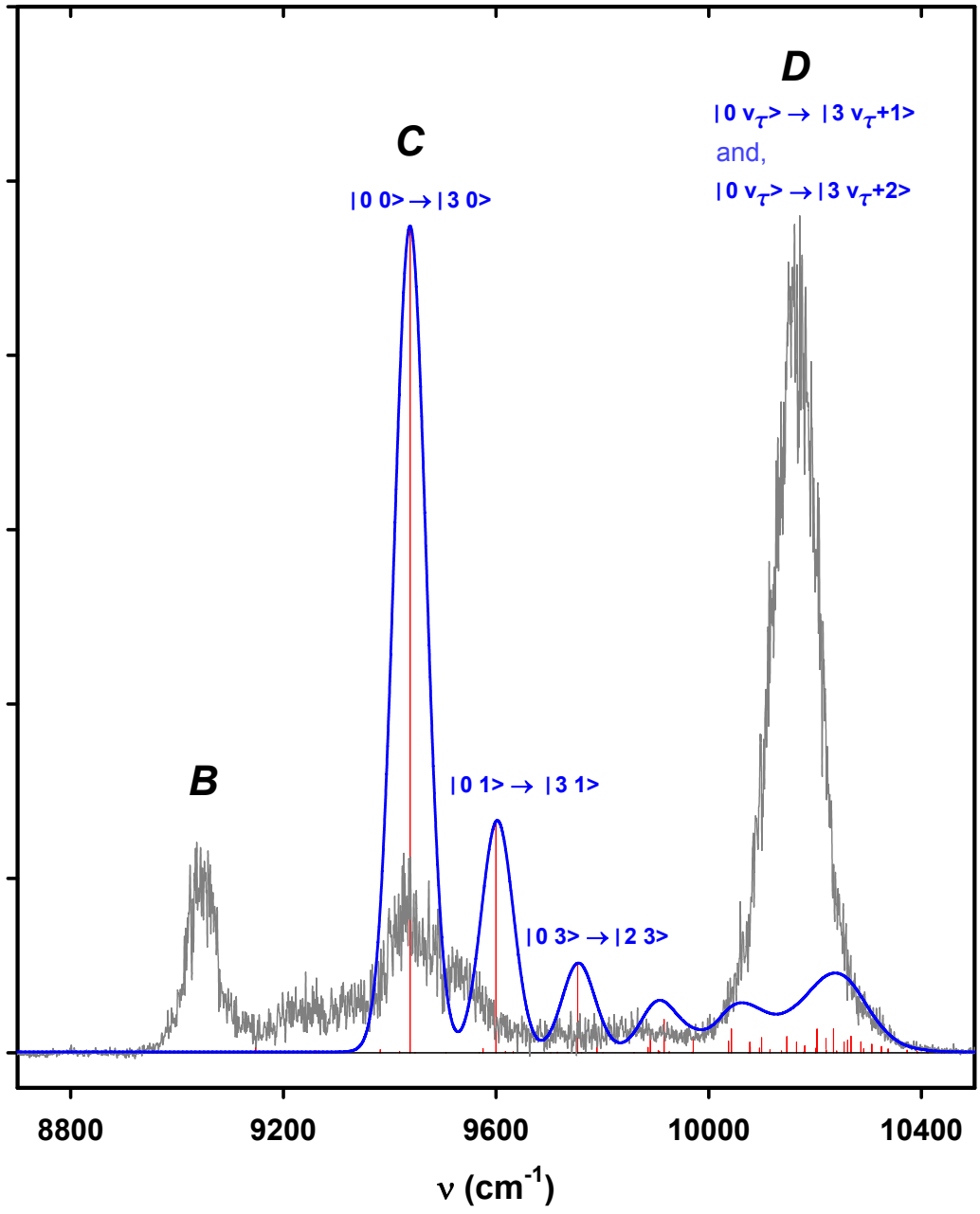

Figure 5.5: Simulated overtone action spectrum (smooth line) resulting from the 2-D intensity calculation. The vertical lines in the stick spectrum are the effective strengths of each vibrational transition weighted by their respective oscillator strength and Boltzmann factor. Each stick is further broadened using a 50 cm^{-1} Gaussian envelope to account for the associated rotational distributions. [File: F5.5_simulation]

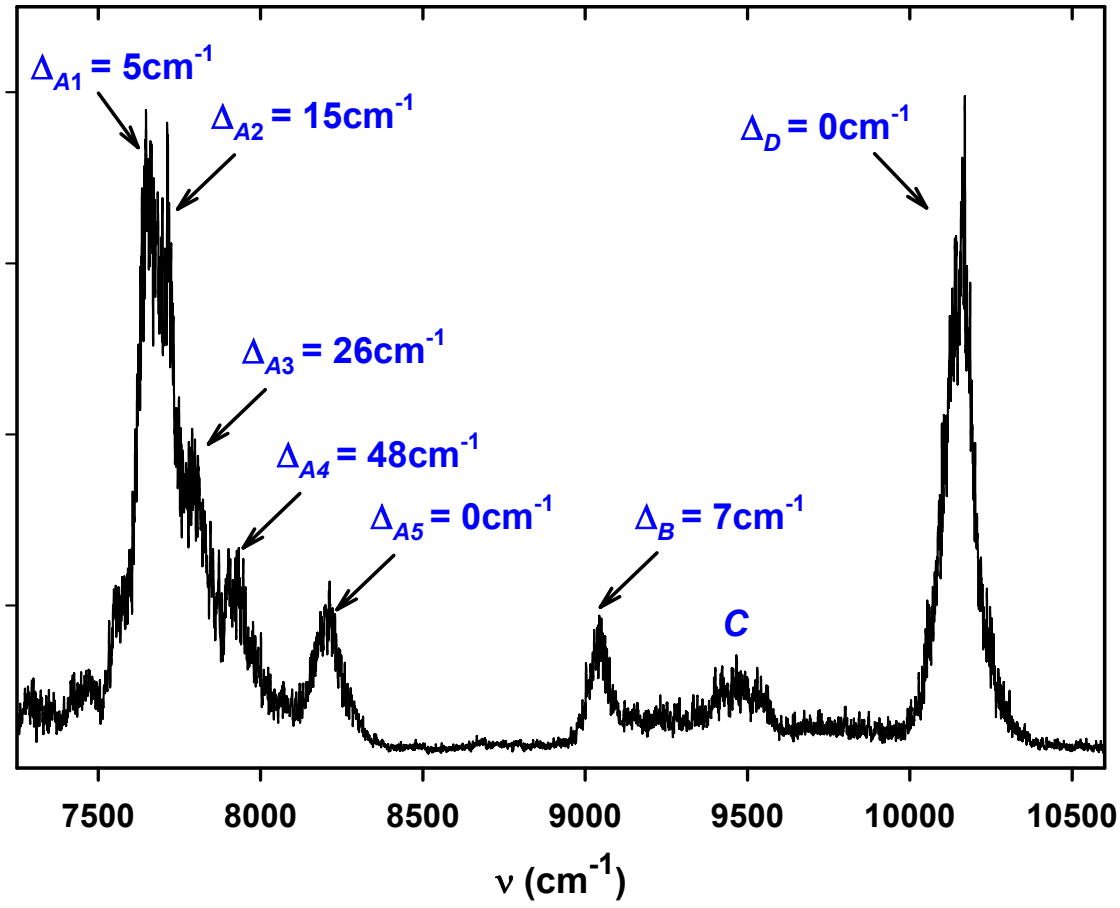

Figure 5.6: Action spectrum HOONO of the bend-stretch combination mode ($2\nu_1 + \nu_3$) and the second ($3\nu_1$) OH-stretching overtone regions. The observed isotopic ^{15}N shifts (cm^{-1}) relative to ^{14}N are indicated with the Δ symbol above each band.
[File: F5.6_shifts]

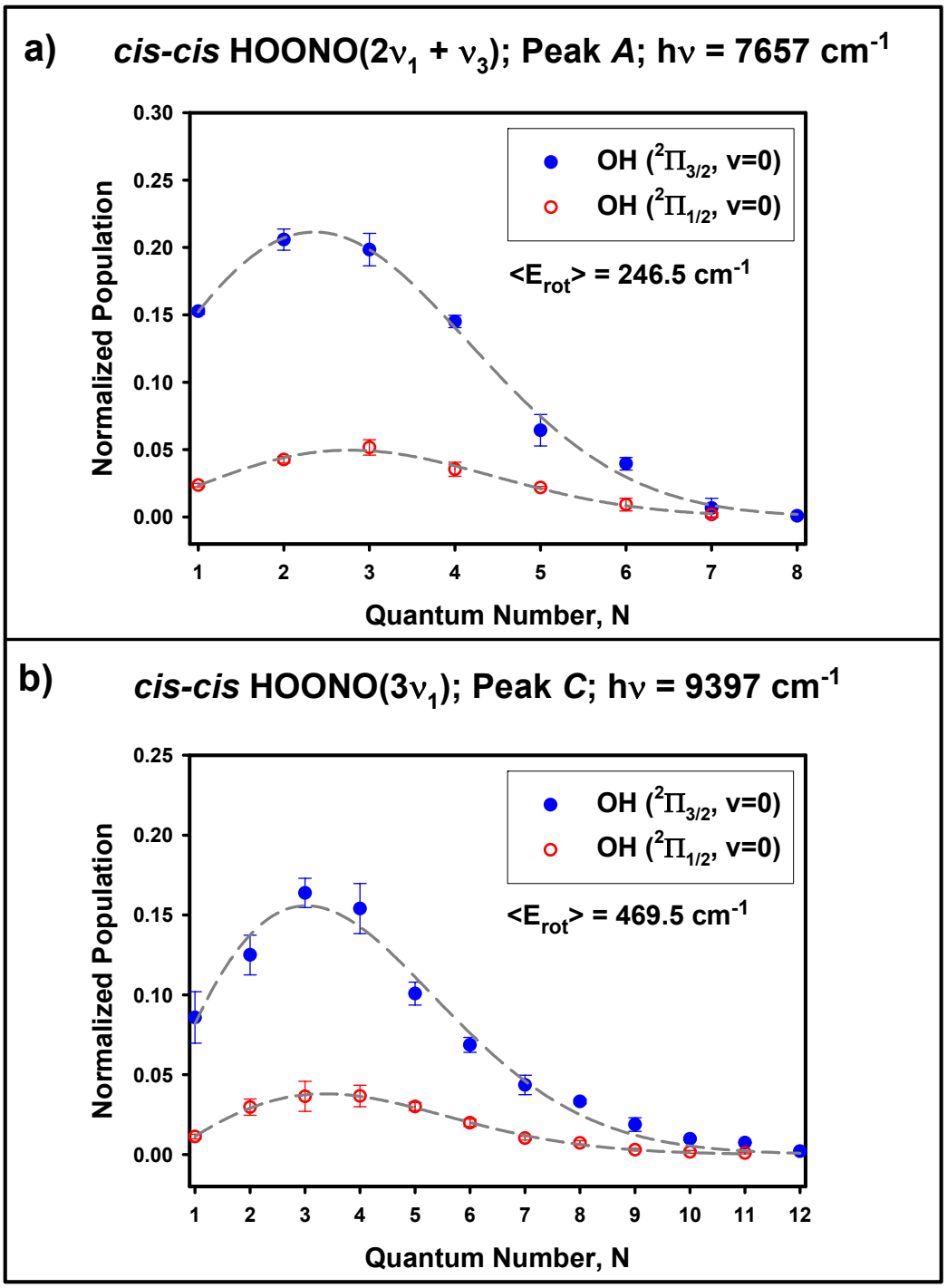

Figure 5.7: Nascent rotational state distributions of the OH (v=0, $^2\Pi_{3/2}$) and OH (v=0,$^2\Pi_{1/2}$) states in close and open circles respectively resulting from excitation at peaks *A* and *C* in the vicinity of the $3\nu_{OH}$ band. a) Distributions resulting from excitation within peak *A*. b) Distributions resulting from excitation within peak *C*.
[File: F5.7_psd_bend_stretch]

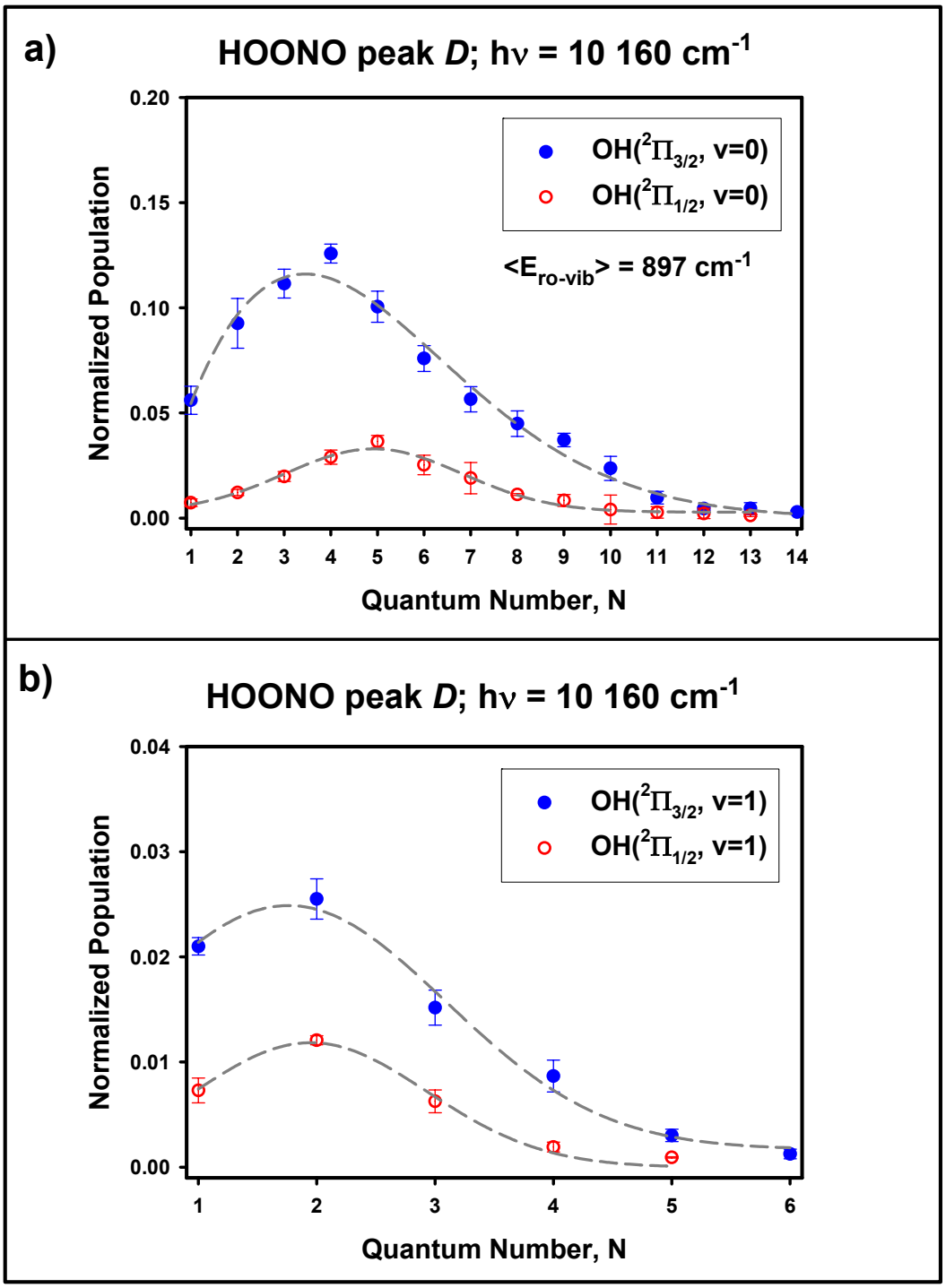

Figure 5.8: Nascent rotational state distributions of the OH($^2\Pi_{3/2}$) and OH($^2\Pi_{1/2}$) states in close and open circles respectively resulting from excitation at peaks *D*. a) Distributions monitoring the OH(v=0) fragment. b) Distributions monitoring OH(v=1) product. [File: F5.8_psd_hotband]

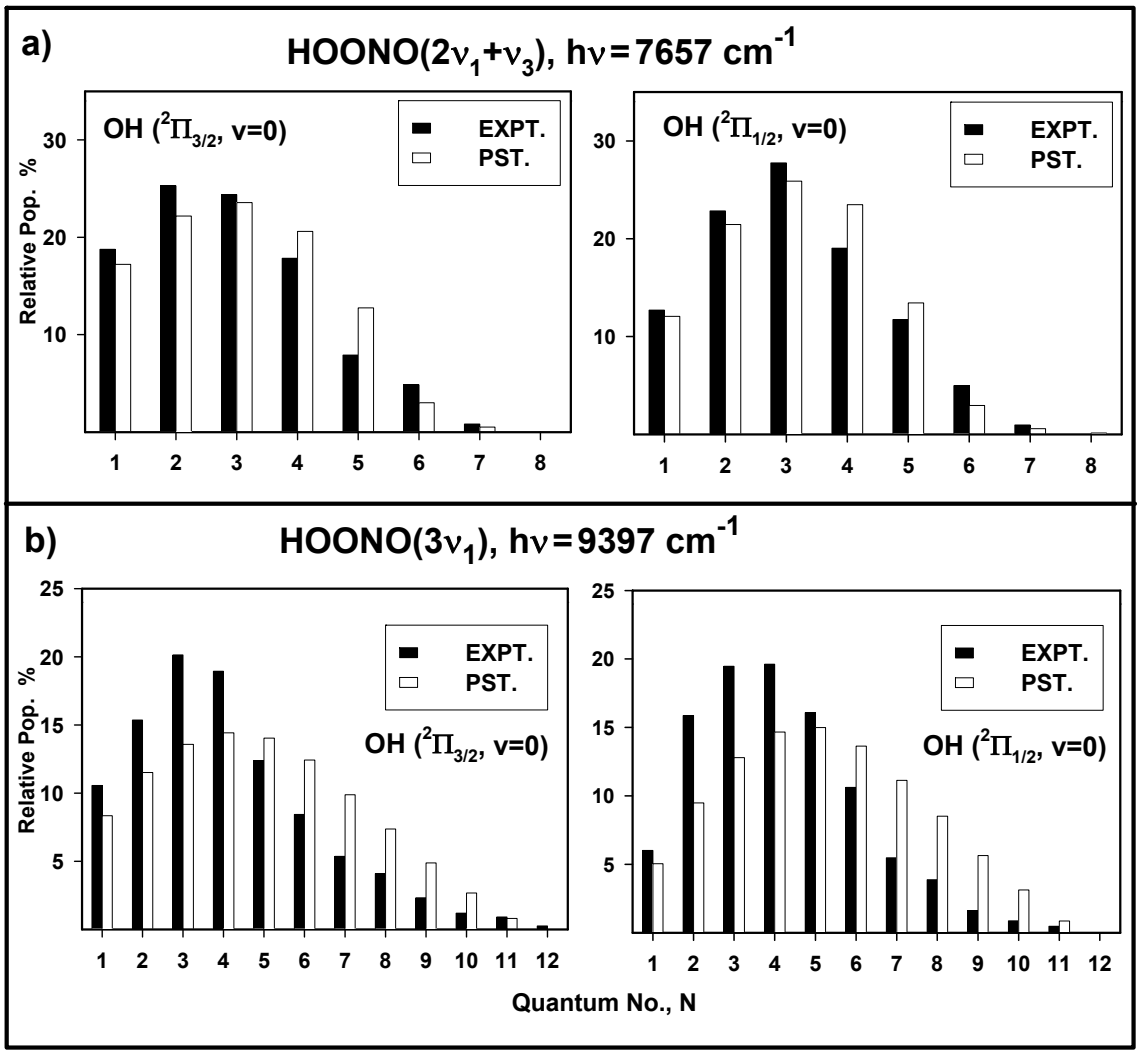

Figure 5.9: Comparison of experimental and phase-space simulation of the OH (v=0, $^2\Pi_{3/2}$) and OH (v=0,$^2\Pi_{1/2}$) product state distributions. The phase space simulation uses D_0 = 19.9 kcal/mol, $C_6 = 2.0 \times 10^{-58}$erg/cm^6, *cis-cis* HOONO spectroscopic parameters and averages over the thermal distribution of initial *cis-cis* HOONO states. a) Results for excitation within peak *A*. b) Results for excitation within peak *C*. [File: F5.9_pst_a_c]

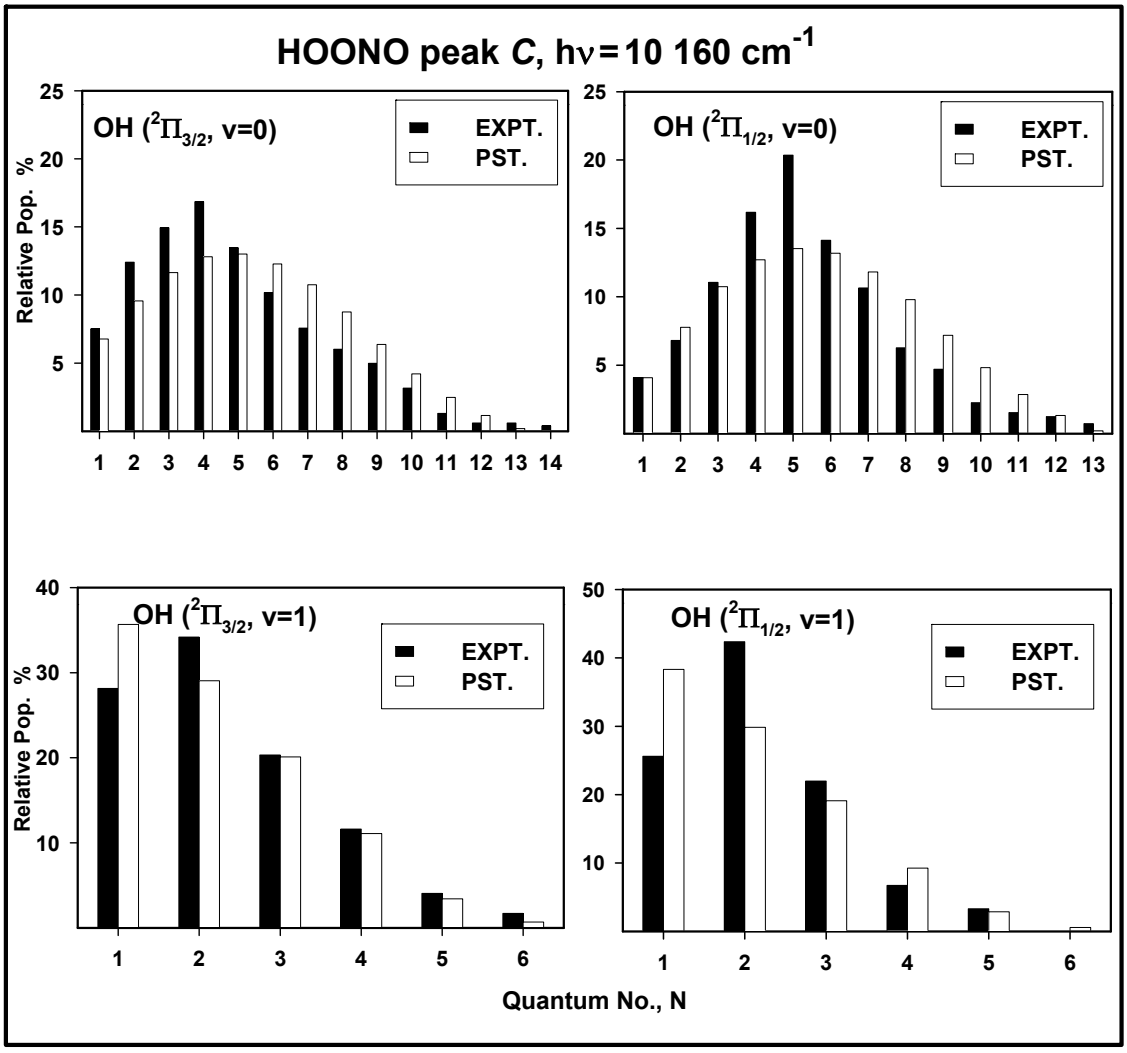

Figure 5.10: Comparison of experimental and phase-space simulation of the OH (v=0, $^2\Pi_{3/2}$) and OH (v=0,$^2\Pi_{1/2}$) product state distributions as well as comparison of experimental and phase-space simulation of the OH (v=1, $^2\Pi_{3/2}$) and OH (v=1,$^2\Pi_{1/2}$) product state distributions associated with peak *D*. The phase space simulation uses D_0 = 19.9 kcal/mol, $C_6 = 2.0 \times 10^{-58}$erg/cm^6, *cis-cis* HOONO spectroscopic parameters and averages over the thermal distribution of initial *cis-cis* HOONO states.
[File: F5.10_pst_d]

5.7 References

1. M. P. McGrath, F. S. Rowland, J. Phys. Chem. **98**, 1061 (1994).

2. Y. Zhao, K. N. Houk, and L. P. Olson, J. Phys. Chem. A **108**, 5864 (2004).

3. Y. Li, J. S. Francisco, J. Chem. Phys. **113**, 7976 (2000).

4. D. A. Dixon, D. Feller, C. G. Zhan, J. S. Francisco, J. Phys. Chem. A **106**, 3191 (2002).

5. H. W. Jin, Z.Z. Wang, Q.S. Li, and X. R. Huang, Theo.Chem. **624**, 115 (2003).

6. R. Sumathi, S. D. Peyerihoff, J. Chem. Phys. **107**, 1872 (1997).

7. D. Chakraborty, J. Park, M. C. Lin, Chem. Phys. **231**, 39 (1998).

8. H. Hippler, S. Nasterlack, F. Striebel, Phys. Chem. Chem. Phys. **4**, 2959 (2002).

9. P. Pechukas, J. C. Light, and C. Rankin, J. Chem. Phys. **44**, 794 (1966); P. Pechukas and J. C. Light, ibid. **42**, 3281 (1965); J. C. Light, Faraday Discuss. Chem. Soc. **44**, 14 (1967).

10. Gaussian 03, Revision B.04, M. J. Frisch, G. W. Trucks, H. B. Schlegel, G. E. Scuseria, M. A. Robb, J. R. Cheeseman, J. A. Montgomery, Jr., T. Vreven, K. N. Kudin, J. C. Burant, J. M. Millam, S. S. Iyengar, J. Tomasi, V. Barone, B. Mennucci, M. Cossi, G. Scalmani, N. Rega, G. A. Petersson, H. Nakatsuji, M. Hada, M. Ehara, K. Toyota, R. Fukuda, J. Hasegawa, M. Ishida, T. Nakajima, Y. Honda, O. Kitao, H. Nakai, M. Klene, X. Li, J. E. Knox, H. P. Hratchian, J. B. Cross, V. Bakken, C. Adamo, J. Jaramillo, R. Gomperts, R. E. Stratmann, O. Yazyev, A. J. Austin, R. Cammi, C. Pomelli, J. W. Ochterski, P. Y. Ayala, K. Morokuma, G. A. Voth, P. Salvador, J. J. Dannenberg, V. G. Zakrzewski, S. Dapprich, A. D. Daniels, M. C. Strain, O. Farkas, D. K. Malick, A. D. Rabuck, K. Raghavachari, J. B. Foresman, J. V. Ortiz, Q. Cui, A. G. Baboul, S. Clifford, J. Cioslowski, B. B. Stefanov, G. Liu, A. Liashenko, P. Piskorz, I. Komaromi, R. L. Martin, D. J. Fox, T. Keith, M. A. Al-Laham, C. Y. Peng, A. Nanayakkara, M. Challacombe, P. M. W. Gill, B. Johnson, W. Chen, M. W. Wong, C. Gonzalez, and J. A. Pople, Gaussian, Inc., Wallingford CT, 2004.

11. D. P. Schofield and H. G. Kjaergaard, J. Phys. Chem. A **109**, 1810 (2005).

12. D. P. Schofield, and H. G. Kjaergaard; J. Matthews, and A. Sinha, J. Chem. Phys. 125, 134318 (2005).

13. I. B. Pollack, I. M. Konen, E. X. Li, and M. I. Lester, J. Chem. Phys. **119**, 9981 (2003).

14. I. M. Konen, I. B. Pollack, E. X. J. Li, and M. I. Lester, J. Chem. Phys. **122**, 094320 (2005).

15. I. M. Konen, E. X. J. Li, T. A. Stephenson, M. I. Lester, J. Chem. Phys. **123**, 204318 (2005).

16. J. L. Fry, S. A. Nizkorodov, M. Okumura, C. M. Roehl, J. S. Francisco, and P. O. Wennberg, J. Chem. Phys. **121**, 1432 (2004).

17. E. X. J. Li, I. M. Konen, and M. I. Lester, and A. B. McCoy, J. Phys. Chem. A **110**, 5607 (2006).

18. P. W. Atkins, *Molecular Quantum Mechanics, 2nd ed*. (Oxford University Press: Oxford, 1983).

19. H. G. Kjaergaard, B. R. Henry, J. Chem. Phys. **96**, 4841 (1992).

20. G. H. Dieke and H.M. Crosswhite, J. Quant. Spectrosc. Radiat. Transfer **2**, 97 (1962).

21. W. L. Dimpfl and J. L. Kinsey, J. Quant. Spectrosc. Radiat. Transfer **21**, 223 (1979).

22. A. Sinha, R. L. Van Der Wal, and F. F. Crim, J. Chem. Phys. **91**, 2929 (1989); **92**, 401 (1989).

23. C. Wittig, I. Nadler, H. Reisler, M. Noble, J. Catanzarite, and G. Radhakrishnan, J. Chem. Phys. **83**, 5581 (1985).

24. I. M. Konen, E. X. J. Li, M. I. Lester, J. Vazqez, and J. F. Stanton, J. Chem. Phys. **125**, 074310 (2006).

25. M. W. Chase, NIST-JANAF Tables 4th ed.; J. Phys. Chem. Ref. Data Mono. **9**, Suppl. 1 (1998).

Chapter 6

Unimolecular Dissociation and Thermochemistry of Methyl Hydroperoxide

6.1 Introduction

This chapter is the first chapter in a series (Chapter 6 through Chapter 10) providing details on the bound and dissociating vibrational and electronic states of methyl hydroperoxide (MHP, CH_3OOH). These experiments utilize several of the experimental techniques described in Chapter 1 to probe both the ground and electronic excited states of MHP under room temperature and molecular beam conditions. CH_3OOH is the smallest organic peroxide and can intrinsically serve as a benchmark in the investigation of properties common to other hydroperoxide such as their dissociation dynamics, thermochemistry, spectroscopy and absorption cross-sections; in particular, properties which are likely common to other organic hydroperoxides such as ethyl hydroperoxide, t-butyl hydroperoxide, hydroxymethyl hydroperoxide. Recently, Watts and Francisco have shown in an *ab initio* ground and electronically excited study that the electronic structure of MHP is very similar to that of hydrogen peroxide, thus bridging between organic and inorganic peroxides as well.[1] The combination of molecular properties such as those noted above are also important in understanding the chemistry of the atmosphere. As mentioned in Chapter 1, in general, hydroperoxides are important tropospheric trace gases because of their contribution to the HOx reservoir.[2-6]

Laboratory studies have shown that CH_3OOH absorbs strongly over the region between 200 – 360 nm resulting in excitation to a dissociative electronic excited state and that the dissociation mainly produces OH and methoxy (CH_3O) fragments.[7,8] Branching ratio measurements at 193 and 248 nm have also confirmed that the quantum yield for the OH + CH_3O channel is near unity.[9,10] Since the absorption cross-section measurements by Ravishankara and coworkers[8] from 190 – 365 nm suggest the molecule absorbs U.V. radiation favorably, it is likely that the U.V. photochemistry of CH_3OOH plays a central role in the atmosphere in terms of OH production.[3-6]

In contrast to photochemistry on its excited state, the photochemistry of CH_3OOH on its ground electronic surface has not been previously reported. *Ab initio* calculations reveal that there are two potential pathways for unimolecular dissociation on the ground electronic surface corresponding respectively to simple bond fission and molecular elimination (see Fig. 6.1).[11] The pathway with the lowest threshold energy involves simple bond cleavage giving rise to the CH_3O + OH radical products. This pathway, however, does not correspond to the most stable fragments. The molecular elimination channel leading to the production of water and formaldehyde (H_2O + H_2CO), generates products that are more stable. Accessing this molecular elimination channel however, requires overcoming a barrier that is calculated to be ~ 3.4 kcal/mol higher than the simple bond fission pathway.

This chapter presents results on the energetics of the unimolecular dissociation of CH_3OOH resulting from excitation of its third ($4\nu_{OH}$) and fourth ($5\nu_{OH}$) OH-stretching overtones regions. Based on the potential energy diagram shown in Fig. 6.1, the OH + CH_3O channel is expected to be the primary products accessible at these excitation

energies. From the measured energy disposal (internal and translational) which is discussed in Appendix *C* and in Chapters 4 and 5 with HOONO, the nascent OH fragment is used to estimate the CH_3O-OH bond dissociation energy. As shown in figure 6.1 and based on simple bond fission of CH_3OOH, D_0[CH3O–OH] = 44.6 kcal/mol. From estimations of band origins of typical OH-stretching modes (such as H_2O_2 and CH_3OH)[12,13], it is likely that while the fourth OH-stretching overtone ($5\nu_{OH}$) lies above the bond dissociation limit, the photodissociation of the third OH-stretching overtone ($4\nu_{OH}$) would only occur under thermally assisted conditions. This fact leads us to predominantly focus on the $5\nu_{OH}$ region where we obtain our D_0 value.

Our experimental D_0 is then compared with the results of *ab initio* calculation. The *ab initio* calculations utilizes the CCSD(T) method in conjunction with an isodesmic reaction scheme to compute the heat of formation of CH_3OOH using a series of basis sets in a similar manner introduced in Chapter 2 for peroxynitric acid. The series of basis sets calculations (CCSD(T)/cc-pVξZ (ξ = D, T, Q)) are then extrapolated to the complete basis set limit (CBS). This enables us to obtain the heat of formation for CH_3OOH, which when combined with the known heats of formation of CH_3O and OH fragments, provides a theoretical estimate of the CH_3O-OH bond dissociation energy for comparison with experiment.

In the subsequent chapters, other important properties of methyl hydroperoxide are discussed. In Chapter 7 the spectroscopy of the overtones obtained in the regions of $2\nu_{OH} - 5\nu_{OH}$ are examined with a two-dimensional dipole moment surface generated at the CCSD(T)/cc-pVTZ level of theory. In Chapter 8, the spectroscopy and band structure predicted by the *ab initio* model are then reexamined in a set of molecular beam

experiments investigating CH_3OOH in its first and second OH-stretching overtones as well as their corresponding torsional COOH states. Intramolecular vibrational energy distribution (IVR) and state-to-state interactions observed in these molecular beam experiments are also discussed. At room temperature, IVR is also apparently affecting the extent of vibrationally excited OH product observed from the photo-initiated dissociation of vibrationally excited C-H and O-H stretching modes. These findings are presented in Chapter 9. And, lastly, Chapter 10 delegates the importance of the near U.V. – VIS photo-initiated dissociation of the CH_3OOH molecule and hydroperoxide in general under atmospheric conditions.

6.2 Experiment

6.2.1 Synthesis of Methyl Hydroperoxide

CH_3OOH is synthesized in a similar manner to that described by Vaghijiani and Ravishankara.[8,9] Some of the steps in the procedure described in Refs. 8-9 are modified leading to smaller quantities of MHP produced in order to reduce the risk of potential explosions. All components coming in contact with methyl hydroperoxide in the synthesis are made from glass or Teflon to minimize losses due to decomposition and secondary reactions. The reagents are given with their Fisher part numbers. Dimethyl sulfate (AC11682-0010, 75mL) is mixed with H_2O_2 (H325-500, 30%, 150mL) and deionized (DI) water (250mL) in a round flat-bottom, tooled-mouth 1000 mL Pyrex flask. The flask is immersed in an ice water bath maintained at 273 K. To the mixture, we add *dropwise* potassium hydroxide (AC23255-0010, 40%) over a period of 40 – 60 minutes under constant stirring. The potassium hydroxide is prepared prior to the synthesis by adding 126 mL of DI water to 84 g of KOH flakes. The reaction leads to formation of

bubbles which are allowed to escape from the open flask. In order to keep the reaction form overheating, it is advisable to add ice to the bath as needed. When bubbling subsides, sulfuric acid (~25mL, 50%) is added, resulting in an acidified clear mixture rich with methyl hydroperoxide. The acidic PH of the solution is verified with PH paper. Please note that as with the potassium hydroxide, sulfuric acid (A300S-500) is purchased in pure form, and is required to be diluted with water prior to the synthesis of CH_3OOH.

We then cap the flask and slowly bring the mixture to ~325 K while vigorously bubbling N_2 carrier gas through the input port in the cap. The carrier gas and vapor are allowed to escape through a second port in the cap made of Teflon tubing attached with drilled-through Swagelok connector to a trap maintained at ice bath temperature. Again, to ensure efficient trapping, continuously add ice to the reservoir. We collect about 30 – 35 mL of clear liquid in the trap over a period of two hours. This step is key to ensure that no hydrogen peroxide or other impurities are present in the final product.

Since CH_3OOH is two orders of magnitude less soluble in water than hydrogen peroxides, it is possible to use ether extraction to separate between MHP and water.[4,14-15] The sample is transferred to a second 250 mL flask filled with diethyl ether in order to separate between the water and CH_3OOH by constant stirring for 1 – 2 hrs. Next, the two layers are separated with a separation column and the ether mixture is dried over anhydrous sodium sulfate (AC21926-0010, 5 g) over an hour period. The ether is then pumped out using the vacuum lines in the hood. During the pumping period the cold liquid will condense the MHP on the bottom of the flask. The final product, ~2mL of pure CH_3OOH, is then further pumped-on in the photolysis chamber until the high vapors from ether is eliminated. Note that a sample of pure MHP has a vapor pressure of ~12 –

15 Torr while the vapor pressure of ether is ~ 500 Torr. A typical sample lasts for about five days under typical cell experiments where the reservoir is kept at 273 K. Between uses, the sample is stored in a freezer at temperatures below -20^{o} C.

6.2.2 Experimental Apparatus

The experimental apparatus is similar to that described in the previous chapters. CH_3OOH is slowly introduced into our glass photolysis cell. The sample pressure in the cell is typically set around 40 – 60 mTorr. The CH_3OOH $5\nu_{OH}$ vibrational overtone band around 620 nm, is excited by focusing the output of a Nd:Yag laser (Continuum: NY82-20) pumped dye laser (Continuum: ND60) operating with DCM + R640 mixture into the reaction cell using a 50 cm lens. Typical pulse energies range between 25 – 27 mJ for the 600 – 640 nm region. The CH_3OOH $4\nu_{OH}$ vibrational overtone bands around 750 nm are excited by the same laser system operating with LDS 750 + LDS 765 mixture providing pulse energies ranging between 18 – 22 mJ in the 730 – 765 nm region. Because of the potential interferences arising from the strong single-color two-photon dissociation process of methyl hydroperoxide in the third OH-stretching overtone region, we modify the focusing conditions in the photolysis chamber by increasing the beam diameter inside the photolysis chamber from 1 mm→ 2 mm by bringing the 50 mm lens backward toward the laser and away from the photolysis cell. The beam diameter is measured by taking a burn-mark inside the cell.

The OH photofragments resulting from unimolecular dissociation are probed via the *A–X* transition at ~308 nm using laser induced fluorescence (LIF). The 308 nm laser radiation, which has a bandwidth of ~0.13 cm^{-1}, is generated by frequency doubling the output of a second Nd:YAG laser (Continuum: NY81-20) pumped dye laser (Continuum:

ND60). The probe laser propagates collinearly with the vibrational excitation laser and typically fires ~ 15 ns after the vibrational excitation laser. Fig. 6.2 shows the experimental apparatus used to investigate the overtones of MHP. The intensity of the probe laser is greatly attenuated in order to avoid saturating the OH LIF transitions. Typical probe laser pulse energies are ~ 0.1 μJ and the fluency is ~ 3×10^{-6} J cm^{-2}. The OH fluorescence excited by the probe laser is collected using an f/1 lens system and imaged onto an end-on photomultiplier (EMI 9813QB). A color glass filter (Schott UG-11) located in front of the photomultiplier provides discrimination against scattered laser light. Signal from the PMT is sent to a gated charge integrator (LeCroy, 2249SG ADC) and subsequently digitized and passed to a laboratory computer for storage and analysis.

6.2.3 Computation Methods

We use the GAUSSIAN03 program to determine the optimized geometries, energies, vibrational frequencies, of methyl hydroperoxide, water (H_2O), hydrogen peroxide (H_2O_2), methanol (CH_3OH), methoxy (CH_3O) and hydroxyl (OH).[16] For detailed description of running GAUSSIAN03 on our workstations refer to Appendix *B*. All stationary points were characterized by vibrational frequency calculations at the (U)CCSD(T)/cc-pVDZ level. Two *ab initio* methods are used in this study. The first is the quadratic configuration interaction theory with single and double excitations as well as perturbative correction for triple excitations (QCISD(T) method). Coupled-cluster theory with single and double excitation with perturbative correction for triple excitations (CCSD(T) method) is also used.[17] These wavefunctions are used in conjunction to the Dunning basis sets including the cc-pVDZ, aug-cc-pVDZ, cc-pVTZ and aug-cc-pVTZ and cc-pVQZ.[18-20] In order to evaluate the bonds dissociation energies of CH_3OOH, we

use CCSD(T)/complete basis set (CBS) limit (CCSD(T)/cc-pVξZ (ξ = D, T, Q)) and the isodesmic reaction scheme in a similar manner used with HO_2NO_2 in Chapter 3 as follows:[19,21]

$$CH_3OOH + H_2O \rightarrow H_2O_2 + CH_3OH \qquad \Delta_r H^o_{0\,k} \qquad (6.1)$$

In the above reaction, the number and types of bonds breaking and forming are preserved leading to cancellation of errors in the Hamiltonian; errors which arise with incorporating electron correlations (electron-electron repulsion forces) in the Schrödinger equation.

6.3 Results and Analysis

6.3.1 Vibrational Action Spectrum of $4\nu_{OH}$ and $5\nu_{OH}$

Based on fission bond energies (see Fig. 6.1) it is likely that the $4\nu_{OH}$ band lies below the dissociation threshold ($D_0^{est.} \approx 15\,600$ cm^{-1}). Therefore, our investigation of methyl hydroperoxide begins by looking for its vibrational signature in the $5\nu_{OH}$ region. Figure 6.3 shows the action spectrum of the CH_3OOH $5\nu_{OH}$ band. The top panel is generated by scanning the frequency of the vibrational overtone excitation laser while probing the yield of OH fragments in the (v"=0, N=2) quantum state under high pressure conditions where 1.5 Torr of molecular nitrogen is added and the delays between the pump and probe are increased to 500 ns to help in collapsing the OH rotational population. The spectrum in the lower panel was generated under nascent conditions (40 mTorr and 10 ns delays) by scanning the wavelength of the vibrational overtone excitation laser while probing the yield of OH fragments in the (v"=0, N=3) quantum state. The OH rotational transitions in the $A - X(0,0)$ manifold are identified using the

assignment of Dieke and Crosswhite.[22] The scans speed is set to 0.12 Å/s averaging 30 shots/bin.

The similarities between the high and low pressures spectra suggest that the energetics associated with these vibrational bands is greater than the bond dissociation energy of MHP. In addition, the position of the two strong central peaks in the action spectrum in Figs. 6.3(a) and 6.3(b) agree fairly well with earlier results from the photoacoustic measurements of Homitsky *et al.*[23] However, unlike the photoacoustic spectrum which primarily reveals the excitation wavelengths absorbed by the sample, the action spectrum contains additional information arising from it being a convolution of the absorption probability and dissociation quantum yield. Thus the $5\nu_{OH}$ spectrum in Fig. 6.3 not only indicates that the CH_3OOH molecule absorbs light in the vicinity of 16 140 cm^{-1}, but additionally, it shows that after doing so it gains enough energy to dissociate and produce OH fragments.

The action spectra in Fig. 6.3 also provide information about the purity of our sample. Hydrogen peroxide, a common impurity, has strong spectral features associated with its $5\nu_{OH}$ band that appear at ~16 260 cm^{-1}.[12] The action spectrum of pure H_2O_2 taken under identical conditions to CH_3OOH is shown in Fig. 6.4(b). It is a well known fact that states in H_2O_2 not only undergoes thermally assisted predissociation but also show a strong decomposition via the one color two-photon dissociation in the fourth and third OH stretching overtone regions.[12] Thus, the absence of these features confirms that the level of this impurity is negligible. The assignment of vibrational transitions giving rise to the main spectral features in the action spectrum is indicated above the peaks in Fig.

6.3(a) and is based on the analysis of Homitsky *et al.*[23] A more rigorous vibrational band analysis is presented in Chapters 7 and 8.

The torsional potential of CH_3OOH in both its ground state, $0\nu_{OH}$ and its fourth OH stretching overtone state, $5\nu_{OH}$, support two types of torsional vibrational levels corresponding to wave-functions that are of symmetric (*S*) and anti-symmetric (*A*) symmetry. We use the standard notation S^j_i and A^j_i to indicate transitions between torsional levels of *S* or *A* symmetry which originate from the initial torsional level-i in the ground OH stretching state ($0\nu_{OH}$) and end up in the j^{th} torsional level of the vibrationally excited OH stretching state ($5\nu_{OH}$). Transitions from $A \rightarrow S$ and $S \rightarrow A$ account for about 10 % based on our torsion analysis presented in Chapter 7. Using this notation the feature at 16 142 cm^{-1} is assigned to transitions between initial and final levels without any torsional excitation; namely the S_0^0 and A_0^0 transitions. While the strong feature to the blue at 16 359 cm^{-1} corresponds to transitions originating from the ground state and ending up with one quantum of torsional excitation in the final $5\nu_{OH}$ level; namely the S_0^1 and A_0^1 transitions.

This assignment is also consistent with the bands appearing in the predissociation spectrum of MHP resulting from excitation in the $4\nu_{OH}$ region shown in Fig. 6.5(a). This spectrum is generated as before, by tuning our excitation laser and subsequently monitoring the formation of the OH fragment in its N=1 rotational state using LIF. The weaker signal-to-noise associated with the $4\nu_{OH}$ is due to several reasons. The first reason involves the fact that the $4\nu_{OH}$ band lies below the dissociation threshold (~2300 cm^{-1}) thus, the expected low dissociation quantum yield could lead to reduced signal levels.

This is consistent with the observation that the (S_0^1 / A_0^1) band which lies at a higher frequency, carries higher intensity than the pure OH stretching mode (S_0^0 / A_0^0). In addition, initial attempts to generate spectrum from the $4\nu_{OH}$ band have instead yielded interferences from one-color two-photon dissociation. This has forced us to increase the overtone excitation laser beam diameter which further reduced the intensity from this vibrational band. Fig. 6.5(b) shows the one-color two-photon spectrum of pure H_2O_2 sample in the third OH-stretching overtone region ($4\nu_{OH}$) under tight focusing conditions. After increasing the beam diameter, we estimate that the signal arising from the two-photon process is less than 0.1 %.

6.3.2 Fragment Energy Release from $4\nu_{OH}$ and $5\nu_{OH}$ Excitation

Based on gas phase enthalpy data[24] and the spectrum collected, the $5\nu_{OH}$ band lies above the dissociation threshold by at least ~1.5 kcal/mol. In contrast, the $4\nu_{OH}$ state lies ~6.6 kcal/mol below the dissociation limit. Thus, the fact that the $5\nu_{OH}$ is closer to the dissociation limit, in principle, may serve as a good probe of the dissociation fragment energy release of the OH + CH_3O channel. We have investigated the energy disposal associated with the $5\nu_{OH}$ initiated dissociation by monitoring the OH fragments resulting from excitation at both 16 142 cm^{-1} and 16 359 cm^{-1}. At these excitation frequencies we find that the dissociation resulting in OH production is prompt and is occurring on a time scale faster than 5 ns (the temporal resolution limit in our measurements).

Figures 6(a) and 6(b) show the rotational state distributions for the OH ($^2\Pi_{3/2}$, v=0) and ($^2\Pi_{1/2}$, v=0) states arising from excitation of the S_0^0 /A_0^0 and S_0^1/A_0^1 transitions. The average energy in OH rotation (averaged over both OH($^2\Pi_{2/3}$) and OH($^2\Pi_{1/2}$) spin-

orbit states) are 313 cm^{-1} for excitation of the S_0^0/A_0^0 spectral feature and 330 cm^{-1} for excitation of the S_0^1/A_0^1 band. These product states are generated by scanning the probe laser over the populated rotational states at 5 μsteps using the external BURST mode and 30 shots/bin averaging by the PROBE SCAN routine (see Appendix *A*). For the procedure on how to convert these OH rotational lines to population refer to Appendix *C*. The product states associated with these excitation energies (16 142 cm^{-1} and 16 359 cm^{-1}) are similar. For the OH($^2\Pi_{3/2}$, v=0), the distribution peaks at N=3 and slowly decreasing to where the last observed state is N=10. Similarly, the OH($^2\Pi_{1/2}$, v=0) distributions arising from the same excitation energy have a maxima at N=2 and monotonically decreasing to N=9. In the absent of a barrier along the reaction coordinate, OH product state distributions with maximum at N=1 suggest that the probed vibrational band lies below the dissociation threshold[25]. The fact that our distributions peak at N=3 indicate that the $5\nu_{OH}$ bands lie above the dissociation limit. Our measurements also indicate that no vibrationally excited OH (v=1) product is observed within our detection limit, consistent with bond dissociation energy and excitation at $5\nu_{OH}$.[24]

We obtain an estimate of the CH_3O-OH bond dissociation energy, D_0, by noting that the highest OH rotational level detected from excitation at 16 139 cm^{-1} and 16359 cm^{-1} is N=10. Applying energy conservation at this N level:

$$E_{therm}(CH_3OOH) + h\nu - D_0 = \qquad (6.2)$$

$$E_{int}(OH(N=10)) + E_{tran}(OH + CH_3O) + E_{int}(CH_3O)$$

In the above equation E_{trans} is the total translational energy of the two fragments, E_{int} is internal energy of the specified fragment, E_{therm} is the internal thermal energy of the room temperature parent molecule calculated using the ro-vibrational expressions:[26]

$$<E_{rot}> = \Sigma\,(2J+1) \times \varepsilon_i \times \exp[-\varepsilon_i / kT] \,/\, \Sigma\,(2J+1) \times \exp[-\varepsilon_i / kT] \qquad (6.3)$$

$$< E_{vib} >= k * \sum_{i=1}^{3*n-6} \left(\frac{\nu_j * Exp\left[-\frac{\nu_i}{kT}\right]}{1 - Exp\left[-\frac{\nu_i}{kT}\right]} \right) \qquad (6.4)$$

In the above equations k, T and ν_j are the respective Boltzmann constant, temperature and vibrational frequencies. We assume that CH_3OOH is a near prolate top ($\kappa = -0.914$). J is the angular momentum quantum number, ε_i is the rotational energy associated with a particular rotational state given by $\varepsilon_i = B\,J(J+1) + (A - C)K^2$. Where, K is the quantum number associated with the angular momentum projection onto the principle axis. *A*, *B*, *C* are the rotational constants of CH_3OOH. The code used in computing these average quantities is provided in Appendix *D*. For CH_3OOH we find that the room temperature internal energy is 630 cm^{-1} (with ~310 cm^{-1} in rotation and 320 cm^{-1} in vibration) using the *ab initio* frequencies and rotational constant given in Ref. 27. At excitation energy $h\nu$ = 16 142 cm^{-1}, assuming that the highest OH state observed from this excitation (v=0, N=10; E ≈ 2017 cm^{-1}) corresponds to the energtics limit and hence negligible translational and internal excitation of the CH_3O fragment, the dissociation energy is estimated through Eq. 6.2 to be $D_0 \approx 42.2$ kcal/mol. This value however is an upper bound estimate as there may be some small amounts of internal excitation associated with CH_3O fragments that correlate with the highest detected OH energy level.

We can also estimate the bond dissociation energy using the average values for the OH rotational product state distribution and fragment translational energy release. Measurement of the OH Doppler profile for the most populated states in the rotational distribution, N = 1 – 6, suggests that the OH + CH_3O fragments have population weighted average ~1400 cm^{-1} of relative translational excitation. The translational energy is obtained by scanning the probe laser over these OH rotational states at 3 μstep and 30 shots/bin averaging as discussed in Appendices *A* and *C*. Table 6.1 summarizes the translational energy obtained from these OH N-levels. Using the average value for the translational energy and the corresponding average OH fragment rotational energy (313 cm^{-1}) in Eq. 6.2, gives a value of ~43 kcal/mol for D_0. Thus our best estimate for the CH_3O–OH bond dissociation energy is ~ 42.6 ± 1 kcal/mol. Using this value for D_0 along with the corresponding experimental values for the heats of formation of OH (8.85 ± 0.07 kcal/mol) and CH_3O (6.8 ± 0.4 kcal/mol),[28,29] we estimate the heat of formation of CH_3OOH to be $\Delta H_f^0 = -27 \pm 1$ kcal/mol.

After completing characterizing the dissociation of methyl hydroperoxide from the fourth OH-stretching overtone, we proceed by investigating the energetics associated with excitation of $4\nu_{OH}$ bands. The nascent OH($^2\Pi_{3/2}$, v=0) product state distributions collected in that region for the $4\nu_{OH}$ and $4\nu_{OH} + \nu_{COOH}$ bands are shown in Fig. 6.7. These distributions are qualitatively different than those obtained at $5\nu_{OH}$ where about 60 % of the population is at N=1. N=2 and 3 rotational states carry the rest of population (~30 %) which rapidly decreasing to where the last observable state is N=5 ($E_{N=5}$ ~ 545 cm^{-1}). These trends in the distributions suggest that unlike the$5\nu_{OH}$ region, the $4\nu_{OH}$ bands are

energetically deficient confirming that indeed these bands lie below the dissociation threshold (~1600 cm^{-1}). These findings are consistent with our D_0 value inferred from the $5\nu_{OH}$ region. Due to poor signal levels, we are unable to obtain nascent OH product state distributions for the $^2\Pi_{1/2}$ spin-orbit state which has a small fraction of the total population.

The plot in Fig. 6.7 also shows the subtle differences in the OH rotational distributions resulting from excitation of the S_0^0/A_0^0 and S_0^1/A_0^1 at 13 292.4 cm^{-1} and 13 473.6 cm^{-1} respectively. The torsional state has slightly less population in the N=1 OH rotational state and slightly more population in the N=2 rotational state. This suggests a warmer distribution for the torsional state which is similar to the situation in the $5\nu_{OH}$ region. These warmer torsional OH product state distributions in essence convey that these energy differences are due to the fact that the S_0^1/A_0^1 are ~180 cm^{-1} and ~220 cm^{-1} higher in energy in the third and fourth OH stretching overtones regions respectively. This also indicates that the origin of these transitions is the S_0/A_0 *and not* transitions originating from torsionally excited hot bands such as S_1/A_1, S_2/A_2 *etc*. These transitions are expected to carry additional internal energy which would materialize in the OH product state distributions and translational energy release.

6.3.3 *Ab initio* Determination of CH_3OOH Thermochemistry

We next compare the experimental CH_3O–OH bond energy and heat of formation with results from *ab initio* calculations carried out at the CCSD(T)/CBS limit.
All electronic structure calculations are carried out using the GAUSSIAN03 program implementing the CCSD(T) method in a similar manner described in Chapter 3 for PNA.[16-18] As before, in order to ascertain that the CCSD(T) method is sufficiently

accurate to be implemented for D_0 calculation of MHP, we compare its results with the QCISD(T) method using Dunning's basis sets cc-PVξZ (ξ = D, T, Q) and aug-cc-pVξZ (ξ = D, T).[19,20] A sample Z-matrices inputs at the CCSD(T)/cc-pVξZ (ξ = D, T, Q) levels are provided in Table 6.2. For keywords description and tutorial on running GAUSSIAN03 on the workstations refer to Appendix *B*. The equilibrium geometries and energies of the QCISD(T) and CCSD(T) calculations are shown in Table 6.3. Looking at the table we find that both methods produce near identical geometries and energies for a given basis-set suggesting that both methods are likely to converge similarly in a CBS calculation. We can also compare the *ab initio* structure of MHP to the experimental structure by comparing the calculated rotational constants with available microwave data.[27] Table 6.4 shows that the deviations in the *A*, *B* and *C* rotational constants for the QCISD(T)/cc-pVQZ method are 0.4 %, 0.7 % and 1.4 % respectively and for the CCSD(T)/cc-pVQZ method the respective deviations are 0.3 %, 0.8 % and 1.5 %. This again, suggests good agreement between experiments and *ab initio* theories.

As shown in Chapter 3 with PNA, we use the isodesmic reaction 6.1 in order to estimate the heat of formation for methyl hydroperoxide. Since isodesmic reactions preserve the number and types of bonds in going from reactants to products, they typically lead to favorable cancellation of errors in the calculated energies arising from deficiencies in the basis set and the presence of electron correlation. We optimize the structure for each species involved in the isodesmic reaction at the CCSD(T) level using the cc-pVξZ (ξ = D, T, Q).[19,20] The energies and the zero-point corrections for the species in reaction 6.1 are provided in Table 6.5. We extrapolate the CCSD(T) total energies to

the complete basis set (CBS) limit, using the 3-parameter mixed exponential/Gaussian function of the form:

$$E(n) = A(\infty) + B \exp[-(n-1)] + C \exp[-(n-1)^2] \quad (6.5)$$

This extrapolation function is appropriate when energies computed with basis sets ranging from cc-pVDZ , cc-pVTZ, and cc-pVQZ (corresponding to n = 2, 3, and 4 respectively) are available.[30] The 3-parameter non-linear solver is included in Appendix *D*.

To back out the heat of formation of CH_3OOH from the above isodesmic reaction, the heat of formation of H_2O, HOOH and CH_3OH are required. The experimental values for these in kcal/mol are H_2O (-57.10 ± 0.10), HOOH (-31.02 ± 0.05), and CH_3OH (-45.4 ± 0.1).[31] The enthalpy of reaction for the isodesmic reaction predicted using the various basis sets and the corresponding heat of formation of CH_3OOH extracted from them, are summarized in Table 6.6 and obtained by noting that:

$$\Delta H_r^0 = \Sigma \text{ E[products]} - \Sigma \text{ E[reactants]} \quad (6.6)$$

$$\Delta H_f^0 [CH_3OOH] = \Delta H_f^0 [H_2O_2] + \Delta H_f^0 [CH_3OH] - \Delta H_f^0 [H_2O] - \Delta H_r^0 \quad (6.7)$$

Where the Σ E[products] term is the sum of the energies of H_2O_2 and CH_3OH and the Σ E[reactants] term is the sum of the CH_3OOH and H_2O energies (including the ZPE corrections). From the table we see that the CCSD(T)/cc-pVQZ level of theory is essentially converged as determined by the fact that the difference between the CCSD(T)/cc-pVQZ and the CCSD(T)/CBS-∞ result for the heat of formation of CH_3OOH is only 0.1 kcal/mol. From this computational analysis we conclude that our best theoretical estimate for the heat of formation, ΔH_f^0, of CH_3OOH is –27.3 kcal/mol.

Using this value for $\Delta H_f^0[CH_3OOH]$ along with the corresponding experimental ΔH_f^0 values for the OH and CH_3O fragments, the theoretical bond dissociation energy for the CH_3O-OH is found to be 43.0 kcal/mol. This value is in good agreement with the experimental value found through the OH product state distribution measurements.

We can also test the viability of the *ab initio* results by comparing the isodesmic reaction scheme to the direct method. In the direct method, D_0 is determined by calculating the energies and ZPEs of the species in the reaction below:

$$CH_3OOH \rightarrow OH + CH_3O \qquad (6.8)$$

Reaction 6.8 is a computational challenge since it directly comparing the energy of the parent molecule in a singlet state with fragment molecules in doublet states. This can potentially lead to un-cancelable errors associated with spin contamination for the OH and CH_3O fragments. Even though this method is not as accurate as the isodesmic reaction method, it can be used in a sense as an *ab initio* "accuracy gauge meter".

As with CH_3OOH, the hydroxyl and methoxy radicals equilibrium and ZPE energies are calculated with the UCCSD(T)/cc-pVξZ (ξ = D, T, Q).[19,20,30] The spin unrestricted CCSD(T) wavefunctions are appropriate for open shell species. The input Z-matrices for the OH and CH_3O are provided in Tables 6.7 and 6.8 respectively. Their energies are summarized in Table 6.9. In order to obtain the CH_3O-OH dissociation energy, we take energy differences of products and reactant which are shown in the last column in the table for a given level of theory. We also obtain the (U)CCSD(T)/CBS using the non-linear fit and extracting the parameter $A(\infty)$ in Eq. 6.5.30 The agreement between the two methods (isodesmic and direct) is excellent. Recall that the isodesmic reaction provide D_0 value of 43 kcal/mol while the direct method gives a value of 42.7

kcal/mol at the CCSD(T)/CBS level. These values are also in remarkable agreement with the experimental average value of 42.6 kcal/mol.

6.4 Summary

Vibrational overtone excitation is used to initiate unimolecular decomposition of CH_3OOH by exciting the molecule in the vicinity of its $4\nu_{OH}$ and $5\nu_{OH}$ bands. The measured energy disposal in the OH fragment from the dissociation at $5\nu_{OH}$ provides an estimate of the CH_3O-OH bond dissociation energy of $D_0[CH_3O\text{-}OH] = 42.6$ kcal/mol (see Fig. 6.6 and Table 6.1). This value is also consistent with the OH fragment rotational product state distributions arising from excitation in the $4\nu_{OH}$ region (Fig. 6.7). The fact that the entire $4\nu_{OH}$ region lies below the dissociation limit (~1600 cm^{-1}) results in rotationally "cold" OH product state distributions. We can estimate the dissociation quantum yield, Φ, using the expression:

$$\Phi = \exp[(h\nu + E_{rot} - D_0)/kT] \qquad (6.9)$$

In the above equation, $h\nu$ is the photon excitation energy, E_{rot} it the MHP average rotational energy calculated at room temperature to be ~310 cm^{-1}. Taking the excitation energies for the $4\nu_{OH}$ and $4\nu_{OH} + \nu_{COOH}$ bands to be 13 292.4 cm^{-1} and 13 473.6 cm^{-1} and noting that both bands (S_0^0/A_0^0 and S_0^1/A_0^1) originate from the ground vibrational state of MHP, we find that $\Phi[4\nu_{OH}] \approx 0.2$ % and $\Phi[4\nu_{OH} + \nu_{COOH}] \approx 0.5$ %. These values suggest that under atmospheric conditions, photodissociation of methyl hydroperoxide resulting from $4\nu_{OH}$ excitation is tenuous compared with photo-initiated dissociation from $5\nu_{OH}$ region. Chapter 10 provides analysis on the importance of photo-initiated dissociation of MHP under atmospheric conditions.

The bond dissociation energy suggests that at 0 K, the heat of formation is ΔH_f^0 [CH_3OOH] = −27 ± 1 kcal/mol. This value for the heat of formation is in good agreement with results of *ab initio* calculations which, at the CCSD(T)/CBS and isodesmic reaction (see Eq. 6.1) finds ΔH_f^0 [CH_3OOH] = −27.3 kcal/mol. Similarly, the direct method (see Eq. 6.8) predicts the heat of formation of CH_3OOH to be ΔH_f^0 [CH_3OOH] = –27.1 kcal/mol. Applying a thermal correction to the *ab initio* heat of formation at 0 K, we obtain a value of ΔH_f^{298} [CH_3OOH] = −30.4 kcal/mol for its isodesmic reaction value and ΔH_f^{298} [CH_3OOH] = −30.2 kcal/mol for its direct method at 298 K. Applying the same correction factor to the experimental results gives the experimental heat of formation at 298 K to be ΔH_f^{298} [CH_3OOH] = −30.1 ± 1 kcal/mol. Comparing the present experimental heat of formation results with data appearing in Ref. 31 (ΔH_f^{298} [CH_3OOH] = −31.3 kcal/mol), this value is slightly too low compared to the present value by about 1.2 kcal/mole. On the other hand, the value recommended by the atmospheric database,[24] ΔH_f^{298} [CH_3OOH] = −33.2 kcal/mol (based on the work of Ref. 32) is lower then our measured value by 3.1 kcal/mol.

Lastly, an interesting observation not addressed in this chapter regarding the $4\nu_{OH}$ and $5\nu_{OH}$ bands shape. These bands exhibit significant structure due to torsional activity. Studies on methanol, hydrogen peroxide and peroxynitic acid indicate that this behavior is unique to methyl hydroperoxide. These issues will be addressed in the following chapters where we examine the spectroscopy of the vibrational overtones of CH_3OOH.

6.5 Acknowledgements

Chapter 6, in part, is a reprint of the material as it appears in Journal of Chemical Physics 122, 221101 (2005). J. Matthews, J. S. Francisco, and A. Sinha, American Institute of Physics, 2005. The dissertation author was the primary investigator and author of this paper.

Table 6.1: Fragment Energy Disposal CH_3OOH ($5\nu_{OH}$ region) → OH + CH_3O [a]

Band / Excitation	OH N-level	OH Population	Translational Total	Population Weighted Translational[b]
S_0^0 / A_0^0 (16 139 cm^{-1})	1	0.16	998	160
	2	0.19	1321	251
	3	0.24	2177	523
	4	0.19	1210	230
	5	0.13	1121	146
	6	0.04	794	32
Σ				1342
S_0^1 / A_0^1 (16 356 cm^{-1})	1	0.13	1174	154
	2	0.18	1546	278
	3	0.24	2494	588
	4	0.22	1581	349
	5	0.14	986	135
	6	0.04	790	46
Σ				1551

[a] In cm^{-1}.

[b] The translational energy in a particular OH level is multiplied by its OH N-level normalized population to obtain the weighted translational energy associated with a particular rotational state. We then sum the contribution to obtain the total weighted translational energy.

Table 6.2: CH_3OOH Z-matrices Used with CCSD(T)/cc-pVξZ (ξ = D, T, Q) Calculations

CCSD(T) /cc-pVDZ

#p ccsd(t,maxcyc=300)/cc-pvdz scf=(direct,tight) trans=iabc opt= ef freq=noraman

CH3OOH optimization and ZPE at ccsd(t)/cc-pvdz

0 1
C
O,1,r1
O,2,r2,1,a1
H,3,r3,2,a2,1,d1,0
H,1,r4,2,a3,3,d2,0
H,1,r5,2,a4,3,d3,0
H,1,r6,2,a5,3,d4,0
Variables:
r1=1.43225505
r2=1.47961411
r3=0.97235865
r4=1.10424861
r5=1.10578389
r6=1.10457794
a1=104.73897209
a2=99.43661444
a3=104.4336185
a4=111.05983384
a5=110.60927617
d1=114.73360406
d2=177.41762582
d3=-63.78608253
d4=58.96125574

CCSD(T) /cc-pVTZ

#p ccsd(t,maxcyc=300)/cc-pvtz scf=(direct,tight) trans=iabc opt=(ef,readfc) geom=check guess=read

CH3OOH optimization at ccsd(t)/cc-pvtz

0 1

CCSD(T) /cc-pVQZ

#p ccsd(t,Maxcyc=300)/cc-pvqz scf=(direct,tight) trans=iabc opt=(ef,readfc) freq=noraman geom=check guess=read

CH3OOH optimization at ccsd(t)/cc-pvqz

0 1

Table 6.3: Equilibrium Geometry Parameters for CH_3OOH (Distances in Å, Angles in degrees)

	QCISD(T)					CCSD(T)				
	cc-pVDZ	aug-cc-pVDZ	cc-pVTZ	aug-cc-pVTZ	cc-pVQZ	cc-pVDZ	aug-cc-pVDZ	cc-pVTZ	aug-cc-pVTZ	cc-pVQZ
r(H-O)	0.973	0.973	0.965	0.967	0.964	0.973	0.972	0.965	0.967	0.964
r(O-O)	1.469	1.480	1.457	1.462	1.453	1.469	1.480	1.457	1.462	1.453
r(O-C)	1.420	1.433	1.417	1.421	1.415	1.419	1.432	1.417	1.421	1.415
r(C-H1)	1.105	1.104	1.091	1.092	1.090	1.105	1.104	1.091	1.092	1.090
r(C-H2)	1.109	1.106	1.093	1.094	1.092	1.108	1.106	1.093	1.094	1.092
r(C-H3)	1.107	1.105	1.092	1.092	1.091	1.107	1.105	1.092	1.092	1.091
∠(HOO)	98.8	99.5	99.6	99.8	99.9	98.8	99.4	99.6	99.8	99.9
∠(OOC)	105.0	104.8	104.9	105.3	105.4	105.0	104.8	105.3	105.3	105.4
∠(OCH1)	104.8	104.4	105.3	104.6	104.8	104.8	104.4	104.9	104.6	104.8
∠(OCH2)	111.7	111.1	111.4	111.2	111.3	111.7	111.1	111.4	111.2	111.3
∠(OCH3)	111.4	110.6	111.0	110.7	110.8	111.4	110.6	111.0	110.7	110.8
τ(HOOC)	116.8	114.4	113.9	116.3	114.4	117.2	114.7	113.9	116.3	114.7
τ(H1COO)	177.8	177.5	177.4	177.1	177.1	177.7	177.4	177.4	177.1	177.1
τ(H2COO)	-63.4	-63.7	-63.8	-64.0	-64.1	-63.5	-63.8	-63.8	-64.0	-64.1
τ(H3COO)	59.3	59.0	58.9	58.7	58.6	59.2	59.0	58.9	58.7	58.6
E (hartree)	-190.38359	-190.43806	-190.58831	-190.60659	-190.64896	-190.38326	-190.43745	-190.58767	-190.60587	-190.64831

Table 6.4: Equilibrium Rotational Constants of CH_3OOH

		Rotational constants (cm^{-1})[a]		
Method	**Basis Set**	***A***	***B***	***C***
QCISD(T)	**cc-pVDZ**	**1.390766**	**0.348796**	**0.302228**
	aug-cc-pVDZ	**1.368516**	**0.345326**	**0.298931**
	cc-pVTZ	**1.414872**	**0.352079**	**0.305628**
	aug-cc-pVTZ	**1.410666**	**0.350054**	**0.303698**
	cc-pVQZ	**1.422678**	**0.352743**	**0.306377**
CCSD(T)	**cc-pVDZ**	**1.391659**	**0.348906**	**0.302291**
	aug-cc-pVDZ	**1.369296**	**0.345461**	**0.299024**
	cc-pVTZ	**1.414872**	**0.352079**	**0.305628**
	aug-cc-pVTZ	**1.410666**	**0.350054**	**0.303698**
	cc-pVQZ	**1.423864**	**0.352921**	**0.306521**
Expt.[b]		**1.428604**	**0.350249**	**0.302044**

[a] Calculated constants correspond to equilibrium structure while experimental values are for vibrational ground state.

[b] From Ref. 27, the values are for the $|0, 0^+>$ state.

Table 6.5: Sum of Electronic and ZPE[a] for Species in the Isodesmic Reaction:
$CH_3OOH + H_2O \rightarrow H_2O_2 + CH_3OH$

Method	H_2O[b]	H_2O_2[c]	CH_3OH[d]	CH_3OOH[e]
CCSD(T)/cc-pVDZ	**-76.219800**	**-151.167856**	**-115.369284**	**-190.328703**
CCSD(T)/cc-pVTZ	**-76.310712**	**-151.332447**	**-115.499289**	**-190.533118**
CCSD(T)/cc-pVQZ	**-76.338293**	**-151.382055**	**-115.537436**	**-190.593811**
CCSD(T)/CBS	**-76.353789**	**-151.409889**	**-115.558719**	**-190.627758**

[a] From CCSD(T)/cc-pVDZ level of theory in hartree units.

[b] ZPE[H_2O] = 0.021505 E_h

[c] ZPE[H_2O_2] = 0.026164 E_h

[d] ZPE[CH_3OH] = 0.051497 E_h

[e] ZPE[CH_3OOH] = 0.054556 E_h

Table 6.6: Thermochemistry of CH_3OOH using the isodesmic reaction: [a]
$CH_3OOH + H_2O \rightarrow H_2O_2 + CH_3OH \quad \Delta H_r^o$

	ΔH_r^o	$\Delta H_f^o(CH_3OOH)$	$D_0(CH_3O–OH)$
CCSD(T)/cc-pVDZ	**7.1**	**-26.4**	**42.05**
CCSD(T)/cc-pVTZ	**7.6**	**-26.9**	**42.55**
CCSD(T)/cc-pVQZ	**7.9**	**-27.2**	**42.85**
CCSD(T)/CBS	**8.0**	**-27.3**	**42.95**

[a] In units of kcal/mol

Table 6.7: OH Z-matrices Used with UCCSD(T)/cc-pVξZ (ξ = D, T, Q) Calculations

UCCSD(T) /cc-pVDZ
#p uccsd(t,maxcyc=300)/cc-pvdz scf=(direct,tight) trans=iabc opt= ef freq=noraman OH optimization and ZPE at ccsd(t)/cc-pvdz 0 2 H O,1,r1 Variables: r1=1.43225505
UCCSD(T) /cc-pVTZ
#p uccsd(t,maxcyc=300)/cc-pvtz scf=(direct,tight) trans=iabc opt=(ef,readfc) geom=check guess=read OH optimization at ccsd(t)/cc-pvtz 0 2
UCCSD(T) /cc-pVQZ
#p uccsd(t,Maxcyc=300)/cc-pvqz scf=(direct,tight) trans=iabc opt=(ef,readfc) freq=noraman geom=check guess=read OH optimization at ccsd(t)/cc-pvqz 0 2

Table 6.8: CH_3O Z-matrices Used with UCCSD(T)/cc-pVξZ (ξ = D, T, Q) Calculations

UCCSD(T) /cc-pVDZ

```
#p uccsd(t,maxcyc=300)/cc-pvdz  scf=(direct,tight) trans=iabc opt= ef
freq=noraman

CH3O optimization and ZPE at ccsd(t)/cc-pvdz

0 2
O
C,1,rco
H,2,rh1,1,ah1
H,2,rh2,1,ah2,3,dh2,0
H,2,rh2,1,ah2,3,-dh2,0
     Variables:
rco=1.38113903
rh1=1.11662085
rh2=1.11134698
ah1=105.20607558
ah2=113.2667189
dh2=116.40550173
```

UCCSD(T) /cc-pVTZ

```
#p uccsd(t,maxcyc=300)/cc-pvtz  scf=(direct,tight) trans=iabc
opt=(ef,readfc) geom=check guess=read

CH3O optimization at ccsd(t)/cc-pvtz

0 2
```

UCCSD(T) /cc-pVQZ

```
#p uccsd(t,Maxcyc=300)/cc-pvqz  scf=(direct,tight) trans=iabc
opt=(ef,readfc) freq=noraman geom=check guess=read

CH3O optimization at ccsd(t)/cc-pvqz

0 2
```

Table 6.9: Sum of Electronic and ZPE[a] for Species in the Reaction:
$CH_3OOH \rightarrow OH + CH_3O$

Method	CH_3OOH[b]	OH[c]	CH_3O[d]	D_0[f]
CCSD(T)/cc-pVDZ	**-190.328703**	**-75.550917**	**-114.718381**	**37.3**
CCSD(T)/cc-pVTZ	**-190.533118**	**-75.629286**	**-114.837862**	**41.4**
CCSD(T)/cc-pVQZ	**-190.593811**	**-75.653196**	**-114.873238**	**42.3**
CCSD(T)/CBS	**-190.627758**	**-75.666645**	**-114.893013**	**42.7**

[a] From CCSD(T)/cc-pVDZ level of theory in hartree units.

[b] ZPE[CH_3OOH] = 0.054556 E_h

[c] ZPE[OH] = 0.008438 E_h

[d] ZPE[CH_3O] = 0.036956 E_h

[f] In units of kcal/mol.

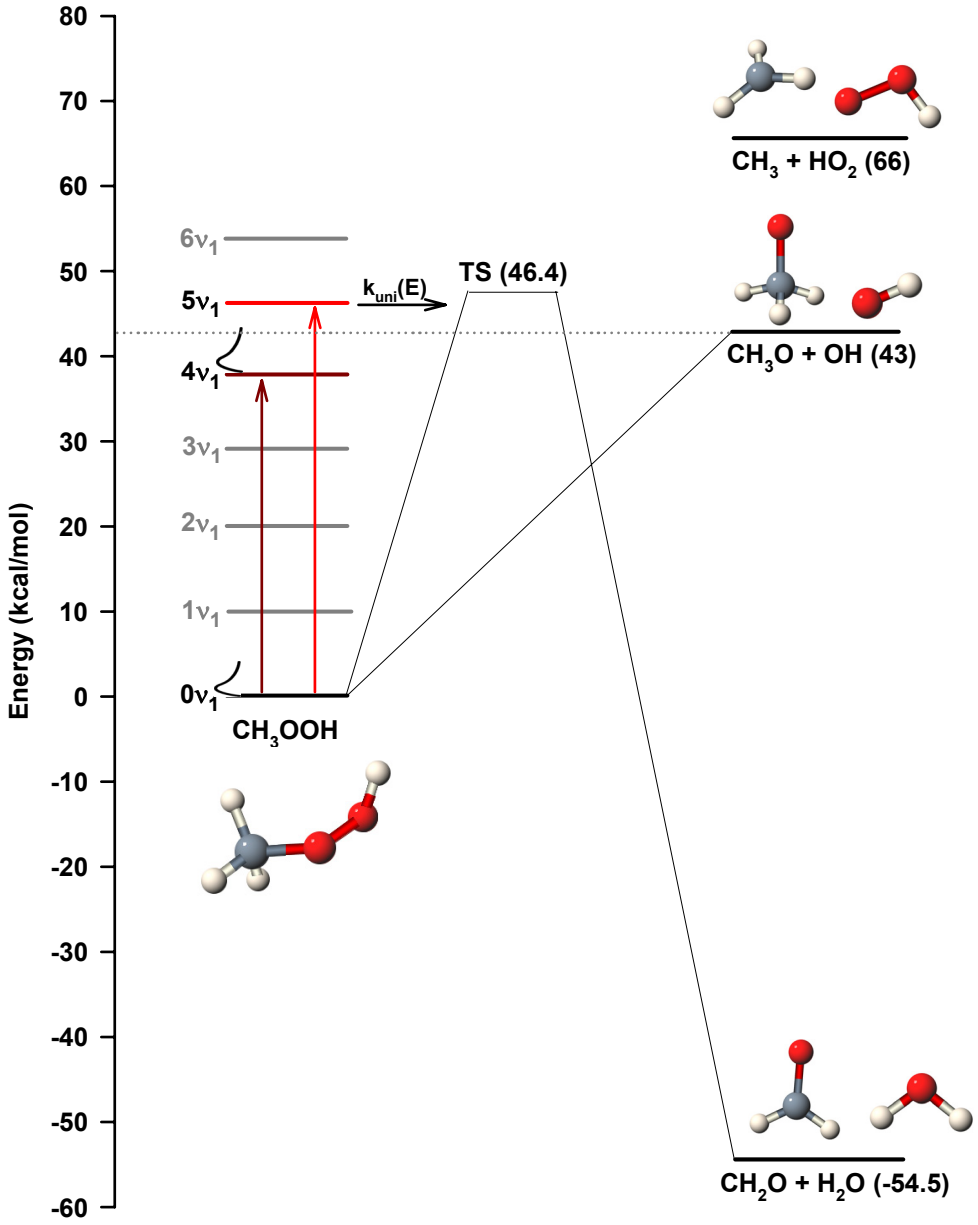

Figure 6.1: Schematic energy level diagram showing the energy associated with the various OH stretching overtone levels of CH_3OOH and its lowest energy pathways for unimolecular decomposition. The dashed line in the figure represents the threshold energy for dissociation into the OH + CH_3O fragments. The energy of the transition state associated with the molecular elimination channel is obtained using the CBS-APNO method from Ref.11. [File: F6.1_ped]

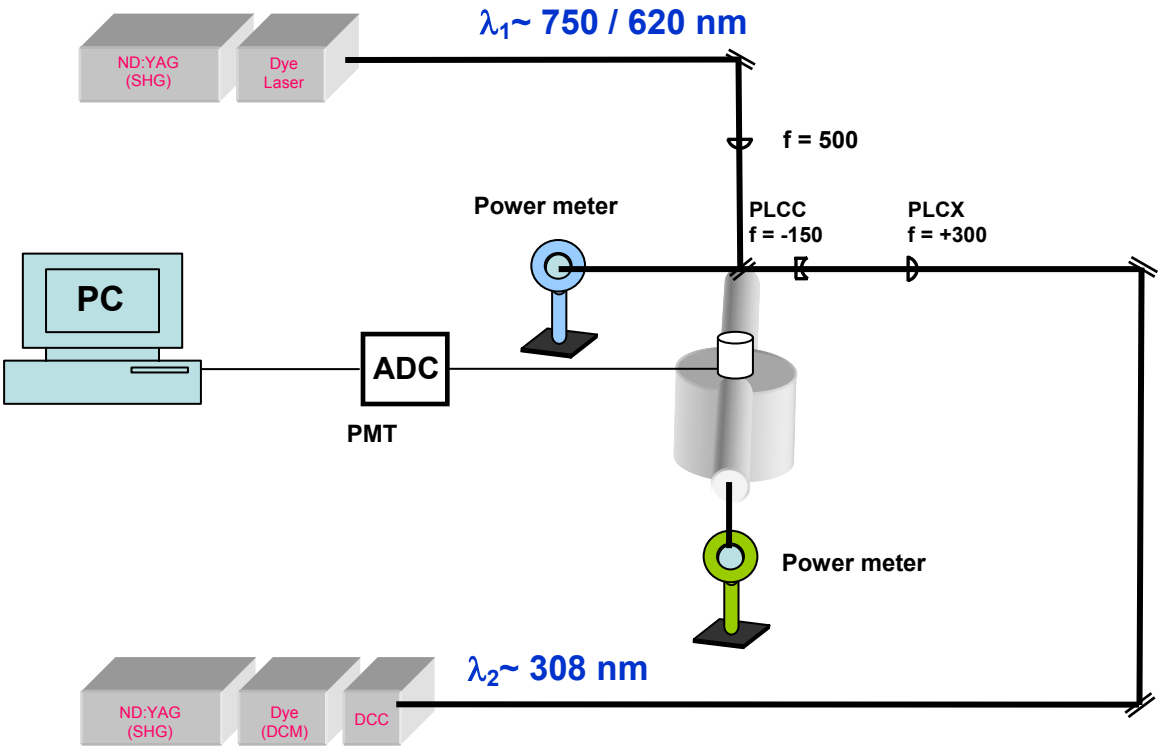

Figure 6.2: Schematic of the experimental apparatus. The tunable VIS. and near IR radiation used for the vibrational excitation (λ_1) is generated by the dye laser system and the U.V. radiation used to probe the OH transition via the $A - X(0,0)$ diagonal transition is generated by the doubled output of a second dye laser (λ_2). The temporal delay between the pump and probe lasers is set to 15 ns and the probe laser is counter propagating to the IR laser. A set of plano-convex (+300 mm) and plano-concave (-150 mm) lenses collimate the probe beam to reduce scatter light. [File: F6.2_apparatus]

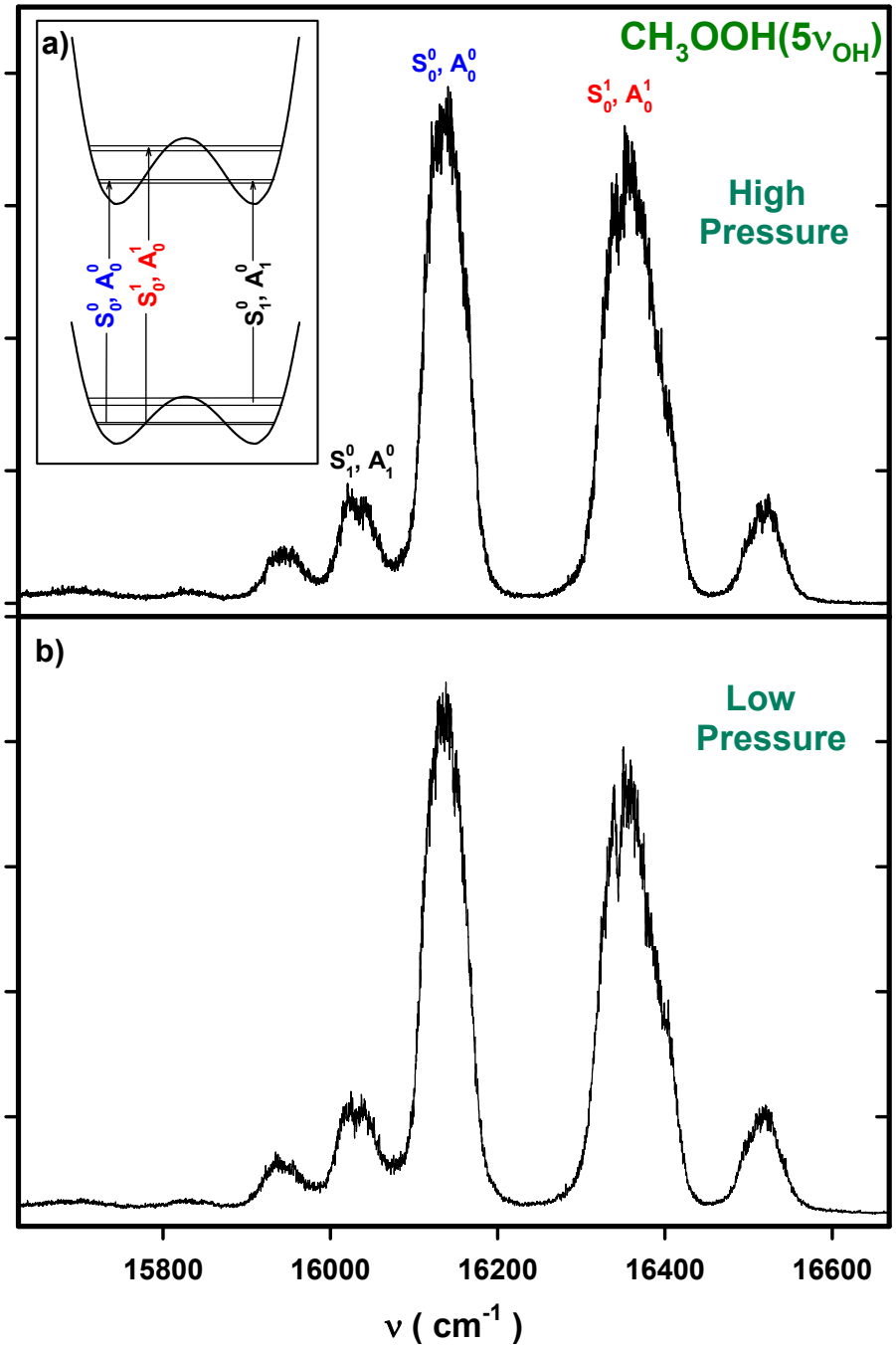

Figure 6.3: Vibrational overtone action spectrum of the CH_3OOH $5\nu_{OH}$ band obtained by monitoring a) the OH ($^2\Pi_{3/2}$, N=2) fragments under "high" pressure conditions and b) the OH ($^2\Pi_{3/2}$, N=3) fragments under low pressure conditions The inset shows a schematic of the ground and excited state torsional potential and the transitions under consideration. Each torsional level corresponds to two closely spaced states one that is symmetric (*S*) and the other anti-symmetric(*A*) relative to reflection through the middle of the potential. The assignments shown are based on Ref. 23. [File: F6.3_5nu]

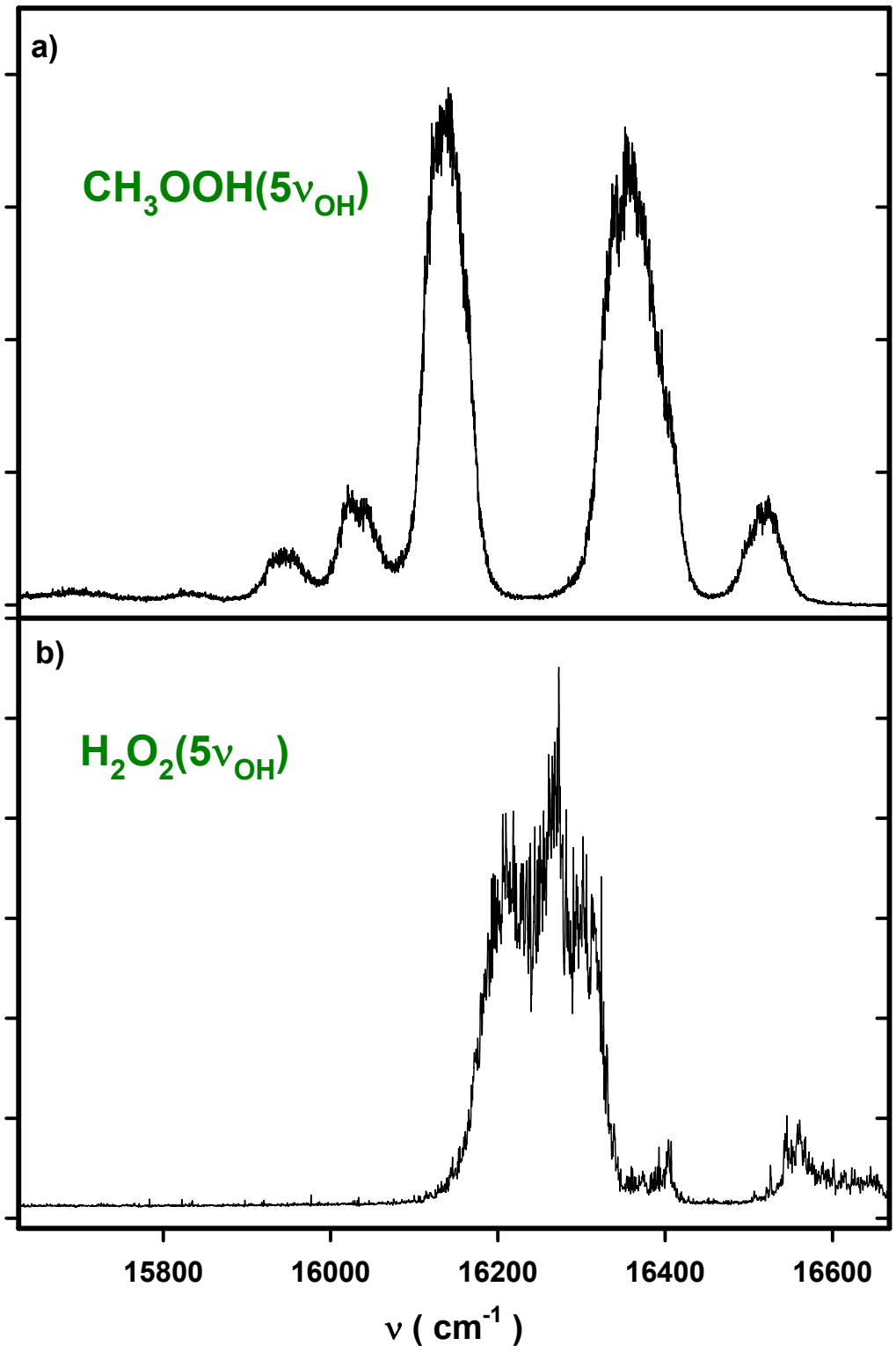

Figure 6.4: a) Vibrational overtone action spectrum of the CH_3OOH $5\nu_{OH}$ band. b) Vibrational overtone action spectrum of the HOOH $5\nu_{OH}$ band. The figure shows that HOOH, a common impurity, *is not* present in our MHP sample. [File: F6.4_5nu_h2o2]

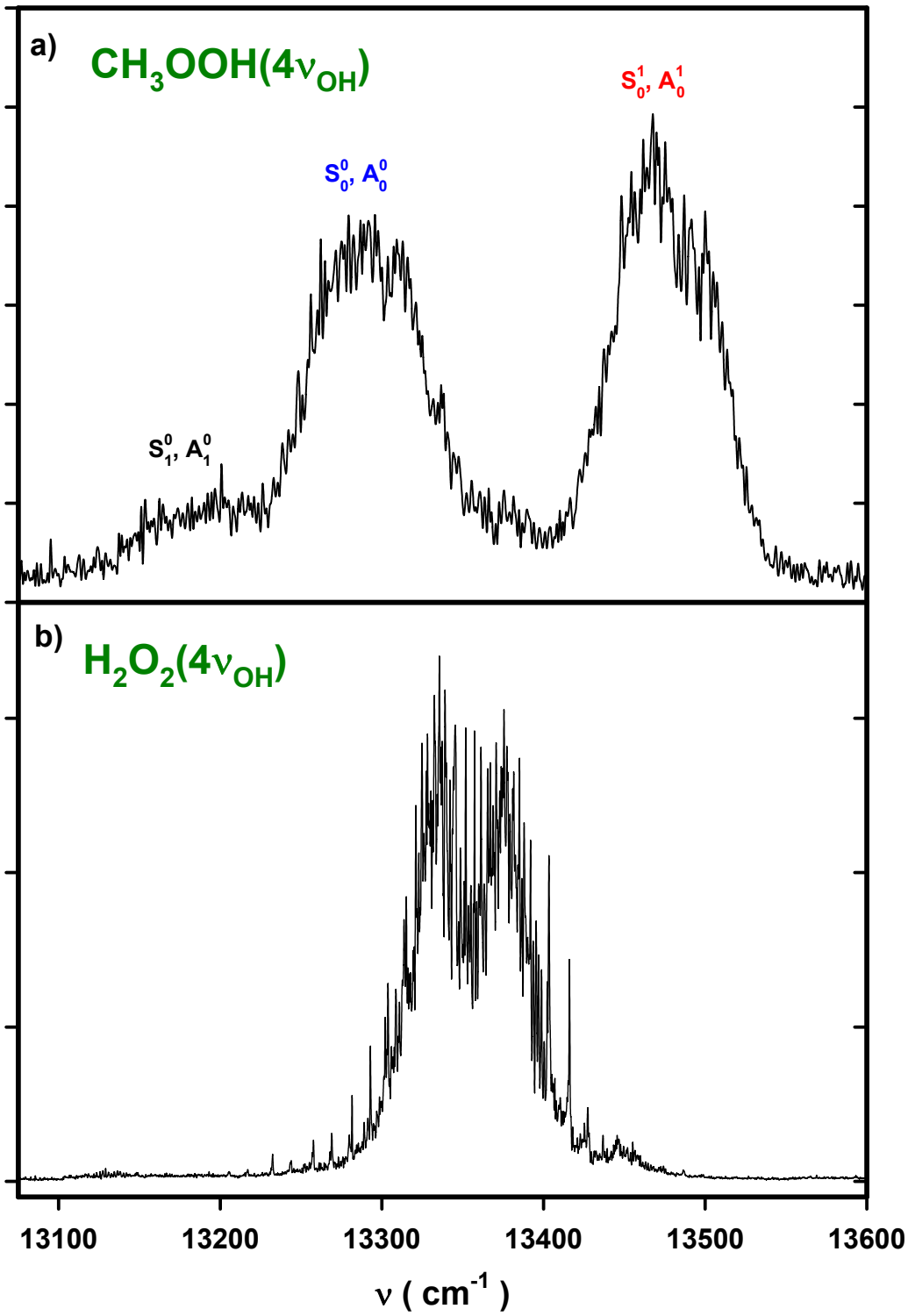

Figure 6.5: a) Vibrational overtone action spectrum of the CH_3OOH $4\nu_{OH}$ band obtained by monitoring the nascent OH ($^2\Pi_{3/2}$, N=1) fragments. b) One-color two-photons vibrational overtone action spectrum of "pure" HOOH $4\nu_{OH}$ band obtained by monitoring OH ($^2\Pi_{3/2}$, N=5) fragments. [File: F6.5_4nu_h2o2]

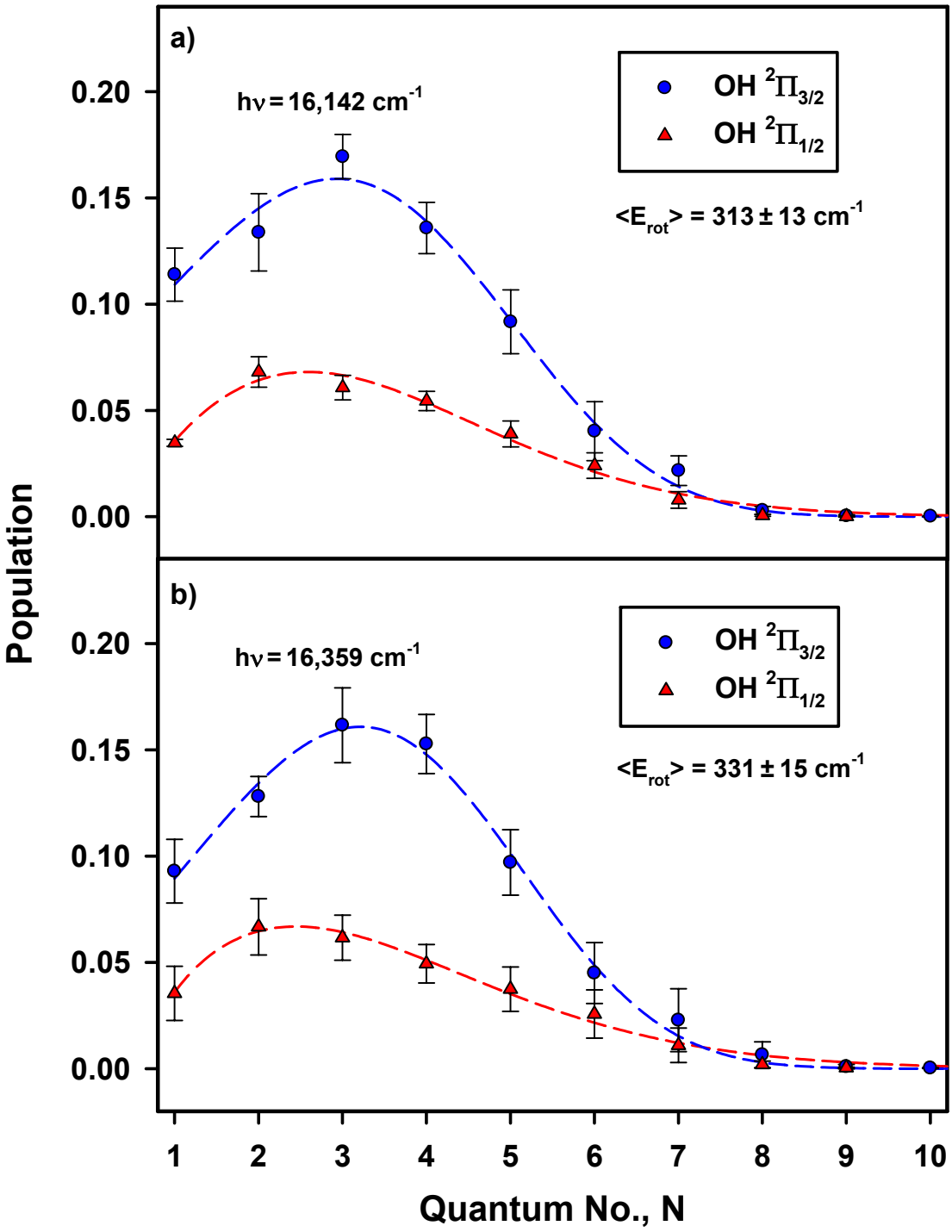

Figure 6.6: The nascent rotational product state distributions OH($^2\Pi_{3/2}$) indicated by the closed circles and OH ($^2\Pi_{1/2}$) indicated by the closed triangles from excitation of features a) S_0^0/A_0^0 and b) S_0^1/A_0^1. [File: F6.6_psd_5nu]

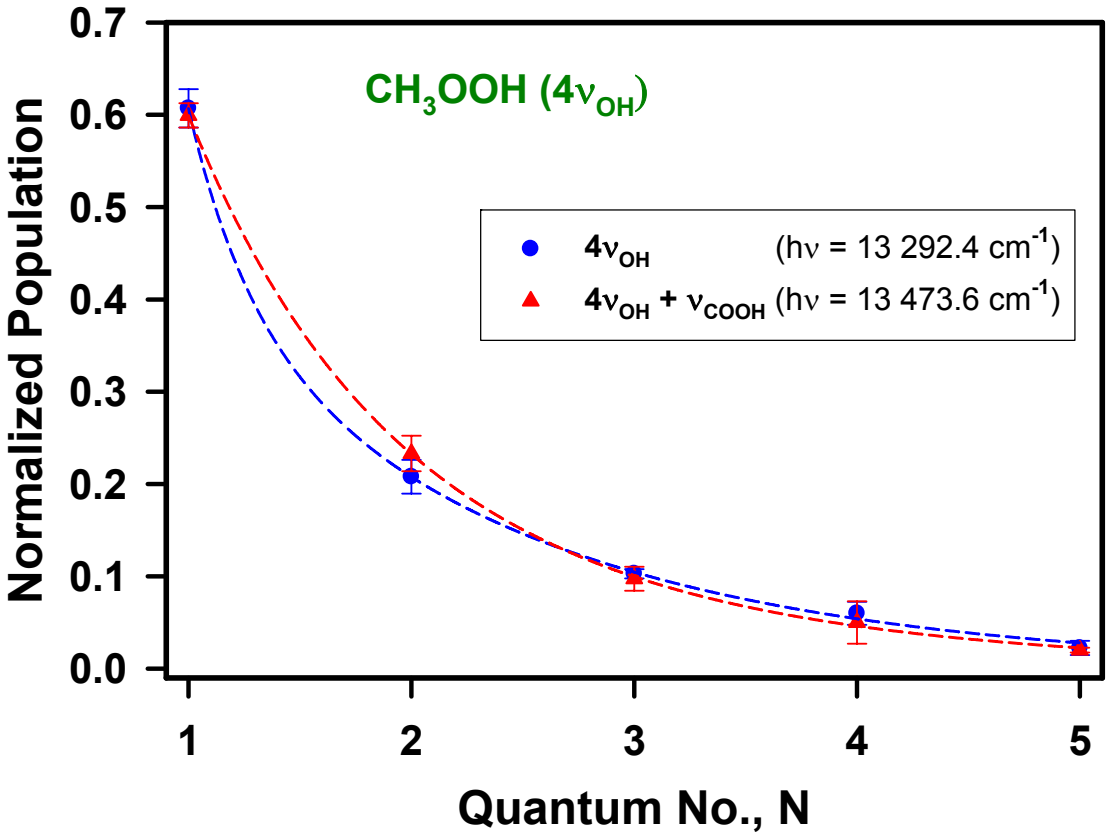

Figure 6.7: The nascent rotational product state distributions OH($^2\Pi_{3/2}$). The closed circles are for excitation with in the S_0^0/A_0^0 band at 13 292 cm^{-1} while the closed triangles are for excitation with the S_0^1/A_0^1 band at 13 474 cm^{-1}. [File: F6.7_psd_4nu]

6.6 References

1. J. D. Watts and J. S. Francisco, J. Chem. Phys. **125**, 104301 (2006).

2. G. P.Brasseur, J. J. Orlando, & G. S.Tyndall, *Atmospheric Chemistry and Global Change* (Oxford University Press, New York, 1999).

3. L. Jaegle′, *et al.*, J. Geophys. Res. **105**, 3877 (2000).

4. M. J. Prather and D. J. Jacob, Geophys. Res. Lett. **24**, 3189 (1997).

5. L . Jaegle′, *et al.,* Geophys. Res. Lett. **24**, 3181 (1997).

6. F. Ravetta, *et al.*, J. Geophys. Res.-Atmos. **106(D23)**, 32709 (2001).

7. M. J. Molina and G. Arguello, Geophys. Res. Lett. **6**, 953 (1979).

8. G. L. Vaghijiani and A. R. Ravishankara, J. Geophys. Res. **94**, 3487 (1989).

9. G. L.Vaghijiani and A. R. Ravishankara, J. Chem. Phys. **92**, 996 (1990).

10. M. A. Thelen, P. Felder, & J. R. Huber, Chem. Phys. Lett. **213**, 275(1993).

11. J. S. Francisco (to be published).

12. T. M. Ticich, M. D. Likar, H. –R. Dübal, L. J. Butler, F. F. Crim, J. Chem. Phys. **87**, 5820 (1987).

13. O. V. Boyarkin, L. Lubich, R. D. F. Settle, D. S. Perry, T. R. Rizzo, J. Chem Phys. **107**, 8409 (1997).

14. R. B. Chatfield and P. J. Crutzen, J. Geophys. Res. **95**, 22319 (1990).

15. L. Jaeglé, D. J. Jacob, P. O. Wennberg, C. M. Spivakovsky, T. F. Hanisco, E. J. Lanzendorf, E. J. Hintsa, D. W. Fahey, E. R. Keim, M. H. Proffitt, E. L. Atlas, F. Flocke, S. Schauffler, C. T. McElroy, C. Midwinter, L. Pfister, and J. C. Wilson, Geophys. Res. Lett. **24**, 3181 (1997).

16. M. J. Frisch G. W. Trucks, H. B. Schlegel, G. E. Scuseria, M. A. Robb, J. R. Cheeseman, J. A. Montgomery, Jr., T. Vreven, K. N. Kudin, J. C. Burant, J. M. Millam, S. S. Iyengar, J. Tomasi, V. Barone, B. Mennucci, M. Cossi, G. Scalmani, N. Rega, G. A. Petersson, H. Nakatsuji, M. Hada, M. Ehara, K. Toyota, R. Fukuda, J. Hasegawa, M. Ishida, T. Nakajima, Y. Honda, O. Kitao, H. Nakai, M. Klene, X. Li, J. E. Knox, H. P. Hratchian, J. B. Cross, C. Adamo, J. Jaramillo, R. Gomperts, R. E. Stratmann, O. Yazyev, A. J. Austin, R. Cammi, C. Pomelli, J. W. Ochterski, P. Y. Ayala, K.

Morokuma, G. A. Voth, P. Salvador, J. J. Dannenberg, V. G. Zakrzewski, S. Dapprich, A. D. Daniels, M. C. Strain, O. Farkas, D. K. Malick, A. D. Rabuck, K. Raghavachari, J. B. Foresman, J. V. Ortiz, Q. Cui, A. G. Baboul, S. Clifford, J. Cioslowski, B. B. Stefanov, G. Liu, A. Liashenko, P. Piskorz, I. Komaromi, R. L. Martin, D. J. Fox, T. Keith, M. A. Al-Laham, C. Y. Peng, A. Nanayakkara, M. Challacombe, P. M. W. Gill, B. Johnson, W. Chen, M. W. Wong, C. Gonzalez, and J. A. Pople, Gaussian 03, Revision B.04, (Gaussian, Inc., Pittsburgh PA, 2003).

17. K. Raghavachari, G. W. Trucks, M. Head-Gordon and J. A. Pople, Chem. Phys. Lett. **157**, 479 (1989).

18. J. D. Watts, J. Gauss, R. Bartlett, J. Chem. Phys. **98**, 8718 (1993).

19. T. H. Dunning, Jr. J. Chem. Phys. **90**, 1007 (1989); K. A. Peterson, D. E. Woon, T. H. Dunning Jr., J. Chem. Phys. **100**, 7410 (1994).

20. R. A. Kendall, T. H. Dunning, Jr. and R. J. Harrison, J. Chem. Phys. **96**, 6796 (1992).

21. J. S. Francisco, J. Chem. Phys. **115**, 6373 (2001).

22. G. H. Dieke and H.M. Crosswhite, J. Quant. Spectrosc. Radiat. Transfer **2**, 97 (1962).

23. S. C. Homitsky, S. M. Dragulin, L. M. Haynes, and S. Hsieh, J. Phys. Chem. A. **108**, 9492 (2004).

24. S. P. Sander, *et al.* Chemical kinetics and photochemical data for use in stratospheric modeling, Evaluation #14, *JPL Publ.* **02-25** (2003).

25. A. Sinha, R. L. Vander Wal, and F. F. Crim, J. Chem. Phys. **92**, 401 (1989).

26. D. A. McQuarrie, *Statistical Mechanics* (HarperCollins, New York, 1976).

27. M. Tyblewski, T. –K. Ha, R. Meyer, A. Bauder, C. E. Blom, J. Chem. Phys. **97**, 6168 (1992).

28. B. Ruscic. A. F. Wagner, L. B. Harding *et al.*, J. Phys. Chem. A. **106**, 2727 (2002).

29. D. L. Osborn, D. J. Leahy, and D. M. Neumark, J. Phys. Chem. A. **101**, 6583 (1997).

30. K. A. Peterson, D. E. Woon, and T. H. Dunning, Jr., J Chem. Phys. **100**, 7410 (1994).

31. M. W. Chase, Jr., J. Phys. Chem. Ref. Data Monograph **9** (1998).

32. V. D. Knyazev and I. R. Slagle, *J. Phys. Chem. A.* **102**, 1770 (1998).

Chapter 7

Probing the Room Temperature Vibrational Overtones of Methyl Hydroperoxide

7.1 Introduction

In the previous chapter, action spectroscopy is used to probe the third ($4\nu_{OH}$) and fourth ($5\nu_{OH}$) OH-stretching overtones which lie near the unimolecular dissociation threshold. More specifically, from these vibrational bands, measurements of the OH fragment energy release, and high level *ab initio* study (using CCSD(T)/CBS level) has resulted in the determination of the O-O bond dissociation energy of methyl hydroperoxide (CH_3OOH, MHP) to be 42.6 ± 1 kcal/mol. Hence, we concluded that while the $5\nu_{OH}$ band fully undergoes dissociation upon photon absorption, the $4\nu_{OH}$ band predissociation spectrum has a small dissociation quantum yield of $\Phi = 0.2 – 0.5$ %. Regardless of quantum yields issues however, in the previous chapter we have shown that with the use of a single excitation laser one may obtain the spectral signature of these dissociating states.

In order to investigate the bound vibrational states of MHP, states which *do not* undergo dissociation upon excitation, several methods are available. A well established method one may use in order to probe the bound overtones involves preparing the ground vibrational state of interest prior to initiating electronic excitation to a dissociating state. The vibrationally mediated photodissociation (ViMP) method which is discussed in

further detail in Chapter 1 and developed by Crim,[1-5] is utilized with MHP in the following manner:

$$CH_3OOH(v''=0) + h\nu\ (\lambda_1 = 0.72 - 1.5\ \mu m) \rightarrow CH_3OOH^{\#}(v') \qquad (7.1)$$

In the above reactions, the ground state is vibrationally excited using infrared radiation. The prepared vibrational state, in the absent of collisions, typically has sufficiently long lifetime to undergo absorption of a second photon (λ_2) promoting the vibrationally excited MHP molecule to a dissociating electronically excited state:[1]

$$CH_3OOH^{\#}(v') + h\nu\ (\lambda_2 = 532\ nm) \rightarrow OH + CH_3O \qquad (7.2)$$

This pump-dissociate-probe technique has been used successfully to probe the overtones of peroxynitric acid (HO_2NO_2, PNA) in Chapter 2, with the exception that there, we initiate electronic excitation with a near UV photon (λ = 390 nm).

One reason for the interest in the low-lying bound states overtones of MHP is the observation arising from our action spectra involving the trends shown in Figs. 6.3 and 6.5. As the vibrational order of the overtone increases, the numbers of peaks appearing in the various spectra also increase. This observation was also noted by Hsieh and coworkers who used photoacoustic spectroscopy to record the room temperature absorption spectra of the $3\nu_{OH}$ to $6\nu_{OH}$ bands.[6-7] From their *ab initio* predictions of a torsion-vibration model, Hsieh and coworkers concluded that enhanced coupling between the OH-stretch and its HOOC-torsional mode lead to the observed activity in these regions.[6-7] Torsional activity has been extensively investigated with the methanol (CH_3OH) molecule where strong mixing of the methyl rotor leads to extensive state mixing in the OH stretching moiety which it is directly attached to.[8-14]

Since in CH_3OOH, the OH group is separated by an oxygen atom from the perturbing CH_3 group, investigating CH_3OOH can provide a useful comparison to the methanol molecule. In fact, quasiclassical trajectory calculations carried out on vibrationally excited states of CH_3OOH indicate that the OH stretch and HOO bend are strongly coupled to each other, but are rather isolated from the other modes in the molecule.[15] As a consequence of restricted intramolecular vibrational energy redistribution (IVR), the calculations predict that the vibrationally excited OH stretching overtone have a dissociation rate that is twice as fast as that of an excited C-H stretching overtone state having comparable energy. Thus, in overtones studies one could potentially obtain information regarding the state-to-state interactions where the initially prepared state will dictate the extent of the interactions with the nearby manifold of states.[1,15-19]

This chapter presents first results of experiments investigating the room temperature vibrational overtone spectra of CH_3OOH using vibrationally mediated photodissociation technique. We use this technique to record room temperature spectra of the bound OH stretching overtone states of CH_3OOH covering the $2\nu_{OH}$ to the $4\nu_{OH}$ bands. We then interpret the vibrational overtone spectra using high level *ab initio* calculations at the CCSD(T)/cc-pVTZ level in conjunction with a two-dimensional vibration-torsion model in order to obtain OH-stretch/HOOC-torsion band assignment and transitions strength. In utilizing two different dipole moment surfaces (DMF) where in the first, the dependence of the overtone transition dipole moment on the HOOC torsional angle is neglected and in the second where the transition dipole moment dependence on the torsion angle is included, we show that even though both models

provide with similar room temperature band shape and absorption cross-sections, the two models lead to different band composition. In particular, we show that inclusion of the anti-symmetric component of the transition dipole moment provides significant intensity to transitions between torsional states of different symmetry. These transitions, which have been neglected in previous studies on molecules such as hydrogen peroxide (H_2O_2),[20] and *tert*-butyl hydroperoxide ($(CH_3)_3COOH$),[21] are essential for interpreting the detailed spectra of jet cooled CH_3OOH presented in Chapter 8; especially for the lower overtones ($2\nu_{OH}$ and $3\nu_{OH}$) where contribution of transitions between states of different symmetry appears to be the largest.

In addition, results of a natural bond orbital analysis (NBO) exploring the changes in the methyl hydroperoxide HOOC torsional potential with increasing OH stretching excitation are also discussed. A look at the transformations occurring in the CH_3OOH molecular orbitals as the OH bond is stretched, provides insight to changes in adiabatic torsional potential barrier height and equilibrium angle with increasing OH vibrational overtone excitation and allows correlating these changes with corresponding changes appearing in the experimental spectra.[22]

7.2 Experiment

7.2.1 Room Temperature Apparatus

The apparatus used in present experiment is similar to the one used to study peroxynitric acid HO_2NO_2 in Chapter 2. MHP is synthesized as described in Chapter 6, and typically, low pressure measurements are taken under 40 – 60 mTorr of sample while the high pressure measurements are taken in the presence of ~3 Torr N_2 buffer gas used in order to thermalized the rotational distribution of the OH fragment. Tunable infrared

radiation (λ_1) in the vicinity of the first and second OH-stretching overtones is generated by optical parametric oscillator laser system. Typical idler pulse energies range between 4 to 6 mJ in the first ($2\nu_{OH}$) OH-stretching overtone and 10 to 12 mJ in the second ($3\nu_{OH}$) OH-stretching overtone regions. We use this tunable light source which has bandwidth full width at half max (FWHM) of ~0.4 cm^{-1} to scan over the 6000 – 11 000 cm^{-1} region covering the $2\nu_{OH}$ and $3\nu_{OH}$ regions. The laser light for exciting the third and fourth OH-stretching overtones is generated by the NY82-20 dye laser system as described in Chapter 6. Typical laser pulse energies range between 18 to 20 mJ in the third ($4\nu_{OH}$) OH-stretching overtone and 25 to 27 mJ for the fourth ($5\nu_{OH}$) OH-stretching overtone with bandwidth of 0.08 cm^{-1} (FWHM).

The doubled output of the third laser ND:YAG (Continuum: NY81-20) is split with R = 60 % reflectance, 2" diameter × 1 mm in thickness diachoric centered at 620 nm for the $4\nu_{OH}$ measurements. This portion of the light is used to promote the vibrationally excited molecule ($4\nu_{OH}$) to a dissociating electronic state (λ_2 = 532nm). The beam, with typical pulse energies of ~50 mJ, is counter propagating to the IR beams and is gently focused inside the photolysis chamber using 500 mm lens with focal point shifted by 2" from the center of interaction. Similarly, for the $2\nu_{OH}$ and $3\nu_{OH}$ overtones measurements, the doubled output of the NY82-20 is directly used in order to dissociate the vibrationally excited molecule on the electronically excited state. The OH product is probed (λ_3) via the $A^2\Sigma$–$X^2\Pi(1,0)$ transition by the doubled output (using the DCCIII crystal) of a second dye laser operating with R590 dye, pumped by the remaining output of the above ND:YAG laser. The 282 nm output with ~0.13 cm^{-1} bandwidth (FWHM) is greatly

attenuated to prevent direct photolysis of CH_3OOH, line-delayed by 10 ns subsequent to the photolysis laser (λ_2 = 532 nm) and co-propagating to the photolysis laser.

Figure 7.1 shows an overview of the vibrationally mediated excitation scheme used in this experiment. The OH fluorescence is collected using *f*/1 lens system and imaged onto an end-on photomultiplier tube. A color glass filter (Schott UG-11, 2 mm) and a set of 266 nm diachroics provide an excellent rejection against the 532 nm (λ_2) and 282 nm (λ_3) photons while enabling OH fluorescence transmission efficiency of ~60 %. Figure 7.2 shows the schematics of the experimental apparatus used in studying the $2\nu_{OH}$ and $3\nu_{OH}$ overtones of methyl hydroperoxide and Fig. 7.3 shows the experimental schematics used in studying the $4\nu_{OH}$ overtone. For studies involving the $4\nu_{OH}$ and $5\nu_{OH}$ unimolecular dissociation of MHP the excitation and detection scheme are discussed in Chapter 6.

7.2.2 Computational Methods

We use GAUSSIAN03 and ACESII programs to determine the optimized geometries, energies, vibrational frequencies, anharmonicities and dipole moment of CH_3OOH.[23, 24] For detailed description of running GAUSSIAN03 and ACESII program on our workstations refer to Appendix *B*. We use the CCSD(T) wavefunctions in conjunction to the Dunning cc-pVTZ basis set in order to obtain the energies and the dipole moment components (μ_a, μ_b, μ_c) associated with a specific O-H bond separation, r, and COOH torsion angle, τ, configuration.[25] The CCSD(T)/cc-pVTZ has been proven in the previous chapter to provide reliable structure and energies for CH_3OOH. Figure 7.4 shows equilibrium geometry of MHP molecule obtained from the CCSD(T)/cc-pVTZ

calculation orientated along its principle axes. From the figure, as will be shown, The COOH-torsion motion affects drastically the displacement of the hydrogen atom along the c-axis.

7.3 Results

7.3.1 Room Temperature Overtones Action Spectra

The OH stretching overtones spectra of methyl hydroperoxide and their corresponding HOOC-torsional states covering the $2\nu_{OH} - 5\nu_{OH}$ bands are shown in Fig. 7.5. For those vibrational levels with band origin below the unimolecular dissociation limit, such as the $2\nu_{OH} - 4\nu_{OH}$ bands, we use the ViMP technique (see Fig. 7.1) to record their spectra. This involves scanning the wavelength of the vibrational excitation laser (λ_1), while keeping the photolysis laser wavelength (λ_2) fixed at 532 nm and monitoring the yield of $OH(^2\Pi_{3/2}, v=0)$ fragments in the N=5 rotational state using LIF (λ_3). *Ab initio* calculations by Watts and Francisco suggest that the lowest accessible electronic excited state in CH_3OOH is the 2^1A state located 5.9 eV above the equilibrium position of the ground electronic state;[26] we believe we are accessing this dissociative excited electronic state in the ViMP process.

The Choice to probe the N=5 rotational state has minimized interferences from one-color two-photon dissociation induced by λ_1 alone. We find that this background signal occurs in the region of the $2\nu_{OH}$ band and, to a lesser extent, in the region of the $4\nu_{OH}$ band as well. The $2\nu_{OH}$ ViMP spectrum monitoring the N=5 OH rotational state and the one-color two-photon dissociation induced by λ_1 generated by probing the N=1 OH rotational state are shown in Figs. 7.6(a) and 7.6(b) respectively. Even though these scans

are taken under similar scan rates (0.008 nm/s) and averaging conditions (30 shots/bin), the two spectra appears different. The two "horns" appear more diffused in the one-color two-photons process (see Fig. 7.6(b)). At excitation corresponding to 7025 cm^{-1}, the total energy from the two-photon process corresponds to 40.3 kcal/mol. At this excitation energy, we are accessing a state which lies 2.3 kcal/mol below the O-O bond dissociation level and has an estimated dissociation quantum yield of $\Phi \approx 10$ %. Under focused IR beam conditions, with the electronic excitation laser (λ_2) blocked, the signal generated from the two-photon process at N=1 is ~50 % and at N=5 is ~20 % relative to the ViMP signal levels. We minimize the two-photon contribution in the ViMP spectrum by collimating the IR beam using a 1000 and 400 mm lens system; under these conditions, the two-photon signal is reduced to < 0.1 %.

Obtaining a "clean" $4\nu_{OH}$ + 532 nm ViMP signal is a bit more challenging. As the CH_3OOH $4\nu_{OH}$ level is ~4.6 kcal/mol below the dissociation limit for the O-O bond breakage, an additional OH background signal arising from unimolecular dissociation of hot bands and highly excited rotationally states induced by λ_1 can contribute to the signal for this vibrational level. In addition, to a lesser extent, the spectrum is also contaminated with one-color two-photons induced by λ_1 in the absent of λ_2 (532 nm). Since the one- and two- color ViMP produce similar OH rotational distributions, probing different N-level does not help in differentiating between the two signals. However, reducing the excitation laser power density will preferentially reduce the squared signal dependence from the one-color ViMP process. To minimize the contribution from the unimolecular

background signals to the recorded spectra, we adjust the relative focusing of the λ_1 and λ_2 lasers as well as select to probe the N=5 OH fragment rotational state via λ_3.

The action spectra obtained by monitoring the OH(V=0, $^2\Pi_{3/2}$) fragments in the N=1 rotational state, arising solely from overtone induced unimolecular dissociation (i.e. λ_2 absent), is shown in Fig. 7.7(a). For comparison, the two-color ViMP signal, obtained by monitoring the OH(V=0, $^2\Pi_{3/2}$) products in the N=5 state, is shown in Fig. 7.7(b). These spectra are generated by scanning the excitation laser (λ_1) at 0.12 Å/s and averaging 30 shots/bin. The enhanced contribution from hot bands and rotationally excited states to the $4\nu_{OH}$ unimolecular dissociation spectra is evident from the substantial broadening (~1.7 times broader) associated with the spectra in Fig. 7.7(a) relative to the ViMP spectrum in Fig. 7.7(b). The role of energy restrictions on dissociation quantum yield is also reflected in these spectra and can be seen from the changes in relative intensities occurring between the two primary spectral features, appearing at ~13 292 cm^{-1} and ~13 474 cm^{-1}. As discussed in Chapter 6, the estimated dissociation quantum yield arising from these excitation frequencies are 0.2 and 0.5 % respectively. The ViMP spectrum is also consistent with the photoacoustic spectrum of Hsieh and coworkers,[6-7] but is taken with a much better signal to noise ratio and without interferences from H_2O_2 and H_2O appearing in their spectrum.

Unlike the other vibrational bands shown in Fig. 7.5, the $5\nu_{OH}$ band in Fig. 7.5(d) lies entirely above the dissociation threshold and its spectrum is obtained by recording action spectrum generated by vibrational overtone induced unimolecular dissociation through λ_1 and monitoring the OH(V=0, $^2\Pi_{3/2}$) fragments in the N=3 rotational state as

described in Chapter 6. Also, it is important to note that at the $3\nu_{OH}$ level we do not detect any signal from secondary dissociation process and the band shown in Fig. 7.5(b) is of the "pure" $3\nu_{OH}$ + 532 nm ViMP spectrum with no additional complications.

An interesting trend that stands out when looking at the series of overtone spectra from the $2\nu_{OH}$ through the $5\nu_{OH}$ in Fig. 7.5 is that as the order of the overtone increases, the number peaks appearing in the various spectra also increases. In other words, as a result of increased OH vibrational excitation, the number of additional states contributing to the spectra is also increased. Thus, based on our action spectra, it is likely that the coupling of the OH stretching mode with the other vibrational state(s) is increasing as a function of O-H vibrational excitation.[27]

7.3.2 *Ab Initio* Spectral Simulation using Vibration-Torsion Model

The action spectra of CH_3OOH in Fig. 7.5 can be simulated using a two-dimensional (2-D) model involving the OH stretch and the HOOC torsion. As with our 2-D simulation of the HOONO spectra in Chapter 4, we take advantage of the large disparity in the frequencies of the OH stretch and the torsion, in order to invoke adiabatic separation of these two vibrational degrees-of-freedom.[28,29] This method, has worked well in analyzing the spectra of several molecules including hydrogen peroxide and *tert*-butyl hydroperoxide.[20,21] Based on initial *ab initio* MP2/aug-cc-pVTZ anharmonic frequency calculation obtained by running GAUSSIAN03,[23] and shown in Table 7.1, the OH stretching mode (ω_1) has harmonic frequency of 3777 cm^{-1} versus the HOOC torsion (ω_{15}) which has a frequency of 171 cm^{-1}. Also, looking at the first column in the table, we find that aside from the anticipated strong coupling of the OH stretch to its HOO bend (ω_8),[15] the OH stretch, as expected, exhibit significant coupling to its HOOC torsion. The

MP2 frequency calculation can also produce the absorption spectrum of MHP in the fundamental region. And although we do not show data in the fundamental region, for completion, the simulated spectrum is shown in Fig. 7.8. Looking at the figure, we note that in the fundamental region, the spectrum is dominated by the OH stretch (ν_1), its HOO bend (ν_8), the various CH stretching modes ($\nu_2 - \nu_4$) and the HOOC torsion (ν_{15}).

Unfortunately, as outlined in Refs. 20 – 21, the procedure for generating overtones absorption spectrum is more involved. This procedure requires we first generate 1-D adiabatic potentials for HOOC torsional motion associated with each O-H stretching vibrational overtone state. These adiabatic potentials are subsequently used to calculate transition frequencies and oscillator strengths for simulating the overtone spectra by solving the Schrödinger equation.[30,31]

We start the procedure for generating the adabatic torsional potentials by first calculating the equilibrium geometry of the molecule using the ACES II *ab initio* software package at the CCSD(T)/cc-pVTZ level with the frozen-core option.[24] See Appendix *B* for tutorial of running the ACESII program. The starting equilibrium geometry parameters of MHP are given in Table 6.3. The result of the unconstrained optimization of the torsional potential is shown in Fig. 7.9(a). The potential in the figure is generated by incrementally changing the HOOC torsion angle, τ, in steps of $\pm 10^o$ covering the entire range from $0 - 360^o$. Changing the angle τ, basically involves bringing the H-atom of the HOOC moiety in and out of the a-b plane of which the COO group lies in (see Fig. 7.4). For each value of τ considered, all other degrees of freedom

are fully optimized. Table 7.2 shows a sample ACESII Z-matrix frozen-core optimization for the $\tau = 60^o$.

As shown in Fig. 7.9(a) this procedure generate a torsional potential with a barrier of 158 cm^{-1} in the *trans* position which steadily increases to 2061 cm^{-1} in the *cis* position. The torsional potential is symmetric about $\tau = 180^o$ and the two stationary points appearing in the figure at $\tau \sim 114^o$ and $\sim 246^o$ correspond to the two possible HOOC torsional angles at the molecule's equilibrium geometry. Our values for the barrier heights and torsion equilibrium geometries are consistent with the values reported by Tonmunphean *et al*.,[32] who obtained their CCSD(T)/cc-pVTZ energies based on MP2/cc-pVTZ structure calculation (CCSD(T)/cc-pVTZ//MP2/cc-pVTZ).

The torsional potential generated in the procedure above is then used to determine the corresponding potential along the O-H stretching coordinate. At each grid point associated with the optimized torsion angles shown in Fig. 7.9(a), we stretch and compress the O-H bond distance, r, from its equilibrium position, r_e, to cover a range of displacements of $-0.4 \leq r_e \leq +0.6$ Å in increments of 0.1 Å. For efficiency purpose, the O-H potentials are evaluated under constrained optimization, where, all other degrees of freedom are frozen at their equilibrium value; i.e. single point (SP) calculations. Note however, that typically, the light H-atom motion does not induce significant changes in the geometry of other atoms. This approach has been implemented successfully with numerous other systems, and thus, validate our approach.[20,21,33-40] The O-H displacement range is also worth commenting. Due to the high excitation in the OH-stretching mode considered (for example, at the $5\nu_{OH}$ level), we find it necessary to extend the potential to cover displacements as large as +0.6 Å from the equilibrium geometry in order to ensure

proper solutions to Schrödinger's equation. A sample Z-matrix for the grid point where $\tau = 60^o$ and $r = r_e + 0.3$ Å is provided in Table 7.3 for reference.

The above procedure generates a 1-D OH-stretching potential for each of the optimized torsional angles in Fig. 7.9(a). Analysis of these O-H stretching potentials revels that unlike in the case with HOONO (see Chapter 6), where the HOON-torsion angle has significantly affected the stiffness of the O-H stretching potential, in CH_3OOH, these effects are minuscule. Next, the eigenfunctions and eigenvalues associated with each of these OH stretching potentials are determined.[41] This is accomplished by inserting the OH potential obtained for each τ into the 1-D time-independent Schrödinger equation and numerically solving the differential equation using a fixed value for the reduced mass associated with the CH_3OO-H motion ($\mu_{OH} = 0.9791666$ amu) using the FGH1D code (see Appendix *F*).[41] For a given τ value, the v-th eigenfunction and eigenvalue for the OH stretch thus generated, are labeled respectively as $\psi_v^{OH}(r|\tau)$ and $E_v^{OH}(\tau)$. The above process is repeated over the entire grid of τ values covering the range from $0 - 360^o$ in increments of 10^0, and leads to evaluations of eigenvalues and eigenfunctions for 38 OH-stretching potentials. However, due to the symmetry of the torsional potential about the COO plane (see Fig. 7.4), the number of OH-stretching potentials we actually evaluate is cut in half.

Fig 7.10(a) shows one of the O-H potential, evaluated at $\tau = \tau_{eq.} \approx 114^o$, and its corresponding wavefunctions. It is interesting to also see how the harmonic frequency and anharmonicity Morse parameters of the OH stretching coordinate changes as a function of the HOOC torsion angle and this is shown in Fig. 7.10(b).[42] From the figure,

we see that these parameters vary by only a few percent (3 – 5 %) over the range of accessible angles. Finally the adiabatic torsional potential associated with the v-th OH stretching vibrational level is generated by considering at each grid point τ, the v-th energy eigenvalue $E_v^{OH}(\tau)$ associated with the OH stretching potential and then connecting these energies (all having the same v- quantum number) over the entire range of torsional angles. The adiabatic torsion potentials obtained in this manner for the $0\nu_{OH}$, $2\nu_{OH}$ and $5\nu_{OH}$ levels are shown in Fig. 7.11; the energy scale of the $2\nu_{OH}$ and $5\nu_{OH}$ is arbitrarily shifted down towards the $0\nu_{OH}$ level. It is clear, by inspection of Fig. 7.11 that as the order of the OH stretching overtone excitation increases, there is a significant change in the molecular geometry with the equilibrium torsional angle decreasing from 112^o to 90^o as we go from $V_{OH} = 0$ to $V_{OH} = 5$. In addition, we find that the height of the trans barrier also increases as the OH stretch is progressively vibrationally excited; the reasons for these changes will be discussed in a later section.

Having determined the adiabatic torsional potentials, we next proceed to determine their associated energies and wavefunctions which are needed to carry out the spectral simulations. As noted by Likar *et al.*,[21] the eigenfuntions and eigenvalues associated with the 1-D adiabatic torsional potential , $U_v(\tau)$, for the v-th OH stretching state can obtained by solving the following form of the Schrödinger equation given in Eq.7.3:[43]

$$[-d/d\tau\ \alpha_v(\tau)d/d\tau + U_v(\tau)]\ \chi^v{}_m(\tau) = E_{vm}\ \chi^v{}_m(\tau) \qquad (7.3)$$

$$\alpha_v(\tau) = (\hbar/4\pi c)\ 1/I_r(\tau) = \alpha^0{}_v + \alpha^1{}_v \cos(\tau) \qquad (7.4)$$

Part of the difficulty in solving Eq. 7.3 arises from the fact that the effective moment of inertia, $I_r(\tau)$, is a function of τ and so it changes as the torsional angle changes.[21] This variation in the moment of inertia with torsion angle is represented through the kinetic energy cofactor $\alpha_v(\tau)$, which in turn is related to the inverse of the moment of inertia as given in Eq. 7.4. The kinetic energy cofactor can be further factored into primary part, α^0_v, that is independent of the torsional angle and a smaller part, $\alpha^1_v \cos(\tau)$, that depends on this angle: [21]

$$\begin{aligned}\alpha^0_v = (\hbar/4\pi c) \times [&1/(\mu_{OH} (r_{OH})^2 \sin^2(\alpha_{OOH})) \\ &+1/(\mu_{OX} (r_{OX})^2 \sin^2(\alpha_{OOX})) \\ &+ 2/(m_O (r_{OO})^2) \times [\cot^2(\alpha_{OOX}) + \cot^2(\alpha_{OOH})] \\ &- 2/(m_O(r_{OO})) \times [\cot(\alpha_{OOH})/((r_{OH})\sin(\alpha_{OOH})) \\ &+ \cot(\alpha_{OOX})/((r_{OX})\sin(\alpha_{OOX}))]]\end{aligned} \tag{7.5}$$

and,

$$\begin{aligned}\alpha^1_v = (\hbar/4\pi c) \times [&(4 \cot(\alpha_{OOX}) \cot(\alpha_{OOH}))/(m_O(r_{OO})^2) - 2/(m_O(r_{OO})) \\ &\times [\cot(\alpha_{OOX})/((r_{OH})\sin(\alpha_{OOH})) + \cot(\alpha_{OOH})/((r_{OX})\sin(\alpha_{OOX}))]]\end{aligned} \tag{7.6}$$

Where for methyl hydroperoxide, r_{OH}, r_{OX} and r_{OO} correspond to the O-H, O-OCH_3 and O-O bond distances respectively. Similarly, the α_{OOH} and α_{OOX} represent the respective OOH and OOC bond angles respectively. m_O, μ_{OH} and μ_{OX} refer to the mass of oxygen atom and the reduce masses of O-H and O-CH_3 respectively. $\hbar$ is Planck's constant divided by 2π and c is the speed of light in vacuum. All the parameters of methyl hydroperoxide are obtained from the CCSD(T)/cc-pVTZ level and provided in Table 6.3.

Table 7.4 provides a summary of the potential energies in the *cis* and *trans* positions, effective moments of inertia and kinetic energy cofactor terms for CH_3OOH evaluated at the equilibrium torsion angle appropriate for the various OH-stretching overtone levels. As the table shows, relative to α^0_v, the magnitude of the angle dependent kinetic energy cofactor term α^1_v is quite small in CH_3OOH. Hence, in solving the Schrödinger equation for the adiabatic torsional potentials (Eq. 7.3),[41] we fix the α^1_v $\cos(\tau)$ term to its value at the equilibrium position, $\tau_{eq.}$, at the specific OH overtone state being considered. The table also shows that as the vibrational excitation in OH increases, the torsional barrier in the *trans* position increase dramatically from 173 to 735 cm^{-1} going from $V_{OH} = 0$ to 6, while in the *cis* position, the increase is less dramatic changing from 2050 to 2195 cm^{-1} for the same overtones. The factors contributing to the changes in barrier height are discussed at a later time.

The resulting torsional wavefunctions for the ground (v=0) and the first OH-stretching overtone (v=2), for example, are shown in Fig. 7.12. Due to the symmetry of the HOOC adiabatic torsional potentials about $\tau = 180^o$, the vibrational levels associated with the potential are split (see Fig. 7.12). These pair of wavefunctions are either symmetric or antisymmetric with respect to reflection about the *trans* barrier at $\tau = 180^o$ and are denoted by $|\chi^v_m(\tau)^+>$ and $|\chi^v_m(\tau)^->$ respectively; where the (+) and (–) symbols as superscripts to denote these symmetries.[44] Furthermore, the vibrational excitation quantum number for torsional motion is designated by "m", for the v^{th} (in superscript) OH stretching level. As illustrated in Fig. 7.12, the energy separation between the corresponding (+) and (–) pairs of levels increases as the torsional excitation quantum

number "m" increases of a certain torsional potential. Due to the increase in the *trans* barrier-height however, the splitting decrease for increasing OH vibrational excitation. In addition to splitting due to tunneling through the *trans* barrier, the *cis* barrier is also expected to split the (+) and (–) levels further. However, because of the substantially larger height of this barrier (~2000 cm^{-1}), the corresponding splitting is expected to be very small and is neglected in the present analysis.[44]

Finally, using the above results, the overall wavefunction associated with a vibration-torsion state, $\Psi_{v,m}(r,\tau)$ can be written as a product:

$$\Psi_{v,m}(r,\tau) = |\psi_v^{OH}(r|\tau)\rangle |\chi^v{}_m(\tau)^{+/-}\rangle = |v\ m^{+/-}\rangle \qquad (7.7)$$

The term $\psi_v^{OH}(r|\tau)$ designates an OH-stretch wavefunction evaluated for a fixed value of torsional angle.

To evaluate the transition strength for excitation from some initial state $|i\rangle = |v,m^{+/-}\rangle$ to some final state $|j\rangle = |v'\ m'^{+/-}\rangle$, The standard expression for the oscillator strength is used:[30,31]

$$f = 4.702 \times 10^{-7}\ [cm\ D^{-2}]\ \nu_{ij}\ |\mu_{ij}|^2 \qquad (7.8)$$

In the above expression ν_{ij} is the transition frequency, obtained by taking energy differences between the initial and final states while $|\mu|^2$ corresponds to the sum of the squares of the transition dipole moment matrix elements components in the molecular reference frame, defined by the inertial axes: [30,31]

$$|\mu|^2 = \Sigma_{\alpha=a,b,c} \langle j|\mu_\alpha(r,\tau)|\ i\rangle^2 \qquad (7.9)$$

In order to evaluate Eq. 7.9 we the ACESII software package at the CCSD(T)/cc-pVTZ level of theory to compute the three-components (μ_a, μ_b, μ_c) of the dipole moment in the

molecular frame for CH_3OOH over a discrete set of 2-D grid points (see Appendix *B*).[24] We then fit each component of this discrete *ab initio* dipole moment surface to a two-dimensional tenth-order Taylor expansion about the molecular equilibrium ($r \sim 0.965$Å, $\tau \sim 114^o$) geometry. The resulting a-, b-, and c- dipole component surfaces are shown in Figs. 7.9(b) – 7.9(d) respectively. For each component of the molecular frame dipole moment function, $\mu_\alpha(r, \tau)$, we separate the evaluation of its contribution to the transition moment matrix element into two-step where we first integrate over the r-dependence associated with the OH-stretching coordinate to obtain:

$$\mu_\alpha(\tau) = \langle \psi_v^{OH}(r|\tau) \, |\mu_\alpha(r,\tau)| \, \psi_0^{OH}(r|\tau) \rangle \qquad (7.10)$$

And then integrate the resulting function, $\mu_\alpha(\tau)$, over its τ dependence to get μ_α:

$$\mu_\alpha = \langle \chi^{v'}{}_{m'}(\tau) | \mu_\alpha(\tau) | \chi^{v}{}_{m}(\tau) \rangle \qquad (7.11)$$

Figures 7.13(a) – 7.13(d) show the results of integrating the dipole moment in Eq. 7.10 associated with the $V_{OH} = 0 \rightarrow 2, 3, 4, 5$ transitions over the OH stretching coordinate respectively. Hence, revealing the variation in the dipole moment function with torsional angle (i.e. $\mu_a(\tau)$, $\mu_b(\tau)$ and $\mu_c(\tau)$) for these transitions. While we find that both the $\mu_a(\tau)$ and $\mu_b(\tau)$ components are symmetric upon reflection about OOC plane formed by the a-b inertial axes, $\mu_c(\tau)$ is antisymmetric; hence, it is *this* component of the dipole moment that, in principle, can connect transitions between vibrational states of different (+) ↔ (–) symmetry. We also note from the figures that the magnitude of the integrals is decreasing by about an order of magnitude with increasing vibrational transition. The codes used to evaluate expressions 7.8 through 7.11 are provided in Appendix *D*.

In contrast to the above situation, if the dipole moment is assumed to be independent of the torsional angle then expressions 7.10 and 7.11 takes on an even simpler form, which is suggestive of a Frank-Condon model:[7,30,45]

$$|\boldsymbol{\mu}|^2 = \Sigma_{\alpha=a,b,c} |\langle \psi_{v'}^{OH}(r|\tau) |\boldsymbol{\mu}_\alpha(r)| \psi_v^{OH}(r|\tau)\rangle \langle \chi^{v'}_{m'}(\tau)|\chi^{v}_{m}(\tau)\rangle|^2 \qquad (7.12)$$

To the extent that the dipole moment does not depend on τ and the Frank-Condon model is valid, one expects the transition intensity to be also controlled by the overlap integral ($\langle \chi^{v'}_{m'}(\tau)|\chi^{v}_{m}(\tau)\rangle$) between wavenfuctions of the initial and final torsional states. In this case only transitions between states of the same symmetry (i.e. (+) → (+), and (–) → (–)) will be allowed based on the $\langle \chi^{v'}_{m'}(\tau)|\chi^{v}_{m}(\tau)\rangle$ term. The previous statement, off course, is only valid in situations where the torsional potential associated with v and v' have similar equilibrium angles. Since, methyl hydroperoxide has a decreasing torsion angles corresponding to increasing OH vibrational states, the assumption of transitions between states of same symmetry is only valid for low vibrational states. In this chapter analysis of both models will be shown and will be discussed below. A plot of the three dipole moment functions, $\boldsymbol{\mu}_a(r)$, $\boldsymbol{\mu}_b(r)$, and $\boldsymbol{\mu}_c(r)$ used in Eq. 7.12 and evaluated at $\tau_{eq.} \approx 114^o$ are shown in Fig. 7.14.

The matrix elements for each of the three components of the dipole moments $\boldsymbol{\mu}_\alpha$ found from Eq. 7.9 and 7.12 are then individually squared then summed, and subsequently multiplied by the transition frequency to get the overall transition oscillator strength (see Eq. 7.8).[30,31] We then weigh each transition's oscillator strength by the appropriate Boltzmann factor for the initial vibrational state. The total vibrational

population over the entire distribution of thermally populated states considered is normalized using the vibrational partition function ($Q_v \sim 3.4$) at 298 K.[46]

The results of the two models (top panel- with torsion dependence, lower panel- without torsion dependence) represented by the stick diagrams which are superimposed on top of the measured action spectra in Figs. 7.15 – 7.18 for the $2\nu_{OH}$ through the $5\nu_{OH}$ regions respectively. Each stick in the plot represents a particular vibrational transition starting from initial state $|\psi^{OH}{}_{v=0}(r|\tau)\,\chi^{v=0}{}_{m}(\tau)^{+/-}>$ to a final state $|\psi^{OH}{}_{v'}(r|\tau)\,\chi^{v}{}_{m'}(\tau)^{+/-}>$. We further broaden each stick with a 50 cm^{-1} Gaussian envelope to account for the rotational distribution associated with each vibrational transition at room temperature and the resulting sum of these broadened features is represented by the solid line passing through each spectra in Figs. 7.15 – 7.18. The calculated oscillator strengths can easily be converted to integrated cross sections with units of cm/molecule by multiplying by 8.85×10^{-13},[31] and finally to peak cross-sections by dividing the total integrated absorption cross-section by the transition width (50 cm^{-1}) and the appropriate partition function in unit of cm^2/molecule as shown along the vertical axis in the above figures.

7.4 Discussion

The results of the two vibration-torsion models with and without the torsion dipole moment dependence are shown in Figs 7.15 – 7.18 in the respective $2\nu_{OH} – 5\nu_{OH}$ stretching overtone regions. Looking at the figures we see that, in general, both models simulate the experimental action spectra quite well and are able account for most of the features appearing in the spectra in terms of their relative position as well as intensities.

In terms of absolute bands positions, we linearly shift the simulations by 52, 70, 102.5 and 124 cm^{-1} (or by [$\nu_{abs} = 1.0082\nu_{sim} - 8.302$] cm^{-1}) in the $2\nu_{OH}$, $3\nu_{OH}$, $4\nu_{OH}$ and $5\nu_{OH}$ respectively. In addition, as noted in a previous section, the trend that stands out in the experimental spectra and, which is picked up by the simulations, is that the number of features appearing in the spectra increases as the order of the overtone transition increases from $2\nu_{OH}$ to $5\nu_{OH}$. As noted by Hsieh and coworkers,[6,7] this trend is primarily due to changes in the adiabatic torsional potential that occur upon OH stretching excitation.

An inspection of the calculated adiabatic torsion potentials, shown in Fig. 7.11, and the tabulated data in Table 7.4, we see that as the OH stretching excitation increases, the height of the trans barrier increases and the equilibrium torsional angle, $\tau_{eq.}$, shifts further away from its value in the OH stretch ground state. Thus, a qualitative analysis using the Frank-Condon model as given Eq. 7.12, then would suggest that the number of transitions having significant vibrational overlap, hence intensity, should increase as the OH stretch is progressively vibrationally excited and the corresponding excited state adiabatic torsional potentials gradually shifts outward relative to that of the ground state.

We have explored the reasons for the changes in the HOOC adiabatic torsional potential upon OH stretching excitation using natural bond orbital (NBO) analysis of the CH_3OOH molecular structure optimized at V_{OH}= 0 and V_{OH}=5. We estimate the molecular structure at these vibrational levels by calculating the root mean squared values for the OH bond displacements $\langle r^2 \rangle^{1/2} = \langle \psi_v{}^{OH}(r|\tau_{eq.}) \, |r^2| \, \psi_0{}^{OH}(r|\tau_{eq.}) \rangle^{1/2}$ and running the optimization routine in GAUSSIAN03 with O-H coordinate frozen at $\langle r^2 \rangle^{1/2} = 0.983897$

and 1.197020 Å at the $0\nu_{OH}$ and $5\nu_{OH}$ levels respectively.[23] From the second-order perturbation theory analysis we find that there are four major interactions involving the OH bond (see Table 7.5).[22,47] Second-order energies, $\Delta E^{(2)}$, is a stabilization energy, and in essence, is a measure of how strong the interactions between donor orbitals and acceptor anti-bonding orbitals are.[22] In Table 7.5, the first three interactions between donor orbitals denoted by σ_{OH}, and acceptor anti-bonding orbitals denoted by $\sigma*$, are similar in energies at $0\nu_{OH}$ and $5\nu_{OH}$. For example, in exciting the molecule to the $5\nu_{OH}$ state, the interaction energy between the σ_{OH} and the Rydberg state of the carbon bonded oxygen ($RY_{O(\alpha)}$) increases only by 0.4 kcal/mol. In contrast, significant differences in interactions occur between the α-oxygen π-type lone pair orbital ($n^{\pi}_{O(\alpha)}$) and the sigma $\sigma*$ orbital of the OH bond (σ^*_{OH}). These $n^{\pi}_{O(\alpha)} \rightarrow \sigma^*_{OH}$ interactions are shown in Fig. 7.19. For $0\nu_{OH}$ (see Fig. 7.19(a) and 7.19(c)), this interaction energy is 1.89 kcal/mol, while the same interaction energy at the $5\nu_{OH}$ level is 5.60 kcal/mol (see Fig. 7.19(b) and 7.19(d)). This interaction energy between $n^{\pi}_{O(\alpha)}$ and the σ^*_{OH} orbitals at the fourth OH stretching overtone makes it difficult for the COO–H bond to rotate freely relative to rotation at the $0\nu_{OH}$ state. These results, in essence, leading to the observed gradual increase in the torsional *trans* barrier as a function of OH vibrational excitation.

Next, we take a closer look at the vibration-torsion transitions that contribute to the overall intensity of the overtone bands using the fourth overtone, $5\nu_{OH}$, as an example. The stick diagram in Fig. 7.18(a) shows that the primary transitions that make up the $5\nu_{OH}$ spectrum are mainly composed of transitions connecting (+) → (+) and (–) → (–) states. However, we also see that transitions connecting states of different

symmetry (+) ↔ (–) also occur and contribute about 12 % to the overall spectral intensity. The strongest feature in the $5\nu_{OH}$ band at 16 142 cm^{-1} involves primarily the $|0\ 0^{+}> \rightarrow |5\ 0^{+}>$ and $|0\ 0^{-}> \rightarrow |5\ 0^{-}>$ transitions. Transitions with $\Delta m = -1, -2\ldots$ are localized predominantly to the red of this main band (at 16 142 cm^{-1}) while features to its blue involve transition of $\Delta m = +1, +2\ldots$ nature. The most intense of these "blue" bands occurs at ~16 359cm^{-1} and are attributed to transitions originating from the initially populated $|0\ 0^{+}>$ and $|0\ 0^{-}>$ levels and connecting respectively to the $|5\ 1^{+}>$ and $|5\ 1^{-}>$ final states. In contrast, Fig. 7.18(b) shows the results of the so-called Franck-Condon model where the dipole moment is only a function of the OH stretching mode ($\mu(r)$). In this case, the model predict that the make up of the $5\nu_{OH}$ spectrum is strictly composed of transitions connecting (+) → (+) and (–) → (–) states. Transitions of different symmetry (+) ↔ (–) contribute negligibly (~ 2×10^{-4} %) to the overall spectral intensity.

In the region of the second ($3\nu_{OH}$) and third ($4\nu_{OH}$) OH stretching overtone, shown in Figs. 7.16(a) and 7.17(a) respectively, we find that the situation is similar to that discussed above for the $5\nu_{OH}$ band with both simulations reproducing the experimental data nicely. And, as with the $5\nu_{OH}$ region, we find similar results in terms of the band make up; when we include of the dependence of dipole moment function on the torsion motion, our results indicate that transitions of different symmetry, (+) ↔ (–), contribute 34 and 12 % for the $3\nu_{OH}$ and $4\nu_{OH}$ respectively. On the other hand, going back to the Franck-Condon model simulations shown in Figs. 7.16(b) and 7.17(b), leads to the conclusion that transitions of (+) ↔ (–) nature are unimportant as they contribute about 6 $\times 10^{-6}$ and 1×10^{-7} % in these two regions respectively.

It is interesting to summarize what we observe in going from the higher to the lower overtones in terms of the relative contribution of the symmetry changing (+) ↔ (–) transitions in our models. In Table 7.6 the upper half corresponds to transition strengths predicted by our full model where the dipole moment surface depends on r and τ, $\mu(r,\tau)$, while the lower half corresponds to transition strings predicted by our Franck-Condon model where the τ dependence is dropped ($\mu(r)$). Looking at the table we see that when considering $\mu(r,\tau)$, as the order of the OH overtone decreases, the contribution of the (+) ↔ (–) transitions relative to those associated with the (+) ↔ (+) and (–) ↔ (–) transition increases. Their contribution is estimated to be 12 % at $5\nu_{OH}$ and goes up to 66 % at the first overtone, $2\nu_{OH}$. Note that while (+) ↔ (+) and (–) ↔ (–) transitions involve connectivity through the μ_a and μ_b components of the transition moment, the (+) ↔ (–) transitions rely solely on the antisymmetric μ_c component of the DMF (see Figs. 7.9(b) – 7.9(d) and 7.13). Tables 7.7 – 7.10 summarize the oscillator strengths associated with $V_{OH} = 0 \rightarrow 2$, 3, 4, and 5 and $V_\tau = 0^{+/-}$, $1^{+/-}$, $2^{+/-}$, $3^{+/-}$ respectively. As the rotational selection rules depend on the component of the transition moment that is active, one expects different rotational band contours to be associated with these different transitions.[9,10,12-14,48] This is our starting point for investigating CH_3OOH under free jet conditions discussed in the following chapter.

In contrast to the $\mu(r,\tau)$ surface, the $\mu(r)$ gives an opposite trend. Looking at the lower half of Table 7.6 reveals that as the excitation in the OH stretching mode increases, the relative contribution from (+) ↔ (–) transitions, though negligible compared with (+) ↔ (+) and (–) ↔ (–), is increasing from 5×10^{-6} to 2×10^{-4} % going from $2\nu_{OH}$ to $5\nu_{OH}$.

At $6\nu_{OH}$ the contribution is 0.02 %. These results are consistent with the fact that in the absence of $\mu_c(r,\tau)$ dipole moment component, the matrix elements of (+) ↔ (–) transitions are essentially zero because of the symmetry of the overlap integral $\langle\chi^{v'}{}_{m'}(\tau)|\chi^{v}{}_{m}(\tau)\rangle$. This is also suggesting that the spectroscopy of the bands, in particular, of the low lying OH stretching modes, the band makeup will differ depending on which of the two models more accurate. For example, in the $2\nu_{OH}$ region, under molecular beam conditions, one may expect to find either two states- as predicted by our $\mu(r)$ model or four states- as predicted by our $\mu(r,\tau)$ model. Namely, for the Franck-Condon model, these are the $|0\ 0^+\rangle \rightarrow |2\ 0^+\rangle$ and $|0\ 0^-\rangle \rightarrow |2\ 0^-\rangle$ states and in the case of our full model, $\mu(r,\tau)$, additional contribution from the $|0\ 0^+\rangle \rightarrow |2\ 0^-\rangle$ and $|0\ 0^-\rangle \rightarrow |2\ 0^+\rangle$ states.

In addition to using spectroscopic methods, we can also compare how well our simulations predict absolute absorption cross-sections by comparing them with experiments. The peak cross sections associated with the experimental $5\nu_{OH}$ spectra in Fig. 7.18 are absolute cross sections, and were determined by calibrating the band against known UV absorption cross sections of CH_3OOH (see Chapter 10). The agreement between computed intensity and experiment is quite good for our $\mu(r,\tau)$ generated fit. In contrast, the fit generated with our $\mu(r)$ surface predicts absorption cross-sections that are 35 % smaller than actually observed.

As it is difficult to measure absolute absorption cross-sections for transitions using the ViMP scheme, we calibrated the peak cross-sections for the experimental $3\nu_{OH}$ and $4\nu_{OH}$ overtones bands using the absorption cross section data of Hsieh and coworkers who used known water transitions appearing in their photoacoustic spectra to establish

the absolute cross-sections.[6,7] Based on the $4\nu_{OH}$ data in Fig. 7.16, we conclude that our $\mu(r,\tau)$ model is, again, in good agreement with the observed absorption cross-sections and band shapes, while the $\mu(r)$ model predict peaks intensities that are 25 % weaker than observed. In the $3\nu_{OH}$ region in Fig 7.15 and in the $2\nu_{OH}$ region shown in Fig. 7.14, the disparities between the two models are small, predicting similar results. However, based on the $4\nu_{OH}$ and $5\nu_{OH}$ regions, we conclude that our $\mu(r,\tau)$ model is likely to properly depict the spectroscopy of MHP.

In comparing CH_3OOH to CH_3OH,[9,11-12,14] at the current resolution, we find no evidence of interaction between the methyl rotor and the OH group in methyl hydroperoxide in the regions shown. We do however, as noted by Tyblewski *et al.*,[44] and discuss above, find interactions between states of different symmetry. The small undetected interactions between the CH_3 group and the OH groups in methyl hydroperoxide are likely due to the fact that not only these moieties are separated by an oxygen atom, but also, the barrier associated with the internal rotation of the CH_3 group is ~1120 cm^{-1}. This barrier height suggests that unlike in the case of methanol where the barrier is three fold smaller, in MHP, the methyl rotor is more hindered.[44,49]

In the following Chapter, rigorous analysis of the $2\nu_{OH}$ and $3\nu_{OH}$ bands and their corresponding torsional states under free jet expansion will show that indeed, predictions made by our 2-D model which do take into account the dipole moment dependence on the torsion, $\mu(r,\tau)$, are indeed accurate. In addition, IVR effects from the CH_3 rotor which are apparent in jet cooled environment are also discussed.

7.5 Conclusions

The overtones of methyl hydroperoxide are investigated using the ViMP scheme where the molecule is vibrationally excited and subsequently photodissociated on the electronically excited state under room temperature conditions. Not only this excitation-detection scheme enables selective investigation of CH_3OOH without interferences from impurities which often present in synthesis of various molecules, but also, as shown here, also provide us with a method of probing the bound states with excellent signal-to-noise ratio. A two-dimensional *ab initio* model at the CCSD(T)/cc-pVTZ level which takes into account the influence of the COOH-torsional mode on the OH-stretching mode is constructed in order to aid in the vibrational band analysis. We compare this model with a standard "Franck-Condon" model where the influence of the COOH-torsional mode on the dipole moment function is neglected. The good agreement between our models predictions and the observed overtone action spectra in both band shape and intensity suggests that indeed, the torsional mode of methyl hydroperoxide is strongly coupled to the OH-stretching mode and that the increased coupling with increasing OH-stretching amplitude can explain the observed spectra. Comparison between measured absorption cross-sections in the $3\nu_{OH}$ through $5\nu_{OH}$ regions and the two models suggest however that unlike the case of H_2O_2,[20] and CH_3OH,[50] in methyl hydroperoxide, the dipole moment function dependence on the torsion can not be neglected. This also suggests that in the absence of spectroscopic information on the $(CH_3)_3COOH$ molecule,[21] a full 2-D dipole moment surface may shed light on the true bands makeup. Finally, under molecular beam conditions, at the $2\nu_{OH}$ level, one is expected to find contribution from four transitions. In the following chapter it will be shown that indeed, the matrix elements of the $\langle \Psi_{v,m}(r,\tau)|\boldsymbol{\mu}_c(r,\tau)|\Psi_{v,m}(r,\tau)\rangle$ expression give rise to (+) ↔ (–) transitions.

Lastly, *ab initio* NBO overtone analysis of the $0\nu_{OH}$ and $5\nu_{OH}$ shows that out of the four major orbital interactions, it is the $n^{\pi}_{O(\alpha)} \rightarrow \sigma^*_{OH}$ interactions that leads to the increase in the torsional barrier height in the *trans* position ($\tau = 180^o$). In addition, these $n^{\pi}_{O(\alpha)} \rightarrow \sigma^*_{OH}$ interactions are also found to affect the equilibrium torsion angle where in going from the $0\nu_{OH}$ to the $5\nu_{OH}$ state, the torsion angle, τ, changes from 112 to 91^o.

7.6 Acknowledgements

Chapter 7, in part, is a reprint of the material as it appears in Journal of Chemical Physics 129, 074316 (2008). J. Matthews, M. Martínez-Avilés, J. S. Francisco, and A. Sinha, American Institute of Physics, 2008. The dissertation author was the primary investigator and author of this paper.

Table 7.1: Harmonic Frequencies, Anharmonicities and Isotope Shifts of CH_3OOH Computed at MP2/aug-cc-pVTZ (cm^{-1})

$(\omega_e)_i$	3777	3179	3151	3061	1532	1490	1464	1359	1211	1181	1060	870	447	261	171
d_3 -shift	0	820	812	870	454	391	109	3.5	111	150	78.7	55.0	41.6	59.5	1.9
$(\omega_e\chi_e)_{ij}$	1	2	3	4	5	6	7	8	9	10	11	12	13	14	15
1	-84.4														
2	-0.84	-36.7													
3	-0.71	-28.8	-31.4												
4	-0.82	-53.4	-87.2	-19.0											
5	-0.43	-3.84	-17.5	-20.5	-3.58										
6	-0.02	-17.8	-10.4	-0.42	-5.28	-8.75									
7	-0.28	-13.4	-7.30	19.9	-4.63	-6.43	-10.6								
8	-27.6	-0.73	0.74	0.06	-0.83	-0.80	-1.37	-9.89							
9	0.11	-5.05	-3.40	-3.03	-3.95	-5.13	-8.33	-29.5	-2.63						
10	-0.56	-3.04	-3.06	-3.98	-10.7	-6.67	-3.07	-1.48	-0.08	-1.82					
11	-2.78	-1.16	3.78	1.17	-2.13	-2.69	-6.17	-5.86	-10.4	-7.98	-6.91				
12	-3.06	-1.26	0.32	-0.13	-0.79	-0.99	-1.19	-11.4	-2.53	-0.67	-6.71	-4.56			
13	0.27	-0.66	0.43	0.17	0.42	-1.04	-0.26	-1.15	-1.55	0.55	-4.99	-4.56	0.38		
14	0.24	-0.68	2.14	1.23	-1.71	1.16	2.10	-0.06	-3.52	-1.62	0.43	-1.33	2.14	-6.16	
15	9.13	2.83	-2.84	0.09	1.71	-1.40	-0.13	-8.83	14.0	1.04	8.98	0.11	-2.30	-5.39	-50.4

Table 7.2: CH_3OOH ACESII Z-matrices Used with CCSD(T)/cc-pVTZ

CCSD(T) /cc-pVTZ
CH3OOH CCSDT/ccpVTZ optimization t=60 C O 1 r1* O 2 r2* 1 a1* H 3 r3* 2 a2* 1 d1 H 1 r4* 2 a3* 3 d2* H 1 r5* 2 a4* 3 d3* H 1 r6* 2 a5* 3 d4* r1=1.41652837 r2=1.45666696 r3=0.96516718 r4=1.09087394 r5=1.09316978 r6=1.09169994 a1=105.30791014 a2=99.59294054 a3=104.87110715 a4=111.40380445 a5=110.97005336 d1=60.0 d2=177.3636104 d3=-63.81333294 d4=58.85585791 *ACES2(PRINT=1,REFERENCE=RHF,CALC=CCSD(T),BASIS=CC-PVTZ,CHARGE=0,SPHERICAL=ON,MULTI=1,SCF_CONV=7, MEMORY_SIZE=800MB,DROPMO=1-3)

Table 7.3: CH_3OOH ACESII Z-matrices Used with CCSD(T)/cc-pVTZ SP Energy and Dipole Moments Calculations

CCSD(T) /cc-pVTZ

```
CH3OOH CCSDT/cc-pVTZ Torsion Grid t = 60 r = re + 0.3
C
O 1 r1
O 2 r2 1 a1
H 3 r3 2 a2 1 d1
H 1 r4 2 a3 3 d2
H 1 r5 2 a4 3 d3
H 1 r6 2 a5 3 d4

r1   =    1.4146368965
r2   =    1.4508122347
a1   =  106.8617575681
r3   =    1.2684317082
a2   =  101.5052253687
r4   =    1.0903421554
a3   =  105.2963477398
d2   =  177.8967881815
r5   =    1.0971321186
a4   =  111.2303568515
d3   =  -64.1793608451
r6   =    1.0919719976
a5   =  111.3018881145
d4   =   58.4716050139
d1   =  60.0

*ACES2(PRINT=0,REFERENCE=RHF,CALC=CCSD(T),BASIS=CC-
PVTZ,CHARGE=0,SPHERICAL=ON,MULTI=1,SCF_CONV=7,
MEMORY_SIZE=800MB,DROPMO=1-3,PROPS=1)
```

Table 7.4: Potential and Kinetic Energy Parameters for the OH Vibrational Levels of CH_3OOH[a]

V_{OH}	$U_v^{cis}(\tau)$	$U_v^{trans}(\tau)$	$\tau_{eq.}$	$\alpha^0{}_v$	$\alpha^1{}_v$	$\alpha_v(\tau)\|_{\tau eq.}$	$I_r(\tau)\|_{\tau eq.}$
0	**2050**	**173**	**112**	**20.84**	**0.679**	**20.59**	**0.818594**
1	**2035**	**212**	**108**	**19.37**	**0.663**	**19.17**	**0.879035**
2	**2029**	**267**	**103**	**18.05**	**0.648**	**17.90**	**0.941293**
3	**2038**	**344**	**99**	**16.85**	**0.634**	**16.75**	**1.00635**
4	**2066**	**445**	**95**	**15.71**	**0.620**	**15.66**	**1.07614**
5	**2117**	**575**	**91**	**14.62**	**0.606**	**14.62**	**1.15305**
6	**2195**	**735**	**87**	**13.59**	**0.593**	**13.62**	**1.23747**

[a] energies (U_v) in cm^{-1}, angles (τ) in degrees, and moment of inertia (I_r) in $Å^2$.

Table 7.5: Bond Interaction Energies of CH_3OOH at Vibrational Excitation Corresponding to $0\nu_{OH}$ and $5\nu_{OH}$ (kcal/mol)[a]

Interaction	$\Delta E^{(2)}$ $(0\nu_{OH})$	$\Delta E^{(2)}$ $(5\nu_{OH})$
$\sigma_{OH} \rightarrow RY_{O(\alpha)}$	0.84	1.23
$\sigma_{OH} \rightarrow \sigma^*_{CO(\alpha)}$	1.90	1.11
$\sigma_{OH} \rightarrow \sigma^*_{OO(\alpha)}$	1.48	2.51
$n^{\pi}_{O(\alpha)} \rightarrow \sigma^*_{OH}$	**1.89**	**5.60**

[a] Where σ = sigma bond, n = lone pair, RY = Rydberg orbital, * = anti-bonding, and O(α) =oxygen bonded to carbon.

Table 7.6: Calculated Oscillator Strength for the Various Transitions in CH_3OOH[a]

Transitions	Oscillator Strength				
	$2\nu_{OH}$	$3\nu_{OH}$	$4\nu_{OH}$	$5\nu_{OH}$	$6\nu_{OH}$
	Considering $\mu(r,\tau)$				
(+) → (+)	4.9×10^{-7}	3.2×10^{-8}	3.6×10^{-9}	2.1×10^{-10}	2.7×10^{-11}
(–) → (–)	5.1×10^{-7}	3.6×10^{-8}	4.2×10^{-9}	2.5×10^{-10}	3.3×10^{-11}
(+) → (–)	3.1×10^{-7}	1.1×10^{-8}	4.1×10^{-10}	2.5×10^{-11}	7.5×10^{-13}
(–) → (+)	3.5×10^{-7}	1.2×10^{-8}	4.9×10^{-10}	3.0×10^{-11}	1.0×10^{-12}
$\frac{[(+) \rightarrow (-)] + [(-) \rightarrow (+)]}{[(+) \rightarrow (+)] + [(-) \rightarrow (-)]}$	0.66	0.34	0.12	0.12	0.03
	Considering $\mu(r)$				
(+) → (+)	8.8×10^{-7}	3.7×10^{-8}	2.1×10^{-9}	1.6×10^{-10}	8.6×10^{-12}
(–) → (–)	9.3×10^{-7}	4.2×10^{-8}	2.5×10^{-9}	1.9×10^{-10}	1.1×10^{-12}
(+) → (–)	5.6×10^{-14}	3.0×10^{-15}	3.1×10^{-16}	6.6×10^{-16}	3.2×10^{-15}
(–) → (+)	4.0×10^{-14}	1.6×10^{-15}	2.9×10^{-16}	1.9×10^{-16}	2.7×10^{-16}
$\frac{[(+) \rightarrow (-)] + [(-) \rightarrow (+)]}{[(+) \rightarrow (+)] + [(-) \rightarrow (-)]}$	5.3×10^{-8}	5.8×10^{-8}	1.3×10^{-7}	2.4×10^{-6}	1.8×10^{-4}

[a] **Computed at the CCSD(T)/cc-pVTZ level.**

Table 7.7: CCSD(T)/cc-pVTZ OH-Stretch / COOH-Torsion Vibrational Levels (in cm^{-1}) and Oscillator Strengths in the First ($2\nu_{OH}$) OH-Stretching Overtone Region

	Final State $\|v'_{OH},v'_{\tau}\rangle$							
Initial State[a] $\|v''_{OH},v''_{\tau}\rangle$	**$\|2,0^+\rangle$ 8901**	**$\|2,1^+\rangle$ 9050**	**$\|2,2^+\rangle$ 9178**	**$\|2,3^+\rangle$ 9379**	**$\|2,0^-\rangle$ 8902**	**$\|2,1^-\rangle$ 9082**	**$\|2,2^-\rangle$ 9271**	**$\|2,3^-\rangle$ 9496**
$\|0,0^+\rangle$ 1927	**4.90*E*-7**	**1.43*E*-7**	**4.02*E*-10**	**1.23*E*-10**	**3.06*E*-7**	**1.10*E*-8**	**9.47*E*-10**	**2.16*E*-11**
$\|0,1^+\rangle$ 2051	**4.74*E*-8**	**4.94*E*-7**	**1.65*E*-7**	**1.70*E*-10**	**7.86*E*-8**	**9.15*E*-8**	**1.74*E*-8**	**1.37*E*-12**
$\|0,2^+\rangle$ 2232	**1.58*E*-8**	**4.85*E*-8**	**4.36*E*-7**	**1.22*E*-7**	**4.45*E*-9**	**1.78*E*-7**	**5.70*E*-8**	**2.25*E*-8**
$\|0,3^+\rangle$ 2478	**1.99*E*-9**	**9.88*E*-9**	**4.60*E*-8**	**4.19*E*-7**	**6.28*E*-10**	**1.12*E*-9**	**1.73*E*-7**	**5.92*E*-8**
$\|0,0^-\rangle$ 1935	**3.45*E*-7**	**4.30*E*-10**	**9.63*E*-9**	**5.90*E*-12**	**5.06*E*-7**	**9.49*E*-8**	**1.51*E*-10**	**4.05*E*-11**
$\|0,1^-\rangle$ 2124	**3.79*E*-8**	**1.86*E*-7**	**3.33*E*-8**	**1.99*E*-8**	**3.59*E*-8**	**4.70*E*-7**	**1.22*E*-7**	**5.46*E*-10**
$\|0,2^-\rangle$ 2349	**6.42*E*-12**	**1.15*E*-8**	**1.73*E*-7**	**5.73*E*-8**	**7.04*E*-9**	**4.60*E*-8**	**4.33*E*-7**	**1.18*E*-7**
$\|0,3^-\rangle$ 2614	**5.04*E*-10**	**7.96*E*-10**	**4.14*E*-11**	**1.64*E*-7**	**3.77*E*-10**	**7.47*E*-9**	**5.45*E*-8**	**4.08*E*-7**

Table 7.8: CCSD(T)/cc-pVTZ OH-Stretch / COOH-Torsion Vibrational Levels (in cm^{-1}) and Oscillator Strengths in the Second ($3\nu_{OH}$) OH-Stretching Overtone Region

	Final State $\|v'_{OH},v'_{\tau}\rangle$							
Initial State[a] $\|v''_{OH},v''_{\tau}\rangle$	**$\|3,0^+\rangle$ 12 109**	**$\|3,1^+\rangle$ 12 283**	**$\|3,2^+\rangle$ 12 401**	**$\|3,3^+\rangle$ 12 572**	**$\|3,0^-\rangle$ 12 110**	**$\|3,1^-\rangle$ 12 296**	**$\|3,2^-\rangle$ 12 473**	**$\|3,3^-\rangle$ 12 679**
$\|0,0^+\rangle$ 1927	**3.24*E*-8**	**1.21*E*-8**	**4.17*E*-10**	**1.70*E*-11**	**1.05*E*-8**	**9.77*E*-10**	**2.80*E*-12**	**2.29*E*-12**
$\|0,1^+\rangle$ 2051	**7.74*E*-9**	**1.95*E*-8**	**1.79*E*-8**	**3.48*E*-10**	**4.26*E*-9**	**1.97*E*-9**	**9.37*E*-10**	**1.13*E*-11**
$\|0,2^+\rangle$ 2232	**2.11*E*-9**	**1.13*E*-8**	**2.06*E*-8**	**9.58*E*-9**	**1.02*E*-9**	**7.76*E*-9**	**8.13*E*-10**	**9.04*E*-10**
$\|0,3^+\rangle$ 2478	**2.34*E*-10**	**1.63*E*-9**	**5.48*E*-9**	**2.82*E*-8**	**3.64*E*-14**	**8.87*E*-10**	**7.74*E*-9**	**1.17*E*-9**
$\|0,0^-\rangle$ 1935	**1.23*E*-8**	**5.39*E*-10**	**2.41*E*-10**	**7.63*E*-12**	**3.58*E*-8**	**8.37*E*-9**	**2.49*E*-10**	**1.26*E*-12**
$\|0,1^-\rangle$ 2124	**3.35*E*-9**	**6.49*E*-9**	**5.12*E*-11**	**8.12*E*-10**	**5.85*E*-9**	**2.78*E*-8**	**1.03*E*-8**	**3.11*E*-10**
$\|0,2^-\rangle$ 2349	**1.45*E*-10**	**2.63*E*-9**	**6.22*E*-9**	**9.08*E*-10**	**7.38*E*-10**	**6.95*E*-9**	**2.73*E*-8**	**8.26*E*-9**
$\|0,3^-\rangle$ 2614	**1.99*E*-11**	**1.54*E*-11**	**5.59*E*-10**	**7.62*E*-9**	**6.70*E*-11**	**7.55*E*-10**	**5.52*E*-9**	**2.97*E*-8**

Table 7.9: CCSD(T)/cc-pVTZ OH-Stretch / COOH-Torsion Vibrational Levels (in cm^{-1}) and Oscillator Strengths in the Third ($4\nu_{OH}$) OH-Stretching Overtone Region

	Final State $\|v'_{OH},v'_{\tau}\rangle$							
Initial State[a] $\|v''_{OH},v''_{\tau}\rangle$	**$\|4,0^+\rangle$ 15 123**	**$\|4,1^+\rangle$ 15 318**	**$\|4,2^+\rangle$ 15 456**	**$\|4,3^+\rangle$ 15 592**	**$\|4,0^-\rangle$ 15 123**	**$\|4,1^-\rangle$ 15 321**	**$\|4,2^-\rangle$ 15 498**	**$\|4,3^-\rangle$ 15 685**
$\|0,0^+\rangle$ 1927	**3.59*E*-9**	**1.68*E*-9**	**3.60*E*-10**	**7.59*E*-14**	**4.12*E*-10**	**7.26*E*-11**	**1.12*E*-12**	**9.41*E*-14**
$\|0,1^+\rangle$ 2051	**1.52*E*-9**	**8.01*E*-10**	**2.80*E*-9**	**3.38*E*-10**	**2.39*E*-10**	**3.11*E*-11**	**4.82*E*-11**	**3.08*E*-12**
$\|0,2^+\rangle$ 2232	**6.40*E*-10**	**2.44*E*-9**	**7.49*E*-10**	**1.61*E*-9**	**1.18*E*-10**	**3.33*E*-10**	**1.17*E*-12**	**3.66*E*-11**
$\|0,3^+\rangle$ 2478	**5.53*E*-11**	**7.50*E*-10**	**1.38*E*-9**	**2.30*E*-9**	**4.53*E*-12**	**1.40*E*-10**	**3.26*E*-10**	**9.16*E*-12**
$\|0,0^-\rangle$ 1935	**4.89*E*-10**	**6.45*E*-11**	**1.17*E*-12**	**1.69*E*-12**	**4.15*E*-9**	**1.38*E*-9**	**1.59*E*-10**	**1.02*E*-12**
$\|0,1^-\rangle$ 2124	**2.48*E*-10**	**1.88*E*-10**	**2.10*E*-11**	**2.68*E*-11**	**1.43*E*-9**	**2.28*E*-9**	**1.71*E*-9**	**1.89*E*-10**
$\|0,2^-\rangle$ 2349	**3.68*E*-11**	**2.70*E*-10**	**1.68*E*-10**	**1.37*E*-12**	**2.25*E*-10**	**1.83*E*-9**	**2.17*E*-9**	**1.28*E*-9**
$\|0,3^-\rangle$ 2614	**6.60*E*-14**	**2.84*E*-11**	**1.09*E*-10**	**3.20*E*-10**	**1.07*E*-11**	**2.41*E*-10**	**1.49*E*-9**	**2.97*E*-9**

Table 7.10: CCSD(T)/cc-pVTZ OH-Stretch / COOH-Torsion Vibrational Levels (in cm^{-1}) and Oscillator Strengths in the Forth ($5\nu_{OH}$) OH-Stretching Overtone Region

	Final State $\|v'_{OH},v'_{\tau}\rangle$							
Initial State[a] $\|v''_{OH},v''_{\tau}\rangle$	**$\|5,0^+\rangle$ 17 944**	**$\|5,1^+\rangle$ 18 156**	**$\|5,2^+\rangle$ 18 331**	**$\|5,3^+\rangle$ 18 452**	**$\|5,0^-\rangle$ 17 944**	**$\|5,1^-\rangle$ 18 156**	**$\|5,2^-\rangle$ 18 343**	**$\|5,3^-\rangle$ 18 521**
$\|0,0^+\rangle$ 1927	**2.12*E*-10**	**1.04*E*-10**	**4.18*E*-11**	**3.16*E*-12**	**2.46*E*-11**	**4.56*E*-12**	**1.99*E*-13**	**2.41*E*-15**
$\|0,1^+\rangle$ 2051	**1.40*E*-10**	**6.58*E*-12**	**1.08*E*-10**	**7.17*E*-11**	**2.05*E*-11**	**3.54*E*-13**	**1.88*E*-12**	**2.62*E*-13**
$\|0,2^+\rangle$ 2232	**1.01*E*-10**	**1.68*E*-10**	**2.03*E*-12**	**8.73*E*-11**	**1.86*E*-11**	**1.93*E*-11**	**3.61*E*-13**	**1.15*E*-12**
$\|0,3^+\rangle$ 2478	**1.67*E*-11**	**1.44*E*-10**	**1.38*E*-10**	**3.05*E*-11**	**3.02*E*-12**	**2.42*E*-11**	**1.72*E*-11**	**8.94*E*-16**
$\|0,0^-\rangle$ 1935	**2.99*E*-11**	**4.62*E*-12**	**4.19*E*-14**	**7.60*E*-14**	**2.53*E*-10**	**1.01*E*-10**	**2.35*E*-11**	**1.06*E*-12**
$\|0,1^-\rangle$ 2124	**2.68*E*-11**	**6.07*E*-12**	**2.85*E*-12**	**2.85*E*-13**	**1.64*E*-10**	**7.01*E*-11**	**1.10*E*-10**	**3.11*E*-11**
$\|0,2^-\rangle$ 2349	**9.61*E*-12**	**2.82*E*-11**	**3.94*E*-12**	**5.28*E*-13**	**4.94*E*-11**	**2.01*E*-10**	**4.71*E*-11**	**8.59*E*-11**
$\|0,3^-\rangle$ 2614	**3.63*E*-13**	**1.21*E*-11**	**2.09*E*-11**	**1.23*E*-11**	**3.52*E*-12**	**6.84*E*-11**	**1.89*E*-10**	**9.76*E*-11**

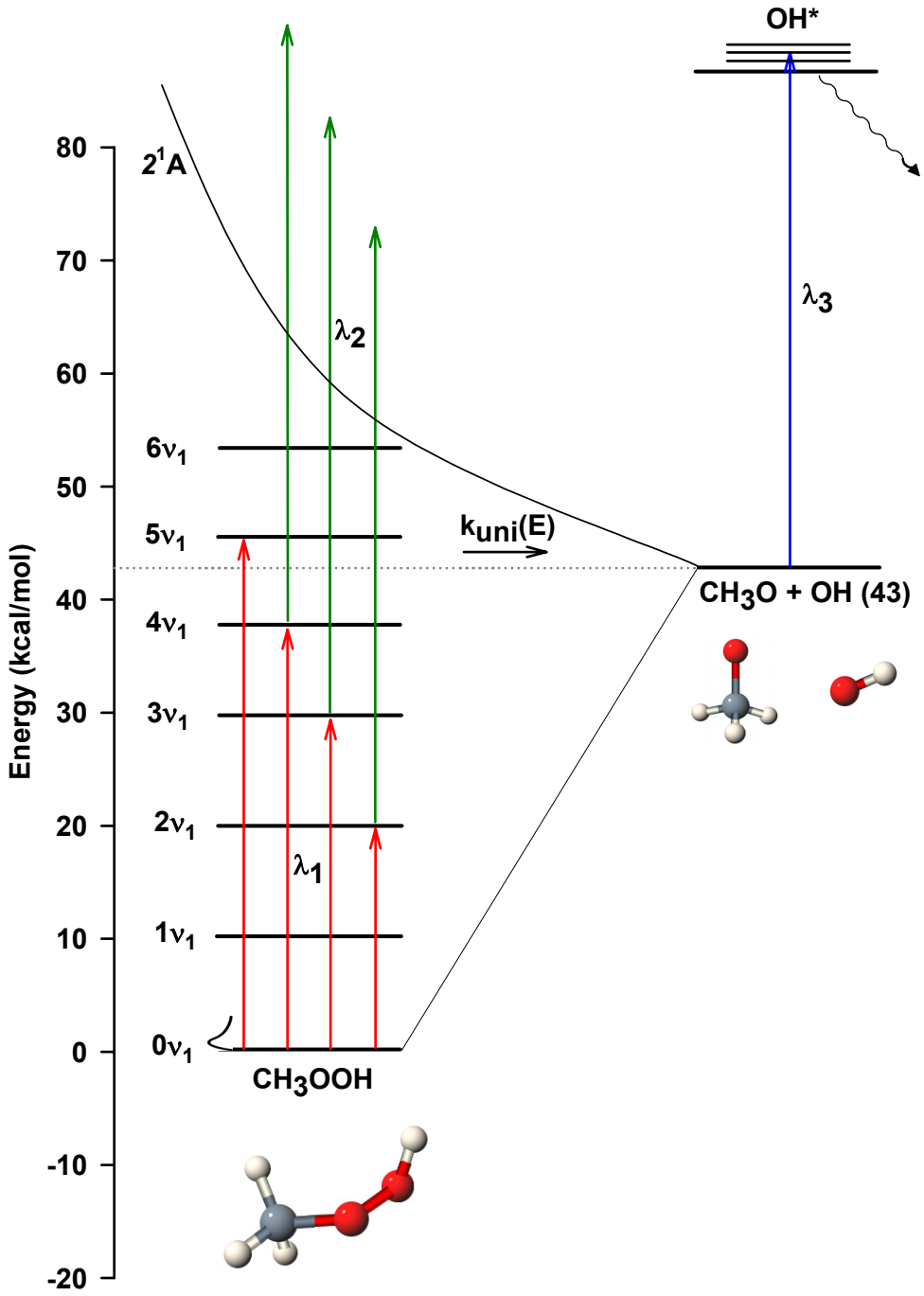

Figure 7.1: Schematic of the ViMP experiments conducted on the CH_3OOH molecule. Initially, the molecule is vibrationally excited (λ_1) on the ground electronic state in the vicinity of the first, second and third OH stretching overtone regions. The vibrationally excited molecule is then dissociated on the electronically excited state using a visible light (λ_2 = 532 nm). The resulting OH fragments are subsequently probed (λ_3) using LIF. The $5\nu_{OH}$ is investigated directly using the pump-probe technique as described in Chapter 6. [File: F7.1_mhp_vimp]

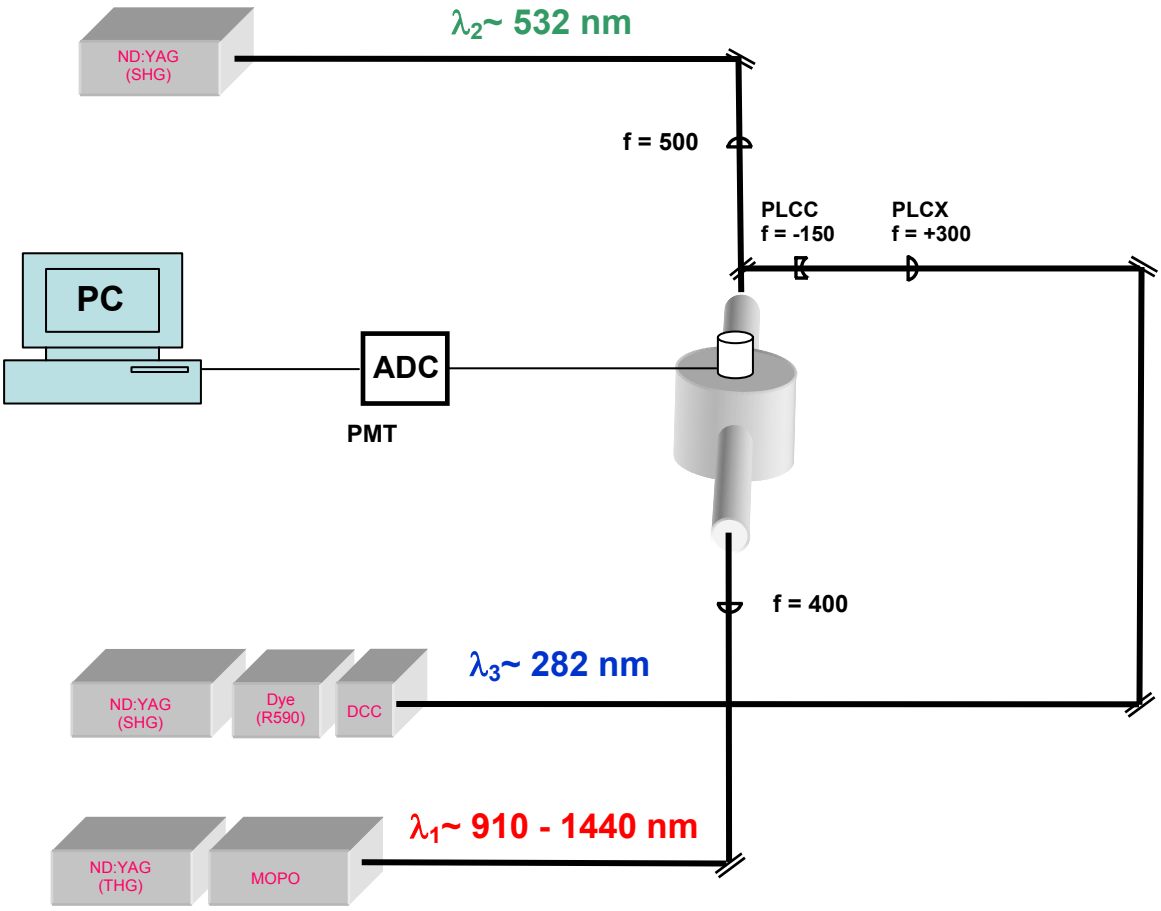

Figure 7.2: Schematic of the experimental apparatus used in recording the $2\nu_{OH}$ and $3\nu_{OH}$ overtone regions. The tunable IR radiation used for the vibrational excitation (λ_1) is generated by the OPO laser system. The 532 nm photolysis beam is generated by the second harmonic of the NY82-20 system (λ_2). The UV radiation used to probe the OH transition via the $A - X(1,0)$ off-diagonal transition is generated by the doubled output of the NY81-20 dye laser system(λ_3). The temporal delay between the pumps and probe lasers is set to 15 ns. A set of plano-convex (+300 mm) and plano-concave (-150 mm) lenses collimate the probe beam to reduce scatter light. [File: F7.2_apparatus1]

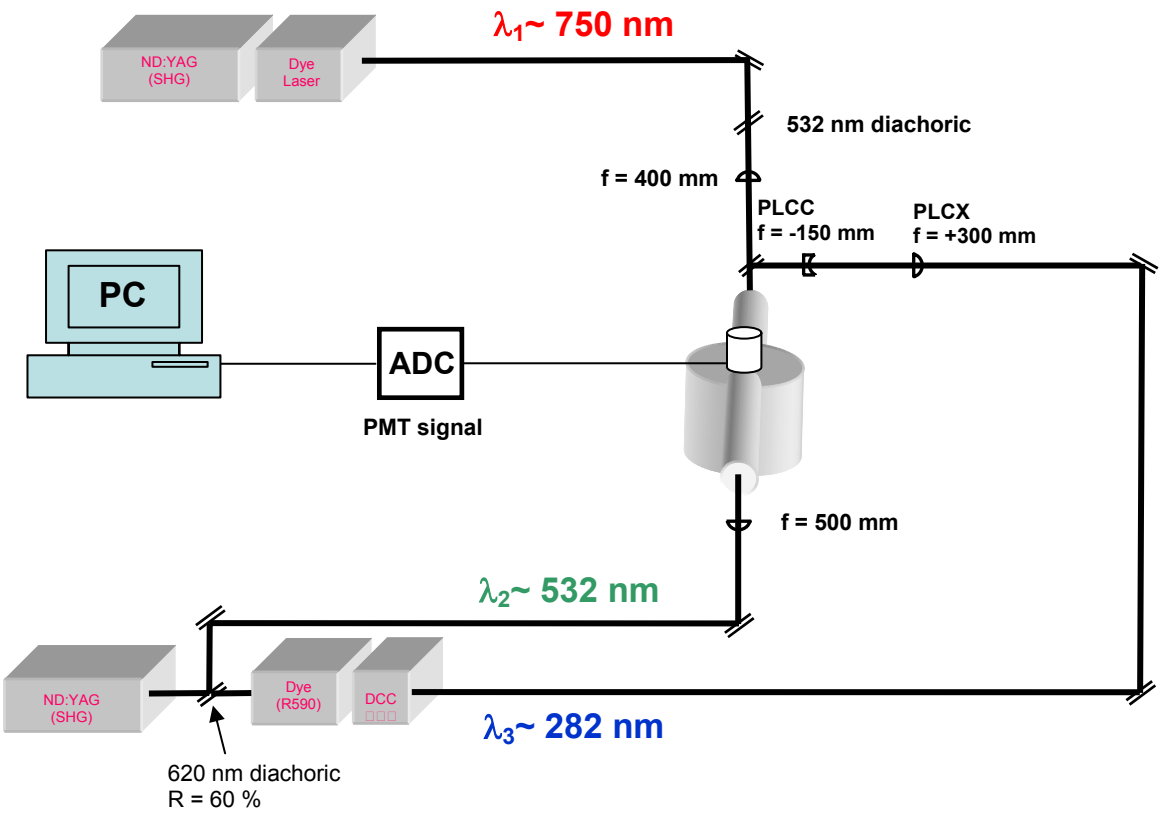

Figure 7.3: Schematic of the experimental apparatus used in recording the $4\nu_{OH}$ overtone region. The tunable IR radiation used for the vibrational excitation (λ_1) is generated by the NY82-20 laser system. The 532 nm photolysis beam is generated by the second harmonic of the NY82-10 system (λ_2). The UV radiation used to probe the OH transition via the $A - X(1,0)$ off-diagonal transition is generated by the doubled output of the NY81-20 dye laser system (λ_3). [File: F7.3_apparatus2]

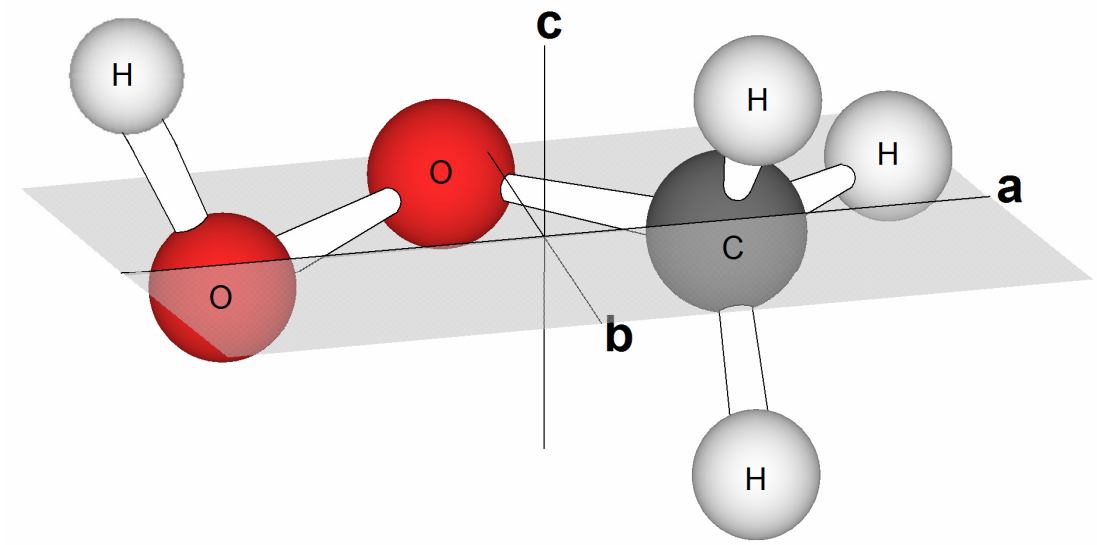

Figure 7.4: CH_3OOH molecule oriented along its a-, b- and c- principle inertial axes. Note that as the figure illustrates, motion along the a-b plane (OOC plane) will have strong effects on the c-component of the dipole moment function.
[File: F7.4_mhp_molecule]

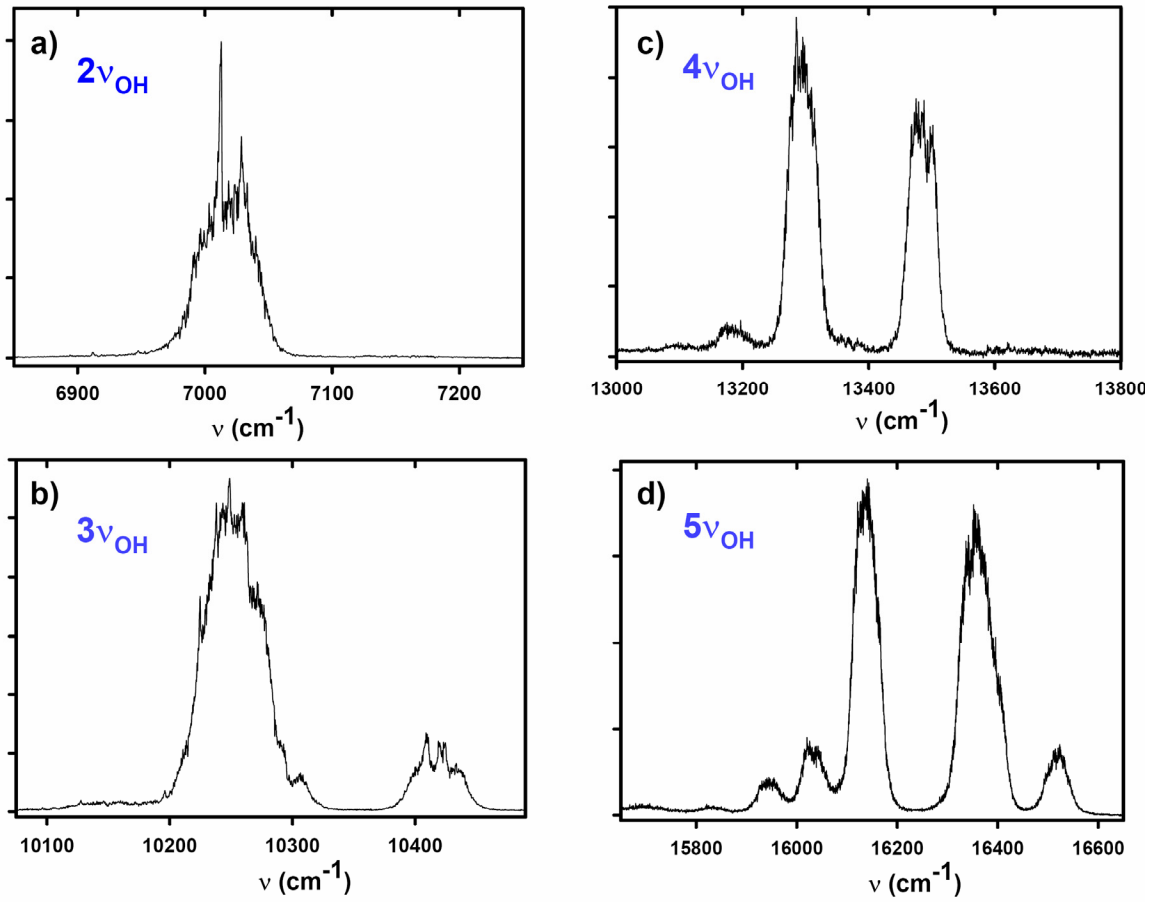

Figure 7.5: The low pressure vibrational overtone spectra of CH_3OOH generated using the ViMP technique in the a) $2\nu_{OH}$, b) $3\nu_{OH}$ and c) $4\nu_{OH}$ regions. Since the $5\nu_{OH}$ band lies entirely above the dissociation threshold, its spectrum shown in panel (d) is generated by directly probing the resulting OH-photoproducts from the overtone induced photodissociation process (see Chapter 6). From these panels we observed the trend where as the vibrational excitation in the OH increases, the spectrum becomes richer with additional vibrational states. [File: F7.5_overtones]

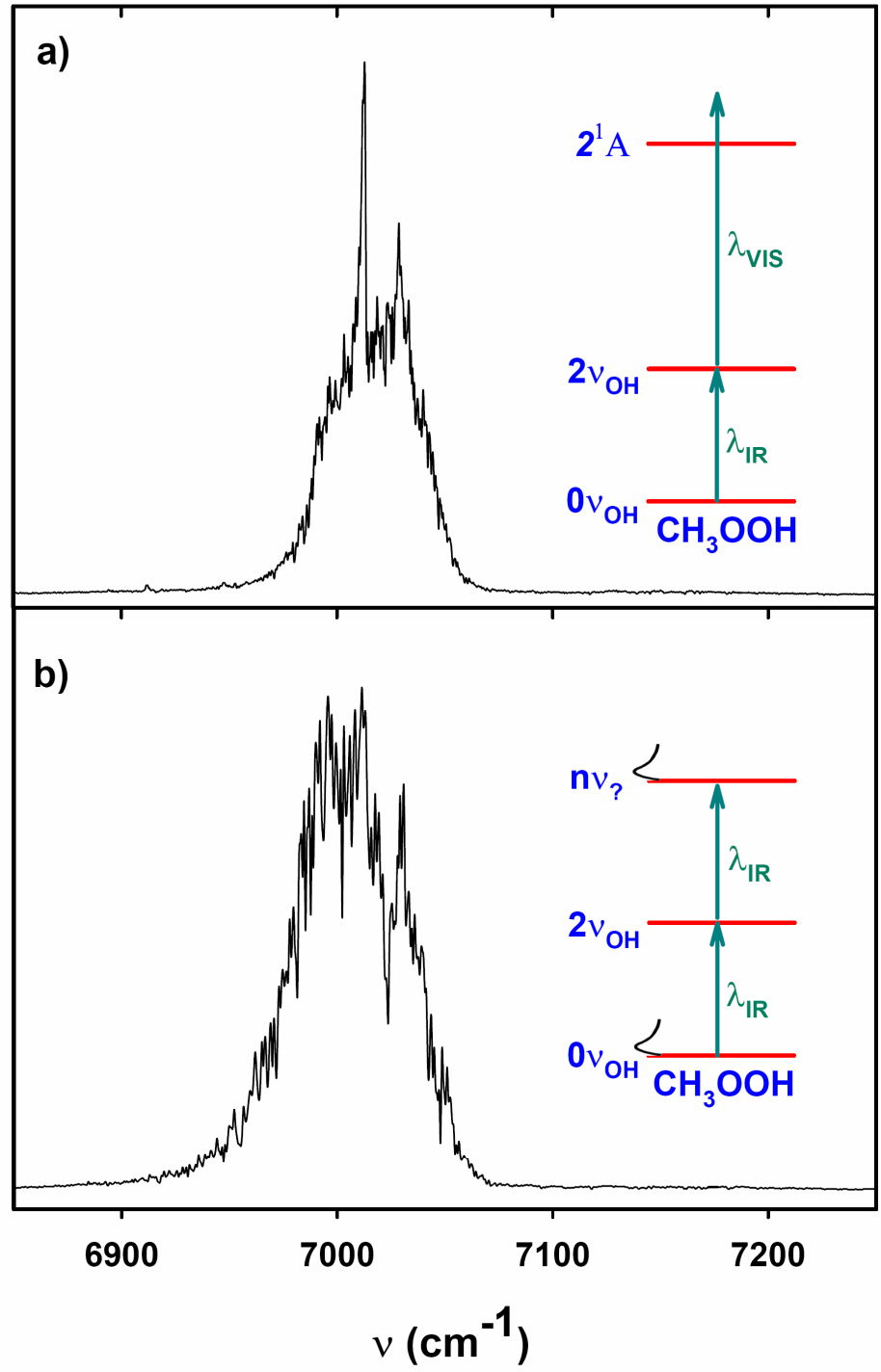

Figure 7.6: The $2\nu_{OH}$ action spectra of methyl hydroperoxide generated from: a) The ViMP $2\nu_{OH}$ + 532 nm process generated by collimated beam conditions using 1000 and 400 mm lens system. b) The one-color two-photon dissociation process which is induced by the focused ~4 mJ of the OPO laser (λ_1). [File: F7.6_2nOH]

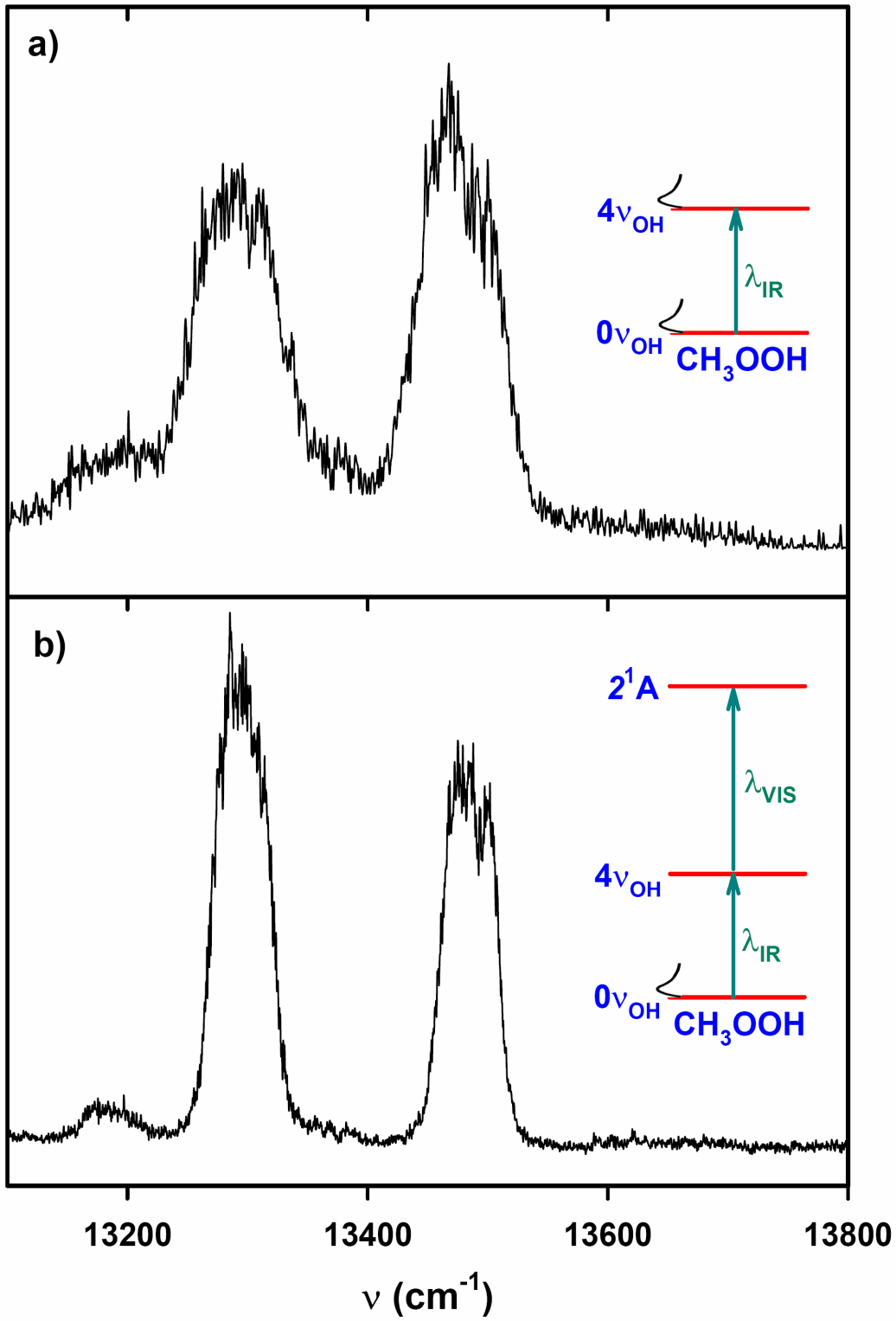

Figure 7.7: The $4\nu_{OH}$ action spectra of methyl hydroperoxide generated from: a) The thermally assisted unimolecular photodissociation process. b) The ViMP $4\nu_{OH}$ + 532 nm photodissociation process. [File: F7.7_4nOH]

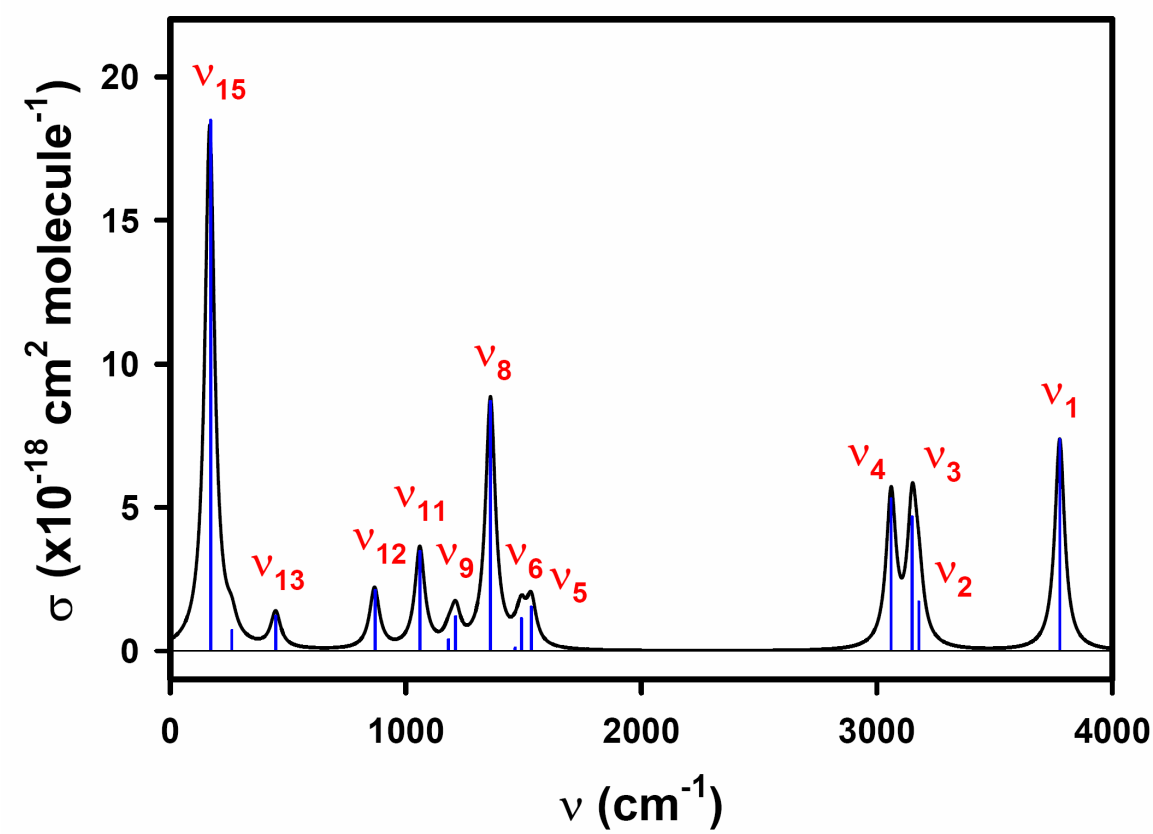

Figure 7.8: Simulated absorption cross-section of MHP molecule in the fundamental region generated by running GAUSSIAN03 [23] at the MP2/aug-cc-pVTZ level of theory. Note that the spectrum is dominated by the HOOC-torsion (ν_{15}), OH-stretch (ν_1), its HOO-bend (ν_8), and the various CH-stretching (ν_2-ν_4) modes. [File: F7.8_1nu]

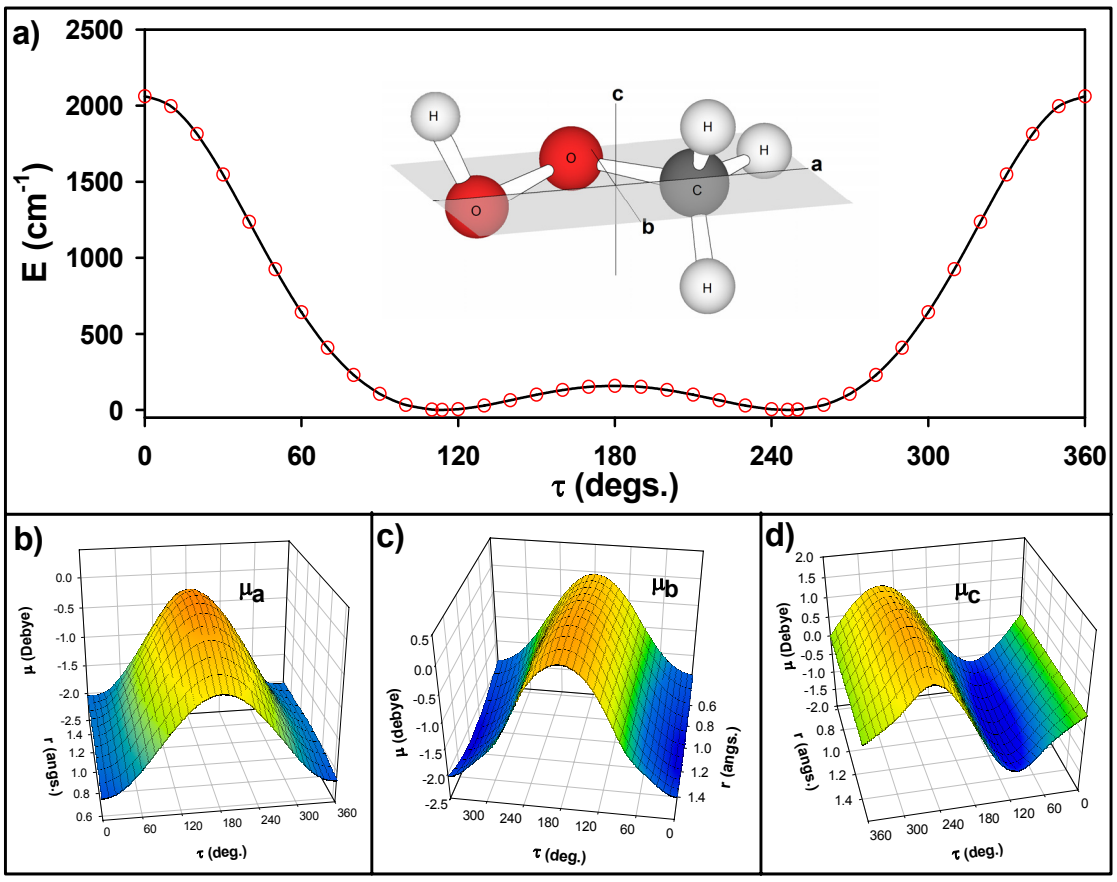

Figure 7.9: a) *Ab initio* potential for HOOC torsional motion calculated at the CCSD(T)/cc-pVTZ level of theory. We consider torsional angles between $\tau = \pm 180^{o}$ in steps of 10 degrees and for each fixed value of the torsional angle, we optimize all the other coordinates. b) Two-dimensional dipole moment function (DMF) of the symmetric $\mu_a(r,\tau)$ as a function O-H separation, r, and HOOC torsion angle, τ. c) Two-dimensional DMF of the symmetric $\mu_b(r,\tau)$ as a function O-H separation, r, and HOOC torsion angle, τ. d) Two-dimensional DMF of the antisymmetric $\mu_c(r,\tau)$ as a function O-H separation, r, and HOOC torsion angle, τ. These dipole moment surfaces are also computed at the CCSD(T)/cc-pVTZ level using ACESII.[24] [File: F7.9_potential]

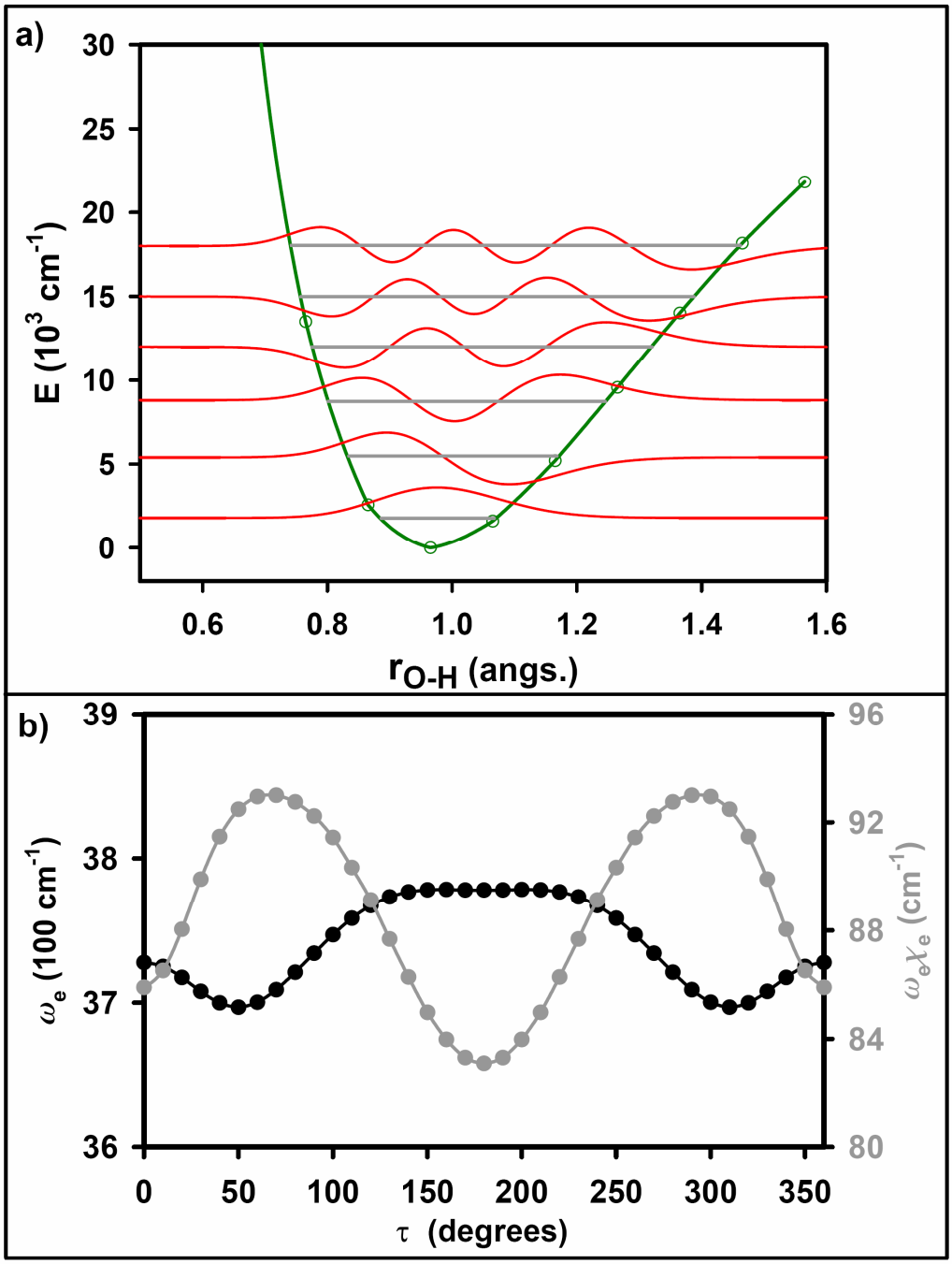

Figure 7.10: a) *Ab initio* potential slice for O-H stretching motion, r, calculated at the CCSD(T)/cc-pVTZ level of theory at $\tau \approx 114^{o}$. We consider separation of $-0.4 \leq r_e \leq +0.6$ Å in steps of 0.1 Å. We then use the FGH1D code to obtain the shown eigenfunctions of these OH potentials.[41] b) Variation in OH stretching frequency (ω_e) and anharmonicity ($\omega_e\chi_e$) with torsion angle that were also obtained from the FGH1D code. Their values at $\tau_{eq.} \approx 114^{o}$ are respectively $\omega_e = 3762$ cm^{-1} and $\omega_e\chi_e = 90$ cm^{-1}.
[File: F7.10_oh]

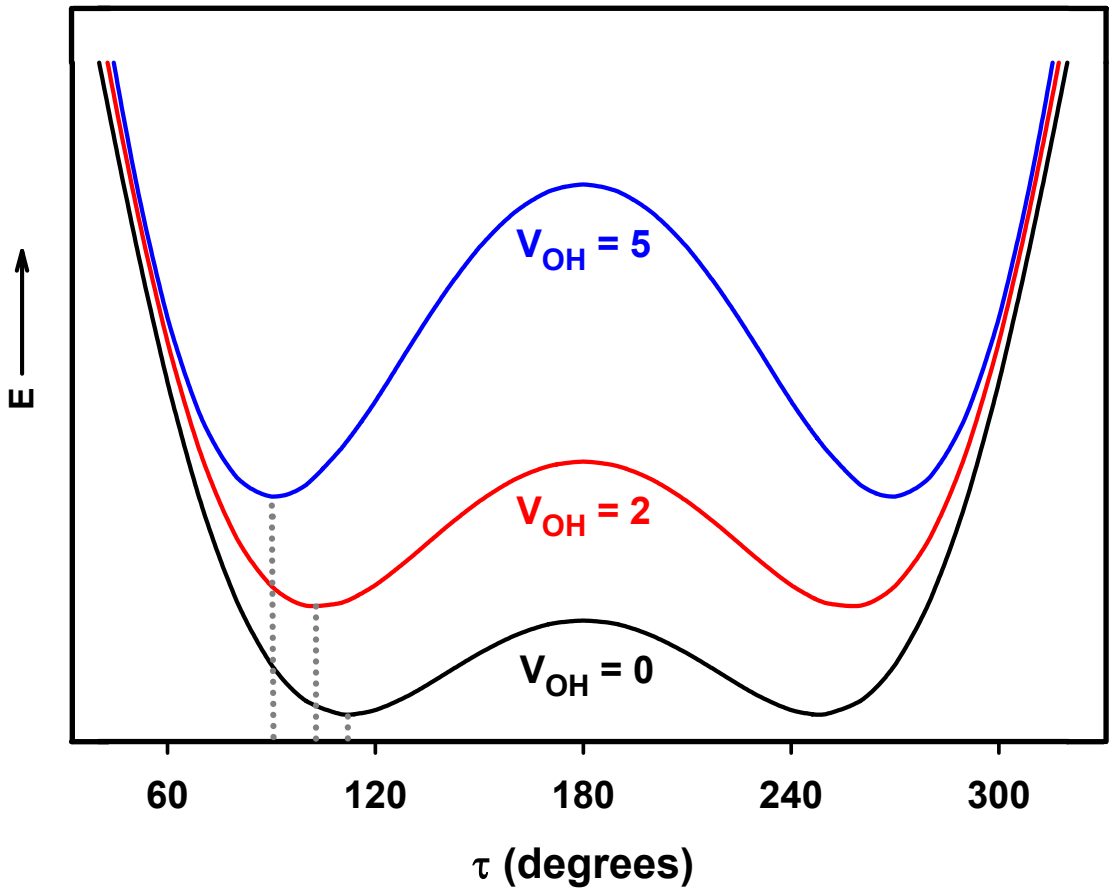

Figure 7.11: CCSD(T)/cc-pVTZ adiabatic torsional potentials associated with excitation of the OH stretching states $0\nu_{OH}$, $2\nu_{OH}$ and $5\nu_{OH}$. The energy scale is arbitrary. This diagram illustrates that as the OH vibrational excitation increases, the torsional barrier at $\tau = 180^{o}$ gradually increases from 173 to 575 cm^{-1} and $\tau_{eq.}$ gradually shifts from 112 to 91^{o} in going from $0\nu_{OH}$ to $5\nu_{OH}$ (see Table 7.4). [File: F7.11_v0_v2_v5]

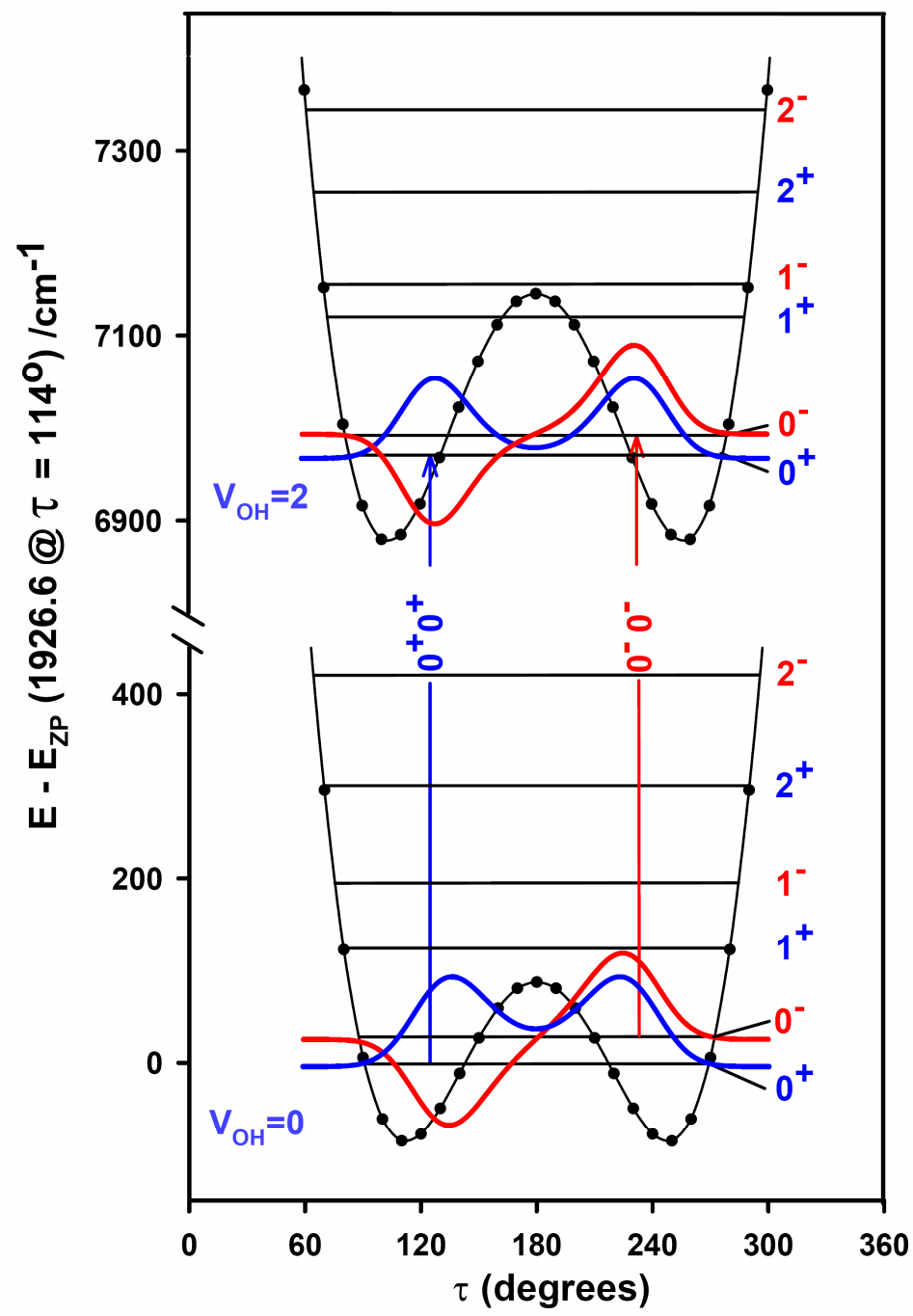

Figure 7.12: Adiabatic torsional potentials for the OH stretching states. The zero-point energy (~1927 cm^{-1}) has been subtracted out in the vertical energy scale. The OH stretching states are labeled by the quantum number V_{OH} while their corresponding torsional states are labeled by the quantum number $0^{\pm}$, $1^{\pm}$, $2^{\pm}$. The barrier in the *trans* position causes splitting of the wavefunctions into symmetric (+) and antisymmetric (–) types. We consider all transitions (+) → (+), (–) → (–) and (+) ↔ (–) allowed in our simulations. [File: F7.12_torsion_diagram]

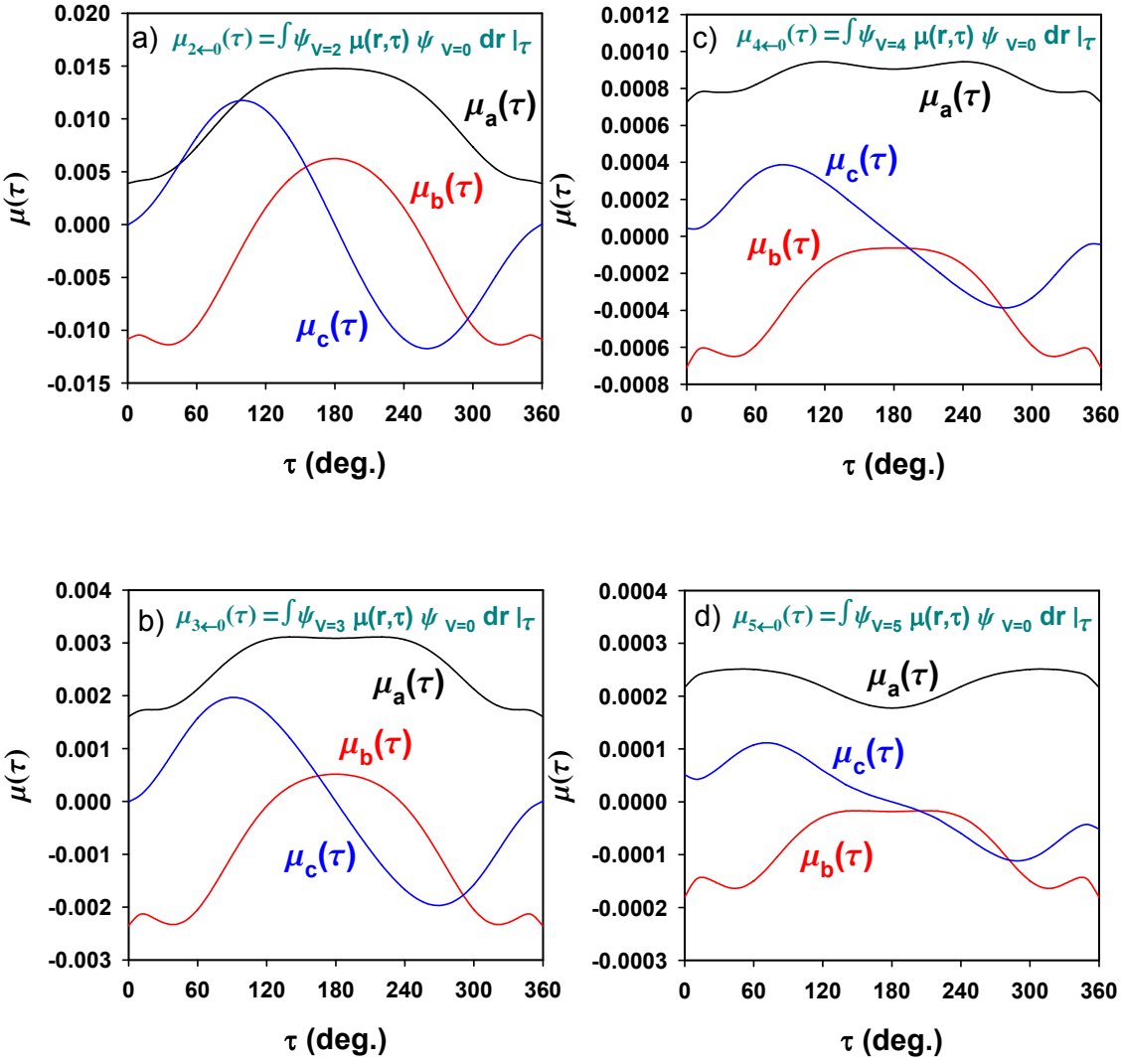

Figure 7.13: $\mu_\alpha(\tau)$ transition dipole moment functions obtain by integrating $\mu(r,\tau)$ along the O-H stretching coordinate -r for the transitions between $V_{OH} = 0$ and the final state: a) $V_{OH} = 2$. b) $V_{OH} = 3$. c) $V_{OH} = 4$. d) $V_{OH} = 5$. For all these transitions we observe that while both $\mu_a(\tau)$ and $\mu_b(\tau)$ components are symmetric about the *trans* barrier at $\tau = 180^o$, the $\mu_c(\tau)$ component is antisymmetric. [File: F7.13_dipole_ut]

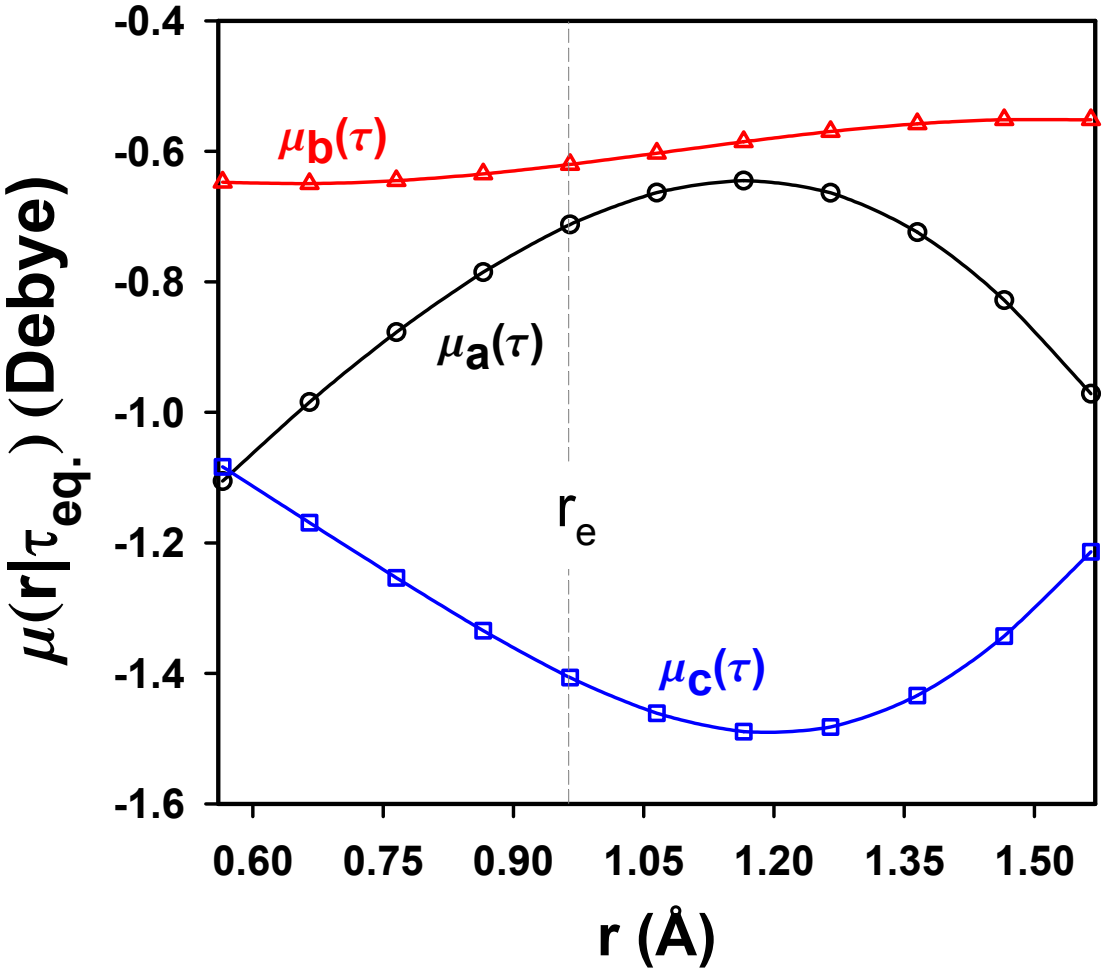

Figure 7.14: $\mu_\alpha(r|\tau_{eq.})$ transition dipole moment functions obtain by evaluating the $\mu(r,\tau)$ at $\tau_{eq.}$. The procedure leads to the removal of the dependence of the DMF on the torsion motion. In turns, this produce intensities that depend on the product of $\langle\psi_v{}'^{OH}(r|\tau)|\mu_\alpha(r)|\psi_v{}^{OH}(r|\tau)\rangle$, and the overlap integral $\langle\chi^{v'}{}_{m'}(\tau)|\chi^{v}{}_{m}(\tau)\rangle$ (see text).
[File: F7.14_dipole_ur]

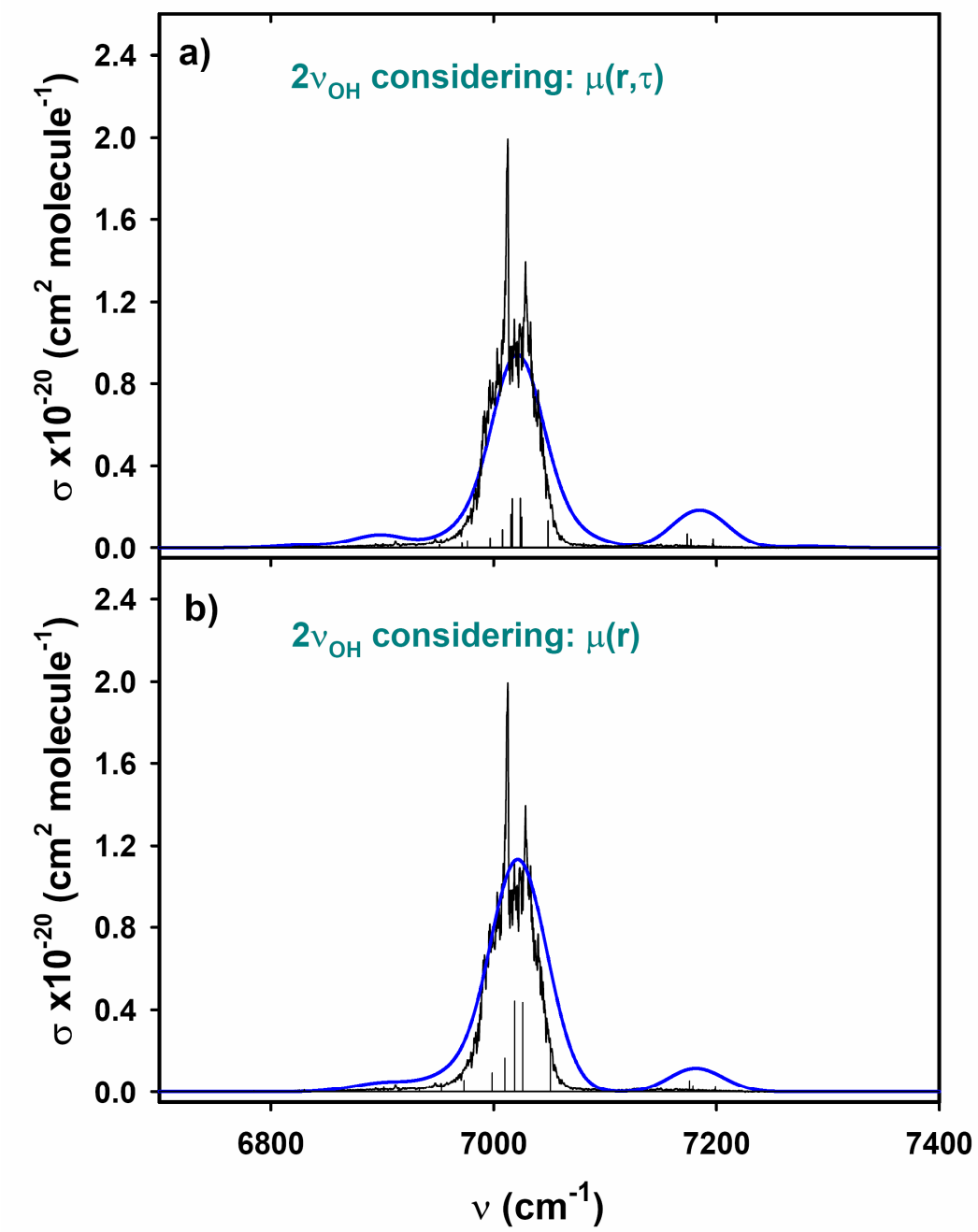

Figure 7.15: Simulated $2\nu_{OH}$ action spectrum resulting from the two-dimensional intensity calculation using a dipole surface computed at the CCSD(T)/cc-pVTZ level of theory and the adiabatic torsional potential considering the a) **$\mu(r,\tau)$** and b) **$\mu(r)$** dependencies. The vertical lines in the stick spectrum are the effective strengths of the vibrational transitions weighted by their respective oscillator strength and Boltzmann factor. A 50 cm^{-1} Gaussian envelope accounts for the rotational distributions within these vibrational states and is shown with the smooth line. The intensity of the experimental spectrum is normalized to the predicted *ab initio* values. [File: F7.15_2nOH_fits]

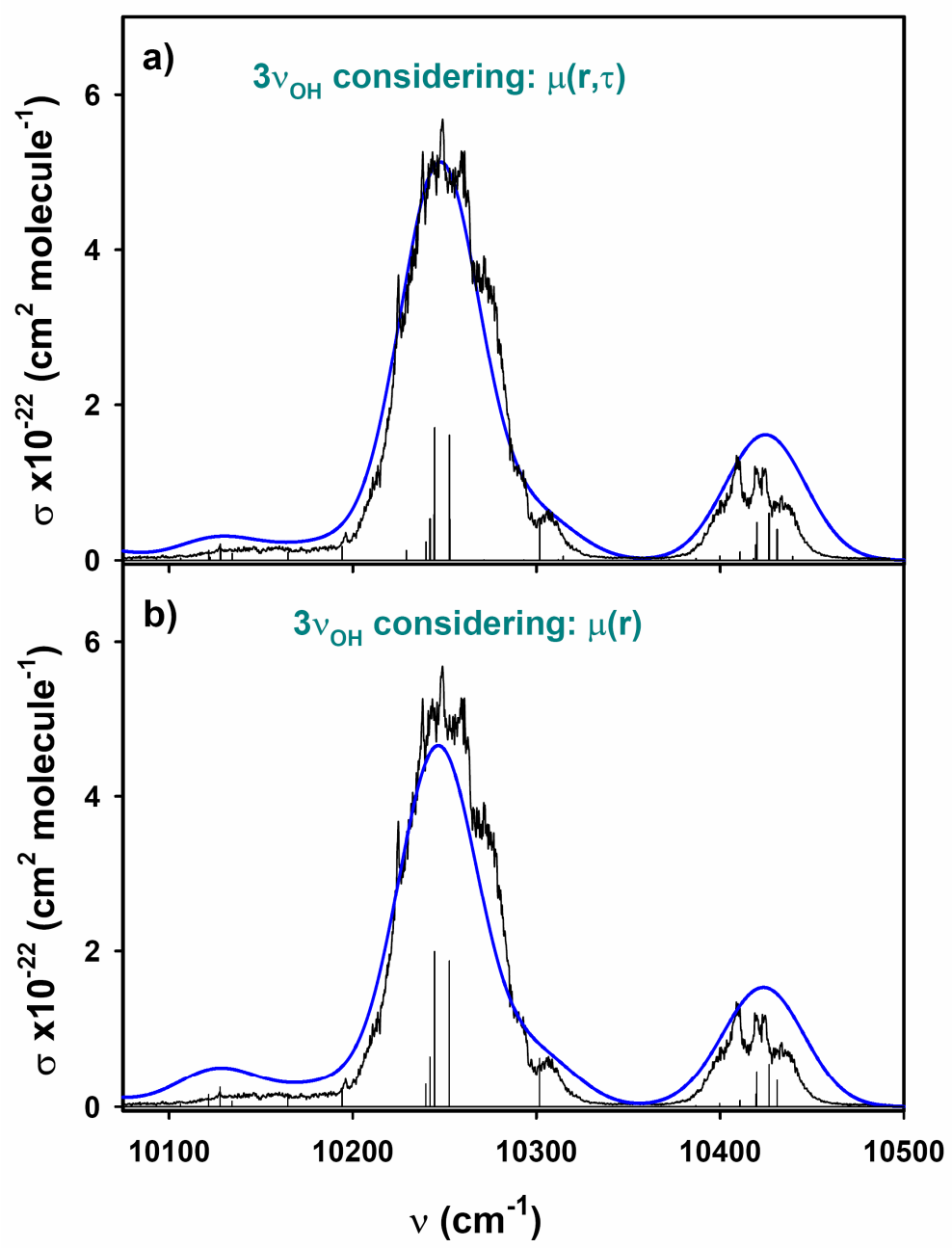

Figure 7.16: Simulated $3\nu_{OH}$ action spectrum resulting from the two-dimensional intensity calculation using a dipole surface computed at the CCSD(T)/cc-pVTZ level of theory and the adiabatic torsional potential considering the a) **$\mu(r,\tau)$** and b) **$\mu(r)$** dependencies. The vertical lines in the stick spectrum are the effective strengths of the vibrational transitions weighted by their respective oscillator strength and Boltzmann factor. A 50 cm^{-1} Gaussian envelope accounts for the rotational distributions within these vibrational states and is shown with the smooth line. The intensity of the experimental spectrum is normalized to data in Ref. 7. [File: F7.16_3nOH_fits]

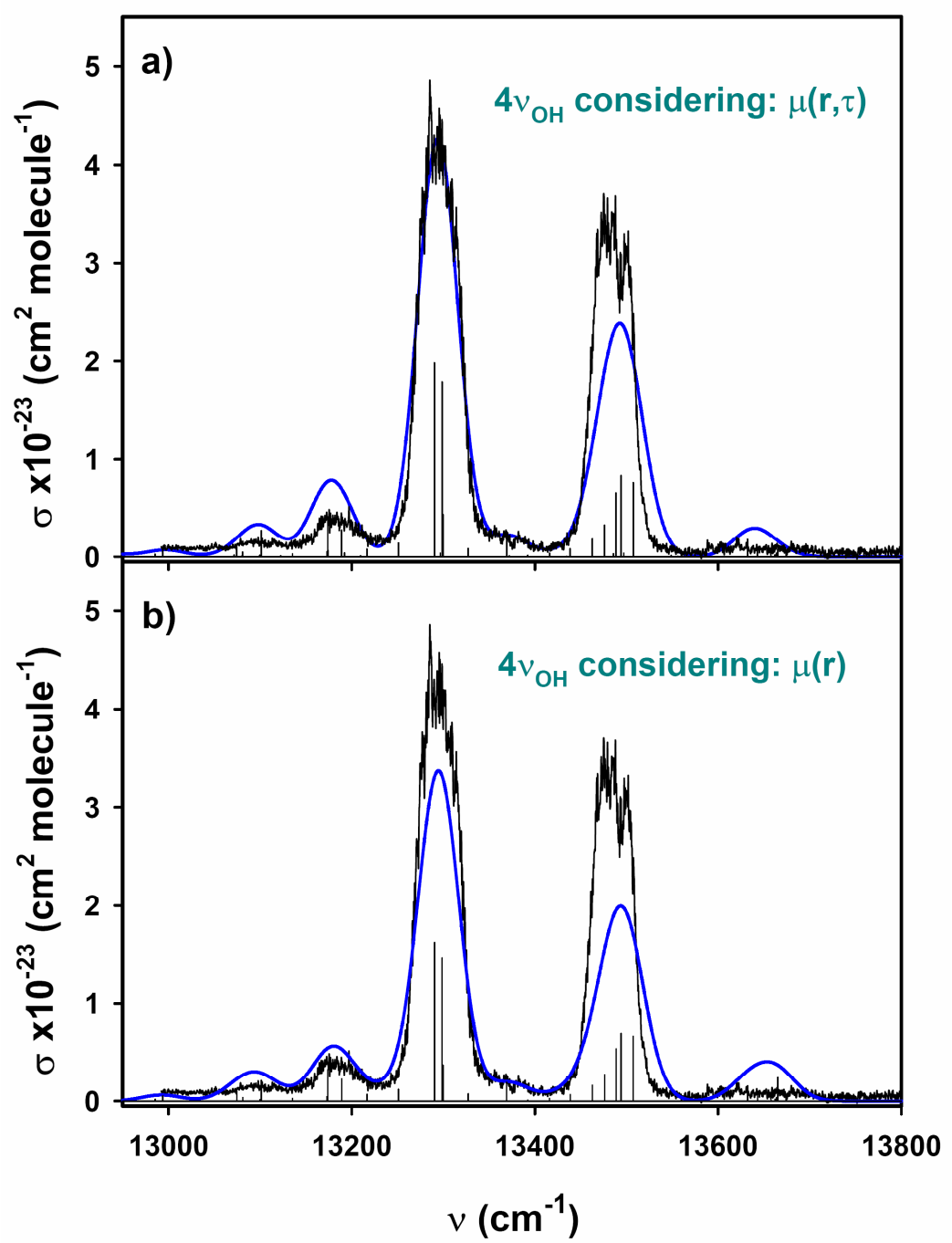

Figure 7.17: Simulated $4\nu_{OH}$ action spectrum resulting from the two-dimensional intensity calculation using a dipole surface computed at the CCSD(T)/cc-pVTZ level of theory and the adiabatic torsional potential considering the a) **$\mu(r,\tau)$** and b) **$\mu(r)$** dependencies. The vertical lines in the stick spectrum are the effective strengths of the vibrational transitions weighted by their respective oscillator strength and Boltzmann factor. A 50 cm^{-1} Gaussian envelope accounts for the rotational distributions within these vibrational states and is shown with the smooth line. The intensity of the experimental spectrum is normalized to data in Ref. 6. [File: F7.17_4nOH_fits]

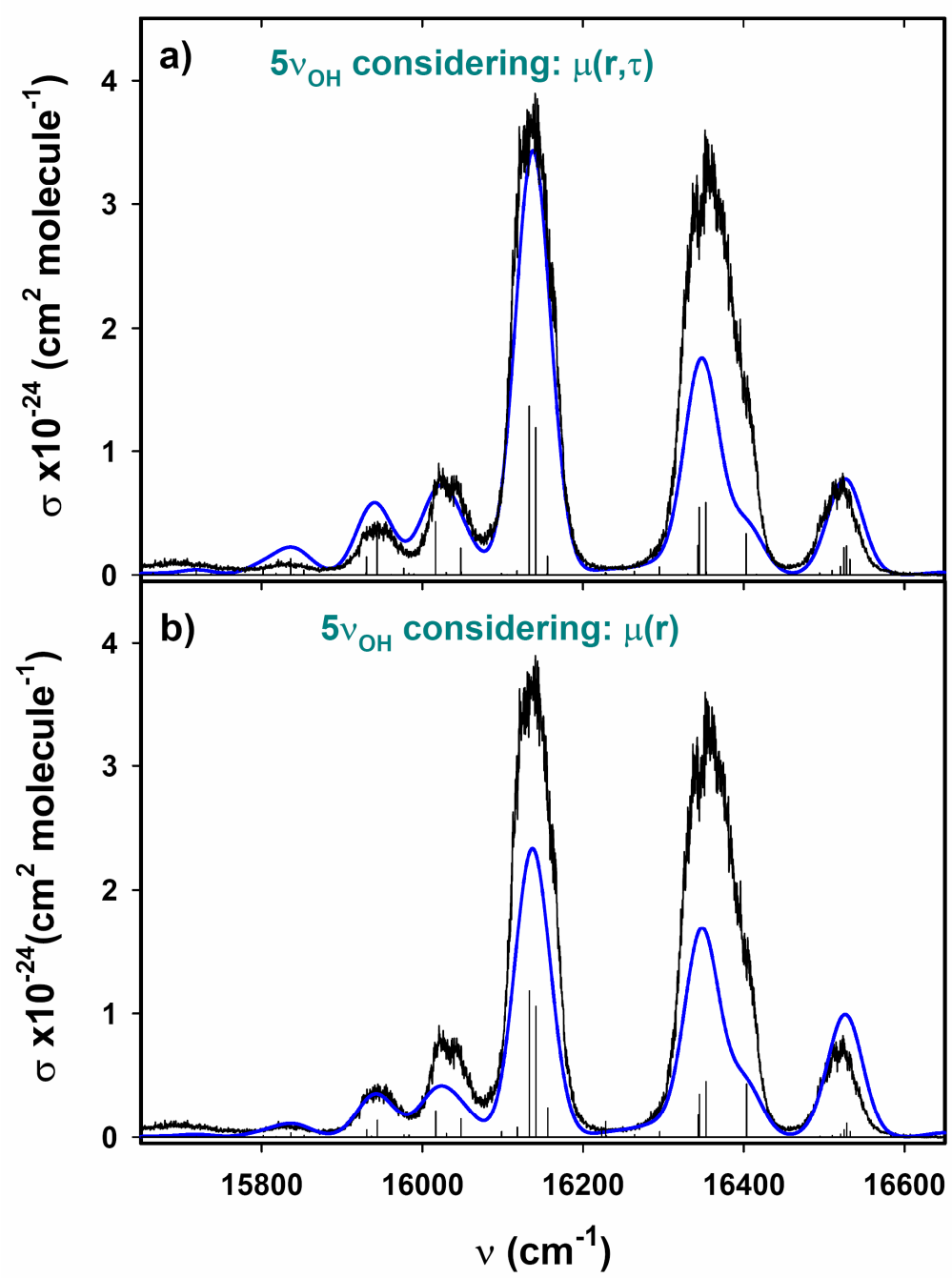

Figure 7.18: Simulated $5\nu_{OH}$ action spectrum resulting from the two-dimensional intensity calculation using a dipole surface computed at the CCSD(T)/cc-pVTZ level of theory and the adiabatic torsional potential considering the a) **μ(r,τ)** and b) **μ(r)** dependencies. The vertical lines in the stick spectrum are the effective strengths of the vibrational transitions weighted by their respective oscillator strength and Boltzmann factor. A 50 cm^{-1} Gaussian envelope accounts for the rotational distributions within these vibrational states and is shown with the smooth line. The intensity of the experimental spectrum is normalized for data in Chapter 10. [File: F7.18_5nOH_fits]

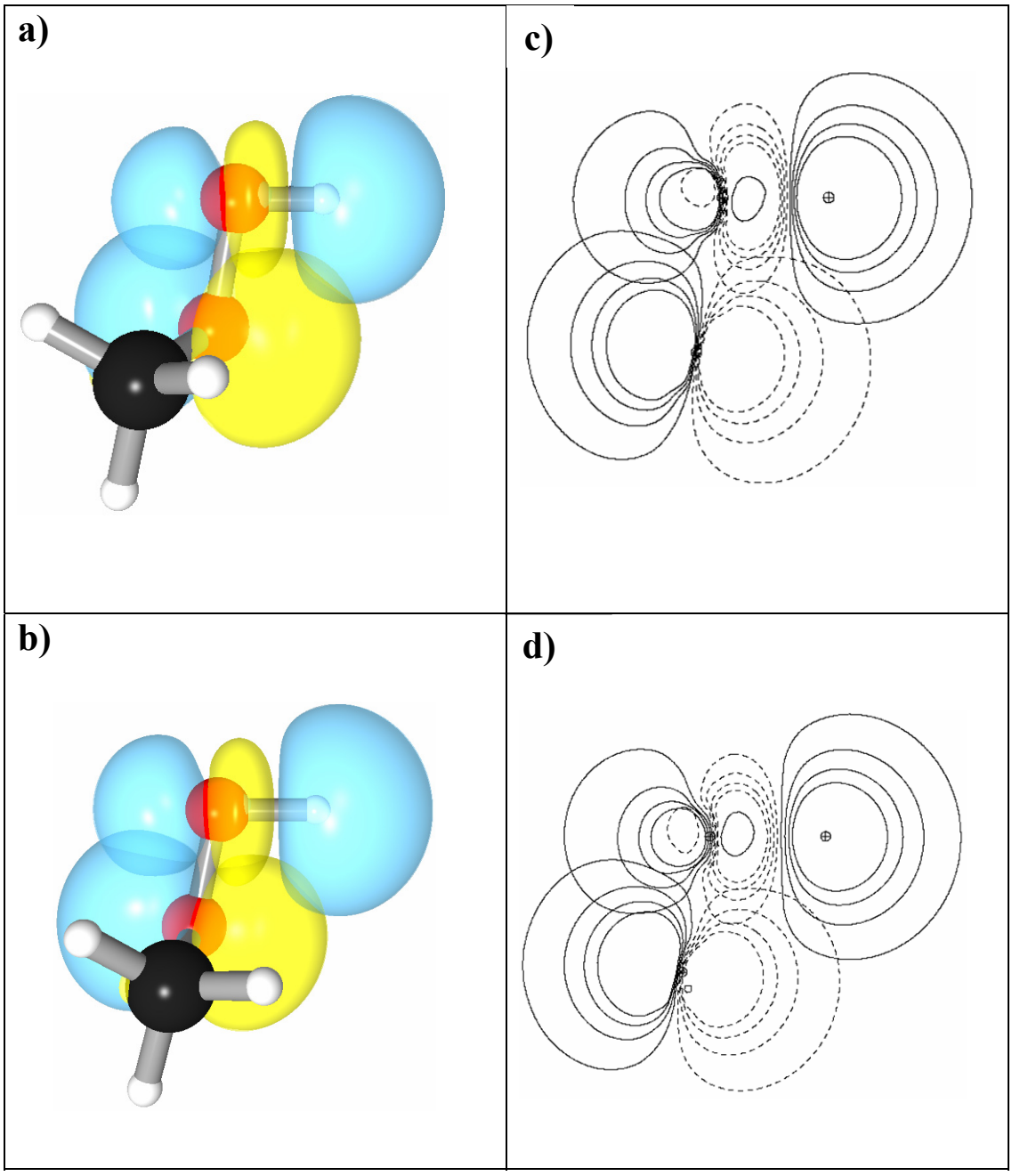

Figure 7.19: a) 3-D representations of the natural bond orbital (NBO) for the $n^{\pi}_{O(\alpha)} \rightarrow \sigma^*_{OH}$ interaction in CH_3OOH at a) V_{OH} =0 and b) V_{OH} =5. The same interactions are also represented in the 2-D contours in c) for the V_{OH} =0 state and d) for the V_{OH} =5 state. At $0\nu_{OH}$ these interaction energies are ~1.9 kcal/mol and at $0\nu_{OH}$ they are increased to ~5.6 kcal/mol which, in turns, makes it harder for the H-atom to rotate in the COO plane. [File: F7.19_orbitals]

7.7 References

1. F. F. Crim, Annu. Rev. Phys. Chem. **44**, 397 (1993).

2. T. M. Ticich, M. D. Likar, H. –R. Dübal, L. J. Butler, F. F. Crim, J. Chem. Phys. **87**, 5820 (1987).

3. S. M. Holland, R. J. Stickland, M. N. R. Ashfold, D. A. Newnham, I. M. Mills, J. Chem. Soc. Faraday Trans. **87**, 3461 (1991).

4. A. Sinha, R. L. Vander Wal, F. F. Crim, J. Chem. Phys. **91**, 2929 (1989).

5. R. J. Barnes, P. J. Dagdigian, H. M. Lambert, and A. Sinha, J. Chem. Phys. **111**, 151 (1999).

6. S. C. Homitsky, S. M. Dragulin, L. M. Haynes, and S. Hsieh, J. Phys. Chem. A. **108**, 9492 (2004).

7. L. M. Haynes, K. M. Vogelhuber, J. L. Pippin, and S. Hsieh, J. Chem. Phys. **123**, 234306 (2005).

8. M. R. Wedlock, R. Jost, and T. R. Rizzo, J. Chem. Phys. **107**, 10344 (1997).

9. O. V. Boyarkin, L. Lubich, R. D. F. Settle, D. S. Perry, T. R. Rizzo, J. Chem. Phys. 107, 8409 (1997).

10. X. Wang, and D. S. Perry, J. Chem. Phys. **109**, 10795 (1998).

11. F. Reiche, B. Abel, R. D. Beck, and T. R. Rizzo, J. Chem. Phys. **116**, 10267 (2002).

12. D. Rueda, O. V. Boyarkin, T. R. Rizzo, A. Chirokolava, and D. S. Perry, J. Chem. Phys. **122**, 044314 (2005).

13. T. N. Clasp and D. S. Perry, J. Chem. Phys. **125**, 104313 (2006).

14. P. Maksyutenko, O. V. Boyarkin, T. R. Rizzo, and D. S. Perry, J. Chem. Phys. **126**, 044311 (2007).

15. H. Gai, D. L. Thompson, G. A. Fisk, J. Chem. Phys. **90**, 7055 (1989).

16. F. F. Crim, J. Phys. Chem **100**, 12725 (1996).

17. M. Gruebele, and P. G. Wolynes, Acc. Chem. Res. **37**, 261 (2004).

18. B. G. Sumpter, and D. L. Thompson, J. Chem. Phys. **82**, 4557 (1985).

19. T. Uzer, J. T. Hynes, and W. P . Reinhardt, J. Chem. Phys. **85**, 5791 (1986).

20. H. –R. Dübal, and F. F. Crim, J. Chem. Phys. **83**, 3863 (1985).

21. M. D. Likar, J. E. Baggott, and F. F. Crim, J. Chem. Phys. **90**, 6266 (1989).

22. F. Weinhold, and C. R. Landis, *Valency and Bonding: A Natural Bond Orbital Donor-Acceptor Perspective* (Cambridge University Press, Cambridge 2003).

23. M. J. Frisch G. W. Trucks, H. B. Schlegel, G. E. Scuseria, M. A. Robb, J. R. Cheeseman, J. A. Montgomery, Jr., T. Vreven, K. N. Kudin, J. C. Burant, J. M. Millam, S. S. Iyengar, J. Tomasi, V. Barone, B. Mennucci, M. Cossi, G. Scalmani, N. Rega, G. A. Petersson, H. Nakatsuji, M. Hada, M. Ehara, K. Toyota, R. Fukuda, J. Hasegawa, M. Ishida, T. Nakajima, Y. Honda, O. Kitao, H. Nakai, M. Klene, X. Li, J. E. Knox, H. P. Hratchian, J. B. Cross, C. Adamo, J. Jaramillo, R. Gomperts, R. E. Stratmann, O. Yazyev, A. J. Austin, R. Cammi, C. Pomelli, J. W. Ochterski, P. Y. Ayala, K. Morokuma, G. A. Voth, P. Salvador, J. J. Dannenberg, V. G. Zakrzewski, S. Dapprich, A. D. Daniels, M. C. Strain, O. Farkas, D. K. Malick, A. D. Rabuck, K. Raghavachari, J. B. Foresman, J. V. Ortiz, Q. Cui, A. G. Baboul, S. Clifford, J. Cioslowski, B. B. Stefanov, G. Liu, A. Liashenko, P. Piskorz, I. Komaromi, R. L. Martin, D. J. Fox, T. Keith, M. A. Al-Laham, C. Y. Peng, A. Nanayakkara, M. Challacombe, P. M. W. Gill, B. Johnson, W. Chen, M. W. Wong, C. Gonzalez, and J. A. Pople, Gaussian 03, Revision B.04, (Gaussian, Inc., Pittsburgh PA, 2003).

24. ACESII is a program product of the Quantum Theory Project, University of Florida. Authors: J. F. Stanton, J. Gauss, J. D. Watts, M. Nooijen, N. Oliphant, S. A. Perera, P. G. Szalay, W. J. Lauderdale, S. A. Kucharski, S. R. Gwaltney, S. Beck, A. Balková D. E. Bernholdt, K. K. Baeck, P. Rozyczko, H. Sekino, C. Hober, and R. J. Bartlett. Integral packages included are VMOL (J. Almlöf and P. R. Taylor); VPROPS (P. Taylor) ABACUS; (T. Helgaker, H. J. Aa. Jensen, P. Jørgensen, J. Olsen, and P. R. Taylor).

25. T. H. Dunning Jr., J. Chem. Phys. 90, 1007 (1989); K. A. Peterson, D. E. Woon, T. H. Dunning Jr., J. Chem. Phys. **100**, 7410 (1994).

26. J. D. Watts, and J. S. Francisco, J. Chem. Phys. **125**, 104301 (2006).

27. D. J. Nesbitt, and R. W. Field, J. Phys. Chem. **100**, 12735 (1996).

28. K. Doclo and U. Rothlisberger, Chem. Phys. Lett. **297**, 205 (1998).

29. B. Ruscic, D. Feller, D. A. Dixon, K. A. Peterson, L. B. Harding, R. L. Asher, and A. F. Wagner, J. Phys. Chem. A **105**, 1 (2001).

30. P. W. Atkins, *Molecular Quantum Mechanics, 2nd ed*. (Oxford University Press, Oxford 1983).

31. H. G. Kjaergaard, B. R. Henry, J. Chem. Phys. **96**, 4841 (1992).

32. S. Tonmunphean, V. Parasuk, and A. Karpfen, J. Phys. Chem. A **106**, 438 (2002).

33. D. J. Donaldson, J. J. Orlando, A. Amann, G. S. Tyndall, R. J. Proos, B. R. Henry, and V. Vaida, J. Phys. Chem. A, **102**, 5171 (1998).

34. K. A. Peterson, Spectrochimica Acta Part A **53**, 1051 (1997).

35. G. R. Low, and H. G. Kjaergaard, J. Chem. Phys. **110**, 9104 (1999).

36. L. Fono, D. J. Donaldson, R. J. Proos, B. R. Henry, Chem. Phys. Lett. **311**, 131 (1999).

37. D. Hurtmans, F. Herregodts, M. Herman, J. Lievin, A. Campargue, A. Garnache, A. A. Kachanov, J. Chem. Phys. **113**, 1535 (2000).

38. H. G. Kjaergaard, H. Yu, B. J. Schattka, B. R. Henry, and A. W. Tarr, J. Chem. Phys. **93**, 6239 (1990).

39. T. J. Lee, and A. P. Rndell, J. Chem. Phys. **94**, 6229 (1991).

40. K. Takahashi, M. Sugawara, and S. Yabushita, J. Phys. Chem. **109**, 4242 (2005).

41. R. D. Johnson III, FGH1D program version 1.01
http://www.nist.gov/compchem/johnson/fgh/fgh1d.html

42. P. M. Morse, Phys. Rev. **34**, 57 (1929).

43. J. C. Decius, J. Chem. Phys. **16**, 1025 (1948).

44. M. Tyblewski, T. –K. Ha, R. Meyer, and A. Bauder, J. Chem. Phys. **97**, 6168 (1992).

45. P. W. Atkins, *Physical Chemistry, 6th ed*. (W. H. Freeman, New York 1998).

46. I. N. Levine, *Physical Chemistry, 4th ed*. (McGraw-Hill, New York 1995).

47. I. N. Levine, *Quantum Chemistry, 5th ed.* (Prentice Hall, New Jersey 2000).

48. P. A. Giguere, J. Chem. Phys. **18**, 88 (1950).

49. D. Rueda, O. V. Boyarkin, T. R. Rizzo, I. Mukhopadhyay, D. S. Perry, J. Chem. Phys. **116**, 91 (2002).

50. M. A. Temsamani, L. –H. Xu, and D. S. Perry, Can. J. Phys. **79**, 467 (2001).

Chapter 8

State-Resolved First and Second OH-Stretching Overtones Action Spectra of Jet Cooled Methyl Hydroperoxide

8.1 Introduction

In the previous dissertation chapter, the ground vibrational states of methyl hydroperoxide (CH_3OOH, MHP) has been investigated in series of room temperature bulb experiments. In these experiments the OH stretching overtones and their corresponding COOH torsional states are recorded in the regions of the $2\nu_{OH} - 5\nu_{OH}$. From the measurements, not only we find significant COOH-torsion activity due to strong coupling with the OH-stretch, but also that the torsion activity depends on the prepared vibrationally excited OH-stretching modes (see Fig. 7.5 in Chapter 7). Through a series of high level *ab initio* calculations using ACESII [1] and GAUSSIAN03 [2] at the CCSD(T)/cc-pVTZ level of theory,[3] a two-dimensional model involving the OH-stretching/COOH-torsion motion was constructed to aid in the vibrational band assignment shown in Fig. 7.5.

The adiabatic torsional potentials associated with the $V_{OH} = 0$, 2 and 3 and, of which their construction have been described in the previous chapter, are shown in Fig. 8.1. The tunneling of the light H-atom through the classically forbidden region of the potential at $\tau = 180^o$ gives rise to splitting of the torsion vibrational levels to symmetric (+) and antisymmetric (–) wavefunctions. Tyblewski *et al.* have measured the splitting on the ground state by recording millimeter-wave spectra of the vibrational ground state and

the lowest lying COOH vibrational mode (ν_{15}).[4] They report that the levels $|0\ 0^+\rangle$ and $|0\ 0^-\rangle$ are separated by 14.97 cm^{-1} (see Fig. 8.1). In addition, from their rotational line analysis Tyblewski *et al.* list the rotational constants associated with the COOH-torsional substates 0^+, 0^-, 1^+, and 1^-.[4] Similarly to their notation, we designate the 0^+ and 0^- levels as symmetric (+) and antisymmetric (–) torsional ground state as well as 1^+ and 1^- as the symmetric and antisymmetric torsionally excited state respectively henceforth. Thus, for example, the notation $|v\ m^{+/-}\rangle$ indicates "m" quanta excitation in the torsion for the "v"-th OH stretching level. The +/– superscript indicates the state symmetry. The experimental and *ab initio* rotational and vibrational parameters for the torsional substates associated with the OH vibrational ground state, $|0\ m^{+/-}\rangle$, are listed in Table 8.1. The table shows that the rotational constants of the torsional states associated with $V_{OH} = 0$ differ slightly from one another and that the predictions made by the MP2/aug-cc-pVTZ and CCSD(T)/calculations are in good agreement with experimental values.

The adiabatic torsion potential energy curves in Fig. 8.1 also show that as the excitation in the OH-stretching increases, the barrier height at $\tau = 180^o$ increases as well, and as a result, the separation between the symmetric and the antisymmetric levels get smaller giving rise to decreasing levels splitting. In the CCSD(T)/cc-pVTZ *ab initio* simulations described in Chapter 7, the splitting between the $|0\ 0^+\rangle$ and the $|0\ 0^-\rangle$ levels are calculated to be 8.4 cm^{-1} (see Table 8.1) and at the first OH-stretching overtone ($2\nu_{OH}$), the predicted splitting between the $|2\ 0^+\rangle$ and the $|2\ 0^-\rangle$ levels is 1.2 cm^{-1}. At $3\nu_{OH}$, the splitting is predicted to be as small as 0.27 cm^{-1}.

In the previous chapter, the spectral congestion and vibrational bands overlap have obstructed the identity of the individual vibrational transitions that contribute at room temperature. In principle however, the levels splitting could lead to four types of transitions; namely, these transitions are the symmetric → symmetric ($|0\ 0^+> \rightarrow |v\ 0^+>$), symmetric → antisymmetric ($|0\ 0^+> \rightarrow |v\ 0^->$), antisymmetric → antisymmetric ($|0\ 0^-> \rightarrow |v\ 0^->$) and antisymmetric → symmetric ($|0\ 0^-> \rightarrow |v\ 0^+>$). Indeed, a central issue which was left unanswered in the previous chapter was whether our *ab initio* simulations predicting four different types of transitions between the OH ground state and its first overtone are correct. Recall that these simulations predict that symmetric ↔ antisymmetric contribution accounts for about ~ 66 % of the $2\nu_{OH}$ state (see Fig. 7.15(a)).

By contrast, previous *ab initio* models using two-dimensional surfaces on molecules such as hydrogen peroxide,[5] *tert*-butyl hydroperoxide,[6] methanol,[7-8] and even methyl hydroperoxide,[9] have neglected the contribution arising from symmetric ↔ antisymmetric transitions based on the assumption that the transition dipole moment does not depend strongly on the torsional mode. In essence, these models approximate the dipole moment function (DMF) dependence *only* on the OH-stretching, r:[5-9]

$$<\psi_v^{OH}(r|\tau)\,\chi^{v'}{}_{m'}(\tau)^{+/-}\,|\boldsymbol{\mu}(r)|\,\psi_{v''}{}^{OH}(r|\tau)\,\chi^{v''}{}_{m''}(\tau)^{+/-}> \qquad (8.1)$$

Where, $\psi_{v'}{}^{OH}(r|\tau)$ and $\chi^{v'}{}_{m'}(\tau)^{+/-}$ are the respective OH-stretch and COOH-torsion wavefunctions and $\boldsymbol{\mu}(r)$ is the DMF which depends solely on the O-H separation, r. Since in Eq. 8.1 the dipole moment function $\boldsymbol{\mu}(r)$ does not depend on the torsion angle, τ, the expression is equivalent to:

$$<\psi_{v'}^{OH}(r|\tau)|\mu(r)|\psi_{v''}^{OH}(r|\tau)><\chi^{v'}{}_{m'}(\tau)^{+/-}|\chi^{v''}{}_{m''}(\tau)^{+/-}> \quad (8.2)$$

Where the term $<\chi^{v'}{}_{m'}(\tau)^{+/-}|\chi^{v''}{}_{m''}(\tau)^{+/-}>$ is the overlap integral between initial and final torsion states, analogous to the Franck-Condon treatment of electronic transition between adiabatic surfaces.[10]

In the previous chapter, we compared the predictions of the Franck-Condon model with a 2-D model which *preserves* the dependence of the dipole moment function on the torsion motion such that the transition dipole moment is evaluated using the following expression:

$$<\psi_{v}^{OH}(r|\tau)\,\chi^{v'}{}_{m'}(\tau)^{+/-}|\mu(r,\tau)|\,\psi_{v''}^{OH}(r|\tau)\,\chi^{v''}{}_{m''}(\tau)^{+/-}> \quad (8.3)$$

In equation 8.3, the DMF $\mu(r,\tau)$ is a function of both the O-H separation, r, *and* the torsion angle, τ. In Fig 8.2, these $\mu_\alpha(r,\tau)$ (= $\mu_a(r,\tau)$, $\mu_b(r,\tau)$, $\mu_c(r,\tau)$) surfaces, which are generated at the CCSD(T)/cc-pVTZ level of theory,[1,3] show that while both the dipole moment functions μ_a and μ_b are symmetric about the *trans* barrier where $\tau = 180^o$, the μ_c component is antisymmetric. Therefore, we anticipate that symmetric → symmetric and antisymmetric → antisymmetric transitions will depend on the μ_a- and μ_b-components of the dipole, whereas symmetric ↔ antisymmetric transitions will predominantly depend on the μ_c component of the dipole moment function. Even though our room temperature spectra do not favor exclusively either model, spectroscopically speaking, each of the models predicts significantly different band structure and makeup.

This chapter extends the previous work on the overtones of CH_3OOH where we predominately focus on interpreting the action spectra of the MHP molecule obtained under molecular beam conditions. By examining the first and second OH-stretching

overtones and their corresponding torsional combination bands, the structure and spectroscopy of these overtones are characterized. From fits obtained using rotational band contours, we report the effective rotational constants as well as band origins and transition frequencies associated with these levels. We also investigate the dipole moment function dependence on the torsion angle in the $2\nu_{OH}$ and $3\nu_{OH}$ and show that for methyl hydroperoxide, only the *ab initio* model constructed using both r and τ dependence ($\mu(r,\tau)$) depicts correctly the band structure.

This chapter also provides an insight to the intramolecular vibrational redistribution (IVR) in the $2\nu_{OH}$ and $3\nu_{OH}$ region which affects both the OH-stretching mode as well as its torsional combination band. The interactions due to IVR between states are reveled from the transition linewidths and from the intensity distribution of the vibrational bands. An isotope study of CD_3OOH (MHP-d_3) is then used to examine whether the interactions are the result of coupling between the methyl rotor and the OH stretching modes. At room temperature, the study of MHP-d_3 is also used to provide positive identification of the CH-stretching modes observed in the regions to the red (6000 cm^{-1}) and blue (8500 cm^{-1}) of the $2\nu_{OH}$ band.

8.2 Experiment

8.2.1 Room Temperature Apparatus

The room temperature apparatus has been described entirely in Chapter 7. The synthesis of MHP is described in Chapter 6. The synthesis of its deuterated analog, CD_3OOH (MHP-d_3), is followed in a similar manner except that we use $^1/_3$ the quantities used for the synthesis of CH_3OOH due to the high cost of dimethyl-d_6 sulfate ($(CD_3)_2SO_4$, Fisher part: AC17291-0010). We use the vibrationally mediated

photodissociation scheme (ViMP) $n\nu_x$ + 532 nm to record the spectra of the second CH stretching overtones ($3\nu_{CH}$) and the OH-stretch/HOO-bend combination modes ($2\nu_{OH} + \nu_{HOO}$). The MOPO system also enables probing of the first CH stretching ($2\nu_{CH}$) overtones. In this region, due to the weak $2\nu_{CH}$ + 532 nm signal levels we use sum frequency mixing to triple the output of the dye laser (NY81-20 system) to generate λ = 203 nm photon. Because the large excess energy associated with the $2\nu_{CH}$ + 203 nm ViMP process ($E_{excess} \approx 115$ kcal/mol), the resulting OH fragments are formed electronically excited in the $A^2\Sigma$ state where we can monitor their fluorescence without the use of a probe laser.

8.2.2 Molecular Beam Apparatus

The molecular beam apparatus described here is used for the first time to investigate methyl hydroperoxide. In designing the apparatus the unstable nature of hydroperoxides and their relatively high decomposition rate are accommodated with temperature control and by reduction of contact with metal.[12] A stainless steel chamber with a several ports and baffled arm (7" in length and 1" in diameter) to reduce scatter light is attached to a diffusion pump (Varian VHS-6) through Aluminum gate valve. A custom made Kel-F face-plate (54 mm diameter and 17 mm width) is horizontally attached to the valve with a Viton O-ring seal. An input port on top of the face-plate attached to ¼ inch Teflon tubing delivers methyl hydroperoxide seeded in various pressures of helium ranging from 500 – 2280 Torr to the pulse valve.

Proper sample passivation is important, and can be achieved by passing the He carrier gas above the liquid phase of methyl hydroperoxide sample which maintained at

280 K. The gas mixture flows into a halocarbon wax coated pulse valve (General Valve, Series 9) operating at 20Hz with modified Teflon coated springs and plunger with Kel-F poppet. From various tests described in Appendix *A*, we find that the Kel-F poppet is more resilient to wear and tear than the Teflon poppet and just like Teflon, Kel-F is chemically inert. A pulse driver (General Valve: Iota One) synchronizes the opening of the valve with the lasers. Typically, in order to see signal from the molecular beam apparatus, we set the valve to trigger anywhere between 300 and 800 μs, with an open time set to 400 – 600 μs, prior to the lasers Q-switch trigger. By setting the valve to trigger ~584 μs prior to the laser Q-switching and setting the valve open time to 450 μs maximizes signal levels (see Appendix *A*).

The sample is introduced to the photolysis chamber through the pulsed valve using one of the two available faceplates. In these experiments, we use both the 0.4 mm and 1.0 mm diameter orifice faceplate depending on the carrier gas backing pressure. Larger hole-size provides more efficient cooling for a given backing pressure, but also put higher load on the pumps. Therefore, for measurements with backing pressure greater than 1000 Torr, we use the 0.4 mm orifice size faceplate. The valve faceplate is positioned 10 mm from the interaction region where we find it to give good combination of cooling, particle density and minimal scatter light.

The low resolution scans are obtained in similar manner to that described above for the room temperature measurements using the MOPO system with the exception that under molecular beam conditions we increase the 532 nm photolysis laser pulse energies to ~65 mJ. This provides with the necessary signal to noise levels to record clean spectra. For the high resolution scans we use difference frequency mixing (DFM) in a lithium

niobate ($LiNbO_3$) crystal pumped by the dye laser system (NY82-20) operating with R610 + R640 mixture and the fundamental output of a seeded ND:YAG laser (Continuum: NY82-20). Typical dye laser and ND:YAG fundamental input pulse energies range between 22 – 25 mJ and 30 – 35 mJ respectively. Typical output power from the crystal in the first OH-stretching overtone is 1.5 – 2.5 mJ with 0.08 cm^{-1} bandwidth (FWHM). The signal from the PMT (EMI 9813QB) is amplified with a preamp (SRS: SR445A) and in order to ensure proper calibration of the spectrum and the laser linewidths, a portion of the output IR beam is directed towards a photoacoustic cell containing water vapor. The water spectrum is compared against known lines in the HITRAN database as described in Appendix *F*.[12] The schematic for the high resolution DMF mixing experimental apparatus is shown in Fig. 8.3. A liquid nitrogen trap and mechanical pump (Edwards: E2M30) are connected to the diffusion pump down stream to aid evacuating the chamber between consecutive laser pulses.

8.3 Results and Analysis

8.3.1 Comparison between Room Temperature and Molecular Beam Action Spectra

The room temperature overview action spectrum of methyl hydroperoxide is shown in Fig 8.4(a). The bands appearing in the spectrum are the focus of this study. The spectrum is obtained by tuning the OPO at 0.015 nm/s averaging 30 shots/bin in the region of 6500 and 11 000 cm^{-1} while monitoring the OH fragment in the N = 2 rotational state via the $A^2\Sigma$–$X^2\Pi(1,0)$ off diagonal transition at ~ 282 nm. The temporal delay between the IR vibrational excitation laser (λ_1) and the photolysis laser (λ_2) is set to 15 ns and the temporal delay between the photolysis laser and the probe (λ_3) is increased to

1400 ns. N_2 buffer gas is added (~0.7 Torr) to ensure rotational relaxation of the OH photoproduct. The band appearing at ~7000 cm^{-1} corresponds to the first OH-stretching overtone ($2\nu_{OH}$) and the band appearing at ~10 260 cm^{-1} corresponds to the second OH-stretching overtone ($3\nu_{OH}$). The band with the weaker intensity at ~10 420 cm^{-1} corresponds to the OH-stretch/COOH torsion combination band ($3\nu_{OH} + \nu_{COOH}$). These band assignments are supported by the *ab initio* two-dimensional model presented in Chapter 7 and Ref. 13.

There are additional bands in the mid region of Fig. 8.4(a) between the $2\nu_{OH}$ and the $3\nu_{OH}$ bands. We attribute the pronounced sharp feature at ~8290 cm^{-1} to the OH-stretch /HOO-bend combination mode ($2\nu_{OH} + \nu_{OOH}$). The series of peaks to the red and blue of the $2\nu_{OH} + \nu_{OOH}$ at 8203, 8417, 8538 and 8676 cm^{-1} are attributed to the second CH stretching overtones ($3\nu_{CH}$). This assignment, though tentative, can be experimentally justified with the spectrum of the isotopomer CD_3OOH shown in Fig. 8.4(b), taken under similar conditions. Upon deuteration at the methyl site, the 8300 cm^{-1} spectral region appears cleaner, dominated by a single band, consistent with the assignment of the $2\nu_{OH} + \nu_{OOH}$. From an *ab initio* frequencies and anharmonicites of CH_3OOH and CD_3OOH at the MP2/aug-cc-pVTZ level,[2] we find that the OH-stretch/HOO-bend combination mode is not expected to shift substantially upon deuterium substitution at methyl group. On the other hand, the C-D stretching modes are likely to shift by about 800 cm^{-1} per quanta of excitation.

Table 8.2 lists the frequencies, anharmonic coupling and MHP-d_3 isotope shifts calculated at the MP2/aug-cc-pVTZ level of theory.[2] The strongest coupling of the OH-

stretch on the ground state occurs with its bending mode. Strong coupling indicates that the bending mode may borrow intensity from the OH stretching mode similar to the situation in other hydroperoxide such as discussed for the hydrogen peroxide (HOOH) in Chapter 9 and Ref. 14, peroxynitrous acid (HOONO) in Chapter 5, and peroxynitric acid ($HOONO_2$) in Chapter 2 and Ref. 15. The combined predicted isotopic shift of the bend-stretch combination mode ($2\nu_1 + \nu_8$) in MHP-d_3 relative to MHP is ~4 cm^{-1}. Experimentally, we find small shifts (~8 cm^{-1}) which are consistent with the *ab initio* values. Reviewing the shifts listed in Table 8.2 for the CH stretching modes (ν_2, ν_3 and ν_4) we find that the corresponding CD stretching modes should red shift by 812 – 870 cm^{-1} per quanta. Thus, the $3\nu_{CD}$ stretching modes are expected to shift by ~2500 cm^{-1} outside the region to around 6000 cm^{-1}. Additional conformation that these bands are CH stretching modes comes from extensive studies on methanol where the CH stretching modes have also relatively weak diffuse intensities compared with the OH stretching modes.[16,17]

From the frequencies and anharmonicities in Table 8.2 one may also predict the line positions of the first CH stretching overtone ($2\nu_{CH}$) and the $\nu_{OH} + 2\nu_{HOO}$ combination band which are also commonly observed in other molecules.[15,16] The MP2/aug-cc-pVTZ calculation predicts the $2\nu_{OH}$ line position at 7021 cm^{-1} which is ~4 cm^{-1} away from the experimental band position. It also predicts that the three first CH-stretching overtones occur around 5861, 5960 and 6009 cm^{-1} for $2\nu_4$, $2\nu_3$ and $2\nu_2$ respectively and that the $\nu_{OH} + 2\nu_{HOO}$ band occurs around 6109 cm^{-1}. Scanning the OPO in this region has resulted in very weak $2\nu_{CH}$ + 532 nm ViMP signal levels. This signal is estimated to be 50 – 100

times weaker that the signal levels arising from excitation of the $2\nu_{OH}$ band. In order to overcome these low signal levels, we have generated the spectrum using an alternative approach shown in Fig. 8.5. In this new approach we use the $2\nu_{CH}$ + 203 nm ViMP scheme where the resulting OH photoproduct is formed in the fluorescing $A^2\Sigma$ state. Looking at the spectrum in Fig. 8.5 we indeed find that the 5800 – 6000 cm^{-1} region shows multiple peaks which most likely involve C-H excitation. Based on the *ab initio* predictions, the band at 6175 cm^{-1} is the $\nu_{OH} + 2\nu_{HOO}$ state.

In order to extract additional information from the vibrational bands in Fig. 8.4 and their spectroscopy, we turn our attention to molecular beam experiments. We hope that in cooling the molecule, the reduced ro-vibrational spectral congestion will provide insight of the bands structure. Close-up figures of the $2\nu_{OH}$, $3\nu_{CH}/2\nu_{OH} + \nu_{OOH}$ and $3\nu_{OH}$ regions under molecular beam and room temperature conditions are shown in Figs. 8.6(a) – 8.6(c) respectively. The poor signal levels have precluded us from obtaining jet cooled spectrum of the $2\nu_{CH}$ region. The spectra shown in Fig. 8.6 are obtained with the OPO system at 0.4 cm^{-1} bandwidth (FWHM) and ~500 Torr of helium carrier gas backing pressure. The scan rate is set to 0.002 nm/s averaging 50 shots/bin and the signal from the PMT is amplified by $\times$ 5. The sample is maintained at 7^o C and it is introduced to the molecular beam chamber through the 1 mm orifice faceplate.

In each of the panels in Fig. 8.6 the effects of the thermal population on the action spectra are significant. Aside from the fact that the bands appear narrower and more resolved, some of the band-origins appear to shift away from what appears to be the band center at room temperature. In addition, in the $2\nu_{OH}$ region the molecular beam spectrum

shows that around 7150 cm^{-1} there is an additional band which is not observed under room temperature conditions. Based on our two-dimension OH-stretch/COOH-torsion *ab initio* model, this band *is* the $2\nu_{OH} + \nu_{COOH}$ combination band. The reason behind its low signal level at room temperature will be discussed at a later section.

It is also worth noting that while we observe significant band narrowing of the modes associated with OH motion (stretch, bend and torsion), the CH-stretching modes appear significantly broader even under molecular beam conditions. As with the room temperature action spectra of the CH stretching modes, these bands span over a 500 cm^{-1} region and further more, their intensity still appear significantly diffuse compared with the second OH stretching overtone ($3\nu_{OH}$). This suggests that these modes are strongly coupled to other vibrational states which, as a result, lead to significant state mixing which in turns lead to broadening of their natural linewidths. This observation has been pointed out by Rizzo and co-workers in their work on methanol where they observed similar broadening and state mixing occurring due to the internal rotation of the methyl rotor.[16-22] More on the effects of intramolecular vibrational energy redistribution on the product state distributions are discussed in the following chapter.

8.3.2 The $2\nu_{OH}$ Band

While the low resolution molecular beam action spectrum of the $2\nu_{OH}$ band in Fig. 8.6(a) can provide information on the bands origin and general band-shape, in order to extract the finer details from these vibrational action spectra, additional experimental effort is needed. To attain this goal we increase both the resolution of the overtone excitation laser and the expansion pressure of the carrier gas. The action spectra of the $2\nu_{OH}$ and the $2\nu_{OH} + \nu_{COOH}$ bands under 2280 Torr (3 atm) of helium carrier gas and 0.08

cm^{-1} bandwidth (FWHM) using the Inrad Autotracker unit are shown in Figs. 8.7(a) and 8.7(b) respectively. To prevent the drilled-through Swagelok connectors from giving out under high back-pressure conditions, we reinforce them by wrapping electrical tape around them. Another consequence of the high back pressure is that in order to prevent overloading the diffusion pump with excess helium, we use the 0.4 mm face-plate. The increase in the helium carrier gas pressure and the resulting diluted sample vapor lead to significant cooling of the molecule. Both spectra in Fig. 8.7 are generated by scanning the dye laser system at 0.0025 Å/s and averaging 100 shots/bin. The pulsed-valve is triggered 584 μs prior to the laser Q-switch trigger and its open-time is set to 290 μs between consecutive laser pulses. The resulting OH($^2\Pi_{3/2}$, v=0) fragments in the N=5 rotational state are probed via the *A*-*X*(1,0) transition at ~283 nm. To properly calibrate the vibrational bandorigin and line positions, a portion of the IR beam exiting the molecular beam chamber is directed towards a photoacoustic cell containing water vapor using a microscope slide. The 2-channel data acquisition occurs simultaneously (see Appendix *A*).

The $2\nu_{OH}$ band structure in Fig. 8.7(a) appears to be comprised of a main congested spectral region between 7020 to 7028 cm^{-1} and a secondary more structured region lying further to the blue around 7029 to 7035 cm^{-1}. According to microwave data,[4] and the 2-D torsion model, the vibrational ground state of methyl hydroperoxide is split into two levels. In Fig. 8.1, these levels are labeled as the 0^+ (symmetric) and 0^- (antisymmetric). Since the 0^- level lies 14.97 cm^{-1} above the 0^+ level, under our molecular beam conditions (estimated at ~5 K), the population of the 0^- level is expected

to contribute less than 1 % assuming a statistical (Boltzmann) distribution of vibrational states. In essence, this simplifies the action spectrum as it leads to the removal of all possible transitions originating from the $|0\ 0^-\rangle$ level. Therefore, in fitting the rotational band contour we need only to consider transitions originating from the symmetric level. As mentioned above, we pick the standard notation to account for these transitions. Namely, for example, the $|0\ 0^+\rangle \rightarrow |2\ 0^+\rangle$ simply indicates transitions originating from the OH vibrational ground state ($V_{OH} = 0$) and symmetric torsion ground level going to vibrationally excited OH ($V_{OH} = 2$) and symmetric torsion ground level (see Fig. 8.1).

In order to examine the predictions made by our *ab initio* model in the previous chapter of whether both $|0\ 0^+\rangle \rightarrow |2\ 0^+\rangle$ and $|0\ 0^+\rangle \rightarrow |2\ 0^-\rangle$ transitions should be taken into account, we initially compute their corresponding transition dipole moments:

$$\mu_\alpha = \langle 2\ 0^+|\mu_\alpha(r, \tau)|\ 0\ 0^+\rangle \qquad \alpha = a, b, \text{ or } c \tag{8.4}$$

And,

$$\mu_\alpha = \langle 2\ 0^-|\mu_\alpha(r, \tau)|\ 0\ 0^+\rangle \qquad \alpha = a, b, \text{ or } c \tag{8.5}$$

The intensity, or oscillator strength, *f*, is proportional to the square of the transition dipole moments in the molecular reference frame $|\mu_a|^2$, $|\mu_b|^2$, and $|\mu_c|^2$.[23,24] Table 8.3 shows the calculated transition moments for the four possible transition involving the initial states, $|0\ 0^+\rangle$, $|0\ 0^-\rangle$ and final states, $|2\ 0^+\rangle$, $|2\ 0^-\rangle$. The first row in Table 8.3 shows that both the $|0\ 0^+\rangle \rightarrow |2\ 0^+\rangle$ and the $|0\ 0^+\rangle \rightarrow |2\ 0^-\rangle$ transitions have negligible μ_b component. Interestingly, we also find that while the $|0\ 0^+\rangle \rightarrow |2\ 0^+\rangle$ transition carries only μ_a contribution, the $|0\ 0^+\rangle \rightarrow |2\ 0^-\rangle$ transition relies solely on contribution originating from the μ_c component. In essence, the *ab initio* calculation confirms our

hypothesis that these transitions are of different rotational type where the $|0\ 0^+> \rightarrow |2\ 0^+>$ transition is of "a-" type and the $|0\ 0^+> \rightarrow |2\ 0^->$ transition is of "c-" type.

Aside from the transition moments, in order to obtain a rotational band contour, the rotational constants associated with the initial and final states are also required. As the ground state rotational parameters are known for the starting $|0\ 0^+>$ level,[4] we limit our search over a range of rotational constants associated with the final states $|2\ 0^{+/-}>$. We start off the simulations using the *ab initio* transition moments and the ground state rotational constants, $|0\ 0^+>$, as a starting point for the upper $|2\ 0^{+/-}>$ states (see Table 8.1). We take the molecule as an asymmetric top with C_1 point group symmetry and using the Ir reduction we simulate the spectrum using the PGOPHER rotational simulation package by varying the upper state parameters and transition moments from their initial values.[22] Tutorial for using PGOPHER is provided in Appendix *F*. The simulation parameters are provided in Table 8.4.

The best fit obtained for the $2\nu_{OH}$ band from the simulations at 5 K, where two transitions originating from the $|2\ 0^+>$ level are considered, is shown in Fig. 8.8(a) with dashed line going through the experimental spectrum. These rotational band contours are obtained by running the simulation searching over a large range of values of transition moments and upper state rotational constants. We also allow the temperature and the transition linewidths to vary for the different bands. The rotational band contour simulation reveals that indeed, as predicted by our two-dimensional *ab initio* model, two vibrational transitions comprise the observed spectrum. These transitions, although having similar upper rotational constants (see Table 8.4) which here, are treated as

effective rotational constants (*A'* = 1.4067 cm^{-1}, *B'* = 0.3480 cm^{-1} and *C'* = 0.3030 cm^{-1}), have rotational band type characteristics that are inherently different. The band at ν_0 = 7024.65 cm^{-1} is characterized by its 1:0 a- to c-ratio with no contribution arising from the b- component. In essence, this band can be labeled as "pure" a-type. The second band with band origin at ν_0 = 7028.55 cm^{-1} is characterized by its 0:1 a- to c- type and similarly to the $|0\ 0^+> \rightarrow |2\ 0^+>$ transition, has no b- component. In other word, this band is a "pure" c- type transition.

These results are encouraging in a sense that our *ab initio* model does indeed predict the symmetric ↔ antisymmetric torsion transitions to appear in the spectrum. In fact, all attempts to fit the spectrum using a *single transition* ($|0\ 0^+> \rightarrow |2\ 0^+>$) with various combinations of transition moments and rotational constants parameters have not yielded satisfactory results. The de-convoluted band shapes obtained from the rotational band contour for the $|0\ 0^+> \rightarrow |2\ 0^+>$ and the $|0\ 0^+> \rightarrow |2\ 0^+>$ transitions are shown in solid lines in Fig. 8.8(a). The P-, Q-, and R- branches in the figure are labeled according to their prolate symmetric top limit ($^{\Delta Ka}\Delta J_{K"a}$). For example, the peak labeled $^{R}Q_0$ contain several transition involving ΔJ = 0 with $K"_a = 0$ and $K'_a = 1$. Based on these findings which are summarized in Table 8.4, we find that the at the first OH stretching overtone region, the experimental splitting between the $|2\ 0^+>$ and the $|2\ 0^->$ states is 3.9 cm^{-1}. Recall that our torsional model predicts splitting of 1.2 cm^{-1} between these levels; on the ground state, the splitting between the $|0\ 0^+>$ and the $|0\ 0^->$ levels is 14.97 cm^{-1}. The trend that the separation of the torsion levels at $V_{OH} = 2$ compared with $V_{OH} = 0$ is smaller is consistent with the fact that the barrier at $\tau = 180^o$ is increasing (see Fig. 8.1). It is also

fascinating to note that the relative intensity of the $|0\ 0^+> \rightarrow |2\ 0^->$ transition is about 70 % of the $|0\ 0^+> \rightarrow |2\ 0^+>$ transition. Looking at Table 8.3 we find that the *ab initio* intensity which is proportional to the square of the transition dipole moments, is agreeing very well with our experimental value producing a ratio of 69 %.

The $2\nu_{OH}$ rotational band contours in Fig. 8.8(a) lead to an additional important observation. Even though the rotational contours appear to fit reasonably, particularly the $|0\ 0^+> \rightarrow |2\ 0^->$ transition, it is clear that the simulation underestimates the intensity distribution of the $|0\ 0^+> \rightarrow |2\ 0^+>$ transition. Moreover, we find significant differences in the rotational linewidths for these two vibrational transitions where the $|2\ 0^+>$ and $|2\ 0^->$ levels are broaden by 0.70 cm^{-1} and 0.25 cm^{-1} (FWHM) respectively. This can be seen in from individual rotational band contour of the two transitions shown in Fig. 8.8(a). The significant broadening of the $|2\ 0^+>$ level, suggest that it is more strongly coupled to an interacting state(s) due to state mixing.[25]

8.3.3 The $2\nu_{OH} + \nu_{COOH}$ Band

In order to evaluate the extent of IVR in the $2\nu_{OH}$ spectrum and to obtain a qualitative picture of whether other states are affected by state mixing, we proceed to investigate the torsion combination band. Its rotational band contour, shown in Fig. 8.8(b), is obtained in a similar manner to that described in fitting the OH-stretching mode. *Ab initio* transition dipole moments of 1:0.62 a- to b-type and negligible c-type contributions are calculated for the $|0\ 0^+> \rightarrow |2\ 1^+>$ transition, and as before, were allowed to vary.

Initial attempts of fitting the spectrum have not been successful. In the first place, as with the $|0\ 0^+> \rightarrow |2\ 0^+>$ transition, we find that the transition linewidth associated with the combination band at 7151.04 cm^{-1} is again, broaden significantly with rotational transition widths of 0.5 cm^{-1} (FWHM). Secondly, we find that in order to obtain a reasonable fit, an additional vibrational transition, which carries ~20 % the intensity of the $|2\ 1^+>$ state is required at $\nu_0 = 7145.9\ cm^{-1}$. It is important to note that this newly discovered band is unaccounted by our two-dimension simulation and likely to involve modes other than the OH stretch/torsion. The best fit for the $|2\ 1^+>$ level shown in Fig. 8.8(b) with the smooth dashed line is therefore the sum of two transitions. Although we cannot identify the interacting zero-order dark state, we point out that its origin is not hot-bands because changing the jet temperature does not affect the relative band intensities. The final parameters used in fitting this band are summarized in Table 8.5. Comparing the rotational transition type obtained experimentally to the predicted *ab initio* value for the $|0\ 0^+> \rightarrow |2\ 1^+>$ transition, we find once again that the *ab initio* μ_a:μ_b ratio of 1:0.62 is in good accord with the 1:0.5 we obtain from the rotational band contour fit.

The proximity of the unidentified state in Fig. 8.8(b) to the $|2\ 1^+>$ state could, in principle, lead to the line broadening observed in the torsionally excited state (~0.5 cm^{-1}). In essence, the coupling of the "dark state" (directly or indirectly) to the torsion combination band which is considered the "bright state", leads to the perturbation in the $|2\ 1^+>$ level in the form of linewidth broadening.[20,25-28] Under this scenario, the transition linewidth associated with the $|2\ 1^+>$ state can be interpreted in terms of simple state-to-state interactions. This however, leaves the observed broadened lines and intensity

distribution of the $|2\ 0^+>$ state unexplained. As one expects, couplings, which are observed in the action spectrum in the form of linewidth broadening will depended on the separation of the two unperturbed zero-order states. Since we observe linewidths associated with $|0\ 0^+> \rightarrow |2\ 0^+>$ transition which are ~40 % broader than the $|0\ 0^+> \rightarrow |2\ 1^+>$ transition, it is not likely that the band at 7145.9 cm^{-1} lying merely 5.14 cm^{-1} apart from the $|2\ 1^+>$ state would lead to a greater perturbation in the $|2\ 0^+>$ state which is separated by 121.25 cm^{-1} away from it. More on state mixing will be discussed at a later part of this chapter.

8.3.4 The $3\nu_{OH}$ Band

The rotational band contour of the first OH stretching overtones ($2\nu_{OH}$) and the torsion combination band ($2\nu_{OH} + \nu_{COOH}$) has underlined the presence of state(s) that interact with the excited vibrational state and giving rise to broadened bands shape. We expect similar interactions between the bright states of the molecule with its dark states to affect the $3\nu_{OH}$ region as well. The extent of IVR in the vibrationally excited CH_3OOH molecule in the second OH-stretching overtone could provide additional information complementary to that acquired in the $2\nu_{OH}$ region. In Fig. 8.6(c), the jet cooled $3\nu_{OH}$ spectrum appears to have similar features as the $2\nu_{OH}$ band in Fig. 8.6(a). Both regions show a main band and further to the blue, the corresponding torsionally excited combination band. A close-up figure of the $3\nu_{OH}$ and the $3\nu_{OH} + \nu_{COOH}$ bands are shown in Figs. 8.9(a) and 8.9(b) respectively. The main $3\nu_{OH}$ band at 10 267 cm^{-1} appears more congested than the $2\nu_{OH}$ band. It also has a satellite band which is carrying $^1/_4{}^{th}$ the intensity centered at 10 254 cm^{-1} (see Fig. 8.9(a)). The torsion band in the $3\nu_{OH}$ region

($3\nu_{OH} + \nu_{COOH}$) shown in Fig. 8.9(b) has similar a-type band shape as the $2\nu_{OH} + \nu_{COOH}$ state. However, unlike the $|2\ 1^+>$ state, the combination band, $|3\ 1^+>$, which has band origin at $\nu_0 = 10\ 407.85\ cm^{-1}$, also has a partially resolved band lying further to the blue at 10 421.10 cm^{-1}. The 13.25 cm^{-1} separation between the $|3\ 1^+>$ state and the partially resolved band differs from 5.14 cm^{-1} separation found between the $|2\ 1^+>$ and the unknown (labeled $|\upsilon_x^+>$) states. The spectrum in Fig. 8.9(a) was generated with the 0.4 mm orifice faceplate with back pressure of 1520 Torr (2 atm) and ×25 amplification. The scans over the $|3\ 1^+>$ state were taken with the 1.0 mm orifice faceplate with back pressure of 500 Torr and ×25 amplification. The scan rate in both scans was 0.002 nm/s averaging 50 shots/bin.

We proceed with the fitting routine of the torsion band in a similar manner that was used in fitting the $2\nu_{OH}$ region. We fix the initial states ($|0\ 0^+>$ and $|0\ 0^->$) rotational parameters to their known values,[4] and search for best fit parameters for the upper state constants. Because the $3\nu_{OH} + \nu_{COOH}$ band appears more structured relative to the $3\nu_{OH}$ band, we start with fitting it first. We calculate transition dipole moments ratio to be 1:0.23 a- to b-type and negligible c-component for the $|0\ 0^+> \rightarrow |3\ 1^+>$ transition. Our 2-D *ab initio* model in Chapter 7 also tells us that the combination band at $\nu_0 = 10\ 407.85\ cm^{-1}$ is comprised of the $|0\ 0^-> \rightarrow |3\ 1^->$ transition, which, at ~19 K (our coldest temperature in which we obtain the spectrum with good signal-to-noise ratio) will carry about a third the intensity relative to that arising from the $|0\ 0^+> \rightarrow |3\ 1^+>$ transition. According to our two-dimension *ab initio* model, the separation between the $|3\ 1^+>$ and the $|3\ 1^->$ states is only 27.77 cm^{-1} due to the increase in the torsion barrier at $V_{OH} = 3$ (see Fig. 8.1). In

addition, the *ab initio* transition dipole moment for the $|0\ 0^-\rangle \rightarrow |3\ 1^-\rangle$ transition is also computed and found to be 1:0.26 a- to b- hybrid type. The best fit for the rotational band contour for the torsion band ($3\nu_{OH} + \nu_{COOH}$) is shown in Fig. 8.10. The dash line going through the spectrum is obtained from the sum of the two transitions mentioned above ($|0\ 0^+\rangle \rightarrow |3\ 1^+\rangle$ and $|0\ 0^-\rangle \rightarrow |3\ 1^-\rangle$) as well as the unidentified transition (labeled $|\upsilon_y^+\rangle$), $|0\ 0^+\rangle \rightarrow |\upsilon_y^+\rangle$. The individual bands contributing to the sum are also shown in Fig. 8.10. The best fit parameters are listed in Table 8.6 and as before, the values given are the effective rotational constants used in the fitted spectrum. The agreement between the *ab initio* and experimental values is noteworthy, albeit fortuitous, as the intermediate laser linewidth resolution (~0.4 cm^{-1}) reduces the sensitivity of the rotational band contour on the molecular parameters.

Aside from the laser linewidth issue, we find that the transition linewidth associated with these states are significantly broader in this region compared with the $|2\ 1^+\rangle$ state. Recall, the $2\nu_{OH}$ combination band has a linewidth of 0.5 cm^{-1} which is a factor of two narrower compared with the linewidth of 1.0 cm^{-1} found for the $3\nu_{OH}$ combination band. Since the density of states in this region is significantly larger in this region (~2452 states/cm^{-1}) compared with the $2\nu_{OH}$ region (~184 states/cm^{-1}) and since the unidentified state lies further away from the $|3\ 1^+\rangle$ state than the state appearing near the $|2\ 1^+\rangle$ state, we infer that the ~1.0 cm^{-1} linewidth broadening associated with the $|3\ 1^+\rangle$ state is likely increased due to the higher order weak coupling of the state with the denser bath of dark states.[14] In other words, the broadening of the linewidths in the $3\nu_{OH}$ region can be attributed to the increase in the density of states over this region.

The coupling in the second overtone region is also affecting the OH-stretching mode. In Fig. 8.9(a), the $3\nu_{OH}$ band taken under 2 atmospheres of helium carrier gas appears featureless. Based on the *ab initio* model, the transitions from symmetric → antisymmetric and antisymmetric → symmetric only account for ~34 % in this region, where it was found to account for ~70 % at the $2\nu_{OH}$ level. In other words, 66 % of the $3\nu_{OH}$ band is comprised of symmetric (+) → symmetric (+) and antisymmetric (–) → antisymmetric (–) transitions. This means that under cold molecular beam conditions we expect to observe mostly contribution from the $|0\ 0^+> \rightarrow |3\ 0^+>$ transition with the $|0\ 0^+> \rightarrow |3\ 0^->$ contributing about a third. In addition, since the adiabatic torsion well associated with the $V_{OH} = 3$ (see Fig. 8.1) is increased in the *trans* position ($\tau = 180^o$) by a factor of two relative to the $V_{OH} = 0$, going from 173 to 344 cm^{-1}, the separation between the $|3\ 0^+>$ and the $|3\ 0^->$ states is likely to be unresolved with our intermediate laser linewidth (~0.4 cm^{-1}). As a result, the band in Fig. 8.9(a) appears structureless. Moreover, ~12 cm^{-1} to the red of the main $3\nu_{OH}$ band, with band origin at $\nu_0 = 10\ 247.4$ cm^{-1}, we find an additional vibrational band. This band, similar to the one appearing in the combination band region, is unaccounted by the two-dimensional *ab initio* model. It is likely that this state is also perturbing the second OH stretching overtone ($3\nu_{OH}$) and lead to the unresolved band shape.

8.4 Discussion

The overview room temperature action spectra of CH_3OOH and CD_3OOH shown in Figs. 8.4(a) and 8.4(b) respectively are partially interpreted with the assistance of the high level CCSD(T)/cc-pVTZ two-dimensional *ab initio* model. The 2-D model predicts

quite accurately the bands position and intensities of the OH-stretching and COOH-torsional states (see Chapter 7). In addition, anharmonic frequency calculation at the MP2/aug-cc-pVTZ level has also aided with the assignment for the CH-stretching modes ($2\nu_{CH}$ and $3\nu_{CH}$) and the bending combination mode associated with the OH-stretching mode ($\nu_{OH} + 2\nu_{OOH}$ and $2\nu_{OH} + \nu_{OOH}$) shown in Fig. 8.5. The assignments are also verified using an isotopic substitution of the hydrogen atoms with deuterium at the methyl site. The jet spectrum of the $3\nu_{CH}$ / $2\nu_{OH} + \nu_{OOH}$ in Fig. 8.6(b) is then utilized in order to determine with higher accuracy the bands origins. We find that the $2\nu_{OH} + \nu_{OOH}$ band has a band origin at $\nu_0 = 8287.72$ cm^{-1}, and the various $3\nu_{CH}$ vibrational modes have band origins at $\nu_0 = 8393.03$ cm^{-1}, 8446.98 cm^{-1}, and 8549.3 cm^{-1}. In addition, the jet spectrum of methyl hydroperoxide has shown that in the CH stretching regions strong state mixing results in the broad transition linewidths and structureless vibrational bands. As with methanol,[16] the rotationally unresolved spectrum in the CH stretching mode region does not permit further investigation of these states. The structureless band shape indicates that IVR is faster for the CH modes than for the OH stretching modes.[16,25] Also, in the $2\nu_{OH}$ mode region, the relatively strong signal-to-noise and the higher resolution laser source allowed for deeper analysis of these bands compared to the other spectral regions.

As previously noted, the fits for the $2\nu_{OH}$ band in Fig. 8.8(a) are reasonable. However, interactions of the $|2\ 0^+>$ state with other state(s) preclude more rigorous fits. The fits are reasonable enough however, to provide with positive identification and assignment of the $|2\ 0^+>$ and $|2\ 0^->$ levels and enables to accurately pin the bands origin

at ν_0 = 7024.65 cm^{-1} and 7028.55 cm^{-1} respectively. These values yield adiabatic torsion levels separation of $\Delta_{VOH=2}$ = 3.9 cm^{-1} between the 0^+ and 0^- at the V_{OH} = 2. The level separation is in good accord with the *ab initio* numbers which give torsion levels splitting of $\Delta_{VOH=2}$ = 1.12 cm^{-1}. For the ground state we predict a reasonable $\Delta_{VOH=0}$ = 8.4 cm^{-1} torsion level splitting where the experimental value of $\Delta_{VOH=0}$ = 14.97 cm^{-1} is reported in Ref. 4. The apparent differences of the level splitting between the experimental values on the ground state and at the first OH-stretching overtone are due to the increase of the barrier in the torsional potential (see Fig. 8.1). As the vibrational excitation of the OH-stretching mode increases, so do the interactions between n^{π}_{OC} and the σ^*_{OH} orbitals which in essence makes it difficult for the H-atom to rotate freely about the COO plane at V_{OH}=2 (see Figs. 7.11 and 7.19 in Chapter 7) relative to the less hindered rotation at V_{OH}=0.[29-31]

The experimental values for the transition dipole moments are also in excellent agreement with the *ab initio* values. Both experimental and *ab initio* values confirm a "pure" a-type rotational transition for the $|2\ 0^+>$ level and a "pure" c-type rotational band for the $|2\ 0^->$ level originating form the $|0\ 0^+>$ state. It is interesting to rationalize why the $|0\ 0^+> \rightarrow |2\ 0^+>$ and the $|0\ 0^+> \rightarrow |2\ 0^->$ transition are either "pure" a- or c- types with no b- contribution especially because Fig. 8.2(b) shows a large $\boldsymbol{\mu_b}$ component. Figure 8.11 shows the dependence of the transition dipole moment components $\boldsymbol{\mu_a(\tau)}$, $\boldsymbol{\mu_b(\tau)}$, and $\boldsymbol{\mu_c(\tau)}$, as a function of τ for the V_{OH} = 2 ← 0 transition. From the figure it is clear transitions with similar symmetry (i.e. (+) ↔ (+) and (–) ↔ (–)) will rely on the symmetric dipole moments components $\boldsymbol{\mu_a(\tau)}$ and $\boldsymbol{\mu_b(\tau)}$. In contrast, transitions with

different symmetry (i.e. (+) ↔ (–)), can only connect via the antisymmetric $\mu_c(\tau)$ component. Figure 8.12(a) shows the product wavefunctions involving the $|0\ 0^+> \rightarrow |2\ 0^+>$ transition and Fig. 8.12(b) shows similar product for the $|0\ 0^+> \rightarrow |2\ 0^->$ transition. As mentioned above, the symmetric and antisymmetric nature of the product wavefunctions, require respectively symmetric and antisymmetric dipole moment components to produce non-zero matrix elements. What is not clear from Figs. 8.11 and 8.12 is why the matrix elements associated with the $\mu_b(\tau)$ component are zero. To clarify, Figs. 8.13(a) and 8.13(b) show the results of integrating the matrix elements $<2\ 0^+|\mu_a(r, \tau)|\ 0\ 0^+>$ and $<2\ 0^+|\mu_b(r, \tau)|\ 0\ 0^+>$ respectively. From these two figures, it is clear that while the $<\mu_a>$ results in a positive area, the $<\mu_b>$ component results in positive and negative regions which cancel each other out. From the rotational band contour we also obtain effective average rotational constants for the $|2\ 0^+>$ and $|2\ 0^->$ levels (see Table 8.4). The fact that two transitions are observed is important, as it highlights the significance of including the dependence of the DMF on the torsion motion. This dependence has been previously neglected in studies of H_2O_2,[5] CH_3OH,[7,8] $(CH_3)_2COOH$,[6,9] CH_3CH_2OOH,[9] and even CH_3OOH [9]. However, we find it to be crucial in explaining the $2\nu_{OH}$ jet spectrum.

Unfortunately, the line broadening and spectral congestion of the spectral feature, even at temperature as cold as 5 K, do not permit for obtaining distinct rotational constants for the two levels. In fact, the reported rotational constants are predominantly influenced by the $|2\ 0^->$ level as it is more sensitive to the choice of rotational constants. Basically, the rotational band contour is able to captures the general band shape of the |0

$0^+> \rightarrow |2\ 0^->$ transition very well, but fails to predict the exact band shape for the $|0\ 0^+> \rightarrow |2\ 0^+>$ transition. More specifically, comparison between the rotational bands contour of the $|0\ 0^+> \rightarrow |2\ 0^+>$ transition and the spectrum suggest that the former underestimates the intensity around ~7025 cm^{-1} and overestimates the intensity distribution to the red. Also, since both transitions are said to originate from the same initial $|0\ 0^+>$ level, it is likely that the inadequate simulation rests on the fact that the $|2\ 0^+>$ level in the upper state is perturbed and that perturbation by additional state(s) near by affects mainly the 0^+ and not the 0^- level. This assumption is in fact supported by the differences in the observed linewidth of these transitions.

Careful laser linewidth measurements with monitor etalon and water lines have established that the overtone excitation laser has linewidth of ~0.08 cm^{-1}. These measurements have also shown that the laser linewidth is constant throughout the scan region. Despite the narrow laser bandwidth, we find it necessary, in order to obtain reasonable rotational band contours, to use a ~0.8 cm^{-1} Lorentzian lineshape for the rotational transitions associated with the $|2\ 0^+>$ level and 0.25 cm^{-1} for the transitions associated with the $|2\ 0^->$ level. This suggests that IVR plays a more prominent role in the stronger perturbation of the $|2\ 0^+>$ level compared with the weakly perturbed the $|2\ 0^->$ state. These weak interactions which appear to mainly affect the linewidth but not the shape of the $|2\ 0^->$ band are likely due to weak coupling of the state with the molecule's dark bath of states.[20,25,27]

Interactions between states have been observed in many molecules and recently with nitric acid in the first OH-stretching overtone as well. Konen *et al.* show that the

$2\nu_{OH}$ band of nitric acid is directly coupled to the $\nu_1 + 2\nu_2$ state (OH/NO stretching combination mode).[32] They also report that the first overtone also coupled indirectly to $3\nu_2 + \nu_3 + \nu_7$ state (NO-stretch/HON-bend/HONO-torsion).[32] In the case of direct coupling, the extent of the perturbation of interacting states to a large extent depends on the frequency separation between the two interacting states.[17,19,27,32,33] Two states can perturb one another more strongly if they are closer to each other in frequency as opposed to states lying further away. In addition, the extent of the perturbation may also be reflected in the intensity the perturbing state borrows from the bright OH-stretching mode.

In order to evaluate which of the states might interact with the first OH-stretching overtone we restrict our search to ±200 cm^{-1} spectral window from the band origin. In this region, with a tenth the intensity of the $2\nu_{OH}$ band we locate the $|2\ 1^+>$ state with band origin at $\nu_0 = 7151.04\ cm^{-1}$. Interestingly, this band does not appear to carry significant intensity at the room temperature (see Figs. 8.4 and 8.6(a)). This is mainly due to the fact that at room temperature, the rotational population associated with this state is spread over many more states leading to a very spread and diffuse feature relative to the $2\nu_{OH}$ band.

From the rotational band contour of the $2\nu_{OH} + \nu_{COOH}$ molecular beam spectrum shown in Fig. 8.7(b) we obtain the effective rotational constant for the torsionally excited state ($A' = 1.4067\ cm^{-1}$, $B' = 0.3480\ cm^{-1}$ and $C' = 0.3030\ cm^{-1}$) with transition dipole moment components 1:0.5 a- to b- band type. The respective *ab initio* values for the transition dipole moment for the $|0\ 0^+> \rightarrow |2\ 1^+>$ state are 1:0.62 a- to b- type hybrid

which again are with good agreement with the results obtained from the rotational band contour. Unlike the case with the $|0\ 0^+> \rightarrow |2\ 0^+>$ state, this band is an hybrid band because the matrix elements of the integral $<2\ 1^+|\mu_b(r, \tau)|\ 0\ 0^+>$ are non-zero. In fact, as shown in Fig. 8.13(c), the matrix elements of $<\mu_a>$ have non-canceling positive and negative lobes which reduce the magnitude of the integral while the $<\mu_b>$ in Fig. 8.13(d) has only positive lobes which do not cancel out.

The rotational band contour also suggests that the torsionally excited state is likely interacting as well. The state mixing is inferred from the ~0.50 cm^{-1} transition linewidth. The shoulder to the red of the main $2\nu_{OH} + \nu_{COOH}$ peak in Fig. 8.7(b) at 7145.9 cm^{-1} can not be accounted in the rotational band simulations with a single $|0\ 0^+> \rightarrow |2\ 1^+>$ band fit and therefore, an additional band with similar rotational constants and transition dipole moments to the $|0\ 0^+> \rightarrow |2\ 1^+>$ is added to the simulation and labeled in the figure with the υ_x symbol. It is likely that due to the overlapping frequencies of these two bands, and, as evident from the line broadening, that these two states do indeed interact although the extent of the interaction is not quantified.

The perturbation of states as a result of IVR has been extensively studied in methanol where the high rotational resolution and *ab initio* local mode studies resulted for comprehensive bands analysis.[7-8,14-21] In methanol, it has been proposed that the methyl rotor which is also common to CH_3OOH molecule interacts strongly with the OH-stretching modes and their excited torsional states.[17,18] We anticipate similar interactions in methyl hydroperoxide though to a lesser extant since the hydroxyl group is separated from the methyl rotor by an oxygen atom. In fact, trajectory calculations on highly

excited vibrational state of CH_3OOH have shown that the OH group is somewhat isolated due to its neighboring oxygen atom.[34]

In order to obtain a qualitative picture to the extant of the perturbation resulting from the methyl rotor in the $2\nu_{OH}$ region, we re-synthesize the isotopomer of methyl hydroperoxide where the methyl group is replaced with methyl-d_3 to form CD_3OOH. Typically, isotopic substitutions result in an increase of the number of low frequencies vibrational modes in the molecule and an increase the density of states (see Table 8.2). More importantly, the vibrational modes associated with the deuterium motion are expected to shift significantly with respect to the OH-stretching mode. In fact, based on the values given in Table 8.2, many modes are expected to shift upon deuterium substitution. If, for example, the perturbing state shifts by some wavenumber further away from the $|2\ 0^+>$ state, its perturbing effects should be lifted from the $|2\ 0^+>$ state.

The CD_3OOH $2\nu_{OH}$ action spectrum taken at 4.2 and 9.5 K as well as the $2\nu_{OH} + \nu_{COOH}$ action spectra taken at 4.3 and 10.3 K are shown in Figs. 8.14(a) – 8.14(d) respectively. The effects of the deuterium substitution appear most dramatic for the stretch-torsion combination band. The rotational band contours are also shown in Fig. 8.14 for the MHP-d_3 spectra. In generating these fits we fix the rotational constants for the $|0\ 0^+>$ and $|0\ 0^->$ levels to scaled microwave rotational constants. The scaling factors for the microwave constants were obtained by taking the ratio of the *ab initio* rotational constants from the MP2/aug-cc-pVTZ calculation for CD_3OOH and CH_3OOH. The rotational constants used for the ground state are given in Table 8.7. We then, as before, vary the parameters associated with upper states. For the two rotational temperatures the spectra in Figs. 8.14(c) and 8.14(d) were obtained, we find that contribution from a single

band to the spectrum resulting from the $|0\ 0^+> \rightarrow |2\ 1^+>$ excitation. Furthermore, the rotational band contours superimposed on the spectrum with the dashes lines agree very well with the experimental spectra. We also find significant narrowing in the linewidths associated with the torsional state; these linewidths are reduced from ~0.50 cm^{-1} in CH_3OOH to ~0.21 cm^{-1} in CD_3OOH. Comparing the two band origins, we find that that the isotopic substitution has resulted in -0.32 cm^{-1} shifts to the $|2\ 1^+>$ level. These small shifts are expected from OH-stretching and COOH-torsion modes since these modes are not significantly affected by the deuteration of the methyl group (see Table 8.2). It is also worth noting that at 4.3 K there is significantly lower number of populated states relative to the number of populated states at 10.3 K. The rotational quantum number J_{max} increases from 3 to 7 as a result of 6 K change in rotational temperature. The rotational parameters extracted from these band contour simulations of the $|2\ 1^+>$ level are listed in Table 8.8.

Also shown in Figs 8.14(a) and 8.14(b) are the rotational band contours of CD_3OOH $2\nu_{OH}$ band. The fits, as with the torsion band are in excellent agreement with the spectrum compared with those obtained for the CH_3OOH $2\nu_{OH}$ state. The cold 4.2 K spectrum in Fig. 8.14(a) is fitted by taking into account the two transitions originating from the $|0\ 0^+>$ level with the final states $|0\ 0^+>$ and $|0\ 0^->$. As before, we fix the ground level rotational constants to the *ab initio* scaled constants (A'' = 1.1135 cm^{-1}, B'' = 0.3004 cm^{-1} and C'' = 0.2627 cm^{-1}),[4] and vary the upper rotational constants and transition dipole moments. The effective rotational constant for the two transition are found to be A' = 1.1077 cm^{-1}, B' = 0.3013 cm^{-1} and C' = 0.2670 cm^{-1} with 1:0 a- to c- type for the $|0$

$0^+> \rightarrow |2\ 0^+>$ transition and 0:1 a- to c- type for the $|0\ 0^+> \rightarrow |2\ 0^->$ transtion. As with CH_3OOH, neither transition have μ_b component.

In terms of transition linewidths, the $|0\ 0^+> \rightarrow |2\ 0^+>$ transtion, previously broadened by 0.8 cm^{-1} (FWHM) in CH_3OOH now have narrower linewidths of 0.65 cm^{-1}. Interestingly, we find that the $|0\ 0^+> \rightarrow |2\ 0^->$ transtion has a 0.45 cm^{-1} linewidth which is almost a factor of two broader than that of CH_3OOH. Unfortunately, our data does not provide evidence to whether the broadening is due to direct or indirect coupling of this state to the dark bath of states. As we pointed out previously, the density of states for CH_3OOH ($2\nu_{OH}$) is significantly smaller compared with CD_3OOH. From Whitten-Rabinovich density of states calculation we find that there are ρ = 165 states/cm^{-1} for CH_3OOH and ρ = 581 states/cm^{-1} for CD_3OOH in the $2\nu_{OH}$ region. This suggests that while the isotopic substitution reduces the effects from perturbation on the $|2\ 0^+>$ and $|2\ 1^+>$ states drastically, the three-and-a-half fold increase of the density of states in CD_3OOH leads to the increased linewidths associated with the $|2\ 0^->$ level. The Whitten-Rabinovich code is provided in Appendix *D* for PNA and can be modified with the harmonic frequencies of MHP and MHP-d_3 from Table 8.2.

The ro-vibrational parameters obtained for the $2\nu_{OH}$ band of CD_3OOH shown in Figs. 8.14(a) and 8.14(b) are provided in Table 8.9 and Table 8.10 respectively. From these tables we find that the ground state separation between the $|0\ 0^+>$ and $|0\ 0^->$ levels is reduced from 14.97 cm^{-1} in CH_3OOH to 14.85 cm^{-1} in CD_3OOH and the separation between the $|2\ 0^+>$ and $|2\ 0^->$ levels is reduced form 3.90 cm^{-1} to 3.54 cm^{-1} due to zero-

point energy considerations. In terms of absolute band positions, the isotopic substitution has resulted in red shift of 0.28 cm^{-1} for the $|2\ 0^+>$ state.

To this point, our analysis has mainly focused on transitions originating from the $|0\ 0^+>$ level (ground state). The relatively low concentration of methyl hydroperoxide in the expansion relative to helium have collapsed the ro-vibrational population in methyl hydroperoxide to $|0\ 0^+\ J_{max}\sim7>$. Even then, the presence of perturbations has lessened our ability to obtain precise fits to the $2\nu_{OH}$ band of CH_3OOH and, have raised the issue of how well one expects the rotational band contour perform in terms of fitting the transitions originating from the $|0\ 0^->$ level. As mentioned previously, the population of the $|0\ 0^->$ level is expected to contribute less than 1 % based on Boltzmann distribution of vibrational states at 4 K. In order to determine the contribution of the $|0\ 0^->$ level, we warm up our spectrum initially to ~17 K by reducing the helium backing pressure to 600 Torr. Under these conditions, the population of the $|0\ 0^->$ level is expected to be ~28 percent. The spectrum and the rotational band contours are shown in Fig. 8.15(a). The new sharp peak appearing at 7013.58 cm^{-1} is the band origin for the $|0\ 0^-> \rightarrow |2\ 0^->$ transition. This transition is fitted using microwave data available for the $|0\ 0^->$ level,[4] and the effective rotational constants used for the fits obtained for the $|2\ 0^->$ level. The transition dipole moment is found to match the *ab initio* value with "pure" a- type band. Similarly, the band at ν_0 = 7009.68 cm^{-1} which corresponds to the $|0\ 0^-> \rightarrow |2\ 0^+>$ transtion is fitted using a "pure" c- type band and no b- component. The overall contour which is the sum of the contribution of these four transitions normalized to their relative population appears to captures the general band shape. The parameters used in

fitting Fig. 8.15(a) are given in Table 8.11. As before, we find that the overall band contour fails to account completely for the intensity distribution in the spectrum. Similar to the situation with the cold spectrum in Fig. 8.8, the rotational band contour around the $|0\ 0^+> \rightarrow |2\ 0^+>$ transition at $\nu_0 = 7024.65\ cm^{-1}$ does not fill up the spectral feature entirely.

Similarly, the $2\nu_{OH}$ band of CD_3OOH shown in Fig. 8.14(b) is also obtained with lower backing helium pressure. As with the fits for the spectrum obtained at 4 K in Fig. 8.14(a), the overall rotational band contour is in good agreement with the CD_3OOH action spectrum. However, in fitting the warm spectrum, we find that the fit of MHP-d_3 ($2\nu_{OH}$) requires an additional band with origin at $\nu_0 = 7020.33\ cm^{-1}$ to be added to the rotational band contour in addition to the standard four transitions originating from the $|0\ 0^+>$ and $|2\ 0^->$ levels. The convolution of the five states contributing to the $CD_3OOH(2\nu_{OH})$ at 9.5 K is shown in Fig. 8.16. The fact that this band (referred to as υ_z) does not appear in the cold spectrum of CD_3OOH suggests that its origin is associated with the $|0\ 0^->$ level. A summary of the transitions originating from the $|0\ 0^->$ levels and their corresponding transition moments and bands origin of CD_3OOH are also listed in Table 8.10.

With the information obtained from fitting the cold and warm action spectra of CH_3OOH, we proceed to fit the room temperature action spectrum. We anticipate that if the extent of IVR is significant or, alternatively, it affects high and low rotational states alike, it would be transparent from the room temperature rotational band contour. The room temperature action spectrum and its rotational band contour are shown in Fig.

8.15(b). The rotational band contour is obtained by using the rotational constants, transition moments and band origins obtained for the four transitions from the molecular beam experiments with their appropriate populations at 298 K. To these transitions we add the contribution from two additional transitions which are also predicted by our two-dimensional *ab initio* model. Namely, these hot bands transitions are the $|0\ 1^+> \rightarrow |2\ 1^+>$ and $|0\ 1^-> \rightarrow |2\ 1^->$. Since the $|2\ 1^+>$ level has been investigated under molecular beam conditions, its rotational constants, transition frequencies and transition moments are known. For the $|2\ 1^->$ level we use the calculated *ab initio* values for the transition moments while using the same rotational constants which were used to fit the $|2\ 1^+>$ level. A summery of the rotational constants, transition moments, and band origins of these room temperature bands are given in Table 8.12. The quartic centrifugal distortions parameters ΔK, ΔJK and ΔJ are also used as input in the simulations; they are fixed in the lower and upper states to the values from Ref. 4. The reasonable agreement between the rotational band contour and the room temperature action spectrum in Fig. 8.15(b) suggests that even though the $2\nu_{OH}$ band is perturbed, it is clear that the effects of the perturbations are not substantial at room temperature. We are basing this on the fact that the rotational band contour which does not include states interactions does well in fitting the room temperature $2\nu_{OH}$ spectrum.

We also evaluate the behavior of the rotational band contour in the room temperature spectrum of the $3\nu_{OH} + \nu_{COOH}$ band at 10 407.85 cm^{-1}. The room temperature $3\nu_{OH} + \nu_{COOH}$ spectrum of MHP, its rotational band simulation, and the convoluted contribution of the individual states are shown in Fig. 8.17. The rotational band-contours

assume rotational transition line-broadening of 1.0 cm^{-1} which is the result of stronger interactions in this region. A total of five transitions give rise to the observed vibrational band in which four of these transitions are accounted for by the *ab initio* model. These states originate from the ground state symmetric $|0\ 0^+> \rightarrow |3\ 1^+>$ and antisymmetric $|0\ 0^-> \rightarrow |3\ 1^->$ transitions as well as the torsionally excited state $|0\ 1^+> \rightarrow |3\ 2^+>$ and $|0\ 1^-> \rightarrow |3\ 2^->$ transitions (hot bands). In addition, we include in the simulation the contribution of an unidentified state which appears in the molecular beam spectrum around 10 421.1 cm^{-1}. The fitting parameters are shown in Table 8.13. The reasonable agreement between the rotational band contour and the spectrum at room temperature implies that although perturbation due to intramolecular vibrational energy redistribution is present in the vibrationally excited molecule, its influence is not strongly noted at room temperature.

8.5 Conclusions

The first and second OH-stretching overtones are examined in molecular beam and room temperature using the vibrationally mediated photodissociation scheme. The rotational structure of the vibrationally excited methyl hydroperoxide is determined using rotational band contours. We find that mainly four transitions associated with symmetric and antisymmetric levels make up the $2\nu_{OH}$ band and that these observations are in excellent agreement with our CCSD(T)/cc-pVTZ two-dimensional *ab initio* model which takes into account the influence of the COOH torsion and OH stretching motion on the dipole moment function. These results imply that in general, one must consider the dependence of the torsion on the dipole moment function. This dependence has been

ignored in the analysis of several hydroperoxides,[5,6,9] and has been shown to be important to correctly analyze the vibrational band structure of MHP.

The rotational band contours generated to fit the spectrum have shown that the $2\nu_{OH}$ and its corresponding torsional state are perturbed as a result of intermolecular vibrational energy redistribution and that while the extent of IVR on the torsionally excited state is predominately observed as linewidth broadening, it is also affecting the intensity distribution of the $|2\ 0^+>$ state. This apparent IVR behavior is likely due to the fact that the $|2\ 0^+>$ state is coupled more strongly to other states compared with the $|2\ 0^->$ state. This in essence suggests that IVR is faster, more complete for the $|2\ 0^+>$ state. Lines broadening are also observed with the torsionally excited state associated with the second OH stretching overtones, $|3\ 1^+>$. These bands however, can be readily fitted at room temperature suggesting that IVR is not strongly controlling the band intensity distributions. IVR is also apparent in the CH-stretching modes where even under molecular beam condition span over a large range of frequencies. Experiments involving isotopic substitution of the methyl group with deuterium (MHP-d_3) suggest that as with methanol,[16] the $2\nu_{OH}$ and $2\nu_{OH} + \nu_{COOH}$ bands of MHP do indeed interact with states associated with the methyl rotor. In order to qualitatively asses the strength of the interactions we use the rotational band contour to fit the room temperature spectrum. The fact that the agreement of the rotational band contour with the spectrum is reasonable implies that these IVR controlled interactions are not strongly noted at room temperature for the first OH-stretching overtone.

Table 8.1: Rotational and Vibrational Parameters for the Torsion Substates Associated with the OH Vibrational Ground State, $|0\ m^{+/-}>$, of CH_3OOH (cm^{-1})

	$\|0\ 0^+>$ Substate		$\|0\ 0^->$ Substate		$\|0\ 1^+>$ Substate		$\|0\ 1^->$ Substate	
	Observed[a]	Predicted[b]	Observed[a]	Predicted[b]	Observed[a]	Predicted[b]	Observed[a]	Predicted[b]
A″	1.42860	1.41228	1.42386	1.41228	1.42888	1.42026	1.42216	1.42026
B″	0.35025	0.35014	0.34952	0.35014	0.35106	0.35270	0.35018	0.35270
C″	0.30204	0.30178	0.30271	0.30178	0.30177	0.30038	0.30255	0.30038
ν_0	0	0	14.97	8.4[c]	130[d]	124.8[c]	191[d]	197.4[c]

[a] From Ref. 4 except where noted otherwise.

[b] From MP2/aug-cc-pVTZ except where noted otherwise.

[c] From CCSD(T)/cc-pVTZ 2-D model.

[d] This work, from room temperature rotational band contours.

Table 8.2: Harmonic Frequencies, Anharmonicities and Isotope Shifts of CH_3OOH Computed at MP2/aug-cc-pVTZ (cm^{-1})

$(\omega_e)_i$	3777	3179	3151	3061	1532	1490	1464	1359	1211	1181	1060	870	447	261	171
d_3 -shift	0	820	812	870	454	391	109	3.5	111	150	78.7	55.0	41.6	59.5	1.9
$(\omega_e\chi_e)_{ij}$	1	2	3	4	5	6	7	8	9	10	11	12	13	14	15
1	-84.4														
2	-0.84	-36.7													
3	-0.71	-28.8	-31.4												
4	-0.82	-53.4	-87.2	-19.0											
5	-0.43	-3.84	-17.5	-20.5	-3.58										
6	-0.02	-17.8	-10.4	-0.42	-5.28	-8.75									
7	-0.28	-13.4	-7.30	19.9	-4.63	-6.43	-10.6								
8	-27.6	-0.73	0.74	0.06	-0.83	-0.80	-1.37	-9.89							
9	0.11	-5.05	-3.40	-3.03	-3.95	-5.13	-8.33	-29.5	-2.63						
10	-0.56	-3.04	-3.06	-3.98	-10.7	-6.67	-3.07	-1.48	-0.08	-1.82					
11	-2.78	-1.16	3.78	1.17	-2.13	-2.69	-6.17	-5.86	-10.4	-7.98	-6.91				
12	-3.06	-1.26	0.32	-0.13	-0.79	-0.99	-1.19	-11.4	-2.53	-0.67	-6.71	-4.56			
13	0.27	-0.66	0.43	0.17	0.42	-1.04	-0.26	-1.15	-1.55	0.55	-4.99	-4.56	0.38		
14	0.24	-0.68	2.14	1.23	-1.71	1.16	2.10	-0.06	-3.52	-1.62	0.43	-1.33	2.14	-6.16	
15	9.13	2.83	-2.84	0.09	1.71	-1.40	-0.13	-8.83	14.0	1.04	8.98	0.11	-2.30	-5.39	-50.4

Table 8.3: CCSD(T)/cc-pVTZ Transition Dipole Moments for the Various Matrix Elements $<0\ 0^{+/-}|\mu_\alpha|2\ 0^{+/-}>$ [a]

	$<2\ 0^+\|$ Substate			$<2\ 0^-\|$ Substate		
	$\|\mu_a\|$	$\|\mu_b\|$	$\|\mu_c\|$	$\|\mu_a\|$	$\|\mu_b\|$	$\|\mu_c\|$
$\|0\ 0^+>$	1.2×10^{-2} (1.0)	4.8×10^{-4} (0.04)	2.5×10^{-6} (~0)	3.1×10^{-6} (~0)	8.4×10^{-8} (~0)	1.0×10^{-2} (0.83)
$\|0\ 0^->$	2.6×10^{-6} (~0)	4.8×10^{-8} (~0)	1.0×10^{-2} (0.83)	1.2×10^{-2} (1.0)	1.1×10^{-4} (0.01)	2.0×10^{-6} (~0)

[a] The values in parenthesis are normalized with respect to the $<2\ 0^+|\mu_a|0\ 0^+>$ transition.

Table 8.4: Experimental Parameters used for the $2\nu_{OH}$ Rotational Band Contour at 5 K [a]

	$\|0\ 0^+> \rightarrow \|2\ 0^+>$	$\|0\ 0^+> \rightarrow \|2\ 0^->$
ν_0	7024.65	7028.55
$\Delta\nu$ (FWHM)	0.7	0.25
A'	1.4067	1.4067
B'	0.3480	0.3480
C'	0.3030	0.3030
μ_a	1	0
μ_b	0	0
μ_c	0	1
f [b]	1	0.7

[a] In cm^{-1}. The transition moments are relative to the $<2\ 0^+|\mu_a|0\ 0^+>$ transition.

[b] Intensities are relative to the $|0\ 0^+> \rightarrow |2\ 0^+>$ transition.

Table 8.5: Experimental Parameters used for the $2\nu_{OH} + \nu_{COOH}$ Rotational Band Contour at 9 K [a]

	$\|0\ 0^+\rangle \rightarrow \|2\ 1^+\rangle$	$\|0\ 0^+\rangle \rightarrow \|\upsilon_x^+\rangle$
ν_0	7151.04	7145.90
$\Delta\nu$ (FWHM)	0.5	0.5
A'	1.4067	1.4067
B'	0.3480	0.3480
C'	0.3030	0.3030
μ_a	1	0
μ_b	0.50	0.63
μ_c	0	0
f [b]	1	0.2

[a] In cm^{-1}. The transition moments are relative to the $\langle 2\ 1^+|\mu_a|0\ 0^+\rangle$ transition.

[b] Intensities are relative to the $|0\ 0^+\rangle \rightarrow |2\ 1^+\rangle$ transition.

Table 8.6: Experimental Parameters used for the $3\nu_{OH} + \nu_{COOH}$ Rotational Band Contour at 19 K [a]

	$\|0\ 0^+\rangle \rightarrow \|3\ 1^+\rangle$	$\|0\ 0^-\rangle \rightarrow \|3\ 1^-\rangle$	$\|0\ 0^+\rangle \rightarrow \|\upsilon_y^+\rangle$
ν_0	10 407.85	10 420.65	10 421.1
$\Delta\nu$ (FWHM)	1.0	1.0	1.0
A'	1.4140	1.4140	1.4140
B'	0.3562	0.3562	0.3562
C'	0.3062	0.3062	0.3062
μ_a	1	1	1
μ_b	0.23	0.26	0.23
μ_c	0	0	0
f [b]	1	0.33	0.25

[a] In cm^{-1}. The transition moments are relative to the $\langle 3\ 1^+|\mu_a|0\ 0^+\rangle$ transition.

[b] Intensities are relative to the $|0\ 0^+\rangle \rightarrow |3\ 1^+\rangle$ transition.

Table 8.7: Scaled Rotational Parameters for the Torsion Substates Associated with the OH Vibrational Ground State, $|0\ 0^{+/-}\rangle$, of CD_3OOH (cm^{-1}). [a]

	$\|0\ 0^+\rangle$ Substate	$\|0\ 0^-\rangle$ Substate
A''	1.1135	1.1135
B''	0.3004	0.3004
C''	0.2627	0.2627
ν_0	0	14.85 [b]

[a] The values from Ref. 4 are scaled using the ratio of rotational constants from the MP2/aug-cc-pVTZ level.

[b] Obtained experimentally.

Table 8.8: Experimental Parameters used for the $2\nu_{OH} + \nu_{COOH}$ Rotational Band Contours of CD_3OOH [a]

	$\|0\ 0^+\rangle \rightarrow \|2\ 1^+\rangle$
ν_0	7149.68
$\Delta\nu$ (FWHM)	0.21
A'	1.1077
B'	0.3013
C'	0.2610
μ_a	1
μ_b	0.52
μ_c	0

[a] In cm^{-1}. The transition moments are relative to the $\langle 2\ 1^+|\mu_a|0\ 0^+\rangle$ transition.

Table 8.9: Experimental Parameters used for the $2\nu_{OH}$ Rotational Band Contour of CD_3OOH at 4.2 K [a]

	$\|0\ 0^+\rangle \rightarrow \|2\ 0^+\rangle$	$\|0\ 0^+\rangle \rightarrow \|2\ 0^-\rangle$
ν_0	7024.93	7028.47
$\Delta\nu$ (FWHM)	0.65	0.45
A'	1.1077	1.1077
B'	0.3013	0.3013
C'	0.2610	0.2610
μ_a	1	0
μ_b	0	0
μ_c	0	1
f [b]	1	0.7

[a] In cm^{-1}. The transition moments are relative to the $\langle 2\ 0^+|\mu_a|0\ 0^+\rangle$ transition.

[b] Intensities are relative to the $|0\ 0^+\rangle \rightarrow |2\ 0^+\rangle$ transition.

Table 8.10: Experimental Parameters Used for the $2\nu_{OH}$ Rotational Band Contour of CD_3OOH at 9.5 K[a]

	$\|0\ 0^+\rangle \rightarrow \|2\ 0^+\rangle$	$\|0\ 0^+\rangle \rightarrow \|2\ 0^-\rangle$	$\|0\ 0^-\rangle \rightarrow \|2\ 0^-\rangle$	$\|0\ 0^-\rangle \rightarrow \|2\ 0^+\rangle$	$\|0\ 0^-\rangle \rightarrow \|\upsilon_z^-\rangle$
ν_0	7024.93	7028.47	7028.57	7024.93	7035.30
$\Delta\nu$ (FWHM)	0.65	0.45	0.45	0.65	1.0
A'	1.1077	1.1077	1.1077	1.1077	1.1077
B'	0.3013	0.3013	0.3013	0.3013	0.3013
C'	0.2610	0.2610	0.2610	0.2610	0.2610
μ_a	1	0	1	0	1
μ_b	0	0	0	0	0
μ_c	0	1	0	1	0
f[b]	1	0.7	0.3	0.15	0.35

[a] In cm^{-1}. The transition moments are relative to the $\langle 2\ 0^+|\mu_a|0\ 0^+\rangle$ transition.

[b] Intensities are relative to the $|0\ 0^+\rangle \rightarrow |2\ 0^+\rangle$ transition.

Table 8.11: Experimental Parameters used for the $2\nu_{OH}$ Rotational Band Contour of CH_3OOH at 17 K[a]

	$\|0\ 0^+\rangle \rightarrow \|2\ 0^+\rangle$	$\|0\ 0^+\rangle \rightarrow \|2\ 0^-\rangle$	$\|0\ 0^-\rangle \rightarrow \|2\ 0^-\rangle$	$\|0\ 0^-\rangle \rightarrow \|2\ 0^+\rangle$
ν_0	**7024.65**	**7028.55**	**7028.55**	**7024.65**
$\Delta\nu$ **(FWHM)**	**0.80**	**0.25**	**0.25**	**0.80**
A'	**1.4067**	**1.4067**	**1.4067**	**1.4067**
B'	**0.3480**	**0.3480**	**0.3480**	**0.3480**
C'	**0.3030**	**0.3030**	**0.3030**	**0.3030**
μ_a	**1**	**0**	**1**	**0**
μ_b	**0**	**0**	**0**	**0**
μ_c	**0**	**1**	**0**	**1**
f[b]	**1**	**0.7**	**0.16**	**0.3**

[a] In cm^{-1}. The transition moments are relative to the $\langle 2\ 0^+|\mu_a|0\ 0^+\rangle$ transition.

[b] Intensities are relative to the $|0\ 0^+\rangle \rightarrow |2\ 0^+\rangle$ transition.

Table 8.12: Experimental Parameters Used for the $2\nu_{OH}$ Rotational Band Contour of CH_3OOH at 298 K[a]

	$\|0\ 0^+\rangle \rightarrow \|2\ 0^+\rangle$	$\|0\ 0^+\rangle \rightarrow \|2\ 0^-\rangle$	$\|0\ 0^-\rangle \rightarrow \|2\ 0^-\rangle$	$\|0\ 0^-\rangle \rightarrow \|2\ 0^+\rangle$	$\|0\ 1^+\rangle \rightarrow \|2\ 1^+\rangle$	$\|0\ 1^-\rangle \rightarrow \|2\ 1^-\rangle$
ν_0	7024.65	7028.55	7028.55	7024.65	7151.04	7192.0
$\Delta\nu$ (FWHM)	0.80	0.25	0.25	0.80	0.5	0.5
A'	1.4067	1.4067	1.4067	1.4067	1.4067	1.4067
B'	0.3480	0.3480	0.3480	0.3480	0.3480	0.3480
C'	0.3030	0.3030	0.3030	0.3030	0.3030	0.3030
μ_a	1	0	1	0	1	1
μ_b	0	0	0	0	0.50	0.50
μ_c	0	1	0	1	0	0
f[b]	1	0.7	1	0.7	0.53	0.35

[a] In cm^{-1}. The transition moments are relative to the $\langle 2\ 0^+|\mu_a|0\ 0^+\rangle$ transition.

[b] Intensities are relative to the $|0\ 0^+\rangle \rightarrow |2\ 0^+\rangle$ transition.

Table 8.13: Experimental Parameters Used for the $3\nu_{OH} + \nu_{COOH}$ Rotational Band Contour of CH_3OOH at 298 K[a]

	$\|0\ 0^+\rangle \rightarrow \|3\ 1^+\rangle$	$\|0\ 0^-\rangle \rightarrow \|3\ 1^-\rangle$	$\|0\ 1^+\rangle \rightarrow \|3\ 2^+\rangle$	$\|0\ 1^-\rangle \rightarrow \|3\ 2^-\rangle$	$\|0\ 1^+\rangle \rightarrow \|2\ 1^+\rangle$
ν_0	10 407.85	10 420.65	10 551.0	10 607.0	10 421.1
$\Delta\nu$ (FWHM)	1.0	1.0	1.0	1.0	1.0
A'	1.4140	1.4140	1.4140	1.4140	1.4140
B'	0.3562	0.3562	0.3562	0.3562	0.3562
C'	0.3062	0.3062	0.3062	0.3062	0.3062
μ_a	1	1	1	0	1
μ_b	0.23	0.26	0.23	0.23	0.23
μ_c	0	0	0	0	0
f[b]	1	0.94	0.5	0.45	0.20

[a] In cm^{-1}. The transition moments are relative to the $\langle 3\ 1^+|\mu_a|0\ 0^+\rangle$ transition.

[b] Intensities are relative to the $|0\ 0^+\rangle \rightarrow |3\ 1^+\rangle$ transition.

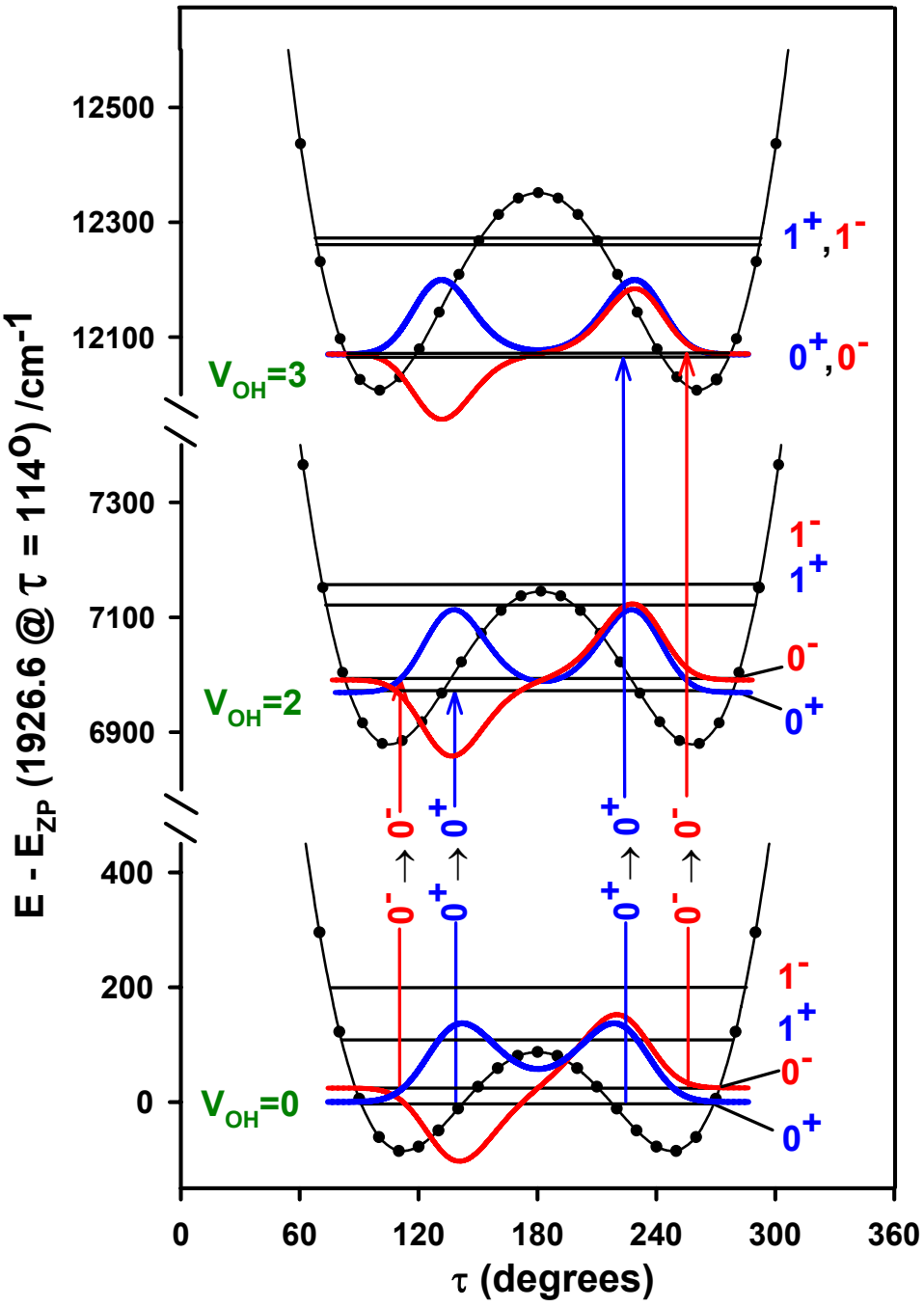

Figure 8.1: Adiabatic torsional potentials for the first few OH stretching states. The zero-point energy (~1927 cm^{-1}) has been subtracted out in the vertical energy scale. The OH stretching states are labeled by the quantum number V_{OH} while their corresponding torsional states are labeled by the quantum number $0^{\pm}$, $1^{\pm}$, $2^{\pm}$. The barrier in the *trans* position causes splitting of the wavefunctions into symmetric (+) and antisymmetric (–) types. Whether the (+) ↔ (–) transitions are allowed motivate this study.
[File: F8.1_torsion_diagram]

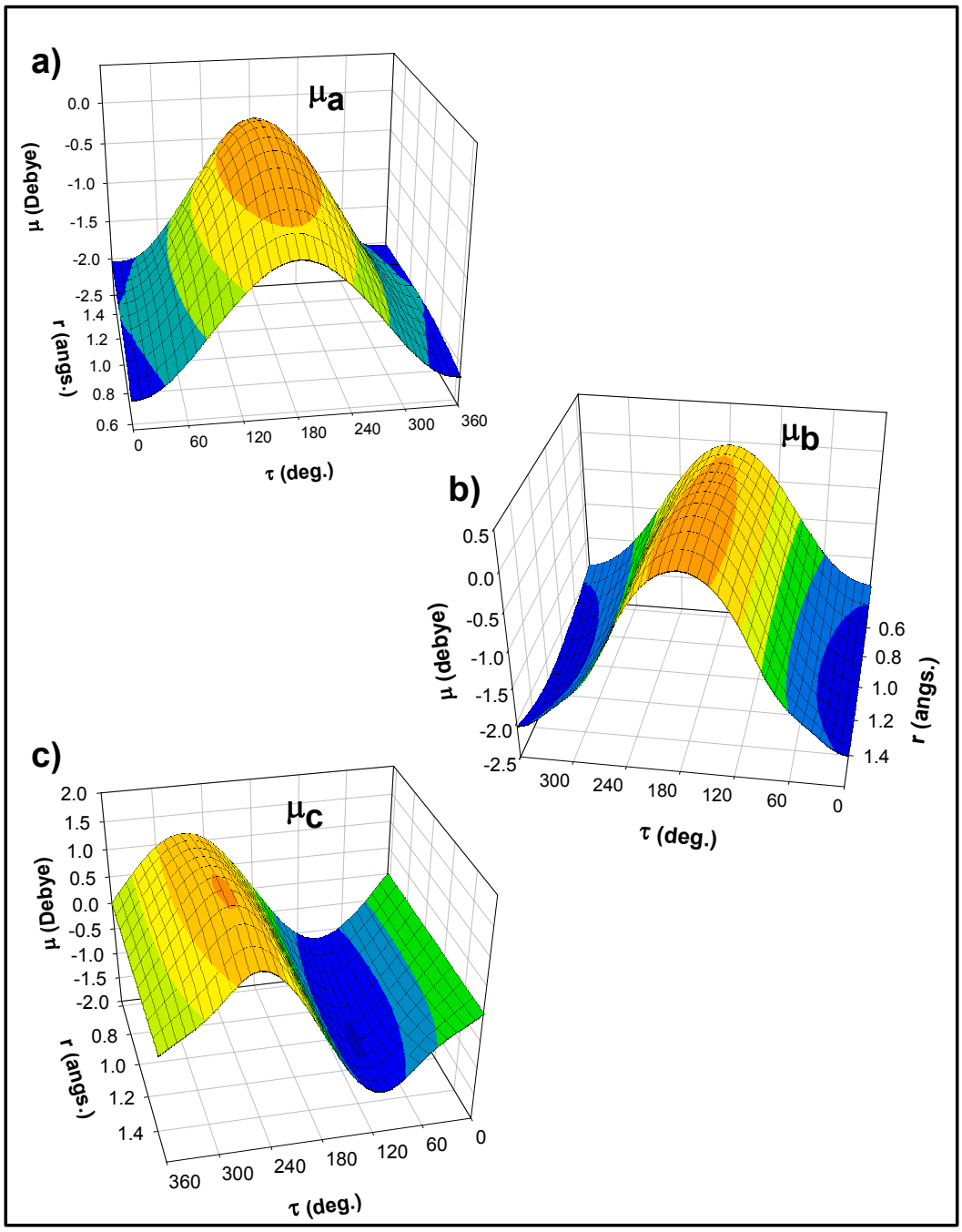

Figure 8.2: a) Two-dimensional dipole moment function (DMF) of the symmetric $\mu_a(r,\tau)$ component as a function O-H separation, r, and HOOC torsion angle, τ. b) Two-dimensional DMF of the symmetric $\mu_b(r,\tau)$ component as a function O-H separation, r, and HOOC torsion angle, τ. c) Two-dimensional DMF of the antisymmetric $\mu_c(r,\tau)$ as a function O-H separation, r, and HOOC torsion angle, τ. These dipole moment surfaces are computed at the CCSD(T)/cc-pVTZ level.[24] [File: F8.2_dipole_surface]

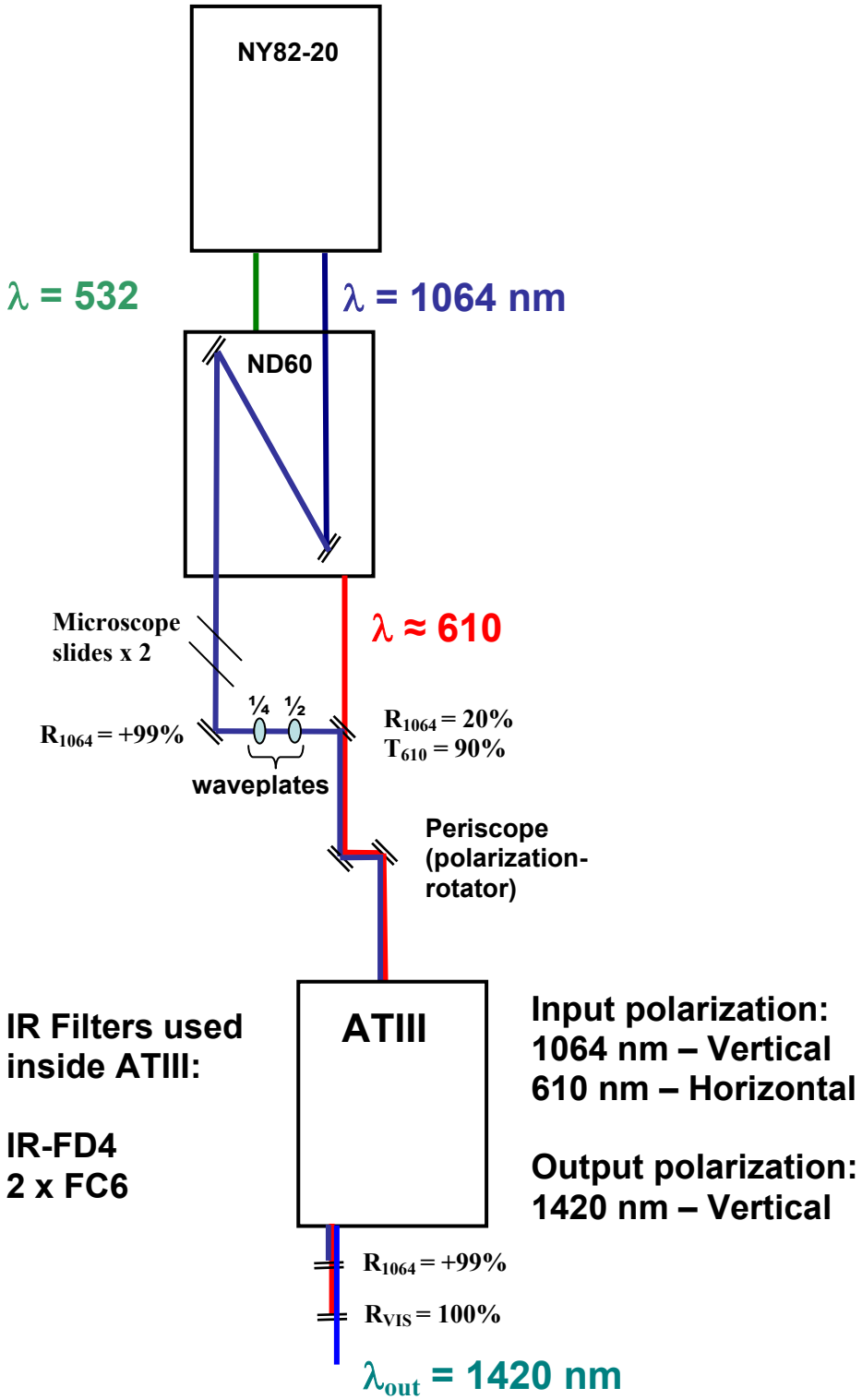

Figure 8.3: Schematic of the DFM IR apparatus used in generating the tunable IR radiation for the vibrational excitation step (λ_1) in the high resolution scans. [File: F8.3_apparatus]

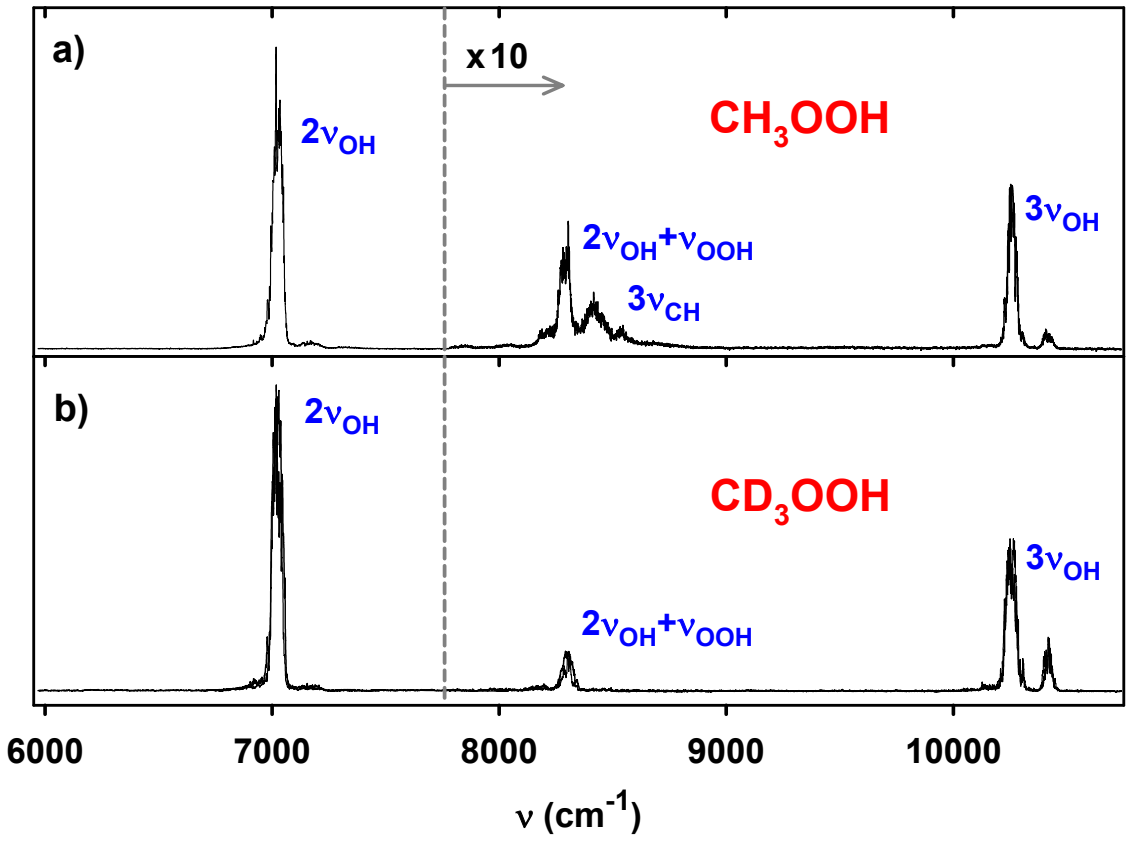

Figure 8.4: The room temperature high pressure overview action spectra of a) CH_3OOH and b) CD_3OOH generated using the ViMP technique in the $2\nu_{OH}$ through the $3\nu_{OH}$ regions. The OH-photoproducts from the overtone induced photodissociation process are probed in their N=2 rotational state at ~283 nm. The bands showing in these spectra are the focus of this study. The band around 7000 cm^{-1} corresponds to the $2\nu_{OH}$ band. The sharp feature around 8300 cm^{-1} corresponds to the $2\nu_{OH} + \nu_{OOH}$ combination band and the more diffused bands in this region correspond to the various CH-stretching modes. The bands around 10 240 cm^{-1} and 10 400 cm^{-1} correspond to the $3\nu_{OH}$ and $3\nu_{OH} + \nu_{COOH}$ respectively. [File: F8.4_CH3_CD3]

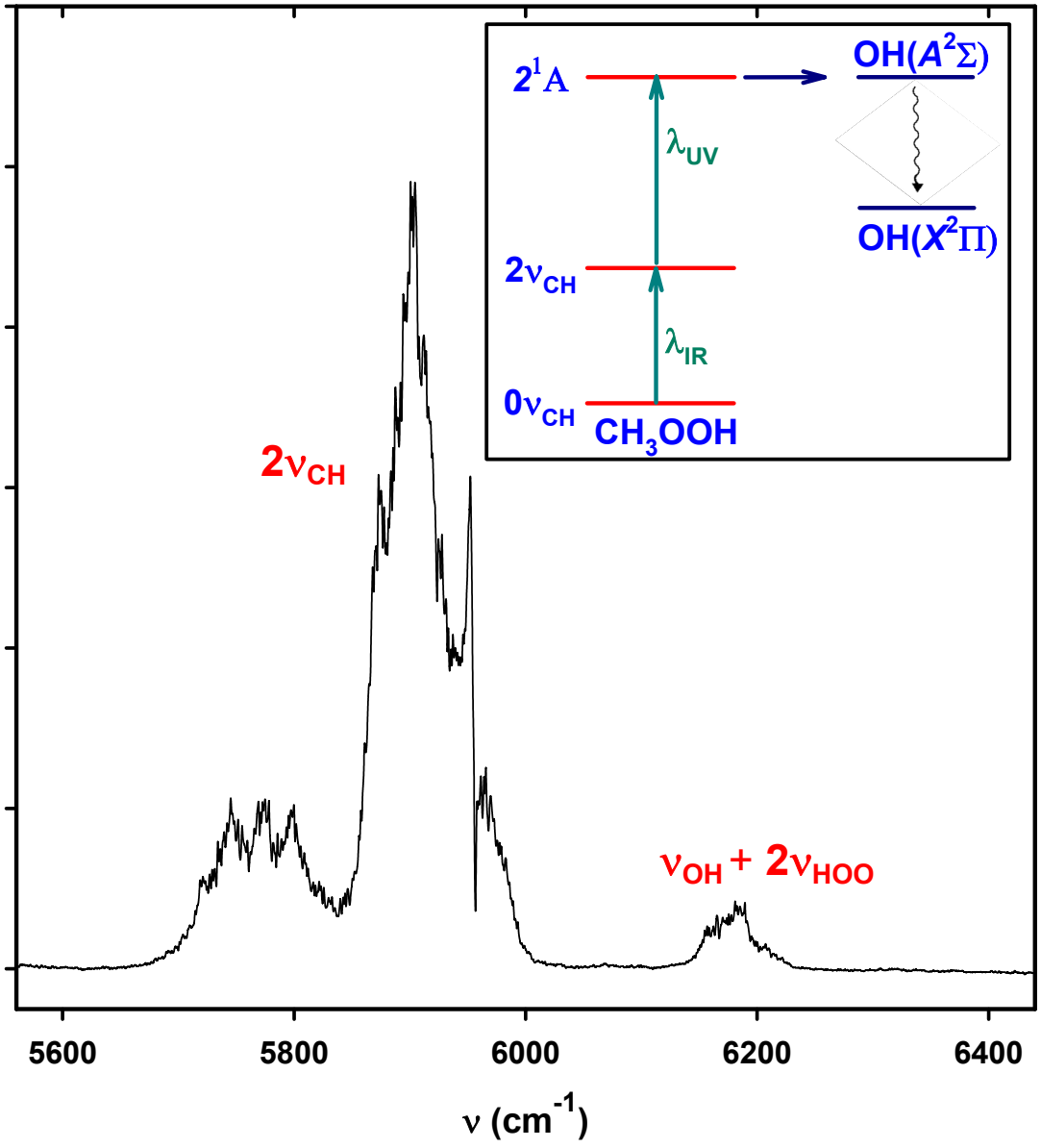

Figure 8.5: The $2\nu_{CH}$ region action spectrum of CH_3OOH generated using the ViMP technique $2\nu_{CH}$ + 203 nm. The OH-photoproducts from the overtone induced photodissociation are formed in their electronically excited $A^2\Sigma$ state. in their N=2 rotational state at ~283 nm. Based on MP2/aug-cc-pVTZ calculation, the bands in the 5600 – 7000 cm^{-1} region correspond to the $2\nu_{CH}$ states and the band around 6200 cm^{-1} corresponds to the $1\nu_{OH} + 2\nu_{OOH}$ combination band. [File: F8.5_2nch]

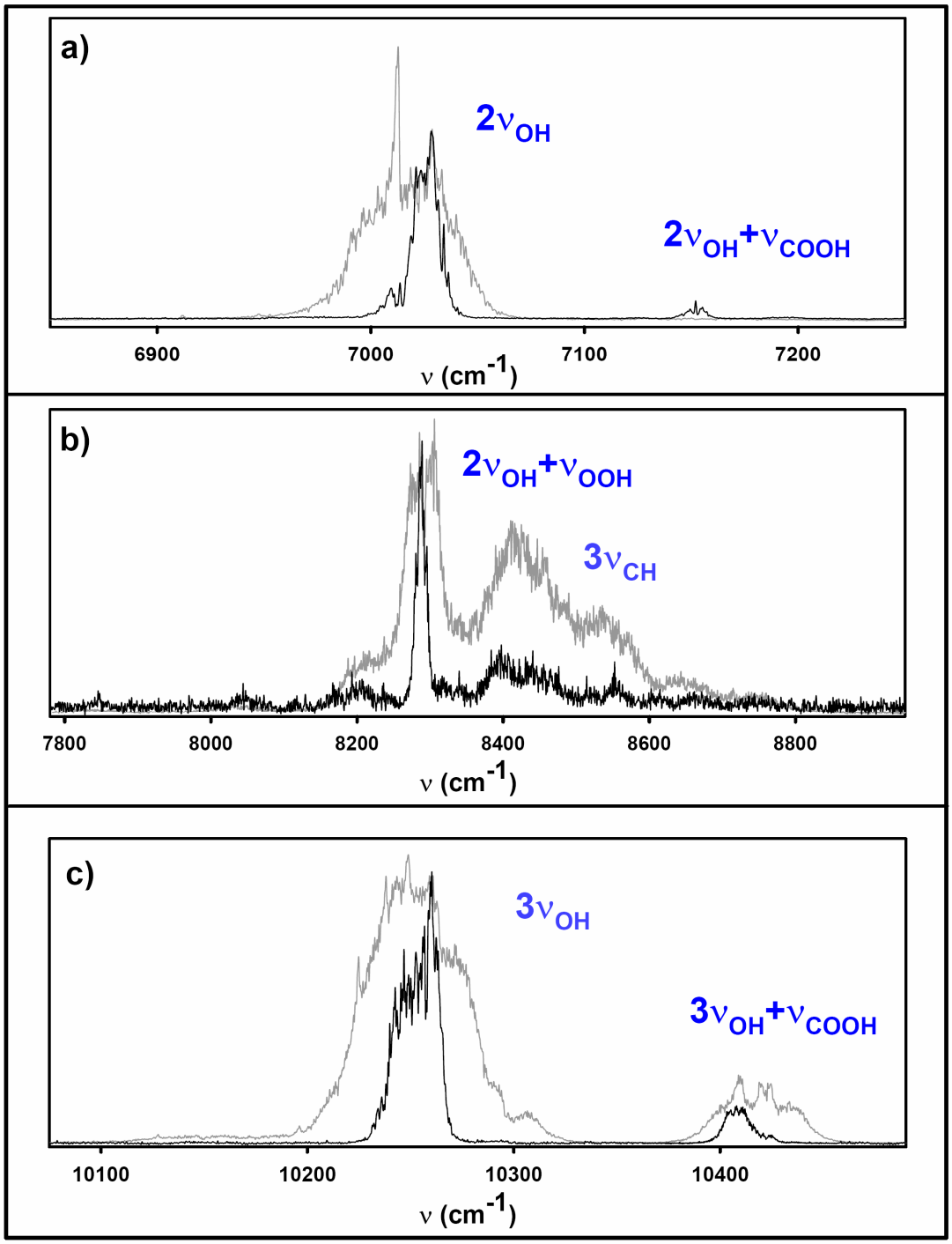

Figure 8.6: The "low resolution" jet spectra of MHP (in black) super imposed on top of the room temperature spectra (in gray) in the a) First OH stretching overtone ($2\nu_{OH}$) region. b) Second CH stretching overtone ($3\nu_{CH}$) region. c) Second OH stretching overtone ($3\nu_{OH}$) region. The OH fragment is probed in its N=5 rotational state. The rotational temperature of the jet spectra is estimated to be T ≈ 20 K.
[File: F8.6_jet_overview]

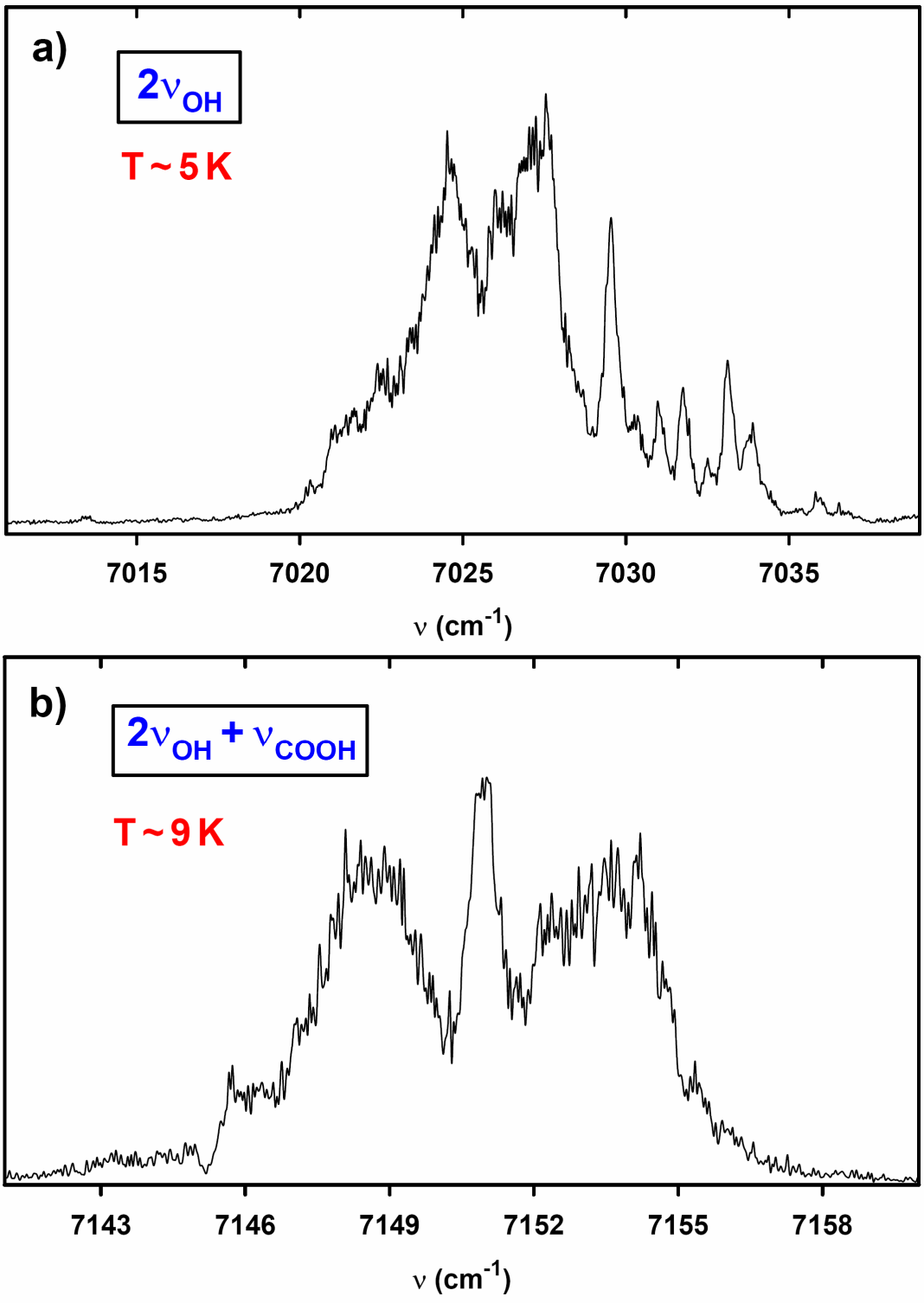

Figure 8.7: The "high resolution" jet spectra of MHP in the a) First OH stretching overtone ($2\nu_{OH}$) region taken at T ≈ 5 K. b) In the torsional combination band region ($2\nu_{OH} + \nu_{COOH}$) taken at T ≈ 9 K [File: F8.7_2nu_5k]

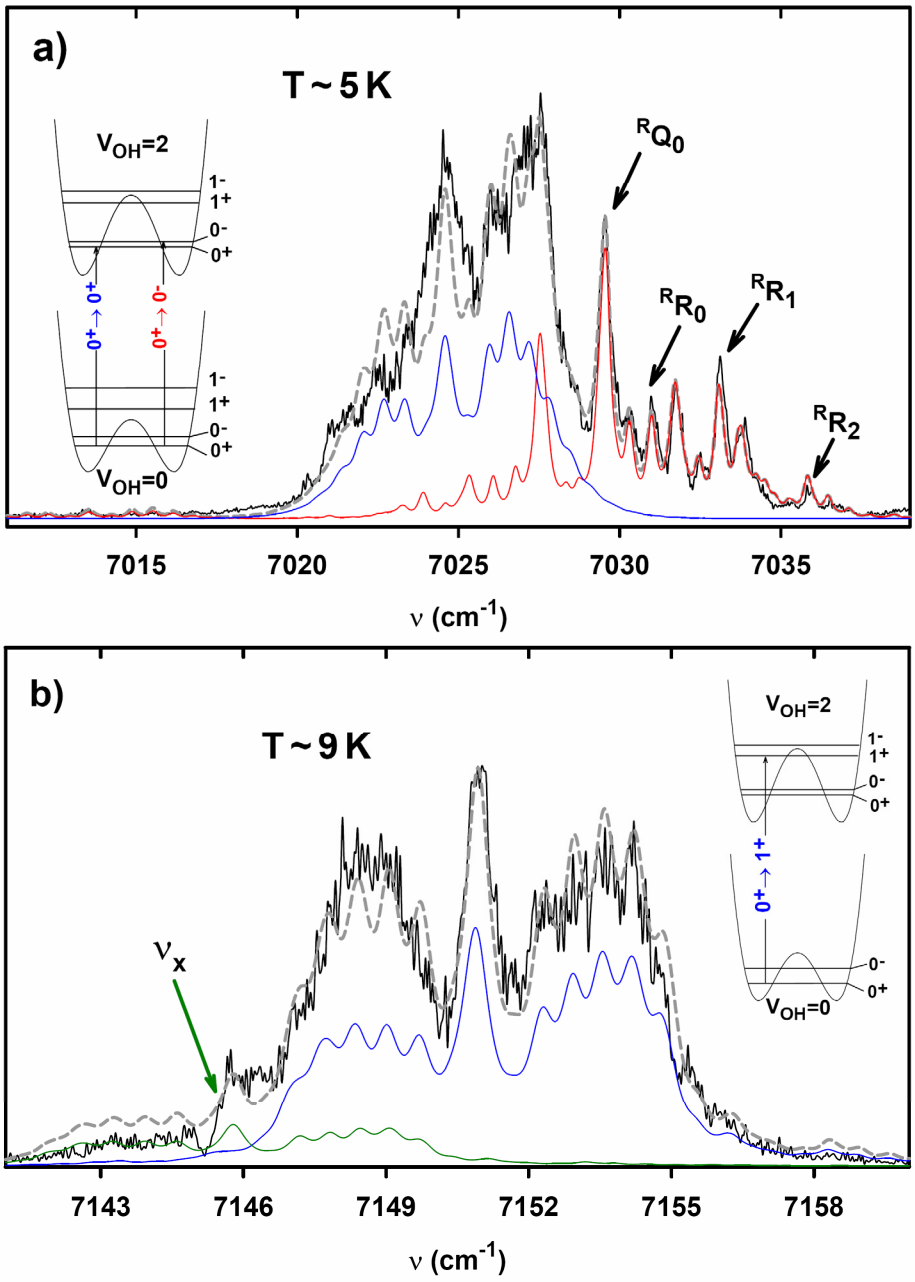

Figure 8.8: a) Rotational band contour simulations at 5 K superimposed on the $2\nu_{OH}$ action spectrum. The solid blue line corresponds to the simulation of the $|0\ 0^+\rangle \rightarrow |2\ 0^+\rangle$ transition and the solid red line corresponds to the simulation of the $|0\ 0^+\rangle \rightarrow |2\ 0^-\rangle$ transition. The weighted sum of these transitions is shown in dashed gray line. b) Rotational band contour simulations at 9K superimposed on the $2\nu_{OH} + \nu_{COOH}$ action spectrum. The solid blue line corresponds to the simulation of the $|0\ 0^+\rangle \rightarrow |2\ 1^+\rangle$ transition and the solid green line corresponds to the simulation of the $|0\ 0^+\rangle \rightarrow |\nu_x\rangle$ transition. The weighted sum of these transitions is shown in dashed gray line. [File: F8.8_2nu_fit_5k]

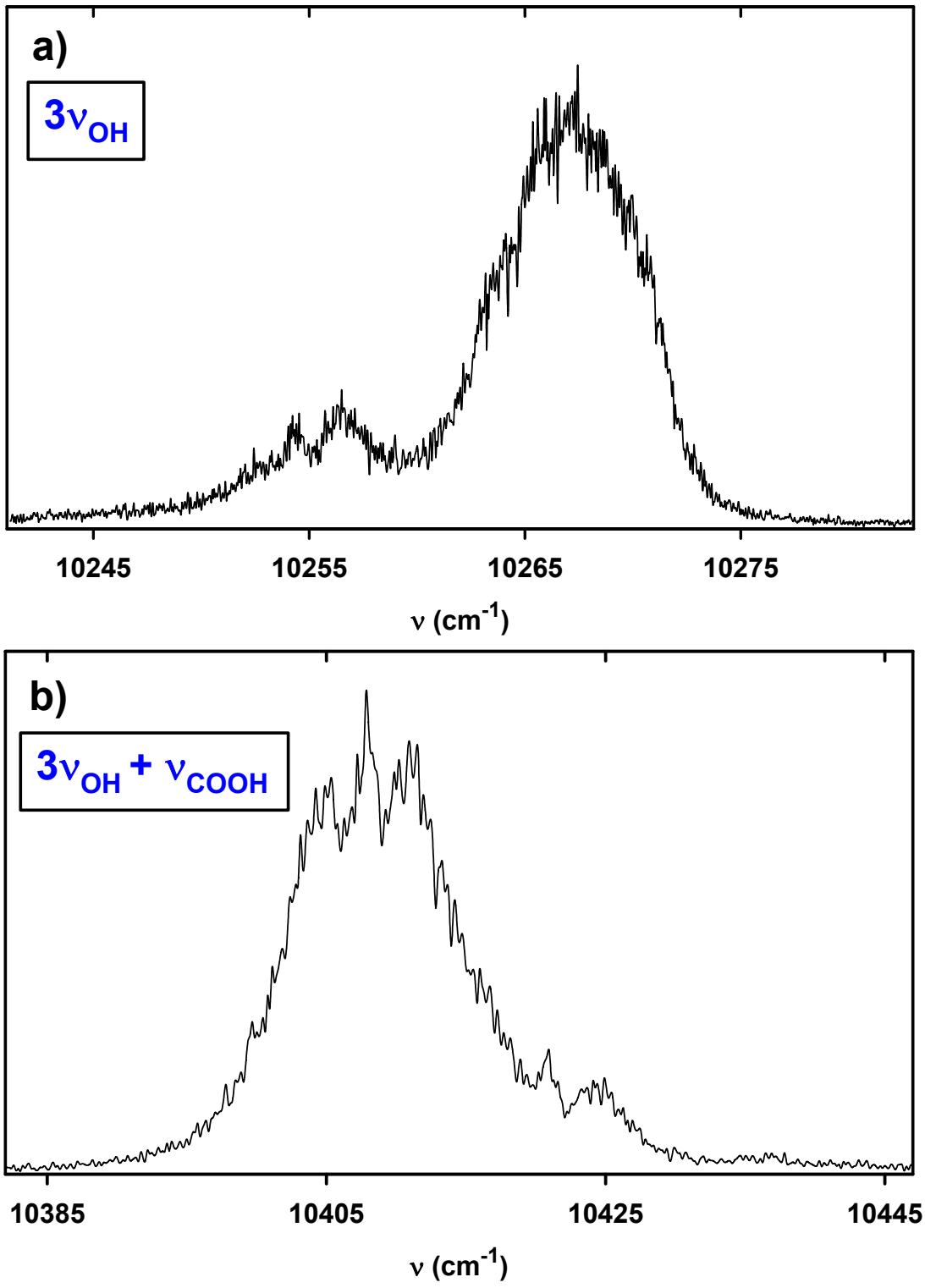

Figure 8.9: a) The jet spectrum of MHP in the second OH stretching overtone ($3\nu_{OH}$). b) The jet spectrum of MHP in the second OH stretch/HOOC torsion ($3\nu_{OH} + \nu_{COOH}$) region. [File: F8.9_3nu]

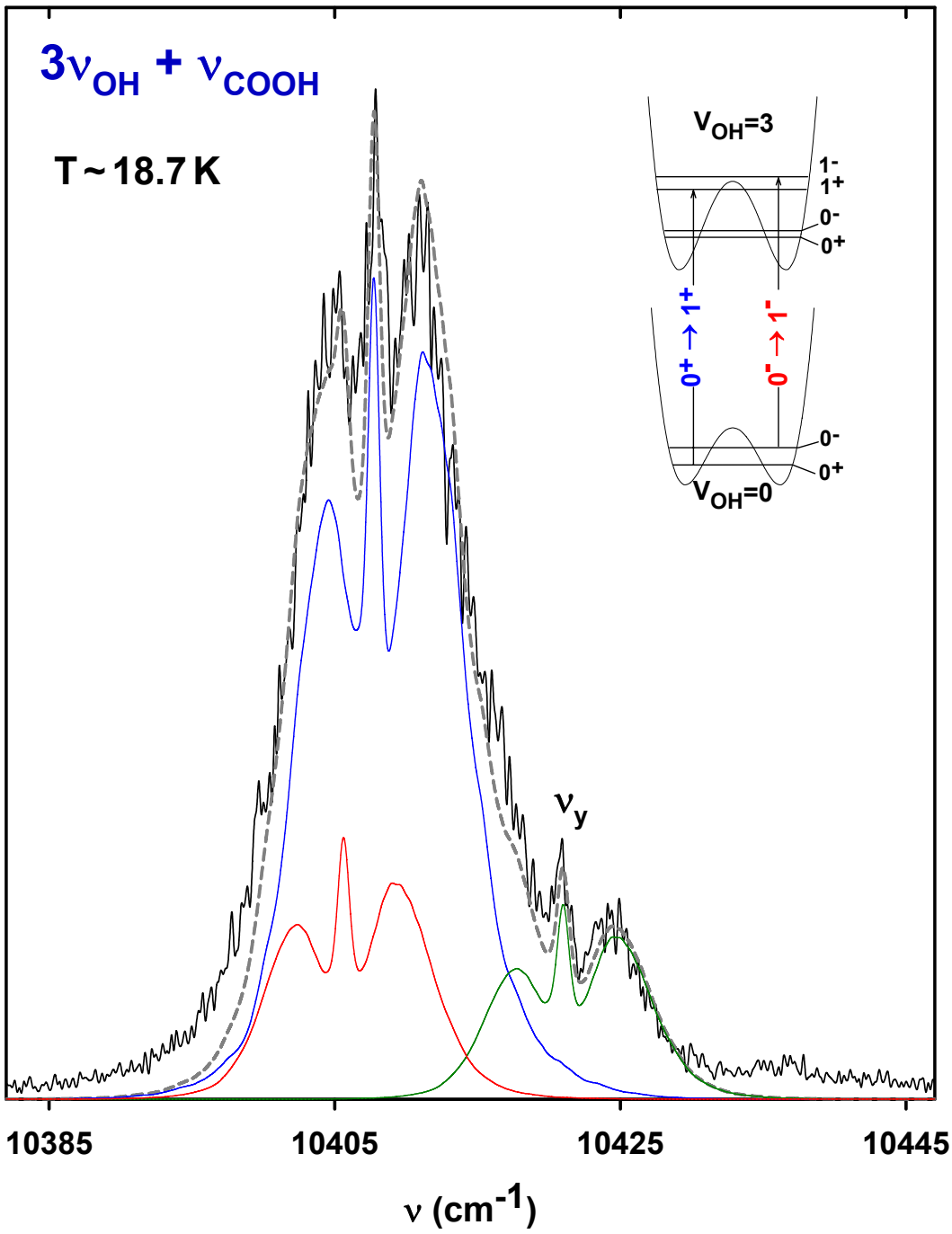

Figure 8.10: Rotational band contour simulations at T = 18.7 K superimposed on the $3\nu_{OH} + \nu_{COOH}$ action spectrum. The solid blue line corresponds to the simulation of the $|0\ 0^+\rangle \rightarrow |3\ 1^+\rangle$ transition and the solid red line corresponds to the simulation of the $|0\ 0^-\rangle \rightarrow |3\ 1^-\rangle$ transition. The simulation also includes contribution from the unidentified $|0\ 0^+\rangle \rightarrow |\nu_y\rangle$ transition. The weighted sum of these transitions is shown in dashed gray line. [File: F8.10_3nu_fit_19k]

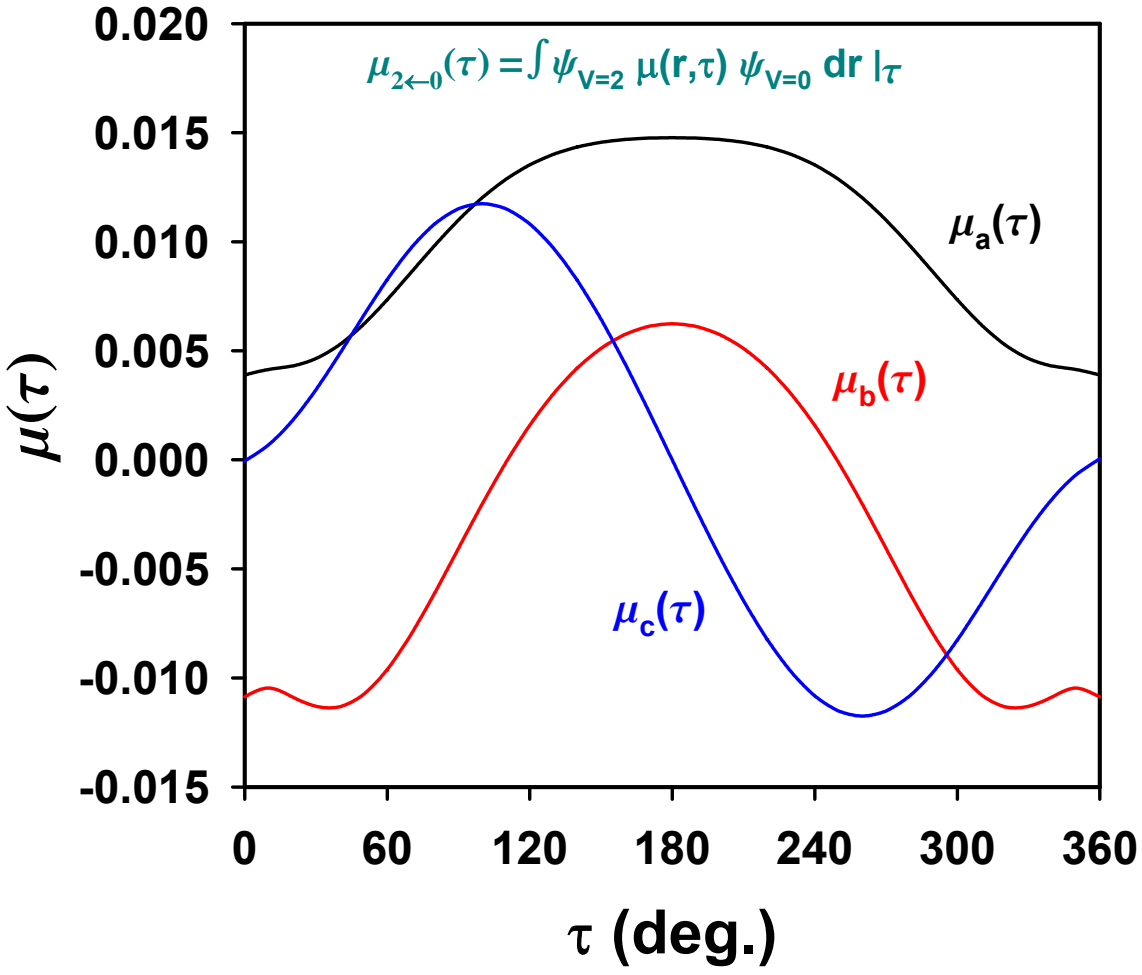

Figure 8.11: $\mu_\alpha(\tau)$ (= $\mu_a(\tau)$, $\mu_b(\tau)$, $\mu_c(\tau)$) transition dipole moment functions obtain by integrating $\mu(r,\tau)$ along the O-H stretching coordinate -r for the transitions between V_{OH} = 0 and the final state V_{OH} = 2. For all these transitions we observe that while both $\mu_a(\tau)$ and $\mu_b(\tau)$ components are symmetric about the *trans* barrier at $\tau = 180^o$, the $\mu_c(\tau)$ component is antisymmetric. [File: F8.11_dipole_ut]

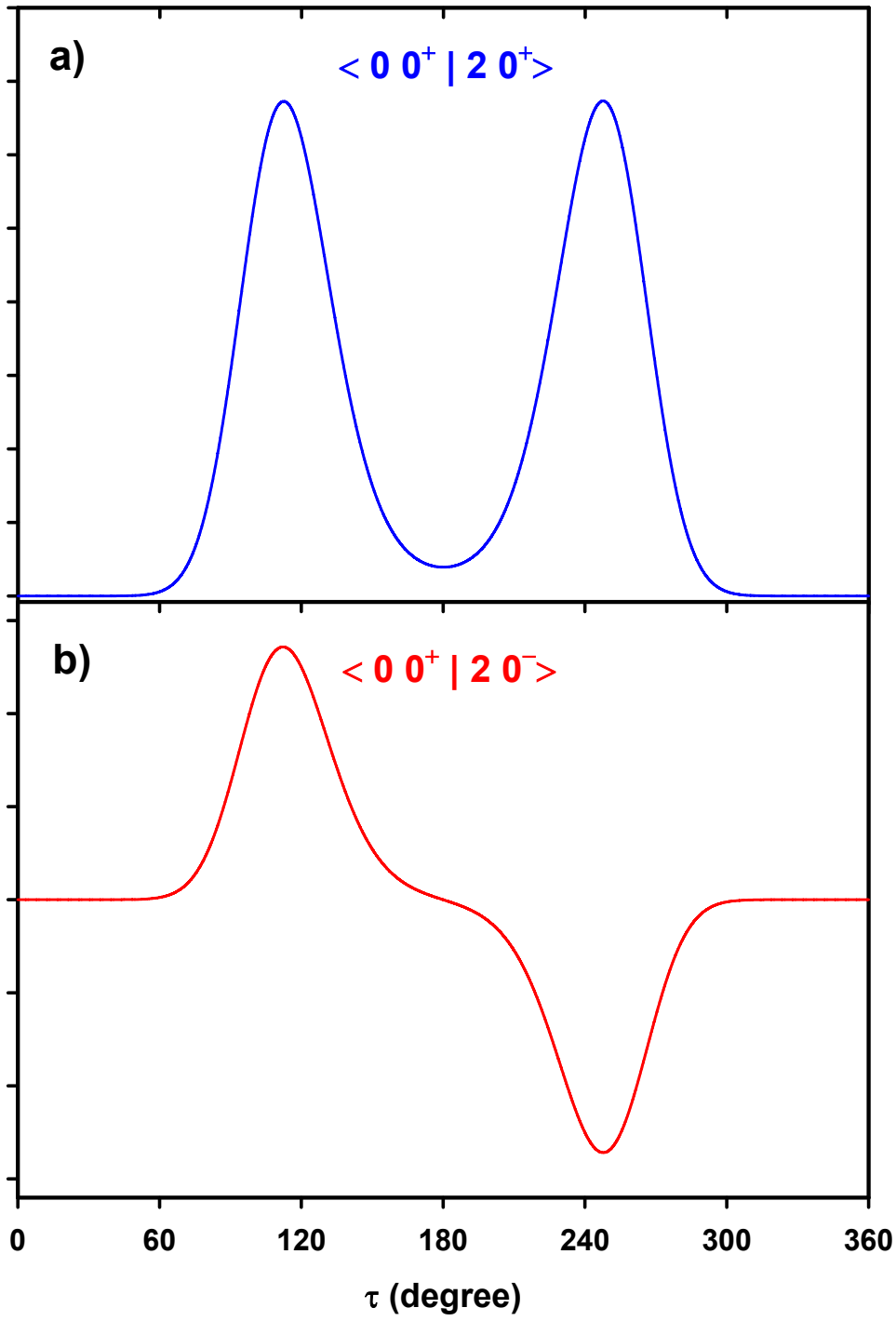

Figure 8.12: a) Product of $|0\ 0^+>$ and $|2\ 0^+>$ torsion wavefunctions showing their symmetric nature. b) Product of $|0\ 0^+>$ and $|2\ 0^->$ torsion wavefunctions showing their antisymmetric nature. [File: F8.12_wavefunctions]

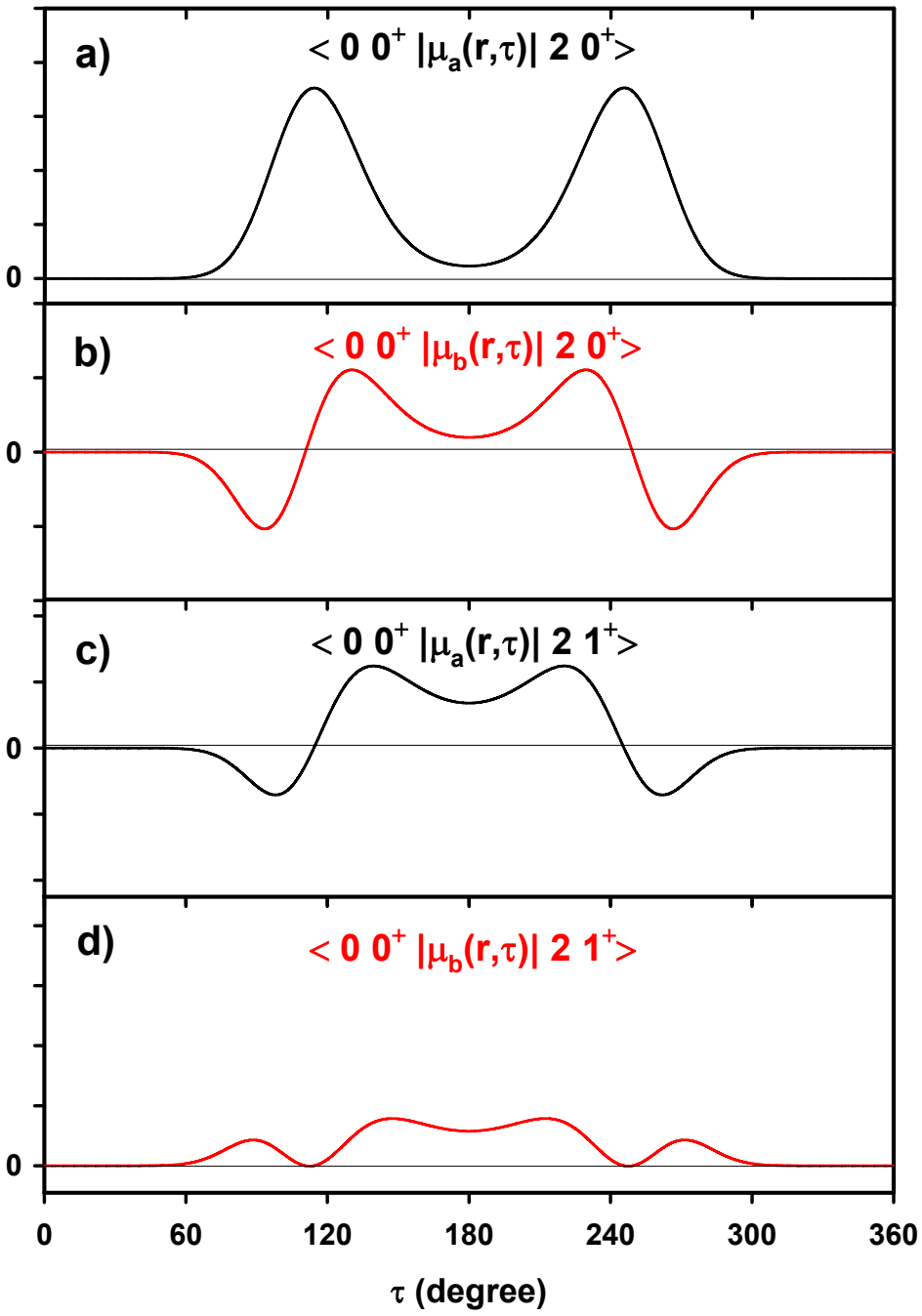

Figure 8.13: a) Transition dipole moment μ_a associated with the $|0\ 0^+> \rightarrow |2\ 0^+>$ transition. b) Transition dipole moment μ_b associated with the $|0\ 0^+> \rightarrow |2\ 0^+>$ transition. c) Transition dipole moment μ_a associated with the $|0\ 0^+> \rightarrow |2\ 1^+>$ transition. d) Transition dipole moment μ_b associated with the $|0\ 0^+> \rightarrow |2\ 1^+>$ transition.
[File: F8.13_transitions]

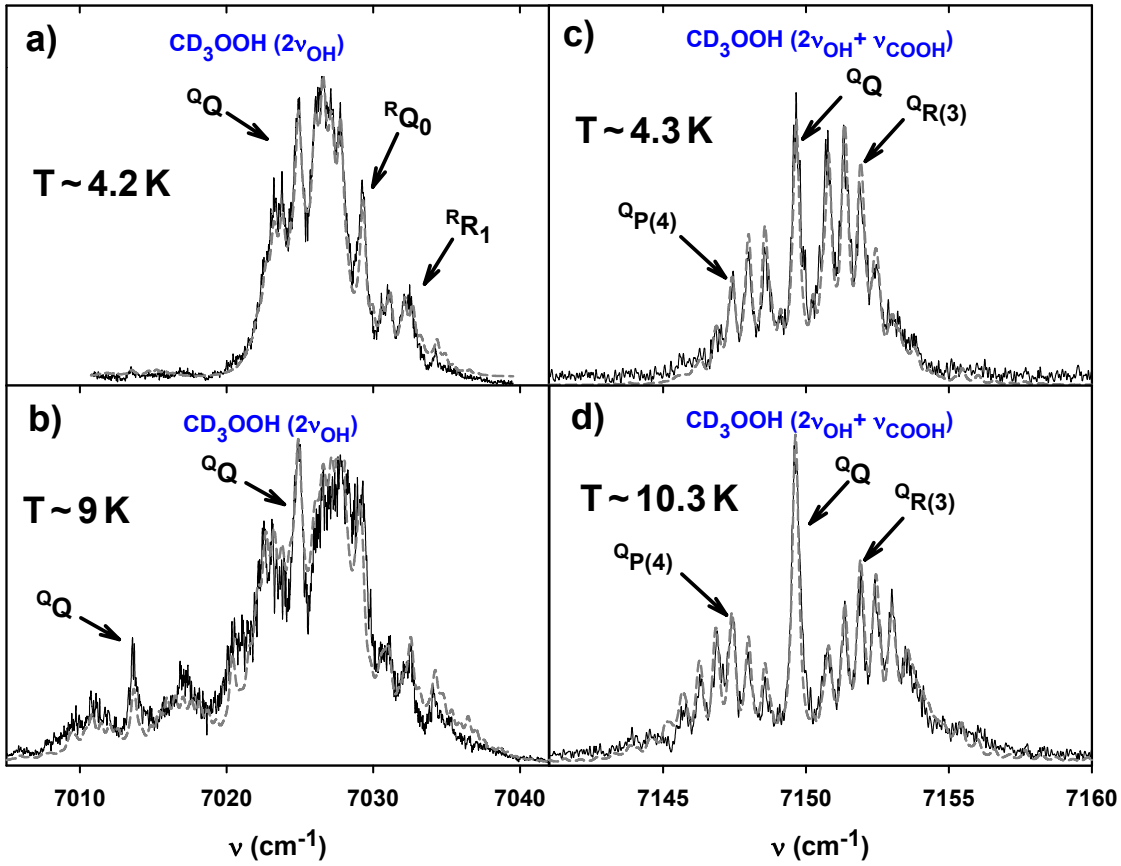

Figure 8.14: Action spectra of CD_3OOH (in black) and band contour simulations (in gray) for the a) $2\nu_{OH}$ band at T = 4.2 K. b) $2\nu_{OH}$ band at T = 9.0 K. c) $2\nu_{OH} + \nu_{COOH}$ band at T = 4.3 K. d) $2\nu_{OH} + \nu_{COOH}$ band at T = 10.3 K. [File: F8.14_cd3ooh_5k9k]

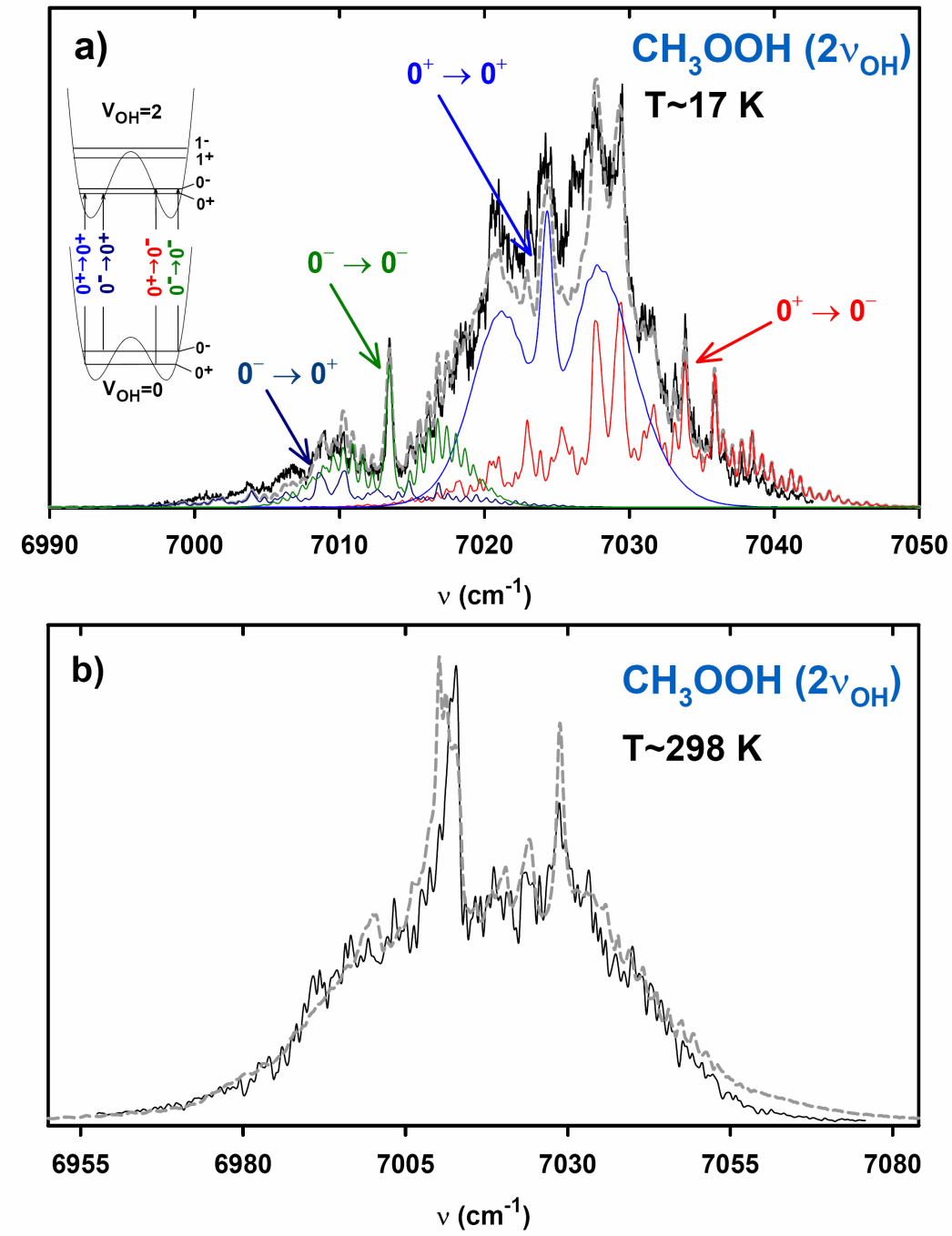

Figure 8.15: a) Action spectra of jet cooled CH_3OOH (in black) and rotational band contour simulation (in gray) at T = 17 K. The $2\nu_{OH}$ band is comprised of the four transitions: $|0\ 0^+> \rightarrow |2\ 0^+>$ transition (in blue), $|0\ 0^+> \rightarrow |2\ 0^->$ transition (in red), $|0\ 0^-> \rightarrow |2\ 0^->$ transition (in green), and $|0\ 0^-> \rightarrow |2\ 0^+>$ transition (in dark blue). b) Action spectra of room temperature CH_3OOH (in black) and rotational band contour simulation (in gray). The $2\nu_{OH}$ band is comprised of the four transitions in part (a) as well as the hot bands $|0\ 1^+> \rightarrow |2\ 1^+>$ and $|0\ 1^-> \rightarrow |2\ 1^->$. [File: F8.15_ch3ooh_2nu_17k298k]

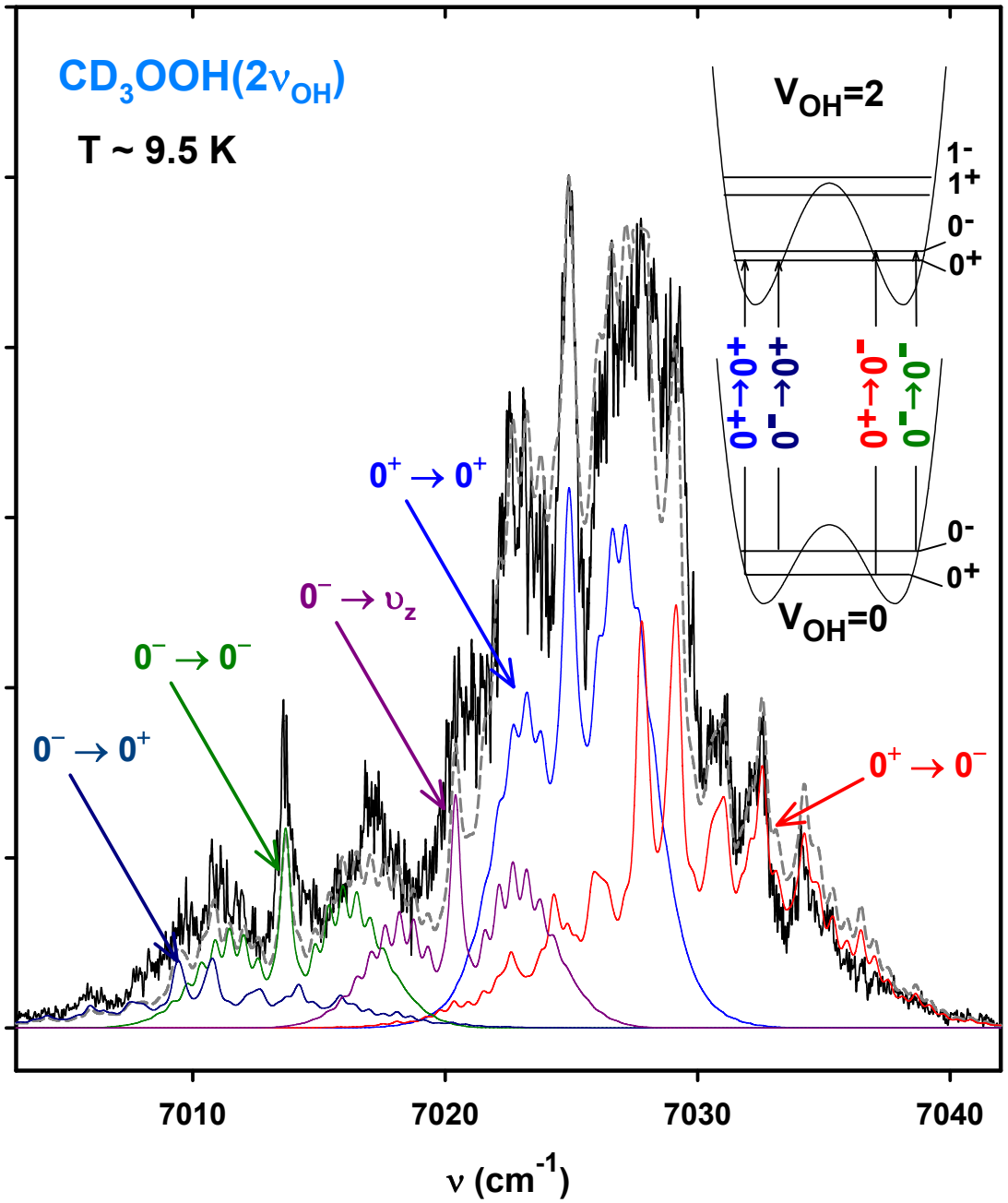

Figure 8.16: Action spectra of jet cooled CD_3OOH (in black) and rotational band contour simulation (in gray) at T = 10 K. The $2\nu_{OH}$ band is comprised of the four transitions: $|0\ 0^+> \rightarrow |2\ 0^+>$ transition (in blue), $|0\ 0^+> \rightarrow |2\ 0^->$ transition (in red), $|0\ 0^-> \rightarrow |2\ 0^->$ transition (in green), and $|0\ 0^-> \rightarrow |2\ 0^+>$ transition (in dark blue). An addition transition (in purple) labeled as $|0\ 0^-> \rightarrow |\upsilon_z>$ is also added to the simulation.
[File: F8.16_cd3ooh_10k]

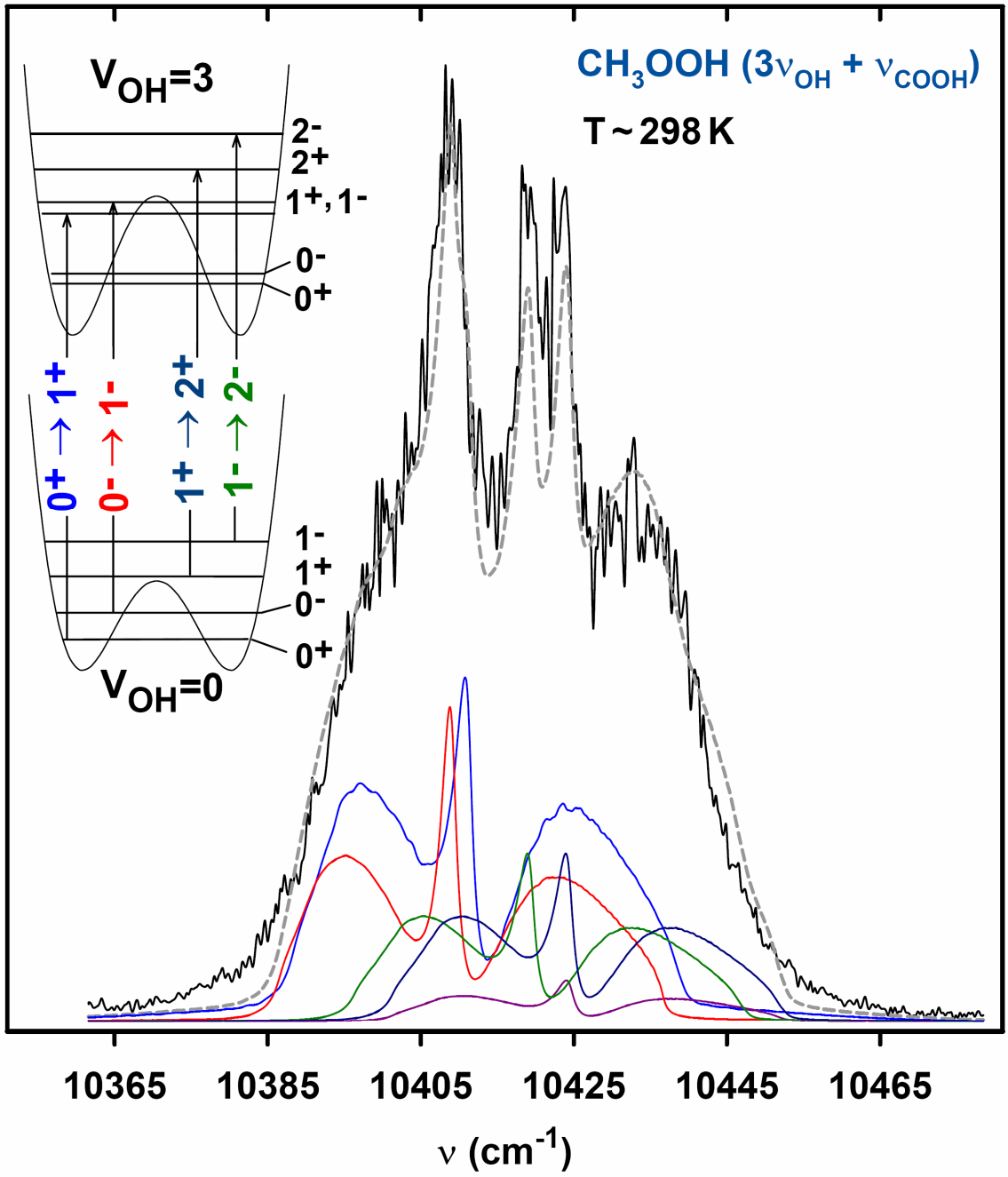

Figure 8.17: Action spectra of CH_3OOH (in black) and rotational band contour simulation (in gray) at room temperature of the $3\nu_{OH} + \nu_{COOH}$ band. The band is comprised of five transitions: $|0\ 0^+> \rightarrow |3\ 1^+>$ transition (in blue), $|0\ 0^-> \rightarrow |3\ 1^->$ transition (in red), $|0\ 1^+> \rightarrow |3\ 2^+>$ transition (in dark blue), and $|0\ 1^-> \rightarrow |3\ 2^->$ transition (in green). The simulation also includes contribution from the $|0\ 0^+> \rightarrow |\upsilon_y>$ state (in purple). [File: F8.17_ch3ooh_3nu_298k]

8.6 References

1. ACESII is a program product of the Quantum Theory Project, University of Florida. Authors: J. F. Stanton, J. Gauss, J. D. Watts, M. Nooijen, N. Oliphant, S. A. Perera, P. G. Szalay, W. J. Lauderdale, S. A. Kucharski, S. R. Gwaltney, S. Beck, A. Balková D. E. Bernholdt, K. K. Baeck, P. Rozyczko, H. Sekino, C. Hober, and R. J. Bartlett. Integral packages included are VMOL (J. Almlöf and P. R. Taylor); VPROPS (P. Taylor) ABACUS; (T. Helgaker, H. J. Aa. Jensen, P. Jørgensen, J. Olsen, and P. R. Taylor).

2. M. J. Frisch G. W. Trucks, H. B. Schlegel, G. E. Scuseria, M. A. Robb, J. R. Cheeseman, J. A. Montgomery, Jr., T. Vreven, K. N. Kudin, J. C. Burant, J. M. Millam, S. S. Iyengar, J. Tomasi, V. Barone, B. Mennucci, M. Cossi, G. Scalmani, N. Rega, G. A. Petersson, H. Nakatsuji, M. Hada, M. Ehara, K. Toyota, R. Fukuda, J. Hasegawa, M. Ishida, T. Nakajima, Y. Honda, O. Kitao, H. Nakai, M. Klene, X. Li, J. E. Knox, H. P. Hratchian, J. B. Cross, C. Adamo, J. Jaramillo, R. Gomperts, R. E. Stratmann, O. Yazyev, A. J. Austin, R. Cammi, C. Pomelli, J. W. Ochterski, P. Y. Ayala, K. Morokuma, G. A. Voth, P. Salvador, J. J. Dannenberg, V. G. Zakrzewski, S. Dapprich, A. D. Daniels, M. C. Strain, O. Farkas, D. K. Malick, A. D. Rabuck, K. Raghavachari, J. B. Foresman, J. V. Ortiz, Q. Cui, A. G. Baboul, S. Clifford, J. Cioslowski, B. B. Stefanov, G. Liu, A. Liashenko, P. Piskorz, I. Komaromi, R. L. Martin, D. J. Fox, T. Keith, M. A. Al-Laham, C. Y. Peng, A. Nanayakkara, M. Challacombe, P. M. W. Gill, B. Johnson, W. Chen, M. W. Wong, C. Gonzalez, and J. A. Pople, Gaussian 03, Revision B.04, (Gaussian, Inc., Pittsburgh PA, 2003).

3. T. H. Dunning Jr., J. Chem. Phys. 90, 1007 (1989); K. A. Peterson, D. E. Woon, T. H. Dunning Jr., J. Chem. Phys. **100**, 7410 (1994).

4. M. Tyblewski, T. –K. Ha, R. Meyer, and A. Bauder, J. Chem. Phys. **97**, 6168 (1992).

5. H. –R. Dübal, and F. F. Crim, J. Chem. Phys. **83**, 3863 (1985).

6. M. D. Likar, J. E. Baggott, and F. F. Crim, J. Chem. Phys. **90**, 6266 (1989).

7. M. A. Temsamani, L. –H. Xu, and D. S. Perry, Can. J. Phys. **79**, 467 (2001).

8. D. Rueda, O. V. Boyarkin, T. R. Rizzo, I. Mukhopadhyay, and D. S. Perry, J. Chem. Phys. **116**, 91 (2002).

9. S. C. Homitsky, S. M. Dragulin, L. M. Haynes, and S. Hsieh, J. Phys. Chem. A. **108**, 9492 (2004).

10. G. Herzberg, *Molecular Spectra and Molecular Structure. I. Spectra of Diatomic Molecules 2nd Edition* (Van Nostrand Reinhold, New York 1950).

11. B. –Z. Zhu, H. –T. Zhao, B. Kalyanaraman, J. Liu, G. –Q. Shan, Y. –G. Du., and B. Frei, PNAS, **104**, 3698 (2007).

12. L. S. Rothman *et al*., *J. Quant. Spectrosc. Radiat. Transfer* **82,** 5 (2003).

13. L. M. Haynes, K. M. Vogelhuber, J. L. Pippin, and S. Hsieh, J. Chem. Phys. **123**, 234306 (2005).

14. X. Luo, and T. R. Rizzo, J. Chem. Phys. **94**, 889 (1991).

15. C. M. Roehl, S. A. Nizkorodov, H. Zhang, G. A. Blake, P. O. Wennberg, J. Phys. Chem. A **106**, 3766 (2002).

16. D. Rueda, O. V. Boyarkin, T. R. Rizzo, A. Chirokolava, and D. S. Perry, J. Chem. Phys. **122**, 044314 (2005).

17. X. Wang, and D. S. Perry, J. Chem. Phys. **109**, 10795 (1998).

18. T. N. Clasp, and D. S. Perry, J. Chem. Phys. **125**, 104313 (2006).

19. O. V. Boyarkin, L. Lubich, R. D. F. Settle, D. S. Perry, and T. R. Rizzo, J. Chem. Phys. **107**, 8409 (1997).

20. O. V. Boyarkin, T. R. Rizzo, and D. S. Perry, J. Chem. Phys. **110**, 11346 (1999); J. Chem. Phys. **110**, 11359 (1999).

21. A. Chirokolava, D. S. Perry, O. V. Boyarkin, M. Schmid, and T. R. Rizzo, J. Chem. Phys. **113**, 10068 (2000).

22. C. M. Western, PGOPHER version 5.2.343 a program for simulating rotational structure, University of Bristol, http://pgopher.chm.bris.ac.uk

23. P. W. Atkins, *Molecular Quantum Mechanics, 2nd ed*. (Oxford University Press, Oxford 1983).

24. H. G. Kjaergaard, B. R. Henry, J. Chem. Phys. **96**, 4841 (1992).

25. D. J. Nesbitt, and R. W. Field, J. Phys. Chem. **100**, 12735 (1996).

26. F. F. Crim, J. Phys. Chem. **100**, 12725 (1996).

27. G. Dutton, R. J. Barnes, and A. Sinha, J. Chem. Phys. **111**, 4976 (1999).

28. M. Gruebele, and R. Bigwood, Int. Rev. Phys. Chem. **17**, 91 (1998).

29. F. Weinhold, and C. R. Landis, *Valency and Bonding: A Natural Bond Orbital Donor-Acceptor Perspective* (Cambridge University Press, Cambridge 2003).

30. J. E. Carpenter and F. Weinhold, J. Phys. Chem. **92**, 4295 (1988); Phys. Chem. **92**, 4306 (1988).

31. H. Hernández-Soto, F. Weinhold, and J. S. Francisco, J. Chem. Phys. **127**, 164102 (2007).

32. I. M. Konen, E. X. J. Li, M. I. Lester, J. Vázquez, and J. F. Stanton, J. Chem. Phys. **125**, 074310 (2006).

33. D. L. Howard and H. G. Kjaergaard, J. Chem. Phys. **121**, 136 (2004).

34. H. Gai, D. L. Thompson, G. A. Fisk, J. Chem. Phys. **90**, 7055 (1989).

Chapter 9

Intramolecular Vibrational Energy Redistribution Controlled Photodissociation Dynamics of Hydrogen Peroxide and Methyl Hydroperoxide

9.1 Introduction

Hydrogen peroxide (H_2O_2) and methyl hydroperoxide (CH_3OOH; MHP) are respectively, the two smallest inorganic and organic hydroperoxides. Aside from their important contribution to the atmospheric HOx (= OH + HO_2) radical production,[1-3] hydroperoxides can potentially provide a wealth of information on the dissociation dynamics,[4,5] as well as insight on the flow of vibrational energy within a molecule.[6] Several state-selected experiments involving hydroperoxides have shown that the outcome of a photodissociation event is not solely controlled by the prepared final electronic state which typically depends on the total photon energy, but is also influenced by the selected intermediate state and the coupling of this state to other vibrational modes in the molecule.[7-9] For example, by indirect excitation of the dissociation coordinate (O-O), Crim and coworkers have shown that the OH fragment resulting from one-color two-photon dissociation from vibrational excitation of the fourth ($4\nu_{OH}$) OH-stretching state in H_2O_2 is formed with a different distribution of quantum states compared with single photon photodissociation having equivalent photon energy.[10]

The extent of the coupling between the bright vibrational overtone excited and the dissociating coordinate affects the flow of energy out of the bright state in a process which is generally controlled by intramolecular vibrational energy redistribution (IVR).[6]

In essence, IVR leads to energy redistribution from the zero-order molecular bright state to the other states of the molecule. Therefore, several experiments and theoretical studies have focused on the dissociation mechanisms and dissociation rates arising from IVR.[11-23] Both HOOH and CH_3OOH molecules have been the subject of several IVR studies as well.[8,21-23] In addition, in the previous dissertation chapter IVR has been held accountable for the observed line broadening and vibrational band structure. Simplified schematics of how the intramolecular vibrational energy redistribution occurs in a small and a large molecule are shown in Figs. 9.1(a) and 9.1(b) respectively. In the tier model of Fig. 9.1(a), the bright state, |**s**>, is initially prepared by absorbing a photon from the ground state, |**g**>. Other states within this energy range typically carry no oscillator strength and therefore can not absorb a photon from the ground state. Subsequently, the energy deposited in the |**s**> state is transferred to other states at IVR controlled rate. The coupling between the initially prepared bright state, |**s**>, with the dark states, |$\boldsymbol{\ell}$>, results in the formation of the eigenstates, |**n**>. In essence, the more interacting dark states the molecule have, the greater the fractionation of the bright state, |**s**> and the less bright state character would be available for each of the eigenstates |**n**>. The extent of fractionation depends on the strength of the coupling between the bright and dark states as well as the number of interacting states. Since the interaction between the bright state and the manifold of the interacting substates, |$\boldsymbol{\ell}$>, typically occurs on a timescale which is faster than the rate of dissociation,[6,9,15,19] a typical action spectrum such as a $2\nu_{OH}$ band is simply a molecular eigenstate |**n**> that is formed between the bright OH character (|**s**>) and other molecular dark states (|$\boldsymbol{\ell}$>).

In general, as shown in Fig. 9.1(a), for a small molecule where the array of vibrational states is restricted, the energy flows from the initially prepared zero-order state to the rest of the molecule via coupling through a smaller subset of states.[6,9,15,19] In contrast, for a large molecule, one expects to find a greater density of states for a given spectral region, which in turns also comes to reason that this enhanced state-density results in greater fractionation of the bright state. Fig. 9.1(b) represents how IVR affects the flow of the energy in a large molecule where significantly more dark substates, $|\boldsymbol{\ell}\rangle$, are available to interact with $|\mathbf{s}\rangle$ and lead to said enhanced fractionation and state mixing.[15]

This dissertation chapter compares the intramolecular vibrational redistribution of energy arising from excitation in the vicinity of the first ($2\nu_{OH}$) and second ($3\nu_{OH}$) OH-stretching overtones as well as in the HOO-bending ($2\nu_{OH} + \nu_{HOO}$) combination mode region in hydrogen peroxide and methyl hydroperoxides. By investigating the resulting OH fragment vibrational product state distribution we find that upon excitation of the bending modes (and CH-stretching), there is a significantly less vibrational excitation in the OH product for both H_2O_2 and CH_3OOH. These results are supported by the fact that the coupling of stretch-bend combination band (and CH-stretching modes) to the tier of states is enhanced significantly compared to the coupling of the "pure" OH-stretching mode.[19,21-23] In essence, by investigating these modes, we demonstrate that the relatively isolated OH-stretching states in hydroperoxides results in a restricted IVR controlled photodissociation while the other vibrational modes such as C-H stretching and bending modes lead to photodissociation which is resulting from a more complete IVR. This apparent mode selective behavior has also been observed in $HOCH_2OOH$ discussed in

Chapter 11, where restricted IVR associated with the peroxide OH gives rise to different dissociation rates compared with the alcohol OH of which enhanced IVR results in greater state mixing.

We also compare within each molecule (HOOH and CH_3OOH) how the densities of states affect the intramolecular vibrational redistribution of energy by comparing the vibrationally excited OH product resulting from excitation of the first ($2\nu_{OH}$) and second ($3\nu_{OH}$) OH-stretching overtones. Despite the ~20 fold increase in the density of states at the $3\nu_{OH}$ region, we find comparable vibrationally excited OH product as with the $2\nu_{OH}$ region. This again is supporting the fact that the peroxide OH is relatively isolated and that the local density of coupled states in these two energy regions is likely similar. We also draw conclusions about how the molecular size affects IVR rates. We find that when comparing similar vibrational states, even though the two molecules differ significantly in their size and atomic composition, their densities of states, the local environment of the OH-stretching mode, and the coupling of these bright states are similar in both molecules thus leading to similar product state distribution.

9.2 Experiment

The synthesis of MHP follows the procedure described in Chapter 6 and is similar to the synthesis procedure of Vaghijiani and Ravishankara.[25] The vibrationally mediated photodissociation (ViMP) experiments $n\nu_x$ + 532 nm, and $n\nu_x$ + 532 nm, where the molecule is initially excited in the vicinities of the first ($2\nu_{OH}$) OH-stretching overtone, its bending combination mode ($2\nu_{OH} + \nu_{OOH}$), second ($3\nu_{OH}$) stretching overtones, and second ($3\nu_{CH}$) stretching overtones regions have also been described in Chapter 7 and

Chapter 8.[4,9,10] The experiment on both HOOH and CH_3OOH are conducted with 60 – 80 mTorr of the samples that are introduced to a glass photolysis cell along with 1400 mTorr N_2 buffer gas to ensure relaxation of the OH rotational states without inducing vibrational relaxation of the parent molecule or the vibrational excitation in the OH photofragment.

The tunable IR radiation (λ_1) is produced by a MOPO laser system which has pulse energies of ranging from 4 – 6 mJ in the $2\nu_{OH}$ region, 6 – 9 mJ in the $3\nu_{CH}$ region and 8 – 12 in the $3\nu_{OH}$ region. The vibrationally excited molecule is subsequently undergoes photodissociation by promoting it to the electronic repulsive excited state using counter propagating beam of 532 or 355 nm generated respectively by the second and third harmonics of the NY82-20 laser (λ_2). The temporal delay between the two lasers is kept fixed at ~15 ns to minimize the vibrational relaxation of the parent molecule. Typical pulse energies for the 532 and 355 nm light are set to 50 and 15 mJ respectively.

The OH fragment ground and vibrational levels are probed via the $A^2\Sigma$–$X^2\Pi(0,0)$, $A^2\Sigma$–$X^2\Pi(1,1)$, $A^2\Sigma$–$X^2\Pi(2,2)$ diagonal transitions using the NY82-10 laser system (λ_3). The rotational assignment of the OH spectrum is based on the work of Dickie and Crosswhite.[25] The probe laser is greatly attenuated to prevent saturation of the OH lines and photolysis of the parent molecules. The probe beam is counter propagating to the IR beam (λ_1), co-propagating to the VIS/UV laser (λ_2) and its temporal delay is set to ~1400 ns in order to allow probing of the vibrationally excited – rotationally thermalized OH fragment in the N=2 rotational states. The resulting laser-induced fluorescence (LIF) is collected using an *f*/1 lens system and imaged onto an end-on photomultiplier. A color

glass filter (Schott UG-11) and a set of 355 nm edge filters enable rejection of the visible and UV laser light while transmitting the OH fluorescence. The vibrational branching ratio are obtained by performing back-to-back measurements comparing the ratio of the integrated signals of OH(v=1) to OH(v=0) and OH(v=2) to OH(v=0) and converting them to relative population using the appropriate Einstein B-coefficients and Franck-Condon factors as described in Appendix *C*.[26]

9.3 Results and Discussion

The overview action spectrum of H_2O_2 is shown in Fig. 9.2(a). The spectrum is obtained by tuning the vibrational excitation laser, λ_1, at 0.015 nm/s averaging 30 shots/bin over the frequencies shown and subsequently promoting the vibrationally excited molecule to an electronic excited state using 532 nm light (λ_2). The resulting OH product undergoes collisions with nitrogen buffer gas prior to its detection via the diagonal A–X(0,0) $Q_1(2)$ transition using ~308 nm light (λ_3). Rotational structure measurements of the $2\nu_{OH}$ band around ~7050 cm^{-1} assign the hybrid band to the $\nu_1 + \nu_5$ which involves excitation in the symmetric (ν_1) and antisymmetric (ν_2) OH-stretching modes respectively.[27,28] With a much weaker intensity, the small bump around ~7350 cm^{-1} is assigned to the OH-stretch/torsion combination mode ($\nu_1 + \nu_5$) + ν_4 similarly to the fourth ($5\nu_{OH}$) and fifth ($6\nu_{OH}$) OH-stretching overtones regions.[29] The band around ~8280 cm^{-1} corresponds to antisymmetric bending ($\nu_1 + \nu_5$) + ν_6 while the band further to the blue around ~8400 cm^{-1} corresponds to the symmetric bend ($\nu_1 + \nu_5$) + ν_2. The $3\nu_{OH}$ band (~10 290 cm^{-1}) which involves excitation of the $2\nu_1 + \nu_5$ or $3\nu_5$ states, has similar band shape as the $2\nu_{OH}$ but an order of magnitude lower in intensity.[27,28] For reference,

illustrations depicting the normal modes of HOOH mentioned above are shown in Fig. 9.3. Based on frequency calculation at the MP2/cc-pVQZ level of theory using GAUSSIAN03 series of programs,[30] both the symmetric and antisymmetric OH-stretching modes have similar frequencies ($\omega_1 = \omega_5 \approx 3817$ cm^{-1}) but the symmetric and antisymmetric bending modes, have different frequencies. Table 9.1 lists the harmonic frequencies and anharomonicities of the HOOH molecule at the MP2/cc-pVQZ level of theory.

Also shown in Fig. 9.2(b) for reference is the overview spectrum of CH_3OOH. As with hydrogen peroxide, methyl hydroperoxide has similar observed overtone transitions where the band around ~7025 cm^{-1} corresponds to the first ($2\nu_1$) OH-stretching overtone and the band around ~7150 cm^{-1} corresponds to the OH-stretch/torsion combination band ($2\nu_1 + \nu_{15}$). Similarly, the second ($3\nu_1$) OH-stretching overtone and its torsion combination band ($3\nu_1 + \nu_{15}$) appearing in the action spectrum around 10 260 cm^{-1} and 10 420 cm^{-1} respectively. The sharp vibrational band feature in the mid range region around ~8287 cm^{-1} is assigned to the combination band involving stretch-bend combination mode ($2\nu_1 + \nu_8$). The other broad features in the mid range region correspond to the three C-H stretching modes associated with the methyl rotor. The assignment of the spectrum in Fig. 9.2(b) is based on high level *ab initio* model at the CCSD(T)/cc-pVTZ level from Chapter 7, molecular beam experiments as well anharmonic frequencies calculations at the MP2/aug-cc-pVTZ (see Table 8.2 in Chapter 8). The overview action spectra of HOOH and MHP which are normalized to laser

powers indicate that the second overtones ($3\nu_{OH}$) are ~10 weaker for HOOH and 20 times weaker for CH_3OOH than their first OH-stretching overtone.

To asses the distribution of the resulting vibrationally excited OH product we initially reproduce the overview action spectra of H_2O_2 and CH_3OOH monitoring the $OH(^2\Pi_{3/2})$ in the N=2 rotational states associated with the v = 0, 1, 2 vibrational levels via the $A^2\Sigma^+ - X^2\Pi$ electronic transition. In Figs. 9.4(a) – 9.4(c) each panel correspond to the spectra of H_2O_2 monitoring the $OH(^2\Pi_{3/2})$ in its vibrational state v = 0, 1 and 2. Looking at panels 9.4(a) and 9.4(b) we find that the overtones spectra for the $2\nu_1$ and $3\nu_1$ bands are similar. Both bands have similar band shape when detecting OH(v=0) vs. OH(v=1) product. Also, the relative bands intensity of the first ($2\nu_1$) and second ($3\nu_1$) OH-stretching overtones in these OH(v=0) and OH(v=1) detected action spectra are similar. By contrast, both symmetric and antisymmetric bending modes result in significantly weaker intensity when monitoring OH(v=1).

Since HOOH has a rotationally resolved structure at room temperature, we reduce the scan rate to 0.002 nm/s and average 30 shots/bin in order to capture the rotational band structure. Figures 9.5(a) – 9.5(c) show the band structure in the first ($\nu_1 + \nu_5$) OH-stretching band, bend-stretch ($\nu_1 + \nu_5$) + ν_2/ν_6 combination band, and second ($2\nu_1 + \nu_5$ or $3\nu_5$) OH-stretching overtone band respectively. These spectra are generated by the ViMP process where the vibrationally excited state is dissociated via excitation at 220 nm ($n\nu_x$ + 220 nm) where, as discussed with methyl hydroperoxide in Chapter 8, the OH fragment is formed directly in the $A^2\Sigma$ fluorescing state.[31,32] The three panels show the manifold of P- and R- rotational states of each band. The high rotational spectral congestion is mainly

due to the fact that the double-well torsion potential gives rise to symmetric (*S*) and antisymmetric (*A*) transitions in each vibrational band, thus doubling the number of ro-vibrational transitions as discussed with MHP in Chapters 7 and 8.[27-30] In the $2\nu_{OH}$ state the splitting is on the order of 5.2 cm^{-1} and in the $3\nu_{OH}$ state the $S \rightarrow S$ and $A \rightarrow A$ splitting is 7.5 cm^{-1}.[27]

Similar to HOOH, Figs. 9.6(a) and 9.6(b) show the trends in the overtones spectra of CH_3OOH. As with the spectra of hydrogen peroxide, photodissociation of methyl hydroperoxide results in vibrationally excited OH product upon excitation of the OH stretching overtone ($2\nu_1$ and $3\nu_1$) shown in Fig. 9.6(b). By contrast, excitation of the stretch-bend combination band ($2\nu_1 + \nu_8$) or the various second ($3\nu_{CH}$) overtones CH-stretching modes result in vibrationally excited OH(v=1) product that is below our detection limits. To confirm that indeed we excite the reported ro-vibrational OH states, we also generate OH rotational spectra in the v = 0, 1, and 2 regions from methyl hydroperoxide and hydrogen peroxide. The ro-vibrational OH spectra shown in Figs. 9.7(a) – 9.7(c) for the v = 0, 1, and 2 respectively are taken at 0.012 /s averaging 30 shots/bin and compared against known OH ro-vibrational lines, thus confirming our assignment.[25]

It is important to note that in the case of H_2O_2 as with MHP, the vibrationally mediated photodissociation process provides the molecule with sufficient energy to dissociate it and produce vibrationally excited OH product over the entire excitation region. For example, at excitation energy corresponding to $2\nu_1$ + 532 nm the total photon energy corresponds to ~74 kcal/mol while the O-O bond dissociation energies are $D_0[H_2O_2]$ = 49 kcal/mol,[8] and $D_0[CH_3OOH]$ = 42.6 kcal/mol. This means that at this

photon excitation energy, there is an excess of ~25 kcal/mol over the HO-OH bond breakage and ~31 kcal/mol over the CH_3O-OH bond breakage. To form vibrationally excited OH fragment in the v = 0, 1, and 2 the minimum required energy above the D_0 value is ~0, 10, and 20 kcal/mol respectively.[25] Panels 9.4(c) and 9.6(c) show scans monitoring OH(v=2, N=2) for HOOH and CH_3OOH respectively. In this OH ro-vib state, we find that at our detection sensitivity limit, only the first ($\nu_1 + \nu_5$) OH-stretching overtone of HOOH gives signal; other states of HOOH and MHP do not produce vibrationally excited OH(v=2) product.

To quantify the resulting vibrational OH product systematically, we park our vibrational excitation laser (λ_1) on the corresponding overtones bands of HOOH and CH_3OOH and compare the resulting OH(v=0, N=2), OH(v=1, N=2), and OH(v=2, N=2) fragment in back-to-back measurements where we scan over these ro-vibrational OH states using the BURST mode at 5 μsteps averaging 20 shots/bin (see Appendix *A*). The branching ratios for hydrogen peroxide and methyl hydroperoxide are found in Tables 9.2 and 9.3 respectively for photolysis wavelength λ_2 = 532 nm. The listed values are obtained by converting the integrated LIF intensities to relative population using the Einstein's B-coefficient and Franck-Condon factors associated with each OH ro-vib states normalized to laser powers.[25,26]

About ~10% of the resulting OH fragment is found vibrationally excited in H_2O_2 ($2\nu_{OH}$) with OH(v=2) accounting for about 0.5% of the vibrational excited product (see Table 9.2). To our surprise, we find that similar amounts of vibrationally excited OH fragment are produced upon excitation of the second overtone ($3\nu_{OH}$). This finding is

surprising considering the fact that the band at ~10 290 cm^{-1} lies ~3240 cm^{-1} above the $2\nu_{OH}$ band. As one may expect, the density of states is larger in the $3\nu_{OH}$ region which in turn, may lead to a greater fractionation of the vibrational excitation in the prepared O-H stretching mode through enhance coupling, thus leading to reduction in the amounts of vibrationally excited OH fragment present. Indeed, based on a Whitten-Rabinovitch vibrational density of state calculation with parameters in Table 9.1, the state density increases by a factor of ~3.3 from 0.25 states/cm^{-1} in the $2\nu_{OH}$ region to 0.82 states/cm^{-1} in the $3\nu_{OH}$ region.[33] Furthermore, Crim and coworkers have measured the resulting vibrationally excited OH product from one-color two-photon photodissociation in the third ($4\nu_{OH}$) OH-stretching overtone.[34] They also find that ~11% of the OH product is formed vibrationally excited despite the 8-fold increase in the density of states compared with the $2\nu_{OH}$ region.

In contrast to the OH-stretching overtones, excitation of the two bending modes associated with the antisymmetric and symmetric bends around ~8280 cm^{-1} and 8400 cm^{-1} lead to significantly less vibrationally excited OH(v=1) product. If one assumes that the of flow of energy from the excited coordinate via intramolecular vibrational redistribution solely depends on the number of available states, an increase in densities of vibrational states should lead to more complete IVR and to reduction in the excitation of the OH product by fractionation of the bright state according to:

$$|\mathbf{n}\rangle = C^{n}_{s}\,|\mathbf{s}\rangle + \Sigma\, C^{n}_{\ell}\,|\boldsymbol{\ell}\rangle \qquad (9.1)$$

In this equation, the prepared zeroth-order bright state, $|\mathbf{s}\rangle$, corresponds to the OH-stretch or bend-stretch combination band. The state $|\boldsymbol{\ell}\rangle$ correspond to the manifold of dark states

in the molecule that fall in the range of interacting frequencies. An increase in the number of interacting dark states will result in smaller expansion coefficient C^n_s and therefore smaller |**s**> character in the eigenstate |**n**> due to an increase in the sum of interacting states C^n_ℓ |**ℓ**>.[4,6,9,15] In other words, intramolecular vibrational energy redistribution tends to dilute the amount of OH-stretch bright state character presented in the prepare eigenstate |**n**>. Based on a simple density of states consideration, the prepared state, |**n**>, which is formed upon excitation of the $2\nu_{OH}$ band, should in principle, contain more of the zero-order |**s**> state character than upon excitation of the $3\nu_{OH}$ band because there are less of the |**ℓ**> dark states available in the $2\nu_{OH}$ region to interact with compared to the $3\nu_{OH}$ region (see Fig. 9.1). In our case, for an intermediate state to contain more of the |**s**> character simply means production of more vibrationally excited OH product. Based on our findings however, this is not the case. As Table 9.2 shows, in HOOH, excitation of the $2\nu_{OH}$ and $3\nu_{OH}$ bands results in roughly ~10 % of vibrationally excited OH(v=1) product. Similarly, in CH_3OOH as shown in Table 9.3, excitation of the $2\nu_{OH}$ and $3\nu_{OH}$ bands result in 0.8 % of vibrationally excited OH(v=1) product.

A more reasonable approach for interpreting our findings invokes the notion that it is the *local* densities of state, that is to say, the chemical environment and the coupling of the prepared bright state to a smaller subset of states that affect the initial energy redistribution in the molecule.[18,35-38] In other words, IVR does not scale with the total density of vibrational states. This approach limits the actual number of available dark states |**ℓ**> with which the zeroth-order bright state may interact with. Since excitation of "pure" OH stretching mode such as in the case of the $2\nu_{OH}$, $3\nu_{OH}$,or $4\nu_{OH}$ involve

elongation of the O-H bond, it is likely that this motion is preserving a similar local chemical environment where the coupling between the OH stretch and the interacting states remain unchanged. In the case of methyl hydroperoxide and hydrogen peroxide, as seen from the coupling matrices associated with the ground state in Tables 8.2 and 9.1 respectively, the OH stretch is mainly coupled to its bend and torsion. By contrast, energy deposited into the stretch-bend combination modes (and CH stretching modes) of these hydroperoxides apparently leads to chemical environment that is changing the formation of molecular eigenstates with significantly less vibrationally excited OH character as indicated by the reduced vibrationally excited OH product. In essence, even though excitation of the combination mode involves two quanta of OH vibrational energy and one quanta of HOO bend to be deposited in a region where the density of states is *lower* than that of the second and third stretching overtones, *less* vibrationally excited OH product is formed. Hence, we conclude that the energy deposited into these combination modes is able to mix more extensively with the background dark states compared to excitation of the $2\nu_{OH}$ and $3\nu_{OH}$ bands.

Fragment vibrational product state distribution measurements of methyl hydroperoxide of which the spectra are shown in Fig. 9.6 and summarized in Table 9.3 also appear similar to HOOH. Aside from the fact that there is less resulting vibrationally excited OH product from the dissociation of methyl hydroperoxide compared with hydrogen peroxides, the spectra indicate that the OH fragment is formed vibrationally excited from both the $2\nu_{OH}$ and $3\nu_{OH}$ stretching overtones but not from excitation of the stretch-bend combination mode ($2\nu_1 + \nu_8$). Within our detection sensitivity, we also do not observe vibrationally excited OH from excitation of the various CH-stretching modes

($3\nu_{CH}$) either. For methyl hydroperoxide, the densities of states in the regions of the $2\nu_1$, $2\nu_1 + \nu_8$, and $3\nu_1$ are 180, 486 and 2205 states/cm^{-1} respectively. These enhanced vibration state densities could provide reasonable account for the reduction in the vibrationally excited OH product from CH_3OOH compared with H_2O_2, where the respective densities of states are ~720, ~1200, and ~2700 times smaller. More importantly however, these MHP state densities suggest that over an order of magnitude increase by going from $2\nu_{OH}$ to $3\nu_{OH}$ does not significantly change the resulting fraction of vibrationally excited OH product formed.

Interestingly, strong coupling in the stretch-bend and CH stretching regions to the manifold of "dark" background of vibrational states affect significantly the photodissociation outcome in the midrange region. In contrast to the situation in the region of the $2\nu_{OH}$ and $3\nu_{OH}$ bands where IVR is more restricted and incomplete, which result in vibrationally excited OH product, the bending modes and CH-stretching modes undergo a more extensive IVR prior to photodissociation due to stronger coupling between these mode and the substates in the first-tier. In other words, the bottleneck due to the restricted IVR at the $2\nu_{OH}$ and $3\nu_{OH}$ in MHP and H_2O_2 lead to significantly larger amounts of vibrationally excited product. Quasiclassical trajectories of CH_3OOH $2\nu_{OH}$ also support the finding of restricted intramolecular vibrational energy redistribution where the energy transfers out of the excited OH more slowly compared with CH excitation.[19-21] Gai *et al.* also note that for MHP excitation of the fifth ($6\nu_{CH}$) CH-stretching overtone results in energy transfer that is on the order of 0.2 picoseconds.[19] IVR redistributes the energy from this vibrational state mainly to the various CH bending

modes while the vibrational energy in the OH stretching mode remains constant over the picoseconds time scale. By contrast, excitation of the fifth ($6\nu_{OH}$) OH stretching overtone shows different behavior. Energy migrates out of this mode very slowly (> 1.0 ps) where initially the main recipient of the energy is the HOO bend. Hence, this slow bottled-neck energy flow from the vibrationally excited OH states is consistent with the observed OH(v=1) product.

Extensive IVR studies of the methyl rotor in methanol also suggest that the internal rotation leads to strong mixing and inhomogeneous linewidths in the modes involving CH motion. As evident from their studies, in the presence of strong mixing, the coupling of the prepared CH state to the first-tier of substates followed by coupling to the second higher order tier of states lead to fractionation of these CH stretching modes and their distribution to the "dark" bath of states very efficiently.[22,39-43] Also, as shown in Chapter 8, in CH_3OOH, the first ($2\nu_{CH}$) and second ($3\nu_{CH}$) CH stretching overtones behave similarly to methanol. In the first place, the room temperature action spectra show broad and diffused feature for these bands. Secondly, these bands show no rotational structure under jet-cooled environment suggesting rotational line broadening as a result of state mixing. On the other hand, the OH-stretching modes of methyl hydroperoxide, under room temperature and jet-cooled conditions show rotational structure. Based on our current findings and the quasiclassical overtone dissociation trajectories of Gai *et al.*,[19] it is clear that excitation of the OH chromophore in CH_3OOH, results in a more restricted distribution of the vibrational energy thus conserving more efficiently the energy in the O-H coordinate and in turns leading to the observed mode selective behavior. Similar theoretical studies of hydrogen peroxide by Uzer *et al.* and Sumpter *et al.* have

demonstrated that energy deposited in the O-H stretching mode, though dependent on the initial excitation, is slow to redistribute even at high vibrational excitation and is on the order of ~5 picoseconds.[20,21] Thus, our findings are strongly supported by these trajectories calculations which involve state evolution in time domain.

As a final check, to confirm that the contribution of the vibrationally excited product is not a result of dissociation dynamics on the electronically excited state, we change the electronic excitation wavelength (λ_2) going from 532 nm to 355 nm. This significant difference in photon energy for the second step could potentially result in different Franck-Condon factors and therefore result in accessing different regions in the global electronic surface that could in turn lead to enhanced vibrationally excited OH fragment from the bending modes and CH-stretching modes of HOOH and CH_3OOH. When we quantify the vibrational branching ratio resulting from excitation λ_2 = 355 nm, we find however that the branching ratio values are similar to those obtained at λ_2 = 532 nm photolysis wavelength. As shown in Table 9.4, we find again that for the $2\nu_{OH}$ state of H_2O_2 ~11 % of the OH product is in v=1 and ~0.3 % is in v=2. Consistent values for the $2\nu_{OH}$ band of CH_3OOH are also obtained at ~355 nm photolysis wavelength (see Table 9.5). Due to background OH(v=0) LIF signal from direct photolysis at ~355 nm from both HOOH and MHP, we unable to quantify the vibrational branching ratio from the second ($3\nu_{OH}$) OH stretching overtones and the bend-stretch combination modes. At these excitation frequencies, signal levels from direct photolysis at 355 nm suppress the IR + UV ViMP signal levels when monitoring the OH(v=0) product. Despite the inability to quantify the vibrationally excited OH product from $3\nu_{OH}$ and stretch-bend combination

modes, we are still able to report formation of vibrationally excited OH product for these two species. The fact that the measurements at the first ($2\nu_{OH}$) OH stretching overtone give similar OH product branching ratio values from photolysis at 532 nm and 355 nm suggest that the OH vibrational product states are independent of the photolysis laser (λ_2) and therefore *affected predominantly by the vibrational character of the prepared vibrational state.* In essence, the two photolysis photons which are used to promote the vibrationally excited molecule are substantially different in frequency and the regions in which they access the electronically excited surface, yet they produce similar values for the branching ratios.

Additional measurements involving single-photon photodissociation of H_2O_2 and CH_3OOH at 355, 285, 266, and 248 nm do not result in measurable amounts of vibrationally excited OH fragment.[9,44,45] Watts and Francisco have recently investigated a few of the low-lying electronically excited singlet states of H_2O_2 and CH_3OOH using *ab initio* methods.[32] They report that the two hydroperoxides have similar electronic potential along the O-O reaction coordinate where the two lowest repulsive electronic states (2^1A and 2^1B) require vertical excitation from the ground state (X^1A) of 5.99 eV and 6.99 eV respectively for H_2O_2. Similarly, for CH_3OOH, the vertical excitations from the ground state (X^1A) to the 2^1A and 4^1A states are 5.85 eV and 6.75 eV.[32] In our experiments, excitation from the first overtone using 532 nm light gives the molecule ~3.2 eV of combined energy while similar excitation from the second ($3\nu_1$) OH stretching overtone gives a total photon energy of ~3.6 eV. These values suggest that in order for photodissociation to occur, energy from the O-H stretching mode must transfer to the reaction coordinate and lead to extension of the O-O bond in order to allow the electronic

excitation photon (λ_2 = 532 nm) to access the upper state and promote dissociation not accessible from the ground state. This indicates that despite the fact that the energy in the O-H mode is somewhat localized, as suggested by the vibrationally excited OH yields, in order to induce photodissociation, energy must first redistribute to the O-O bond to induce dissociation by enhancing the overlap between the ground and excited state.

9.4 Conclusions

To summarize, in this work the OH vibrational product state distributions of methyl hydroperoxide and hydrogen peroxide resulting from excitation in the vicinity of the first ($2\nu_{OH}$) and second ($3\nu_{OH}$) OH-stretching overtones as well as in the vicinity of the OH-stretch / OOH-bend ($2\nu_{OH} + \nu_{OOH}$) combination regions are investigated by IR-VIS and IR-UV ViMP excitation scheme. We find that the OH fragment vibrational state distributions depend on the initially prepared vibrational band with the stretch-bend combination state producing significant less vibrationally excited OH product. The disparity in the vibrationally excited OH product is likely reflects the enhanced intramolecular vibrational energy redistribution (IVR) associated with bending modes compared with excitation of a "pure" OH stretch.

Despite the differences in size and composition of the two compounds, we find similarities upon excitation of their OH stretching overtones where there is significantly more vibrationally excited OH product when compared with the vibrational overtone excitation of the OOH bending (and CH stretching) modes. Since energy constraints play no role in producing vibrationally excited product under our experimental conditions, these results suggest that both the CH-stretching and HOO-bending modes are more extensively mixed. In quantifying the resulting vibrationally excited OH product from

photodissociation of a vibrationally excited OH stretching mode, we find that as proposed by theoretical studies,[18,35-38] these modes are more isolated thus leading to more restricted energy flow. It is essential to identify restricted IVR and mode selective behavior in small and large molecules in order to categorize when statistical theories which relay on complete randomization of the energy in the excited molecule may or may not be used to model dissociation dynamics of hydroperoxides.[18] Chapter 11, which studies the unimolecular dissociation of hydroxymethyl hydroperoxide, also shows non-statistical mode-selective dissociation dynamics which perhaps is common to other hydroperoxide as well.

Table 9.1: Harmonic Frequencies, and Anharmonicities of HOOH Computed at MP2/cc-pVQZ (cm^{-1})

$(\omega_e)_i$	3817	1435	937	385	3817	1331
$(\omega_e\chi_e)_{ij}$	1	2	3	4	5	6
1	-43.5					
2	-17.5	-10.6				
3	-4.40	-16.6	-6.86			
4	2.85	23.7	-0.98	-36.4		
5	-172	-18.2	-4.03	6.51	-42.9	
6	-11.3	-12.3	-14.1	-18.0	-10.6	-10.6

Table 9.2: The OH Fragment Vibrational Product State Branching Ratio of Hydrogen Peroxide in the Stretching Overtones and Bend-Stretch Regions at Photolysis Wavelength λ_2 = 532 nm

Excitation Band	OH(v=0)	OH(v=1)	OH(v=2)
$\nu_1 + \nu_5$ (7050 cm^{-1})	89.8	9.7	0.5
$(\nu_1 + \nu_5) + \nu_6$ (8300 cm^{-1})	97.2	2.8	0
$2\nu_1 + \nu_5$ / $3\nu_5$ (10 290 cm^{-1})	90.5	9.5	0

Table 9.3: The OH Fragment Vibrational Product State Branching Ratio of Methyl Hydroperoxide in the Stretching Overtones and Bend-Stretch Regions at Photolysis Wavelength λ_2 = 532 nm

Excitation Band	OH(v=0)	OH(v=1)	OH(v=2)
$2\nu_1$ (7025 cm^{-1})	99.2	0.8	0
$2\nu_1 + \nu_8$ (8290 cm^{-1})	100	0	0
$3\nu_1$ (10 260 cm^{-1})	99.25	0.75	0

Table 9.4: The OH Fragment Vibrational Product State Branching Ratio of Hydrogen Peroxide in the Stretching Overtones and Bend-Stretch Regions at Photolysis Wavelength λ_2 = 355 nm [a]

Excitation Band	OH(v=0)	OH(v=1)	OH(v=2)
$\nu_1 + \nu_5$ (7050 cm^{-1})	88.7	11.0	0.3
$(\nu_1 + \nu_5) + \nu_6$ (8300 cm^{-1})	...	...	0
$2\nu_1 + \nu_5$ / $3\nu_5$ (10 290 cm^{-1})	...	...	...

[a] "..." indicates values that could not be measured due to interference from the 355 nm photolysis wavelength.

Table 9.5: The OH Fragment Vibrational Product State Branching Ratio of Methyl Hydroperoxide in the Stretching Overtones and Bend-Stretch Regions at Photolysis Wavelength λ_2 = 355 nm [a]

Excitation Band	OH(v=0)	OH(v=1)	OH(v=2)
$2\nu_1$ (7025 cm^{-1})	99.24	0.76	0
$2\nu_1 + \nu_8$ (8290 cm^{-1})	...	0	0
$3\nu_1$ (10 260 cm^{-1})	...	...	0

[a] "..." indicates values that could not be measured due to interference from the 355 nm photolysis wavelength.

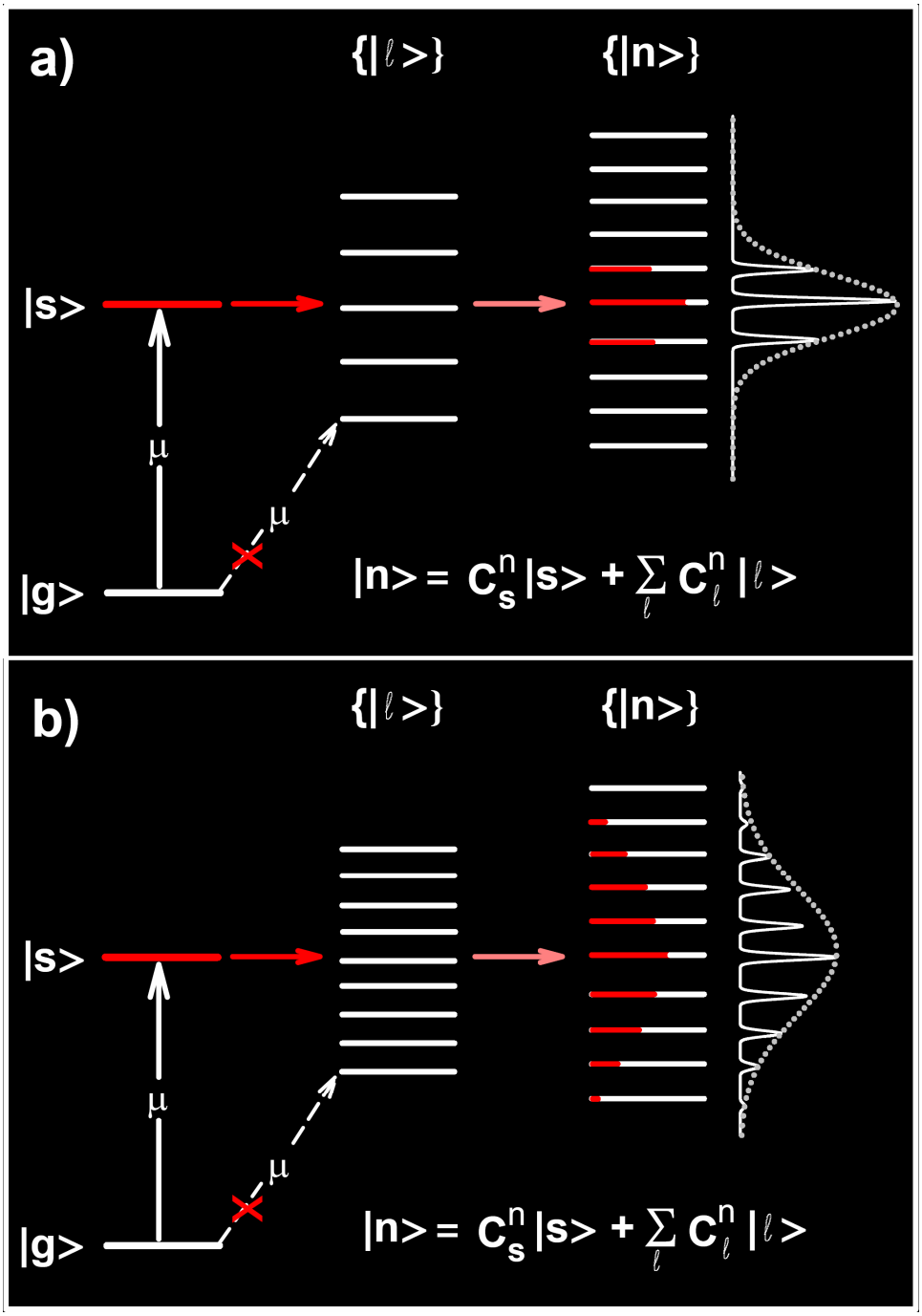

Figure 9.1: Schematic diagram illustrating IVR. a) For small molecule the zeroth-order bright state, |**s**>, is accessed via a transition from the ground state. Other states in this frequencies range, |***ℓ***>, typically do not carry oscillator strength from the ground state. However, coupling of the bright state to the dark states result in formation of eigenstates, |**n**>, and fractionation of the bright state character. b) Same as above, except that for a large molecule the increase in the densities of the dark bath of states results in additional fractionation of the zeroth-order bright state. [File: F9.1_tier_model]

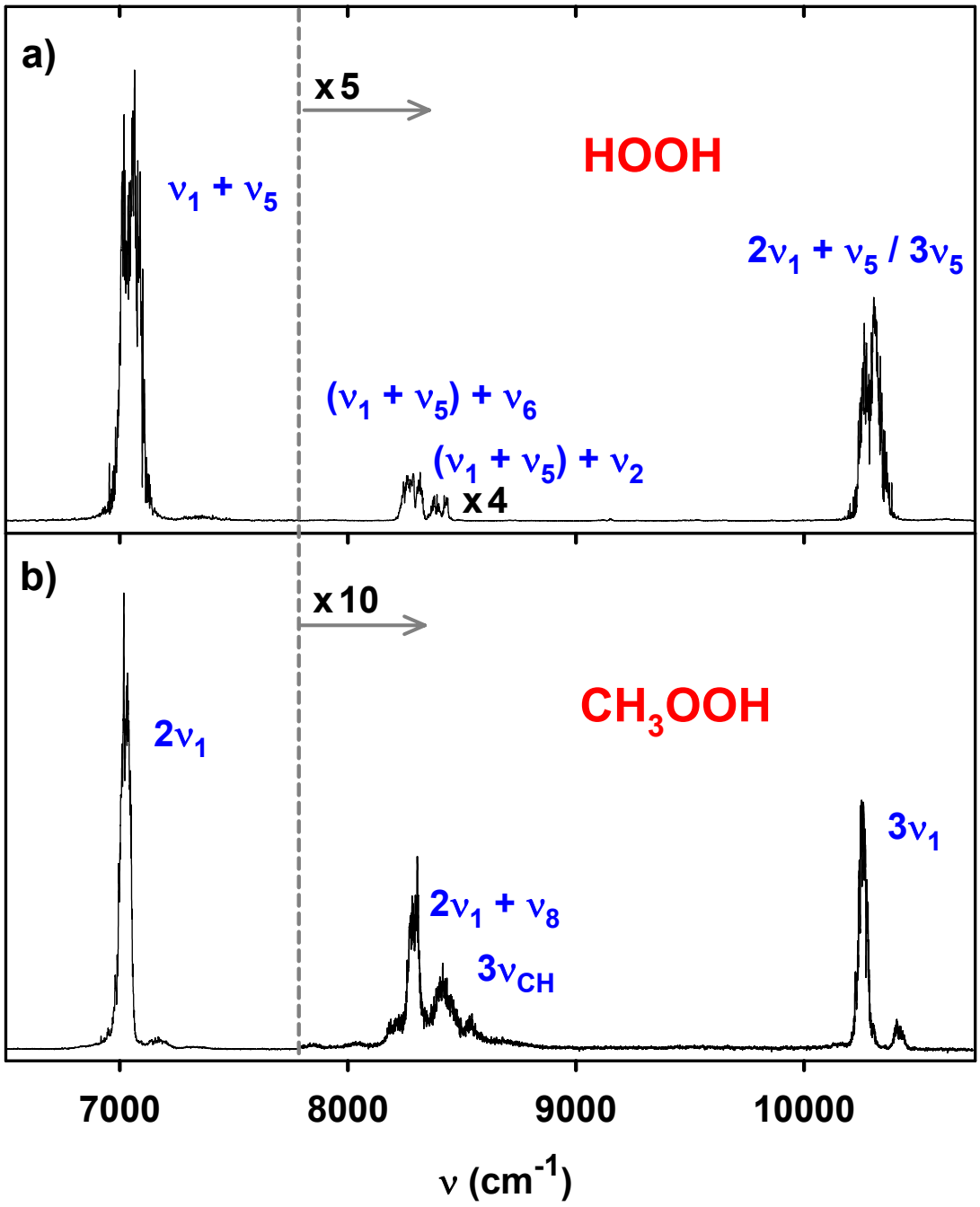

Figure 9.2: Overview action spectra in the regions of the first ($2\nu_{OH}$) through second ($3\nu_{OH}$) OH stretching overtones of a) HOOH. b) CH_3OOH. The "high" pressure spectra are generated by using the $n\nu_x$ + 532 nm ViMP process while monitoring the resulting OH fragment in its N=2 rotational state via the A–X(0,0) transition. The high frequency region is magnified by the indicated values. The bending mode of HOOH is further magnified by a factor of 4. [File: F9.2_overview]

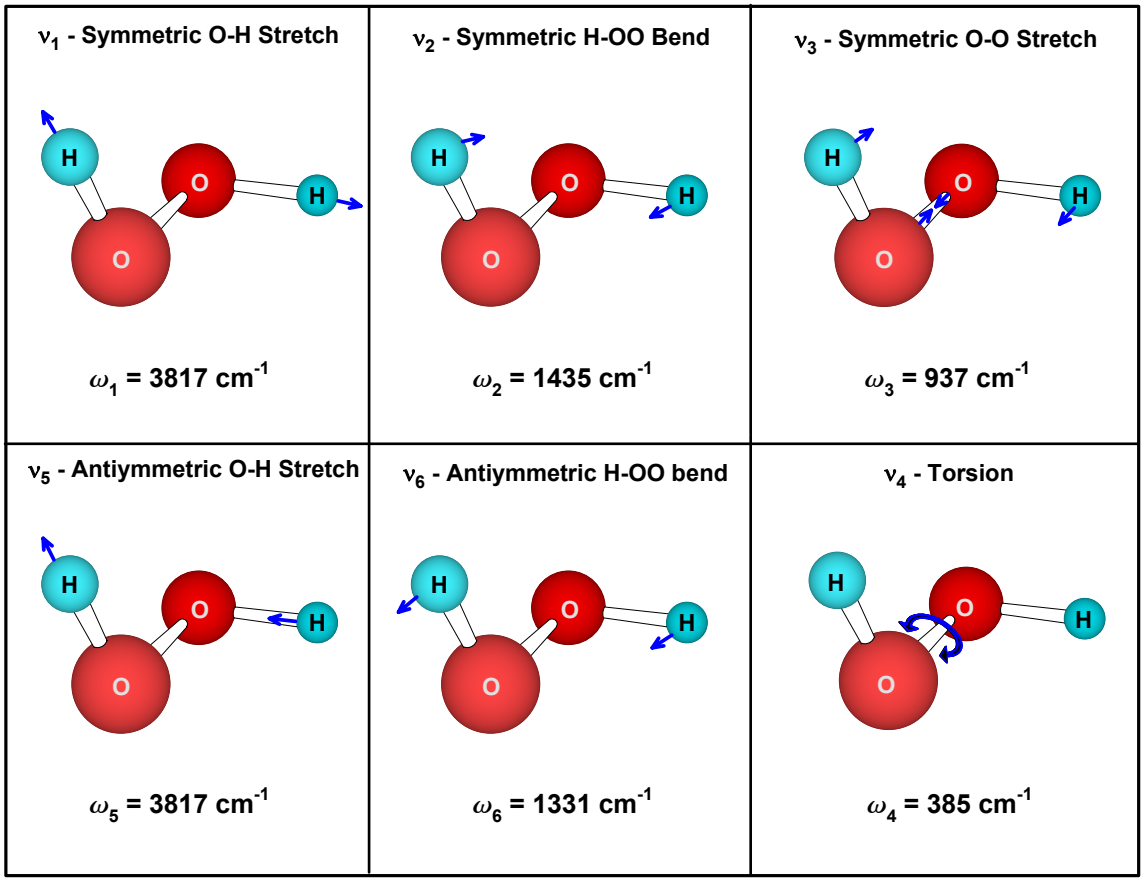

Figure 9.3: Normal modes representation of hydrogen peroxide calculated at the MP2/cc-pVQZ level of theory. In our experiment we detect all the modes except of the O-O symmetric stretch (ω_3). [File: F9.3_h2o2]

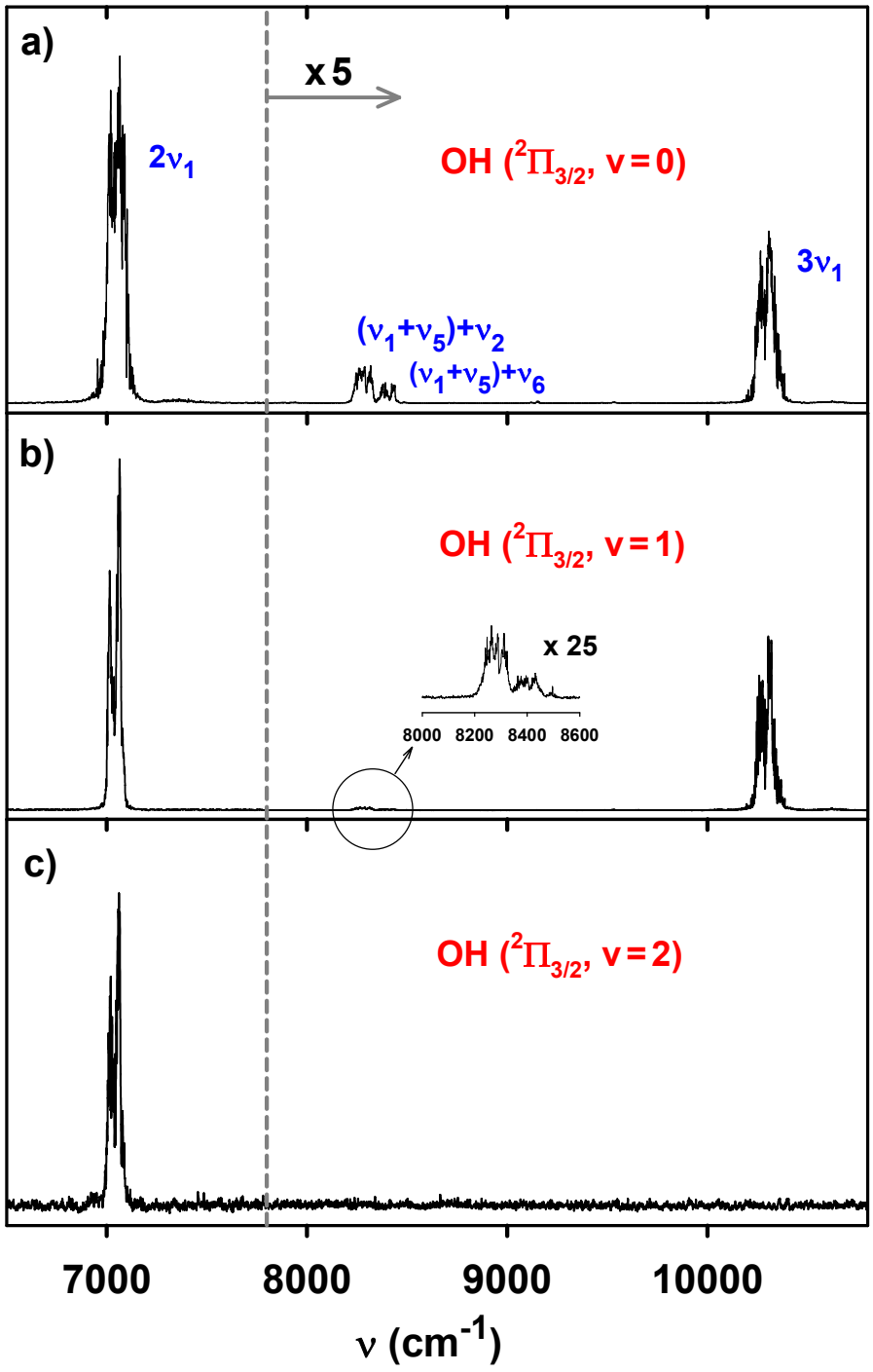

Figure 9.4: a) ViMP action spectrum of HOOH monitoring the OH(v=0,N=2) via the A–X(0,0) transition. b) ViMP action spectrum of HOOH monitoring the OH(v=1,N=2) via the A–X(1,1) transition. The insert shows ×25 magnification of bending mode region. c) ViMP action spectrum of HOOH monitoring the OH(v=2,N=2) via the A–X(2,2) transition. The high frequency region is magnified by a factor of 5.
[File: F9.4_h2o2_v012_532]

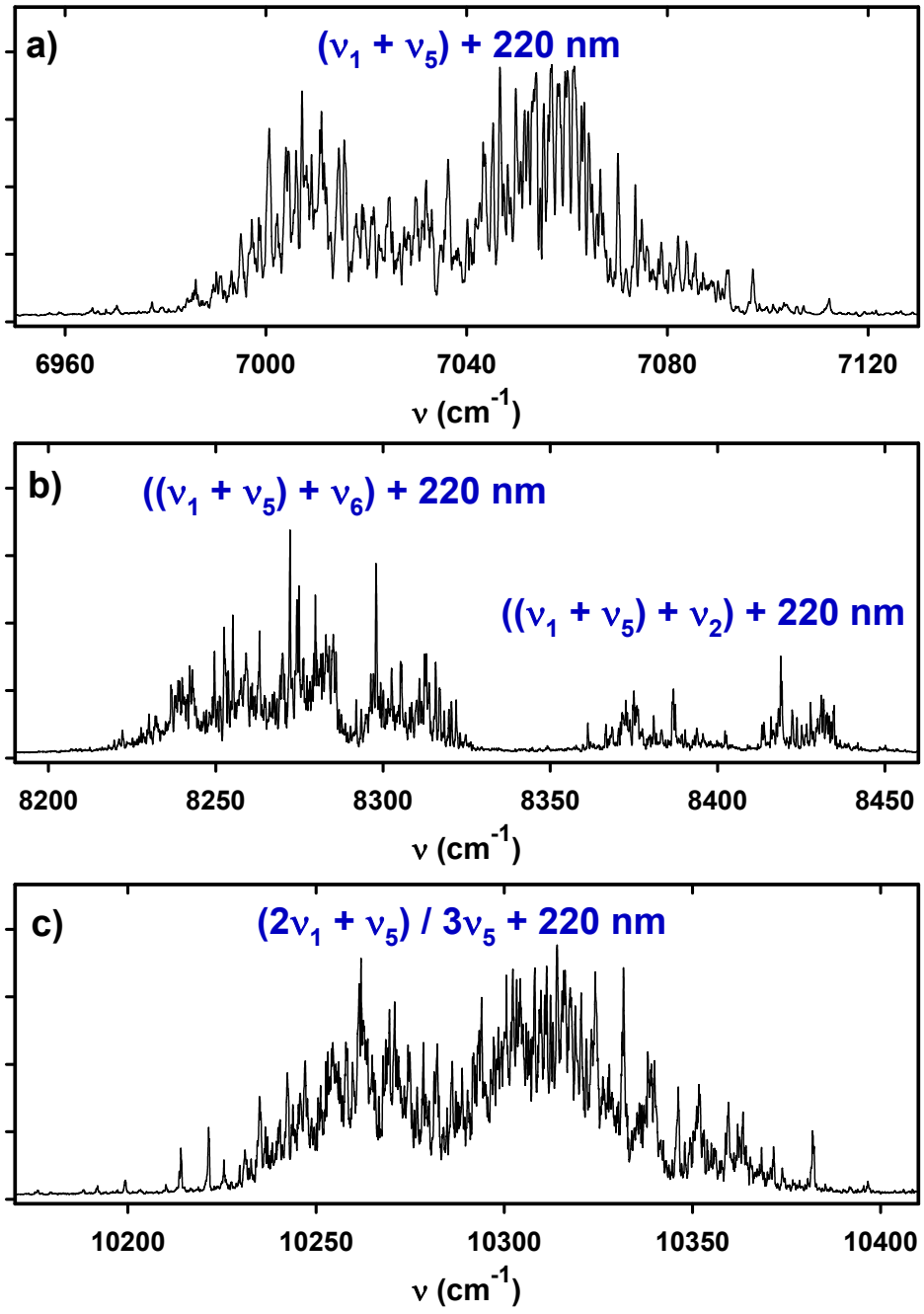

Figure 9.5: Expended view of the vibrational states of HOOH showing its rotational structure. These spectra are obtained with the ViMP $n\nu_x$ + 205 nm excitation scheme where the resulting OH fragment is formed directly in the $A^2\Sigma$ fluorescing state. a) ViMP action spectrum of HOOH in the $\nu_1 + \nu_5$ region. b) ViMP action spectrum of HOOH in the $(\nu_1 + \nu_5) + \nu_6/\nu_2$ region. c) ViMP action spectrum of HOOH in the $(2\nu_1 + \nu_5) / 3\nu_5$ region. [File: F9.5_slow_scan]

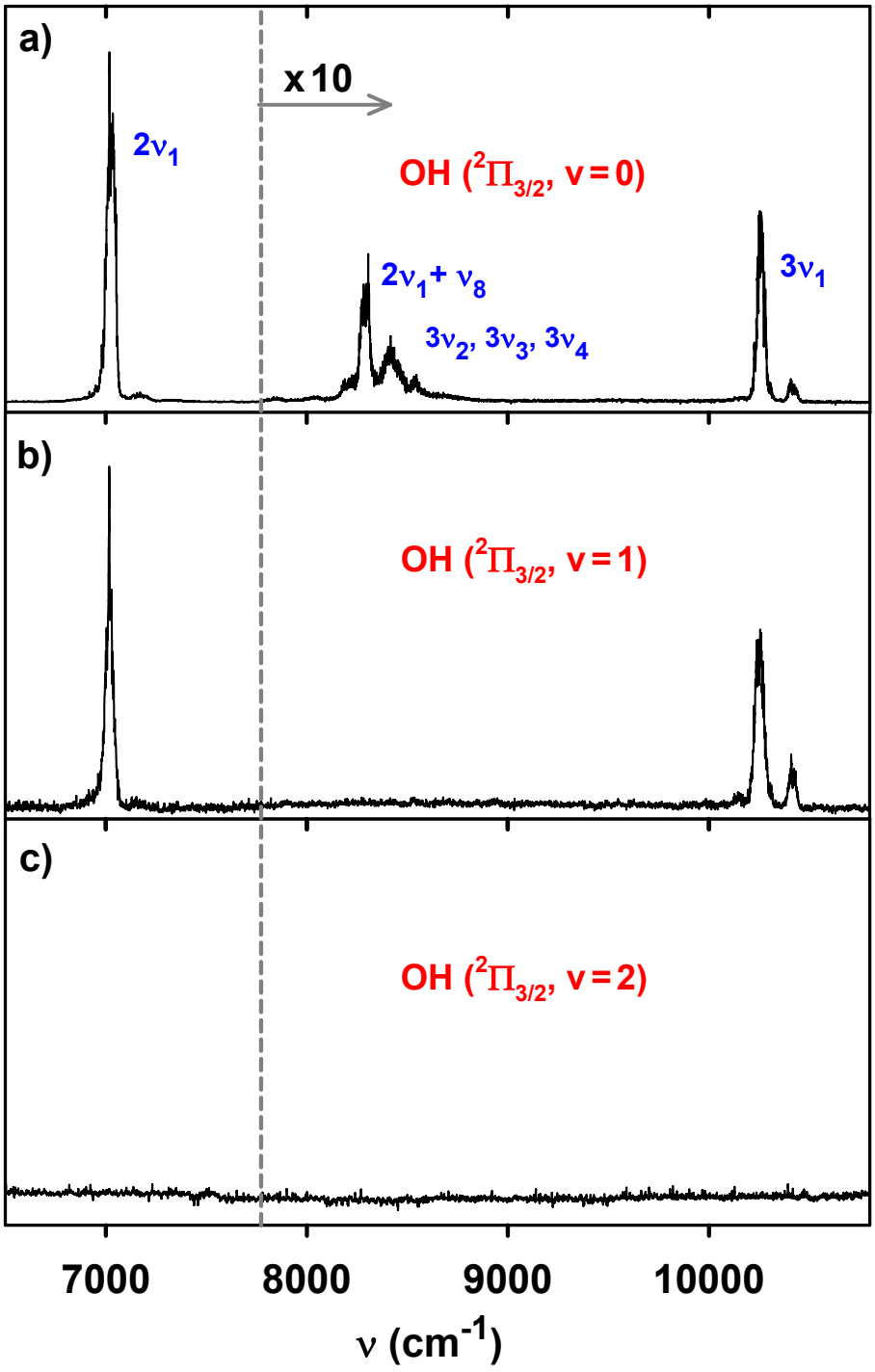

Figure 9.6: a) ViMP action spectrum of CH_3OOH monitoring the OH(v=0,N=2) via the A–X(0,0) transition. b) ViMP action spectrum of CH_3OOH monitoring the OH(v=1,N=2) via the A–X(1,1) transition. c) ViMP action spectrum of CH_3OOH monitoring the OH(v=2,N=2) via the A–X(2,2) transition. The high frequency region is magnified by a factor of 10. [File: F9.6_ch3ooh_v012_532]

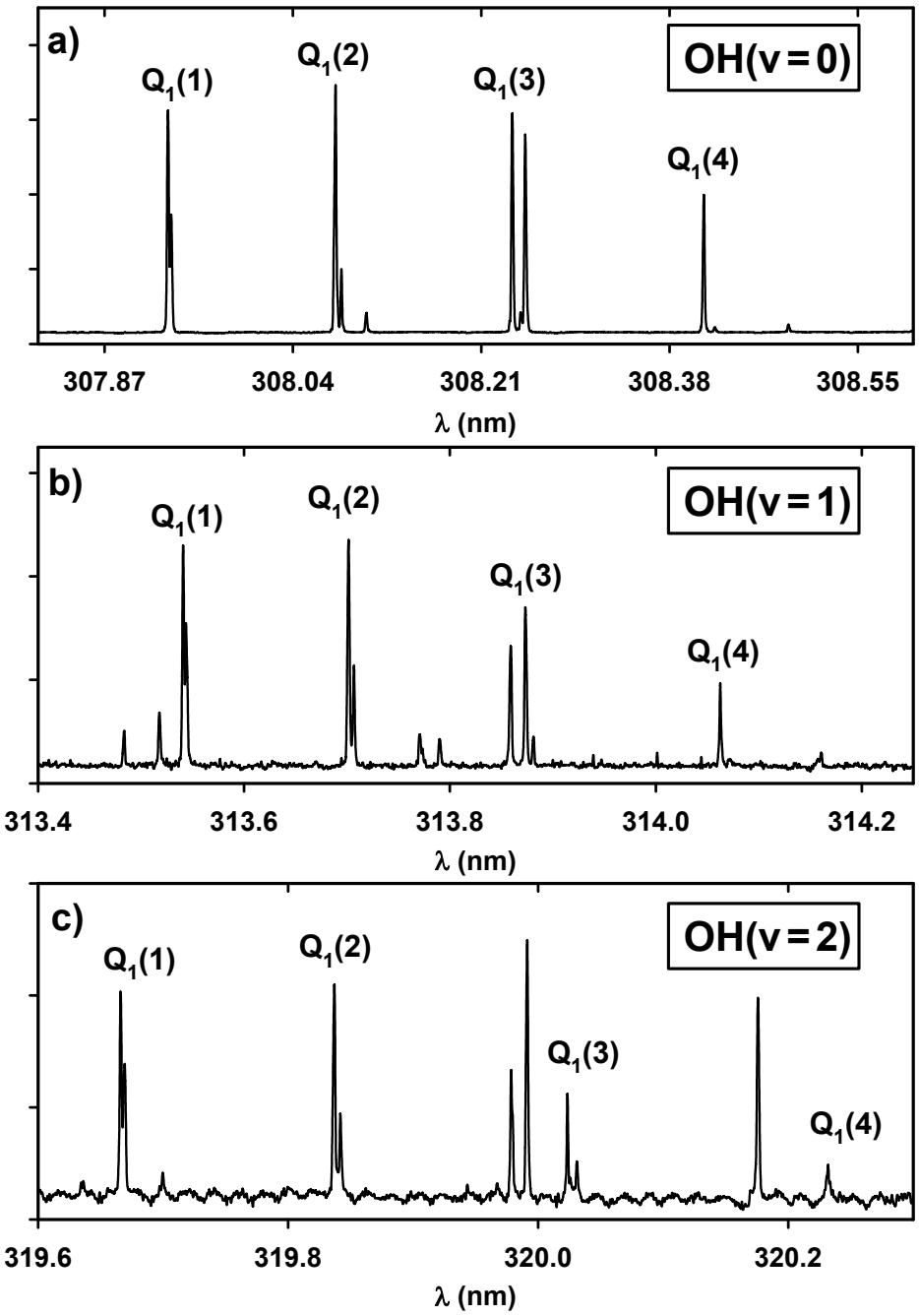

Figure 9.7: a) Relaxed OH product LIF spectra from the ViMP of CH_3OOH ($2\nu_{OH}$ + 532 nm). The OH is probed via the *A*–*X*(0,0) transition. b) Relaxed OH product LIF spectra from the ViMP of CH_3OOH $2\nu_{OH}$ + 532 nm. The OH is probed via the *A*–*X*(1,1) transition. c) Relaxed OH product LIF spectra from the ViMP of HOOH $2\nu_{OH}$ + 532 nm. The OH is probed via the *A*–*X*(2,2) transition. The assignment is based on the work in Ref. 25. [File: F9.7_oh_lines]

9.5 References

1. G. P. Brasseur, J. J. Orlando, and G. S. Tyndall, *Atmospheric Chemistry and Global Change* (Oxford University Press, New York 1999).

2. S. P. Sander, R. R. Friedl, D. M. Golden, M. J. Kurylo, R. E. Huie, V. L. Orkin, G. K. Moortgat, A. R. Ravishankara, C. E. Kolb, M. J. Molina, B. J. Finlayson-Pitts, Chemical kinetics and photochemical data for use in stratospheric modeling, Evaluation #14, *JPL Publ.*, **02-25** (2003).

3. B. J. Finlayson-Pitts, and J. N. Pitts Jr., *Atmospheric Chemistry: Fundamental and Experimental Techniques* (Wiley, New York 1986).

4. F. F. Crim, J. Phys. Chem. **100**, 12725 (1996).

5. L. J. Butler, D. M. Newmark, J. Phys. Chem. **100**, 12801 (1996).

6. D. J. Nesbitt, and R. W. Field, J. Phys. Chem. **100**, 12735 (1996).

7. M. D. Likar, J. E. Baggott, and F. F. Crim, J. Chem. Phys. **90**, 6266 (1989).

8. B. Kuhn, and T. R. Rizzo, J. Chem. Phys. **112**, 7461 (2000).

9. F. F. Crim, Annu. Rev. Phys. Chem. **44**, 397 (1993).

10. T. M. Ticich, M. D. Likar, H. –R. Dübal, L. J. Butler, F. F. Crim, J. Chem. Phys. **87**, 5820 (1987).

11. T. Gilbert, T. L. Grebner, I. Fischer, and P. Chen, J. Chem. Phys. **110**, 5485 (1999).

12. J. C. Owrutsky and A. P. Baronavski, J. Chem. Phys. **110**, 11206 (1999).

13. S. H. Courtney, M. W. Balk, L. A. Philips, S. P. Webb, D. Yang, D. H. Levy, and G. R. Fleming, J. Chem. Phys. **89,** 6697 (1988).

14.Y. S. Choi, and C. B. Moore, J. Chem. Phys. **94**, 5414(1991).

15. G. Dutton, R. J. Barnes, and A. Sinha, J. Chem. Phys. **111,** 4976 (1999).

16. M. R. Wedlock, R. Jost, and T. R. Rizzo, J. Chem. Phys. **107**, 10344 (1997).

17. F. Reiche, B. Abel, R. D. Beck, and T. R. Rizzo, J. Chem. Phys. **116**, 10267 (2002).

18. M. Quack, Annu. Rev. Phys. Chem. **41**, 839 (1990).

19. K. K. Lehmann, G. Scoles, B. H. Pate, Annu. Rev. Phys. Chem. 45, 241 (1994).

18. M. Gruebele, and P. G. Wolynes, Acc. Chem. Res. **37**, 261 (2004).

19. H. Gai, D. L. Thompson, G. A. Fisk, J. Chem. Phys. **90**, 7055 (1989).

20. B. G. Sumpter, and D. L. Thompson, J. Chem. Phys. **82**, 4557 (1985).

21. T. Uzer, J. T. Hynes, and W. P. Reinhardt, J. Chem. Phys. **85,** 5791 (1986).

22. O. V. Boyarkin, T. R. Rizzo, and D. S. Perry, J. Chem. Phys. **110**, 11346 (1999).

23. M. Quack and M. Willeke, J. Chem. Phys. **110**, 11958 (1999).

24. G. L. Vaghijiani, and A. R. Ravishankara, J. Geophys. Res. **94**, 3487 (1989).

25. G. H. Dieke and H. M. Crosswhite, J. Quant. Spectrosc. Radiat. Transfer **2**, 97 (1962).

26. W. L. Dimpfl and J. L. Kinsey, J. Quant. Spectrosc. Radiat. Transfer **21**, 223 (1979).

27. P. A. Giguere, J. Chem. Phys. **18**, 88 (1950).

28. E. Hirota, J. Chem. Phys. **28**, 839 (1958).

29. H. –R. Dubal, F. F. Crim, J. Chem. Phys. **83**, 3863 (1985).

30. GAUSSIAN03, Revision B.04, M. J. Frisch, G. W. Trucks, H. B. Schlegel, G. E. Scuseria, M. A. Robb, J. R. Cheeseman, J. A. Montgomery, Jr., T. Vreven, K. N. Kudin, J. C. Burant, J. M. Millam, S. S. Iyengar, J. Tomasi, V. Barone, B. Mennucci, M. Cossi, G. Scalmani, N. Rega, G. A. Petersson, H. Nakatsuji, M. Hada, M. Ehara, K. Toyota, R. Fukuda, J. Hasegawa, M. Ishida, T. Nakajima, Y. Honda, O. Kitao, H. Nakai, M. Klene, X. Li, J. E. Knox, H. P. Hratchian, J. B. Cross, V. Bakken, C. Adamo, J. Jaramillo, R. Gomperts, R. E. Stratmann, O. Yazyev, A. J. Austin, R. Cammi, C. Pomelli, J. W. Ochterski, P. Y. Ayala, K. Morokuma, G. A. Voth, P. Salvador, J. J. Dannenberg, V. G. Zakrzewski, S. Dapprich, A. D. Daniels, M. C. Strain, O. Farkas, D. K. Malick, A. D. Rabuck, K. Raghavachari, J. B. Foresman, J. V. Ortiz, Q. Cui, A. G. Baboul, S. Clifford, J. Cioslowski, B. B. Stefanov, G. Liu, A. Liashenko, P. Piskorz, I. Komaromi, R. L. Martin, D. J. Fox, T. Keith, M. A. Al-Laham, C. Y. Peng, A. Nanayakkara, M. Challacombe, P. M. W. Gill, B. Johnson, W. Chen, M. W. Wong, C. Gonzalez, and J. A. Pople, Gaussian, Inc., Wallingford CT, 2004.

31. K. H. Gericke, S. Klee, F. J. Comes, and R. N. Dixon, J. Chem. Phys. **85**, 4463 (1986).

32. J. D. Watts, J. S. Francisco, J. Chem. Phys. **125**, 104301 (2006).

33. K. A. Holbrook, M. J. Pilling, and S. H. Robertson, *Unimolecular Reactions -2nd Edition* (Wiley, New York, 1996).

34. T. M. Ticich, M. D. Likar, H. R. Dubal, L. J. Butler, and F. F. Crim, J. Chem. Phys. **87**, 5820 (1987).

35. J. E. Gambogi, R. P. L'Esperance, K. K. Lehmann, B. H. Pate, and G. Scoles, J. Chem. Phys. **98**, 1116 (1993).

36. R. Bigwood, M. Gruebele, D. M. Leitner, and P. G. Wolynes, Proc. Natl. Acad. Sci. **95**, 5960 (1998).

37. D. J. Nesbitt and R. W. Field, J. Phys. Chem. **100**, 12735 (1996).

38. K. Lehmann, G. Scoles and B. H. Pate, Annu. Rev. Phys. Chem. **45**, 241 (1994).

39. D. Rueda, O. V. Boyarkin, T. R. Rizzo, A. Chirokolava, and D. S. Perry, J. Chem. Phys. **122**, 044314 (2005).

40. X. Wang, and D. S. Perry, J. Chem. Phys. **109**, 10795 (1998).

41. T. N. Clasp, and D. S. Perry, J. Chem. Phys. **125**, 104313 (2006).

42. O. V. Boyarkin, L. Lubich, R. D. F. Settle, D. S. Perry, and T. R. Rizzo, J. Chem. Phys. **107**, 8409 (1997).

43. A. Chirokolava, D. S. Perry, O. V. Boyarkin, M. Schmid, and T. R. Rizzo, J. Chem. Phys. **113**, 10068 (2000).

44. G. L. Vaghijiani, and A. R. Ravishankara, J. Chem. Phys. **92**, 996 (1990).

45. M .A. Thelen, P. Felder, J. R. Huber, Chem. Phys. Lett. **213**, 275 (1993).

Chapter 10

The near-UV and Overtone Absorption Cross Sections of Methyl Hydroperoxide: A Mechanism of Tropospheric OH Production

10.1 Introduction

This chapter ties together some of the ideas introduced in Chapter 1 and in essence, it applies some of the concepts introduced earlier and highlights the importance associated with some of the studies we carried out on the various hydroperoxide molecules. More specifically, this part of the dissertation illustrates that in quantifying the thermochemistry (see Chapter 6), spectroscopy (Chapters 7 – 8) and photochemical dissociation dynamics (Chapter 9) of methyl hydroperoxide we can better assess by applying new, non-traditional approach its atmospheric importance. As discussed in Chapter 1, many atmospheric hydroperoxide molecules though exist in trace amounts, significantly affect the composition of the atmosphere.[1] While some of these molecules are transient (short lived) like we have seen with HOONO and HO_2NO_2 because of their weak bond dissociation energy, others have long lifetime; hence, they can serve as reservoir to the HOx (where HOx ≡ OH + HO_2) radical. The differences in behavior between reservoir and temporary reservoir in terms of atmospheric contribution will be discussed below.

Based on findings in Chapter 6 of this dissertation, MHP has a CH_3O–OH bond dissociation energy of 42.6 kcal/mol. Under atmospheric conditions, overtones initiated photodissociation is expected to be low due to the weak absorption cross-section

estimations presented in Chapter 7. However, in contrast to nitric acid molecule, the strong UV absorption features of methyl hydroperoxide and hydroperoxides in general, these systems considered an excellent source of the HOx radical.[1,2] Hence, accurate modeling of the oxidizing or cleansing capacity of the atmosphere requires knowledge of all significant sources of the hydroxyl radicals such as UV photochemistry. This is particularly important because several studies have suggested large changes in OH abundances in the atmosphere over the past decades; the direction of the change is apparently unclear. Studies by Krol *et al.*,[3] show a significant global increase in OH while those by Prinn *et al.*,[4] show a decline in OH levels after 1988. Recent studies in the upper troposphere have also reported discrepancies between model predictions and measured HO_x concentrations that are strongly dependent on solar zenith angles.[5-8] These differences between predictions and observation not only highlight the difficulties associated with measuring atmospheric OH concentrations, but also potential variability arising from incomplete accounting of all significant sources and sinks of the OH radical.

This chapter demonstrates that absorption from often-neglected weak tails of electronic absorption bands can lead to significant amounts of photochemically generated OH radicals that, apparently, are currently unaccounted for in tropospheric models. Methyl hydroperoxide (CH_3OOH), which is the prototypical organic peroxide (ROOH) and acts as a sink as well as a temporary reservoir for HO_x and RO_x species in the atmosphere, is used to highlight the process under consideration.[9-11] The average tropospheric lifetime of CH_3OOH of about one day (22 hrs),[10] and the relatively large concentration of CH_3OOH in the troposphere, combined with the fact that this dissociation is initiated by the portion of the solar flux that readily penetrates into the

troposphere and hence can initiate photochemistry over a broad range of solar zenith angles, makes this neglected source an important addition to the tropospheric OH budget.

This "eccentric" photochemical source is inline with recent interest in various "unconventional" photochemical sources of atmospheric HOx radicals at high-solar zenith angles.[6-8] Donaldson *et al.* have argued for the importance of vibrational overtone induced dissociation as being a significant source of HO_x yields in the atmosphere.[12-14] However, thus far, only HO_2NO_2 have positively identified as a significant overtone photo-initiated HOx source in the atmosphere.[12] Moreover, as discussed previously, vibrational overtone excitation relies on the anharmonicity associated with molecular vibrations. Thus, typically, OH-stretching overtone excitation is most efficient for exciting these high frequency motions.[15,16] However, in Chapter 9 we have observed that strong intramolecular vibrational energy redistribution (IVR) associated with C-H stretching overtone modes can hamper the IR absorption of otherwise strong anharmonic oscillators and lead to poor signal levels. Furthermore, since these transitions typically involve excitation at relatively long wavelengths which are quantized over small regions of the absorption spectrum, this process is expected to be especially important at high solar zenith angles where absorption and scattering remove much of the energetic short wavelengths present in the solar actinic flux. Hence the need to find other mechanisms that will lead to HOx production and do not rely on weak overtones absorption.

In this work we examine the possibility that excitation in the weak tail region of electronic absorption bands, which are frequently neglected because of the apparent difficulty associated in determining their contributions,[17] can give rise to additional atmospheric radical sources whose influence may be stronger than those arising from

vibrational overtone induced dissociation of the same molecule. The contribution from these weak electronic absorption tails can, in many cases, persist over a wide range of solar-zenith angles as well as wide range of frequencies and hence be significant in modeling tropospheric chemistry. Organic peroxides are one class of molecules where this effect is expected to be important and we illustrate this using CH_3OOH as the prototypical system.

We choose to demonstrate this with MHP because in the first place, the near UV photodissociation of CH_3OOH is known to be a significant source of OH radicals.[7] Secondly, current tropospheric models only include the photochemistry associated with UV photodissociation of CH_3OOH between 210 – 360 nm.[2] Several laboratory studies[18,19] have shown that CH_3OOH absorbs strongly over this wavelength region resulting in excitation to a dissociative electronic excited sate and the concomitant production of OH photofragments with near unity quantum yield.[20-22] We demonstrate that photons in selected regions between 365 – 640 nm can also photodissociate CH_3OOH. Photochemistry over the 365 – 640 nm spectral region has not been investigated previously and covers excitation within the continuum tail of the molecule's first electronic absorption band and extends down to the structured region of the fourth overtone of its OH stretching vibration; the $5\nu_{OH}$ band is the lowest OH stretching vibrational overtone state having sufficient energy to undergo unimolecular dissociation with unit quantum yield. We also project our findings with CH_3OOH and compare them with the near-UV photodissociation of HO_2NO_2. A comparison between the near-UV photochemistry and overtone initiated dissociation is also presented.

10.2 Experimental

The experimental apparatus used for measuring the UV and overtones absorption cross-sections of CH_3OOH is similar to the apparatus used in Chapter 2 and Chapter 6. The synthesis of MHP is outlined in Chapter 6. Tunable photolysis light covering the region between 365 – 405 nm is generated by sum frequency mixing (using the MCC-I crystal) of a dye laser (Continuum: ND60) output with that of a Nd:Yag laser's fundamental (Continuum: NY82-20). The tunable photolysis light is introduced into the cell and the OH fragments generated from the photodissociation are monitored by laser-induced fluorescence (LIF) at 308 nm using a second Nd:Yag (Continuum: NY81-20) pumped dye laser (Continuum: ND60). For excitation of the CH_3OOH $5\nu_{OH}$ vibrational overtone band in the 600 – 640 nm range, the dye laser output of the photolysis laser system is used directly as described in Chapter 6.

A 355 nm light is also introduced into the cell in order to provide a reference point for the absorption cross-section. The beam is generated from the third harmonic of the Nd:Yag laser (Spectra Physics: GCR-270). The absorption cross section at 355 nm is known from previous measurements to be $\sim 2.1 \times 10^{-22}$ cm^2/molecule.[19] The fixed wavelength reference beam has the same beam diameter and power densities as the near-UV wavelengths generated by the NY82-20 laser system. The beam enters the cell collinearly with the tunable photolysis beam. Figure 10.1 shows the experimental schematic used to obtain the absorption cross-sections. The pressure in the cell is typically set around 2 Torr by the addition of nitrogen or argon buffer gas to the 30 mTorr CH_3OOH sample. The time delay between the excitation and probe lasers is set to ~2 μs providing with about ~40 collisions in order to thermalize the nascent OH fragments. We conduct the experiments under large number of collisions because the

populations of the OH fragment resulting from excitation at 355 nm and 619.6 nm are expected to be significantly different with excitation at 355 nm giving rise to larger number of populated OH rotational states. To verify our thermalized OH product results, we also measure the total OH population from the reference and the overtone excitation under nascent conditions without the addition of nitrogen buffer gas at short temporal delays (15 ns). These measurements are conducted to ensure that under "high" pressure conditions there is sufficient number of collisions to equally thermalize the two OH rotational distributions.

Comparing back-to-back yields of OH at the desired photolysis wavelength with that from the 355 nm reference beam at 30 shots/bin and normalizing for the laser powers, gives us an estimate of the absorption cross-section at the desired wavelengths relative to the known value at 355 nm. Typical pulse energies used at 355 nm and 365 – 405 nm are 2.2 – 2.5 mJ and for the overtone laser at ~619.6 nm are 40 – 45 mJ. The pulse energies are monitored right in front and right past the photolysis chamber before and after the collection of each data set.

10.3 Results

The absorption cross-sections for CH_3OOH measured at several selected points between 365 – 640 nm and their uncertainties are given in Table 10.1. These values are obtained by comparing the average signal ($S(\lambda)$) ratio of OH at the particular wavelength to that at 355 nm and multiplying these ratios by the 355 nm absorption cross-section ($\sigma(355)$) from Ref. 19:

$$\sigma(\lambda) = S(\lambda) / S(355\text{ nm}) \times \sigma(355) \qquad [\text{cm}^2\text{ molecule}^{-1}] \qquad (10.1)$$

The corresponding absorption cross-section plot with the uncertainties is shown in Fig. 10.2. The blue curve is obtained by interpolating through the data points. The plot shows that the absorption has a maximum at 355 nm and is decayed slowly to where the absorption at 405 nm is ~70 times weaker than the absorption at 355 nm.

Figure 10.3 gives a detailed view of the CH_3OOH $5\nu_{OH}$ band and their absorption cross-sections. This action spectrum of the vibrational band was generated by scanning the wavelength of the vibrational excitation laser (i.e. photolysis laser) while probing the yield of OH ($^2\Pi_{3/2}$) fragments in their vibrational ground state corresponding to the N=2 rotational level in the presence of nitrogen buffer gas. As with the UV absorption cross-section measurements, the $5\nu_{OH}$ region absorption cross-section is obtained by comparing the average signal levels resulting from back-to-back measurements at 355 nm and 619.6 nm. The overtone absorption cross-section obtained in this region is in excellent agreement with the *ab initio* study presented in Chapter 7. Also, as concluded from Chapter 6, the $5\nu_{OH}$ band lies above the dissociation barrier, hence, we take the dissociation quantum yield associated with the $5\nu_{OH}$ excitation to be unity. Under atmospheric conditions, as collisions with background gases in the atmosphere (mainly nitrogen), are expected to remove ~100 – 200 cm^{-1} of energy on every collision,[2] six or more collisions will be required to remove enough energy to quench the dissociation of a CH_3OOH molecule excited to the $5\nu_{OH}$ level. Under tropospheric conditions, at collision rate of 1×10^7 s^{-1} $Torr^{-1}$, this process will take ~7 ns. As mentioned in Chapter 6, varying the time delay between the vibrational overtone excitation laser and probe laser while looking at the time evolution of the OH fragment in our experiment, reveals that the

dissociation from the $5\nu_{OH}$ level occurs on a time scale faster than ~5 ns (which is the temporal resolution limit in our measurements). From these observations we conclude that dissociation of CH_3OOH from the $5\nu_{OH}$ level, occurs sufficiently rapidly and sufficiently above the dissociation threshold to be unaffected by collisions under atmospheric conditions.

The absorption spectrum of CH_3OOH in the two regions (UV + VIS) is shown in Fig. 10.4, where the dashed line on the electronic absorption curve represents previous measurements and the solid line represents present results obtained by interpolating through the data points of Table 10.1. *Ab initio* calculations indicate that although there are three excited singlet electronic states, only one of the states is likely responsible for absorption in this region.[23] As the excitation wavelength is increased towards the visible ($\lambda > 450$nm) in Fig. 10.4, we enter the spectral region where the CH_3OOH absorption is dominated by vibrational overtone excitation resulting in the dissociation of the molecule on its ground electronic surface. We consider only the $5\nu_{OH}$ band of CH_3OOH, occurring in the vicinity of 620 nm, as this is the lowest order OH stretching overtone state having unit dissociation quantum yield (at $4\nu_{OH}$ the dissociation quantum yield is estimated to be about 0.3 – 0.5 %). Figure 10.4 also shows the photon flux emitted by the sun at 10 km.[24] The blue trace corresponds to total solar flux when the sun is at 20^o (around midday) and the red trace corresponds to total solar flux when the sun is at 90^o (around 6 pm; sundown). From the plot it is clear that at high solar zenith angles aside from the fact that the transmitted light emitted by the sun is depleted at all wavelengths due to the longer absorption path, there is also a preferential depletion of UV radiation transmitted into the

troposphere. Hence, the plot implies that at high SZA the longer wavelength are likely to be important. These concepts will be developed further in the following section.

10.4 Discussion

The UV absorption cross-sections shown in Fig. 10.2 and Table 10.1 appear to be structureless. This lack of structure is consistent with the fact that the low-lying electronic excited states of MHP are not bound. In the 3 – 3.5 eV vertical excitation regions which are accessible with our excitation photon, Watts and Francisco have shown in an *ab initio* study[23] that the 2^1A is accessible if sufficient ground state excitation is deposited along the O–O reaction coordinate. Interestingly, H_2O_2 has a similar electronically excited structure as CH_3OOH.[23] In fact, in several other hydroperoxides such as HO_2NO_2,[25] and HOONO,[26] promoting of electron via the $n \rightarrow \pi^*$ transition is the main dissociation pathway at these excitation wavelengths. The similarities in the electronic structure of these molecules suggest that hydroperoxide molecules such as $HOCH_2OOH$,[27] and t-butyl hydroperoxide are likely to also have similar absorption cross-sections at the tail of the absorption region.

The $5\nu_{OH}$ overtone action spectrum is shown in Fig. 10.3. This action spectrum is converted to absorption spectrum by measuring the peak cross-section of MHP at ~619.6 nm. We focus on this band since it is the lowest lying vibrational state where the dissociation quantum yield is unity. We note however, that absorption and dissociation from the $6\nu_{OH}$ (~532 nm) and $7\nu_{OH}$ (~ 470 nm) vibrational bands can also occur, but these excitations are expected to be substantially weaker as vibrational overtone cross-sections decrease roughly a by an order of magnitude for each unit increase in the order of the overtone.[15] Thus, by only considering the $5\nu_{OH}$ overtone band our present analysis

gives a fairly accurate, although strictly speaking, a lower limit estimate, of the total contribution coming from these neglected absorption features.

In figure 10.4, the full absorption features including the $5\nu_{OH}$ overtone of CH_3OOH are shown. In order to assess the importance of excitation arising from the tail of the CH_3OOH electronic absorption between 365 – 405 nm and the $5\nu_{OH}$ vibrational overtone band under tropospheric conditions, we have calculated the enhancement of the photolysis rate due to inclusion of this previously neglected spectral region. In the figure, also plotted in blue and red respectively, are the solar flux corresponding to an altitude of 10 km and a solar zenith angle of 20^o and 90^o.[24] We see from the figure that although the absorption cross-section for CH_3OOH peaks at short wavelengths, the solar flux reaching the troposphere at these wavelengths ($\lambda < 290$) is very much attenuated by the upper atmosphere. The partial photolysis rate, J_λ, for particular wavelength range is given by:[28]

$$J_\lambda = \sigma(\lambda) \times I(\lambda)\, d\lambda \ [s^{-1}\ nm^{-1}] \qquad (10.2)$$

In Eq. 10.2 the terms $\sigma(\lambda)$ and $I(\lambda)$ are the respective wavelength dependent absorption cross section and solar flux. Hence under *tropospheric* conditions, even relatively weak absorptions features occurring in the near-UV and visible region of the spectrum, where the solar flux is high, can contribute significantly towards the overall photolysis rate. Figure 10.5 shows the integrated J_λ value for methyl hydroperoxide over the absorption region under atmospheric conditions at altitude of 10 km and a solar zenith angle of $\theta = 90^o$. The area shaded in gray represents current wavelengths which are considered in atmospheric modeling while area shaded in blue represents wavelengths which are considered here to carry significant contribution to the total photolysis rate. At this

altitude and SZA we find a maximum in the photolysis rate at $\lambda \approx 330$ nm. We also find that while the shorter wavelengths ($\lambda < 290$ nm) have a much larger absorption cross-section (see Fig. 10.4), in the troposphere, their contribution to the photolysis rate is negligible. Only at wavelengths where $\lambda > 290$ nm, photolysis may occur and lead to OH production. It is also important to note that while it is likely, as seen from the figure, that photolysis contribution from the overtone is small, the $\lambda > 360$ nm region appears to have significant contribution to the total photolysis rate of CH_3OOH.

To obtain quantitative data for the near-UV and overtone dissociation rate relative to the dissociation at shorter wavelengths we calculate the percent enhancement defined as:

$$\% \text{ enhancement} = J(\text{tail}) / (J(\text{tail}) + J(\text{UV})) \times 100 \qquad (10.3)$$

Where J(tail) corresponds to photolysis rate resulting from excitation in the 365 – 640 nm region and J(UV) corresponds to excitation in the 230 – 365 nm region. Figure 10.6 displays the enhancement in the photolysis rate arising from inclusion of the new absorption data for the altitudes of 1, 5 and 10 km as a function of solar zenith angles. We find that the photolysis rate enhancement varies between ~7% to about 20% depending on the particular range of solar zenith angle considered. Decomposing this enhancement to extract the relative contribution arising from electronic absorption versus vibrational excitation, we find that as expected, dissociation initiated through excitation of the $5\nu_{OH}$ vibrational overtone band of CH_3OOH contributes a maximum of ~1.8 % to the overall enhancement; this is occurring at a solar zenith angle of ~90^o. Donaldson and coworkers have observed similar findings in their overtone analysis of nitric acid and hydrogen

peroxide.[12] Thus, the major portion of the calculated ~20% enhancement in the OH yield that occurs at a solar zenith angle of ~90^{o}, is due to excitation in the electronic absorption tail and illustrates the important influence that these weak electronic absorptions can have on tropospheric radical production.

Interestingly, Donaldson *et al.* have also shown that with PNA, a molecule which undergoes dissociation from low-lying overtones ($\geq 2\nu_{OH}$), its overtones contribute amply to the % enhancement.[12] To test whether with PNA the "tail" of absorption competes with its overtone initiated photo-dissociation, we recalculate the % enhancement using the near-UV "tail" from methyl hydroperoxide with overtone absorption cross-sections provided in Ref. 29 and UV cross-sections from Ref. 2. These PNA absorption cross-sections are shown in Fig. 10.7. The absorption cross-section at $2\nu_{OH}$ is scaled in order to account for the dissociation quantum yield based on the work in Chapter 2. Unlike in the situation with methyl hydroperoxide, the low-lying overtones have significant absorption cross-section which clearly, compete even with the absorption at short wavelengths. The percent enhancement from PNA is shown in Figs. 10.8(a) and 10.8(b) at 5 km as a function of SZA. The figure shows that without including the contribution from overtones (Fig. 10.8(a)), the % enhancement from PNA is comparable to that from methyl hydroperoxide ranging from 7 – 27 % for the various solar zenith angles. This finding is important as it illustrates that indeed CH_3OOH can be used as a prototype for other hydroperoxide molecules which are considered to contribute to the HOx budget. However, as Fig 10.8(b) shows, when including the overtones ($2\nu_{OH}$ and $3\nu_{OH}$) of PNA, the total % enhancement from tail + overtone is increased significantly varying from few hundreds to few thousands percent as a function of solar zenith angle. This indicates that

in the case of PNA, or, in general, molecules with low lying dissociative vibrational states such as $2\nu_{OH}$ and $3\nu_{OH}$ will produce HOx more readily on the ground state than from the UV absorption tail. These findings highlight the differences between molecules which are considered reservoir species and molecules which are considered temporary reservoir species. In the latter, the near-UV photodissociation cannot compete with photo-initiated overtone photodissociation.

10.5 Conclusions

The present experimental findings demonstrate that excitation of weak absorption features in the region between 365 – 640 nm, can photodissociate CH_3OOH to give OH fragments with unit quantum yield. The relatively large concentration of CH_3OOH in the troposphere, the unit quantum yield associated with the dissociation process, combined with the fact that this dissociation is initiated by the portion of the solar flux that readily penetrates into the troposphere, and hence can initiate dissociation over a broad range of solar zenith angles, makes this OH source important. As CH_3OOH is the prototypical organic hydroperoxide molecule, one can expect similar photochemistry and contributions from other organic hydroperoxides and inorganic hydroperoxides as shown with PNA.[30]

The findings indicate that the percent enhancement for HOx budget from CH_3OOH is ~20 % and from HO_2NO_2 is ~25 %. Since OH radicals are central to determining the oxidative capacity of the atmosphere, photodissociation from these weak absorption features will need to be included in future modeling studies in order to more completely understand the tropospheric OH budget. However, for atmospheric molecules which have low-lying dissociative vibrational overtones such as HO_2NO_2, HOONO and

the recently investigated HO_3 molecule,[31] the dominating process is likely to remain the overtone initiated photodissociation as originally proposed by Donaldson and coworkers.[12] Therefore, we can conclude that the overtones of transient hydroperoxides, or temporary reservoir species, are more important than their UV absorption tail.

Lastly, the present measurements highlight the need to measure absorption cross sections for molecules over a wider dynamic range, especially over the wavelength regions where the solar flux is high, in order to fully quantitate their contributions to atmospheric photochemistry. Recently, similar efforts to characterize another important atmospheric hydroperoxide by Roehl *et al.*,[27] and Fry *et al.*,[32] have shown that photochemically speaking, hydroxymethyl hydroperoxide behaves similarly to methyl hydroperoxide. HMHP is discussed in further details in Chapter 11.

10.6 Acknowledgements

Chapter 10, in part, is a reprint of the material as it appears in Proceedings of the National Academy of Sciences 102, 7449 (2005). J. Matthews, J. S. Francisco, and A. Sinha, National Academy of Sciences of the USA, 2005. The dissertation author was the primary investigator and author of this paper.

Table 10.1: Absorption Cross-Sections for CH_3OOH

Wavelength [nm]	σ [$\times 10^{-22}$ cm^2 molecule^{-1}]
355	2.1 [a]
365	1.14 ± 0.05
370	0.75 ± 0.05
375	0.52 ± 0.05
380	0.40 ± 0.06
383	0.30 ± 0.05
387	0.21 ± 0.06
390	0.14 ± 0.06
395	0.07 ± 0.05
400	0.06 ± 0.05
405	0.03 ± 0.05
620 [b]	0.036 ± 0.004

[a] Reference 19.

[b] Cross sections for the entire $5\nu_{OH}$ band is given in Fig. 10.3.

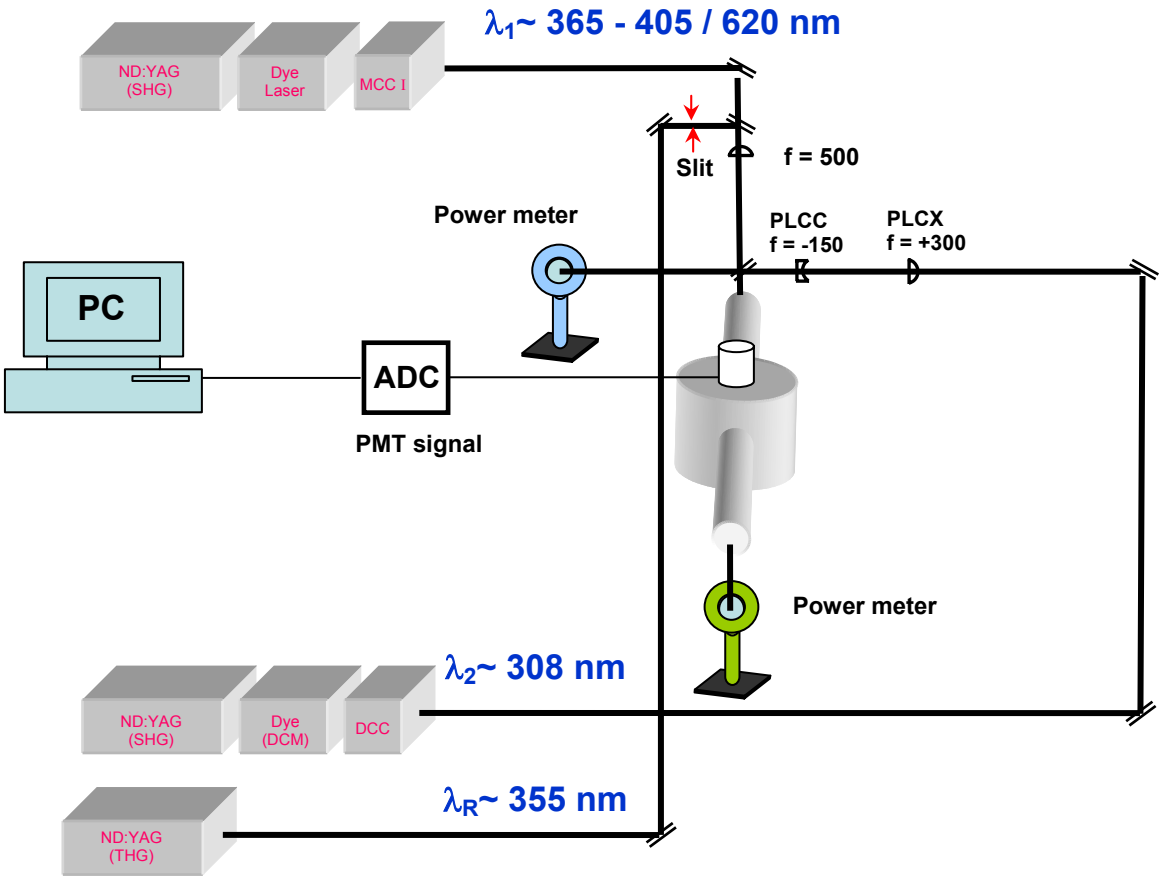

Figure 10.1: Schematic of the experimental apparatus. The tunable near-UV/VIS used for the electronic and vibrational excitation (λ_1) is generated by the NY82-20 laser system. The reference 355 nm beam is generated by the third harmonic of the MOPO system (λ_R). The UV radiation used to probe the OH transition via the $A - X(0,0)$ diagonal transition is generated by the doubled output of the NY81-20 dye laser system(λ_2). The temporal delay between the pumps and probe lasers is set to 2 μs and the probe laser is co-propagating with the other lasers. A set of plano-convex (+300 mm) and plano-concave (-150 mm) lenses collimate the probe beam to reduce scatter light. [File: F10.1_apparatus]

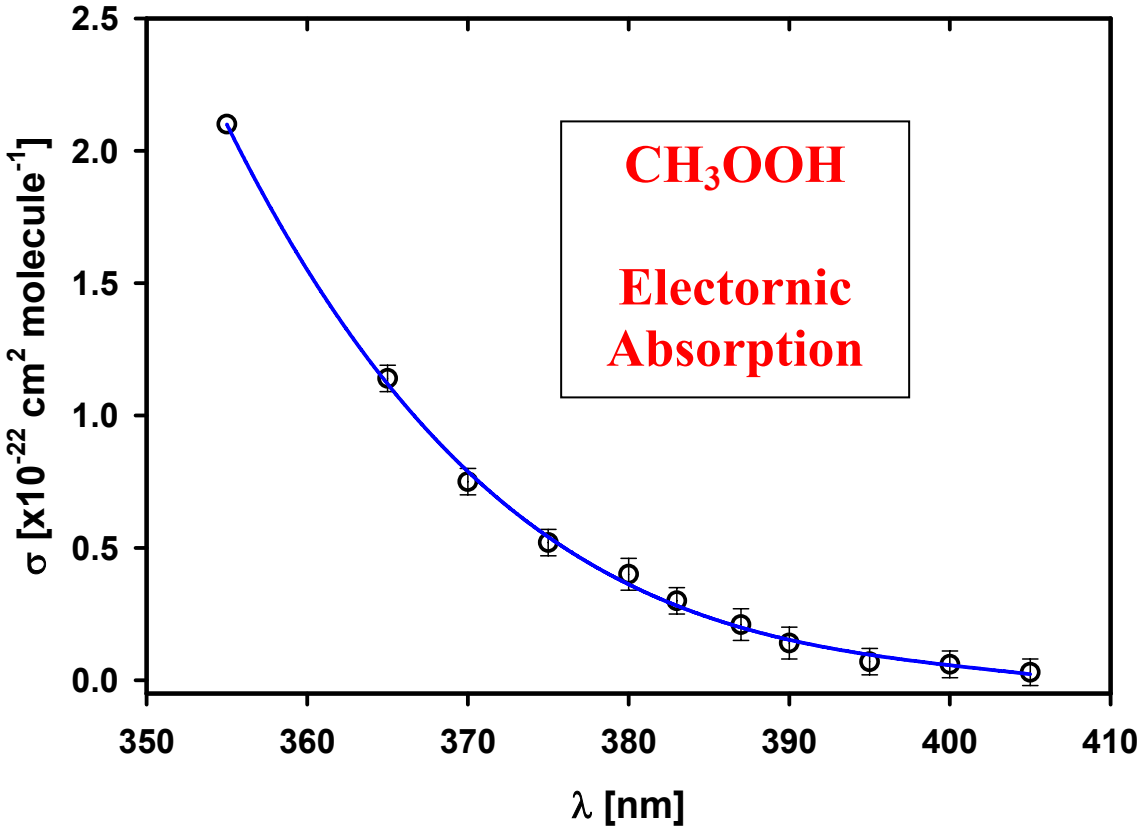

Figure 10.2: The room temperature electronic UV absorption cross-sections of methyl hydroperoxide generated by excitation from molecule's ground state. The solid line represents interpolation through the data points in the 355 – 405 nm absorption region. The cross-section for this absorption is normalized relative to the electronic absorption cross-section at 355 nm.[19] [File: F10.2_xsections]

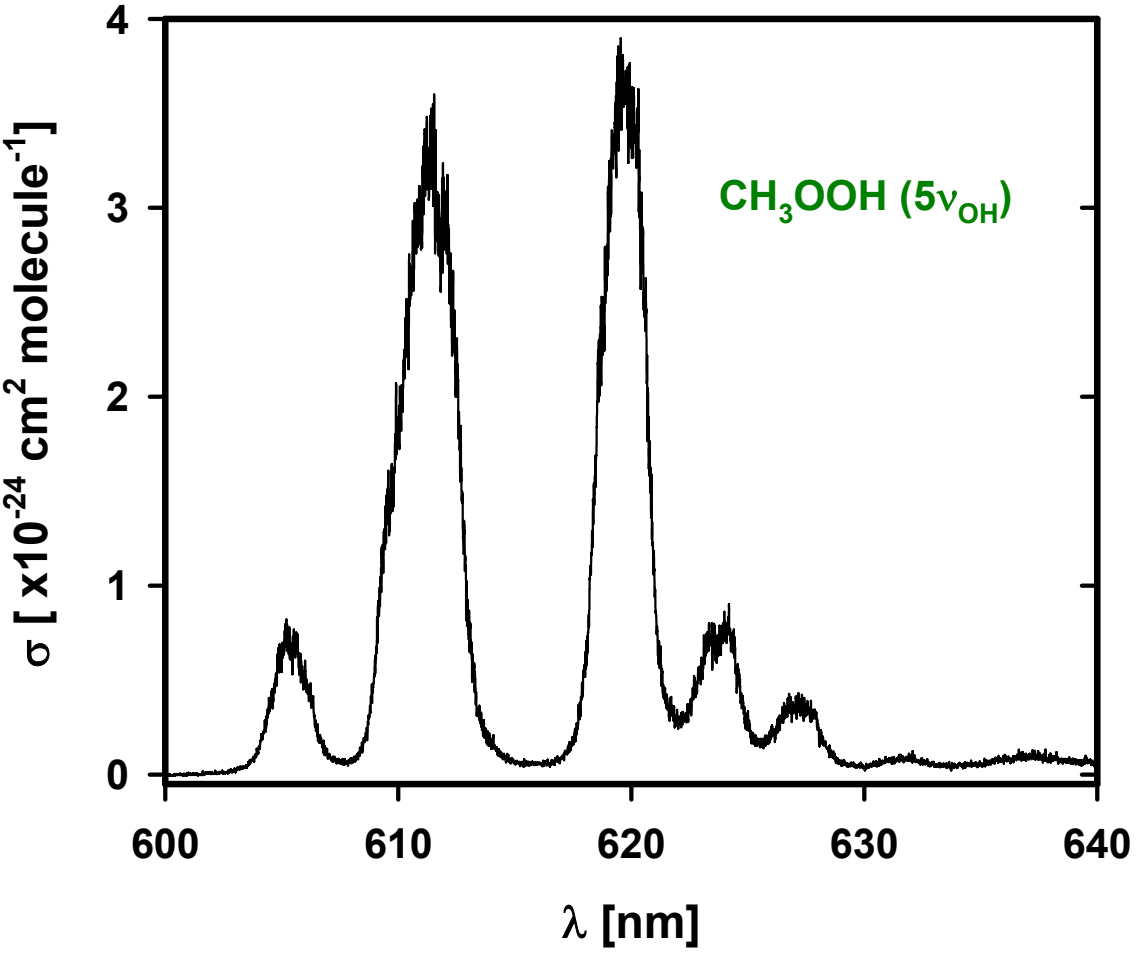

Figure 10.3: Room temperature action spectrum of the CH_3OOH $5\nu_{OH}$ band between 600 – 640 nm. The cross-section for this band is normalized relative to the electronic absorption cross-section at 355 nm.[19] The peak absorbance of $\sigma = 3.95 \times 10^{-24}$ occurs at λ = 619.607 nm [File: F10.3_5nu]

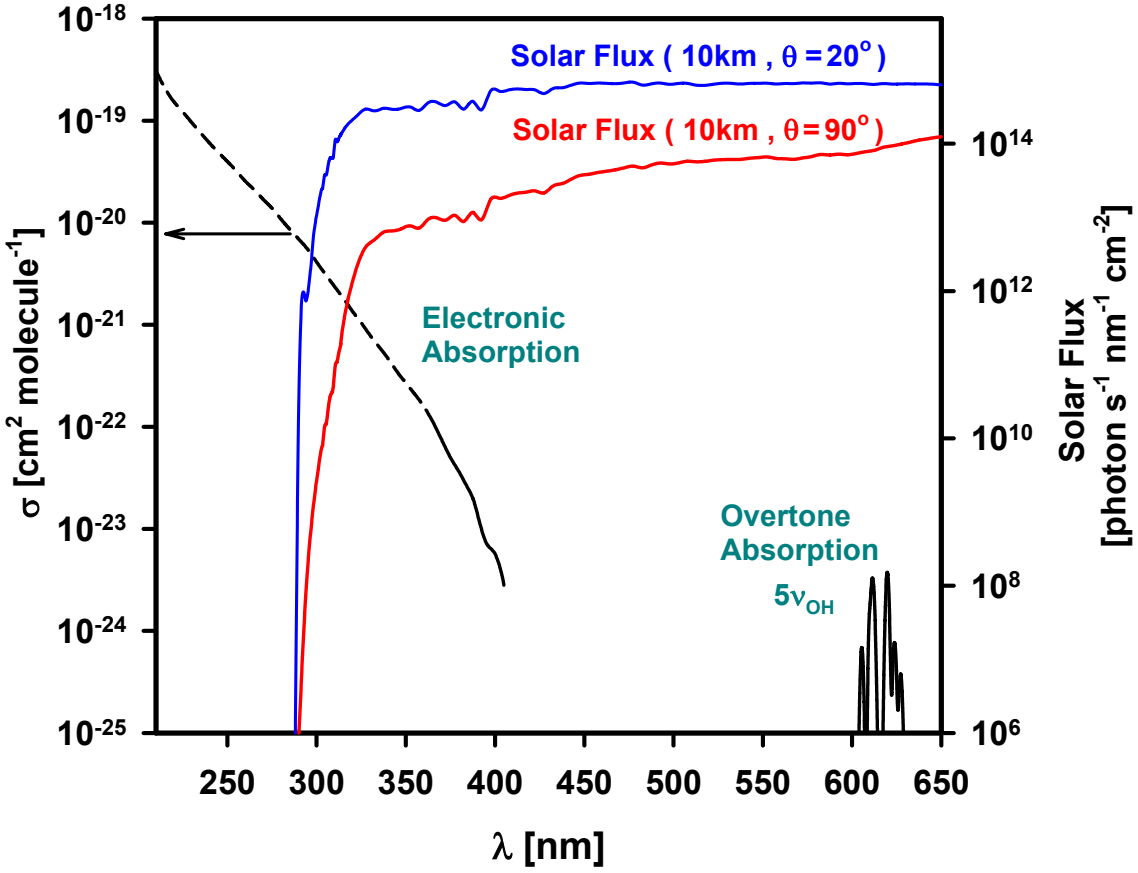

Figure 10.4: The UV electronic absorption data reported in Refs. 2, 18-19 is represented by the black dashed line. The black solid line represents interpolation through the present absorption data. The blue and red solid lines show the solar flux over the region of 10 km and zenith angle of 20° and 90° respectively.[24] The observed $5\nu_{OH}$ vibrational overtone band is also shown in black between 600 to 640 nm. [File: F10.4_solar_flux]

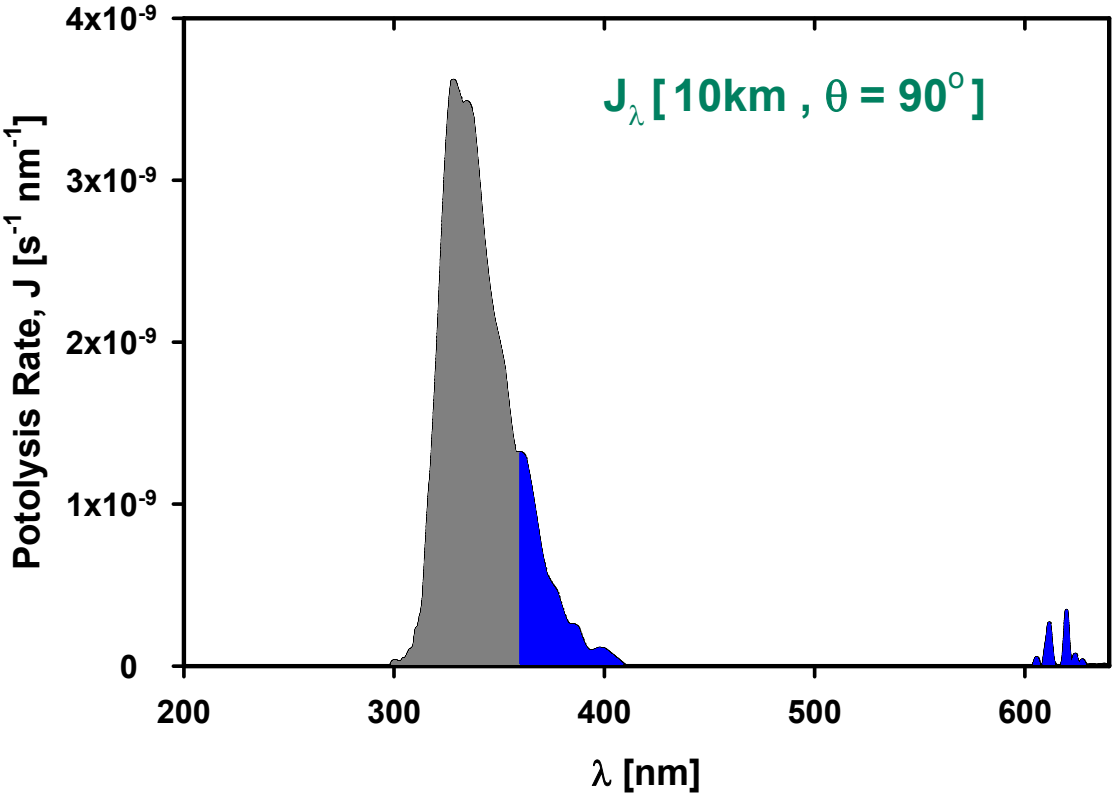

Figure 10.5: The fractional photolysis rate, J_λ as a function of wavelength. The gray shaded area represents the photolysis region currently considered in models while the area in blue is the region under investigation. [File: F10.5_J_value]

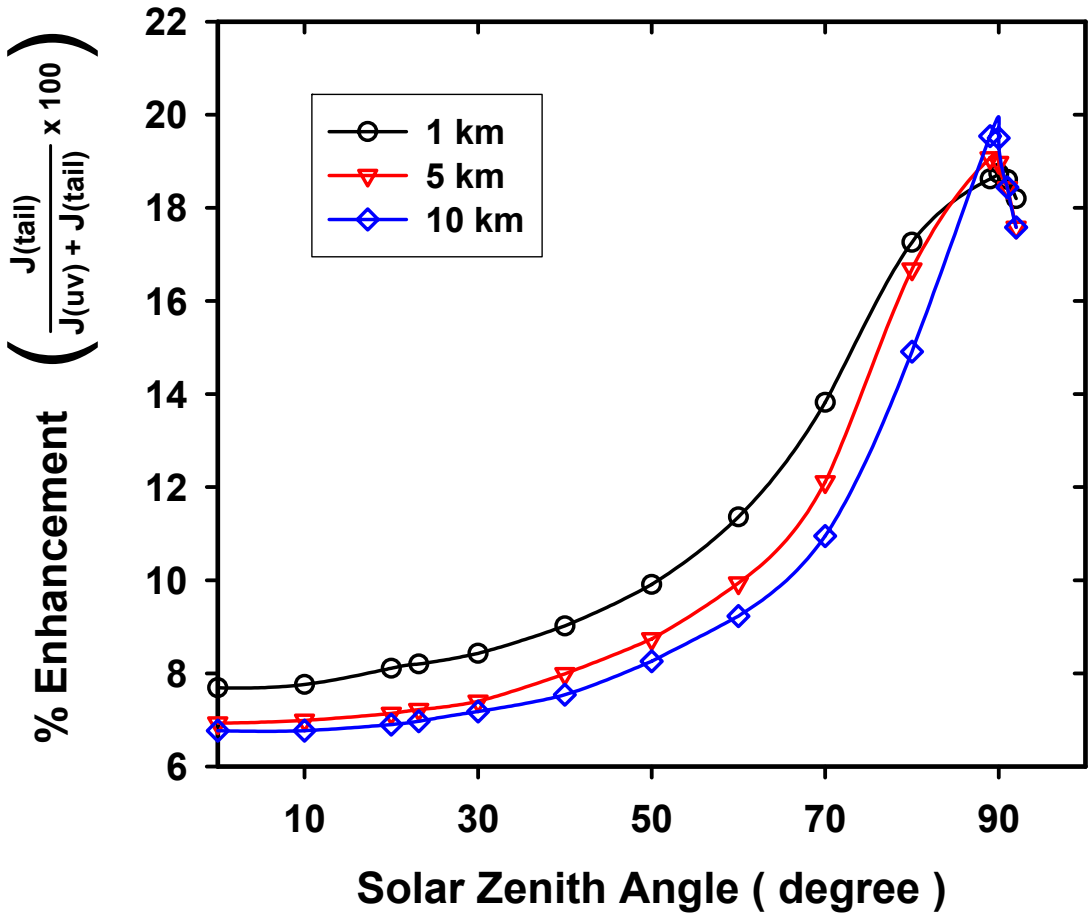

Figure 10.6: The percent enhancement in the yield of OH radicals resulting from inclusion of the UV tail absorption between 365 – 405 nm plus the $5\nu_{OH}$ vibrational overtone, for various solar zenith angles and altitudes. The dependent variable is calculated by taking the ratio of photolysis rate of the tail, J(tail), which also includes the overtone and the sum of photolysis rate of the UV, J(uv), covering the 210 – 360 nm and the tail regions. [File: F10.6_enhancement]

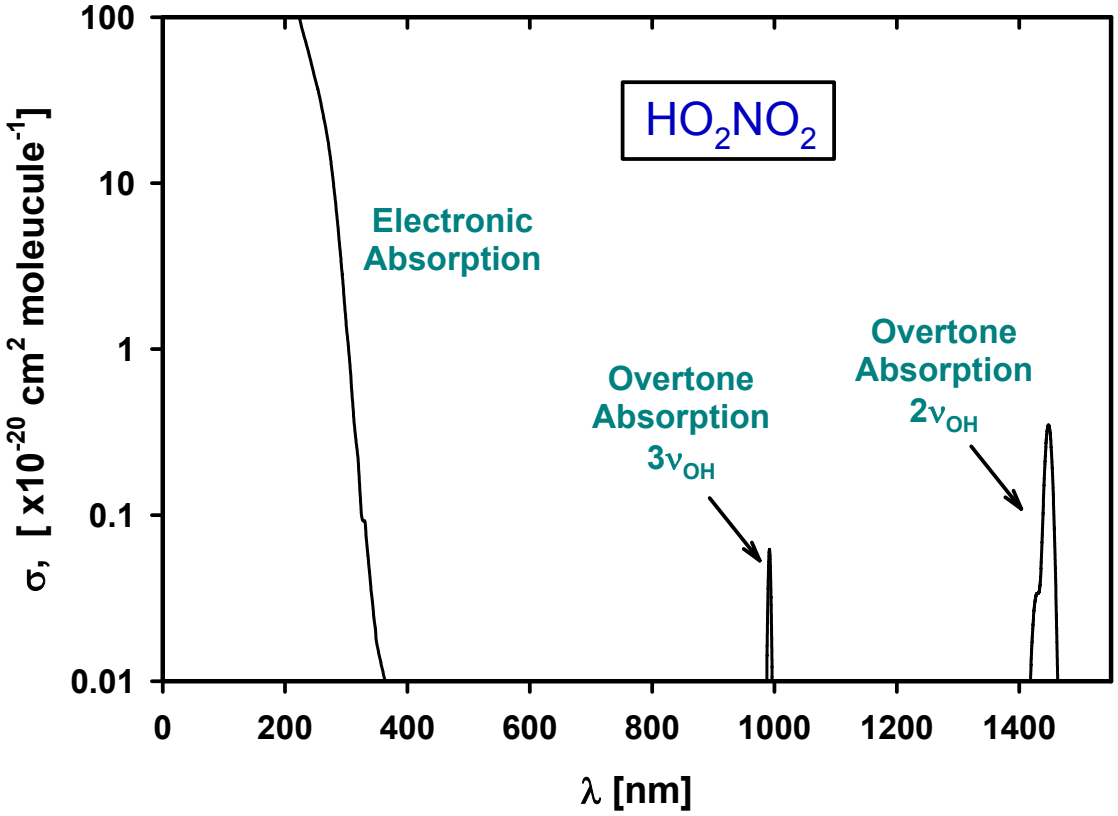

Figure 10.7: The room temperature electronic,[2] and overtones,[29] absorption cross-sections of HO_2NO_2. The solid line represents interpolation through the data points in the 190 – 405 nm absorption region. The cross-section for the $2\nu_{OH}$ is normalized to the dissociation quantum yield from Chapter 2. [File: F10.7_pna_xsections]

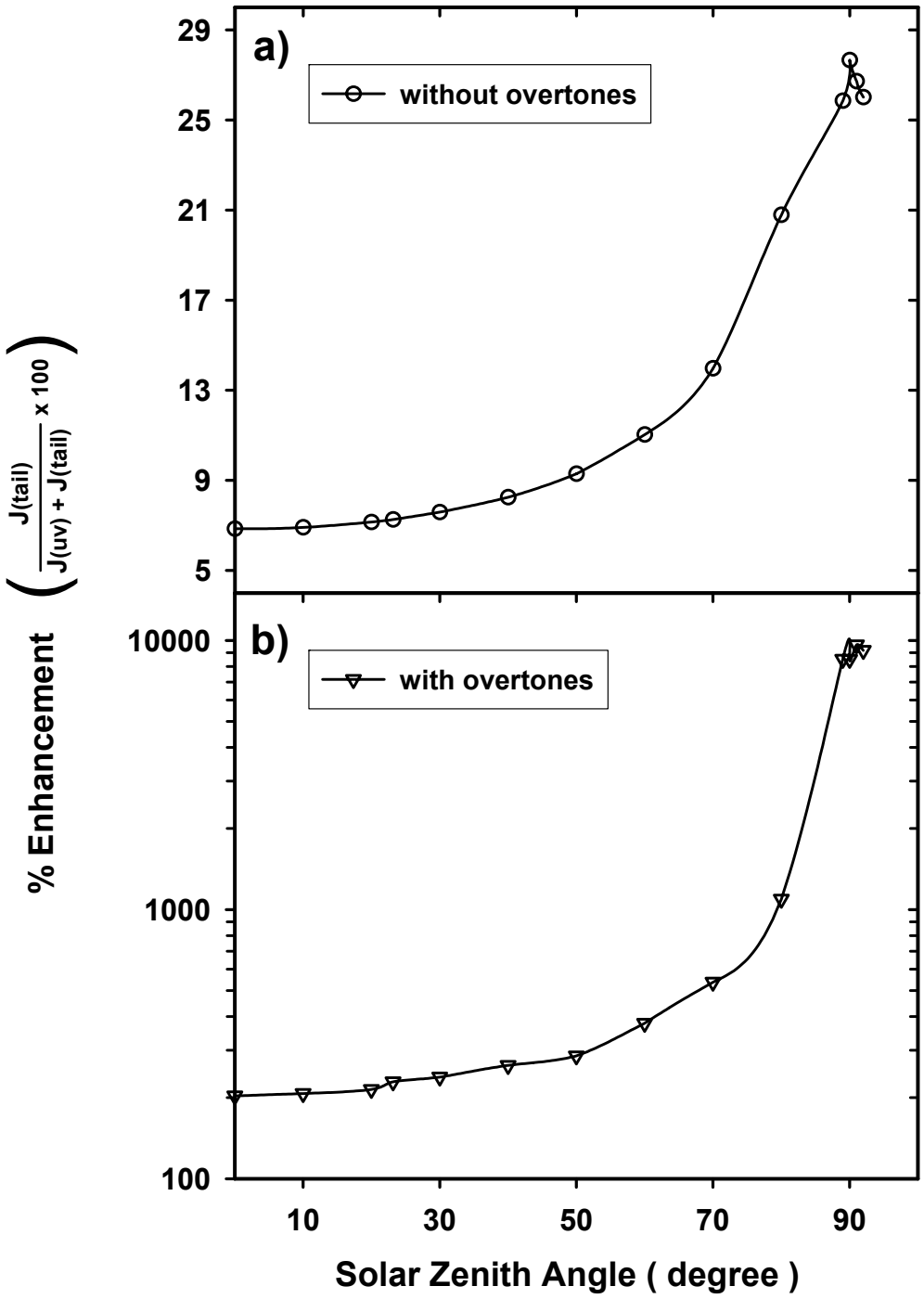

Figure 10.8: The percent enhancement in the yield of HO_2 radicals from PNA resulting from a) inclusion of the UV tail absorption between 365 – 405 nm for the various solar zenith angles at 10 km. b) Including the absorption tail plus the vibrational overtones for various solar zenith angles at 10 km altitude. The plots show that with PNA, the contribution to the % enhancement is much more significant from overtones photolysis than from the near-UV tail. [File: F10.8_pna_enhancement]

10.7 References

1. G. P. Brasseur, J. J. Orlando, and G. S. Tyndall, *Atmospheric Chemistry and Global Change* (Oxford University Press, New York 1999).

2. S. P. Sander, R. R. Friedl, D. M. Golden, M. J. Kurylo, R. E. Huie, V. L. Orkin, G. K. Moortgat, A. R. Ravishankara, C. E. Kolb, M. J. Molina, B. J. Finlayson-Pitts, Chemical kinetics and photochemical data for use in stratospheric modeling, Evaluation #14, *JPL Publ.*, **02-25** (2003).

3. M. Krol, P. J. Van Leeuwen, J. Lelieveld, J. Geophys. Res. Atmos. **103**, 10697 (1998).

4. R. G. Prinn, J. Huang, R. F. Weiss, D. M. Cunnold, P. J. Fraser, P. G. Simmonds, A. McCulloch, C. Harth, P. Salameh, S. O'Doherty, *et al.*, Science **292**, 1882 (2001).

5. P. O. Wennberg, T. F. Hanisco, L. Jaegle′, D. J. Jacob, E. J. Hintsa, E. J. Lanzendorf, J. G. Anderson, R. S. Gao, E. R. Keim, S. G, Donnelly, *et al.*, Science **279**, 49 (1998).

6. P. O. Wennberg, R. J. Salawitch, D. J. Donaldson, T. F. Hanisco, E. J. Lanzendorf, K. K. Perkins, S. A. Lloyd, V. Vaida, R. S. Gao, E. J. Hintsa, *et al.*, Geophys. Res. Lett. **26**, 1373 (1999).

7. L. Jaegle′, D. J. Jacob W. H. Brune, I. Faloona, D. Tan, B. G. Heikes, Y. Kondo, G. W. Sachse, B. Anderson, G. L. Gregory, *et al.*, J. Geophys. Res. **105**, 3877 (2000).

8. R. J. Salawitch, P. O. Wennberg, G. C. Toon, B. Sen, J. F. Blavier, Geophys. Res. Lett. **29**, 1762 (2002).

9. M. J. Prather, and D. J. Jacob, Geophys. Res. Lett. **24**, 3189 (1997).

10. L. Jaegle′, D. J. Jacob, P. O. Wennberg, C. M. Spivakovsky, T. F. Hanisco, E. J. Lanzendorf, E. J. Hinsta, D. W. Fahey, E. R. Keim, M. H. Proffitt, *et al.*, Geophys. Res. Lett. **24**, 3181 (1997).

11. F. Ravetta, D. J. Jacob, W. H. Brune, B. G. Heikes, B. E. Anderson, D. R. Blake, G. L. Gregory, G. W. Sachse, S. T. Sandholm, R. E. Shetter, *et al.*, *J.* Geophys. Res.-Atmos. **106(D23)**, 32709 (2001).

12. D. J. Donaldson, G. J. Frost, K. H. Rosenlof, A. F. Tuck, V. Vaida, Geophys. Res. Lett. **24**, 2651 (1997).

13. D. J. Donaldson, J. J. Orlando, S. Amann, G. S. Tyndall, R. J. Proos, B. R. Henry, V. Vaida, J. Phys. Chem. A **102**, 5171 (1998).

14. D. J. Donaldson, A. F. Tuck, V. Vaida, Phys. Chem. Earth C **25**, 223 (2000).

15. F. F. Crim, Annu. Rev. Phys. Chem. **35**, 657 (1984).

16. F. F. Crim, J. Phys. Chem. **100**, 12725 (1996).

17. C. G. Waschewsky, R. Horansky, V. Vaida, J. Phys. Chem. **100,** 11559 (1996).

18. M. J. Molina, and G. Arguello, Geophys. Res. Lett. **6**, 953 (1979).

19. G. L. Vaghijiani, and A. R. Ravishankara, J. Geophys. Res. **94**, 3487 (1989).

20. G. L. Vaghijiani, and A. R. Ravishankara, J. Chem. Phys. **92**, 996 (1990).

21. M .A. Thelen, P. Felder, J. R. Huber, Chem. Phys. Lett. **213**, 275 (1993).

22. S. W. Novicki, and R. Vasudev, J. Chem. Phys. **93**, 8725 (1990).

23. J. D. Watts, and J. S. Francisco, J. Chem. Phys. **125**, 104301 (2006).

24. S. Madronich, S. Flocke, J. Zeng, I. Petropavlovskikh, J. Lee-Taylor, Tropospheric Ultraviolet-Visible Model, version 4.1 (2002).
http://cprm.acd.ucar.edu/Models/TUV/Interactive_TUV/

25. C. M. Rohel, T. L. Mazely, R. R. Friedl, Y. Li, J. S. Francisco, S. P. Sander, J. Phys. Chem. A. **105**, 1592 (2001).

26. Y. M. Li, J. S. Francisco, J. Chem. Phys. **113**, 7976 (2000).

27. C. M. Roehl, Z. Marka, J. L. Fry, P. O. Wennberg, Atmos. Chem. Phys. **7**, 713 (2007).

28. B. J. Finlayson-Pitts, and J. N. Pitts Jr., *Atmospheric Chemistry: Fundamental and Experimental Techniques* (Wiley, New York 1986).

29. C. M. Roehl, S. A. Nizkorodov, H. Zhang, G. A. Blake, P. O. Wennberg, J. Phys. Chem. A **106**, 3766 (2002).

30. S. Bauerle, and G. K. Moortgat, Chem. Phys. Lett. **309**, 43 (1999).

31. C. Murray, E. L. Derro, T. D. Sechler, M. I. Lester, J. Phys. Chem. A **111**, 4727 (2007).

32. J. L. Fry, J. Matthews, J. R. Lane, C. M. Roehl, A. Sinha, H. G. Kajaergaard, P. O. Wennberg, J. Phys. Chem. A **110**, 7072 (2006).

Chapter 11

Vibrational Overtone Initiated Unimolecular Dissociation of Hydroxymethyl Hydroperoxide: Thermochemistry and Dissociation Rates

11.1 Introduction

Hydroxymethyl hydroperoxide ($HOCH_2OOH$, HMHP) is the largest hydroperoxide investigated by the dissertation author. Despite of its size, it is an important atmospheric molecule with concentrations ranging as high as 1 – 5 ppbv.[1-5] It is mainly formed via the sequential reactions of ethylene (C_2H_4) with ozone (O_3) and water (H_2O) as follows:[6]

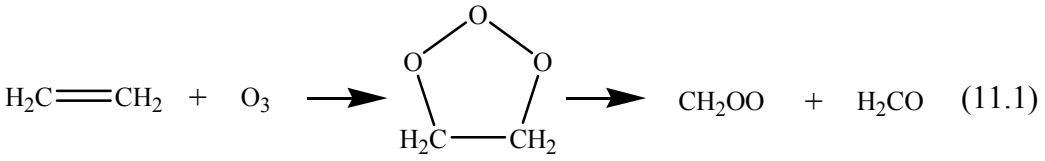

(11.1)

$$CH_2OO + H_2O \longrightarrow HOCH_2OOH\ (HMHP) \qquad (11.2)$$

In the atmosphere, upon absorption of UV photon between 205 and 360 nm,[7,8] HMHP is expected to dissociate to produce 2 • HO_x ($HO_x \equiv OH + HO_2$) molecules and formic acid (CHOOH) in the presence of molecular oxygen (O_2):

$$HOCH_2OOH + h\nu \rightarrow HOCH_2O + OH \qquad (11.3)$$

$$HOCH_2O + O_2 \rightarrow HCOOH + HO_2 \qquad (11.4)$$

As discussed in Chapter 1, the quantifying the sources leading to HOx formation is key to understanding oxidation capacity of the global atmosphere.

Aside from its atmospheric significance,[7] HMHP is an interesting molecule to study in terms of its physical properties in the spirit of some of the other hydroperoxide presented in this dissertation. To start, HMHP contains two OH chromophores that have similar vibrational frequencies, but which are located at different sites relative to the reaction center associated with the breakage of the O-O bond. Hence, one can use direct vibrational overtone excitation to excite these chromophores and investigate differences in the dissociation dynamics arising from excitation of the OH moiety directly attached to the peroxide reaction center versus the OH group situated further away, at the carbon end of the molecule.

Ab initio studies have suggested that HMHP has three stable conformers. At the CCSD(T)/aug'-cc-pVTZ level including zero-point energy correction from the QCISD/aug'-cc-pVTZ level, these conformers have relative energies of 0, 13 and 215 cm^{-1} respectively for HMHP-A, HMHP-B and HMHP-C (see Fig. 11.1).[9] In all three conformers the two hydrogen atoms are situated perpendicular to the OCO and OOC planes (τ_{HOCO} ranging from 68 to 80 deg. and τ_{HOOC} ranging from 74 to 114 deg.). At room temperature, the Boltzmann factors for these conformers are calculated to be 1: 0.94: 0.35. This suggests that all three conformers are likely present in our sample. In fact, overtone FTIR measurements and spectroscopic analysis confirm that indeed, the room temperature vapor of HMHP contains all three conformers conformers.[9]

In this study we present results of investigating the vibrational overtone initiated unimolecular dissociation dynamics of hydroxymethyl hydroperoxide under low pressure room temperature conditions. As with HOONO and methyl hydroperoxide presented in Chapters 4 and 6 respectively, the thermochemistry of HMHP has not been investigated

previously. Thus, we present results of near threshold unimolecular dissociation from excitation of thermal HMHP sample in the region of its third OH stretching overtone ($4\nu_{OH}$) as well as OH fragment product state distribution resulting from excitation of both the $4\nu_{OH}$ and $5\nu_{OH}$ vibrational state. Then, as with HOONO, we use the OH fragment rotational state distributions from the $4\nu_{OH}$ and $5\nu_{OH}$ unimolecular dissociations in conjunction with phase space theory[10] simulations to estimate D_0 for HMHP. Since the structure of $HOCH_2OOH$ is similar to CH_3OOH with hydrogen atom on the carbon displaced by an additional oxygen atom, we expect that the bond dissociation energy occur around excitation of these overtones (see Fig. 11.2). Recent absorption cross-sections measurements of HMHP by Roehl *et al.* have hinted that the topology of the excited state is also very similar to MHP as well.[8]

As shown in Fig. 11.2, the peroxide OH dissociation occurs near threshold as a result of excitation of the $4\nu_{OH}$ band. In fact, at these excitation wavelengths we also are able to measure dissociation rates involving excitation of the two OH chromophores. Interestingly, our rate measurements in the $4\nu_{OH}$ region indicate that vibrational excitation of the lower energy peroxide OH stretch (ν_2) in HMHP results in a unimolecular dissociation rate that is ~ 40% faster than that arising from excitation of the higher frequency alcohol OH stretch (ν_1), thus suggesting the presence of mode selective behavior in this molecule.

Although the vast majority of studies involving molecules excited above their reaction threshold satisfy the requirements for rapid intramolecular vibrational energy redistribution (IVR), there are examples of systems where IVR is slow or incomplete,

resulting in the molecule exhibiting "non-statistical" or mode selective behavior.[11-18] This mode selective behavior, again, is also observed with CH_3OOH where the strong mixing in the methyl group leads to apparently more complete intramolecular vibrational energy redistribution as discussed in Chapter 9.

Additional measurements of the relative unimolecular dissociation rates from excitation of the $4\nu_{OH}$ peroxide and alcohol OH stretching chromophores in $HOCD_2OOH$ (HMHP-d_2) have produced similar trends with the peroxide OH (ν_2) dissociating ~120 % faster than the higher frequency alcohol OH (ν_1). Apart from differences in the dissociation rates arising from excitation of the two *distinct* OH sites in each isotopomer, our measurements also reveal interesting variations in the dissociation rates associated with excitation of *equivalent* OH sites in the two isotopomers (HMHP vs. HMHP-d_2). We find that the dissociation rate resulting from excitation of the alcohol $4\nu_{OH}$ stretching state decreases sharply, by almost a factor of two, in going from HMHP to HMHP-d_2. By contrast, however, the dissociation rate for excitation of the peroxide $4\nu_{OH}$ state is only reduced slightly (~18%) in going to the deuterated isotopomer.

In order to interpret the above findings and compare this behavior with statistical behavior expected for a molecule of this size, we have also carried out RRKM calculations. Implementing these calculations involves using *ab initio* methods, available on GAUSSIAN03,[19] to first investigate the HMHP potential along the O-O bond breaking reaction coordinate in order to locate the transition state for unimolecular dissociation and then calculate the vibrational frequencies and rotational constants associated with this critical configuration. The computed *ab initio* vibrational frequencies for both the critical configuration as well as the reactant HMHP (HMHP-d_2) molecule are

used to estimate the sum and densities of states required for implementing the RRKM theory. As we discuss below, the rate calculations provide additional support for our conclusion regarding the non-statistical nature of the HMHP unimolecular dissociation process. Furthermore, the deviation between the calculated and measured rates appear to suggest that not only is the energy flow restricted in the energized HMHP molecule, but that the extent of this restriction is different for the alcohol versus the peroxide OH stretching states in the region of the $4\nu_{OH}$ band.

11.2 Experiment

11.2.1 Synthesis of Hydroxymethyl Hydroperoxide

HMHP is synthesized in a similar manner described in Ref. 7 and of which, the details were furnished to the dissertation author by the Wennberg group. The chemicals used are given with their respective Fisher catalog numbers. About 7 mL of hydrogen peroxide (H_2O_2) 70 – 90 % is placed in a long narrow test tube. The test tube is immersed in a beaker filled with ethylene glycol bath (Fisher, E178-4) maintained at 333 ± 5 K (60^o C) under constant stirring. Since hydrogen peroxide is not commercially available to us at these concentrations, it is prepared by bubbling N_2 gas vigorously through 50 % H_2O_2 solution (Fisher, H341-500) to evaporate as much of the water as possible by noting the difference between the initial and final volumes.

In a round bottom 100 mL two-neck flask we place about 5 – 15 g of paraformaldehyde (Fisher, +95%, 04042-500) and paraformaldehyde-d_2 (Acros, +99 %, AC27879-0050) in order to generate $HOCH_2OOH$ and $HOCD_2OOH$ respectively. The flask is capped with a single-hole rubber stopper with a ¼ inch tube inserted through, facilitating a slow, gentle flow of nitrogen carrier gas over the solid paraformaldehyde

powder. The second neck is attached to a glass port containing a piece of glass wool (Fisher, 11-390) which acts as filter, preventing the powder from directly flowing to the H_2O_2 sample. The flask is placed on a second hotplate maintained at 383 ± 10 K (110^o C). At this temperature range, evaporation of mono formaldehyde is maximized. It is important to note that at temperature greater than 120^o C paraformaldehyde becomes liquid and at 178^o C it becomes vaporous. In order to prevent contamination of the H_2O_2 with paraformaldehyde, which could lead to formation of bis-HMHP ($HOCH_2OOCH_2OH$),[20] it is important to keep the flask within the above temperature range. The formaldehyde/N_2 vapor mixture is flowed into the H_2O_2 filled test tube through $^1/_8$ inch OD tubing. Typically, the synthesis is left to run overnight for a period of 15 – 18 h. Do however, watch for variations in the paraformaldehyde temperature and N_2 gas flow rate. The resulting product, a mixture of H_2O_2 / H2O / HMHP, is transferred to a glass vial stored in a freezer at -20^o C for a period of up to several months. Small amounts (1 – 2 mL) of the raw sample are used at a time.

11.2.2 Experimental Apparatus

The experimental apparatus used for investigating HMHP and HMHP-d_2 is identical to the experimental apparatus used to study the unimolecular dissociation of methyl hydroperoxide in Chapter 6 (see Fig. 6.2). HMHP is generated in a manner described above and about 1 – 2 mL of the raw, unpurified sample is placed in a round bottom flask, situated inside a sturdy Plexiglass housing, for the duration of the experiments. The Plexiglass box serves as a barrier against potential peroxide explosions which have occurred at the Wennberg lab.[8,9] Typically, this amount of HMHP sample lasts for about a week worth of experiments. The round bottom sample flask is connected

to the photolysis chamber with ¼ inch tubing. A glass bulb located directly above the sample flask containing ~30 mL of water and is situated outside of the Plexiglass box. It is used after the completion of each experiment to quench the sample with water prior to exposing the sample to atmospheric pressure. This procedure is essential, because the residue left from the neat peroxide sample can explode when the sample is exposed to the atmosphere.

Prior to experimenting, we pump on the raw HMHP sample for several hours (6 – 10 hours) in order to minimize contaminants such as H_2O, HCOOH, and H_2O_2 typically present in the sample.[9] The sample pressure in the photolysis cell is maintained around 60 – 80 mTorr in these measurements. As with methyl hydroperoxide, we investigate the unimolecular dissociation of HMHP in the regions of the third ($4\nu_{OH}$) and fourth OH stretching overtones ($5\nu_{OH}$) with the Continuum NY82-20 and NY81-20 laser systems. The overtone excitation dye laser (λ_1) operates in the region of 600 – 650 nm (Rhodamine 640 + DCM mixture, 40 mJ/pulse) for the $5\nu_{OH}$ experiments and in the 720 – 770 nm region (LDS 750 + LDS 765 mixture, 20 mJ/pulse) for the $4\nu_{OH}$ measurements. The OH photofragments resulting from unimolecular dissociation are probed via the *A*–*X*(0,0) transition at ~308 nm (λ_2). The pump-probe delay is typically fixed at 20 ns for measurement of the fragment product state distribution while this delay is scanned in the unimolecular dissociation rate measurements.

11.3 Results and Discussion

11.3.1 Vibrational Overtone Spectra

The room temperature action spectra of HMHP and HMHP-d_2 in the vicinity of the $4\nu_{OH}$ bands are shown in Figs. 11.3(a)-11.3(b). These spectra were generated by monitoring yields of nascent OH(v=0, $^2\Pi_{3/2}$) fragments in the N=1 rotational states as the wavelength of the vibrational excitation laser is scanned at 0.2 Å/s over the region of the $4\nu_{OH}$ bands and averaging 20 shots/bin. These spectra are obtained after pumping on the sample for an ample period (6 – 10 hrs.) to remove much of the excess H_2O_2 impurity which undergoes single-color two-photon dissociation. The spectra in Figs. 11.4(a) – 11.4(c) shows the variations in the relative $4\nu_{OH}$ band shape and intensities as function of pumping duration. The first panel corresponds to spectrum collected at the beginning of the day after only a few hours of pumping on a fresh sample. After additional several hours, the intensity of the hydrogen peroxide peak at ~13 350 cm^{-1} begin to drop, giving rise to a more pronounced $4\nu_1$ band associated with HMHP at ~13 580 cm^{-1} (see Fig. 11.4(b)). Finally, after a significant pumping period, the signal from H_2O_2 diminishes, and we obtain a fairly "clean" spectrum of HMHP. It is important to note that signal from H_2O_2 is always present and is observed as shoulders in our spectra at $4\nu_{OH}$ and $5\nu_{OH}$ bands as well as in our product state distributions.

One dimensional spectral simulation using an *ab initio* dipole surface and potential along the OH stretching coordinate (CCSD(T)/aug'-cc-pVTZ), suggest that the two most prominent features appearing in the $4\nu_{OH}$ spectrum shown in Fig. 11.3(a) are associated with the two zeroth order OH stretching motions in the molecule, with the feature at lower frequency (13 330 cm^{-1}) corresponding to the peroxide OH stretch (labeled $4\nu_2$) and the one at higher frequency (13 580 cm^{-1}) to the alcohol OH stretch

(labeled $4\nu_1$).[9] As D_0 for breaking the peroxide O-O bond in HMHP is estimated to be ~13 950 cm^{-1} (~39.9 kcal/mol),[9] spectral features associated with the $4\nu_{OH}$ bands lie close to the dissociation threshold. Therefore, it is likely that dissociation quantum yields play a major role with the peroxide OH stretching band (~13 330 cm^{-1}) being of lower intensity than the alcohol OH stretching band (~13 580 cm^{-1}).

As mentioned above and shown in Fig. 11.1, these a*b initio* calculations also reveal that there are three stable conformers of HMHP.[9] Because of the OH stretching frequencies and anharmonicities of these conformers, their bands overlap sufficiently such that they are not resolved in these room temperature experiments. Also shown in Fig. 11.3(b) is the corresponding spectrum of $HOCD_2OOH$ (HMHP-d_2). At the resolution of the present study, the spectra of the two isotopomers look nearly identical over the region of the $4\nu_{OH}$ band.

The spectra for both HMHP and HMHP-d_2 in the $5\nu_{OH}$ spectral region are shown in Figs. 11.5(a) and 11.5(b) respectively. As in the $4\nu_{OH}$ region, there are also two primary features in the $5\nu_{OH}$ region corresponding to the two different OH stretches. The peak at 16 205 cm^{-1} is assigned to the peroxide OH stretch ($5\nu_2$) while the one at 16 550 cm^{-1} is assigned to the alcohol OH group ($5\nu_1$).[9] Also, similar to the third OH stretching overtone, is the signal detected from H_2O_2 in the forth OH-stretching overtone region. At these excitation wavelengths, H_2O_2 undergoes several dissociation processes; namely, single photon unimolecular dissociation, one-color two-photon photodissociation, and three-photon dissociation.[21] Fig. 6.4 in Chapter 6 shows the two former processes taking place, and the latter three-photon signal from H_2O_2 is shown in Fig. 11.6. This signal is

obtain by exciting the transitions of H_2O_2 in the vicinity of the $5\nu_{OH}$ band present in our HMHP sample and by probing the OH fragments with the *same* excitation laser which results in the OH fragment undergoing one-color two-photons transition from the $X^2\Pi$ state to the $A^2\Sigma$ state without the use of the probe laser. In other words, the overtone excitation laser also serves as a probe for the resulting HO + OH fragments.

Also, from Fig. 11.5, unlike in the $4\nu_{OH}$ region, the spectra of the two isotopomers in the $5\nu_{OH}$ region exhibit noticeable differences in the vicinity of 16 550 cm^{-1} corresponding to the alcohol OH stretch. As noted in Ref. 9, Fermi resonance interaction between the zeroth-order $5\nu_{OH}$ state and the $4\nu_{OH} + \nu_{CH}$ combination band, associated with the alcohol OH stretch in HMHP, results in significant state mixing among these vibrational levels, and leads to the splitting seen in the HMHP spectrum in this region. Similar interactions have also been reported in the $5\nu_{OH}$ spectrum of methanol and formic acid.[22,23] Upon deuteration, the lower frequency of the C-D stretch removes the resonance between the $4\nu_{OH} + \nu_{CH}$ combination band and the $5\nu_{OH}$ stretching states of the alcohol moiety resulting in a single peak of higher intensity for HMHP-d_2 shown in Fig. 11.5(b).

Comparing the $5\nu_{OH}$ spectra of the two isotopomers in the region of the peroxide OH stretch we see that at the present resolution, deuteration has very little visible effect on the spectral features in this region. The shoulder seen around 16 600 cm^{-1} in the HMHP-d_2 $5\nu_{OH}$ spectrum, is likely due to slight separation in the OH frequencies of the structural conformers at this higher overtone;[9] this is supported by the presence of a weak, less well resolved, shoulder appearing in the corresponding HMHP peak as well.

11.3.2 OH Fragment Product State Distribution

We probe the OH fragment rotational distribution arising from unimolecular dissociation of HMHP in a manner similar to HOONO and CH_3OOH in Chapters 4 and 6 respectively using the BURST mode at 5 μstep scan rate with 30 shots/bin in the $4\nu_{OH}$ region and 20 shots/bin in the $5\nu_{OH}$ region. The integrated LIF line intensities are converted to relative population using the OH Einstein B coefficients[24] as described in previous chapters and Appendix *C*. These measured OH product state distributions are used to estimate D_0 associated with breaking the O-O bond in HMHP; a parameter which we in turn is also utilized in the RRKM calculations discussed below.

The different panels in Fig. 11.7 display the normalized nascent rotational distributions for the OH ($X^2\Pi_{3/2}$; v"=0) and OH ($X^2\Pi_{1/2}$; v"=0) spin-orbit manifolds resulting from excitation of various spectral features in the HMHP $4\nu_{OH}$ and $5\nu_{OH}$ bands. For excitation at 13 324 cm^{-1} corresponding to the peroxide $4\nu_{OH}$ stretch in panel 11.7(a), poor signal-to-noise prevents us from measuring the OH($^2\Pi_{1/2}$) state populations and only the distribution associated with the lower $^2\Pi_{3/2}$ spin-orbit state is presented. It is important to point out that the feature at 13 324 cm^{-1} has background contribution from HOOH the one-color two-photon photodissociation as well.[21] The OH rotational distribution associated with this two-photon electronic photodissociation process, however, is well characterized[21] and the distribution arising from the unimolecular dissociation of HMHP, shown in Fig. 11.7(a), has this background contribution subtracted out. The raw, un-subtracted OH product state distribution for both HMHP and H_2O_2 is shown in Fig. 11.8. It is clear from the figure that the combined distribution giving rise to a much hotter OH product consistent with the fact that the combined photon energy is ~375 nm. The

contribution from H_2O_2 to the low N- rotational states typically ranges from 20 to 50 % and for N > 5 up to 100 %.

Figure 11.7(b) shows that similarly to the product state resulting from excitation of the peroxide OH, photolysis at 13 580 cm^{-1} corresponding to excitation in the alcohol OH stretch, the maximum in the nascent rotational population for the lower OH ($^2\Pi_{3/2}$) spin-orbit sate occurs at N=1 and then monotonically decrease as the OH rotational quantum number N increases. The less-populated, higher energy $^2\Pi_{1/2}$ spin-orbit state has a maximum at N=2 before decreasing towards zero at higher values of N.

In contrast to the $4\nu_{OH}$ rotational state distributions, which arise from excitation near the dissociation threshold, the OH rotational distributions resulting from excitation of spectral features in the $5\nu_1$ band have a qualitatively different appearance (Fig. 11.7(c)). The OH $^2\Pi_{3/2}$ rotational state distributions from spectral features associated with this higher energy vibrational band exhibit a maximum peaking around N= 2 or 3 before decreasing towards zero at N= 10. Within our detection limits, we do not observe any measurable population in the excited vibrational state of OH from excitation of the HMHP $5\nu_1$ band at 16 580 cm^{-1}.

11.3.3 Phase-Space Simulations and D_0 Estimate

In order to determine how well the measured OH rotational distributions are described by statistical theory, we model them using phase-space theory (PST). As shown in Chapter 4, in using phase-space theory, we invoke the energy and angular momentum conservation constraints and perform the calculations on HMHP analogously to that described for HOONO in Chapter 4 and nitric acid.[25] We approximate $HOCH_2OOH$ (κ =

-0.826) as a prolate symmetric top which have vibrational partition function (q_{vib}) of 3.05 and rotational partition function (q_{rot}) of 38 502.3 calculated based on equations E.1 and E.2 in Appendix *E* respectively. The vibrational and rotational constants for both the parent and fragment molecules used in the phase space calculations are listed in Table 11.1.[19,26]

Apart from the spectroscopic parameters, the dissociation energy, D_0, and long-range attraction parameter, C_6, are also needed to implement the PST calculations. C_6 is given by the sum of the *dipole–dipole* ($C_{d\text{-}d}$), *dipole–induced-dipole* ($C_{d\text{-}id}$), and the *dispersion energy* (C_{disp}) constants:[27]

$$C_{d\text{-}d} = -2/3kT \times (p_1\, p_2)^2 / (4\pi\varepsilon_0)^2 \qquad (11.5)$$

$$C_{d\text{-}id} = -(p_1^2\, \alpha_2 + p_2^2\, \alpha_1) / (4\pi\varepsilon_0)^2 \qquad (11.6)$$

$$C_{disp} \approx -\,^3/_2 \times I_1\, I_2 / (I_1 + I_2) \times \alpha_1\alpha_2 / (4\pi\varepsilon_0)^2 \qquad (11.7)$$

Where p_1 and p_2 are the dipole moments, α_1 and α_2 are the polorizabilities, I_1 and I_2 are the ionization energies of the OH and $HOCH_2O$ fragments respectively. Also appearing in the equations, k is the Boltzmann factor, T is the temperature and ε_0 is permittivity of vacuum. These calculated parameters are given in Table 11.2. See Appendix *B* for "how to" calculate these quantities with GAUSSIAN03. The estimated total attractive interaction parameter C_6 based on these parameter is found to be 1.7 x 10^{-58} erg cm^6.[27] We leave the dissociation energy D_0 as a fitting parameter and determine it by fitting the measured OH rotational state distributions to PST simulations using the above spectroscopic parameters and C_6 coefficient. The phase-space code used in obtaining the D_0 value for HMHP is given in Appendix *E*.

Results of the PST calculations associated with the peroxide $4\nu_2$ band are shown in Fig. 11.9 for three trial D_0 values of 37, 38 and 39 kcal/mol. From these simulations, we find that a value of $D_0 = 38 \pm 0.7$ kcal/mol gives the best fit to the measured HMHP OH rotational product state distributions arising from near threshold dissociation. This value is further confirmed by fitting the OH distributions arising from excitation of the alcohol $4\nu_1$ band at 13 580 cm^{-1} using the same D_0 and C_6 values as shown in Fig. 11.10(a). While the PST simulation fits the $4\nu_1$ data reasonably well, we find that as with the $3\nu_{OH}$ bands associated with HOONO (see Chapter 5), the fits to the $5\nu_1$ band in Fig. 11.10(b) are not as good. This trend likely reflects the breakdown in the applicability of phase space theory for states substantially above the dissociation threshold, where the critical configuration no longer corresponds to a "loose" transition state and vibrationally excited products can form.[28]

11.3.4 Unimolecular Dissociation Rate Measurements

The dissociation rates arising from excitation of various spectral features in the higher energy $5\nu_{OH}$ band are too fast to be measured with our laser system, which has a temporal resolution of ~7 ns. However, in the $4\nu_{OH}$ band we find that the rates are sufficiently slow to directly measure them. Figures 11.11(a) – (b) display results of the rate measurements associated with excitation at the peak of the primary spectral features associated respectively with the $4\nu_{OH}$ bands of HMHP and HMHP-d_2. We obtain these rates measurement by varying the vibrational excitation laser (λ_1) with respect to the LIF probe laser (λ_2) monitoring the OH ($^2\Pi_{3/2}$, N=1, v=0) state under low pressure conditions. The solid lines through the data points in Fig. 11.11 is obtained by a non-linear least

square fit program "tails.udf" written by G. J. Dutton and R. J. Barnes for PeakFit.[29] The code is located in the chapter "udf" folder.

In the case of HMHP, Fig. 11.11(a) compares rates arising from excitation at ~13 330 cm^{-1} ($4\nu_2$) indicated by the closed circle symbols versus excitation at 13 580 cm^{-1} ($4\nu_1$) indicated by the open circle symbols. In addition to measuring the rates at the peak maxima, we have also measured rates at points on either side of the main peaks; points defining the peak's full width at half maximum (FWHM), and find that the variation in rates between a peak maximum and its associated shoulders to be substantially less than that between the respective peak maxima. These rate measurements are shown in Fig. 11.12 and summarized in Table 11.3. Interestingly, as figures 11.11 and 11.12 show, we find that the dissociation rate from excitation of the *lower energy* peroxide $4\nu_{OH}$ stretch of HMHP is ~40% faster than the rate associated with excitation of the higher energy alcohol $4\nu_{OH}$ stretch.

In order to see if these differences in measured rates might be due to differences in internal energies, arising from the presence of underlying vibrational hot bands, we compare the measured OH fragment product state distributions arising from excitation of these bands. As with HOONO $2\nu_{OH}$ band, we expect that transitions not originating from the ground state (i.e hot bands) to generate product state distributions which are warmer due to the initial thermal energy. Figure 11.13 compares the OH ($^2\Pi_{3/2}$) rotational state distributions arising from exciting at 13 324 cm^{-1} ($4\nu_2$) versus that from 13 580 cm^{-1} ($4\nu_1$). Consistent with its higher energy, we find that the OH rotational distribution associated with excitation at 13 580 cm^{-1} is slightly hotter than that arising from

excitation at 13 324 cm^{-1}. Thus, different initial state internal energies do not appear to be the reason for the observed differences in the dissociation rates.

We have also attempted to compare the translational energy associated with the OH + $HOCH_2O$ channel arising from excitation of the $4\nu_1$ and $4\nu_2$ bands. Although the total translational energy associated with excitation of the alcohol OH ($4\nu_1$) is consistent with near threshold dissociation process (E_t [OH + HOCH2O] ≈ 900 cm^{-1}), we find that excitation in the peroxide OH results in translationally hot product (E_t [OH + HOCH2O] ≈ 2500 cm^{-1}). This significant translational energy is the result of interferences arising from H_2O_2 which, we are unable to convolute out due to the relatively modest amount of translational energy in the HMHP compared with H_2O_2 OH fragment.

To further explore the apparent trend in the dissociation rate, we have also carried out analogous measurements on HMHP-d_2, where the two hydrogen atoms attached to the carbon site are replaced by deuterium atoms. As Figs. 11.3(a) and 11.3(b) indicate, the vibrational bands associated with the two OH stretching chromophores in HMHP-d_2 occur roughly at the same frequency as in HMHP. Figure 11.11(b) shows the corresponding rate data from HMHP-d_2 resulting from excitation of its OH chromophores in the $4\nu_{OH}$ region. A comparison of Figs. 11.11(a) and 11.11(b) show that although HMHP-d_2 follows a trend similar to that found in HMHP, with the higher energy alcohol OH stretching state giving rise to a slower dissociation rate compared to the lower energy peroxide OH stretching state, HMHP-d_2 exhibits a much larger differential between the rates for its two OH sites.

In addition to comparing dissociation rates arising from excitation of the two *distinct* OH sites in each isotopomer, we can also compare relative dissociation rates

associated with excitation of *equivalent* OH sites in the two isotopomers (HMHP vs HMHP-d_2). We find that deuteration at the carbon site has a large affect on the dissociation rate associated with excitation of the alcohol OH stretch, increasing its lifetime from 54 ns in HMHP to 100 ns in HMHP-d_2 while it has almost negligible affect on the lifetime associated with the peroxide OH site, where it increases slightly from 39 ns in HMHP to 46 ns in HMHP-d_2. Hence, the measured rates indicate that there is almost a factor of two difference in the rates between the $4\nu_{OH}$ alcohol OH stretch of HMHP versus HMHP-d_2 while for the $4\nu_{OH}$ peroxide OH stretch, the rate changes by only ~18 % between the two isotopomers.

11.3.5 RRKM Calculations

In order to provide a benchmark for comparison with the measured rates, RRKM calculations were carried out on both HMHP and HMHP-d_2. The D_0 value required for the RRKM calculation was obtained from the phase space theory simulations discussed in the previous section. In applying phase space theory, we assumed that the unimolecular dissociation occurred on a potential with negligible barrier. This assumption is reasonable as the reverse reaction involving the association of radicals, the OH and $HOCH_2O$ fragments, is expected to occur with minimal or no barrier. The issue of whether a barrier actually exists along the reaction coordinate is, however, more critical for implementation of RRKM theory.

To check if the HMHP potential contains a barrier along the reaction coordinate, the OPT=QST2 routine in conjunction with unconstrained optimization was used to examine the potential along the peroxide O-O bond dissociation coordinate using GAUSSIAN03.[19] The QST2 routine is initially used in order to obtain the transition

structure by specifying the initial (equilibrium) and final (large O-O bond separation) geometries. We also verify these results by performing unconstrained incremental optimization at the UCCSD(T)/cc-pVDZ stretching the O-O bond and allowing relaxation in all other degrees of freedom similar to the procedure used for generating the HOONO and CH_3OOH torsional potentials (see Chapters 4, 7 and Appendix *B*). The routine reveals the presence of a small ~ 0.9 kcal/mol barrier at a O-O bond separation distance of 2.5 Å. In addition, prior to running the UCCSD(T) calculation, the energy potential surface was also optimized using the UMP2/cc-pVDZ and UCCSD/cc-pVDZ levels. As shown in Fig. 11.14, the routine at the UCCSD level of theory finds the transitions state to be at 2.05 Å. The transition state for HMHP unimolecular dissociation was taken to be this barrier maximum and the vibrational frequencies and rotational constants associated with this critical configuration calculated at the UCCSD(T)/cc-pVDZ level. These computed spectroscopic parameters for the transition state along with those of the reagent molecule are given in Table 11.4.

In implementing the RRKM calculations we treated the rotational angular momentum projection quantum number, K_a, as being adiabatic.[30] Thus, this quantum number is assumed to be conserved in both the energized reactant molecule and the transition state. The rate calculation is carried out by separately considering each thermally populated reactant state characterized by the vibrational and rotational quantum numbers (v, J, K_a) and corresponding ro-vibrational internal energy given by $E_v + E_r(J, K_a)$. Each of these states is then promoted by the vibrational overtone excitation laser photon to generate an energized molecule with energy equal to the sum of the initial

internal energy plus the photon energy. The difference between this total energy, E, and the barrier height E_0, gives the excess energy available for the reaction:

$$E = E_v + E_r(J, K_a) + h\nu \quad (11.8)$$

$$E_{excess} = E - E_0 \geq 0 \quad (11.9)$$

Only energized states having positive excess energy are considered in the calculation. For each such state, the Boltzmann factor $P(v, J, K_a, T)$ is calculated using the expression:

$$P(v, J, K_a, T) = (2J + 1)\exp[-(E_v + E_r(J, K_a))/kT] \quad (11.10)$$

The corresponding unimolecular rate $k(E, J, K_a)$ for each dissociating state is then calculated using the expressions:[31]

$$k(E, J, K_a) = G^{\#}[E - E_0 - E^{\#}_r(J, K_a)]/\ h\ N[\ E - E_r(J, K_a)] \quad (11.11)$$

In the above rate expression, "h" is Plank's constant, $G^{\#}$ is the sum of vibrational states for the transition state at the given energy and N is the density of vibrational states for the reactant molecule. The sum and density of states were calculated using the standard Whitten-Rabinovitch expressions using the scaled vibrational frequencies given in Table 11.4. This procedure is repeated for each thermally populated reactant state having total energy up to 1100 cm^{-1} above the ground state. This involves considering each vibrational state falling within this energy limit, and for each such vibrational state considering values of the rotational quantum number $J \leq 80$. Furthermore, for a given J value, K_a for each state is restricted to the usual range of (2J+1) values. The overall RRKM rate constant is then given by the weighted average over the Boltzmann distribution:

$$k(T) = \sum_{v,J,Ka} P(v,J, K_a,T)\ k(E,J, K_a) \Big/ \sum_{v,J,Ka} P(v,J, K_a,T) \quad (11.12)$$

In the above expression the sum runs over the range of v, J, and K_a states as noted. The code used in calculating the RRKM rate constant is provided in Appendix *D*.

The results of the rate calculation for T = 298 K and several values of D_0 are given in Table 11.5. Looking at the entries associated with HMHP in the upper half of Table 11.5, we see that for a D_0 value of 38 kcal/mole, the RRKM calculation predicts a rate that is in good agreement with the measurement for excitation of the $4\nu_{OH}$ alcohol OH stretch. However, the same calculation predicts that the rate of the corresponding peroxide OH stretch should be substantially slower and gives a value that is ~3 times lower than what is experimentally observed. The RRKM calculation for HMHP-d_2, shown in the lower half of Table 11.5, also exhibit similar deviations when compared with experiment. Looking at the HMHP-d_2 entries in Table 11.5 corresponding to D_0 = 38 kcal/mole, we find that the RRKM calculations again predicts a dissociation rate for excitation of the $4\nu_{OH}$ alcohol stretch that is in accord with measurements (within ~20%). However, as before, the calculation predicts a rate for the corresponding peroxide OH stretch that is substantially slower (by a factor of 6) than what is experimentally observed.

11.4 Summary and Conclusions

This chapter present results on the overtone initiated dissociation of HMHP and HMHP-d_2. The findings provide information about the O-O bond dissociation energies as well as dissociation rates. We estimate that for HMHP, $D_0 = 38 \pm 0.7$ kcal/mole based on phase-space simulations of the OH rotational product state distributions. A comparison of the HMHP D_0 with that of other organic peroxides shows that it is similar in value to that of t-butyl hydroperoxide (37.6 kcal/mole)[32] but substantially lower than our results of

methyl hydroperoxide (42.6 kcal/mole) in Chapter 6. This D_0 value and overtones lifetimes also suggest that under atmospheric conditions, the photolysis rate from the overtones is likely small. Taking the pressure to be $^1/_3$ atm and the dissociation lifetime of 39 ns, under atmospheric conditions (at 8 km), the overtone population will deplete rapidly undergoing ~ 100 collisions mainly with molecular nitrogen and oxygen.

The dissociation rates resulting from excitation of the two distinct OH stretching chromophores in $HOCH_2OOH$ over the region of its $4\nu_{OH}$ band are found to be different, with the lower energy peroxide OH stretch exhibiting a measurable faster rate compared to the higher energy alcohol OH stretch (see figures 11.11 and 11.12). Yet, the OH fragment product state distributions arising from excitation of these two bands, show that the fragment rotational state distribution associated with excitation of the peroxide $4\nu_{OH}$ band at 13 324 cm^{-1} is colder than the distribution arising from excitation of the alcohol $4\nu_{OH}$ feature at 13 580 cm^{-1}. Thus, the observed trend in dissociation rate does not appear to be a result of hot bands preferentially enhancing the dissociation rate of the lower energy peroxide OH stretch. This non-statistical trend in dissociation rate observed in $HOCH_2OOH$ is further supported by our measurements of the corresponding rates in $HOCD_2OOH$, which also exhibits similar behavior (see Fig. 11.11(b)).

Results of RRKM calculations, shown in Table 11.5, are unable to account for the observed relative rates. On an absolute scale, for D_0 value of 38 kcal/mol, the RRKM calculations are in good accord with unimolecular dissociation rates arising from excitation of the alcohol OH stretch in both HMHP and HMHP-d_2 ($4\nu_1$), but gives values for rates arising from the peroxide OH stretch ($4\nu_2$) that are substantially lower than the measurements. The observed deviation between experiment and RRKM calculation

appear to suggest that indeed, HMHP molecule is exhibiting non-statistical or mode selective unimolecular dissociation.

Differences in the dissociation rates associated with excitation of *equivalent* OH sites in HMHP versus HMHP-d_2 are also apparent in our measurements. *Ab initio* calculations show that replacement of the two hydrogen atoms at the carbon site with deuterium alters the frequencies of the lowest vibrational modes of the molecule only slightly (see Table 11.4). Thus, the initial thermal distribution of vibrational states, which is primarily governed by the low frequency modes, is expected to be very similar in HMHP and HMHP-d_2. This is consistent with the similarity of the relative intensities and band positions appearing in the near threshold $4\nu_{OH}$ action spectra for the two isotopomers as shown in Fig. 11.3.

Deuterium substitution, however, does affect the relative zero-point energy associated with the reaction as well as the total density of vibrational states of the energized molecule. Based on the difference in zero-point energy between the reactant molecule and transition state, we estimate the dissociation threshold of HMHP-d_2 to be ~85 cm^{-1} higher in comparison to HMHP while the total density of vibrational states in the $4\nu_{OH}$ region is expected to increase from 4.05×10^5 states/cm^{-1} in HMHP to 1.16×10^6 states/cm^{-1} in HMHP-d_2. Hence, on the basis of both these factors one expects the $4\nu_{OH}$ unimolecular dissociation rates for HMHP-d_2 to be slower than those of HMHP as is indeed experimentally observed.

The slower rate upon deuteration is in fact also reflected in the results of the RRKM calculations shown in Table 11.5. However, what is interesting about the present data and which the RRKM calculation is unable to reconcile, is the fact that the degree to

which the rate slows down upon deuteration is experimentally found to be very different for the $4\nu_{OH}$ peroxide OH stretching state versus the alcohol OH state. We find that the dissociation rate associated with excitation of the alcohol $4\nu_1$ stretching state decreases by almost a factor of two in going from HMHP to HMHP-d_2 while the dissociation rate for excitation of the peroxide $4\nu_{OH}$ state decreases by only ~18%. This suggests that deuteration at the carbon site affects the coupling of the reaction coordinate to the alcohol OH moiety to a different extent than its coupling to the peroxide OH stretch.

One possible explanation for the present findings is that the OH chromophores associated with the two different functional groups, one on the methyl and the other on the peroxide moiety, exhibit different degrees of vibrational state mixing and hence different rates of intramolecular vibrational energy redistribution.[33,34] The OH attached to the methyl group, whose unimolecular dissociation rate is in fairly good agreement with the results of RRKM calculations in both HMHP and HMHP-d_2, is apparently strongly coupled to the dense manifold of "dark" background vibrational states resulting in its IVR being rather complete, which is a key requirement for the applicability of RRKM theory. By contrast, IVR is apparently more restricted in the OH chromophore associated with the peroxide functional group, thus causing its unimolecular dissociation rate to differ considerably from RRKM predictions.

The initial flow of energy out of the vibrationally excited state is generally controlled by low order resonances which strongly couple the zero-order vibrational overtone excited state, $|s\rangle$, to a subset of background states forming a first-tier of states (see Fig 11.15(a)). In the figure, additional coupling between the first-tier states, $|\ell\rangle$, and secondary tiers of background states, $|n\rangle$, which themselves are not directly coupled

strongly to the zero-order overtone state, redistributes the energy further among the total density of bath states over a longer time scale. Thus in an energized molecule the initial stages of IVR, which is controlled by the local-density of coupled states and not the total vibrational state density, may be fast.[33-35] However, complete energy redistribution among the entire energetically accessible set of bath states, associated with the later stages of IVR, may act as a bottleneck, channeling the energy flow along a specific coordinate. By contrast, in figure 11.15(b), the more significantly coupled first-tier of states and the zero-order overtone state lead to the statistical redistribution of energy and dissociation rate.

The trend for more complete IVR for the alcohol OH compared to the peroxide OH in HMHP is supported by studies on CH_3OH and CH_3OOH;[36-38] with methanol representing a situation where the OH is directly attached to the methyl group and methyl hydroperoxide representing the other situation where the OH group is attached to the peroxide site. Detailed spectroscopic measurements and theoretical analysis of the methanol $5\nu_{OH}$ and $4\nu_{OH}$ bands indicate that the OH stretching state is extensively mixed with bath states consisting of C-H stretch as well various bending modes of the molecule.[36,37]

By contrast, quasiclassical trajectory calculations carried out on vibrational overtone excited states of CH_3OOH, where the OH is located further away from the methyl rotor, indicate that this OH stretch is somewhat more isolated.[38] The calculations find that the OH stretch and HOO bending modes are strongly coupled to each other but are rather isolated from the other modes in the molecule. As a consequence of this restricted IVR, the quasiclassical trajectory calculations predict CH_3OOH to exhibit mode

selective behavior with respect to overtone induced unimolecular dissociation; vibrationally excited OH stretching overtone state of CH_3OOH is predicted to have a dissociation rate that is twice as fast as that of an excited C-H stretching overtone state having comparable energy.[38] Also, as shown in Chapters 8 and 9, is clear that as with the case in methanol, the CH_3 group in methyl hydroperoxide is strongly mixed leading to inhomogeneous line broadening and complete IVR as indicated from the jet cooled action spectrum and the resulting vibrationally excited OH product.

These observations, when applied to HMHP, would then suggest that the molecule is likely to exhibit vastly different IVR rates for its two OH stretching states. The ability of different functional groups to promote IVR to different extents has been reported in the literature with several studies noting that IVR is faster when the initially excited vibration is in close proximity to a methyl rotor or to a bond about which torsional motion occurs.[39-41] So our observation of the differences in the dissociation rate for the alcohol versus the peroxide OH stretch in HMHP and HMHP-d_2 is likely a manifestation of these effects.

11.5 Future Studies

As shown in the previous sections and in Fig. 11.2, in the current excitation scheme, due to the thermal energy in HMHP, our initial state is undefined and manifested by the thermal energy. Thus, in principle, the $4\nu_1$ and $4\nu_2$ bands could possibly be originating from two different initial states. If indeed the $4\nu_2$ originate from a higher energy state, its faster dissociation can be explained on the basis of energetics rather than restricted IVR. Double-resonance experiments, where a laser is used to prepare an initial state, i.e. $2\nu_{OH}$, and subsequently use a second laser to excess the $4\nu_1$ and $4\nu_2$ state will

eliminate the possibility of unequal thermal contribution in these two OH stretching overtones. Thus, the double-resonance technique can potentially provide conclusively evidence for mode selective behavior.

Additional mode selective behavior can also be inferred from the vibrationally mediated photodissociation of HMHP $2\nu_{OH}$ + 532 shown in Fig. 11.16. The vibrational assignment in this region is based on FTIR data.[9] Experiments conducted in Chapter 9 on CH_3OOH where the resulting vibrationally excited OH product from excitation of OH-stretching modes, CH-stretching modes and HOO-bending mode are found to exhibit mode-selective behavior. Since HMHP has two OH-stretching chromophores with similar vibrational frequencies but different chemical environment, it should be possible to quantify the resulting OH vibrationally excited OH product as a function of excitation a strongly "mixed" alcohol OH stretching mode with a more "isolated" peroxide OH stretching mode. Based on our findings in this Chapter, it is likely that one may observe more vibrationally excited OH yield from the excitation of the $2\nu_2$ band because the more restricted IVR will to lead to smaller fractionation of the OH character in this mode relative to the $2\nu_1$ state.

11.6 Acknowledgements

Chapter 11, in part, is a reprint of the material as it appears in Journal of Chemical Physics 128, 184306 (2008). J. Matthews, J. L. Fry, C. M. Roehl, P. O. Wennberg, A. Sinha, American Institute of Physics, 2008. The dissertation author was the primary investigator and author of this paper.

Table 11.1: Rotational Constants and Scaled[a] Harmonic Frequencies for Reactant and Products Used with Phase-Space Simulation (cm^{-1})

	Molecule		
	HMHP	**$HOCH_2O$**	**OH[b]**
A	**0.55786**	**1.64046**	**-**
B	**0.20105**	**0.35134**	**16.978[c]**
C	**0.16754**	**0.31194**	**-**
D_J	**6.07×10^{-6}**	**-**	**-**
D_{JK}	**-2.1×10^{-6}**	**-**	**-**
D_K	**2.0×10^{-6}**	**-**	**-**
ν_1	**3728**	**3815**	**3768**
ν_2	**3644**	**3094**	**-**
ν_3	**3077**	**2972**	**-**
ν_4	**2989**	**1415**	**-**
ν_5	**1459**	**1383**	**-**
ν_6	**1406**	**1325**	**-**
ν_7	**1371**	**1130**	**-**
ν_8	**1358**	**1094**	**-**
ν_9	**1249**	**1003**	**-**
ν_{10}	**1087**	**793**	**-**
ν_{11}	**1033**	**544**	**-**
ν_{12}	**1025**	**287**	**-**
ν_{13}	**805**	**-**	**-**
ν_{14}	**628**	**-**	**-**
ν_{15}	**446**	**-**	**-**
ν_{16}	**395**	**-**	**-**
ν_{17}	**334**	**-**	**-**
ν_{18}	**178**	**-**	**-**

[a] Using scaling factor of 0.9788 for harmonic frequencies from *ab initio* CCSD(T)/cc-pVDZ calculations.

[b] The OH rotational lines are entered numerically in the phase-space simulations based on levels given in Ref. 26.

[c] Ref. 26.

Table 11.2: Dipoles, Ionization Potentials and Polarizabilities for Reactants and Products Used with Phase-Space Simulation [a]

	Molecule		
	HMHP	**$HOCH_2O$**	**OH[c]**
Dipole (D)	-	1.479	1.660
I **(eV)**	-	12.36	15.96
α (m^3)	-	3.58×10^{-30}	1.01×10^{-30}
$C_{d\text{-}d}$	9.75×10^{-59}		
$C_{d\text{-}id}$	1.21×10^{-59}		
C_{disp}	6.04×10^{-59}		
C_6 **(erg cm^6)**	1.70×10^{-58}		

[a] **From *ab initio* (U)CCSD(T)/cc-pVDZ calculations.**

Table 11.3: HMHP Dissociation Rates Resulting from Excitation at Various Wavelengths in the Vicinity of Peroxide and Alcohol $4\nu_{OH}$ Bands

Freq., ν (cm^{-1})	**Lifetime (nsec.)**	**Rate ($sec.^{-1}$)**
O-OH band		
13 301	**40.3**	24.8×10^6
13 330	**39.0**	25.6×10^6
13 357	**42.7**	23.4×10^6
C-OH band		
13 556	**50.2**	19.9×10^6
13 580	**53.6**	18.7×10^6
13 620	**46.9**	21.3×10^6

Table 11.4: CCSD(T)/cc-pVDZ Rotational Constants and Scaled[a] Harmonic Frequencies Used with RRKM Rates Calculations for HMHP and HMHP-d_2

	Ground State (cm^{-1})		Transition State (cm^{-1})	
	HMHP	**HMHP-d_2**	**HMHP**	**HMHP-d_2**
A	0.55786	0.48638	0.33305	0.31634
B	0.20105	0.19348	0.18158	0.17012
C	0.16754	0.16121	0.13017	0.12577
ν_1	3728	3727	3725	3725
ν_2	3644	3644	3595	3595
ν_3	3077	2291	3004	2217
ν_4	2989	2174	2868	2088
ν_5	1459	1368	1403	1309
ν_6	1406	1327	1353	1153
ν_7	1371	1157	1306	1019
ν_8	1358	1103	1117	958
ν_9	1249	982	1087	944
ν_{10}	1087	975	1003	844
ν_{11}	1033	942	821	673
ν_{12}	1025	871	566	559
ν_{13}	805	773	542	538
ν_{14}	628	604	466	465
ν_{15}	446	440	315	311
ν_{16}	395	373	169	167
ν_{17}	334	321	157	138
ν_{18}	178	174	-	-

[a] **Using scaling factor of 0.9788 for harmonic frequencies from *ab initio* calculations.**

Table 11.5: RRKM Rates Calculated for Excitation of the Peroxide and Alcohol $4\nu_{OH}$ Stretching Overtones of HMHP and HMHP-d_2

	O-OH band		C-OH band	
D_0 (kcal/mol)	Lifetime (nsec.)	Rates (sec^{-1})	Lifetime (nsec.)	Rates (sec^{-1})
		HMHP		
37	35	28.6×10^6	19	52.6×10^6
37.50	63	15.9×10^6	32	31.3×10^6
37.75	87	11.5×10^6	42	23.8×10^6
37.90	105	9.52×10^6	50	20.0×10^6
38	**120**	$\mathbf{8.33 \times 10^6}$	**56**	$\mathbf{17.9 \times 10^6}$
39	259	3.86×10^6	162	6.17×10^6
40	448	2.23×10^6	361	2.77×10^6
41	725	1.38×10^6	649	1.54×10^6
Expt.	**39 ± 3**	$\mathbf{(25.6 \pm 2.0) \times 10^6}$	**54 ± 4**	$\mathbf{(18.5 \pm 1.4) \times 10^6}$
		HMHP-d_2		
37	75	13.3×10^6	39	25.6×10^6
37.50	140	7.14×10^6	68	14.7×10^6
37.75	195	5.13×10^6	91	11.0×10^6
37.90	241	4.15×10^6	109	9.18×10^6
38	**277**	$\mathbf{3.61 \times 10^6}$	**124**	$\mathbf{8.06 \times 10^6}$
39	653	1.53×10^6	382	2.62×10^6
40	1200	0.83×10^6	885	1.13×10^6
41	1973	0.51×10^6	1684	0.59×10^6
Expt.	**46 ± 4**	$\mathbf{(21.7 \pm 1.9) \times 10^6}$	**100 ± 8**	$\mathbf{(10.0 \pm 0.8) \times 10^6}$

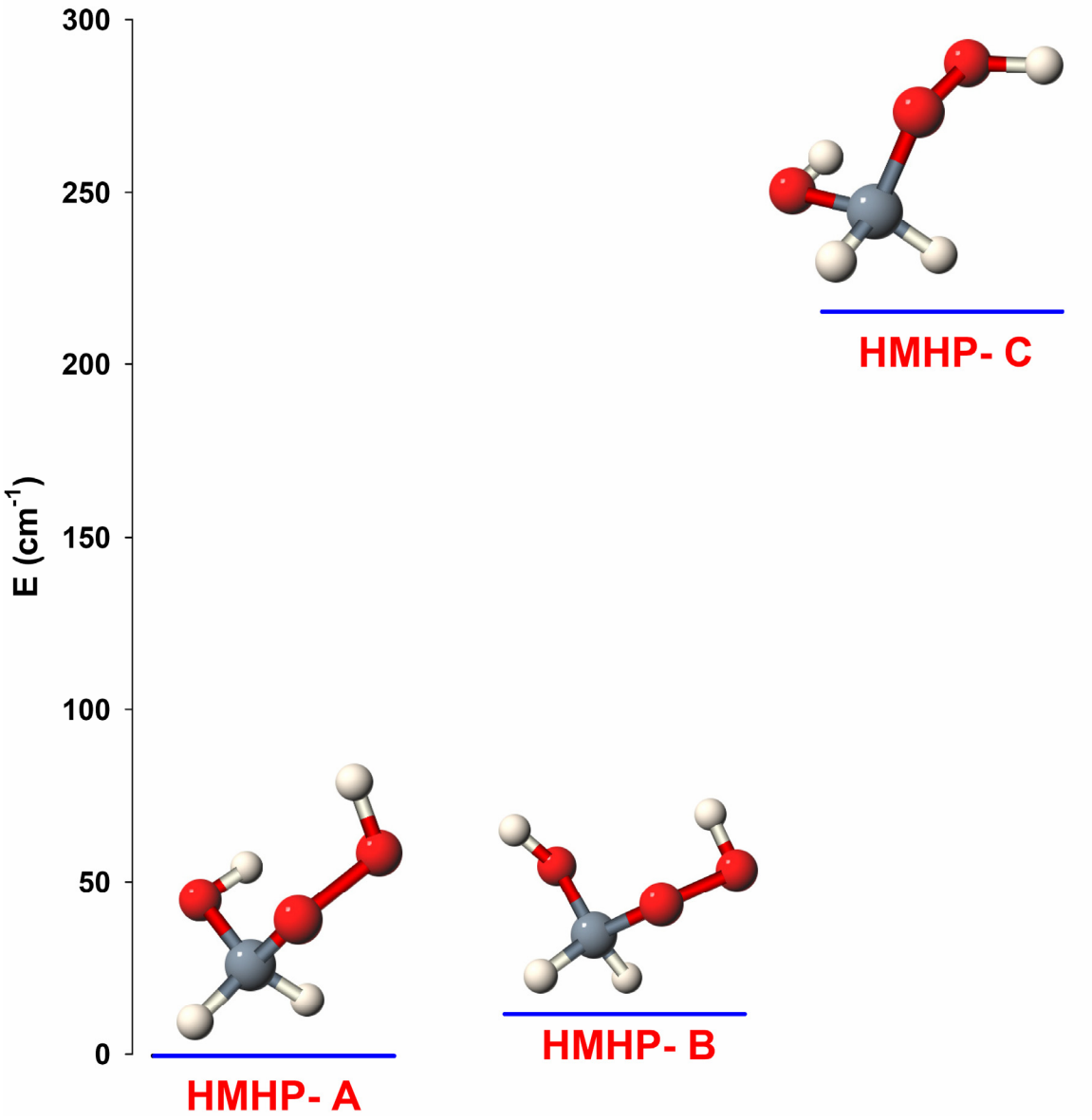

Figure 11.1: Energy level diagram of the three room temperature conformers of HMHP. The relative energies between HMHP-A, HMHP-B and HMHP-C are 0, 13, 215 cm^{-1} respectively as calculated at the CCSD(T)/aug'-cc-pVTZ level.[9] [File: F11.1_conf]

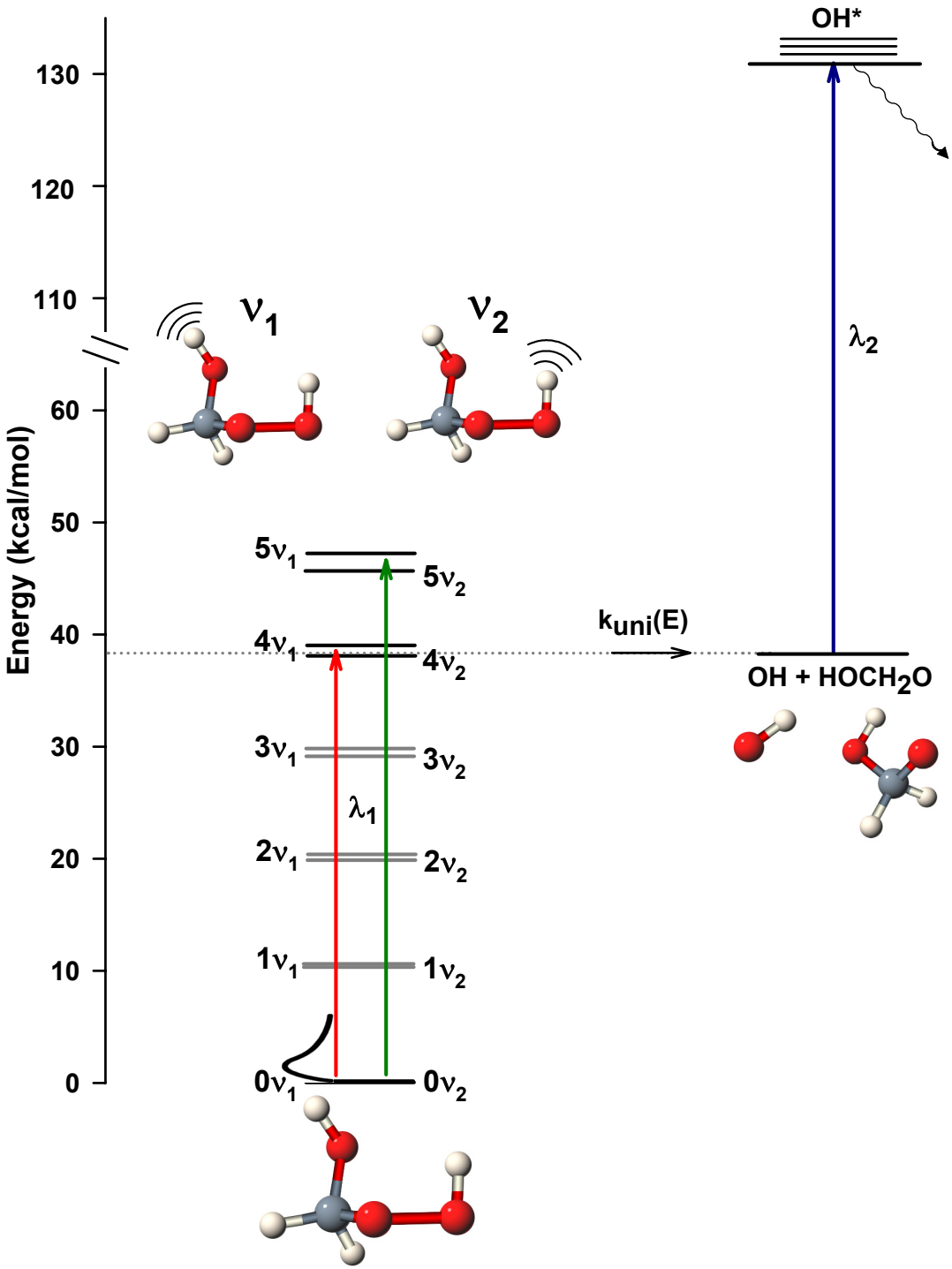

Figure 11.2: Schematic energy level diagram for vibrational overtone initiated unimolecular dissociation of HMHP. The higher frequency alcohol OH stretch is ν_1 while the peroxide OH stretch is ν_2. [File: F11.2_ped]

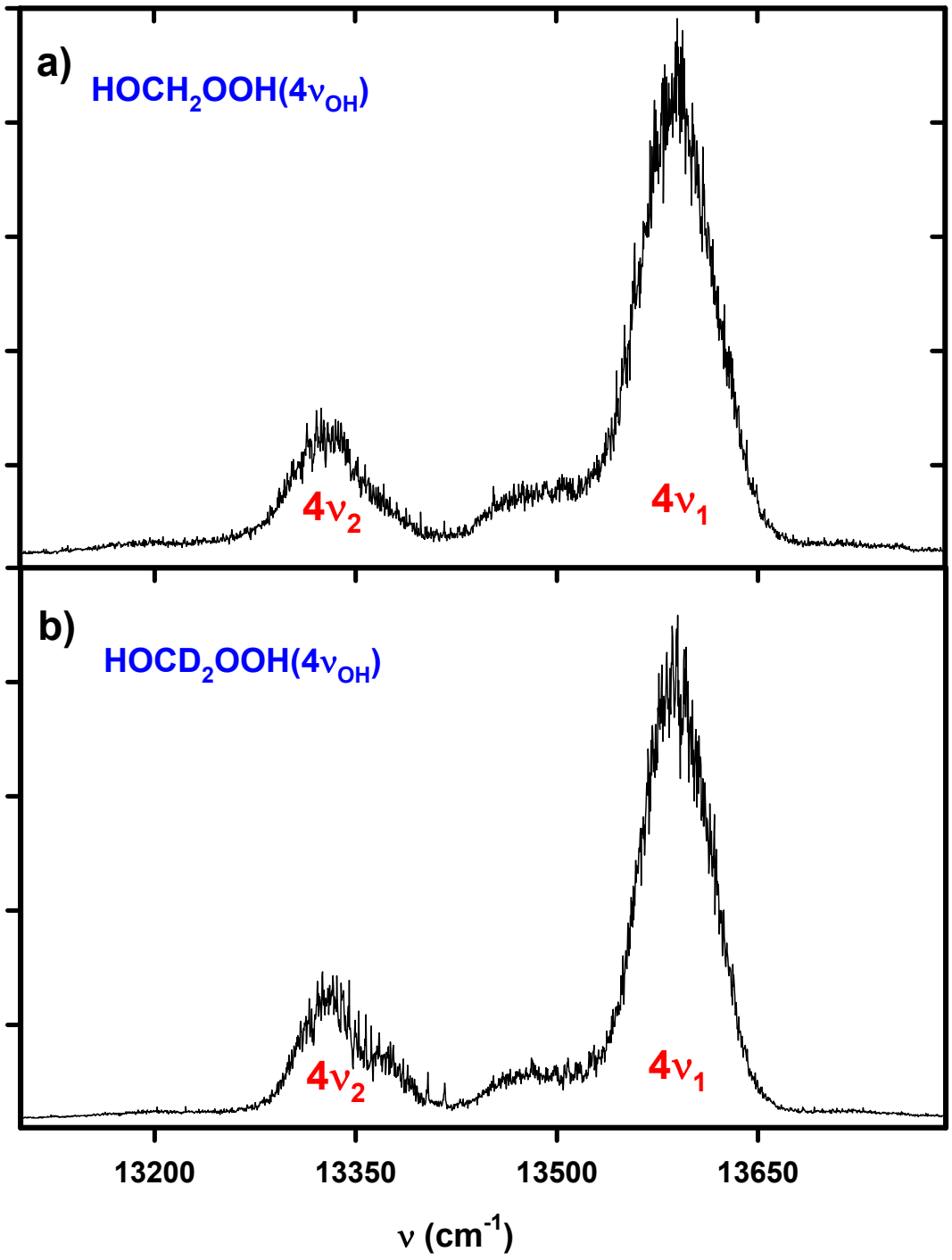

Figure 11.3: The room temperature action spectra of a) HMHP and b) HMHP-d_2 in the region of the third ($4\nu_{OH}$) OH-stretching overtones generated by monitoring the nascent OH(N=1, $^2\Pi_{3/2}$; v=0) rotational state. The low frequency feature appearing in the spectrum corresponds to the peroxide OH (~13 330 cm^{-1}) and the higher intensity band around ~10 580 cm^{-1} corresponds to the alcohol OH. [File:F11.3_4nu]

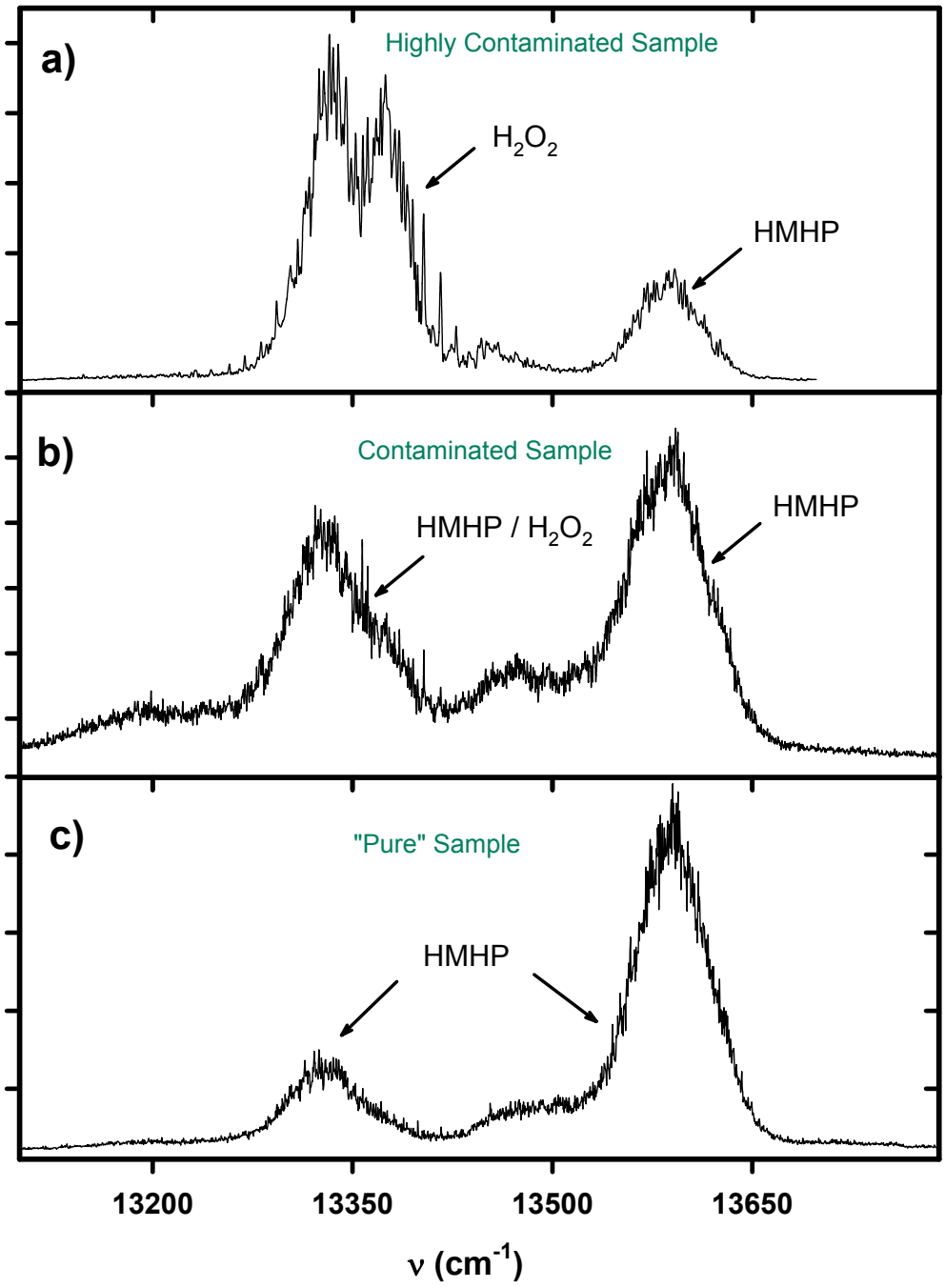

Figure 11.4: The variations in the HMHP ($4\nu_{OH}$) band shape and intensity as a function of H_2O_2 concentration. a) Initially, after short pumping periods the spectrum is dominated by signal from one-color two-photon dissociation of H_2O_2. b) After additional pumping, the H_2O_2 signal is reduced, giving rise to more pronounced HMHP ($4\nu_1$) signal. The $4\nu_2$ band however, remains contaminated. c) After significant pumping time, most of the H_2O_2 is removed from the sample and we obtain a fairly clean HMHP signal.
[File: F11.4_4nu_h2o2]

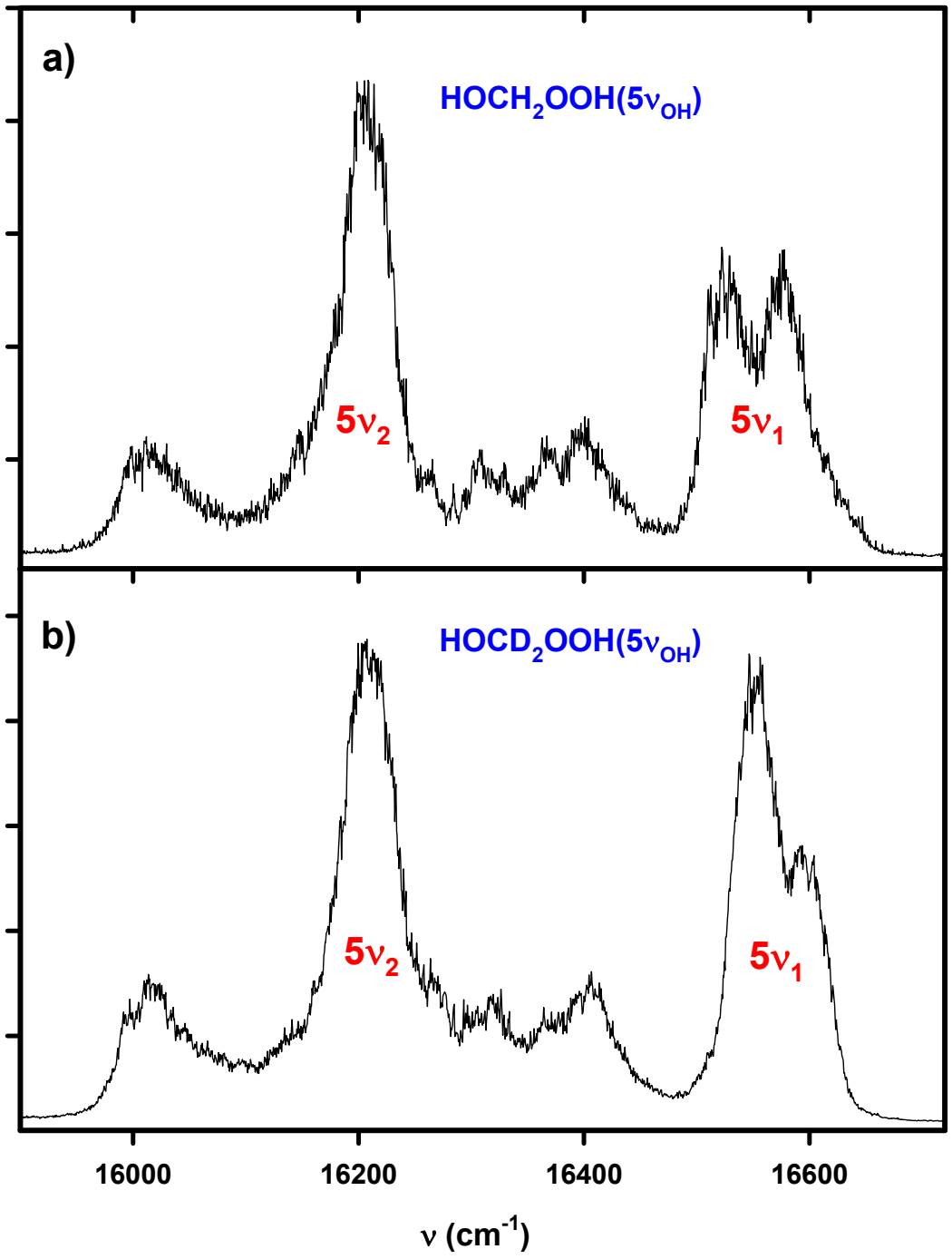

Figure 11.5: The room temperature action spectra of a) HMHP and b) HMHP-d_2 in the region of the fourth ($5\nu_{OH}$) OH-stretching overtones generated by monitoring the nascent OH(N=3, $^2\Pi_{3/2}$; v=0) rotational state. The peroxide OH ($5\nu_2$) is assigned to the band around ~16 200 cm^{-1} and the alcohol OH stretch around 16 526 cm^{-1}. Fermi resonance interaction between the alcohol $5\nu_{OH}$ and $4\nu_{OH} + \nu_{CH}$ states affects the $5\nu_1$ band shape.[9] [File: F11.5_5nu]

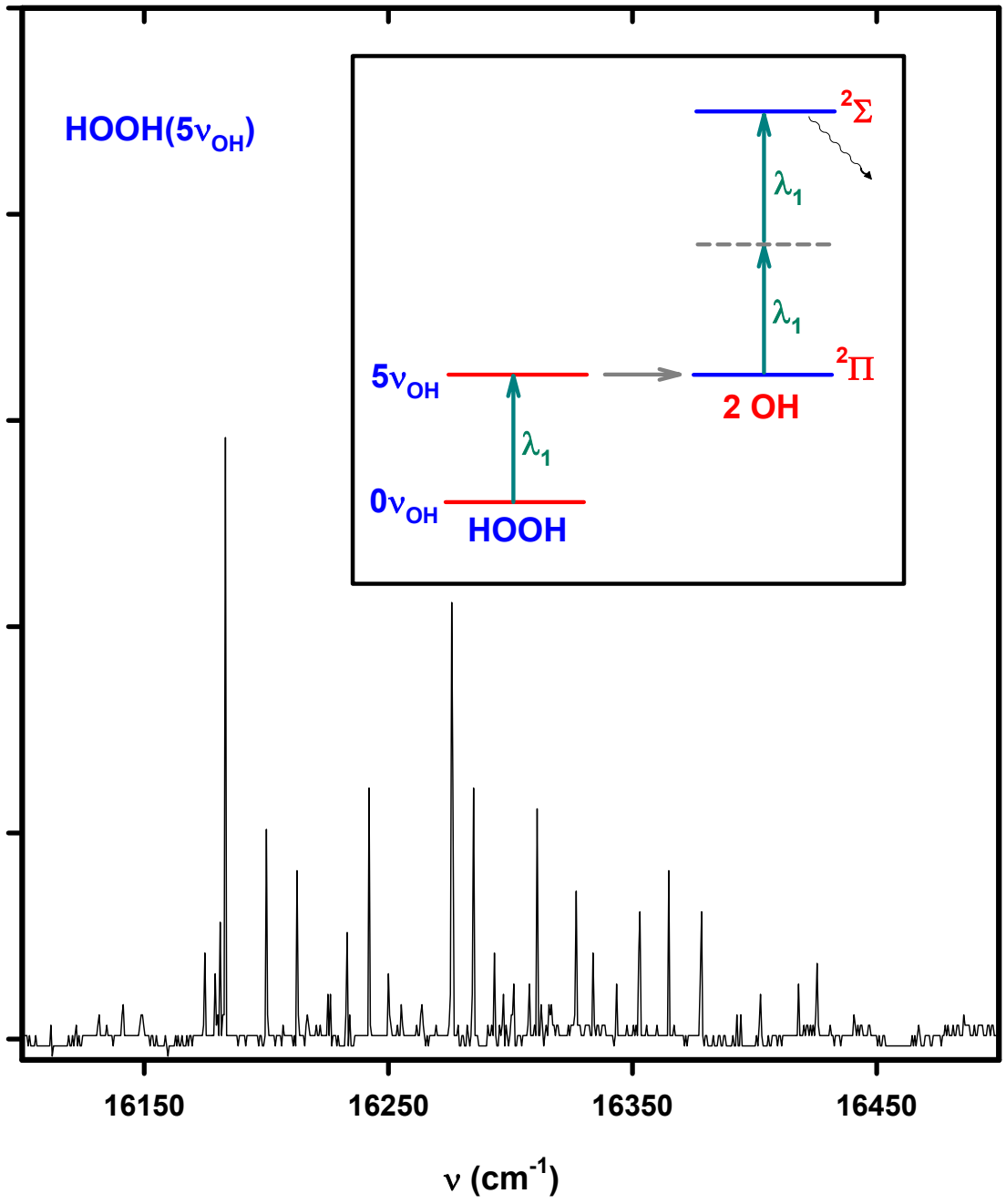

Figure 11.6: The one-color three-photon dissociation of H_2O_2 in the $5\nu_{OH}$ band. The spectrum is generated by vibrationally dissociating H_2O_2 present as an impurity in the HMHP sample and subsequently promoting the resulting 2·OH fragments from the $X^2\Pi$ state to the $A^2\Sigma$ state with one-color two-photon process. The spectrum shown corresponds to resonance excitation of transitions in H_2O_2 ($5\nu_{OH}$) and OH ($A^2\Sigma \leftarrow X^2\Pi(0,0)$). [File: F11.6_three_photon]

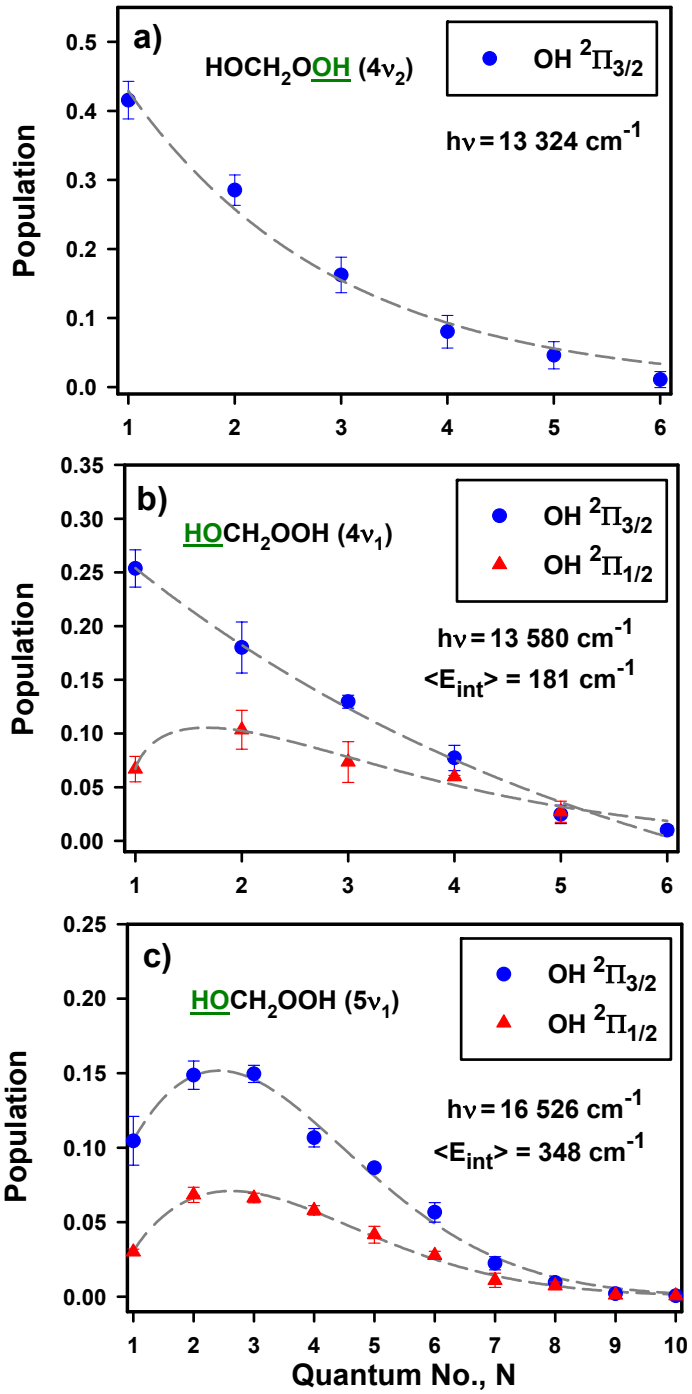

Figure 11.7: Nascent rotational state distributions of the OH (v=0, $^2\Pi_{3/2}$) and OH (v=0, $^2\Pi_{1/2}$) states resulting from excitation of HMHP in the region of the $4\nu_{OH}$ and $5\nu_{OH}$ bands. a) OH product state distribution resulting from excitation of the peroxide $4\nu_{OH}$ state at ~13 324 cm^{-1}. b) OH product state distributions resulting from excitation of alcohol $4\nu_{OH}$ state at ~13 580 cm^{-1}. c) OH product state distributions resulting from excitation of the $5\nu_{OH}$ alcohol band at ~16 526 cm^{-1}. [File: F11.7_psd]

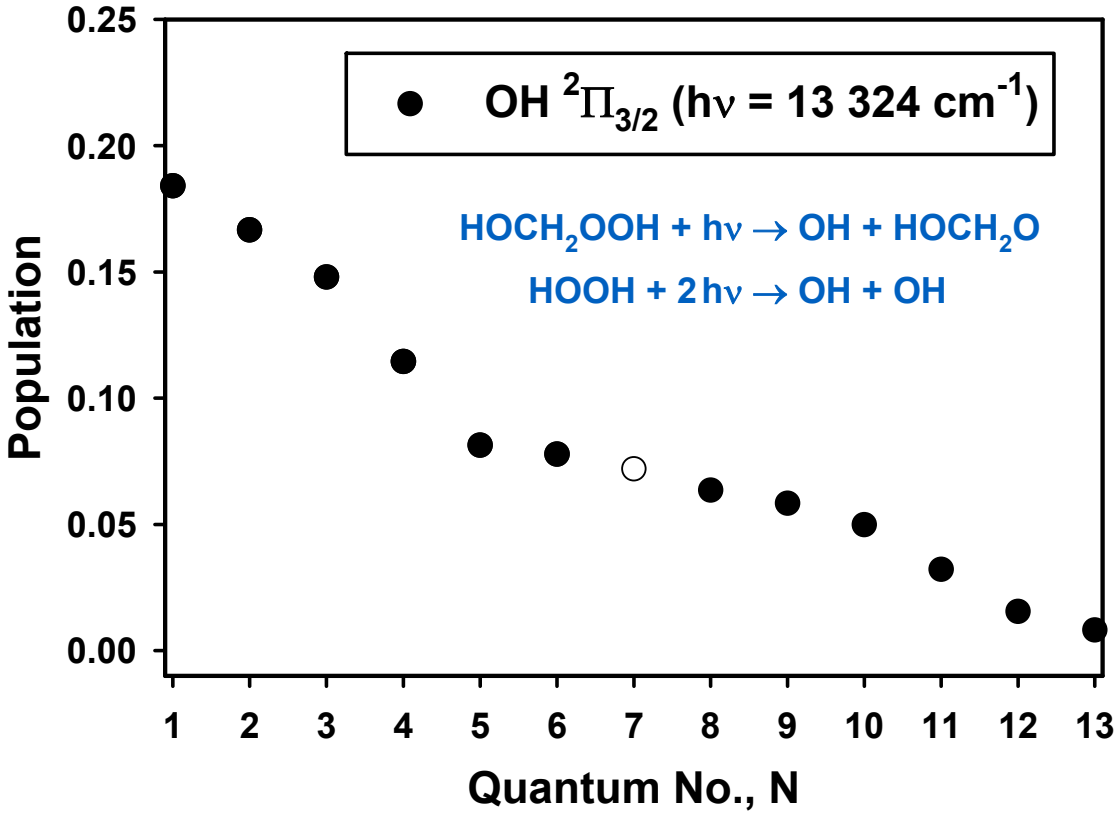

Figure 11.8: Raw sum of the nascent rotational state distributions of the OH (v=0, $^2\Pi_{3/2}$) state resulting from excitation of HMHP and overlapping H_2O_2 in the region of the peroxide OH bands at ~13 324 cm^{-1}. The hydrogen peroxide contribution is subtracted out using data from Ref. 21. The population at N=7 is not measured because of contaminations from the $Q_{21}(3)$ state. [File: F11.8_psd_raw]

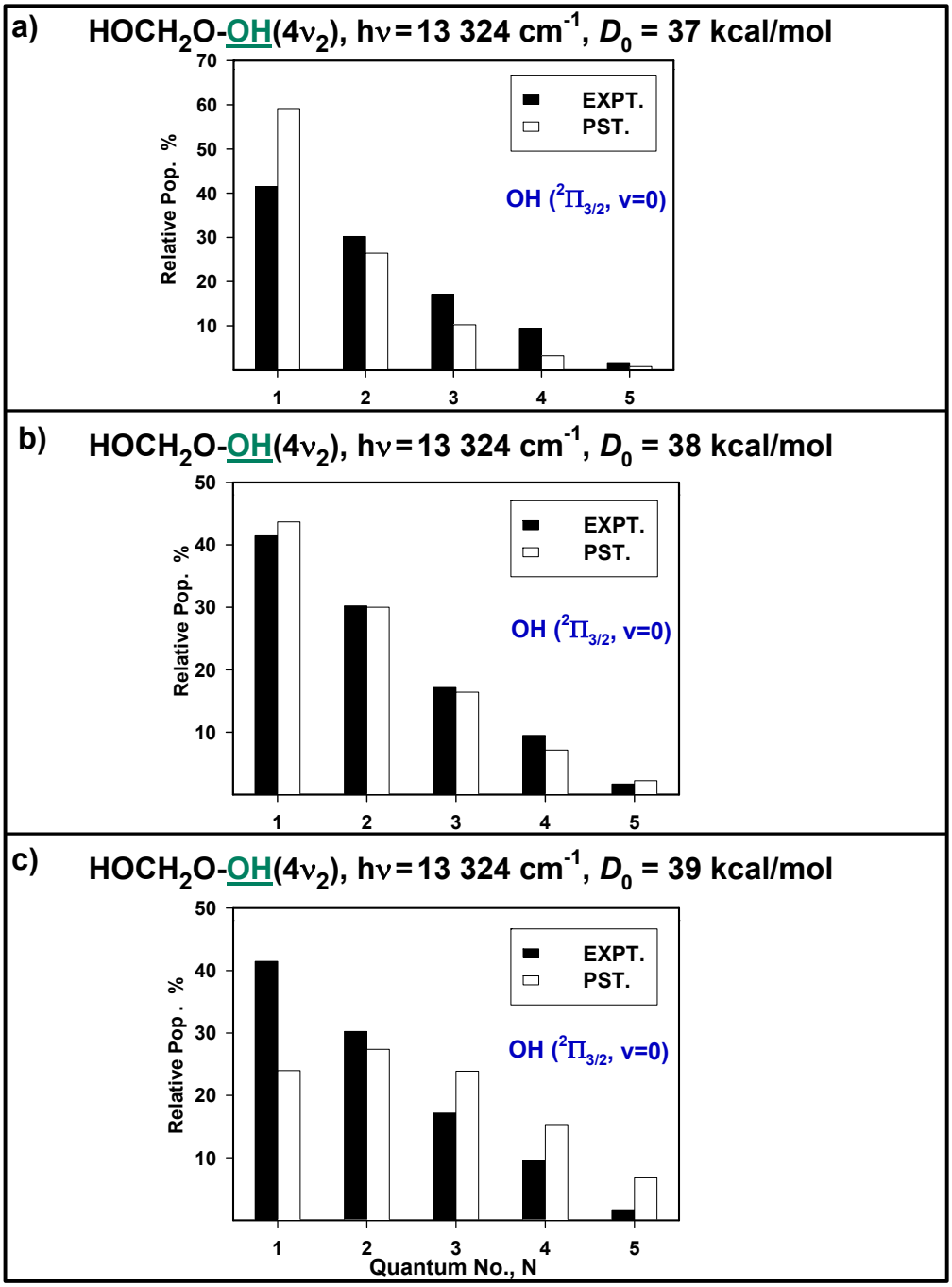

Figure 11.9: Comparison of experimental and phase-space simulation of the OH (v=0, $^2\Pi_{3/2}$) and OH (v=0,$^2\Pi_{1/2}$) rotational product state distributions resulting from peroxide O-H excitation of HMHP in the region of its third OH stretching overtones ($4\nu_2$). a) Results for D_0 = 37 kcal/mol. b) Results for D_0 = 38 kcal/mol. c) Results for D_0 = 39 kcal/mol. From these simulations we find that a value of D_0 = 38 ± 0.7 kcal/mol gives the best fit to the measured HMHP OH rotational product state distributions.
[File: F11.9_pst_4n2]

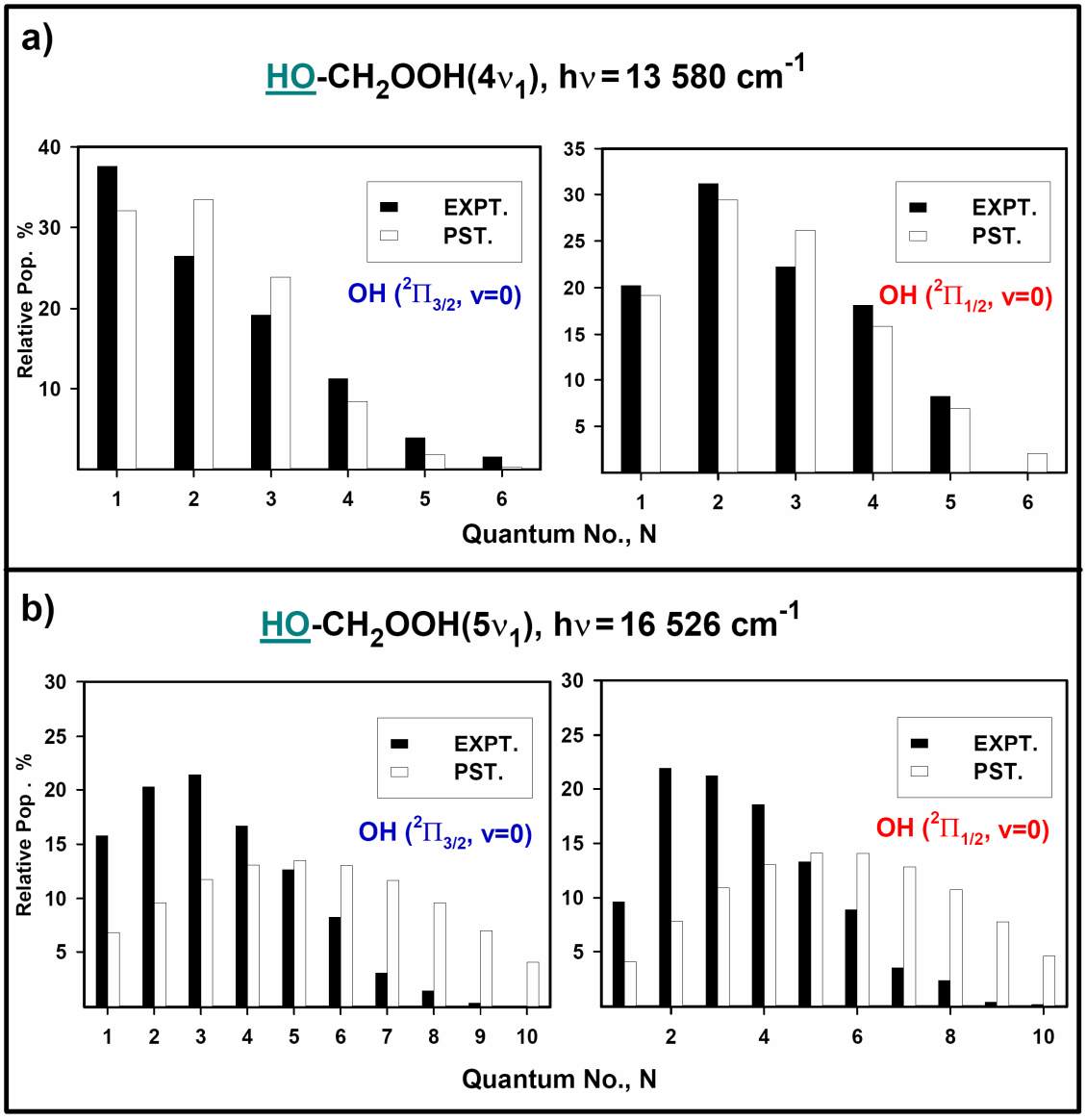

Figure 11.10: Comparison of experimental and phase-space simulation of the OH (v=0, $^2\Pi_{3/2}$) and OH (v=0,$^2\Pi_{1/2}$) rotational product state distributions resulting from vibrational overtone initiated unimolecular dissociation of HMHP in the region of its third ($4\nu_1$) and fourth ($5\nu_1$) OH stretching overtones. The simulation uses D_0 = 38 kcal/mol obtained from data in Fig. 11.9. a) Results for excitation of the alcohol $4\nu_{OH}$ state at 13 580 cm^{-1}. b) Results for excitation of the alcohol $5\nu_{OH}$ state at 16 526 cm^{-1}. [File: F11.10_pst_n1]

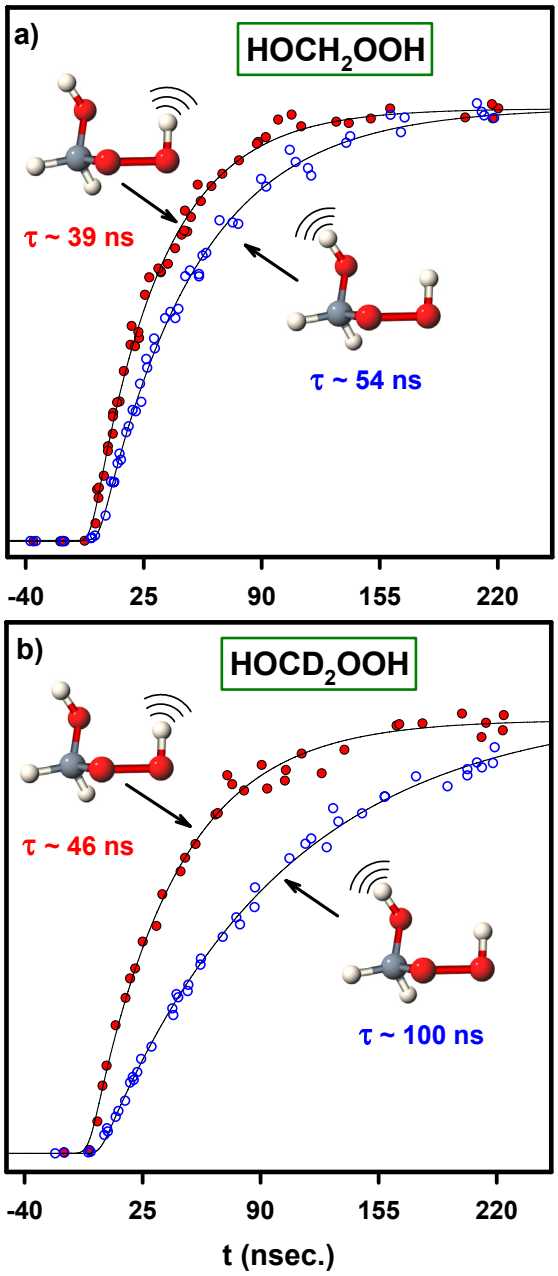

Figure 11.11: Unimolecular dissociation rate measurements resulting from excitation of the $4\nu_{OH}$ peroxide and alcohol OH stretching states in HMHP and HMHP-d_2. The rates are obtained by varying the temporal delay between the overtone excitation and the probe lasers while monitoring the yield of the OH ($^2\Pi_{3/2,}$ N=1, v=0) fragments. The indicated dissociation lifetimes are obtained by non-linear least square fitting of the data.[29] a) Comparison of dissociation rates resulting from excitation of the $4\nu_{OH}$ peroxide versus alcohol OH-stretching states in HMHP. b) Comparison of dissociation rates resulting from excitation of the $4\nu_{OH}$ peroxide versus alcohol OH-stretching states in HMHP-d_2. [File: F11.11_rates]

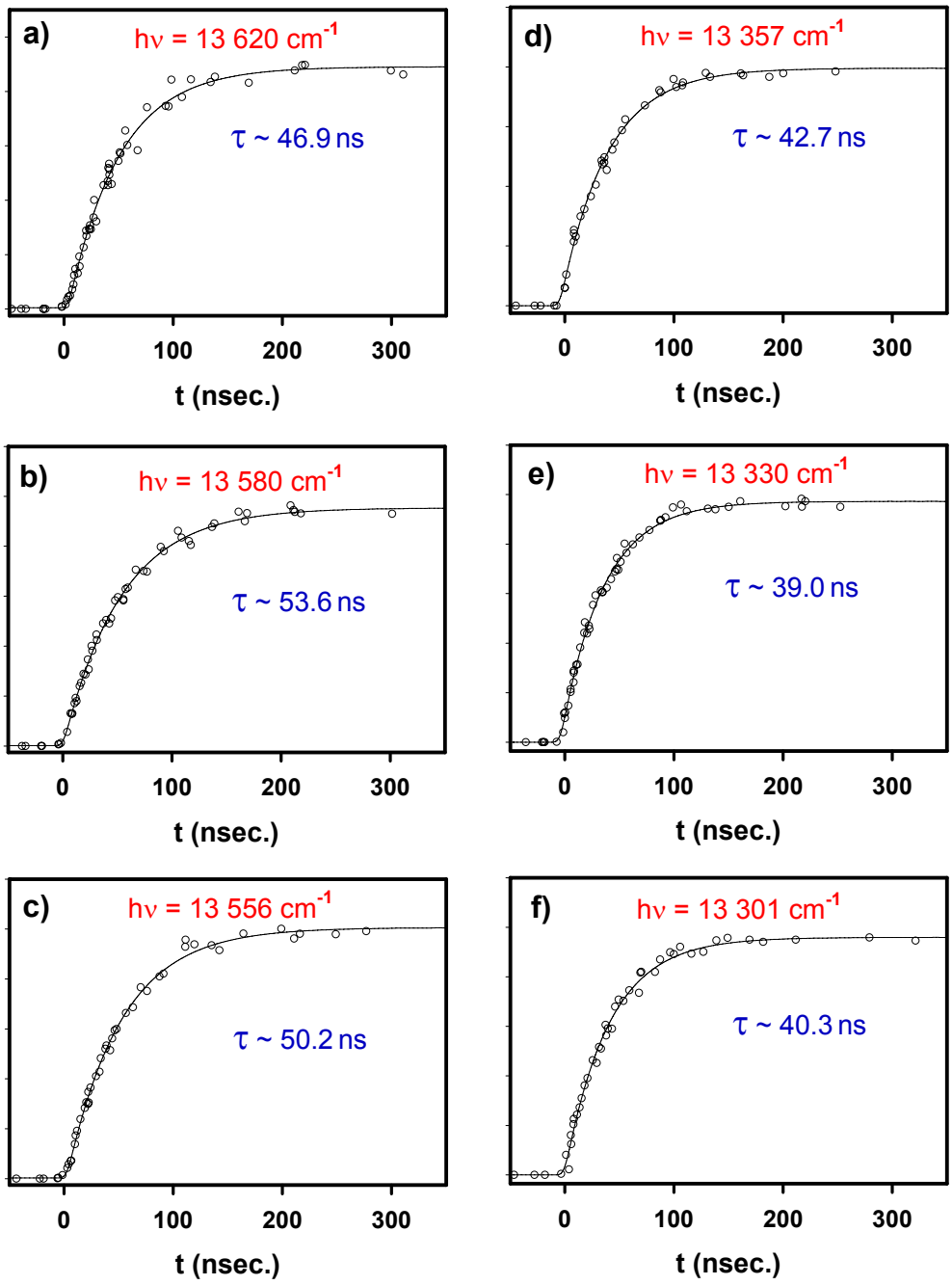

Figure 11.12: Unimolecular dissociation rate measurement resulting from various excitations corresponding to FWHM locations of the $4\nu_{OH}$ peroxide and alcohol OH stretching states in HMHP. The indicated dissociation lifetimes are obtained by non-linear least square fitting of the data.[29] a) Excitation of the $4\nu_1$ band at 732.4 nm. b) Excitation of the $4\nu_1$ band at 736.4 nm. c) Excitation of the $4\nu_1$ band at 737.7 nm. d) Excitation of the $4\nu_2$ band at 748.7 nm. e) Excitation of the $4\nu_2$ band at 750.2 nm. f) Excitation of the $4\nu_2$ band at 751.8 nm. [File: F11.12_bands_rates]

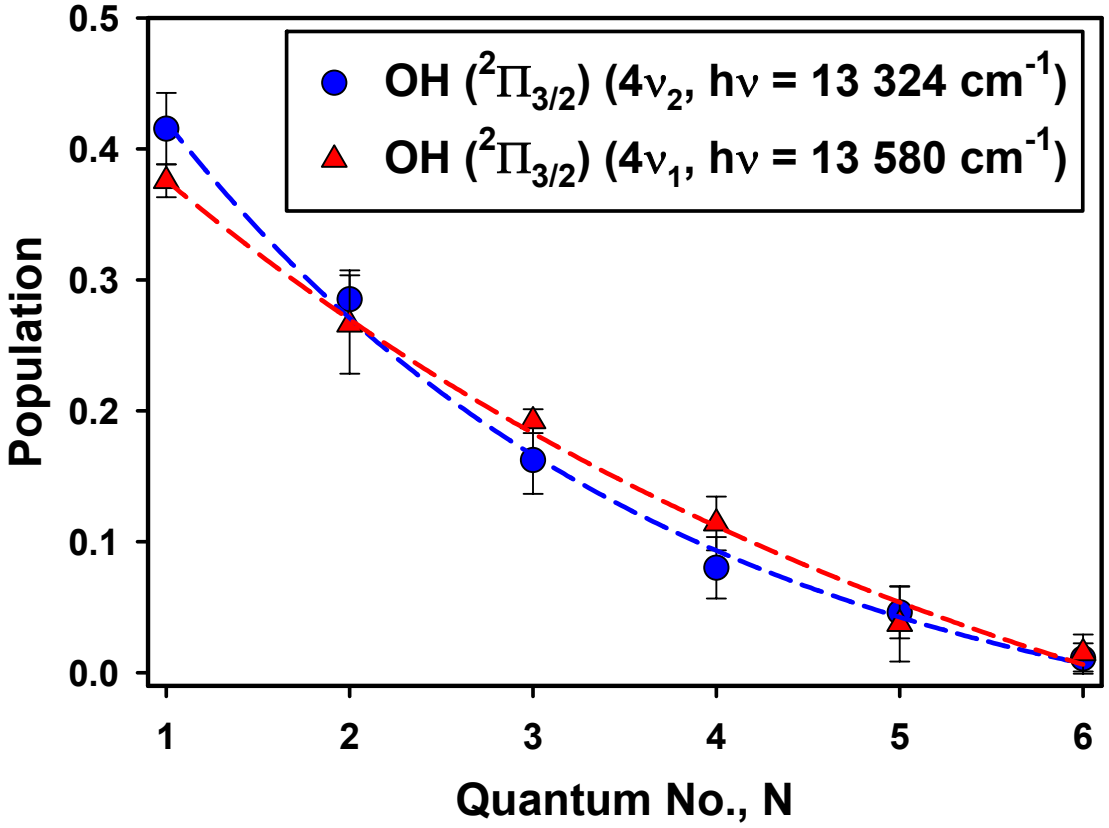

Figure 11.13: Direct comparison of the measured OH (v=0, $^2\Pi_{3/2}$) rotational product state distributions resulting from excitation of the HMHP $4\nu_{OH}$ peroxide stretching mode at 13 324 cm^{-1}and $4\nu_{OH}$ alcohol stretching mode at 13 580 cm^{-1}. The distributions are similar with the $4\nu_{OH}$ alcohol stretching mode exhibiting a slightly warmer rotational temperature consistent with its lower frequency. [File: F11.13_psd_comapre]

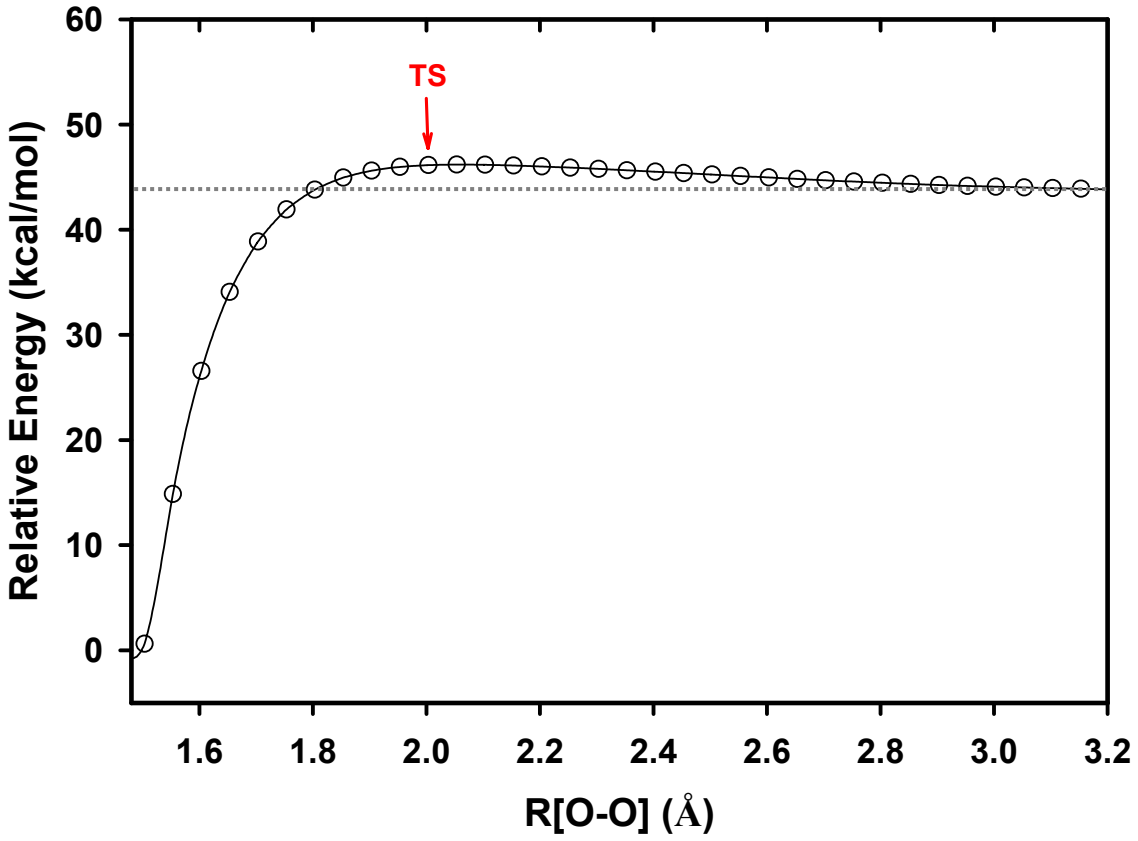

Figure 11.14: CCSD/cc-pVDZ potential energy diagram of the ground state of HMHP as a function of O-O bond distance. The distance is in Å and energy is in kcal/mol. The transition state is located around 2.05 Å with a barrier height of ~1 kcal/mol.
[File: F11.14_barrier]

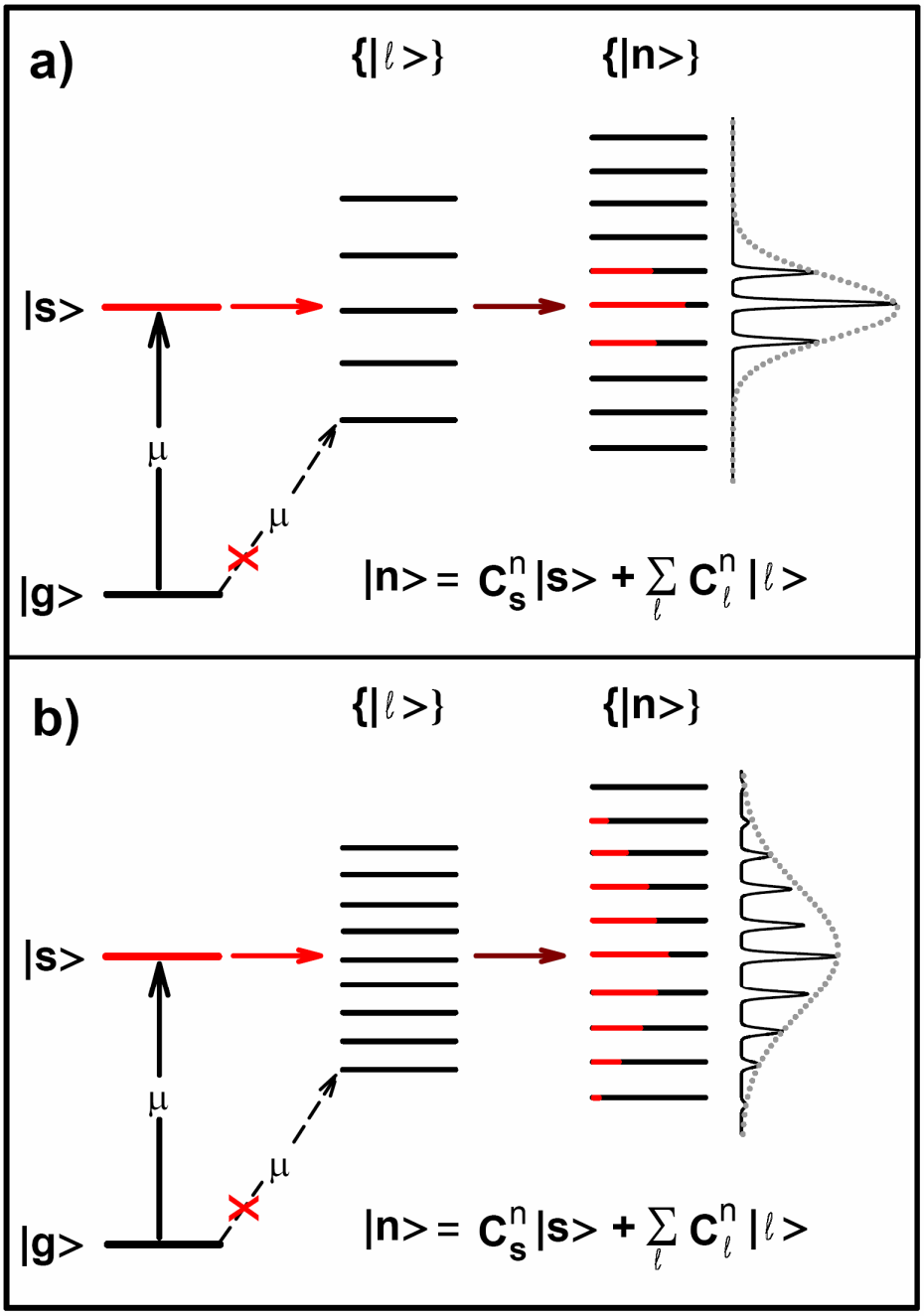

Figure 11.15: Schematic illustrating the IVR in HMHP molecule. a) This panel illustrates restricted IVR process where the bright state, | s >, is coupled to only small number of substates, | ℓ >. This poor-coupling scenario acts as a bottle-neck for distributing the energy among the other vibrational states. b) Illustration of efficient IVR process where the bright state fractionates efficiently due to strong coupling with the other sub-states , | ℓ >. In this scenario, rapid IVR leads to randomized distribution of the energy deposited in the | s> state among the rest of the eigenstates.
[File: F11.15_tier_model]

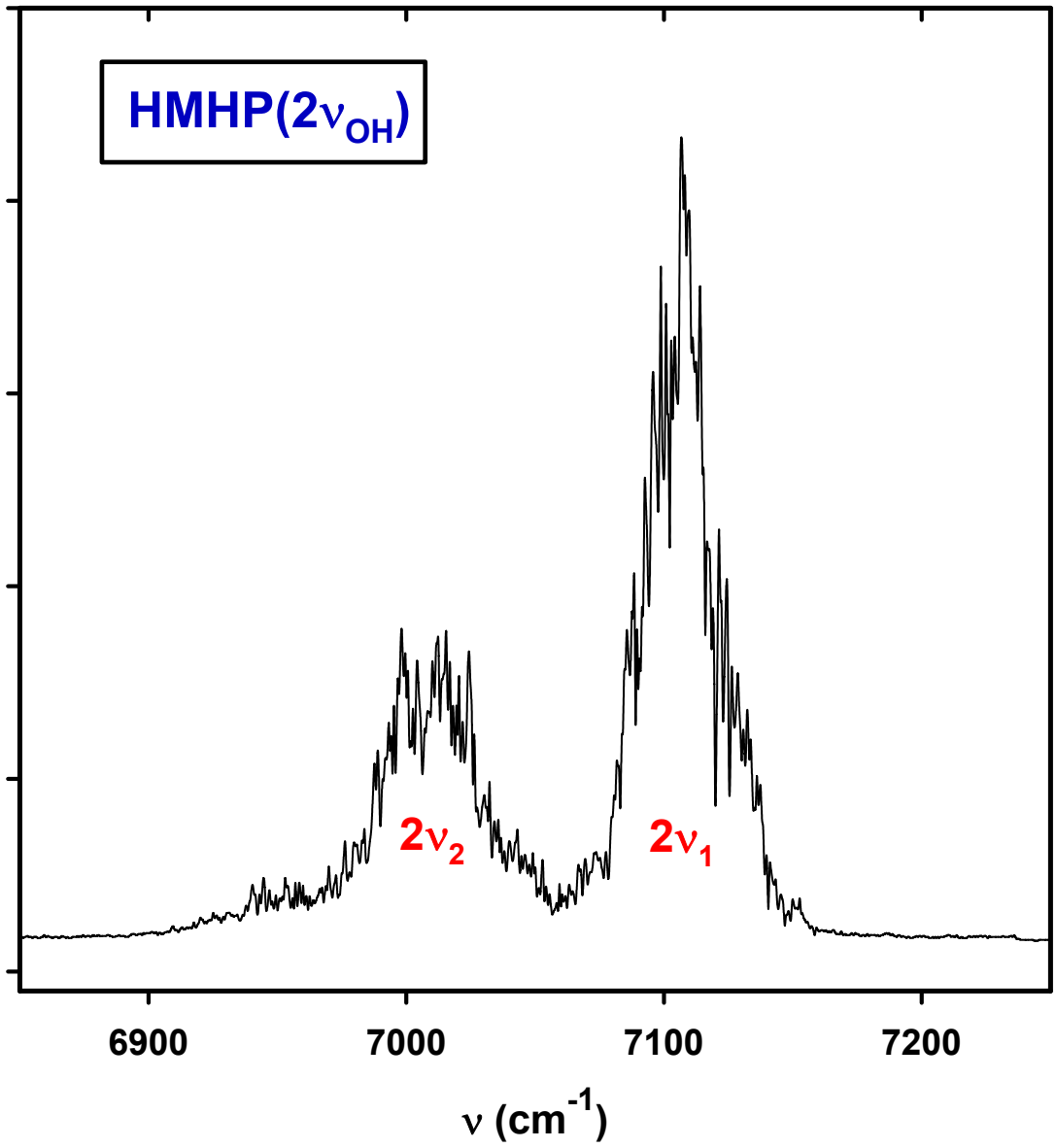

Figure 11.16: The room temperature action spectra of HMHP in the region of the first ($2\nu_{OH}$) OH-stretching overtones region generated by dissociating the molecule with 532 nm light and monitoring the nascent OH(N=5, $^2\Pi_{3/2}$; v=0) rotational state. This spectrum is generated in a similar manner used in probing the overtones of CH_3OOH in Chapter 7 ($2\nu_{OH}$ + 532 nm). The low frequency feature appearing in the spectrum corresponds to the peroxide OH (~7010 cm^{-1}) and the higher intensity band around ~7106 cm^{-1} corresponds to the alcohol OH. The assignment is based on FTIR measurements of Ref. 9. [File: F11.16_2nuoh]

11.7 References

1. P. Neeb, F. Sauer, O. Horie, G. K. Moortgat, Atmos. Environ. **31**, 1417 (1997).

2. E. Hellpointer, and S. Gab, Nature **337**, 631 (1989).

3. C. N. Hewitt, and G. L. Kok, J. Atmos. Chem. **12**, 181 (1991).

4. J. B. Weinstein-Lloyd, H. J. Lee, P. H. Daum, L. I. Klienman, L. J. Nunnermacker, S. R. Springston, J. Geophys. Res. Atmos. **103**, 22361 (1998).

5. J. H. Lee, D. F. Leahy, I. N. Tang, L. Newman, J. Geophys. Res. Atmos. **98**, 2911 (1993).

6. D. Grosssmann, G. K. Moortgat, M. Kibler, S. Schlomski, K. Bachmann, B. Alicke, A. Geyer, U. Platt, M. U. Hummer, B. Vogel, D. Mihelcic, A. Hofzumahaus, F. Holland, A. Volz-Thomas, J. Geophys. Res. Atmos. **108** (2003).

7. S. Bauerle, and G. K. Moortgat, Chem. Phys. Lett. **309**, 43 (1999).

8. C. M. Roehl, Z. Marka, J. L. Fry, P. O. Wennberg, Atmos. Chem. Phys. **7**, 713 (2007).

9. J. L. Fry, J. Matthews, J. R. Lane, C. M. Roehl, A. Sinha, H. G. Kjaergaard, and P. O. Wennberg, J. Phys. Chem. A. **110**, 7072 (2006).

10. P. Pechukas, J. C. Light, and C. Rankin, J. Chem. Phys. **44**, 794 (1966); P. Pechukas and J. C. Light, ibid. **42**, 3281 (1965); J. C. Light, Faraday Discuss. Chem. Soc. **44**, 14 (1967).

11. T. Gilbert, T. L. Grebner, I. Fischer, and P. Chen, J. Chem. Phys. **110**, 5485 (1999).

12. J. C. Owrutsky and A. P. Baronavski, J. Chem. Phys. **110**, 11206 (1999).

13. S. H. Courtney, M. W. Balk, L. A. Philips, S. P. Webb, D. Yang, D. H. Levy, and G. R. Fleming, J. Chem. Phys. **89,** 6697 (1988).

14.Y. S. Choi, and C. B. Moore, J. Chem. Phys. **94**, 5414 (1991).

15. G. Dutton, R. J. Barnes, and A. Sinha, J. Chem. Phys. **111,** 4976 (1999).

17. M. R. Wedlock, R. Jost, and T. R. Rizzo, J. Chem. Phys. **107**, 10344 (1997).

18. F. Reiche, B. Abel, R. D. Beck, and T. R. Rizzo, J. Chem. Phys. **116**, 10267 (2002).

19. GAUSSIAN03, Revision B.04, M. J. Frisch, G. W. Trucks, H. B. Schlegel, G. E. Scuseria, M. A. Robb, J. R. Cheeseman, J. A. Montgomery, Jr., T. Vreven, K. N. Kudin, J. C. Burant, J. M. Millam, S. S. Iyengar, J. Tomasi, V. Barone, B. Mennucci, M. Cossi, G. Scalmani, N. Rega, G. A. Petersson, H. Nakatsuji, M. Hada, M. Ehara, K. Toyota, R. Fukuda, J. Hasegawa, M. Ishida, T. Nakajima, Y. Honda, O. Kitao, H. Nakai, M. Klene, X. Li, J. E. Knox, H. P. Hratchian, J. B. Cross, V. Bakken, C. Adamo, J. Jaramillo, R. Gomperts, R. E. Stratmann, O. Yazyev, A. J. Austin, R. Cammi, C. Pomelli, J. W. Ochterski, P. Y. Ayala, K. Morokuma, G. A. Voth, P. Salvador, J. J. Dannenberg, V. G. Zakrzewski, S. Dapprich, A. D. Daniels, M. C. Strain, O. Farkas, D. K. Malick, A. D. Rabuck, K. Raghavachari, J. B. Foresman, J. V. Ortiz, Q. Cui, A. G. Baboul, S. Clifford, J. Cioslowski, B. B. Stefanov, G. Liu, A. Liashenko, P. Piskorz, I. Komaromi, R. L. Martin, D. J. Fox, T. Keith, M. A. Al-Laham, C. Y. Peng, A. Nanayakkara, M. Challacombe, P. M. W. Gill, B. Johnson, W. Chen, M. W. Wong, C. Gonzalez, and J. A. Pople, Gaussian, Inc. (Wallingford CT, 2004).

20. S. Marklund, Acta. Chem. Scand. **25**, 3517 (1971).

21. T. M. Ticich, M. D. Likar, H. R. Dubal, L. J. Butler, and F. F. Crim, J. Chem. Phys. **87**, 5820 (1987).

22. D. L. Howard, H. G. Kjaergaard, J. Chem. Phys. **121**, 136 (2004).

23. O. V. Boyarkin, L. Lubich, R. D. F. Settle, D. S. Perry, T. R. Rizzo, J. Chem. Phys. **107**, 8409 (1997).

24. W. L. Dimpfl and J. L. Kinsey, J. Quant. Spectrosc. Radiat. Transfer **21**, 223 (1979).

25. A. Sinha, R. L. Vanderwal, and F. F. Crim, J. Chem. Phys. **92**, 401 (1990).

26. G. H. Dieke and H. M. Crosswhite, J. Quant. Spectrosc. Radiat. Transfer **2**, 97 (1962).

27. I. N. Levine, *Physical Chemistry*, 4th edition (McGraw Hill, New York, 1995).

28. C. Wittig, I. Nadler, H. Reisler, M. Noble, J. Catanzarite, and G. Radhakrishnan, J. Chem. Phys. **83**, 5581 (1985).

29. R. J. Barnes, *The State-Resolved Photochemistry of Small Molecules on Their Ground and Electronic Excited States* (University of California-San Diego, 1999); G. Dutton, R. J. Barnes, and A. Sinha, J. Chem. Phys. **111**, 4976 (1999).

30. L. Zhu, W. C. Chen, W. L. Hase, and E. W. Kaiser, J. Phys. Chem. **97**, 311 (1993).

31. K. A. Holbrook, M. J. Pilling, and S. H. Robertson, *Unimolecular Reactions -2nd Edition* (Wiley, New York, 1996); W. Frost, *Theory of Unimolecular Reactions*

(Academic, New York, 1973); T. Baer and W. L. Hase, *Unimolecular Reaction Dynamics*.(Oxford University Press, New York, 1996); R. G. Gilbert and S.C. Smith, *Theory of Unimolecular and Recombination Reactions*. (Blackwell Scientific Publications, Oxford, 1990).

32. B. G. Ryu, C. R. Park, Y. Lee, S. K. shin, and H. L. Kim, J. Photochem. and Photobiol. A: Chem. **149**, 15 (2002).

33. D. J. Nesbitt and R. W. Field, J. Phys. Chem. **100**, 12735 (1996).

34. K. Lehmann, G. Scoles and B. H. Pate, Annu. Rev. Phys. Chem. **45**, 241 (1994).

35. Gruebele and P. G. Wolynes, Acc. Chem. Res. **37**, 261 (2004).

36. O. V. Boyarkin, T. R. Rizzo, and D. S. Perry, J. Chem. Phys. **110**, 11346 (1999).

37. M. Quack and M. Willeke, J. Chem. Phys. **110**, 11958 (1999).

38. H. Gai, D. L. Thompson, and G. A. Fisk, J. Chem. Phys. **90**, 7055 (1989).

39. C. S. Parmenter and B. M. Stone, J. Chem. Phys. **84**, 4710 (1986).

40. G. A. Bethardy, X. L. Wang, and D. S. Perry, Can. J. Chem. **72**, 652 (1994).

41. D. S. Perry, G. A. Bethardy, and X. L. Wang, Berich. Der Buns. Gesell. **99**, 530 (1995).

Appendix A

Supplementary Equipment Operation and Maintenance

A.1 Introduction

The experiments covered in the dissertation chapters make use of equipment that requires proper operation and regular maintenance. This appendix covers these topics for the laser systems, data acquisition program and electronic devices. As written, ambient temperature of 20 ± 1^{o} C (68 ± 2^{o} F) is found to be optimal for all the laser systems.

A.2 GCR-270 Laser System

A.2.1 Basic Turning-On Procedure

The Spectra Physics ND:Yag laser that pumps the OPO requires a warm-up procedure to ensure optimal power output and to prevent damage to optical components in the YAG and the OPO. As with all the lasers, the YAG requires an external trigger pulse generated which is generated by the BNC Delay Generator discussed in a separate section. The following steps will ensure proper warm-up of the laser:

1. Make sure the external water supply is circulating at pressure greater than 22 psi. Also make sure that the internal DI water reservoir in the back of the power supply unit is in the normal operating level. Turn on the delay generator.

2. Check that the nitrogen cylinder has sufficient purge gas and that the regulator is set to ~6.5 PISG and that flow rate is set to 0.2 SCFH. The OPO also purged with the nitrogen line but the dial is set too low to record the flow rate.

3. Make sure that the knobs on the YAG controllers are set as follows: LAMP ENERGY for the oscillator and amplifier set to 0. REP RATE is set to FIXED and Q-SWITCH is set to LONG PULSE. Also, check that the toggle switches are pointing towards INT, REP and LAMP ON positions and away from the FIRE position as shown in Fig. A.1.

4. Open the YAG cover. The extra air flow apparently increases the output power and stability.

5. Switch the ON key on the power supply unit. The POWER ON and INTERLOCK FAULT indicators on the power supply unit as well as the OFF indicator on the controller should turn on.

6. On the controller, push the ENABLE toggle switch. As a result, the power supply high voltage will energize. The oscillator and amplifier SIMMER indicator lights should turn on after a short charge period.

5. Check the seeder beam using an infrared card right past the second and third harmonic generator (SHG/THG) housing (see Fig. A.2). Warning: Pumping the OPO without seeded beam may damage optical components.

6. SLOWLY turn the oscillator knob clockwise from 0 to 10 to increase the pumping voltages on the flashlamps. This should be done in a continuous manner at a rate of 5 seconds per mark. Then, SLOWLY repeat the step with the amplifier stage (see Fig. A.3). In essence, the process should take about two minutes to increase gradually the voltage of the oscillator and amplifier stages.

7. Once both oscillator stage and amplifier stage are all the way up, there is a 45 minute wait to allow the system to warm-up and equilibrate.

8. After the warm-up stage is done, the system can be switched to external mode. Note that the following steps should be preformed rather quickly to prevent the system from cooling down. If planning to pump the OPO, first turn ON the MOPO controller main power switch located in the rear of the controller.

9. *Quickly* bring the amplifier down from 10 to 0 by turning the LAMP ENERGY dial counter-clockwise. Then reduce the oscillator lamp energy to 0 in a similar manner.

10. Switch the REP RATE dial from FIXED to EXT and then the Q-SWITCH dial from LONG PULSE to EXT as shown in Fig. A.4. The laser is now ready to lase.

11. Bring the oscillator lamp-energy up from 0 to 10 at a faster rate than the warm-up procedure spending about 2 to 3 seconds per mark. At the same rate bring the amplifier lamp energy up from 0 to 5. Do NOT exceed the '5' mark with the amplifier stage.

12. Press the MONITOR key on the MOPO controller. The left bar graph corresponds to the PUMP POWER; it useful to monitor the bar graph levels while increasing the amplifier LAMP ENERGY on the GCR controller. With the LAMP ENERGY on the oscillator at 10 and the amplifier at 5 one expects, depending on alignment, flashlamps age and photodiode gain to read between 8 and 15 out of 99.

13. The amplifier stage needs to be raise slowly in interval to prevent thermal shock to optical components and hotspots in the beam profile. As a general rule the amplifier can be raise every few minutes (2 – 3 minutes) in half interval steps. I.e. in going from 5 to 5.5 one should wait for 2 to 3 minutes before raising the lamp energy again from 5.5 to 6. Because the pulse energy increases non-linearly however, it is important to also monitor the PUMP POWER bar graph on the MOPO controller and only raise the LAMP ENERGY up to 5 units at a time. It is apparent that around 9 on the amplifier LAMP

ENERGY scale, that energy increases very quickly with each turn because in going from 5 → 9, the YAG produces 300 mJ/pulse while going from 9 → 10 leads to additional 200 – 250 mJ gain!

14. When the amplifier stage is increased to 10, the YAG is ready. Normal pump operating power ranges between 495 – 550 mJ/pulse of 355 nm light (THG).

A.2.2 Basic Turning-Off Procedure

To turn the Yag off, follow these basic steps to ensure proper cooling and to make sure the system is ready to be used again next time:

1. *Quickly* bring the amplifier LAMP ENERGY from 10 to 0 in a counter-clockwise rotation.

2. *Quickly* bring the oscillator LAMP ENERGY from 10 to 0 in a counter-clockwise rotation.

3. Switch the Q-SWITCH dial from EXT to LONG PULSE and the REP RATE dial from EXT to FIXED.

4. If the OPO has been used, turn off the main power switch on the MOPO controller.

5. Wait for 5 minutes or longer to allow the water heat exchangers to cool the cavities down.

6. Press the STOP toggle switch on the YAG controller shown in Fig. A.1. The system will halt.

7. Turn the power supply key to OFF position.

8. Turn off the Delay Generator unit.

A.2.3 Maximizing the Power Output

In some occasions, the YAG power output may drop. Even though the SGH/THG housing is temperature regulated, power output may drop when the ambient room temperature changes, or when the voltages on the flashlamps have been changed, or, when realigning the laser. In some cases it may be possible to recover to power output by adjusting the SHG and THG angles (phase-matching). This should be attempted only after the system has been running in full-out mode for at least an hour to ensure that thermal equilibrium has been reached. The procedure can be done by placing a power meter in front of the OPO however, since the MOPO controller PUMP POWER graph bar reads intensities from a photodiode inside the OPO, using it to optimize the phase-matching is more practical.

To phase-match the crystals simply turn very slowly the SHG and THG knobs shown in Fig. A.5 *one at a time* while monitoring the PUMP POWER level. The top knob tunes the SHG crystal and the lower knob tunes the THG crystal. After maximizing the power output, stop ajusting the knobs and wait to see whether the power drifts. If the power remains constant, the optimization procedure is complete. If the power keeps drifting under constant ambient temperature conditions, it is likely that the SHG/THG temperature controller unit is not adjusted properly. In that case, order a service visit.

A.2.4 Internal Cooling System Maintenance

Aside from keeping internal water reservoir filled to the normal operating levels, the internal DI water system requires periodic maintenance. There are two filters inside the power supply unit. According to the manufacturer, the Deionizing Filter (Spectra-Physics part number 9800-0600) and Particle Filter (Spectra-Physics part number 9800-0620) should be replaced with every 6 months of use. To replace the filters, make sure

the power key is in the OFF position. Open the power supply unit by releasing the four screws (two of each side) on the base and lift up the power supply cover. The DI and particle filters are shown in Fig. A.5. To drain the water lines:

1. Pull the reservoir return line shown in Fig. A.5 and place it in a bucket.
2. Turn the power switch key to ON.
3. Push the ENABLE toggle switch on the YAG controller and allow the water to drain from the lines and reservoir.
4. When finished, push the STOP switch on the YAG controller and turn the key OFF.

The particle filter is located on the top level of the rack. To replace it, pull the tube going into the reservoir, allow the water to drain back and disconnect the clip located above the deionizing filter. Using kimwipes, dry any water drops. Next reroute the tubes of the new particle filter and mount the filter with provided fasteners.

The Deionizing filter is located next to the reservoir. A new filter contains amino acids residues and therefore, to prevent contamination of the laser, it must be rinsed thoroughly before installing inside.

1. Start off by rinsing the new filter by attaching it to the DI water faucet and by flowing DI water until the water passing through the filter are colorless (~5 minutes at reasonable flow rate).
2. Disconnect the old filter tubes by pressing on the retaining clips located above and below the filter.
3. Loosen the two filter mounts and remove the filter.
4. Install the new deionizing filter, reconnect the tubes and lock in place with the filter mounts.

5. Refill the water reservoir; it is recommended to use Millipore DI water (from Mark Thiemens' lab) or Nanopore water (from Judy Kim' lab). Turn the system on by turning the key to the ON position and pressing the ENABLE toggle switch on the YAG controller.

6. Make sure there are no leaks anywhere and that air bubbles in the lines have been flushed out.

7. Turn system off by pressing the STOP toggle switch and turning the key to OFF position.

8. Cover the power supply unit and fasten the four screws at the base of the unit.

A.2.5 Flashlamps Maintenance and Replacement

Newly installed flashlamps (Spectra Physics part number: 0450-9080) typically generate sufficient power to pump the OPO for $18 – 21 \times 10^6$ shots before needing replacement. There is a quote # 310409A filed with Spectra Physics that prorate the price of the flashlamps based on performance against 25×10^6 shots corresponding to a discount of 0.72 of the full price.

Even flashlamps that have less than 18×10^6 shots needs some tweaking as they age. Mainly, this involves raising the pumping voltages of the oscillator lamps every ~8 $\times 10^6$ shots or when the 355 nm pump pulse energy drops below ~490 mJ. The current base voltage setting for a new set of flash lamp is 6.54 V as measured at checkpoint (TP) 23 on the oscillator board. Every time the voltage is raised, it is done at 0.03 V increments (ie. 6.54 → 6.57 → 6.60 V). To raise the voltages when the power output is low and the lamps have less than 18×10^6 shots:

1. Measure and record the current power output of the 355 nm.

2. Allow the system to cool and turn it off, as discussed in section A.2.1.

3. Remove power supply cover as discussed in section A.2.4.

4. Attach a voltmeter leads to checkpoint TP23 on the oscillator board and to ground as shown in Fig. A.7.

5. Defeat the interlock on main power supply by pulling up (see Fig x).

6. Switch the main power supply key to ON and turn oscillator dial in the LAMP ENERGY from 0 to 10 WITHOUT pressing the ENABLE toggle switch. Even though the YAG is not firing, the voltmeter should display current voltage settings.

7. Bring the voltages up slowly by using a sharpen wooden Q-Tip turning clockwise the variable resistor R179 on the oscillator board shown in Fig. A.7. If currently the voltage setting is at 6.57 V, you should raise it to 6.60 V. Do not exceed 6.60 V unless the baseline voltage setting has been changed by a service engineer. In essence this allows raising the voltages twice per set of flashlamps. Once at ~8×10^6 shots and another time at ~16×10^6 shots which will bring the voltages from 6.54 → 6.57 → 6.60 V. After that, new flashlamps must be installed.

8. Cover the power supply and recheck the 355 nm power output prior to pumping the OPO. The SHG/THG may require optimization (see section A.2.3). The pulse energy must not exceed 550 mJ; if the pulse energy exceeds 550 mJ, reduce the voltage at checkpoint 23.

9. At full power-out, also take a burn mark in front of the OPO using a Polaroid photography paper to make sure the beam has no hotspots.

Older flashlamps which unable to produce sufficient power output to pump the OPO (490 mJ) need to be replaced. The following steps describe the flashlamp replacement procedure:

1. As described above, the voltages at checkpoint TP23 must be reduced to their base voltage (currently 6.54 V). Follow the steps above to reduce the voltage to the baseline setting and turn the system off.

2. Remove the YAG cover. As shown in Fig. A.8, there are two oscillators cavities and two amplifiers cavities.

3. Short together the terminals of each flashlamp using a screwdriver with insulated plastic handle (see Fig. A.9). CAUTION: The terminal may store few kilovolts.

3. Loosen the terminal posts and disconnect flashlamp wires.

4. Loosen and remove four thumb screws and two blocks from the flashlamp ends. Place kimwipe underneath each block to prevent water from dripping on the dust tubes. There is an O-ring on each side, remove them as well and inspect for wear.

5. Remove flashlamp by slowly pulling it out anode end (red) first.

6. Clean a new flashlamp with methanol and optical tissue from dust and fingerprints. Do not stain flashlamp with fingerprints.

7. Install new lamp by inserting it through the housing cathode end (black) first.

8. Center the lamp and place the O-rings, Teflon blocks and thumb screws.

9. Connect the wire terminals.

10. Repeat above steps for the other flashlamps.

11. Defeat the two YAG interlocks (see Fig. A.8).

12. Switch the main power key ON and press the ENABLE toggle switch on the YAG controller. Warning: High Voltage- keep a way from the YAG.

13. The four lamps should glow. Let the water circulate for 5 minutes and check for leaks all around before turning the system off.

14. Place the YAG cover back on.

15. Reset the shot meter located on the power supply unit.

16. The flashlamps need 6 hours of break-in period in LONG-PULSE mode as described in section A.2.1 prior to lasing.

17. Measure the 355 nm power output after the break-in period and adjust the SHG/THG crystals as needed. Take burn-marks to make sure that the beam has no prior to pumping the OPO. If the pulse energy exceeds 550 mJ reduce the voltage settings at TP23.

A.3 MOPO-730 Laser

A.3.1 Basic Operation Procedure

The OPO laser is pumped by the third harmonic of the GCR-270 and it can generate signal output wavelengths ranging from 440 to 680 nm and idler output wavelengths ranging from 742 to 1830 nm. Typical signal pulse energies range between 60 – 75 mJ and Idler pulse energies range between 4 – 25 mJ. This section describes basic operating procedure for the OPO. There are three function screens a user can toggle between to operate the OPO; these are MONITOR, OPERATE and SCAN SETUP.

The MONITOR screen can be viewed by selecting the MONITOR key. The screen displays graphically the PUMP POWER ranging from 0 to 99, M-OSC POWER (Master Oscillator Power) ranging from 0 to 99, and Tracking Mode. To select the desire tracking mode simply press on the key underneath and toggle between the available

modes using the UP/DOWN arrow keys. After selecting an operation mode, press and hold the key for 2 seconds to activate the mode. The available options are:

1. M-OSC TBL, should be selected when (a) initially warming up the YAG before reaching full-out, (b) when writing a MANUAL TABLE and (c) whenever the laser is sitting on a wavelength without scanning and a calibration table has not been generated.

2. M-OSC TRK, should be chosen when generating a calibration table automatically using the TRACK mode.

3. M-OSC TBL TO, should be used after generating a calibration table in TABLE or TRACK modes but when scanning the laser is not needed.

4. M-OSC TRK TO, should be used when scanning the OPO after generating a track calibration table in TRACK mode.

In essence, the M-OSC-TBL and M-OSC TRK are used in generating manual or automatic calibration tables respectively. After writing either the table, the M-OSC TBL TO (Master Oscillator Table Time Out) and M-OSC TRK TO modes are used for sitting on a particular wavelength or scanning respectively.

The OPERATE screen shows the current wavelengths and allows the user to use the GOTO, START SCAN and MOVE commands:

1. The GOTO command sends the laser to a particular wavelength that is keyed in using the GOTO key and the UP/DOWN arrow keys. To send the laser to the desire wavelength, hold the GOTO key for two seconds. The input wavelength corresponds to the signal output beam which is ranging from 410 to 690 nm. To convert the signal beam to idler wavelengths in cm^{-1} and nm use the following relationships respectively:

$$\nu_{idler}\ [cm^{-1}] = 1 \times 10^7\ (1/354.72\ [nm] - 1/\lambda_{signal}\ [nm]) \qquad (A.1)$$

$$\lambda_{idler}\,[nm] = (1/354.72\,[nm] - 1/\lambda_{signal}\,[nm])^{-1} \quad (A.2)$$

Where the ND:YAG third harmonic is $\lambda_{THG} = 354.72$ nm.

2. START SCAN allows the user to begin and stop the scan by holding down the key for 2 seconds. The scan parameters are controlled from the SCAN SETUP screen discussed below.

3. MOVE allows the user to manually change the wavelength. Simply press the MOVE key and use the UP/DOWN arrow keys to change the wavelength to the red and blue.

The SCAN SETUP screen allows the user to set the scan parameters such as number of scans, initial and final wavelengths, and scan rate.

1. SCAN sets the number of scans desired and it is typically set to 1.

2. BEGIN indicates the initial wavelength.

3. END indicates the final wavelength.

4. CONT. indicates the scan rate in nm/sec ranging from 0.002 – 0.25 nm/sec. The dissertation author finds that using scan rates faster than 0.030 makes it hard on the system to track the power while scanning. Optimal scan rates for overview spectrum covering large ranges (such as $2\nu_{OH} - 3\nu_{OH}$ bands) can be taken at 0.015 – 0.025 nm/sec while averaging 20 or 30 shots/bin averaging, and for scans over a single vibrational band scan rates of 0.002 – 0.010 nm/sec while averaging 30 or 50 shots/bin averaging generate neat spectra.

5. To start the scan, switch to the OPERATE screen, then press and hold the START SCAN key for 2 second. When the scan completes, the program sends the OPO to the initial wavelengths.

A.3.2 Writing Calibration Table

The OPO optimizes the power output for a given wavelengths position based on values obtained from a calibration table generated by the user. Prior to scanning the OPO over a new range of wavelength or whenever alignment and/or YAG output power have changed, it is recommended to re-write the calibration table. There are several manual calibration modes and one automatic calibration mode. It is recommended start with the automatic calibration mode and if it fails, use manual calibration instead. To generate automatic calibration table:

1. Allow the YAG power output to equilibrate for a little awhile.
2. Press the SCAN SETUP key and set the initial and final desire wavelength to write a table over. The scan rate is not relevant.
3. Press OPERATE key twice to access the calibration menu.
4. Press the M-MIKE key and using the UP/DOWN arrow keys and select the TRK mode.
5. Press and hold the M-MIKE key for 2 seconds to set the TRK mode.
6. Press the CALIB. key and using the UP/DOWN arrow keys and select the TRACK mode.
7. Press and hold the CALIB. key to start the calibration.
8. The laser will go the initial wavelength and procedure to optimize the power output.

When calibration table completes successfully, press the MONITOR key and select the M-OSC TRK TO mode as described above.

The laser should now have a useable calibration table over the selected range of wavelengths.

In some situations, such as low pump power or poor initial calibration table, it may be difficult for the automatic table writing routine to generate a good calibration table. When this occurs, the automatic calibration table routine will terminate unsuccessfully and it may be necessary to first generate a manual table:

1. As with the automatic calibration routine, in the SCAN SETUP menu, select a range of wavelengths, however, choose a range covering *only* 6 nm at a time. i.e. $\lambda_i \leq \lambda \leq \lambda_i + 6$ nm. For example, $\lambda_i = 470$ and , $\lambda_f = 476$ nm.

2. Press OPERATE key twice to access the calibration menu.

4. Press the M-MIKE key and using the UP/DOWN arrow keys and select the TBL mode.

5. Press and hold the M-MIKE key for 2 seconds to set the TBL mode.

6. Press the CALIB. key and using the UP or DOWN arrow keys and select the MODIFY mode.

7. Press and hold the CALIB. key for 2 seconds.

8. Press the METHOD key and toggle using the UP/DOWN arrow keys and select the LAGRNG.

9. Press and hold the METHOD key for 2 seconds. The OPO will go the initial wavelength.

10. Press the ADJUST key and using the UP/DOWN arrow keys, optimize the M-OSC power levels. When maximum values obtained, press CONT to continue.

11. The wavelength will increase by one unit from 470 to 471 and the process is repeated over the 6 chosen wavelengths.

12. When all 6 wavelengths have been optimized, press and hold the SAVE? Key for 2 seconds to save the calibration table.

13. Repeat steps 1 through 12 over a new range of wavelengths as needed, i.e. 476 to 482 nm.

14. After the entire range of desired wavelengths has been covered, rerun the automatic calibration routine to optimize the calibration values between non-integer wavelengths values.

A.3.3 MOPO Alignment

From time to time the frequency overlap between the Master Oscillator (MO) and the Power Oscillator (PO) needs optimization because of beam drifting due to vibrations. The MOPO optical layout is shown in Fig. A.10. The MO-TM2 and PO-TP2 diachroics highlighted in the figure are very sensitive to adjustments and ONLY the VERTICAL (top) degree of freedom should be adjusted.

1. Allow the YAG power output to equilibrate for a little awhile.

2. Make sure the M-OSC in the MONITOR screen is set to TBL.

3. Remove the OPO cover slowly by lifting straight-up.

4. Slowly turn in clockwise and/or counter-clockwise motion the VERTICAL degree of freedom of the MO-TM2 (see Fig. A.10) *while* monitoring the M-OSC POWER level in the MONITOR screen of the MOPO controller. Do not use a power meter to adjust the M-OSC power.

5. Stop tweaking the knob when maximum level is found.

6. Adjust the VERTICAL (top) degree of freedom of the PO-TP2 diachroic by monitoring the idler power output using a power meter.

7. When the maximum power is achieved, place the MOPO cover slowly and rewrite the automatic calibration table as needed.

A.3.4 Optics Replacement

There are several optical components that have been replaced in the MOPO laser system with parts from vendors other than Spectra-Physics due to significant price difference. Table A.1 lists these original Spectra-Physics parts and their compatible parts that were obtained from other vendors. The location of the optical components inside the MOPO is indicated in Fig. A.11.

A.4 NY82-10 / NY82-20 Laser System

A.4.1 Basic YAG Turning-On Procedure

The Continuum ND:Yag lasers NY82-20 and NY81-20 are very similar to one another in operation except that the NY82-20 has a seeder and an preamplifier pass. Specs powers for the NY82-20 and NY81-20 are 550 mJ and 320 mJ respectively. Currently, the power outputs are 510 at 1.29 kV and 210 mJ at 1.34 kV respectively for the two lasers. Also, the NY82-20 has a THG crystal for 355 nm generation and the NY81-20 has a FHG crystal for 266 generation. As with the OPO system, the Continuum YAGs also require warm-up procedure:

1. Make sure the external water supply is circulating at pressure greater than 22 PSI. Also make sure that the internal DI water reservoir is in the normal operating level.
2. Turn on the delay generator.
3. Turn main power switch located on the right side of the power supply unit ON.
4. Make sure that the NY82-20 power supply settings are as follows: Voltage (PU620A) should not exceed 1.29 kV, Oscillator delay (CB631A) = 75 μs, Amplifier delay

(CB632A) = 50 μs. The NY81-20 power supply settings are as follows: Voltage (PU620A) should not exceed 1.34 kV, Oscillator delay (CB630A) = 60 μs, Amplifier delay (CB630A) = 55 μs.

5. Check that the DI water resistivity light is green; if red, see below internal DI water supply section below.

6. Switch the key on power supply unit to ON. The laser will pulse in Long Pulse mode.

7. If the seeder is needed, switch the seeder key located underneath the NY82-20 laser to ON to allow the seeder beam to stabilize.

8. Wait for 20 minutes for the laser to warm up.

9. On the YAG controller, press the AUTO/MANUAL key once. Then press the UP arrow twice to access PROGRAM 2 (PGM 2 – 20 Hz, 165 μs). Press the ACITVE key to activate the program (see Fig. A.12).

NOTE: If the dye laser is used in conjunction to the YAG laser, make sure you read the dye laser operating procedure prior to lasing.

10. To lase, simply hit the SHUTTER key (see Fig. A.12). To stop lasing, simply press the SHUTTER key again.

A.4.2 YAG Turning-Off Procedure

To turn the Yag off, follow these basic steps to ensure the laser is properly cooled:

1. If the laser is lasing, press the SHUTTER key (see Fig. A.12).

2. Switch the key to OFF position.

3. Allow the system to cool for at least 5 minutes.

4. Turn the main power switch OFF.

A.4.3 Dye Laser Turning-On Procedure

Before pumping the Dye laser, follow the procedure described below:

1. The oscillator cavity in the dye laser is thermally regulated and maintained 31.6^{o} C. The ND60 dye laser pump by the NY81-20 YAG laser requires an external power source to power the heater. The external power supply currently provides 9 V and 1.8 Amps to hold 31.6^{o} C in the oscillator cavity.

2. Turn the PC monitor ON.

3. Run the Dye Laser Program ND62:

A:> ND62

4. After the program loads, while holding the SHIFT key, press the 5 key (SHIFT + 5 or %) to reset the optical arm and to calibrate the laser.

5. Turn ON the dye circulator.

6. The dye laser can be pumped now.

A.4.4 Basic Dye Laser Turning-Off Procedure

To turn the dye laser off, follow the procedure described below:

1. SHUTTER the YAG laser and stop it from lasing.

2. Turn OFF the dye circulator.

3. Press “Q” to quit the dye laser program.

4. Turn the monitor OFF.

A.4.5 Basic Dye Laser Operation

There are several menus in the dye laser software that allow for tuning the laser. To select an option click the first letter associated with the option.

The (**G**)OTO option allows the user to send the laser to a particular wavelength. To send the laser, press ‘G’ and type the desire wavelength in nm followed by ENTER key.

The (**D**)ISPLACEMENT option is similar to the GOTO key except that it displaces the wavelength by ± λ nm from its current position. For example, to change current wavelength by 5 nm, press ‘D’, type the number of wavelength to change (5 nm), and press ENTER.

The (**M**)anual option allows changing the wavelength manually. Simply press ‘M’ and select the manual tuning rate and use the RIGHT/LEFT arrow keys to displace the wavelength.

The (**N**)ew Parameters option allows changing the current Dye used, select initial and final scan wavelength and scan rate. Press ‘D’ to load the (**D**)ye List. Toggle through the list using the UP/DOWN arrow keys to select the current dye and press **F10** to save choice. Press ‘B’ to select the (**B**)EGIN scan wavelength (nm) and press ‘E’ to select the (**E**)ND scan wavelength (nm). Select ‘V’ to choose (**V**)ELOCITY (Å/s). Lastly, select ‘N’ to input the (**N**)umber of scans.

For molecular beam experiments, reasonable scan rates are found to be 0.00050 – 0.0025 Å/s while averaging 100 or 50 shots respectively. And, for room temperature experiments, rates of 0.012 and 0.12 Å/s averaging 30 shots generate neat rotational and vibrational spectra respectively.

Pressing the (**P**)ROGRAMMED SCAN option executes the scan programmed.

(**B**)URST MODE permits generating scans that are synchronized with data acquisition program (DAP) LIF31 as used for product state distributions and Doppler

profile measurements. To initiate, press ‘B’ followed by ‘E’ for (**E**)XTERNAL mode. Next, enter the initial wavelength and the micro-steps to take between each wavelength. Press ENTER or ‘Y’ to execute, and ‘N’ to cancel. The laser will go to the desire wavelength and wait for handshake pulses from the DAP. As the laser changes wavelength, the number of micro-steps taken is shown but the current wavelength position is only shown when the scan completes.

A.4.6 Internal Dieonized Water System

As with the MOPO system, the NY82-20 and NY81-20 also require periodic maintenance to their internal water cooling system. Aside from keeping the water level at its operating level with Millipore or NanoPore water (see section A.2.4), the two filters used in the system are the DI water filter (Continuum part 313-0099) and PALL capsule 3 μm particle filter (VWR part 28145-780). When the resistivity light stays red instead of changing to green, it is time to replace the DI water filter. To replace the filter:

1. Open the filter cover on the bottom of the power supply unit (CG603A), pull the unit out a little for better access, and disconnect the filter (see Fig. A.13).
2. Remove the female connectors from both sides of the filter.
3. Wrap a fresh piece of Teflon on the connectors and reattach to the new filter.
4. Reconnect the filter.
5. Turn ON the main power switch and check for leaks.
6. Allow the water to circulate up to four hours for light to change to green again. The laser can be used in the meantime.

The external water filter requires replacement when the user receives “water interlock” error message on the YAG controller. This error message simply indicates insufficient flow rate due to a clogged external filter. To replace the external filter:

1. Place a Pyrex tray underneath the filters.
2. Disconnect the hose clamps from one side and pull the hose from the old filter.
3. Connect the hose to the new filter and clamp.
4. Remove the hose clamp from the other side of the old filter and remove the hose.
5. Reconnect to the new filter and clamp.
6. Turn ON the main power switch and check for leaks.
7. Purge excess air from the filter using the purge nipple on the filter prior to lasing.

If the internal water system is contaminated with algae, hydrogen peroxide treatment is recommended. To treat with H_2O_2:

1. Remove the internal DI filter.
2. Remove, external water filter and reattach a glass or a plastic tube instead.
3. Drain old water from reservoir and refill with fresh DI water.
4. Add 500 mL of 30 % H_2O_2 and allow circulating for an hour.
5. Drain the reservoir and refill with fresh water and circulate. Repeat until no H_2O_2 is present (~10 refills).
6. Reattach the filters- preferably a new set.

Lastly, the DI water system is driven by magnetic pump drive (part number MD-30RZ-220N) which can be purchased from “Pumping Solutions” (909) 930-6600.

A.4.7 Dye Circulator

The dye laser circulator pump is supposed to provide a constant flow of 1 liter / 40 sec through the oscillator/amplifier cuvettes. If flow rate is low, the particle filter located past the pump/motor assembly may require cleaning. To remove the filter, unscrew the cap remove the filter (9 μm, Continuum part 313-0274) and place in a sonicator with methanol. If the flow rate is still slow, the pump may need to be replaced. The pump/motor assembly is manufactured by TUTHILL (part number B10059T) and can be purchased from Fluid Handling System (562-483-6094). To replace the pump:

1. Drain the Dye solution and rinse the line with methanol.
2. Remove the 10 screws holding the circulator housing (4 in front, 6 in rear).
3. Remove the housing.
4. Remove the input and output dye flow tubes from the pump and unscrew the 4 screws holding the pump.
5. Replace pump and reconnect tubes.
6. Check the flow rate. If the flow is slower than the spec (1 L/40 sec.) adjust the screw at the base of the pump to increase or decrease the flow rate as necessary.

A.4.8 NY82-20 and NY81-20 Flashlamps Replacement

The following section describes the flashlamps replacement procedure for the NY81-20 and NY82-20. The procedure itself is the same for the two lasers except where noted otherwise. Three lamps are required for the NY82-20, one oscillator (Continuum part 203-0019) and two amplifier lamps (Continuum part 203-0032). The NY81-20 requires one oscillator lamp (Continuum part 203-0019) and one amplifier lamp (Continuum part 203-0019); both lamps are identical. To change lamps:

1. With power OFF, open the laser cover.

2. Remove dust covers.

3. Slowly remove cladding covers; the Faraday Isolator in the NY82-20 has a strong magnet that will attract the cover (see Fig. A.14).

4. Remove the anode/cathode leads from the cladding and the heater sensor wires (see Fig. A.15).

5. Unscrew the cladding by turning the bolt underneath the cladding *clockwise* (see Fig. A.16).

6. Watch for water spilling out of the cladding; use kimwipes to dry out water drops.

7. Place the cladding on a clean counter on top of kimwipes.

8. Loosen and remove two Alan screws attached to the Teflon block from each side of the flashlamp.

9. Remove the Teflon washers and O-rings; inspect for wear.

10. Remove flashlamp by slowly pulling it out in any direction.

11. Clean a new flashlamp with methanol and optical tissue from dust and fingerprints; do not touch the flashlamp with hands.

12. Insert new lamp; the oscillator in the NY82-20 and the NY81-20 requires a single flashlamp (Continuum part 203-0019). The amplifier in the NY81-20 requires the same flashlamp as the oscillator. The amplifier in the NY82-20 requires two flashlamps (Continuum part 203-0032).

13. Center the lamps and place the O-rings, washers, Teflon blocks and Alan screws. Place cladding back in laser and tighten the bolt underneath by turning *counter clockwise* (see Fig. A.16).

14. Reattach the lamp leads and heater sensor wire terminals.

15. Repeat above steps for the other cladding.

16. Turn main power switch ON and search for leaks.

17. Place back cladding covers and dust covers.

18. Reset the shot counter.

19. Cover the laser and measure power output.

A.5 Frequency Mixing using Inrad Autotracker III

The lab has four Autotrackers (labeled I – IV) that are used to generate additional frequencies via doubling (λ/2), tripling (sum frequency mixing, λ/3) and difference frequency mixing (DFM, $1/(1/\lambda_{dye} - 1/1064)$). Currently, two units are configured for IR DFM generation, another unit is configured for frequency doubling and the last unit is configured for tripling.

The Autotracker units operate similarly to one another. The differences between each unit are in the filters installed, compensation blocks, input polarization and photodiodes detectors assemblies. These components depend on the crystals and the type of mixing process. The crystals that are currently available to generate the various frequencies are listed below:

A $LiNBO_3$ (lithium naobate) crystal (Type I, Theta = 50.0 deg) that is used to mix (DFM) a horizontally polarized dye (657 – 841 nm) with a vertically polarized 1064 nm to generate 1.72 – 4.0 μm light. The crystal dimensions are 18.5 W × 13.5 H × 30.0 L mm. The crystal was purchased from Conex Systems Technology (925-735-8825). Typical input energies for the 730 nm and the 1064 nm were 50 and 120 mJ respectively. The output energies were ~0.25 mJ.

A $LiNBO_3$ (lithium naobate) crystal (Type I, Theta = 59.9 deg) that is used to mix (DFM) a horizontally polarized dye laser (585 – 690 nm) with a vertically polarized 1064 nm to generate 1.3 – 1.96 μm light. The crystal dimensions are 18.5 W × 13.5 H × 30.0 L mm. The crystal was purchased from Photop Technologies (818-678-1999). Typical input energies for the 608 nm and the 1064 nm were 25 and 35 mJ respectively. The output pulse energies were 2 – 3 mJ but the crystals were damaged during use. The same crystal was also purchased from Conex Systems Technology (925-735-8825) but has yet to be tested.

A KDP doubling crystal (Continuum, DCC2) is used to double the output of the vertically polarized dye laser (590 – 730 nm) to generate 295 – 365 nm light. The crystal is housed in an old Continuum housing that no longer fits the company's autotracker unit but works well with the Inrad Autotracker III unit.

A BBO crystal (Type I, Theta = 65 deg) for THG by mixing vertically polarized 608 – 687 nm dye output with its vertically polarized doubled output to generate 203 – 229 nm output. The crystal dimensions are 8 W × 10 H × 6.5 L mm. The crystal is coated with magnesium fluoride and is mounted as purchased from Inrad (BBO Type C, 201-767-1910). The crystal typically generates 1.5 – 2 mJ when pumped with 55 mJ of 630 nm light. The crystal can be used for NO laser-induced fluorescence detection via the $A^2\Sigma - X^2\Pi$ band at 220 nm.

A BBO crystal (Type I, Theta = 53.2 deg) for THG by mixing vertically polarized 645 – 825 nm dye output with its vertically polarized doubled output to generate 215 – 275 nm output. The crystal dimensions are 8 W × 10 H × 8 L mm. The crystal is coated with magnesium fluoride and is unmounted as purchased from Photop Technologies

(818-678-1999). The crystal can be used for HCO laser-induced fluorescence detection via the $B^2A - X^2A$ band at 258 nm.

To generate the above frequencies, a proper input polarization is required. In addition, different sets of filters and compensator blocks used required inside the Autotracker unit:

For IR generation (Autotrackers labeled I and IV), since the YAG output is circularly polarized, a ¼ and ½ waveplates (CVI part numbers: QWPM-1064-10-4 and QWPM-1064-10-2) are placed sequentially along the beam-path and resulting in a horizontally polarized 1064 nm beam. The dye laser is vertically polarized. The $LiNBO_3$ crystals require a horizontally polarized dye laser and vertically polarized 1064 nm input beams. In order to reverse the relative polarization of the two beams, a periscope is placed in front of the crystal as shown in Fig. 8.3. Inside the Autotracker unit, a CB-1 compensator block is used to direct the beam to the photodiodes. Two FC-6 (block the dye output) and IR-FD (IR neutral density) filters are placed in front of the photodiodes assembly.

For doubling (using Autotracker labeled III), the vertically polarized dye laser is directed to the DCC crystal through a CB-1 compensator block. The beam is directed to the photodiodes detectors with a FR-ϕ filter. A set of two FC-2 (to blocks the visible), and several FD (neutral density) filters are placed as needed in front of the photodiodes detector.

For tripling (using Autotracker labeled II), the vertically polarized dye laser is first doubled in a DCC crystal. Subsequently, the doubled output (horizontal) is rotated with a Quartz rotator (Inrad 741-251/02 for 311 – 362 nm) or Quartz rotator (Inrad

SY6777-3 for 380 – 415 nm) and combined with the residual dye fundamental. The beams are directed to the BBO crystal through a CB-4T6 compensator block. A portion of the beam is directed to the photodiodes detectors with a FR-4 filter (198 – 220 nm) or FR-2 filter (217 – 235 nm) or FR-1 filter (235 – 270 nm). Several FD (neutral density) filters are placed in front of the photodiodes detector as needed.

The number of FD or IR-FD filters actually used, depend on the amount of output light generated. Since the gain on the photodiodes ranges from 1 to 21, it best to place as many neutral-density filters such that the display readout is at 75% filled at peak power when the gain is set to around ~10 (7 – 14); this permits the unit to autotrack properly while scanning the laser.

The Autotracker has several control features worth mentioning. All the features discussed below are shown in Fig. A.17:

The LIGHT key turn ON and OFF the display light.

The AUTO feature switches the unit from MANUAL mode to autotracking mode. To autotrack:

1. Before switching to AUTO mode, make sure that correct filters and beam polarization are used.
2. Set the DSP to 4 by using the AVG /ALT+AVG keys to increase or decrease the averaging value respectively.
3. Set the Ctl to 4 by pressing ALT+AUTO key and selecting at the prompt the value 4 and confirming with the ENTER key; this value affect the averaging rate for the AUTO mode.

4. Set the ARATE to 1 by pressing the ARATE/ALT+ARATE to increase or decrease the rate value respectively.

5. Maximize the power output by changing the TILT angle using the RED/BLUE keys.

6. Slowly turn the detector knob located on the Autotracker unit until the PD1 and PD2 on the display are equal. If the fluctuations are large, also change the focusing condition to reduce the scatter on the photodiodes.

7. Press the AUTO key to switch to autotracking mode and check that the power output remains constant.

8. Change the wavelength and check that the unit is autotracking monitoring PD1 and PD2; they should equal each other as the laser scans. If the scan rate is too fast for the current autotracking speed, the ARATE can be increased (see step 4).

The MANUAL key switches from AUTO mode to manual mode. The crystal tilt angle is controlled using the RED/BLUE keys and the GOTO key. The rate the angle is changing can be controlled using the MRATE/ALT+MRATE key to increase or decrease the rate value respectively.

A.6 Photomultiplier Tube

Two UV/VIS photo-multiplier tubes (PMT) were used in collecting the measurements reported in the dissertation chapters. The EMI-9635QB and EMI-9813QB PMTs have spectral responds in the 160 – 650 nm range. However, the EMI-9813QB has a higher gain, which also has a gating circuit. As a higher gain PMT, it can be pumped with maximum of 2.45 KV compared the 1.15 KV allowed for the EMI-9635QB. The gating circuitry requires a 5 V pulse with minimum of 2 μs gate width and minimum of 2

μs gate delay. The actual parameters used are discussed below in the delay generator section.

Before turning the PMT on turn the main lights in the room OFF to prevent the ambient scattered light from reaching to the PMT. Also, before dismounting the PMT from the photolysis cell, turn OFF *all* light sources, including computer monitors, etc in the room to prevent damaging the PMT.

A.7 Delay Generator

The delay generator (BNC series 555) is externally triggered by Rhett's pulse generator. Therefore, t_0 is defined as the pulse received from Rhett's box. The delay generator has 8 channels, each producing 5 V signals. Each of the three YAG lasers requires a lamp fire pulse and a Q-switch pulse. The other two delay generator channels send trigger signal to the PMT gate and Pulse Valve. To turn the delay generator on, turn the power switch ON and allow the software to boot. After booting, press the RUN/STOP key to enable trigger pulses.

Since the pulsed valve requires ample response time, the lasers and PMT triggers are delayed by 1100 μs with respect to t_0. This section details the current parameters which are saved as PROGRAM 12 and load automatically when the delay generator is turned on:

Channel *A*: NY82-20 Lamp Fire

Pulse Width: 10 μs
Delay: 800 μs
Polarity: Active low
Output: TTL/CMOS
Mode: Normal
Gate: Disable
Pol: Active high

Channel *B*: NY82-20 Q-Switch

Pulse Width: 10 μs
Delay: 1100.1 μs
Polarity: Active low
Output: TTL/CMOS
Mode: Normal
Gate: Disable
Pol: Active high

Channel *C*: OPO Lamp Fire

Pulse Width: 0.1 μs
Delay: 912 μs
Polarity: Active high
Output: TTL/CMOS
Mode: Normal
Gate: Disable
Pol: Active high

Channel *D*: OPO Q-Switch

Pulse Width: 0.1 μs
Delay: 1100.08 μs
Polarity: Active high
Output: TTL/CMOS
Mode: Normal
Gate: Disable
Pol: Active high

Channel *E*: Pulsed Valve

Pulse Width: 10 μs
Delay: 516 μs
Polarity: Active high
Output: TTL/CMOS
Mode: Normal
Gate: Disable
Pol: Active high

Channel *F*: NY81-20 Lamp Fire

Pulse Width: 10 μs
Delay: 800 μs
Polarity: Active low

Output: TTL/CMOS
Mode: Normal
Gate: Disable
Pol: Active high

Channel *G*: NY81-20 Q-Switch

Pulse Width: 10 μs
Delay: 1100.17 μs
Polarity: Active low
Output: TTL/CMOS
Mode: Normal
Gate: Disable
Pol: Active high

Channel *H*: PMT Gate

Pulse Width: 8 μs
Delay: 1092.6 μs
Polarity: Active high
Output: TTL/CMOS
Mode: Normal
Gate: Disable
Pol: Active high

Looking at Channels A and B which send pulses to the NY82-20 YAG laser, we see that the both the lamp and Q-switch require a negative (active low) 5 V (TTL/CMOS), 10 μs-wide trigger pulses. These pulses are at 50 ms (20 Hz) rate (Normal) and are un-gated. There is also a ~300 μs delay between the lamp firing pulse and the Q-switch pulse where the lamp firing pulse is sent 800 μs after receiving t_0 pulse from Rhett's box. This is design to accommodate for the valve which requires a pulse 400 – 800 μs (currently fixed at 1100 – 516 = 584 μs) prior to the laser firing to allow for a sample flowing through the pulsed valve to reach the interaction region inside the vacuum chamber.

It is also important to note that while the lamp firing and Q-switch channels are independent of one another, changing of the Q-switch timing also requires changing the

Lamp firing timing by same Δt in order to maintain peak power. This is especially important when changing the Q-switch delay by more than ± 2 μs.

A.8 Data Acquisition Program

The data acquisition program (DAQ), LIF31, is used to record all the measurements in the dissertation chapters. For the program to collect data, the following equipment must be turned on:

1. Turn the delay generator ON and enable trigger (see section A.7).
2. Turn the NY81-20 main power switch ON. The trigger from the laser is sent to the electronic rack.
3. Turn ON the three power switches (integrator, main and stepper power switches) on the electronic rack (see Fig. A.18).
4. Run "LIF31" program.

C:> LIF31.EXE

The program has several menus:

The PROBE SCAN option allows for running the BURST mode using the dye lasers. It should be initiated only after setting the BURST mode discussed in section A.4.5. To start the routine, press '3'. Leave the delay settings at 0 by pressing ENTER. Next, choose the number of shots/μstep the program should average. 20 or 30 shots/μstep works well with 3 or 5 laser μstep (see section A.4.5). Leave the DATA CHANNELS FOR A/D CONVERTER with the value '3'. When asked for initial and final wavelengths, you may choose to change the values or leave unchanged. As discussed in Appendix *C*, the data analysis is independent of these values. If this scan is using the doubled output of the dye laser, select 'Y' for UV SCAN. Select 'N' for DUPLEX scan

and add comments for the scan as wanted. To start the scan, press ENTER. To stop the scan, lift and hold the HALT knob on the stepper (see Fig. A.18) unit in the electronic rack and choose whether to save the file.

The BLANK SCAN calls for the unsynchronized scanning routine. To start the routine, press ‘3’. Leave the delay settings at 0 by pressing ENTER. Enter the scan lengths in minutes and press ENTER. Choose the number of shots per bin and press ENTER. Normally, 20 or 30 shots per bin work well in terms of averaging. For the number of A/D channel, select 1 for PMT data acquisition and 2 for photoacoustic data acquisition. In either case, both channels are acquired and can be accessed after the file has been saved, but only the channel chosen will be displayed on screen. To start the scan press ENTER. To stop the scan, lift and hold the HALT knob on the stepper unit in the electronic rack and choose whether to save the file.

To display a saved file, select ‘5’ from the main menu and input the file name. All the files are stored in the C:\DATA\MOLEC_NAME where MOLEC_NAME correspond to the directory named after the molecule. For example, CH_3OOH data is stored in the C:\DATA\CH3OOH directory. To change the working directory, select ‘7’ from the main menu and ‘8’ to change the directory path. Enter the new path and press enter. To save updates press ‘S’ and ENTER, to exit without saving ‘X’.

The experiments discussed in the dissertation chapters are taken with certain integrator settings. Typically, the PMT signal is attenuated by 10 dB prior to entering the integrator (SRS, SR250) and the signal is attenuated by 6 dB exiting the integrator . The integrator averages the fluorescence signal of 10 laser shots. The gate width is chosen to be 500 or 1500 ns which correspond to OH fluorescence lifetime in the photolysis cell

and molecular beam cell respectively. Lastly, the signal sensitivity multiplier is chosen based on signal to noise ratios.

A.9 Molecular Beam Apparatus

Some measurements are taken under molecular beam environment. This section gives operating procedure of the chamber.

1. Switch the pressure controller ON. Do not turn on the ion gauge.

2. Fill the trap with liquid nitrogen (LN_2).

3. The vacuum line has two gate valves by the LN_2 trap. The valve closer to the mechanical pump is typically left open. Open the second valve and wait until the back pressure in the flexible tube drops to baseline.

4. Open the chilled water supply and return lines going to the diffusion pump.

5. Slowly open the gate valve attached to the vacuum chamber by turning *counter clockwise*. Allow the air to evacuate and close the valve by turning *clockwise* to isolate the chamber.

6. Plug the diffusion pump to the 14/16 electrical socket and allow at least 45 minutes to warm-up.

7. Slowly open the gate valve attached to the vacuum chamber and wait for 15 minutes.

8. Measure the pressure inside the chamber by turning the ion gauge on by pressing the filament button. Make sure that the range selected on the dial is initially set to 10^{-4} and work your way down needed. Typical pressure in evacuated chamber should initially ~5 $\times 10^{-6}$ Torr. This value should drop to 1×10^{-6} Torr or under by the end of the day.

9. Switch back the ion gauge range to 10^{-4} and pulse the valve. Typically, good signal levels are obtained when the pressure inside the chamber is around ~2×10^{-5} Torr but

make sure that the helium pressure going to the mechanical pump through the LN_2 trap is not greater than 100 mTorr.

10. To check the signal level. Turn OFF the ion gauge and cover with a blind to prevent laser and ambient light from scattering.

11. Also cover the pulsed valve with a blind. Laser light tends to penetrate through the transparent Kel-F faceplate.

12. Make sure the lasers go cleanly through the chamber and turn the PMT on.

To turn off the vacuum chamber:

1. Turn PMT, lasers and pulsed valve off.

2. Slowly close the gate valve attached to the vacuum chamber.

3. Disconnect the diffusion pump electric cable.

4. Switch off the pressure controller.

5. Wait for ~2 hours for the chamber to cool down.

6. Close the gate valve leading to the flexible vacuum line.

7. Close the chilled water supply and return lines.

The pulsed valve (General Valve, Series 9) assembly is modified from it original design in order to reduce the decomposition rate of molecules by reducing their contact with metal surfaces. There are two custom faceplates that are made out of Kel-F. One has 0.4 mm orifice and the other has a 1.0 mm orifice to allow greater gas flow over shorter valve open time. The pulsed valve is coated with halocarbon wax and the plunger/spring assembly is Teflon coated. The poppets that work with both faceplates are commercially available and are made out of either Teflon or Kel-F. They can be purchased from General Valve (Teflon part 003-0023-050-002 and Kel-F part 009-0185-020-002). It

appears that the Kel-F poppet is more resilient and less likely to wear down as quickly as the Teflon poppet. Its influence on the decomposition rate of molecules has not been tested. The pulsed valve components are shown in Fig. A.19.

The valve is screwed into the faceplate which has an O-ring for a seal. In order to seal from external leaks, the valve must be screwed-in sufficiently. There is a small range in which the faceplate and the pulse valve seal from external leak while the poppet seals the orifice *but* not too tightly such that the valve motion is restricted and the poppet does not fully open. This is best achieved by energizing the valve to keep the plunger retracted while slowly screwing the valve into the faceplate a few turns. Energizing the valve is important to prevent grinding the poppet on the surface of the faceplate. Next, check for leaks by hooking up the input lines to a mechanical pump to see if the poppet seals in the mTorr range. If the orifice leaks, re-energize the valve and tighten a bit more and recheck for leaks. If no leaks found, pulse the valve. While the valve pulses, the sound resonating from the motion should sound 'crisp'. One should also check if the pressure rises when the valve is pulsating. If all appears well, attach to the vacuum chamber and test for leaks.

The Iota One controller which powers the pulsed valve is configured in the following manner. The On Time Duration is set depending on the desire pressure to 350 – 750 μsec. The Off Time duration is configured at 20.0 Hz and is controlled externally (One Shot) by the delay generator that plugs into the Input TTL.

A.10 Liquid Nitrogen Level Controller

The liquid nitrogen trap has a dual level controller which automatically fills the Dewar when the liquid level gets below the lower senor and stops when the upper sensor is immersed in the liquid. The lower level sensor is typically placed about ¼ of an inch

above the base of the trap and the upper sensor is placed about ¾ of an inch below the trap cover.

To ensure proper operation of the controller in terms starting and stopping filling up the trap, the voltages on the board should be adjusted as follows:

1. Fully immerse the two sensors in liquid nitrogen.
2. Open the controller cover.
3. Place the negative lead of the voltmeter in position labeled R1 in Fig. A.20.
4. Place the positive lead of the voltmeter in position labeled R2 in Fig. A.20.
5. Adjust the voltages on the variable resistor labeled *B* in Fig. A.20 until the voltage reads between 104 and 110 VDC.
6. Leave the negative lead in position R1 and connect the positive lead to R3 and adjust the voltages on the variable resistor labeled *C* until the voltage reads between 104 and 110 VDC (see Fig. A.20).

The controller is now calibrated. The controller and accessories are commercially available from JC Controls (http://ln2.net, 887-837-8877).

Table A.1: MOPO System Optical Components Replacement Parts

Product	Size	Spectra-Physics Part	Vendor Part	Location in MOPO [a]
Lens +300 (AR355) PL/CX	1”	0449-2340	CVI PLCX-25.4-154.5-UV-355	MO-PL
Lens +200 (AR355) PL/CX	1”	0448-8860	CVI PLCX-25.4-103.0-UV-355	PO-PL
Lens -150 (AR355) PL/CC	1”	0448-8880	CVI PLCC-25.4-77.3-UV-355	PO-NL MO-NL
Lens -100 (AR355) PL/CC	1”	0448-8890	CVI PLCC-25.4-51.5-UV-355	PO-NL MO-NL
Beamsplitter 1% (AR 355) 45deg, s- polarization (vertical)	1” x 1/4”	0448-8500	CVI BS1-355-02-1025-45S	BS1
OPO input window (AR355)	1” x 1/8”	0449-1910	CVI W2-PW1-1012-UV-355-0	OPO Cover
BBO Type I Crystals. P and AR coated at 355 nm $\theta = 28^{o}$, $\Phi = 0^{o}$	12W × 8H × 13T mm	0447-9961	Photop Technologies 818-648-1999	MO / PO
Pockels Cell (KD*P)		0100-4460	Cleveland Crystals 216-486-6100	YAG [b]
High energy 355 nm diachroics	1.5’’ × 0.25”	0449-5370	CVI BSR-31-1525	YAG [b]

[a] See Fig. A.11

[b] See Fig. A.8

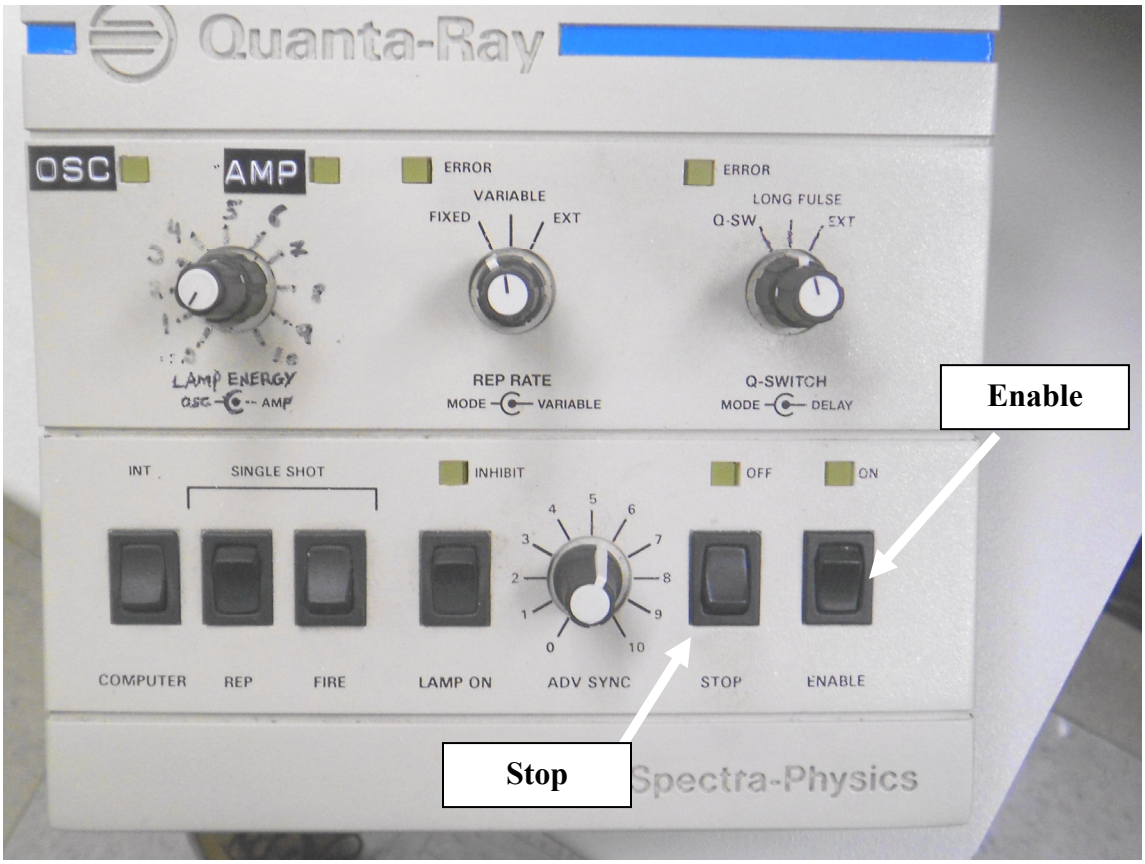

Figure A.1: The GCR-270 YAG controller. [File: FA.1]

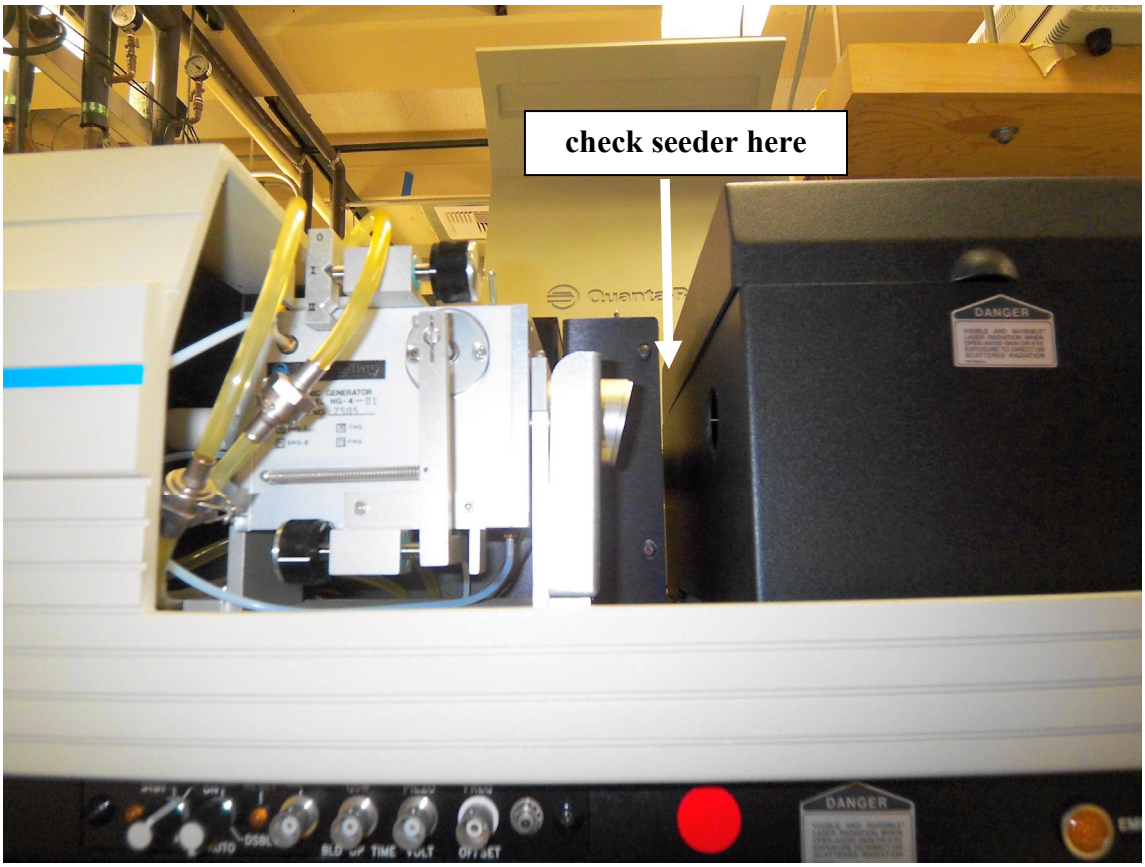

Figure A.2: The GCR-270 YAG with cover open. [File: FA.2]

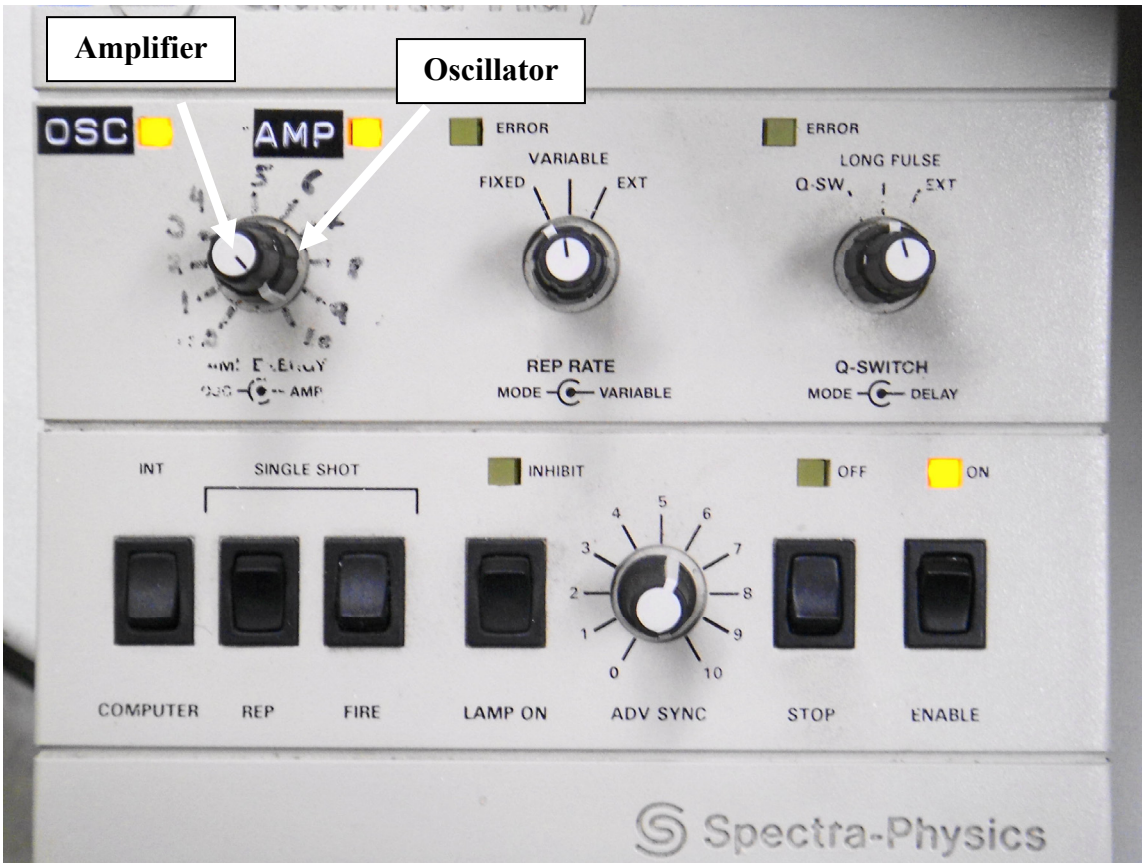

Figure A.3: The GCR-270 YAG controller in LONG PULSE MODE. [File: FA.3]

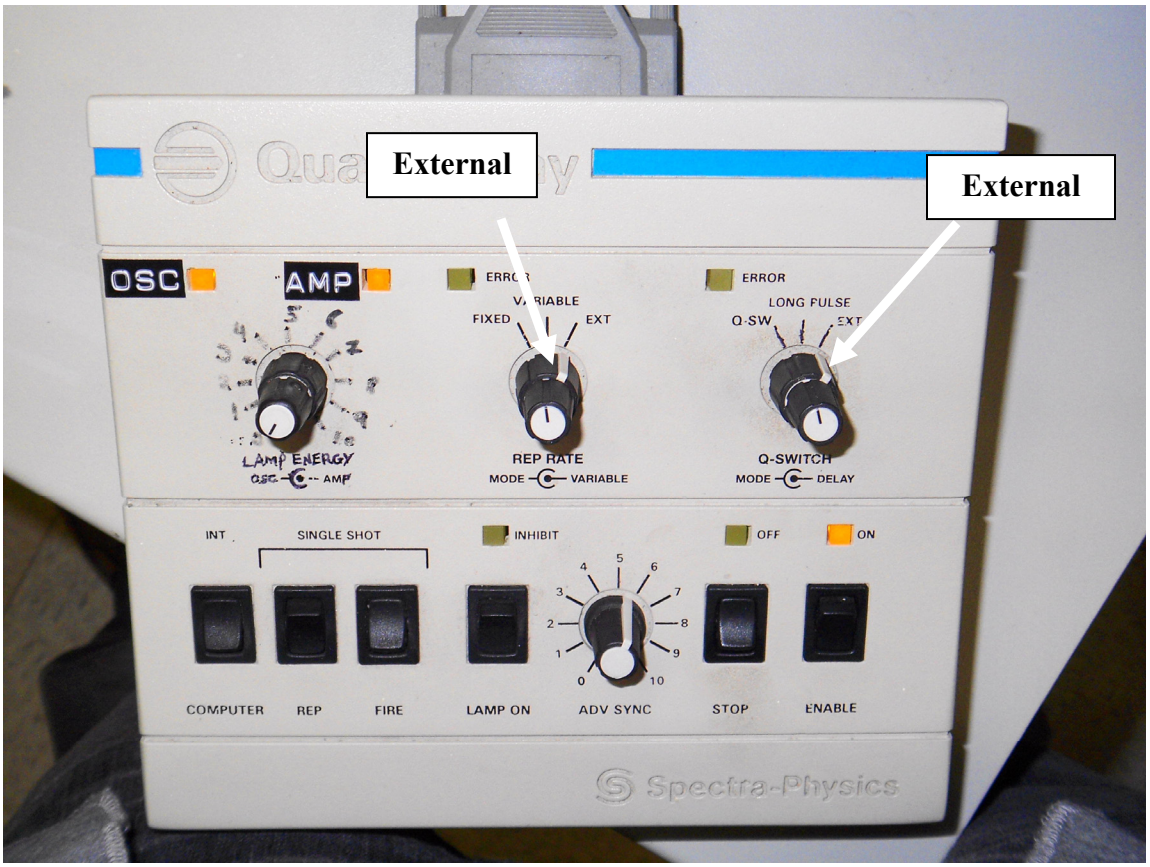

Figure A.4: The GCR-270 YAG controller in EXTERNAL Q-SWITCH MODE. [File: FA.4]

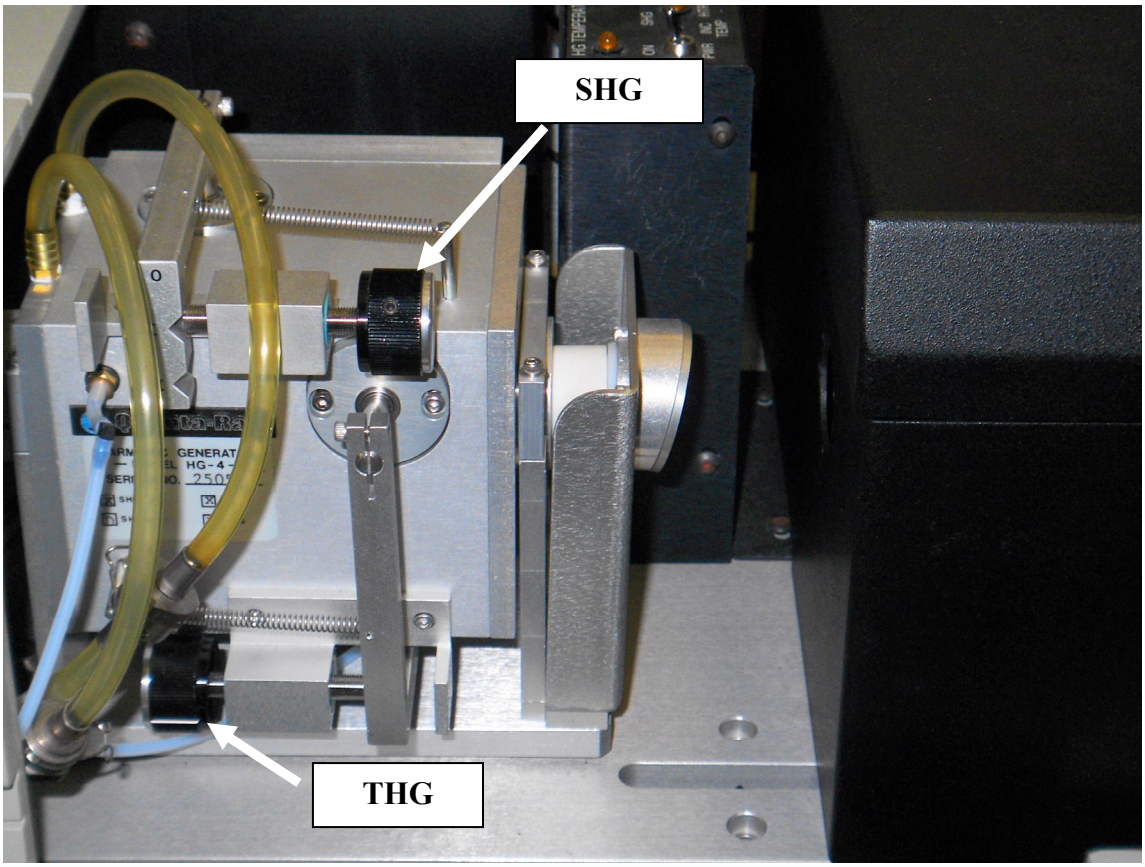

Figure A.5: The GCR-270 YAG SHG/THG harmonic generator housing. [File: FA.5]

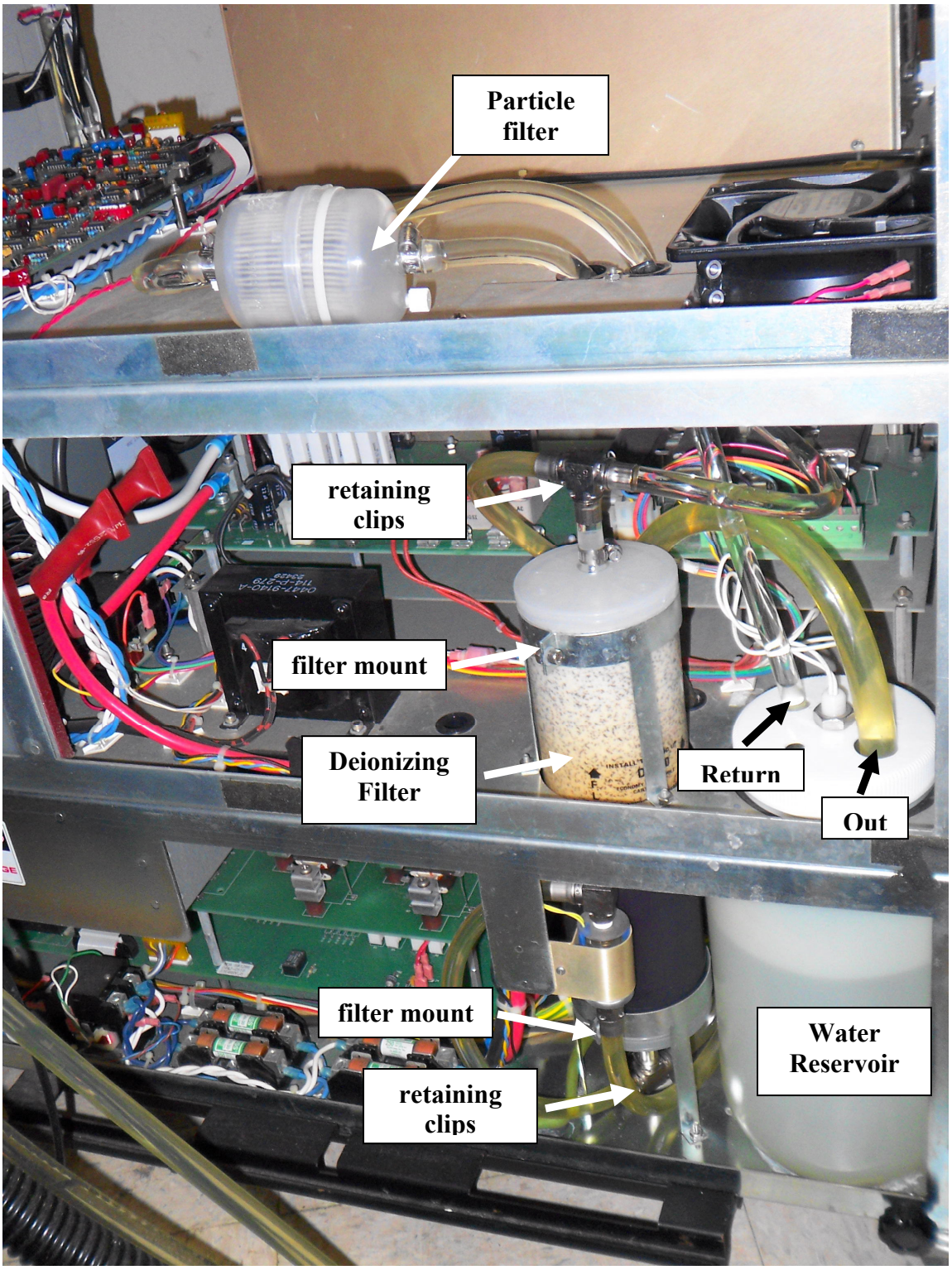

Figure A.6: The GCR-270 power supply unit showing the DI and particle filters. [File: FA.6]

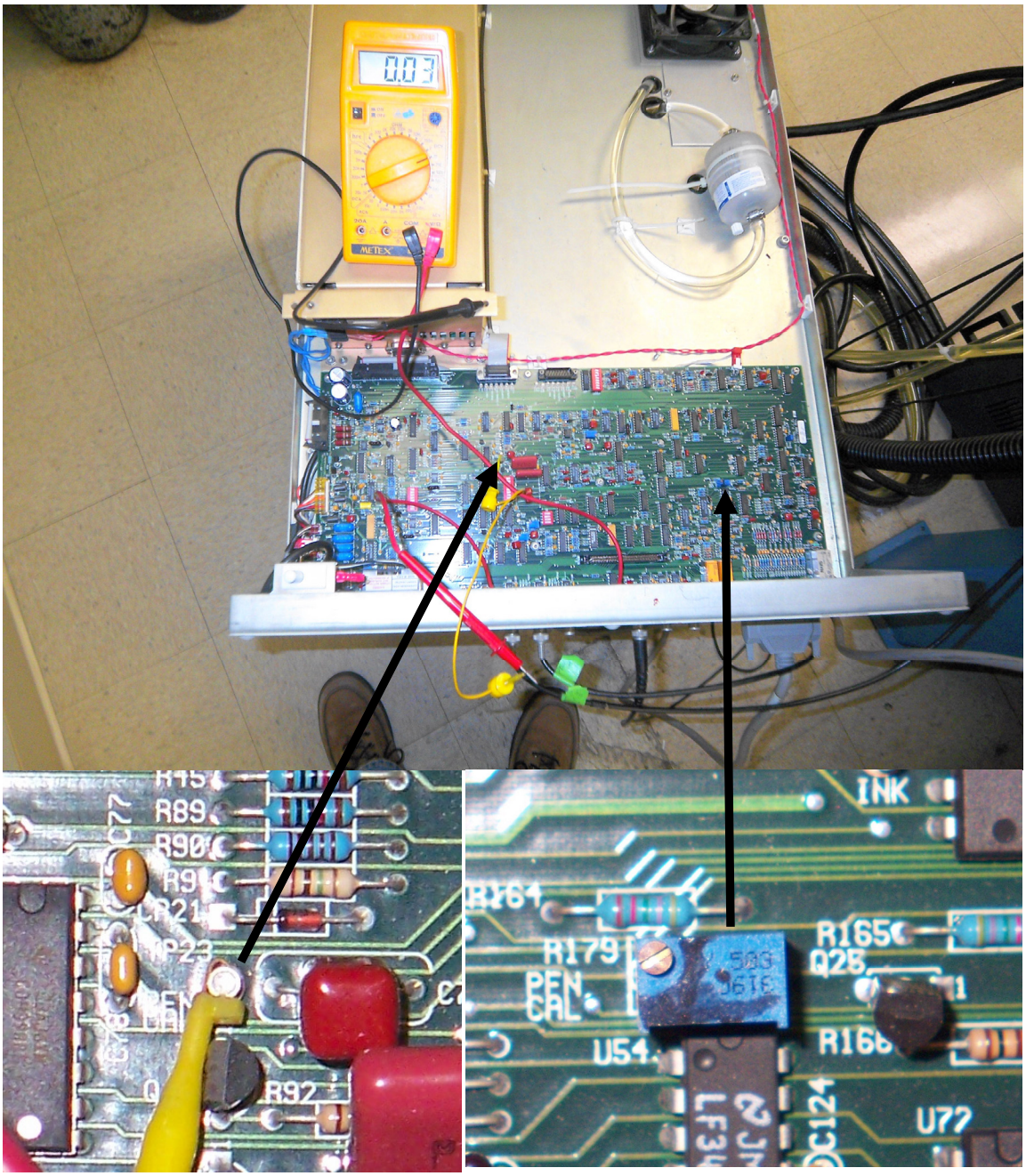

Figure A.7: The GCR-270 power supply unit showing oscillator board. [File: FA.7]

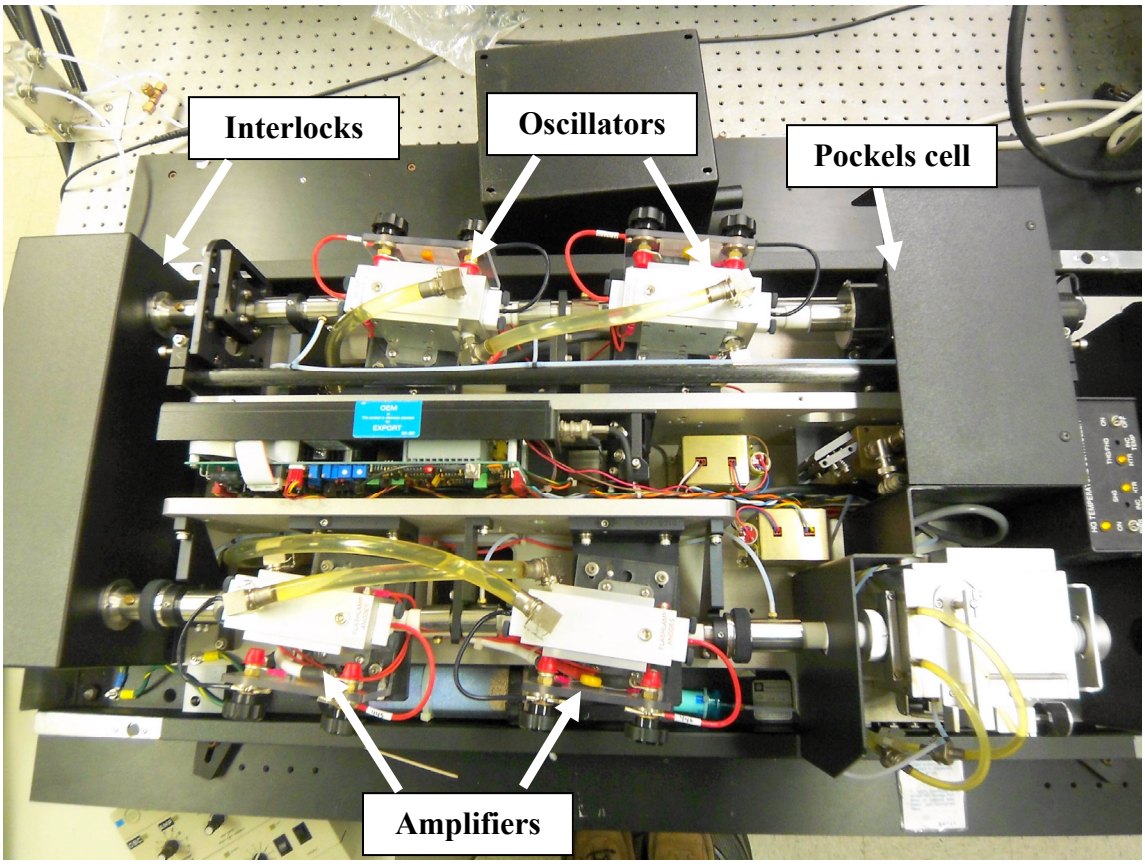

Figure A.8: Top view of the GCR-270 laser. [File: FA.8]

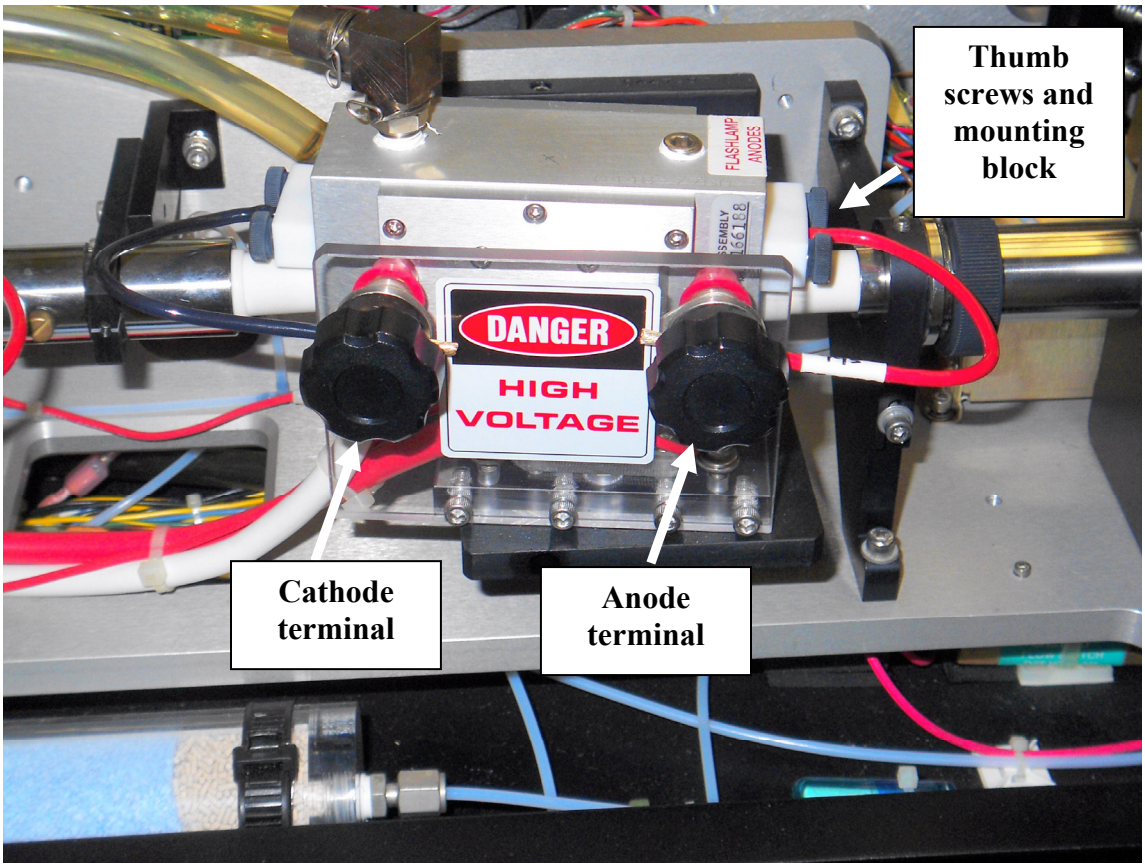

Figure A.9: GCR-270 flashlamp housing. [File: FA.9]

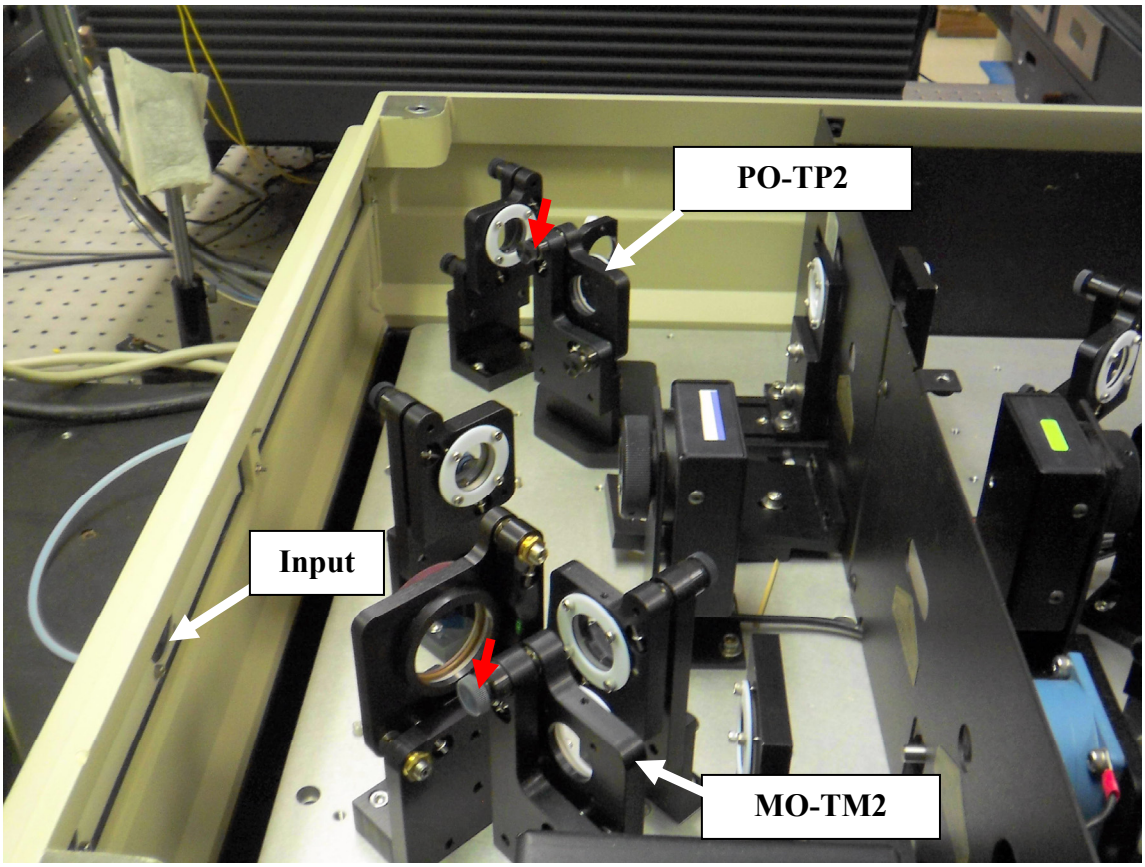

Figure A.10: MOPO-730 showing the power oscillator (PO) and master oscillator (MO) stages. Only the vertical adjustments pointed with arrows should be changed.
[File: FA.10]

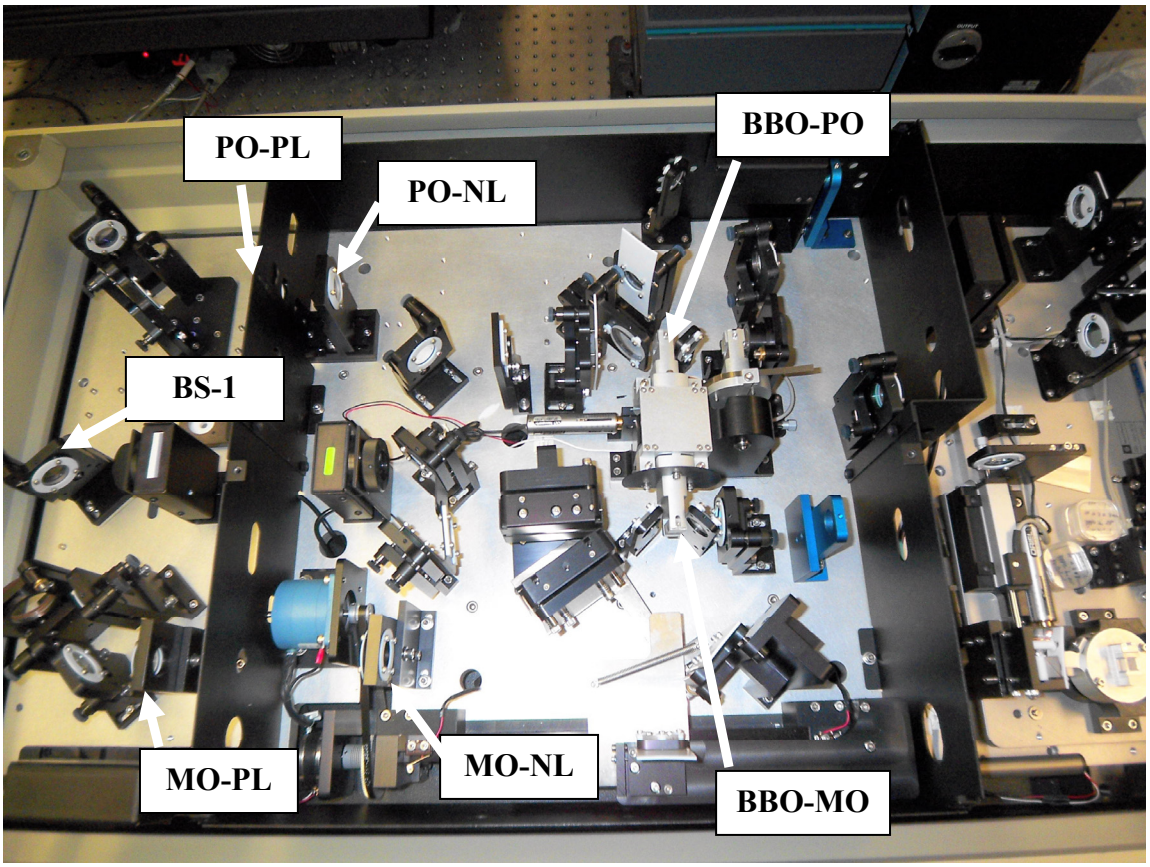

Figure A.11: MOPO-730 schematics. [File: FA.11]

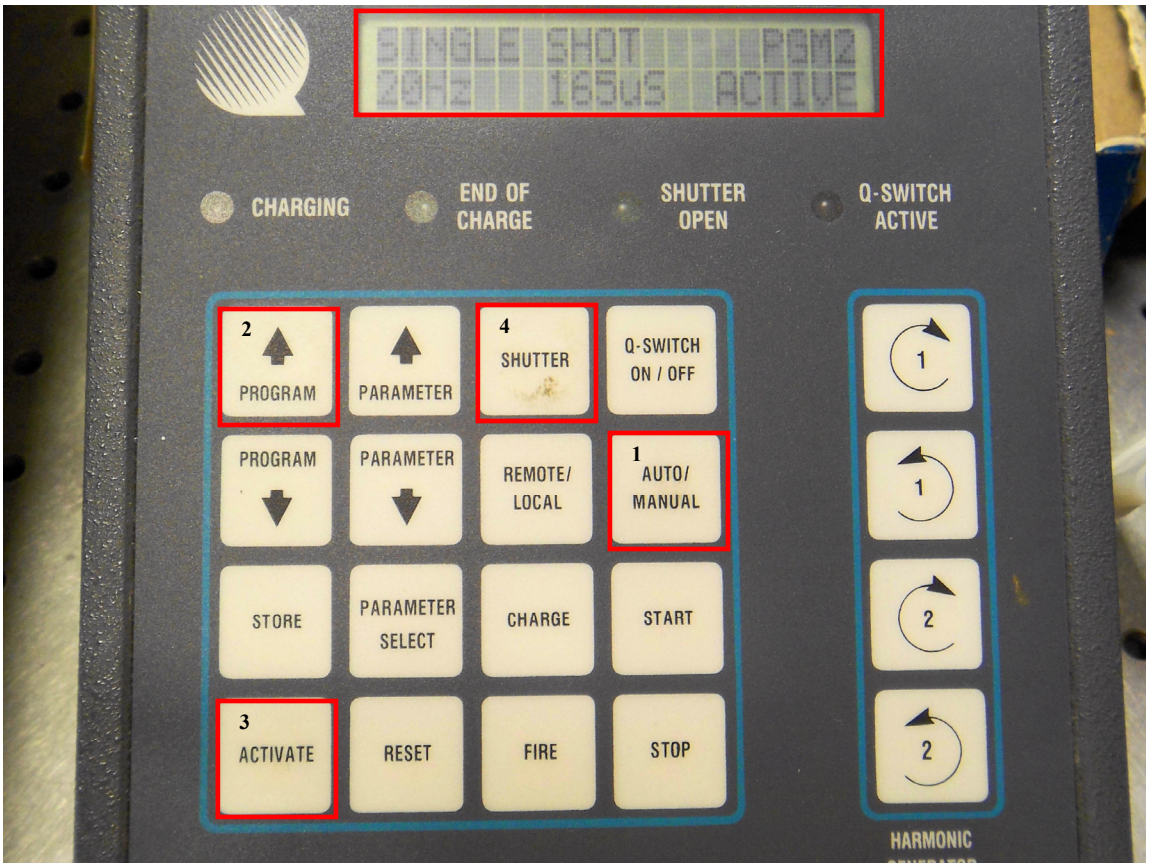

Figure A.12: NY82-20/NY81-20 YAG controller. [File: FA.12]

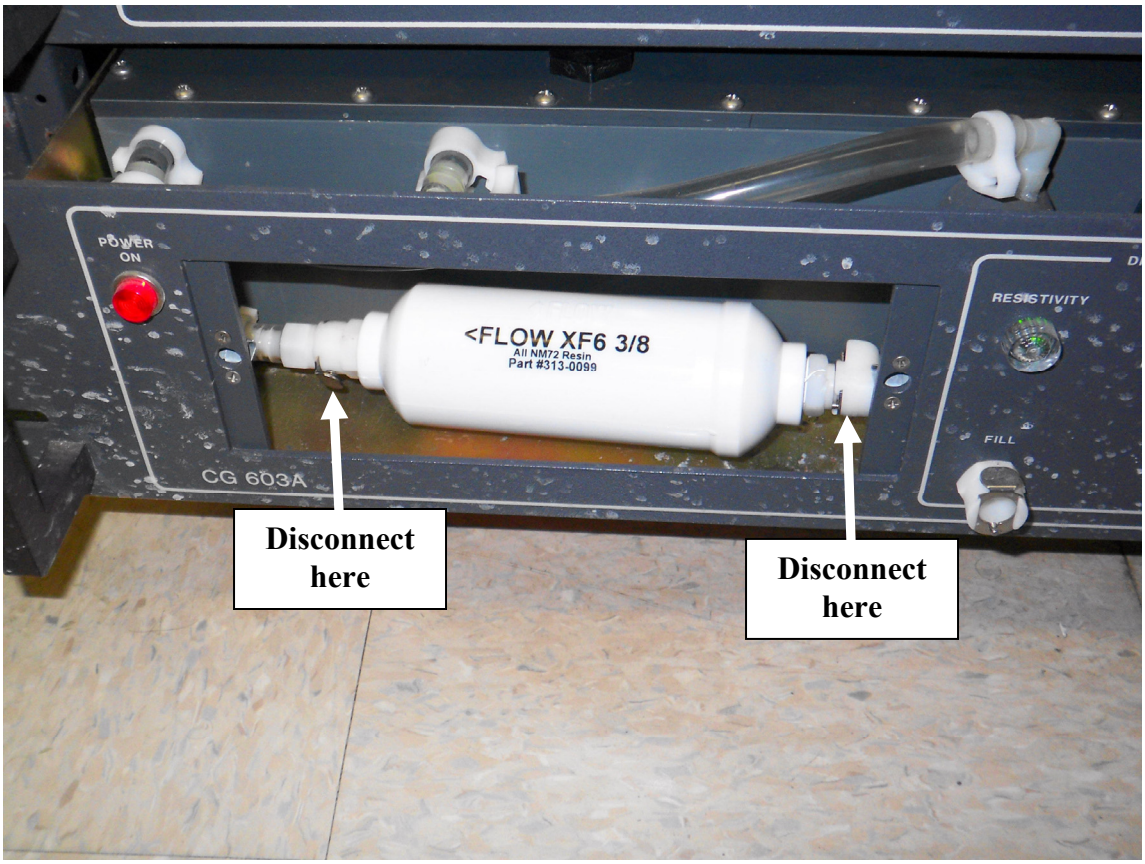

Figure A.13: NY81-20/NY82-20 Deionizing filter. [File: FA.13]

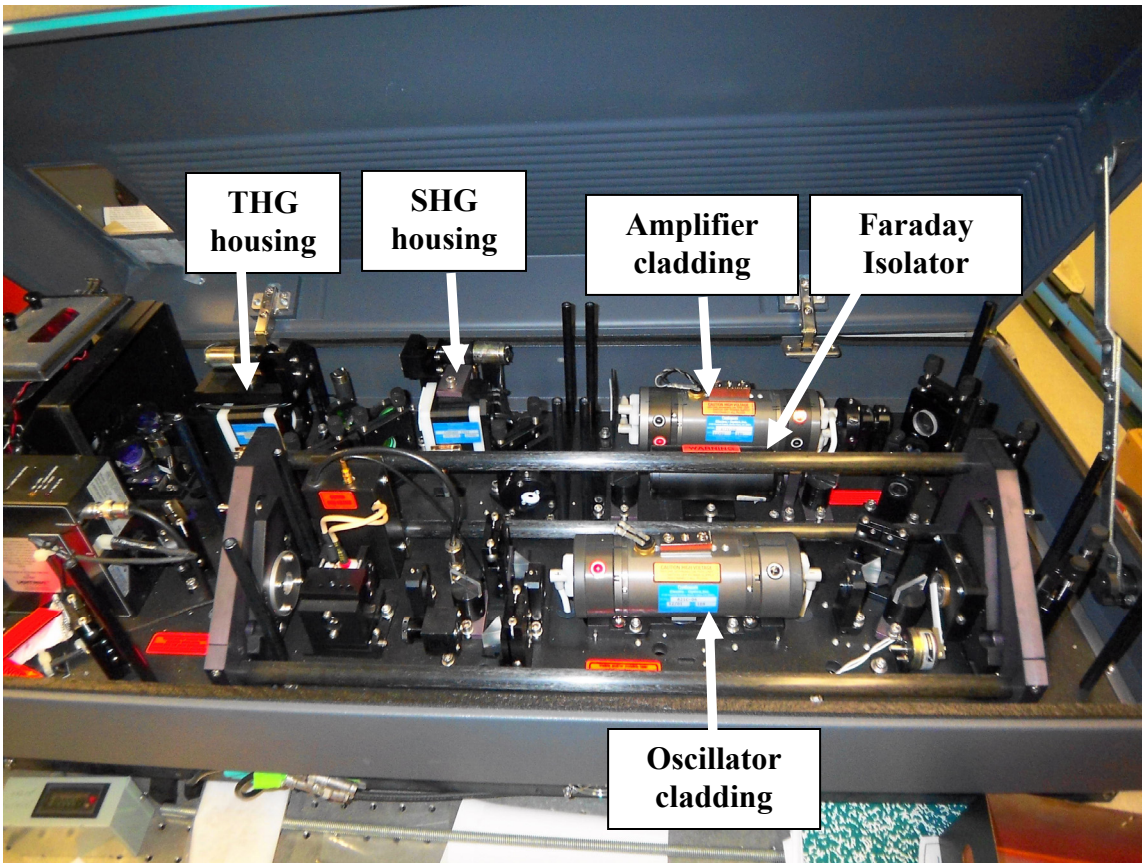

Figure A.14: NY82-20 YAG laser. [File: FA.14]

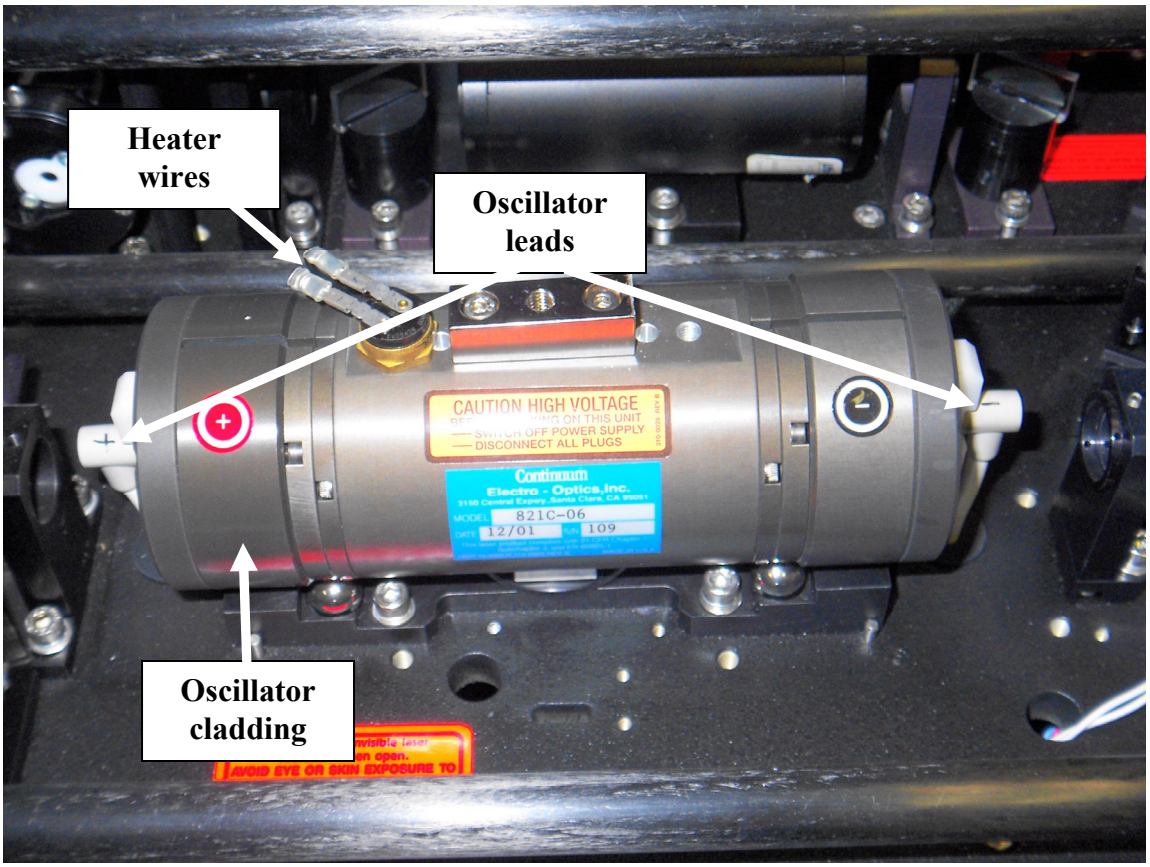

Figure A.15: NY82-20 YAG laser showing oscillator cladding. [File: FA.15]

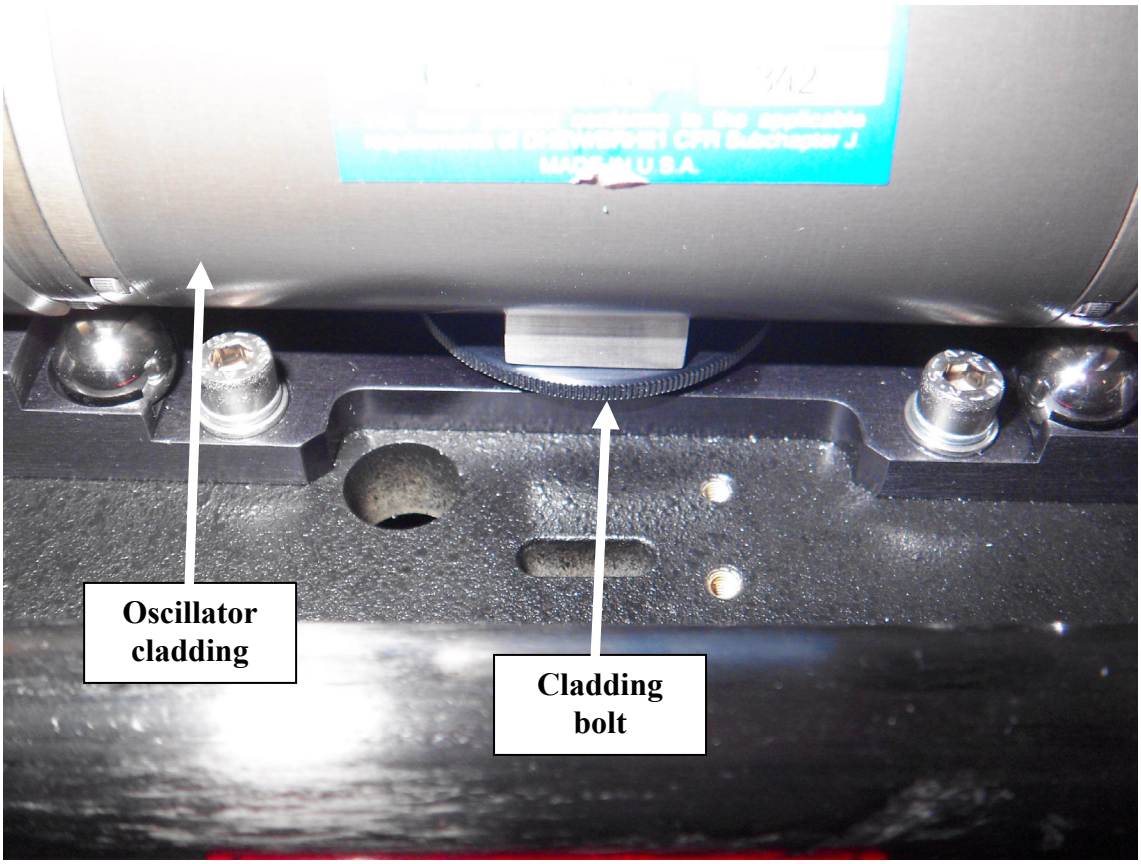

Figure A.16: NY82-20 YAG laser showing oscillator cladding bolt. [File: FA.16]

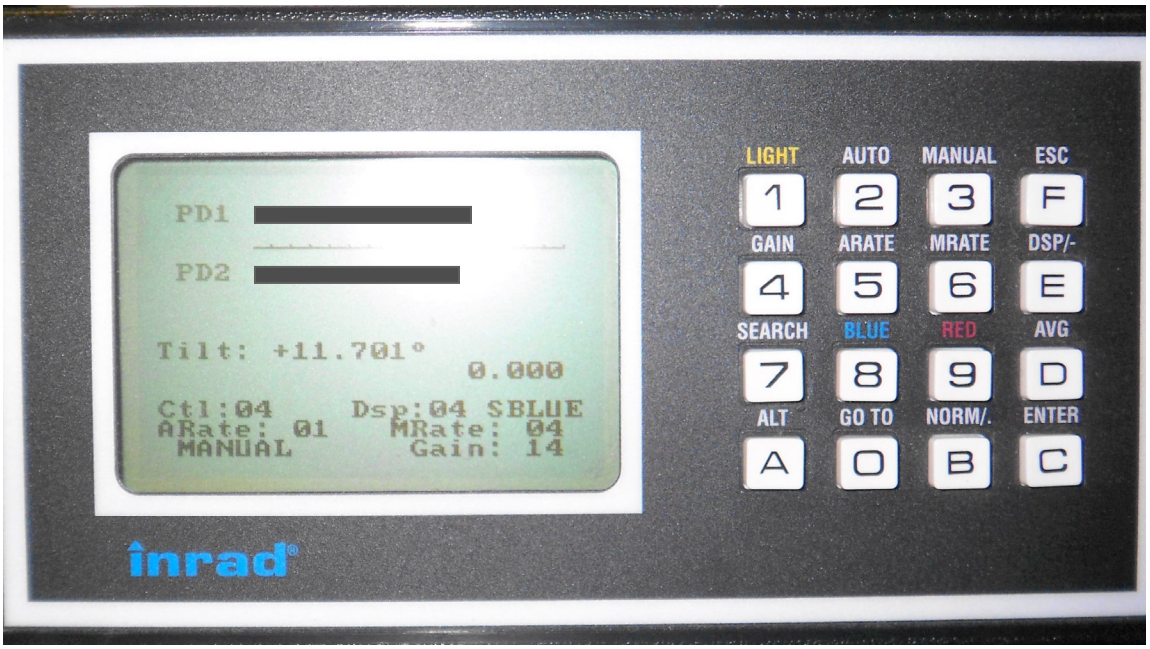

Figure A.17: Inrad Autotracker controller [File: FA.17]

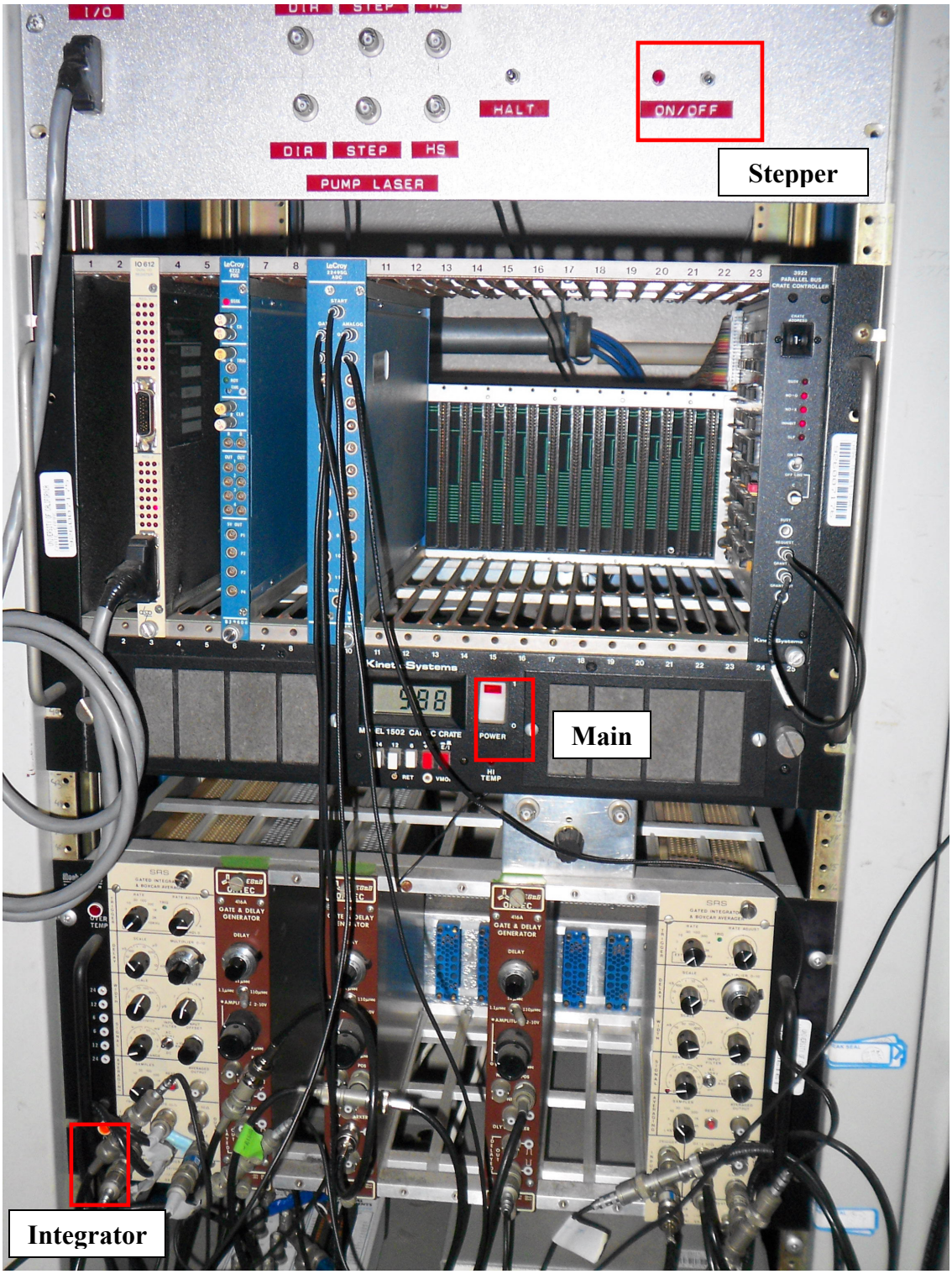

Figure A.18: Electronics rack. [File: FA.18]

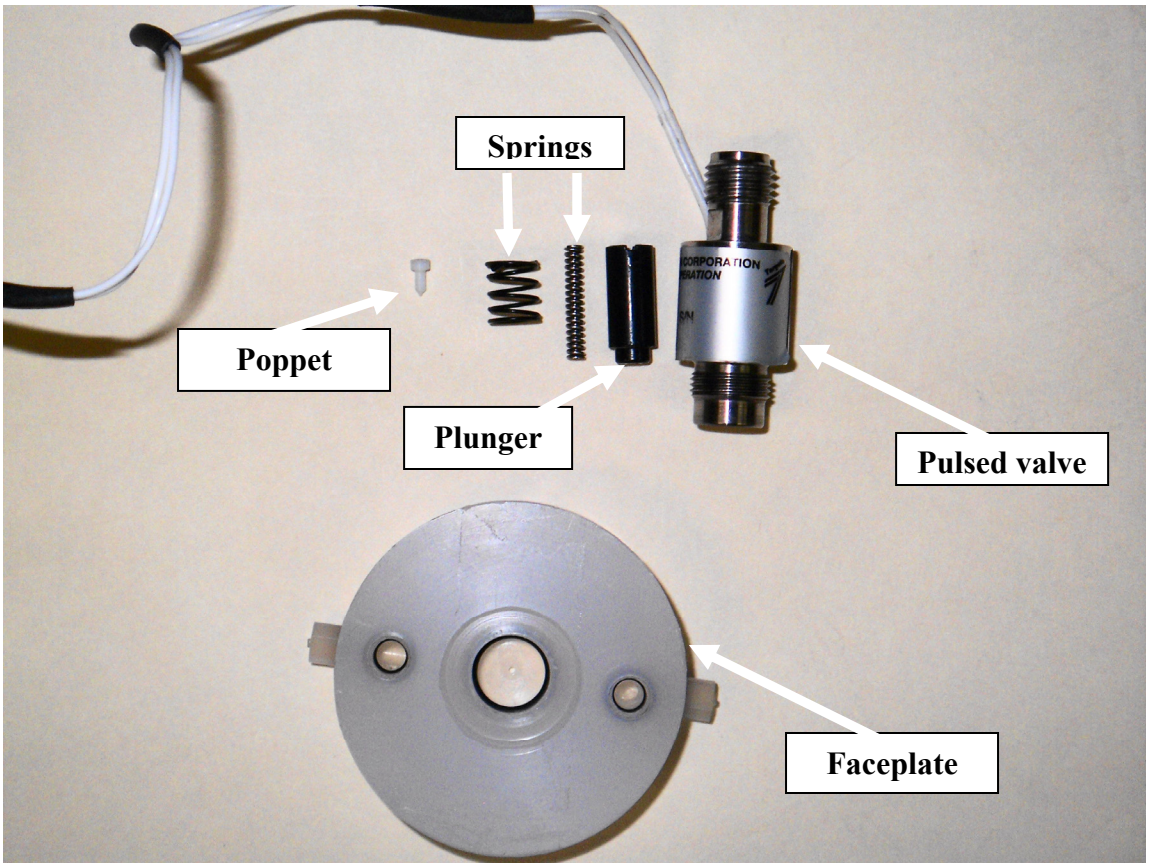

Figure A.19: Pulsed-valve assembly [File: FA.19]

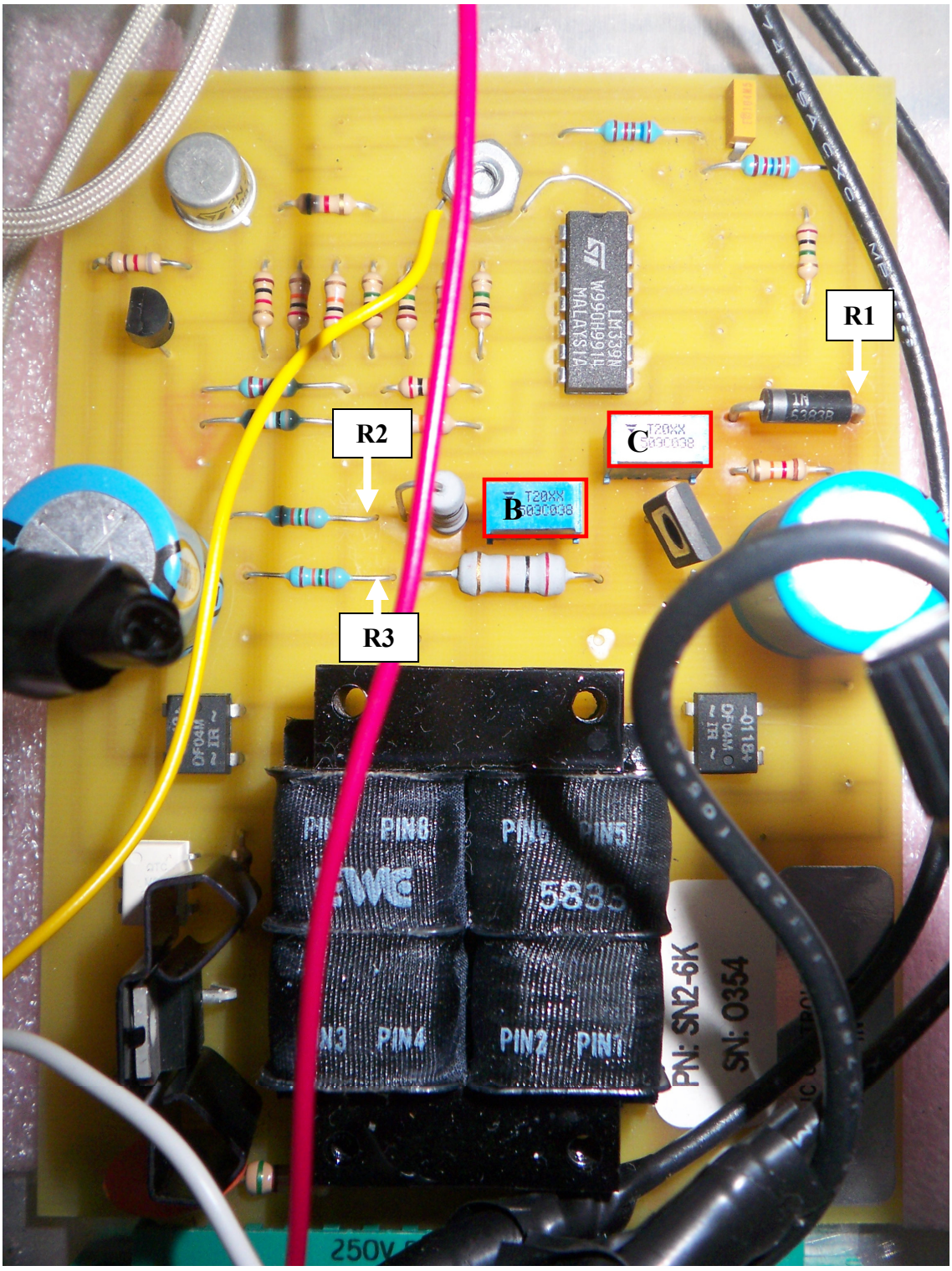

Figure A.20: Liquid nitrogen controller board. [File: FA.20]

Appendix B

GAUSSIAN03 and ACESII Operation

B.1 GAUSSIAN03 Operation

B.1.1 Basic Linux and GAUSSIAN03 Commands

This section explains how to operate GAUSSIAN03 program [1] on the workstations in the lab and provide information on the keywords used in the calculations of the various molecular properties throughout the dissertation chapter.

The GAUSSIAN03 program is compiled (as purchased) to run under the Linux Red Hat 9.0 operating system and is located in the /home/g03 directory of each machine. Under current permission policies, the program runs under the "root" administrator user. Logging in as "root" also gives the user full unrestricted access in Linux. Red Hat hosts several UNIX shells which are sets of programs that design to execute other programs and commands such as GAUSSIAN03. Although the GAUSSIAN03 program can run in all available shells, at startup, the initialized environment variable contains script for running GAUSSIAN03 only under the BASH and CSH shells. The BASH shell is the default and even though the two shells are very similar to one another, the CSH has the advantage that programs can be left to run as a background process even after the user has logged off.

To start a new BASH shell, click on the terminal window which opens a new command line screen. This, by default is the BASH shell. To switch to CSH, in the command prompt type:

csh

The symbol "#" indicates the prompt and should not be typed. To switch back from CSH to BASH shell, type:

exit

Or,

bash

None that all Linux commands are case-sensitive. The GAUSSIAN03 executable, g03, which is located in the /home/g03 directory can run from any directory and operate on any GAUSSIAN03 input file. Data files which include input (com) and output (log) files are located in /home/data/foldername/ folder. Where, "foldername" is a directory for a specific molecule such as HOONO, CH3OOH, etc. To access a particular directory such as CH_3OOH type in BASH or CSH:

cd /home/data/ch3ooh

To execute GAUSSIAN03 on an input file type:

g03 filename.com

When initialized, GAUSSIAN03 generates an output text file which has the same filename as the input file but with a "log" extension, i.e. "filename.log".

To view files in the directory type:

ls –l

To view the content of log file as it being written:

tail –f filename.log

And to exit viewing the log file, type:

CTRL + C

Note that while GAUSSIAN03 is running, the terminal will not be available to perform other operations. To run GAUSSIAN03 as a background process where other operations such as running the tail command, or to close the terminal without terminating GAUSSIAN03 prematurely, first switch to the CSH shell:

csh

Then, run the program using the nohup command as follows:

nohup g03 filename.com &

The no hang-up command, nohup, enables running any program as background process and the "&" symbol releases the terminal to perform other tasks.

B.1.2 GAUSSIAN03 Input File

GAUSSIAN03 requires specific basic file structure which has different sections.[2] Some of these sections require a blank line between them:

Link 0 Command
Route Section
Blank line
Title Section
Blank line
Molecular Specification
Blank line

The Link 0 Command contains the location of the scratch files and checkpoint file. The scratch files are input-output files that GAUSSIAN03 uses while running. There are four types of scratch files (Int, D2E, Scr, Rwf) which can not exceed the two gigabytes file-size limit. Therefore, for calculations that require more than a single scratch file due to file-size limit, the Link 0 Command should contain the following:

%MEM=2GB
%NProcShared=2
%SCR=scr1,2GB,scr2,2GB,scr3,2GB,scr4,2GB,…

```
%RWF=rwf1,2GB,rwf2,2GB,rwf3,2GB,rwf4,2GB,…
%D2E=d2e1,2GB
%Int=int1,2GB
%NoSave
%chk=/home/data/foldername/filename.chk
```

Note that each command in the Link 0 starts with "%" and that there are no spaces anywhere. The MEM keyword defines the maximum amount of memory to allocate for the job which must not exceed the amount of *free* RAM available. The NProcShared keyword tells GAUSSIAN03 how many processors to utilize in the calculation (if omitted from the Link 0 command, it defaults to 2). The default scratch file directory is /scr/; this is where all the scratch files are stored. Generally speaking, only the Scr and Rwf files may exceed the 2GB and require splitting while the D2E and Int files should not. The "NoSave" command deletes any file generated above its location in the route section automatically upon successful completion of the job and saves all files below it. In this case all scratch files will be erased and the checkpoint file "filename.chk" will be saved. Note that it is best to generate the checkpoint file in the same directory where the input and output files are stored by explicitly pointing out the save directory.

The route section contains the job type such as optimization and/or frequency calculation as well as wavefunction and basis set. The route section is initiated by the pound sign (#) and the letter N- for normal print level, T- for terse print level and P- for additional output (recommended).[2] Other keywords will depend on the job type, convergent criteria and calculation level. Most calculations performed throughout the dissertation chapters involve optimization and subsequent frequency calculation using tight self-consistent field (SCF) convergence criteria and the CCSD(T) wavefunctions in conjunction to the Dunning basis-set:[2-5]

#P CCSD(T)/cc-pVDZ opt=ef freq=noraman scf=tight trans=iabc

The above route section requests structure optimization (OPT) using the eigenvalue-following algorithm (EF) and subsequent frequency calculation without Raman intensities (FREQ=NORAMAN).[2] These calculations also request tight SCF convergence criteria (SCF=TIGHT) and produce IABC integrals (TRANS=IABC) for orbital transformation.[2] Note that the route section is case insensitive and keywords can be placed in any order in the route section. For example, switching the location of the FREQ and OPT keywords in the route section will maintain the order in which structure optimization occurs prior to computing its frequency.

The title contains a description of the job type. This can be anything and include any character.

Lastly, molecular specifications include the multiplicity, charge, and molecular connectivity in Cartesian or Z-matrix internal coordinates. In the Z-matrix format, the bond lengths, bond angles, and dihedral angles are specified between atoms. The general format of each line in the Z-matrix is as follows:

charge, multiplicity
atom, form-a-bond-with, bond-length, form-angle-with, angle-length, form-dihedral-with, dihedral-angle, format-code
•
•
•

Variables:
bond-lengths
bond-angles
dihedrals
•
•
•

Constants:

bond-lengths in angstrom
bond-angles in degrees
dihedrals in degrees
•
•
•

The charge is the molecule's overall charge and spin is indicated by the multiplicity (2S+1). Each subsequent line defines the molecular structure in internal coordinates in terms of connectivity between atoms. For example, HOONO molecule may have the following Z-matrix matrix:

```
0 1
N
O 1 R1
O 1 R2 2 A1
O 3 R3 1 A2 2 D1 0
H 4 R4 3 A3 1 D2 0
        Variables:
R1=1.1915513
R2=1.38482706
R3=1.43318804
R4=0.9822377
A1=114.39570514
A2=112.95094938
A3=99.80958663
        Constants:
D1=0.0
D2=0.0
```

…

Looking at the above section, note that commas are optional and as shown here, have been omitted. It is also important to point out that the section must terminate with a blank line at the end of the input file. The charge associated with HOONO is 0 and as a closed-shell molecule, its multiplicity is 1. The encore atom (atom number 1) is chosen to be the nitrogen atom. The terminal oxygen atom (atom number 2 in the list) is connected to the

nitrogen atom and has a bond length R1. The second oxygen atom (atom number 3) is connected to the nitrogen atom, and has a bond length of R2. It also forms an angle A1 with the second oxygen atom (ONO –bond angle). The addition of the fourth atom, which is also an oxygen atom, results in the addition of the dihedral angle, D1, between the OONO atoms. The last atom in the Z-matrix is the H-atom which forms the second dihedral angle, D2. The "Variable:" section contains all bond distances, angles and dihedral angles that get optimized by the OPT keyword. The "Constants:" section contains all parameters that are requested not to be optimized. As shown, the optimization routine of the *cis-cis* HOONO conformer constrains the two dihedral angles to 0^{o}.

The complete input file for HOONO which combines all the above sections is shown below:

```
%MEM=2GB
%SCR=scr1,2GB,scr2,2GB,scr3,2GB,scr4,2GB,…
%RWF=rwf1,2GB,rwf2,2GB,rwf3,2GB,rwf4,2GB,…
%D2E=d2e1,2GB
%Int=int1,2GB
%NoSave
%chk=/home/data/HOONO/cchoono.chk
#P CCSD(T)/cc-pVDZ opt=ef freq=noraman scf=tight trans=iabc

cis-cis HOONO optimization at cc-pvdz

0 1
N
O 1 R1
O 1 R2 2 A1
O 3 R3 1 A2 2 D1 0
H 4 R4 3 A3 1 D2 0
     Variables:
R1=1.1915513
R2=1.38482706
R3=1.43318804
R4=0.9822377
A1=114.39570514
A2=112.95094938
```

```
A3=99.80958663
     Constants:
D1=0.0
D2=0.0

…
```

The calculation generates output file (see next section) which includes text output of the optimization parameters and also a checkpoint binary file which also contains the optimization information. The checkpoint file can then be used for subsequent calculations, or for restarting a failed calculation, or for changing the calculation level as follows:[2,3]

```
%MEM=2GB
%SCR=scr1,2GB,scr2,2GB,scr3,2GB,scr4,2GB,…
%RWF=rwf1,2GB,rwf2,2GB,rwf3,2GB,rwf4,2GB,…
%D2E=d2e1,2GB
%Int=int1,2GB
%NoSave
%chk=/home/data/HOONO/cchoono.chk
#P CCSD(T)/cc-pVTZ opt=(ef,readfc) scf=tight trans=iabc
guess=read geom=check

cis-cis HOONO optimization at cc-pvtz from cc-pvdz

0 1

…
```

The Link 0 command remains unchanged, including the checkpoint file that contains the information from an earlier cc-pVDZ calculation. In the route section, the basis-set is increased from cc-pVDZ to cc-pVTZ. The OPT keyword is also modified to instruct the program to extract the force constants from the checkpoint file. The GUESS=READ keyword requests that the initial Hartree-Fock wavefunctions be read from the checkpoint file. The GEOM keyword instructs the program to also read the optimized structure from the previous calculation from the checkpoint file (GEOM=CHECK); therefore, the Z-matrix is omitted from the molecular specification section. Only the charge and

multiplicity are includes in molecular parameters section and the file is terminated with a blank line. When the calculation completes successfully, the checkpoint file stores the information from the new calculation.

The Linux text editors VI or VIM are useful to generate input files. Of course, any text editor would work fine. To start vim or vi type:

vi(m) filename.com

When the screen loads, the editor creates the file in the current directory. To start editing the file click on the letter "i" to insert characters to the input file. Do not forget to terminate with a blank line. When editing is finished, press the "ESC" key twice and then ":wq". This saves the changes to the file and quits the editor.

B.1.3 GAUSSIAN03 Output File

The GAUSSIAN03 output file contains several useful parameters that can be extracted when the calculation completes. For example, in the case of HOONO CCSD(T)/cc-pVTZ optimization routine, the initial part of the output files contains the copied input parameters which are useful in order to verify that GAUSSIAN03 understands what job to perform:

```
*****************************************
 Gaussian 03:  x86-Linux-G03RevB.04 2-Jun-2003
                7-Aug-2004
 *****************************************
 %chk=/home/data/HOONO/hoonocc_ccsdt_ccpvtz.chk
 Default route:  MaxDisk=1960MW
 ----------------------------------------------------------------------
 #p ccsd(t,maxcyc=300)/cc-pvtz scf=(direct,tight) TRANS=IABC geom=check
  guess=read opt=(readfc,ef)
 ----------------------------------------------------------------------
```

•
•
•

The output file also prints out the initial optimization parameter:

```
-----------------
 cis cis structure
 -----------------
 Z-Matrix taken from the checkpoint file:
 /home/data/HOONO/hoonocc_ccsdt_ccpvtz.chk
 Charge =  0 Multiplicity = 1
 N
 O,1,no1
 O,1,no2,2,ono2
 O,3,oo,1,oon,2,d1,0
 H,4,ho,3,hoo,1,d2,0
      Variables:
 no1=1.1915513
 no2=1.38482706
 oo=1.43318804
 ho=0.9822377
 ono2=114.39570514
 oon=112.95094938
 hoo=99.80958663
     Constants:
d1=0.0
d2=0.0
•
•
•
Force constant matrix read from checkpoint file:
 /home/data/HOONO/hoonocc_ccsdt_ccpvtz.chk
                      ----------------------------
                      !    Initial Parameters    !
                      ! (Angstroms and Degrees)  !
 ---------------------                            ----------------------
 !      Name          Value   Derivative information (Atomic Units)     !
 ---------------------------------------------------------------------------
 !       no1         1.1916   D2E/DX2 =    0.7808                       !
 !       no2         1.3848   D2E/DX2 =    0.2271                       !
 !       oo          1.4332   D2E/DX2 =    0.3036                       !
 !       ho          0.9822   D2E/DX2 =    0.4552                       !
 !      ono2       114.3957   D2E/DX2 =    0.7458                       !
 !       oon       112.9509   D2E/DX2 =    0.614                        !
 !       hoo        99.8096   D2E/DX2 =    0.2888                       !
 ---------------------------------------------------------------------------
•
•
•
```

The rest of the output file contains the optimization iterations which typically are not useful. The final part of the output file contains the optimized parameters:

```
      ITEM                 VALUE      THRESHOLD  CONVERGED?
 MAXIMUM FORCE            0.000278     0.000450     YES
 RMS     FORCE            0.000133     0.000300     YES
 MAXIMUM DISPLACEMENT     0.000664     0.001800     YES
 RMS     DISPLACEMENT     0.000338     0.001200     YES
```

```
 ********************************************
 **  CONVERGENCE CRITERIA APPARENTLY SATISFIED  **
 ********************************************


                      ----------------------------
                      !   Optimized Parameters   !
                      ! (Angstroms and Degrees)  !
 ---------------------                            ----------------------
 !      Name          Value   Derivative information (Atomic Units)     !
 --------------------------------------------------------------------------
 !       no1         1.1916   -DE/DX =   -0.0001                        !
 !       no2         1.3848   -DE/DX =    0.0                          !
 !       oo          1.4332   -DE/DX =    0.0                          !
 !       ho          0.9822   -DE/DX =    0.0                          !
 !      ono2       114.3957   -DE/DX =   -0.0001                        !
 !       oon       112.9509   -DE/DX =   -0.0003                        !
 !       hoo        99.8096   -DE/DX =   -0.0002                        !
 --------------------------------------------------------------------------
 PREDICTED CHANGE IN ENERGY   0.000000
```

•
•
•

The calculation also contains Dipole moments and higher order moments which are computed from the SCF Hartree-Fock wavefunction:

```
Dipole moment (field-independent basis, Debye):
    X=     -0.1408    Y=     -1.1063    Z=      0.0000  Tot=      1.1153
 Quadrupole moment (field-independent basis, Debye-Ang):
   XX=    -22.6277   YY=    -23.1939   ZZ=    -21.1861
   XY=     -2.4189   XZ=      0.0000   YZ=      0.0000
 Traceless Quadrupole moment (field-independent basis, Debye-Ang):
   XX=     -0.2918   YY=     -0.8580   ZZ=      1.1498
   XY=     -2.4189   XZ=      0.0000   YZ=      0.0000
 Octapole moment (field-independent basis, Debye-Ang**2):
  XXX=      2.2558  YYY=      0.5303  ZZZ=      0.0000  XYY=      2.7933
  XXY=     -2.6276  XXZ=      0.0000  XZZ=     -0.4948  YZZ=     -0.5805
  YYZ=      0.0000  XYZ=      0.0000
 Hexadecapole moment (field-independent basis, Debye-Ang**3):
 XXXX=   -122.3628 YYYY=    -92.9621 ZZZZ=    -15.4650 XXXY=    -21.9555
 XXXZ=      0.0000 YYYX=    -20.0997 YYYZ=      0.0000 ZZZX=      0.0000
 ZZZY=      0.0000 XXYY=    -34.3050 XXZZ=    -22.6401 YYZZ=    -17.7080
 XXYZ=      0.0000 YYXZ=      0.0000 ZZXY=     -6.1118
```

•
•
•

The final block also contains the input route section, Z-matrix, optimized parameters and variational or perturbation energies which are calculated from the various wavefunctions at the optimized geometry:[2,3]

```
1\1\GINC-CHESINH5\FOpt\RCCSD(T)-FC\CC-pVTZ\H1N1O3\ROOT\07-Aug-2004\1\\
#P CCSD(T,MAXCYC=300)/CC-PVTZ SCF=(DIRECT,TIGHT) TRANS=IABC GEOM=CHECK
 GUESS=READ OPT=(READFC,EF)\\cis cis structure\\0,1\N\O,1,no1\O,1,no2,
2,ono2\O,3,oo,1,oon,2,0.,0\H,4,ho,3,hoo,1,0.,0\\no1=1.1915513\no2=1.38
482706\oo=1.43318804\ho=0.9822377\ono2=114.39570514\oon=112.95094938\h
oo=99.80958663\\Version=x86-Linux-G03RevB.04\State=1-A'\HF=-279.501647
6\MP2=-280.4312847\MP3=-280.4120242\MP4D=-280.437979\MP4DQ=-280.412857
7\MP4SDQ=-280.4311936\CCSD=-280.4263567\CCSD(T)=-280.4736514\RMSD=1.43
6e-09\RMSF=1.332e-04\PG=CS [SG(H1N1O3)]\\@


TIMES HAVE CHANGED. IN THE BIBLE WHEN AN ASS
SPOKE IT WAS CONSIDERED A MIRACLE.
Job cpu time:  0 days  3 hours 21 minutes 11.9 seconds.
File lengths (MBytes):  RWF=    568 Int=      0 D2E=      0 Chk=      8
Scr=      1
Normal termination of Gaussian 03 at Sat Aug  7 14:25:35 2004.
```

B.1.4 Useful GAUSSIAN03 Keywords

The dissertation chapters contain molecular properties that are calculated with the GAUSSIAN03 program. This section provides explanation on those keywords and points out where the information is located inside the output file.

Optimization to a minima involves searching for the equilibrium structure and it is utilized with the OPT keyword in the route section. It is available with all wavefunctions and basis-sets. When the calculation complete the energy and structure are printed in the log file. Often, the keyword is initiated with the OPT=EF option which prints to the log file the final optimized structure in internal Z-matrix coordinates instead of the default Cartesian coordinates.[2] As explained in the previous section, the checkpoint file contains force constants that can be read by subsequent calculations and help speeding up the convergence of the optimization at high level of theory by using the OPT=(EF, READFC) routine.[2] This routine is usually accompanied by the GEOM=CHECK and GUESS=READ keywords which respectively instruct the program to read the optimized geometry and the initial SCF wavefunctions from the checkpoint file as well.[2] The optimized geometry, rotational constants and energy can be found in the end of the log

file. For example, the CCSD(T)/cc-pVTZ calculation for *cis-cis* HOONO gives the following geometry parameters and energies (in bold):

Rotational constants (GHZ): 21.3049023 8.0828457 5.8597289

1\1\GINC-CHESINH5\FOpt**RCCSD(T)-FC\CC-pVTZ**\H1N1O3\ROOT\07-Aug-2004\1\\ #P CCSD(T,MAXCYC=300)/CC-PVTZ SCF=(DIRECT,TIGHT) TRANS=IABC **GEOM=CHECK GUESS=READ OPT=(READFC,EF)**\\cis cis structure\\0,1\N\O,1,no1\O,1,no2,2,ono2\O,3,oo,1,oon,2,0.,0\H,4,ho,3,hoo,1,0.,0**no1=1.1915513\no2=1.38482706\oo=1.43318804\ho=0.9822377\ono2=114.39570514\oon=112.95094938\hoo=99.80958663**\\Version=x86-Linux-G03RevB.04\State=1-A'\HF=-279.5016476\MP2=-280.4312847\MP3=-280.4120242\MP4D=-280.437979\MP4DQ=-280.4128577\MP4SDQ=-280.4311936\CCSD=-280.4263567**CCSD(T)=280.4736514**\RMSD=1.436e-09\RMSF=1.332e-04\PG=CS [SG(H1N1O3)]\\@

TIMES HAVE CHANGED. IN THE BIBLE WHEN AN ASS
SPOKE IT WAS CONSIDERED A MIRACLE.
Job cpu time: 0 days 3 hours 21 minutes 11.9 seconds.
File lengths (MBytes): RWF= 568 Int= 0 D2E= 0 Chk= 8 Scr= 1
Normal termination of Gaussian 03 at Sat Aug 7 14:25:35 2004.

The OPT=RESTART keyword can be used to restart the calculation from the last saved point in the checkpoint file in the event of computer failure etc.

Optimization to Transition State requests optimization to a transition state instead of a minimum energy point.[2-3] One practice method of doing so is by specifying the reactant and product and requesting the GAUSSIAN03 program to search for a maximum in the pathway via the OPT=QST2 keyword. The input file requires an input as follows:

Link 0 Command
Route Section with OPT=QST2
Blank line
Title Section for Reactant
Blank line
Molecular Specification for Reactant
Blank line
Title Section for Product
Blank line
Molecular Specification for Product

Blank line

Often, the transition state is verified by running a frequency calculation (see below) which must result with one imaginary frequency.[3] It is also important to instruct the software to use unrestricted wavefunctions such as UCCSD etc., and GUESS=(MIX,ALWAYS) in order to help in producing unrestricted HF wavefunctions during the SCF cycle and generate initial wavefunctions guess for each optimization step.[2-3] For HMHP, the transition state is shown below as taken from the log file:

```
Final structure in terms of initial Z-matrix:
O
C,1,R2
H,1,R3,2,A3
H,2,R4,1,A4,3,D4,0
H,2,R5,1,A5,4,D5,0
O,2,R6,1,A6,4,D6,0
O,6,R7,2,A7,1,D7,0
H,7,R8,6,A8,2,D8,0
     Variables:
R2=1.4112237
R3=0.96801305
R4=1.10546164
R5=1.11699884
R6=1.36267579
R7=2.39998886
R8=0.98001811
A3=106.59716729
A4=106.4537704
A5=112.0822891
A6=114.58585969
A7=92.43379531
A8=79.69245727
D4=178.06640439
D5=-118.18508632
D6=122.78345204
D7=-59.29108177
D8=46.12149821
1\1\ UCSD-CHESINH4\FTS\UCCSD-FC\CC-pVDZ\C1H4O3\JAMIE\04-May-
2006\0\\#P UCCSD(MAXCYC=300)/CC-PVDZ TRANS=IABC
SCF=(DIRECT,MAXCYC=3000) OPT=(Z-MATRIX,MAXCYCLE=100,QST2)
GUESS=(MIX,ALWAYS)\\HMHP products\\0,1\O,-0.0025201247,
0.7568300716,-1.1425306821\C,0.0462324791,0.9481099565,
0.2548194983\H,0.9148633465,0.7337602457,-1.45062906\H,-
0.0024149042,1.0095307793,0.599219819\H,0.5614502782,
1.9000378065,0.5306281063\O,0.7224158556,-0.019042899,
```

```
0.9361980278\O,-0.7424374428,-1.7463032866,0.1420173704\H,-
0.5709598999,-1.2638596587,-0.6936135845\\Version=x86-Linux-
G03RevB.04\State=1-A\HF=-264.6978662\MP2=-265.3216038\MP3=-
265.355975\MP4D=-265.3683097\MP4DQ=-265.3600534\PUHF=-
264.7193642\PMP2-0=-265.342939\PMP3-0=-265.3771379\MP4SDQ=-
265.3653795\CCSD=-265.3679875\S2=0.99251\S2-1=0.976762\
S2A=0.093178\RMSD=9.011e-09\RMSF=4.221e-05\Dipole=
0.3710559,0.9750806,-0.5233586\PG=C01[X(C1H4O3)]\\@
```

The OPT=(QST2,RESTART) keyword can be used to restart the calculation from the last saved point in the checkpoint file in the event of computer failure etc.

Single Point Energy is simply used to obtain the energy associated with a structure at a particular level. The molecular parameters are not optimized when utilizing the SP keyword even when they appear as variables in the molecular specification section. When the SP keyword is used, the OPT keyword must be omitted from the route section. SP is also the GAUSSIAN03 default when no other calculation type keyword (such as OPT or FREQ) is specified.[2]

Harmonic Frequency calculation is used to calculate force constants and normal modes and to verify minima, transition states and saddle points.[2-3] In addition, the calculation gives zero-point energies (ZPE), thermodynamic properties (such as partition functions, heat of formation, enthalpy and entropy).[2-3] When analytical methods (such as HF, DFT, MP2, MP3, MP4(SDQ), QCISD, CCD, CCSD, CID and CISD and SAC-CI methods) are used, infrared and Raman intensities are also available.[2] To calculate frequencies add the FREQ keyword to the route section. The FREQ=NORAMAN suppresses the Raman intensity calculation (when available) and as a result, saves ~20 % in computation time. As an example, for HOOH, the resulting output section that contains the frequencies is shown below:

```
                     1                      2                      3
                     A                      A                      B
```

```
Frequencies --    328.3174                861.5239                1295.2061
Red. masses --      1.0832                 14.2675                   1.0994
Frc consts  --      0.0688                  6.2393                   1.0867
IR Inten    --      0.0000                  0.0000                   0.0000

                      4                       5                        6
                      A                       B                        A
Frequencies --   1432.3515               3782.6264                3784.5762
Red. masses --      1.0856                  1.0676                   1.0701
Frc consts  --      1.3123                  9.0000                   9.0305
IR Inten    --      0.0000                  0.0000                   0.0000
```

ZPE and thermal corrections are also given:

```
Zero-point correction=                           0.026164 (Hartree/Particle)
Thermal correction to Energy=                    0.029463
Thermal correction to Enthalpy=                  0.030407
Thermal correction to Gibbs Free Energy=         0.004435
Sum of electronic and zero-point Energies=          -151.167856
Sum of electronic and thermal Energies=             -151.164558
Sum of electronic and thermal Enthalpies=           -151.163613
Sum of electronic and thermal Free Energies=        -151.189586
```

Where 1 Hartree = 219 474.6314 cm^{-1} = 627.503 kcal/mol = 27.2107 eV. Once a frequency calculation completes and a checkpoint file is generated, isotope data can also be extracted readily by specifying in the route section FREQ=(READFC,READISO) and GEOM=CHECK.[2] These keywords instruct GAUSSIAN03 to read the force constants that are stored in the checkpoint file as well as the optimized geometry (GEOM=CHECK). The READISO specifies that the isotope data should be read from the molecular specification section where atomic symbols are replaced with the integer isotope mass (the program will replace the integer with the exact mass automatically):[2-3]

0 1

298.150 1.0
2
16
18
1

…

HOOH, has charge and multiplicity of 0 and 1 respectively. The default temperature and pressure (298.150 K and 1.0 atm respectively) are used to calculate thermodynamic

properties, but can be altered. Lastly, the atomic masses instead of atomic symbols are listed in the order of appearance in the original Z-matrix. In this case, the frequencies associated with $D^{16}O^{18}OH$ are evaluated. The FREQ=RESTART keyword can be used to restart the frequency calculation from the last saved point in the checkpoint file in the event of computer failure etc.

Anharmonic Frequency is very useful calculation in obtaining transition frequencies and coupling constants. It is however only available for the HF, DFT, CIS and MP2 methods.[2] To run anharmonic frequency calculation, simply add to the route section the FREQ=ANHARMONIC keyword.[2] In addition to the properties obtained from the FREQ calculation, one also obtains anharmonic frequencies, and anharmonic coupling. As an example, here is the output from HOOH anharmonic frequency calculation at the MP2/cc-pVQZ level of theory:

```
 Vibrational Energies and Rotational Constants (cm-1)
 Mode(Quanta)     E(harm)     E(anharm)    Aa(z)       Ba(x)       Ca(y)
 Equilibrium Geometry                    10.104701    0.889925    0.860977
 Ground State    5861.357     5760.843    9.999957    0.880169    0.846358
 Fundamental Bands (DE w.r.t. Ground State)
  1(1)           3817.422     3629.474    9.834155    0.878633    0.845707
  2(1)           1435.146     1393.588   10.102638    0.874888    0.843985
  3(1)            937.364      903.588    9.986488    0.870289    0.836713
  4(1)            384.697      318.847    9.965173    0.880749    0.838178
  5(1)           3817.179     3632.459    9.780906    0.878348    0.845642
  6(1)           1330.908     1276.508   10.120892    0.878595    0.838682
 Sovratones (DE w.r.t. Ground State)
  1(2)           7634.843     7132.993    9.668353    0.877097    0.845056
  2(2)           2870.293     2766.017   10.205320    0.869606    0.841612
  3(2)           1874.727     1793.452    9.973019    0.860409    0.827069
  4(2)            769.394      564.813    9.930390    0.881330    0.829997
  5(2)           7634.357     7218.048    9.561855    0.876526    0.844926
  6(2)           2661.815     2531.785   10.241827    0.877022    0.831007
 Combination Bands (DE w.r.t. Ground State)
  2(1)   1(1)    5252.568     5005.584    9.936837    0.873352    0.843334
  3(1)   1(1)    4754.785     4528.665    9.820686    0.868753    0.836063
  3(1)   2(1)    2372.510     2280.625   10.089169    0.865008    0.834340
  4(1)   1(1)    4202.119     3951.171    9.799372    0.879213    0.837527
  4(1)   2(1)    1819.843     1736.147   10.067855    0.875468    0.835805
  4(1)   3(1)    1322.061     1221.453    9.951705    0.870869    0.828533
  5(1)   1(1)    7634.600     7090.404    9.615104    0.876812    0.844991
  5(1)   2(1)    5252.325     5007.860    9.883588    0.873066    0.843269
  5(1)   3(1)    4754.542     4532.012    9.767437    0.868467    0.835998
  5(1)   4(1)    4201.876     3957.818    9.746123    0.878928    0.837462
  6(1)   1(1)    5148.329     4894.662    9.955090    0.877059    0.838032
  6(1)   2(1)    2766.054     2657.808   10.223573    0.873314    0.836309
  6(1)   3(1)    2268.271     2165.963   10.107423    0.868715    0.829038
  6(1)   4(1)    1715.605     1577.328   10.086108    0.879176    0.830502
```

```
  6(1)   5(1)    5148.086     4898.394    9.901841    0.876774    0.837967
```

The first column is the vibrational mode number. The second and third columns are the harmonic and anharmonic frequencies respectively. The last three columns are the respective *A*, *B* and *C* rotational constants associated with the particular vibration. The calculation also produces the coupling matrix:

```
X matrix of Anharmonic Constants (cm-1)
              1             2             3             4             5
      1 -0.435057D+02
      2 -0.174782D+02 -0.105802D+02
      3 -0.439668D+01 -0.165523D+02 -0.686258D+01
      4  0.285041D+01  0.237112D+02 -0.983084D+00 -0.364408D+02
      5 -0.171529D+03 -0.181877D+02 -0.403496D+01  0.651164D+01 -0.429068D+02
      6 -0.113197D+02 -0.122879D+02 -0.141330D+02 -0.180265D+02 -0.105720D+02
              6
      6 -0.106152D+02
```

Dipole Moments and higher order moments are produced with every single point (SP) and optimization calculation. However, unless specified, these moments *are not* the correct analytical derivatives of the energy. Only methods in which analytical derivatives are available (HF, DFT, MP2, MP3, MP4(SDQ), QCISD, CCD, CCSD, CID and CISD and SAC-CI), *if* specified, can produce correct moments. [2] For all other methods in GAUSSIAN03 (such as CCSD(T), QCISD(T) etc.), the moments are computed from the SCF density matrix (HF). To obtain dipole moments that are correct derivatives of the energy, the keyword DENSITY=CURRENT must be specified.[2] For example, at the QCISD/cc-pVDZ level, the output file of *cis-cis* HOONO gives the following values:

```
 Dipole moment (field-independent basis, Debye):
    X=     0.0546    Y=    -1.0654    Z=     0.0000  Tot=     1.0668
 Quadrupole moment (field-independent basis, Debye-Ang):
   XX=   -22.8426   YY=   -23.1208   ZZ=   -21.1157
   XY=    -2.2067   XZ=     0.0000   YZ=     0.0000
 Traceless Quadrupole moment (field-independent basis, Debye-Ang):
   XX=    -0.4829   YY=    -0.7611   ZZ=     1.2440
   XY=    -2.2067   XZ=     0.0000   YZ=     0.0000
 Octapole moment (field-independent basis, Debye-Ang**2):
  XXX=     2.6854  YYY=     0.8101  ZZZ=     0.0000  XYY=     2.3616
  XXY=    -2.7744  XXZ=     0.0000  XZZ=    -0.2919  YZZ=    -0.6847
  YYZ=     0.0000  XYZ=     0.0000
 Hexadecapole moment (field-independent basis, Debye-Ang**3):
 XXXX=  -121.8030 YYYY=   -93.3191 ZZZZ=   -14.7780 XXXY=   -22.0106
 XXXZ=     0.0000 YYYX=   -20.2033 YYYZ=     0.0000 ZZZX=     0.0000
```

```
 ZZZY=      0.0000 XXYY=    -34.2242 XXZZ=    -22.4628 YYZZ=    -17.4366
 XXYZ=      0.0000 YYXZ=      0.0000 ZZXY=     -6.0937
```

The total dipole moment in the second line is the trigonometric sum of $(\mu_x^2 + \mu_y^2 + \mu_z^2)^{0.5}$. In GAUSSIAN03, in contrast to ACESII, the dipole moments (in Debye) are not given in the molecular reference frame (the *A*, *B* and *C* inertial axes) but in the standard orientation frame which is chosen by the GAUSSIAN03 program. Therefore these values are referred to as the X Y and Z axes.

The polarizability of molecules can also be calculated with the GAUSSIAN03 program,[1-3] and as with the dipole moment, the DENSITY=CURRENT must be specified in conjunction to frequency calculation. GAUSSIAN03 prints the polarizability tensor right below the Hexadecapole moment. For example, for the $HOCH_2O$ radical GAUSSIAN03 predicts:

Exact polarizability: 26.647 -0.268 24.424 -0.168 -0.227 21.482

The above tensor has the form of α_{XX}, α_{XY}, α_{YY}, α_{XZ}, α_{YZ}, α_{ZZ} which in essence corresponds to:

	X	Y	Z
X	26.647	-0.268	-0.168
Y	-0.268	24.424	-0.227
Z	-0.168	-0.227	21.482

The polarizability is the average sum of the diagonal values (26.647 + 24.424 + 21.482) / 3 = 24.1843 a_0^3. To convert the polarizability from a.u. to m^3 units simply divide these value by the cubed value of the Bohr radius (a_0 = 0.529177249) to obtain 3.58 m^3.

B.2 ACESII Operation

B.2.1 Basic ACESII Commands

This section explains how to operate ACESII program,[6] and provides information on the keywords used to calculate the various molecular properties throughout the dissertation chapter. As with GAUSSIAN03,[1] the ACESII [6] program is compiled to run under Linux Red Hat 9.0 operating system and is located in the /home/acesii directory of each machine. It also requires admin (root) permissions to execute. Also, since it was purchased at a much later time relative to GAUSSIAN03, it was used less extensively. Nonetheless, the program is indispensable in terms of computation of density properties such as dipole moments (field-independent basis) which are correct analytical derivative of the energy.[7]

ACESII is installed to run in CSH shell. To switch from BASH to CSH shell type in terminal:

csh

The recommended syntax for running ACESII in the CSH shell is:

nohup xaces2 >output.log &

Where "NOHUP" causes the "XACES2" program to run as a service, and as discussed in section B.1.1, the "&" enables the terminal to run other applications. The ">" character directs ACESII to print its output to a "output.log" file of choice. ACESII can execute from any directory as long as the directory contains the basis-set file "GENBAS",[8] which is located in the /home/acesii/Basis/ directory and can be copied to the directory where the input file is prepared. Also note that with ACESII one does not specify the input file but instead, provides the name of the output file. That is because the input file ACESII searches for is the ZMAT file.[7] In essence, the input file in ACESII is called the "ZMAT" (in caps).

B.2.2 ACESII Input ZMAT File

The ZMAT file is the ACESII input file and by default, the program reads the job from it. Similarly to GAUSSIAN03,[1] it contains the following sequential structure:

Title
Z-matrix
Blank Line
Variables /Constants
Blank Line
Name List
Blank Line

The title line contains a brief description of the job type. The Z-matrix contains the molecule connectivity just as described with GAUSSIAN03. For example for CH_3OOH, the Z-matrix may look like:

```
C
O 1 r1
O 2 r2 1 a1
H 3 r3 2 a2 1 d1
H 1 r4 2 a3 3 d2
H 1 r5 2 a4 3 d3
H 1 r6 2 a5 3 d4
```

Note that with the ACESII program, the charge and multiplicity are not specified in the Z-matrix section but in the name list section instead. Also, atomic symbols must be capitalized; for example, chlorine atom must be specified as CL and *not* Cl. The Variable/Constant section contains all the bond lengths, angles and dihedrals:

```
r1=1.41652837
r2=1.45666696
a1=105.30791014
r3=0.96516718
a2=99.59294054
d1=113.84859166
r4=1.09087394
a3=104.87110715
d2=177.3636104
r5=1.09316978
a4=111.40380445
d3=-63.81333294
```

```
r6=1.09169994
a5=110.97005336
d4=58.85585791
```

As shown below, optimized parameters are specified in the Z-matrix section.[7] The name list section has the following syntax:

*ACES2(Job Control Parameters)

Thus, for example, the ZMAT file that is used to calculate the dipole moment of CH_3OOH molecule at $\tau_{eq.}$ and $r_{eq.}$ at the CCSD(T)/cc-pVTZ level of theory involves the following syntax:

```
CH3OOH CCSDT/ccpVTZ ENERGY CALCULATION
C
O 1 r1
O 2 r2 1 a1
H 3 r3 2 a2 1 d1
H 1 r4 2 a3 3 d2
H 1 r5 2 a4 3 d3
H 1 r6 2 a5 3 d4

r1=1.41652837
r2=1.45666696
a1=105.30791014
r3=0.96516718
a2=99.59294054
d1=113.84859166
r4=1.09087394
a3=104.87110715
d2=177.3636104
r5=1.09316978
a4=111.40380445
d3=-63.81333294
r6=1.09169994
a5=110.97005336
d4=58.85585791

*ACES2(PRINT=0,REFERENCE=RHF,CALC=CCSD(T),BASIS=CC-
PVTZ,CHARGE=0,SPHERICAL=ON,MULTI=1,SCF_CONV=7,MEMORY_SIZE=80
0MB,DROPMO=1-3,PROPS=1)
```

The various keywords in the ZMAT file are discussed at a later time.

B.2.3 ACESII Output File

The output file of ACESII contains the calculated properties as well as intermediate iteration information.[7] The PRINT keyword controls the amount of printed energy derivatives that is dumped into the output file.[7] For all purposes PRINT=0 produce sufficient iteration information. At this print level, the output file initially displays keywords and parameters validation log, and subsequently, proceeds with the job. For the CCSD(T) single point energy (SP) calculation, ACESII printout includes SCF energy (in Hartree):

```
@OOFCOR: SCF has converged.
     E(SCF)=      -189.8756745056              0.8851776867E-07
```

And, CCSD(T) energy:

```
@TRPS-I,  CCSD            =    -190.561361795930
          CCSD + T(CCSD)  =    -190.588593817907
          CCSD(T)         =    -190.587674058146
```

If requested (see next section), the program also computes the SCF Moments as well as post SCF Moments which are the correct analytical derivatives of the energy in the molecular reference frame: [7]

```
  @DRVPRP-I, Properties computed from the SCF density matrix follow.
   Components of electric dipole moment
        X =   -0.3297283793   Y =   -0.2780968407   Z =   -0.5972636572
   Components of second moment
       XX =  108.8714439120  YY =   34.8875868729  ZZ =   20.8579572808
       XY =    1.8911384073  XZ =   -0.0074330427  YZ =    0.1427151418
   Components of electric quadrupole moment
       XX =    2.3588722738  YY =   -2.5183339355  ZZ =    0.1594616616
       XY =    0.6775657638  XZ =   -3.0253497992  YZ =   -0.0248948105
   Components of electric octopole moment
      XXX =   -1.0509985396 YYY =   -0.6433711859 ZZZ =    6.8306430634
      XXY =    3.4189641594 XXZ =  -10.8675655064 XYY =   -4.4267572588
      YYZ =    4.0369224430 XZZ =    5.4777557984 YZZ =   -2.7755929735
      XYZ =    0.2022289231
•
•
•
@DRVPRP-I, Properties computed from the correlated density matrix
follow.
   Components of electric dipole moment
        X =   -0.2801843659   Y =   -0.2439804678   Z =   -0.5533855081
```

```
Components of second moment
    XX =  109.0225965124  YY =   34.9555322364  ZZ =   21.0963807102
    XY =    2.0232560877  XZ =   -0.1254648994  YZ =    0.1616398613
Components of electric quadrupole moment
    XX =    2.3609040872  YY =   -2.3914912905  ZZ =    0.0305872033
    XY =    0.4793892592  XZ =   -2.8483019988  YZ =   -0.0532818839
Components of electric octopole moment
   XXX =   -1.1024232899 YYY =   -0.2862649149 ZZZ =    6.4249457742
   XXY =    3.0224827336 XXZ =  -10.2711791903 XYY =   -4.0426612935
   YYZ =    3.8462334162 XZZ =    5.1450845834 YZZ =   -2.7362178187
   XYZ =    0.1849707919
```

The ACESII job terminates successfully with following message:

```
@ACES2: The ACES2 program has completed successfully in  66084 seconds.
```

After the job is complete, the scratch files that were generated in the working directory while the program was running can be deleted.

B.2.4 Useful ACESII Keywords

The dissertation chapters contain molecular properties that are calculated with the ACESII program.[6] This section provides explanation on the optimization, constrained optimization, frequencies and dipole moments jobs as well as the keywords that were used to compute these properties.

The optimization and constrained optimization routines are controlled by selecting which degrees of freedom to minimize in the Z-matrix section of the ZMAT file.[7] For example, the ZMAT file which results in constrained optimization of CH_3OOH structure at the CCSD(T)/cc-pVTZ level of theory where HOOC torsion angle, τ, is fixed at 100^o and all other degrees of freedom are allowed to relax, is shown below:

```
CH3OOH CCSD(T)/cc-pVTZ Torsion=100
C
O 1 r1*
O 2 r2* 1 a1*
H 3 r3* 2 a2* 1 d1
H 1 r4* 2 a3* 3 d2*
H 1 r5* 2 a4* 3 d3*
H 1 r6* 2 a5* 3 d4*
```

```
r1   =    1.4165283700
r2   =    1.4566669600
a1   =  105.3079101400
r3   =    0.9651671800
a2   =   99.5929405400
d1   =  100.0
r4   =    1.0908739400
a3   =  104.8711071500
d2   =  177.3636104000
r5   =    1.0931697800
a4   =  111.4038044500
d3   =  -63.8133329400
r6   =    1.0916999400
a5   =  110.9700533600
d4   =   58.8558579100

*ACES2(PRINT=0,REFERENCE=RHF,CALC=CCSD(T),BASIS=CC-PVTZ,
SPHERICAL=ON,CHARGE=0,MULTI=1, MEMORY_SIZE=800MB,SCF_CONV=7,
DROPMO=1-3)
```

The asterisk (*) instructs the program to optimize all degrees of freedom but the d1 dihedral angle. To obtain the fully relaxed structure, simply add an asterisk next to d1 in the Z-matrix as well. Conversely, for single point energy calculation (SP), all asterisks should be removed from the Z-matrix. Also, as discussed below, dipole moments and other electronic properties can not be performed in conjunction to optimization but only in subsequent SP calculation.

There are several keywords that are worth discussing in the above example. As mentioned previously, the PRINT command controls the amount of intermediate iteration information that is dumped into the output file.[7] The REFERENCE keyword controls the SCF Hartree-Fock (HF) wavefunctions that are generated.[7] Generally speaking, RHF refers to restricted HF wavefunctions that are normally used for closed-shell species and UHF refers to unrestricted HF wavefunctions that are normally used for opened-shell species.[2,3] The CALC keyword controls the level of calculation and in this example is set

to the CCSD(T) level of theory.[7] The BASIS keyword refers to the basis-set that is read from the GENBAS file and here, Dunning's cc-pVTZ basis functions are chosen.[4,5,8] SPHERICAL keyword specifies whether spherical harmonics or Cartesian basis-functions should be used; set to ON with Dunnning's correlated-consistent basis-functions.[7] The CHARGE and MULTI for CH_3OOH are the charge and multiplicity and are set to 0 and 1 respectively.[7] The MEMORY_SIZE keyword controls the amount of RAM allocated for the job and SCF_CONV refers to the convergence criteria of the HF SCF wavefunctions; the SCF_CONV=7 ($=10^{-7}$) is the default and the SCF_CONV=8 ($=10^{-8}$) is synonymous with the SCF=TIGHT keyword in GAUSSIAN03.[2,7]

Lastly, the DROPMO keyword controls the number of orbitals that are excluded from the post SCF calculation.[7] This keyword is synonymous with the Frozen-Core (FC) option which is the default in GAUSSIAN03 and which excludes the inner-shell orbitals from the correlation calculation.[2] By default, ACESII does not use the frozen-core approximation and thus, can be computationally expensive. The orbitals are numbered in ascending order, and in the case of CH_3OOH, the 1S atomic orbital of the Carbon and the two oxygen atoms are assumed to not form molecular orbitals and therefore can be omitted from the correlation calculation. When the FC approximation is used, GAUSSIAN and ACESII should produce similar energy and geometry for a given calculation. When the job completes, the output file will contain the rotational constants (*A*, *B* and *C*), CCSD(T) energy, and the optimized structure:

```
   Rotational constants (in cm-1):
     0.30663        0.35223        1.40746
•
•
•
@TRPS-I,  CCSD           =    -190.561131019328
```

```
           CCSD + T(CCSD) =     -190.588427756369
           CCSD(T)        =     -190.587499932424
•
•
•
r1    =      1.4171894668
r2    =      1.4531902934
a1    =    105.8317147015
r3    =      0.9660564440
a2    =    100.1005746004
r4    =      1.0908713685
a3    =    104.9387395932
d2    =    177.4061520164
r5    =      1.0939352153
a4    =    111.4377934698
d3    =    -63.9960814955
r6    =      1.0913721222
a5    =    111.0460723866
d4    =     58.6397480157

@ACES2: The ACES2 program has completed successfully in
404262 seconds.
```

Note that d1 is a constant and therefore does not appear in the optimized parameters list.

Frequency calculation in ACESII is performed in a separate job from the optimization job. Thus, all asterisks must be removed from the Z-matrix while the VIB=FINDIF keyword is added to the ACESII name list section:

```
CH3OOH CCSDT/ccpVTZ VIBRATION ANALYSIS
C
O 1 r1
O 2 r2 1 a1
H 3 r3 2 a2 1 d1
H 1 r4 2 a3 3 d2
H 1 r5 2 a4 3 d3
H 1 r6 2 a5 3 d4

r1=1.41652837
r2=1.45666696
a1=105.30791014
r3=0.96516718
a2=99.59294054
d1=113.84859166
r4=1.09087394
a3=104.87110715
d2=177.3636104
r5=1.09316978
```

```
a4=111.40380445
d3=-63.81333294
r6=1.09169994
a5=110.97005336
d4=58.85585791

*ACES2(PRINT=0,REFERENCE=RHF,CALC=CCSD(T),BASIS=CC-PVTZ,
SPHERICAL=ON,CHARGE=0,MULTI=1, MEMORY_SIZE=800MB,SCF_CONV=7,
DROPMO=1-3,VIB=FINDIF)
```

The finite difference (FINDIF) is recommended for vibrational normal mode analysis.[7]

The program generates a printout of the vibrational frequencies in cm^{-1} in several location of the output file:

```
   Principal axis orientation for molecule:
       -2.206109878501   -0.550653468713   -0.027648274958
       -0.109385391012    1.112709001333    0.022353513281
        2.108483539623   -0.515839151212    0.101431826227
        2.832803096295   -0.122169549573   -1.525529180853
       -3.859127188389    0.680629510505    0.004967486822
       -2.217867264730   -1.697412817953   -1.745873706157
       -2.215165601175   -1.777265643047    1.631076022065
*****************************************************************************
   The full molecular point group is C1  .
   The largest Abelian subgroup of the full molecular point group is C1  .
   The computational point group is C1  .
*****************************************************************************
 @GEOPT-W, Archive file not created for single-point calculation.
                     Normal Coordinate Analysis
-----------------------------------------------------------------
    Irreducible         Harmonic       Infrared        Type
   Representation       Frequency      Intensity
-----------------------------------------------------------------
                          (cm-1)        (km/mol)
-----------------------------------------------------------------
      ----                  0.0000i        0.0000       ---------
      ----                  0.0000i        0.0000       ---------
      ----                  0.0000i        0.0000       ---------
      ----                  0.0000         0.0000       ---------
      ----                  0.0000         0.0000       ---------
      ----                  0.0000         0.0000       ---------
         A                195.8309       108.4226       VIBRATION
         A                257.9685         6.1205       VIBRATION
         A                448.3821         5.6433       VIBRATION
         A                861.5893        11.7760       VIBRATION
         A               1061.2822        19.7445       VIBRATION
         A               1179.4913         2.7337       VIBRATION
         A               1213.3423         6.0914       VIBRATION
         A               1371.6180        50.1620       VIBRATION
         A               1455.9602         2.3539       VIBRATION
         A               1475.1713         5.2849       VIBRATION
         A               1521.0715         8.5837       VIBRATION
         A               3024.5285        35.5171       VIBRATION
         A               3100.5737        40.0569       VIBRATION
         A               3129.7705        17.2074       VIBRATION
         A               3795.0929        31.9058       VIBRATION
-----------------------------------------------------------------

                              Normal Coordinates
                        [Dimensions are Mass**-1/2 Distance]
```

	A 195.83 VIBRATION X	 Y	 Z	A 257.97 VIBRATION X	 Y	 Z	A 448.38 VIBRATION X	 Y	 Z
C	0.0008	-0.0150	-0.1044	0.0093	-0.0039	0.0311	0.4465	-0.1049	0.0018
O	0.0197	-0.0166	0.1116	-0.0019	0.0205	-0.3383	0.0168	0.4496	0.0286
O	0.1025	0.2098	0.1122	-0.0393	-0.0148	0.2390	-0.5244	-0.2491	-0.0292
H	-0.4824	-0.7021	-0.3841	0.1166	0.0046	0.1188	-0.0745	-0.1148	0.0054
H	-0.0011	-0.0075	0.0409	-0.0029	-0.0240	0.5633	-0.0237	-0.2385	-0.0195
H	-0.0267	0.0823	-0.0918	-0.3313	0.2964	-0.1905	0.2992	-0.0489	0.0126
H	0.0208	-0.0905	-0.0963	0.3493	-0.2867	-0.2034	0.2805	-0.0345	-0.0023

	A 861.59 VIBRATION X	 Y	 Z	A 1061.28 VIBRATION X	 Y	 Z	A 1179.49 VIBRATION X	 Y	 Z
C	0.2665	0.0655	0.0101	0.5402	0.2507	0.0046	0.0082	-0.0463	0.4108
O	0.3095	-0.5179	0.0037	-0.6519	-0.1841	-0.0326	-0.0182	0.0387	-0.2095
O	-0.5637	0.3947	-0.0248	0.1626	-0.1442	0.0374	-0.0072	0.0103	-0.0148
H	-0.0150	0.0373	0.0397	-0.1233	0.0671	-0.0409	0.1037	-0.0743	0.0227
H	0.2057	0.1874	0.0066	0.2417	0.2018	0.0076	0.0307	0.0352	-0.2131
H	-0.0458	0.0220	-0.0036	-0.0176	0.0895	-0.0174	0.3759	0.4079	-0.1626
H	-0.0518	0.0182	0.0064	-0.0155	0.0843	0.0160	-0.4377	-0.4043	-0.1713

	A 1213.34 VIBRATION X	 Y	 Z	A 1371.62 VIBRATION X	 Y	 Z	A 1455.96 VIBRATION X	 Y	 Z
C	0.0995	-0.4746	-0.0499	0.0157	0.0995	-0.0409	0.3346	0.1427	-0.0085
O	0.0250	0.3882	0.0522	-0.2029	-0.0719	0.1520	0.0498	0.0093	0.0012
O	-0.0518	-0.0331	-0.0299	-0.0144	0.1228	-0.1716	-0.0159	0.0092	-0.0043
H	0.1060	-0.1003	0.0227	0.7285	-0.5547	0.1292	0.0162	-0.0070	0.0042
H	0.3945	0.3677	0.0291	-0.0409	-0.0327	0.0423	-0.3374	-0.5259	0.0289
H	-0.4080	-0.0578	-0.0595	0.0487	-0.0257	0.0278	-0.4588	-0.0273	0.0375
H	-0.3291	0.0133	0.0910	0.0749	0.0671	0.0200	-0.5095	-0.0059	-0.0288

	A 1475.17 VIBRATION X	 Y	 Z	A 1521.07 VIBRATION X	 Y	 Z	A 3024.53 VIBRATION X	 Y	 Z
C	0.0207	-0.0020	0.2000	0.0061	0.2164	0.0148	0.0933	0.1173	0.0373
O	-0.0048	-0.0078	0.0429	-0.0153	0.0570	0.0050	0.0061	0.0040	0.0001
O	-0.0030	0.0037	-0.0082	0.0025	-0.0066	-0.0019	-0.0010	-0.0008	0.0005
H	0.0329	-0.0127	0.0103	0.0115	-0.0076	0.0019	0.0036	0.0008	-0.0034
H	-0.0263	-0.0218	-0.7144	0.0856	0.1500	-0.0302	-0.3575	0.2678	0.0099
H	-0.4686	0.1657	-0.0774	-0.0582	-0.5488	0.3828	0.0071	-0.3742	-0.5833
H	0.4215	-0.1082	-0.0471	-0.0093	-0.5410	-0.4178	0.0042	-0.3119	0.4459

	A 3100.57 VIBRATION X	 Y	 Z	A 3129.77 VIBRATION X	 Y	 Z	A 3795.09 VIBRATION X	 Y	 Z
C	0.0399	-0.0140	-0.3078	0.1906	-0.2379	0.0405	0.0010	0.0020	0.0001
O	0.0012	-0.0007	0.0002	0.0030	-0.0035	-0.0003	-0.0045	0.0012	0.0016
O	-0.0002	0.0007	0.0015	-0.0030	0.0021	-0.0002	0.0993	0.0526	-0.2186
H	-0.0036	-0.0005	-0.0006	-0.0008	0.0009	0.0008	-0.3790	-0.2174	0.8652
H	-0.1414	0.1061	-0.0163	-0.6689	0.4994	0.0157	-0.0020	-0.0002	0.0004
H	-0.0104	0.3557	0.5276	0.0073	0.0990	0.1824	0.0009	-0.0021	-0.0030
H	0.0137	-0.4128	0.5444	0.0045	0.2272	-0.3369	-0.0009	-0.0018	0.0014

Normal modes in internal coordinates

	0.000	0.000	0.000	0.000	0.000
r1	0.000000	0.000000	0.000000	0.000000	0.000000
r2	0.000000	0.000000	0.000000	0.000000	0.000000
a1	0.000000	0.000000	0.000000	0.000000	0.000000
r3	0.000000	0.000000	0.000000	0.000000	0.000000
a2	0.000000	0.000000	0.000000	0.000000	0.000000
d1	0.000000	0.000000	0.000000	0.000000	0.000000
r4	0.000000	0.000000	0.000000	0.000000	0.000000
a3	0.000000	0.000000	0.000000	0.000000	0.000000
d2	0.000000	0.000000	0.000000	0.000000	0.000000
r5	0.000000	0.000000	0.000000	0.000000	0.000000
a4	0.000000	0.000000	0.000000	0.000000	0.000000
d3	0.000000	0.000000	0.000000	0.000000	0.000000

r6	0.000000	0.000000	0.000000	0.000000	0.000000
a5	0.000000	0.000000	0.000000	0.000000	0.000000
d4	0.000000	0.000000	0.000000	0.000000	0.000000
	0.000	195.831	257.968	448.382	861.589
r1	0.000000	0.008312	-0.000602	-0.051792	-0.261805
r2	0.000000	-0.028760	0.003208	-0.035433	-0.886378
a1	0.000000	0.038678	-0.012963	-0.879110	0.180616
r3	0.000000	0.005196	-0.000799	0.000518	-0.011382
a2	0.000000	0.038057	0.008851	0.083080	0.243493
d1	0.000000	-0.990662	0.177367	0.031097	0.058440
r4	0.000000	0.000573	-0.000726	-0.010610	-0.006778
a3	0.000000	0.002310	0.004093	0.315999	-0.167591
d2	0.000000	-0.060629	-0.580061	0.071606	-0.000957
r5	0.000000	0.005618	0.004723	-0.004658	0.012687
a4	0.000000	0.002968	0.019911	-0.162340	0.079512
d3	0.000000	-0.074467	-0.560787	0.226699	-0.065524
r6	0.000000	-0.003399	-0.004425	-0.003138	0.010840
a5	0.000000	0.001743	-0.025295	-0.156801	0.086246
d4	0.000000	-0.073757	-0.562348	-0.088871	0.062218
	1061.282	1179.491	1213.342	1371.618	1455.960
r1	-0.770207	0.010006	0.230705	-0.124256	-0.166341
r2	0.377694	0.013729	0.083149	0.011921	-0.024497
a1	0.017486	-0.019697	-0.195057	0.044128	-0.021569
r3	0.004742	0.002982	0.000813	0.018636	0.002365
a2	-0.221359	0.098248	0.137293	0.969933	0.020071
d1	-0.055520	0.132315	-0.006527	-0.027330	0.003438
r4	0.021216	0.001800	0.016658	0.000902	0.018342
a3	-0.271405	-0.053071	-0.675121	0.064004	0.622139
d2	-0.012081	0.260057	-0.009988	0.005309	-0.043517
r5	0.017104	-0.003064	-0.007739	-0.005197	0.014705
a4	0.193137	-0.591851	0.350952	0.028505	0.463818
d3	-0.185607	-0.290312	-0.315930	0.141900	-0.228892
r6	0.013341	0.001643	-0.005879	0.004484	0.017583
a5	0.203328	0.643288	0.223829	-0.101915	0.484128
d4	0.154584	-0.230879	0.391897	0.071403	0.281308
	1475.171	1521.071	3024.529	3100.574	3129.771
r1	-0.014191	-0.065272	-0.040056	-0.004481	-0.000577
r2	-0.003253	0.024606	-0.000698	-0.000437	-0.001945
a1	-0.001561	0.017237	0.002856	-0.002743	-0.030812
r3	-0.001165	0.001746	0.004769	-0.000648	-0.000673
a2	0.046833	0.011214	0.000539	-0.001334	-0.000058
d1	0.046414	0.005685	0.004777	-0.034230	0.003835
r4	0.001865	-0.029618	0.441075	0.179233	0.870249
a3	0.048966	-0.085100	0.024004	-0.003605	-0.041224
d2	0.751594	0.036276	0.003348	-0.033004	0.005592
r5	0.044069	0.047207	0.709753	-0.673635	-0.222112
a4	0.233100	0.391256	0.003894	0.050347	0.018286
d3	-0.442960	0.570175	-0.000704	0.023907	-0.044153
r6	-0.042742	0.037149	0.546989	0.711295	-0.431413
a5	-0.217076	0.367137	0.014604	-0.039785	0.031396
d4	-0.355952	-0.607175	-0.005608	0.034024	0.035304

Dipole Moment Function
(Normal Coordinate Basis)

Mode	Symmetry	d(Mu(x))/dQ	d(Mu(y))/dQ	d(Mu(z))/dQ
Q7	A	-0.176491	-0.251543	-0.129595
Q8	A	0.049330	-0.000944	0.062000
Q9	A	0.067912	-0.034203	0.002619
Q10	A	0.097445	0.050110	0.008552
Q11	A	0.078572	0.118659	0.000162

```
     Q12          A        0.019303     -0.022773      0.043738
     Q13          A       -0.012824     -0.077620     -0.007686
     Q14          A        0.201180     -0.104000     -0.012873
     Q15          A        0.048879      0.005026     -0.000315
     Q16          A        0.014506      0.004147     -0.072066
     Q17          A        0.087763     -0.032056     -0.008656
     Q18          A        0.145974      0.116030      0.040761
     Q19          A        0.024548     -0.013878     -0.200734
     Q20          A        0.055160     -0.119242      0.019739
     Q21          A       -0.125792     -0.028158      0.126932
-----------------------------------------------------------------
   Vibrational frequencies after rotational projection  of
   Cartesian force constants:
            1               0.0000i
            2               0.0000i
            3               0.0000
            4               0.0000
            5               0.0000
            6               0.0001
            7             195.8309
            8             257.9685
            9             448.3821
           10             861.5893
           11            1061.2822
           12            1179.4913
           13            1213.3423
           14            1371.6180
           15            1455.9602
           16            1475.1713
           17            1521.0715
           18            3024.5285
           19            3100.5737
           20            3129.7705
           21            3795.0929
  Zero-point vibrational energy =   34.4408 kcal/mole.


 @ACES2: The ACES2 program has completed successfully in  874529 seconds.
```

Unlike the situation in GAUSSIAN03, The ACESII program can compute CCSD(T) dipole moments and as with the frequency calculation, electron properties and optimization must be computed separately.[7] Again, picking the optimized structure of CH_3OOH at $\tau = 100^o$ as an example, the ZMAT must contain the PROP=1 in name list:[7]

```
CH3OOH CCSD(T)/cc-pVTZ Torsion=100 dipole moment calculation
C
O 1 r1
O 2 r2 1 a1
H 3 r3 2 a2 1 d1
H 1 r4 2 a3 3 d2
H 1 r5 2 a4 3 d3
H 1 r6 2 a5 3 d4

r1=1.4171894668
r2=1.4531902934
a1=105.8317147015
r3=0.9660564440
```

```
a2=100.1005746004
r4=1.0908713685
a3=104.9387395932
d2=177.4061520164
r5=1.0939352153
a4=111.4377934698
d3=-63.9960814955
r6=1.0913721222
a5=111.0460723866
d4=58.6397480157
d1=100.0

*ACES2(PRINT=0,REFERENCE=RHF,CALC=CCSD(T),BASIS=CC-PVTZ,
SPHERICAL=ON,CHARGE=0,MULTI=1,MEMORY_SIZE=800MB,SCF_CONV=7,
DROPMO=1-3,PROPS=1)
```

This results in printout containing the SCF dipole moments μ_a, μ_b and μ_c:

```
 @DRVPRP-I, Properties computed from the SCF density matrix follow.
   Components of electric dipole moment
        X =   -0.4166189254   Y =   -0.4138204482   Z =   -0.6246847573
```

And, more importantly, the post SCF dipole moments μ_a, μ_b and μ_c:

```
@DRVPRP-I, Properties computed from the correlated density matrix
follow.
   Components of electric dipole moment
        X =   -0.3606546645   Y =   -0.3695461051   Z =   -0.5787761825
```

The above dipole moments values are given in a.u. units but can be converted to Debye units by dividing them by 0.393456 a.u./Debye. Note that in ACESII, the X, Y, and Z components correspond to the a-, b-, and c- inertial axes.[7]

B.3 Acknowledgment

The dissertation author would like to warmly acknowledge Professor H. G. Kjaergaard of the University of Otago, Professor J. D. Watts of Jackson State University, Dr. S. A. Perera of the University of Florida, and Professor J. S. Francisco of Purdue University for their help with the operation of GAUSSIAN03 and ACESII programs.

B.4 References

1. Gaussian 03, Revision B.04, M. J. Frisch, G. W. Trucks, H. B. Schlegel, G. E. Scuseria, M. A. Robb, J. R. Cheeseman, J. A. Montgomery, Jr., T. Vreven, K. N. Kudin,

J. C. Burant, J. M. Millam, S. S. Iyengar, J. Tomasi, V. Barone, B. Mennucci, M. Cossi, G. Scalmani, N. Rega, G. A. Petersson, H. Nakatsuji, M. Hada, M. Ehara, K. Toyota, R. Fukuda, J. Hasegawa, M. Ishida, T. Nakajima, Y. Honda, O. Kitao, H. Nakai, M. Klene, X. Li, J. E. Knox, H. P. Hratchian, J. B. Cross, V. Bakken, C. Adamo, J. Jaramillo, R. Gomperts, R. E. Stratmann, O. Yazyev, A. J. Austin, R. Cammi, C. Pomelli, J. W. Ochterski, P. Y. Ayala, K. Morokuma, G. A. Voth, P. Salvador, J. J. Dannenberg, V. G. Zakrzewski, S. Dapprich, A. D. Daniels, M. C. Strain, O. Farkas, D. K. Malick, A. D. Rabuck, K. Raghavachari, J. B. Foresman, J. V. Ortiz, Q. Cui, A. G. Baboul, S. Clifford, J. Cioslowski, B. B. Stefanov, G. Liu, A. Liashenko, P. Piskorz, I. Komaromi, R. L. Martin, D. J. Fox, T. Keith, M. A. Al-Laham, C. Y. Peng, A. Nanayakkara, M. Challacombe, P. M. W. Gill, B. Johnson, W. Chen, M. W. Wong, C. Gonzalez, and J. A. Pople, Gaussian, Inc., Wallingford CT, 2004.

2. A. Frisch, M. J. Frisch, G. W. Trucks, *Gaussian 03 User's Reference* and *IOps Reference* (Gaussian, Carnegie, PA 2003).

3. J. B. Foresman, and A. Frisch, *Exploring Chemistry with Electronic Structure Methods 2nd edition* (Gaussian, Carnegie, PA 1996).

4. T. H. Dunning Jr., J. Chem. Phys. **90**, 1007 (1989).

5. K. A. Peterson, D. E. Woon, T. H. Dunning Jr., J. Chem. Phys. **100**, 7410 (1994).

6. ACESII is a program product of the Quantum Theory Project, University of Florida. Authors: J. F. Stanton, J. Gauss, J. D. Watts, M. Nooijen, N. Oliphant, S. A. Perera, P. G. Szalay, W. J. Lauderdale, S. A. Kucharski, S. R. Gwaltney, S. Beck, A. Balková D. E. Bernholdt, K. K. Baeck, P. Rozyczko, H. Sekino, C. Hober, and R. J. Bartlett. Integral packages included are VMOL (J. Almlöf and P. R. Taylor); VPROPS (P. Taylor) ABACUS; (T. Helgaker, H. J. Aa. Jensen, P. Jørgensen, J. Olsen, and P. R. Taylor).

7. J. F. Stanton *et al.*, *ACESII Release 2.5.0 User Manual* (University of Florida, Fl 2006) http://www.qtp.ufl.edu/Aces2/

8. Basis sets were obtained from the Extensible Computational Chemistry Environment Basis Set Database, Version 1.0, as developed and distributed by the Molecular Science Computing Facility, Environmental and Molecular Sciences Laboratory which is part of the Pacific Northwest Laboratory, P.O. Box 999, Richland, Washington 99352, USA, and funded by the U.S. Department of Energy. The Pacific Northwest Laboratory is a multi-program laboratory operated by Battelle Memorial Institute for the U.S. Department Energy under contract DE-AC06-76RLO 1830. Contact Karen Schuchardt for further information.

Appendix C

OH Fragment Translational and Rotational Energy Release Analysis

C.1 Introduction

Several chapters in this dissertation include the investigation of the dissociation dynamics of the molecule of interest. In part, this involves investigation of the energy partitioning in the OH fragment. In general, the excess energy in a unimolecular photodissociation process which can be described as C → A + B where A, B and C are molecules, will produce energized fragments. The partitioning of the energy into internal (rotational, vibrational, electronic) and translational degrees of freedom typically depends on the prepared state in the parent molecule which results in fragmentation of the molecule.[1] For photodissociation of OH containing molecules presented in this dissertation, i.e. HOX → OH + X (X= OH, CH_3O, ONO, ONO_2, OCH_2OH), we typically find that, depending on the dissociation process, the resulting OH fragment is rotationally excited and in some cases vibrationally excited as well. Due to the large energy separation (~4.05 eV) between the ground state OH($X^2\Pi_\Omega$) and first electronic excited state OH($A^2\Sigma^+$),[2,3] it is quite uncommon to observe direct fluorescence of electronically excited OH with our lasers excitation energies. In contrast, since the OH is the smaller of the two fragments, the largest fraction of the translational energy is transferred to it upon dissociation.

This chapter focuses on the theoretical aspects of obtaining the translational energy release information from scans over the OH rotational transitions as well as conversion of these rotational lines to population and to average rotational energy by

convoluting out the contributions of the laser linewidth and the parent motion. The physical approach to obtaining these values using the PeakFit program is also explained in the sections to follow.

C.2 OH Fragment Translational Energy Release

In a two-body photodissociation of HO-X molecule, the resulting OH and X products are formed in quantum states specified by their rotational and vibrational quantum numbers. In addition, the breaking of the bonding in HO-X molecule leads the fragments to translate in opposite direction such that:

$$Et_{tot.} = Et_{OH} + Et_x \qquad (C.1)$$

In the above equation the total translational energy available is the sum of the translational energies in the OH and X fragments. The momentum P, carried by each fragment is simply equals to $Et^2 / 2m$. The general approach for obtaining the translational energy in the OH fragment (Et_{OH}) and the total translational energy (Et_{tot}) involves investigation of the Doppler profiles of the OH ro-vibrational transitions between the $A - X$ states. The linewidths associated with these transitions are assume to be a convolution of the natural transition width $\Delta\nu_n$, associated with the lifetime of the OH in the *A* state, the initial motion of the parent molecule due to the thermal energy $\Delta\nu_P$, the laser linewidth $\Delta\nu_L$ and the Doppler broadening $\Delta\nu_D$.[4] Since the lifetime of the OH fragment in the *A* state is long, the lifetime broadening $\Delta\nu_n$, is expected to be much smaller then the broadening due to the laser linewidth and the Doppler broadening and therefore ignored. Thus, we treat the total transition linewidth $\Delta\nu$, as a geometrical sum encompassing the following terms:

$$\Delta\nu^2 = \Delta\nu_P^2 + \Delta\nu_L^2 + \Delta\nu_D^2 \qquad (C.2)$$

Where the Doppler linewidth $\Delta\nu_D$, can be extracted using:

$$\Delta\nu_D = (\Delta\nu^2 - \Delta\nu_P^2 - \Delta\nu_L^2)^{0.5} \qquad (C.3)$$

In order to evaluate the above expression we fit the raw OH rotational transition ($\Delta\nu$) with a Gaussian function and extract the linewidth (FWHM) in the manner described in section C.5.3 using the PeakFit program. The velocity distribution of a gaseous sample in thermal equilibrium can be described by Maxwell-Boltzmann distribution function.[4] It can be shown that under this treatment the Doppler linewidth (FWHM) associated with the motion of the thermalized parent molecules ($\Delta\nu_P$) is simply:[4,5]

$$\Delta\nu_P = 2\nu_0(2\ k\ T\ \ln(2) / m_p\ c^2)^{0.5} \qquad (C.4)$$

Or, for parent molecules at room temperature 298.15 K:

$$\Delta\nu_P = 1.22596\times10^{-5}\ m_p^{-0.5}\ \nu_0 \qquad (C.5)$$

In the above expression, k is the Boltzmann constant, T is the temperature m is the mass of the parent molecule in amu units, c is the speed of light in vacuum and ν_0 is the line position of the probed transition in cm^{-1} units. For example, the contribution of HOONO molecule to the linewidth of the probed OH($^2\Pi_{3/2}$, v=0) fragment in its N=1 rotational state with transition frequency ν_0 = 32 474.58 cm^{-1} and m_p[HOONO] = 63 amu results in $\Delta\nu_P = 1.22596\times10^{-5} \times 63^{-0.5} \times 32\ 474.58 = 0.050159\ cm^{-1}$ broadening.

Having found the contribution of the parent motion to the line profile, we now turn our attention to the laser contribution to the line profile. The term $\Delta\nu_L$ in essence is verified in a separate set of experiments where we generate OH radicals in a side reactor by discharging hydrogen gas (~5 mTorr) diluted in 50 mTorr of helium in an Evenson cavity microwave operating at 2450 MHz with 30 W of power. NO_2 (~5 mTorr) and

additional helium gas (~3 – 5 Torr) are introduced down stream the reactor to generate OH radicals via the $H + NO_2 + M \rightarrow OH + NO + M$ reaction scheme. The large amounts of helium gas ensure collision relaxation and thermalization of the OH radical. Probing the various N levels provide an indication to the variability of the laser linewidth over the region of interest. The laser linewidth $\Delta\nu_L$, obtained from these scans is then approximated per equation C.3 as:

$$\Delta\nu_L = (\Delta\nu^2 - \Delta\nu_P^2)^{0.5} \qquad (C.6)$$

Where as before, $\Delta\nu$ is the raw transition linewidth (FWHM) obtained from analysis shown in section C.5.3 and $\Delta\nu_P$ is the linewidth broadening due to the parent motion (OH molecule in this case) of thermal sample (298 K). Using equation C.5, $\Delta\nu_P$, the Doppler width of OH transition probed at N=2 at 298 K will have $\Delta\nu_P = 1.22596\text{x}10^{-5}$ x $17^{-0.5}$ x 32 458.65 = 0.0965 cm^{-1} (FWHM). If, for example, we measure raw linewidth of $\Delta\nu$ = 0.165 cm^{-1} at N=2, then based on equation C.6, our laser linewidth is, $\Delta\nu_L$ = 0.134 cm^{-1}. Several linewidth measurements of our laser system have confirmed linewidth of $\Delta\nu_L$ = 0.13(3) cm^{-1} for the doubled output of the dye laser pumped by the NY81-20 laser system in the 308 nm and 282 nm regions corresponding to excitation of the $A - X$ (0,0) and $A - X$ (1,0) bands. This also indicates that the dye laser output has a linewidth of $0.133 / 2^{0.5}$ = 0.095 cm^{-1}.

Having found the laser linewidth ($\Delta\nu_L$) and parent ($\Delta\nu_P$) motion contributions to the raw linewidth ($\Delta\nu$) the Doppler profile ($\Delta\nu_D$) in equation C.3 can be easily deconvoluted out. To calculate the translational energy of the probed fragment (Et_{OH}) and

the total translational energy in the two-body dissociation process one can use the following expressions:[5]

$$Et_{OH} = 3.7574\times10^{12}\, m_{OH}\, (\Delta\nu_D / \nu_0)^2 \qquad (C.7)$$

And,

$$Et_{tot} = 3.7574\times10^{12}\, m_{OH}\, m_p\, m_x^{-1} (\Delta\nu_D / \nu_0)^2 \qquad (C.8)$$

Where m_{OH}, m_x and m_p are the respective masses for the OH, its partner fragment x, and the mass of the dissociating parent molecule and $\Delta\nu_D$, ν_0 have the usual meaning. We point out that these equations provide with the translational energies of the probed fragment and the probed fragment + partner in the parent molecule reference frame and applying momentum conservation using equation C.1, the translational energy of the fragment x can be obtained as well.

C.3 OH Fragment Ro-Vibrational Population and Energy

In a two-body photodissociation, in addition to the fragments containing translation energy, they may also contain vibrational and rotation excitation (internal excitation). Since several chapters in this dissertation include extensive investigation of the internal energy in the OH fragment via product state distributions, this section provides a summary of the analysis preformed in order to extract the average ro-vibrational energy in the OH fragment.

The basic approach to product state distributions is mapping out the specific quantum numbers the fragment is formed in as a function of its population according to:

$$HO–X\ (v_1, J_1) + h\nu \rightarrow OH(\Omega_2, v_2, J_2) + X(\Omega_3, v_3, J_3) \qquad (C.9)$$

Since our laser system interacts with many populated vibrational (v) and rotational (J) states in the HOX parent molecule, its photodissociation results in a distribution of states

in the fragment molecules consistent with energy and angular momentum conservation. The relative population of the OH forming in a specific electronic (Ω) ro-vibrational state is hence related to the integrated signal intensities:

$$S \alpha B(\Omega, v, J) E P(\Omega, v, J) \quad (C.10)$$

According to Eq. C.10 the population P(Ω, v, J) of the OH fragment in the various quantum states is proportional to the integrated signal intensity and inversely proportional to Einstein's B-coefficients for stimulated emission and probe-laser power (E). To eliminate the dependence of the product states on the probe-laser power, we keep the laser power fixed to low power levels (< 1μJ) to ensure the transitions remain unsaturated and un-broadened. From time to time we check for saturation effects of the rotational states by comparing the ratios of $Q_1(1)$ and $Q_1(2)$ to their respective satellite peaks. Under no-saturation conditions their integrated signal intensities ratio of a thermal sample of OH should equal to their Einstein's B-coefficient ratios given in Ref. 6. These values are also given in Ref. 7 as conversion coefficients which take into account Einstein's A-coefficient for spontaneous emission and pressure-dependent nonradiative relaxation rates. The population ratios of the i^{th} and j^{th} states are simply:

$$P(\Omega_i, v_i, J_i) / P(\Omega_j, v_j, J_j) = S_i B(\Omega_j, v_j, J_j) f_j / S_j B(\Omega_i, v_i, J_i) f_i \quad (C.11)$$

In the above equation the f–terms correspond to the Franck-Condon factors associated with the transition overlap term ($\left| \int \Psi_{Vj}^* \Psi_{Vi} d\tau \right|^2$) of two OH vibrational state in the *A* – *X*(j, i) system. For comparing rotational populations in different vibrational states i.e. $v_i \neq v_j$ these factors must be included as well. The Franck-Condon factors for the various combinations of vibrational bands are given in Table 7 of Ref. 3. For example, in order to

obtain the fraction of population in $Q_1(2)$ and $Q_1(4)$ from their integrated signal intensities (see Fig C.1), we first use PeakFit to obtain their raw areas. This step is discussed in section C.5.2; for the time being, let's assume the resulting integrated signal intensities for the $Q_1(2)$ and $Q_1(4)$ lines taken under near-identical conditions are ~134 and ~111 au. respectively. This suggest that the population of $Q_1(2)$ is greater than that of $Q_1(4)$. To find the population values we simply multiply these values by their respective conversion coefficients from Ref. 7 which are inversely proportion to the B-coefficients. For $Q_1(2)$: 134 x 0.216 = 28.94 and for $Q_1(4)$: 111 x 0.185 = 20.54. Alternatively, one may divide by the B-coefficient given in Ref. 6. To normalize the population, we may sum the probabilities for being in the N^{th} state according to $\Sigma P_i = 28.94 + 20.54 = 49.48$. Thus the normalized population for $Q_1(2)$ and $Q_1(4)$ are $P[Q_1(2)] / \Sigma P[Q_1(2) + Q_1(4)] = 28.94 / 49.48 = 0.585$ and $P[Q_1(4)] / \Sigma P[Q_1(2) + Q_1(4)] = 20.54 / 49.48 = 0.415$. Thus, in this example, ~58.5 % of the OH population is formed in the N=2 state and ~41.5 in the N=4 rotational state. To fully quantify the OH product state distribution, one must scan over all the populated rotational states in order to obtain a complete and normalized picture of the product state distribution.

From the normalized product state distributions it is then possible to obtain the average internal (rotation + vibration) in the OH fragment using the following expression:

$$\langle E_{int} \rangle = \Sigma\, \varepsilon_i\, P_i / \Sigma\, P_i \qquad (C.12)$$

In the above equation, the denominator is the normalization constant, the ε_i, is the energy of the i^{th} state with P_i probability. For the OH molecule, these values are given in Tables 12 and 13 of Ref. 3 for the v=0 and v=1 respectively. Table C.I uses the normalized

product state distribution obtained from *cis-cis* HOONO($2\nu_1$) band to show how the average rotational energy associated with excitation at 6381 cm^{-1} was calculated. From the nascent OH product state distributions we find that ~66 cm^{-1} of rotation energy associated with photodissociation of this band, of which 31 cm^{-1} are in the OH($^2\Pi_{3/2}$, v=0) state and 35 cm^{-1} are in the OH($^2\Pi_{1/2}$, v=0) spin-orbit state. Despite the fact that only ~17 % of OH population is formed in the low spin-orbit state, its contribution to the total average rotational energy is significant in this example.

C.4 OH Fragment Λ-Doublet splitting

Another aspect of characterizing the dissociation dynamics via population analysis and translational energy release involves the investigation of the orientation of the unpaired electron in the OH fragment. In some photodissociation processes, for states carrying large rotational excitation ("high" J-limit), the singly occupied P_π orbital may be aligned perpendicular to the plane of rotation and parallel to J (Λ(A")) or, in the plane of rotation perpendicular to J (Λ(A')). The two λ-doublet components which further split the OH $^2\Pi_\Omega$ electronic states to f and f' levels can be investigated via Q, P and R transitions.[3-5] In the "high" J-limit, selection rules constrain the Q-branch transitions to probing the anti-symmetric states (A") while the P- or R-branches transitions to probing the symmetric states (A'). In order to investigate the propensity and fragment alignment (if any), all that is required is to scan over Q_1[N] and P_1[N] (or R_1[N]) lines and compare their relative *population*. Since the energy spacing associated with these symmetric and antisymmetric wavefunctions is negligible[3], energy constraints play no role in preference of the population of Q- vs. P- (or R-) branches thus, providing with insight to the

dissociation dynamics. None of the systems discussed in this dissertation exhibit alignment propensity.

C.5 Linewidth and Area Analysis with PeakFit

C.5.1 Differences in Integrated Intensities and Linewidths

The analysis in the previous sections have been preformed using the PeakFit program where the population was obtain by looking at the areas (integrated intensities) and the translational energy release was obtained by looking at the transition linewidths (FWHM). A second difference between the rotational and translational part involves the scan rates used. Since the translational energy releases is proportional to the square of the linewidth (see Eq. C.7-C.8), it requires a more careful analysis which can be achieved with a slower scan rate and higher averaging. All linewidths measurements presented in this dissertation involved scanning in BURST mode over the OH lines at 3 μstep scan-rate and 30 shots / bin averaging by the LIF31 software (see Appendix *A*). Since the fluctuations in the areas are not drastically affected by scan-rate and averaging, we find that typically, using BURST mode with 5 μstep scan-rate and 20 or 30 shots / bin averaging (depending on how good the signal-to-noise is) works well. Lastly, while the relative intensity (y-axis) of the rotational lines is insignificant for the linewidth analysis, the widths require extremely careful calibration of the cm^{-1} scale (x-axis). In order to achieve that, when possible, we scan over at least two rotational lines with known absolute frequency position to ensure properly calibrated x-axis scale. In contrast, population analysis requires tight measurements of the relative intensities of the lines therefore require keeping all parameters affecting these intensities such as sample pressure (number density), flow rates, laser beams size, laser powers, focusing

conditions, timing and PMT settings constant. The following sections will provide a guide to how to perform the analysis using the PeakFit program. Note that Appendix *A* covers in details the experimental methods used to obtaining these scans.

C.5.2 Evaluating the Integrated Signal Intensities

To obtain the area associated with a rotational transition shown in figure C.2, start PeakFit and use the "File" menu and select "Import" to load a file (see Fig C.3). Select the file you want to load. In this example, we open the file MA2187.O11 in the "figures" directory which was obtained using BURST mode using scan rate of 5 μstep and 30 shots / bin. When asked "Read multi-column data?" select YES. Pick channel "1" for the x-column and channel "6" for the y-column if collected data from channel-1 using LIF31 data acquisition software. Pick channel "1" for the x-column and channel "7" for the y-column if collected data from channel-2 using LIF31 data acquisition software (see Fig. C.4). Hit "OK" and provide a "Title" if desired and accept by hitting "OK" again. The program will load the file and display pictorially the spectrum shown in fig C.2. To extract the area associated with this line we fit the line by selecting "AutoFit Peaks I Residuals…" in the "AutoFit" menu (see Fig. C.5). On the left panel of the newly open screen (see Fig. C.6) for the "Baseline" select "Constant 2D", For "Smoothing" select "Convolved" and we will pick for this example the "Voigt Area G/L" function in order to obtain best fit. We then run the "Full Peak Fit with Graphical Update" option (see mouse curser on screen caption C.7). When the routine completes, select "Addl Adjust" to make additional fitting attempts or "Review Fit" to obtain a closer look at the fit and obtain the parameters. If you obtained satisfactory fitting (see fig. C.8), select the "Numeric" button to obtain the integrated intensity. In Fig. C.9, the "Amplitude" – or intensity (~911 au.)

and “Analytical Area” (76 422 au.) are highlighted in red. We find that these values will change depending on fitting methods (peak types and smoothing conditions). However, if one uses a consistent fitting method for all the lines within a set of product state distribution, the inconsistencies in the areas tend to cancel out and the relative areas appear unaffected by the choice of fitting routine. In the case the fitting routine fails to produce satisfactory fit, go back to the screen shown in figure C.7 and adjust the peak parameters to aid with the fitting by right-mouse click on the top of the peak to open the parameters menu. For the chosen Voigt function, the parameters box in figure C.10 control the peak’s area (a0), intensity (a1), Gaussian width (a2) and Lorentzian width (a3). Note that the a3 parameter (Lorentzian width) is the half-width at half-max (HWHM) which is the FWHM / 2 and the a2 (Gaussian width) parameter is the FWHM $/(8 \ln 2)^{-0.5} \approx$ FWHM / 2.355. Use these parameters to manually improve the fitting before rerunning the auto fitting routine. It is also possible to control these values by left-mouse click-and-hold on the squares appearing at the midpoints and the bases of each of the peaks using a stretch and compress type of action. The midpoints affect the Gaussian components and the wings affect the Lorentzian components of the Voigt function.

C.5.3 Evaluating the Transition Linewidth

To evaluate the transition linewidth (FWHM) open the file as described above. In the present example we choose the file labeled AP2887.O21 (in the /figures/ directory of Appendix *C*) of $Q_1(2)$ in the region of 616.060 – 616.091 nm (dye laser output) which was taken using BURST mode at 3 μstep and 30 shots / bin (see figure C.11). The x-axis needs to be converted from time scale to wave number scale and to this end, select “Data” → “Enter Calculation…”. Subtract one data point by evaluating in line 1 (X=) X-

1 and apply the calculation. Now the minimum data points becomes "0" and the maximum data points becomes "718". This information is available by clicking the "Section and Graphically Process XY Data" button in the main screen (see Fig. C.12). In order to obtain a properly calibrated scale, we need to find out the exact separation between the two lines $Q_1(2)$ and $Q_{21}(2)$ as their current data point separation relates to their known frequency separation of $\Delta_{freq} = 0.58$ cm^{-1} given in Ref. 3. To find their current position, we utilize the same procedure as before to find the area using the "AutoFit Peaks I Residuals…" in the "AutoFit" menu (see Figs. C.5 and C.6) only now we are interesting in their band centers. As shown if figure C.13, the respective band centers for $Q_1(2)$ and $Q_{21}(2)$ are 346.118109 and 591.863425. Thus, their separation on the current scale $\Delta_{pts} = 245.745316$. To convert our spectrum to we again use the "Data" → "Enter Calculation…" screen and in the "X=" line enter 2E7 / λ_I – Δ_{freq} / Δ_{pts} * X. The first term simply converts the initial dye output wavelength to doubled output in cm^{-1} and the second term converts the scale from steps in points to steps in cm^{-1}. In this case this results in X_{new}= 2E7 / 616.060 – 0.58 / 245.745316*X_{old}. Apply the calculation and now check again by fitting the peaks to see if indeed the separation is 0.58 cm^{-1} as intended. As shown in figure C.14, the separation between the two centers now corresponds to Δ_{freq} = 0.58 cm^{-1} but the band positions do not match absolute line position. As a final calibration, we linearly shift their position by noting their current and absolute line position of 32 463.5534 and 32 458.65 for $Q_1(2)$ respectively. Thus, we require subtracting 4.9034 cm^{-1} to shift the bands to their known calibrated position using the "Data" → "Enter Calculation…" screen and applying X= X – 4.9034. The lines can now be fit and as shown in figure C.15, we find that the two linewidths (FWHM) associated

with the $Q_1(2)$ and $Q_{21}(2)$ are 0.163 and 0.158 respectively and both lines positioned properly.

Table C.1: OH Fragment Rotational Energy Distribution

OH Rotational Level, N	$OH(^2\Pi_{3/2}, v=0)$		$OH(^2\Pi_{1/2}, v=0)$	
	$\varepsilon_i[N]$[a]	$P_i[N]$	$\varepsilon_i[N]$[a]	$P_i[N]$
1	0.03	0.5894	126.43	0.0516
2	83.90	0.1614	187.71	0.0740
3	202.37	0.0648	289.01	0.0366
4	355.87	0.0092	429.45	0.0089
5	544.82	0.0012		
$\Sigma P_i[N]$		0.83		0.17
$<E_{int}> = \Sigma \varepsilon_i P_i$	31		35	

[a] All energies and widths in cm^{-1} .

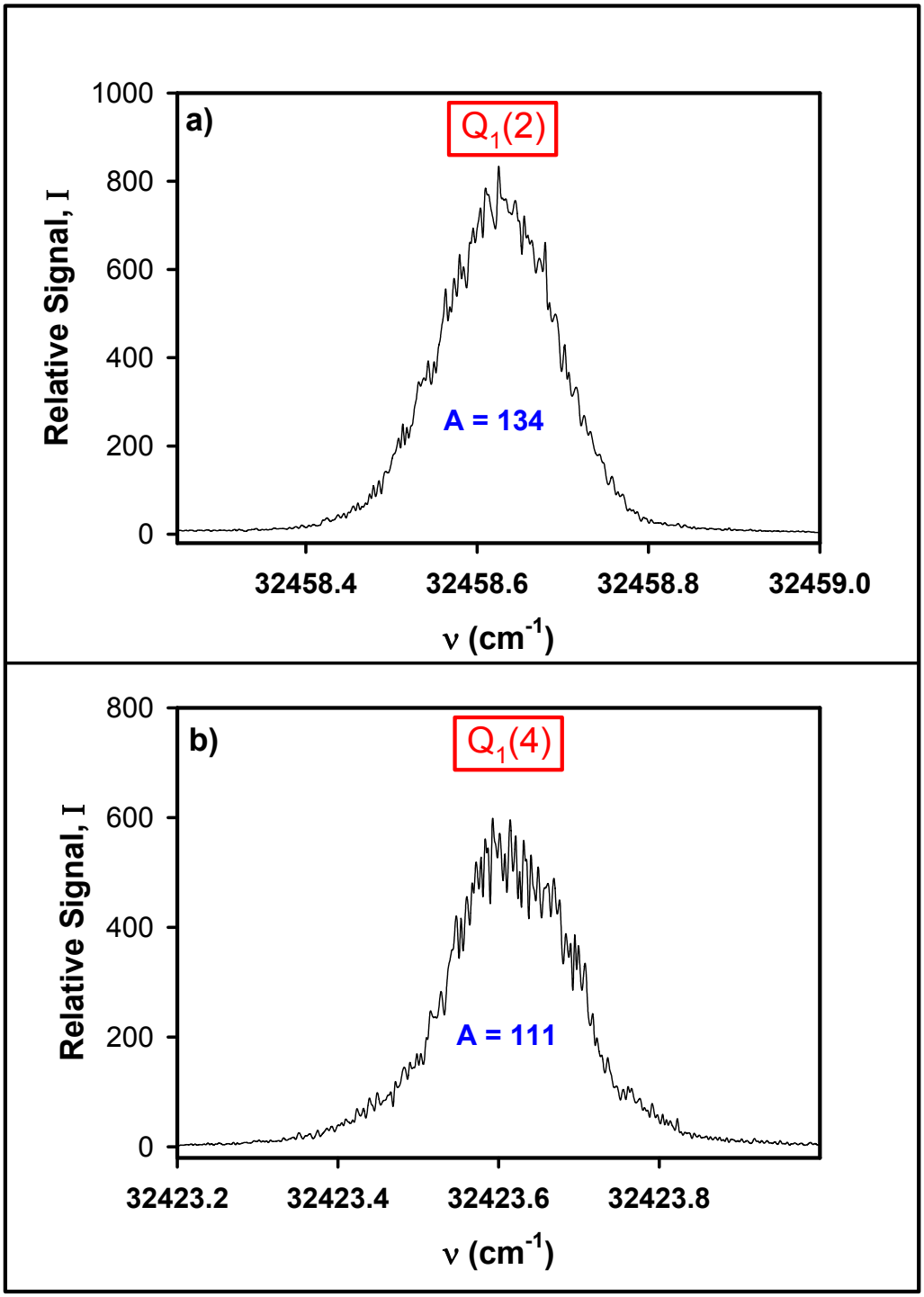

Figure C.1: OH (v=0, $^2\Pi_{3/2}$) in its N=2 (a) and N=4 (b) rotational states. The areas under the curves are found in a manner described in section C.5.2.
[File: FC.1_q12q14]

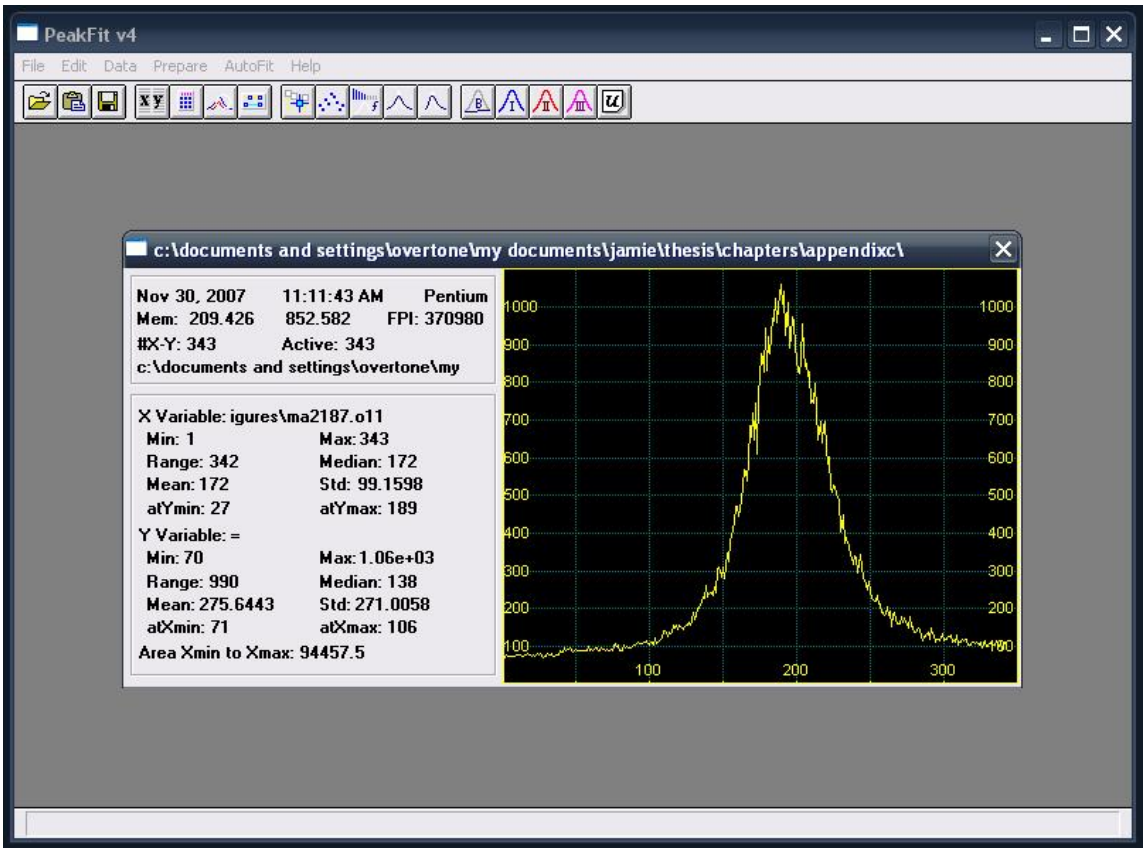

Figure C.2: Screen caption of the PeakFit program main menu. [File: FC.2_pf1]

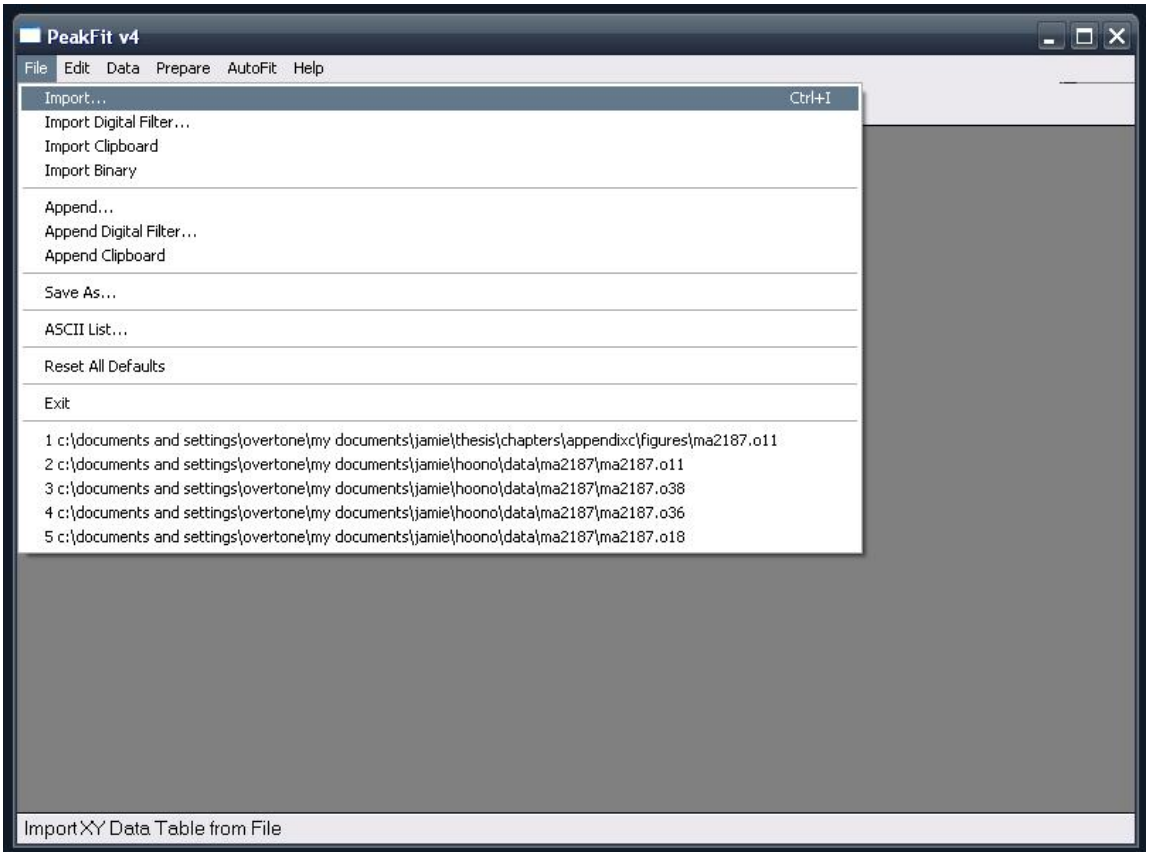

Figure C.3: The import menu used in loading files in PeakFit program.
[File: FC.3_pf2]

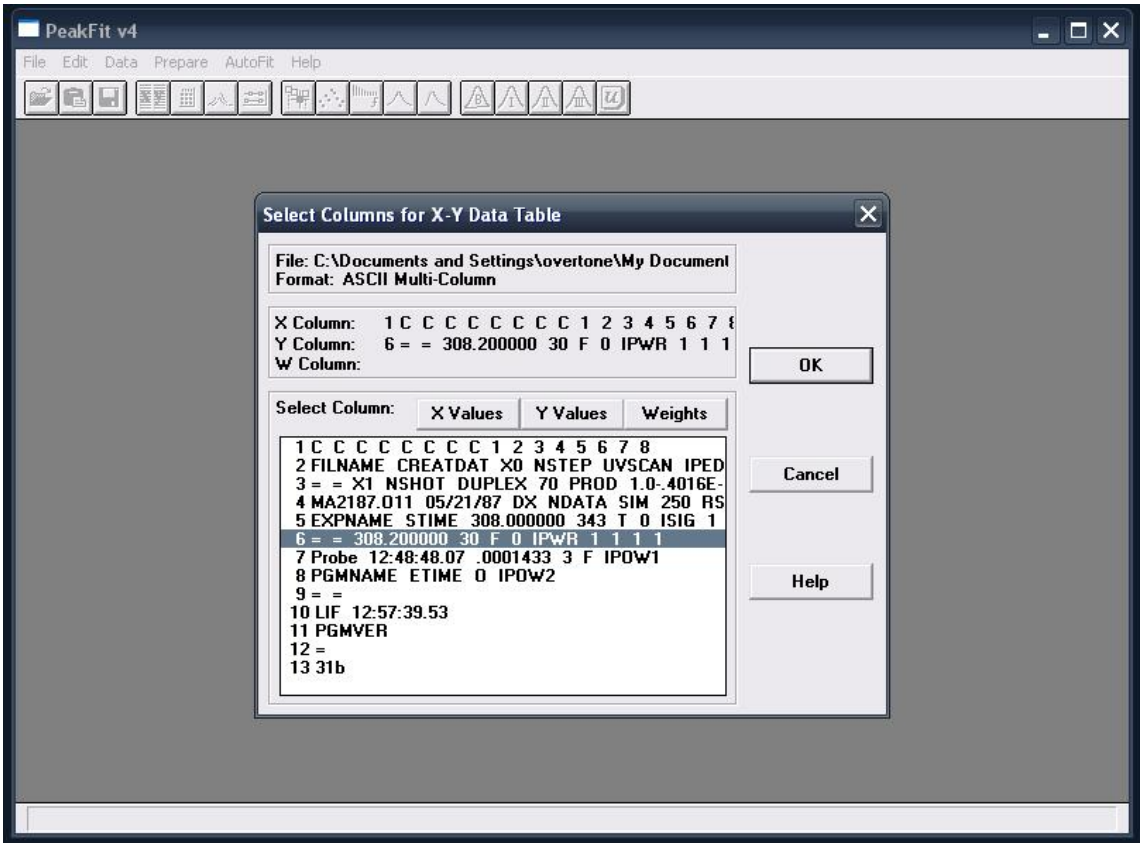

Figure C.4: Selecting X and Y columns to load in PeakFit program. [File: FC.4_pf3]

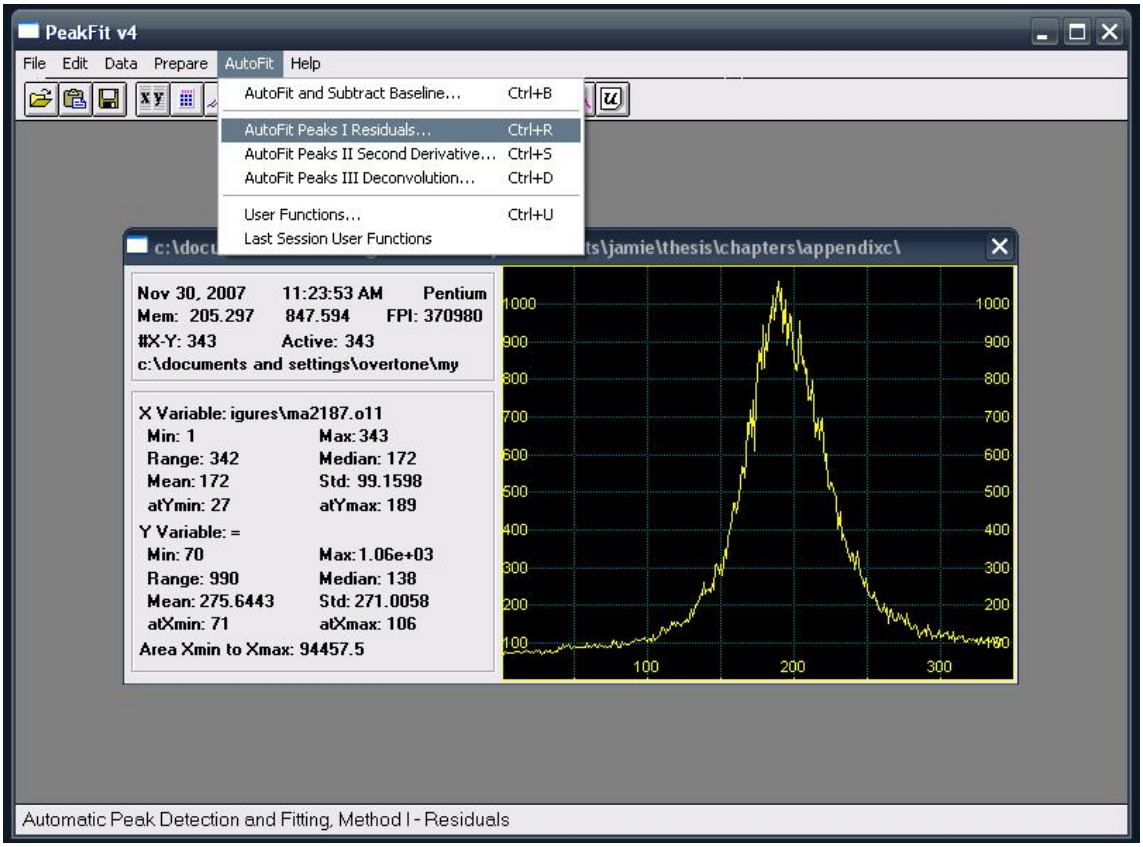

Figure C.5: Selecting from the "AutoFit" menu the Fitting routine involving automatic fitting Method I. [File: FC.5_pf4]

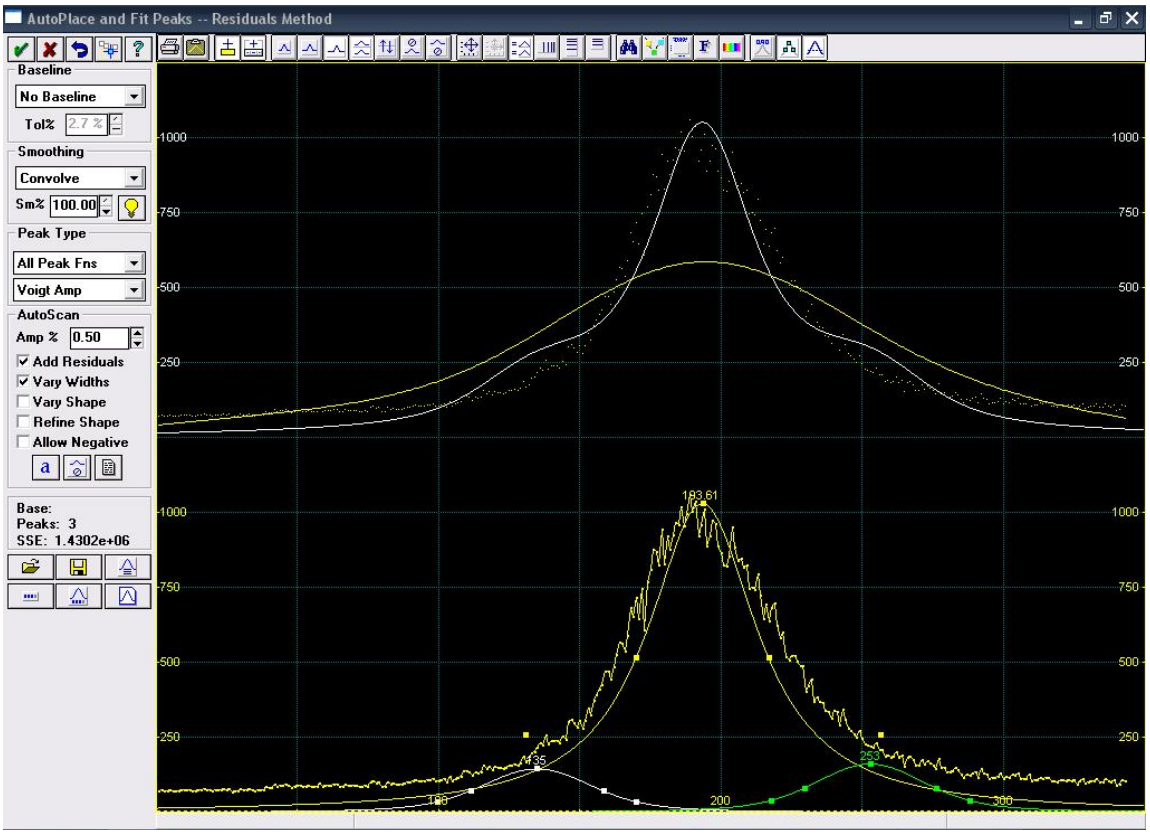

Figure C.6: Initial AutoFit screen caption of the auto-fitting Method I in PeakFit. [File: FC.6_pf5]

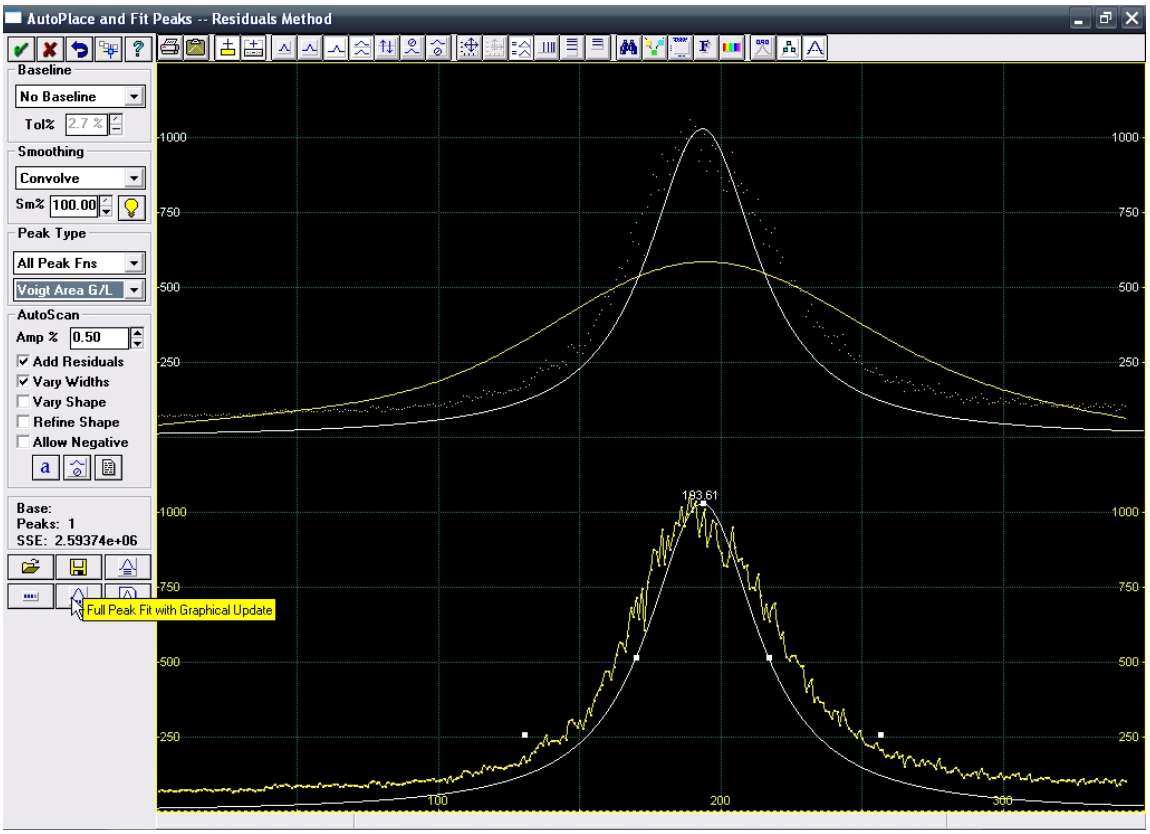

Figure C.7: Selecting the "Full Peak Fit with Graphical Update" option runs the Auto Fit routine. [File: FC.7_pf6]

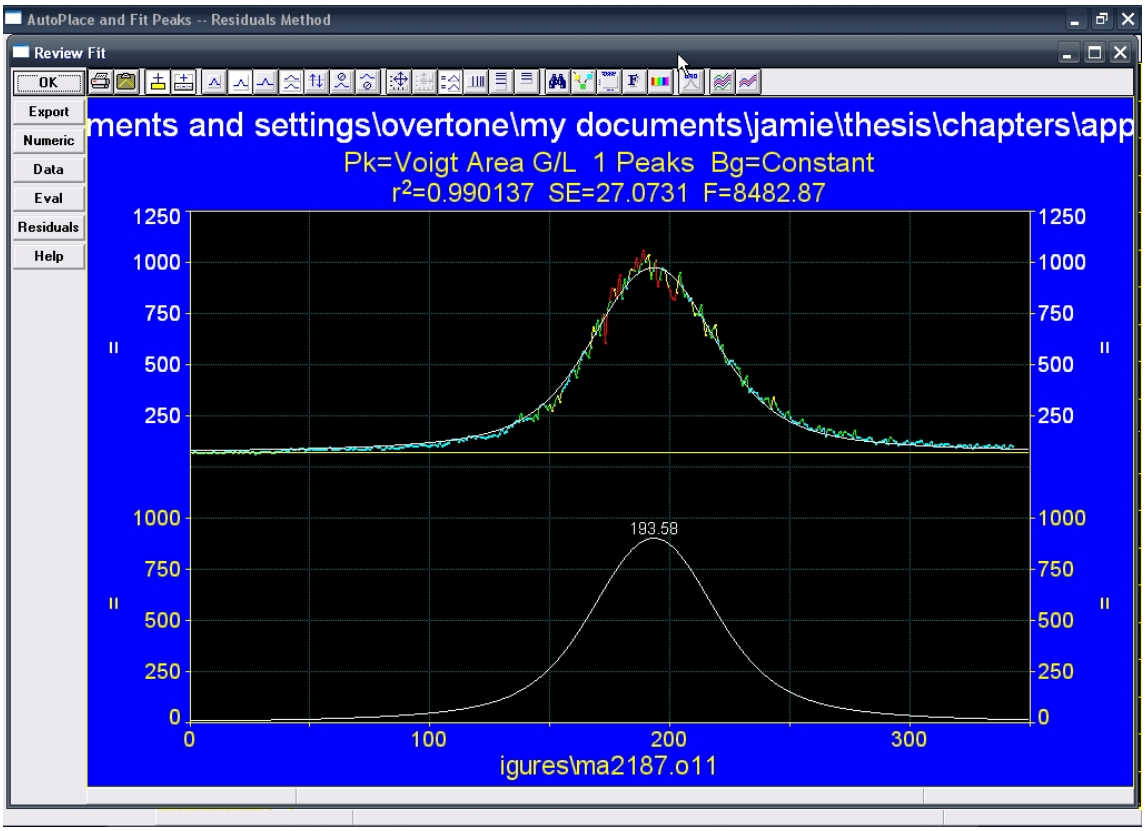

Figure C.8: The resulting fit using the Auto Fit routine are shown along with the R^2 value and standard errors in the PeakFit program. [File: FC.8_pf7]

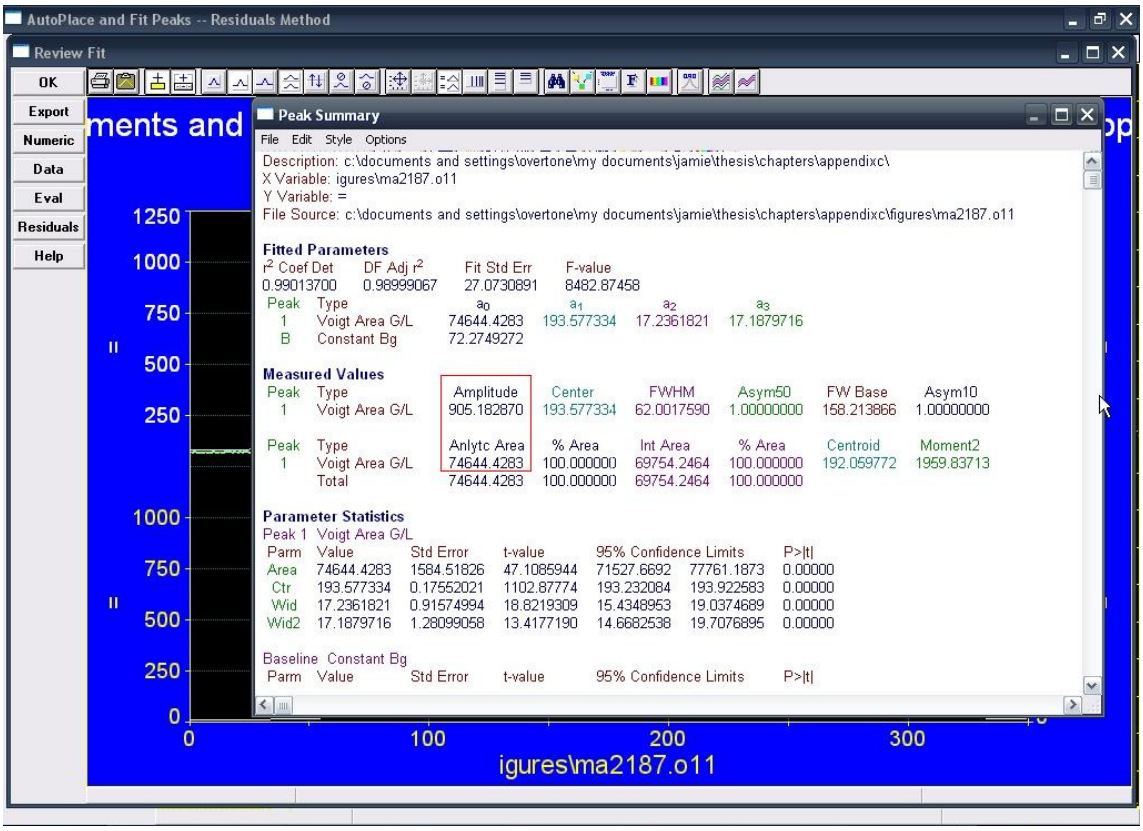

Figure C.9: Additional values are shown post fitting by clicking on the "Numeric" button. The Amplitude and Area are highlighted with the red box. [File: FC.9_pf8]

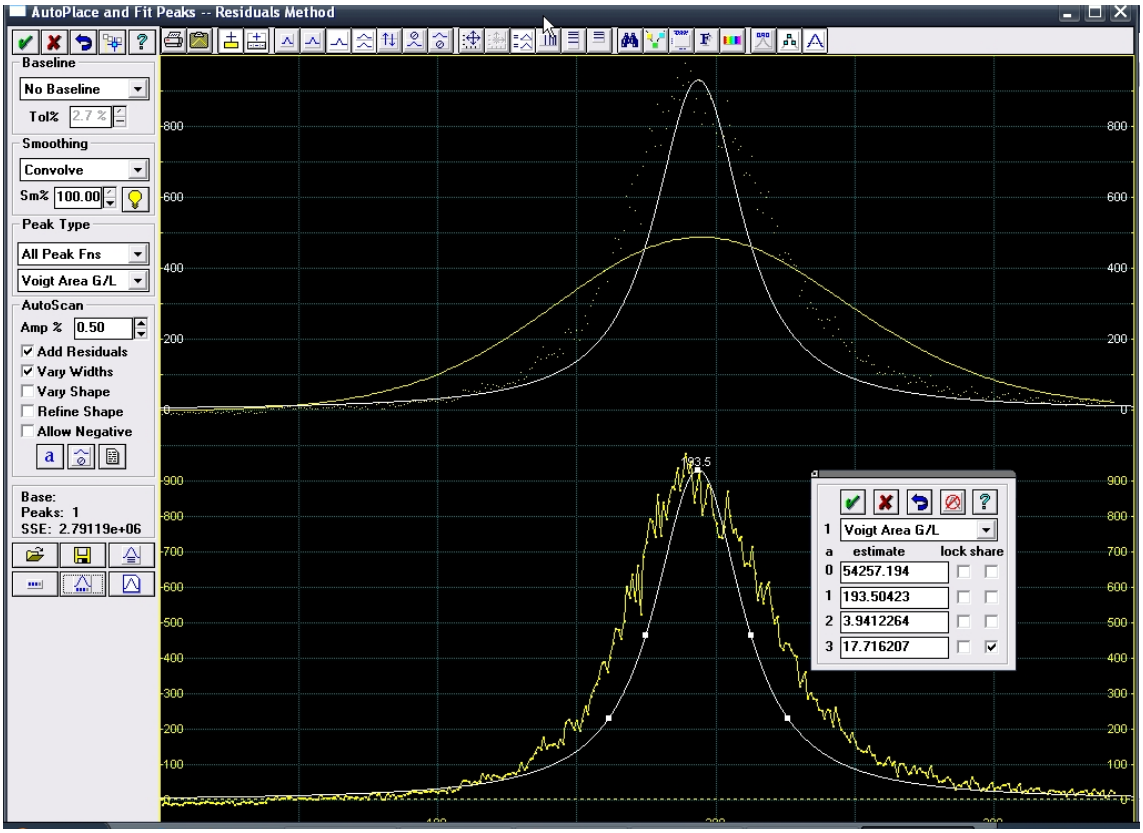

Figure C.10: Manual adjustments to the position, intensities and widths can be chosen for the individual peaks using the right-mouse-click on the peak's maxima. [File: FC.10_pf9]

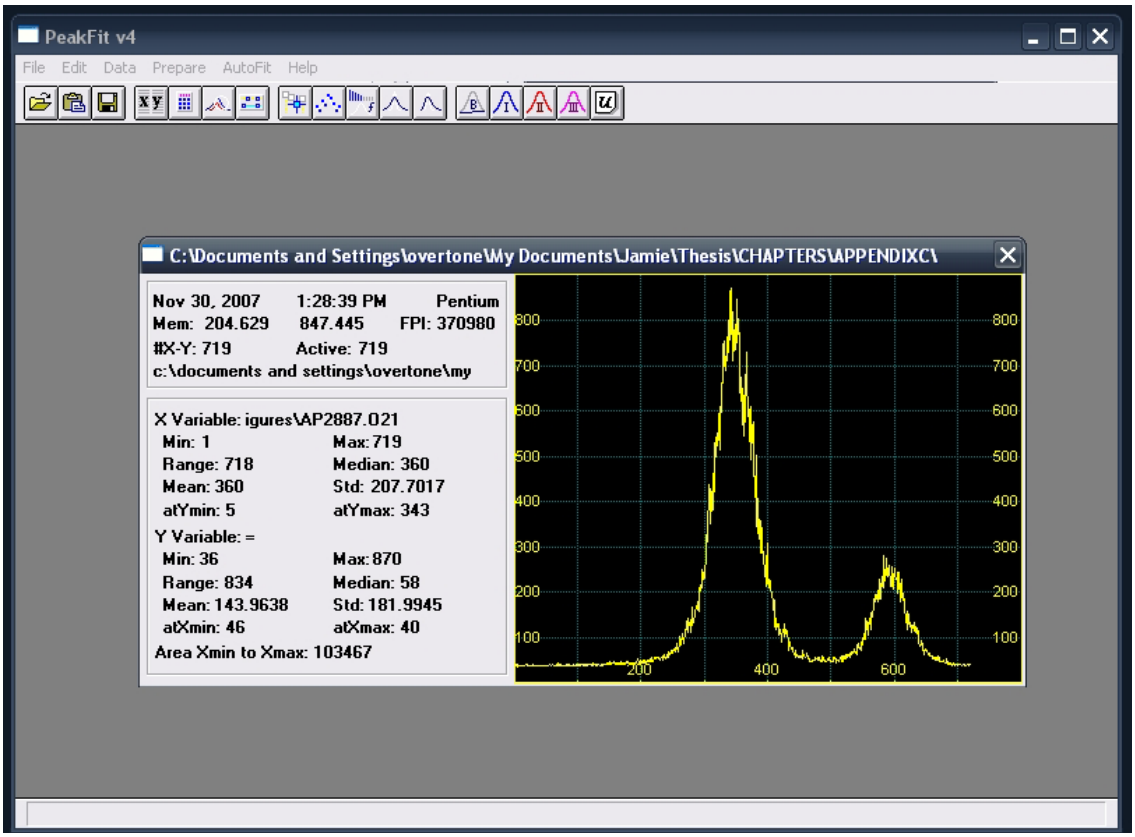

Figure C.11: Screen capture of PeakFit main screen showing graphical display of un-calibrated OH(v=0, $^2\Pi_{3/2}$) lines in their $Q_1(2)$ and $Q_{21}(2)$ states. [File: FC.11_pf10]

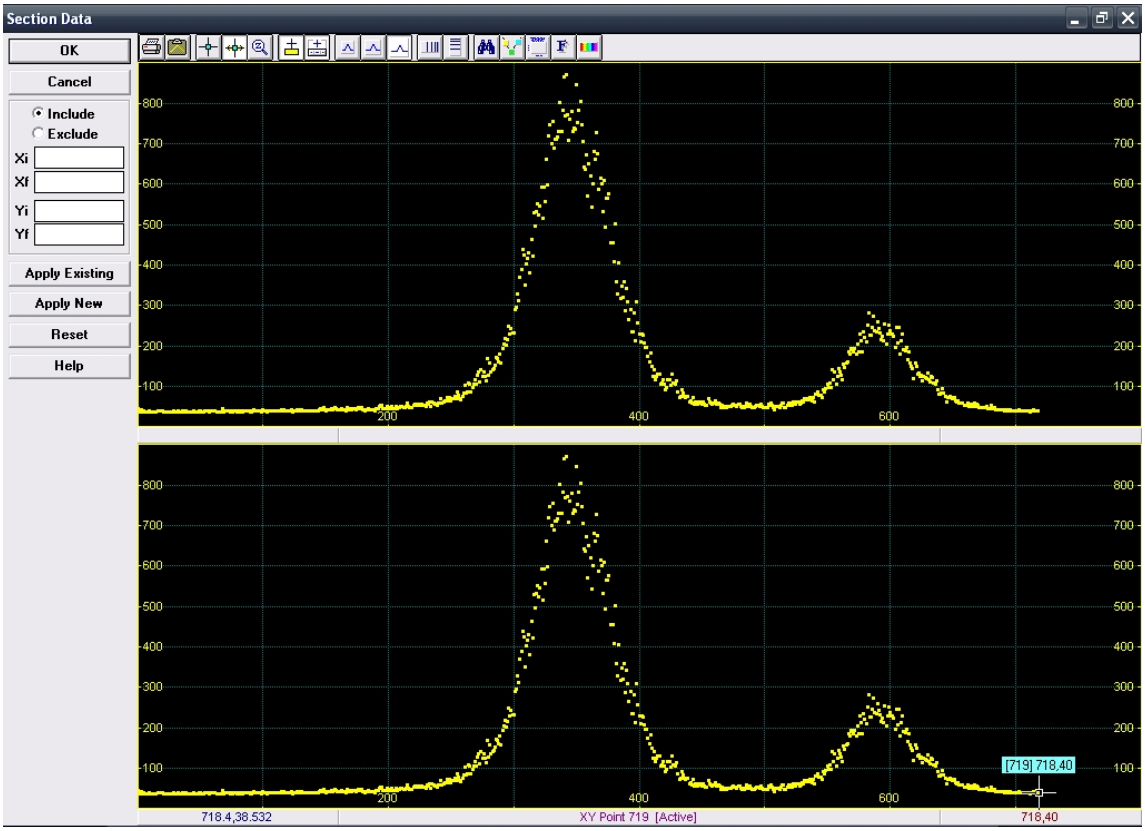

Figure C.12: Screen capture of PeakFit showing graphical display of un-calibrated OH(v=0, $^2\Pi_{3/2}$) lines as data points. The first scan point is zero (0) and the last scan point is 718. Originally the first and last points were 1 and 719. [File: FC.12_pf11]

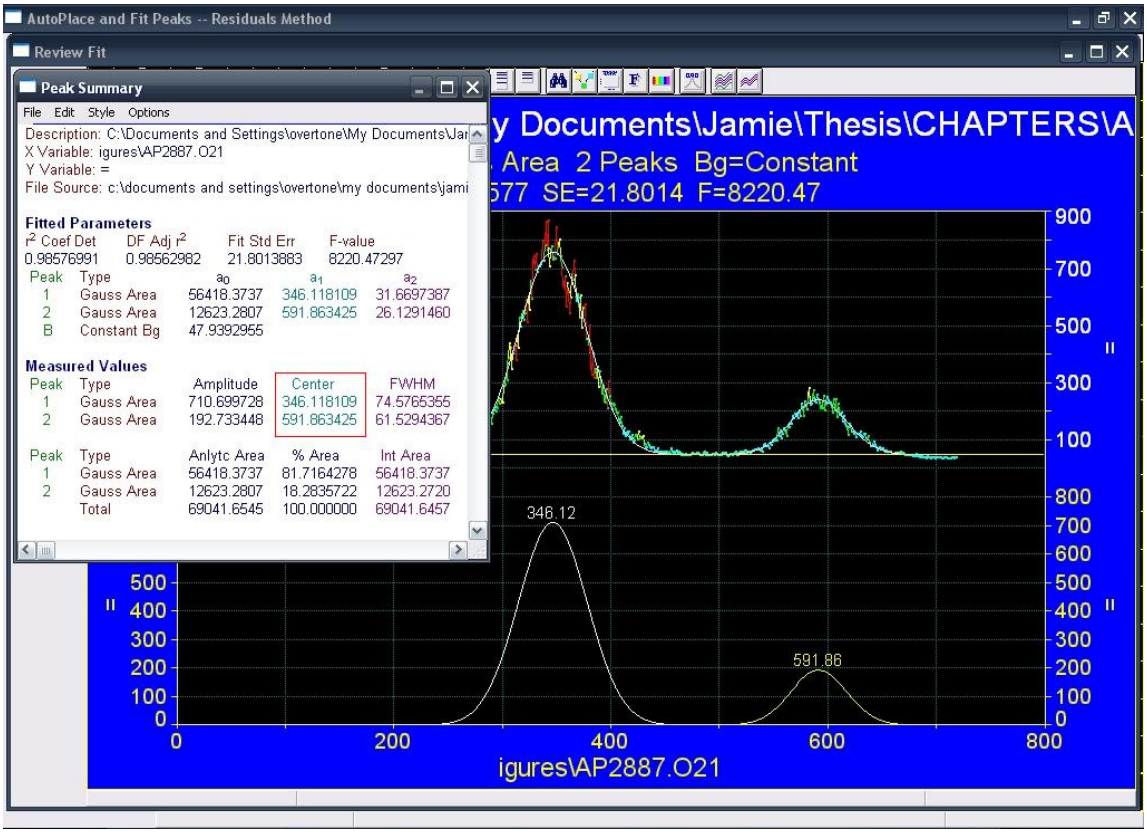

Figure C.13: Screen capture of PeakFit showing the points separation between the centers of each of the OH lines. [File: FC.13_pf12]

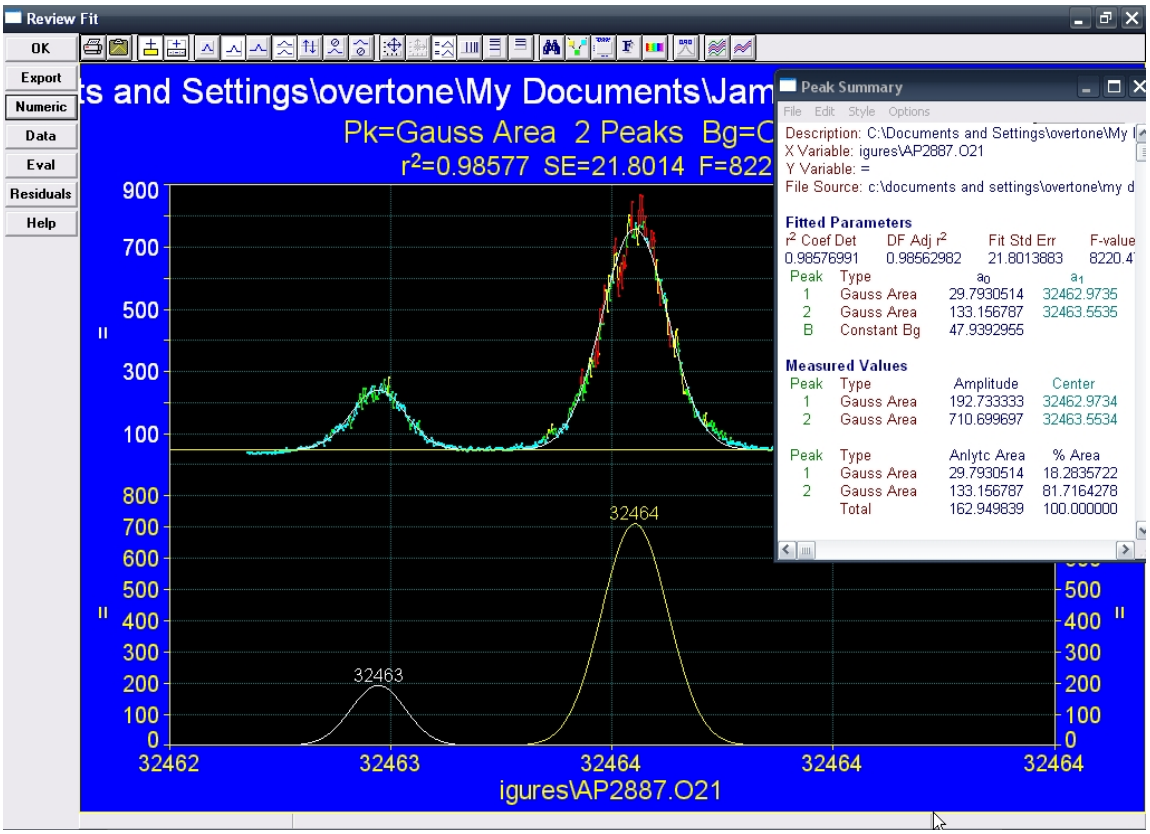

Figure C.14: Screen capture of PeakFit showing the frequency separation between the two OH lines. Even though the band centers do not match absolute line positions, their post calibration relative separation is 0.58 cm^{-1}
[File: FC.14_pf13]

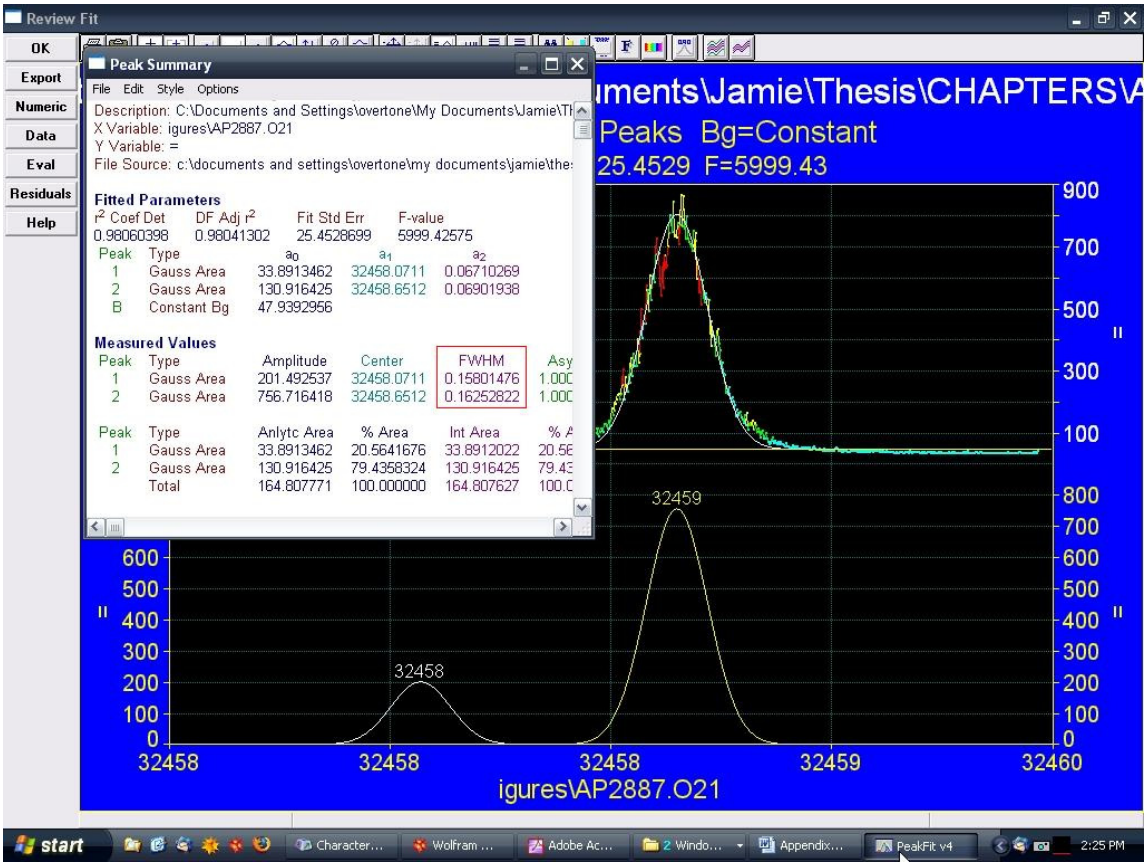

Figure C.15: Screen capture of PeakFit showing now the fully calibrated spectra. At this point, the linewidths (FWHM) can be extracted from the fitting routine and the file can be saved for additional analysis. [File: FC.15_pf14]

C.6 References

1. F. F. Crim, Annu. Rev. Phys. Chem. **44**, 397 (1993).

2. G. Hertzberg, *Molecular Spectra and Molecular Structure Vol. I.* (Von Nostrand Reinhold Co., New York, 1950).

3. G. H. Dieke and H. M. Crosswhite, J. Quant. Spectrosc. Radiat. Transfer **2**, 97 (1962).

4. P. F. Bernath, *Spectra of Atoms and Molecules* (Oxford University Press, New York, 1995).

5. R. J. Barnes, *The State-Resolved Photochemistry of Small Molecules on Their Ground and Electronic Excited States* (University of California-San Diego, 1999).

6. W. L. Dimpfl and J. L Kinsey, J. Quant. Spectrosc. Radiat. Transfer **21**, 233 (1979).

7. T. M. Ticich, *Overtone Vibration Initiated Predissociation and Vibrationally Mediated Photodissociation of Hydrogen Peroxide in Room Temperature Samples and in A Free-Jet Expansion* (University of Wisconsin-Madison, 1988).

Appendix D

Mathematica Codes Used with Data Analysis

D.1 Introduction

In order to assist with the interpretation of the data collected in the lab, several codes have been developed using Mathematica. The codes which are provided in this appendix are also available as mathematica .nb files in Appendix *D* directory in the folder labeled the “codes”. It is important to note that these codes where written and used with version 5 of Mathematica and may not work with older or newer version of the program. Expressions appearing in “double quotation marks” are commented and do not get evaluated by Mathematica. The codes are used to evaluate mathematical expressions such as ro-vibrational internal energies, densities of states, transition moments, basis sets limit extrapolations and RRKM calculations.

D.2 Evaluating the Average Rotational-Vibrational internal energy of PNA

Mathematica Program VibrotPNA.nb:

This code evaluates the average vibrational and rotational internal energies of PNA at thermal equilibrium. n- number of modes, k- Boltzmann constant in cm^{-1} Θ- is the vibrational temperature, υ- are the normal modes of PNA and T- is the temperature. The rotational and vibrational parameters are taken from Chapter 3.

```
n = 6;
k = 0.6950387;
Θj = υj / k ;
υ12 = 145;
υ11 = 300;
υ10 = 340;
υ9 = 483;
υ8 = 654;
υ7 = 722;
υ6 = 803;
υ5 = 945;
υ4 = 1304;
υ3 = 1397;
υ2 = 1728;
υ1 = 3540;

Θ1 = υ1 / k;
Θ2 = υ2 / k;
Θ3 = υ3 / k;
Θ4 = υ4 / k;
Θ5 = υ5 / k;
Θ6 = υ6 / k;
Θ7 = υ7 / k;
Θ8 = υ8 / k;
Θ9 = υ9 / k;
Θ10 = υ10 / k;
Θ11 = υ11 / k;
Θ12 = υ12 / k;


T = 298;
```

```
Print["At Temperature= ",
 T "K, the Vibrational Energy is (neglecting zeroth pt. energy):"]
```

$$E_{vib} = k * \sum_{j=1}^{3*n-6} \left(\frac{\theta_j * \text{Exp}\left[-\frac{\theta_j}{T}\right]}{1 - \text{Exp}\left[-\frac{\theta_j}{T}\right]} \right);$$

```
Print[E_vib, " cm^-1"]
```

This portion of the code evaluates the average rotational internal energy of PNA at thermal equilibrium a, b and c- are the rotational constants, β- PNA is estimated as prolate top (κ = -0.704).

```
k = 0.6950387;
T = 298;
a = 0.400093;
b = 0.155611;
c = 0.113170;
```

$$\beta = \frac{b + c}{2};$$

$$n = \text{Sum}\left[(2J+1) * e^{-\frac{\beta*J*(J+1) + (a-\beta)*Ka^2}{k*T}} * \left(\beta * J * (J+1) + (a-\beta) * Ka^2\right), \{J, 0, 500\}, \{Ka, -J, J\}\right];$$

$$d = \text{Sum}\left[(2J+1) * e^{-\frac{\beta*J*(J+1) + (a-\beta)*Ka^2}{k*T}}, \{J, 0, 500\}, \{Ka, -J, J\}\right];$$

```
Print["At Temperature= ", T "K, the ave. rotational Energy is= ",
 n/d, " cm^-1"]
Print["At Temperature= ", T "K, the ave. rot-vib Energy is= ",
 n/d + E_vib, " cm^-1" ]
```

D.3 Evaluating the Densities of States in PNA using Whitten-Rabinovitch Approximation

The formulation for the Whitten-Rabinovitch approximation is given in: K. A. Holbrook, M. J. Pilling, and S. H. Robertson, *Unimolecular Reactions* (John Wiley & Son, New York, 1996). The vibrational parameters used are from Chapter 3.

Mathematica Program WhittRabDosPNA.nb:

```
" Here are the vibrational modes ";
υj = {υ1, υ2, υ3, υ4, υ5, υ6, υ7, υ8, υ9, υ10, υ11, υ12};
υ12 = 145 ;
υ11 = 300 ;
```

$\upsilon_{10} = 340$;
$\upsilon_9 = 483$;
$\upsilon_8 = 654$;
$\upsilon_7 = 722$;
$\upsilon_6 = 803$;
$\upsilon_5 = 945$;
$\upsilon_4 = 1304$;
$\upsilon_3 = 1397$;
$\upsilon_2 = 1728$;
$\upsilon_1 = 3540$;

"n - number of atoms, s - number of normal modes";
n = 6;
s = 3 * n - 6;

"Select oscillator energy";
$\varepsilon_v = 6950$;

"β - modified frequency dispersion parameter";

$$\beta = \frac{s-1}{s} * \left(\frac{\frac{\sum_{j=1}^{s} \upsilon_j^2}{s}}{\left(\frac{\sum_{j=1}^{s} \upsilon_j}{s} \right)^2} \right);$$

"ε_z - zeroth point energy, ε_p - reduced energy";

$$\varepsilon_z = \sum_{j=1}^{s} 0.5\, \upsilon_j;$$

$\varepsilon_p = \varepsilon_v / \varepsilon_z$

$\omega_i = \{\omega_1, \omega_2\}$;
$\omega_1 = \left(5.00 * \varepsilon_p + 2.73 * \varepsilon_p^{0.5} + 3.51\right)^{-1}$;
$\omega_2 = \text{Exp}\left[-2.4191 * \varepsilon_p^{0.25}\right]$;
$d\omega_1 = -\left(5.00 + 1.365 * \varepsilon_p^{-0.5}\right) * \omega_1^2$;
$d\omega_2 = -\left(0.60478 * \varepsilon_p^{-0.75}\right) * \omega_2$;

If[0.1 < ε_p < 1.0, {$\omega = \omega_1$, $d\omega = d\omega_1$},
 If[1.0 < ε_p < 8.0, {$\omega = \omega_2$, $d\omega = d\omega_2$}]]

```
" Evaluate the density - ρ, and the sum - W ";
  with the appropriate ω from above

a = 1 - β * ω;
ρ = (εv + a * εz)^(s-1) / (Factorial[s - 1] * ∏j=1^s υj) * (1 - β * dω);
W = (εv + a * εz)^s / (Factorial[s] * ∏j=1^s υj);
Print["ρ , the density of states is ", ρ, " per cm^-1"]
Print["W , the sum of states is ", W]
Print["for oscillator energy εv of ", εv, "cm^-1"]
```

D.4 3-Parameter Extrapolation of $E(n \rightarrow \infty)$: Basis Set Limit Evaluations

The formulation of the code used in obtaining the extrapolated energies of PNA, its fragments, and reference molecules used is taken from K. A. Peterson, D. E. Woon, T. H. Dunning, Jr. J. Chem. Phys. **100**, 7410 (1994)

Mathematica Program CBS_PNA.nb:

```
"3 parameters CSB limit for PNA. See Ref. JCP
   100, 7410 (1994)";
Clear[ℓ, b, c, ε]

"Here is the 3-parameter equation. yyy is the
   energy associated with -ℓ- the cardinal number
   in the cc-pVζZ basis sets with DZ( =2) , TZ
   ( =3) and QZ ( =4). ε is the estimated CSB
   limit as ℓ → ∞ and is the parameter of interest. ";

yyy = ε + b * Exp[-(ℓ - 1)] + c * Exp[-(ℓ - 1)^2];

"Enter the CCSD(T) energies as a function of basis
   set. DZ( =2) , TZ ( =3) and QZ ( =4), etc." ;
zzz = {{2, -355.1671966}, {3, -355.5241934},
   {4, -355.6355336}};

ss = ListPlot[zzz, PlotStyle -> PointSize[0.02],
  PlotLabel → "E(n) vs n" ]
```

```
ff = Plot[yyy /. mmm, {ℓ, 2, 4},
  PlotLabel → "Fit E(n) vs n"]
Show[ff, ss]
Print[
 "The results of the non-linear fit are found
   below (ε is the extrapolated value: "]
mmm = FindFit[zzz, yyy, {b, c, ε}, ℓ]
```

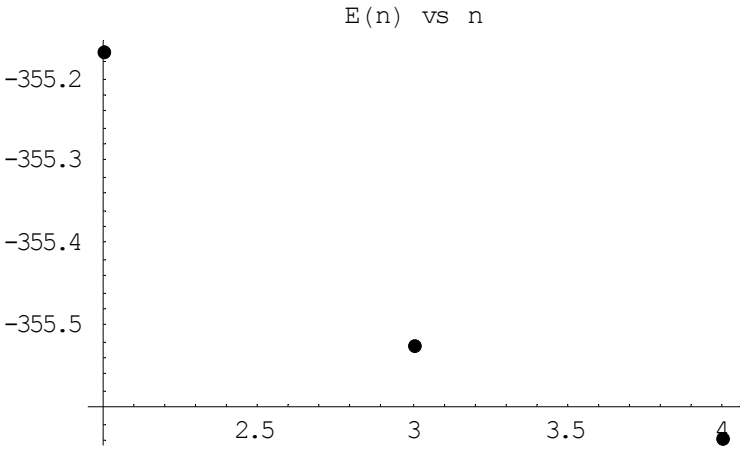

-Graphics-

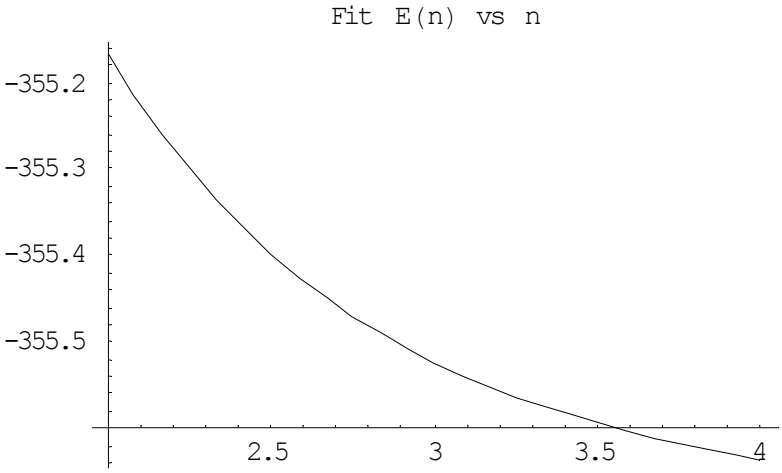

-Graphics-

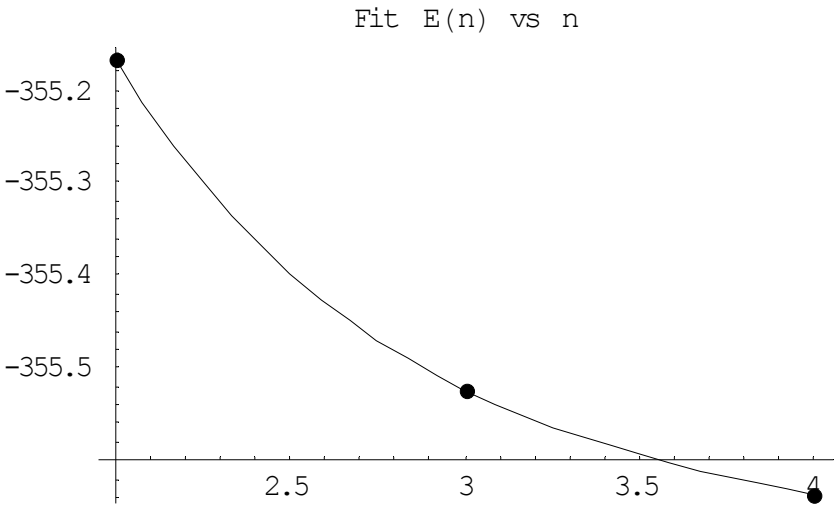

-Graphics-

The results of the non-linear fit are found below (ε is the extrapolated value of interest):

{b→1.26298,c→0.181075,ε→-355.698}

D.5 HO_2NO_2 O-H Stretching Polynomial Fit and Morse Parameters (ω_e, $\omega_e\chi_e$)

This code computes Morse parameters (ω_e, $\omega_e\chi_e$) for PNA by differentiation of a 7th order polynomial fit which was used in fitting the potential energy V(r) as a function of O-H stretching (r) generated using CCSD(T)/aug-cc-pVTZ level of theory. The code itself initially imports that data and fit the data points using a non-linear polynomial fit. The second and third derivatives of the polynomial are then used in obtaining the Morse parameters according to:

$$\omega_e\ (cm^{-1}) = (F_{ii}G_{ii})^{1/2}/2\pi c$$

$$\omega_e\chi_e\ (cm^{-1}) = (hG_{ii}/72\pi^2 c)\ (F_{iii}/F_{ii})^2$$

Where ω_e and $\omega_e\chi_e$ are the respective harmonic and anharmonic frequencies, h is Planck's constant, c is the speed of light, G_{ii} is the reciprocal of the reduced mass for the O-H, F_{ii} and F_{iii} are the respective second and third derivatives of the 7th order polynomial evaluated at $q = r\text{-}r_e$.

Mathematica Program pna_energy_atz.nb:

```
<<Statistics`NonlinearFit`
"here R is in meters and energy in joules";
```

Load the file pnaenadz.txt containing the potential data points and fit them using a 7th order polynomial:

```
Off[General::spelll]
Clear[x, epd, δ, r];
epd =
  Import["C:\Documents and Settings\overtone\My Documents\Jamie\
    Thesis\CHAPTERS\APPENDIXD\codes\pna\pnaenazt.txt", "Table"];
δ = Extract[epd[[5]], 1];

sss = ListPlot[epd, PlotStyle → PointSize[0.02]];
fitt = Fit[epd, {1, (x - δ), (x - δ)^2, (x - δ)^3, (x - δ)^4, (x - δ)^5,
   (x - δ)^6, (x - δ)^7}, x]
sds = Plot[fitt, {x, 0.4 * 10^-10, 1.5 * 10^-10}, PlotRange → {0, 1 * 10^-18}]
Show[sds, sss, Background → RGBColor[1, 1, 0]]
TableForm[epd];
```

The plots for the raw data and the fit and the polynomial are shown below:

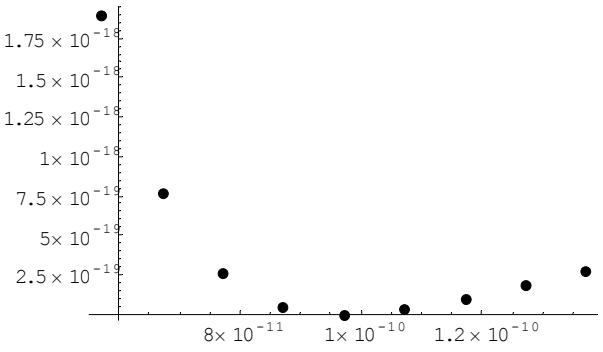

$$-7.78333\times10^{-23} - 1.09834\times10^{-12}\,(-9.70658\times10^{-11}+x) + 388.591\,(-9.70658\times10^{-11}+x)^2 - 9.10336\times10^{12}\,(-9.70658\times10^{-11}+x)^3 + 1.32447\times10^{23}\,(-9.70658\times10^{-11}+x)^4 - 1.76808\times10^{33}\,(-9.70658\times10^{-11}+x)^5 + 3.05464\times10^{43}\,(-9.70658\times10^{-11}+x)^6 - 3.25124\times10^{53}\,(-9.70658\times10^{-11}+x)^7$$

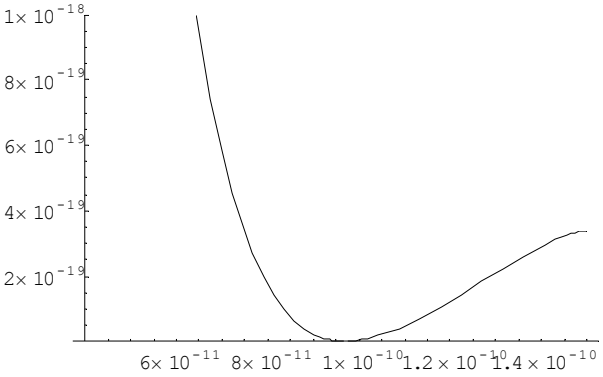

-Graphics-

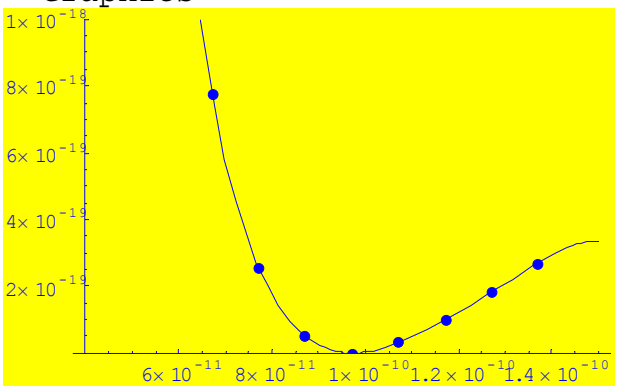

Differentiate and evaluate at q = r - r_e to obtain the harmonic and anharmonic frequencies:

In[150]:=
```
Clear[x]
D1x = N[D[fitt, {x, 1}], x = 6];
Clear[x]
D2x = N[D[fitt, {x, 2}], x = 6];
Clear[x]
D3x = N[D[fitt, {x, 3}], x = 6];
Clear[x]

rmass = 1.574306 * 10^-27;
Gmass = 1/rmass;
c = 2.99792458 * 10^10;
h = 6.626 * 10^-34;

ω = (D2x * Gmass)^(1/2) / (2 * π * c);

ωχ = (h * Gmass) / (72 * π^2 * c) * (D3x / D2x)^2;

Print["ω= ", ω, " cm^-1"]

Print["ωχ= ", ωχ, " cm^-1"]

Print["The vibrational freq. at V=0 is = ", ω - 2 * ωχ, " cm^-1"]
```

ω= 3730.06 cm^{-1}

ωχ= 97.5821 cm^{-1}

The vibrational freq. at V=0 is = 3534.9 cm^{-1}

D.6 PNA Vibrational Transition Strengths

This code is used to compute the vibrational transition dipole moments and cross-sections of PNA using the generalized Laguerre polynomials as basis functions for the Morse oscillator and 7th order Taylor expansion in the dipole moments functions.

Mathematica Program pnadipole.nb:

Load the X, Y and Z dipole moment points (in Debye units) vs. separation r (in Å units).

```
Off[General::spell]
Off[General::spell1]
SetDirectory[
 "C:\Documents and Settings\overtone\My
   Documents\Jamie\Thesis\CHAPTERS\APPENDIXD\pna\codes"]
xfun = Import["pnaXdip.txt", "Table"]
yfun = Import["pnaYdip.txt", "Table"]
zfun = Import["pnaZdip.txt", "Table"]
```

```
C:\Documents and Settings\overtone\My
  Documents\Jamie\Thesis\CHAPTERS\APPENDIXD\codes
```

```
{{0.565689, 1.0812}, {0.665689, 1.2055}, {0.765689, 1.317},
 {0.865689, 1.4146}, {0.965689, 1.4954}, {1.06569, 1.5554},
 {1.16569, 1.5904}, {1.26569, 1.5969}, {1.36569, 1.573}}

{{0.565689, 0.2972}, {0.665689, 0.3525}, {0.765689, 0.4046},
 {0.865689, 0.4529}, {0.965689, 0.4959}, {1.06569, 0.5307},
 {1.16569, 0.5541}, {1.26569, 0.5635}, {1.36569, 0.5568}}

{{0.565689, 1.0867}, {0.665689, 1.1705}, {0.765689, 1.2565},
 {0.865689, 1.3423}, {0.965689, 1.4225}, {1.06569, 1.4893},
 {1.16569, 1.5343}, {1.26569, 1.5502}, {1.36569, 1.5324}}
```

```
xf = ListPlot[xfun, PlotStyle → PointSize[0.02]];
yf = ListPlot[yfun, PlotStyle → PointSize[0.02]];
zf = ListPlot[zfun, PlotStyle → PointSize[0.02]];
Show[xf, yf, zf];
```

Plot the dipole moment data points:

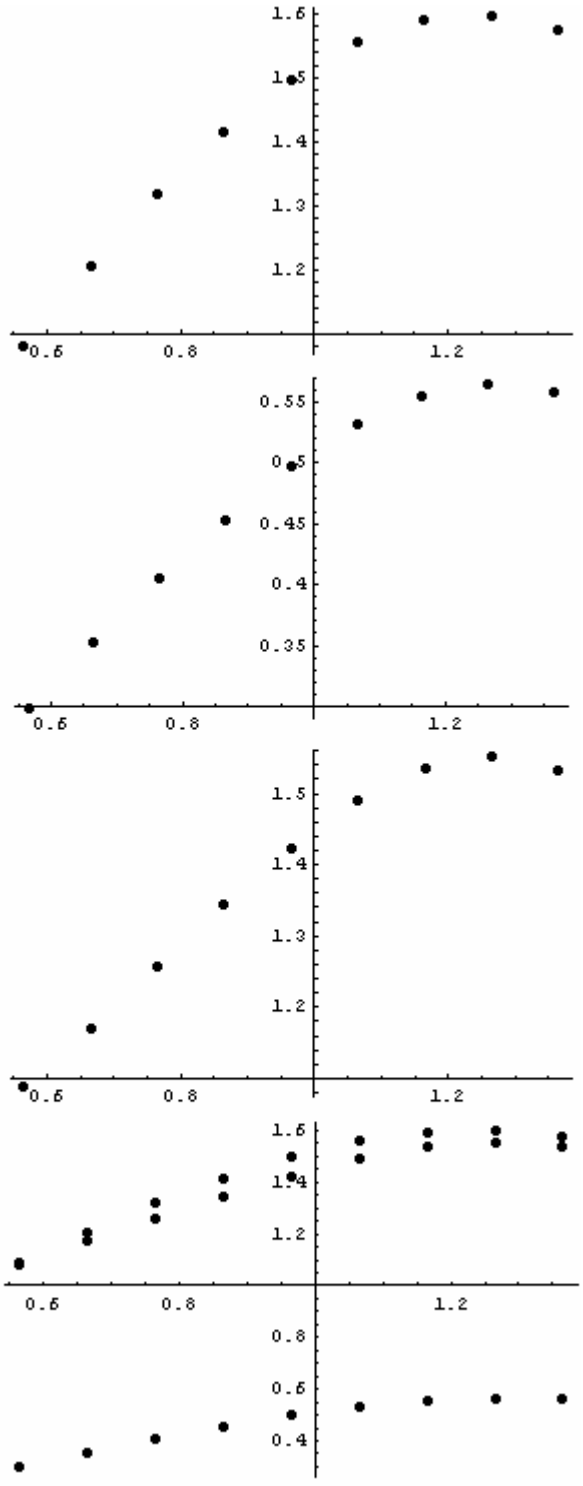
1.6
1.5
1.4
1.3
1.2
0.6
0.8
1.2
0.55
0.5
0.45
0.4
0.35
0.6
0.8
1.2
1.5
1.4
1.3
1.2
0.6
0.8
1.2
1.6
1.4
1.2
0.6
0.8
1.2
0.8
0.6
0.4

- Graphics -

Fit the data to a 7^{th} order polynomial:

```
δ = Extract[xfun[[5]], 1]
fitx = Fit[xfun, {1, x - δ, (x - δ)^2, (x - δ)^3, (x - δ)^4, (x - δ)^5, (x - δ)^6,
   (x - δ)^7}, x]

fity = Fit[yfun, {1, y - δ, (y - δ)^2, (y - δ)^3, (y - δ)^4, (y - δ)^5, (y - δ)^6,
   (y - δ)^7}, y]

fitz = Fit[zfun, {1, z - δ, (z - δ)^2, (z - δ)^3, (z - δ)^4, (z - δ)^5, (z - δ)^6,
   (z - δ)^7}, z]

plotx = Plot[fitx, {x, 0.5, 1.4}]
Show[plotx, xf]
ploty = Plot[fity, {y, 0.5, 1.4}]
Show[ploty, yf]
plotz = Plot[fitz, {z, 0.5, 1.4}]
Show[plotz, zf]
```

```
0.965689
```

$$1.4954 + 0.71114\,(-0.965689 + x) - 1.03888\,(-0.965689 + x)^2 - 0.721806\,(-0.965689 + x)^3 - 0.0930199\,(-0.965689 + x)^4 + 0.777778\,(-0.965689 + x)^5 + 0.0740741\,(-0.965689 + x)^6 - 0.198413\,(-0.965689 + x)^7$$

$$0.495895 + 0.39451\,(-0.965689 + y) - 0.407435\,(-0.965689 + y)^2 - 0.562639\,(-0.965689 + y)^3 - 0.159544\,(-0.965689 + y)^4 + 1.19444\,(-0.965689 + y)^5 + 0.0925926\,(-0.965689 + y)^6 - 2.57937\,(-0.965689 + y)^7$$

$$1.42249 + 0.74913\,(-0.965689 + z) - 0.665701\,(-0.965689 + z)^2 - 1.42924\,(-0.965689 + z)^3 - 0.306019\,(-0.965689 + z)^4 + 1.63889\,(-0.965689 + z)^5 + 0.342593\,(-0.965689 + z)^6 - 1.28968\,(-0.965689 + z)^7$$

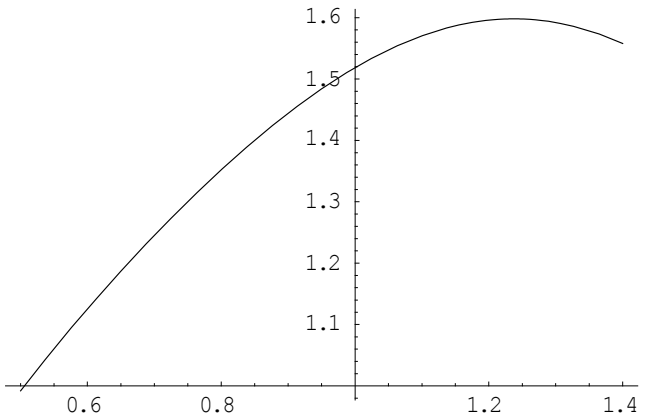

- Graphics -

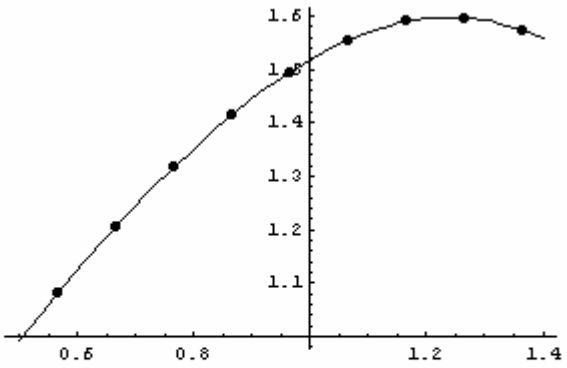

- Graphics -

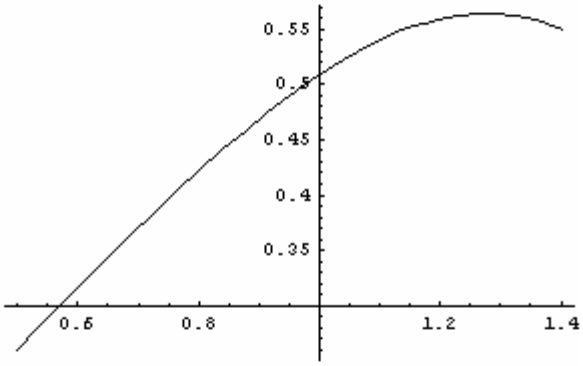

- Graphics -

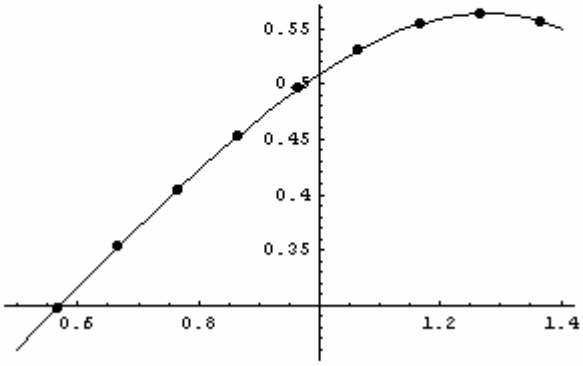

- Graphics -

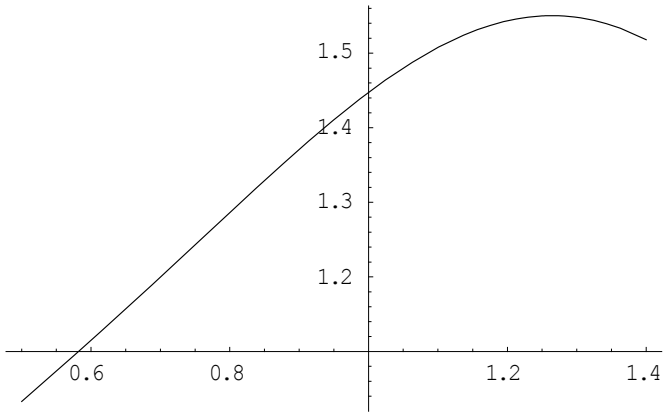

- Graphics -

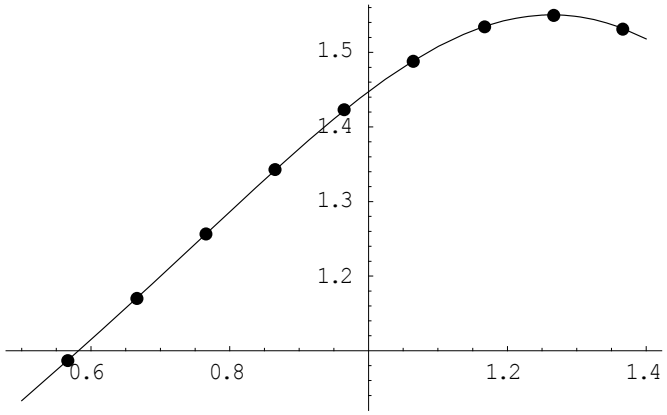

- Graphics -

Now obtain the first 7 derivatives for each of the X, Y and Z polynomials:

```
Clear[x, y, z]
D1x = N[D[fitx, {x, 1}], x = 6];
D1y = N[D[fity, {y, 1}], y = 6];
D1z = N[D[fitz, {z, 1}], z = 6];
Clear[x, y, z]
D2x = N[D[fitx, {x, 2}], x = 6];
D2y = N[D[fity, {y, 2}], y = 6];
D2z = N[D[fitz, {z, 2}], z = 6];
Clear[x, y, z]
D3x = N[D[fitx, {x, 3}], x = 6];
D3y = N[D[fity, {y, 3}], y = 6];
D3z = N[D[fitz, {z, 3}], z = 6];
Clear[x, y, z]
D4x = N[D[fitx, {x, 4}], x = 6];
D4y = N[D[fity, {y, 4}], y = 6];
D4z = N[D[fitz, {z, 4}], z = 6];
```

```
Clear[x, y, z]
D5x = N[D[fitx, {x, 5}], x = 6];
D5y = N[D[fity, {y, 5}], y = 6];
D5z = N[D[fitz, {z, 5}], z = 6];
Clear[x, y, z]
D6x = N[D[fitx, {x, 6}], x = 6];
D6y = N[D[fity, {y, 6}], y = 6];
D6z = N[D[fitz, {z, 6}], z = 6];
Clear[x, y, z]
D7x = N[D[fitx, {x, 7}], x = 6];
D7y = N[D[fity, {y, 7}], y = 6];
D7z = N[D[fitz, {z, 7}], z = 6];
Clear[x, y, z]
Clear[q]
Print["D1x=", D1x];
Print["D1y=", D1y];
Print["D1z=", D1z];
Print["D2x=", D2x];
Print["D2y=", D2y];
Print["D2z=", D2z];
Print["D3x=", D3x];
Print["D3y=", D3y];
Print["D3z=", D3z];
Print["D4x=", D4x];
Print["D4y=", D4y];
Print["D4z=", D4z];
Print["D5x=", D5x];
Print["D5y=", D5y];
Print["D5z=", D5z];
Print["D6x=", D6x];
Print["D6y=", D6y];
Print["D6z=", D6z];
Print["D7x=", D7x];
Print["D7y=", D7y];
Print["D7z=", D7z];
```

Express these derivatives using a 7^{th} order Taylor expansion. Where $q = r - r_e$.

```
mux = (q) * D1x + (q) ^ 2 * D2x / 2 + (q) ^ 3 * D3x / 6 + (q) ^ 4 * D4x / 4 ! + (q) ^ 5 * D5x / 5 ! +
   (q) ^ 6 * D6x / 6 ! + q^ 7 * D7x / 7 !
```

```
muy = (q) * D1y + (q) ^2 * D2y / 2 + (q) ^3 * D3y / 6 + (q) ^4 * D4y / 4 ! + (q) ^5 * D5y / 5 ! +
   (q) ^6 * D6y / 6 ! + q^7 * D7y / 7 !

muz = (q) * D1z + (q) ^2 * D2z / 2 + (q) ^3 * D3z / 6 + (q) ^4 * D4z / 4 ! + (q) ^5 * D5z / 5 ! +
   (q) ^6 * D6z / 6 ! + q^7 * D7z / 7 !
```

Lastly, using equations 3.8 – 3.20 evaluate the vibrational transition dipole moments using transition frequencies, dipole moments Taylor expansion and Morse oscillator wave functions. “m” and “n” are the respective initial and final vibrational states, with m = 0 being the ground state.

```
δ = Extract[xfun[[5]], 1];
q = r - δ;
rmass = 1.574306 * 10^-27 / 1.6605402 * 10^-27;
ω = 3714;
ωχ = 85;
κ = ω / ωχ;


a = 0.243559 * (rmass * ωχ)^0.5;
ξ = κ * Exp[-a * (r - δ)];

n = 1;
m = 0;
b1 = κ - 2 n - 1;
b2 = κ - 2 m - 1;
nu1 = n * ω - ωχ * n (n + 1);
nu2 = m * ω - ωχ * m (m + 1);
nu = Abs[nu1 - nu2];
Print["ν= ", nu, " for v=", m, "⟶", n];
η1 = Sqrt[a * b1 * Factorial[n] / Gamma[κ - n]];
η2 = Sqrt[a * b2 * Factorial[m] / Gamma[κ - m]];

Ψ[n] = η1 * Exp[-ξ / 2.0] * ξ^(b1/2) * LaguerreL[n, b1, ξ];
Ψ[m] = η2 * Exp[-ξ / 2.0] * ξ^(b2/2) * LaguerreL[m, b2, ξ];

Ψ[n];
Ψ[m];
```

```
Øx = NIntegrate[Ψ[n] * mux * Ψ[m], {r, 0, ∞}];
Øy = NIntegrate[Ψ[n] * muy * Ψ[m], {r, 0, ∞}];
Øz = NIntegrate[Ψ[n] * muz * Ψ[m], {r, 0, ∞}];
μ = Øx^2 + Øy^2 + Øz^2;
ℓ = 4.70165 * 10^-7 * nu * μ;
Print["∑(<Ψe|μ|Ψg>)^2= ", μ, " and ", "Oscillator strengths= ", ℓ,
 " for v=", m, "⟶", n]
Print["or, in km/mol units=", 16.1941 * μ * nu * 0.393427217^2, "km/mol"]
Print["Also, ∫σ(ν)dν=", ℓ / (1.1296 * 10^12), "cm/molec"]
norma = Integrate[Ψ[n] * Ψ[m], {r, 0, ∞}];
Print["∫_0^∞ Ψ[n]*Ψ[m]dr= ", norma]
ss = 6;
Plot[Evaluate[Ψ[n]], {r, 0, 2}, PlotRange → {-ss, ss}, AxesOrigin → {0.5, 0},
  PlotLabel → "Ψ[n]"];
Plot[Evaluate[Ψ[n]^2], {r, 0, 2}, PlotRange → {0, ss}, AxesOrigin → {0.5, 0},
  PlotLabel → "Ψ[n]^2"];
Plot[Evaluate[Ψ[m]], {r, 0, 2}, PlotRange → {-ss, ss}, AxesOrigin → {0.5, 0},
  PlotLabel → "Ψ[m]"];
Plot[Evaluate[Ψ[m]^2], {r, 0, 2}, PlotRange → {0, ss}, AxesOrigin → {0.5, 0},
  PlotLabel → "Ψ[m]^2"];
Plot[Evaluate[Ψ[m] * Ψ[n]], {r, 0, 2}, PlotRange → {-ss, ss}, AxesOrigin → {0.5, 0},
  PlotLabel → "Ψ[m]Ψ[n]"];
Plot[Evaluate[Ψ[m] * mux * Ψ[n]], {r, 0, 2}, PlotRange → {-ss, ss},
  AxesOrigin → {0.5, 0}, PlotLabel → "Ψ[m]muxΨ[n]"];
Plot[Evaluate[Ψ[m] * muy * Ψ[n]], {r, 0, 2}, PlotRange → {-ss, ss},
  AxesOrigin → {0.5, 0}, PlotLabel → "Ψ[m]muyΨ[n]"];
Plot[Evaluate[Ψ[m] * muz * Ψ[n]], {r, 0, 2}, PlotRange → {-ss, ss},
  AxesOrigin → {0.5, 0}, PlotLabel → "Ψ[m]muzΨ[n]"];
Clear[n, m, nu, nu1, nu2, η1, η2, ℓ];
```

```
ν= 3344 for v=0⟶1
∑(<Ψe|μ|Ψg>)^2= 0.00522101 and
 Oscillator strengths= 8.20865×10^-6 for v=0⟶1
or, in km/mol units=43.763km/mol
Also, ∫σ(ν)dν=7.26686×10^-18cm/molec
∫_0^∞ Ψ[n]*Ψ[m]dr= -3.10862×10^-14
```

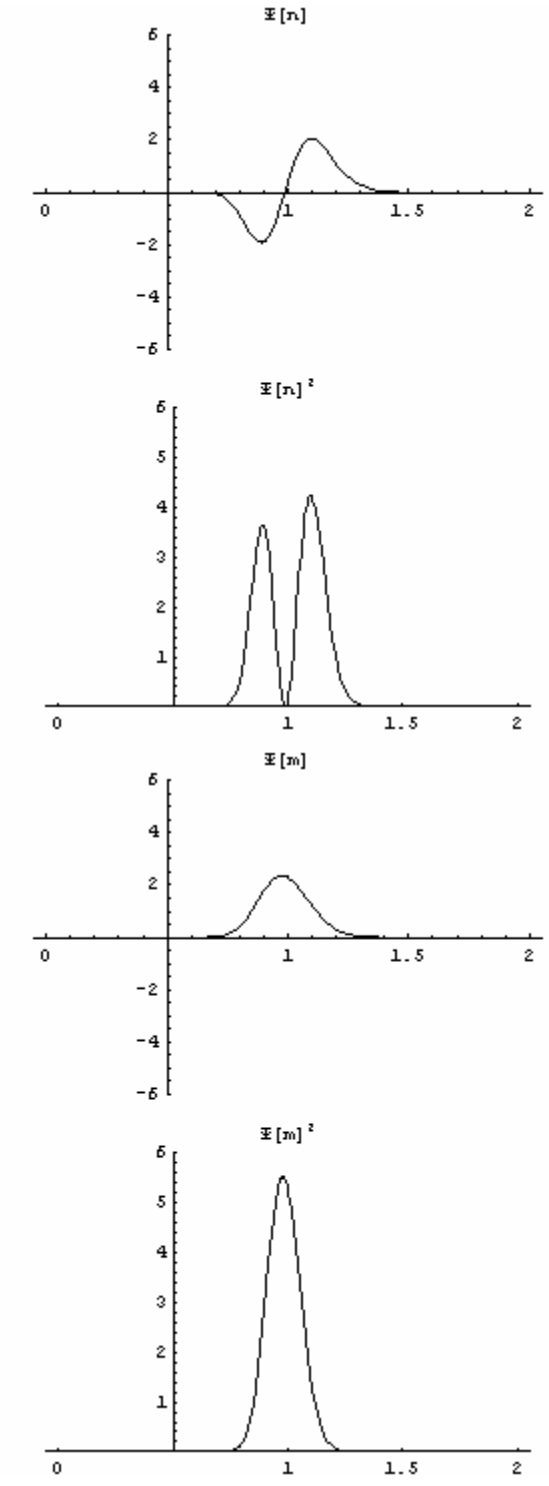
Ψ[n]
6
4
2
0
1
1.5
2
-2
-4
-6
Ψ[n]²
6
5
4
3
2
1
0
1
1.5
2
Ψ[m]
6
4
2
0
1
1.5
2
-2
-4
-6
Ψ[m]²
6
5
4
3
2
1
0
1
1.5
2

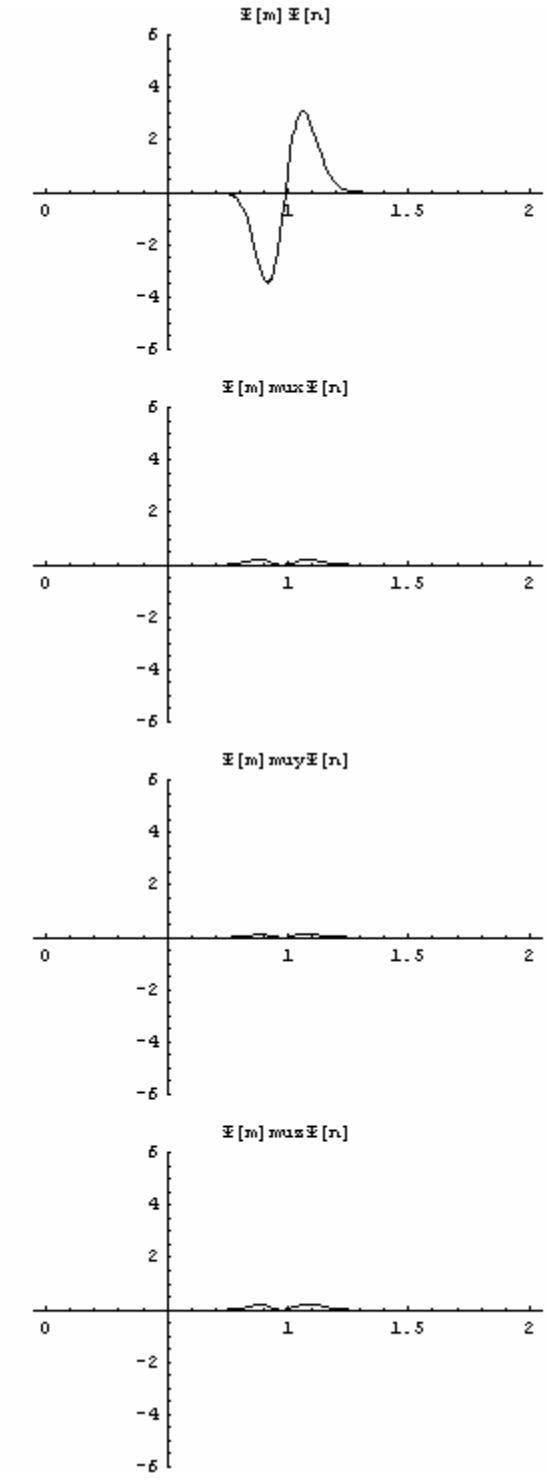
E[m] E[n]
6
4
2
0
1
1.5
2
-2
-4
-6
E[m] maxE[n]
6
4
2
0
1
1.5
2
-2
-4
-6
E[m] maxE[n]
6
4
2
0
1
1.5
2
-2
-4
-6
E[m] maxE[n]
6
4
2
0
1
1.5
2
-2
-4
-6

D.7 Internal Energy of *cis-cis* HOONO

This code is used to compute room temperature average internal energy (ro-vibrational) of cis-cis HOONO. The code initially evaluates the Boltzmann weighted of a particular ro-vibrational states within energy range and assign it to a bin. The normalized distribution of states is then used to evaluate the average energy according to the expression: $\langle E_{ro\text{-}vib} \rangle = \Sigma P_i \times \varepsilon_i$

Mathematica Program cchoonoie.nb:

General parameters and definitions: T is the temperature, kb is Boltzmann constant, blz is the Boltzmann factor. HOONO has 9 modes.

```
Off[General::spelll]
Off[General::spell]
Off[General::nffil]
Off[InterpolatingFunction::dmval]
modes = 9;
T = 298.15;
kb = 0.6950387;
blz = (2 J + 1) Exp[- εi / (kb * T)];
probi = blz;
β = 0.2291427845;
α = 0.714040412;
ω0 = 0;
ω1 = 3460;
ω2 = 1568;
ω3 = 1451;
ω4 = 971;
ω5 = 836;
ω6 = 726;
ω7 = 419;
ω8 = 523;
ω9 = 383;
grain = 10;
Do[εi = ai * ωi + β * J (J + 1) + K^2 (α - β), {i, 0, modes}]

SetDirectory[
  "C:\Documents and Settings\overtone\My
    Documents\Jamie\Thesis\CHAPTERS\APPENDIXD\codes\cchoonoie"];
```

Set the directory where the bins will be generated. In this case, we choose an energy grain of 1 cm^{-1}, so for n = 2000 cm^{-1} maximum energy state, there will be 2000 energy bins:

```
n = 2000;
DeleteFile["lst.txt"]
Do[{DeleteFile[ToString[InputForm[a]]]}, {a, grain, n, grain}]
Do[{PutAppend[0, ToString[InputForm[a]]]}, {a, grain, n, grain}]
Do[abc_i = ToExpression["If[(q-grain)≤(ε_i)<q, PutAppend[blz,xxx]]"],
  {i, 0, modes}];
Do[pqr_i = Table[abc_i /. xxx → ToString[InputForm[q]],
    {q, grain, n, grain}], {i, 0, modes}];

Do[
 {pqr_i, {J, K, ε_i} >> lst.txt}, {i, 0, 0}, {J, 0, 100}, {K, -J, J}]
Do[
 {pqr_i, {a_i, i, J, K, ε_i} >> lst.txt}, {i, 1, modes},
 {a_i, 1, Round[n / ω_i]}, {J, 0, 100}, {K, -J, J}]


Print["done", "  ", TimeUsed[], "s"]
```

The cells above generate the bins and/or delete old bins before evaluating the loops considering up to 2000 cm^{-1} energy state, J_{max} within each vibration is set to 100 and K allowed to run from –J → +J. According to the expression $\varepsilon_i = a_i\,\omega_i + B\,J(J+1) + K^2(A - B)$, each particular energy state is assigned a bin according to the grain size.

```
done  5126.92s
```

Add, normalize the bins and plot the result:

```
DeleteFile[{"dos.txt"}]; DeleteFile[{"en.txt"}];
Do[d >>> en.txt, {d, grain, n, grain}]
Do[
 {ReadList[ToString[InputForm[a]]]^0.5 .
    ReadList[ToString[InputForm[a]]]^0.5 >>> dos.txt},
 {a, grain, n, grain}]
pros = ReadList["dos.txt"]^0.5 .ReadList["dos.txt"]^0.5;
```

Sum the product of the probability and the energy of a particular bin ranging from $\varepsilon_I = 0$ → 2000 cm^{-1} to obtain the average energy:

```
n = 2000;
zzz = {ReadList["en.txt"], ReadList["dos.txt"]/pros};
yyy = Transpose[zzz];
bbb = ListPlot[yyy, PlotRange → {{0, n + 100}, {0, 0.03}},
  PlotJoined → False, PlotStyle → PointSize[0.02]]
```

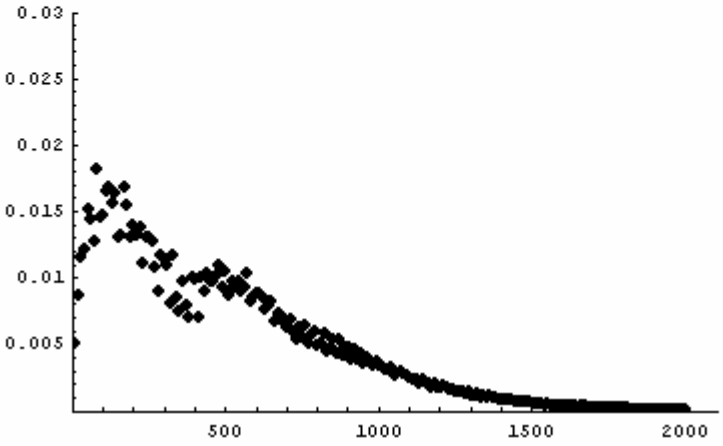


```
- Graphics -
```

```
sss = Interpolation[yyy, InterpolationOrder → 3];
mmm = Plot[sss[x], {x, 0, n}, PlotRange → {{0, n}, {0, 0.03}}]
Show[bbb, mmm]
```

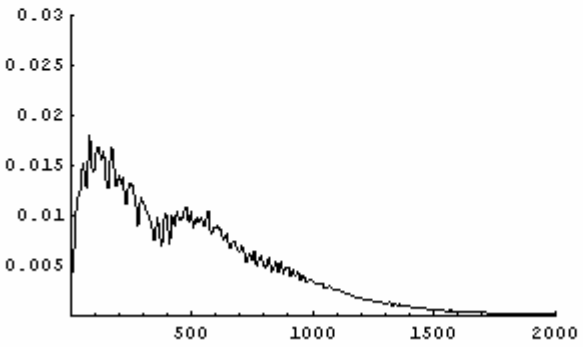


```
- Graphics -
```

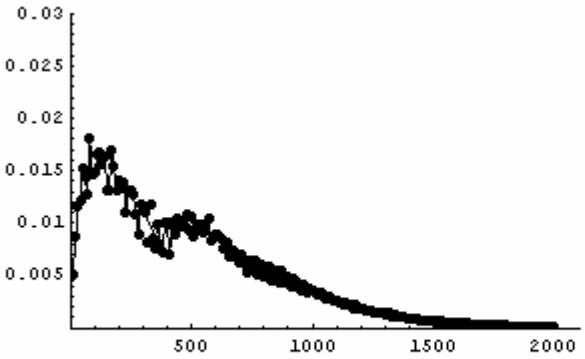


```
- Graphics -
```

```
inte = Sum[yyy[[i, 1]] * yyy[[i, 2]], {i, 1, n / grain}] /
  Sum[yyy[[i, 2]], {i, 1, n / grain}]
jave = Solve[{inte / β == J^2 + J}, J];
Print["The Average ro-vibrational energy of cis cis HOONO= ",
 inte, " cm^-1"]
Print["Ave. J associated with this energy level is: ", jave]
```

```
485.212
```

```
The Average ro-vibrational energy of cis cis HOONO= 485.212 cm^-1
Ave. J associated with this energy level is:
 {{J → -46.5191}, {J → 45.5191}}
```

D.8 Two-Dimension OH-Stretch / HOON-Torsion Oscillator Strength Evaluation for *cis-cis* HOONO Using CCSD(T)/cc-pVTZ Dipole Moment Surface

This code is used to compute the oscillator strength of the transitions associated with *cis-cis* HOONO. The two-dimensional potential and dipole moment surfaces take into account the influence of the HOON-torsion on the OH-stretching mode. The model was constructed using the CCSD(T)/cc-pVTZ level of theory. The Mathematica program HOONO_osc_str.nb was designed to evaluate the transition strength for the transition $|V_{OH}, V_\tau>' \leftarrow |V_{OH}, V_\tau>$". It features numerical integration of equation 4.17 and thus, requires that appropriate wavefunctions, transition frequencies and dipole moments surfaces which are located in the "evhoono" directory.

Mathematica Program hoono_osc_str.nb:

```
Off[General::spelll]
Off[General::spell]
Off[NIntegrate::slwcon]
Off[NIntegrate::ploss]
Off[NIntegrate::ncvb]
Off[NIntegrate::tmap]
"first ind. always describes the electronic surface";
```

```
SetDirectory[
 "C:\Documents and Settings\overtone\My
   Documents\Jamie\Thesis\CHAPTERS\APPENDIXD\codes\evhoono"]
"Dipole Functions Imports";
dipZ = Import["Zsurface_ccsdt.txt", "Table"];
dipY = Import["Ysurface_ccsdt.txt", "Table"];
dipX = Import["Xsurface_ccsdt.txt", "Table"];

"wavefuctions for Tau v=0-5 at ground state imports";

v00 = Import["efzerozero.txt", "Table"];
v01 = Import["efzeroone.txt", "Table"];
v02 = Import["efzerotwo.txt", "Table"];
v03 = Import["efzerothree.txt", "Table"];
v04 = Import["efzerofour.txt", "Table"];
v05 = Import["efzerofive.txt", "Table"];
v06 = Import["efzerosix.txt", "Table"];
v07 = Import["efzeroseven.txt", "Table"];
v08 = Import["efzeroeight.txt", "Table"];
v09 = Import["efzeronine.txt", "Table"];
v010 = Import["efzeroten.txt", "Table"];

"wavefuctions for OH at ground state (V=0) imports";

n00 = Import["evzerozero.txt", "Table"];
n01 = Import["evzeroone.txt", "Table"];
n02 = Import["evzerotwo.txt", "Table"];
n03 = Import["evzerothree.txt", "Table"];
n04 = Import["evzerofour.txt", "Table"];
n05 = Import["evzerofive.txt", "Table"];
n06 = Import["evzerosix.txt", "Table"];
n07 = Import["evzeroseven.txt", "Table"];
n08 = Import["evzeroeight.txt", "Table"];
n09 = Import["evzeronine.txt", "Table"];
n010 = Import["evzeroten.txt", "Table"];
```

```
"wavefuctions for Tau v=0-5 1st Excited state imports";

v10 = Import["efonezero.txt", "Table"];
v11 = Import["efoneone.txt", "Table"];
v12 = Import["efonetwo.txt", "Table"];
v13 = Import["efonethree.txt", "Table"];
v14 = Import["efonefour.txt", "Table"];
v15 = Import["efonefive.txt", "Table"];
v16 = Import["efonesix.txt", "Table"];
v17 = Import["efoneseven.txt", "Table"];
v18 = Import["efoneeight.txt", "Table"];
v19 = Import["efonenine.txt", "Table"];
v110 = Import["efoneten.txt", "Table"];

"wavefuctions for OH at 1st Excited state (V=1) imports";

n10 = Import["evonezero.txt", "Table"];
n11 = Import["evoneone.txt", "Table"];
n12 = Import["evonetwo.txt", "Table"];
n13 = Import["evonethree.txt", "Table"];
n14 = Import["evonefour.txt", "Table"];
n15 = Import["evonefive.txt", "Table"];
n16 = Import["evonesix.txt", "Table"];
n17 = Import["evoneseven.txt", "Table"];
n18 = Import["evoneeight.txt", "Table"];
n19 = Import["evonenine.txt", "Table"];
n110 = Import["evoneten.txt", "Table"];

"wavefuctions for Tau v=0-5 at 2nd Excited State imports";

v20 = Import["eftwozero.txt", "Table"];
v21 = Import["eftwoone.txt", "Table"];
v22 = Import["eftwotwo.txt", "Table"];
v23 = Import["eftwothree.txt", "Table"];
v24 = Import["eftwofour.txt", "Table"];
v25 = Import["eftwofive.txt", "Table"];
v26 = Import["eftwosix.txt", "Table"];
v27 = Import["eftwoseven.txt", "Table"];
v28 = Import["eftwoeight.txt", "Table"];
v29 = Import["eftwonine.txt", "Table"];
v210 = Import["eftwoten.txt", "Table"];
```

```
"wavefuctions for OH at 2nd Excited state (V=2) imports";

n20 = Import["evtwozero.txt", "Table"];
n21 = Import["evtwoone.txt", "Table"];
n22 = Import["evtwotwo.txt", "Table"];
n23 = Import["evtwothree.txt", "Table"];
n24 = Import["evtwofour.txt", "Table"];
n25 = Import["evtwofive.txt", "Table"];
n26 = Import["evtwosix.txt", "Table"];
n27 = Import["evtwoseven.txt", "Table"];
n28 = Import["evtwoeight.txt", "Table"];
n29 = Import["evtwonine.txt", "Table"];
n210 = Import["evtwoten.txt", "Table"];

"wavefuctions for Tau v=0-5 3rd Excited State imports";

v30 = Import["efthreezero.txt", "Table"];
v31 = Import["efthreeone.txt", "Table"];
v32 = Import["efthreetwo.txt", "Table"];
v33 = Import["efthreethree.txt", "Table"];
v34 = Import["efthreefour.txt", "Table"];
v35 = Import["efthreefive.txt", "Table"];
v36 = Import["efthreesix.txt", "Table"];
v37 = Import["efthreeseven.txt", "Table"];
v38 = Import["efthreeeight.txt", "Table"];
v39 = Import["efthreenine.txt", "Table"];
v310 = Import["efthreeten.txt", "Table"];

"wavefuctions for OH at 3rd Excited state (V=3) imports";

n30 = Import["evthreezero.txt", "Table"];
n31 = Import["evthreeone.txt", "Table"];
n32 = Import["evthreetwo.txt", "Table"];
n33 = Import["evthreethree.txt", "Table"];
n34 = Import["evthreefour.txt", "Table"];
n35 = Import["evthreefive.txt", "Table"];
n36 = Import["evthreesix.txt", "Table"];
n37 = Import["evthreeseven.txt", "Table"];
n38 = Import["evthreeeight.txt", "Table"];
n39 = Import["evthreenine.txt", "Table"];
n310 = Import["evthreeten.txt", "Table"];
```

```
"Load Transition Frequencies Matrix";
transfreq = Import["evfreq.txt", "Table"];
"Load quantum yield per JF";
qy = Import["quantumyield.txt", "Table"];

Print["import complete"]
```

```
 C:\Documents and Settings\overtone\My
   Documents\Jamie\Thesis\CHAPTERS\APPENDIXD\codes\evhoono

import complete
```

```
"Plots for quantum yield";

qylp = ListPlot[qy, PlotStyle → PointSize[0.025]]

"Plots for dipole surfaces";
<< Graphics`Graphics3D`
<< Graphics`Graphics`

dipZplot = ScatterPlot3D[dipZ, PlotRange → {-2, 2}, AspectRatio → Automatic,
  BoxRatios → {1, 1, 2}, PlotStyle → PointSize[0.02],
  ViewPoint → {1.0, 2.0, 1.0}, PlotJoint → True, ImageSize → 300]
dipYplot = ScatterPlot3D[dipY, PlotRange → {-2, 2}, AspectRatio → Automatic,
  BoxRatios → {1, 1, 2}, PlotStyle → PointSize[0.02],
  ViewPoint → {1.0, 2.0, 1.0}, PlotJoint → True, ImageSize → 300]
dipXplot = ScatterPlot3D[dipX, PlotRange → {-2, 2.5},
  AspectRatio → Automatic, BoxRatios → {1, 1, 2},
  PlotStyle → PointSize[0.02], ViewPoint → {1.0, 2.0, 1.0},
  PlotJoint → True, ImageSize → 300]


"Plots for eigenvectors of Tau on Ground State";

%0,0 = ListPlot[v00, PlotStyle → PointSize[0.015], PlotRange → {-0.3, 0.3},
  DefaultColor → RGBColor[0.8, 0.1, 0.1]]
%0,1 = ListPlot[v01, PlotStyle → PointSize[0.015], PlotRange → {-0.3, 0.3}]
%0,2 = ListPlot[v02, PlotStyle → PointSize[0.015], PlotRange → {-0.3, 0.3}]
%0,3 = ListPlot[v03, PlotStyle → PointSize[0.015], PlotRange → {-0.3, 0.3}]
%0,4 = ListPlot[v04, PlotStyle → PointSize[0.015], PlotRange → {-0.3, 0.3}]
%0,5 = ListPlot[v05, PlotStyle → PointSize[0.015], PlotRange → {-0.3, 0.3}]
```

```
γ0,6 = ListPlot[v06, PlotStyle → PointSize[0.015], PlotRange → {-0.3, 0.3}]
γ0,7 = ListPlot[v07, PlotStyle → PointSize[0.015], PlotRange → {-0.3, 0.3}]
γ0,8 = ListPlot[v08, PlotStyle → PointSize[0.015], PlotRange → {-0.3, 0.3}]
γ0,9 = ListPlot[v09, PlotStyle → PointSize[0.015], PlotRange → {-0.3, 0.3}]
γ0,10 = ListPlot[v010, PlotStyle → PointSize[0.015], PlotRange → {-0.3, 0.3}]

"Plots for eigenvectors of OH on Ground State";

β0,0 = ListPlot[n00, PlotStyle → PointSize[0.015], PlotRange → {-0.25, 0.25},
  DefaultColor → RGBColor[0.2, 0.1, 0.9]]
β0,1 = ListPlot[n01, PlotStyle → PointSize[0.015], PlotRange → {-0.25, 0.25}]
β0,2 = ListPlot[n02, PlotStyle → PointSize[0.015]]
β0,3 = ListPlot[n03, PlotStyle → PointSize[0.015]]
β0,4 = ListPlot[n04, PlotStyle → PointSize[0.015]]
β0,5 = ListPlot[n05, PlotStyle → PointSize[0.015]]
β0,6 = ListPlot[n06, PlotStyle → PointSize[0.015]]
β0,7 = ListPlot[n07, PlotStyle → PointSize[0.015]]
β0,8 = ListPlot[n08, PlotStyle → PointSize[0.015]]
β0,9 = ListPlot[n09, PlotStyle → PointSize[0.015]]
β0,10 = ListPlot[n010, PlotStyle → PointSize[0.015]]

"Plots for eigenvectors of Tau on 1st Excited State";

γ1,0 = ListPlot[v10, PlotStyle → PointSize[0.015], PlotRange → {-0.3, 0.3},
  DefaultColor → RGBColor[0.8, 0.1, 0.1]]
γ1,1 = ListPlot[v11, PlotStyle → PointSize[0.015], PlotRange → {-0.3, 0.3}]
γ1,2 = ListPlot[v12, PlotStyle → PointSize[0.015], PlotRange → {-0.3, 0.3}]
γ1,3 = ListPlot[v13, PlotStyle → PointSize[0.015], PlotRange → {-0.3, 0.3}]
γ1,4 = ListPlot[v14, PlotStyle → PointSize[0.015], PlotRange → {-0.3, 0.3}]
γ1,5 = ListPlot[v15, PlotStyle → PointSize[0.015], PlotRange → {-0.3, 0.3}]
γ1,6 = ListPlot[v16, PlotStyle → PointSize[0.015], PlotRange → {-0.3, 0.3}]
γ1,7 = ListPlot[v17, PlotStyle → PointSize[0.015], PlotRange → {-0.3, 0.3}]
γ1,8 = ListPlot[v18, PlotStyle → PointSize[0.015], PlotRange → {-0.3, 0.3}]
γ1,9 = ListPlot[v19, PlotStyle → PointSize[0.015], PlotRange → {-0.3, 0.3}]
γ1,10 = ListPlot[v110, PlotStyle → PointSize[0.015], PlotRange → {-0.3, 0.3}]

"Plots for eigenvectors of OH on 1st Excited State";

β1,0 = ListPlot[n10, PlotStyle → PointSize[0.015], PlotRange → {-0.25, 0.25},
  DefaultColor → RGBColor[0.2, 0.1, 0.9]]
β1,1 = ListPlot[n11, PlotStyle → PointSize[0.015], PlotRange → {-0.25, 0.25}]
```

```
ß1,2 = ListPlot[n12, PlotStyle → PointSize[0.015], PlotRange → {-0.25, 0.25}]
ß1,3 = ListPlot[n13, PlotStyle → PointSize[0.015], PlotRange → {-0.25, 0.25}]
ß1,4 = ListPlot[n14, PlotStyle → PointSize[0.015], PlotRange → {-0.25, 0.25}]
ß1,5 = ListPlot[n15, PlotStyle → PointSize[0.015], PlotRange → {-0.25, 0.25}]
ß1,6 = ListPlot[n16, PlotStyle → PointSize[0.015]]
ß1,7 = ListPlot[n17, PlotStyle → PointSize[0.015]]
ß1,8 = ListPlot[n18, PlotStyle → PointSize[0.015]]
ß1,9 = ListPlot[n19, PlotStyle → PointSize[0.015]]
ß1,10 = ListPlot[n110, PlotStyle → PointSize[0.015]]


"Plots for eigenvectors of Tau on 2nd Excited State";

ɣ2,0 = ListPlot[v20, PlotStyle → PointSize[0.015], PlotRange → {-0.3, 0.3},
  DefaultColor → RGBColor[0.8, 0.1, 0.1]]
ɣ2,1 = ListPlot[v21, PlotStyle → PointSize[0.015], PlotRange → {-0.3, 0.3}]
ɣ2,2 = ListPlot[v22, PlotStyle → PointSize[0.015], PlotRange → {-0.3, 0.3}]
ɣ2,3 = ListPlot[v23, PlotStyle → PointSize[0.015], PlotRange → {-0.3, 0.3}]
ɣ2,4 = ListPlot[v24, PlotStyle → PointSize[0.015], PlotRange → {-0.3, 0.3}]
ɣ2,5 = ListPlot[v25, PlotStyle → PointSize[0.015], PlotRange → {-0.3, 0.3}]
ɣ2,6 = ListPlot[v26, PlotStyle → PointSize[0.015], PlotRange → {-0.3, 0.3}]
ɣ2,7 = ListPlot[v27, PlotStyle → PointSize[0.015], PlotRange → {-0.3, 0.3}]
ɣ2,8 = ListPlot[v28, PlotStyle → PointSize[0.015], PlotRange → {-0.3, 0.3}]
ɣ2,9 = ListPlot[v29, PlotStyle → PointSize[0.015], PlotRange → {-0.3, 0.3}]
ɣ2,10 = ListPlot[v210, PlotStyle → PointSize[0.015], PlotRange → {-0.3, 0.3}]

"Plots for eigenvectors of OH on 2nd Excited State";

ß2,0 = ListPlot[n20, PlotStyle → PointSize[0.015], PlotRange → {-0.25, 0.25},
  DefaultColor → RGBColor[0.2, 0.1, 0.9]]
ß2,1 = ListPlot[n21, PlotStyle → PointSize[0.015], PlotRange → {-0.25, 0.25}]
ß2,2 = ListPlot[n22, PlotStyle → PointSize[0.015], PlotRange → {-0.25, 0.25}]
ß2,3 = ListPlot[n23, PlotStyle → PointSize[0.015], PlotRange → {-0.25, 0.25}]
ß2,4 = ListPlot[n24, PlotStyle → PointSize[0.015], PlotRange → {-0.25, 0.25}]
ß2,5 = ListPlot[n25, PlotStyle → PointSize[0.015], PlotRange → {-0.25, 0.25}]
ß2,6 = ListPlot[n26, PlotStyle → PointSize[0.015]]
ß2,7 = ListPlot[n27, PlotStyle → PointSize[0.015]]
ß2,8 = ListPlot[n28, PlotStyle → PointSize[0.015]]
ß2,9 = ListPlot[n29, PlotStyle → PointSize[0.015]]
ß2,10 = ListPlot[n210, PlotStyle → PointSize[0.015]]
```

```
"Plots for eigenvectors of Tau on 3rd Excited State";

γ3,0 = ListPlot[v30, PlotStyle → PointSize[0.015], PlotRange → {-0.3, 0.3},
  DefaultColor → RGBColor[0.8, 0.1, 0.1]]
γ3,1 = ListPlot[v31, PlotStyle → PointSize[0.015], PlotRange → {-0.3, 0.3}]
γ3,2 = ListPlot[v32, PlotStyle → PointSize[0.015], PlotRange → {-0.3, 0.3}]
γ3,3 = ListPlot[v33, PlotStyle → PointSize[0.015], PlotRange → {-0.3, 0.3}]
γ3,4 = ListPlot[v34, PlotStyle → PointSize[0.015], PlotRange → {-0.3, 0.3}]
γ3,5 = ListPlot[v35, PlotStyle → PointSize[0.015], PlotRange → {-0.3, 0.3}]
γ3,6 = ListPlot[v36, PlotStyle → PointSize[0.015], PlotRange → {-0.3, 0.3}]
γ3,7 = ListPlot[v37, PlotStyle → PointSize[0.015], PlotRange → {-0.3, 0.3}]
γ3,8 = ListPlot[v38, PlotStyle → PointSize[0.015], PlotRange → {-0.3, 0.3}]
γ3,9 = ListPlot[v39, PlotStyle → PointSize[0.015], PlotRange → {-0.3, 0.3}]
γ3,10 = ListPlot[v310, PlotStyle → PointSize[0.015], PlotRange → {-0.3, 0.3}]

"Plots for eigenvectors of OH on 3rd Excited State";

β3,0 = ListPlot[n30, PlotStyle → PointSize[0.015], PlotRange → {-0.25, 0.25},
  DefaultColor → RGBColor[0.2, 0.1, 0.9]]
β3,1 = ListPlot[n31, PlotStyle → PointSize[0.015], PlotRange → {-0.25, 0.25}]
β3,2 = ListPlot[n32, PlotStyle → PointSize[0.015], PlotRange → {-0.25, 0.25}]
β3,3 = ListPlot[n33, PlotStyle → PointSize[0.015], PlotRange → {-0.25, 0.25}]
β3,4 = ListPlot[n34, PlotStyle → PointSize[0.015], PlotRange → {-0.25, 0.25}]
β3,5 = ListPlot[n35, PlotStyle → PointSize[0.015], PlotRange → {-0.25, 0.25}]
β3,6 = ListPlot[n36, PlotStyle → PointSize[0.015]]
β3,7 = ListPlot[n37, PlotStyle → PointSize[0.015]]
β3,8 = ListPlot[n38, PlotStyle → PointSize[0.015]]
β3,9 = ListPlot[n39, PlotStyle → PointSize[0.015]]
β3,10 = ListPlot[n310, PlotStyle → PointSize[0.015]]
```

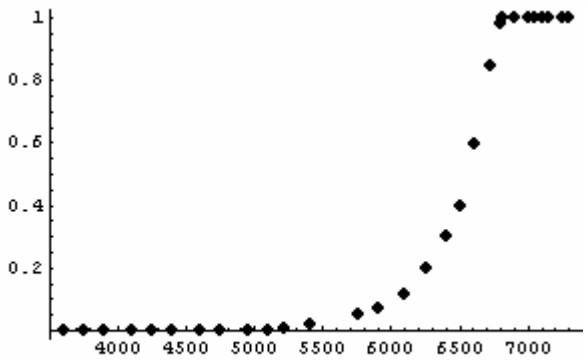

- Graphics -

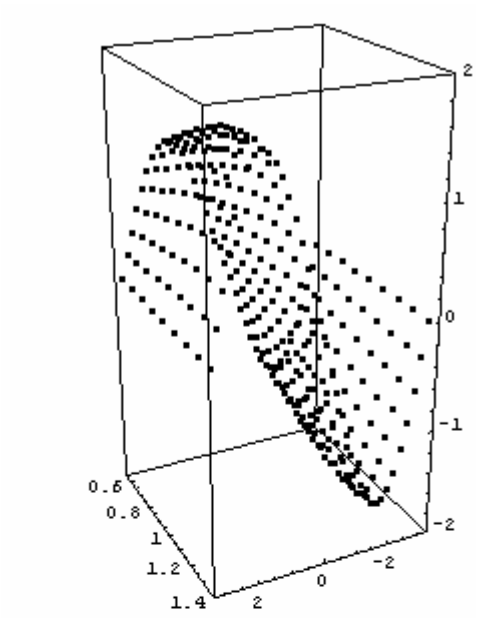

- Graphics3D -

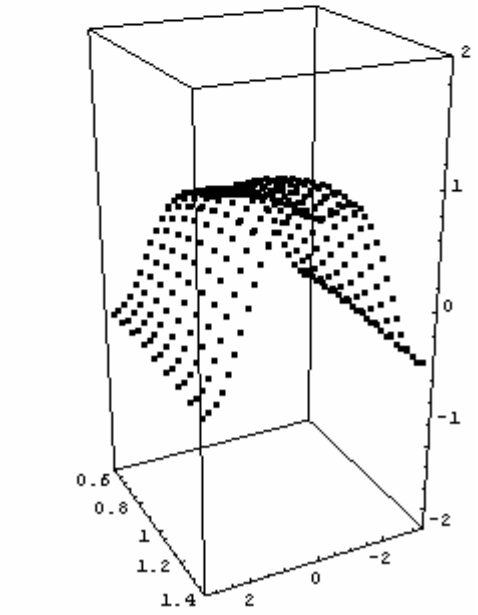

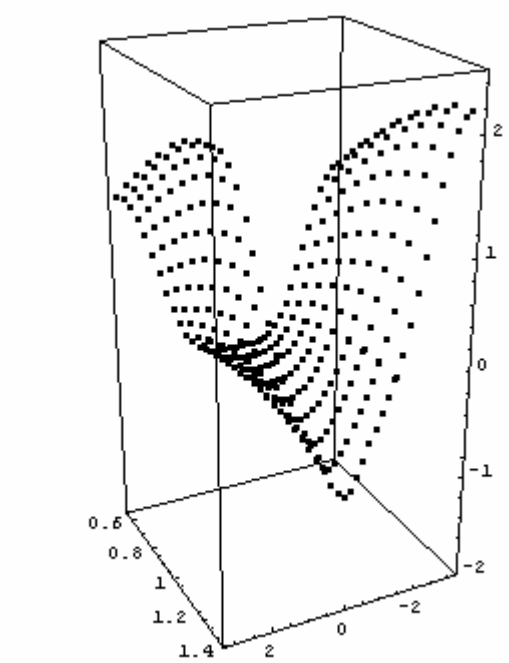


```
" Quantum Yield Fit ";

qyf = Fit[qy, {1, w, w^2, w^3, w^4, w^5, w^6, w^7, w^8, w^9, w^10,
    w^11, w^12, w^13, w^14, w^15, w^16} , w];
qyp = Plot[qyf, {w, 3500, 7500}]
Show[qyp, qylp]

" Dipole Surface fit using Taylor expansion ";
t = (x - to);
r = (y - ro);
to = Extract[dipZ[[176]], 1];
ro = Extract[dipZ[[176]], 2];
μz = Fit[dipZ, {1, r, t, r^2, r t, t^2, r^3, r^2 t, r t^2, t^3, r^4, r^3 t, r^2 t^2,
    r t^3, t^4, r^5, r^4 t, r^3 t^2, r^2 t^3, r t^4, t^5, r^6, r^5 t, r^4 t^2, r^3 t^3, r^2 t^4,
    r t^5, t^6, r^7, r^6 t, r^5 t^2, r^4 t^3, r^3 t^4, r^2 t^5, r t^6, t^7, r^8, r^7 t, r^6 t^2,
    r^5 t^3, r^4 t^4, r^3 t^5, r^2 t^6, r t^7, t^8, r^9, r^8 t, r^7 t^2, r^6 t^3, r^5 t^4, r^4 t^5,
    r^3 t^6, r^2 t^7, r t^8, t^9, r^10, r^9 t, r^8 t^2, r^7 t^3, r^6 t^4, r^5 t^5, r^4 t^6,
    r^3 t^7, r^2 t^8, r t^9, t^10}, {x, y}];
μY = Fit[dipY, {1, r, t, r^2, r t, t^2, r^3, r^2 t, r t^2, t^3, r^4, r^3 t, r^2 t^2,
    r t^3, t^4, r^5, r^4 t, r^3 t^2, r^2 t^3, r t^4, t^5, r^6, r^5 t, r^4 t^2, r^3 t^3, r^2 t^4,
    r t^5, t^6, r^7, r^6 t, r^5 t^2, r^4 t^3, r^3 t^4, r^2 t^5, r t^6, t^7, r^8, r^7 t, r^6 t^2,
    r^5 t^3, r^4 t^4, r^3 t^5, r^2 t^6, r t^7, t^8, r^9, r^8 t, r^7 t^2, r^6 t^3, r^5 t^4, r^4 t^5,
    r^3 t^6, r^2 t^7, r t^8, t^9, r^10, r^9 t, r^8 t^2, r^7 t^3, r^6 t^4, r^5 t^5, r^4 t^6,
    r^3 t^7, r^2 t^8, r t^9, t^10}, {x, y}];
```

```
μX = Fit[dipX, {1, r, t, r^2, r t, t^2, r^3, r^2 t, r t^2, t^3, r^4, r^3 t, r^2 t^2,
    r t^3, t^4, r^5, r^4 t, r^3 t^2, r^2 t^3, r t^4, t^5, r^6, r^5 t, r^4 t^2, r^3 t^3, r^2 t^4,
    r t^5, t^6, r^7, r^6 t, r^5 t^2, r^4 t^3, r^3 t^4, r^2 t^5, r t^6, t^7, r^8, r^7 t, r^6 t^2,
    r^5 t^3, r^4 t^4, r^3 t^5, r^2 t^6, r t^7, t^8, r^9, r^8 t, r^7 t^2, r^6 t^3, r^5 t^4, r^4 t^5,
    r^3 t^6, r^2 t^7, r t^8, t^9, r^10, r^9 t, r^8 t^2, r^7 t^3, r^6 t^4, r^5 t^5, r^4 t^6,
    r^3 t^7, r^2 t^8, r t^9, t^10}, {x, y}];
muZplot = Plot3D[μZ, {x, -3.14, 3.14}, {y, 0.565, 1.37}, Mesh → False,
  PlotPoints → 50]
Show[muZplot, dipZplot, ViewPoint → {1.0, 2.0, 1.0}]
Pause[1];
muYplot = Plot3D[μY, {x, -3.14, 3.14}, {y, 0.565, 1.37}, Mesh → False,
  PlotPoints → 50]
Show[muYplot, dipYplot, ViewPoint → {1.0, 2.0, 1.0}]
Pause[1];
muXplot = Plot3D[μX, {x, -3.14, 3.14}, {y, 0.565, 1.37}, Mesh → False,
  PlotPoints → 50]
Show[muXplot, dipXplot, ViewPoint → {1.0, 2.0, 1.0}]
Pause[1];

"wavefunctions interpolation for Tau on Ground state";

Ψ0,0 = Interpolation[v00, InterpolationOrder → 3];
χ0,0 = Plot[Evaluate[Ψ0,0][x], {x, -3.2, 3.2}, PlotPoints → 100,
  PlotRange → {-0.25, 0.25}]
Show[γ0,0, χ0,0]
Ψ0,1 = Interpolation[v01, InterpolationOrder → 3];
χ0,1 = Plot[Evaluate[Ψ0,1][x], {x, -3.2, 3.2}, PlotPoints → 100,
  PlotRange → {-0.25, 0.25}]
Show[γ0,1, χ0,1]
Ψ0,2 = Interpolation[v02, InterpolationOrder → 3];
χ0,2 = Plot[Evaluate[Ψ0,2][x], {x, -3.2, 3.2}, PlotPoints → 100,
  PlotRange → {-0.25, 0.25}]
Show[γ0,2, χ0,2]
Ψ0,3 = Interpolation[v03, InterpolationOrder → 3];
χ0,3 = Plot[Evaluate[Ψ0,3][x], {x, -3.2, 3.2}, PlotPoints → 100,
  PlotRange → {-0.25, 0.25}]
Show[γ0,3, χ0,3]
Ψ0,4 = Interpolation[v04, InterpolationOrder → 3];
χ0,4 = Plot[Evaluate[Ψ0,4][x], {x, -3.2, 3.2}, PlotPoints → 100,
  PlotRange → {-0.25, 0.25}]
Show[γ0,4, χ0,4]
```

```
Ψ0,5 = Interpolation[v05, InterpolationOrder → 3];
χ0,5 = Plot[Evaluate[Ψ0,5][x], {x, -3.2, 3.2}, PlotPoints → 100,
  PlotRange → {-0.25, 0.25}]
Show[γ0,5, χ0,5]
Ψ0,6 = Interpolation[v06, InterpolationOrder → 3];
χ0,6 = Plot[Evaluate[Ψ0,6][x], {x, -3.2, 3.2}, PlotPoints → 100,
  PlotRange → {-0.25, 0.25}]
Show[γ0,6, χ0,6]
Ψ0,7 = Interpolation[v07, InterpolationOrder → 3];
χ0,7 = Plot[Evaluate[Ψ0,7][x], {x, -3.2, 3.2}, PlotPoints → 100,
  PlotRange → {-0.25, 0.25}]
Show[γ0,7, χ0,7]
Ψ0,8 = Interpolation[v08, InterpolationOrder → 3];
χ0,8 = Plot[Evaluate[Ψ0,8][x], {x, -3.2, 3.2}, PlotPoints → 100,
  PlotRange → {-0.25, 0.25}]
Show[γ0,8, χ0,8]
Ψ0,9 = Interpolation[v09, InterpolationOrder → 3];
χ0,9 = Plot[Evaluate[Ψ0,9][x], {x, -3.2, 3.2}, PlotPoints → 100,
  PlotRange → {-0.25, 0.25}]
Show[γ0,9, χ0,9]
Ψ0,10 = Interpolation[v010, InterpolationOrder → 3];
χ0,10 = Plot[Evaluate[Ψ0,10][x], {x, -3.2, 3.2}, PlotPoints → 100,
  PlotRange → {-0.25, 0.25}]
Show[γ0,10, χ0,10]
"wavefunctions interpolation for OH on Ground State ";

Φ0,0 = Interpolation[n00, InterpolationOrder → 3];
Υ0,0 = Plot[Evaluate[Φ0,0][y], {y, 0.3, 2.0}, PlotPoints → 100,
  PlotRange → {-0.25, 0.25}]
Show[Υ0,0, β0,0]
Φ0,1 = Interpolation[n01, InterpolationOrder → 3];
Υ0,1 = Plot[Evaluate[Φ0,1][y], {y, 0.3, 2.0}, PlotPoints → 100,
  PlotRange → {-0.25, 0.25}]
Show[Υ0,1, β0,1]
Φ0,2 = Interpolation[n02, InterpolationOrder → 3];
Υ0,2 = Plot[Evaluate[Φ0,2][y], {y, 0.3, 2.0}, PlotPoints → 100,
  PlotRange → {-0.25, 0.25}]
Show[Υ0,2, β0,2]
Φ0,3 = Interpolation[n03, InterpolationOrder → 3];
Υ0,3 = Plot[Evaluate[Φ0,3][y], {y, 0.3, 2.0}, PlotPoints → 100,
  PlotRange → {-0.25, 0.25}]
Show[Υ0,3, β0,3]
```

```
Ø0,4 = Interpolation[n04, InterpolationOrder → 3];
Υ0,4 = Plot[Evaluate[Ø0,4][y], {y, 0.3, 2.0}, PlotPoints → 100,
  PlotRange → {-0.25, 0.25}]
Show[Υ0,4, ß0,4]
Ø0,5 = Interpolation[n05, InterpolationOrder → 3];
Υ0,5 = Plot[Evaluate[Ø0,5][y], {y, 0.3, 2.0}, PlotPoints → 100,
  PlotRange → {-0.25, 0.25}]
Show[Υ0,5, ß0,5]
Ø0,6 = Interpolation[n06, InterpolationOrder → 3];
Υ0,6 = Plot[Evaluate[Ø0,6][y], {y, 0.3, 2.0}, PlotPoints → 100,
  PlotRange → {-0.25, 0.25}]
Show[Υ0,6, ß0,6]
Ø0,7 = Interpolation[n07, InterpolationOrder → 3];
Υ0,7 = Plot[Evaluate[Ø0,7][y], {y, 0.3, 2.0}, PlotPoints → 100,
  PlotRange → {-0.25, 0.25}]
Show[Υ0,7, ß0,7]
Ø0,8 = Interpolation[n08, InterpolationOrder → 3];
Υ0,8 = Plot[Evaluate[Ø0,8][y], {y, 0.3, 2.0}, PlotPoints → 100,
  PlotRange → {-0.25, 0.25}]
Show[Υ0,8, ß0,8]
Ø0,9 = Interpolation[n09, InterpolationOrder → 3];
Υ0,9 = Plot[Evaluate[Ø0,9][y], {y, 0.3, 2.0}, PlotPoints → 100,
  PlotRange → {-0.25, 0.25}]
Show[Υ0,9, ß0,9]
Ø0,10 = Interpolation[n010, InterpolationOrder → 3];
Υ0,10 = Plot[Evaluate[Ø0,10][y], {y, 0.3, 2.0}, PlotPoints → 100,
  PlotRange → {-0.25, 0.25}]
Show[Υ0,10, ß0,10]

"wavefunctions interpolation for Tau on 1st Excited State";

Ψ1,0 = Interpolation[v10, InterpolationOrder → 3];
χ1,0 = Plot[Evaluate[Ψ1,0][x], {x, -3.2, 3.2}, PlotPoints → 100,
  PlotRange → {-0.25, 0.25}]
Show[ϒ1,0, χ1,0]
Ψ1,1 = Interpolation[v11, InterpolationOrder → 3];
χ1,1 = Plot[Evaluate[Ψ1,1][x], {x, -3.2, 3.2}, PlotPoints → 100,
  PlotRange → {-0.25, 0.25}]
Show[ϒ1,1, χ1,1]
```

```
Ψ1,2 = Interpolation[v12, InterpolationOrder → 3];
χ1,2 = Plot[Evaluate[Ψ1,2][x], {x, -3.2, 3.2}, PlotPoints → 100,
  PlotRange → {-0.25, 0.25}]
Show[γ1,2, χ1,2]
Ψ1,3 = Interpolation[v13, InterpolationOrder → 3];
χ1,3 = Plot[Evaluate[Ψ1,3][x], {x, -3.2, 3.2}, PlotPoints → 100,
  PlotRange → {-0.25, 0.25}]
Show[γ1,3, χ1,3]
Ψ1,4 = Interpolation[v14, InterpolationOrder → 3];
χ1,4 = Plot[Evaluate[Ψ1,4][x], {x, -3.2, 3.2}, PlotPoints → 100,
  PlotRange → {-0.25, 0.25}]
Show[γ1,4, χ1,4]
Ψ1,5 = Interpolation[v15, InterpolationOrder → 3];
χ1,5 = Plot[Evaluate[Ψ1,5][x], {x, -3.2, 3.2}, PlotPoints → 100,
  PlotRange → {-0.25, 0.25}]
Show[γ1,5, χ1,5]
Ψ1,6 = Interpolation[v16, InterpolationOrder → 3];
χ1,6 = Plot[Evaluate[Ψ1,6][x], {x, -3.2, 3.2}, PlotPoints → 100,
  PlotRange → {-0.25, 0.25}]
Show[γ1,6, χ1,6]
Ψ1,7 = Interpolation[v17, InterpolationOrder → 3];
χ1,7 = Plot[Evaluate[Ψ1,7][x], {x, -3.2, 3.2}, PlotPoints → 100,
  PlotRange → {-0.25, 0.25}]
Show[γ1,7, χ1,7]
Ψ1,8 = Interpolation[v18, InterpolationOrder → 3];
χ1,8 = Plot[Evaluate[Ψ1,8][x], {x, -3.2, 3.2}, PlotPoints → 100,
  PlotRange → {-0.25, 0.25}]
Show[γ1,8, χ1,8]
Ψ1,9 = Interpolation[v19, InterpolationOrder → 3];
χ1,9 = Plot[Evaluate[Ψ1,9][x], {x, -3.2, 3.2}, PlotPoints → 100,
  PlotRange → {-0.25, 0.25}]
Show[γ1,9, χ1,9]
Ψ1,10 = Interpolation[v110, InterpolationOrder → 3];
χ1,10 = Plot[Evaluate[Ψ1,10][x], {x, -3.2, 3.2}, PlotPoints → 100,
  PlotRange → {-0.25, 0.25}]
Show[γ1,10, χ1,10]
```

```
"wavefunctions interpolation for OH on 1st Excited State ";

Ø1,0 = Interpolation[n10, InterpolationOrder → 3];
Υ1,0 = Plot[Evaluate[Ø1,0][y], {y, 0.3, 2.0}, PlotPoints → 100,
  PlotRange → {-0.25, 0.25}]
Show[Υ1,0, ß1,0]
Ø1,1 = Interpolation[n11, InterpolationOrder → 3];
Υ1,1 = Plot[Evaluate[Ø1,1][y], {y, 0.3, 2.0}, PlotPoints → 100,
  PlotRange → {-0.25, 0.25}]
Show[Υ1,1, ß1,1]
Ø1,2 = Interpolation[n12, InterpolationOrder → 3];
Υ1,2 = Plot[Evaluate[Ø1,2][y], {y, 0.3, 2.0}, PlotPoints → 100,
  PlotRange → {-0.25, 0.25}]
Show[Υ1,2, ß1,2]
Ø1,3 = Interpolation[n13, InterpolationOrder → 3];
Υ1,3 = Plot[Evaluate[Ø1,3][y], {y, 0.3, 2.0}, PlotPoints → 100,
  PlotRange → {-0.25, 0.25}]
Show[Υ1,3, ß1,3]
Ø1,4 = Interpolation[n14, InterpolationOrder → 3];
Υ1,4 = Plot[Evaluate[Ø1,4][y], {y, 0.3, 2.0}, PlotPoints → 100,
  PlotRange → {-0.25, 0.25}]
Show[Υ1,4, ß1,4]
Ø1,5 = Interpolation[n15, InterpolationOrder → 3];
Υ1,5 = Plot[Evaluate[Ø1,5][y], {y, 0.3, 2.0}, PlotPoints → 100,
  PlotRange → {-0.25, 0.25}]
Show[Υ1,5, ß1,5]
Ø1,6 = Interpolation[n16, InterpolationOrder → 3];
Υ1,6 = Plot[Evaluate[Ø1,6][y], {y, 0.3, 2.0}, PlotPoints → 100,
  PlotRange → {-0.25, 0.25}]
Show[Υ1,6, ß1,6]
Ø1,7 = Interpolation[n17, InterpolationOrder → 3];
Υ1,7 = Plot[Evaluate[Ø1,7][y], {y, 0.3, 2.0}, PlotPoints → 100,
  PlotRange → {-0.25, 0.25}]
Show[Υ1,7, ß1,7]
Ø1,8 = Interpolation[n18, InterpolationOrder → 3];
Υ1,8 = Plot[Evaluate[Ø1,8][y], {y, 0.3, 2.0}, PlotPoints → 100,
  PlotRange → {-0.25, 0.25}]
Show[Υ1,8, ß1,8]
Ø1,9 = Interpolation[n19, InterpolationOrder → 3];
Υ1,9 = Plot[Evaluate[Ø1,9][y], {y, 0.3, 2.0}, PlotPoints → 100,
  PlotRange → {-0.25, 0.25}]
Show[Υ1,9, ß1,9]
```

```
Ø1,10 = Interpolation[n110, InterpolationOrder → 3];
Υ1,10 = Plot[Evaluate[Ø1,10][y], {y, 0.3, 2.0}, PlotPoints → 100,
  PlotRange → {-0.25, 0.25}]
Show[Υ1,10, ß1,10]
"wavefunctions interpolation for Tau on 2nd Excited State";

Ψ2,0 = Interpolation[v20, InterpolationOrder → 3];
χ2,0 = Plot[Evaluate[Ψ2,0][x], {x, -3.2, 3.2}, PlotPoints → 100,
  PlotRange → {-0.25, 0.25}]
Show[ϒ2,0, χ2,0]
Ψ2,1 = Interpolation[v21, InterpolationOrder → 3];
χ2,1 = Plot[Evaluate[Ψ2,1][x], {x, -3.2, 3.2}, PlotPoints → 100,
  PlotRange → {-0.25, 0.25}]
Show[ϒ2,1, χ2,1]
Ψ2,2 = Interpolation[v22, InterpolationOrder → 3];
χ2,2 = Plot[Evaluate[Ψ2,2][x], {x, -3.2, 3.2}, PlotPoints → 100,
  PlotRange → {-0.25, 0.25}]
Show[ϒ2,2, χ2,2]
Ψ2,3 = Interpolation[v23, InterpolationOrder → 3];
χ2,3 = Plot[Evaluate[Ψ2,3][x], {x, -3.2, 3.2}, PlotPoints → 100,
  PlotRange → {-0.25, 0.25}]
Show[ϒ2,3, χ2,3]
Ψ2,4 = Interpolation[v24, InterpolationOrder → 3];
χ2,4 = Plot[Evaluate[Ψ2,4][x], {x, -3.2, 3.2}, PlotPoints → 100,
  PlotRange → {-0.25, 0.25}]
Show[ϒ2,4, χ2,4]
Ψ2,5 = Interpolation[v25, InterpolationOrder → 3];
χ2,5 = Plot[Evaluate[Ψ2,5][x], {x, -3.2, 3.2}, PlotPoints → 100,
  PlotRange → {-0.25, 0.25}]
Show[ϒ2,5, χ2,5]
Ψ2,6 = Interpolation[v26, InterpolationOrder → 3];
χ2,6 = Plot[Evaluate[Ψ2,6][x], {x, -3.2, 3.2}, PlotPoints → 100,
  PlotRange → {-0.25, 0.25}]
Show[ϒ2,6, χ2,6]
Ψ2,7 = Interpolation[v27, InterpolationOrder → 3];
χ2,7 = Plot[Evaluate[Ψ2,7][x], {x, -3.2, 3.2}, PlotPoints → 100,
  PlotRange → {-0.25, 0.25}]
Show[ϒ2,7, χ2,7]
Ψ2,8 = Interpolation[v28, InterpolationOrder → 3];
χ2,8 = Plot[Evaluate[Ψ2,8][x], {x, -3.2, 3.2}, PlotPoints → 100,
  PlotRange → {-0.25, 0.25}]
Show[ϒ2,8, χ2,8]
```

```
Ψ2,9 = Interpolation[v29, InterpolationOrder → 3];
χ2,9 = Plot[Evaluate[Ψ2,9][x], {x, -3.2, 3.2}, PlotPoints → 100,
  PlotRange → {-0.25, 0.25}]
Show[ϒ2,9, χ2,9]
Ψ2,10 = Interpolation[v210, InterpolationOrder → 3];
χ2,10 = Plot[Evaluate[Ψ2,10][x], {x, -3.2, 3.2}, PlotPoints → 100,
  PlotRange → {-0.25, 0.25}]
Show[ϒ2,10, χ2,10]

"wavefunctions interpolation for OH on 2nd Excited State ";

Φ2,0 = Interpolation[n20, InterpolationOrder → 3];
Υ2,0 = Plot[Evaluate[Φ2,0][y], {y, 0.3, 2.0}, PlotPoints → 100,
  PlotRange → {-0.25, 0.25}]
Show[Υ2,0, β2,0]
Φ2,1 = Interpolation[n21, InterpolationOrder → 3];
Υ2,1 = Plot[Evaluate[Φ2,1][y], {y, 0.3, 2.0}, PlotPoints → 100,
  PlotRange → {-0.25, 0.25}]
Show[Υ2,1, β2,1]
Φ2,2 = Interpolation[n22, InterpolationOrder → 3];
Υ2,2 = Plot[Evaluate[Φ2,2][y], {y, 0.3, 2.0}, PlotPoints → 100,
  PlotRange → {-0.25, 0.25}]
Show[Υ2,2, β2,2]
Φ2,3 = Interpolation[n23, InterpolationOrder → 3];
Υ2,3 = Plot[Evaluate[Φ2,3][y], {y, 0.3, 2.0}, PlotPoints → 100,
  PlotRange → {-0.25, 0.25}]
Show[Υ2,3, β2,3]
Φ2,4 = Interpolation[n24, InterpolationOrder → 3];
Υ2,4 = Plot[Evaluate[Φ2,4][y], {y, 0.3, 2.0}, PlotPoints → 100,
  PlotRange → {-0.25, 0.25}]
Show[Υ2,4, β2,4]
Φ2,5 = Interpolation[n25, InterpolationOrder → 3];
Υ2,5 = Plot[Evaluate[Φ2,5][y], {y, 0.3, 2.0}, PlotPoints → 100,
  PlotRange → {-0.25, 0.25}]
Show[Υ2,5, β2,5]
Φ2,6 = Interpolation[n26, InterpolationOrder → 3];
Υ2,6 = Plot[Evaluate[Φ2,6][y], {y, 0.3, 2.0}, PlotPoints → 100,
  PlotRange → {-0.25, 0.25}]
Show[Υ2,6, β2,6]
```

```
Ø2,7 = Interpolation[n27, InterpolationOrder → 3];
Υ2,7 = Plot[Evaluate[Ø2,7][y], {y, 0.3, 2.0}, PlotPoints → 100,
  PlotRange → {-0.25, 0.25}]
Show[Υ2,7, ß2,7]
Ø2,8 = Interpolation[n28, InterpolationOrder → 3];
Υ2,8 = Plot[Evaluate[Ø2,8][y], {y, 0.3, 2.0}, PlotPoints → 100,
  PlotRange → {-0.25, 0.25}]
Show[Υ2,8, ß2,8]
Ø2,9 = Interpolation[n29, InterpolationOrder → 3];
Υ2,9 = Plot[Evaluate[Ø2,9][y], {y, 0.3, 2.0}, PlotPoints → 100,
  PlotRange → {-0.25, 0.25}]
Show[Υ2,9, ß2,9]
Ø2,10 = Interpolation[n210, InterpolationOrder → 3];
Υ2,10 = Plot[Evaluate[Ø2,10][y], {y, 0.3, 2.0}, PlotPoints → 100,
  PlotRange → {-0.25, 0.25}]
Show[Υ2,10, ß2,10]

"wavefunctions interpolation for Tau on 3rd Excited State";

Ψ3,0 = Interpolation[v30, InterpolationOrder → 3];
χ3,0 = Plot[Evaluate[Ψ3,0][x], {x, -3.2, 3.2}, PlotPoints → 100,
  PlotRange → {-0.25, 0.25}]
Show[γ3,0, χ3,0]
Ψ3,1 = Interpolation[v31, InterpolationOrder → 3];
χ3,1 = Plot[Evaluate[Ψ3,1][x], {x, -3.2, 3.2}, PlotPoints → 100,
  PlotRange → {-0.25, 0.25}]
Show[γ3,1, χ3,1]
Ψ3,2 = Interpolation[v32, InterpolationOrder → 3];
χ3,2 = Plot[Evaluate[Ψ3,2][x], {x, -3.2, 3.2}, PlotPoints → 100,
  PlotRange → {-0.25, 0.25}]
Show[γ3,2, χ3,2]
Ψ3,3 = Interpolation[v33, InterpolationOrder → 3];
χ3,3 = Plot[Evaluate[Ψ3,3][x], {x, -3.2, 3.2}, PlotPoints → 100,
  PlotRange → {-0.25, 0.25}]
Show[γ3,3, χ3,3]
Ψ3,4 = Interpolation[v34, InterpolationOrder → 3];
χ3,4 = Plot[Evaluate[Ψ3,4][x], {x, -3.2, 3.2}, PlotPoints → 100,
  PlotRange → {-0.25, 0.25}]
Show[γ3,4, χ3,4]
```

```
Ψ3,5 = Interpolation[v35, InterpolationOrder → 3];
χ3,5 = Plot[Evaluate[Ψ3,5][x], {x, -3.2, 3.2}, PlotPoints → 100,
  PlotRange → {-0.25, 0.25}]
Show[γ3,5, χ3,5]
Ψ3,6 = Interpolation[v36, InterpolationOrder → 3];
χ3,6 = Plot[Evaluate[Ψ3,6][x], {x, -3.2, 3.2}, PlotPoints → 100,
  PlotRange → {-0.25, 0.25}]
Show[γ3,6, χ3,6]
Ψ3,7 = Interpolation[v37, InterpolationOrder → 3];
χ3,7 = Plot[Evaluate[Ψ3,7][x], {x, -3.2, 3.2}, PlotPoints → 100,
  PlotRange → {-0.25, 0.25}]
Show[γ3,7, χ3,7]
Ψ3,8 = Interpolation[v38, InterpolationOrder → 3];
χ3,8 = Plot[Evaluate[Ψ3,8][x], {x, -3.2, 3.2}, PlotPoints → 100,
  PlotRange → {-0.25, 0.25}]
Show[γ3,8, χ3,8]
Ψ3,9 = Interpolation[v39, InterpolationOrder → 3];
χ3,9 = Plot[Evaluate[Ψ3,9][x], {x, -3.2, 3.2}, PlotPoints → 100,
  PlotRange → {-0.25, 0.25}]
Show[γ3,9, χ3,9]
Ψ3,10 = Interpolation[v310, InterpolationOrder → 3];
χ3,10 = Plot[Evaluate[Ψ3,10][x], {x, -3.2, 3.2}, PlotPoints → 100,
  PlotRange → {-0.25, 0.25}]
Show[γ3,10, χ3,10]
"wavefunctions interpolation for OH on 3rd Excited State ";

Ø3,0 = Interpolation[n30, InterpolationOrder → 3];
Υ3,0 = Plot[Evaluate[Ø3,0][y], {y, 0.3, 2.0}, PlotPoints → 100,
  PlotRange → {-0.25, 0.25}]
Show[Υ3,0, β3,0]
Ø3,1 = Interpolation[n31, InterpolationOrder → 3];
Υ3,1 = Plot[Evaluate[Ø3,1][y], {y, 0.3, 2.0}, PlotPoints → 100,
  PlotRange → {-0.25, 0.25}]
Show[Υ3,1, β3,1]
Ø3,2 = Interpolation[n32, InterpolationOrder → 3];
Υ3,2 = Plot[Evaluate[Ø3,2][y], {y, 0.3, 2.0}, PlotPoints → 100,
  PlotRange → {-0.25, 0.25}]
Show[Υ3,2, β3,2]
Ø3,3 = Interpolation[n33, InterpolationOrder → 3];
Υ3,3 = Plot[Evaluate[Ø3,3][y], {y, 0.3, 2.0}, PlotPoints → 100,
  PlotRange → {-0.25, 0.25}]
Show[Υ3,3, β3,3]
```

```
Ø3,4 = Interpolation[n34, InterpolationOrder → 3];
Υ3,4 = Plot[Evaluate[Ø3,4][y], {y, 0.3, 2.0}, PlotPoints → 100,
  PlotRange → {-0.25, 0.25}]
Show[Υ3,4, β3,4]
Ø3,5 = Interpolation[n35, InterpolationOrder → 3];
Υ3,5 = Plot[Evaluate[Ø3,5][y], {y, 0.3, 2.0}, PlotPoints → 100,
  PlotRange → {-0.25, 0.25}]
Show[Υ3,5, β3,5]
Ø3,6 = Interpolation[n36, InterpolationOrder → 3];
Υ3,6 = Plot[Evaluate[Ø3,6][y], {y, 0.3, 2.0}, PlotPoints → 100,
  PlotRange → {-0.25, 0.25}]
Show[Υ3,6, β3,6]
Ø3,7 = Interpolation[n37, InterpolationOrder → 3];
Υ3,7 = Plot[Evaluate[Ø3,7][y], {y, 0.3, 2.0}, PlotPoints → 100,
  PlotRange → {-0.25, 0.25}]
Show[Υ3,7, β3,7]
Ø3,8 = Interpolation[n38, InterpolationOrder → 3];
Υ3,8 = Plot[Evaluate[Ø3,8][y], {y, 0.3, 2.0}, PlotPoints → 100,
  PlotRange → {-0.25, 0.25}]
Show[Υ3,8, β3,8]
Ø3,9 = Interpolation[n39, InterpolationOrder → 3];
Υ3,9 = Plot[Evaluate[Ø3,9][y], {y, 0.3, 2.0}, PlotPoints → 100,
  PlotRange → {-0.25, 0.25}]
Show[Υ3,9, β3,9]
Ø3,10 = Interpolation[n310, InterpolationOrder → 3];
Υ3,10 = Plot[Evaluate[Ø3,10][y], {y, 0.3, 2.0}, PlotPoints → 100,
  PlotRange → {-0.25, 0.25}]
Show[Υ3,10, β3,10]

"Normalization for Tau on Ground Surface ";

λ = 3.2;

α0,0 =
  NIntegrate[Evaluate[Ψ0,0][x] * Evaluate[Ψ0,0][x], {x, -λ, λ},
    MaxRecursion → 100]^-0.5;
α0,1 =
  NIntegrate[Evaluate[Ψ0,1][x] * Evaluate[Ψ0,1][x], {x, -λ, λ},
    MaxRecursion → 100]^-0.5;
α0,2 =
  NIntegrate[Evaluate[Ψ0,2][x] * Evaluate[Ψ0,2][x], {x, -λ, λ},
    MaxRecursion → 100]^-0.5;
```

```
α0,3 =
  NIntegrate[Evaluate[Ψ0,3][x] * Evaluate[Ψ0,3][x], {x, -λ, λ},
    MaxRecursion → 100]^-0.5;
α0,4 =
  NIntegrate[Evaluate[Ψ0,4][x] * Evaluate[Ψ0,4][x], {x, -λ, λ},
    MaxRecursion → 100]^-0.5;
α0,5 =
  NIntegrate[Evaluate[Ψ0,5][x] * Evaluate[Ψ0,5][x], {x, -λ, λ},
    MaxRecursion → 100]^-0.5;
α0,6 =
  NIntegrate[Evaluate[Ψ0,6][x] * Evaluate[Ψ0,6][x], {x, -λ, λ},
    MaxRecursion → 100]^-0.5;
α0,7 =
  NIntegrate[Evaluate[Ψ0,7][x] * Evaluate[Ψ0,7][x], {x, -λ, λ},
    MaxRecursion → 100]^-0.5;
α0,8 =
  NIntegrate[Evaluate[Ψ0,8][x] * Evaluate[Ψ0,8][x], {x, -λ, λ},
    MaxRecursion → 100]^-0.5;
α0,9 =
  NIntegrate[Evaluate[Ψ0,9][x] * Evaluate[Ψ0,9][x], {x, -λ, λ},
    MaxRecursion → 100]^-0.5;
α0,10 =
  NIntegrate[Evaluate[Ψ0,10][x] * Evaluate[Ψ0,10][x], {x, -λ, λ},
    MaxRecursion → 100]^-0.5;

"Normalization for OH wavefunctions on Ground Surface";

η = 0.3;
θ = 2.0;

β0,0 =
  NIntegrate[Evaluate[Ø0,0][y] * Evaluate[Ø0,0][y], {y, η, θ},
    MaxRecursion → 100]^-0.5;
β0,1 =
  NIntegrate[Evaluate[Ø0,1][y] * Evaluate[Ø0,1][y], {y, η, θ},
    MaxRecursion → 100]^-0.5;
β0,2 =
  NIntegrate[Evaluate[Ø0,2][y] * Evaluate[Ø0,2][y], {y, η, θ},
    MaxRecursion → 100]^-0.5;
β0,3 =
  NIntegrate[Evaluate[Ø0,3][y] * Evaluate[Ø0,3][y], {y, η, θ},
    MaxRecursion → 100]^-0.5;
```

```
p0,4 =
  NIntegrate[Evaluate[Ø0,4][y] * Evaluate[Ø0,4][y], {y, η, θ},
    MaxRecursion → 100]^-0.5;
p0,5 =
  NIntegrate[Evaluate[Ø0,5][y] * Evaluate[Ø0,5][y], {y, η, θ},
    MaxRecursion → 100]^-0.5;
p0,6 =
  NIntegrate[Evaluate[Ø0,6][y] * Evaluate[Ø0,6][y], {y, η, θ},
    MaxRecursion → 100]^-0.5;
p0,7 =
  NIntegrate[Evaluate[Ø0,7][y] * Evaluate[Ø0,7][y], {y, η, θ},
    MaxRecursion → 100]^-0.5;
p0,8 =
  NIntegrate[Evaluate[Ø0,8][y] * Evaluate[Ø0,8][y], {y, η, θ},
    MaxRecursion → 100]^-0.5;
p0,9 =
  NIntegrate[Evaluate[Ø0,9][y] * Evaluate[Ø0,9][y], {y, η, θ},
    MaxRecursion → 100]^-0.5;
p0,10 =
  NIntegrate[Evaluate[Ø0,10][y] * Evaluate[Ø0,10][y], {y, η, θ},
    MaxRecursion → 100]^-0.5;

"Normalization for Tau on 1st Excited State ";

α1,0 =
  NIntegrate[Evaluate[Ψ1,0][x] * Evaluate[Ψ1,0][x], {x, -λ, λ},
    MaxRecursion → 100]^-0.5;
α1,1 =
  NIntegrate[Evaluate[Ψ1,1][x] * Evaluate[Ψ1,1][x], {x, -λ, λ},
    MaxRecursion → 100]^-0.5;
α1,2 =
  NIntegrate[Evaluate[Ψ1,2][x] * Evaluate[Ψ1,2][x], {x, -λ, λ},
    MaxRecursion → 100]^-0.5;
α1,3 =
  NIntegrate[Evaluate[Ψ1,3][x] * Evaluate[Ψ1,3][x], {x, -λ, λ},
    MaxRecursion → 100]^-0.5;
α1,4 =
  NIntegrate[Evaluate[Ψ1,4][x] * Evaluate[Ψ1,4][x], {x, -λ, λ},
    MaxRecursion → 100]^-0.5;
α1,5 =
  NIntegrate[Evaluate[Ψ1,5][x] * Evaluate[Ψ1,5][x], {x, -λ, λ},
    MaxRecursion → 100]^-0.5;
```

```
α1,6 =
  NIntegrate[Evaluate[Ψ1,6][x] * Evaluate[Ψ1,6][x], {x, -λ, λ},
    MaxRecursion → 100]^-0.5;
α1,7 =
  NIntegrate[Evaluate[Ψ1,7][x] * Evaluate[Ψ1,7][x], {x, -λ, λ},
    MaxRecursion → 100]^-0.5;
α1,8 =
  NIntegrate[Evaluate[Ψ1,8][x] * Evaluate[Ψ1,8][x], {x, -λ, λ},
    MaxRecursion → 100]^-0.5;
α1,9 =
  NIntegrate[Evaluate[Ψ1,9][x] * Evaluate[Ψ1,9][x], {x, -λ, λ},
    MaxRecursion → 100]^-0.5;
α1,10 =
  NIntegrate[Evaluate[Ψ1,10][x] * Evaluate[Ψ1,10][x], {x, -λ, λ},
    MaxRecursion → 100]^-0.5;

"Normalization for OH wavefunctions on 1st Excited Surface";

p1,0 =
  NIntegrate[Evaluate[Ø1,0][y] * Evaluate[Ø1,0][y], {y, η, θ},
    MaxRecursion → 100]^-0.5;
p1,1 =
  NIntegrate[Evaluate[Ø1,1][y] * Evaluate[Ø1,1][y], {y, η, θ},
    MaxRecursion → 100]^-0.5;
p1,2 =
  NIntegrate[Evaluate[Ø1,2][y] * Evaluate[Ø1,2][y], {y, η, θ},
    MaxRecursion → 100]^-0.5;
p1,3 =
  NIntegrate[Evaluate[Ø1,3][y] * Evaluate[Ø1,3][y], {y, η, θ},
    MaxRecursion → 100]^-0.5;
p1,4 =
  NIntegrate[Evaluate[Ø1,4][y] * Evaluate[Ø1,4][y], {y, η, θ},
    MaxRecursion → 100]^-0.5;
p1,5 =
  NIntegrate[Evaluate[Ø1,5][y] * Evaluate[Ø1,5][y], {y, η, θ},
    MaxRecursion → 100]^-0.5;
p1,6 =
  NIntegrate[Evaluate[Ø1,6][y] * Evaluate[Ø1,6][y], {y, η, θ},
    MaxRecursion → 100]^-0.5;
p1,7 =
  NIntegrate[Evaluate[Ø1,7][y] * Evaluate[Ø1,7][y], {y, η, θ},
    MaxRecursion → 100]^-0.5;
```

```
p1,8 =
  NIntegrate[Evaluate[Ø1,8][y] * Evaluate[Ø1,8][y], {y, η, θ},
    MaxRecursion → 100]^-0.5;
p1,9 =
  NIntegrate[Evaluate[Ø1,9][y] * Evaluate[Ø1,9][y], {y, η, θ},
    MaxRecursion → 100]^-0.5;
p1,10 =
  NIntegrate[Evaluate[Ø1,10][y] * Evaluate[Ø1,10][y], {y, η, θ},
    MaxRecursion → 100]^-0.5;


"Normalization for Tau on 2nd Excited State ";


α2,0 =
  NIntegrate[Evaluate[Ψ2,0][x] * Evaluate[Ψ2,0][x], {x, -λ, λ},
    MaxRecursion → 100]^-0.5;
α2,1 =
  NIntegrate[Evaluate[Ψ2,1][x] * Evaluate[Ψ2,1][x], {x, -λ, λ},
    MaxRecursion → 100]^-0.5;
α2,2 =
  NIntegrate[Evaluate[Ψ2,2][x] * Evaluate[Ψ2,2][x], {x, -λ, λ},
    MaxRecursion → 100]^-0.5;
α2,3 =
  NIntegrate[Evaluate[Ψ2,3][x] * Evaluate[Ψ2,3][x], {x, -λ, λ},
    MaxRecursion → 100]^-0.5;
α2,4 =
  NIntegrate[Evaluate[Ψ2,4][x] * Evaluate[Ψ2,4][x], {x, -λ, λ},
    MaxRecursion → 100]^-0.5;
α2,5 =
  NIntegrate[Evaluate[Ψ2,5][x] * Evaluate[Ψ2,5][x], {x, -λ, λ},
    MaxRecursion → 100]^-0.5;
α2,6 =
  NIntegrate[Evaluate[Ψ2,6][x] * Evaluate[Ψ2,6][x], {x, -λ, λ},
    MaxRecursion → 100]^-0.5;
α2,7 =
  NIntegrate[Evaluate[Ψ2,7][x] * Evaluate[Ψ2,7][x], {x, -λ, λ},
    MaxRecursion → 100]^-0.5;
α2,8 =
  NIntegrate[Evaluate[Ψ2,8][x] * Evaluate[Ψ2,8][x], {x, -λ, λ},
    MaxRecursion → 100]^-0.5;
```

```
α2,9 =
  NIntegrate[Evaluate[Ψ2,9][x] * Evaluate[Ψ2,9][x], {x, -λ, λ},
    MaxRecursion → 100]^-0.5;
α2,10 =
  NIntegrate[Evaluate[Ψ2,10][x] * Evaluate[Ψ2,10][x], {x, -λ, λ},
    MaxRecursion → 100]^-0.5;

"Normalization for OH wavefunctions on 2nd Excited Surface";

p2,0 =
  NIntegrate[Evaluate[Φ2,0][y] * Evaluate[Φ2,0][y], {y, η, θ},
    MaxRecursion → 100]^-0.5;
p2,1 =
  NIntegrate[Evaluate[Φ2,1][y] * Evaluate[Φ2,1][y], {y, η, θ},
    MaxRecursion → 100]^-0.5;
p2,2 =
  NIntegrate[Evaluate[Φ2,2][y] * Evaluate[Φ2,2][y], {y, η, θ},
    MaxRecursion → 100]^-0.5;
p2,3 =
  NIntegrate[Evaluate[Φ2,3][y] * Evaluate[Φ2,3][y], {y, η, θ},
    MaxRecursion → 100]^-0.5;
p2,4 =
  NIntegrate[Evaluate[Φ2,4][y] * Evaluate[Φ2,4][y], {y, η, θ},
    MaxRecursion → 100]^-0.5;
p2,5 =
  NIntegrate[Evaluate[Φ2,5][y] * Evaluate[Φ2,5][y], {y, η, θ},
    MaxRecursion → 100]^-0.5;
p2,6 =
  NIntegrate[Evaluate[Φ2,6][y] * Evaluate[Φ2,6][y], {y, η, θ},
    MaxRecursion → 100]^-0.5;
p2,7 =
  NIntegrate[Evaluate[Φ2,7][y] * Evaluate[Φ2,7][y], {y, η, θ},
    MaxRecursion → 100]^-0.5;
p2,8 =
  NIntegrate[Evaluate[Φ2,8][y] * Evaluate[Φ2,8][y], {y, η, θ},
    MaxRecursion → 100]^-0.5;
p2,9 =
  NIntegrate[Evaluate[Φ2,9][y] * Evaluate[Φ2,9][y], {y, η, θ},
    MaxRecursion → 100]^-0.5;
```

```
β2,10 =
  NIntegrate[Evaluate[Ø2,10][y] * Evaluate[Ø2,10][y], {y, η, θ},
    MaxRecursion → 100]^-0.5;


"Normalization for Tau on 3rd Excited State ";


α3,0 =
  NIntegrate[Evaluate[Ψ3,0][x] * Evaluate[Ψ3,0][x], {x, -λ, λ},
    MaxRecursion → 100]^-0.5;
α3,1 =
  NIntegrate[Evaluate[Ψ3,1][x] * Evaluate[Ψ3,1][x], {x, -λ, λ},
    MaxRecursion → 100]^-0.5;
α3,2 =
  NIntegrate[Evaluate[Ψ3,2][x] * Evaluate[Ψ3,2][x], {x, -λ, λ},
    MaxRecursion → 100]^-0.5;
α3,3 =
  NIntegrate[Evaluate[Ψ3,3][x] * Evaluate[Ψ3,3][x], {x, -λ, λ},
    MaxRecursion → 100]^-0.5;
α3,4 =
  NIntegrate[Evaluate[Ψ3,4][x] * Evaluate[Ψ3,4][x], {x, -λ, λ},
    MaxRecursion → 100]^-0.5;
α3,5 =
  NIntegrate[Evaluate[Ψ3,5][x] * Evaluate[Ψ3,5][x], {x, -λ, λ},
    MaxRecursion → 100]^-0.5;
α3,6 =
  NIntegrate[Evaluate[Ψ3,6][x] * Evaluate[Ψ3,6][x], {x, -λ, λ},
    MaxRecursion → 100]^-0.5;
α3,7 =
  NIntegrate[Evaluate[Ψ3,7][x] * Evaluate[Ψ3,7][x], {x, -λ, λ},
    MaxRecursion → 100]^-0.5;
α3,8 =
  NIntegrate[Evaluate[Ψ3,8][x] * Evaluate[Ψ3,8][x], {x, -λ, λ},
    MaxRecursion → 100]^-0.5;
α3,9 =
  NIntegrate[Evaluate[Ψ3,9][x] * Evaluate[Ψ3,9][x], {x, -λ, λ},
    MaxRecursion → 100]^-0.5;
α3,10 =
  NIntegrate[Evaluate[Ψ3,10][x] * Evaluate[Ψ3,10][x], {x, -λ, λ},
    MaxRecursion → 100]^-0.5;
```

```
"Normalization for OH wavefunctions on 3rd Excited Surface";

p3,0 =
  NIntegrate[Evaluate[Ø3,0][y] * Evaluate[Ø3,0][y], {y, η, θ},
    MaxRecursion → 100]^-0.5;
p3,1 =
  NIntegrate[Evaluate[Ø3,1][y] * Evaluate[Ø3,1][y], {y, η, θ},
    MaxRecursion → 100]^-0.5;
p3,2 =
  NIntegrate[Evaluate[Ø3,2][y] * Evaluate[Ø3,2][y], {y, η, θ},
    MaxRecursion → 100]^-0.5;
p3,3 =
  NIntegrate[Evaluate[Ø3,3][y] * Evaluate[Ø3,3][y], {y, η, θ},
    MaxRecursion → 100]^-0.5;
p3,4 =
  NIntegrate[Evaluate[Ø3,4][y] * Evaluate[Ø3,4][y], {y, η, θ},
    MaxRecursion → 100]^-0.5;
p3,5 =
  NIntegrate[Evaluate[Ø3,5][y] * Evaluate[Ø3,5][y], {y, η, θ},
    MaxRecursion → 100]^-0.5;
p3,6 =
  NIntegrate[Evaluate[Ø3,6][y] * Evaluate[Ø3,6][y], {y, η, θ},
    MaxRecursion → 100]^-0.5;
p3,7 =
  NIntegrate[Evaluate[Ø3,7][y] * Evaluate[Ø3,7][y], {y, η, θ},
    MaxRecursion → 100]^-0.5;
p3,8 =
  NIntegrate[Evaluate[Ø3,8][y] * Evaluate[Ø3,8][y], {y, η, θ},
    MaxRecursion → 100]^-0.5;
p3,9 =
  NIntegrate[Evaluate[Ø3,9][y] * Evaluate[Ø3,9][y], {y, η, θ},
    MaxRecursion → 100]^-0.5;
p3,10 =
  NIntegrate[Evaluate[Ø3,10][y] * Evaluate[Ø3,10][y], {y, η, θ},
    MaxRecursion → 100]^-0.5;
```

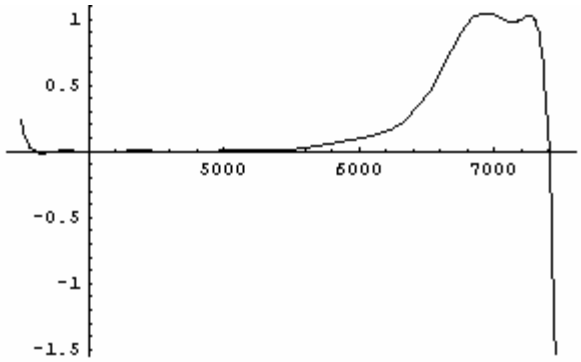

- Graphics -

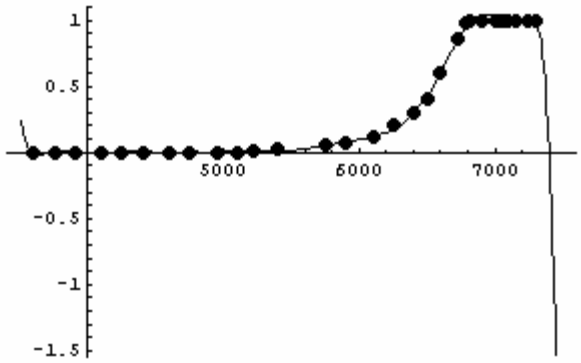

- Graphics -

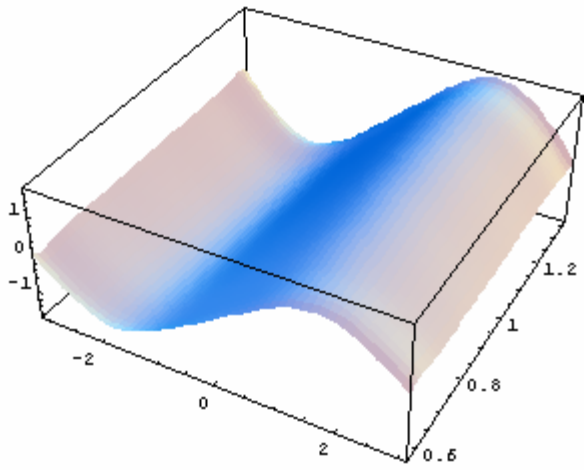

- SurfaceGraphics -

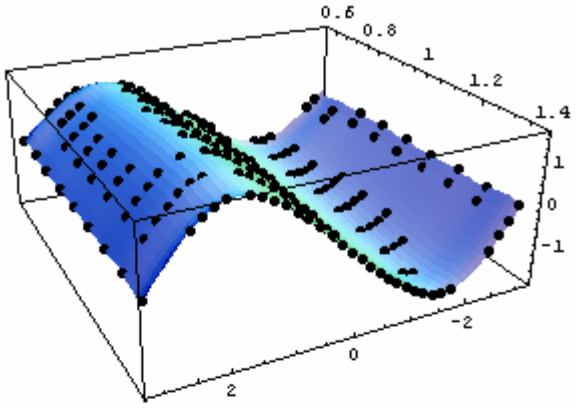

- Graphics3D -

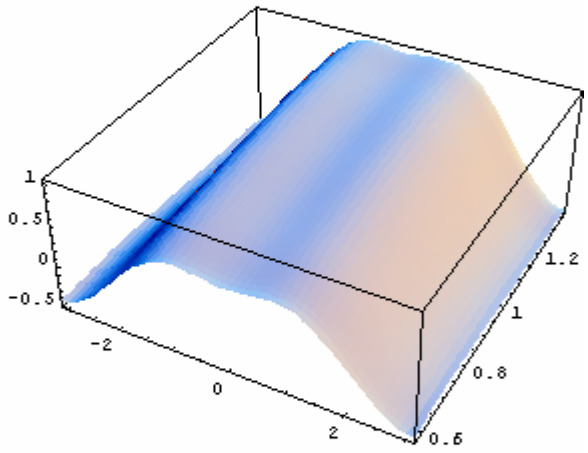

- SurfaceGraphics -

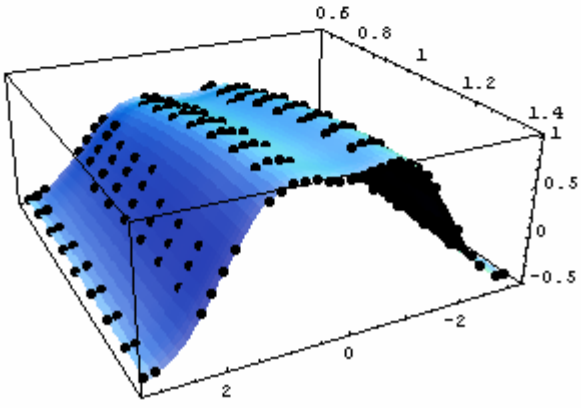

- Graphics3D -

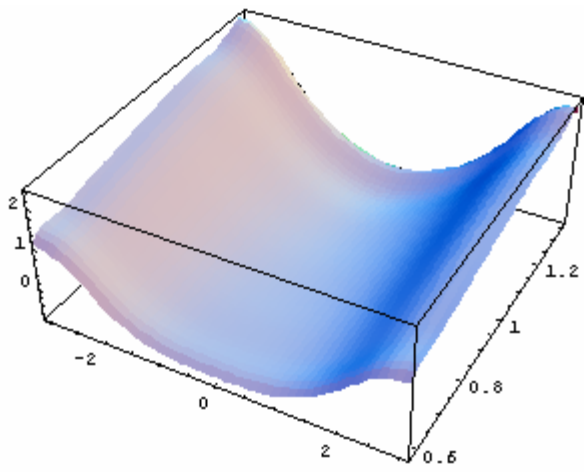

- SurfaceGraphics -

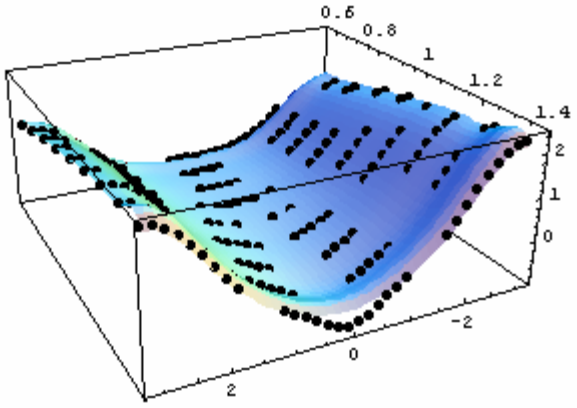

- Graphics3D -

```
"Dipole Moments Integration |j,k> → |m,n>";

Off[NIntegrate::inum]
Off[Part::pspec]
freq = transfreq;
ν = (freq[[m + 1, n + 1]] - freq[[j + 1, k + 1]]);
Clear[m, n, j, k]
σE =
  NIntegrate[Evaluate[Ø_{j,k}][γ] * Evaluate[Ψ_{j,k}][x] * μE * Evaluate[Ψ_{m,n}][x] *
     Evaluate[Ø_{m,n}][γ], {γ, η, θ}, {x, -λ, λ}] * (p_{j,k} * p_{m,n}) * (α_{j,k} * α_{m,n});
σY =
  NIntegrate[Evaluate[Ø_{j,k}][γ] * Evaluate[Ψ_{j,k}][x] * μY * Evaluate[Ψ_{m,n}][x] *
     Evaluate[Ø_{m,n}][γ], {γ, η, θ}, {x, -λ, λ}] * (p_{j,k} * p_{m,n}) * (α_{j,k} * α_{m,n});
σX =
  NIntegrate[Evaluate[Ø_{j,k}][γ] * Evaluate[Ψ_{j,k}][x] * μX * Evaluate[Ψ_{m,n}][x] *
     Evaluate[Ø_{m,n}][γ], {γ, η, θ}, {x, -λ, λ}] * (p_{j,k} * p_{m,n}) * (α_{j,k} * α_{m,n});
```

```
blz = Exp[-(freq[[j + 1, k + 1]] - freq[[1, 1]]) / (kb * T)];
f = 4.702*^-7 * ν * Σ;
kb = 0.695;
T = 300;
Σ = σX^2 + σY^2 + σB^2;
w = ν;
Print["2nu"]
Do[Print[AccountingForm[{, ν, f, blz * f, blz * f * qyf, j, k, m, n,}]],
 {j, 0, 0}, {k, 0, 10}, {m, 2, 2}, {n, 0, 10}]
Print["3nu"]
Do[Print[AccountingForm[{, ν, f, blz * f, blz * f * 1, j, k, m, n,}]],
 {j, 0, 0}, {k, 0, 10}, {m, 3, 3}, {n, 0, 10}]
Print["1nu"]
Do[Print[AccountingForm[{, ν, f, blz * f, blz * f * 1, j, k, m, n,}]],
 {j, 0, 0}, {k, 0, 10}, {m, 1, 1}, {n, 0, 10}]
Print["done!!!"]

"MERGE, COPY AS FORMATTED TEXT, PASTE IN WORD PAD, SAVE
   AS TEXT DOCUMENT!";
```

The output is comma separated where the values in each row correspond to:
{ Transition Frequency, Oscillator Strength, Oscillator Strength × Boltzmann Factor, Oscillator Strength × Boltzmann Factor × quantum yield, V^i_{OH}, V^i_{τ}, V^f_{OH}, V^f_{τ} }. Note that this program only considers the first ten (10) eigenstates associated with each adiabatic torsion curve. Also, this output only computes transitions between $V_{OH} = 0 \rightarrow 1$, 2 and 3. Values in parentheses are negative due to quantum yield interpolation error. These values however do not contribute in the $2\nu_{OH}$ region and can be ignored or be used without their quantum yield factor (as it is unity in this region). The quantum yield values are taken from J. L. Fry, S. A. Nizkorodov, M. Okumura, C. M. Roehl, J. S. Francisco, and P. O. Wennberg, J. Chem. Phys. 121, 1432(2004) but are not used in the final values reported in Chapter 4. Instead, the code in the next section is used to properly evaluate the quantum yield of *cis-cis* HOONO.

2nu
{Null,6485.3,0.000000275864,0.000000275864,0.000000113,0,0,2,0,Null}
{Null,6882.9,0.0000000114777,0.0000000114777,0.0000000118495,0,0,2,1,Null}
{Null,7203.7,0.00000000300837,0.00000000300837,0.00000000301481,0,0,2,2,Null}
{Null,7437.5,0.0000000000407305,0.0000000000407305,(0.0000000000454795),0,0,2,3,Null}
{Null,7573.2,0.0000000000202283,0.0000000000202283,(0.0000000003282),0,0,2,4,Null}
{Null,7653.,0.000000000000122212,0.000000000000122212,(0.000000000000536703),0,0,2,5,Null}
{Null,7739.4,0.0000000000103954,0.0000000000103954,(0.0000000011465),0,0,2,6,Null}
{Null,7838.1,0.000000000000187546,0.000000000000187546,(0.000000000000521391),0,0,2,7,Null}
{Null,7936.9,0.0000000000399149,0.0000000000399149,(0.00000000254273),0,0,2,8,Null}
{Null,8035.6,0.000000000000119922,0.000000000000119922,(0.000000000162653),0,0,2,9,Null}
{Null,8129.,0.0000000000168664,0.0000000000168664,(0.00000000443433),0,0,2,10,Null}
{Null,6195.1,0.00000000949613,0.00000000236089,0.00000000035471,0,1,2,0,Null}

{Null,6592.7,0.000000289106,0.0000000718763,0.000000043026,0,1,2,1,Null}
{Null,6913.5,0.0000000348841,0.00000000867273,0.00000000903354,0,1,2,2,Null}
{Null,7147.3,0.0000000120492,0.00000000299561,0.00000000293291,0,1,2,3,Null}
{Null,7283.,0.000000000560764,0.000000000139415,0.000000000141574,0,1,2,4,Null}
{Null,7362.8,0.000000000205767,0.000000000051157,0.000000000320702,0,1,2,5,Null}
{Null,7449.2,0.0000000000872679,0.0000000000216962,(0.0000000000353854),0,1,2,6,Null}
{Null,7547.9,0.0000000000484713,0.0000000000120507,(0.000000000136225),0,1,2,7,Null}
{Null,7646.7,0.0000000000150032,0.00000000000373003,(0.000000000152343),0,1,2,8,Null}
{Null,7745.4,0.0000000000123019,0.00000000000305846,(0.000000000358025),0,1,2,9,Null}
{Null,7838.8,0.00000000000156089,0.000000000000388061,(0.000000000108552),0,1,2,10,Null}
{Null,5977.5,0.00000000236203,0.000000000206807,0.0000000000201945,0,2,2,0,Null}
{Null,6375.1,0.0000000135933,0.00000000119016,0.000000000318632,0,2,2,1,Null}
{Null,6695.9,0.000000270089,0.0000000236476,0.0000000188521,0,2,2,2,Null}
{Null,6929.7,0.0000000939562,0.00000000822631,0.00000000857956,0,2,2,3,Null}
{Null,7065.4,0.0000000460329,0.0000000040304,0.00000000400622,0,2,2,4,Null}
{Null,7145.2,0.00000000554164,0.000000000485197,0.000000000474882,0,2,2,5,Null}
{Null,7231.6,0.00000000263537,0.000000000230739,0.00000000023487,0,2,2,6,Null}
{Null,7330.3,0.000000000534856,0.0000000000468291,0.0000000000413842,0,2,2,7,Null}
{Null,7429.1,0.000000000260128,0.0000000000227755,(0.0000000000181942),0,2,2,8,Null}
{Null,7527.8,0.0000000000872719,0.00000000000764107,(0.0000000000633228),0,2,2,9,Null}
{Null,7621.2,0.0000000000388097,0.00000000000339798,(0.000000000102496),0,2,2,10,Null}
{Null,5856.5,0.0000000000166147,0.000000000000814207,0.000000000000059069,0,3,2,0,Null}
{Null,6254.1,0.00000000343024,0.0000000001681,0.0000000000296438,0,3,2,1,Null}
{Null,6574.9,0.00000000903542,0.000000000442783,0.0000000002501,0,3,2,2,Null}
{Null,6808.7,0.000000221566,0.0000000108579,0.0000000105579,0,3,2,3,Null}
{Null,6944.4,0.000000229936,0.0000000112681,0.0000000117435,0,3,2,4,Null}
{Null,7024.2,0.000000145585,0.00000000713443,0.0000000072356,0,3,2,5,Null}
{Null,7110.6,0.0000000273819,0.00000000134186,0.00000000131403,0,3,2,6,Null}
{Null,7209.3,0.00000000652678,0.000000000319846,0.00000000032158,0,3,2,7,Null}
{Null,7308.1,0.000000000177967,0.00000000000872131,0.00000000000846615,0,3,2,8,Null}
{Null,7406.8,0.000000000216298,0.0000000000105997,(0.00000000000140082),0,3,2,9,Null}
{Null,7500.2,0.00000000000357122,0.000000000000175009,(0.000000000000903579),0,3,2,10,Null}
{Null,5799.8,0.0000000000783254,0.00000000000292444,0.000000000000176074,0,4,2,0,Null}
{Null,6197.4,0.0000000000433821,0.00000000000161976,0.000000000000244742,0,4,2,1,Null}
{Null,6518.2,0.00000000853107,0.000000000318525,0.000000000147511,0,4,2,2,Null}
{Null,6752.,0.0000000132657,0.000000000495303,0.000000000442885,0,4,2,3,Null}
{Null,6887.7,0.000000265381,0.00000000990854,0.0000000102497,0,4,2,4,Null}
{Null,6967.5,0.000000322806,0.0000000120526,0.0000000125063,0,4,2,5,Null}
{Null,7053.9,0.000000155845,0.00000000581879,0.00000000581504,0,4,2,6,Null}
{Null,7152.6,0.0000000245716,0.000000000917432,0.000000000899174,0,4,2,7,Null}
{Null,7251.4,0.0000000100724,0.000000000376075,0.000000000385527,0,4,2,8,Null}
{Null,7350.1,0.000000000251672,0.00000000000939669,0.00000000000704777,0,4,2,9,Null}
{Null,7443.5,0.0000000000887456,0.0000000000033135,(0.00000000000453728),0,4,2,10,Null}
{Null,5730.2,0.00000000000201425,0.000000000000538616,0.0000000000000245258,0,5,2,0,Null}
{Null,6127.8,0.00000000113404,0.0000000000303247,0.00000000000392845,0,5,2,1,Null}
{Null,6448.6,0.00000000181959,0.0000000000486565,0.0000000000173102,0,5,2,2,Null}
{Null,6682.4,0.0000000458508,0.00000000122606,0.000000000946511,0,5,2,3,Null}
{Null,6818.1,0.0000000180353,0.00000000048227,0.000000000473991,0,5,2,4,Null}
{Null,6897.9,0.000000230927,0.00000000617507,0.0000000064099,0,5,2,5,Null}
{Null,6984.3,0.000000308314,0.00000000824441,0.00000000850934,0,5,2,6,Null}
{Null,7083.,0.000000151651,0.00000000405521,0.00000000400174,0,5,2,7,Null}
{Null,7181.8,0.0000000229079,0.000000000612565,0.000000000606688,0,5,2,8,Null}
{Null,7280.5,0.0000000124606,0.000000000333201,0.000000000339115,0,5,2,9,Null}
{Null,7373.9,0.00000000102604,0.0000000000274365,0.0000000000134309,0,5,2,10,Null}

{Null,5643.1,0.0000000000553351,0.000000000000974413,0.0000000000000289005,0,6,2,0,Null}
{Null,6040.7,0.0000000000276518,0.000000000000486929,0.0000000000000536337,0,6,2,1,Null}
{Null,6361.5,0.00000000428312,0.0000000000754226,0.0000000000191815,0,6,2,2,Null}
{Null,6595.3,0.00000000751734,0.000000000132375,0.0000000000799015,0,6,2,3,Null}
{Null,6731.,0.0000000541019,0.000000000952696,0.000000000819012,0,6,2,4,Null}
{Null,6810.8,0.000000012957,0.000000000228164,0.000000000222409,0,6,2,5,Null}
{Null,6897.2,0.000000225677,0.000000003974,0.00000000412428,0,6,2,6,Null}
{Null,6995.9,0.000000303368,0.0000000053421,0.0000000054889,0,6,2,7,Null}
{Null,7094.7,0.000000168732,0.00000000297125,0.00000000292063,0,6,2,8,Null}
{Null,7193.4,0.0000000205669,0.000000000362168,0.000000000360839,0,6,2,9,Null}
{Null,7286.8,0.0000000139381,0.00000000024544,0.000000000248245,0,6,2,10,Null}
{Null,5558.,0.00000000000423818,0.000000000000496206,0.0000000000000091564,0,7,2,0,Null}
{Null,5955.6,0.000000000350508,0.00000000000410375,0.000000000000382814,0,7,2,1,Null}
{Null,6276.4,0.000000000284964,0.00000000000333636,0.000000000000630199,0,7,2,2,Null}
{Null,6510.2,0.00000000781143,0.0000000000914563,0.000000000041126,0,7,2,3,Null}
{Null,6645.9,0.00000000931289,0.000000000109035,0.0000000000765259,0,7,2,4,Null}
{Null,6725.7,0.0000000486439,0.000000000569523,0.000000000484434,0,7,2,5,Null}
{Null,6812.1,0.0000000133971,0.000000000156853,0.000000000153127,0,7,2,6,Null}
{Null,6910.8,0.000000240356,0.00000000281409,0.00000000292988,0,7,2,7,Null}
{Null,7009.6,0.000000305863,0.00000000358105,0.00000000365732,0,7,2,8,Null}
{Null,7108.3,0.000000188505,0.00000000220702,0.00000000216217,0,7,2,9,Null}
{Null,7201.7,0.000000013233,0.000000000154932,0.000000000155086,0,7,2,10,Null}
{Null,5472.3,0.0000000000142054,0.000000000000110262,0.0000000000000132609,0,8,2,0,Null}
{Null,5869.9,0.0000000000196525,0.000000000000152543,0.0000000000000115078,0,8,2,1,Null}
{Null,6190.7,0.00000000113339,0.0000000000879739,0.0000000000130768,0,8,2,2,Null}
{Null,6424.5,0.00000000138193,0.0000000000107266,0.0000000000347492,0,8,2,3,Null}
{Null,6560.2,0.000000006478,0.0000000000502824,0.0000000000270266,0,8,2,4,Null}
{Null,6640.,0.0000000117253,0.0000000000910118,0.0000000000628308,0,8,2,5,Null}
{Null,6726.4,0.0000000558331,0.000000000433377,0.000000000369151,0,8,2,6,Null}
{Null,6825.1,0.00000000915084,0.000000000071029,0.0000000000703266,0,8,2,7,Null}
{Null,6923.9,0.000000242516,0.00000000188241,0.00000000196285,0,8,2,8,Null}
{Null,7022.6,0.0000002889,0.00000000224244,0.00000000227602,0,8,2,9,Null}
{Null,7116.,0.000000220273,0.00000000170977,0.00000000167294,0,8,2,10,Null}
{Null,5388.1,0.0000000000416802,0.000000000000216033,0.0000000000000000209368,0,9,2,0,Null}
{Null,5785.7,0.000000000118038,0.000000000000611805,0.0000000000000349702,0,9,2,1,Null}
{Null,6106.5,0.000000000053266,0.000000000000276084,0.0000000000000343156,0,9,2,2,Null}
{Null,6340.3,0.0000000021387,0.0000000000110851,0.0000000000260652,0,9,2,3,Null}
{Null,6476.,0.00000000172132,0.0000000000892179,0.0000000000352742,0,9,2,4,Null}
{Null,6555.8,0.00000000644455,0.0000000000334028,0.0000000000176845,0,9,2,5,Null}
{Null,6642.2,0.000000016557,0.0000000000858165,0.0000000000596119,0,9,2,6,Null}
{Null,6740.9,0.0000000618747,0.000000000320704,0.000000000281016,0,9,2,7,Null}
{Null,6839.7,0.00000000475283,0.0000000000246344,0.0000000000247288,0,9,2,8,Null}
{Null,6938.4,0.000000256161,0.00000000132771,0.00000000138442,0,9,2,9,Null}
{Null,7031.8,0.000000263714,0.00000000136686,0.00000000138101,0,9,2,10,Null}
{Null,5325.7,0.0000000000458042,0.000000000000176003,0.0000000000000000167718,0,10,2,0,Null}
{Null,5723.3,0.0000000000019107,0.000000000000000734187,0.0000000000000000324155,0,10,2,1,Null}
{Null,6044.1,0.000000000385274,0.00000000000148042,0.000000000000164076,0,10,2,2,Null}
{Null,6277.9,0.00000000041468,0.00000000000159341,0.000000000000302422,0,10,2,3,Null}
{Null,6413.6,0.0000000014586,0.00000000000560469,0.00000000000174033,0,10,2,4,Null}
{Null,6493.4,0.00000000198699,0.00000000000763503,0.00000000000322468,0,10,2,5,Null}
{Null,6579.8,0.00000000967648,0.0000000000371819,0.0000000000213449,0,10,2,6,Null}
{Null,6678.5,0.0000000179726,0.0000000000690598,0.0000000000528041,0,10,2,7,Null}
{Null,6777.3,0.0000000589049,0.000000000226342,0.000000000210961,0,10,2,8,Null}
{Null,6876.,0.000000000245223,0.000000000000942271,0.000000000000969653,0,10,2,9,Null}

{Null,6969.4,0.00000025399,0.000000000975957,0.00000000101217,0,10,2,10,Null}
3nu
{Null,9438.3,0.0000000237122,0.0000000237122,0.0000000237122,0,0,3,0,Null}
{Null,9890.1,0.000000000541844,0.000000000541844,0.000000000541844,0,0,3,1,Null}
{Null,10261.1,0.000000000364434,0.000000000364434,0.000000000364434,0,0,3,2,Null}
{Null,10544.9,0.00000000000996186,0.00000000000996186,0.00000000000996186,0,0,3,3,Null}
{Null,10728.2,0.000000000000340049,0.000000000000340049,0.000000000000340049,0,0,3,4,Null}
{Null,10832.2,0.000000000000773765,0.000000000000773765,0.000000000000773765,0,0,3,5,Null}
{Null,10920.3,0.000000000000741504,0.000000000000741504,0.000000000000741504,0,0,3,6,Null}
{Null,11022.7,0.000000000000135555,0.000000000000135555,0.000000000000135555,0,0,3,7,Null}
{Null,11128.2,0.000000000000263623,0.000000000000263623,0.000000000000263623,0,0,3,8,Null}
{Null,11234.1,0.000000000000381576,0.000000000000381576,0.000000000000381576,0,0,3,9,N
ull}
{Null,11337.7,0.0000000000000692415,0.0000000000000692415,0.0000000000000692415,0,0,3,10,
Null}
{Null,9148.1,0.000000000760963,0.000000000189188,0.000000000189188,0,1,3,0,Null}
{Null,9599.9,0.0000000268714,0.00000000668067,0.00000000668067,0,1,3,1,Null}
{Null,9970.9,0.00000000190572,0.000000000473792,0.000000000473792,0,1,3,2,Null}
{Null,10254.7,0.00000000126271,0.00000000031393,0.00000000031393,0,1,3,3,Null}
{Null,10438.,0.0000000000572126,0.000000000014224,0.000000000014224,0,1,3,4,Null}
{Null,10542.,0.00000000000485734,0.00000000000120761,0.00000000000120761,0,1,3,5,Null}
{Null,10630.1,0.00000000000150255,0.00000000000373559,0.00000000000373559,0,1,3,6,Null}
{Null,10732.5,0.00000000000179378,0.00000000000445962,0.00000000000445962,0,1,3,7,Null}
{Null,10838.,0.00000000000227163,0.00000000000564764,0.00000000000564764,0,1,3,8,Null}
{Null,10943.9,0.00000000000472257,0.00000000000117411,0.00000000000117411,0,1,3,9,Null}
{Null,11047.5,0.00000000000034185,0.00000000000000849894,0.00000000000000849894,0,1,3,10,Nul
l}
{Null,8930.5,0.000000000645263,0.0000000000564958,0.0000000000564958,0,2,3,0,Null}
{Null,9382.3,0.00000000112573,0.0000000000985633,0.0000000000985633,0,2,3,1,Null}
{Null,9753.3,0.0000000294688,0.00000000258013,0.00000000258013,0,2,3,2,Null}
{Null,10037.1,0.00000000390003,0.000000000341466,0.000000000341466,0,2,3,3,Null}
{Null,10220.4,0.00000000470048,0.000000000411549,0.000000000411549,0,2,3,4,Null}
{Null,10324.4,0.000000000402311,0.0000000000352243,0.0000000000352243,0,2,3,5,Null}
{Null,10412.5,0.0000000000333759,0.0000000000292222,0.0000000000292222,0,2,3,6,Null}
{Null,10514.9,0.00000000000990451,0.00000000000867186,0.00000000000867186,0,2,3,7,Null}
{Null,10620.4,0.0000000000137337,0.00000000000120245,0.00000000000120245,0,2,3,8,Null}
{Null,10726.3,0.0000000000022051,0.00000000000193067,0.00000000000193067,0,2,3,9,Null}
{Null,10829.9,0.0000000000014549,0.00000000000127383,0.00000000000127383,0,2,3,10,Null}
{Null,8809.5,0.0000000000305409,0.0000000000149666,0.0000000000149666,0,3,3,0,Null}
{Null,9261.3,0.00000000133701,0.0000000000655204,0.0000000000655204,0,3,3,1,Null}
{Null,9632.3,0.000000000699205,0.0000000000342647,0.0000000000342647,0,3,3,2,Null}
{Null,9916.1,0.0000000196208,0.000000000961522,0.000000000961522,0,3,3,3,Null}
{Null,10099.4,0.0000000893185,0.000000000437708,0.000000000437708,0,3,3,4,Null}
{Null,10203.4,0.0000000140234,0.000000000687221,0.000000000687221,0,3,3,5,Null}
{Null,10291.5,0.00000000247643,0.000000000121358,0.000000000121358,0,3,3,6,Null}
{Null,10393.9,0.000000000334195,0.0000000000163773,0.0000000000163773,0,3,3,7,Null}
{Null,10499.4,0.00000000000347374,0.00000000000170232,0.00000000000170232,0,3,3,8,Null}
{Null,10605.3,0.000000000119258,0.0000000000584428,0.0000000000584428,0,3,3,9,Null}
{Null,10708.9,0.0000000000013277,0.00000000000000650642,0.00000000000000650642,0,3,3,10,Null}
{Null,8752.8,0.0000000000684962,0.0000000000255745,0.0000000000255745,0,4,3,0,Null}
{Null,9204.6,0.0000000000858642,0.0000000000320592,0.0000000000320592,0,4,3,1,Null}
{Null,9575.6,0.00000000345493,0.000000000128997,0.000000000128997,0,4,3,2,Null}
{Null,9859.4,0.000000000330801,0.0000000000123511,0.0000000000123511,0,4,3,3,Null}
{Null,10042.7,0.0000000185403,0.00000000069224,0.00000000069224,0,4,3,4,Null}

{Null,10146.7,0.0000000126095,0.000000000470799,0.000000000470799,0,4,3,5,Null}
{Null,10234.8,0.0000000185397,0.000000000692216,0.000000000692216,0,4,3,6,Null}
{Null,10337.2,0.00000000312436,0.000000000116654,0.000000000116654,0,4,3,7,Null}
{Null,10442.7,0.000000000984785,0.000000000036769,0.000000000036769,0,4,3,8,Null}
{Null,10548.6,0.0000000000101781,0.000000000000380022,0.000000000000380022,0,4,3,9,Null}
{Null,10652.2,0.0000000000929276,0.000000000000346964,0.000000000000346964,0,4,3,10,Null}
{Null,8683.2,0.0000000000118512,0.000000000000316905,0.000000000000316905,0,5,3,0,Null}
{Null,9135.,0.000000000745157,0.0000000000199257,0.0000000000199257,0,5,3,1,Null}
{Null,9506.,0.000000000392559,0.0000000000104971,0.0000000000104971,0,5,3,2,Null}
{Null,9789.8,0.00000000994613,0.000000000265963,0.000000000265963,0,5,3,3,Null}
{Null,9973.1,0.0000000000533293,0.000000000000142604,0.000000000000142604,0,5,3,4,Null}
{Null,10077.1,0.0000000116888,0.000000000312562,0.000000000312562,0,5,3,5,Null}
{Null,10165.2,0.0000000117638,0.000000000314567,0.000000000314567,0,5,3,6,Null}
{Null,10267.6,0.0000000178242,0.000000000476625,0.000000000476625,0,5,3,7,Null}
{Null,10373.1,0.00000000298038,0.0000000000796962,0.0000000000796962,0,5,3,8,Null}
{Null,10479.,0.00000000131112,0.0000000000350598,0.0000000000350598,0,5,3,9,Null}
{Null,10582.6,0.000000000000263115,0.0000000000000703578,0.0000000000000703578,0,5,3,10,Nul
l}
{Null,8596.1,0.00000000004759,0.000000000000838026,0.000000000000838026,0,6,3,0,Null}
{Null,9047.9,0.0000000000675099,0.0000000000011888,0.0000000000011888,0,6,3,1,Null}
{Null,9418.9,0.00000000217369,0.0000000000382772,0.0000000000382772,0,6,3,2,Null}
{Null,9702.7,0.000000000463937,0.0000000000081696,0.0000000000081696,0,6,3,3,Null}
{Null,9886.,0.00000000913741,0.000000000160903,0.000000000160903,0,6,3,4,Null}
{Null,9990.,0.000000000000299743,0.0000000000000527826,0.0000000000000527826,0,6,3,5,Null}
{Null,10078.1,0.00000000996176,0.00000000017542,0.00000000017542,0,6,3,6,Null}
{Null,10180.5,0.0000000116397,0.000000000204966,0.000000000204966,0,6,3,7,Null}
{Null,10286.,0.000000017988,0.000000000316757,0.000000000316757,0,6,3,8,Null}
{Null,10391.9,0.00000000315545,0.0000000000555653,0.0000000000555653,0,6,3,9,Null}
{Null,10495.5,0.0000000016678,0.0000000000293688,0.0000000000293688,0,6,3,10,Null}
{Null,8511.,0.000000000000389436,0.000000000000000455952,0.000000000000000455952,0,7,3,0,Null}
{Null,8962.8,0.00000000029333,0.000000000000343431,0.000000000000343431,0,7,3,1,Null}
{Null,9333.8,0.000000000154599,0.000000000000181004,0.000000000000181004,0,7,3,2,Null}
{Null,9617.6,0.00000000331723,0.0000000000388381,0.0000000000388381,0,7,3,3,Null}
{Null,9800.9,0.000000000372362,0.000000000000435961,0.000000000000435961,0,7,3,4,Null}
{Null,9904.9,0.00000000594678,0.000000000069625,0.000000000069625,0,7,3,5,Null}
{Null,9993.,0.000000000000222423,0.000000000000000260413,0.000000000000000260413,0,7,3,6,Null}
{Null,10095.4,0.000000012108,0.00000000014176,0.00000000014176,0,7,3,7,Null}
{Null,10200.9,0.000000011603,0.000000000135848,0.000000000135848,0,7,3,8,Null}
{Null,10306.8,0.0000000216724,0.00000000025374,0.00000000025374,0,7,3,9,Null}
{Null,10410.4,0.00000000293035,0.0000000000343085,0.0000000000343085,0,7,3,10,Null}
{Null,8425.3,0.000000000186319,0.000000000000144621,0.000000000000144621,0,8,3,0,Null}
{Null,8877.1,0.000000000212587,0.000000000000016501,0.000000000000016501,0,8,3,1,Null}
{Null,9248.1,0.0000000008608,0.000000000000668154,0.000000000000668154,0,8,3,2,Null}
{Null,9531.9,0.00000000019528,0.000000000000151577,0.000000000000151577,0,8,3,3,Null}
{Null,9715.2,0.00000000279403,0.0000000000216873,0.0000000000216873,0,8,3,4,Null}
{Null,9819.2,0.000000000339677,0.000000000000263658,0.000000000000263658,0,8,3,5,Null}
{Null,9907.3,0.00000000605444,0.0000000000469947,0.0000000000469947,0,8,3,6,Null}
{Null,10009.7,0.000000000241041,0.000000000000187096,0.000000000000187096,0,8,3,7,Null}
{Null,10115.2,0.000000011532,0.000000000895118,0.000000000895118,0,8,3,8,Null}
{Null,10221.1,0.0000000109844,0.000000000085261,0.000000000085261,0,8,3,9,Null}
{Null,10324.7,0.0000000240893,0.000000000186981,0.000000000186981,0,8,3,10,Null}
{Null,8341.1,0.000000000000142556,0.000000000000000738881,0.000000000000000738881,0,9,3,0,Null}
{Null,8792.9,0.000000000121455,0.000000000000629517,0.000000000000629517,0,9,3,1,Null}
{Null,9163.9,0.000000000068122,0.000000000000353084,0.000000000000353084,0,9,3,2,Null}

{Null,9447.7,0.0000000012824,0.0000000000066468,0.0000000000066468,0,9,3,3,Null}
{Null,9631.,0.000000000171143,0.00000000000887055,0.00000000000887055,0,9,3,4,Null}
{Null,9735.,0.00000000178358,0.00000000000924447,0.00000000000924447,0,9,3,5,Null}
{Null,9823.1,0.00000000044743,0.00000000000231908,0.00000000000231908,0,9,3,6,Null}
{Null,9925.5,0.00000000704755,0.0000000000365282,0.0000000000365282,0,9,3,7,Null}
{Null,10031.,0.000000000169583,0.00000000000878966,0.00000000000878966,0,9,3,8,Null}
{Null,10136.9,0.0000000114436,0.0000000000593136,0.0000000000593136,0,9,3,9,Null}
{Null,10240.5,0.00000001111,0.0000000000575844,0.0000000000575844,0,9,3,10,Null}
{Null,8278.7,0.00000000000659022,0.00000000000000025323,0.00000000000000025323,0,10,3,0,Null}
{Null,8730.5,0.00000000000942967,0.00000000000000362335,0.00000000000000362335,0,10,3,1,Null}
{Null,9101.5,0.0000000000301301,0.00000000000115775,0.00000000000115775,0,10,3,2,Null}
{Null,9385.3,0.0000000000905965,0.00000000000000348118,0.00000000000000348118,0,10,3,3,Null}
{Null,9568.6,0.000000000853083,0.00000000000327798,0.00000000000327798,0,10,3,4,Null}
{Null,9672.6,0.00000000033899,0.00000000000130257,0.00000000000130257,0,10,3,5,Null}
{Null,9760.7,0.00000000169144,0.00000000000649938,0.00000000000649938,0,10,3,6,Null}
{Null,9863.1,0.0000000000426455,0.00000000000163866,0.00000000000163866,0,10,3,7,Null}
{Null,9968.6,0.00000000604248,0.0000000000232182,0.0000000000232182,0,10,3,8,Null}
{Null,10074.5,0.0000000000879333,0.00000000000337884,0.00000000000337884,0,10,3,9,Null}
{Null,10178.1,0.00000000531903,0.0000000000204384,0.0000000000204384,0,10,3,10,Null}
lnu
{Null,3331.7,0.00000377461,0.00000377461,0.00000377461,0,0,1,0,Null}
{Null,3675.,0.000000207193,0.000000207193,0.000000207193,0,0,1,1,Null}
{Null,3944.8,0.0000000372135,0.0000000372135,0.0000000372135,0,0,1,2,Null}
{Null,4124.8,0.00000000193776,0.00000000193776,0.00000000193776,0,0,1,3,Null}
{Null,4214.8,0.00000000353556,0.00000000353556,0.00000000353556,0,0,1,4,Null}
{Null,4282.2,0.000000000886619,0.000000000886619,0.000000000886619,0,0,1,5,Null}
{Null,4370.6,0.00000000179312,0.00000000179312,0.00000000179312,0,0,1,6,Null}
{Null,4463.,0.000000000436942,0.000000000436942,0.000000000436942,0,0,1,7,Null}
{Null,4555.1,0.00000000056437,0.00000000056437,0.00000000056437,0,0,1,8,Null}
{Null,4646.3,0.000000000171023,0.000000000171023,0.000000000171023,0,0,1,9,Null}
{Null,4726.6,0.000000000180304,0.000000000180304,0.000000000180304,0,0,1,10,Null}
{Null,3041.5,0.00000000600208,0.00000000149221,0.00000000149221,0,1,1,0,Null}
{Null,3384.8,0.00000205105,0.000000509923,0.000000509923,0,1,1,1,Null}
{Null,3654.6,0.000000435264,0.000000108214,0.000000108214,0,1,1,2,Null}
{Null,3834.6,0.000000148346,0.0000000368812,0.0000000368812,0,1,1,3,Null}
{Null,3924.6,0.0000000012864,0.000000000319819,0.000000000319819,0,1,1,4,Null}
{Null,3992.,0.0000000327615,0.00000000814503,0.00000000814503,0,1,1,5,Null}
{Null,4080.4,0.00000000241138,0.000000000599507,0.000000000599507,0,1,1,6,Null}
{Null,4172.8,0.00000000998737,0.00000000248302,0.00000000248302,0,1,1,7,Null}
{Null,4264.9,0.0000000012975,0.00000000032258,0.00000000032258,0,1,1,8,Null}
{Null,4356.1,0.0000000029266,0.000000000727598,0.000000000727598,0,1,1,9,Null}
{Null,4436.4,0.000000000591737,0.000000000147115,0.000000000147115,0,1,1,10,Null}
{Null,2823.9,0.00000000548307,0.000000000480069,0.000000000480069,0,2,1,0,Null}
{Null,3167.2,0.0000000618902,0.00000000541878,0.00000000541878,0,2,1,1,Null}
{Null,3437.,0.000000913841,0.0000000800111,0.0000000800111,0,2,1,2,Null}
{Null,3617.,0.00000152801,0.000000133785,0.000000133785,0,2,1,3,Null}
{Null,3707.,0.000000422085,0.0000000369555,0.0000000369555,0,2,1,4,Null}
{Null,3774.4,0.000000000219458,0.0000000000192146,0.0000000000192146,0,2,1,5,Null}
{Null,3862.8,0.0000000815072,0.00000000713634,0.00000000713634,0,2,1,6,Null}
{Null,3955.2,0.00000000130727,0.000000000114457,0.000000000114457,0,2,1,7,Null}
{Null,4047.3,0.0000000136658,0.0000000011965,0.0000000011965,0,2,1,8,Null}
{Null,4138.5,0.000000000597612,0.0000000000523237,0.0000000000523237,0,2,1,9,Null}
{Null,4218.8,0.000000003989,0.000000000349256,0.000000000349256,0,2,1,10,Null}
{Null,2702.9,0.00000000487986,0.000000000239139,0.000000000239139,0,3,1,0,Null}

{Null,3046.2,0.00000000790975,0.000000000387619,0.000000000387619,0,3,1,1,Null}
{Null,3316.,0.000000131107,0.00000000642493,0.00000000642493,0,3,1,2,Null}
{Null,3496.,0.00000101543,0.0000000497617,0.0000000497617,0,3,1,3,Null}
{Null,3586.,0.00000263489,0.000000129124,0.000000129124,0,3,1,4,Null}
{Null,3653.4,0.00000112736,0.0000000552464,0.0000000552464,0,3,1,5,Null}
{Null,3741.8,0.0000000170465,0.00000000083537,0.00000000083537,0,3,1,6,Null}
{Null,3834.2,0.0000000838049,0.00000000410688,0.00000000410688,0,3,1,7,Null}
{Null,3926.3,0.00000000147334,0.0000000000722016,0.0000000000722016,0,3,1,8,Null}
{Null,4017.5,0.00000000304256,0.000000000149102,0.000000000149102,0,3,1,9,Null}
{Null,4097.8,0.0000000000813424,0.00000000000398621,0.00000000000398621,0,3,1,10,Null}
{Null,2646.2,0.00000000014329,0.00000000000535003,0.00000000000535003,0,4,1,0,Null}
{Null,2989.5,0.0000000384482,0.00000000143554,0.00000000143554,0,4,1,1,Null}
{Null,3259.3,0.0000000182717,0.00000000068221,0.00000000068221,0,4,1,2,Null}
{Null,3439.3,0.00000000247854,0.0000000000925412,0.0000000000925412,0,4,1,3,Null}
{Null,3529.3,0.00000150969,0.0000000563675,0.0000000563675,0,4,1,4,Null}
{Null,3596.7,0.00000199314,0.0000000744179,0.0000000744179,0,4,1,5,Null}
{Null,3685.1,0.00000102305,0.0000000381977,0.0000000381977,0,4,1,6,Null}
{Null,3777.5,0.0000000187118,0.000000000698642,0.000000000698642,0,4,1,7,Null}
{Null,3869.6,0.000000049769,0.00000000185823,0.00000000185823,0,4,1,8,Null}
{Null,3960.8,0.00000000447574,0.000000000167111,0.000000000167111,0,4,1,9,Null}
{Null,4041.1,0.00000000227084,0.0000000000847863,0.0000000000847863,0,4,1,10,Null}
{Null,2576.6,0.00000000315778,0.00000000008444,0.00000000008444,0,5,1,0,Null}
{Null,2919.9,0.00000000263642,0.0000000000704988,0.0000000000704988,0,5,1,1,Null}
{Null,3189.7,0.000000112426,0.00000000300632,0.00000000300632,0,5,1,2,Null}
{Null,3369.7,0.00000021203,0.00000000566976,0.00000000566976,0,5,1,3,Null}
{Null,3459.7,0.000000336559,0.0000000089997,0.0000000089997,0,5,1,4,Null}
{Null,3527.1,0.00000174078,0.0000000465491,0.0000000465491,0,5,1,5,Null}
{Null,3615.5,0.00000181286,0.0000000484764,0.0000000484764,0,5,1,6,Null}
{Null,3707.9,0.00000136074,0.0000000363867,0.0000000363867,0,5,1,7,Null}
{Null,3800.,0.00000000768832,0.000000000205588,0.000000000205588,0,5,1,8,Null}
{Null,3891.2,0.0000000691975,0.00000000185036,0.00000000185036,0,5,1,9,Null}
{Null,3971.5,0.0000000144059,0.000000000385217,0.000000000385217,0,5,1,10,Null}
{Null,2489.5,0.0000000000636662,0.00000000000112112,0.00000000000112112,0,6,1,0,Null}
{Null,2832.8,0.0000000162292,0.000000000285785,0.000000000285785,0,6,1,1,Null}
{Null,3102.6,0.0000000173249,0.00000000030508,0.00000000030508,0,6,1,2,Null}
{Null,3282.6,0.00000000000237394,0.000000000000418033,0.000000000000418033,0,6,1,3,Null}
{Null,3372.6,0.000000487614,0.00000000858653,0.00000000858653,0,6,1,4,Null}
{Null,3440.,0.000000453321,0.00000000798266,0.00000000798266,0,6,1,5,Null}
{Null,3528.4,0.00000171309,0.0000000301662,0.0000000301662,0,6,1,6,Null}
{Null,3620.8,0.00000275315,0.000000048481,0.000000048481,0,6,1,7,Null}
{Null,3712.9,0.00000171334,0.0000000301707,0.0000000301707,0,6,1,8,Null}
{Null,3804.1,0.00000000140948,0.00000000002482,0.00000000002482,0,6,1,9,Null}
{Null,3884.4,0.0000000914292,0.00000000161,0.00000000161,0,6,1,10,Null}
{Null,2404.4,0.00000000105907,0.0000000000123996,0.0000000000123996,0,7,1,0,Null}
{Null,2747.7,0.000000000703476,0.00000000000823631,0.00000000000823631,0,7,1,1,Null}
{Null,3017.5,0.0000000294839,0.000000000345198,0.000000000345198,0,7,1,2,Null}
{Null,3197.5,0.0000000676057,0.000000000791529,0.000000000791529,0,7,1,3,Null}
{Null,3287.5,0.0000000153296,0.000000000179479,0.000000000179479,0,7,1,4,Null}
{Null,3354.9,0.000000501196,0.00000000586801,0.00000000586801,0,7,1,5,Null}
{Null,3443.3,0.000000336698,0.00000000394206,0.00000000394206,0,7,1,6,Null}
{Null,3535.7,0.00000186979,0.0000000218916,0.0000000218916,0,7,1,7,Null}
{Null,3627.8,0.00000191401,0.0000000224093,0.0000000224093,0,7,1,8,Null}
{Null,3719.,0.00000201853,0.000000023633,0.000000023633,0,7,1,9,Null}
{Null,3799.3,0.00000000810324,0.0000000000948728,0.0000000000948728,0,7,1,10,Null}

{Null,2318.7,0.0000000000191426,0.000000000000148585,0.000000000000148585,0,8,1,0,Null}
{Null,2662.,0.00000000617846,0.0000000000479573,0.0000000000479573,0,8,1,1,Null}
{Null,2931.8,0.00000000415924,0.0000000000322841,0.0000000000322841,0,8,1,2,Null}
{Null,3111.8,0.00000000205888,0.0000000000159811,0.0000000000159811,0,8,1,3,Null}
{Null,3201.8,0.0000000681193,0.000000000528743,0.000000000528743,0,8,1,4,Null}
{Null,3269.2,0.0000000243427,0.000000000188949,0.000000000188949,0,8,1,5,Null}
{Null,3357.6,0.000000430926,0.00000000334486,0.00000000334486,0,8,1,6,Null}
{Null,3450.,0.000000328779,0.00000000255199,0.00000000255199,0,8,1,7,Null}
{Null,3542.1,0.00000173043,0.0000000134317,0.0000000134317,0,8,1,8,Null}
{Null,3633.3,0.00000185214,0.0000000143764,0.0000000143764,0,8,1,9,Null}
{Null,3713.6,0.00000273488,0.0000000212282,0.0000000212282,0,8,1,10,Null}
{Null,2234.5,0.000000000386107,0.00000000000200123,0.00000000000200123,0,9,1,0,Null}
{Null,2577.8,0.000000000161682,0.000000000000838015,0.000000000000838015,0,9,1,1,Null}
{Null,2847.6,0.0000000101802,0.0000000000527652,0.0000000000527652,0,9,1,2,Null}
{Null,3027.6,0.0000000147901,0.0000000000766588,0.0000000000766588,0,9,1,3,Null}
{Null,3117.6,0.000000000133831,0.000000000000693659,0.000000000000693659,0,9,1,4,Null}
{Null,3185.,0.0000000822907,0.000000000426522,0.000000000426522,0,9,1,5,Null}
{Null,3273.4,0.0000000207417,0.000000000107506,0.000000000107506,0,9,1,6,Null}
{Null,3365.8,0.000000495706,0.0000000025693,0.0000000025693,0,9,1,7,Null}
{Null,3457.9,0.000000219457,0.00000000113747,0.00000000113747,0,9,1,8,Null}
{Null,3549.1,0.00000212964,0.0000000110382,0.0000000110382,0,9,1,9,Null}
{Null,3629.4,0.00000190768,0.00000000988772,0.00000000988772,0,9,1,10,Null}
{Null,2172.1,0.0000000000600604,0.000000000000230782,0.000000000000230782,0,10,1,0,Null}
{Null,2515.4,0.00000000185201,0.0000000000711636,0.0000000000711636,0,10,1,1,Null}
{Null,2785.2,0.000000000793332,0.0000000000304838,0.0000000000304838,0,10,1,2,Null}
{Null,2965.2,0.00000000121544,0.0000000000467035,0.0000000000467035,0,10,1,3,Null}
{Null,3055.2,0.0000000112687,0.0000000000433001,0.0000000000433001,0,10,1,4,Null}
{Null,3122.6,0.000000000106071,0.000000000000407578,0.000000000000407578,0,10,1,5,Null}
{Null,3211.,0.000000073915,0.000000000284019,0.000000000284019,0,10,1,6,Null}
{Null,3303.4,0.0000000348848,0.000000000134045,0.000000000134045,0,10,1,7,Null}
{Null,3395.5,0.000000271198,0.00000000104208,0.00000000104208,0,10,1,8,Null}
{Null,3486.7,0.0000000883223,0.000000000339379,0.000000000339379,0,10,1,9,Null}
{Null,3567.,0.00000370069,0.0000000142199,0.0000000142199,0,10,1,10,Null}
done!!!

D.9 Quantum Yield Calculation of *cis-cis* HOONO in the $2\nu_{OH}$ Region

In Chapter 4 we used a two-dimension ab initio model to simulate the action spectrum in the $2\nu_{OH}$ region of HOONO. To do this properly, the oscillator strength associated with a particular transition was scaled by the quantum yield factor in order to reflect the correct "transition weight". This program computes the quantum yield factor by approximating the dissociation quantum yield for each vibrational band by first shifting the entire thermal distribution of rotational states associated with its initial vibrational level by the energy of the vibrational overtone excitation photon and then determining the fraction of these states that have energies greater than D_0 = 19.9 kcal/mol.

Mathematica Program hoono_qy.nb:

Obtain HOONO parameter.

```
Off[General::spelll]
Off[General::spell]
Off[General::nffil]
T = 298;
kb = 0.6950387;
a = 0.714040412;
b = 0.265118544;
c = 0.193167025;
β = (b + c)/2;
g = 2 J + 1;
ε_r = β * J * (J + 1) + (a - β) * K^2;
blz = Exp[-ε_r/(kb * T)];
probε = g * blz * ε_r;
probi = g * blz;

Print["kappa= " , (2 * b - a - c) / (a - c)]
If[(2 * b - a - c) / (a - c) > 0, Print["Oblate Top"], Print["Prolate Top"]]
SetDirectory[
  "C:\Documents and Settings\overtone\My
    Documents\Jamie\Thesis\CHAPTERS\APPENDIXD\codes\qyhoono"];
```

```
kappa= -0.723727
Prolate Top
```

Using the expression for a Prolate top, evaluate the Boltzmann factor a particular E_J carry. J = 0 – 100 and runs $-J \leq K \leq +J$.

```
DeleteFile[{"er.txt"}];
DeleteFile[{"pr.txt"}];
DeleteFile[{"ddd.txt"}];

n = 100;
prob = Sum[g * blz, {J, 0, n}, {K, -J, J}];
Print["Partition function Q= ", prob]
```

```
d = 0;
Do[{Do[{If[d ≤ (ε_r) ≤ d + 10, probi / prob >>> er.txt]}, {J, 0, n}, {K, -J, J}];
  Inner[Times, ReadList["er.txt"], ReadList["er.txt"] / ReadList["er.txt"], Plus] >>> pr.txt,
  DeleteFile[{"er.txt"}], d >>> ddd.txt}, {d, 0, 2500, 10}]
```

These values are normalized by the partition function Q :

Partition function Q= 27295.2

```
zzz = {ReadList["ddd.txt"], ReadList["pr.txt"]};
yyy = Transpose[zzz];
bbb = ListPlot[yyy, PlotRange → {{0, 2500}, {0, 0.03}}, PlotJoined → False]
```

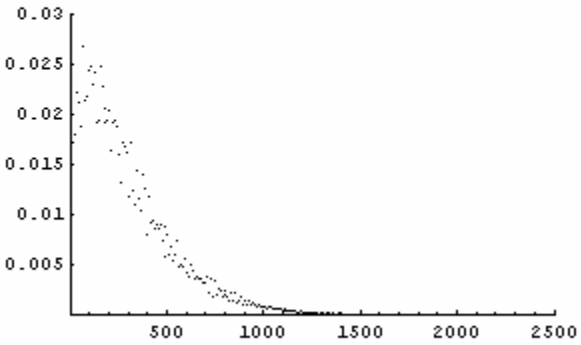

- Graphics -

Interpolate the data:

```
sss = Interpolation[yyy, InterpolationOrder → 3];
mmm = Plot[sss[x], {x, 0, 2500}]
Show[bbb, mmm]
```

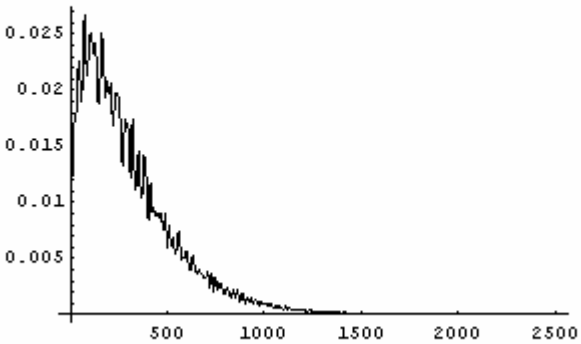

- Graphics -

Now pick a value for the photon energy, hv, - the excitation energy and the initial vibrational energy, vib, this particular energy this state carries:

```
hv = 6592;
vib = 290;
d0kcal = 19.9;
d0 = d0kcal * 349.7552764;
viblz = Exp[-vib / (kb * T)];
Print["Vibrational Bolzmann Factor= ", viblz]
Print["rotational energy required = ", d0 - hv - vib, "cm-1"]
```

```
Vibrational Bolzmann Factor= 0.246561
rotational energy required = 78.13cm-1
```

```
i = 80; f = 2500;
numeric = Take[ReadList["pr.txt"], {(i / 10 + 1), (f / 10 + 1), 1}];
Print["Quantum Yield = ",
 Inner[Times, numeric, numeric/numeric, Plus] /
  Inner[Times, Take[ReadList["pr.txt"], {1, 251, 1}],
   Take[ReadList["pr.txt"], {1, 251, 1}]/Take[ReadList["pr.txt"], {1, 251, 1}], Plus], " for states between ", i,
 " and ", f, " cm-1"]
```

```
Quantum Yield = 0.854203 for states between 80 and 2500 cm-1
```

```
i = 590; f = 2500;
numeric = Take[ReadList["pr.txt"], {(i / 10 + 1), (f / 10 + 1), 1}];

Print["f(diss)/f(survive) = ",
 Inner[Times, numeric, numeric/numeric, Plus] / (1 - Inner[Times, numeric, numeric/numeric, Plus]),
 " for states between ", i, " and ", f, " cm-1"]
```

```
f(diss)/f(survive) = 0.145626 for states between 590 and 2500 cm-1
```

D.10 Vibrational Term Value Calculation *cis-cis* HOONO

This program calculates the vibrational term values using the frequencies and anharmonicites of cis-cis obtained from the *ab initio* MP2/aug-cc-pVTZ calculation. ^{15}N data is also factored into the calculation which places additional constrains on the assignment in the $2\nu_{OH}$ region.

Mathematica Program vtv_cc.nb:

```
"This code computes the vibrational term value for a molecule
    based on anharmonicities and frequencies.
n is the # of atoms. " Go " is the zero pt energy";
"ωi are the harmonic frequencies and χi,j are the anharmonic
   frequencies.";
n = 5;
ω1 = 3487.2; ω2 = 1568.4; ω3 = 1433.7; ω4 = 971.0; ω5 = 836.6;
ω6 = 716.2; ω7 = 397.3; ω8 = 524.0; ω9 = 355.4;

χ1,1 = -111.0; χ1,2 = -2.7398; χ1,3 = -39.6613; χ1,4 = 3.73989; χ1,5 = 5.11222;
χ1,6 = 12.1801; χ1,7 = 2.20820; χ1,8 = 23.5844; χ1,9 = 65.1103;

χ2,1 = 0; χ2,2 = -9.72092; χ2,3 = -9.10827; χ2,4 = -3.40512; χ2,5 = -1.06247;
χ2,6 = 28.8206; χ2,7 = 0.383901; χ2,8 = 0.723536; χ2,9 = 4.39989;

χ3,1 = 0; χ3,2 = 0; χ3,3 = -5.94696; χ3,4 = -4.97211; χ3,5 = -8.55963; χ3,6 = -1.80166;
χ3,7 = -0.786474; χ3,8 = 3.53046; χ3,9 = 12.2089;

χ4,1 = 0; χ4,2 = 0; χ4,3 = 0; χ4,4 = -2.85769; χ4,5 = -9.11970; χ4,6 = -9.38890;
χ4,7 = -4.76739; χ4,8 = -2.52283; χ4,9 = -6.01977;

χ5,1 = 0; χ5,2 = 0; χ5,3 = 0; χ5,4 = 0; χ5,5 = -3.40467; χ5,6 = -4.72425;
χ5,7 = -3.12952; χ5,8 = -4.87140; χ5,9 = -3.98472;

χ6,1 = 0; χ6,2 = 0; χ6,3 = 0; χ6,4 = 0; χ6,5 = 0; χ6,6 = -28.3659; χ6,7 = -9.57796;
χ6,8 = -16.0073; χ6,9 = -39.5811;

χ7,1 = 0; χ7,2 = 0; χ7,3 = 0; χ7,4 = 0; χ7,5 = 0; χ7,6 = 0; χ7,7 = -3.53355;
χ7,8 = -6.54043; χ7,9 = -15.3504;

χ8,1 = 0; χ8,2 = 0; χ8,3 = 0; χ8,4 = 0; χ8,5 = 0; χ8,6 = 0; χ8,7 = 0; χ8,8 = -8.47216;
χ8,9 = -48.2422;
```

```
χ9,1 = 0; χ9,2 = 0; χ9,3 = 0; χ9,4 = 0; χ9,5 = 0; χ9,6 = 0; χ9,7 = 0; χ9,8 = 0;
χ9,9 = -38.1953;

νi = {ν1, ν2, ν3, ν4, ν5, ν6, ν7, ν8, ν9};
G[νi] = Sum[ωi * (νi + 0.5), {i, 1, 3n-6}] + Sum[(Sum[χi,k * (νi + .5) * (νk + .5), {i, 1, 3n-6}]), {k, 1, 3n-6}];

mi = {m1 = 0, m2 = 0, m3 = 0, m4 = 0, m5 = 0, m6 = 0, m7 = 0, m8 = 0, m9 = 0};
Go = Sum[ωi * (mi + 0.5), {i, 1, 3n-6}] + Sum[(Sum[χi,k * (mi + .5) * (mk + .5), {i, 1, 3n-6}]), {k, 1, 3n-6}];
Print["Go=", Go, "cm-1"]
ΔG = G[νi] - Go;
```

```
Go=5068.55cm-1
```

```
"αi -are the relative shifts.";
"a- parameter controls how many quantas for each mode to consider";
a = 6;
νi = {ν1, ν2, ν3, ν4, ν5, ν6, ν7, ν8, ν9};
αi = {α1 = -0.008, α2 = -24.46, α3 = -4.295, α4 = -6.561, α5 = -6.126,
   α6 = -9.993, α7 = -0.309, α8 = -6.075, α9 = -1.296};
Print["Energy      ν1→νi"]
Timing[
 Do[ If[6200 < ΔG < 11000 && Sum[νi, {i, 1, 3n-6}] < 6 && -11 < Sum[(νi * αi), {i, 1, 3n-6}] < 0,
   Print[ΔG, "    ", ν1, ν2, ν3, ν4, ν5, ν6, ν7, ν8, ν9, "  Sum of Quanta=  ",
    Sum[νi, {i, 1, 3n-6}], "  relative shift= ", N[Sum[(νi * αi), {i, 1, 3n-6}], 2], "cm-1" ]],
  {ν9, 0, a}, {ν8, 0, a}, {ν7, 0, a}, {ν6, 0, a}, {ν5, 0, a},
  {ν4, 0, a}, {ν3, 0, a}, {ν2, 0, a}, {ν1, 0, a}]]
```

```
Energy      ν1→νi
6377.93    200000000  Sum of Quanta=  2  relative shift= -0.016cm-1
9233.9    300000000  Sum of Quanta=  3  relative shift= -0.024cm-1
7695.84    201000000  Sum of Quanta=  3  relative shift= -4.311cm-1
10512.1    301000000  Sum of Quanta=  4  relative shift= -4.319cm-1
```

9001.86 202000000 Sum of Quanta= 4 relative shift= -8.606cm^{-1}

7332.47 200100000 Sum of Quanta= 3 relative shift= -6.577cm^{-1}

10192.2 300100000 Sum of Quanta= 4 relative shift= -6.585cm^{-1}

8645.41 201100000 Sum of Quanta= 4 relative shift= -10.872cm^{-1}

7202.78 200010000 Sum of Quanta= 3 relative shift= -6.142cm^{-1}

10063.9 300010000 Sum of Quanta= 4 relative shift= -6.15cm^{-1}

8512.13 201010000 Sum of Quanta= 4 relative shift= -10.437cm^{-1}

7041.72 200001000 Sum of Quanta= 3 relative shift= -10.009cm^{-1}

9909.87 300001000 Sum of Quanta= 4 relative shift= -10.017cm^{-1}

6753.8 200000100 Sum of Quanta= 3 relative shift= -0.325cm^{-1}

9611.98 300000100 Sum of Quanta= 4 relative shift= -0.333cm^{-1}

8070.93 201000100 Sum of Quanta= 4 relative shift= -4.62cm^{-1}

10889.4 301000100 Sum of Quanta= 5 relative shift= -4.628cm^{-1}

6375.3 102000100 Sum of Quanta= 4 relative shift= -8.907cm^{-1}

9376.15 202000100 Sum of Quanta= 5 relative shift= -8.915cm^{-1}

7703.57 200100100 Sum of Quanta= 4 relative shift= -6.886cm^{-1}

10565.5 300100100 Sum of Quanta= 5 relative shift= -6.894cm^{-1}

7575.52 200010100 Sum of Quanta= 4 relative shift= -6.451cm^{-1}

10438.8 300010100 Sum of Quanta= 5 relative shift= -6.459cm^{-1}

8884.08 201010100 Sum of Quanta= 5 relative shift= -10.746cm^{-1}

7408.01 200001100 Sum of Quanta= 4 relative shift= -10.318cm^{-1}

10278.4 300001100 Sum of Quanta= 5 relative shift= -10.326cm^{-1}

7122.61 200000200 Sum of Quanta= 4 relative shift= -0.634cm^{-1}

9982.99 300000200 Sum of Quanta= 5 relative shift= -0.642cm^{-1}

8438.94 201000200 Sum of Quanta= 5 relative shift= -4.929cm^{-1}

6740.32 102000200 Sum of Quanta= 5 relative shift= -9.216cm^{-1}

8067.61 200100200 Sum of Quanta= 5 relative shift= -7.195cm^{-1}

7941.19 200010200 Sum of Quanta= 5 relative shift= -6.76cm^{-1}

7767.24 200001200 Sum of Quanta= 5 relative shift= -10.627cm^{-1}

7484.34 200000300 Sum of Quanta= 5 relative shift= -0.943cm^{-1}

6906.99 200000010 Sum of Quanta= 3 relative shift= -6.091cm^{-1}

9786.54 300000010 Sum of Quanta= 4 relative shift= -6.099cm^{-1}

8228.42 201000010 Sum of Quanta= 4 relative shift= -10.386cm^{-1}

```
7276.31   200000110  Sum of Quanta=  4  relative shift= -6.4cm-1
10158.1   300000110  Sum of Quanta=  5  relative shift= -6.408cm-1
8596.97   201000110  Sum of Quanta=  5  relative shift= -10.695cm-1
7638.58   200000210  Sum of Quanta=  5  relative shift= -6.709cm-1
6771.43   200000001  Sum of Quanta=  3  relative shift= -1.312cm-1
9692.51   300000001  Sum of Quanta=  4  relative shift= -1.32cm-1
8101.55   201000001  Sum of Quanta=  4  relative shift= -5.607cm-1
10983.    301000001  Sum of Quanta=  5  relative shift= -5.615cm-1
6356.02   102000001  Sum of Quanta=  4  relative shift= -9.894cm-1
9419.78   202000001  Sum of Quanta=  5  relative shift= -9.902cm-1
7719.95   200100001  Sum of Quanta=  4  relative shift= -7.873cm-1
10644.8   300100001  Sum of Quanta=  5  relative shift= -7.881cm-1
7592.3    200010001  Sum of Quanta=  4  relative shift= -7.438cm-1
10518.5   300010001  Sum of Quanta=  5  relative shift= -7.446cm-1
7131.95   200000101  Sum of Quanta=  4  relative shift= -1.621cm-1
10055.2   300000101  Sum of Quanta=  5  relative shift= -1.629cm-1
8461.28   201000101  Sum of Quanta=  5  relative shift= -5.916cm-1
6712.76   102000101  Sum of Quanta=  5  relative shift= -10.203cm-1
8075.7    200100101  Sum of Quanta=  5  relative shift= -8.182cm-1
7949.68   200010101  Sum of Quanta=  5  relative shift= -7.747cm-1
7485.41   200000201  Sum of Quanta=  5  relative shift= -1.93cm-1
7252.24   200000011  Sum of Quanta=  4  relative shift= -7.387cm-1
10196.9   300000011  Sum of Quanta=  5  relative shift= -7.395cm-1
7606.22   200000111  Sum of Quanta=  5  relative shift= -7.696cm-1
7088.54   200000002  Sum of Quanta=  4  relative shift= -2.608cm-1
10074.7   300000002  Sum of Quanta=  5  relative shift= -2.616cm-1
8430.87   201000002  Sum of Quanta=  5  relative shift= -6.903cm-1
8031.04   200100002  Sum of Quanta=  5  relative shift= -9.169cm-1
7905.42   200010002  Sum of Quanta=  5  relative shift= -8.734cm-1
7433.71   200000102  Sum of Quanta=  5  relative shift= -2.917cm-1
7521.11   200000012  Sum of Quanta=  5  relative shift= -8.683cm-1
7329.26   200000003  Sum of Quanta=  5  relative shift= -3.904cm-1
{26316.8 Second, Null}
```

D.11 Internal Energy of CH_3OOH

This code is used to compute room temperature average internal energy (ro-vibrational) of methyl hydroperoxide in a same manner used with PNA above.

Mathematica Program int_mhp.nb:

```
n = 7;
r = 0.6950387;

ν15 = 195.8 / r;
ν14 = 257.97 / r;
ν13 = 448.4 / r;
ν12 = 861.6 / r;
ν11 = 1061.3 / r;
ν10 = 1179.5 / r;
ν9 = 1213.3 / r;
ν8 = 1371.6 / r;
ν7 = 1455.96 / r;
ν6 = 1475.2 / r;
ν5 = 1521.1 / r;
ν4 = 3024.5 / r;
ν3 = 3100.6 / r;
ν2 = 3129.8 / r;
ν1 = 3795.1 / r;

a = 1.434543727;
b = 0.350825727;
c = 0.301985161;
β = (b + c) / 2;
Print["kappa= " , (2 * b - a - c) / (a - c)]
If[(2 * b - a - c) / (a - c) > 0, Print["Oblate Top"], Print["Prolate Top"]]

T = 298;

Print["At Temperature= ",
 T "K, the Vibrational Energy is (neglecting zeroth pt. energy):"]
Evib = r * Sum[(νj * Exp[-νj / T]) / (1 - Exp[-νj / T]), {j, 1, 3*n-6}];
Print[Evib , " cm^-1"]
```

```
n = Sum[(2 J + 1) * e^-(β*J*(J+1)+(a-β)*K^2)/(r*T) * (β*J*(J+1)+(a-β)*K^2), {J, 0, 500},
    {K, -J, J}];
d = Sum[(2 J + 1) * e^-(β*J*(J+1)+(a-β)*K^2)/(r*T), {J, 0, 500}, {K, -J, J}];
Print["At Temperature= ", T "K, the Rotational Energy is:"]
NSolve[n / d,];
Print[n / d, " cm^-1"]
Print["<Eint>= ", n / d + E_vib, " cm^-1"]
```

```
kappa= -0.913752
Prolate Top
At Temperature= 298 K, the Vibrational Energy is (neglecting zeroth pt. energy):
319.565 cm^-1
At Temperature= 298 K, the Rotational Energy is:
310.58 cm^-1
<Eint>= 630.145 cm^-1
```

D.12 Two-Dimension OH-Stretch / HOON-Torsion Oscillator Strength Evaluation for CH_3OOH Using CCSD(T)/cc-pVTZ Dipole Moment Surface

This code is used to compute the oscillator strength of the vibrational transitions of CH_3OOH. The two-dimensional potential and dipole moment surfaces take into account the influence of the HOOC-torsion on the OH-stretching mode. The model was constructed using the CCSD(T)/cc-pVTZ level of theory. The Mathematica program is split into two parts. The first program, mhp_full_part1.nb, evaluates the $\mu_\alpha(\tau) = <\psi_v^{OH}(r|\tau)\,|\mu_\alpha(r,\tau)|\,\psi_0^{OH}(r|\tau)>$ matrix elements (see Eq. 7.10) and mhp_full_part2.nb evaluate $\mu_\alpha = <\chi^{v'}{}_{m'}(\tau)|\mu_\alpha(\tau)|\chi^{v}{}_{m}(\tau)>$ matrix elements in Eq. 7.11 as well as the transition strength $f = 4.702 \times 10^{-7}$ [cm D^{-2}] $\nu_{ij}\,|\mu_{ij}|^2$ from equation 7.8.

Mathematica Program mhp_full_part1.nb:

```
Off[General::spelll]
Off[General::spell]
Off[General::nffil]
Off[NIntegrate::slwcon]
Off[NIntegrate::inum]
<< Graphics`Graphics3D`
<< Statistics`DataManipulation`
SetDirectory[
  "C:/Documents and Settings/overtone/My
    Documents/Jamie/Thesis/CHAPTERS/APPENDIXD/codes/mhp_full"];

"Dipole Functions Imports";
dipZ = Import["Zsurface_ccsdt.txt", "Table"];
dipY = Import["Ysurface_ccsdt.txt", "Table"];
dipX = Import["Xsurface_ccsdt.txt", "Table"];

"wavefuctions for all OH wavefunctions imports";

Do[n_{w,g} = Column[Import[ToString[InputForm[g]], "Table"], {1, w + 2}],
 {w, 0, 6}, {g, 0, 360, 10}]

"Load Transition Frequencies Matrix";
transfreq = Import["evfreq.txt", "Table"];
```

```
"Plots for dipole surfaces";
```

```
dipZplot = ScatterPlot3D[dipZ, PlotRange → {-2, 2}, AspectRatio → Automatic,
  BoxRatios → {1, 1, 2}, PlotStyle → PointSize[0.02], ViewPoint → {1.0, 2.0, 1.0},
  PlotJoint → True, ImageSize → 300]

dipYplot = ScatterPlot3D[dipY, PlotRange → {-2, 1}, AspectRatio → Automatic,
  BoxRatios → {1, 1, 2}, PlotStyle → PointSize[0.02], ViewPoint → {1.0, 2.0, 1.0},
  PlotJoint → True, ImageSize → 300]
dipXplot = ScatterPlot3D[dipX, PlotRange → {-2, 0.5}, AspectRatio → Automatic,
  BoxRatios → {1, 1, 2}, PlotStyle → PointSize[0.02], ViewPoint → {1.0, 2.0, 1.0},
  PlotJoint → True, ImageSize → 300]
```

```
Do[{
  β_{w,g} = ListPlot[n_{w,g}, PlotStyle → PointSize[0.015], PlotRange → {-0.25, 0.25},
    DefaultColor → RGBColor[0.2, 0.1, 0.9], DisplayFunction → Identity]},
 {w, 0, 6}, {g, 0, 360, 10}]
Show[GraphicsArray[Table[β_{w,g}, {w, 0, 6}, {g, 0, 360, 10}]]]
```

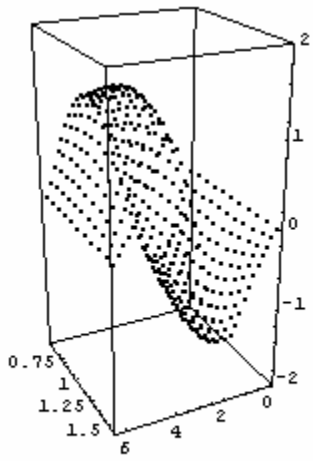

- Graphics3D -

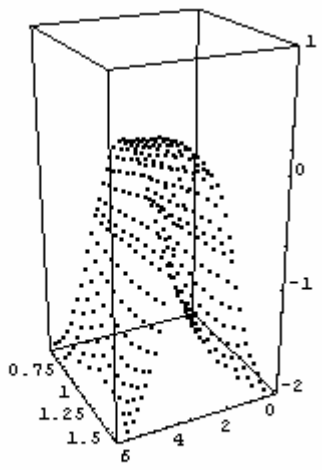

- Graphics3D -

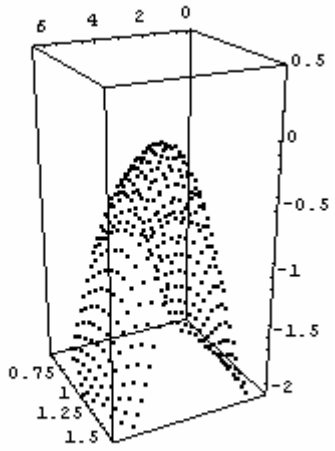

- Graphics3D -

```
" Dipole Surface fit using Taylor expansion ";
t = (x - to);
r = (y - ro);
to = Extract[dipZ[[137]], 1];
ro = Extract[dipZ[[137]], 2];
μz_m = Fit[dipZ, {1, r, t, r^2, r t, t^2, r^3, r^2 t, r t^2, t^3, r^4, r^3 t, r^2 t^2, r t^3,
    t^4, r^5, r^4 t, r^3 t^2, r^2 t^3, r t^4, t^5, r^6, r^5 t, r^4 t^2, r^3 t^3, r^2 t^4, r t^5, t^6,
    r^7, r^6 t, r^5 t^2, r^4 t^3, r^3 t^4, r^2 t^5, r t^6, t^7, r^8, r^7 t, r^6 t^2, r^5 t^3, r^4 t^4,
    r^3 t^5, r^2 t^6, r t^7, t^8, r^9, r^8 t, r^7 t^2, r^6 t^3, r^5 t^4, r^4 t^5, r^3 t^6, r^2 t^7, r t^8,
    t^9, r^10, r^9 t, r^8 t^2, r^7 t^3, r^6 t^4, r^5 t^5, r^4 t^6, r^3 t^7, r^2 t^8, r t^9, t^10}, {x, y}];
```

```
μY_m = Fit[dipY, {1, r, t, r^2, r t, t^2, r^3, r^2 t, r t^2, t^3, r^4, r^3 t, r^2 t^2, r t^3,
    t^4, r^5, r^4 t, r^3 t^2, r^2 t^3, r t^4, t^5, r^6, r^5 t, r^4 t^2, r^3 t^3, r^2 t^4, r t^5, t^6,
    r^7, r^6 t, r^5 t^2, r^4 t^3, r^3 t^4, r^2 t^5, r t^6, t^7, r^8, r^7 t, r^6 t^2, r^5 t^3, r^4 t^4,
    r^3 t^5, r^2 t^6, r t^7, t^8, r^9, r^8 t, r^7 t^2, r^6 t^3, r^5 t^4, r^4 t^5, r^3 t^6, r^2 t^7, r t^8,
    t^9, r^10, r^9 t, r^8 t^2, r^7 t^3, r^6 t^4, r^5 t^5, r^4 t^6, r^3 t^7, r^2 t^8, r t^9, t^10}, {x, y}];
μx_m = Fit[dipX, {1, r, t, r^2, r t, t^2, r^3, r^2 t, r t^2, t^3, r^4, r^3 t, r^2 t^2, r t^3,
    t^4, r^5, r^4 t, r^3 t^2, r^2 t^3, r t^4, t^5, r^6, r^5 t, r^4 t^2, r^3 t^3, r^2 t^4, r t^5, t^6,
    r^7, r^6 t, r^5 t^2, r^4 t^3, r^3 t^4, r^2 t^5, r t^6, t^7, r^8, r^7 t, r^6 t^2, r^5 t^3, r^4 t^4,
    r^3 t^5, r^2 t^6, r t^7, t^8, r^9, r^8 t, r^7 t^2, r^6 t^3, r^5 t^4, r^4 t^5, r^3 t^6, r^2 t^7, r t^8,
    t^9, r^10, r^9 t, r^8 t^2, r^7 t^3, r^6 t^4, r^5 t^5, r^4 t^6, r^3 t^7, r^2 t^8, r t^9, t^10}, {x, y}];
muZplot = Plot3D[μz_m, {x, 0, 2π}, {y, 0.566, 1.56}, Mesh → False, PlotPoints → 50]
Show[muZplot, dipZplot, ViewPoint → {1.0, 2.0, 1.0}]

muYplot = Plot3D[μy_m, {x, 0, 2π}, {y, 0.566, 1.56}, Mesh → False, PlotPoints → 50]
Show[muYplot, dipYplot, ViewPoint → {1.0, 2.0, 1.0}]

muXplot = Plot3D[μx_m, {x, 0, 2π}, {y, 0.566, 1.56}, Mesh → False, PlotPoints → 50]
Show[muXplot, dipXplot, ViewPoint → {1.0, 2.0, 1.0}]

Do[
 {μz_m =
   Fit[dipZ, {1, r, t, r^2, r t, t^2, r^3, r^2 t, r t^2, t^3, r^4, r^3 t, r^2 t^2,
      r t^3, t^4, r^5, r^4 t, r^3 t^2, r^2 t^3, r t^4, t^5, r^6, r^5 t, r^4 t^2, r^3 t^3,
      r^2 t^4, r t^5, t^6, r^7, r^6 t, r^5 t^2, r^4 t^3, r^3 t^4, r^2 t^5, r t^6, t^7, r^8,
      r^7 t, r^6 t^2, r^5 t^3, r^4 t^4, r^3 t^5, r^2 t^6, r t^7, t^8, r^9, r^8 t, r^7 t^2,
      r^6 t^3, r^5 t^4, r^4 t^5, r^3 t^6, r^2 t^7, r t^8, t^9, r^10, r^9 t, r^8 t^2, r^7 t^3,
      r^6 t^4, r^5 t^5, r^4 t^6, r^3 t^7, r^2 t^8, r t^9, t^10}, {x, y}] /. x → (m * π / 180)},
 {m, 0, 360, 10}]
Do[
 {μY_m =
   Fit[dipY, {1, r, t, r^2, r t, t^2, r^3, r^2 t, r t^2, t^3, r^4, r^3 t, r^2 t^2,
      r t^3, t^4, r^5, r^4 t, r^3 t^2, r^2 t^3, r t^4, t^5, r^6, r^5 t, r^4 t^2, r^3 t^3,
      r^2 t^4, r t^5, t^6, r^7, r^6 t, r^5 t^2, r^4 t^3, r^3 t^4, r^2 t^5, r t^6, t^7, r^8,
      r^7 t, r^6 t^2, r^5 t^3, r^4 t^4, r^3 t^5, r^2 t^6, r t^7, t^8, r^9, r^8 t, r^7 t^2,
      r^6 t^3, r^5 t^4, r^4 t^5, r^3 t^6, r^2 t^7, r t^8, t^9, r^10, r^9 t, r^8 t^2, r^7 t^3,
      r^6 t^4, r^5 t^5, r^4 t^6, r^3 t^7, r^2 t^8, r t^9, t^10}, {x, y}] /. x → (m * π / 180)},
 {m, 0, 360, 10}]
```

```
Do[
 {μx_m =
   Fit[dipX, {1, r, t, r^2, r t, t^2, r^3, r^2 t, r t^2, t^3, r^4, r^3 t, r^2 t^2,
     r t^3, t^4, r^5, r^4 t, r^3 t^2, r^2 t^3, r t^4, t^5, r^6, r^5 t, r^4 t^2, r^3 t^3,
     r^2 t^4, r t^5, t^6, r^7, r^6 t, r^5 t^2, r^4 t^3, r^3 t^4, r^2 t^5, r t^6, t^7, r^8,
     r^7 t, r^6 t^2, r^5 t^3, r^4 t^4, r^3 t^5, r^2 t^6, r t^7, t^8, r^9, r^8 t, r^7 t^2,
     r^6 t^3, r^5 t^4, r^4 t^5, r^3 t^6, r^2 t^7, r t^8, t^9, r^10, r^9 t, r^8 t^2, r^7 t^3,
     r^6 t^4, r^5 t^5, r^4 t^6, r^3 t^7, r^2 t^8, r t^9, t^10}, {x, y}] /. x → (m * π / 180)},
 {m, 0, 360, 10}]
"wavefunctions interpolation for all OH ";
Do[{
  Ø_oh,ang = Interpolation[n_oh,ang, InterpolationOrder → 3];
  Υ_oh,ang = Plot[Evaluate[Ø_oh,ang][y], {y, 0.3, 2.0}, PlotPoints → 100,
    PlotRange → {-0.25, 0.25}, DisplayFunction → Identity];},
 {oh, 0, 6}, {ang, 0, 360, 10}]
Show[GraphicsArray[Table[Υ_oh,ang, {oh, 0, 6}, {ang, 0, 360, 10}]]]

"Normalization for all OH wavefunctions ";

Do[{
  p_oh,ang =
    NIntegrate[Evaluate[Ø_oh,ang][y] * Evaluate[Ø_oh,ang][y], {y, 0.3, 2.0},
      MaxRecursion → 100, WorkingPrecision → 15]^-0.5;}, {oh, 0, 6},
 {ang, 0, 360, 10}]
```

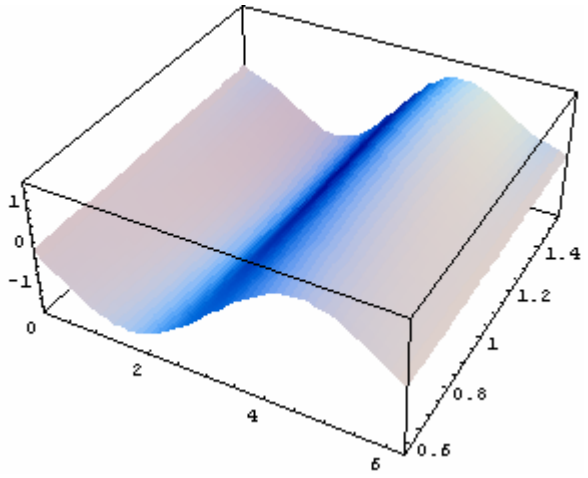

- SurfaceGraphics -

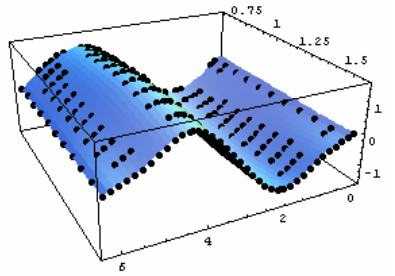

- Graphics3D -

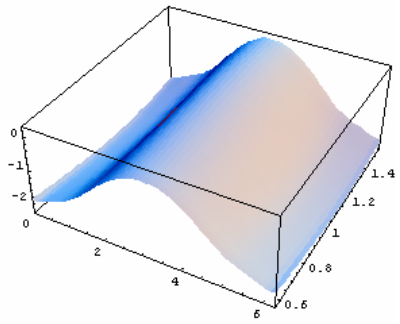

- SurfaceGraphics -

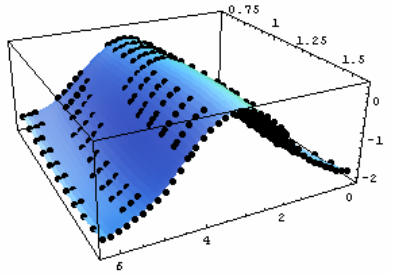

- Graphics3D -

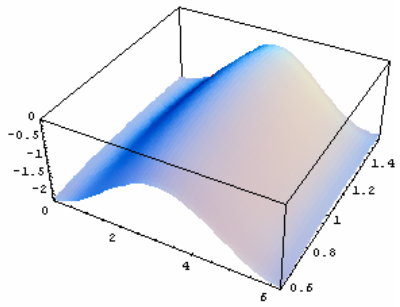

- SurfaceGraphics -

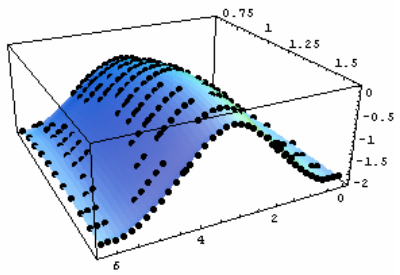

```
"Do NOT RERUN ";

Do[{DeleteFile[ToString[InputForm[a]]]}, {a, 11, 13}]
Do[{DeleteFile[ToString[InputForm[a]]]}, {a, 21, 23}]
Do[{DeleteFile[ToString[InputForm[a]]]}, {a, 31, 33}]
Do[{DeleteFile[ToString[InputForm[a]]]}, {a, 41, 43}]
Do[{DeleteFile[ToString[InputForm[a]]]}, {a, 51, 53}]
Do[{DeleteFile[ToString[InputForm[a]]]}, {a, 61, 63}]

"Do NOT RERUN ";
Clear[x, y, tor, v];

σZ = NIntegrate[Evaluate[Ø0,tor][y] * μztor * Evaluate[Øv,tor][y] *
     (p0,tor * pv,tor), {y, 0.3, 2.0}, MaxRecursion → 100];
σY = NIntegrate[Evaluate[Ø0,tor][y] * μytor * Evaluate[Øv,tor][y] *
     (p0,tor * pv,tor), {y, 0.3, 2.0}, MaxRecursion → 100];
σX = NIntegrate[Evaluate[Ø0,tor][y] * μxtor * Evaluate[Øv,tor][y] *
     (p0,tor * pv,tor), {y, 0.3, 2.0}, MaxRecursion → 100];



Do[{PutAppend[σZ, ToString[InputForm[v * 10 + 1]]] ,
  PutAppend[σY, ToString[InputForm[v * 10 + 2]]],
  PutAppend[σX, ToString[InputForm[v * 10 + 3]]] ,
  Print[AccountingForm[{ , tor, σZ, σY, σX, }]]}, {v, 1, 6},
 {tor, 0, 360, 10}]
```

{Null,0,0.000406082,(0.0329515),0.0063903,Null}
{Null,10,0.00189184,(0.0299917),0.0047779,Null}
{Null,20,0.0055242,(0.0298226),0.0044730,Null}
{Null,30,0.0080315,(0.0302709),0.0051496,Null}
{Null,40,0.0078552,(0.0300499),0.0066476,Null}
{Null,50,0.0046059,(0.0285163),0.0088891,Null}
{Null,60,(0.00131405),(0.0254514),0.0118300,Null}
{Null,70,(0.0090144),(0.0209070),0.0154221,Null}
{Null,80,(0.0173884),(0.0151126),0.0195845,Null}
{Null,90,(0.0253413),(0.0084177),0.0241879,Null}
{Null,100,(0.0319181),(0.00121592),0.0290711,Null}
{Null,110,(0.0363915),0.0060923,0.0340399,Null}
{Null,120,(0.0382954),0.0131377,0.0388925,Null}
{Null,130,(0.0374258),0.0195996,0.0434185,Null}
{Null,140,(0.0338299),0.0252151,0.047427,Null}
{Null,150,(0.0277747),0.0297792,0.050741,Null}
{Null,160,(0.0197090),0.0331409,0.053221,Null}
{Null,170,(0.0102217),0.0351974,0.054753,Null}
{Null,180,(0.000000126413),0.0358894,0.055272,Null}
{Null,190,0.0102215,0.0351974,0.054753,Null}
{Null,200,0.0197088,0.0331409,0.053221,Null}
{Null,210,0.0277745,0.0297792,0.050741,Null}

{Null,220,0.0338297,0.0252151,0.047427,Null}
{Null,230,0.0374256,0.0195996,0.0434185,Null}
{Null,240,0.0382953,0.0131377,0.0388925,Null}
{Null,250,0.0363914,0.0060923,0.0340399,Null}
{Null,260,0.0319180,(0.00121592),0.0290711,Null}
{Null,270,0.0253413,(0.0084177),0.0241879,Null}
{Null,280,0.0173885,(0.0151126),0.0195845,Null}
{Null,290,0.0090144,(0.0209070),0.0154221,Null}
{Null,300,0.00131410,(0.0254514),0.0118300,Null}
{Null,310,(0.0046058),(0.0285163),0.0088891,Null}
{Null,320,(0.0078552),(0.0300499),0.0066476,Null}
{Null,330,(0.0080315),(0.0302709),0.0051496,Null}
{Null,340,(0.0055242),(0.0298226),0.0044730,Null}
{Null,350,(0.00189183),(0.0299917),0.0047779,Null}
{Null,360,(0.000406045),(0.0329515),0.0063903,Null}
{Null,0,(0.000051041),0.0108660,(0.00389207),Null}
{Null,10,0.00068652,0.0104610,(0.00414146),Null}
{Null,20,0.00178640,0.0108657,(0.00430003),Null}
{Null,30,0.00321343,0.0112968,(0.0046440),Null}
{Null,40,0.0048659,0.0113207,(0.0052817),Null}
{Null,50,0.0066018,0.0107593,(0.0062067),Null}
{Null,60,0.0082646,0.0096176,(0.0073427),Null}
{Null,70,0.0097093,0.0080110,(0.0085849),Null}
{Null,80,0.0108203,0.0061031,(0.0098306),Null}
{Null,90,0.0115140,0.00405763,(0.0109964),Null}
{Null,100,0.0117492,0.00202455,(0.0120185),Null}
{Null,110,0.0115111,0.000117350,(0.0128632),Null}
{Null,120,0.0108213,(0.00158401),(0.0135243),Null}
{Null,130,0.0097107,(0.00303307),(0.0140088),Null}
{Null,140,0.0082343,(0.00420974),(0.0143441),Null}
{Null,150,0.0064534,(0.0051112),(0.0145595),Null}
{Null,160,0.0044370,(0.0057444),(0.0146867),Null}
{Null,170,0.00225900,(0.0061192),(0.0147520),Null}
{Null,180,0.000000066369,(0.0062431),(0.0147715),Null}
{Null,190,(0.00225886),(0.0061192),(0.0147520),Null}
{Null,200,(0.0044368),(0.0057444),(0.0146867),Null}
{Null,210,(0.0064533),(0.0051112),(0.0145595),Null}
{Null,220,(0.0082342),(0.00420974),(0.0143441),Null}
{Null,230,(0.0097106),(0.00303307),(0.0140088),Null}
{Null,240,(0.0108212),(0.00158401),(0.0135243),Null}
{Null,250,(0.0115110),0.000117350,(0.0128632),Null}
{Null,260,(0.0117491),0.00202455,(0.0120185),Null}
{Null,270,(0.0115140),0.00405763,(0.0109964),Null}
{Null,280,(0.0108202),0.0061031,(0.0098306),Null}
{Null,290,(0.0097093),0.0080110,(0.0085849),Null}
{Null,300,(0.0082646),0.0096176,(0.0073427),Null}
{Null,310,(0.0066017),0.0107593,(0.0062067),Null}
{Null,320,(0.0048659),0.0113207,(0.0052817),Null}
{Null,330,(0.00321340),0.0112968,(0.0046440),Null}
{Null,340,(0.00178637),0.0108657,(0.00430003),Null}
{Null,350,(0.00068648),0.0104610,(0.00414146),Null}
{Null,360,0.000051076,0.0108660,(0.00389207),Null}
{Null,0,0.0000062342,(0.00235441),0.00160538,Null}
{Null,10,(0.000115977),(0.00213800),0.00171896,Null}

{Null,20,(0.000343077),(0.00218556),0.00173448,Null}
{Null,30,(0.00064168),(0.00229145),0.00175077,Null}
{Null,40,(0.00097202),(0.00232965),0.00181982,Null}
{Null,50,(0.00129516),(0.00224989),0.00194904,Null}
{Null,60,(0.00157585),(0.00204740),0.00212714,Null}
{Null,70,(0.00178812),(0.00174763),0.00233210,Null}
{Null,80,(0.00192001),(0.00139240),0.00253857,Null}
{Null,90,(0.00197018),(0.00102309),0.00272353,Null}
{Null,100,(0.00193882),(0.00066859),0.00287624,Null}
{Null,110,(0.00183349),(0.000352069),0.00298903,Null}
{Null,120,(0.00166964),(0.000087402),0.00306285,Null}
{Null,130,(0.00145478),0.000122419,0.00310152,Null}
{Null,140,(0.00120479),0.000279306,0.00311399,Null}
{Null,150,(0.00092426),0.000390179,0.00311118,Null}
{Null,160,(0.00062655),0.00046220,0.00310102,Null}
{Null,170,(0.000316477),0.00050260,0.00309175,Null}
{Null,180,(0.00000000141751),0.00051528,0.00308805,Null}
{Null,190,0.000316474,0.00050260,0.00309175,Null}
{Null,200,0.00062654,0.00046220,0.00310102,Null}
{Null,210,0.00092426,0.000390179,0.00311118,Null}
{Null,220,0.00120478,0.000279306,0.00311399,Null}
{Null,230,0.00145477,0.000122419,0.00310152,Null}
{Null,240,0.00166962,(0.000087402),0.00306285,Null}
{Null,250,0.00183346,(0.000352069),0.00298903,Null}
{Null,260,0.00193879,(0.00066859),0.00287624,Null}
{Null,270,0.00197015,(0.00102309),0.00272353,Null}
{Null,280,0.00191998,(0.00139240),0.00253857,Null}
{Null,290,0.00178808,(0.00174763),0.00233210,Null}
{Null,300,0.00157580,(0.00204740),0.00212714,Null}
{Null,310,0.00129511,(0.00224989),0.00194904,Null}
{Null,320,0.00097197,(0.00232965),0.00181982,Null}
{Null,330,0.00064163,(0.00229145),0.00175077,Null}
{Null,340,0.000343028,(0.00218556),0.00173448,Null}
{Null,350,0.000115928,(0.00213800),0.00171896,Null}
{Null,360,(0.0000062832),(0.00235441),0.00160538,Null}
{Null,0,0.0000432740,0.00070988,(0.00072528),Null}
{Null,10,0.0000424814,0.00061232,(0.00077734),Null}
{Null,20,0.000079994,0.00061108,(0.00078161),Null}
{Null,30,0.000140135,0.00063489,(0.00077889),Null}
{Null,40,0.000210124,0.00064969,(0.00078141),Null}
{Null,50,0.000278342,0.00063744,(0.00079384),Null}
{Null,60,0.000332650,0.00059005,(0.00082009),Null}
{Null,70,0.000369518,0.00051959,(0.00085096),Null}
{Null,80,0.000386045,0.000435721,(0.00088276),Null}
{Null,90,0.000383690,0.000350048,(0.00091010),Null}
{Null,100,0.000364962,0.000271037,(0.00093007),Null}
{Null,110,0.000333203,0.000204021,(0.00094119),Null}
{Null,120,0.000292715,0.000151934,(0.00094396),Null}
{Null,130,0.000247612,0.000114677,(0.00093946),Null}
{Null,140,0.000197600,0.000089921,(0.00093132),Null}
{Null,150,0.000148636,0.000075254,(0.00092124),Null}
{Null,160,0.000098393,0.000067501,(0.00091238),Null}
{Null,170,0.000048856,0.000064160,(0.00090644),Null}
{Null,180,(0.0000000205273),0.000063273,(0.00090413),Null}

{Null,190,(0.000048896),0.000064160,(0.00090644),Null}
{Null,200,(0.000098433),0.000067501,(0.00091238),Null}
{Null,210,(0.000148673),0.000075254,(0.00092124),Null}
{Null,220,(0.000197633),0.000089921,(0.00093132),Null}
{Null,230,(0.000247640),0.000114677,(0.00093946),Null}
{Null,240,(0.000292739),0.000151934,(0.00094396),Null}
{Null,250,(0.000333221),0.000204021,(0.00094119),Null}
{Null,260,(0.000364974),0.000271037,(0.00093007),Null}
{Null,270,(0.000383696),0.000350048,(0.00091010),Null}
{Null,280,(0.000386045),0.000435721,(0.00088276),Null}
{Null,290,(0.000369512),0.00051959,(0.00085096),Null}
{Null,300,(0.000332639),0.00059005,(0.00082009),Null}
{Null,310,(0.000278327),0.00063744,(0.00079384),Null}
{Null,320,(0.000210106),0.00064969,(0.00078141),Null}
{Null,330,(0.000140116),0.00063489,(0.00077889),Null}
{Null,340,(0.000079975),0.00061108,(0.00078161),Null}
{Null,350,(0.0000424627),0.00061232,(0.00077734),Null}
{Null,360,(0.0000432557),0.00070988,(0.00072528),Null}
{Null,0,(0.000051497),(0.000180586),0.000216592,Null}
{Null,10,(0.0000426675),(0.000146571),0.000238002,Null}
{Null,20,(0.000049744),(0.000145326),0.000245485,Null}
{Null,30,(0.000064726),(0.000155229),0.000249053,Null}
{Null,40,(0.000082088),(0.000163195),0.000250815,Null}
{Null,50,(0.000097479),(0.000161699),0.000251409,Null}
{Null,60,(0.000107684),(0.000149544),0.000250830,Null}
{Null,70,(0.000111776),(0.000129601),0.000248641,Null}
{Null,80,(0.000109323),(0.000105263),0.000245691,Null}
{Null,90,(0.000100834),(0.000080295),0.000241415,Null}
{Null,100,(0.000089029),(0.000058521),0.000235158,Null}
{Null,110,(0.000074677),(0.0000408596),0.000227245,Null}
{Null,120,(0.000059451),(0.0000284798),0.000218094,Null}
{Null,130,(0.000046083),(0.0000211304),0.000207870,Null}
{Null,140,(0.0000326185),(0.0000174742),0.000198279,Null}
{Null,150,(0.0000225315),(0.0000166968),0.000189664,Null}
{Null,160,(0.0000136179),(0.0000173187),0.000183006,Null}
{Null,170,(0.0000065258),(0.0000180216),0.000179046,Null}
{Null,180,0.0000000197498,(0.0000182931),0.000177459,Null}
{Null,190,0.0000065650,(0.0000180216),0.000179046,Null}
{Null,200,0.0000136564,(0.0000173187),0.000183006,Null}
{Null,210,0.0000225689,(0.0000166968),0.000189664,Null}
{Null,220,0.0000326543,(0.0000174742),0.000198279,Null}
{Null,230,0.000046117,(0.0000211304),0.000207870,Null}
{Null,240,0.000059482,(0.0000284798),0.000218094,Null}
{Null,250,0.000074706,(0.0000408596),0.000227245,Null}
{Null,260,0.000089055,(0.000058521),0.000235158,Null}
{Null,270,0.000100856,(0.000080295),0.000241415,Null}
{Null,280,0.000109342,(0.000105263),0.000245691,Null}
{Null,290,0.000111792,(0.000129601),0.000248641,Null}
{Null,300,0.000107698,(0.000149544),0.000250830,Null}
{Null,310,0.000097491,(0.000161699),0.000251409,Null}
{Null,320,0.000082099,(0.000163195),0.000250815,Null}
{Null,330,0.000064736,(0.000155229),0.000249053,Null}
{Null,340,0.000049755,(0.000145326),0.000245485,Null}
{Null,350,0.0000426786,(0.000146571),0.000238002,Null}

{Null,360,0.000051508,(0.000180586),0.000216592,Null}
{Null,0,0.0000336390,(0.000044395),0.000061247,Null}
{Null,10,0.0000282638,(0.000053539),0.000051400,Null}
{Null,20,0.0000305615,(0.000051285),0.000045734,Null}
{Null,30,0.0000352687,(0.000046063),0.0000401882,Null}
{Null,40,0.0000401665,(0.0000390131),0.0000387635,Null}
{Null,50,0.0000422804,(0.0000366236),0.0000393269,Null}
{Null,60,0.0000412811,(0.0000380641),0.0000423855,Null}
{Null,70,0.0000370862,(0.0000422416),0.000047672,Null}
{Null,80,0.0000319822,(0.000045531),0.000056016,Null}
{Null,90,0.0000227833,(0.000051293),0.000062547,Null}
{Null,100,0.0000157145,(0.000053676),0.000071326,Null}
{Null,110,0.0000063762,(0.000056248),0.000078496,Null}
{Null,120,0.0000000212710,(0.000056011),0.000086674,Null}
{Null,130,(0.00000424828),(0.000054528),0.000094345,Null}
{Null,140,(0.0000069821),(0.000052195),0.000101206,Null}
{Null,150,(0.0000074843),(0.000049614),0.000106678,Null}
{Null,160,(0.0000060943),(0.000047265),0.000110868,Null}
{Null,170,(0.00000363217),(0.000045531),0.000113128,Null}
{Null,180,(0.0000000123094),(0.000044989),0.000114214,Null}
{Null,190,0.00000360761,(0.000045531),0.000113128,Null}
{Null,200,0.0000060699,(0.000047265),0.000110868,Null}
{Null,210,0.0000074601,(0.000049614),0.000106678,Null}
{Null,220,0.0000069582,(0.000052195),0.000101206,Null}
{Null,230,0.00000422471,(0.000054528),0.000094345,Null}
{Null,240,(0.000000044361),(0.000056011),0.000086674,Null}
{Null,250,(0.0000063987),(0.000056248),0.000078496,Null}
{Null,260,(0.0000157363),(0.000053676),0.000071326,Null}
{Null,270,(0.0000228043),(0.000051293),0.000062547,Null}
{Null,280,(0.0000320025),(0.000045531),0.000056016,Null}
{Null,290,(0.0000371058),(0.0000422416),0.000047672,Null}
{Null,300,(0.0000413001),(0.0000380641),0.0000423855,Null}
{Null,310,(0.0000422989),(0.0000366236),0.0000393269,Null}
{Null,320,(0.0000401850),(0.0000390131),0.0000387635,Null}
{Null,330,(0.0000352875),(0.000046063),0.0000401882,Null}
{Null,340,(0.0000305807),(0.000051285),0.000045734,Null}
{Null,350,(0.0000282835),(0.000053539),0.000051400,Null}
{Null,360,(0.0000336591),(0.000044395),0.000061247,Null}

```
Do[{
  l$a = {ReadList["cord.txt"], ReadList[ToString[InputForm[a]]]};
  d$a = Transpose[l$a];
  ListPlot[d$a, PlotJoined → False, PlotStyle → PointSize[0.02]]},
 {a, kkk, kkk + 2}, {kkk, 11, 61, 10}]
```

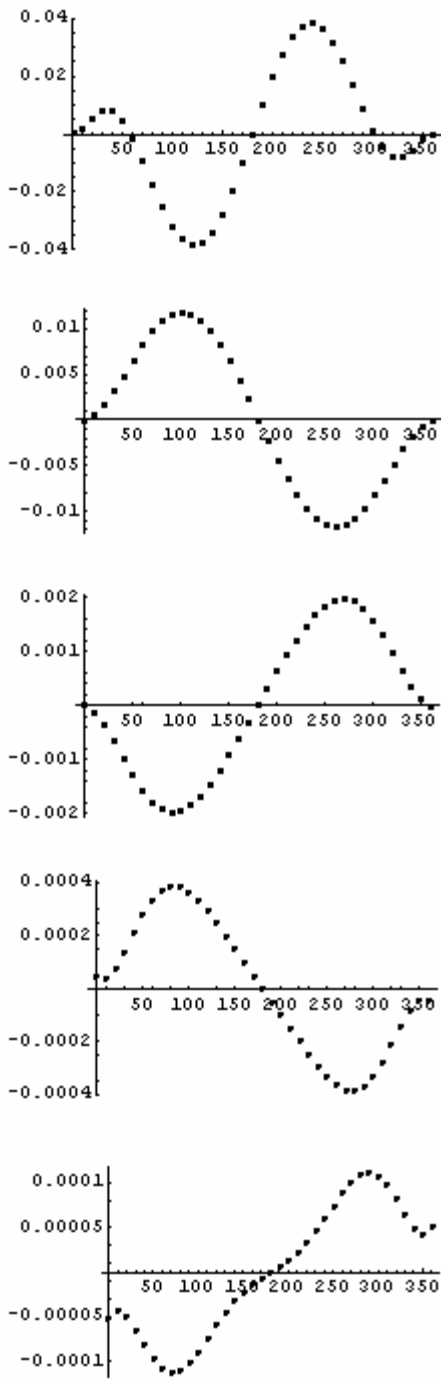
0.04
0.02
50 100 150 200 250 300 350
-0.02
-0.04
0.01
0.005
50 100 150 200 250 300 350
-0.005
-0.01
0.002
0.001
50 100 150 200 250 300 350
-0.001
-0.002
0.0004
0.0002
50 100 150 200 250 300 350
-0.0002
-0.0004
0.0001
0.00005
50 100 150 200 250 300 350
-0.00005
-0.0001

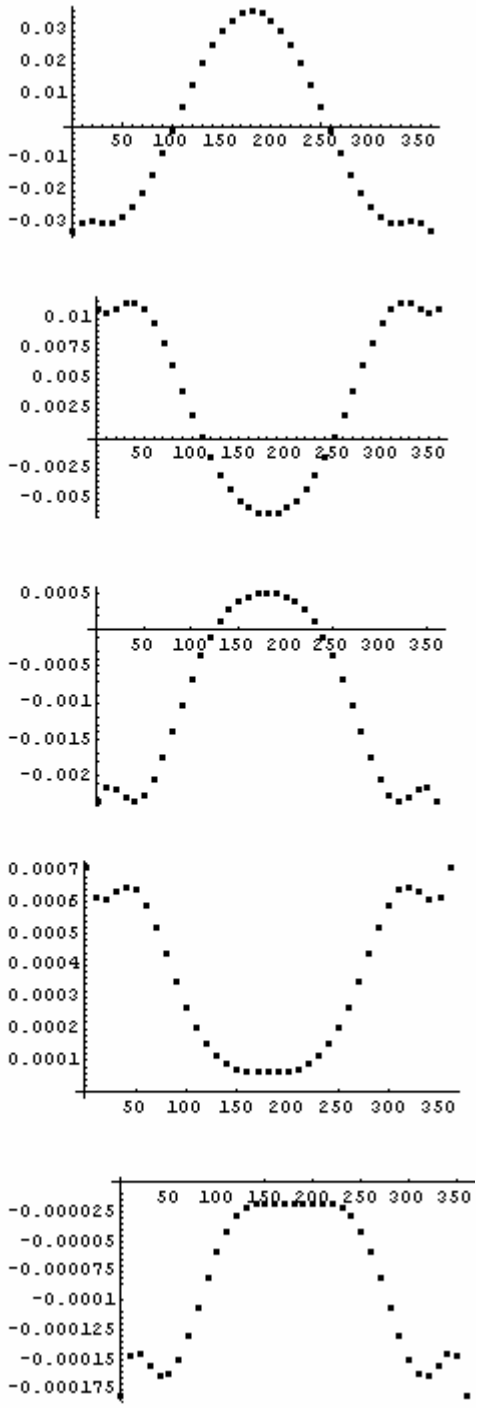
0.03
0.02
0.01
50 100 150 200 250 300 350
-0.01
-0.02
-0.03
0.01
0.0075
0.005
0.0025
50 100 150 200 250 300 350
-0.0025
-0.005
0.0005
50 100 150 200 250 300 350
-0.0005
-0.001
-0.0015
-0.002
0.0007
0.0006
0.0005
0.0004
0.0003
0.0002
0.0001
50 100 150 200 250 300 350
50 100 150 200 250 300 350
-0.000025
-0.00005
-0.000075
-0.0001
-0.000125
-0.00015
-0.000175

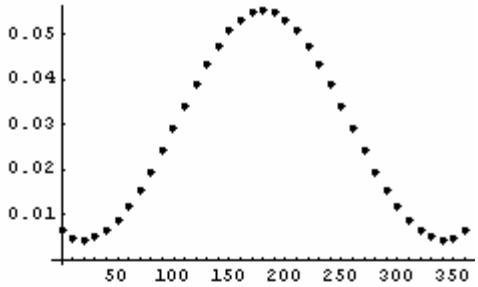
0.05
0.04
0.03
0.02
0.01
50 100 150 200 250 300 350

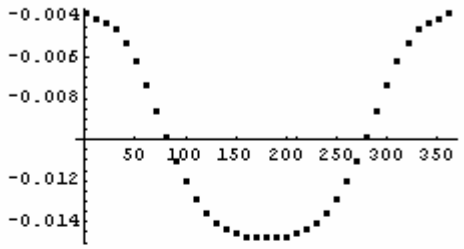
-0.004
-0.006
-0.008
-0.012
-0.014
50 100 150 200 250 300 350

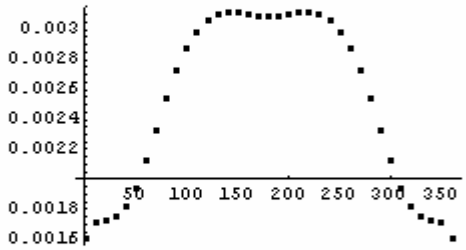
0.003
0.0028
0.0026
0.0024
0.0022
0.0018
0.0016
50 100 150 200 250 300 350

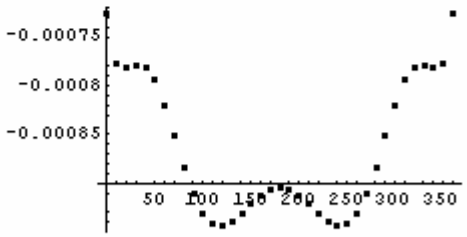
-0.00075
-0.0008
-0.00085
50 100 150 200 250 300 350

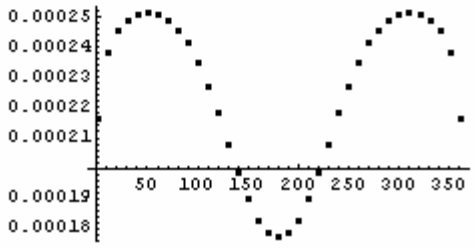
0.00025
0.00024
0.00023
0.00022
0.00021
0.00019
0.00018
50 100 150 200 250 300 350

Mathematica Program mhp_full_part2.nb:

```
Off[General::spelll]
Off[General::spell]

<< Graphics`Graphics3D`
<< Statistics`DataManipulation`
"first ind. describe the electronic surface";
SetDirectory[
  "C:/Documents and Settings/overtone/My
    Documents/Jamie/Thesis/CHAPTERS/APPENDIXD/codes/mhp_full"];
"Dipole Functions Imports";

Do[dipZ_g = Column[Import["Zsurface.txt", "Table"], {1, g + 1}], {g, 1, 6}];
Do[dipY_g = Column[Import["Ysurface.txt", "Table"], {1, g + 1}], {g, 1, 6}];
Do[dipX_g = Column[Import["Xsurface.txt", "Table"], {1, g + 1}], {g, 1, 6}];

"wavefuctions for Tau v=0-9 at ground state imports";

Do[v_{0,w} = Column[Import["efzero.txt", "Table"], {1, w + 2}] , {w, 0, 9}]

"wavefuctions for Tau v=0-9 1st Excited state imports";

Do[v_{1,w} = Column[Import["efone.txt", "Table"], {1, w + 2}] , {w, 0, 9}]

"wavefuctions for Tau v=0-9 at 2nd Excited State imports";

Do[v_{2,w} = Column[Import["eftwo.txt", "Table"], {1, w + 2}] , {w, 0, 9}]

"wavefuctions for Tau v=0-9 3rd Excited State imports";

Do[v_{3,w} = Column[Import["efthree.txt", "Table"], {1, w + 2}] , {w, 0, 9}]

"wavefuctions for Tau v=0-9 4th Excited State imports";

Do[v_{4,w} = Column[Import["effour.txt", "Table"], {1, w + 2}] , {w, 0, 9}]

"wavefuctions for Tau v=0-9 5th Excited State imports";

Do[v_{5,w} = Column[Import["effive.txt", "Table"], {1, w + 2}] , {w, 0, 9}]
```

```
"wavefuctions for Tau v=0-9 6th Excited State imports";

Do[v6,w = Column[Import["efsix.txt", "Table"], {1, w + 2}] , {w, 0, 9}]

"Load Transition Frequencies Matrix";
transfreq = Import["evfreq.txt", "Table"];

Print["import complete"]

" OH wavefunctions run from 0-->ohfinal ";
ohfinal = 6;

" Tau wavefunctions run from 0-->taufinal ";
taufinal = 9;

"Plots for quantum yield";

" qylp=ListPlot[qy,PlotStyle→PointSize[0.025]] ";

"Plots for dipole surfaces";

Do[
 {dipZplotg = ListPlot[dipZg, PlotStyle → PointSize[0.02],
    DefaultColor → RGBColor[0.8, 0.1, 0.1], DisplayFunction → Identity]}, {g, 1, 6}]
Show[GraphicsArray[Table[dipZplotg, {g, 1, 6}]]]

Do[
 {dipYplotg = ListPlot[dipYg, PlotStyle → PointSize[0.02],
    DefaultColor → RGBColor[0.8, 0.1, 0.1], DisplayFunction → Identity]}, {g, 1, 6}]
Show[GraphicsArray[Table[dipYplotg, {g, 1, 6}]]]

Do[
 {dipXplotg = ListPlot[dipXg, PlotStyle → PointSize[0.02],
    DefaultColor → RGBColor[0.8, 0.1, 0.1], DisplayFunction → Identity]}, {g, 1, 6}]
Show[GraphicsArray[Table[dipXplotg, {g, 1, 6}]]]
```

```
"Plots for all eigenvectors of Tau";
Do[{
  γ_{str,tor} = ListPlot[v_{str,tor}, PlotStyle → PointSize[0.015], PlotRange → {-0.3, 0.3},
    DefaultColor → RGBColor[0.8, 0.1, 0.1], DisplayFunction → Identity]},
 {str, 0, ohfinal}, {tor, 0, taufinal}]
Show[GraphicsArray[Table[γ_{str,tor}, {str, 0, 6}, {tor, 0, 9}]]]
" Dipole Surface fit using Taylor expansion ";

Do[μz_g = Interpolation[dipZ_g, InterpolationOrder → 3], {g, 1, 6}]
Do[μy_g = Interpolation[dipY_g, InterpolationOrder → 3], {g, 1, 6}]
Do[μx_g = Interpolation[dipX_g, InterpolationOrder → 3], {g, 1, 6}]

Do[Plot[Evaluate[μz_g][x], {x, 0, 2π}], {g, 1, 5}]
Pause[1];
Do[Plot[Evaluate[μy_g][x], {x, 0, 2π}], {g, 1, 5}]
Pause[1];
Do[Plot[Evaluate[μx_g][x], {x, 0, 2π}], {g, 1, 5}]
Pause[1];


"wavefunctions interpolation for all Tau";
Do[{
  Ψ_{str,tor} = Interpolation[v_{str,tor}, InterpolationOrder → 3];
  χ_{str,tor} = Plot[Evaluate[Ψ_{str,tor}][x], {x, 0, 2π}, PlotPoints → 100,
    PlotRange → {-0.25, 0.25}];
  Show[γ_{str,tor}, χ_{str,tor}]}, {str, 0, ohfinal}, {tor, 0, taufinal}]


"Normalization for all Tau wavefunctions ";


Do[{
  α_{str,tor} =
    NIntegrate[Evaluate[Ψ_{str,tor}][x] * Evaluate[Ψ_{str,tor}][x], {x, 0, 2π},
      MaxRecursion → 100]^(-0.5);}, {str, 0, ohfinal}, {tor, 0, taufinal}]
```

```
"Calculate the Partition function:";
freq = transfreq;
kb = 0.695;
T = 298;
vibpartfunc =
 Sum[(Exp[-(freq[[1, k + 1]] - freq[[1, 1]]) / (kb * T)]), {k, 0, 9}]
Do[Print[(Exp[-(freq[[1, k + 1]] - freq[[1, 1]]) / (kb * T)])], {k, 0, 9}]
```

```
3.38523
1.
0.960253
0.547398
0.385538
0.229318
0.129969
0.069885
0.0360666
0.0180296
0.00877676
```

```
"DO LOOPS";
"Format: |j,k> → |m,n>  j, m - electronic surface, k ,n -tau functions
   on associated surface";
Off[NIntegrate::inum]
Off[Part::pspec]
freq = transfreq;
ν = (freq[[m + 1, n + 1]] - freq[[j + 1, k + 1]]);
Clear[m, n, j, k]
σZ = NIntegrate[Evaluate[Ψj,k][x] * Evaluate[μzm][x] * Evaluate[Ψm,n][x], {x, 0, 2 π}] *
    (αj,k * αm,n);
σY = NIntegrate[Evaluate[Ψj,k][x] * Evaluate[μym][x] * Evaluate[Ψm,n][x], {x, 0, 2 π}] *
    (αj,k * αm,n);
σX = NIntegrate[Evaluate[Ψj,k][x] * Evaluate[μxm][x] * Evaluate[Ψm,n][x], {x, 0, 2 π}] *
    (αj,k * αm,n);
blz = Exp[-(freq[[j + 1, k + 1]] - freq[[1, 1]]) / (kb * T)];
f = 4.702*^-7 * ν * Σ;
kb = 0.695;
T = 298;
Σ = σX^2 + σY^2 + σZ^2;
w = ν;
```

```
Print["1nu"]
Do[Print[AccountingForm[{, ν, f, σ_Z^2, σ_Y^2, σ_X^2, blz * f, j, k, m, n,}]],
 {j, 0, 0}, {k, 0, 9}, {m, 1, 1}, {n, 0, 9}]
Print["2nu"]
Do[Print[AccountingForm[{, ν, f, σ_Z^2, σ_Y^2, σ_X^2, blz * f, j, k, m, n,}]],
 {j, 0, 0}, {k, 0, 9}, {m, 2, 2}, {n, 0, 9}]
Print["3nu"]
Do[Print[AccountingForm[{, ν, f, σ_Z^2, σ_Y^2, σ_X^2, blz * f, j, k, m, n,}]],
 {j, 0, 0}, {k, 0, 9}, {m, 3, 3}, {n, 0, 9}]
Print["4nu"]
Do[Print[AccountingForm[{, ν, f, σ_Z^2, σ_Y^2, σ_X^2, blz * f, j, k, m, n,}]],
 {j, 0, 0}, {k, 0, 9}, {m, 4, 4}, {n, 0, 9}]
Print["5nu"]
Do[Print[AccountingForm[{, ν, f, σ_Z^2, σ_Y^2, σ_X^2, blz * f, j, k, m, n,}]],
 {j, 0, 0}, {k, 0, 9}, {m, 5, 5}, {n, 0, 9}]
Print["6nu"]
Do[Print[AccountingForm[{, ν, f, σ_Z^2, σ_Y^2, σ_X^2, blz * f, j, k, m, n,}]],
 {j, 0, 0}, {k, 0, 9}, {m, 6, 6}, {n, 0, 9}]


Print["done!!!"]

" MERGE, COPY AS FORMATTED TEXT, PASTE IN WORD PAD, SAVE AS TEXT DOCUMENT! ";
" The printout is read in columns as follows: 1) Transition Frequency.
   2) Oscillator strenght. 3) μ_Z^2 component. 4) μ_Y^2 component. 5) μ_X^2
   component. 6) Boltzmann Scaled Oscillator Strength. 7) V_i^OH . 8) V_i^T
   . 9) V_f^OH . 10) V_f^T .";
```

1nu

{Null	3568.7	2.62344E-06	2.62344E-06	0	0	1	0	Null}
{Null	3572.4	1.70283E-06	1.70283E-06	0	0	1	1	Null}
{Null	3700.3	7.95784E-07	7.95784E-07	0	0	1	2	Null}
{Null	3753.6	9.92236E-08	9.92236E-08	0	0	1	3	Null}
{Null	3853.1	2.83741E-08	2.83741E-08	0	0	1	4	Null}
{Null	3959.2	2.36861E-08	2.36861E-08	0	0	1	5	Null}
{Null	4077.5	8.56876E-10	8.56876E-10	0	0	1	6	Null}
{Null	4204.5	1.95037E-10	1.95037E-10	0	0	1	7	Null}
{Null	4338.5	6.38477E-11	6.38477E-11	0	0	1	8	Null}
{Null	4478.5	8.52445E-11	8.52445E-11	0	0	1	9	Null}
{Null	3560.3	1.81607E-06	1.74389E-06	0	1	1	0	Null}
{Null	3564	2.35808E-06	2.26435E-06	0	1	1	1	Null}
{Null	3691.9	1.50215E-09	1.44244E-09	0	1	1	2	Null}
{Null	3745.2	5.78548E-07	5.55553E-07	0	1	1	3	Null}
{Null	3844.7	1.34306E-07	1.28968E-07	0	1	1	4	Null}

{Null	3950.8	2.62642E-10	2.52203E-10	0	1	1	5	Null}
{Null	4069.1	1.68379E-09	1.61687E-09	0	1	1	6	Null}
{Null	4196.1	5.8123E-10	5.58128E-10	0	1	1	7	Null}
{Null	4330.1	3.92162E-10	3.76574E-10	0	1	1	8	Null}
{Null	4470.1	3.97766E-12	3.81956E-12	0	1	1	9	Null}
{Null	3443.9	1.46129E-07	7.9991E-08	0	2	1	0	Null}
{Null	3447.6	1.4307E-07	7.83162E-08	0	2	1	1	Null}
{Null	3575.5	3.88383E-06	0.000002126	0	2	1	2	Null}
{Null	3628.8	5.80438E-07	3.17731E-07	0	2	1	3	Null}
{Null	3728.3	8.44852E-07	4.62471E-07	0	2	1	4	Null}
{Null	3834.4	1.88614E-07	1.03247E-07	0	2	1	5	Null}
{Null	3952.7	1.32352E-10	7.24491E-11	0	2	1	6	Null}
{Null	4079.7	1.11641E-09	6.11119E-10	0	2	1	7	Null}
{Null	4213.7	6.91359E-10	3.78449E-10	0	2	1	8	Null}
{Null	4353.7	5.56126E-10	3.04422E-10	0	2	1	9	Null}
{Null	3371.3	1.0622E-10	4.09517E-11	0	3	1	0	Null}
{Null	3375	2.12779E-07	8.20342E-08	0	3	1	1	Null}
{Null	3502.9	8.21699E-07	3.16796E-07	0	3	1	2	Null}
{Null	3556.2	2.57786E-06	9.93863E-07	0	3	1	3	Null}
{Null	3655.7	2.30279E-07	8.87814E-08	0	3	1	4	Null}
{Null	3761.8	7.94032E-07	3.06129E-07	0	3	1	5	Null}
{Null	3880.1	2.50272E-07	9.64893E-08	0	3	1	6	Null}
{Null	4007.1	1.91744E-09	7.39246E-10	0	3	1	7	Null}
{Null	4141.1	9.26851E-11	3.57336E-11	0	3	1	8	Null}
{Null	4281.1	6.27068E-10	2.41758E-10	0	3	1	9	Null}
{Null	3263.7	7.69979E-08	1.7657E-08	0	4	1	0	Null}
{Null	3267.4	4.23187E-08	9.70443E-09	0	4	1	1	Null}
{Null	3395.3	2.26012E-07	5.18286E-08	0	4	1	2	Null}
{Null	3448.6	4.98149E-07	1.14234E-07	0	4	1	3	Null}
{Null	3548.1	2.43366E-06	5.58082E-07	0	4	1	4	Null}
{Null	3654.2	2.48442E-07	5.6972E-08	0	4	1	5	Null}
{Null	3772.5	8.27732E-07	1.89814E-07	0	4	1	6	Null}
{Null	3899.5	2.90049E-07	6.65133E-08	0	4	1	7	Null}
{Null	4033.5	5.18127E-09	1.18816E-09	0	4	1	8	Null}
{Null	4173.5	1.53463E-09	3.51917E-10	0	4	1	9	Null}
{Null	3146.1	3.34574E-08	4.34842E-09	0	5	1	0	Null}
{Null	3149.8	1.94864E-08	2.53263E-09	0	5	1	1	Null}
{Null	3277.7	4.0993E-08	5.32781E-09	0	5	1	2	Null}
{Null	3331	3.49245E-07	4.53909E-08	0	5	1	3	Null}
{Null	3430.5	4.62635E-07	6.01281E-08	0	5	1	4	Null}
{Null	3536.6	2.08578E-06	2.71087E-07	0	5	1	5	Null}
{Null	3654.9	1.89579E-07	2.46394E-08	0	5	1	6	Null}
{Null	3781.9	8.46715E-07	1.10047E-07	0	5	1	7	Null}
{Null	3915.9	3.22088E-07	4.18613E-08	0	5	1	8	Null}
{Null	4055.9	9.90245E-09	1.28701E-09	0	5	1	9	Null}
{Null	3017.6	1.22471E-09	8.55888E-11	0	6	1	0	Null}
{Null	3021.3	1.13634E-08	7.94131E-10	0	6	1	1	Null}
{Null	3149.2	2.31509E-08	1.6179E-09	0	6	1	2	Null}
{Null	3202.5	1.11544E-07	7.79522E-09	0	6	1	3	Null}
{Null	3302	4.06831E-07	2.84314E-08	0	6	1	4	Null}
{Null	3408.1	3.58965E-07	2.50863E-08	0	6	1	5	Null}
{Null	3526.4	1.86578E-06	1.3039E-07	0	6	1	6	Null}
{Null	3653.4	1.47628E-07	1.0317E-08	0	6	1	7	Null}
{Null	3787.4	8.64584E-07	6.04214E-08	0	6	1	8	Null}

{Null	3927.4	3.45327E-07	2.41331E-08	0	6	1	9	Null}
{Null	2880.6	8.99849E-10	3.24545E-11	0	7	1	0	Null}
{Null	2884.3	3.04422E-11	1.09795E-12	0	7	1	1	Null}
{Null	3012.2	1.28551E-08	4.63641E-10	0	7	1	2	Null}
{Null	3065.5	1.07868E-08	3.89042E-10	0	7	1	3	Null}
{Null	3165	1.50428E-07	5.42542E-09	0	7	1	4	Null}
{Null	3271.1	4.73362E-07	1.70725E-08	0	7	1	5	Null}
{Null	3389.4	2.7919E-07	1.00694E-08	0	7	1	6	Null}
{Null	3516.4	1.68234E-06	6.06763E-08	0	7	1	7	Null}
{Null	3650.4	1.11371E-07	4.01676E-09	0	7	1	8	Null}
{Null	3790.4	8.77573E-07	3.16511E-08	0	7	1	9	Null}
{Null	2737	1.59304E-10	2.87218E-12	0	8	1	0	Null}
{Null	2740.7	8.15342E-12	1.47003E-13	0	8	1	1	Null}
{Null	2868.6	9.0888E-11	1.63867E-12	0	8	1	2	Null}
{Null	2921.9	6.4738E-09	1.1672E-10	0	8	1	3	Null}
{Null	3021.4	5.56335E-09	1.00305E-10	0	8	1	4	Null}
{Null	3127.5	1.9432E-07	3.50351E-09	0	8	1	5	Null}
{Null	3245.8	5.2402E-07	9.44787E-09	0	8	1	6	Null}
{Null	3372.8	2.10963E-07	3.80357E-09	0	8	1	7	Null}
{Null	3506.8	1.53173E-06	2.76165E-08	0	8	1	8	Null}
{Null	3646.8	8.16834E-08	1.47272E-09	0	8	1	9	Null}
{Null	2587.9	1.25137E-10	1.0983E-12	0	9	1	0	Null}
{Null	2591.6	9.39895E-11	8.24923E-13	0	9	1	1	Null}
{Null	2719.5	6.50134E-11	5.70607E-13	0	9	1	2	Null}
{Null	2772.8	6.23993E-10	5.47664E-12	0	9	1	3	Null}
{Null	2872.3	3.01022E-09	2.642E-11	0	9	1	4	Null}
{Null	2978.4	1.84642E-09	1.62056E-11	0	9	1	5	Null}
{Null	3096.7	2.28126E-07	2.00221E-09	0	9	1	6	Null}
{Null	3223.7	5.65318E-07	4.96166E-09	0	9	1	7	Null}
{Null	3357.7	1.54852E-07	1.3591E-09	0	9	1	8	Null}
{Null	3497.7	1.40451E-06	1.2327E-08	0	9	1	9	Null}
2nu								
{Null	6974.1	4.90188E-07	4.90188E-07	0	0	2	0	Null}
{Null	6975.3	3.05808E-07	3.05808E-07	0	0	2	1	Null}
{Null	7123.8	1.42803E-07	1.42803E-07	0	0	2	2	Null}
{Null	7155.5	1.1005E-08	1.1005E-08	0	0	2	3	Null}
{Null	7251.7	4.0199E-10	4.0199E-10	0	0	2	4	Null}
{Null	7344	9.46635E-10	9.46635E-10	0	0	2	5	Null}
{Null	7452.3	1.22572E-10	1.22572E-10	0	0	2	6	Null}
{Null	7569.4	2.15756E-11	2.15756E-11	0	0	2	7	Null}
{Null	7694.1	2.69774E-12	2.69774E-12	0	0	2	8	Null}
{Null	7825.3	4.49375E-13	4.49375E-13	0	0	2	9	Null}
{Null	6965.7	3.45348E-07	3.31622E-07	0	1	2	0	Null}
{Null	6966.9	5.06199E-07	4.86079E-07	0	1	2	1	Null}
{Null	7115.4	4.30118E-10	4.13022E-10	0	1	2	2	Null}
{Null	7147.1	9.49202E-08	9.11474E-08	0	1	2	3	Null}
{Null	7243.3	9.63425E-09	9.25132E-09	0	1	2	4	Null}
{Null	7335.6	1.50505E-10	1.44523E-10	0	1	2	5	Null}
{Null	7443.9	5.90073E-12	5.66619E-12	0	1	2	6	Null}
{Null	7561	4.04913E-11	3.88819E-11	0	1	2	7	Null}
{Null	7685.7	1.05847E-11	1.0164E-11	0	1	2	8	Null}
{Null	7816.9	1.29041E-13	1.23912E-13	0	1	2	9	Null}
{Null	6849.3	4.74415E-08	2.59694E-08	0	2	2	0	Null}
{Null	6850.5	7.85963E-08	4.30235E-08	0	2	2	1	Null}

{Null	6999	4.94073E-07	2.70455E-07	0	2	2	2	Null}
{Null	7030.7	9.15307E-08	5.01037E-08	0	2	2	3	Null}
{Null	7126.9	1.64723E-07	9.01689E-08	0	2	2	4	Null}
{Null	7219.2	1.74064E-08	9.52823E-09	0	2	2	5	Null}
{Null	7327.5	1.70154E-10	9.31422E-11	0	2	2	6	Null}
{Null	7444.6	1.37223E-12	7.51157E-13	0	2	2	7	Null}
{Null	7569.3	4.79399E-11	2.62422E-11	0	2	2	8	Null}
{Null	7700.5	1.20474E-11	6.59475E-12	0	2	2	9	Null}
{Null	6776.7	3.78962E-08	1.46104E-08	0	3	2	0	Null}
{Null	6777.9	3.58614E-08	1.38259E-08	0	3	2	1	Null}
{Null	6926.4	1.8564E-07	7.15711E-08	0	3	2	2	Null}
{Null	6958.1	4.70152E-07	1.81261E-07	0	3	2	3	Null}
{Null	7054.3	3.32791E-08	1.28303E-08	0	3	2	4	Null}
{Null	7146.6	1.22354E-07	4.71721E-08	0	3	2	5	Null}
{Null	7254.9	1.98841E-08	7.66608E-09	0	3	2	6	Null}
{Null	7372	5.45931E-10	2.10477E-10	0	3	2	7	Null}
{Null	7496.7	5.70454E-11	2.19931E-11	0	3	2	8	Null}
{Null	7627.9	3.96071E-11	1.527E-11	0	3	2	9	Null}
{Null	6669.1	1.57627E-08	3.61466E-09	0	4	2	0	Null}
{Null	6670.3	4.45026E-09	1.02052E-09	0	4	2	1	Null}
{Null	6818.8	4.84522E-08	1.11109E-08	0	4	2	2	Null}
{Null	6850.5	1.78114E-07	4.08446E-08	0	4	2	3	Null}
{Null	6946.7	4.35813E-07	9.99396E-08	0	4	2	4	Null}
{Null	7039	5.69865E-08	1.3068E-08	0	4	2	5	Null}
{Null	7147.3	1.21563E-07	2.78766E-08	0	4	2	6	Null}
{Null	7264.4	2.2481E-08	5.1553E-09	0	4	2	7	Null}
{Null	7389.1	7.84655E-10	1.79935E-10	0	4	2	8	Null}
{Null	7520.3	1.47616E-10	3.3851E-11	0	4	2	9	Null}
{Null	6551.5	6.42074E-12	8.34495E-13	0	5	2	0	Null}
{Null	6552.7	7.04014E-09	9.14998E-10	0	5	2	1	Null}
{Null	6701.2	1.15112E-08	1.49609E-09	0	5	2	2	Null}
{Null	6732.9	4.59509E-08	5.97218E-09	0	5	2	3	Null}
{Null	6829.1	1.73141E-07	2.25029E-08	0	5	2	4	Null}
{Null	6921.4	4.33034E-07	5.62808E-08	0	5	2	5	Null}
{Null	7029.7	5.72536E-08	7.44118E-09	0	5	2	6	Null}
{Null	7146.8	1.18463E-07	1.53965E-08	0	5	2	7	Null}
{Null	7271.5	2.43851E-08	3.1693E-09	0	5	2	8	Null}
{Null	7402.7	1.04522E-09	1.35846E-10	0	5	2	9	Null}
{Null	6423	1.99464E-09	1.39396E-10	0	6	2	0	Null}
{Null	6424.2	6.27783E-10	4.38726E-11	0	6	2	1	Null}
{Null	6572.7	9.87909E-09	6.904E-10	0	6	2	2	Null}
{Null	6604.4	1.11683E-09	7.80496E-11	0	6	2	3	Null}
{Null	6700.6	4.60436E-08	3.21776E-09	0	6	2	4	Null}
{Null	6792.9	1.73099E-07	1.2097E-08	0	6	2	5	Null}
{Null	6901.2	4.19366E-07	2.93074E-08	0	6	2	6	Null}
{Null	7018.3	5.92362E-08	4.13972E-09	0	6	2	7	Null}
{Null	7143	1.17787E-07	8.23153E-09	0	6	2	8	Null}
{Null	7274.2	2.60354E-08	1.81948E-09	0	6	2	9	Null}
{Null	6286	5.04059E-10	1.81797E-11	0	7	2	0	Null}
{Null	6287.2	3.76785E-10	1.35894E-11	0	7	2	1	Null}
{Null	6435.7	7.96491E-10	2.87267E-11	0	7	2	2	Null}
{Null	6467.4	7.47114E-09	2.69459E-10	0	7	2	3	Null}
{Null	6563.6	4.1378E-11	1.49236E-12	0	7	2	4	Null}
{Null	6655.9	5.44853E-08	1.9651E-09	0	7	2	5	Null}

{Null	6764.2	1.63543E-07	5.89843E-09	0	7	2	6	Null}
{Null	6881.3	4.0784E-07	1.47094E-08	0	7	2	7	Null}
{Null	7006	5.95717E-08	2.14855E-09	0	7	2	8	Null}
{Null	7137.2	1.17633E-07	4.24262E-09	0	7	2	9	Null}
{Null	6142.4	5.0372E-11	9.08187E-13	0	8	2	0	Null}
{Null	6143.6	1.74072E-10	3.13846E-12	0	8	2	1	Null}
{Null	6292.1	5.68918E-10	1.02574E-11	0	8	2	2	Null}
{Null	6323.8	1.63204E-09	2.9425E-11	0	8	2	3	Null}
{Null	6420	6.30956E-09	1.13759E-10	0	8	2	4	Null}
{Null	6512.3	8.02037E-10	1.44604E-11	0	8	2	5	Null}
{Null	6620.6	6.0253E-08	1.08634E-09	0	8	2	6	Null}
{Null	6737.7	1.51513E-07	2.73172E-09	0	8	2	7	Null}
{Null	6862.4	3.97131E-07	7.16011E-09	0	8	2	8	Null}
{Null	6993.6	5.9047E-08	1.06459E-09	0	8	2	9	Null}
{Null	5993.3	2.10505E-11	1.84755E-13	0	9	2	0	Null}
{Null	5994.5	3.66911E-11	3.22029E-13	0	9	2	1	Null}
{Null	6143	2.69997E-10	2.3697E-12	0	9	2	2	Null}
{Null	6174.7	2.11063E-10	1.85245E-12	0	9	2	3	Null}
{Null	6270.9	1.90561E-09	1.67251E-11	0	9	2	4	Null}
{Null	6363.2	5.52406E-09	4.84833E-11	0	9	2	5	Null}
{Null	6471.5	3.3267E-09	2.91976E-11	0	9	2	6	Null}
{Null	6588.6	6.57943E-08	5.77461E-10	0	9	2	7	Null}
{Null	6713.3	1.37352E-07	1.2055E-09	0	9	2	8	Null}
{Null	6844.5	3.87314E-07	3.39937E-09	0	9	2	9	Null}
3nu								
{Null	10182.6	3.23552E-08	3.23552E-08	0	0	3	0	Null}
{Null	10182.9	1.05486E-08	1.05486E-08	0	0	3	1	Null}
{Null	10356.6	1.21445E-08	1.21445E-08	0	0	3	2	Null}
{Null	10369.4	9.77269E-10	9.77269E-10	0	0	3	3	Null}
{Null	10474.8	4.1731E-10	4.1731E-10	0	0	3	4	Null}
{Null	10546.8	2.80388E-12	2.80388E-12	0	0	3	5	Null}
{Null	10645.8	1.69504E-11	1.69504E-11	0	0	3	6	Null}
{Null	10752.4	2.29445E-12	2.29445E-12	0	0	3	7	Null}
{Null	10867.9	7.95676E-15	7.95676E-15	0	0	3	8	Null}
{Null	10990.3	7.66579E-15	7.66579E-15	0	0	3	9	Null}
{Null	10174.2	1.22669E-08	1.17793E-08	0	1	3	0	Null}
{Null	10174.5	3.57625E-08	3.43411E-08	0	1	3	1	Null}
{Null	10348.2	5.39112E-10	5.17684E-10	0	1	3	2	Null}
{Null	10361	8.36948E-09	8.03682E-09	0	1	3	3	Null}
{Null	10466.4	2.4094E-10	2.31364E-10	0	1	3	4	Null}
{Null	10538.4	2.49204E-10	2.39299E-10	0	1	3	5	Null}
{Null	10637.4	7.62938E-12	7.32613E-12	0	1	3	6	Null}
{Null	10744	1.26115E-12	1.21102E-12	0	1	3	7	Null}
{Null	10859.5	2.00147E-13	1.92192E-13	0	1	3	8	Null}
{Null	10981.9	3.4121E-14	3.27648E-14	0	1	3	9	Null}
{Null	10057.8	7.73833E-09	4.23595E-09	0	2	3	0	Null}
{Null	10058.1	4.26362E-09	2.3339E-09	0	2	3	1	Null}
{Null	10231.8	1.94983E-08	1.06733E-08	0	2	3	2	Null}
{Null	10244.6	1.97301E-09	1.08002E-09	0	2	3	3	Null}
{Null	10350	1.78771E-08	9.78588E-09	0	2	3	4	Null}
{Null	10422	9.37242E-10	5.13045E-10	0	2	3	5	Null}
{Null	10521	3.48168E-10	1.90587E-10	0	2	3	6	Null}
{Null	10627.6	1.12827E-11	6.17612E-12	0	2	3	7	Null}
{Null	10743.1	1.70461E-12	9.33098E-13	0	2	3	8	Null}

{Null	10865.5	1.77312E-13	9.70601E-14	0	2	3	9	Null}
{Null	9985.2	3.35323E-09	1.2928E-09	0	3	3	0	Null}
{Null	9985.5	5.85045E-09	2.25557E-09	0	3	3	1	Null}
{Null	10159.2	6.49308E-09	2.50333E-09	0	3	3	2	Null}
{Null	10172	2.77792E-08	1.07099E-08	0	3	3	3	Null}
{Null	10277.4	5.12337E-11	1.97525E-11	0	3	3	4	Null}
{Null	10349.4	1.03086E-08	3.97436E-09	0	3	3	5	Null}
{Null	10448.4	8.12329E-10	3.13183E-10	0	3	3	6	Null}
{Null	10555	3.10992E-10	1.19899E-10	0	3	3	7	Null}
{Null	10670.5	2.14461E-11	8.26828E-12	0	3	3	8	Null}
{Null	10792.9	7.35464E-13	2.83549E-13	0	3	3	9	Null}
{Null	9877.6	2.10691E-09	4.83152E-10	0	4	3	0	Null}
{Null	9877.9	1.01622E-09	2.33038E-10	0	4	3	1	Null}
{Null	10051.6	1.12699E-08	2.58438E-09	0	4	3	2	Null}
{Null	10064.4	7.75627E-09	1.77865E-09	0	4	3	3	Null}
{Null	10169.8	2.06349E-08	4.73195E-09	0	4	3	4	Null}
{Null	10241.8	8.12519E-10	1.86325E-10	0	4	3	5	Null}
{Null	10340.8	9.58103E-09	2.1971E-09	0	4	3	6	Null}
{Null	10447.4	9.04146E-10	2.07337E-10	0	4	3	7	Null}
{Null	10562.9	3.06952E-10	7.03894E-11	0	4	3	8	Null}
{Null	10685.3	2.70622E-11	6.20583E-12	0	4	3	9	Null}
{Null	9760	1.454E-10	1.88974E-11	0	5	3	0	Null}
{Null	9760.3	7.37864E-10	9.58993E-11	0	5	3	1	Null}
{Null	9934	2.62646E-09	3.41358E-10	0	5	3	2	Null}
{Null	9946.8	6.94998E-09	9.0328E-10	0	5	3	3	Null}
{Null	10052.2	6.22477E-09	8.09025E-10	0	5	3	4	Null}
{Null	10124.2	2.73041E-08	3.54868E-09	0	5	3	5	Null}
{Null	10223.2	9.07544E-10	1.17952E-10	0	5	3	6	Null}
{Null	10329.8	8.25501E-09	1.07289E-09	0	5	3	7	Null}
{Null	10445.3	9.22322E-10	1.19873E-10	0	5	3	8	Null}
{Null	10567.7	3.04315E-10	3.95514E-11	0	5	3	9	Null}
{Null	9631.5	2.34455E-10	1.63848E-11	0	6	3	0	Null}
{Null	9631.8	3.6363E-14	2.54123E-15	0	6	3	1	Null}
{Null	9805.5	1.62537E-09	1.13589E-10	0	6	3	2	Null}
{Null	9818.3	8.87222E-10	6.20035E-11	0	6	3	3	Null}
{Null	9923.7	5.47796E-09	3.82827E-10	0	6	3	4	Null}
{Null	9995.7	7.74315E-09	5.4113E-10	0	6	3	5	Null}
{Null	10094.7	2.82358E-08	1.97326E-09	0	6	3	6	Null}
{Null	10201.3	1.1709E-09	8.18284E-11	0	6	3	7	Null}
{Null	10316.8	7.44101E-09	5.20015E-10	0	6	3	8	Null}
{Null	10439.2	9.41167E-10	6.57734E-11	0	6	3	9	Null}
{Null	9494.5	1.99349E-11	7.18983E-13	0	7	3	0	Null}
{Null	9494.8	6.69642E-11	2.41517E-12	0	7	3	1	Null}
{Null	9668.5	1.54302E-11	5.56515E-13	0	7	3	2	Null}
{Null	9681.3	7.55252E-10	2.72394E-11	0	7	3	3	Null}
{Null	9786.7	5.58912E-10	2.0158E-11	0	7	3	4	Null}
{Null	9858.7	5.51948E-09	1.99069E-10	0	7	3	5	Null}
{Null	9957.7	7.62162E-09	2.74886E-10	0	7	3	6	Null}
{Null	10064.3	2.97247E-08	1.07207E-09	0	7	3	7	Null}
{Null	10179.8	1.35861E-09	4.90002E-11	0	7	3	8	Null}
{Null	10302.2	6.76373E-09	2.43944E-10	0	7	3	9	Null}
{Null	9350.9	1.57871E-11	2.84636E-13	0	8	3	0	Null}
{Null	9351.2	2.12749E-11	3.83578E-13	0	8	3	1	Null}
{Null	9524.9	1.53516E-10	2.76784E-12	0	8	3	2	Null}

{Null	9537.7	3.08656E-11	5.56494E-13	0	8	3	3	Null}
{Null	9643.1	5.63432E-10	1.01585E-11	0	8	3	4	Null}
{Null	9715.1	2.26552E-10	4.08465E-12	0	8	3	5	Null}
{Null	9814.1	5.01889E-09	9.04885E-11	0	8	3	6	Null}
{Null	9920.7	7.435E-09	1.3405E-10	0	8	3	7	Null}
{Null	10036.2	3.07158E-08	5.53793E-10	0	8	3	8	Null}
{Null	10158.6	1.52199E-09	2.74409E-11	0	8	3	9	Null}
{Null	9201.8	8.38263E-12	7.35723E-14	0	9	3	0	Null}
{Null	9202.1	5.84192E-12	5.12731E-14	0	9	3	1	Null}
{Null	9375.8	4.58454E-11	4.02374E-13	0	9	3	2	Null}
{Null	9388.6	5.98915E-11	5.25653E-13	0	9	3	3	Null}
{Null	9494	5.54556E-11	4.8672E-13	0	9	3	4	Null}
{Null	9566	5.26217E-10	4.61848E-12	0	9	3	5	Null}
{Null	9665	5.26182E-11	4.61817E-13	0	9	3	6	Null}
{Null	9771.6	4.6276E-09	4.06153E-11	0	9	3	7	Null}
{Null	9887.1	6.99118E-09	6.136E-11	0	9	3	8	Null}
{Null	10009.5	3.15321E-08	2.7675E-10	0	9	3	9	Null}
4nu								
{Null	13196.1	3.59294E-09	3.59294E-09	0	0	4	0	Null}
{Null	13196.2	4.11871E-10	4.11871E-10	0	0	4	1	Null}
{Null	13391.5	1.67848E-09	1.67848E-09	0	0	4	2	Null}
{Null	13394.5	7.25666E-11	7.25666E-11	0	0	4	3	Null}
{Null	13529.6	3.60486E-10	3.60486E-10	0	0	4	4	Null}
{Null	13571	1.11518E-12	1.11518E-12	0	0	4	5	Null}
{Null	13665.2	7.58517E-14	7.58517E-14	0	0	4	6	Null}
{Null	13758.6	9.40573E-14	9.40573E-14	0	0	4	7	Null}
{Null	13864.5	1.20954E-13	1.20954E-13	0	0	4	8	Null}
{Null	13977.8	6.11952E-15	6.11952E-15	0	0	4	9	Null}
{Null	13187.7	4.89274E-10	4.69827E-10	0	1	4	0	Null}
{Null	13187.8	4.14891E-09	3.984E-09	0	1	4	1	Null}
{Null	13383.1	6.45368E-11	6.19717E-11	0	1	4	2	Null}
{Null	13386.1	1.37535E-09	1.32068E-09	0	1	4	3	Null}
{Null	13521.2	1.17379E-12	1.12714E-12	0	1	4	4	Null}
{Null	13562.6	1.58763E-10	1.52453E-10	0	1	4	5	Null}
{Null	13656.8	1.68665E-12	1.61961E-12	0	1	4	6	Null}
{Null	13750.2	1.02459E-12	9.83868E-13	0	1	4	7	Null}
{Null	13856.1	2.17998E-15	2.09333E-15	0	1	4	8	Null}
{Null	13969.4	8.72434E-15	8.37758E-15	0	1	4	9	Null}
{Null	13071.3	1.52139E-09	8.32806E-10	0	2	4	0	Null}
{Null	13071.4	2.39189E-10	1.30932E-10	0	2	4	1	Null}
{Null	13266.7	8.00699E-10	4.38301E-10	0	2	4	2	Null}
{Null	13269.7	3.11135E-11	1.70315E-11	0	2	4	3	Null}
{Null	13404.8	2.8028E-09	1.53425E-09	0	2	4	4	Null}
{Null	13446.2	4.81633E-11	2.63645E-11	0	2	4	5	Null}
{Null	13540.4	3.38305E-10	1.85188E-10	0	2	4	6	Null}
{Null	13633.8	3.07595E-12	1.68377E-12	0	2	4	7	Null}
{Null	13739.7	1.17201E-12	6.41555E-13	0	2	4	8	Null}
{Null	13853	4.04854E-15	2.21616E-15	0	2	4	9	Null}
{Null	12998.7	2.47518E-10	9.54274E-11	0	3	4	0	Null}
{Null	12998.8	1.42768E-09	5.50424E-10	0	3	4	1	Null}
{Null	13194.1	1.87981E-10	7.24739E-11	0	3	4	2	Null}
{Null	13197.1	2.27816E-09	8.78317E-10	0	3	4	3	Null}
{Null	13332.2	2.09663E-11	8.0833E-12	0	3	4	4	Null}
{Null	13373.6	1.71322E-09	6.6051E-10	0	3	4	5	Null}

{Null	13467.8	2.67596E-11	1.03168E-11	0	3	4	6	Null}
{Null	13561.2	1.89434E-10	7.30338E-11	0	3	4	7	Null}
{Null	13667.1	3.20094E-12	1.23408E-12	0	3	4	8	Null}
{Null	13780.4	1.22905E-12	4.73843E-13	0	3	4	9	Null}
{Null	12891.1	6.40247E-10	1.4682E-10	0	4	4	0	Null}
{Null	12891.2	1.17986E-10	2.70562E-11	0	4	4	1	Null}
{Null	13086.5	2.44147E-09	5.59873E-10	0	4	4	2	Null}
{Null	13089.5	3.33254E-10	7.64209E-11	0	4	4	3	Null}
{Null	13224.6	7.4944E-10	1.7186E-10	0	4	4	4	Null}
{Null	13266	1.17029E-12	2.68368E-13	0	4	4	5	Null}
{Null	13360.2	1.61272E-09	3.69826E-10	0	4	4	6	Null}
{Null	13453.6	3.66213E-11	8.3979E-12	0	4	4	7	Null}
{Null	13559.5	1.70559E-10	3.91122E-11	0	4	4	8	Null}
{Null	13672.8	3.35033E-12	7.6829E-13	0	4	4	9	Null}
{Null	12773.5	3.67766E-11	4.7798E-12	0	5	4	0	Null}
{Null	12773.6	2.24852E-10	2.92237E-11	0	5	4	1	Null}
{Null	12968.9	2.70177E-10	3.51145E-11	0	5	4	2	Null}
{Null	12971.9	1.83311E-09	2.38246E-10	0	5	4	3	Null}
{Null	13107	1.67976E-10	2.18316E-11	0	5	4	4	Null}
{Null	13148.4	2.17243E-09	2.82348E-10	0	5	4	5	Null}
{Null	13242.6	1.37156E-12	1.7826E-13	0	5	4	6	Null}
{Null	13336	1.27639E-09	1.65891E-10	0	5	4	7	Null}
{Null	13441.9	3.66947E-11	4.76916E-12	0	5	4	8	Null}
{Null	13555.2	1.48639E-10	1.93184E-11	0	5	4	9	Null}
{Null	12645	5.5255E-11	3.86149E-12	0	6	4	0	Null}
{Null	12645.1	4.53301E-12	3.16789E-13	0	6	4	1	Null}
{Null	12840.4	7.50157E-10	5.24247E-11	0	6	4	2	Null}
{Null	12843.4	1.3951E-10	9.74967E-12	0	6	4	3	Null}
{Null	12978.5	1.37789E-09	9.62939E-11	0	6	4	4	Null}
{Null	13019.9	3.25889E-10	2.27747E-11	0	6	4	5	Null}
{Null	13114.1	2.30129E-09	1.60826E-10	0	6	4	6	Null}
{Null	13207.5	9.1646E-12	6.40468E-13	0	6	4	7	Null}
{Null	13313.4	1.06291E-09	7.42816E-11	0	6	4	8	Null}
{Null	13426.7	3.73408E-11	2.60956E-12	0	6	4	9	Null}
{Null	12508	6.5955E-14	2.37877E-15	0	7	4	0	Null}
{Null	12508.1	1.0707E-11	3.86166E-13	0	7	4	1	Null}
{Null	12703.4	2.83859E-11	1.02378E-12	0	7	4	2	Null}
{Null	12706.4	2.40614E-10	8.67812E-12	0	7	4	3	Null}
{Null	12841.5	1.08585E-10	3.91629E-12	0	7	4	4	Null}
{Null	12882.9	1.49413E-09	5.38882E-11	0	7	4	5	Null}
{Null	12977.1	3.19859E-10	1.15362E-11	0	7	4	6	Null}
{Null	13070.5	2.96515E-09	1.06943E-10	0	7	4	7	Null}
{Null	13176.4	1.73274E-11	6.2494E-13	0	7	4	8	Null}
{Null	13289.7	8.69551E-10	3.13617E-11	0	7	4	9	Null}
{Null	12364.4	3.2186E-12	5.803E-14	0	8	4	0	Null}
{Null	12364.5	1.41166E-12	2.54517E-14	0	8	4	1	Null}
{Null	12559.8	4.11618E-11	7.42131E-13	0	8	4	2	Null}
{Null	12562.8	7.65225E-13	1.37967E-14	0	8	4	3	Null}
{Null	12697.9	1.97017E-10	3.55215E-12	0	8	4	4	Null}
{Null	12739.3	7.45874E-11	1.34478E-12	0	8	4	5	Null}
{Null	12833.5	1.27701E-09	2.30239E-11	0	8	4	6	Null}
{Null	12926.9	3.58506E-10	6.46373E-12	0	8	4	7	Null}
{Null	13032.8	3.38543E-09	6.1038E-11	0	8	4	8	Null}
{Null	13146.1	2.71085E-11	4.88755E-13	0	8	4	9	Null}

{Null 12215.3 1.3329E-12 1.16986E-14 0 9 4 0 Null}
{Null 12215.4 2.01494E-12 1.76846E-14 0 9 4 1 Null}
{Null 12410.7 2.43842E-12 2.14014E-14 0 9 4 2 Null}
{Null 12413.7 1.03203E-11 9.05785E-14 0 9 4 3 Null}
{Null 12548.8 3.22533E-13 2.83079E-15 0 9 4 4 Null}
{Null 12590.2 1.01142E-10 8.87697E-13 0 9 4 5 Null}
{Null 12684.4 4.39991E-11 3.8617E-13 0 9 4 6 Null}
{Null 12777.8 1.16912E-09 1.02611E-11 0 9 4 7 Null}
{Null 12883.7 3.59027E-10 3.1511E-12 0 9 4 8 Null}
{Null 12997 3.78201E-09 3.31938E-11 0 9 4 9 Null}
5nu
{Null 16017.3 2.12422E-10 2.12422E-10 0 0 5 0 Null}
{Null 16017.3 2.46263E-11 2.46263E-11 0 0 5 1 Null}
{Null 16228.9 1.04454E-10 1.04454E-10 0 0 5 2 Null}
{Null 16229.3 4.56033E-12 4.56033E-12 0 0 5 3 Null}
{Null 16404.1 4.17599E-11 4.17599E-11 0 0 5 4 Null}
{Null 16416.7 1.98532E-13 1.98532E-13 0 0 5 5 Null}
{Null 16525.7 3.16469E-12 3.16469E-12 0 0 5 6 Null}
{Null 16593.9 2.41412E-15 2.41412E-15 0 0 5 7 Null}
{Null 16691 3.8082E-15 3.8082E-15 0 0 5 8 Null}
{Null 16793.3 3.2715E-16 3.2715E-16 0 0 5 9 Null}
{Null 16008.9 2.99258E-11 2.87363E-11 0 1 5 0 Null}
{Null 16008.9 2.53354E-10 2.43284E-10 0 1 5 1 Null}
{Null 16220.5 4.61948E-12 4.43587E-12 0 1 5 2 Null}
{Null 16220.9 1.01422E-10 9.73911E-11 0 1 5 3 Null}
{Null 16395.7 4.18882E-14 4.02233E-14 0 1 5 4 Null}
{Null 16408.3 2.3488E-11 2.25544E-11 0 1 5 5 Null}
{Null 16517.3 7.59912E-14 7.29708E-14 0 1 5 6 Null}
{Null 16585.5 1.0599E-12 1.01778E-12 0 1 5 7 Null}
{Null 16682.6 3.67798E-16 3.53179E-16 0 1 5 8 Null}
{Null 16784.9 9.89768E-15 9.50428E-15 0 1 5 9 Null}
{Null 15892.5 1.39716E-10 7.64803E-11 0 2 5 0 Null}
{Null 15892.5 2.05484E-11 1.12482E-11 0 2 5 1 Null}
{Null 16104.1 6.58489E-12 3.60456E-12 0 2 5 2 Null}
{Null 16104.5 3.54097E-13 1.93832E-13 0 2 5 3 Null}
{Null 16279.3 1.08464E-10 5.93729E-11 0 2 5 4 Null}
{Null 16291.9 1.87958E-12 1.02888E-12 0 2 5 5 Null}
{Null 16400.9 7.1684E-11 3.92397E-11 0 2 5 6 Null}
{Null 16469.1 2.61805E-13 1.43312E-13 0 2 5 7 Null}
{Null 16566.2 1.89165E-12 1.03549E-12 0 2 5 8 Null}
{Null 16668.5 1.59597E-16 8.7363E-17 0 2 5 9 Null}
{Null 15819.9 2.6829E-11 1.03436E-11 0 3 5 0 Null}
{Null 15819.9 1.64259E-10 6.3328E-11 0 3 5 1 Null}
{Null 16031.5 6.07351E-12 2.34157E-12 0 3 5 2 Null}
{Null 16031.9 7.0133E-11 2.70389E-11 0 3 5 3 Null}
{Null 16206.7 2.85435E-12 1.10046E-12 0 3 5 4 Null}
{Null 16219.3 1.09909E-10 4.23739E-11 0 3 5 5 Null}
{Null 16328.3 2.8493E-13 1.09851E-13 0 3 5 6 Null}
{Null 16396.5 3.11234E-11 1.19992E-11 0 3 5 7 Null}
{Null 16493.6 2.19158E-13 8.44938E-14 0 3 5 8 Null}
{Null 16595.9 9.75107E-13 3.7594E-13 0 3 5 9 Null}
{Null 15712.3 1.01384E-10 2.32491E-11 0 4 5 0 Null}
{Null 15712.3 1.85829E-11 4.2614E-12 0 4 5 1 Null}
{Null 15923.9 1.67799E-10 3.84792E-11 0 4 5 2 Null}

{Null	15924.3	1.92877E-11	4.42301E-12	0	4	5	3	Null}
{Null	16099.1	2.02693E-12	4.6481E-13	0	4	5	4	Null}
{Null	16111.7	3.61431E-13	8.28825E-14	0	4	5	5	Null}
{Null	16220.7	8.72648E-11	2.00114E-11	0	4	5	6	Null}
{Null	16288.9	1.14572E-12	2.62733E-13	0	4	5	7	Null}
{Null	16386	2.84954E-11	6.5345E-12	0	4	5	8	Null}
{Null	16488.3	2.26687E-13	5.19832E-14	0	4	5	9	Null}
{Null	15594.7	9.60525E-12	1.24838E-12	0	5	5	0	Null}
{Null	15594.7	4.94379E-11	6.42538E-12	0	5	5	1	Null}
{Null	15806.3	2.8173E-11	3.66161E-12	0	5	5	2	Null}
{Null	15806.7	2.01112E-10	2.61383E-11	0	5	5	3	Null}
{Null	15981.5	3.93661E-12	5.11636E-13	0	5	5	4	Null}
{Null	15994.1	4.71483E-11	6.12781E-12	0	5	5	5	Null}
{Null	16103.1	5.27807E-13	6.85984E-14	0	5	5	6	Null}
{Null	16171.3	8.58882E-11	1.11628E-11	0	5	5	7	Null}
{Null	16268.4	1.16142E-12	1.50948E-13	0	5	5	8	Null}
{Null	16370.7	2.23332E-11	2.90261E-12	0	5	5	9	Null}
{Null	15466.2	1.67024E-11	1.16725E-12	0	6	5	0	Null}
{Null	15466.2	3.01821E-12	2.10928E-13	0	6	5	1	Null}
{Null	15677.8	1.44352E-10	1.00881E-11	0	6	5	2	Null}
{Null	15678.2	2.41762E-11	1.68955E-12	0	6	5	3	Null}
{Null	15853	1.3763E-10	9.61829E-12	0	6	5	4	Null}
{Null	15865.6	1.72339E-11	1.20439E-12	0	6	5	5	Null}
{Null	15974.6	3.04853E-11	2.13046E-12	0	6	5	6	Null}
{Null	16042.8	8.93765E-16	6.24607E-17	0	6	5	7	Null}
{Null	16139.9	7.24454E-11	5.06284E-12	0	6	5	8	Null}
{Null	16242.2	1.29659E-12	9.06121E-14	0	6	5	9	Null}
{Null	15329.2	3.62899E-13	1.30885E-14	0	7	5	0	Null}
{Null	15329.2	3.521E-12	1.2699E-13	0	7	5	1	Null}
{Null	15540.8	1.20587E-11	4.34917E-13	0	7	5	2	Null}
{Null	15541.2	6.84257E-11	2.46788E-12	0	7	5	3	Null}
{Null	15716	2.09128E-11	7.54253E-13	0	7	5	4	Null}
{Null	15728.6	1.88896E-10	6.81281E-12	0	7	5	5	Null}
{Null	15837.6	1.22854E-11	4.43093E-13	0	7	5	6	Null}
{Null	15905.8	9.75984E-11	3.52004E-12	0	7	5	7	Null}
{Null	16002.9	1.44884E-13	5.22548E-15	0	7	5	8	Null}
{Null	16105.2	5.89651E-11	2.12667E-12	0	7	5	9	Null}
{Null	15185.6	4.33101E-13	7.80863E-15	0	8	5	0	Null}
{Null	15185.6	1.3465E-14	2.42768E-16	0	8	5	1	Null}
{Null	15397.2	1.90599E-11	3.43642E-13	0	8	5	2	Null}
{Null	15397.6	2.98352E-12	5.37917E-14	0	8	5	3	Null}
{Null	15572.4	8.85579E-11	1.59666E-12	0	8	5	4	Null}
{Null	15585	1.91469E-11	3.45211E-13	0	8	5	5	Null}
{Null	15694	1.40887E-10	2.54014E-12	0	8	5	6	Null}
{Null	15762.2	2.32851E-11	4.1982E-13	0	8	5	7	Null}
{Null	15859.3	1.36297E-10	2.45738E-12	0	8	5	8	Null}
{Null	15961.6	7.61009E-13	1.37207E-14	0	8	5	9	Null}
{Null	15036.5	1.67089E-13	1.4665E-15	0	9	5	0	Null}
{Null	15036.5	2.87925E-13	2.52705E-15	0	9	5	1	Null}
{Null	15248.1	6.45735E-14	5.66746E-16	0	9	5	2	Null}
{Null	15248.5	2.58179E-12	2.26598E-14	0	9	5	3	Null}
{Null	15423.3	4.63043E-12	4.06402E-14	0	9	5	4	Null}
{Null	15435.9	4.17925E-11	3.66803E-13	0	9	5	5	Null}
{Null	15544.9	1.27828E-11	1.12191E-13	0	9	5	6	Null}

{Null	15613.1	1.7626E-10	1.54699E-12	0	9	5	7	Null}
{Null	15710.2	2.6491E-11	2.32505E-13	0	9	5	8	Null}
{Null	15812.5	1.87526E-10	1.64587E-12	0	9	5	9	Null}
6nu								
{Null	18645.6	2.74267E-11	2.74267E-11	0	0	6	0	Null}
{Null	18645.6	7.50657E-13	7.50657E-13	0	0	6	1	Null}
{Null	18870.3	3.16434E-11	3.16434E-11	0	0	6	2	Null}
{Null	18870.4	1.91527E-14	1.91527E-14	0	0	6	3	Null}
{Null	19072.8	2.45885E-11	2.45885E-11	0	0	6	4	Null}
{Null	19074.5	1.46897E-13	1.46897E-13	0	0	6	5	Null}
{Null	19229.6	1.22113E-11	1.22113E-11	0	0	6	6	Null}
{Null	19257.3	5.16639E-14	5.16639E-14	0	0	6	7	Null}
{Null	19356.9	6.56874E-13	6.56874E-13	0	0	6	8	Null}
{Null	19440.2	9.95735E-16	9.95735E-16	0	0	6	9	Null}
{Null	18637.2	9.53361E-13	9.15468E-13	0	1	6	0	Null}
{Null	18637.2	3.27727E-11	3.14701E-11	0	1	6	1	Null}
{Null	18861.9	2.27639E-14	2.18591E-14	0	1	6	2	Null}
{Null	18862	3.35349E-11	3.2202E-11	0	1	6	3	Null}
{Null	19064.4	1.47481E-13	1.41619E-13	0	1	6	4	Null}
{Null	19066.1	1.91836E-11	1.84211E-11	0	1	6	5	Null}
{Null	19221.2	1.89235E-14	1.81713E-14	0	1	6	6	Null}
{Null	19248.9	4.81103E-12	4.61981E-12	0	1	6	7	Null}
{Null	19348.5	1.19245E-14	1.14506E-14	0	1	6	8	Null}
{Null	19431.8	3.36631E-13	3.23251E-13	0	1	6	9	Null}
{Null	18520.8	1.79268E-11	9.8131E-12	0	2	6	0	Null}
{Null	18520.8	1.16003E-12	6.35E-13	0	2	6	1	Null}
{Null	18745.5	5.98212E-13	3.2746E-13	0	2	6	2	Null}
{Null	18745.6	4.10719E-14	2.24827E-14	0	2	6	3	Null}
{Null	18948	1.40007E-11	7.66395E-12	0	2	6	4	Null}
{Null	18949.7	9.98358E-16	5.465E-16	0	2	6	5	Null}
{Null	19104.8	5.71404E-11	3.12786E-11	0	2	6	6	Null}
{Null	19132.5	1.03955E-13	5.69051E-14	0	2	6	7	Null}
{Null	19232.1	1.76519E-11	9.6626E-12	0	2	6	8	Null}
{Null	19315.4	7.01257E-14	3.83867E-14	0	2	6	9	Null}
{Null	18448.2	2.10253E-12	8.10606E-13	0	3	6	0	Null}
{Null	18448.2	2.02916E-11	7.82317E-12	0	3	6	1	Null}
{Null	18672.9	1.79176E-13	6.9079E-14	0	3	6	2	Null}
{Null	18673	2.23657E-12	8.62282E-13	0	3	6	3	Null}
{Null	18875.4	3.6035E-14	1.38928E-14	0	3	6	4	Null}
{Null	18877.1	3.07727E-11	1.1864E-11	0	3	6	5	Null}
{Null	19032.2	1.64446E-13	6.34E-14	0	3	6	6	Null}
{Null	19059.9	3.17375E-11	1.2236E-11	0	3	6	7	Null}
{Null	19159.5	2.76971E-15	1.06783E-15	0	3	6	8	Null}
{Null	19242.8	6.7544E-12	2.60408E-12	0	3	6	9	Null}
{Null	18340.6	1.1182E-11	2.56424E-12	0	4	6	0	Null}
{Null	18340.6	2.32026E-12	5.32076E-13	0	4	6	1	Null}
{Null	18565.3	1.49359E-11	3.42506E-12	0	4	6	2	Null}
{Null	18565.4	6.66585E-13	1.5286E-13	0	4	6	3	Null}
{Null	18767.8	1.37627E-11	3.15604E-12	0	4	6	4	Null}
{Null	18769.5	8.04133E-14	1.84402E-14	0	4	6	5	Null}
{Null	18924.6	8.64107E-12	1.98155E-12	0	4	6	6	Null}
{Null	18952.3	3.37228E-14	7.73324E-15	0	4	6	7	Null}
{Null	19051.9	3.40648E-11	7.81165E-12	0	4	6	8	Null}
{Null	19135.2	2.97349E-14	6.81873E-15	0	4	6	9	Null}

{Null 18223 2.0059E-12 2.60704E-13 0 5 6 0 Null}
{Null 18223 4.26395E-12 5.5418E-13 0 5 6 1 Null}
{Null 18447.7 1.67371E-12 2.1753E-13 0 5 6 2 Null}
{Null 18447.8 2.2814E-11 2.96511E-12 0 5 6 3 Null}
{Null 18650.2 1.82352E-13 2.37001E-14 0 5 6 4 Null}
{Null 18651.9 7.21794E-14 9.38106E-15 0 5 6 5 Null}
{Null 18807 6.56574E-14 8.5334E-15 0 5 6 6 Null}
{Null 18834.7 2.58812E-11 3.36375E-12 0 5 6 7 Null}
{Null 18934.3 6.11316E-14 7.94519E-15 0 5 6 8 Null}
{Null 19017.6 2.58379E-11 3.35812E-12 0 5 6 9 Null}
{Null 18094.5 7.9169E-13 5.53272E-14 0 6 6 0 Null}
{Null 18094.5 1.20738E-12 8.43776E-14 0 6 6 1 Null}
{Null 18319.2 1.72204E-11 1.20345E-12 0 6 6 2 Null}
{Null 18319.3 2.67538E-12 1.86968E-13 0 6 6 3 Null}
{Null 18521.7 9.55521E-12 6.67765E-13 0 6 6 4 Null}
{Null 18523.4 6.26694E-13 4.37965E-14 0 6 6 5 Null}
{Null 18678.5 3.95248E-12 2.76219E-13 0 6 6 6 Null}
{Null 18706.2 1.82122E-13 1.27276E-14 0 6 6 7 Null}
{Null 18805.8 2.1823E-11 1.5251E-12 0 6 6 8 Null}
{Null 18889.1 2.7095E-14 1.89353E-15 0 6 6 9 Null}
{Null 17957.5 4.53667E-13 1.63622E-14 0 7 6 0 Null}
{Null 17957.5 1.14222E-14 4.1196E-16 0 7 6 1 Null}
{Null 18182.2 2.74143E-12 9.88738E-14 0 7 6 2 Null}
{Null 18182.3 6.93745E-12 2.5021E-13 0 7 6 3 Null}
{Null 18384.7 1.63321E-12 5.89044E-14 0 7 6 4 Null}
{Null 18386.4 2.04472E-11 7.3746E-13 0 7 6 5 Null}
{Null 18541.5 2.97899E-13 1.07442E-14 0 7 6 6 Null}
{Null 18569.2 4.30755E-13 1.55359E-14 0 7 6 7 Null}
{Null 18668.8 2.36307E-13 8.5228E-15 0 7 6 8 Null}
{Null 18752.1 2.57973E-11 9.30422E-13 0 7 6 9 Null}
{Null 17813.9 8.27404E-14 1.49178E-15 0 8 6 0 Null}
{Null 17813.9 6.9809E-14 1.25863E-15 0 8 6 1 Null}
{Null 18038.6 1.07073E-12 1.93048E-14 0 8 6 2 Null}
{Null 18038.7 1.72992E-12 3.11898E-14 0 8 6 3 Null}
{Null 18241.1 1.46494E-11 2.64123E-13 0 8 6 4 Null}
{Null 18242.8 2.68413E-12 4.83938E-14 0 8 6 5 Null}
{Null 18397.9 1.17127E-11 2.11175E-13 0 8 6 6 Null}
{Null 18425.6 9.73586E-13 1.75534E-14 0 8 6 7 Null}
{Null 18525.2 1.22966E-12 2.21704E-14 0 8 6 8 Null}
{Null 18608.5 4.48723E-13 8.09029E-15 0 8 6 9 Null}
{Null 17664.8 8.25526E-16 7.24544E-18 0 9 6 0 Null}
{Null 17664.8 1.08504E-13 9.52316E-16 0 9 6 1 Null}
{Null 17889.5 5.53206E-13 4.85536E-15 0 9 6 2 Null}
{Null 17889.6 1.89074E-14 1.65946E-16 0 9 6 3 Null}
{Null 18092 2.39742E-12 2.10416E-14 0 9 6 4 Null}
{Null 18093.7 4.72653E-12 4.14837E-14 0 9 6 5 Null}
{Null 18248.8 1.61081E-12 1.41377E-14 0 9 6 6 Null}
{Null 18276.5 1.90853E-11 1.67507E-13 0 9 6 7 Null}
{Null 18376.1 1.07941E-12 9.47369E-15 0 9 6 8 Null}
{Null 18459.4 6.25353E-12 5.48858E-14 0 9 6 9 Null}
done!!!

D.13 "Franck-Condon" OH-Stretch / HOON-Torsion Oscillator Model for CH_3OOH Using CCSD(T)/cc-pVTZ Dipole Moment Surface

This code is used to compute the oscillator strength of the vibrational transitions of CH_3OOH using the "Franck-Condon" model (see Chapter 7). The two-dimensional dipole moment surfaces does not take into account the torsional dependence in calculating the oscillator strength but instead, uses Eq. 7.12 where, the transition dipole moment is "scaled" by the overlap intergral:

$$|\mu|^2 = \Sigma_{\alpha=a,b,c} |< \psi_{v'}^{OH}(r|\tau)\, |\mu_\alpha(r)|\, \psi_v^{OH}(r|\tau)> < \chi^{v'}_{m'}(\tau)|\chi^{v}_{m}(\tau)>|^2$$

Mathematica Program mhp_fc.nb:

```
Off[General::spelll]
Off[General::spell]
<< Graphics`Graphics3D`
<< Statistics`DataManipulation`
"first ind. describe the electronic surface";
SetDirectory[
  "C:/Documents and Settings/overtone/My
    Documents/Jamie/Thesis/CHAPTERS/APPENDIXD/codes/mhp_fc"];
"Dipole Functions Imports";
dipZ = Import["Zsurface_ccsdt.txt", "Table"];
dipY = Import["Ysurface_ccsdt.txt", "Table"];
dipX = Import["Xsurface_ccsdt.txt", "Table"];

"wavefuctions for Tau v=0-9 at ground state imports";

Do[v0,w = Column[Import["efzero.txt", "Table"], {1, w + 2}] , {w, 0, 9}]

"wavefuctions for OH imports";

Do[nw = Column[Import["evoh.txt", "Table"], {1, w + 2}] , {w, 0, 6}]

"wavefuctions for Tau v=0-9 1st Excited state imports";

Do[v1,w = Column[Import["efone.txt", "Table"], {1, w + 2}] , {w, 0, 9}]

"wavefuctions for Tau v=0-9 at 2nd Excited State imports";

Do[v2,w = Column[Import["eftwo.txt", "Table"], {1, w + 2}] , {w, 0, 9}]
```

```
"wavefuctions for Tau v=0-9 3rd Excited State imports";

Do[v3,w = Column[Import["efthree.txt", "Table"], {1, w + 2}] , {w, 0, 9}]

"wavefuctions for Tau v=0-9 4th Excited State imports";

Do[v4,w = Column[Import["effour.txt", "Table"], {1, w + 2}] , {w, 0, 9}]

"wavefuctions for Tau v=0-9 5th Excited State imports";

Do[v5,w = Column[Import["effive.txt", "Table"], {1, w + 2}] , {w, 0, 9}]

"wavefuctions for Tau v=0-9 6th Excited State imports";

Do[v6,w = Column[Import["efsix.txt", "Table"], {1, w + 2}] , {w, 0, 9}]



"Load Transition Frequencies Matrix";
transfreq = Import["evfreq.txt", "Table"];

Print["import complete"]
" OH wavefunctions run from 0-->ohfinal ";
ohfinal = 6;

" Tau wavefunctions run from 0-->taufinal ";
taufinal = 9;

"Plots for quantum yield";

" qylp=ListPlot[qy,PlotStyle→PointSize[0.025]] ";

"Plots for dipole surfaces";


dipZplot = ListPlot[dipZ, PlotRange → {-2, 0}]
dipYplot = ListPlot[dipY, PlotRange → {-2, 0}]
dipXplot = ListPlot[dipX, PlotRange → {-2, 0}]
```

```
"Plots for all eigenvectors of Tau";
Do[{
  γstr,tor = ListPlot[vstr,tor, PlotStyle → PointSize[0.015], PlotRange → {-0.3, 0.3},
    DefaultColor → RGBColor[0.8, 0.1, 0.1], DisplayFunction → Identity]},
 {str, 0, ohfinal}, {tor, 0, taufinal}]
Show[GraphicsArray[Table[γstr,tor, {str, 0, 6}, {tor, 0, 9}]]]

"Plots for all eigenvectors of OH ";
Do[{
  βstr = ListPlot[nstr, PlotStyle → PointSize[0.015], PlotRange → {-0.25, 0.25},
    DefaultColor → RGBColor[0.2, 0.1, 0.9], DisplayFunction → Identity]},
 {str, 0, ohfinal}]
Show[GraphicsArray[Table[βstr, {str, 0, 6}]]]

" Dipole Surface fit using interpolation ";

μZ = Interpolation[dipZ, InterpolationOrder → 3];
μY = Interpolation[dipY, InterpolationOrder → 3];
μX = Interpolation[dipX, InterpolationOrder → 3];
muZplot = Plot[μZ[y], {y, 0.56516718, 1.56516718}]
Show[muZplot, dipZplot]
Pause[1];
muYplot = Plot[μY[y], {y, 0.56516718, 1.56516718}]
Show[muYplot, dipYplot]
Pause[1];
muXplot = Plot[μX[y], {y, 0.56516718, 1.56516718}]
Show[muXplot, dipXplot]
Pause[1];

"wavefunctions interpolation for all Tau";
Do[{
  Ψstr,tor = Interpolation[vstr,tor, InterpolationOrder → 3];
  χstr,tor = Plot[Evaluate[Ψstr,tor][x], {x, 0, 2π}, PlotPoints → 100,
    PlotRange → {-0.25, 0.25}];
  Show[{γstr,tor, χstr,tor}], {str, 0, ohfinal}, {tor, 0, taufinal}]

"wavefunctions interpolation for all OH ";
Do[{
  Østr = Interpolation[nstr, InterpolationOrder → 3];
  Υstr = Plot[Evaluate[Østr][y], {y, 0.3, 2.0}, PlotPoints → 100,
    PlotRange → {-0.25, 0.25}];
  Show[{Υstr, βstr}], {str, 0, ohfinal}]
```

```
"Normalization for all Tau wavefunctions ";

Do[{
  α_{str,tor} =
    NIntegrate[Evaluate[Ψ_{str,tor}][x] * Evaluate[Ψ_{str,tor}][x], {x, 0, 2π},
      MaxRecursion → 100]^-0.5;}, {str, 0, ohfinal}, {tor, 0, taufinal}]

"Normalization for all OH wavefunctions ";

η = 0.3;
θ = 2.0;
Do[{
  p_{str} =
    NIntegrate[Evaluate[Ø_{str}][y] * Evaluate[Ø_{str}][y], {y, η, θ},
      MaxRecursion → 100]^-0.5;}, {str, 0, ohfinal}]

"DO LOOP FOR EXPORTS";
"Format: |j,k> → |m,n>  j, m - electronic surface, k ,n -tau
   functions on associated surface";
Off[NIntegrate::inum]
Off[Part::pspec]
freq = transfreq;
ν = (freq[[m + 1, n + 1]] - freq[[j + 1, k + 1]]);
Clear[m, n, j, k]
σ_B =
  NIntegrate[Evaluate[Ø_j][y] * Evaluate[Ψ_{j,k}][x] * Evaluate[μ_B][y] *
     Evaluate[Ψ_{m,n}][x] * Evaluate[Ø_m][y], {y, 0.56516718, 1.56516718},
    {x, 0, 2π}] * (p_j * p_m) * (α_{j,k} * α_{m,n});
σ_Y =
  NIntegrate[Evaluate[Ø_j][y] * Evaluate[Ψ_{j,k}][x] * Evaluate[μ_Y][y] *
     Evaluate[Ψ_{m,n}][x] * Evaluate[Ø_m][y], {y, 0.56516718, 1.56516718},
    {x, 0, 2π}] * (p_j * p_m) * (α_{j,k} * α_{m,n});
σ_X =
  NIntegrate[Evaluate[Ø_j][y] * Evaluate[Ψ_{j,k}][x] * Evaluate[μ_X][y] *
     Evaluate[Ψ_{m,n}][x] * Evaluate[Ø_m][y], {y, 0.56516718, 1.56516718},
    {x, 0, 2π}] * (p_j * p_m) * (α_{j,k} * α_{m,n});

blz = Exp[-(freq[[j + 1, k + 1]] - freq[[1, 1]]) / (kb * T)];
f = 4.702*^-7 * ν * Σ;
kb = 0.695;
T = 298;
```

```
Σ = σX^2 + σY^2 + σS^2;
w = ν;
Print["1nu"]
Do[Print[AccountingForm[{, ν, f, blz * f, j, k, m, n,}]], {j, 0, 0},
 {k, 0, 9}, {m, 1, 1}, {n, 0, 9}]
Print["2nu"]
Do[Print[AccountingForm[{, ν, f, blz * f, j, k, m, n,}]], {j, 0, 0},
 {k, 0, 9}, {m, 2, 2}, {n, 0, 9}]
Print["3nu"]
Do[Print[AccountingForm[{, ν, f, blz * f, j, k, m, n,}]], {j, 0, 0},
 {k, 0, 9}, {m, 3, 3}, {n, 0, 9}]
Print["4nu"]
Do[Print[AccountingForm[{, ν, f, blz * f, j, k, m, n,}]], {j, 0, 0},
 {k, 0, 9}, {m, 4, 4}, {n, 0, 9}]
Print["5nu"]
Do[Print[AccountingForm[{, ν, f, blz * f, j, k, m, n,}]], {j, 0, 0},
 {k, 0, 9}, {m, 5, 5}, {n, 0, 9}]
Print["6nu"]
Do[Print[AccountingForm[{, ν, f, blz * f, j, k, m, n,}]], {j, 0, 0},
 {k, 0, 9}, {m, 6, 6}, {n, 0, 9}]

Print["done!!!", Date[]]

" MERGE, COPY AS FORMATTED TEXT, PASTE IN WORD PAD, SAVE AS TEXT DOCUMENT! ";
```

1nu

{Null	3568.7	4.91052E-06	4.91052E-06	0	0	1	0	Null}
{Null	3572.4	1.25792E-11	1.25792E-11	0	0	1	1	Null}
{Null	3700.3	1.38627E-07	1.38627E-07	0	0	1	2	Null}
{Null	3753.6	3.26918E-15	3.26918E-15	0	0	1	3	Null}
{Null	3853.1	1.0139E-09	1.0139E-09	0	0	1	4	Null}
{Null	3959.2	1.20906E-15	1.20906E-15	0	0	1	5	Null}
{Null	4077.5	1.18741E-10	1.18741E-10	0	0	1	6	Null}
{Null	4204.5	2.73322E-17	2.73322E-17	0	0	1	7	Null}
{Null	4338.5	9.1132E-12	9.1132E-12	0	0	1	8	Null}
{Null	4478.5	9.72998E-17	9.72998E-17	0	0	1	9	Null}
{Null	3560.3	1.28151E-11	1.23058E-11	0	1	1	0	Null}
{Null	3564	4.9791E-06	4.7812E-06	0	1	1	1	Null}
{Null	3691.9	1.74622E-14	1.67682E-14	0	1	1	2	Null}
{Null	3745.2	6.24149E-08	5.99341E-08	0	1	1	3	Null}
{Null	3844.7	3.91565E-16	3.76002E-16	0	1	1	4	Null}
{Null	3950.8	3.92753E-10	3.77143E-10	0	1	1	5	Null}
{Null	4069.1	3.17886E-16	3.05251E-16	0	1	1	6	Null}
{Null	4196.1	6.39232E-11	6.13825E-11	0	1	1	7	Null}
{Null	4330.1	2.47592E-16	2.37751E-16	0	1	1	8	Null}
{Null	4470.1	1.27048E-12	1.21999E-12	0	1	1	9	Null}
{Null	3443.9	1.23892E-07	6.78182E-08	0	2	1	0	Null}

{Null	3447.6	3.96617E-13	2.17108E-13	0	2	1	1	Null}
{Null	3575.5	0.000004837	2.64777E-06	0	2	1	2	Null}
{Null	3628.8	2.02885E-15	1.11059E-15	0	2	1	3	Null}
{Null	3728.3	9.2935E-08	5.08725E-08	0	2	1	4	Null}
{Null	3834.4	1.22739E-14	6.71871E-15	0	2	1	5	Null}
{Null	3952.7	7.83659E-11	4.28974E-11	0	2	1	6	Null}
{Null	4079.7	2.76381E-16	1.5129E-16	0	2	1	7	Null}
{Null	4213.7	8.13601E-11	4.45364E-11	0	2	1	8	Null}
{Null	4353.7	1.17916E-14	6.45473E-15	0	2	1	9	Null}
{Null	3371.3	1.7684E-13	6.81784E-14	0	3	1	0	Null}
{Null	3375	5.58788E-08	2.15434E-08	0	3	1	1	Null}
{Null	3502.9	1.59822E-15	6.16176E-16	0	3	1	2	Null}
{Null	3556.2	4.91371E-06	1.89442E-06	0	3	1	3	Null}
{Null	3655.7	3.74451E-17	1.44365E-17	0	3	1	4	Null}
{Null	3761.8	5.76548E-08	2.22281E-08	0	3	1	5	Null}
{Null	3880.1	1.33837E-16	5.15992E-17	0	3	1	6	Null}
{Null	4007.1	4.70766E-10	1.81498E-10	0	3	1	7	Null}
{Null	4141.1	1.30245E-15	5.02143E-16	0	3	1	8	Null}
{Null	4281.1	8.5103E-11	3.28104E-11	0	3	1	9	Null}
{Null	3263.7	5.7396E-09	1.31619E-09	0	4	1	0	Null}
{Null	3267.4	2.44299E-14	5.60221E-15	0	4	1	1	Null}
{Null	3395.3	7.92452E-08	1.81723E-08	0	4	1	2	Null}
{Null	3448.6	2.65554E-16	6.08963E-17	0	4	1	3	Null}
{Null	3548.1	4.88253E-06	1.11965E-06	0	4	1	4	Null}
{Null	3654.2	9.69491E-15	2.22321E-15	0	4	1	5	Null}
{Null	3772.5	4.65256E-08	1.06691E-08	0	4	1	6	Null}
{Null	3899.5	1.22156E-16	2.80125E-17	0	4	1	7	Null}
{Null	4033.5	8.55842E-10	1.9626E-10	0	4	1	8	Null}
{Null	4173.5	1.99987E-15	4.58606E-16	0	4	1	9	Null}
{Null	3146.1	2.04872E-16	2.66269E-17	0	5	1	0	Null}
{Null	3149.8	3.61063E-10	4.69269E-11	0	5	1	1	Null}
{Null	3277.7	1.66491E-15	2.16386E-16	0	5	1	2	Null}
{Null	3331	5.09985E-08	6.62821E-09	0	5	1	3	Null}
{Null	3430.5	5.51068E-15	7.16216E-16	0	5	1	4	Null}
{Null	3536.6	4.91035E-06	6.38192E-07	0	5	1	5	Null}
{Null	3654.9	4.49313E-15	5.83967E-16	0	5	1	6	Null}
{Null	3781.9	3.59873E-08	4.67722E-09	0	5	1	7	Null}
{Null	3915.9	3.69738E-16	4.80543E-17	0	5	1	8	Null}
{Null	4055.9	1.37468E-09	1.78666E-10	0	5	1	9	Null}
{Null	3017.6	1.13934E-11	7.96224E-13	0	6	1	0	Null}
{Null	3021.3	2.18003E-16	1.52352E-17	0	6	1	1	Null}
{Null	3149.2	3.966E-10	2.77163E-11	0	6	1	2	Null}
{Null	3202.5	1.56383E-16	1.09288E-17	0	6	1	3	Null}
{Null	3302	4.09269E-08	2.86017E-09	0	6	1	4	Null}
{Null	3408.1	6.52311E-15	4.55867E-16	0	6	1	5	Null}
{Null	3526.4	4.91407E-06	3.4342E-07	0	6	1	6	Null}
{Null	3653.4	2.56113E-15	1.78984E-16	0	6	1	7	Null}
{Null	3787.4	2.72541E-08	1.90465E-09	0	6	1	8	Null}
{Null	3927.4	1.31138E-15	9.16456E-17	0	6	1	9	Null}
{Null	2880.6	3.39434E-16	1.22422E-17	0	7	1	0	Null}
{Null	2884.3	4.87294E-11	1.7575E-12	0	7	1	1	Null}
{Null	3012.2	5.11878E-17	1.84617E-18	0	7	1	2	Null}
{Null	3065.5	3.85818E-13	1.39151E-14	0	7	1	3	Null}
{Null	3165	7.21046E-16	2.60056E-17	0	7	1	4	Null}

{Null	3271.1	3.19957E-08	1.15398E-09	0	7	1	5	Null}
{Null	3389.4	2.06993E-15	7.46554E-17	0	7	1	6	Null}
{Null	3516.4	4.91622E-06	1.77311E-07	0	7	1	7	Null}
{Null	3650.4	7.81229E-16	2.81763E-17	0	7	1	8	Null}
{Null	3790.4	1.94635E-08	7.01983E-10	0	7	1	9	Null}
{Null	2737	2.03635E-11	3.67145E-13	0	8	1	0	Null}
{Null	2740.7	3.97985E-16	7.17551E-18	0	8	1	1	Null}
{Null	2868.6	7.40846E-11	1.33572E-12	0	8	1	2	Null}
{Null	2921.9	7.14788E-16	1.28873E-17	0	8	1	3	Null}
{Null	3021.4	9.26618E-11	1.67066E-12	0	8	1	4	Null}
{Null	3127.5	5.02679E-15	9.06311E-17	0	8	1	5	Null}
{Null	3245.8	2.43327E-08	4.38708E-10	0	8	1	6	Null}
{Null	3372.8	7.67463E-16	1.38371E-17	0	8	1	7	Null}
{Null	3506.8	4.91617E-06	8.86367E-08	0	8	1	8	Null}
{Null	3646.8	8.05943E-15	1.45308E-16	0	8	1	9	Null}
{Null	2587.9	1.3799E-15	1.2111E-17	0	9	1	0	Null}
{Null	2591.6	5.14732E-12	4.51768E-14	0	9	1	1	Null}
{Null	2719.5	1.32102E-16	1.15943E-18	0	9	1	2	Null}
{Null	2772.8	1.06779E-10	9.37171E-13	0	9	1	3	Null}
{Null	2872.3	2.017E-15	1.77027E-17	0	9	1	4	Null}
{Null	2978.4	4.01145E-10	3.52076E-12	0	9	1	5	Null}
{Null	3096.7	5.69529E-16	4.99862E-18	0	9	1	6	Null}
{Null	3223.7	1.74807E-08	1.53424E-10	0	9	1	7	Null}
{Null	3357.7	6.70687E-15	5.88646E-17	0	9	1	8	Null}
{Null	3497.7	4.91461E-06	4.31343E-08	0	9	1	9	Null}
2nu								
{Null	6974.1	8.81624E-07	8.81624E-07	0	0	2	0	Null}
{Null	6975.3	5.60893E-14	5.60893E-14	0	0	2	1	Null}
{Null	7123.8	1.11471E-07	1.11471E-07	0	0	2	2	Null}
{Null	7155.5	2.66239E-15	2.66239E-15	0	0	2	3	Null}
{Null	7251.7	4.75013E-11	4.75013E-11	0	0	2	4	Null}
{Null	7344	1.7751E-15	1.7751E-15	0	0	2	5	Null}
{Null	7452.3	1.62787E-10	1.62787E-10	0	0	2	6	Null}
{Null	7569.4	7.41211E-17	7.41211E-17	0	0	2	7	Null}
{Null	7694.1	1.93962E-12	1.93962E-12	0	0	2	8	Null}
{Null	7825.3	1.87651E-15	1.87651E-15	0	0	2	9	Null}
{Null	6965.7	3.96861E-14	3.81087E-14	0	1	2	0	Null}
{Null	6966.9	9.31894E-07	8.94854E-07	0	1	2	1	Null}
{Null	7115.4	4.23301E-14	4.06476E-14	0	1	2	2	Null}
{Null	7147.1	5.89221E-08	5.65802E-08	0	1	2	3	Null}
{Null	7243.3	1.92312E-15	1.84669E-15	0	1	2	4	Null}
{Null	7335.6	5.82218E-10	5.59077E-10	0	1	2	5	Null}
{Null	7443.9	1.21575E-15	1.16742E-15	0	1	2	6	Null}
{Null	7561	3.85754E-11	3.70422E-11	0	1	2	7	Null}
{Null	7685.7	2.32398E-14	2.23161E-14	0	1	2	8	Null}
{Null	7816.9	7.50733E-14	7.20894E-14	0	1	2	9	Null}
{Null	6849.3	9.63504E-08	5.27421E-08	0	2	2	0	Null}
{Null	6850.5	6.62831E-17	3.62833E-17	0	2	2	1	Null}
{Null	6999	7.8501E-07	4.29713E-07	0	2	2	2	Null}
{Null	7030.7	2.06422E-15	1.12995E-15	0	2	2	3	Null}
{Null	7126.9	1.1228E-07	6.14621E-08	0	2	2	4	Null}
{Null	7219.2	2.51318E-15	1.37571E-15	0	2	2	5	Null}
{Null	7327.5	7.33302E-10	4.01409E-10	0	2	2	6	Null}
{Null	7444.6	2.56443E-16	1.40376E-16	0	2	2	7	Null}

{Null	7569.3	4.61988E-11	2.52891E-11	0	2	2	8	Null}
{Null	7700.5	2.89164E-16	1.58288E-16	0	2	2	9	Null}
{Null	6776.7	5.38348E-16	2.07553E-16	0	3	2	0	Null}
{Null	6777.9	5.49681E-08	2.11922E-08	0	3	2	1	Null}
{Null	6926.4	2.22975E-15	8.59653E-16	0	3	2	2	Null}
{Null	6958.1	8.72022E-07	3.36197E-07	0	3	2	3	Null}
{Null	7054.3	8.88087E-16	3.42391E-16	0	3	2	4	Null}
{Null	7146.6	6.06662E-08	2.33891E-08	0	3	2	5	Null}
{Null	7254.9	2.09029E-15	8.05886E-16	0	3	2	6	Null}
{Null	7372	1.1996E-09	4.62491E-10	0	3	2	7	Null}
{Null	7496.7	1.60269E-16	6.17896E-17	0	3	2	8	Null}
{Null	7627.9	3.51936E-11	1.35685E-11	0	3	2	9	Null}
{Null	6669.1	1.06793E-08	2.44895E-09	0	4	2	0	Null}
{Null	6670.3	1.40661E-15	3.22559E-16	0	4	2	1	Null}
{Null	6818.8	9.44996E-08	2.16704E-08	0	4	2	2	Null}
{Null	6850.5	7.5892E-16	1.74034E-16	0	4	2	3	Null}
{Null	6946.7	8.29726E-07	1.90271E-07	0	4	2	4	Null}
{Null	7039	9.83803E-15	2.25603E-15	0	4	2	5	Null}
{Null	7147.3	4.99281E-08	1.14494E-08	0	4	2	6	Null}
{Null	7264.4	3.8922E-16	8.92551E-17	0	4	2	7	Null}
{Null	7389.1	1.52178E-09	3.48971E-10	0	4	2	8	Null}
{Null	7520.3	8.79807E-15	2.01755E-15	0	4	2	9	Null}
{Null	6551.5	1.31027E-15	1.70294E-16	0	5	2	0	Null}
{Null	6552.7	1.38704E-09	1.80272E-10	0	5	2	1	Null}
{Null	6701.2	1.95279E-16	2.53801E-17	0	5	2	2	Null}
{Null	6732.9	5.68152E-08	7.38419E-09	0	5	2	3	Null}
{Null	6829.1	5.26666E-15	6.84501E-16	0	5	2	4	Null}
{Null	6921.4	8.84568E-07	1.14966E-07	0	5	2	5	Null}
{Null	7029.7	1.61074E-15	2.09346E-16	0	5	2	6	Null}
{Null	7146.8	3.84274E-08	4.99436E-09	0	5	2	7	Null}
{Null	7271.5	1.07507E-15	1.39725E-16	0	5	2	8	Null}
{Null	7402.7	1.90009E-09	2.46953E-10	0	5	2	9	Null}
{Null	6423	2.12035E-11	1.48181E-12	0	6	2	0	Null}
{Null	6424.2	3.19229E-15	2.23093E-16	0	6	2	1	Null}
{Null	6572.7	2.65067E-09	1.85242E-10	0	6	2	2	Null}
{Null	6604.4	8.11875E-16	5.67378E-17	0	6	2	3	Null}
{Null	6700.6	4.59777E-08	3.21315E-09	0	6	2	4	Null}
{Null	6792.9	1.50331E-16	1.05059E-17	0	6	2	5	Null}
{Null	6901.2	8.99581E-07	6.28672E-08	0	6	2	6	Null}
{Null	7018.3	3.63218E-15	2.53835E-16	0	6	2	7	Null}
{Null	7143	2.96451E-08	2.07175E-09	0	6	2	8	Null}
{Null	7274.2	3.03046E-15	2.11784E-16	0	6	2	9	Null}
{Null	6286	5.58157E-17	2.01308E-18	0	7	2	0	Null}
{Null	6287.2	3.15037E-11	1.13623E-12	0	7	2	1	Null}
{Null	6435.7	6.72771E-16	2.42645E-17	0	7	2	2	Null}
{Null	6467.4	3.54917E-10	1.28007E-11	0	7	2	3	Null}
{Null	6563.6	3.09024E-16	1.11454E-17	0	7	2	4	Null}
{Null	6655.9	3.77569E-08	1.36176E-09	0	7	2	5	Null}
{Null	6764.2	6.94167E-15	2.50362E-16	0	7	2	6	Null}
{Null	6881.3	9.1437E-07	3.29782E-08	0	7	2	7	Null}
{Null	7006	1.7654E-15	6.36718E-17	0	7	2	8	Null}
{Null	7137.2	2.19988E-08	7.93421E-10	0	7	2	9	Null}
{Null	6142.4	3.66275E-11	6.60379E-13	0	8	2	0	Null}
{Null	6143.6	8.58519E-16	1.54788E-17	0	8	2	1	Null}

{Null	6292.1	5.2903E-11	9.53819E-13	0	8	2	2	Null}
{Null	6323.8	2.26109E-15	4.07666E-17	0	8	2	3	Null}
{Null	6420	4.2037E-11	7.57909E-13	0	8	2	4	Null}
{Null	6512.3	9.23158E-15	1.66442E-16	0	8	2	5	Null}
{Null	6620.6	2.99595E-08	5.40158E-10	0	8	2	6	Null}
{Null	6737.7	1.19708E-15	2.15828E-17	0	8	2	7	Null}
{Null	6862.4	9.25927E-07	1.66941E-08	0	8	2	8	Null}
{Null	6993.6	4.1883E-15	7.55133E-17	0	8	2	9	Null}
{Null	5993.3	1.06148E-16	9.31637E-19	0	9	2	0	Null}
{Null	5994.5	1.46086E-11	1.28216E-13	0	9	2	1	Null}
{Null	6143	1.09521E-13	9.61239E-16	0	9	2	2	Null}
{Null	6174.7	1.38873E-10	1.21886E-12	0	9	2	3	Null}
{Null	6270.9	2.52024E-15	2.21195E-17	0	9	2	4	Null}
{Null	6363.2	5.81929E-11	5.10745E-13	0	9	2	5	Null}
{Null	6471.5	3.87109E-16	3.39757E-18	0	9	2	6	Null}
{Null	6588.6	2.27775E-08	1.99913E-10	0	9	2	7	Null}
{Null	6713.3	9.88597E-15	8.67668E-17	0	9	2	8	Null}
{Null	6844.5	9.35592E-07	8.21147E-09	0	9	2	9	Null}
3nu								
{Null	10182.6	3.74371E-08	3.74371E-08	0	0	3	0	Null}
{Null	10182.9	3.00701E-15	3.00701E-15	0	0	3	1	Null}
{Null	10356.6	1.09842E-08	1.09842E-08	0	0	3	2	Null}
{Null	10369.4	4.8315E-16	4.8315E-16	0	0	3	3	Null}
{Null	10474.8	5.55532E-10	5.55532E-10	0	0	3	4	Null}
{Null	10546.8	3.53386E-14	3.53386E-14	0	0	3	5	Null}
{Null	10645.8	1.73603E-11	1.73603E-11	0	0	3	6	Null}
{Null	10752.4	2.49268E-16	2.49268E-16	0	0	3	7	Null}
{Null	10867.9	7.04208E-14	7.04208E-14	0	0	3	8	Null}
{Null	10990.3	2.58963E-15	2.58963E-15	0	0	3	9	Null}
{Null	10174.2	1.63906E-15	1.57392E-15	0	1	3	0	Null}
{Null	10174.5	4.15146E-08	3.98645E-08	0	1	3	1	Null}
{Null	10348.2	3.18257E-16	3.05607E-16	0	1	3	2	Null}
{Null	10361	7.06746E-09	6.78656E-09	0	1	3	3	Null}
{Null	10466.4	7.76029E-16	7.45185E-16	0	1	3	4	Null}
{Null	10538.4	3.1804E-10	3.05399E-10	0	1	3	5	Null}
{Null	10637.4	6.40727E-17	6.1526E-17	0	1	3	6	Null}
{Null	10744	5.80218E-13	5.57156E-13	0	1	3	7	Null}
{Null	10859.5	2.442E-15	2.34494E-15	0	1	3	8	Null}
{Null	10981.9	2.81536E-14	2.70346E-14	0	1	3	9	Null}
{Null	10057.8	9.11825E-09	4.99132E-09	0	2	3	0	Null}
{Null	10058.1	4.53791E-16	2.48405E-16	0	2	3	1	Null}
{Null	10231.8	2.29787E-08	1.25785E-08	0	2	3	2	Null}
{Null	10244.6	2.71802E-15	1.48784E-15	0	2	3	3	Null}
{Null	10350	1.65189E-08	9.04243E-09	0	2	3	4	Null}
{Null	10422	8.58994E-16	4.70212E-16	0	2	3	5	Null}
{Null	10521	4.65335E-10	2.54724E-10	0	2	3	6	Null}
{Null	10627.6	1.46165E-15	8.00107E-16	0	2	3	7	Null}
{Null	10743.1	7.23267E-13	3.95915E-13	0	2	3	8	Null}
{Null	10865.5	1.74947E-15	9.57659E-16	0	2	3	9	Null}
{Null	9985.2	1.72988E-17	6.66932E-18	0	3	3	0	Null}
{Null	9985.5	6.67483E-09	2.5734E-09	0	3	3	1	Null}
{Null	10159.2	3.39066E-15	1.30723E-15	0	3	3	2	Null}
{Null	10172	3.34373E-08	1.28913E-08	0	3	3	3	Null}
{Null	10277.4	7.41374E-16	2.85827E-16	0	3	3	4	Null}

{Null	10349.4	8.24978E-09	3.1806E-09	0	3	3	5	Null}
{Null	10448.4	1.22092E-15	4.70709E-16	0	3	3	6	Null}
{Null	10555	4.14088E-10	1.59646E-10	0	3	3	7	Null}
{Null	10670.5	9.6138E-16	3.70648E-16	0	3	3	8	Null}
{Null	10792.9	7.07995E-14	2.72959E-14	0	3	3	9	Null}
{Null	9877.6	2.01666E-09	4.62456E-10	0	4	3	0	Null}
{Null	9877.9	2.44911E-15	5.61624E-16	0	4	3	1	Null}
{Null	10051.6	1.35866E-08	3.11565E-09	0	4	3	2	Null}
{Null	10064.4	5.06277E-16	1.16098E-16	0	4	3	3	Null}
{Null	10169.8	2.5314E-08	5.80494E-09	0	4	3	4	Null}
{Null	10241.8	2.11313E-15	4.84579E-16	0	4	3	5	Null}
{Null	10340.8	7.15628E-09	1.64106E-09	0	4	3	6	Null}
{Null	10447.4	7.21247E-16	1.65395E-16	0	4	3	7	Null}
{Null	10562.9	4.20947E-10	9.65305E-11	0	4	3	8	Null}
{Null	10685.3	6.84538E-16	1.56977E-16	0	4	3	9	Null}
{Null	9760	7.93163E-16	1.03086E-16	0	5	3	0	Null}
{Null	9760.3	4.26261E-10	5.54006E-11	0	5	3	1	Null}
{Null	9934	2.18193E-15	2.83583E-16	0	5	3	2	Null}
{Null	9946.8	7.89739E-09	1.02641E-09	0	5	3	3	Null}
{Null	10052.2	2.5587E-15	3.32551E-16	0	5	3	4	Null}
{Null	10124.2	3.42724E-08	4.45434E-09	0	5	3	5	Null}
{Null	10223.2	2.36856E-16	3.07839E-17	0	5	3	6	Null}
{Null	10329.8	6.43501E-09	8.3635E-10	0	5	3	7	Null}
{Null	10445.3	8.42761E-16	1.09533E-16	0	5	3	8	Null}
{Null	10567.7	4.28588E-10	5.5703E-11	0	5	3	9	Null}
{Null	9631.5	3.51843E-11	2.45885E-12	0	6	3	0	Null}
{Null	9631.8	5.19114E-15	3.62782E-16	0	6	3	1	Null}
{Null	9805.5	1.31378E-09	9.18135E-11	0	6	3	2	Null}
{Null	9818.3	3.32721E-15	2.32522E-16	0	6	3	3	Null}
{Null	9923.7	6.17143E-09	4.3129E-10	0	6	3	4	Null}
{Null	9995.7	1.05663E-15	7.38424E-17	0	6	3	5	Null}
{Null	10094.7	3.60994E-08	2.52281E-09	0	6	3	6	Null}
{Null	10201.3	6.29519E-15	4.39939E-16	0	6	3	7	Null}
{Null	10316.8	4.26226E-09	2.97868E-10	0	6	3	8	Null}
{Null	10439.2	1.14582E-15	8.00754E-17	0	6	3	9	Null}
{Null	9494.5	2.54064E-16	9.1632E-18	0	7	3	0	Null}
{Null	9494.8	4.18206E-13	1.50833E-14	0	7	3	1	Null}
{Null	9668.5	2.49955E-15	9.01503E-17	0	7	3	2	Null}
{Null	9681.3	2.55053E-10	9.19888E-12	0	7	3	3	Null}
{Null	9786.7	4.70884E-16	1.69832E-17	0	7	3	4	Null}
{Null	9858.7	5.62591E-09	2.02907E-10	0	7	3	5	Null}
{Null	9957.7	1.20521E-15	4.34678E-17	0	7	3	6	Null}
{Null	10064.3	3.85642E-08	1.39088E-09	0	7	3	7	Null}
{Null	10179.8	2.85506E-15	1.02972E-16	0	7	3	8	Null}
{Null	10302.2	3.23751E-09	1.16766E-10	0	7	3	9	Null}
{Null	9350.9	6.77413E-12	1.22135E-13	0	8	3	0	Null}
{Null	9351.2	2.88334E-14	5.19855E-16	0	8	3	1	Null}
{Null	9524.9	9.85011E-14	1.77594E-15	0	8	3	2	Null}
{Null	9537.7	2.5399E-16	4.57934E-18	0	8	3	3	Null}
{Null	9643.1	1.24442E-10	2.24364E-12	0	8	3	4	Null}
{Null	9715.1	1.49813E-15	2.70107E-17	0	8	3	5	Null}
{Null	9814.1	4.65801E-09	8.39821E-11	0	8	3	6	Null}
{Null	9920.7	2.635E-15	4.75079E-17	0	8	3	7	Null}
{Null	10036.2	4.04036E-08	7.2846E-10	0	8	3	8	Null}

{Null	10158.6	5.80628E-15	1.04685E-16	0	8	3	9	Null}
{Null	9201.8	4.60422E-16	4.04101E-18	0	9	3	0	Null}
{Null	9202.1	4.098E-12	3.59672E-14	0	9	3	1	Null}
{Null	9375.8	3.02992E-15	2.65929E-17	0	9	3	2	Null}
{Null	9388.6	1.5848E-11	1.39094E-13	0	9	3	3	Null}
{Null	9494	3.75473E-15	3.29544E-17	0	9	3	4	Null}
{Null	9566	1.60619E-11	1.40971E-13	0	9	3	5	Null}
{Null	9665	2.12925E-15	1.86879E-17	0	9	3	6	Null}
{Null	9771.6	3.71529E-09	3.26082E-11	0	9	3	7	Null}
{Null	9887.1	4.07954E-16	3.58051E-18	0	9	3	8	Null}
{Null	10009.5	4.20081E-08	3.68695E-10	0	9	3	9	Null}
4nu								
{Null	13196.1	2.13551E-09	2.13551E-09	0	0	4	0	Null}
{Null	13196.2	3.11228E-16	3.11228E-16	0	0	4	1	Null}
{Null	13391.5	1.01492E-09	1.01492E-09	0	0	4	2	Null}
{Null	13394.5	8.86705E-16	8.86705E-16	0	0	4	3	Null}
{Null	13529.6	2.29546E-10	2.29546E-10	0	0	4	4	Null}
{Null	13571	7.27707E-16	7.27707E-16	0	0	4	5	Null}
{Null	13665.2	1.23615E-13	1.23615E-13	0	0	4	6	Null}
{Null	13758.6	5.46753E-16	5.46753E-16	0	0	4	7	Null}
{Null	13864.5	1.67247E-13	1.67247E-13	0	0	4	8	Null}
{Null	13977.8	2.81295E-17	2.81295E-17	0	0	4	9	Null}
{Null	13187.7	2.86456E-16	2.7507E-16	0	1	4	0	Null}
{Null	13187.8	2.46098E-09	2.36317E-09	0	1	4	1	Null}
{Null	13383.1	2.9309E-16	2.8144E-16	0	1	4	2	Null}
{Null	13386.1	8.18713E-10	7.86171E-10	0	1	4	3	Null}
{Null	13521.2	2.19935E-16	2.11193E-16	0	1	4	4	Null}
{Null	13562.6	3.68804E-10	3.54145E-10	0	1	4	5	Null}
{Null	13656.8	3.30233E-16	3.17108E-16	0	1	4	6	Null}
{Null	13750.2	1.14912E-12	1.10344E-12	0	1	4	7	Null}
{Null	13856.1	3.3035E-16	3.1722E-16	0	1	4	8	Null}
{Null	13969.4	1.39734E-15	1.3418E-15	0	1	4	9	Null}
{Null	13071.3	8.71916E-10	4.77285E-10	0	2	4	0	Null}
{Null	13071.4	6.00523E-15	3.28725E-15	0	2	4	1	Null}
{Null	13266.7	5.13578E-10	2.81132E-10	0	2	4	2	Null}
{Null	13269.7	7.02263E-16	3.84418E-16	0	2	4	3	Null}
{Null	13404.8	1.77766E-09	9.73089E-10	0	2	4	4	Null}
{Null	13446.2	5.06037E-16	2.77004E-16	0	2	4	5	Null}
{Null	13540.4	2.36528E-10	1.29475E-10	0	2	4	6	Null}
{Null	13633.8	7.62693E-17	4.17497E-17	0	2	4	7	Null}
{Null	13739.7	1.36075E-12	7.44873E-13	0	2	4	8	Null}
{Null	13853	1.03275E-15	5.65323E-16	0	2	4	9	Null}
{Null	12998.7	2.2752E-16	8.77177E-17	0	3	4	0	Null}
{Null	12998.8	7.96608E-10	3.07122E-10	0	3	4	1	Null}
{Null	13194.1	1.78283E-15	6.87346E-16	0	3	4	2	Null}
{Null	13197.1	1.40995E-09	5.43587E-10	0	3	4	3	Null}
{Null	13332.2	1.06712E-15	4.11416E-16	0	3	4	4	Null}
{Null	13373.6	1.0409E-09	4.01304E-10	0	3	4	5	Null}
{Null	13467.8	4.11026E-16	1.58466E-16	0	3	4	6	Null}
{Null	13561.2	1.35538E-10	5.2255E-11	0	3	4	7	Null}
{Null	13667.1	7.68346E-16	2.96226E-16	0	3	4	8	Null}
{Null	13780.4	1.70953E-12	6.59086E-13	0	3	4	9	Null}
{Null	12891.1	3.34424E-10	7.66893E-11	0	4	4	0	Null}
{Null	12891.2	1.74172E-17	3.99408E-18	0	4	4	1	Null}

{Null	13086.5	1.44347E-09	3.31012E-10	0	4	4	2	Null}
{Null	13089.5	2.98862E-15	6.85343E-16	0	4	4	3	Null}
{Null	13224.6	4.88681E-10	1.12063E-10	0	4	4	4	Null}
{Null	13266	3.27496E-16	7.51005E-17	0	4	4	5	Null}
{Null	13360.2	1.02461E-09	2.3496E-10	0	4	4	6	Null}
{Null	13453.6	4.72479E-16	1.08348E-16	0	4	4	7	Null}
{Null	13559.5	1.24079E-10	2.84535E-11	0	4	4	8	Null}
{Null	13672.8	1.96974E-15	4.51696E-16	0	4	4	9	Null}
{Null	12773.5	8.58675E-16	1.11601E-16	0	5	4	0	Null}
{Null	12773.6	1.02807E-10	1.33617E-11	0	5	4	1	Null}
{Null	12968.9	1.51179E-15	1.96485E-16	0	5	4	2	Null}
{Null	12971.9	1.03357E-09	1.34331E-10	0	5	4	3	Null}
{Null	13107	1.56365E-17	2.03225E-18	0	5	4	4	Null}
{Null	13148.4	1.36901E-09	1.77928E-10	0	5	4	5	Null}
{Null	13242.6	2.93588E-16	3.81573E-17	0	5	4	6	Null}
{Null	13336	7.52244E-10	9.77681E-11	0	5	4	7	Null}
{Null	13441.9	2.45015E-16	3.18443E-17	0	5	4	8	Null}
{Null	13555.2	1.08999E-10	1.41664E-11	0	5	4	9	Null}
{Null	12645	1.71526E-11	1.19871E-12	0	6	4	0	Null}
{Null	12645.1	4.67488E-16	3.26704E-17	0	6	4	1	Null}
{Null	12840.4	3.88921E-10	2.71797E-11	0	6	4	2	Null}
{Null	12843.4	3.06559E-15	2.14239E-16	0	6	4	3	Null}
{Null	12978.5	7.97611E-10	5.5741E-11	0	6	4	4	Null}
{Null	13019.9	3.37067E-17	2.35559E-18	0	6	4	5	Null}
{Null	13114.1	1.44521E-09	1.00999E-10	0	6	4	6	Null}
{Null	13207.5	1.73084E-15	1.20959E-16	0	6	4	7	Null}
{Null	13313.4	6.06667E-10	4.23969E-11	0	6	4	8	Null}
{Null	13426.7	1.69639E-15	1.18552E-16	0	6	4	9	Null}
{Null	12508	4.40433E-16	1.58849E-17	0	7	4	0	Null}
{Null	12508.1	4.8969E-13	1.76614E-14	0	7	4	1	Null}
{Null	12703.4	2.02952E-16	7.31976E-18	0	7	4	2	Null}
{Null	12706.4	1.01223E-10	3.65078E-12	0	7	4	3	Null}
{Null	12841.5	1.93834E-15	6.99092E-17	0	7	4	4	Null}
{Null	12882.9	8.34951E-10	3.01138E-11	0	7	4	5	Null}
{Null	12977.1	3.84374E-15	1.3863E-16	0	7	4	6	Null}
{Null	13070.5	1.84857E-09	6.66714E-11	0	7	4	7	Null}
{Null	13176.4	6.48141E-16	2.33762E-17	0	7	4	8	Null}
{Null	13289.7	4.74115E-10	1.70997E-11	0	7	4	9	Null}
{Null	12364.4	5.52301E-13	9.95777E-15	0	8	4	0	Null}
{Null	12364.5	2.29578E-16	4.13921E-18	0	8	4	1	Null}
{Null	12559.8	7.07727E-12	1.276E-13	0	8	4	2	Null}
{Null	12562.8	1.65438E-15	2.98277E-17	0	8	4	3	Null}
{Null	12697.9	8.06818E-11	1.45466E-12	0	8	4	4	Null}
{Null	12739.3	1.21682E-15	2.19387E-17	0	8	4	5	Null}
{Null	12833.5	6.83776E-10	1.23282E-11	0	8	4	6	Null}
{Null	12926.9	4.72137E-16	8.51245E-18	0	8	4	7	Null}
{Null	13032.8	2.10638E-09	3.79773E-11	0	8	4	8	Null}
{Null	13146.1	4.72791E-16	8.52423E-18	0	8	4	9	Null}
{Null	12215.3	8.60871E-16	7.55566E-18	0	9	4	0	Null}
{Null	12215.4	7.56223E-13	6.63719E-15	0	9	4	1	Null}
{Null	12410.7	1.06236E-15	9.32412E-18	0	9	4	2	Null}
{Null	12413.7	2.19125E-12	1.92321E-14	0	9	4	3	Null}
{Null	12548.8	1.08499E-15	9.52268E-18	0	9	4	4	Null}
{Null	12590.2	2.21825E-11	1.9469E-13	0	9	4	5	Null}

{Null	12684.4	8.75783E-16	7.68654E-18	0	9	4	6	Null}
{Null	12777.8	6.0279E-10	5.29054E-12	0	9	4	7	Null}
{Null	12883.7	3.91489E-16	3.43601E-18	0	9	4	8	Null}
{Null	12997	2.3406E-09	2.05429E-11	0	9	4	9	Null}
5nu								
{Null	16017.3	1.57652E-10	1.57652E-10	0	0	5	0	Null}
{Null	16017.3	6.63555E-16	6.63555E-16	0	0	5	1	Null}
{Null	16228.9	9.72175E-11	9.72175E-11	0	0	5	2	Null}
{Null	16229.3	7.36737E-16	7.36737E-16	0	0	5	3	Null}
{Null	16404.1	4.93051E-11	4.93051E-11	0	0	5	4	Null}
{Null	16416.7	1.53676E-16	1.53676E-16	0	0	5	5	Null}
{Null	16525.7	5.09275E-12	5.09275E-12	0	0	5	6	Null}
{Null	16593.9	2.9452E-15	2.9452E-15	0	0	5	7	Null}
{Null	16691	1.80205E-15	1.80205E-15	0	0	5	8	Null}
{Null	16793.3	4.75164E-17	4.75164E-17	0	0	5	9	Null}
{Null	16008.9	1.82836E-16	1.75569E-16	0	1	5	0	Null}
{Null	16008.9	1.88715E-10	1.81214E-10	0	1	5	1	Null}
{Null	16220.5	1.46481E-15	1.40659E-15	0	1	5	2	Null}
{Null	16220.9	9.34438E-11	8.97298E-11	0	1	5	3	Null}
{Null	16395.7	3.43558E-16	3.29902E-16	0	1	5	4	Null}
{Null	16408.3	2.74747E-11	2.63826E-11	0	1	5	5	Null}
{Null	16517.3	1.31069E-13	1.25859E-13	0	1	5	6	Null}
{Null	16585.5	1.88478E-12	1.80986E-12	0	1	5	7	Null}
{Null	16682.6	1.37252E-16	1.31797E-16	0	1	5	8	Null}
{Null	16784.9	1.84634E-14	1.77296E-14	0	1	5	9	Null}
{Null	15892.5	8.86273E-11	4.85144E-11	0	2	5	0	Null}
{Null	15892.5	2.63785E-16	1.44395E-16	0	2	5	1	Null}
{Null	16104.1	4.74547E-12	2.59766E-12	0	2	5	2	Null}
{Null	16104.5	5.94665E-16	3.25519E-16	0	2	5	3	Null}
{Null	16279.3	1.15755E-10	6.33644E-11	0	2	5	4	Null}
{Null	16291.9	7.48045E-17	4.09479E-17	0	2	5	5	Null}
{Null	16400.9	9.06507E-11	4.9622E-11	0	2	5	6	Null}
{Null	16469.1	1.46326E-16	8.00988E-17	0	2	5	7	Null}
{Null	16566.2	3.58545E-12	1.96267E-12	0	2	5	8	Null}
{Null	16668.5	1.01163E-13	5.53763E-14	0	2	5	9	Null}
{Null	15819.9	3.7482E-16	1.44507E-16	0	3	5	0	Null}
{Null	15819.9	9.68742E-11	3.73486E-11	0	3	5	1	Null}
{Null	16031.5	4.72791E-15	1.82279E-15	0	3	5	2	Null}
{Null	16031.9	5.25125E-11	2.02455E-11	0	3	5	3	Null}
{Null	16206.7	3.12638E-16	1.20534E-16	0	3	5	4	Null}
{Null	16219.3	1.10425E-10	4.2573E-11	0	3	5	5	Null}
{Null	16328.3	6.54997E-17	2.52526E-17	0	3	5	6	Null}
{Null	16396.5	3.90013E-11	1.50365E-11	0	3	5	7	Null}
{Null	16493.6	1.74486E-16	6.72707E-17	0	3	5	8	Null}
{Null	16595.9	2.17902E-12	8.40092E-13	0	3	5	9	Null}
{Null	15712.3	5.28442E-11	1.21181E-11	0	4	5	0	Null}
{Null	15712.3	8.1085E-17	1.85942E-17	0	4	5	1	Null}
{Null	15923.9	1.14809E-10	2.63277E-11	0	4	5	2	Null}
{Null	15924.3	8.94009E-16	2.05012E-16	0	4	5	3	Null}
{Null	16099.1	7.23664E-13	1.65949E-13	0	4	5	4	Null}
{Null	16111.7	1.1791E-16	2.70388E-17	0	4	5	5	Null}
{Null	16220.7	9.37553E-11	2.14997E-11	0	4	5	6	Null}
{Null	16288.9	3.12291E-16	7.16137E-17	0	4	5	7	Null}
{Null	16386	3.67845E-11	8.43534E-12	0	4	5	8	Null}

{Null	16488.3	1.9135E-17	4.38799E-18	0	4	5	9	Null}
{Null	15594.7	1.03336E-15	1.34305E-16	0	5	5	0	Null}
{Null	15594.7	2.1393E-11	2.78042E-12	0	5	5	1	Null}
{Null	15806.3	4.33959E-16	5.64011E-17	0	5	5	2	Null}
{Null	15806.7	1.2283E-10	1.59641E-11	0	5	5	3	Null}
{Null	15981.5	5.85203E-17	7.60581E-18	0	5	5	4	Null}
{Null	15994.1	3.41441E-11	4.43766E-12	0	5	5	5	Null}
{Null	16103.1	5.50178E-16	7.15059E-17	0	5	5	6	Null}
{Null	16171.3	8.99474E-11	1.16903E-11	0	5	5	7	Null}
{Null	16268.4	1.45948E-16	1.89687E-17	0	5	5	8	Null}
{Null	16370.7	3.22529E-11	4.19187E-12	0	5	5	9	Null}
{Null	15466.2	5.40058E-12	3.77419E-13	0	6	5	0	Null}
{Null	15466.2	8.37119E-16	5.8502E-17	0	6	5	1	Null}
{Null	15677.8	7.58487E-11	5.30068E-12	0	6	5	2	Null}
{Null	15678.2	1.81691E-15	1.26975E-16	0	6	5	3	Null}
{Null	15853	9.11484E-11	6.3699E-12	0	6	5	4	Null}
{Null	15865.6	2.43468E-15	1.70148E-16	0	6	5	5	Null}
{Null	15974.6	2.18213E-11	1.52498E-12	0	6	5	6	Null}
{Null	16042.8	1.81884E-15	1.27109E-16	0	6	5	7	Null}
{Null	16139.9	8.24997E-11	5.76549E-12	0	6	5	8	Null}
{Null	16242.2	7.61949E-15	5.32488E-16	0	6	5	9	Null}
{Null	15329.2	5.67222E-16	2.04577E-17	0	7	5	0	Null}
{Null	15329.2	5.36154E-13	1.93372E-14	0	7	5	1	Null}
{Null	15540.8	2.67164E-15	9.63569E-17	0	7	5	2	Null}
{Null	15541.2	2.90493E-11	1.04771E-12	0	7	5	3	Null}
{Null	15716	5.41593E-16	1.95334E-17	0	7	5	4	Null}
{Null	15728.6	1.11278E-10	4.0134E-12	0	7	5	5	Null}
{Null	15837.6	1.44799E-16	5.2224E-18	0	7	5	6	Null}
{Null	15905.8	6.776E-11	2.44387E-12	0	7	5	7	Null}
{Null	16002.9	5.3513E-16	1.93003E-17	0	7	5	8	Null}
{Null	16105.2	6.50527E-11	2.34623E-12	0	7	5	9	Null}
{Null	15185.6	1.64387E-14	2.96383E-16	0	8	5	0	Null}
{Null	15185.6	9.82377E-16	1.77119E-17	0	8	5	1	Null}
{Null	15397.2	5.46668E-12	9.85621E-14	0	8	5	2	Null}
{Null	15397.6	1.68123E-15	3.03119E-17	0	8	5	3	Null}
{Null	15572.4	4.18459E-11	7.54465E-13	0	8	5	4	Null}
{Null	15585	9.3766E-16	1.69056E-17	0	8	5	5	Null}
{Null	15694	8.11429E-11	1.46297E-12	0	8	5	6	Null}
{Null	15762.2	7.50555E-15	1.35322E-16	0	8	5	7	Null}
{Null	15859.3	1.27457E-10	2.29801E-12	0	8	5	8	Null}
{Null	15961.6	1.67531E-16	3.02052E-18	0	8	5	9	Null}
{Null	15036.5	6.38876E-17	5.60727E-19	0	9	5	0	Null}
{Null	15036.5	1.7083E-13	1.49934E-15	0	9	5	1	Null}
{Null	15248.1	1.79043E-16	1.57142E-18	0	9	5	2	Null}
{Null	15248.5	8.73851E-14	7.66958E-16	0	9	5	3	Null}
{Null	15423.3	1.50381E-14	1.31986E-16	0	9	5	4	Null}
{Null	15435.9	1.4715E-11	1.2915E-13	0	9	5	5	Null}
{Null	15544.9	7.13656E-16	6.26359E-18	0	9	5	6	Null}
{Null	15613.1	9.2886E-11	8.15238E-13	0	9	5	7	Null}
{Null	15710.2	1.52722E-15	1.3404E-17	0	9	5	8	Null}
{Null	15812.5	1.29721E-10	1.13853E-12	0	9	5	9	Null}
6nu								
{Null	18645.6	8.63077E-12	8.63077E-12	0	0	6	0	Null}
{Null	18645.6	3.19476E-15	3.19476E-15	0	0	6	1	Null}

{Null	18870.3	6.98466E-12	6.98466E-12	0	0	6	2	Null}
{Null	18870.4	1.2918E-15	1.2918E-15	0	0	6	3	Null}
{Null	19072.8	4.58018E-12	4.58018E-12	0	0	6	4	Null}
{Null	19074.5	1.54178E-16	1.54178E-16	0	0	6	5	Null}
{Null	19229.6	1.98047E-12	1.98047E-12	0	0	6	6	Null}
{Null	19257.3	3.50009E-16	3.50009E-16	0	0	6	7	Null}
{Null	19356.9	2.49566E-13	2.49566E-13	0	0	6	8	Null}
{Null	19440.2	6.8701E-17	6.8701E-17	0	0	6	9	Null}
{Null	18637.2	2.65329E-16	2.54783E-16	0	1	6	0	Null}
{Null	18637.2	1.05559E-11	1.01363E-11	0	1	6	1	Null}
{Null	18861.9	3.32955E-16	3.19721E-16	0	1	6	2	Null}
{Null	18862	7.29904E-12	7.00893E-12	0	1	6	3	Null}
{Null	19064.4	2.73782E-16	2.629E-16	0	1	6	4	Null}
{Null	19066.1	3.54064E-12	3.39991E-12	0	1	6	5	Null}
{Null	19221.2	5.5375E-16	5.3174E-16	0	1	6	6	Null}
{Null	19248.9	7.53217E-13	7.23279E-13	0	1	6	7	Null}
{Null	19348.5	7.37565E-17	7.08249E-17	0	1	6	8	Null}
{Null	19431.8	1.45651E-12	1.39862E-12	0	1	6	9	Null}
{Null	18520.8	6.63978E-12	3.6346E-12	0	2	6	0	Null}
{Null	18520.8	1.03941E-17	5.68971E-18	0	2	6	1	Null}
{Null	18745.5	7.6594E-14	4.19274E-14	0	2	6	2	Null}
{Null	18745.6	7.01044E-16	3.8375E-16	0	2	6	3	Null}
{Null	18948	2.78982E-12	1.52714E-12	0	2	6	4	Null}
{Null	18949.7	4.46293E-16	2.443E-16	0	2	6	5	Null}
{Null	19104.8	1.00116E-11	5.48034E-12	0	2	6	6	Null}
{Null	19132.5	1.27767E-16	6.99396E-17	0	2	6	7	Null}
{Null	19232.1	4.02078E-12	2.20097E-12	0	2	6	8	Null}
{Null	19315.4	5.32142E-16	2.91294E-16	0	2	6	9	Null}
{Null	18448.2	1.81544E-15	6.9992E-16	0	3	6	0	Null}
{Null	18448.2	2.15481E-10	8.30759E-11	0	3	6	1	Null}
{Null	18672.9	2.8546E-16	1.10055E-16	0	3	6	2	Null}
{Null	18673	8.56784E-13	3.30322E-13	0	3	6	3	Null}
{Null	18875.4	3.52234E-17	1.35799E-17	0	3	6	4	Null}
{Null	18877.1	6.21467E-12	2.39599E-12	0	3	6	5	Null}
{Null	19032.2	1.75419E-16	6.76304E-17	0	3	6	6	Null}
{Null	19059.9	5.65787E-12	2.18132E-12	0	3	6	7	Null}
{Null	19159.5	1.42219E-16	5.48306E-17	0	3	6	8	Null}
{Null	19242.8	1.03632E-12	3.9954E-13	0	3	6	9	Null}
{Null	18340.6	5.62594E-12	1.29013E-12	0	4	6	0	Null}
{Null	18340.6	1.29522E-16	2.97017E-17	0	4	6	1	Null}
{Null	18565.3	5.08046E-12	1.16504E-12	0	4	6	2	Null}
{Null	18565.4	5.19518E-16	1.19135E-16	0	4	6	3	Null}
{Null	18767.8	2.74021E-12	6.28377E-13	0	4	6	4	Null}
{Null	18769.5	5.78725E-16	1.32712E-16	0	4	6	5	Null}
{Null	18924.6	1.62751E-12	3.73216E-13	0	4	6	6	Null}
{Null	18952.3	1.10083E-16	2.5244E-17	0	4	6	7	Null}
{Null	19051.9	6.15592E-12	1.41166E-12	0	4	6	8	Null}
{Null	19135.2	2.12852E-17	4.88108E-18	0	4	6	9	Null}
{Null	18223	1.00055E-15	1.3004E-16	0	5	6	0	Null}
{Null	18223	2.86123E-12	3.7187E-13	0	5	6	1	Null}
{Null	18447.7	1.90379E-15	2.47433E-16	0	5	6	2	Null}
{Null	18447.8	9.55421E-12	1.24175E-12	0	5	6	3	Null}
{Null	18650.2	7.83195E-16	1.01791E-16	0	5	6	4	Null}
{Null	18651.9	1.49119E-14	1.93808E-15	0	5	6	5	Null}

```
{Null    18807    3.42638E-16    4.45323E-17    0    5    6    6    Null}
{Null    18834.7  4.91622E-12    6.38955E-13    0    5    6    7    Null}
{Null    18934.3  6.47612E-17    8.41693E-18    0    5    6    8    Null}
{Null    19017.6  1.76649E-11    2.29589E-12    0    5    6    9    Null}
{Null    18094.5  9.38994E-13    6.56215E-14    0    6    6    0    Null}
{Null    18094.5  1.30331E-15    9.10816E-17    0    6    6    1    Null}
{Null    18319.2  8.36118E-12    5.8432E-13     0    6    6    2    Null}
{Null    18319.3  1.34353E-15    9.38929E-17    0    6    6    3    Null}
{Null    18521.7  3.66625E-12    2.56215E-13    0    6    6    4    Null}
{Null    18523.4  3.01906E-17    2.10987E-18    0    6    6    5    Null}
{Null    18678.5  5.86852E-13    4.10121E-14    0    6    6    6    Null}
{Null    18706.2  3.49692E-16    2.44382E-17    0    6    6    7    Null}
{Null    18805.8  3.17922E-11    2.2218E-12     0    6    6    8    Null}
{Null    18889.1  9.21084E-16    6.43699E-17    0    6    6    9    Null}
{Null    17957.5  2.26966E-15    8.18587E-17    0    7    6    0    Null}
{Null    17957.5  1.69255E-13    6.10445E-15    0    7    6    1    Null}
{Null    18182.2  1.81697E-15    6.55318E-17    0    7    6    2    Null}
{Null    18182.3  4.39204E-12    1.58406E-13    0    7    6    3    Null}
{Null    18384.7  6.35808E-16    2.29314E-17    0    7    6    4    Null}
{Null    18386.4  8.06516E-12    2.90883E-13    0    7    6    5    Null}
{Null    18541.5  2.6954E-17     9.72137E-19    0    7    6    6    Null}
{Null    18569.2  4.32586E-11    1.56019E-12    0    7    6    7    Null}
{Null    18668.8  1.08371E-15    3.90858E-17    0    7    6    8    Null}
{Null    18752.1  4.57513E-12    1.65009E-13    0    7    6    9    Null}
{Null    17813.9  4.55613E-15    8.21453E-17    0    8    6    0    Null}
{Null    17813.9  9.07464E-18    1.63612E-19    0    8    6    1    Null}
{Null    18038.6  1.74086E-12    3.13869E-14    0    8    6    2    Null}
{Null    18038.7  1.47682E-15    2.66264E-17    0    8    6    3    Null}
{Null    18241.1  3.94541E-11    7.11341E-13    0    8    6    4    Null}
{Null    18242.8  8.97436E-12    1.61804E-13    0    8    6    5    Null}
{Null    18397.9  4.67867E-12    8.43546E-14    0    8    6    6    Null}
{Null    18425.6  5.5766E-16     1.00544E-17    0    8    6    7    Null}
{Null    18525.2  7.7808E-13     1.40285E-14    0    8    6    8    Null}
{Null    18608.5  4.16669E-15    7.51238E-17    0    8    6    9    Null}
{Null    17664.8  5.37697E-17    4.71924E-19    0    9    6    0    Null}
{Null    17664.8  2.01146E-14    1.76541E-16    0    9    6    1    Null}
{Null    17889.5  2.20966E-16    1.93936E-18    0    9    6    2    Null}
{Null    17889.6  1.237E-13      1.08569E-15    0    9    6    3    Null}
{Null    18092    4.41253E-16    3.87277E-18    0    9    6    4    Null}
{Null    18093.7  3.62201E-12    3.17895E-14    0    9    6    5    Null}
{Null    18248.8  4.87595E-16    4.27951E-18    0    9    6    6    Null}
{Null    18276.5  8.66013E-12    7.60079E-14    0    9    6    7    Null}
{Null    18376.1  1.11095E-15    9.75056E-18    0    9    6    8    Null}
{Null    18459.4  2.48819E-12    2.18383E-14    0    9    6    9    Null}
done!!! {2005    10    15    3    26    14.2998750}
```

D.14 Calculating the Percent Enhancement in OH Yield from CH_3OOH

This code is used to compute the % enhancement to the OH yield from photolysis at wavelengths 361 – 640 nm relative to photolysis of CH_3OOH in 210 – 360 nm regions under tropospheric conditions. The enhancement is defined as the following ratio of photolysis rates: $J_{tail} / (J_{UV} + J_{tail}) \times 100$. The code includes absorptions cross-sections of MHP measured in Chapter 10 and from Ref.: G. L. Vaghjiani and A. R. Ravishankara, J. Geophys. Res. **94**, 3487 (1989). The solarflux is obtained from: S. Madronich, S. Flocke, J. Zeng, I. Petropavlovskikh, J. Lee-Taylor, J. Tropospheric Ultraviolet-Visible Model, version 4.1 (2002). This databases is available online from: http://cprm.acd.ucar.edu/Models/TUV/Interactive_TUV/ . The program includes actinic flux in units of quanta s^{-1} cm^{-2} nm^{-1} from that data base at 1 km, 5 km and 10 km for the following angles: 0^o – 90^o in steps of 10^o as well as 89^o – 92^o in 1^o increments.

Mathematica Program mhp_xsection.nb:

Set the working directory:

```
Off[General::Spell]
Off[General::spell1]
SetDirectory[
 "C:\Documents and Settings\overtone\My
   Documents\Jamie\Thesis\CHAPTERS\APPENDIXD\codes\xsection"]
```

Load the molecule's absorption cross-sections in molec. cm^{-2} vs. nm and the specific solar flux file:

```
xsc = Import["xsection.txt", "Table"];
sof = Import["5k\solarf89.txt", "Table"];
```

In this example, the solar flux is read from the 5 km directory and the SZA is 89^o.

```
C:\Documents and Settings\overtone\My
  Documents\Jamie\Thesis\CHAPTERS\APPENDIXD\codes\xsection

lp = ListPlot[xsc, PlotStyle → PointSize[0.02],
  PlotRange → {{210, 700}, {0, 1*^-20}}]
lpf = ListPlot[sof, PlotStyle → PointSize[0.02]]
fxsc = Interpolation[xsc];
fsof = Interpolation[sof];
dsd = Plot[fxsc[x], {x, 210, 640}, PlotRange → {0, 1*^-22}]
soff = Plot[fsof[x], {x, 121.6, 720}]
Show[{lp, dsd}]
Show[{lpf, soff}]
```

```
Plot[Evaluate[fxsc[x]]*Evaluate[fsof[x]], {x, 230, 640},
 PlotRange→{{200, 640}, {0, 50.0*^-9}}]
```

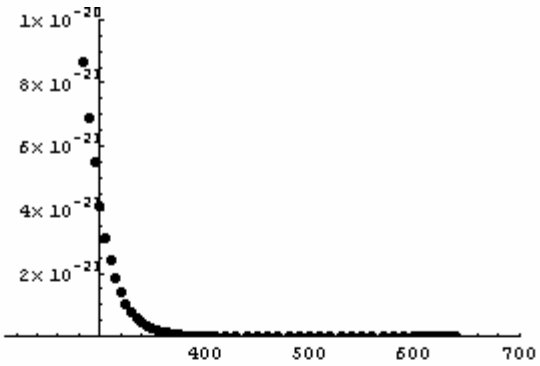

- Graphics -

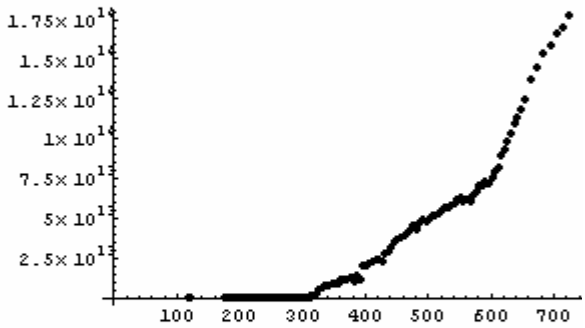

- Graphics -

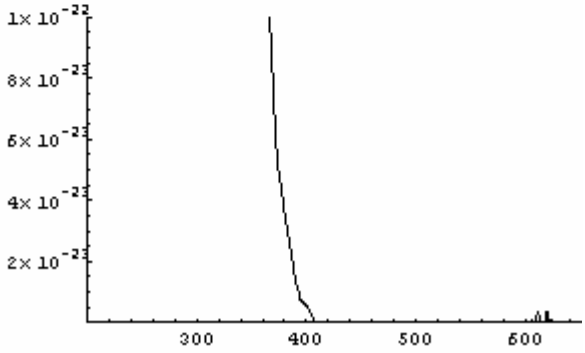

- Graphics -

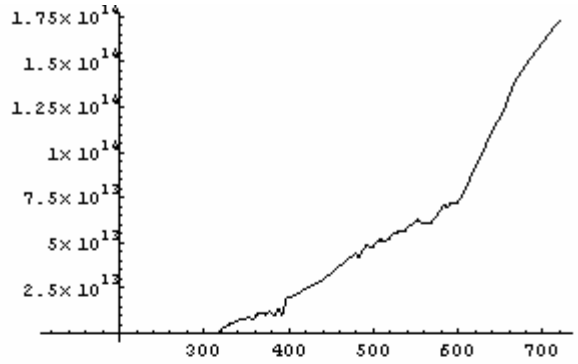

- Graphics -

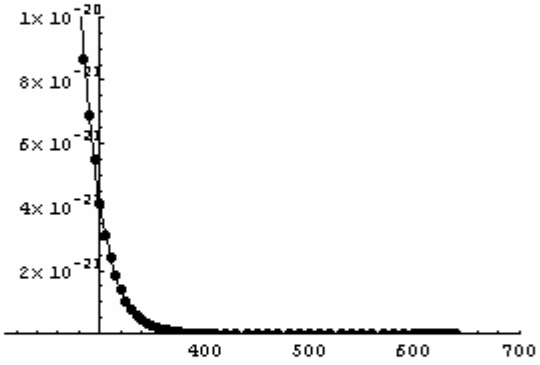

- Graphics -

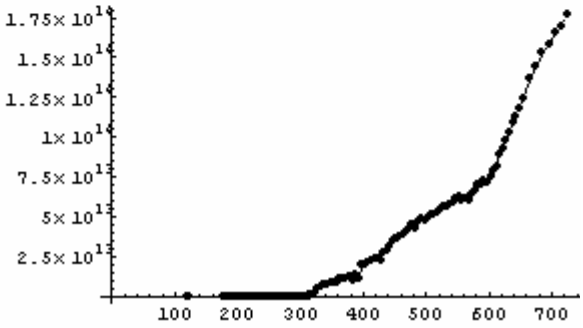

- Graphics -

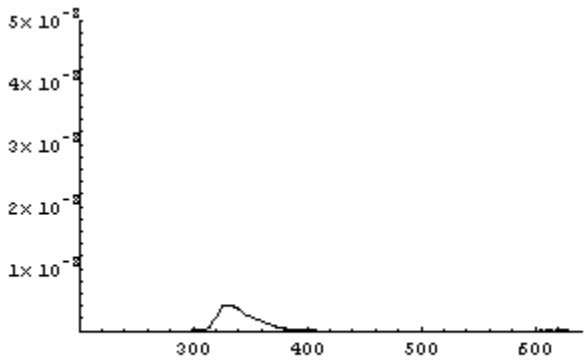


```
- Graphics -
```

```
vis = NIntegrate[Evaluate[fxsc[x]] * Evaluate[fsof[x]],
   {x, 361, 640}, WorkingPrecision → 12];
uv = NIntegrate[Evaluate[fxsc[x]] * Evaluate[fsof[x]],
   {x, 210, 360}, WorkingPrecision → 12];
tot = NIntegrate[Evaluate[fxsc[x]] * Evaluate[fsof[x]],
   {x, 210, 640}, WorkingPrecision → 12];
Print["% enhancement= ", (tot - uv) * 100 / uv, " % "]
```

```
% enhancement= 19.1 %
```

D.15 RRKM Rate Calculation

This code is used to compute the RRKM rate constant for hydroxymethyl hydroperoxide as discussed in Chapter 11. The formulation used is taken from J. I. Steinfeld, J. S. Francisco and W. L. Hase, *Chemical Kinetics and Dynamics* -2nd Edition (Prentice Hall, Upper Saddle River, NJ 1999) where the rate constant $k(E, J, K_a)$, is evaluated according to: $k(E, J, K_a) = G^{\#}[E - E_0 - E^{\#}_r(J, K_a)]/ h N[E - E_r(J, K_a)]$. Where, h is Plank's constant, $G^{\#}$ is the sum of vibrational states for the transition state at the given energy and N is the density of vibrational states for the reactant molecule. J and K_a are the respective angular momentum and its projection onto the top axis quantum numbers. E is the total energy (photon + thermal), E_0 is the barrier height, and $E^{\#}_r(J, K_a)$ is the rotational energy of the transition state. The sum and densities of states are calculated using the Whitten-Rabinovitch expressions from: K. A. Holbrook, M. J. Pilling and P. J. Robinson, *Unimolecular Reactions* -2nd Edition (Wiley, New York, 1996)

Mathematica Program rrkm_coh.nb:

```
Off[General::spell]
Off[General::spell1]
SetDirectory[
  "C:/Documents and Settings/overtone/My
    Documents/Jamie/Thesis/CHAPTERS/APPENDIXD/codes/rrkm"];
vib = Import["vibscaled.txt", "Table"];
Do[νp_z = Extract[vib[[z]], 1], {z, 1, 18}]
vibts = Import["vibTSscaled.txt", "Table"];
Do[νts_z = Extract[vibts[[z]], 1], {z, 1, 17}]
h = 6.6260755*^-34;
conv = 1.986447446*^-23;
DeleteFile[{"counter.txt"}];


"Here are the PARENT parameters";
arp = 0.557858734;
brp = 0.2010469131;
crp = 0.167540372;
bbarp = (brp + crp)/2;
εp_{J,K} = bbarp * J * (J + 1) + (arp - bbarp) * K^2;
εp_νp = Sum[a_i * νp_i, {i, 1, 18}];
εp_t = εp_{J,K} + εp_νp + hn

"Here are the TS parameters";

arts = 0.33305746;
brts = 0.18158271;
crts = 0.13017242;
bbarts = (brts + crts)/2;
ε_rts = bbarts * J * (J + 1) + (arts - bbarts) * K^2;
```

Select the molecular parameters:

```
D0 = 39 * 350.
hn = 13580;
kb = 0.695;
T = 298;
blz = (2 J + 1) Exp[-(εp_{J,K} + εp_νp)/(kb * T)];
```

D0 is the dissociation energy and hn is the photon excitation energy.

$$13580 + 0.184294\,J\,(1+J) + 0.373565\,K^2 + 177.813\,a_1 + 333.679\,a_2 + 394.47\,a_3 + 445.697\,a_4 + 627.693\,a_5 + 804.773\,a_6 + 1024.6\,a_7 + 1032.54\,a_8 + 1086.51\,a_9 + 1248.74\,a_{10} + 1357.71\,a_{11} + 1370.82\,a_{12} + 1406.35\,a_{13} + 1458.58\,a_{14} + 2988.77\,a_{15} + 3076.6\,a_{16} + 3644.15\,a_{17} + 3727.57\,a_{18}$$

13650.

```
Do[If[(Sum[a_i * vp_i, {i, 1, 18}] + hbarp * J * (J + 1) + (arp - hbarp) * K^2 + hn) ≥ D0 &&
    (Sum[a_i * vp_i, {i, 1, 18}] + (hbarp * J * (J + 1) + (arp - hbarp) * K^2) +
       hn - (hbarts * J * (J + 1) + (arts - hbarts) * K^2)) ≥ D0,
  {"n - number of atoms, s - number of normal modes";
   n = 6;
   sp = 3 * n - 6;

   "Select oscillator energy";
   ep_v = Sum[a_i * vp_i, {i, 1, 18}] + hn;

   "β - modified frequency dispersion parameter";
   βp = (sp - 1)/sp * ((Σ_{j=1}^{sp} vp_j^2)/sp) / ((Σ_{j=1}^{sp} vp_j)/sp)^2;

   "ε_z - zeroth point energy, ε_p - reduced energy";
   ep_z = Σ_{j=1}^{sp} 0.5 vp_j;
ep_p = ep_v / ep_z;

ωp_1 = (5.00 * ep_p + 2.73 * ep_p^0.5 + 3.51)^-1;
ωp_2 = Exp[-2.4191 * ep_p^0.25];
dωp_1 = -(5.00 + 1.365 * ep_p^-0.5) * ωp_1^2;
dωp_2 = -(0.60478 * ep_p^-0.75) * ωp_2;

If[0.1 < ep_p < 1.0, {ωp = ωp_1, dωp = dωp_1},
  If[1.0 < ep_p < 8.0, {ωp = ωp_2, dωp = dωp_2}]];
"Select the correct value for ω from above";

ap = 1 - βp * ωp;
pp = (ep_v + ap * ep_z)^(sp-1) / (Factorial[sp - 1] * Π_{j=1}^{sp} vp_j) * (1 - βp * dωp);
```

"n - number of atoms, s - number of normal modes";

$$sts = 3 * n - 6 - 1;$$

"Select oscillator energy";

$$\epsilon ts_v = \text{Sum}[a_i * \upsilon p_i, \{i, 1, 18\}] + \left(bbarp * J * (J+1) + (arp - bbarp) * K^2\right) + hn - \left(bbarts * J * (J+1) + (arts - bbarts) * K^2\right) - D0;$$

"β - modified frequency dispersion parameter";

$$\beta ts = \frac{sts - 1}{sts} * \left(\frac{\frac{\sum_{j=1}^{sts} \upsilon ts_j{}^2}{sts}}{\left(\frac{\sum_{j=1}^{sts} \upsilon ts_j}{sts}\right)^2} \right);$$

"ϵ_z - zeroth point energy, ϵ_p - reduced energy";

$$\epsilon ts_z = \sum_{j=1}^{sp} 0.5\, \upsilon ts_j;$$

$$\epsilon ts_p = \epsilon ts_v / \epsilon ts_z;$$

$$\omega ts_1 = \left(5.00 * \epsilon ts_p + 2.73 * \epsilon ts_p{}^{0.5} + 3.51\right)^{-1};$$

$$\omega ts_2 = \text{Exp}\left[-2.4191 * \epsilon ts_p{}^{0.25}\right];$$

$$d\omega ts_1 = -\left(5.00 + 1.365 * \epsilon ts_p{}^{-0.5}\right) * \omega ts_1{}^2;$$

$$d\omega ts_2 = -\left(0.60478 * \epsilon ts_p{}^{-0.75}\right) * \omega ts_2;$$

$$\text{If}[0.0001 < \epsilon ts_p < 1.0, \{\omega ts = \omega ts_1, d\omega ts = d\omega ts_1\}, \text{If}[1.0 < \epsilon ts_p < 8.0, \{\omega ts = \omega ts_2, d\omega ts = d\omega ts_2\}]];$$

"Select the correct value for ω from above";

$$ats = 1 - \beta ts * \omega ts;$$

$$Wts = \frac{(\epsilon ts_v + ats * \epsilon ts_z)^{sts}}{\text{Factorial}[sts] * \prod_{j=1}^{sts} \upsilon ts_j};$$

$$kr = \frac{Wts * conv}{h * \mu p};$$

```
kr >>> ratescaled_4coh_39kcal.txt;
blz >>> blzscaled_4coh_39kcal.txt;
{a1, a2, a3, a4, J, K} >>> counter.txt;

}],
 {a1, 0, 2}, {a2, 0, 1}, {a3, 0, 1}, {a4, 0, 1}, {a5, 0, 0},
 {a6, 0, 0}, {a7, 0, 0}, {a8, 0, 0}, {a9, 0, 0}, {a10, 0, 0},
 {a11, 0, 0}, {a12, 0, 0}, {a13, 0, 0}, {a14, 0, 0}, {a15, 0, 0},
 {a16, 0, 0}, {a17, 0, 0}, {a18, 0, 0}, {J, 0, 80}, {K, -J, J}]

kblzsum = ReadList["ratescaled_4coh_39kcal.txt"].
  ReadList["blzscaled_4coh_39kcal.txt"]
blzsum = ReadList["blzscaled_4coh_39kcal.txt"]^0.5.
  ReadList["blzscaled_4coh_39kcal.txt"]^0.5
Print["k= ", kblzsum/blzsum]
Print["1/k= ", 1*^9/(kblzsum/blzsum), " ns"]

 4.39595×10^11

 71060.1

k= 6.18624×10^6

1/k= 161.649 ns
```

Appendix E

FORTRAN Code Used in Phase Space Simulations

E.1 Introduction

Several chapters in the dissertation utilize phase space theory (PST) in order to extract additional information regarding the dissociation dynamics of the parent molecule from the resulting OH fragment rotational product state distributions. The FORTRAN code that was used in the analysis of HOONO $2\nu_{OH}$ and $3\nu_{OH}$ bands as well as in the $HOCH_2OOH$ $4\nu_{OH}$ and $5\nu_{OH}$ studies was written by Professor A. Sinha for nitric acid. The code was modified by the dissertation author for these particular studies. As outlined in Chapter 4, several parameters associated with the molecule and its fragments are required in order to use the program properly. These parameters are discussed below in the order they appear in the FORTRAN code.

QVIB is the vibrational partition function calculated using:[1]

$$Q_{vib} = \prod_{j=1}^{3n-6} \frac{1}{(1 - \mathrm{Exp}[-\omega_j / (k*T)])} \qquad \text{(E.1)}$$

Where the product runs over the total number of vibrational modes, ω_j, (nine for HOONO). k is the Boltzmann factor and T is the temperature. QROT is the rotational partition function calculated using the expression:[2]

$$Q_{rot} = \frac{1}{\sigma} \left(\frac{k*T}{h*c}\right)^{3/2} \left(\frac{\pi}{A*B*C}\right)^{1/2} \qquad \text{(E.2)}$$

Where σ is the symmetry number (σ = 1 for HOONO), h is Planck's constant, c is the speed of light, and A, B, C are the molecular rotational constants. The term XKT corresponds to the Boltzmann factor × temperature. Also needed are the reduced mass and the total attractive constant for the long-range interaction between the fragments, C_6, given by the sum of the *dipole–dipole* ($C_{d\text{-}d}$), *dipole–induced-dipole* ($C_{d\text{-}id}$), and the *dispersion energy* (C_{disp}) constants:[1]

$$C_{d\text{-}d} = -2/3kT \times (p_1\, p_2)^2 / (4\pi\varepsilon_0)^2 \qquad \text{(E.3)}$$

$$C_{d\text{-}id} = -(p_1^2\, \alpha_2 + p_2^2\, \alpha_1) / (4\pi\varepsilon_0)^2 \qquad \text{(E.4)}$$

$$C_{disp} \approx -{}^3/_2 \times I_1\, I_2 / (I_1 + I_2) \times \alpha_1\alpha_2 / (4\pi\varepsilon_0)^2 \qquad \text{(E.5)}$$

Where p_1 and p_2 are the dipole moments, α_1 and α_2 are the polorizabilities, I_1 and I_2 are the ionization energies of the OH and NO_2 fragments respectively. Also in the equations k is the Boltzmann factor, T is the temperature and ε_0 is permittivity of vacuum.

In order to consider contribution from "hotbands", the parameter "NV" has to be adjusted. For example, in the sample code, NV=1,6 is set to evaluate the thermal contribution from the first six vibrational states (including the ground state which carries 0 cm^{-1}). To consider hotband contribution in the simulation, say from a state carrying ~630 cm^{-1} of internal energy, set NV=6,6 which in turns will only consider that state in the DO loop.

E.2 Phase-Space Simulation for *cis-cis* HOONO ($h\nu$ = 6381.23 cm^{-1})

FORTRAN Program cHOONO.FOR:

```
C     ***************************************************************
C     PROGRAM cHOONO.FOR, CALCULATES OH(PI-3/2) AND OH(PI-1/2) PRODUCT
C     STATE DISTRIBUTION GENERATED FROM 2NU-OH EXCITATION
C     OF HO-ONO USING PHASE SPACE THEORY. USE TOTAL ANGULAR MOMENTUM-J
C     ***************************************************************

      IMPLICIT REAL*8 (A-H,O-Z)
      IMPLICIT INTEGER*4 (I-N)
      DIMENSION FHNO3(11),FNO2(11),PN(20),PM(20),XPN(20),FOH(20)
C     ***********************************
C     PARTITION FUNCTION FOR HOONO AT 298 K
C     ***********************************
      QVIB=1.61
      QROT=27324.3
      XKT=207.1
C     ***********************************************
C     INPUT DISSOCIATION ENERGY AND PHOTON ENERGY CM-1
C     ***********************************************
      DZERO=6960.13
      EPHOTN=6381.23
      OPEN (UNIT=3,FILE='ciscis.OUT',STATUS='NEW')
C     ************************************
C     INPUT REDUCED MASS AND C6 COEFFICIENT
C     ************************************
      RMASS=2.06D-23
      C6=2.0D-58
      HBAR=1.05D-27
C     ************************************************
C     RELAVENT ROTATIONAL CONSTANTS FOR HOONO (using MW data) AND NO2 CM-1
C     ************************************************
      BBARP=0.229143
      CP=0.714040412
      DJP=.268633D-6
      DJKP=-0.5348204D-6
      DKP=2.000899D-6
      BBAR2=0.422063
      A2=8.00213
C     ********************************************************************
C     ENERGIES OF RELAVENT THERMALLY POPULATED VIB. STATES OF HOONO(CM-1)
C     ********************************************************************
      FHNO3(1)=0.0
      FHNO3(2)=290.2472
      FHNO3(3)=371.0
      FHNO3(4)=482.0
      FHNO3(5)=507.791
      FHNO3(6)=628.828
      FHNO3(7)=643.0
      FHNO3(8)=685.518
      FHNO3(9)=736.0
```

```
      FHNO3(10)=755.1785
      FHNO3(11)=815.0
      FHNO3(12)=842.2629
      FHNO3(13)=927.2964
      FHNO3(14)=946.92
      FHNO3(15)=947.10

C     ******************************************************
C     ENERGIES OF RELAVENT VIB. STATES OF NO2 PRODUCT (CM-1)
C     ******************************************************
      FNO2(1)=0.0
      FNO2(2)=749.6
      FNO2(3)=1319.95
      FNO2(4)=1498.2
      FNO2(5)=1616.05
      FNO2(6)=2059.85
      FNO2(7)=2245.8
      FNO2(8)=2362.95
      FNO2(9)=2623.70
      FNO2(10)=2798.75
      FNO2(11)=2906.20
C     ************************************************************
C     TERM VALUE FOR OH ROTATIONAL STATES (DOUBLET PI-3/2) CM-1
C     ************************************************************
      FOH(1)=0.055
      FOH(2)=83.92
      FOH(3)=202.38
      FOH(4)=355.91
      FOH(5)=544.83
      FOH(6)=769.24
      FOH(7)=1029.118
      FOH(8)=1324.317
      FOH(9)=1654.6
      FOH(10)=2019.52
C     *********************************
C     ENERGY LEVELS FOR OH PI-1/2 STATE
C     *********************************
      FOH(11)=126.46
      FOH(12)=187.76
      FOH(13)=289.03
      FOH(14)=429.42
      FOH(15)=608.12
      FOH(16)=824.43
      FOH(17)=1077.72
      FOH(18)=1367.46
      FOH(19)=1693.10
      FOH(20)=2054.14


      EVIB1=0.0
      NOHMAX=20

C     ************************************************************
C     ADD UP THE CONT-
```

```
C     RIBUTIONS MADE BY THE VARIOUS THERMALLY POPULATED STATES OF
C     HOONO.
C     ********************************************************

      DO 900 NV=1,6
      NVA=NV

C     ****************************************
C     VIBRATIONAL ENERGY OF PARENT MOLECULE: EVIBP
C     ****************************************

      EVIBP=FHNO3(NVA)

C     ****************************************
C     CALCULATE VIBRATIONAL PARTITION FUNCITION
C     ****************************************

      VBOLTZ=DEXP(-1.0*EVIBP/XKT)*(1.0/QVIB)

C     ********************************************************
C     SUM UP THE CONTRIBUTIONS MADE TO THE STATE COUNTING BY THE
C     VARIOUS ROTATIONAL STATES OF THE PARENT MOLECULE.
C     ********************************************************
      DO 800 J=0,80
      JP=J
      KMAX=J
C     ************************************************************
C     FOR EACH J-STATE CONSIDER RELAVENT K STATE. IN THE SYMMETRIC
C     TOP LIMIT CONSIDERED HERE,(+,-) K STATES ARE DEGENERATE. HOONO
C     IS A NEAR OBLATE TOP KAPPA=-0.72
C     ************************************************************
      DO 700 KK=0,KMAX
      RC=0.0
      KP=KK
      RK=DFLOAT(KP)
      RJ=DFLOAT(JP)
      CDP=DJP*((RJ*(RJ+1.))**2)+DJKP*(RJ*(RJ+1.))*(RK**2)+DKP*(RK**2)
      EROTP=(BBARP*RJ*(RJ+1.))+(CP-BBARP)*(RK**2)+CDP
      EPAR=EVIBP+EROTP
C     ********************************************************
C     WE ONLY CONSIDER HOONO STATES WHOSE BOLTZMAN FACTOR
C     IS GREATER THAN 0.0002. THUS, STATES HAVING ENERGY GREATER
C     THAN 1823 CM-1 ARE NOT CONSIDERED.
C     ********************************************************
      PROB=DEXP(-1.0*EPAR/XKT)*100.0
      IF (PROB .LT. .01) GO TO 700
      RBOLTZ=((2.0*RJ)+1.)*DEXP(-1.*EROTP/XKT)*(1./QROT)
C     ****************************************
C     ALL K-STATES ARE DOUBLY DEGENERATE EXCEPT K=0
C     ****************************************
      IF(RK .GT. 0.0) DEGENK=2.0
      IF(RK .EQ. 0.0) DEGENK=1.0
      RBOL0TZ=RBOLTZ*DEGENK
      BOLTZ=VBOLTZ*RBOLTZ
```

```
      ETPAR=EVIBP+EROTP+EPHOTN
      EXCESS=ETPAR-DZERO
C     ************************************************************
C     CHECK THAT THE PARENT STATE BEING CONSIDERED IN CONJUNCTION
C     WITH THE PHOTON ENERGY IS ENERGETIC ENOUGH TO PRODUCE AT LEAST
C     THE LOWEST OH ROTATIONAL STATE .
C     ************************************************************

      IF (EXCESS .LT. FOH(1)) GO TO 700

C     ************************************************************
C     CONSIDER FIRST THE VARIOUS ROTATIONAL STATES OF OH FRAGMENT
C     ************************************************************

      DO 650 NOH=1,NOHMAX
      N1=NOH
      S=0.0
C     ***********************************
C     FOR THE PI-3/2 STATE OF OH : J=N+1/2
C     FOR THE PI-1/2 STATE OF OH : J=N-1/2
C     ***********************************

      RJ1=DFLOAT(N1)+.5
      IF (NOH .GT. 10) RJ1=(DFLOAT(N1)-10.0)-.5
      EROT1=FOH(N1)
      EOH=EVIB1+EROT1
      IF (EXCESS .LT. EOH) GO TO 650
C     ************************************************************
C     COUNT THE NUMBER OF WAYS THE EXCESS ENERGY CAN BE DISTRIBUTED
C     AMONG THE VARIOUS VIBRATIONAL AND ROTATIONAL STATES OF THE
C     NO2 FRAGMENTS. FIRST CONSIDER VIBRATIONAL STATES.
C     ************************************************************
      EAVNO2=EXCESS-EOH
      DO 600 NV2=1,6
      EVIB2=FNO2(NV2)
      EMAXR2=EAVNO2-EVIB2
      IF (EMAXR2 .LT. 0.0 ) GO TO 600
      NNO2MX=IDINT((-.5+DSQRT(.25+(EMAXR2/BBAR2))))

C     ************************************************************
C     WITHIN THE VIBRATIONAL LEVEL OF NO2 BEING CONSIDERED, WHAT ARE
C     THE POSSIBLE ROTATIONAL STATES THAT CAN BE POPULATED WHILE
C     CONSERVING ENERGY. NNO2MX IS THE MAXIMUM VALUE OF ROTATIONAL
C     ANGULAR MOMENTUM THAT THE NO2 FRAGMENT CAN HAVE.
C     ************************************************************
      DO 500 NNO2=0,NNO2MX
      N2=NNO2
      K2MAX=N2
C     ************************************************************
C     THE NO2 FRAGMENT IS BEING CONSIDERED AS A NEAR PROLATE TOP.
C     ALSO NOTE THAT FOR NO2 HALF THE ROTATIONAL STATES WILL BE
C     MISSING. THIS IS APPROXIMATELY ACCOUNTED FOR IN THIS PROGRAM BY
C     COUNTING ONLY THE + K-STATES.
C     ************************************************************
```

```
      DO 400 KK2=0,K2MAX
      K2=KK2
      RN2=DFLOAT(N2)
      RK2=DFLOAT(K2)
      EROT2=(BBAR2*RN2*(RN2+1.0))+(A2-BBAR2)*(RK2**2)
      IF ( EROT2 .GT. EMAXR2 ) GO TO 400
      DO 350 IJK=1,2
      RJ2=RN2-0.5
      IF (IJK .EQ. 2) RJ=RN2+0.5
      IF (RJ2 .LT. 0.0) GO TO 350
C     ************************************************************
C     FOR A GIVEN J1(OH) AND J2(NO2), THE RESULTANT ANGULAR MOMENTUM
C     CAN TAKE ON ANY VALUES BETWEEN (J1+J2) AND |J1-J2| IN STEPS OF
C     ONE.
C     ************************************************************
      RHIGH= RJ1+RJ2
      JRHIGH=IDINT(RHIGH)
      RLOW=DABS(RJ1-RJ2)
      JRLOW=IDINT(RLOW)
      DO 300 JR=JRLOW,JRHIGH
      JRES=JR
      LUPP=JP+JRES
      LLOW=IABS(JP-JRES)
      ETRANS=ETPAR-DZERO-(EROT1+EVIB1+EROT2+EVIB2)
C     ********************************
C     CONVERT ETRANS FROM CM-1 TO ERGS
C     ********************************
      ETRANS=ETRANS*(1./5.03D15)
      ALPHA=RMASS*6*(C6**0.3333)*((ETRANS/2.0)**.6666)*(1./HBAR**2)
C     ***************************************
C     CALCULATE MAXIMUM ALLOWED VALUE FOR L.
C     ***************************************
      LMAX=IDINT((-.5+DSQRT(.25+ALPHA)))
      IF (LUPP .GT. LMAX ) LUPP=LMAX
      DO 200 L=LLOW,LUPP
      S=S+1.
  200   CONTINUE
  300   CONTINUE
  350   CONTINUE
  400   CONTINUE
  500   CONTINUE
  600   CONTINUE
C      BOLTZ=1.0
      PM(N1)=S
      RC=RC+S
  650   CONTINUE
      IF (RC .EQ. 0.0) GO TO 700
      DO 675 MXX=1,NOHMAX
      PM(MXX)=(PM(MXX)/RC)*BOLTZ
      PN(MXX)=PN(MXX)+PM(MXX)
  675   CONTINUE
  700   CONTINUE
  800   CONTINUE
  900   CONTINUE
```

```
C     ***********************************************
C     NORMALIZE RESULTS OF THE COUNTING PROCESS TO 100%
C     ***********************************************
      SNORM=0.0
      DO 2000 M=1,NOHMAX
      SNORM=SNORM+PN(M)
2000  CONTINUE
      DO 3000 MM=1,NOHMAX
      XPN(MM)=(PN(MM)/SNORM)*100.0
      WRITE(3,*)MM,PN(MM),XPN(MM)
3000  CONTINUE
      CLOSE (UNIT=3)
      END
```

Sample Output CISCIS.OUT:

```
 1  4.713057232599519E-003      65.789335676322910
 2  1.287529330417616E-003      17.972559027303770
 3  3.836213760161228E-004       5.354952047848842
 4  1.055494380708538E-004       1.473359449925591
 5  2.787184680736577E-005   3.890617480402337E-001
 6  4.757471188039790E-006   6.640930791068544E-002
 7  2.548727503525234E-007   3.557756271599816E-003
 8  0.000000000000000E+000   0.000000000000000E+000
 9  0.000000000000000E+000   0.000000000000000E+000
10  0.000000000000000E+000   0.000000000000000E+000
11  2.361216418324555E-004       3.296010463762576
12  2.257890591183564E-004       3.151778446404641
13  1.168373122176602E-004       1.630926333726563
14  4.603461691172349E-005   6.425949686729924E-001
15  1.398285901015579E-005   1.951860458580610E-001
16  2.353614850860077E-006   3.285399472872680E-002
17  1.013495360499470E-007   1.414733222781581E-003
18  0.000000000000000E+000   0.000000000000000E+000
19  0.000000000000000E+000   0.000000000000000E+000
20  0.000000000000000E+000   0.000000000000000E+000
```

The output file contains three columns: OH N-level, un-normalized population, normalized population. The OH N-levels 1 – 10 are associated with OH($2\Pi_{3/2}$, N= 1 → 10) rotational states and the OH N-levels 11 – 20 are associated with OH($^2\Pi_{1/2}$, N= 1 → 10) rotational states.

E.3 Phase-Space Simulation for *trans-perp* HOONO ($h\nu = 6971.35\ cm^{-1}$)

FORTRAN Program tHOONO.FOR:

```
C     ************************************************************
C     PROGRAM tHOONO.FOR, CALCULATES OH(PI-3/2) AND OH(PI-1/2) PRODUCT
C     STATE DISTRIBUTION GENERATED FROM 2NU-OH EXCITATION
C     OF HO-ONO USING PHASE SPACE THEORY. USE TOTAL ANGULAR MOMENTUM-J
```

```
C     ************************************************************

      IMPLICIT REAL*8 (A-H,O-Z)
      IMPLICIT INTEGER*4 (I-N)
      DIMENSION FHNO3(14),FNO2(11),PN(20),PM(20),XPN(20),FOH(20)
C     ***********************************
C     PARTITION FUNCTION FOR HNO3 AT 298 K
C     ***********************************
      QVIB=2.91485
      QROT=25096.5
      XKT=2.5715
C     ********************************************
C     INPUT DISSOCIATION ENERGY AND PHOTON ENERGY CM-1
C     ********************************************
      DZERO=5665.14
      EPHOTN=6971.35
      OPEN (UNIT=3,FILE='THOONO.OUT',STATUS='NEW')
C     ***********************************
C     INPUT REDUCED MASS AND C6 COEFFICIENT
C     ***********************************
      RMASS=2.06D-23
      C6=0.2D-58
      HBAR=1.05D-27
C     ************************************************
C     RELAVENT ROTATIONAL CONSTANTS FOR HNO3 AND NO2 CM-1
C     ************************************************
      BBARP=0.16015
      CP=1.8054
      DJP=8.3D-8
      DJKP=-2.2221D-6
      DKP=4.4077D-5
      BBAR2=0.422063
      A2=8.00213
C     ********************************************************************
C     ENERGIES OF RELAVENT THERMALLY POPULATED VIB. STATES OF HNO3(CM-1)
C     ********************************************************************
      FHNO3(1)=0.0
      FHNO3(2)=206.0
      FHNO3(3)=282.8
      FHNO3(4)=334.2
      FHNO3(5)=400.0
      FHNO3(6)=409.0
      FHNO3(7)=525.2
      FHNO3(8)=612.0
      FHNO3(9)=686.1
      FHNO3(10)=729.3
      FHNO3(11)=770.7
      FHNO3(12)=800.3
      FHNO3(13)=814.0
      FHNO3(14)=894.4
      FHNO3(15)=945.0
C     ****************************************************
C     ENERGIES OF RELAVENT VIB. STATES OF NO2 PRODUCT (CM-1)
C     ****************************************************
```

```
      FNO2(1)=0.0
      FNO2(2)=749.6
      FNO2(3)=1319.95
      FNO2(4)=1498.2
      FNO2(5)=1616.05
      FNO2(6)=2059.85
      FNO2(7)=2245.8
      FNO2(8)=2362.95
      FNO2(9)=2623.70
      FNO2(10)=2798.75
      FNO2(11)=2906.20
C     ********************************************************
C     TERM VALUE FOR OH ROTATIONAL STATES (DOUBLET PI-3/2) CM-1
C     ********************************************************
      FOH(1)=0.055
      FOH(2)=83.92
      FOH(3)=202.38
      FOH(4)=355.91
      FOH(5)=544.83
      FOH(6)=769.24
      FOH(7)=1029.118
      FOH(8)=1324.317
      FOH(9)=1654.6
      FOH(10)=2019.52
C     *********************************
C     ENERGY LEVELS FOR OH PI-1/2 STATE
C     *********************************
      FOH(11)=126.46
      FOH(12)=187.76
      FOH(13)=289.03
      FOH(14)=429.42
      FOH(15)=608.12
      FOH(16)=824.43
      FOH(17)=1077.72
      FOH(18)=1367.46
      FOH(19)=1693.10
      FOH(20)=2054.14


      EVIB1=0.0
      NOHMAX=20

C     ***********************************************************
C     ADD UP THE CONT-
C     RIBUTIONS MADE BY THE VARIOUS THERMALLY POPULATED STATES OF
C     HNO3.
C     ***********************************************************

      DO 900 NV=1,1
      NVA=NV

C     ******************************************
C     VIBRATIONAL ENERGY OF PARENT MOLECULE: EVIBP
C     ******************************************
```

```
      EVIBP=FHNO3(NVA)

C     ***************************************
C     CALCULATE VIBRATIONAL PARTITION FUNCITION
C     ***************************************

      VBOLTZ=DEXP(-1.0*EVIBP/XKT)*(1.0/QVIB)

C     ***********************************************************
C     SUM UP THE CONTRIBUTIONS MADE TO THE STATE COUNTING BY THE
C     VARIOUS ROTATIONAL STATES OF THE PARENT MOLECULE.
C     ***********************************************************
      DO 800 J=0,80
      JP=J
      KMAX=J
C     ***************************************************************
C     FOR EACH J-STATE CONSIDER RELAVENT K STATE. IN THE SYMMETRIC
C     TOP LIMIT CONSIDERED HERE,(+,-) K STATES ARE DEGENERATE. NITRIC
C     ACID IS A NEAR OBLATE TOP KAPPA=.7
C     ***************************************************************
      DO 700 KK=0,KMAX
      RC=0.0
      KP=KK
      RK=DFLOAT(KP)
      RJ=DFLOAT(JP)
      CDP=DJP*((RJ*(RJ+1.))**2)+DJKP*(RJ*(RJ+1.))*(RK**2)+DKP*(RK**2)
      EROTP=(BBARP*RJ*(RJ+1.))+(CP-BBARP)*(RK**2)+CDP
      EPAR=EVIBP+EROTP
C     ***********************************************************
C     WE ONLY CONSIDER NITRIC ACID STATES WHOSE BOLTZMAN FACTOR
C     IS GREATER THAN 0.0002. THUS, STATES HAVING ENERGY GREATER
C     THAN 1823 CM-1 ARE NOT CONSIDERED.
C     ***********************************************************
      PROB=DEXP(-1.0*EPAR/XKT)*100.0
      IF (PROB .LT. .01) GO TO 700
      RBOLTZ=((2.0*RJ)+1.)*DEXP(-1.*EROTP/XKT)*(1./QROT)
C     *****************************************
C     ALL K-STATES ARE DOUBLY DEGENERATE EXCEPT K=0
C     *****************************************
      IF(RK .GT. 0.0) DEGENK=2.0
      IF(RK .EQ. 0.0) DEGENK=1.0
      RBOL0TZ=RBOLTZ*DEGENK
      BOLTZ=VBOLTZ*RBOLTZ
      ETPAR=EVIBP+EROTP+EPHOTN
      EXCESS=ETPAR-DZERO
C     ***************************************************************
C     CHECK THAT THE PARENT STATE BEING CONSIDERED IN CONJUNCTION
C     WITH THE PHOTON ENERGY IS ENERGETIC ENOUGH TO PRODUCE AT LEAST
C     THE LOWEST OH ROTATIONAL STATE .
C     ***************************************************************

      IF (EXCESS .LT. FOH(1)) GO TO 700
```

```
C     ********************************************************
C     CONSIDER FIRST THE VARIOUS ROTATIONAL STATES OF OH FRAGMENT
C     ********************************************************

      DO 650 NOH=1,NOHMAX
      N1=NOH
      S=0.0
C     ***********************************
C     FOR THE PI-3/2 STATE OF OH : J=N+1/2
C     FOR THE PI-1/2 STATE OF OH : J=N-1/2
C     ***********************************

      RJ1=DFLOAT(N1)+.5
      IF (NOH .GT. 10) RJ1=(DFLOAT(N1)-10.0)-.5
      EROT1=FOH(N1)
      EOH=EVIB1+EROT1
      IF (EXCESS .LT. EOH) GO TO 650
C     ************************************************************
C     COUNT THE NUMBER OF WAYS THE EXCESS ENERGY CAN BE DISTRIBUTED
C     AMONG THE VARIOUS VIBRATIONAL AND ROTATIONAL STATES OF THE
C     NO2 FRAGMENTS. FIRST CONSIDER VIBRATIONAL STATES.
C     ************************************************************
      EAVNO2=EXCESS-EOH
      DO 600 NV2=1,6
      EVIB2=FNO2(NV2)
      EMAXR2=EAVNO2-EVIB2
      IF (EMAXR2 .LT. 0.0 ) GO TO 600
      NNO2MX=IDINT((-.5+DSQRT(.25+(EMAXR2/BBAR2))))

C     ************************************************************
C     WITHIN THE VIBRATIONAL LEVEL OF NO2 BEING CONSIDERED, WHAT ARE
C     THE POSSIBLE ROTATIONAL STATES THAT CAN BE POPULATED WHILE
C     CONSERVING ENERGY. NNO2MX IS THE MAXIMUM VALUE OF ROTATIONAL
C     ANGULAR MOMENTUM THAT THE NO2 FRAGMENT CAN HAVE.
C     ************************************************************
      DO 500 NNO2=0,NNO2MX
      N2=NNO2
      K2MAX=N2
C     ************************************************************
C     THE NO2 FRAGMENT IS BEING CONSIDERED AS A NEAR PROLATE TOP.
C     ALSO NOTE THAT FOR NO2 HALF THE ROTATIONAL STATES WILL BE
C     MISSING. THIS IS APPROXIMATELY ACCOUNTED FOR IN THIS PROGRAM BY
C     COUNTING ONLY THE + K-STATES.
C     ************************************************************
      DO 400 KK2=0,K2MAX
      K2=KK2
      RN2=DFLOAT(N2)
      RK2=DFLOAT(K2)
      EROT2=(BBAR2*RN2*(RN2+1.0))+(A2-BBAR2)*(RK2**2)
      IF ( EROT2 .GT. EMAXR2 ) GO TO 400
      DO 350 IJK=1,2
      RJ2=RN2-0.5
      IF (IJK .EQ. 2) RJ=RN2+0.5
      IF (RJ2 .LT. 0.0) GO TO 350
```

```
C     ************************************************************
C     FOR A GIVEN J1(OH) AND J2(NO2), THE RESULTANT ANGULAR MOMENTUM
C     CAN TAKE ON ANY VALUES BETWEEN (J1+J2) AND |J1-J2| IN STEPS OF
C     ONE.
C     ************************************************************
      RHIGH= RJ1+RJ2
      JRHIGH=IDINT(RHIGH)
      RLOW=DABS(RJ1-RJ2)
      JRLOW=IDINT(RLOW)
      DO 300 JR=JRLOW,JRHIGH
      JRES=JR
      LUPP=JP+JRES
      LLOW=IABS(JP-JRES)
      ETRANS=ETPAR-DZERO-(EROT1+EVIB1+EROT2+EVIB2)
C     *******************************
C     CONVERT ETRANS FROM CM-1 TO ERGS
C     *******************************
      ETRANS=ETRANS*(1./5.03D15)
      ALPHA=RMASS*6*(C6**0.3333)*((ETRANS/2.0)**.6666)*(1./HBAR**2)
C     ************************************
C     CALCULATE MAXIMUM ALLOWED VALUE FOR L.
C     ************************************
      LMAX=IDINT((-.5+DSQRT(.25+ALPHA)))
      IF (LUPP .GT. LMAX ) LUPP=LMAX
      DO 200 L=LLOW,LUPP
      S=S+1.
 200   CONTINUE
 300   CONTINUE
 350   CONTINUE
 400   CONTINUE
 500   CONTINUE
 600   CONTINUE
C      BOLTZ=1.0
      PM(N1)=S
      RC=RC+S
 650   CONTINUE
      IF (RC .EQ. 0.0) GO TO 700
      DO 675 MXX=1,NOHMAX
      PM(MXX)=(PM(MXX)/RC)*BOLTZ
      PN(MXX)=PN(MXX)+PM(MXX)
 675   CONTINUE
 700   CONTINUE
 800   CONTINUE
 900   CONTINUE

C     ************************************************
C     NORMALIZE RESULTS OF THE COUNTING PROCESS TO 100%
C     ************************************************
      SNORM=0.0
      DO 2000 M=1,NOHMAX
      SNORM=SNORM+PN(M)
2000   CONTINUE
      DO 3000 MM=1,NOHMAX
      XPN(MM)=(PN(MM)/SNORM)*100.0
```

```
      WRITE(3,*)MM,PN(MM),XPN(MM)
3000  CONTINUE
      CLOSE (UNIT=3)
      END
```

Sample Output THOONO.OUT:

```
 1  1.631088879451123E-005      7.278972452119412
 2  2.226875850846397E-005      9.937758865755683
 3  2.551080550311267E-005     11.384569708489500
 4  2.495473273992047E-005     11.136414112823130
 5  1.999423668723658E-005      8.922720268715532
 6  1.619459505088552E-005      7.227074669793155
 7  9.155759856663067E-006      4.085891615991998
 8  3.310974671828133E-012  1.477570825816196E-006
 9  0.000000000000000E+000  0.000000000000000E+000
10  0.000000000000000E+000  0.000000000000000E+000
11  7.112850662660541E-006      3.174213538073285
12  1.311938302546806E-005      5.854716369798332
13  1.701756295951796E-005      7.594336123867296
14  1.764959413700650E-005      7.876389271784523
15  1.533697111496834E-005      6.844347457164489
16  1.264128470792924E-005      5.641358009833249
17  6.814871669013340E-006      3.041236058219574
18  0.000000000000000E+000  0.000000000000000E+000
19  0.000000000000000E+000  0.000000000000000E+000
20  0.000000000000000E+000  0.000000000000000E+000
```

E.4 Phase-Space Simulation for HMHP ($h\nu$ = 13 330 cm^{-1})

FORTRAN Program HMHP4N2.FOR:

```
C     ***************************************************************
C     PROGRAM hmhp.FOR, CALCULATES OH(PI-3/2) AND OH(PI-1/2) PRODUCT
C     STATE DISTRIBUTION GENERATED FROM 2NU-OH EXCITATION
C     OF HO-OCH2OH USING PHASE SPACE THEORY. USE TOTAL ANGULAR MOMENTUM-J
C     ***************************************************************

      IMPLICIT REAL*8 (A-H,O-Z)
      IMPLICIT INTEGER*4 (I-N)
      DIMENSION FHMHP(14),FHOCH2O(9),PN(20),PM(20),XPN(20),FOH(20)
C     ************************************
C     PARTITION FUNCTION FOR HOONO AT 298 K
C     ************************************
      QVIB=3.05
      QROT=38502.3
      XKT=207.1
C     ********************************************
C     INPUT DISSOCIATION ENERGY AND PHOTON ENERGY CM-1
C     ********************************************
      DZERO=13300.0
      EPHOTN=13330.0
      OPEN (UNIT=3,FILE='4nuooh.OUT',STATUS='NEW')
```

```
C     ************************************
C     INPUT REDUCED MASS AND C6 COEFFICIENT
C     ************************************
      RMASS=2.07D-23
      C6=1.7D-58
      HBAR=1.05D-27
C     ************************************************
C     RELAVENT ROTATIONAL CONSTANTS FOR HOCH2OOH AND HOCH2O CM-1
C     ************************************************
      BBARP=0.18450475
      CP=0.557858734
      DJP=6.07D-6
      DJKP=-2.1D-6
      DKP=2.000899D-6
      BBAR2=0.3316294
      A2=1.640457283
C     ********************************************************************
C     ENERGIES OF RELAVENT THERMALLY POPULATED VIB. STATES OF HOCH2OOH(CM-
1)
C     ********************************************************************
          FHMHP(1)=0.0
          FHMHP(2)=177.8
          FHMHP(3)=333.7
          FHMHP(4)=355.6
          FHMHP(5)=394.5
          FHMHP(6)=445.7
          FHMHP(7)=533.4
          FHMHP(8)=627.7
          FHMHP(9)=667.4
          FHMHP(10)=711.3
          FHMHP(11)=788.9
          FHMHP(12)=804.8
          FHMHP(13)=889.1
          FHMHP(14)=891.4
C     ********************************************************
C     ENERGIES OF RELAVENT VIB. STATES OF HOCH2O PRODUCT (CM-1)
C     ********************************************************
      FHOCH2O(1)=0.0
      FHOCH2O(2)=286.8
      FHOCH2O(3)=544.2
      FHOCH2O(4)=573.7
      FHOCH2O(5)=792.7
      FHOCH2O(6)=860.5
      FHOCH2O(7)=1003.2
      FHOCH2O(8)=1088.4
      FHOCH2O(9)=1093.8
C     ***********************************************************
C     TERM VALUE FOR OH ROTATIONAL STATES (DOUBLET PI-3/2) CM-1
C     ***********************************************************
      FOH(1)=0.055
      FOH(2)=83.92
      FOH(3)=202.38
      FOH(4)=355.91
      FOH(5)=544.83
```

```
      FOH(6)=769.24
      FOH(7)=1029.118
      FOH(8)=1324.317
      FOH(9)=1654.6
      FOH(10)=2019.52
C     *********************************
C     ENERGY LEVELS FOR OH PI-1/2 STATE
C     *********************************
      FOH(11)=126.46
      FOH(12)=187.76
      FOH(13)=289.03
      FOH(14)=429.42
      FOH(15)=608.12
      FOH(16)=824.43
      FOH(17)=1077.72
      FOH(18)=1367.46
      FOH(19)=1693.10
      FOH(20)=2054.14


      EVIB1=0.0
      NOHMAX=20

C     ***********************************************************
C     ADD UP THE CONT-
C     RIBUTIONS MADE BY THE VARIOUS THERMALLY POPULATED STATES OF
C     HOCH2OOH.
C     ***********************************************************

      DO 900 NV=1,14
      NVA=NV

C     ****************************************
C     VIBRATIONAL ENERGY OF PARENT MOLECULE: EVIBP
C     ****************************************

      EVIBP=FHMHP(NVA)

C     ****************************************
C     CALCULATE VIBRATIONAL PARTITION FUNCITION
C     ****************************************

      VBOLTZ=DEXP(-1.0*EVIBP/XKT)*(1.0/QVIB)

C     ***********************************************************
C     SUM UP THE CONTRIBUTIONS MADE TO THE STATE COUNTING BY THE
C     VARIOUS ROTATIONAL STATES OF THE PARENT MOLECULE.
C     ***********************************************************
      DO 800 J=0,80
      JP=J
      KMAX=J
C     ***************************************************************
C     FOR EACH J-STATE CONSIDER RELAVENT K STATE. IN THE SYMMETRIC
C     TOP LIMIT CONSIDERED HERE,(+,-) K STATES ARE DEGENERATE. HMHP
```

```
C     IS A NEAR prolate TOP KAPPA=-0.826
C     ************************************************************
      DO 700 KK=0,KMAX
      RC=0.0
      KP=KK
      RK=DFLOAT(KP)
      RJ=DFLOAT(JP)
      CDP=DJP*((RJ*(RJ+1.))**2)+DJKP*(RJ*(RJ+1.))*(RK**2)+DKP*(RK**2)
      EROTP=(BBARP*RJ*(RJ+1.))+(CP-BBARP)*(RK**2)+CDP
      EPAR=EVIBP+EROTP
C     ************************************************************
C     WE ONLY CONSIDER HMHP STATES WHOSE BOLTZMAN FACTOR
C     IS GREATER THAN 0.0002. THUS, STATES HAVING ENERGY GREATER
C     THAN 1823 CM-1 ARE NOT CONSIDERED.
C     ************************************************************
      PROB=DEXP(-1.0*EPAR/XKT)*100.0
      IF (PROB .LT. .01) GO TO 700
      RBOLTZ=((2.0*RJ)+1.)*DEXP(-1.*EROTP/XKT)*(1./QROT)
C     *****************************************
C     ALL K-STATES ARE DOUBLY DEGENERATE EXCEPT K=0
C     *****************************************
      IF(RK .GT. 0.0) DEGENK=2.0
      IF(RK .EQ. 0.0) DEGENK=1.0
      RBOL0TZ=RBOLTZ*DEGENK
      BOLTZ=VBOLTZ*RBOLTZ
      ETPAR=EVIBP+EROTP+EPHOTN
      EXCESS=ETPAR-DZERO
C     ************************************************************
C     CHECK THAT THE PARENT STATE BEING CONSIDERED IN CONJUNCTION
C     WITH THE PHOTON ENERGY IS ENERGETIC ENOUGH TO PRODUCE AT LEAST
C     THE LOWEST OH ROTATIONAL STATE .
C     ************************************************************

      IF (EXCESS .LT. FOH(1)) GO TO 700

C     ************************************************************
C     CONSIDER FIRST THE VARIOUS ROTATIONAL STATES OF OH FRAGMENT
C     ************************************************************

      DO 650 NOH=1,NOHMAX
      N1=NOH
      S=0.0
C     ***********************************
C     FOR THE PI-3/2 STATE OF OH : J=N+1/2
C     FOR THE PI-1/2 STATE OF OH : J=N-1/2
C     ***********************************

      RJ1=DFLOAT(N1)+.5
      IF (NOH .GT. 10) RJ1=(DFLOAT(N1)-10.0)-.5
      EROT1=FOH(N1)
      EOH=EVIB1+EROT1
      IF (EXCESS .LT. EOH) GO TO 650
C     ************************************************************
C     COUNT THE NUMBER OF WAYS THE EXCESS ENERGY CAN BE DISTRIBUTED
```

```
C     AMONG THE VARIOUS VIBRATIONAL AND ROTATIONAL STATES OF THE
C     HOCH2O FRAGMENTS. FIRST CONSIDER VIBRATIONAL STATES.
C     ************************************************************
      EAVHOCH2O=EXCESS-EOH
      DO 600 NV2=1,9
      EVIB2=FHOCH2O(NV2)
      EMAXR2=EAVHOCH2O-EVIB2
      IF (EMAXR2 .LT. 0.0 ) GO TO 600
      NHOCH2OMX=IDINT((-.5+DSQRT(.25+(EMAXR2/BBAR2))))

C     ************************************************************
C     WITHIN THE VIBRATIONAL LEVEL OF HOCH2O BEING CONSIDERED, WHAT ARE
C     THE POSSIBLE ROTATIONAL STATES THAT CAN BE POPULATED WHILE
C     CONSERVING ENERGY. NHOCH2OMX IS THE MAXIMUM VALUE OF ROTATIONAL
C     ANGULAR MOMENTUM THAT THE HOCH2O FRAGMENT CAN HAVE.
C     ************************************************************
      DO 500 NHOCH2O=0,NHOCH2OMX
      N2=NHOCH2O
      K2MAX=N2
C     ************************************************************
C     THE HOCH2O FRAGMENT IS BEING CONSIDERED AS A NEAR PROLATE TOP.
C     ALSO NOTE THAT FOR HOCH2O HALF THE ROTATIONAL STATES WILL BE
C     MISSING. THIS IS APPROXIMATELY ACCOUNTED FOR IN THIS PROGRAM BY
C     COUNTING ONLY THE + K-STATES.
C     ************************************************************
      DO 400 KK2=0,K2MAX
      K2=KK2
      RN2=DFLOAT(N2)
      RK2=DFLOAT(K2)
      EROT2=(BBAR2*RN2*(RN2+1.0))+(A2-BBAR2)*(RK2**2)
      IF ( EROT2 .GT. EMAXR2 ) GO TO 400
      DO 350 IJK=1,2
      RJ2=RN2-0.5
      IF (IJK .EQ. 2) RJ=RN2+0.5
      IF (RJ2 .LT. 0.0) GO TO 350
C     ************************************************************
C     FOR A GIVEN J1(OH) AND J2(HOCH2O), THE RESULTANT ANGULAR MOMENTUM
C     CAN TAKE ON ANY VALUES BETWEEN (J1+J2) AND |J1-J2| IN STEPS OF
C     ONE.
C     ************************************************************
      RHIGH= RJ1+RJ2
      JRHIGH=IDINT(RHIGH)
      RLOW=DABS(RJ1-RJ2)
      JRLOW=IDINT(RLOW)
      DO 300 JR=JRLOW,JRHIGH
      JRES=JR
      LUPP=JP+JRES
      LLOW=IABS(JP-JRES)
      ETRANS=ETPAR-DZERO-(EROT1+EVIB1+EROT2+EVIB2)
C     ********************************
C     CONVERT ETRANS FROM CM-1 TO ERGS
C     ********************************
      ETRANS=ETRANS*(1./5.03D15)
      ALPHA=RMASS*6*(C6**0.3333)*((ETRANS/2.0)**.6666)*(1./HBAR**2)
```

```
C      ************************************
C      CALCULATE MAXIMUM ALLOWED VALUE FOR L.
C      ************************************
       LMAX=IDINT((-.5+DSQRT(.25+ALPHA)))
       IF (LUPP .GT. LMAX ) LUPP=LMAX
       DO 200 L=LLOW,LUPP
       S=S+1.
 200   CONTINUE
 300   CONTINUE
 350   CONTINUE
 400   CONTINUE
 500   CONTINUE
 600   CONTINUE
C      BOLTZ=1.0
       PM(N1)=S
       RC=RC+S
 650   CONTINUE
       IF (RC .EQ. 0.0) GO TO 700
       DO 675 MXX=1,NOHMAX
       PM(MXX)=(PM(MXX)/RC)*BOLTZ
       PN(MXX)=PN(MXX)+PM(MXX)
 675   CONTINUE
 700   CONTINUE
 800   CONTINUE
 900   CONTINUE

C      ************************************************
C      NORMALIZE RESULTS OF THE COUNTING PROCESS TO 100%
C      ************************************************
       SNORM=0.0
       DO 2000 M=1,NOHMAX
       SNORM=SNORM+PN(M)
2000   CONTINUE
       DO 3000 MM=1,NOHMAX
       XPN(MM)=(PN(MM)/SNORM)*100.0
       WRITE(3,*)MM,PN(MM),XPN(MM)
3000   CONTINUE
       CLOSE (UNIT=3)
       END
```

Sample Output 4NUOOH.OUT:

```
 1   1.241369511260666E-001       34.134191688149900
 2   8.524587679483778E-002       23.440233328949510
 3   4.661763157474098E-002       12.818545628720710
 4   2.026532024165795E-002        5.572396610965609
 5   6.286750069890478E-003        1.728680542211823
 6   1.416698296412605E-003   3.895524320144912E-001
 7   2.051406343432579E-004   5.640794036088637E-002
 8   1.771656145548616E-005   4.871559187580754E-003
 9   3.542357688272780E-007   9.740493484224497E-005
10   0.000000000000000E+000   0.000000000000000E+000
11   2.034613631490659E-002        5.594618772141061
12   2.596958951071409E-002        7.140911214430032
```

13	1.927233662592542E-002	5.299353872480877
14	9.635089013707764E-003	2.649380159113862
15	3.329921044706134E-003	9.156352094629145E-001
16	7.974343731573013E-004	2.192721627618201E-001
17	1.198656820687629E-004	3.295971208774789E-002
18	1.036949852116056E-005	2.851322245475685E-003
19	1.470686970802229E-007	4.043978083821854E-005
20	0.000000000000000E+000	0.000000000000000E+000

E.5 References

1. I. N. Levine, *Physical Chemistry, 4th ed*. (McGraw-Hill, New York, 1995).

2. D. A. McQuarrie, *Statistical Mechanics* (HarperCollins, New York, 1976).

Appendix F

Schrödinger Equation Solver FGH1D, HITRAN and Rotational Structure Analysis with PGOPHER

F.1 Schrödinger Equation Solver FGH1D

FGH1D is a program written by Dr. Russell D. Johnson III for generating one-dimensional solution of the Schrödinger equation.[1] The program uses Fourier Grid Hamiltonian method (FGH) developed by Balint-Kurti and coworkers to compute the bound state eigenvalues and eigenfunctions of the Schrödinger equation.[2-6] This section provides a tutorial for using the FGH1D program in order to obtain the solution to the Schrödinger equation from the HOON-torsion potential of HOONO (see Fig. F.1). Details on generating the torsion potential are given in Chapter 4 and Appendix *B*.

Start the FGH program. In Fig. F.2, the top left panel titled "Data" enables the user to choose from the various potentials. In this example we are using the HOONO torsion potential and therefore, we choose the input file to be used from either the "Read File" or "Read Clipboard". In order to use the "Read File" option, a grid of points must initially be generated using distances in Angstrom, angles in Radians and energy in cm^{-1} units:

```
39
-3.141592654  1211.982636
-2.967059728  1203.598706
.
.
.
2.792526803   1176.932542
2.967059728   1203.598706
3.141592654   1211.982636
```

In this example, τ, the torsional angle, is given in radians units and the energy is given in cm^{-1} units. The first line of each file must indicate the number of grid point provided in the file. In this case it is 37 points ($-180^o \leq \tau \leq +180^o$ in $\pm 10^o$ increments). Selecting the "Read File" option will open a dialog box requesting the location and the file name to import (see Fig. F.3). An easier method to importing files can be achieved by using the "Read ClipBoard" option. To use this option, simply copy to memory the two columns needed by using the "Copy" command in Excel or Notepad and select the "Read ClipBoard" option in the FGH program. This will automatically load the data points, update the "Range", and "Data Parameters" panels with the current information as shown in Fig. F.4. Note that using the "Read ClipBoard" option circumvents creating individual data files for each potential and there is no need to let the program know how many data points are to be loaded. The data points used in this example are given in Table F.1.

After importing the data points using whichever method one prefers, two parameters are needed to be adjusted. The first is the "Data Points" in the "Range" panel (see Fig. F.5). This is the number of basis functions used and the dimension of the matrix which is diagonalized to obtain the eigenvalues; the number of points must be an even number.[1] The larger the value, the finer the evaluations would be and the slower the calculation will take. In this example we choose 200 basis functions although for the data presented in Chapter 4, we have chosen 640 data points for the torsion potential and 200 for the OH-stretching potential. The second parameter that one needs to adjust is the "Mass" in units of amu or rather the moment of inertia in units of $Å^2$ if angles are used instead of distances (see Fig. F.6). For this torsion potential we pick $\mu = 1.1266$ $Å^2$. The final appearance of the program before running the code is give in Fig. F.7.

After setting all the required parameters, the program is ready to start calculating the eigenvalues and eigenfunctions by selecting the "Start" option. Depending on the number of points, this process can take several minutes. When completed, the viewing window showing the potential, its eigenvalues as well as the eigenfunctions will open (see Fig. F.8). In the main program, several additional parameters will show. The "Expectation Values" panel will contain the average, $<\tau>$, and root mean square (RMS), $<\tau^2>^{1/2}$ values associated with the eigenfunctions, $V_\tau = 0, 1, 2, \ldots$ Also shown in the main panel, the "Eigenvalues" panel (see Fig. F.9) are the eigenvalues associated with $V_\tau = 0, 1, 2, \ldots$ These values can be copied to clipboard using the "Copy to Clipboard" and pasted in notepad. It is also possible to generate a fit to these eigenvalues using polynomial parameters using the "Fitting" panel (see Fig. F.10) by simply selecting the maximum number of eigenvalues and by choosing the number of fitting parameters according to:

$$E(v) = T_e + \omega(v + {}^1/_2) - x(v + {}^1/_2)^2 + y(v + {}^1/_2)^3 + z(v + {}^1/_2)^4 \qquad (F.1)$$

In Eq. F.1, E(v) is the eigenvalue associated with the vibrational level –v, T_e is the electronic energy, ω and x are the harmonic and anharmonic frequencies respectively, and y and z are second and third correction terms. In this example, fitting the first 7^{th} eigenvalues results in the expression $E(v) = -26.271 + 383.2(v + {}^1/_2) + 66.31(v + {}^1/_2)^2 + 4.434(v + {}^1/_2)^3$. The "Eigenvalues" panel in Fig. F.11, also shows the newly calculated E(v) levels using Eq. F.1 as well as their differences from the "exact" values (Calc E(v) – E(v)).

The eigenvectors associated with the eigenvalues that are shown in the main "Eigenvalues" panel can also be obtained. This is done by selecting "Eigenvectors to

Clipboard" as shown in Fig. F.12. Be patient, this process can take a while. The clipboard, once the process is complete can be dumped to notepad application using the "paste" command. The first row in the output file is the angle τ. In essence, this is the x-axis. Each subsequent row simply corresponds to the probability amplitude, or simply, the y-axis associated with each eigenfunction $V_\tau = 0, 1, 2 \ldots$ These values can be pasted to an excel sheet and be plotted as shown in Fig. F.13. Please note that these eigenfunctions are not normalized and therefore must be normalized prior to usage.

F.2 The HITRAN Database Application

The High Resolution Transmission (HITRAN) molecular spectroscopic database application is developed and maintained by Dr. L. S. Rothman.[7] The program is designed to generate IR (overtone) and U.V (electronic) absorption spectra for atmospherically important molecules such as H_2O, NO_2, HOCl etc. The program is capable of generating these absorption spectra for a particular region of the spectrum as a function of temperature, specific vibrational transitions, and for the various isotopologues. It is of a particular use when the spectra collected in the lab required frequency calibration against absolute lines-position as discussed, for example, in Chapter 9. The program and updates are currently available free online at: http://cfa-www.harvard.edu/hitran/. This section presents basics usage of the HITRAN database as pertained to the chapters in this dissertation.

To start the program, run the JavaHawks program. Figure F.14 show the program main screen. From the menu screen click on the "SELECT" tab which will load the molecular section (see Fig. F.15). Selecting the "HITRAN filename" shown in Fig. F.16 will open a new menu enabling the user to select the correct input filename containing the

molecular parameters of interest. Table F.2 contains the list of files corresponding to available molecules in the "C:\Program Files\JavaHAWKS\DATA\" folder. By clicking "Select local file" option and subsequently "NO" (see Fig. F.17) the program allow the user to select input file. Note that the file name "HITRAN04.PAR" (see Fig. F.18) contains a complete line-list for all the molecules in the database in Table F.2 except those that have been recently updated / corrected indicated with a ¥ symbol. The "Output File Name" shown in Fig. F.19 should be left with the name "C:\Documents and Settings\overtone\My Documents\Specsim\in.out" and the output shown in Fig. F.20 should be left as "Hitran Output".

In the "Selection Parameters" in Fig. F.21, select the "Spectral Range" option. In this example we will generate water absorption spectrum in the $2\nu_{OH}$ region (7000 – 7500 cm^{-1}). Insert the range and click ok. Next, select the "Temperature" key and insert 298 K as shown in Fig. F.22. Lastly, select the "Molecule" key and choose "H_2O" (see Fig. F.23). Note that one may select more than one molecule. Now we are ready to generate the spectrum by selecting the "Run Select" option (see Fig. F.24) and "OK" in Fig. F.25. When the program finish selecting the lines push the "CANCEL" key in the HWAKS select menu and then push the "EXIT" on the "Line Selection" screen. To confirm that the correct spectral region was chosen one may generate quick spectra using the "Plot" and "Plot Line By Line" options shown in Fig. F.26. In figure F.27 simply select "Intensity" option to obtain the spectra shown in Fig. F.28.

The raw file "C:\Documents and Settings\overtone\My Documents\Specsim\in.out" generated in the simulation and plotted in Fig. F.28 can also be converted to an Excel sheet columns data file displaying frequency vs. absorption

cross-section using the "SPECSIM" program located in the "C:\Documents and Settings\overtone\My Documents\Specsim\" folder. To start the program, double-click on the specsim.exe file (see Fig. F.29). The program will immediately read the "in.out" file generated by the HITRAN program and display the total numbers of lines read, initial and final wavelength, as well as their corresponding absorption cross-sections. The program prompts the user to enter the line-shape. Select "1" for Gaussian and "2" for "Lorentzian" lineshape (See Fig. F.29). Next, enter the laser linewidth, where, our MOPO has a linewidth of ~0.4 cm^{-1} (FWHM) and the ND60 dye lasers have ~0.08 cm^{-1} (FWHM). Lastly, (see Fig. F.30) the program asks to enter the number of data points per linewidth (FWHM). Typically, for scans with the MOPO over water lines, we find that 16 points/0.4 cm^{-1} (= 40 points/cm^{-1}) are sufficient for accurate calibration. For short-range high resolution scans (~15 cm^{-1} range) preformed with the Inrad unit discussed in Chapter 9, 40 points/0.08 cm^{-1} (50 points/cm^{-1}) work well. After selecting executing, the program will generate the output file "C:\Documents and Settings\overtone\My Documents\Specsim\OUT.OUT" and immediately exit. The file can be imported normally using Excel. Figure F.31 shows the final $H_2O(2\nu_{OH})$ spectrum generated using HITRAN and Specsim.

F.3 Rotational Band Contour Simulation Program PGOPHER

The program PGOPHER is a program for simulating rotational structure developed by C. M. Western.[8] The code is used throughout the dissertation chapters to generate rotational band contours of multiple vibrational bands. This section contains step by step instructions for generating rotational simulation using the CD_3OOH $2\nu_1 + \nu_{15}$ combination band as an example.

Start the PGOPHER program as shown in Fig. F.32. Typically, using the simulation would be easier by first overlaying an experimental spectrum. To do so, copy from an Excel spreadsheet (CD3OOH.xls) two consecutive columns to memory and paste by using the "paste overlay" command in the "Edit" menu in PGOPHER (see Fig. F.33). Change the plot range to zoom in on spectral region of interest by dragging the mouse and drawing a rectangle over the region of interest as shown in Fig. F.34. Next, save the overlay by selecting the "Properties" option in the "Overlay" menu and subsequently, in the new screen select the "save all overlays" option (see Fig. F.35). Now that the overlay is saved, it can be loaded directly from the "Load Overlay" option in the "File" menu.

Next, we are interested in generating the rotational band contour for the experimental spectrum. To do so, bring the "Constants" option by selecting it from the "View" menu or by clicking CTRL + T as shown in Fig. F.36. Access the "Add New … Species" shown in Fig. F.37 with the right mouse click, and subsequently, right click on "New Species" and select "Add New" and "Asymmetric Molecule" as highlighted in Fig. F.38. Next, add an "Asymmetric Manifold" as shown in Fig. F.39. An important parameter to change in the Asymmetric Manifold is the "Initial" parameter below from "FALSE" to "TRUE". Finally, add "New Asymmetric Top" as shown in Fig. F.40. At this stage, input all the known molecular parameters that are associated with the initial state shown in Fig. F.41. Note that in the figure, we also changed the labels of "New Species" to "CH_3OOH", "New Asymmetric Molecule" to "Combination Band Transition", "New Asymmetric Manifold" to "Ground State", and "New Asymmetric Top" to "Ground State Parameters". Right click again on the "Combination Band Transition" and add another "Asymmetric Manifold". Next, change its name to "Upper

State". To the newly labeled "Upper State" add "New Asymmetric Top" and change its name to "Upper State Parameters" as shown in Fig. F.42. Next, adjust the upper states parameters as shown in Fig. F.43.

In order to simulate the spectrum, the initial and final parameters must be connected via the transition dipole moment. These transitions are generated by right clicking on the "Combination Band Transition" and select the "Add Transition Moment" option as shown in Fig F.44. The upper state is the "Bra" and the ground state is the "Ket". Now right click on the transition moment "<upper state |mu| ground state>" and add three new "Cartesian Transition Moments" a-, b- and c- component by changing their "Axis" parameters as shown in Fig. F.45. Note that the relative intensity is proportional to the square of the transition strength. Therefore only relative transition moments are important and not their absolute values. Since the $|2\ 0^+> \rightarrow |2\ 1^+>$ transition is a 1:0.52 a:b- type, change the strength of "<upper state |b| ground state>" and "<upper state |c| ground state>" to 0.52 and 0 respectively.

Close the constants screen and save file using the "Save" option in the "File" menu. Change the Temperature to 4.3 K. The "Gau:" parameter controls the laser line width. In this scan, the spectrum was obtained with a laser which has 0.08 cm^{-1} bandwidth (FWHM). The transition width corresponds to "Lor:". Change its value from 0 to 0.21 cm^{-1}. Fig. F.46 shows the final screen before running the simulation. The mouse cursor indicates the "Simulate Spectrum" option. When ready, click on it to run the simulation. Figure F.47 shows the simulated spectrum of the CD_3OOH $|2\ 1^+>$ State. To toggle between plots style, click on the "Cycle Through Plots Style" option as indicated

by the mouse cursor in Fig. F.47. Figure F.48 shows the simulated spectrum overlaid on top of the experimental spectrum.

Table F.1: CCSD(T)/cc-pVTZ HOONO Torsion Potential Used with FGH1D Program to Obtain Eigenvalues and Eigenfunctions

τ (degrees)	τ (radians)	E (cm^{-1})	τ (degrees)	τ (radians)	E (cm^{-1})
-180	**-3.14159**	**1211.983**	**10**	**0.174533**	**50.83032**
-170	**-2.96706**	**1203.599**	**20**	**0.349066**	**183.3271**
-160	**-2.79253**	**1176.933**	**30**	**0.523599**	**348.4598**
-150	**-2.61799**	**1127.924**	**40**	**0.698132**	**495.3761**
-140	**-2.44346**	**1054.554**	**50**	**0.872665**	**593.3496**
-130	**-2.26893**	**960.6623**	**60**	**1.047198**	**639.0442**
-120	**-2.0944**	**858.0579**	**70**	**1.22173**	**648.7669**
-110	**-1.91986**	**764.035**	**80**	**1.396263**	**646.9672**
-100	**-1.74533**	**694.5274**	**90**	**1.570796**	**657.0411**
-90	**-1.5708**	**657.0411**	**100**	**1.745329**	**694.5274**
-80	**-1.39626**	**646.9672**	**110**	**1.919862**	**764.035**
-70	**-1.22173**	**648.7669**	**120**	**2.094395**	**858.0579**
-60	**-1.0472**	**639.0442**	**130**	**2.268928**	**960.6623**
-50	**-0.87266**	**593.3496**	**140**	**2.443461**	**1054.554**
-40	**-0.69813**	**495.3761**	**150**	**2.617994**	**1127.924**
-30	**-0.5236**	**348.4598**	**160**	**2.792527**	**1176.933**
-20	**-0.34907**	**183.3271**	**170**	**2.96706**	**1203.599**
-10	**-0.17453**	**50.83032**	**180**	**3.141593**	**1211.983**
0	**0**	**0**			

Table F.2: Molecules Available in the HITRAN Database [a]

Molecule	File Name[b] (xx_HIT_yr.par)	Number of Transitions
H_2O[¥]	01	63 197
CO_2	02	62 913
O_3	03	311 481
N_2O[¥]	04	47 835
CO	05	4477
CH_4	06	251 440
O_2[¥]	07	6428
NO[¥]	08	102 280
SO_2	09	38 853
NO_2	10	104 223
NH_3	11	29 084
HNO_3[¥]	12	271 166
OH[¥]	13	42 373
HF	14	107
HCl	15	613
HBr	16	1293
HI	17	806
ClO[¥]	18	7230
OCS[¥]	19	19 920
H_2CO	20	2702
HOCl	21	16 276
N_2	22	120
HCN	23	4253
CH_3Cl	24	31 119
H_2O_2[¥]	25	100 781
C_2H_2[¥]	26	3517
C_2H_6[¥]	27	4749
PH_3[¥]	28	11 790
COF_2	29	70 601
SF_6	30	22 901
H_2S	31	20 788
HCOOH[¥]	32	24 808
HO_2	33	38 804
O	34	2
$ClONO_2$	35	32 199
NO^+[¥]	36	1206
HOBr	37	4358
C_2H_4	38	12 978
CH_3OH	39	19 899

[a] Available in the file C:\Program Files\JavaHAWKS\DATA\HITRAN04.PAR

[b] xx- indicates the file number listed in the table and yr- indicate the year of the update (1996 (=96), 2002 (=2k), 2004 (=04), etc.)

[¥] Indicates that the molecule's line-list has been updated since the compilation of the HITRAN04.PAR file. For latest updates go to: http://cfa-www.harvard.edu/hitran/

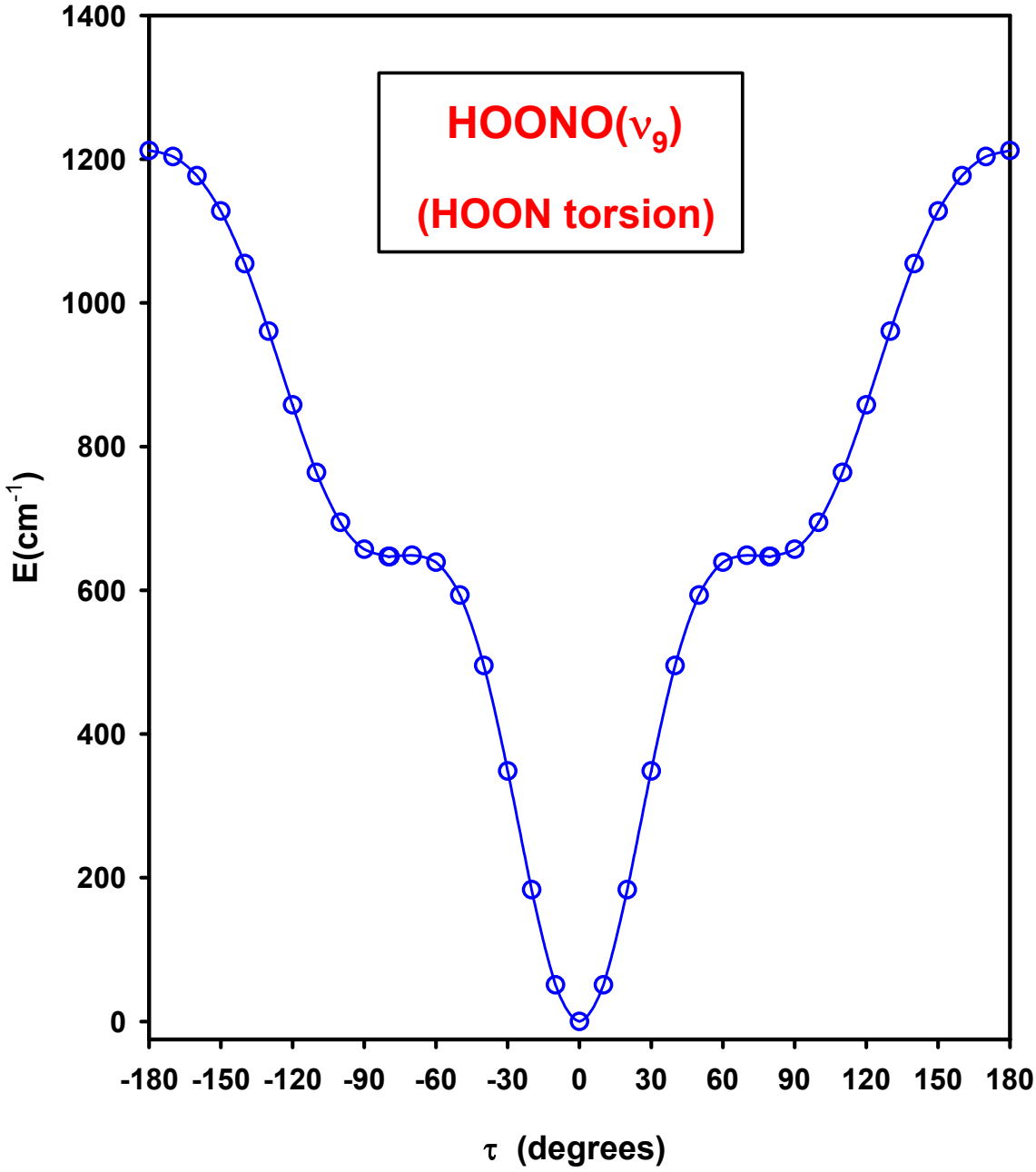

Figure F.1: The HOON-torsion potential of *cis-cis* HOONO generated by changing τ from the equilibrium in the range of ± 180^o in 10^o increments allowing all other degrees of freedom to relax. This potential is generated at the CCSD(T)/cc-pVTZ level of theory. [File: FF.1_torsion]

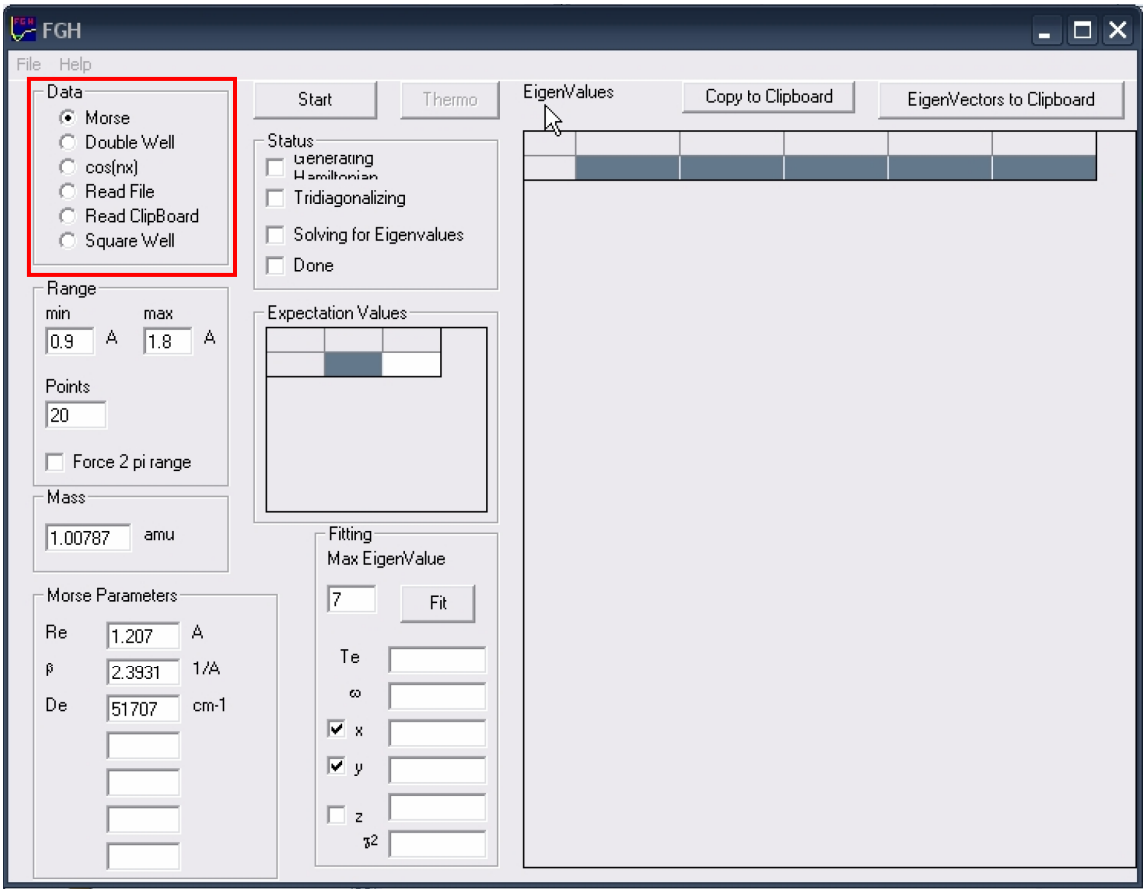

Figure F.2: FGH1D program default settings initially show when the program is loaded. The top left "Data" panel indicates the various potentials the program can use.
[File: FF.2_FGH1]

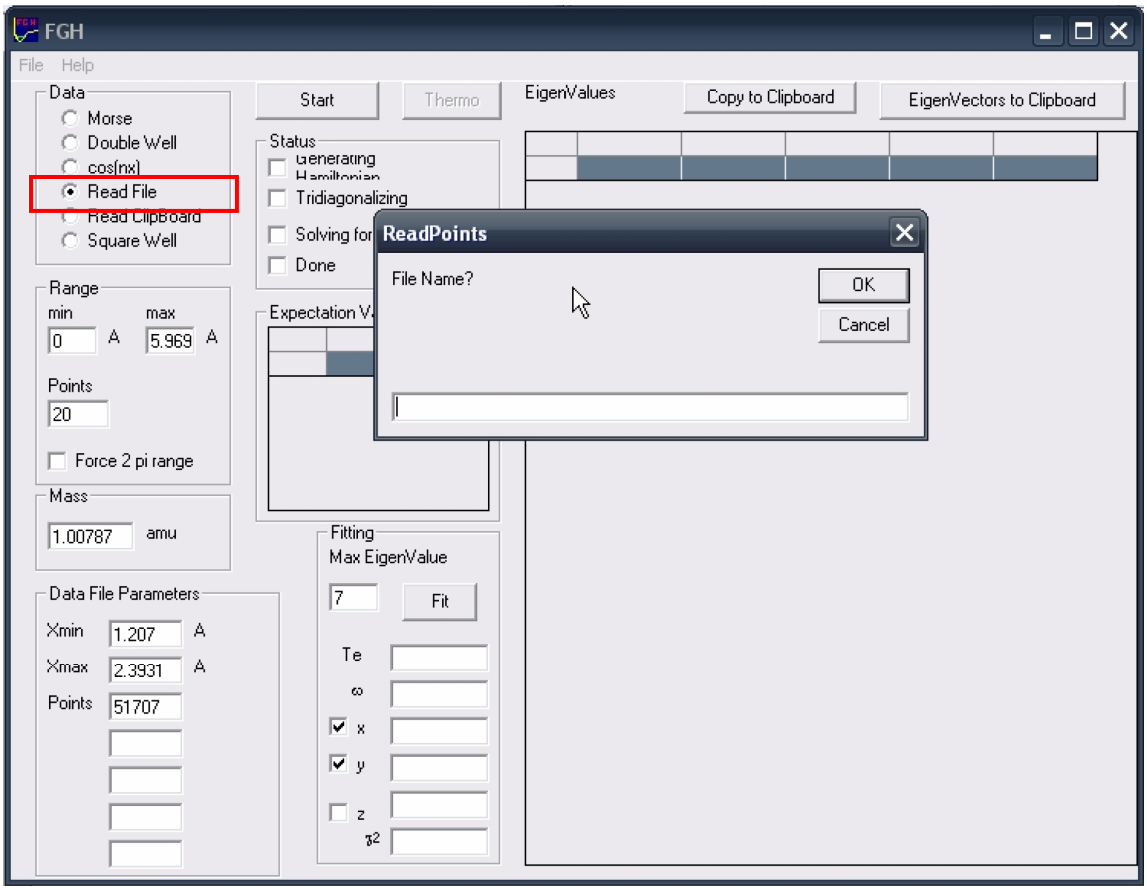

Figure F.3: FGH1D program after selecting the "Read File" in the "Data" panel. The program requests the user to enter the directory and file name to import.
[File: FF.3_FGH2]

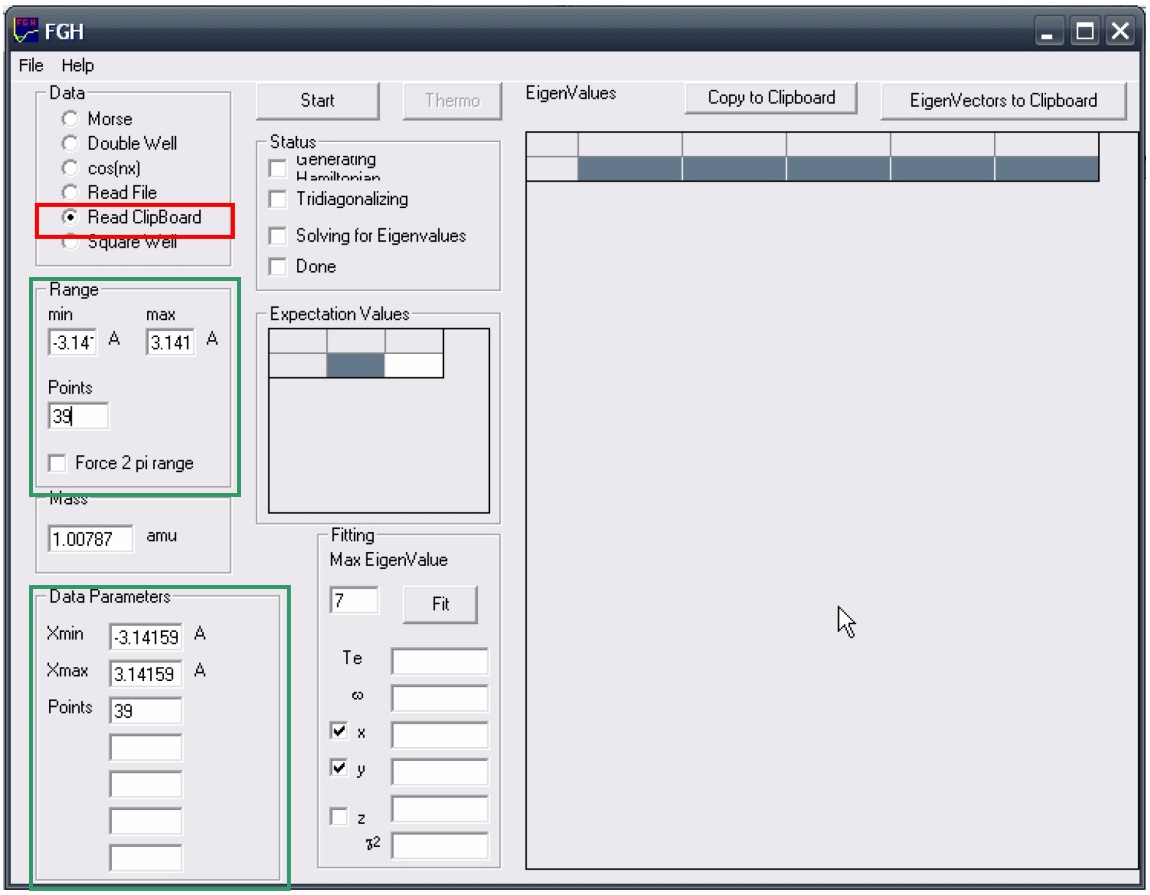

Figure F.4: FGH1D program after selecting the "Read ClipBoard" in the "Data" panel. The program automatically loads the content of the clipboard and adjust the "Range" and "Data Parameters" panels. [File: FF.4_FGH3]

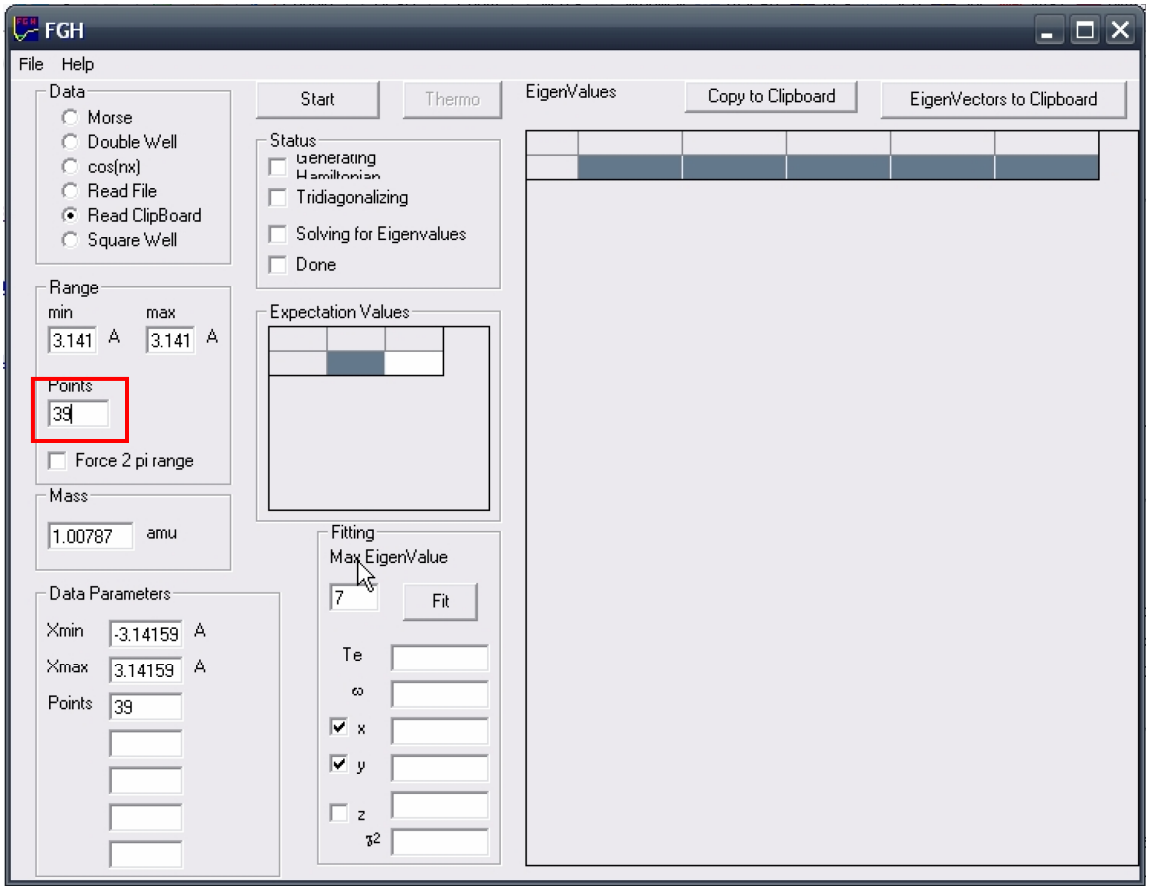

Figure F.5: FGH1D program adjustable "Points" parameter in the "Range" panel. This is the number of basis functions used and the dimension of the matrix which is diagonalized to obtain the eigenvalues; the number of points must be an even number. The larger the value, the finer the evaluations would be and the slower the calculation will take. In this example we choose 200 basis functions. [File: FF.5_FGH4]

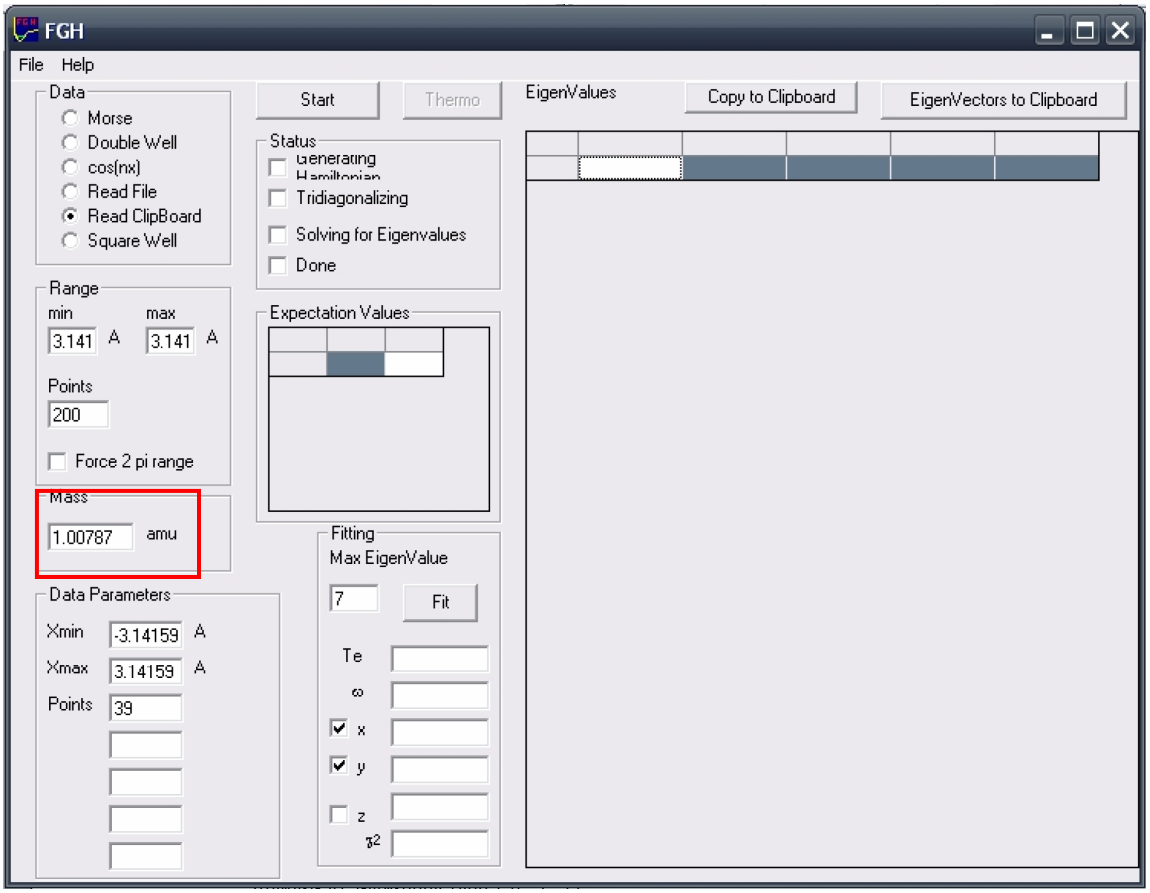

Figure F.6: FGH1D program adjustable "Mass" parameter. This parameter is in units of amu or rather the moment of inertia in units of Å^2 if angles are used instead of distances. For this torsion potential we pick $\mu = 1.1266$ Å^2. [File: FF.6_FGH5]

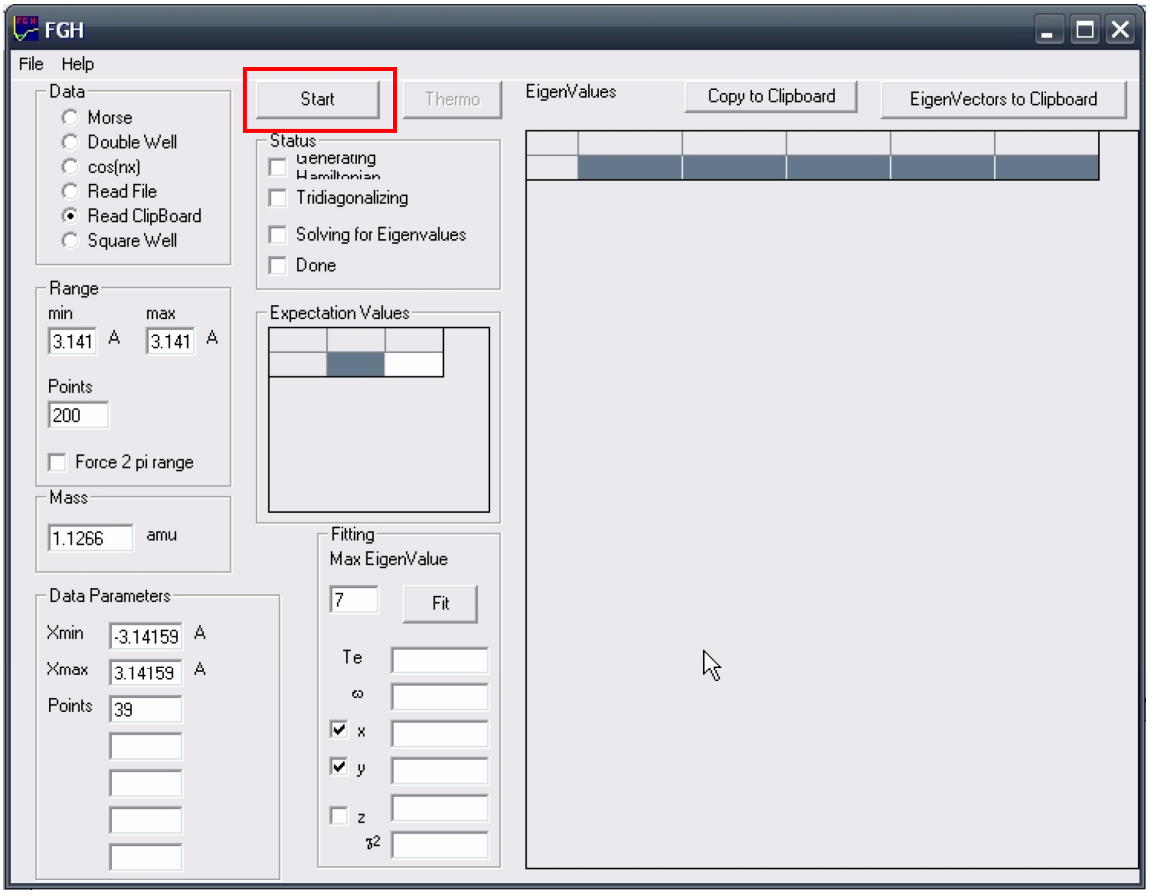

Figure F.7: FGH1D program after all the required parameters are inserted and ready to be executed by selecting the "Start" key. [File: FF.7_FGH6]

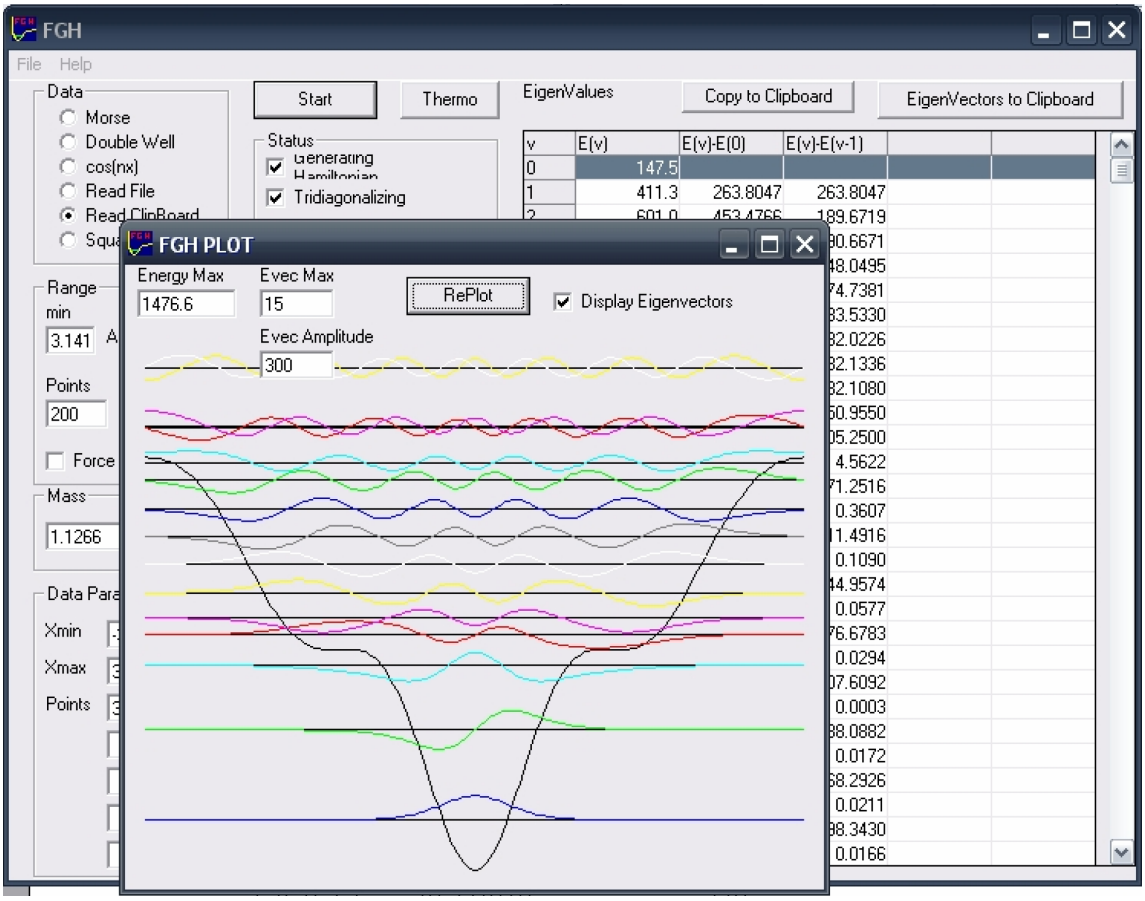

Figure F.8: FGH1D program showing the solutions to the Schrödinger equation. The program display the potential, its eigenvalues and eigenfunctions.
[File: FF.8_FGH7]

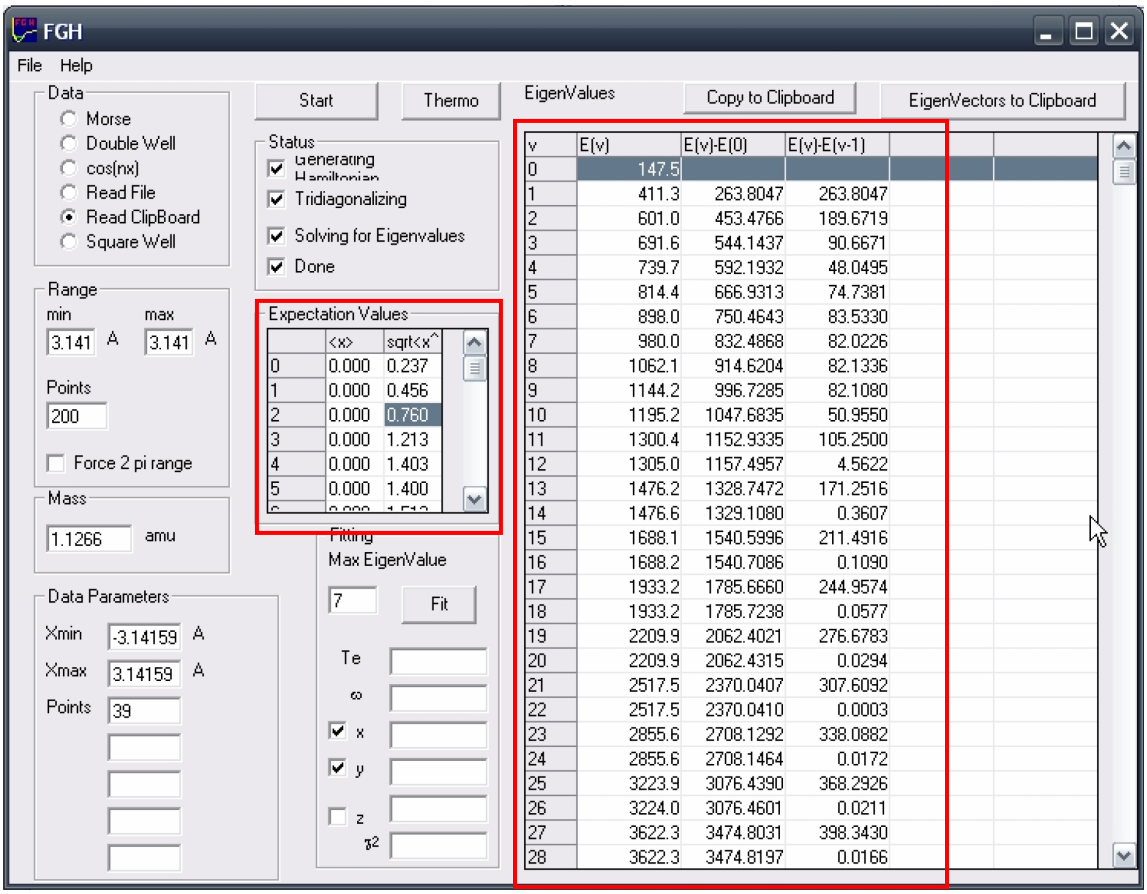

Figure F.9: FGH1D program displaying the expectation $\langle x \rangle$ and $\langle x^2 \rangle^{1/2}$ (RMS) values. The program also shows the eigenvalues in the "Eigenvalues" panel. The first column corresponds to the vibrational eigenstates $V_\tau = 0, 1, 2, \ldots$ The column labeled E(v) lists the energy levels from the bottom of the well and the column E(v) – E(0) subtracts the zero-point energy (ZPE). Also shown are the differences between two consecutive eigenstates in the E(v) – E(v-1) column. [File: FF.9_FGH8]

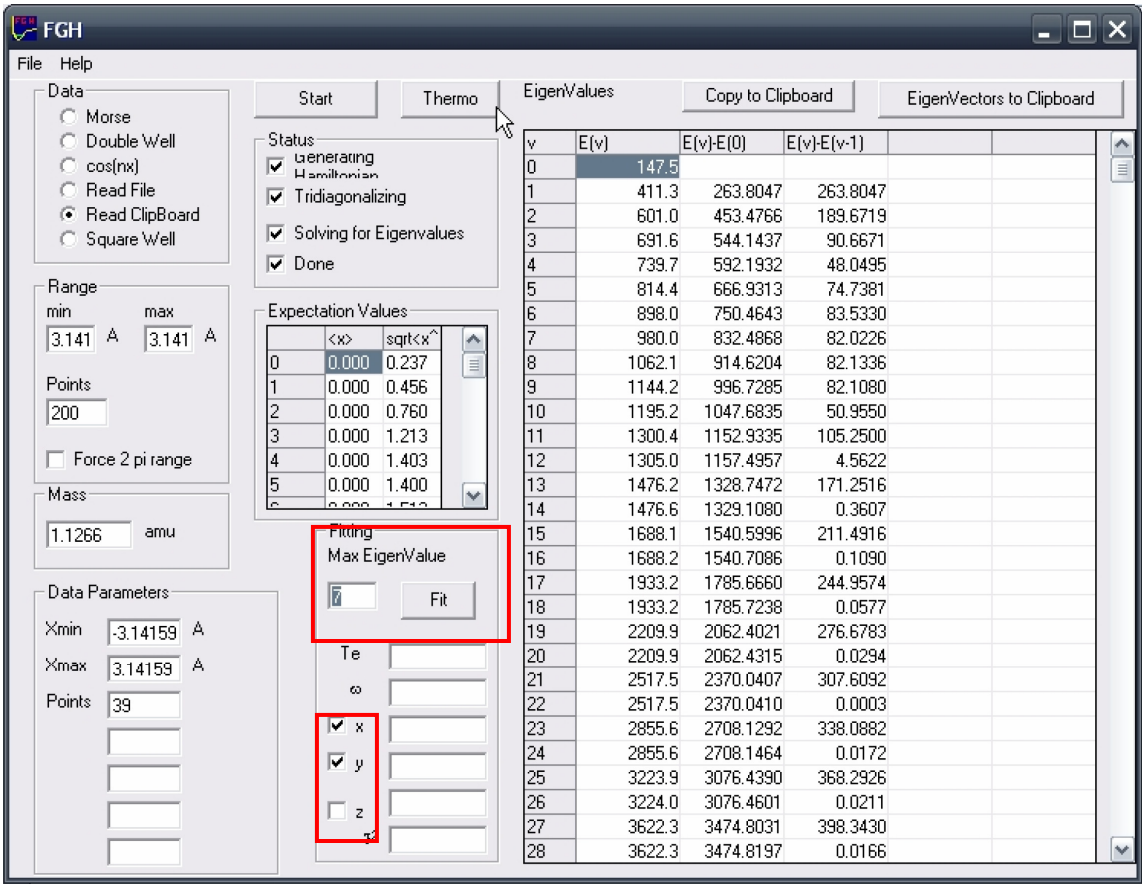

Figure F.10: FGH1D program also allowing the user to obtain fitting parameters for the eigenvalues by choosing the number of eigenvalues to fit and polynomial order according to Eq. F.1. [File: FF.10_FGH9]

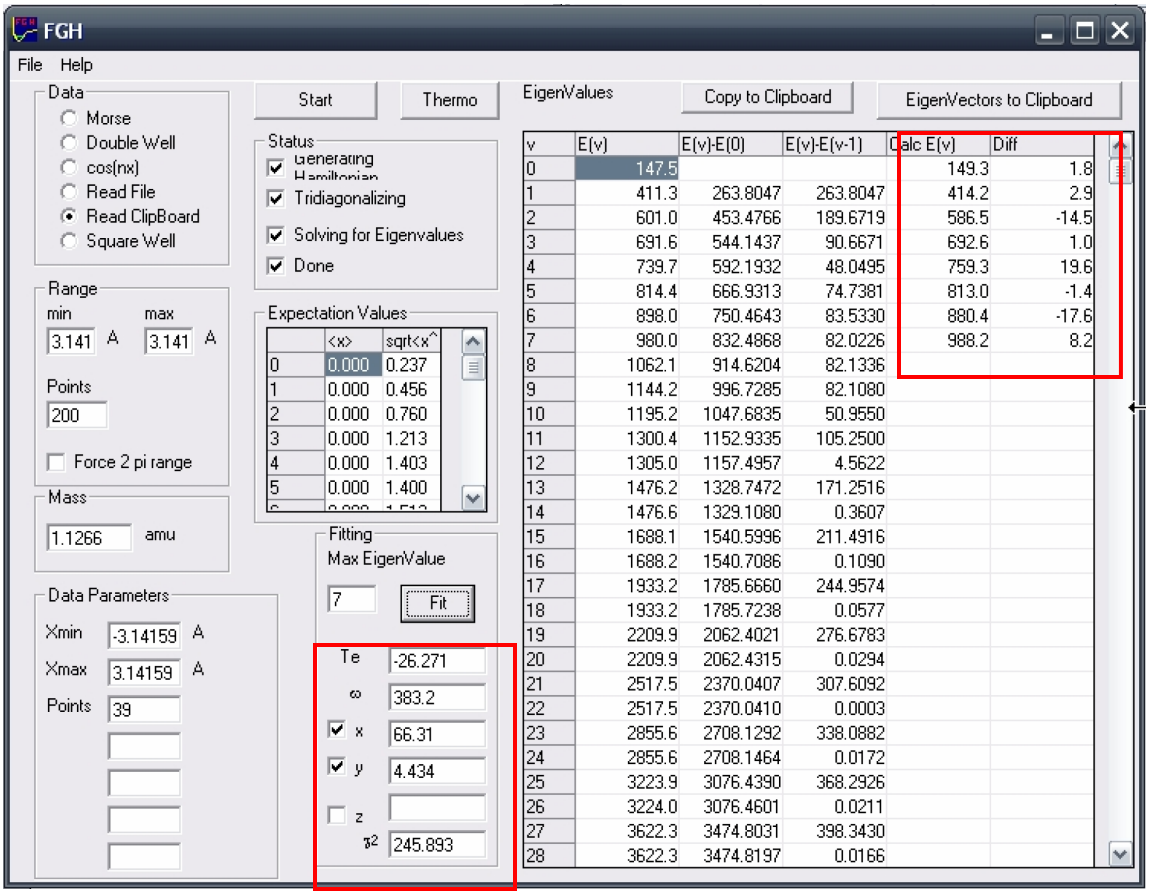

Figure F.11: FGH1D program displaying the fitted eigenvalues parameters and the differences between the "calculated" and "exact" positions. [File: FF.11_FGH10]

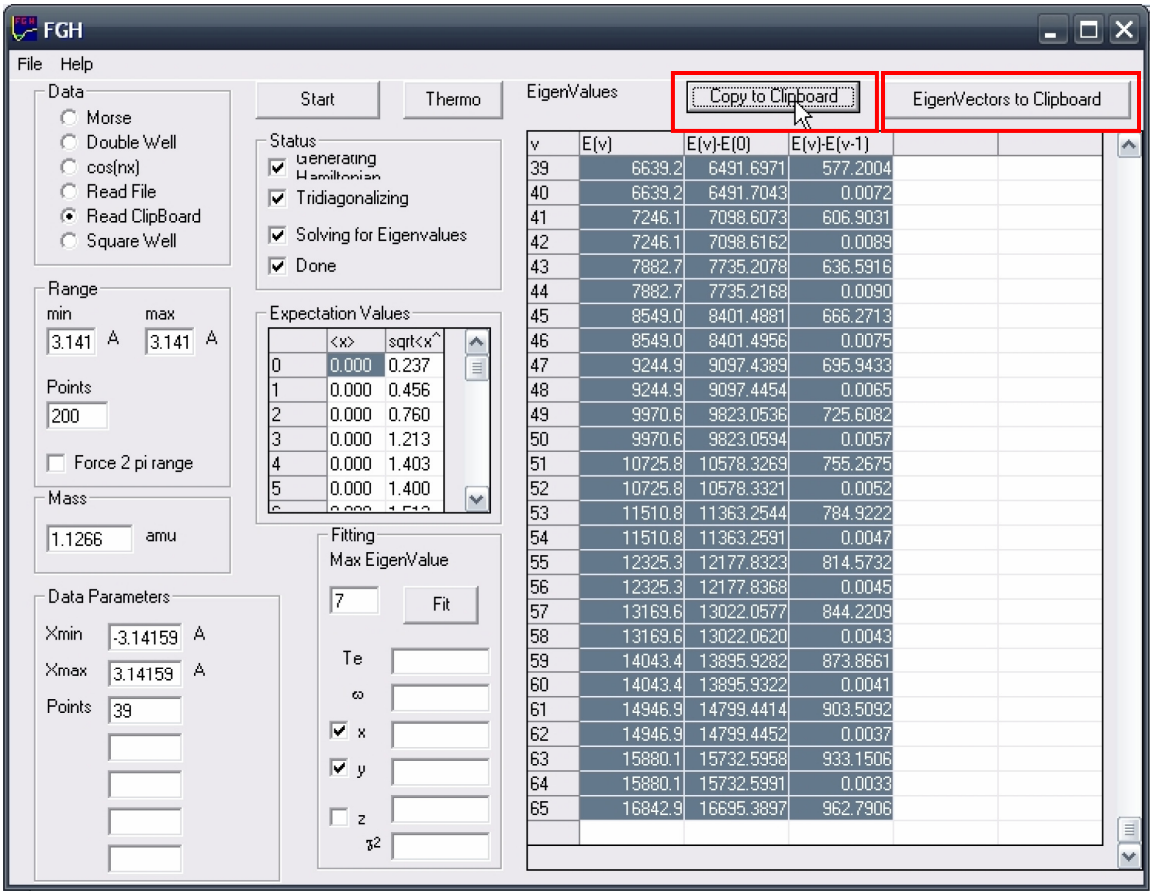

Figure F.12: FGH1D program showing the "Copy to Clipboard" option that can be used to copy and paste with the eigenvalues to a notepad application and the "Eigenvectors to Clipboard" which will generate the numerical values for the eigenfunctions shown in Fig. F.8. [File: FF.12_FGH11]

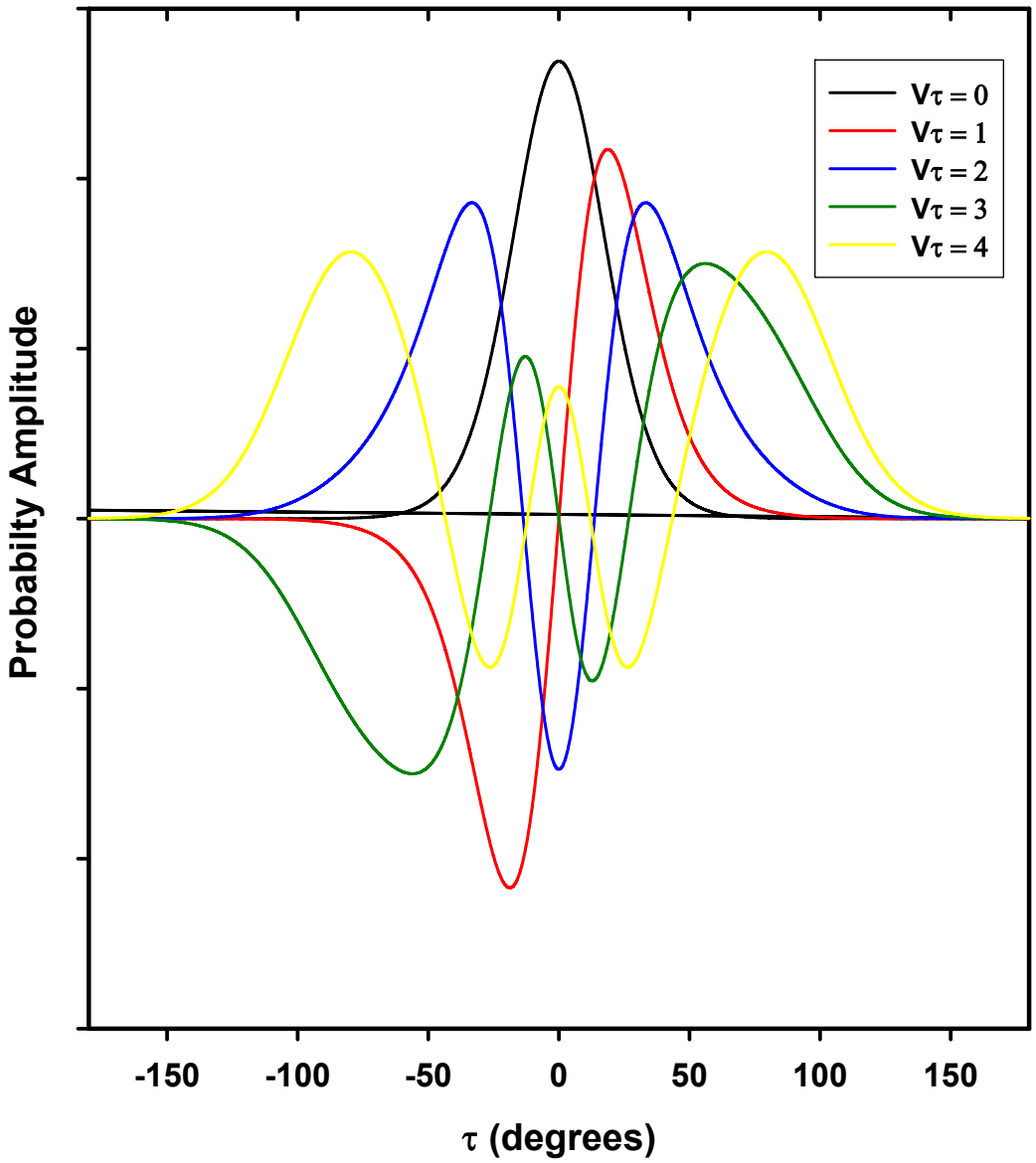

Figure F.13: The first four eigenvectors ($V_\tau = 0 - 4$) associated with the HOON torsion potential of HOONO. The eigenvectors are obtained from the FGH1D solver and are plot as a function of probability amplitude. [File: FF.13_eigenfunctions]

Figure F.14: Computer screen caption of the HITRAN program when initially loaded. [File FF.14_hitran1]

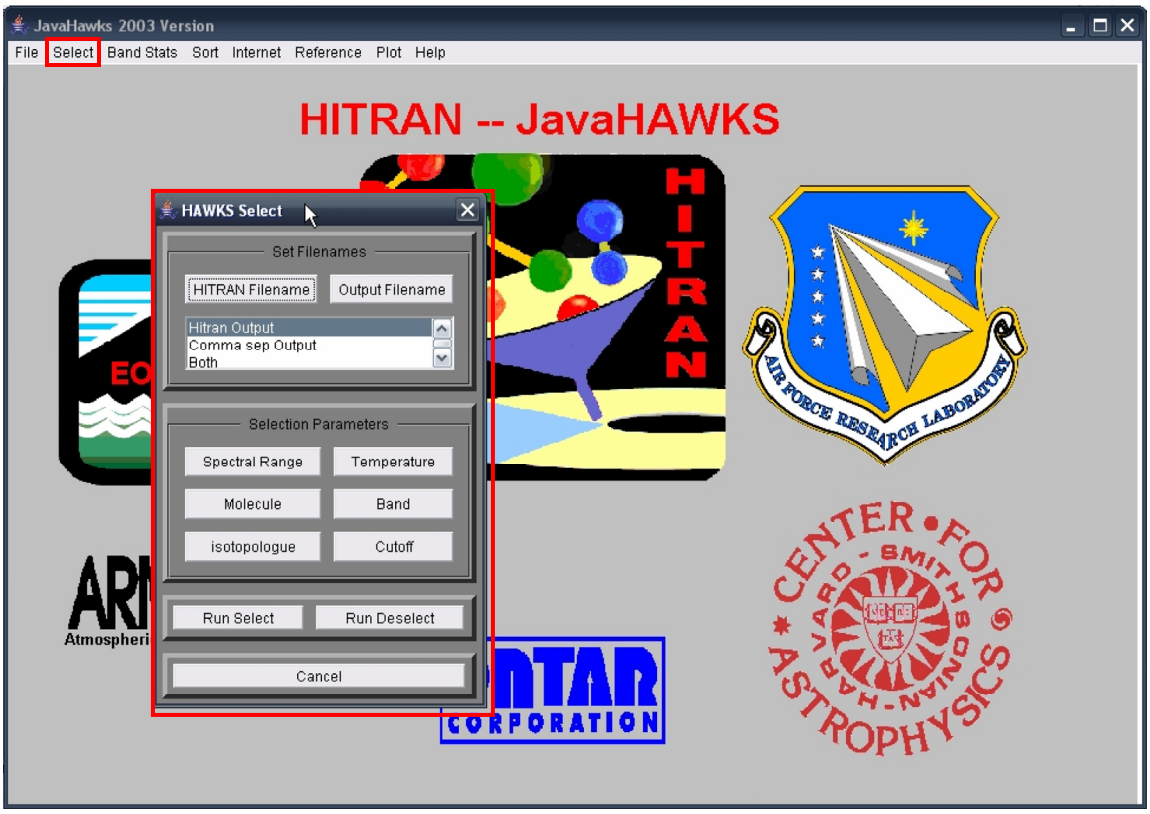

Figure F.15: Computer screen caption of the HITRAN program displaying the various options in the "Select" tab. [File FF.15_hitran2]

Figure F.16: Computer screen caption of the HITRAN program asking the user to select the input file containing the molecular parameters from the "C:\Program Files\JavaHAWKS\DATA\" folder. [File FF.16_hitran3]

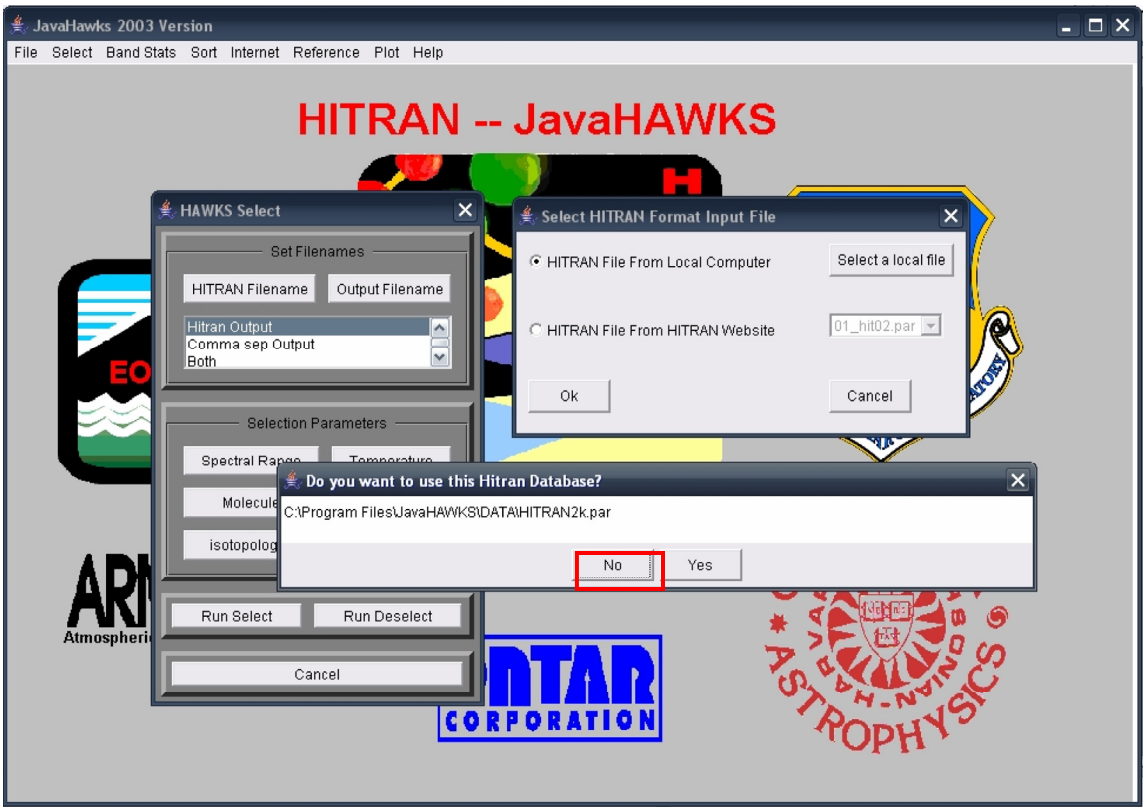

Figure F.17: Computer screen caption of the HITRAN program. Selecting "NO" will enable the user to select the input file containing the molecular parameters from the "C:\Program Files\JavaHAWKS\DATA\" folder. [File FF.17_hitran4]

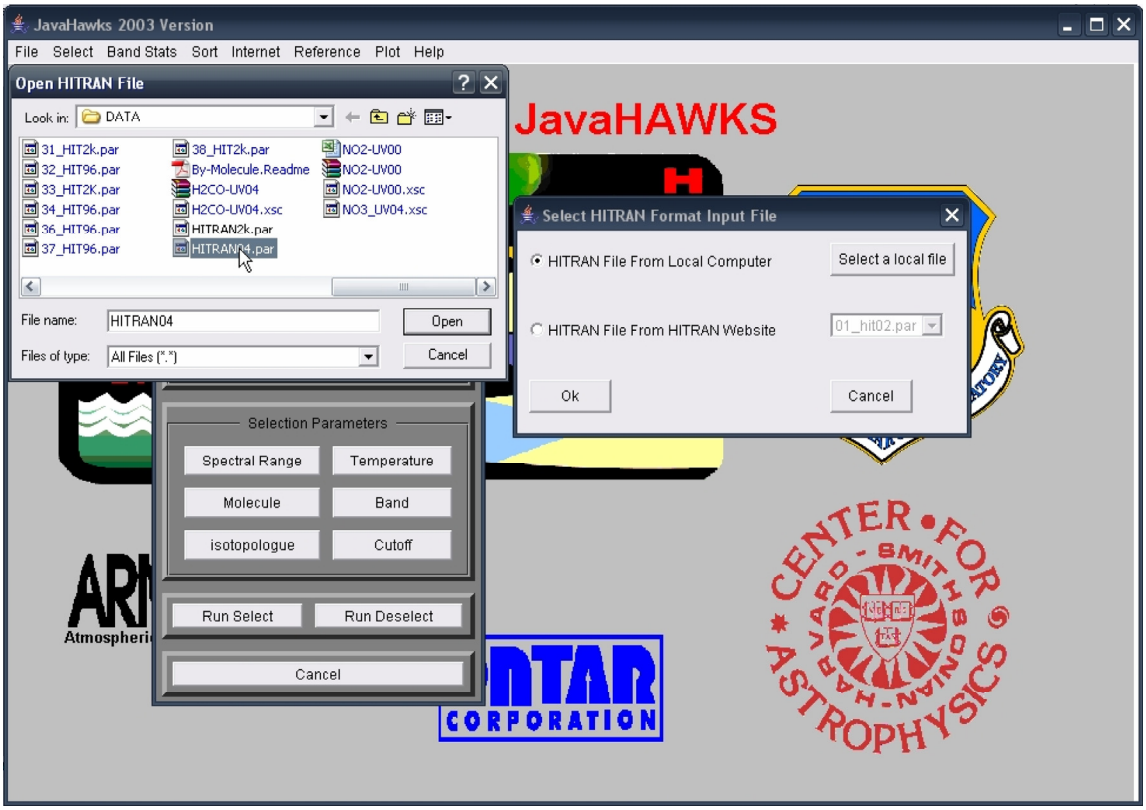

Figure F.18: Computer screen caption of the HITRAN program. In general, the input file HITRAN04.PAR contains the line list for all the molecules in Table F.2.
[File FF.18_hitran5]

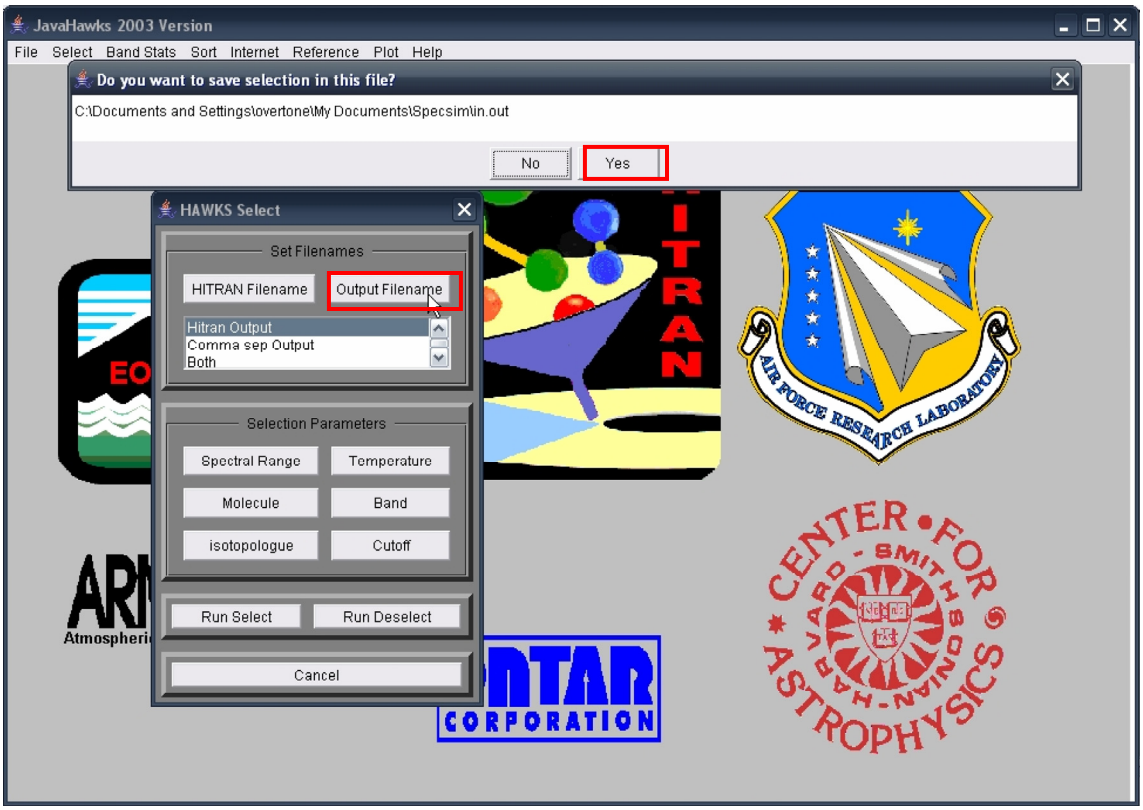

Figure F.19: Computer screen caption of the HITRAN program. The simulation output file name "in.out" should be left unchanged in the "C:\Documents and Settings\overtone\My Documents\Specsim" directory. [File FF.19_hitran6]

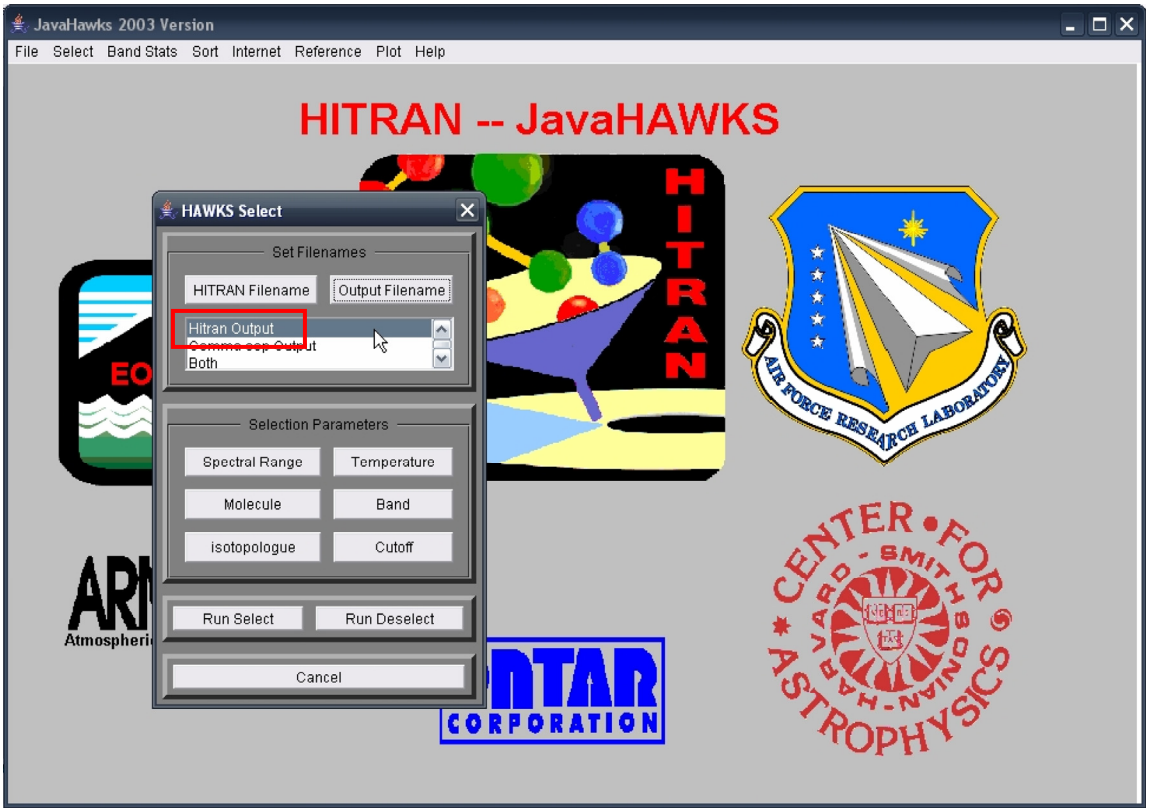

Figure F.20: Computer screen caption of the HITRAN program. Select the "Hitran Output" option for the output file. [File FF.20_hitran7]

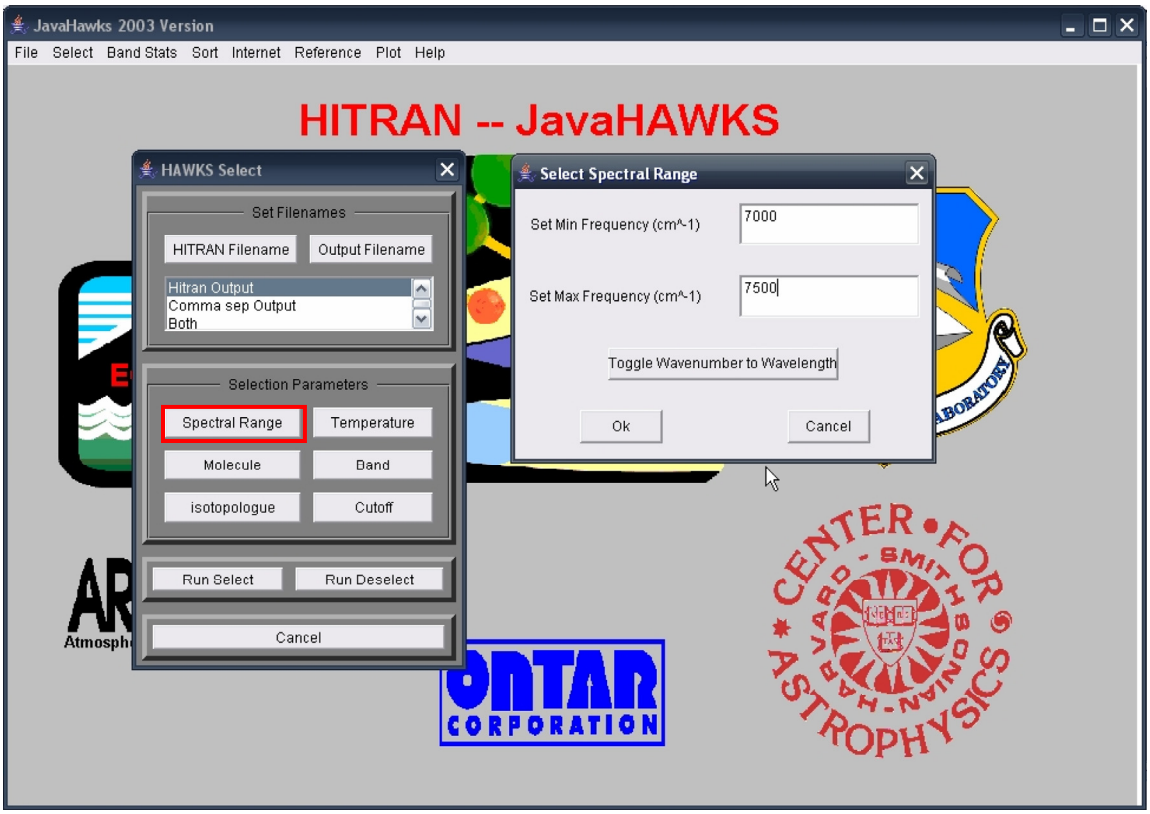

Figure F.21: Computer screen caption of the HITRAN program. Selecting the Spectral Range option prompts the user to set spectral range in cm^{-1} or μm units.
[File FF.21_hitran8]

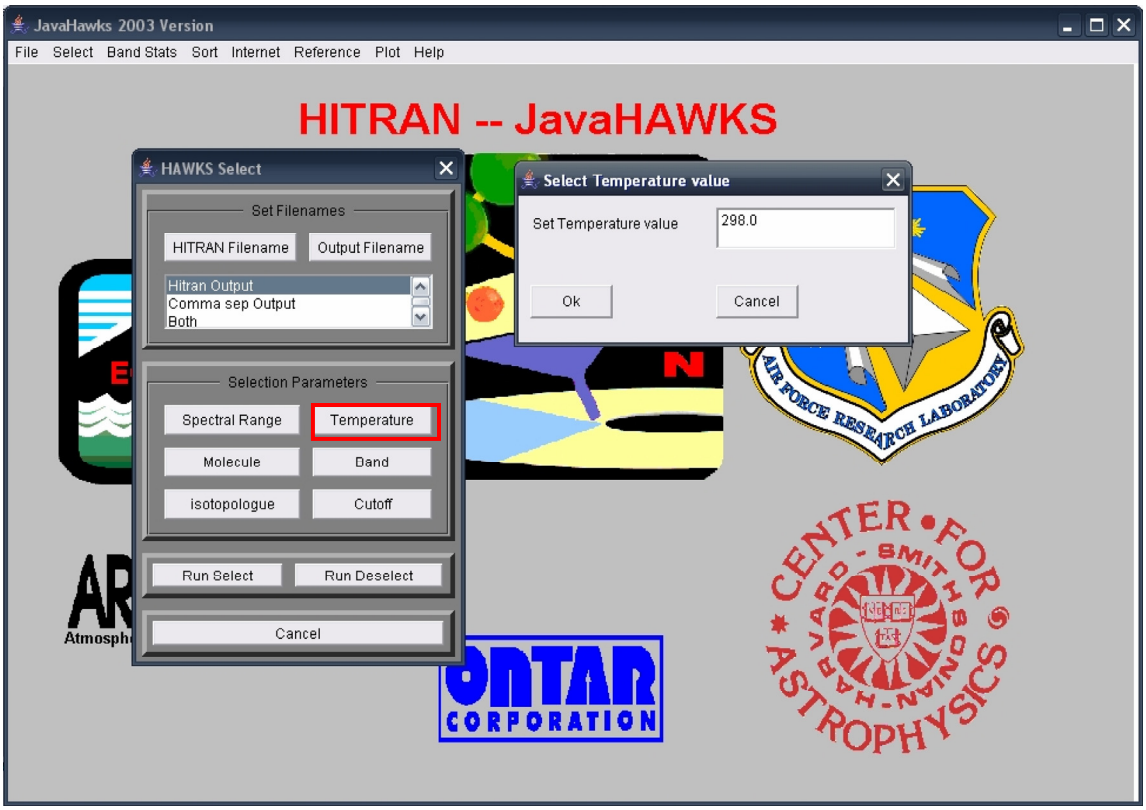

Figure F.22: Computer screen caption of the HITRAN program. Selecting the temperature parameter prompts the user to set the temperature in Kelvin units. [File FF.22_hitran9]

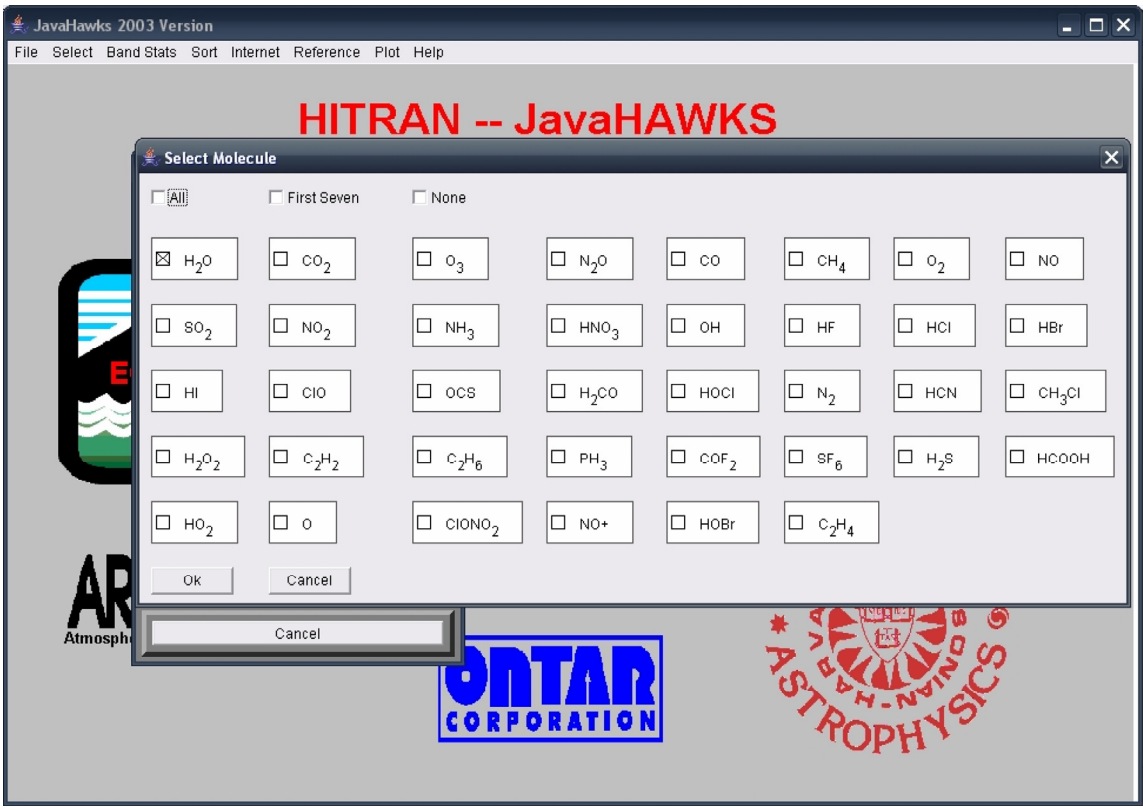

Figure F.23: Computer screen caption of the HITRAN program. Selecting the "Molecule" option prompts the user to choose the molecule(s) to use in the simulation. [File FF.23_hitran10]

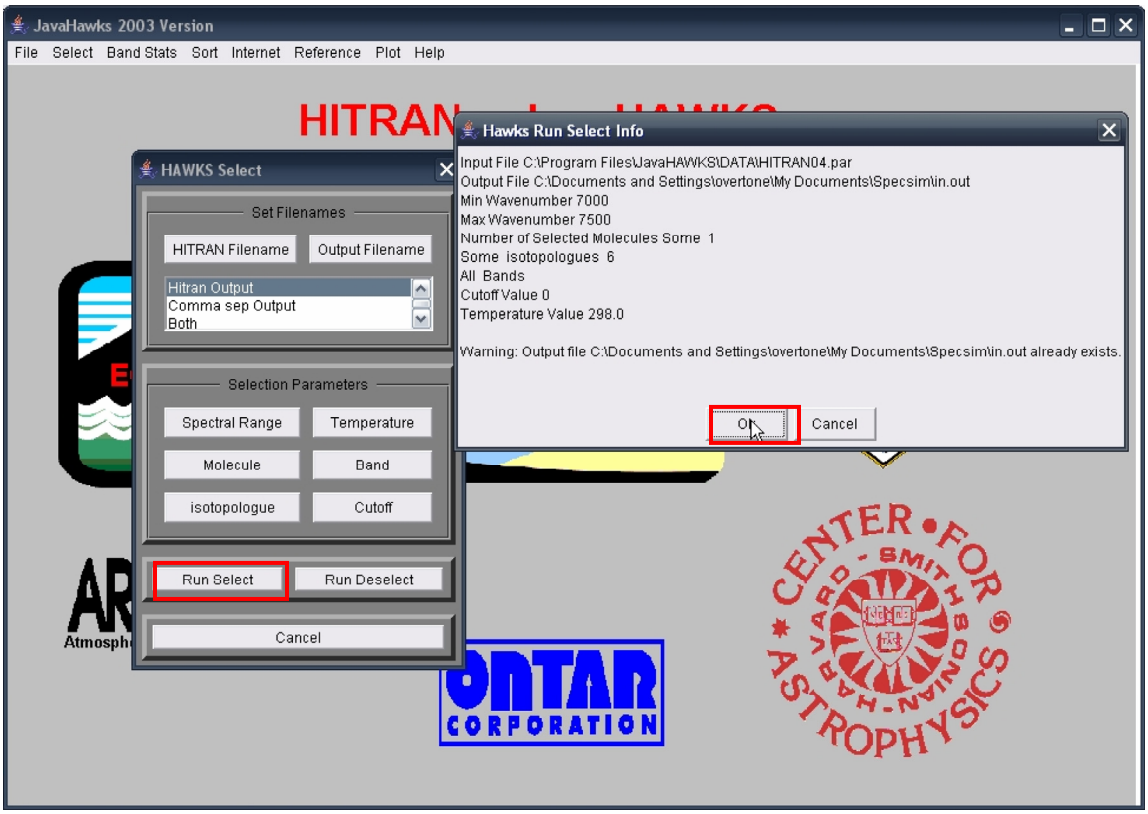

Figure F.24: Computer screen caption of the HITRAN program showing the "Run Select" option highlighted. [File FF.24_hitran11]

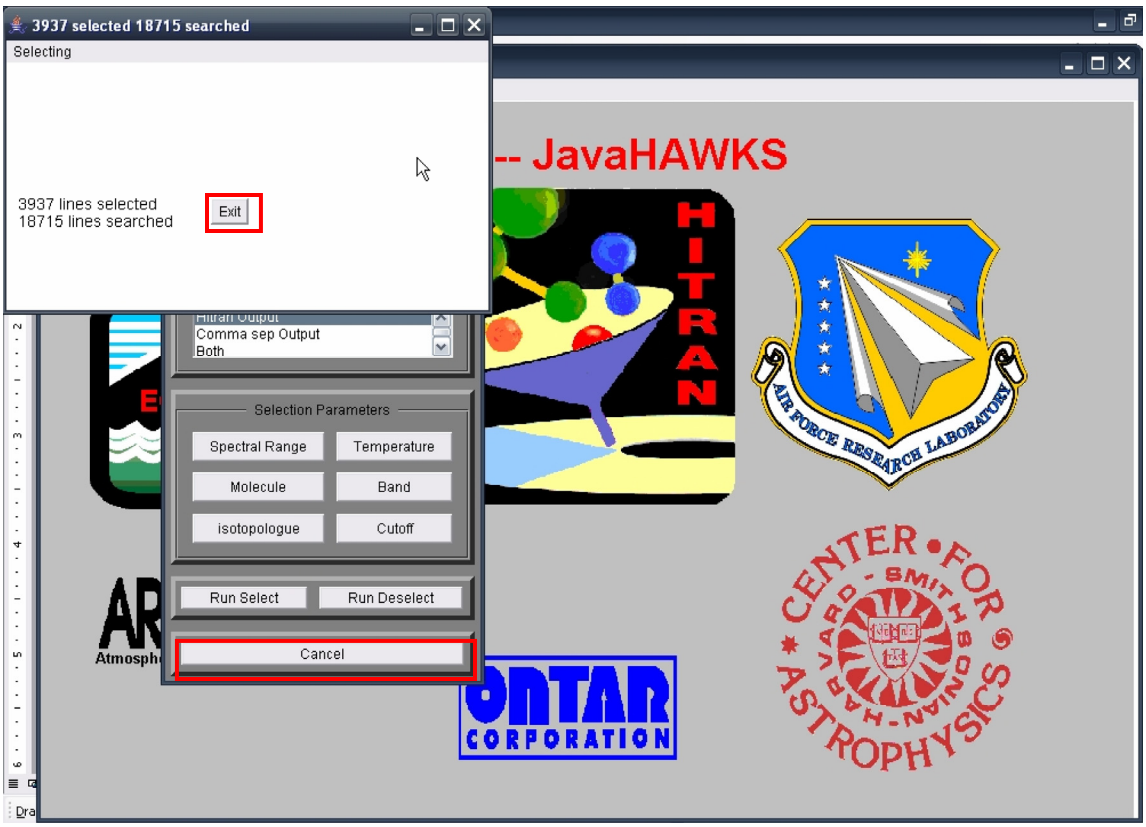

Figure F.25: Computer screen caption of the HITRAN program showing the number water lines selected in the 7000 – 7500 cm^{-1} spectral region. To exit this screen first select "Cancel" on the parameter window and *then* select the "Exit" key on the line window. [File FF.25_hitran12]

Figure F.26: Computer screen caption of the HITRAN program showing the "Plot" option for the generated file. [File FF.26_hitran13]

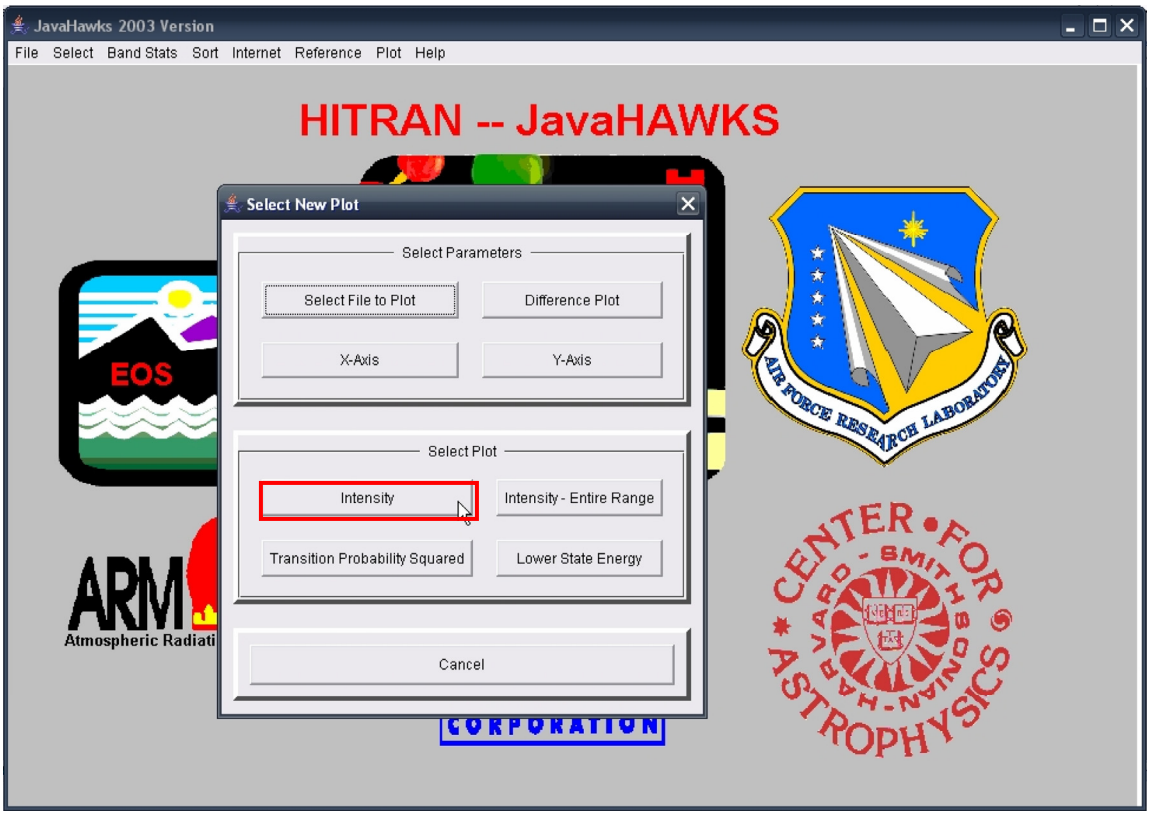

Figure F.27: Computer screen caption of the HITRAN program. To plot the output file generated, simply select the "Intensity" key. [File FF.27_hitran14]

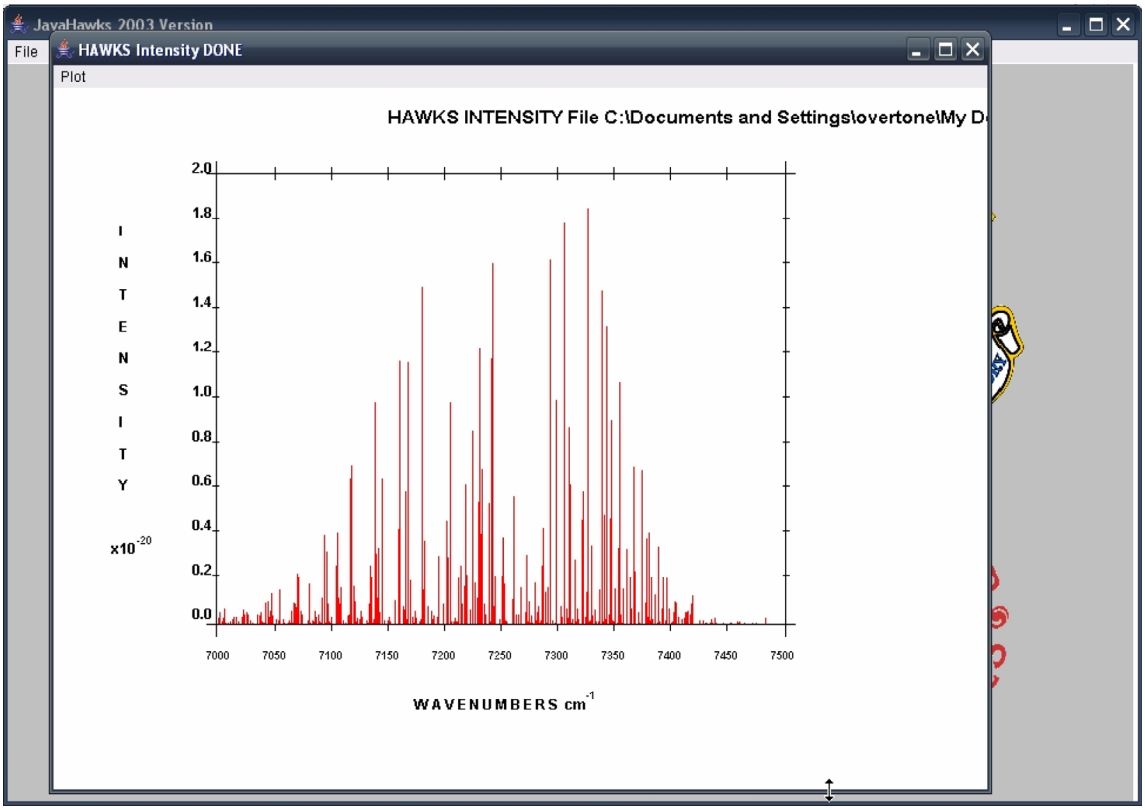

Figure F.28: Computer screen caption of the HITRAN program displaying the transitions of water molecule in the $2\nu_{OH}$ region (7000 – 7500 cm^{-1}).
[File FF.28_hitran15]

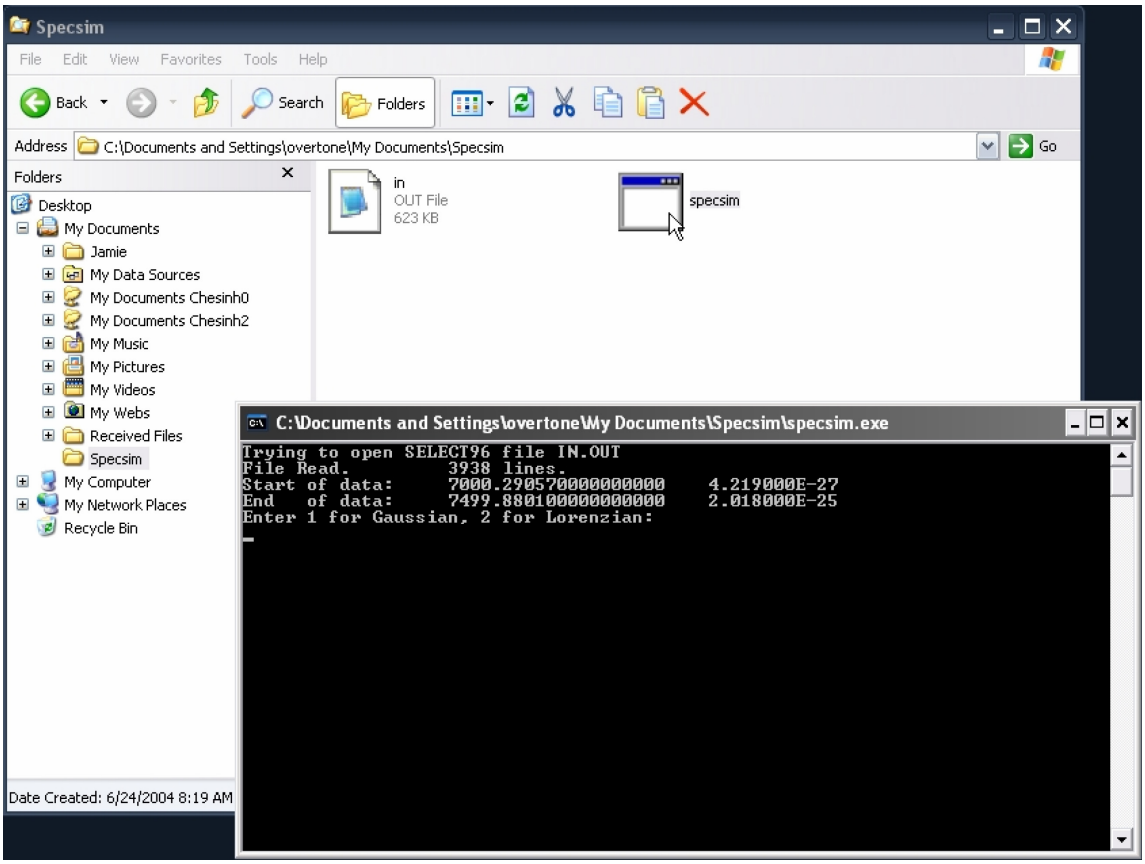

Figure F.29: Computer screen caption of the Specsim code in the "C:\Documents and Settings\overtone\My Documents\Specsim" directory. In this screen caption the program reads the transition lines, initial and final wavelength, and intensity from the "in.out" file generated using HITRAN. The program then prompts the user to enter "1" for Gaussian line-shape and "2" for Lorentzian lines-shape. [File FF.29_hitran16]

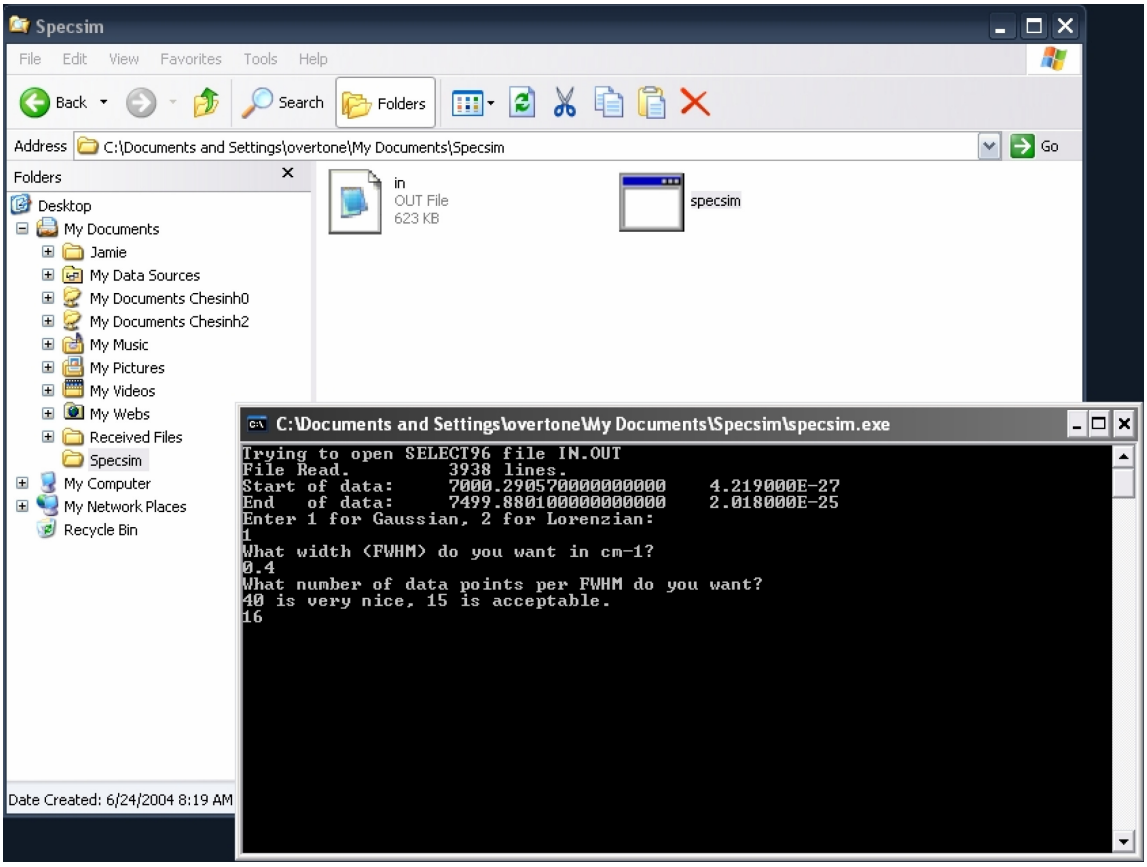

Figure F.30: Computer screen caption of the Specsim code. The program then prompts the user to enter the transition linewidth (cm^{-1}) and number of data points per said FWHM (cm^{-1}). In this example, selecting 0.4 cm-1 for the linewidth and 16 points per 0.4 cm^{-1} results in 40 points / cm^{-1} or 2000 points total for the entire scan range.
[File FF.30_hitran17]

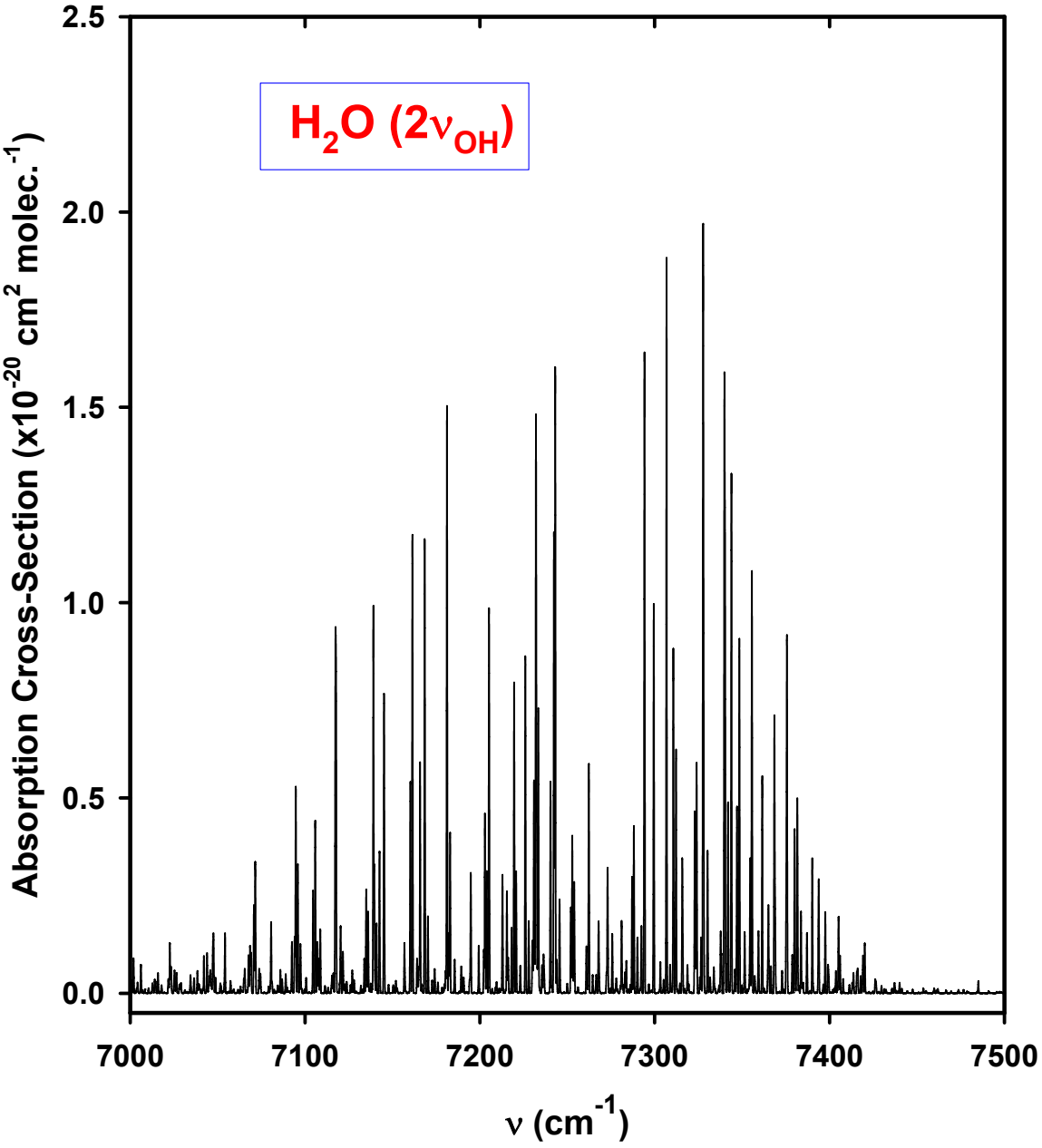

Figure F.31: The simulated absorption spectrum of water in the $2\nu_{OH}$ region (7000 – 7500 cm^{-1}) generated using HITRAN and Specsim programs at 0.4 cm^{-1} FWHM resolution and 298 K. [File FF.31_h2o_spectrum]

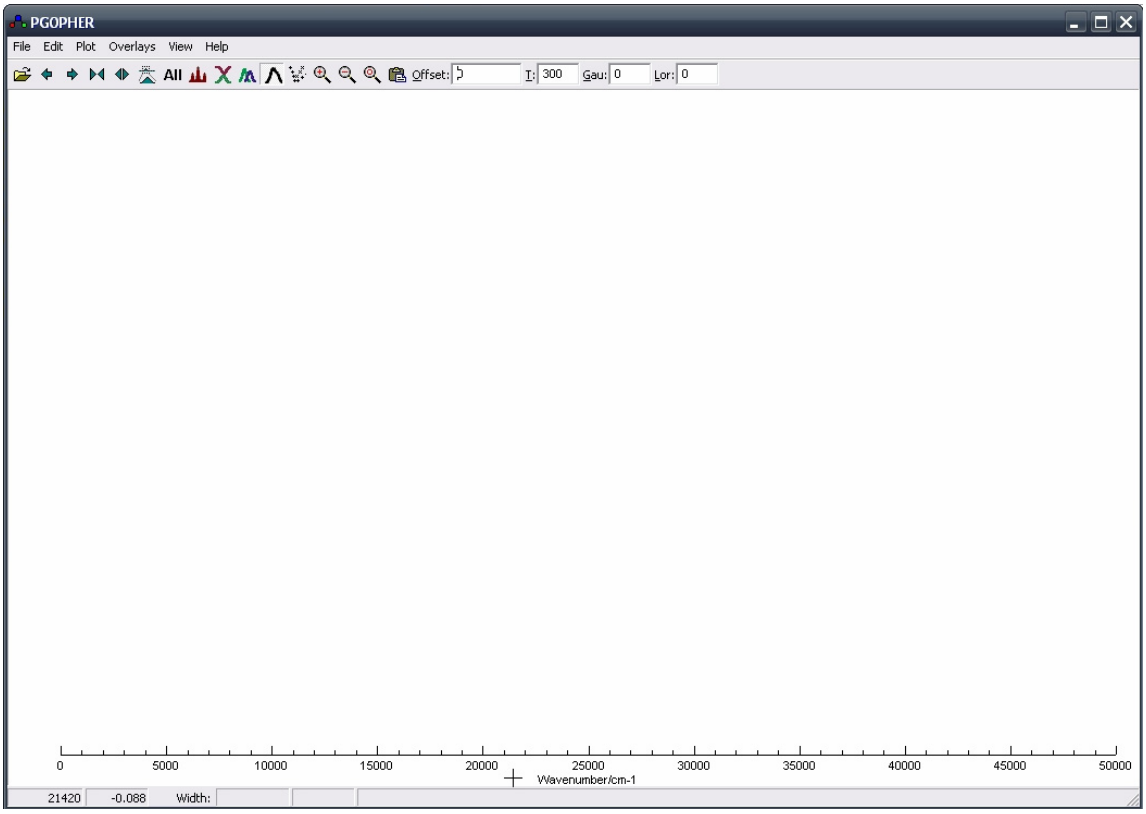

Figure F.32: Computer screen caption of the program PGOPHER. [File: FF.32]

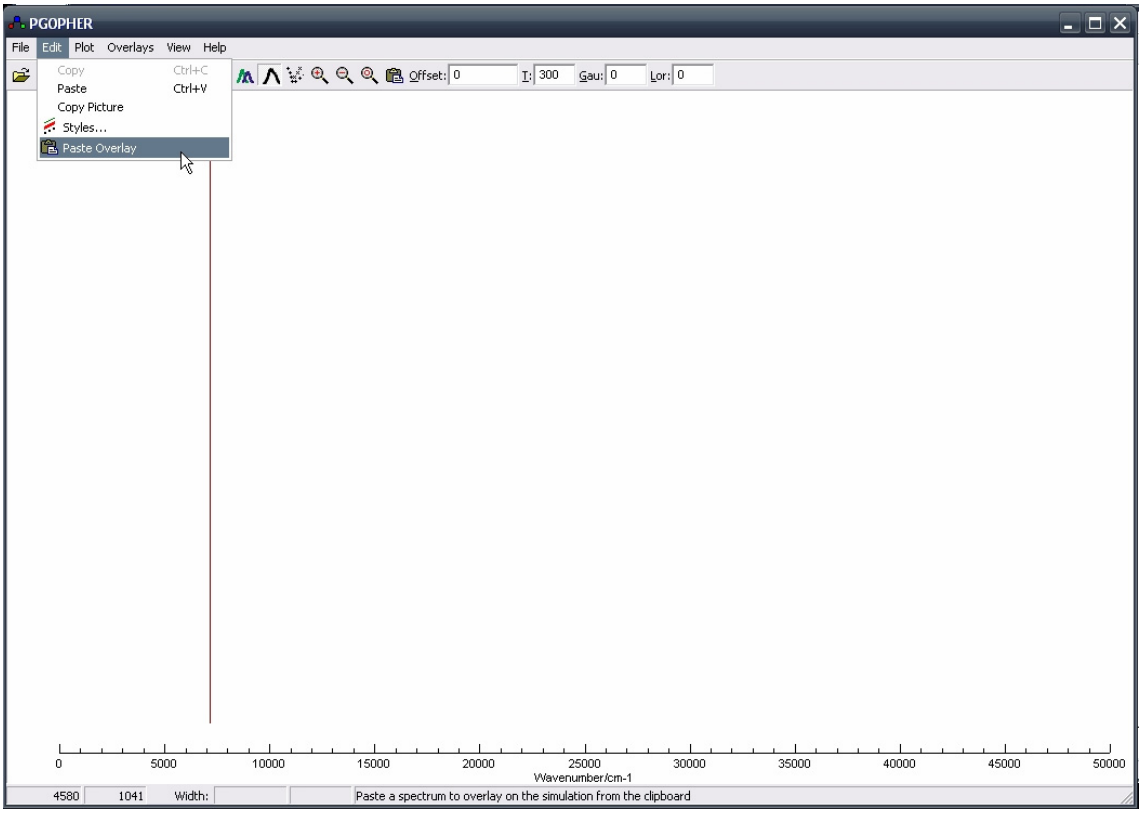

Figure F.33: Computer screen caption of the program PGOPHER showing the "Paste Overlay" option in the "Edit" menu. [File: FF.33]

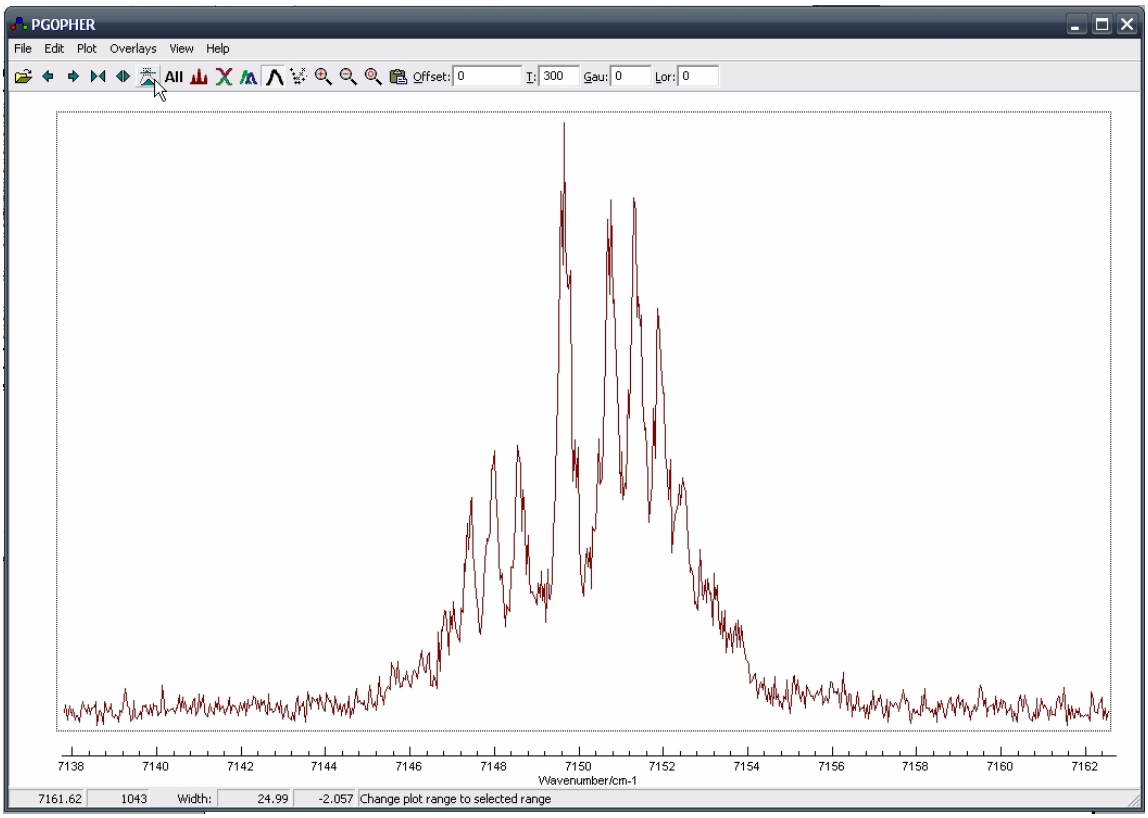

Figure F.34: Computer screen caption of the program PGOPHER showing the expended view of the overlay of CD_3OOH $2\nu_1 + \nu_{15}$ state. [File: FF.34]

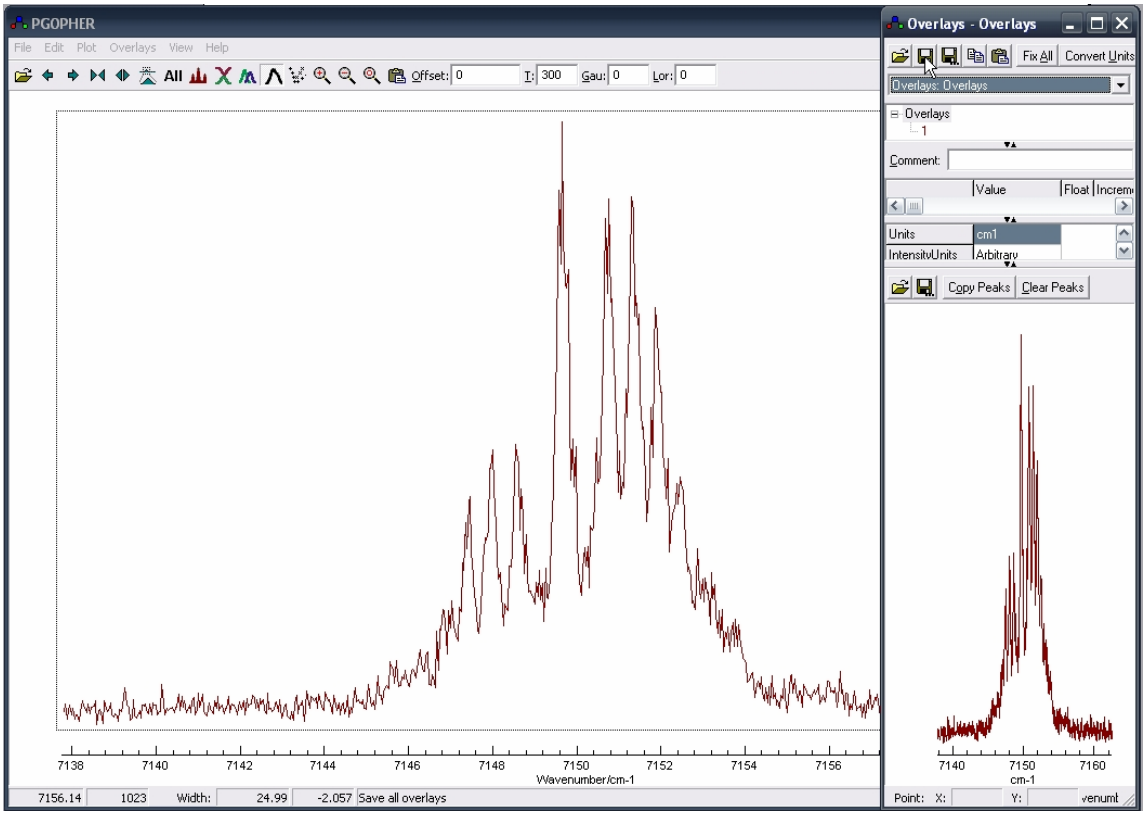

Figure F.35: Computer screen caption of the program PGOPHER showing the "Overlays" screen. The "Save Overlay" option is indicated with the mouse cursor. [File: FF.35]

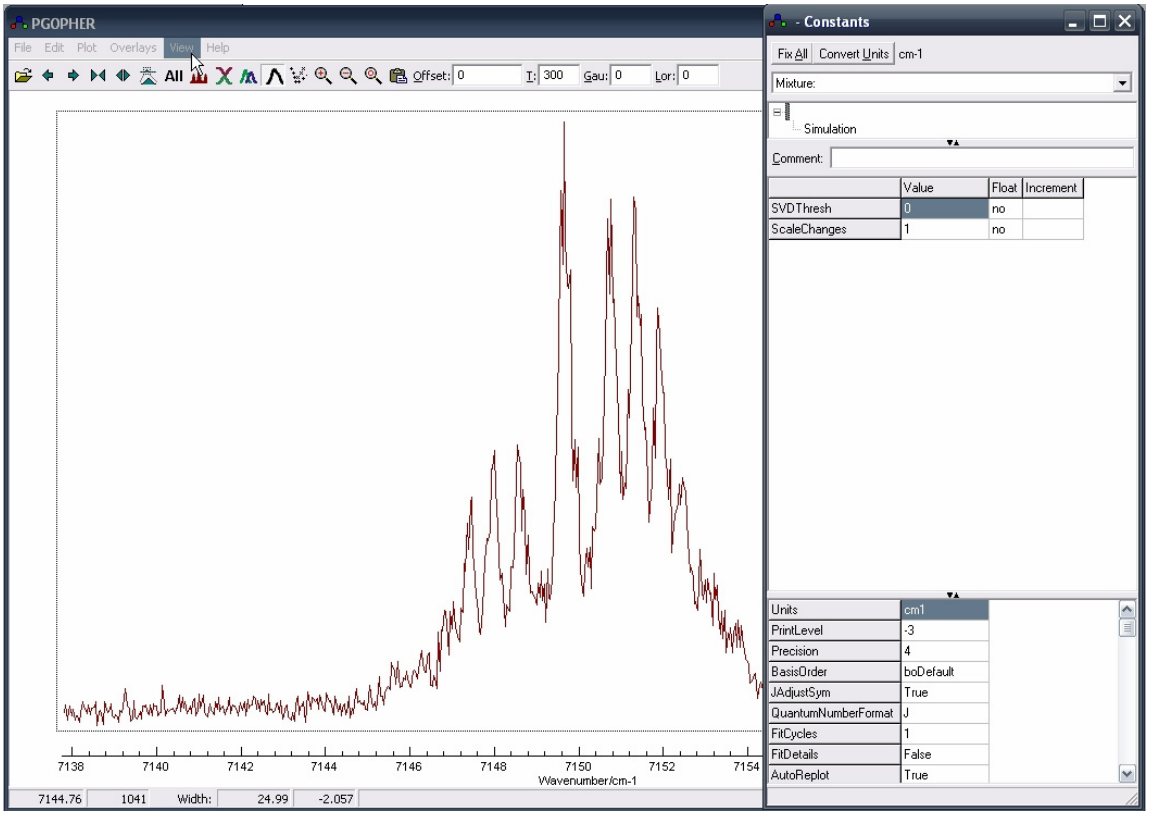

Figure F.36: Computer screen caption of the program PGOPHER showing the "Constants" screen which can be accessed via the "View" menu or by hitting CTRL +T. [File: FF.36]

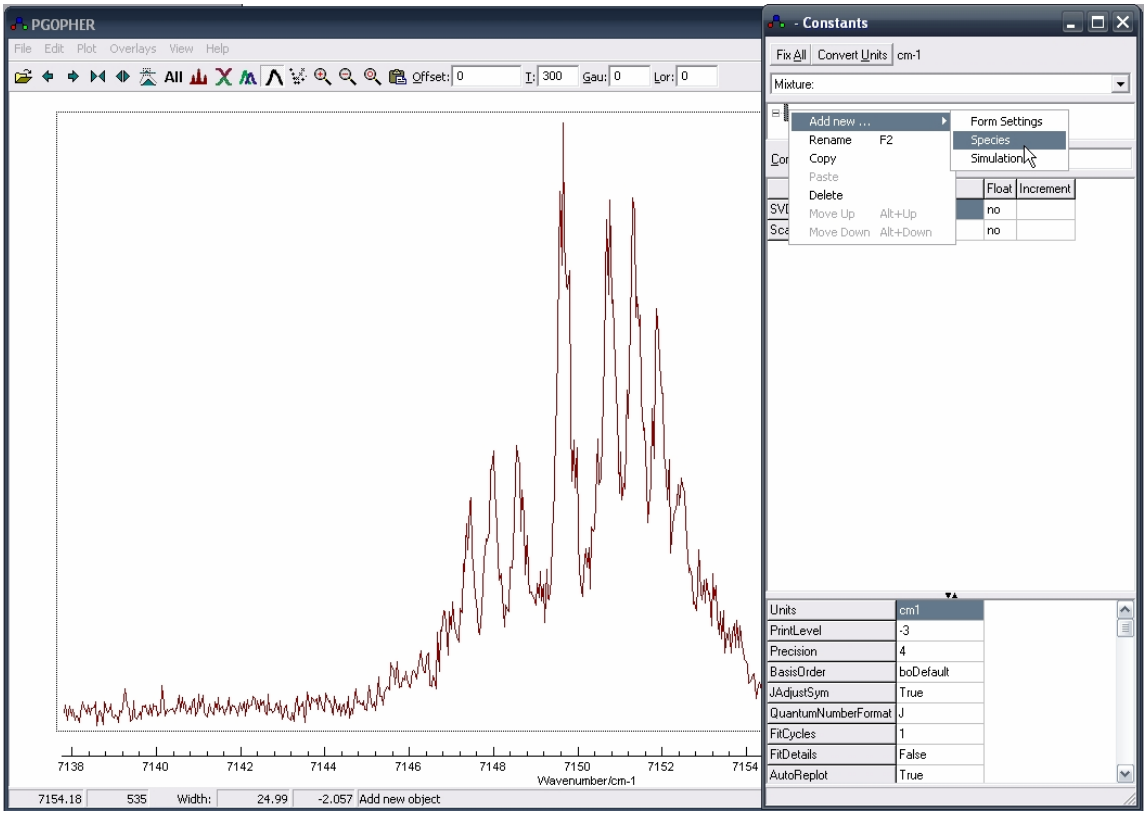

Figure F.37: Computer screen caption of the program PGOPHER showing in the Constant screen the "Add New…" and "Species" options. [File: FF.37]

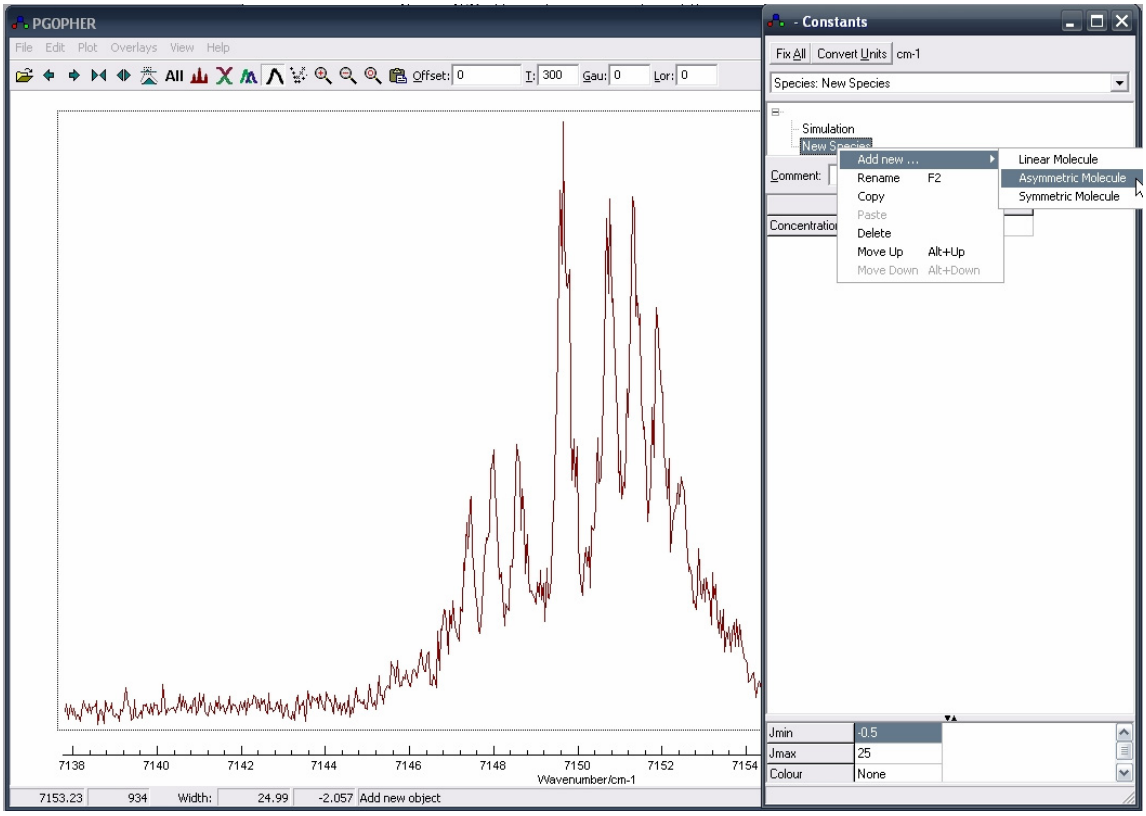

Figure F.38: Computer screen caption of the program PGOPHER showing in the "Constants" screen the "Add New…" and "Asymmetric Molecule" options.
[File: FF.38]

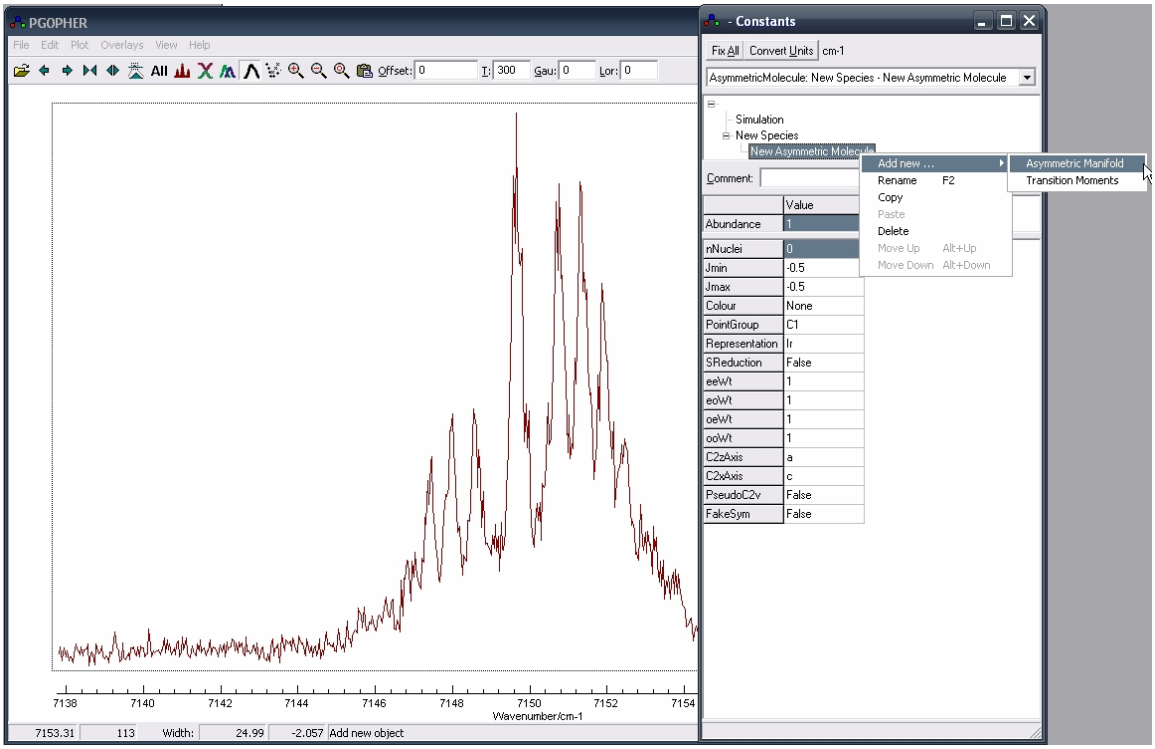

Figure F.39: Computer screen caption of the program PGOPHER showing in the "Constants" screen the "Add New…" and "Asymmetric Manifold" options.
[File: FF.39]

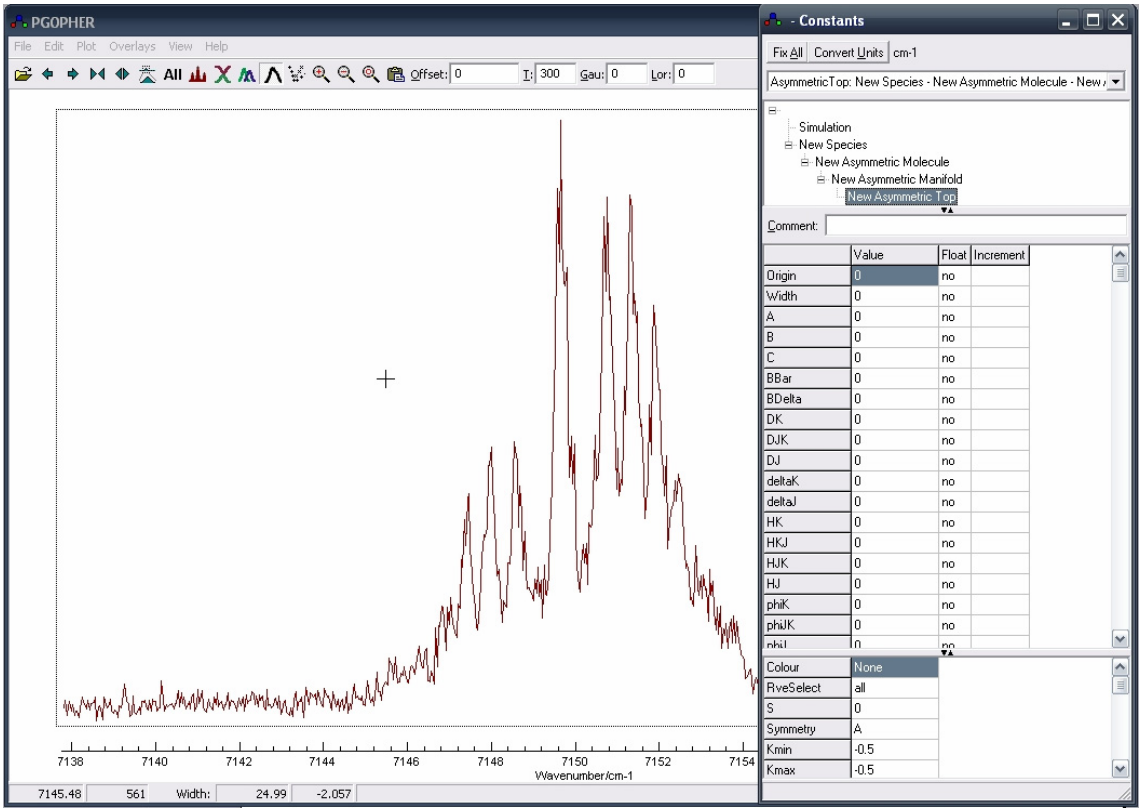

Figure F.40: Computer screen caption of the program PGOPHER showing in the "Constants" screen the "Add New…" and "New Asymmetric Top" options.
[File: FF.40]

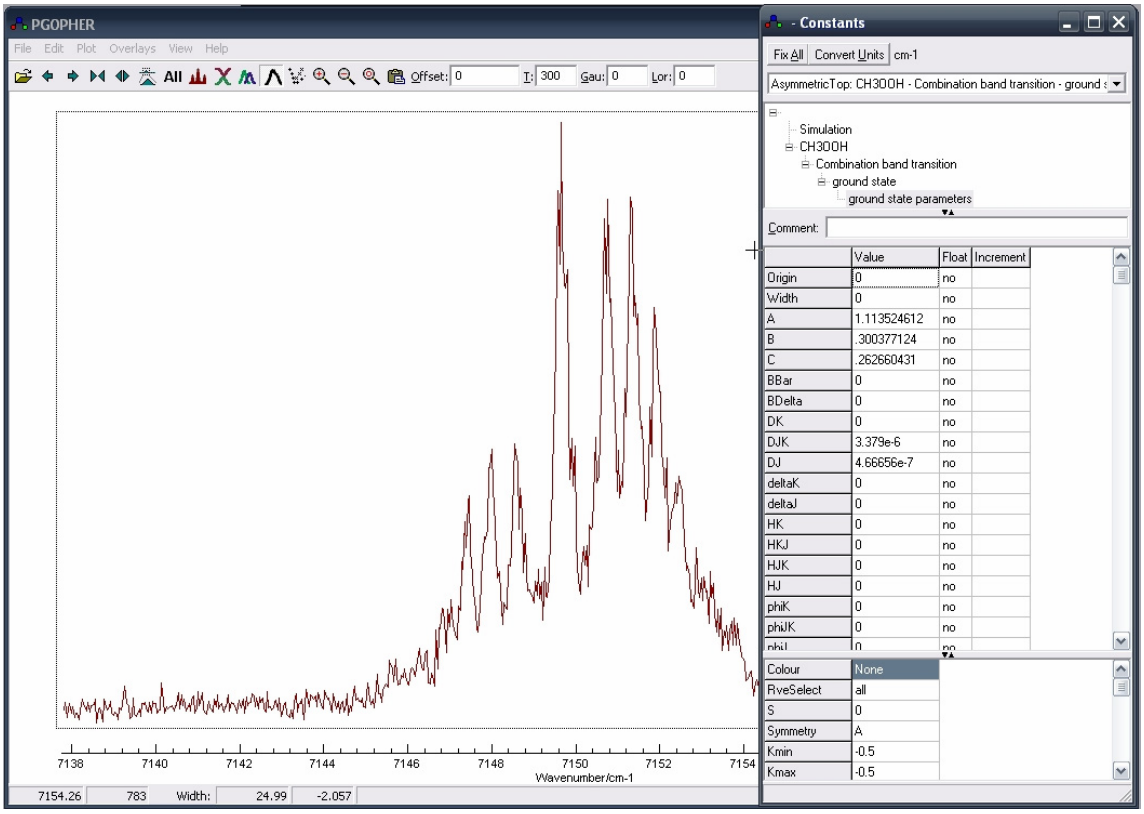

Figure F.41: Computer screen caption of the program PGOPHER showing in the "Constants" screen associated with the parameters of the initial state. The origin is set to 0 cm^{-1}, A = 1.1135 cm^{-1}, B = 0.3004 cm^{-1}, C = 0.2627 cm^{-1}. DJK and DJ are set to 3.379E-6 cm^{-1} and 4.666E-7 cm^{-1} respectively. [File: FF.41]

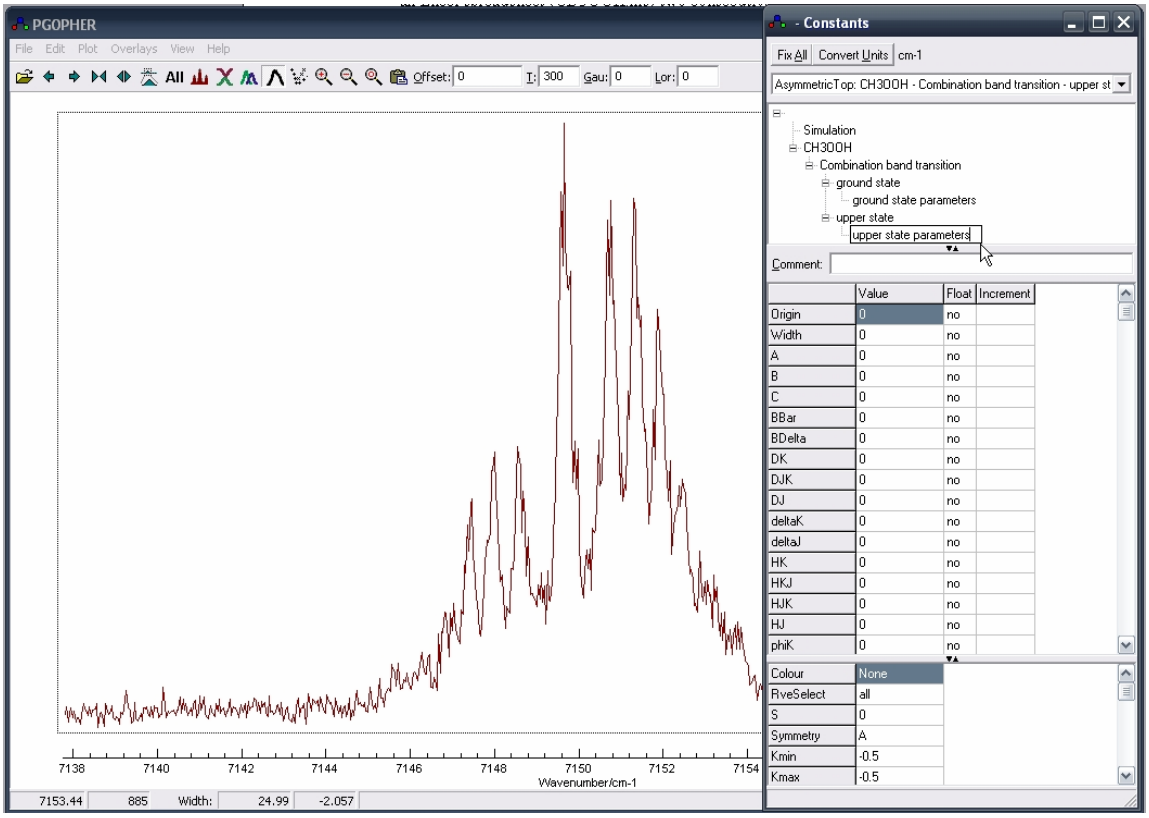

Figure F.42: Computer screen caption of the program PGOPHER showing the "Constants" screen associated with upper state parameters. [File: FF.42]

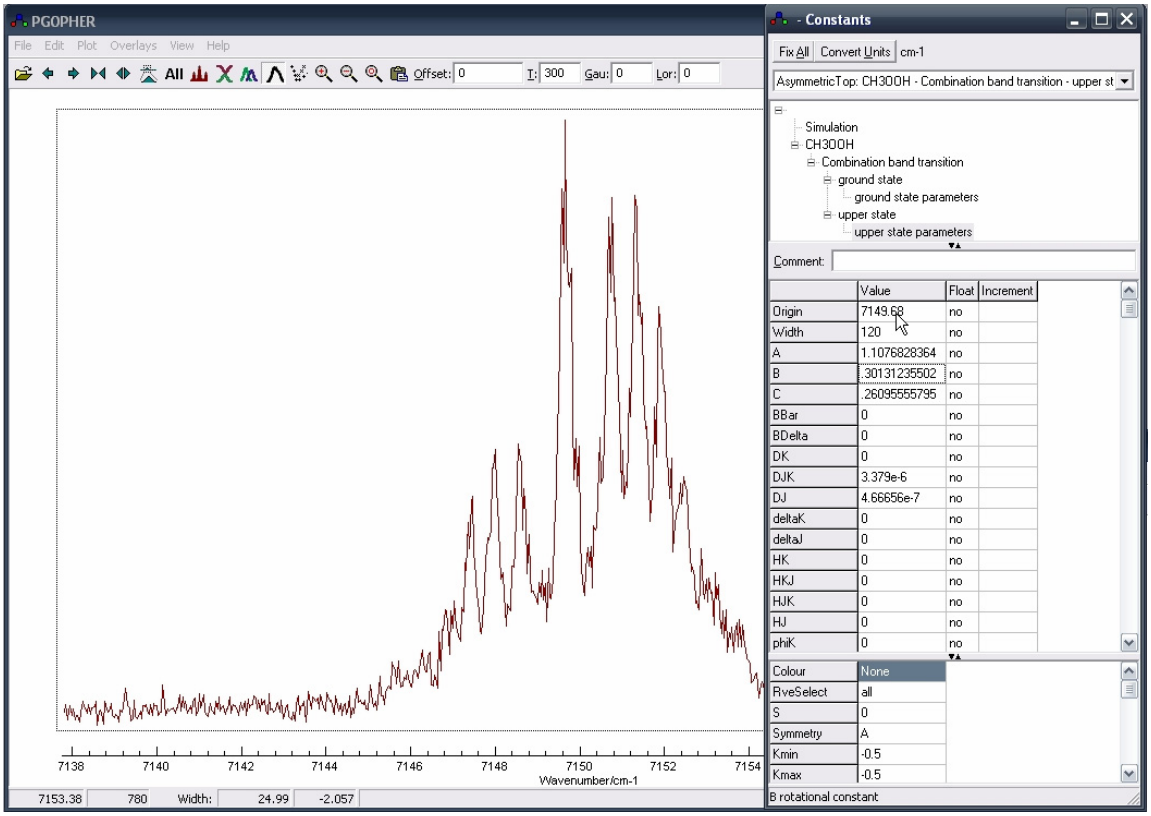

Figure F.43: Computer screen caption of the program PGOPHER showing parameters associated with the upper state constants. The origin is set to 7149.68 cm^{-1}, A = 1.1077 cm^{-1}, B = 0.30131 cm^{-1}, C = 0.2610 cm^{-1}. DJK and DJ are set to 3.379E-6 cm^{-1} and 4.666E-7 cm^{-1} respectively. [File: FF.43]

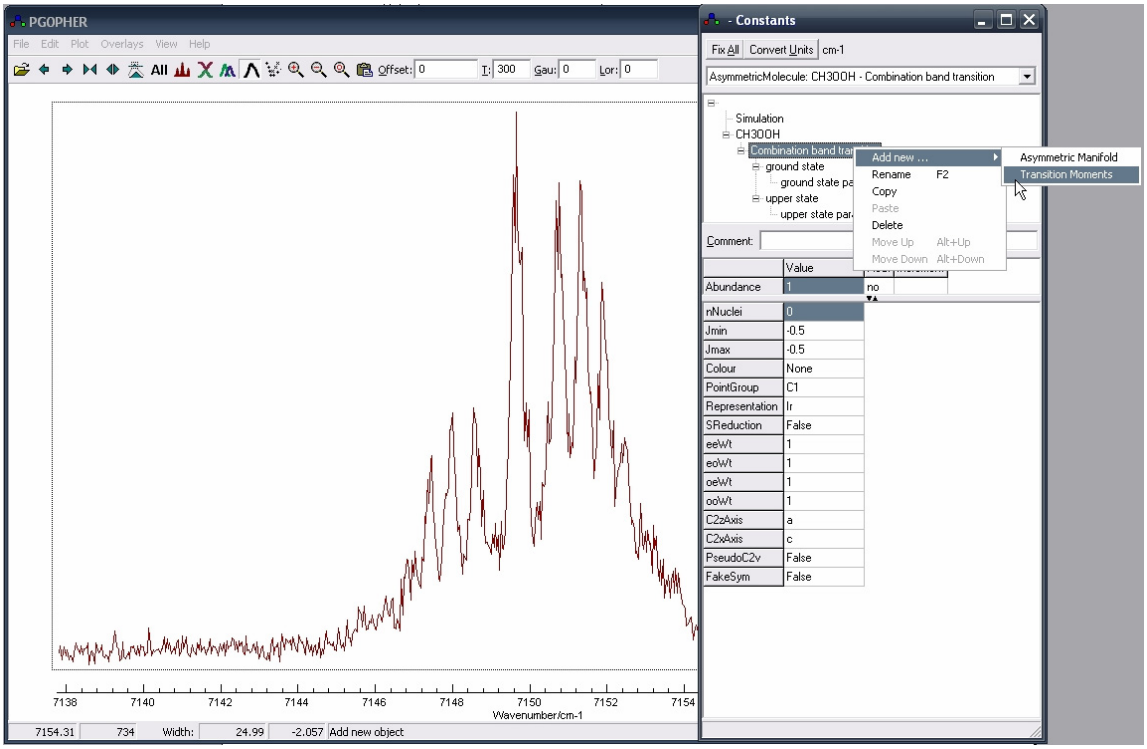

Figure F.44: Computer screen caption of the program PGOPHER showing the "Add Transition Moments" in the "Constants" screen. [File: FF.44]

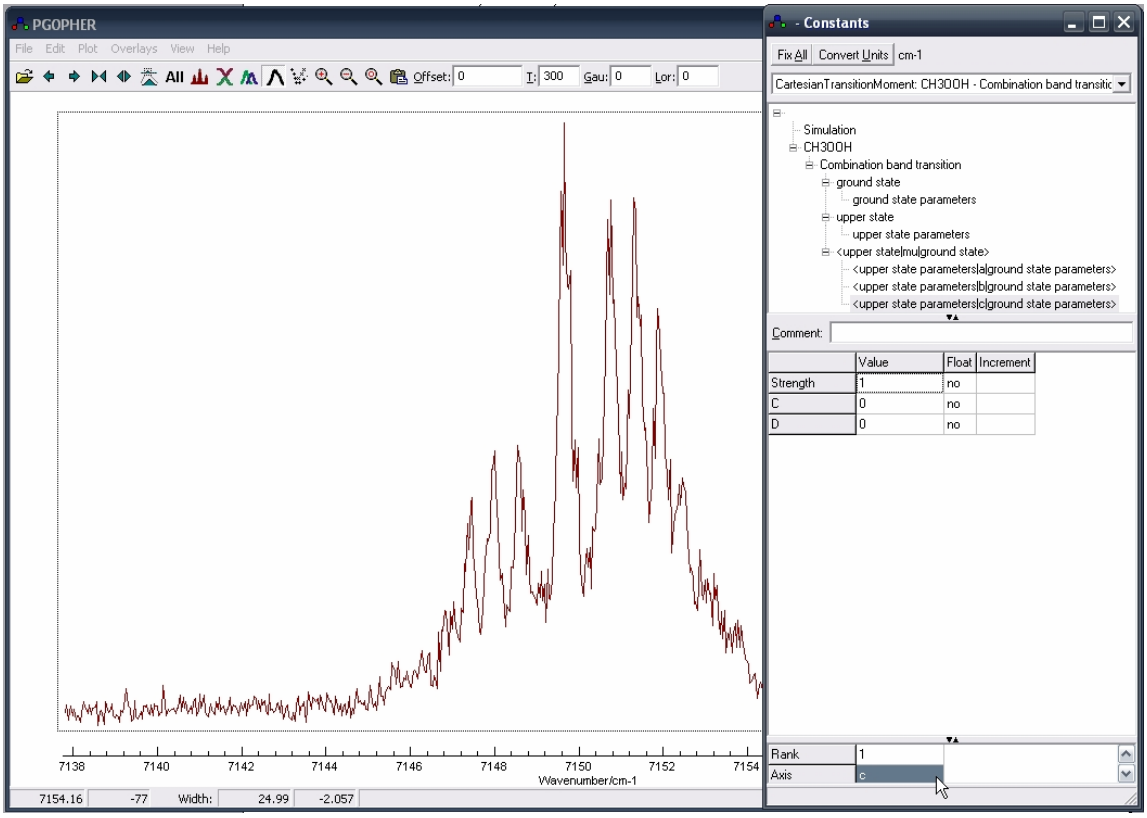

Figure F.45: Computer screen caption of the program PGOPHER showing a-, b-, and c-Cartesian Transition Moments Parameters in the "Constants" screen. The transition strength μ_a is set to 1, μ_b is set to 0.52 and μ_c is set to 0. [File: FF.45]

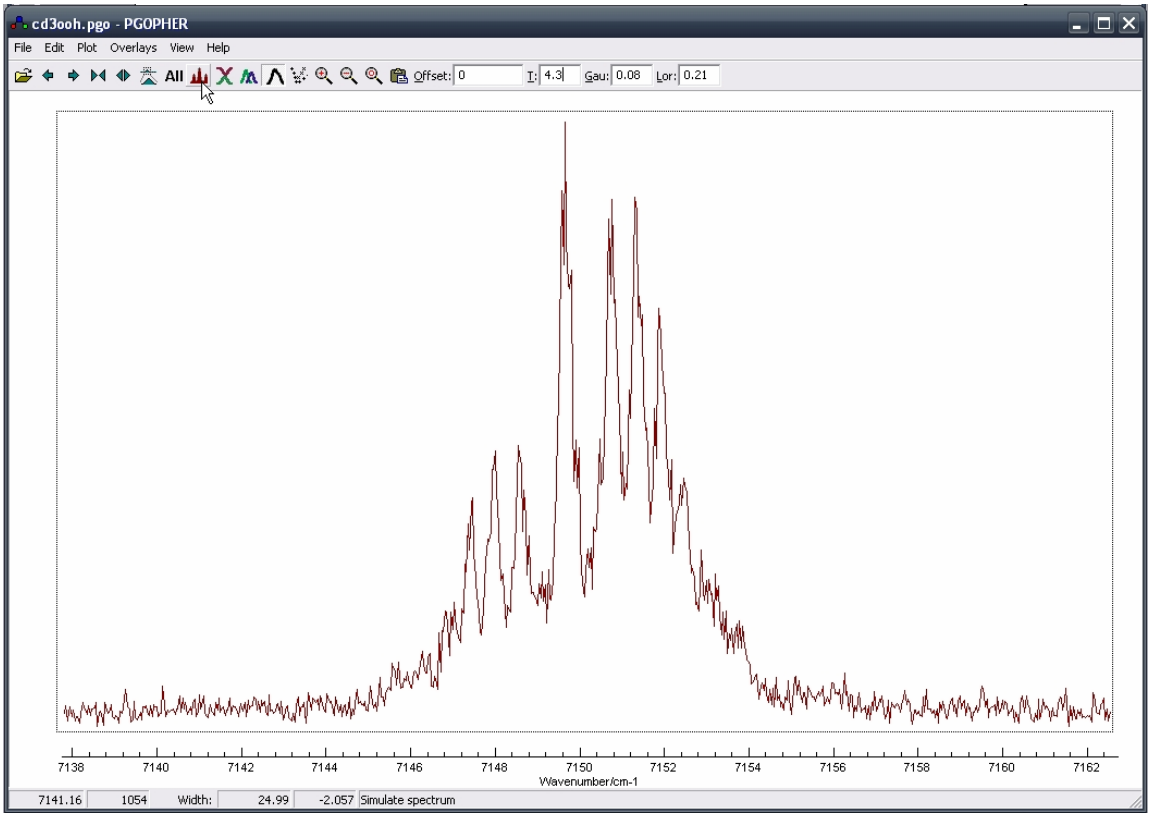

Figure F.46: Computer screen caption of the program PGOPHER showing current simulation temperature (4.3 K), Gaussian and Lorentzian widths (0.08 and 0.21 cm^{-1}) respectively. The cursor indicates the "Simulate Spectrum" key.
[File: FF.46]

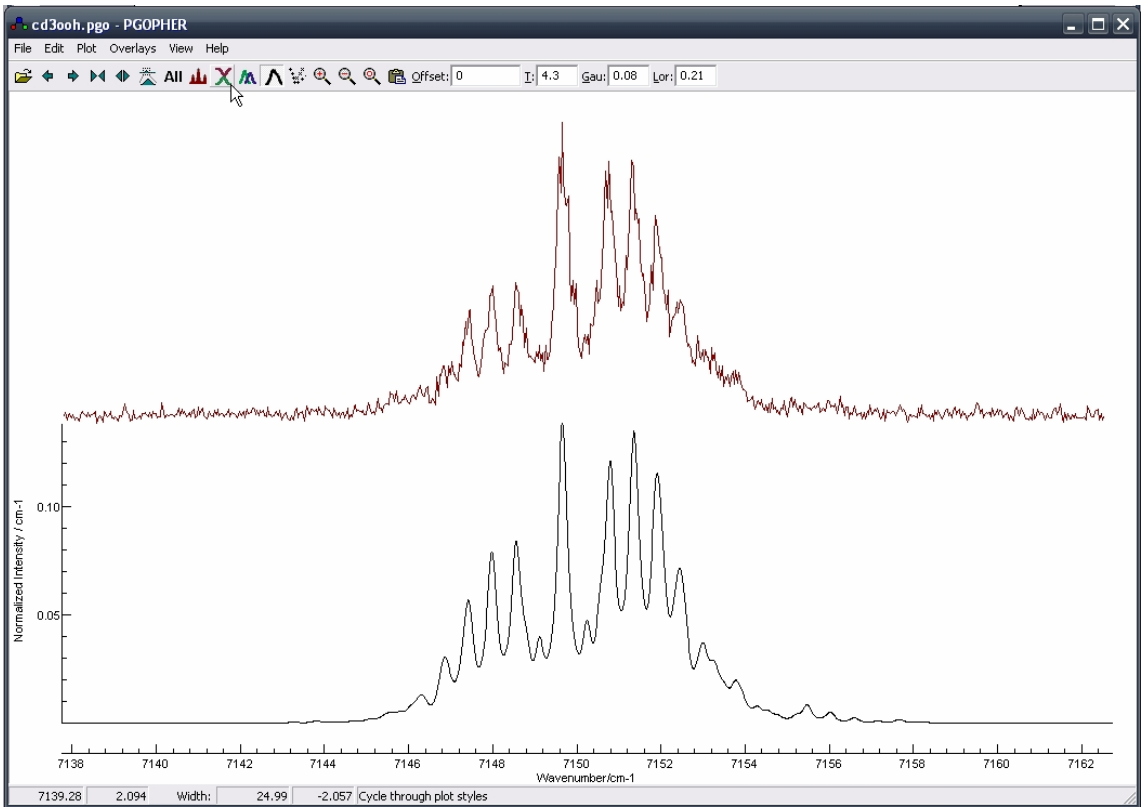

Figure F.47: Computer screen caption of the program PGOPHER showing the simulation of CD_3OOH $|2\ 1^+>$ state. The cursor indicates the "Cycle Through Plots Style" key. [File: FF.47]

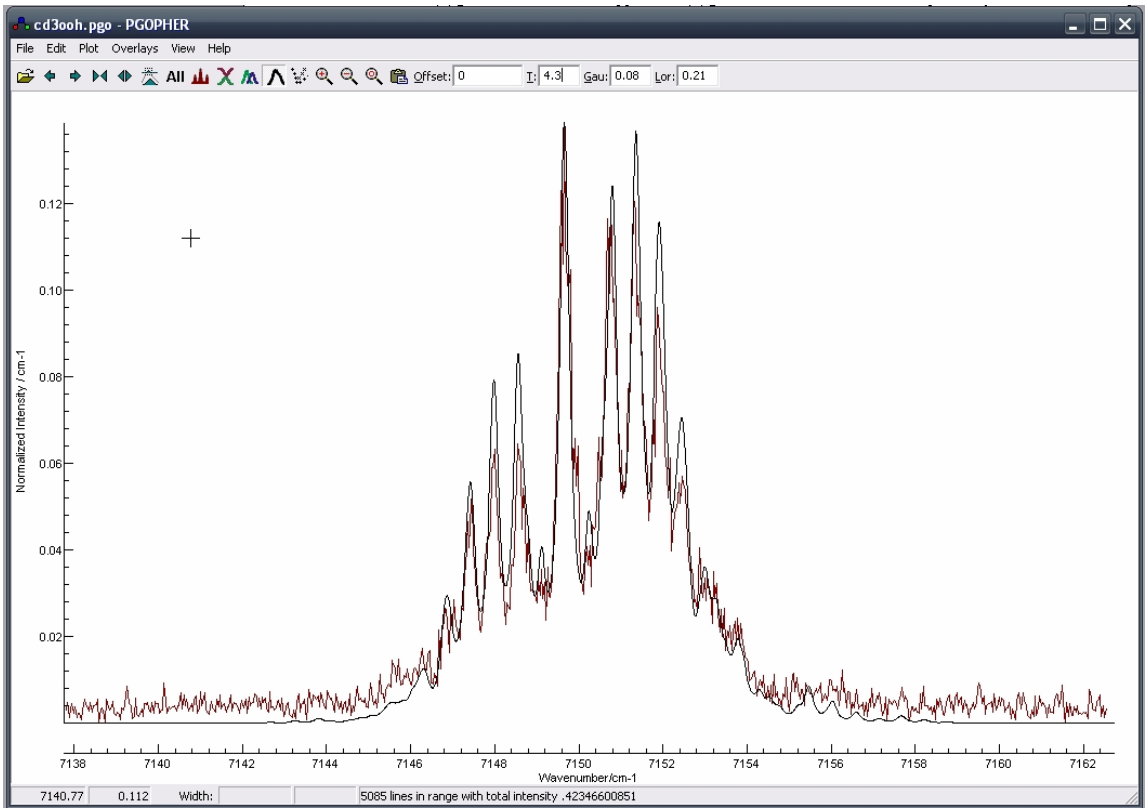

Figure F.48: Computer screen caption of the program PGOPHER showing the overlaid simulation of CD_3OOH $|2\ 1^+>$ state and the experimental spectrum. [File: FF.48]

F.4 References

1. R. D. Johnson III, FGH1D program version 1.01, http://www.nist.gov/compchem/johnson/fgh/fgh1d.html

2. C. C. Marston and G. Balint-Kurti, J. Chem. Phys. **91**, 3571 (1989).

3. G. G. Balint-Kurti, C.L. Ward and C. C. Marston, Computer Physics Communications, **67**, 285 (1991).

4. G. G. Balint-Kurti, R. N. Dixon and C. C. Marston, Internat. Rev. Phys. Chem. **11**, 317 (1992).

5. F. Gögtas, G. G. Balint-Kurti and C. C. Marston, Quantum Chemistry Program Exchange, Program No. 647; published in QCPE Bulletin, **14**, 19 (1994).

6. J. Stare and G. Balint-Kurti, J. Phys. Chem. A, **107**, 7204 (2003).

7. L. S. Rothman, A. Barbe, D. C. Benner, L. R. Brown, C. Camy-Peyret, M. R. Carleer, K. Chance, C. Clerbaux, V. Dana, V. M. Devi, A. Fayt, J. Fischer, J. M. Flaud, R. R. Gamache, A. Goldman, D. Jacquemart, K. W. Jucks, W. J. LaFerty, J. Y. Mandin, S. T. Massie, V. Nemtchinov, D. A. Newnham, A. Perrin, C. P. Rinsland, J. Schroeder, K. M. Smith, M. A. H. Smith, K. Tang, R. A. Toth, J. Vander Auwera, P. Varanasi, K. Yoshino, The HITRAN Molecular Spectroscopic Database: Edition of 2003, J. Quant. Spectrosc. Radiat. Transfer **82,** 5 (2003).

8. C. M. Western, PGOPHER version 5.2.343 a program for simulating rotational structure, University of Bristol, http://pgopher.chm.bris.ac.uk